

FUNDAMENTALS AND TECHNOLOGY OF COMBUSTION



F. El-Mahallawy
S. El-Din Habik

ELSEVIER

**FUNDAMENTALS
AND TECHNOLOGY OF
COMBUSTION**

Elsevier Science Internet Homepage:

<http://www.elsevier.com>

Elsevier Energy Internet Homepage:

<http://www.energyinfo.net>

Consult EnergyInfo.net for full catalogue information on all books, journals, newsletters, magazines and electronic products within the energy and power field.

Elsevier Titles of Related Interest

ISHII

Advanced Pulverized Coal Injection Technology and Blast Furnace Operation

ISBN: 0-08-043651-X

TOMITA

Elsevier Energy Compendia: Emission Reduction: NO_x/SO_x Suppression

ISBN: 0-08-044089-4

Related Journals

Combustion and Flame

Fuel

Fuel and Energy Abstracts

Fuel Processing Technology

International Journal of Heat and Mass Transfer

Progress in Energy and Combustion Science

Fuelfirst (<http://www.fuelfirst.com>)

To Contact the Publisher

Elsevier Science welcomes enquiries concerning publishing proposals: books, journal special issues, conference proceedings, etc. All formats and media can be considered. Should you have a publishing proposal you wish to discuss, without obligation, please visit Energyinfo.net (<http://www.energyinfo.net>) for further information or contact the Publisher directly:

Victoria Thame
Publishing Editor
Elsevier Science Ltd
The Boulevard, Langford Lane
Kidlington, Oxford OX5 1GB
UK

Phone: +44 1865 843402
Fax: +44 1865 843920
Email: v.thame@elsevier.com

General enquiries including placing orders, should be directed to Elsevier's Regional Sales Offices – please access the Elsevier homepage for full contact details (homepage at the top of this page).

FUNDAMENTALS AND TECHNOLOGY OF COMBUSTION

FAWZY EL-MAHALLAWY

*Faculty of Engineering,
Cairo University, Egypt*

SAAD EL-DIN HABIK

*Faculty of Engineering of Port-Said,
Suez Canal University, Egypt*



2002

ELSEVIER

AMSTERDAM – BOSTON – LONDON – NEW YORK – OXFORD – PARIS
SAN DIEGO – SAN FRANCISCO – SINGAPORE – SYDNEY – TOKYO

ELSEVIER SCIENCE Ltd
The Boulevard, Langford Lane
Kidlington, Oxford OX5 1GB, UK

© 2002 Elsevier Science Ltd. All rights reserved.

This work is protected under copyright by Elsevier Science, and the following terms and conditions apply to its use:

Photocopying

Single photocopies of single chapters may be made for personal use as allowed by national copyright laws. Permission of the Publisher and payment of a fee is required for all other photocopying, including multiple or systematic copying, copying for advertising or promotional purposes, resale, and all forms of document delivery. Special rates are available for educational institutions that wish to make photocopies for non-profit educational classroom use.

Permissions may be sought directly from Elsevier Science via their home page (<http://www.elsevier.com>) by selecting 'Customer support' and then 'Permissions'. Alternatively you can send an e-mail to: permissions@elsevier.com or fax to: (+44) 1865 853333.

In the USA, users may clear permissions and make payments through the Copyright Clearance Center, Inc., 222 Rosewood Drive, Danvers, MA 01923, USA; phone: (+1) (978) 7508400, fax: (+1) (978) 7504744, and in the UK through the Copyright Licensing Agency Rapid Clearance Service (CLARCS), 90 Tottenham Court Road, London W1P 0LP, UK; phone: (+44) 207 631 5555; fax: (+44) 207 631 5500. Other countries may have a local reprographic rights agency for payments.

Derivative Works

Tables of contents may be reproduced for internal circulation, but permission of Elsevier Science is required for external resale or distribution of such material.

Permission of the Publisher is required for all other derivative works, including compilations and translations.

Electronic Storage or Usage

Permission of the Publisher is required to store or use electronically any material contained in this work, including any chapter or part of a chapter.

Except as outlined above, no part of this work may be reproduced, stored in a retrieval system or transmitted in any form or by any means, electronic, mechanical, photocopying, recording or otherwise, without prior written permission of the Publisher.

Address permissions requests to: Elsevier Science Global Rights Department, at the mail, fax and e-mail addresses noted above.

Notice

No responsibility is assumed by the Publisher for any injury and/or damage to persons or property as a matter of products liability, negligence or otherwise, or from any use or operation of any methods, products, instructions or ideas contained in the material herein. Because of rapid advances in the medical sciences, in particular, independent verification of diagnoses and drug dosages should be made.

First edition 2002

Library of Congress Cataloging in Publication Data

A catalog record from the Library of Congress has been applied for.

British Library Cataloguing in Publication Data

A catalogue record from the British Library has been applied for.

ISBN: 0-08-044108-8

Ⓢ The paper used in this publication meets the requirements of ANSI/NISO Z39.48-1992 (Permanence of Paper).
Printed in The Netherlands.

To

Mrs. *El-Mahallawy, Fatma El-Awady,*
and Mrs. *Habik, Samira El-Sherif* for their
morale support during the preparation of this book

Acknowledgements

The authors would like to acknowledge their indebtedness to all research workers who worked with them, and to some of their colleagues.

Special thanks are due to Professors Derek Bradley and Graham Dixon-Lewis from Leeds University in England, with whom Professors Saad Habik and Samira El-Sherif have worked during their period of research at both Departments of Mechanical Engineering, and Fuel and Energy. This period was a rare privilege, and it is visible throughout chapters 1, 2 and part of chapter 3 as a special spirit generated by Professors Bradley and Dixon-Lewis.

Special gratitude is also due to Professor Samira El-Sherif, Faculty of Engineering of El-Mataria, Helwan University, for her co-operation in editing chapters 1 and 2. Her contribution is significant and is highly appreciated.

Special thanks also go to Professor Abd El-Razek Abd El-Fattah, the former president of Helwan University, and Professor Nassif Rafat, the former Professor of heat engines, Cairo University, due to their continuous encouragement during the preparation of this book.

Finally, the authors are very grateful to their colleague Dr. Ayman Rezk, Faculty of Engineering, Cairo University, for his valuable assistance during the preparation of the manuscript.

Fawzy El-Mahallawy

Saad Habik

Contents

Acknowledgements	vii
Preface	xvii
CHAPTER 1: COMBUSTION FUNDAMENTALS	1
1.1 Introduction	1
1.2 Energy Sources	2
1.2.1 Fuels	7
1.2.2 Fuel cells	14
1.3 Some Related Thermodynamic Fundamentals	15
1.3.1 Ideal gases and mass conservation	15
1.3.2 Basics of thermodynamics	17
1.4 Combustion Stoichiometry and Thermochemical Calculations	20
1.4.1 Combustion stoichiometry	20
1.4.2 Thermochemical calculations	22
- Enthalpy and enthalpy of formation, 22	
- Internal energy – Entropy, 26	
1.5 Chemical Kinetics and Equilibrium	27
1.5.1 Kinetic theory of gases	27
1.5.2 Chemical kinetics	29
1.5.3 Reaction kinetics	30
1.5.4 Chemical equilibrium	34
- Basic equations, 34	
- Equilibrium modeling, 37	
- Equilibrium composition and temperature, 38	
- Conservation, energy and equilibrium equations, 39	
1.6 Transport Phenomena, and Modeling	41
1.6.1 Real gases	41
1.6.2 Transport phenomena of gases at low density	44
- Theory of viscosity, 44	
- Theory of thermal conductivity, 46	
- Theory of ordinary diffusion, 47	
1.6.3 Transport properties of multi-component mixtures	49
1.6.4 Transport modeling	53

1.7 Modeling in Combustion Chemistry	53
1.8 Combustion Generated Air Pollution	54
1.8.1 Background	54
1.8.2 Air quality and air pollution	55
1.8.3 Legislation of air pollution	59
1.9 Pollutants Formation and Oxidation Kinetics	63
1.9.1 Kinetics of nitrogen compounds	63
1.9.2 Kinetics of pollutants originating from sulphur	66
- Sulphur dioxide formation, 66	
- Sulphur trioxide formation, 66	
1.9.3 Kinetics of carbon monoxide	67
1.10 Pollutant Emissions Reduction Techniques	67
1.10.1 Reduction techniques in combustion equipment	68
- Combustion modification techniques for NO _x reduction, 68	
- Post-combustion techniques for NO _x reduction, 71	
- Sulphur compounds reduction techniques, 73	
1.10.2 Emission reduction techniques in vehicles	74
1.10.3 Greenhouse warming and its reduction techniques	74
 CHAPTER 2: LAMINAR PREMIXED FLAMES	 77
2.1 Introduction	77
2.2 Definitions	80
2.2.1 Flammability limits	80
2.2.2 Laminar flame stabilization	80
2.2.3 Flame temperature	82
2.2.4 Burning velocity of a premixed flame	82
- Stationary methods, 83	
- Propagation methods, 84	
2.2.5 Ignition	85
2.3 Theory and Kinetics of Laminar Premixed Flames	86
2.3.1 Background to flame propagation	86
2.3.2 Kinetic model of premixed flames	86
2.3.3 Transport parameters	92
2.3.4 Reaction mechanisms for simple fuels	93
2.4 Simple Fuels-N₂-O₂ Flames	108
2.4.1 Hydrogen-oxygen-nitrogen flames	108
2.4.2 Hydrogen-H ₂ O-CO-O ₂ -N ₂ flames	119
2.4.3 Methane-oxygen-nitrogen flames	125
2.4.4 Methanol-air flames	142
2.4.5 Methanol-water-air flames	155
2.4.6 Propane-air flames	167
2.4.7 Ethane-air flames	182
2.4.8 Natural gas-air flames	184

2.5	Generalization of Flame Characteristics	198
2.5.1	Laminar burning velocity	198
	- General background, 198	
	- Review of burning velocity data, 199	
	- General correlations of burning velocity, 199	
2.5.2	General correlations of heat release rate	207
2.6	High Hydrocarbon Fuels-Air Flames	212
2.6.1	Background to reduced kinetic models	212
2.6.2	Computational methods and reaction mechanisms	213
	- Computational approach, 213	
	- Reduced reaction mechanisms, 213	
	- Computational procedure, 215	
2.6.3	Experimental and computational results	215
2.7	Effect of Fuel Type and Additives on Emissions and Flame Characteristics	226
2.7.1	Effect of fuel type on nitrogen compounds	226
2.7.2	H ₂ and C ₂ H ₆ addition to C ₃ H ₈ -air flames	228
2.7.3	H ₂ and CO addition to CH ₄ -air flames	234
2.8	Porous Burners	241
2.8.1	Experimental study	242
2.8.2	Computational method and discussion	244
2.9	Flame Extinction Pattern	252
CHAPTER 3: TURBULENT PREMIXED AND DIFFUSION FLAMES		259
3.1	Introduction	259
3.2	Characteristics of Diffusion Flames	261
3.2.1	Diffusion flame length	263
3.2.2	Opposed diffusion flames	268
3.3	Turbulent Burning	270
3.4	Turbulence Models	272
3.5	Interaction Between Turbulence and Chemical Kinetics	273
3.5.1	The influence of turbulence on the chemical reactions	274
3.5.2	Fantasy versus realism in chemical kinetics description	275
3.6	Flame Stabilization	280
3.6.1	Introduction	280
3.6.2	Stability of premixed flames	283
3.6.3	Stability of diffusion flames	287
3.6.4	Flame stabilization by non-streamlined bodies	290
	- Effect of the stabilizer geometry, 291	
	- Stabilization of free diffusion flames, 303	

3.7 Turbulent Premixed Flames	311
3.7.1 Introduction	311
3.7.2 Laminar flamelet model (LFM)	311
3.7.3 Structure and heat release rate	315
- Jet-stirred conical reactor, 316	
- Tunnel burner with annular entry of a pre-mixture, 318	
- Turbulent vertical free flames, 320	
- Turbulent horizontal flat flames, 326	
3.7.4 Turbulent burning velocity	332
- Burning velocity in closed systems, 338	
- Burning velocity in horizontal flat flames, 342	
3.8 Turbulent Free Diffusion Flames	347
3.8.1 Introduction	347
3.8.2 Structure and height of diffusion flames	347
- Theoretical calculation of flame height, 347	
- Effect of buoyancy, 351	
- Effect of relative angle between fuel and air jets, 358	
- Effect of air swirl, 365	
- Structure of vertical flat free flames, 371	
- Structure of lifted turbulent jet flames, 374	
 CHAPTER 4: CHARACTERISTICS OF TURBULENT CONFINED DIFFUSION FLAMES	 377
4.1 Introduction	377
4.2 Mixing and Flow Fields of Jets	378
4.2.1 Free jets	378
4.2.2 Annular and coaxial jets	380
4.2.3 Wall jets	381
4.2.4 Swirling jets	386
4.2.5 Confined jets	387
4.3 Swirling Flows in Combustion Systems	389
4.3.1 Introduction	389
4.3.2 Methods of combustion air swirling	390
4.3.3 Effect of combustion air swirling	392
4.4 Flow and Mixing in Cold Models	397
4.4.1 Co-axial confined jets	398
4.4.2 Asymmetric confined jets	402
4.4.3 Co-flowing jets with large velocity difference	406
4.4.4 Two swirling confined jets	411
4.4.5 Forced flow reversal	412
4.4.6 Furnace and burner geometry	415

4.5	Characteristics of Confined Flames	423
4.5.1	Aerodynamics and turbulent mixing	424
	- Flow pattern, 424	
	- Turbulent mixing, 430	
4.5.2	Heat liberation in confined flames	438
	- Introduction, 438	
	- Heat liberation in flame tubes, 440	
4.5.3	Effect of different parameters	447
	- Effect of air swirl on flow and mixing, 448	
	- Effect of air swirl on heat liberation, 454	
	- Effect of fuel-air ratio, 457	
	- Forced flow reversal, 460	
	- Furnace and burner geometry, 461	
	- Effect of the direction of air and fuel entries, 464	
	- Bluff bodies, 478	
4.6	Emission and Combustion Modeling in Flames	483
4.6.1	PDF model using in situ tabulation chemistry method	483
4.6.2	Coherent flame model	487
4.6.3	Stochastic model	489
4.6.4	Three dimensions CRFD model	490
 CHAPTER 5: COMBUSTION, HEAT TRANSFER, AND EMISSION IN BOILERS AND FURNACES		499
5.1	Steam Boilers	500
5.1.1	Fire and water tube boilers	500
5.1.1.1	Background	500
5.1.1.2	Boiler types and classifications	501
5.1.1.3	Applications of steam generators	503
5.1.2	Radiative heat transfer	505
5.1.2.1	Historical citation	505
5.1.2.2	Equation of radiant energy transfer	508
5.1.2.3	Methodology	509
	- Integrating by use of an integrating factor, 510	
	- Diffusion method, 510	
	- Approximate solutions, 511	
	- The Monte Carlo technique, 513	
	- The engineering treatment of gas radiation, 514	
	- Flux and discrete ordinates methods, 515	
	- Zonal method of analysis, 522	
	- Radiation calculation in boiler furnaces, 524	
5.1.3	Convective heat transfer	528
5.1.4	Combustion and heat transfer in flame tubes	530
5.1.4.1	Horizontal flame tube of circular cross section	531

- Flame structure, 532	
- Heat transfer, 535	
- Computational analysis and results	539
5.1.4.2 Vertical flame tube of circular cross section	545
- Experimental study, 545	
- Computational analysis, 549	
5.1.4.3 Horizontal flame tube of square cross section	552
5.1.5 Combustion and heat transfer in water-tube boilers	555
5.1.5.1 Experimental study	558
- Flame structure, 558	
- Heat transfer, 564	
5.1.5.2 Computational analysis of heat transfer	566
- Zonal method, 566	
- Discrete ordinates transfer method, 569	
- Boiler heat transfer modeling, 575	
- Comparison between different methods, 579	
5.1.5.3 Heat transfer from flame impingement	588
- Overview, 588	
- Experimental and computational analysis, 593	
5.1.6 Emission and Emission Control	597
5.1.6.1 Combustion modification techniques	598
- Flue gas re-circulation (FGR), 598	
- Water and steam injection, 601	
- Air and fuel staging, 602	
- Burner configuration and duration, 603	
- Re-burning, 607	
5.1.6.2 Post-combustion techniques	609
- Nitrogen oxides techniques, 609	
- Sulfur dioxide techniques, 613	
5.1.6.3 Combination of NO _x and SO ₂ control techniques	624
5.2 Tangentially-Fired Furnaces (TFFs)	629
5.2.1 Introduction	629
5.2.2 General background	630
- Overview, 630	
- Configuration, 632	
5.2.3 Flame stability	635
- Ignition limits, 636	
- Effect of burner tripping, 636	
- Temperature-contours maps just before ignition, 642	
- Inclination angle and core-vortex size, 642	
5.2.4 Flow, combustion, and heat transfer	644
5.2.5 Modeling of large scale TFFs	654
- Background to the modeling of TFFs, 655	
- Three-dimensional modeling of TFFs, 656	
5.2.6 Emission and emission control	663
- Emission, 663	

	- Emission control, 666	
5.3	Fluidized-Bed Furnaces (FBFs)	674
5.3.1	Application of FBC	676
5.3.2	The phenomenon of fluidization	677
	- General terminology, 679	
	- Minimum and maximum fluidization velocity, 680	
	- Particle characterization, 685	
	- Packed beds, 686	
	- Bubbling beds, 686	
	- Slugging, 688	
	- Bed expansion, 689	
	- Distributor (or grid) design, 690	
5.3.3	Combustion in FBF	691
5.3.4	Background to heat transfer	699
	- Heat transfer from emulsion phase, 700	
	- Heat transfer by radiation, 703	
	- Total heat transfer, 705	
	- Heat transfer to horizontal and vertical tube banks, 706	
5.3.5	Experimental and computational study of heat transfer	709
	- Calculation of different modes of heat transfer, 709	
	- Heat transfer to the distributor plate, 714	
	- Heat transfer to immersed bodies, 717	
	- Heat transfer in a bubbling fluidized-bed combustor, 721	
	- Heat transfer to a horizontal tube bundle, 730	
5.3.6	Emission and emission control	733
	- Emission, 733	
	- Emissions control, 741	
Appendix A		747
Appendix B		750
Appendix C		760
Appendix D		767
Appendix E		776
References		779
Index		835

Preface

This book is a valuable scientific and technical reference for engineers and scientists as well as for postgraduate students in the academic community. Moreover, the book will help to establish a link between principles and practical applications in the field of combustion. It can also be used as a bibliography to present the background of different combustion researchers.

The book contains brief descriptions of fundamental and combustion processes, followed by an extensive survey of the combustion research technology. It also includes mathematical modeling of the processes covering mainly premixed and diffusion flames, where many chemical and physical processes compete in complex ways, for both laminar and turbulent flows. This provides a unique bridge between combustion fundamentals and combustion technology, which should make the book a valuable technical reference for many engineers and scientists. Moreover, the book gives the reader sufficient background of basic engineering sciences such as chemistry, thermodynamics, heat transfer and fluid mechanics. The mentioned research and mathematical models fit between small-scale laboratory burner flames, and large-scale industrial boilers, furnaces and combustion chambers. The materials of this book have been collected from previous relevant research and some selected papers of the authors and co-workers, which have been presented mainly in different refereed journals, international conferences and symposiums.

Furthermore, the book includes some of the many recent general correlations for the characteristics of laminar, turbulent, premixed and diffusion flames in an easily usable form. The authors believe that further progress in optimizing combustion performance and reducing polluting emissions can only be treated through understanding of combustion chemistry. Therefore, the book involves combustion chemistry models that validate experimental data for different fuels. These models are sufficiently accurate to allow confident predictions of the flame characteristics.

Chapter I presents an introduction to the fundamentals of combustion. The chapter starts with energy sources and fuel types with some related thermodynamic fundamentals, combustion stoichiometry, and thermochemical calculations. Descriptions of chemical reactions, and equilibrium composition and temperature are also presented. Chemical kinetics, including kinetic theory of gases, elementary reactions with transport phenomena, and modeling in combustion chemistry are discussed. Furthermore, the pollutant emissions generated from combustion systems, their formation and oxidation kinetics, as well as the reduction techniques, are also presented.

Preface

In chapter 2, the basic definitions for premixed and diffusion laminar flames are given. Since the tasks of combustion flow diagnostics are to increase the fundamental understanding of aspects of combustion, the study of small-scale laminar flames in this chapter is essential. Therefore, many practical combustion problems can be examined most conveniently under the well defined and controlled conditions which the laminar flame provides. The objective of this chapter is to present some understanding of laminar flames as revealed by detailed numerical kinetic modeling, particularly in relation to the interaction between modeling and experiments. Furthermore, some general correlations are derived for the flame propagation parameters for both gaseous and liquid fuels. This chapter also describes the computational method of the kinetic model with the use of transport parameters and reaction mechanisms for different fuels (H_2 to $C_{16}H_{34}$). These kinetic mechanisms are described, examined, and validated by the experimental results at different pressures, temperatures, equivalence ratios and volumetric ratios of O_2/N_2 .

Laminar burning velocity and volumetric heat release rate in relation to the turbulent flame model are important. Therefore, general correlations for such parameters with the heat of reaction per mole of mixture for different gaseous and liquid fuels are introduced in chapter 2. Furthermore, several expressions for laminar burning velocities as functions of equivalence ratio, pressure, temperature, and gaseous additives have been derived for several practical hydrocarbon fuels. Also, in this chapter, the chemical reactions of nitrogen compounds that occur in combustion processes have been explained with their reduction technologies. In addition, the responses of flames to applied stresses are discussed in the context of flame extinction for premixed flames in both the symmetric back-to-back and the asymmetric unburnt-to-burnt configurations.

Chapter 3 describes mainly the characteristics of turbulent, free premixed, and diffusion flames. The effect of some parameters on the turbulent burning velocity, flame structure, heat release rate, flame height, and flame stability under different conditions is introduced with some problems of combustion in gasoline engines. Furthermore, laminar flamelet models for turbulent combustion processes are presented together with an extensive theoretical and experimental study of flame characteristics for model furnaces and burners. The determination of these characteristics, as well as the experimental methods and techniques, form the principal objective of this chapter. These studies are complementary, and necessary to enhance the understanding of the flow, chemistry, mixing, and heat transfer in burners, furnaces, and combustion chambers, and will be described in chapters 4 and 5.

In a practical combustion system, the length and shape of the confined flame depend, to a large extent, on the mixing processes between the fuel and air, which enter the furnace separately. These processes have been dealt with in chapter 4. They explain how flame characteristics and dimensions depend on some operating and geometrical parameters. These include turbulence level, air-fuel ratio, swirl imparted to either fuel or combustion air, strain rate, burner and furnace geometry, forced flow reversal, and non-streamlined bodies. Most of the work presented in this chapter is devoted to study the effect of such parameters on the aerodynamic flow and mixing patterns in both hot and cold conditions, as well as the flame stability and heat liberation under firing conditions. Furthermore, in order to provide a bridge between the fundamentals of chapters 1 to 3 and the applications given in chapters 4 and 5, modern comprehensive models which

include all physical and chemical phenomena that appear during the combustion process are described in section 4.6.

Chapter 5 describes three important parts of combustion research technology, firstly in conventional steam boilers (section 5.1), secondly in tangentially-fired furnaces (section 5.2), and thirdly in fluidized-bed furnaces (section 5.3). Turbines and I.C. engines are visited briefly. In such industrial flame applications the achievement of high heat transfer rates is a principal objective. Therefore, most of the combustion research in conventional systems such as flame tubes and water-tube boiler furnaces are devoted in this chapter to study the effect of operating parameters such as fuel-air ratio, combustion air swirl, and combustion zone geometry on heat transfer and flame structure. Single and multi-burner systems have been investigated in this part. The basics of radiative and convective heat transfer in combustion zones are covered first in this chapter, followed by simple and modified analytical computations of heat transfer rates in flame tubes and boiler furnaces. Furthermore, modern models to simulate the flame characteristics in real boilers are compared in section 5.1.5.2.

The responsibility of the combustion engineers should be mainly devoted towards the utilization of the energy sources in the most efficient and economical manner. Tangentially-fired furnaces are considered as ones that fulfill these requirements in recent years and become more attractive in the field of power station boilers. Therefore, the objectives of the second part of chapter 5 are to present an overview of tangentially-fired furnaces and to investigate experimentally and computationally the flame stability, flow, combustion, and heat transfer in such type of furnaces. Furthermore, modeling of large-scale tangentially-fired furnaces is also presented.

The third part of chapter 5 explains fluidized-bed combustors. It explains in some detail the applications of fluidized-bed combustors as well as the phenomenon of fluidization and the physical fundamental aspects of the fluidized-bed. Furthermore, the theoretical study of heat balance and heat transfer coefficient calculations in fluidized-beds are set with a background of relevant research. The present applied research on the rectangular cross-sectional fluidized-bed model and fluidized-bed boiler model is described experimentally and theoretically. Most of this work is concerned with the study of the effect of bed temperature, particle diameter, tube diameter, and cooling coil diameter on the heat transfer coefficients between the fluidizing material and both bed walls and immersed bodies under firing conditions. Also, the effect of some of these parameters on the heat transfer to the freeboard and to a horizontal tube bank is considered.

Since NO_x and SO_2 emissions are the major drivers of combustion technology, each of the three parts in this chapter describes the real application of such technology to control NO_x and SO_2 in steam boilers (section 5.1.6), tangentially-fired furnaces (section 5.2.6) and finally in fluidized-bed furnaces (section 5.3.6).

Fawzy El-Mahallawy

Saad Habik

About the Authors

Fawzy El-Mahallawy is an emeritus Professor of Combustion and Heat Engines at Cairo University, Egypt. In 1967 he gained his PhD from Cairo University. He continued his postdoctoral program at the Imperial College in London with Professor Spalding in the period 1970 – 1972. He became a full Professor in 1978. In 1989 he was appointed as the Vice Dean of the Faculty of Engineering, Cairo University, and as the Director of the Development Research and Technological Planning Center, Cairo University in 1993. A total of 25 PhD and 54 MSc degrees have been awarded under his supervision. He has published 117 papers in the field of combustion and heat transfer, and 122 technical reports. He was the Associate Editor of the book entitled “Flow, Mixing and Heat Transfer in Furnaces”, published by Pergamon Press in 1978. He has been twice awarded the National Award for Engineering Activities, in 1975 and 1983, and the First Class Science and Arts Medal for his contribution to the field of Engineering, in 1977 and 1986.

Saad Habik is a Professor of Combustion and Heat Engines at the Mechanical Power Engineering Department, Faculty of Engineering of Port-Said, Suez Canal University, Egypt. He is currently the Director of the Energy Research and Studies Center at the Faculty of Engineering of Port-Said. He gained his PhD from the Mechanical Engineering Department at Leeds University, UK in 1986. He worked as a postdoctoral research fellow at the same department in the period 1986-1990. In 1995 he undertook research at Michigan Technological University, USA. His field of research focuses on combustion chemistry and he has published 35 scientific papers in the same field. Two PhD and one MSc degrees have been awarded under his supervision. Professor Habik is a member of SAE, USA, Associating Energy Engineer, USA, and ILASS, Egypt. He was awarded the National Award for Engineering Activities, and a First Class Medal for his contributions to the field of Engineering.

Chapter

1

Combustion Fundamentals

1.1 Introduction

This chapter is intended as introductory text in the fundamentals of combustion for engineering graduate students, as well as a basis for the next four chapters. Combustion is defined as a rapid exothermic reaction that liberates substantial energy as heat and flames as combustion reactions with the ability to propagate through a suitable medium. This propagation results from the strong coupling of the reaction with the molecular transport process. The chemistry and physics of combustion, i.e. destruction and re-arrangement of certain molecules, rapidly release energy within a few millionths of second. Currently, combustion is a mature discipline and an integral element of diverse research and development programs from fundamental studies of the physics of flames and high-temperature molecular chemistry to applied engineering projects involved with developments such as advanced coal-burning equipment and improved combustion furnaces, boilers, and engines. These developments are important in controlling the pollutant emissions. Therefore, it is appropriate in this chapter to present two very important practical considerations relative to the combustion reaction systems, which are the mass and energy balance used to describe such systems.

The chapter starts with the energy sources including the energy characteristics of various important fuels resources and their physical and chemical properties. This is followed by introducing some definitions of ideal gases, mass conservation and basic thermodynamic principles, as well as, general energy balance for a chemically reactive medium. Description of the practical stoichiometry and thermochemical requirements, which apply during combustion processes such as chemical reaction, equilibrium composition and temperature, are also presented.

Actually, combustion is a result of dynamic, or time-dependent, events that occur on a molecular level among atoms, molecules, radicals and solid boundaries. Therefore, this chapter presents chemical kinetics that include kinetic theory of gases, elementary reactions and reaction rate theory. Furthermore, the rapid reactions produce gradients that transport processes convert into heat and species fluxes that speed-up the reactions. Therefore, further discussions including the primary transport properties and processes are presented with brief discussions on combustion chemistry and modeling.

Finally, combustion generated air pollution; pollutant formation and oxidation kinetics, as well as, their reduction techniques are presented at the end of this chapter.

1.2 Energy Sources

Energy represents the ability to do work. Fifty years ago, the energy demands were relatively low and energy was very cheap, but now engineering and technology recognize that the earth is a finite eco-sphere having limited terrestrial resources and a delicately balanced environment. Tomorrow's energy sources may be divided to two categories:

1. Exhaustible sources, e.g. fossil fuels such as coal, crude oil, natural gas,...etc. Past and future paths for total primary energy supply and CO₂ emissions are presented in Figs. 1.1 (a) and 1.1 (b) [1]. It is expected that the world energy demand will be increased from 8000 million ton oil equivalent in 1990 to about 14000 million ton oil equivalent in 2020 (Fig. 1.1 (a)). This will be corresponding to the increase in population from 5400 to 8000 million persons for the same years [1]. Moreover, oil continues to dominate world energy consumption, with transport use increasing its share. Gas consumption rises to approach coal consumption by the end of this period, while nuclear power stabilizes, hydropower and renewable energy increase steadily, but remain at low levels (see Fig. 1.1 (b)). CO₂ emissions rise with primary energy demand slightly faster than in the past (see more details in section 1.10.3). Contributing factors are the stabilization of nuclear power generation and the continued rapid growth in coal use in China and other Asian countries [1].
2. Inexhaustible or continuous sources, e.g. hydraulic, wind and solar energy, energy from oceans, waste and synthetic fuels,...etc. Atomic or nuclear energy may be considered as an exhaustible source because the uranium and thorium deposits could be completely consumed.

Figure 1.2 shows the proved oil reserves at the end-1996 [2], and if the world's oil reserves were reported with reasonable accuracy and the assessments of potential volumes in yet undiscovered fields proved general reliability, the original recoverable oil endowment of the earth would have been around 2.3 trillion barrel. About one-third of this oil has already been produced and consumed. Should unconstrained modern oil exploitation proceed around the world, the remaining two-thirds of the earth's original oil could sustain world output at its current rate through much of the 21st century, until a declining resource base finally forced down production. In 1980 proved oil reserves were estimated at around 0.7 trillion barrel as compared to the reserve estimate of nearly 1.1 trillion barrel in 1996. However, some geologists hold discordant views that place ultimate world oil recovery at only about 1.75 trillion barrel [2].

It took 50 years (1900-1950) for total annual U.S. energy consumption to go from 4 million barrel of oil equivalent (Mboe) per day to 16 Mboe [3]. It took only 20 years (1950 – 1970) to go from 16 to 32 Mboe. This rapid growth in energy use slowed in the early 1970's, but took a spurt in the late 1970's, reaching almost 40 Mboe in 1979. Energy use slowed again in the early 1980's and dropped to 35 Mboe in 1983. Economic growth in mid 1980's returned the use to 40 Mboe in 1988. Energy use remained fairly steady at just 40 Mboe in the late 1980's, but started growing in the 1990's. By the end of 1996, energy use in U.S. was up to almost 45 Mboe. With only 5 percent of the world's population, the United States consumes about 25 percent of its energy and produces about 25 percent of the world's gross national product (GNP). However, some nations such as Japan, West Germany, and Sweden, produce the same or greater GNP per capita with significantly less energy than the United States [3].

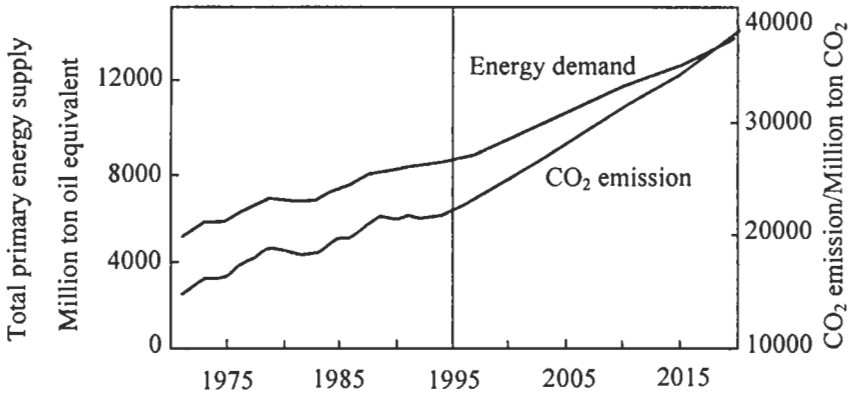


Fig. 1.1 (a): World primary energy supply and CO₂ emission 1971-2020 [1]. Reproduced by permission of OECD/IEA (International Energy Agency).

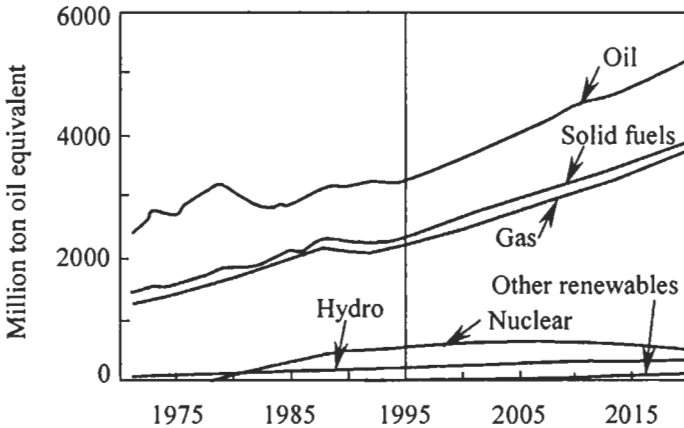


Fig. 1.1 (b): World primary energy by fuel 1971-2020 [1]. Reproduced by permission of OECD/IEA (International Energy Agency).

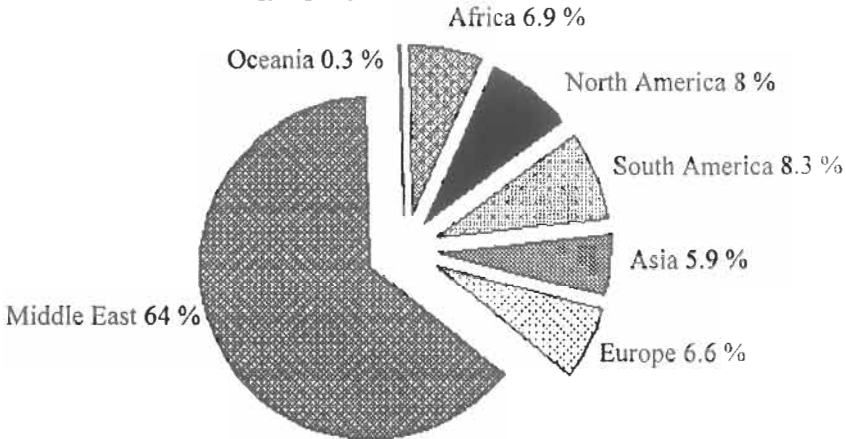


Fig. 1.2: Proved oil reserves at end – 1996: Regional distribution [2]. Reproduced by permission of World Energy Council.

In order to present the main developments in energy demand, it is important to identify the principal purposes for which energy is used. Four major energy-related services [4] have been identified:

- ◆ Electrical services (total consumption of electricity by final consumers).
- ◆ Mobility (non-electricity fuels consumed in all forms of transport).
- ◆ Stationary services (mainly fossil fuels used for heating in buildings and industrial processes).
- ◆ Fuel used in power generation.

A more detailed description of the energy related services is given in Ref. 4. Table 1.1 shows the main indicators of gross inland consumption [5].

Figure 1.3 shows the total energy produced and inland consumed in NAFTA (North American Free Trade Agreement, Canada, Mexico, and the United States of America), USA, European Union and Russia [5]. It is clear from the figure that the energy produced in NAFTA (Fig. 1.3 (a)) increased rapidly since 1985 compared to that in USA (Fig. 1.3 (b)). Furthermore, there is nearly steady state energy produced and consumed in Eu 15 since 1985 till 1997, while in Russia both energies decreased very rapidly since 1989. Figure 1.4 shows the energy production in 1997 in a broader geographical appeal.

From the above figures, and based on more detailed data and energy highlights given by Ref.5, the following points summarize the total energy produced and inland consumed for the world and its main regions:

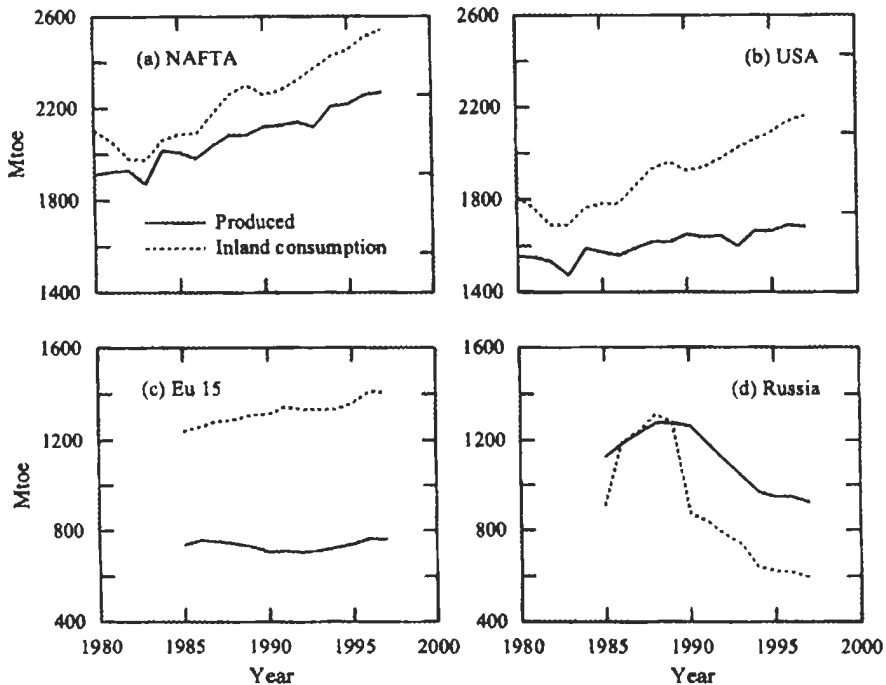


Fig. 1.3: Total energy produced and inland consumed (Mtoe) in: (a) NAFTA, (b) USA, (c) EU 15 and (d) Russia. (According to data given by Ref. [5]).

- ◆ World energy demand grew by only 1.1% in 1997 despite world economic growth by 3.3%. It increased more rapidly in the Middle East, Asia and Latin America.
- ◆ Final energy demand was driven by the transport and tertiary – domestic sectors, and the potential for further demand growth remains enormous in the developing regions.
- ◆ The fuel mix is changing in favor of gas but oil still remains predominant.
- ◆ World-wide CO₂ emissions have increased by 8 % since 1990.
- ◆ Since 1990, natural gas consumption has grown faster than overall energy consumption despite the stagnation registered in 1997 following major increases in 1995 and 1996. In recent years, the bulk of consumption growth arose from power generation. Demand accelerated in developing countries, mainly in Asia and the Middle East, but also in European Union.
- ◆ Oil remains the predominant energy source, keeping its share of 37% since 1990. Oil demand accelerated significantly in 1996 and 1997. Developing regions – Asia, Latin America and the Middle East – which increased their share in the world oil consumption from 22.5% in 1990 to 30.2% in 1997, are driving oil consumptions. The near future will be marked by the increasing contribution of transport in final demand sustained by the enormous potential for development in the emerging regions.
- ◆ Solid fuels have been steadily losing market share since 1990, principally in the European Union. The consumption, increasingly concentrated in the power sector, was progressively located close to the main producers. Asia, in particular, absorbed 41.3% of the world consumption in 1997 against 32.7% in 1990. Consumption also increased substantially in NAFTA region in 1996 and 1997.
- ◆ The carbon – free energy sources (nuclear and renewable) increased by 2% per year on average since 1990. Renewable energy sources accounted for 13.5% of total energy since 1997; showing a small increase since 1990. More than 55% of world biomass production remained located in Asia.

Conversion factors with a short listing of the average energy contained in a number of the most common fuels, as well as some energy units conversions are shown in Tables A1 and A2 (a) to A2 (c) (Appendix A).

Table 1.1: Main indicators of gross inland consumption, Mtoe.

(According to data given by Ref. 5).

Region	Power generation	Energy branch	Industry	Transport	Tertiary-domestic	Total
World (1996)	2524.8	561.3	1969.3	1572.9	2709.5	9341.0
%	27.03	6.00	21.08	16.83	29.00	100.00
European EU (1997)	483	69.2	262.6	288.6	379.0	1406.9
%	32.58	4.66	17.71	19.47	25.56	100.00
NAFTA (1997)	720	166.7	388.3	656.9	530.6	2541.7
%	29.24	6.77	15.77	26.68	21.55	100.00
Asia (1996)	504.7	122.8	658.9	216.2	804.9	2293.4
%	21.87	5.32	28.55	9.36	34.88	100.00
Middle East (1996)	79.5	51.1	49.1	60.8	89	315.8
%	24.12	15.51	14.90	18.45	27.00	100.00

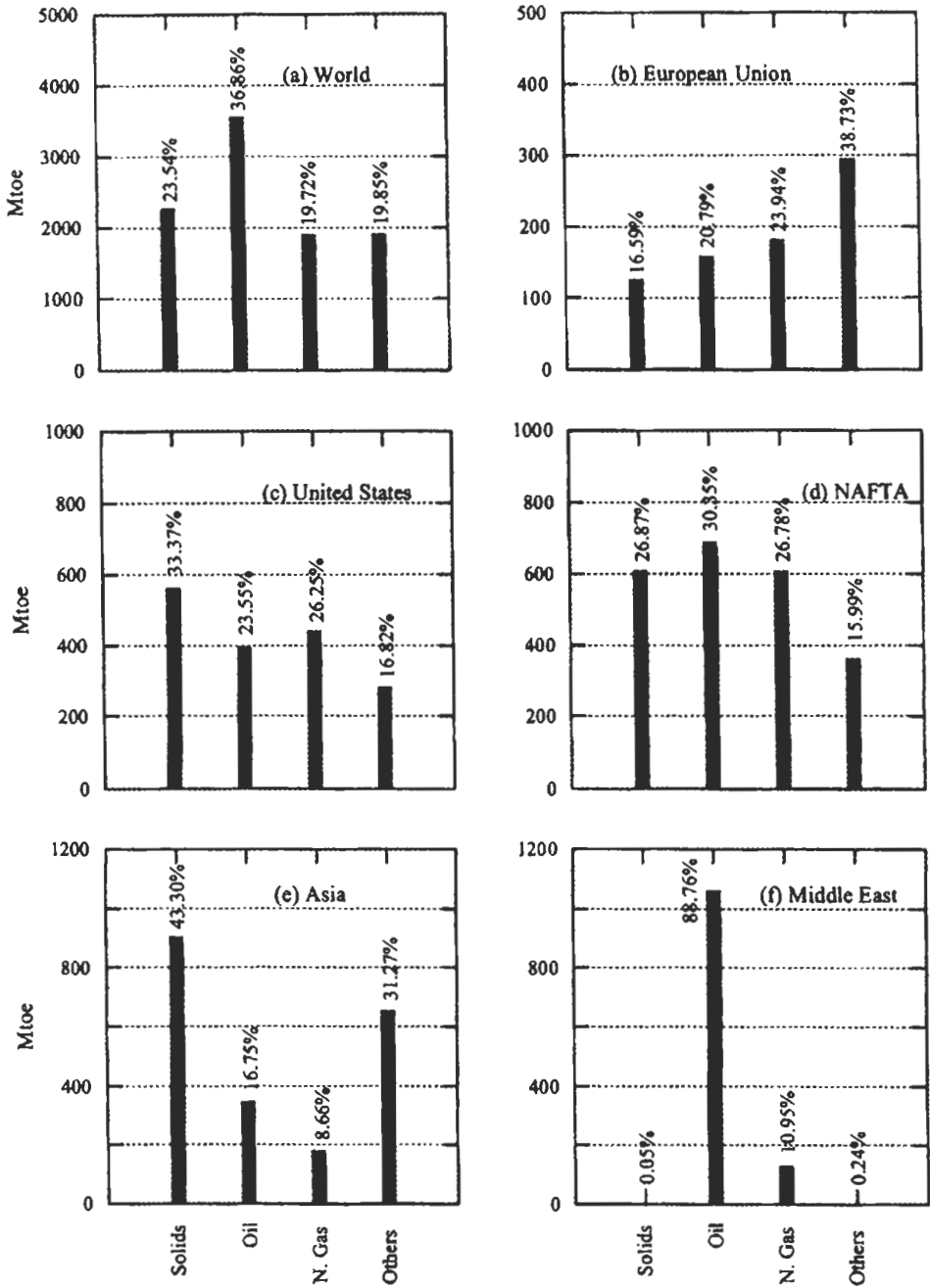


Fig. 1.4: Production of different fuels in 1997 for the world and some of its main regions, Mtoe. (According to data given by Ref. [5]).

1.2.1 Fuels

A fuel can be considered as a finite resource of chemical potential energy in which energy stored in the molecular structure of particular compounds is released via complex chemical reactions.

Chemical fuels can be classified in a variety of ways, including by phase and availability as shown in Table 1.2 [6].

Table 1.2: Classification of chemical fuels by phase and availability [6]. Reproduced by permission of Marcel Dekker Inc.

Naturally available	Synthetically produced
<i>Solid</i>	
Coal	Coke
Wood	Charcoal
Vegetation	Inorganic solid waste
Organic solid waste	
<i>Liquid</i>	
Crude oil	Syncrudes
Biological oils	Petroleum distillates
Fuel plants	Alcohols
	Colloidal fuels
	Benzene
<i>Gas</i>	
Natural gas	Natural gas
Marsh gas	Hydrogen
Biogas	Methane
	Propane
	Coal gasification

Some of the basic requirements of a fuel include: high energy density (content), high heat of combustion (release), good thermal stability (storage), low vapor pressure (volatility) and non-toxicity (environmental impact).

Any combustion system may be operated on fuel in any of the three states, gaseous, liquid, or solid. Crude oil is known to exist at various depths beneath land and sea in most parts of the world. Crude oils are extremely complex mixtures of gases, liquids, and dissolved solids that always consist mainly of hydrocarbons, with small amounts of nitrogenous substances and organic sulfur compounds. Crude oil is separated by a distillation process that exploits the fact that the various components in crude oil have different boiling points. When a crude oil is heated, the first gases evolved are chiefly methane, ethane, propane, and butane. At higher temperatures, vapors are released and then condensed to form light distillates of the kind used in the production of gasoline. As boiling proceeds, the kerosene emerges, followed by the middle distillates used in gas oil and Diesel fuel. Finally, a residue is left and used in the manufacture of lubricating oil, wax and bitumen.

The physical requirements for reactive mixtures and the thermochemical path that fuel and oxidant, or *reactants*, should follow to form *products of combustion* while releasing energy are as shown in Fig. 1.5 [6].

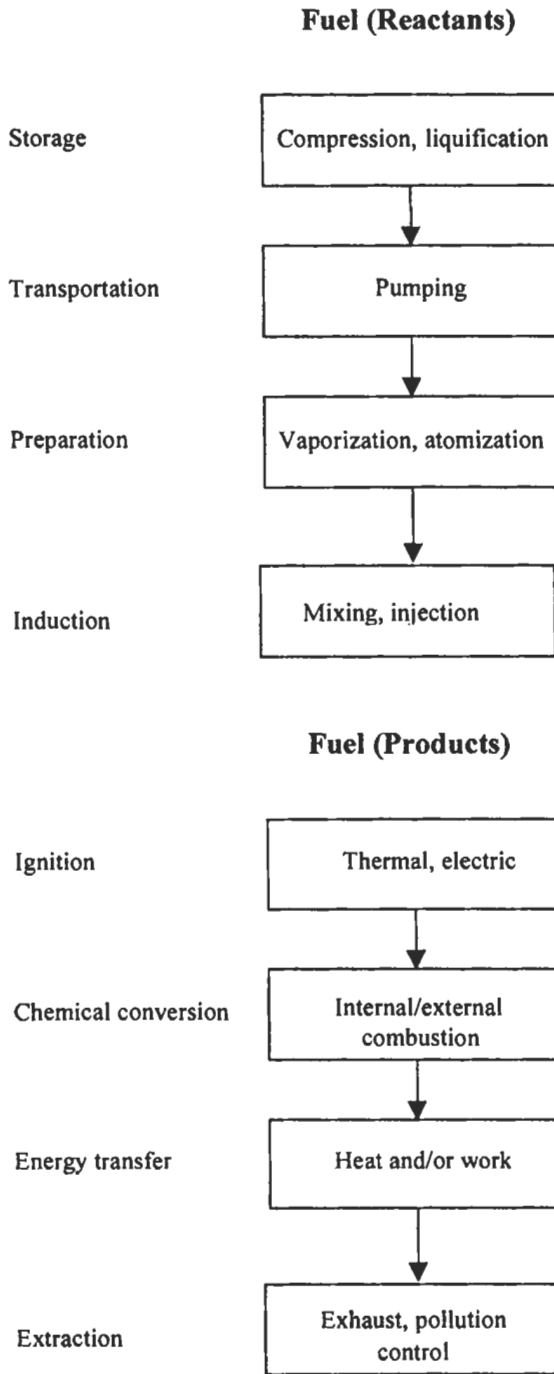


Fig. 1.5: Physical requirements and thermochemical path for fuel combustion [6]. Reproduced by permission of Marcel Dekker Inc.

Knowledge of the properties, structures, safety, reliability of these fuels, as well as the manner in which they affect the combustion system performance are important. Because the burning velocities of different gaseous and liquid fuels are extensively surveyed in chapter 2 (section 2.4.7), it is necessary to have some brief knowledge about the chemical structure and physical properties of most of these fuels. Selection of these fuels is governed by the above-described requirements.

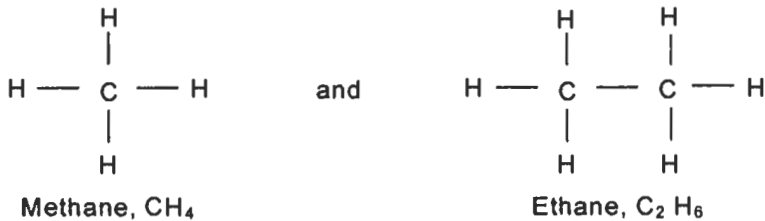
Gaseous fuels present the least difficulty from the standpoint of mixing with air and distributing homogeneously to the various cylinders in a multi-cylinder engine, or burners in a gas turbine, furnace or jet engine. Under good combustion conditions, they leave relatively little combustion deposits as compared with other fuels. However, gaseous fuels for automotive equipment necessitate the use of large containers and restrict the field of operation.

Liquid fuels are used to a much larger extent in most of the combustion systems than gaseous or solid fuels. They offer some advantages such as, large energy quantities per unit volume, ease and safety of handling, storing, and transporting. In addition, liquid fuels must be vaporized, or atomized and at least partially vaporized, during the process of mixing with air. There are some difficulties that occur in distributing and vaporizing the fuel particles in the primary combustion air to obtain complete combustion in combustors or combustion devices.

Pure hydrocarbon fuels are compounds of two elements only, carbon (C) and hydrogen (H). Those with up to four carbon atoms are gaseous; those with twenty or more are solid, and those in between are liquid. Compounds, which contain the element carbon, are known in chemistry as organic chemistry. It eventually became necessary to introduce a systematic form of nomenclature in order that the structure of a carbon compound could be readily deduced from its name, and vice-versa. The nomenclature at present in use was laid down by the International Union of Pure and Applied Chemistry (I.U.P.A.C.) [7], and the rules for naming some of the simpler compounds are presented next and are used in chapter 2 (sections 2.4.7 and 2.4.11). The main physical parameters of gases are given in Table B1, while the thermal and physical properties of various gases are given in Tables B2 (a) to (e) (Appendix B) [8]. Furthermore, Table B3 (Appendix B) contains the heating values of some hydrocarbon fuels.

Alkanes. The general formula is C_nH_{2n+2} . Each member of alkanes is given the suffix *-ane*. The first four retain the names originally given to them: methane (CH_4), ethane (C_2H_6), propane (C_3H_8) and butane (C_4H_{10}). After that, the first part of the name is derived from the Greek for the number of carbon atoms in the molecule: pentane (C_5H_{12}), hexane (C_6H_{14}), heptane (C_7H_{16}), octane (C_8H_{18}), and so on.

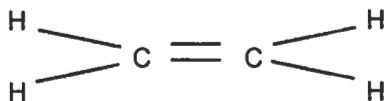
As the number of carbon atoms increases, the boiling point and density increase. The boiling point depends on the attractive forces between the molecules of the liquid. The structural formula for CH_4 and C_2H_6 is:



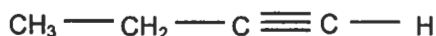
Alkenes. The general formula is C_nH_{2n} . The unsaturated compounds with a $C = C$ double bond which are often referred to as olefines are termed alkenes in the I.U.P.A.C. scheme. Each member is terminated with **-ene**, and the position of the double bond is determined by inserting the lowest possible number before the suffix to describe the carbon atom, which forms one end of the double bond relative to its position in the chain, e.g. pent-1-ene:



Some alkenes are, ethene ($CH_2 = CH_2$), propene ($CH_3 - CH = CH_2$), but-1-ene ($C_2H_5 - CH = CH_2$), and phenylethene ($C_6H_5 - CH = CH_2$). The melting points and boiling points of the alkenes are very close to those of the alkanes with the same number of carbon atoms [7]. The structural formula for ethene is:



Alkynes. The general formula is C_nH_{2n-2} . The compounds are named as for the alkenes but with the suffix **-yne**. For example:

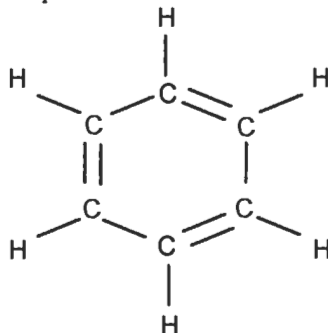


is but-1-yne. However, the first member, ethyne ($CH \equiv CH$) is often described by its original name, acetylene, and its simple derivatives are sometimes described as substituted acetylene: e.g. propyne ($CH_3 - C \equiv CH$) is methyl acetylene.

Some alkynes are ethyne ($CH \equiv CH$), propyne ($CH_3 - C \equiv C - H$), and but-1-yne ($C_2H_5 - C \equiv C - H$). The melting points and boiling points of the alkynes are similar to those of the alkanes with the same number of carbon atoms. The structural formula for ethyne is:



Aromatic compounds. The term "aromatic" was first used to describe a group of compounds, which have a pleasant smell (aroma). These compounds include the cyclic compound, benzene, and its derivatives. The benzene is a simple cyclic compound, with a six-membered ring of six carbon atoms and with one hydrogen atom attached to each carbon atom. Bearing in mind that carbon and hydrogen form four bonds and one bond, respectively, it was natural to represent its structure as:



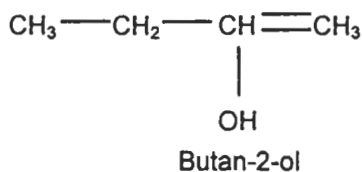
in which single and double bonds alternate around the ring.

The characteristic formula for the aromatics is C_nH_{2n-6} . More complex molecules of the aromatic group are obtained either by replacing one or more of the hydrogen atoms with hydrocarbon groups or by "condensing" one, example of this is toluene, $C_6H_5CH_3$. Aromatics have compact molecular structure, stable when stored, smoky combustion process, highest fuel distillate densities and lowest heating values per unit mass of liquid hydrocarbon fuels.

Alcohols and phenols. The general formula is $R - OH$. Alcohols are compounds containing one or more hydroxyl groups attached to saturated carbon atoms. Those with one hydroxyl group are known as *monohydric* alcohols; examples are methanol (CH_3-OH), ethanol ($C_2H_5 - OH$), and phenyl methanol ($C_6H_5 - CH_2 - OH$). There are also *polyhydric* alcohols, which contain more than one hydroxyl group; examples are ethane-1,2-diol, $HOCH_2 - CH_2OH$ and propane-1,2,3-triol, $HOCH_2 - CH(OH) - CH_2OH$.

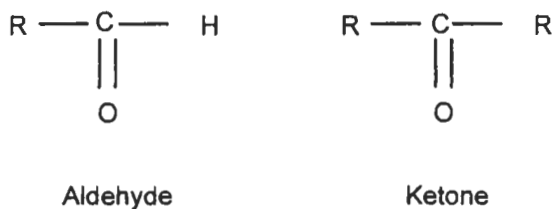
Phenols are compounds containing one or more hydroxyl groups attached to aromatic carbon atoms, the parent member of the series is phenol itself, $C_6H_5 - OH$. Many of the properties of phenols are different from those of alcohols.

Monohydric alcohols are named by replacing the final -e in the corresponding alkane by -ol. The position of the hydroxyl group in the carbon chain is given by numbering the carbon atoms as for alkanes [7]. For example:



Ethers. The general formula is $R - O - R'$. The two R groups in the structural formula $R - O - R'$ can be the same or different, and can be either alkyl groups or aromatic groups. For example, $CH_3 - O - CH_2 - CH_3$ is methoxy ethane. However, it is common practice to use the name compounded from the two groups R and R' followed by ether, example, dimethylether, $CH_3 - O - CH_3$ and ethyl methyl ether, $CH_3 - O - CH_2 - CH_3$. Their boiling points are the same as those of the alkanes of similar formula weight.

Aldehydes and ketones. The general formula is:

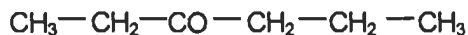


Both aldehydes and ketones contain the *carbonyl group* ($>C = O$). However, the attachment of a hydrogen atom to the carbonyl group in an aldehyde gives aldehydes certain properties, which ketones do not possess and which enable the two classes of compounds to be distinguished from one another.

The I.U.P.A.C. nomenclature uses the suffixes *-al* for aldehydes and *-one* for ketones; the main carbon chain is named as usual and, for ketones, the position of the carbonyl group is specified by inserting the number of its carbon atom from the nearer end of the chain [7]. For example:



Pentanal



Hexan-3-one

Some simple series are, methanal, ethanal, and propanal. Methanal is a gas, other aldehydes and ketones of relatively low formula weight are liquids and the remainders are solids.

The maximum burning velocities are measured by different techniques for most of the above organic compounds fuels, are given in section 2.4.7.

Natural gas and liquefied petroleum gas. The world's most readily available and abundant gaseous fuel resources are found in *natural gas* reserves. Gaseous fuels have been used for centuries in China and for over 100 years in both the United States and Europe. In the United States, when natural gas was originally discovered at oil wells, it was burned, or *flared off*, as a useless by-product of oil production. Today, natural gas is a major industry that transports fuel throughout the United States by a complex interstate pipeline network. Natural gas was formed by *anaerobic*, or bacterial-assisted, decomposition of organic matter under heat and pressure and, therefore, like coal and crude oil, is a variable-composition hydrocarbon fuel. Table B4 (a) (Appendix B) lists properties of certain natural and synthetic gas resources.

Natural gas consists chiefly of methane, ranging anywhere from 75% to 99% by volume, with varying concentrations of low molecular weight hydrocarbons, CO, CO₂, He, N₂, and/or H₂O. Conventional gas well drilling has proved successful in or near oil fields. Natural gas is practically colorless and odorless, and for safety reasons, is "soured" with the familiar rotten egg odor by adding hydrogen sulfide, H₂S. The American Gas Association classifies natural gas as sweet or sour gas and, additionally, as being associated or non-associated gas. Associated, or *wet*, gas is either dissolved in crude oil reserves or confined in pressurized gas caps located on the top of oil ponds. Wet gas has appreciable concentrations of ethene, butene, propane, propylene, and butylenes. Nonassociated, or *dry*, gas can be found in gas pockets trapped under high pressure that have migrated from oil ponds or are the results of an early coalization-gasification stage. The composition of natural gas varies from one place to another. Change in the balance of methane, other hydrocarbons, and inert gases affect both density and the volumetric energy content of the mixture. The increase of higher hydrocarbons leads to an increase in the volumetric energy content. On the other hand, the increase of amount of inert gases reduces the volumetric energy content. High concentration of higher hydrocarbons enriches the mixture and reduces the octane number, which would lead to excessive emissions and knock. Likewise high concentration of inert gases will result in an excessive lean mixture. This would reduce power output and possibly leads to rough operation specifically if the mixture was lean.

Liquid Petroleum gas, or LPG, consists of condensable hydrocarbon vapors recovered by expansion of wet gas reserves. By compressing the condensable fractions, liquefied fuel vapors, such as commercial propane and butane, can be stored and transported at ambient temperatures as a liquid. Liquefied natural gas, LNG, is a condensed state of dry natural gas but requires a cryogenic refrigeration for storage and handling at -102°C . At present, efficient transportation of large Middle Eastern natural gas to the United States, Europe, and Asia by sea requires specially designed LNG tankers. More details about properties of other fuels are given in Ref. 9.

Solid fuels. Naturally available solid fuels include wood and other forms of biomass, lignite, bituminous coal, and anthracite. The modern trend is to go on for clean and efficient fuels with small sized furnaces where solid fuels cannot compete with liquid and gaseous fuels. But because they are cheap and easily available, solid fuels still supply approximately 35 % of the total energy requirements of the world.

In addition to carbon and hydrogen constituents, solid fuels contain significant amounts of oxygen, water, and ash, as well as nitrogen and sulfur. The oxygen is chemically bound in the fuel and varies from 45 % by weight for wood to 2 % for anthracite coal on a dry, ash-free basis. Ash is the inorganic residue remaining after the fuel is completely burned. Wood usually has only a few tenths of a percent ash, while coal typically has 10 % or more of ash. Ash characteristics play an important role in system design in order to minimize slagging, fouling, erosion, and corrosion. The composition of solid fuels is reported on an as-received basis, or on a dry basis, or on a dry, ash-free basis. The moisture content on an as-received basis is the mass of the moisture in the fuel divided by the mass of the moisture plus the mass of the dry fuel and ash.

The world's most prominent natural solid fuel resource is coal. Coal, remnants of plants and other vegetation that have undergone varying degrees of chemical conversion in the biosphere, is not a simple homogeneous material but rather is a complex substance having varying chemical consistency. Plant life first begins to decay by anaerobic, or bacterial, action, often in swamps or other aqueous environments, producing a material known as peat. The decomposing material is next covered and folded into the earth's crust via geological action that provides extreme hydrological pressure and heating required for the coal conversion process, as well as an environment that drives off volatile and water. This complex transformation, or coalification process, results in changes, or metamorphosis, over great periods of time and in a variety of fuels ranging from peat, which is principally cellulose, to hard, black coal.

Coal may be classified according to rank and grade. Coal rank expresses the progressive metamorphism of coal from lignite (low rank) to anthracite (high rank). Rank is based on heating value (HV), and its value and percentage of fixed carbon increase as the rank moves from lignite to low volatile bituminous coal, and the volatile matter decreases. Lignite is a brownish-black coal of low rank, and it also referred to as brown coal, and is similar to peat. It has volatile matter (VM) of about 30 % and heating value of 13,000 to 18,000 kJ/kg. Subbituminous coal is dull-black, shows little woody material, and often appears banded (VM \approx 30 – 35 % and HV \approx 19,000 to 24,000 kJ/kg). Bituminous coal is a dark black color and is often banded (VM \approx 19 % to 45 %, and HV \approx 28,000 % to 35,000 kJ/kg), and it is more resistant to disintegration in air than are lignite and subbituminous coals. Anthracite coal is hard and brittle and has a bright luster (VM \approx 5 % and HV \approx 30,000 to 33,000 kJ/kg).

1.2.2 Fuel Cells

The 1973 oil crisis in the USA stimulated development of alternative automotive power sources, including electric vehicles for urban transportation. During this period, the primary motive was independence from foreign oil suppliers. Available batteries then were lead / acid (Pb / acid) and nickel-cadmium (Ni / Cd), both with low energy density that restricted driving range. This characteristic led research to consider fuel cells as a vehicle power source. In rechargeable batteries, the energy is stored as chemicals at the electrodes, physically limiting the amount of stored energy. In a fuel cell, the energy is stored outside electrodes, as is the gasoline in cars with combustion engines. Therefore, only the amount of fuel stored in the tank limits the driving range.

Fuel Cell Principles

The fuel cell dates to 1839, when Sir William Grove first demonstrated it. Although fuel cells were used in the earliest space exploration, serious efforts to use a fuel engine for an electric car did not begin for the late 1980s, when the USA Department of Energy (DOE) provided incentives for research and development of fuel cell systems for transportation applications. Since 1987, DOE has awarded contracts for the development of a small urban bus powered by a methanol-fueled phosphoric acid fuel cell (PAFC), a 50-kW proton exchange membrane fuel cell (PEMFC) propulsion system with an onboard methanol reformer, and direct hydrogen-fueled PEMFC systems for mid-size vehicles.

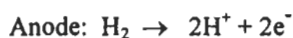
Grove based his discovery on the thermodynamic reversibility of the electrolysis of water. The reversible electrochemical reaction for the electrolysis of water is [10]:



Grove successfully detected the electric current flowing through the external conductors when supplying hydrogen and oxygen to the two electrodes of an electrolysis cell. Joining several of these fuel cells, he observed that a shock could be felt by five of his assistants joining hands. The electrochemical reaction for the fuel cell is:



Fuel cell operation and its accompanying reaction is simple (Fig. 1.6), as hydrogen gas is supplied to the anode and reacts electrochemically at the electrode surface to form protons and electrons. The electrons travel through the electrode and connecting conductors to an electric load, such as a motor, and to the fuel cell's cathode. At the cathode, the electrons react with the oxygen and the previously produced protons to form water. Platinum (Pt) catalysts increase the speed of reactions, producing practical amounts of current. The anodic and cathodic electrochemical reactions are:



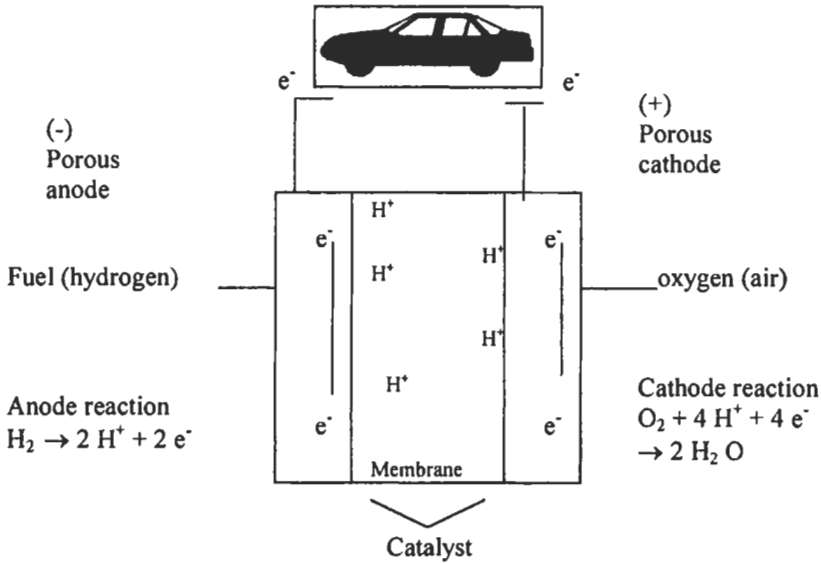
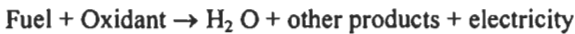


Fig. 1.6: Fuel cell operation.

Overall electrochemical reaction $2 \text{H}_2 + \text{O}_2 \rightarrow 2 \text{H}_2\text{O} + \text{electricity}$

The fuel for operating a fuel cell is not restricted to hydrogen, and the overall electrochemical reaction is:



Water and electricity are the only products of the hydrogen-fueled fuel cell.

1.3 Some Related Thermodynamic Fundamentals

1.3.1 Ideal Gases and Mass Conservation

An equation of state of a substance is a relationship among pressure (P), specific volume (v), and temperature (T), and most equations of state are extremely complicated. Therefore, an ideal gas equation is the convenient approximation and it is easily understood and may be used in most of the computational analysis of this book. An ideal gas molecule has no volume or intermolecular forces and most of the gases can be modeled as ideal [11].

From experimental observations it has been established that the P - v - T behavior of gases at "low" pressure and "high" temperature is simply represented by:

$$P\bar{v} = \bar{R}T \quad (1.1)$$

where \bar{R} is the universal gas constant, which is equal to $8.314 \text{ kJ kmole}^{-1} \text{ K}^{-1}$, and \bar{v} is the molar specific volume.

Dividing Eq. 1.1 by the molecular weight, M , then the equation of state on a unit mass basis can be written as:

$$\frac{P\bar{v}}{M} = \frac{\bar{R}T}{M} \quad \text{or} \quad Pv = RT \quad (1.2)$$

$$\text{where } R = \frac{\bar{R}}{M} \quad (1.3)$$

R is a constant for a particular gas. It follows from Eqs. 1.1 and 1.2 that this equation of state can be written in terms of the total volume, V , as:

$$PV = n\bar{R}T \quad \text{or} \quad PV = mRT \quad (1.4)$$

where m and n are the mass and number of moles, respectively. It should also be noted that Eq. 1.4 could alternately be written as:

$$\frac{P_1 V_1}{T_1} = \frac{P_2 V_2}{T_2} \quad (1.5)$$

and this is the well-known Boyle's and Charles' law.

The conservation of mass principle is a fundamental engineering concept. A description based on mass or weight for a mixture of compounds, existing in either reactant or product state, termed a gravimetric analysis, expresses the total mass in terms of each pure constituent. For a mixture of s total chemical species, a mass fraction mf_i for each i component species can be written as:

$$mf_i = \frac{m_i}{m_t} \quad \text{and} \quad \sum_{i=1}^s mf_i = 1 \quad (1.6)$$

and the total mass m_t is then equal to:

$$m_t = \sum_{i=1}^s m_i \quad (1.7)$$

Even though the total mass of a combustion process may remain constant, concentration of constituents such as oxygen or carbon dioxide may change during a reaction. Often, it is more convenient to describe chemically reactive mixtures on a molar basis. For a mixture of s total chemical species, a mole fraction X_i for each species is:

$$X_i = \frac{n_i}{n_t} \quad \text{and} \quad \sum_{i=1}^s X_i = 1 \quad (1.8)$$

where $n_t = \sum_{i=1}^s n_i$, and $m_i = n_i M_i$, where M_i is the molecular weight of species i . For a mixture of s species, the total molecular weight is:

$$M_t = \sum_{i=1}^s X_i M_i \quad (1.9)$$

The mole, n_i is termed a gmole, since it is an amount of substance in grams equal to the molecular weight. The product of mass and local gravitational acceleration is defined as a force. Weight is really correctly used only as a force. Therefore, the mass of a substance remains constant with elevation, but its weight varies with elevation.

1.3.2 Basics of Thermodynamics

Thermodynamics is the science of energy, the transformation of energy, and the accompanying change in the state of matter. Thermodynamics may be studied from either a microscopic or macroscopic point of view. The first view considers matter to be composed of molecules and concerns itself with the actions of these individual molecules. The second view is concerned with the effect of the action of many molecules, and considers the average properties of a very large number of molecules. Moreover, thermodynamics is a physical theory of great generality affecting practically every phase of human experience. It is based on two concepts, energy and entropy and the principles are the first and second law of thermodynamics.

In elementary treatments of thermodynamics, one is introduced to eight fundamental thermodynamic variables. These are: *pressure*, *temperature*, *volume*, *internal energy* U , *entropy* S , *enthalpy* $H = U + PV$, *Helmholtz free energy* or work function $W_F = U - TS$, and *Gibbs free energy*, $G_F = H - TS = U + PV - TS$

The first five of these variables are fundamentals to the subject, while the last three are defined for operational convenience. The first two are intensive variables, that is, are independent of the quantity of material under consideration. The numerical values of the last six are proportional to the quantity of material under consideration and are therefore called extensive variables [9].

For an ideal gas, the determination of the properties of internal energy, enthalpy, specific heat, and entropy is greatly simplified.

If P and T are taken to be appropriate independent thermodynamic variables, then it is important to determine the different values associated with a change from thermodynamic state to another, such as $U_2(P_2, T_2) - U_1(P_1, T_1)$ and on the absolute value of either U_1 or U_2 .

The *first law of thermodynamics* is a statement of conservation of energy, and in a closed system, the first law may be written as:

$$U_2 - U_1 = Q - W \quad (1.10)$$

where Q is the heat added to the system and W is the work performed on the surroundings. If the process that is used to go from state 1 to state 2 is a reversible process such that a thermodynamic state can be defined for the system during every step of the process, then Eq. 1.10 may be written as:

$$dU = \delta Q_{\text{rev}} - \delta W$$

where the two differentials on the right-hand side indicate that they are path dependent differentials, and the integral form of this equation gives the change of the *internal energy* such as:

$$U_2 - U_1 = \int_1^2 \delta Q_{\text{rev}} - \int_1^2 \delta W \quad (1.11)$$

For compressible PV work on the system, then Eq. 1.11 may be written as:

$$dU = \delta Q_{\text{rev}} - PdV \quad (1.12)$$

where V is the volume of the system and PV path, as well as, δQ term must be known to determine $U_2 - U_1$. All substances have heat capacities, however, because of their innate compressibility, gases have heat capacities that are path dependent.

Two heat capacities are usually defined for a gas. These are the heat capacity when heat is added at constant pressure, $C_p = (\delta H/\delta T)_p$, or at constant volume, $C_v = (\delta U/\delta T)_v$, when heat is added at constant volume. Since the internal energy for an ideal gas is not a function of volume, then the specific heat at constant volume may be written as:

$$C_v = dU/dT \quad \text{or} \quad dU = C_v dT \quad (1.13)$$

At constant pressure a portion of the heat energy added to a gas is used to perform work on the surroundings, as the gas increases its volume against the constant counter-pressure, therefore the *enthalpy* is defined as:

$$H = U + PV = U + RT \quad (1.14)$$

By differentiating Eq. 1.14 and substituting Eq. 1.12, dH is obtained as:

$$dH = \delta Q_{\text{rev}} \quad (\text{for constant } P) \quad (1.15)$$

Since the enthalpy of an ideal gas is a function of the temperature only, and is independent of pressure, the *specific heat at constant pressure* is:

$$C_p = (dH/dT)_p \quad \text{or} \quad dH = C_p dT \quad (1.16)$$

Thus, enthalpy is the natural variable to use when describing a constant pressure process or when defining C_p . From Eqs. 1.13, 1.14 and 1.16, we can obtain the following relation for an ideal gas:

$$dH = dU + RdT \quad \text{and} \quad C_p dT = C_v dT + RdT \quad \text{or} \quad C_p - C_v = R \quad (1.17)$$

The unique feature of Eq. 1.17 is that, whereas C_p and C_v are functions of temperature, $C_p - C_v$ is a constant. For an ideal gas it is convenient to define a *heat capacity ratio* $k(T) = C_p/C_v$, which is a function of temperature only. The specific heat at constant pressure, C_p for different ideal gases is collected from different sources [12-21] and for essentially all purposes in combustion modeling, however, a relation between C_p and temperature for each chemical species is obtained by first order polynomial fits over 300 °K temperature ranges and this will be presented in section 1.4.2. (Eq. 1.39).

Entropy and the **second law of thermodynamics** are concepts related to reversibility. The entropy change for a system undergoing a reversible process is defined as:

$$S_2 - S_1 = \int_1^2 \frac{\delta Q_{\text{rev}}}{T} \quad (1.18)$$

Furthermore, it can be shown that for an isolated system $S_2 - S_1 = 0$ for a reversible process, while a positive value of $S_2 - S_1$ represents a spontaneous process which is not reversible, and a negative value represents an unobservable process.

If the differential definition of entropy is substituted into the first law (Eq. 1.12), then the following expression is obtained:

$$dU = TdS - PdV \quad (1.19)$$

or

$$S_2 - S_1 = \int_1^2 \frac{dU}{T} + \int_1^2 \frac{PdV}{T} \quad (1.20)$$

or in terms of enthalpy, $dH = TdS + VdP$, or

$$S_2 - S_1 = \int_1^2 \frac{dH}{T} - \int_1^2 \frac{VdP}{T} \quad (1.21)$$

For constant C_p and ideal gas ($PV=RT$), Eq. 1.21 may be written in the form:

$$S_2 - S_1 = C_p \ln (T_2/T_1) - R \ln (P_2/P_1) \quad (1.22)$$

Equations 1.20 and 1.21 allow the calculation of the entropy change of any system once an equation of state is known for any ideal gas.

The last two of the eight thermodynamic variables are defined for operational convenience when dealing with questions of thermodynamic equilibrium. Thus the entropy argument, even though useful, may not be conveniently applied in a direct manner. This was first pointed out by Massieu in 1869 approximately forty years after the concept of entropy was first introduced by Clausius [22]. Massieu defined two new functions for discussing equilibrium in constant (P,T) and (V,T) systems. However it was Gibbs who first demonstrated the utility of the newly defined functions and extensively discussed their possible applications [9]. The Helmholtz free energy is useful for discussing equilibrium in a system held at constant volume and temperature and it may be written as:

$$\begin{aligned} dW_F &= dU - TdS - SdT \\ &= \delta Q - PdV - TdS - SdT \end{aligned} \quad (1.23)$$

For a process occurring at constant volume and temperature, this equation reduces to:

$$dW_F = \delta Q - TdS \quad (1.24)$$

However, since $dS = \delta Q_{rev}/T$ and $dS > \delta Q_{rev}/T$, this leads to $dW_F = 0$ for a reversible process and that W_F decreases for a spontaneous process occurring at constant volume and temperature.

Similarly, and at constant pressure and temperature;

$$\begin{aligned} dG_F &= dH - TdS - SdT \\ &= \delta Q - TdS \end{aligned} \quad (1.25)$$

This leads to $dG_F = 0$ for a reversible process and that G_F decreases for a spontaneous process at constant pressure and temperature. Thus, the state of minimum W_F (for V, T held constant) or minimum G_F (for P, T held constant) will be the thermodynamic equilibrium state of that system within the imposed constraints [9].

1.4 Combustion Stoichiometry and Thermochemical Calculations

1.4.1 Combustion Stoichiometry

The word stoichiometry is derived from the Greek “stoicheion”, meaning element. Most practical combustion processes occur when a fossil fuel or fossil-derived fuel burns with the oxidizer, air. The majority of these fuels contains only the elements carbon, hydrogen, oxygen, nitrogen, and sulfur. The aim of stoichiometry is to determine exactly how much air must be used to completely oxidize the fuel to the products carbon dioxide, water vapor, nitrogen, and sulfur dioxide. This does not imply that combustion is necessarily complete in any specific practical device. Nevertheless, a stoichiometrically correct mixture of fuel with air is defined as one that would yield exactly the products listed above and has no excess oxygen if combustion was complete. Figure 1.7 represents a combustion system with a complete combustion of methane with air (oxygen + nitrogen, as reactants), to form carbon dioxide, nitrogen and water (as products).

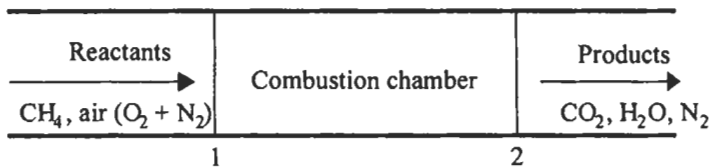
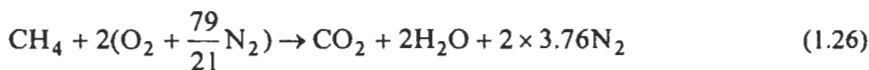


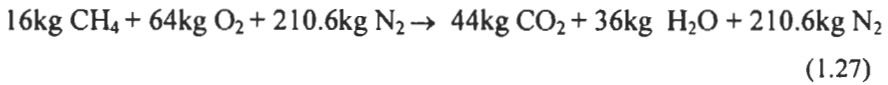
Fig. 1.7: Complete combustion for CH_4 and air.

Thus, a balanced stoichiometric relationship between methane (as fuel) and air (as oxidizer) with the assumption of complete combustion may be expressed by the equation:



This equation describes the breakdown of the bonds between the atoms (or elements) forming the molecules of methane and oxygen, and their re-arrangements to construct molecules of carbon dioxide and water. The chemistry would be unchanged by the inert diluent nitrogen. The coefficients in Eq. 1.26 are determined from considerations of atom conservation. The coefficients in Eq. 1.26 are for the chemically correct, or *stoichiometric*, proportions of reactants – with no excess fuel or oxidant. The coefficients in a chemical equation are more usually regarded as the number of kmoles of substance taking part in the reaction. Where all the substances taking part in a chemical reaction may be treated as ideal gases, the coefficients in the chemical equation may be alternatively considered as the volumetric proportions, since at a fixed temperature and pressure a kmole of any ideal gas will occupy the same volume.

Chemical equations may also be written in terms of masses taking part in the reaction, since a kmole of any substance contains a mass numerically equal its relative molecular mass, therefore Eq. 1.26 might be written as:



The stoichiometric air-methane ratio, AFR_v , by volume (Eq. 1.26) is:

$$\text{AFR}_v = \frac{2(1+3.76)}{1} = 9.52$$

while the stoichiometric air-methane ratio, AFR_m , by mass (Eq. 1.27) is:

$$\text{AFR}_m = \frac{2(32+105.3)}{1 \times 16} = 17.16$$

Non-stoichiometric mixtures. Having considered above, the complete combustion of stoichiometric mixtures, it is necessary now to describe the lean and rich mixtures. The terms lean (or weak) and rich are used where, respectively, oxidant and fuel are available in excess of their stoichiometric proportions. It is possible to have complete combustion to CO_2 and H_2O with a lean mixture, and the excess oxygen appearing on the product side of the chemical equation. It is however, impossible to have complete combustion of a rich mixture, and the product composition is then indeterminate without further information – this will be considered later. A departure from stoichiometric proportions may be described by a number of terms:

i) **Equivalence ratio ϕ and mixture strength, MS.** The equivalence ratio, ϕ , is defined as the ratio of fuel/air available to that required for the stoichiometric quantity of oxidant, i.e.:

$$\phi = \frac{(\text{Fuel/Air})_{\text{actual}}}{(\text{Fuel/Air})_{\text{stoich}}} \quad \text{or} \quad \frac{(\text{FAR})_{\text{actual}}}{(\text{FAR})_{\text{stoich}}} \quad (1.28)$$

With this definition, mixtures with $\phi < 1$ are called fuel-lean, while mixtures in which $\phi > 1$ are called fuel-rich. Moreover, the mixture strength, MS, is in fact the equivalence ratio expressed as a percentage and is often used in reciprocating combustion engines work.

ii) **Relative air-fuel ratio and percent theoretical air.** The relative air-fuel ratio is often called the oxidizer equivalence ratio, and is defined as the actual AFR_{actual} divided by the stoichiometric AFR_{stoich} , i.e. $1 / \phi$. Also, the percent theoretical air is defined as:

$$\text{Percent theoretical air} = 100 / \phi \quad (1.29)$$

iii) **Percentage excess air EA.** This term most usually employed to describe lean or weak mixtures in engine and boiler technology and is defined as:

$$\frac{AFR_{\text{actual}} - AFR_{\text{stoich}}}{AFR_{\text{stoich}}} \times 100\% \quad (1.30)$$

$$EA = \frac{100\%}{\phi} - 100\% = \frac{(1 - \phi)}{\phi} \times 100\% \quad \text{or} \quad \frac{(100 - MS)}{MS} \%$$

Excess air is sometimes employed to ensure complete combustion or to reduce the product temperature. Furthermore, Eqs. 1.29 and 1.30 are commonly used to specify the composition of a combustible mixture relative to the stoichiometric composition.

iv) **Limits of flammability.** Flammability limits bracket the rich-to-lean fuel-air mixture range beyond which fuel-air can not burn after an ignition source is removed, even if the mixture is at its ignition temperature. Some values of lean $(\phi)_L$ and rich $(\phi)_R$ flammability limits for some fuels are given in Table B4 (b) (Appendix B). These values are shown as equivalence ratio, ϕ $((\text{fuel}/\text{air})_{L,R}/(\text{fuel}/\text{air})_{st})$, where $(\text{fuel}/\text{air})_{L,R}$ is the lean or rich limit of fuel to air ratio, and $(\text{fuel}/\text{air})_{st}$ is the stoichiometric ratio.

1.4.2 Thermochemical Calculations

Section 1.4.1 presents the most important fundamental changes that must be followed during a combustion process, which is the change in the thermodynamic state of the system. This section discusses further information on the thermochemical properties of combustion gases including:

- (i) The chemical internal energy, enthalpy, and entropy change for a specific reaction occurring at constant temperature.
- (ii) The physical (sensible) internal energy, enthalpy, and entropy change when the temperature of some reactant or product mixtures is changed without the occurrence of chemical reaction.

Enthalpy and Enthalpy of Formation

Normally in classical thermodynamics, the internal energy and enthalpy of a pure substance (of invariable chemical composition) are defined with respect to some relatively arbitrary datum. Where combustion occurs, it is necessary to define the datum more closely.

Consider for example the situation where carbon and oxygen, supplied at 25 °C and

1 bar, Fig. 1.8, are burned at constant pressure to form carbon dioxide, and assume that the energy liberated is transferred to the surroundings such that the burned gas is also at 25°C. The First Law of Thermodynamics, in the form of steady flow energy equation (in the absence of work, kinetic, and potential energy terms) may be applied to the burner in order to determine the magnitude of the heat transfer:

$$Q = \sum n_p H_p - \sum n_r H_r \quad (1.31)$$

where n is the number of kmoles of substance, H is the enthalpy per kmole of substance, suffices r and p refer to reactants and products respectively.

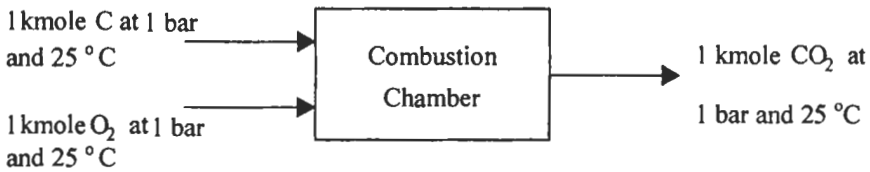


Fig. 1.8: Energy of formation.

Now if the usual temperature datum for gaseous enthalpies are to be adopted (i.e. $H = 0$ at 25°C), then the enthalpies of both reactants and the products would be zero. Eq. 1.31 would then suggest a zero heat transfer. This is clearly not so, experiment shows that for every kmole of carbon consumed there would be a heat transfer of $-393,522$ kJ. The negative sign results from the adoption of the usual heat transfer sign convention, with the heat transfer in fact occurring from the system for this particular *exothermic* reaction. A positive sign would have indicated an *endothermic* reaction; one which absorbs energy.

However, the heat transfer Q gives a measure of the enthalpy of the compound product molecule (CO_2) relative to that of the elements from which it is formed (C , O_2), at a pressure of 1 bar and a temperature of 25°C. Thus if a datum of 1 bar and 25°C is adopted for all elements, the magnitude of the heat transfer per kmole of the compound product molecule may be defined as the *enthalpy of formation* H_f° of that molecule from its elements at the standard state conditions, i.e. for CO_2 , $H_f^\circ = -393,522$ kJ/kmole. The enthalpies of formation of a number of substances are given in Table 1.3.

Hence, in general, the enthalpy of any chemical substance at pressure P and temperature T becomes:

$$H_{P,T} = H_f^\circ + H_{PT/298}^\circ \quad (1.32)$$

where $H_{PT/298}^\circ$ is the more familiar enthalpy of the substance measured from the datum of 25°C and 1 bar. Hereafter, for convenience, the pressure suffices will be omitted as the enthalpies are essentially independent of pressure for normal combustion conditions, and the T suffix will be omitted from the $H_{P,T}$ term. The values of $H_{T/298}^\circ$ may be found in tables of fluid properties or may be calculated using appropriate specific heat data. In combustion work the JANAF compilations [13], are often used.

Table 1.3: Enthalpy of formation, H_f° , Gibbs of formation, G_f° , and absolute Entropy, S° at 298 K and 1 bar (N.B.S = 0 at 0 K, $\bar{R} = 8.3143 \text{ kJ kmol}^{-1} \text{ K}^{-1}$).

ubstance	M	H_f° kJ kmol ⁻¹	G_f° kJ kmol ⁻¹	S° kJ kmol ⁻¹ K ⁻¹
C (graphite)	12.011	0, by definition	0, by definition	5.795
O ₂	31.999			205.142
H ₂	2.016			130.684
N ₂	28.013			191.611
CO	28.011	-110,529	-137,150	197.653
CO ₂	44.011	-393,522	-394,374	213.795
H ₂ O (vap.)	18.015	-241,827	-228,583	188.833
H ₂ O (liq.)	18.015	-285,838	-237,178	70.049
OH	17.007	39,463	34,755	183.703
O	16.000	249,195	231,756	161.060
H	1.008	217,986	203,264	114.718
NO	30.006	90,592	86,899	210.761
NO ₂	46.005	33,723	51,909	239.953
N	14.007	472,646	455,503	153.302

These data, derived for a pressure of 1 bar, use the notation ($H^\circ - H_{298}^\circ$) in place of $H_{T/298}^\circ$. The superscript^o indicates that data are for the standard pressure of 1 bar.

For inter-conversion between enthalpy and temperature, it is necessary in most of the combustion modeling to provide the program with polynomial coefficients which allow molar enthalpies, H_{P,T_i} of the pure components, i , to be expressed as functions of temperature (see chapter 2). However, in the one-dimensional kinetic model developed by Dixon-Lewis, Bradley, Habik, and El-Sherif [15-21], the molar enthalpy of component i is expressed as:

$$H_{P,T_i} = a_{i,0} + a_{i,1}T + a_{i,2}T^2 \quad \text{kJ/kmole} \quad (1.33)$$

where, $a_{i,0}$, $a_{i,1}$ and $a_{i,2}$ are constants and given in Appendix C, Table C1. The values of H_{P,T_i} for different species, i , and at different temperatures (300 – 3000K) were taken from Refs. 12 and 13 and were fitted by Dixon-Lewis et al [15-21] using second order polynomial equation (Eq. 1.33) over 300 K temperature ranges. In terms of the temperature and unit mass, the specific enthalpy of the mixture can be expressed as:

$$h_{P,T_i} = \sum_{i=1}^N \sigma_i (a_{i,0} + a_{i,1}T + a_{i,2}T^2) \quad \text{kJ/kg} \quad (1.33')$$

In an N-component system, $\sigma_i = w_i / M_i$, where w_i and M_i are the mass fraction and molecular weight of species i , respectively. If Eq. 1.33 is of order greater than three (such as 7-term NASA polynomial [12]), then solving this equation for the temperature has to be done numerically. As an alternative, Eq. 1.33 which is equivalent to the equations given in Ref. 12, can be replaced by a quadratic form valid for a small range of T near that estimated for the grid point as described in chapter 2. In general the

7-term NASA polynomial which represents thermodynamic data [12] has widespread use, for example, STANJAN and Sandia software packages [23].

As an illustration of the use of Fig. 1.9, consider the adiabatic constant pressure complete combustion of hydrogen and oxygen (at an initial temperature of 400 K and 1 bar) to form steam. Since there is no heat loss from the system, the energy released in the chemical reaction is absorbed by the product molecules; heating them until they attain the *adiabatic flame temperature*, T_{ad} , where the enthalpy of the product just balances the enthalpy of the reactants plus the enthalpy of formation of the product.

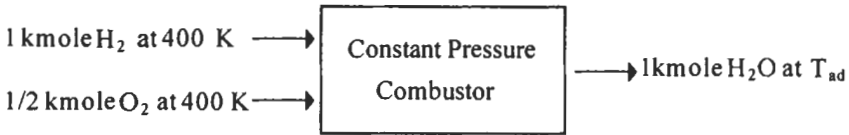


Fig. 1.9: Adiabatic flame temperature.

For such a system, enthalpy in = enthalpy out

$$\text{i.e. } H_r = H_p \tag{1.34a}$$

$$1(H_f^\circ + H_{400/298}^\circ)_{H_2} + \frac{1}{2}(H_f^\circ + H_{400/298}^\circ)_{O_2} = 1(H_f^\circ + H_{T/298}^\circ)_{H_2O} \tag{1.34b}$$

or using the data of Table C1 (Appendix C):

$$\underbrace{1(0 + 2940)}_a + \underbrace{\frac{1}{2}(0 + 3039)}_b = 1(-242838 + H_{T/298}^\circ)_c \tag{1.35}$$

hence $(H_{T/298}^\circ)_{H_2O} = 248817 \text{ kJ/kmol}$, and thus by interpolation in (higher temperature range) Table C1 and using of Eq. 1.33, then $T_{ad} = 5005 \text{ K}$. (In practice at such a temperature a certain amount of dissociation of the product would occur, and this matter will be considered later). The solution is shown graphically in Fig 1.10.

Note that the H-T curve for H_2O is that for an ideal gas. The constant pressure specific heat at any temperature is of course given by the gradient of the curve at that temperature, since $C_p = (dH/dT)_p$. If the gas had been a perfect one, the curve would have been a straight line (constant specific heat), and similarly the curve for the reactants is that for a non-reacting mixture. The step change in enthalpy between the two curves at the standard state temperature represents the enthalpy of formation of H_2O from O_2 and H_2 at 25 oC. The energy of the reactants, together with that released in the chemical reaction, are used to heat up the product molecules until they reach a temperature T, where $|a| + |b| = |c|$ (see Fig. 1.10). Note that the diagram seems to be in contradiction with Eq. 1.34, where $a = b + c$. The apparent anomaly is a function of the sign convention since the enthalpy of formation (b) is negative for this

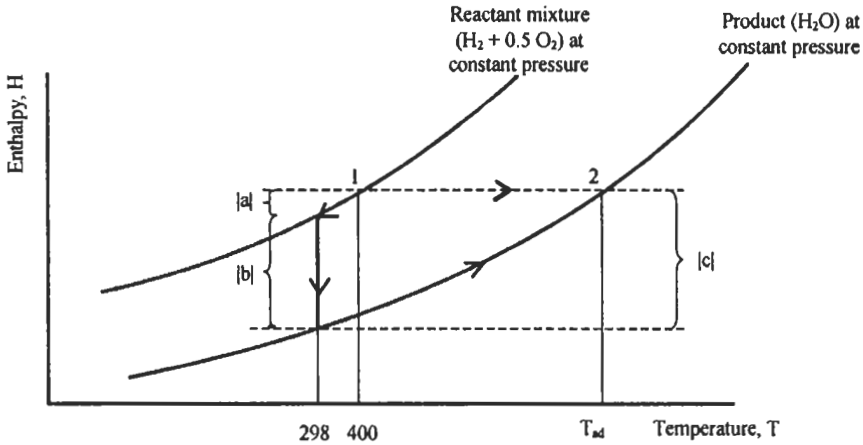


Fig. 1.10: Calculation of adiabatic flame temperature.

(exothermic) reaction. In calculations it is always safest to obey the sign convention and to allow the directions to take care of themselves. When looking at H-T diagrams, in order to appreciate better what is happening in a process, consider magnitudes, e.g., |a| etc.

Internal Energy

Just as the enthalpy of a chemical substance is given by Eq. 1.32, so too the internal energy may be written as:

$$U_{P,T} = H_{P,T} - PV = (H_f^0 + H_{PT/298}) - PV \tag{1.36}$$

, and for an ideal gas $PV = RT$, hence:

$$U_{P,T} = H_f^0 + H_{PT/298} - RT \tag{1.37}$$

Therefore, the internal energy values can be calculated from Eq. 1.37 with the same procedure described above to calculate the enthalpy.

Entropy

In combustion work, one may usually assume ideal gas behavior; for such a gas the entropy of Eq. 1.22 may be written as:

$$S - S^0 = \int_{T_0}^T (C_p / T) dT - R \ln(P / P_0) \tag{1.38a}$$

Thus, unlike enthalpy, entropy is both temperature and pressure dependent. Since the temperature in Eq. 1.38 (a) is the absolute temperature it is useful to adopt a zero Kelvin

datum for entropy rather than the 298 K datum used for enthalpy. The datum pressure is usually the same standard state pressure as used for enthalpy, i.e. $P_o = 1$ bar. Entropy values at the standard state pressure (signified by S°) are readily available in Table C2 (Appendix C) for common gases. Note that the entropy S at any other pressure P is related to the tabulated standard state entropy S° (at the same temperature) by:

$$S = S^\circ - R \ln (P/P_o) \quad (1.38b)$$

As it was shown before, in section 1.3.2, the values of C_p for different gases is fitted by first order polynomial fits over 300 K temperature range as:

$$C_{pi}(T) = a_{i,0} + a_{i,1}T \quad (1.39)$$

C_p in J/kmole °K, $a_{i,0}$ and $a_{i,1}$ are constants and tabulated in Table C3 (Appendix C).

1.5 Chemical Kinetics and Equilibrium

The dynamic study of molecular chemistry, or chemical kinetics, includes kinetic theory of gases, quantum chemistry, and elementary reactions and reaction rate theory.

1.5.1 Kinetic Theory of Gases

A simple model for the microscopic matter in the gas phase developed by using kinetic theory assumes that [6]:

- Matter exists as discrete particles or molecules.
- Molecules can be treated ideally as small spheres of diameter S_i .
- Mean distance between molecules $\gg S_i$.
- Molecules are in continuous three-dimensional motion.
- Each molecule moves in a random direction through space at a different speed.
- No appreciable inter-atomic forces exist between gas molecules except when they collide.
- Speed and directional characteristics for any molecule will remain constant until it interacts with another particle or a solid boundary.

Kinetic theory of gases provides both scientists and engineers with useful molecular descriptions of important ideal-gas mixture properties, including density, pressure, temperature, and internal energy. Density, or mass per unit volume, is simply the total molecular mass associated with molecules contained within a given space divided by that same volume.

Since the direction and speed of any particular molecule will be changing with time, all molecules do not move at the same velocity U . It is more appropriate then to describe molecular motion in terms of a statistical speed distribution function Ψ , developed by Maxwell in 1860 and given as [6]:

$$\Psi < U > = 4\pi \left[\frac{m}{2\pi kT} \right]^{\frac{3}{2}} U^2 \exp \left\{ \frac{-mU^2}{2kT} \right\} \quad (1.40)$$

where

m = molecular mass = M/N_o , g mole/molecule.

M = molecular weight.

U = molecular speed, cm s^{-1} .

N_o = Avogadro's constant = 6.023×10^{23} molecules/mole.

κ = Boltzmann's constant = 1.3804×10^{-16} g $\text{cm}^2\text{s}^{-2}\text{K}^{-1}$.

(i.e. Universal gas constant per molecule).

$\bar{R} = \kappa N_o$, where \bar{R} is the molar universal gas constant for all substances.

The most probable speed, the velocity magnitude associated with the maximum of the Maxwell distribution function, is found to be equaled to:

$$U_{mP} = \sqrt{2\kappa T / m} \quad \text{cm s}^{-1} \quad (1.41)$$

;while mean speed for all molecules is:

$$U_m = \sqrt{\frac{8\kappa T}{\pi m}} \quad \text{or} \quad \sqrt{\frac{8\bar{R}T}{\pi M}} \quad \text{cm s}^{-1} \quad (1.42)$$

For a single A molecule moving through the differential volume at a mean speed U_m , the volume swept out per unit time by this molecule would be equaled to:

$$\pi S_i^2 U_m = \pi S_i^2 \left[\frac{8\kappa T}{\pi m} \right]^{\frac{1}{2}} \quad \text{cm}^3 \text{ s}^{-1} \quad (1.43)$$

The ideal number of molecular collisions of an A molecule per unit time with all other A molecules in this swept volume is (No. A collisions):

$$S_i^2 \left[\frac{8\pi\kappa T}{m} \right]^{\frac{1}{2}} [A] \quad \text{collisions s}^{-1} \quad (1.44a)$$

where, $[A]$ is the molar concentration of A (i.e. number of molecules per unit volume). Also the number of molecular collisions per unit area may be calculated by [6, 9]:

$$Z_A = \frac{1}{4} U_m [A] \quad (1.44b)$$

Thereafter, the total frequency of collisions, Z_{AA} between all molecules of A is given by:

$$Z_{AA} = [A][A] S_i^2 \left[\frac{8\pi\kappa T}{m} \right]^{\frac{1}{2}} \quad (1.45)$$

The average transit distance between collisions is called the *mean free path*. Since a

molecule moving at a velocity U_m suffers $\pi Si^2 U_m [A]$ (collisions s^{-1}), then the mean free path is:

$$B_L = \frac{U_m}{\pi Si^2 U_m [A]} = \frac{1}{\pi Si^2 [A]}$$

If one assumes hard spheres with a Maxwell distribution, this equation becomes:

$$B_L = \frac{1}{\sqrt{2} \pi Si^2 [A]} \quad (1.46)$$

Values of Si for different chemical species are given in section 1.6.

1.5.2 Chemical Kinetics

Chemical kinetics is the study of the rate and mechanism by which one chemical species is converted to another. In order to provide the basic background needed to appreciate the valuable presentation of chapter 2, it is necessary to introduce some languages of chemical kinetics. First, some basic terms: *a chemical reaction* is the conversion of one kind of matter into another chemically different form; *a combustion reaction* is a chemical reaction in which a fuel combines with an oxidizer (usually oxygen from air) to form *combustion products*. Combustion reactions are described by writing chemical symbols for the starting materials, the *reactants*, and the final *products* connected by an arrow that means, "react with one another to form". Thus, for the combustion of methane in air, the combustion reaction is:



where, the stoichiometric coefficients 2, 1, and 2 denote the number of moles of oxygen, carbon dioxide, and water, respectively, that participates in the combustion of one mole of methane.

At the molecular level, a similar form of expression is used to describe molecular events that are responsible for the observed changes. For an example, the attack of hydrogen atoms on oxygen molecules to form hydroxyl radicals and oxygen atoms is:



Chemical transformations that are also real molecular events are called *elementary reactions or elementary steps*.

Combustion reactions occur because large numbers of different elementary reactions combine to produce the transformation of fuel and oxidizer to combustion products as described in the chemical equation.

The whole set of elementary reactions is called the *reaction mechanism*. In summary, combustion reactions can be described at the molecular level by giving the

elementary reactions that comprise the combustion mechanism of the fuel of interest. Determining the mechanism of a reaction is a very difficult task, and may require the work of many investigators over a period of many years. In chapter 2, there are some selections of elementary reactions that one can assemble into a mechanism for the combustion of hydrogen, carbon-monoxide, methane, natural gas, methanol-air mixtures and different practical high hydrocarbon fuels. The overall reaction proceeds via the highly reactive intermediates, the *radicals* O, OH and H reactants in which one radical creates two or more further radicals (e.g. $\text{H} + \text{O}_2 \rightarrow \text{OH} + \text{O}$) are termed *chain branching*. These reactions which result in the net disappearance of radicals (e.g. $\text{H} + \text{OH} + \text{M} \rightarrow \text{H}_2\text{O} + \text{M}$) are termed *chain termination*. Intermediate in character are *chain propagation reactions* (e.g. $\text{OH} + \text{H} \rightarrow \text{H}_2\text{O} + \text{H}$). The termination reactions are all *termolecular* in that a third body, M, is required to remove the energy released in combination.

1.5.3 Reaction Kinetics

It involves knowing how fast each elementary reaction proceeds. In chemical kinetics one defines the *rate* as the mass in moles, of a product produced or reactant consumed, per unit time; thus for the elementary reaction $\text{H} + \text{O}_2 \rightarrow \text{OH} + \text{O}$ the increases in the concentrations of OH and O per unit time due to this reaction would be a measure of its reaction rate. Since the concentrations of H and O₂ are decreased as a result of this reaction, their concentration changes attributable to this reaction would be multiplied by (-1) to get the rate.

Elementary reactions may proceed in either direction; thus an encounter between OH and O may lead to the formation of H and O₂ in what is called a *reverse reaction*. The *net rate*, R_n of an elementary reaction is taken as the difference between the forward and reverse rate:

$$R_n = \text{forward rate} - \text{reverse rate} \quad (1.49)$$

At any time, the net rate must be either positive or negative. As termination reactions are less frequent than bimolecular ones, but are important in chain termination and energy releases, the composition of a reacting system changes in time, and it is possible that the direction of net reaction changes. For purposes of modeling combustion reactions, as will be described in chapter 2, the two opposing directions are considered separately.

The higher the concentrations of the reacting molecules, the faster the reaction will proceed. Since the rate in either direction is proportional to the concentration of each of the reactant molecules, a *mass action rate* law connects the rate of reaction to the reactant concentrations. Thus for the $\text{H} + \text{O}_2 \rightarrow \text{OH} + \text{O}$ elementary reaction, the forward and reverse rates may be written as:

$$\text{forward rate} = k_f [\text{H}] [\text{O}_2]$$

$$\text{reverse rate} = k_r [\text{OH}] [\text{O}]$$

$$R_n = k_f [\text{H}] [\text{O}_2] - k_r [\text{OH}] [\text{O}]$$

$$\text{or } d[\text{OH}] / dt = d[\text{H}][\text{O}_2] / dt - d[\text{OH}][\text{O}] / dt \quad (1.50)$$

where, the proportionality constants k_f and k_r are called the *rate coefficients, rate parameters or rate constants in the forward and reverse directions*, and the brackets are used to denote concentrations. This rate is expressed as a function of temperature in the form of the Arrhenius expression:

$$k = A \exp(-E/RT) \quad (1.51)$$

where, A is constant and E is the activation energy (see also chapter 2). More details about derivation of k will be given below.

The molecularity of a reaction is defined as the number of atoms or molecules taking part in each act leading to the chemical reaction. Elementary reactions like the one above in which there are two reactant molecules (where atoms and radicals also count as molecules) are called *bimolecular* elementary reaction. In combustion reactions, there are also *unimolecular* elementary reactions such as:



for which the forward rate is given by:

$$\text{forward rate} = k_f [\text{C}_3\text{H}_8] \quad (1.52b)$$

and *termolecular* elementary reaction such as:



for which the forward rate is given by:

$$\text{forward rate} = k_f [\text{H}] [\text{CO}] [\text{H}_2\text{O}] \quad (1.53b)$$

It is often convenient to classify reactions by their order rather than molecularity. The *order of a reaction* is the number of atoms or molecules whose concentrations determine the rate of the reaction. Rate coefficient of k_f and k_r for different elementary reactions involved in the combustion of different fuels are given in chapter 2.

The relation of Eq. 1.51 can be derived on the basis of collision theory described above in section 1.5.1, where E may be regarded as a necessary minimum energy at collision for the reaction to occur, Figs 1.11 (a) & (b).

The pre-exponential factor A in the Eq. 1.51 is termed the *Arrhenius constant* or *frequency factor*. Both E and A are constant for any given reaction. Thus it can be seen from Fig. 1.11(c) that as T tends to zero, so also does k. Then as T increases there is a sharp rate of increase of k, which rate then begins to decrease until as T tends to infinity so k approaches A. The values of A and E may be found by measuring k at a number of temperatures and plotting them as shown in Fig.1.11 (c). For a simple reaction a straight line should result, the gradient of that gives the value of E/R with the intercept giving the value of ln(A).

Several theoretical models have been proposed to predict the observed behavior of an elemental rate constant k (in Eq. 1.51), including collision theory, statistical

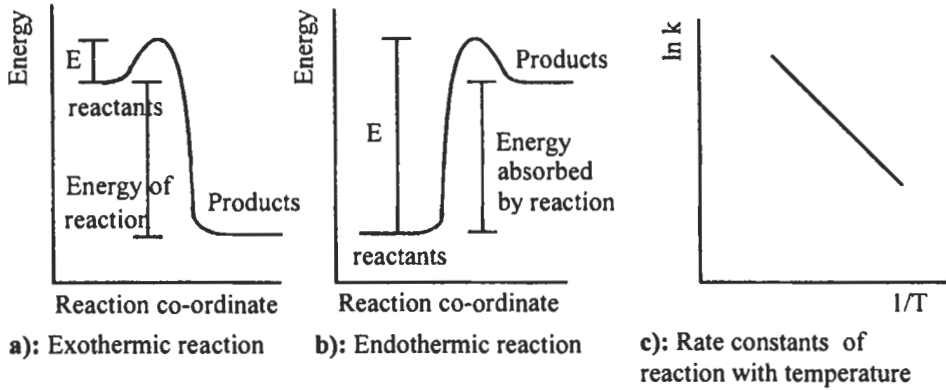


Fig. 1.11: Activation energy and rate constants .

thermodynamics, and quantum mechanics. Recall from section 1.5.1 that the frequency of collisions between two species A and B equals:

$$Z_{A-B} = S_{A-B}^2 \left\{ 8\pi k N_o T \left[\frac{m_A + m_B}{m_A m_B} \right] \right\}^{\frac{1}{2}} [A][B] \quad (1.54)$$

where S_{A-B} is the average collision diameter $(S_A + S_B)/2$, and Z_{A-B} may be written as follows:

$$Z_{A-B} = Z'_{A-B} [A][B] \quad (1.55)$$

Thus the Arrhenius form for the rate is:

$$R_A = Z'_{A-B} [A][B] \exp(-E/RT) \quad (1.56)$$

When compared to the reaction rate written from the law of mass action, the result is found as [24]:

$$k = Z'_{A-B} \exp(-E/RT) = Z''_{A-B} T^{0.5} \exp(-E/RT) \quad (1.57)$$

Thus, the important conclusion is that the specific reaction rate constant is dependent on the temperature alone. Actually, when complex molecules are reacting, not every collision has the proper steric orientation for the specified reaction to take place. Thus k can be written as:

$$k = Z''_{A-B} T^{0.5} \exp(-E/RT) f \quad (1.57')$$

where, f is an experimentally determined steric factor, which can be a very small number. Most generally the Arrhenius form of the reaction rate is written as in Eq. 1.51, where the constant A takes into account the collision terms, the mild temperature

dependence, and the steric factor. This form of expression (Eq. 1.51) holds well for most reactions, shows an increase of k with T , and permits convenient straight line correlation of data on a $\ln k$ versus $(1/T)$ as shown in Fig. 1.11 (c).

An alternate derivation for k is based on the concept of an intermediate state, often called a *transition or activated state*, which is a postulate of the transition-state theory. In this theory reaction is still presumed to occur as a result of collisions between reacting molecules, but what happens after collision is examined in more detail. This examination is based on the concept that molecules possess vibrational and rotational, as well as, translational, energy levels.

The essential postulate is that an activated complex (or transition state) is formed from the reactants, and that this subsequently decomposes to the products. The activated complex is assumed to be in thermodynamic equilibrium with the reactants. Then, the rate-controlling step is the decomposition of the activated complex. The concept of an equilibrium activation step followed by slow decomposition is equivalent to assuming a time lag between activation and decomposition into the reaction products. It is the answer proposed by the theory to the question of why all collisions are not effective in producing a reaction [25]. Suppose that the product C of the reaction,



is formed by decomposition of an activated form of reactants A and B , which will be designated $(AB)^*$. Then the reaction occurs by two elementary steps,



If the first step is comparatively rapid in both forward and reverse directions, $(AB)^*$ will be in equilibrium with A and B so that its concentration is given by:

$$C_{AB^*} = K^* C_A C_B \quad (1.61)$$

where K^* is the equilibrium constant for the formation of $(AB)^*$. The rate of reaction (rate of formation of C) is then given by the rate of the first-order decomposition step. With Eq. 1.61, this may be expressed as:

$$R_C = k^* C_{AB^*} = k^* K^* C_A C_B \quad (1.62)$$

For an elementary reaction whose rates are rapid enough to achieve a dynamic equilibrium the van't Hoff equation states that:

$$d \ln K/dT = \Delta H^0/RT^2 \quad (1.63)$$

If we integrate the van't Hoff equation, (Eq. 1.63), replacing K with K^* and ΔH^0 with ΔH^* , the result is:

$$K^* = I \exp^{(-\Delta H^*/RT)} \quad (1.64)$$

where, I is the constant of integration. Combining Eqs. 1.62 and 1.64 gives:

$$R_C = k^* I e^{-\Delta H^*/RT} C_A C_B \quad (1.65)$$

Comparison with Eq. 1.51 shows that:

$$k = A e^{-\Delta H^*/RT} \quad (1.66)$$

where, $A = k^*I$. Equation 1.66 is also of the form of the Arrhenius equation.

Since ΔH^* is the energy required to form the activated state $(AB)^*$ from A and B, $e^{-\Delta H^*/RT}$ is the *Boltzmann expression* for the fraction of molecules having an energy ΔH^* in excess of the average energy. This gives some meaning to the activation energy E in the Arrhenius equation, and this value is the energy barrier that must be overcome to form $(AB)^*$, and ultimately, product C.

Comprehensive reviews of data of those rate constants which are important in combustion have been prepared by several investigators [26 – 30].

1.5.4 Chemical Equilibrium

A system is said to be in equilibrium when there is no tendency for spontaneous change in its state with respect to time. In the post flame zone, many of the combustion products are in chemical equilibrium or possibly shifting equilibrium. The following will discuss the basic equations of chemical equilibrium as well as the equilibrium program to calculate the adiabatic temperature and compositions.

Basic Equations

It has been noted that chemical reactions such as that given by:



proceed in the forward and reverse directions concurrently. When the forward and reverse rates are in balance, i.e. the concentrations of the constituents are constant with zero net rates of species formation or destruction, the reaction is said to be in a state of *chemical equilibrium*.

$$\text{i.e. } R_f = \left[\frac{-1}{a} \frac{d[A]}{dt} \right]_f = R_r = \left[\frac{1}{a} \frac{d[A]}{dt} \right]_r \quad (1.68)$$

$$\text{or } k_f [A]_e^a [B]_e^b = k_r [Y]_e^y [Z]_e^z \quad (1.69)$$

where, the suffix e denotes the equilibrium concentration. Thus, at equilibrium:

$$\frac{[Y]_e^y [Z]_e^z}{[A]_e^a [B]_e^b} = \left[\frac{k_f}{k_r} \right] = K_n \quad (1.70)$$

where, K_n , the *equilibrium constant*, varies with temperature as do the rate constants. Note that since $(a+b)$ is not necessarily equal to $(y+z)$ in Eq. 1.70, the equilibrium constant is not necessarily dimensionless, thus the suffix n is employed to indicate its definition in terms of molar densities.

The concept of an equilibrium constant may alternatively be derived from the Second Law of Thermodynamics as described in section 1.3.2. For constant temperature and total pressure of the mixture a consequence of the Second Law of Thermodynamics is that equilibrium will pertain where the value of Gibbs Function (G_F) for the mixture is a minimum [31], however, G_F may be written in the form of Gibbs Molar Function G_i and number of moles n_i for species i .

$$G_F = \sum_i n_i G_i = \sum_i n_i (H_i - TS_i) \quad (1.71)$$

Consider for example the mixture of the substances A, B, Z and Y may react according to the chemical Eq. 1.67.

Therefore at equilibrium, G_F is:

$$yG_Y + zG_Z - aG_A - bG_B = 0 \quad (1.72)$$

where, at a temperature T :

$$G_i = H_i - TS_i \quad (1.73)$$

For an ideal gas at a constant temperature, the entropy (S_i) at a pressure (P_i) is related to the absolute entropy (S_i^0) at the standard state pressure (P) by Eq. 1.38 (b), and by combining Eqs. 1.38b and 1.73:

$$\begin{aligned} G_i &= H_i - T S_i^0 + RT \ln (P_i/P_0) \\ &= G_i^0 + RT \ln (P_i/P_0) \end{aligned} \quad (1.74)$$

where, G_i^0 is the value of the Gibbs molar free energy at the standard state pressure (P_0) at the temperature concerned. The value of S_i^0 may be found from a relation similar to that for enthalpy, Eq. 1.32, viz.:

$$G_i^0 = G_f^0 + G_{T/298}^0 \quad (1.75)$$

where G_f^0 is the Gibbs free energy of formation of a compound from its constituent elements at the standard pressure and temperature (the value of G_f^0 for an element being zero by definition), and $G_{T/298}^0$ is the difference in Gibbs free energy between its values at the temperature T and 298 K, at the standard pressure.

Combining Eqs. 1.72 and 1.74 gives:

$$yG_Y^0 + zG_Z^0 - aG_A^0 - bG_B^0 = -\bar{R}T \left[y \ln(P_Y/P_0) + z \ln(P_Z/P_0) - a \ln(P_A/P_0) - b \ln(P_B/P_0) \right]$$

or

$$\frac{(P_Y)^y (P_Z)^z}{(P_A)^a (P_B)^b} \left[\frac{1}{P_0} \right]^{(y+z-a-b)} = \exp \left\{ \frac{-\Delta G_{FT}^0}{\bar{R}T} \right\} = K \quad (1.76)$$

where, ΔG_{FT}^0 is the change in Gibbs function for the reaction given by Eq. 1.67 proceeding completely from left to right, with the reactants are initially separated and each is at a temperature T at the standard state pressure and the products are similarly being finally separated and each is at a temperature T at the standard pressure (note also that $\Delta G_{FT}^0 = \Delta H_T^0 - T\Delta S^0$). ΔG_{FT}^0 is written as a molar quantity, since (for example) its value for $\text{CO} + \frac{1}{2} \text{O}_2 \rightarrow \text{CO}_2$ would differ from that for $2\text{CO} + \text{O}_2 \rightarrow 2\text{CO}_2$, thus values of ΔG_{FT}^0 and K should always be considered in conjunction with their particular chemical equation. K is an equilibrium constant analogous to that given by Eq. 1.70. In Eq. 1.76 the relative proportions are expressed in terms of partial pressures instead of molar concentrations. Since the value of K is dependent on the standard state pressure, the P_0 term in Eq. 1.76 is often incorporated into the R.H.S:

$$\frac{(P_Y)^y (P_Z)^z}{(P_A)^a (P_B)^b} = P_0^{(y+z-a-b)} K = K_p \quad (1.77)$$

where, K_p has dimensions of (pressure) $^{(y+z-a-b)}$. Thus when using tabulated values of K_p , care should be taken that the units used for partial pressure in Eq. 1.77 should be the same as those assumed in compiling the values of K_p .

Note that where the products may all be considered to be ideal gases, one may write (see section 1.3.1):

$$\frac{P_i}{P_e} = \frac{n_i}{\sum n_i} = X_i \quad (1.78)$$

where, P_e is the total system pressure, $\sum n_i$ is the total number of kmols of product and X_i is the mole fraction of species i . The equilibrium condition may then be expressed as:

$$\frac{(X_Y)^y (X_Z)^z}{(X_A)^a (X_B)^b} \left[\frac{P_e}{P_0} \right]^{(y+z-a-b)} = K \quad (1.79)$$

$$\text{or } \frac{(n_Y)^y (n_Z)^z}{(n_A)^a (n_B)^b} \left[\frac{P_e}{P_0} \frac{1}{\sum n} \right]^{(y+z-a-b)} = K \quad (1.80)$$

Comparing Eqs. 1.70, 1.77 and 1.80, then:

$$K_n = K_p \left[\frac{1}{RT} \right]^{(y+z-a-b)} = K \left[\frac{P_o}{RT} \right]^{(y+z-a-b)}$$

Fortunately in many important reactions, $(y+z) = (a+b)$ and then $K_n = K_p = K$.

In combustion modeling, it is necessary to calculate the equilibrium constant, K , from a polynomial equation. Therefore, the equilibrium constant values were taken from JANAF Tables [13] and fitted by Agrawal and Gupta [32] with the following general form:

For the temperature range, 1600-4000 K:

$$\begin{aligned} \log_{10}K = & A_1 + A_2(T-1600)10^{-3} + A_3(T-1600)(T-2000)10^{-6} + \\ & A_4(T-1600)(T-2000)(T-2400)10^{-9} + \\ & A_5(T-1600)(T-2000)(T-2400)(T-2800)10^{-12} + \\ & A_6(T-1600)(T-2000)(T-2400)(T-2800)(T-3200)10^{-15} + \\ & A_7(T-1600)(T-2000)(T-2400)(T-2800)(T-3200)(T-3600)10^{-18} \end{aligned}$$

For the temperature range 4000-6000 K:

$$\begin{aligned} \log_{10}K = & A_8 + A_9(T-4000)10^{-3} + A_{10}(T-4000)(T-4500)10^{-6} + \\ & A_{11}(T-4000)(T-4500)(T-5000)10^{-9} + \\ & A_{12}(T-4000)(T-4500)(T-5000)(T-5500)10^{-12} \end{aligned} \quad (1.81)$$

The values of the coefficients $A_1 - A_{12}$ are given in the Table C4 (Appendix C) for different reactions. These equations are used in the calculation of the equilibrium adiabatic flame temperature and composition, as will be described in the next section.

Equilibrium Modeling

The equilibrium constant, K (described above), together with elementary atom balance considerations can be used to determine the equilibrium composition for a simple chemical reaction at known temperature and pressure. In section 1.4.2 it was shown that the adiabatic flame temperature could be calculated for a completed simple chemical reaction, on the basis of the First Law of Thermodynamics. In much the same way, the corresponding chemical equilibrium adiabatic flame temperature for a more complex mixture can be calculated by using the First Law in conjunction with the solution of the equilibrium composition equations.

However, the problem in determining the adiabatic flame temperature, T_{ad} , for known reactants (Eq. 1.67), is that the product composition is itself a function of T_{ad} . This necessitates an iterative solution whereby one uses an initial temperature "guestimate" (T) to determine the equilibrium composition as described in section 1.4.2. Using this composition, a check can be made for the equivalence of H_p and H_r (see Eq. 1.34a), leading to successively refined estimates of T_{ad} . Therefore, for complex

hydrocarbon reactions it is sensible to computerize the solution procedure. For such programs the specific heat, enthalpy, and equilibrium constant data are readily available in the form of polynomials in temperature such as in Eqs. 1.33, 1.39 and 1.81. There are some available computer programs to calculate the equilibrium adiabatic temperature and composition [33 – 36]. NASA-Lewis CEC code [33] was the first program of this type to be published in its entirety, and this is followed by a less general program published by Olikara and Borman [34], and the maximum temperature from their program was 4000 K with twelve product species.

Harker and Allen [35] have also presented computer programs for constant pressure combustion calculations in C-H-O-N and C-H-O systems, assuming the equilibrium products to be consisting of ten species in the former system, and eight species in the latter. These programs can be used for final temperatures in the range 1500-4000 K. Moreover, Miller and McConnel [36] have published a computer flow chart for constant pressure combustion calculations in C-H-O-N systems assuming the products to be consisting of the same ten species as assumed by Harker [37]. For constant volume combustion calculations in C-H-O-N systems, Agrawal et al [38] have presented a computer program assuming twelve product species; their program is applicable for temperatures up to 3400 K. Also, Agrawal and Gupta [39] have presented a computer program to calculate the equilibrium composition and final temperature with eighteen product species. Sheppard [40] has presented a computer program for constant pressure and volume combustion in hydrocarbon-air and oxygen systems with eleven product species. The program is applicable for temperatures up to 3500 K and is limited to certain ranges of hydrocarbon fuels. Dixon-Lewis and Greenberg [41] also presented a computer program for the calculation of high temperature equilibrium, partial equilibrium, and quasi-steady state properties in C-H-O-N systems. Furthermore, a new simple formula for calculating the adiabatic flame temperature of fuel-air mixture has been developed by Rhee and Chang [42]. The formula is functionally expressed in terms of the fuel-air ratio, the reaction pressure, the initial temperature, and the number of carbon atoms in the individual fuel.

The STANJAN program [23] uses the element potential approach to solve chemical equilibrium problems. In this program the user selects the species to be included in each phase of the system, sets the atomic populations and two thermodynamic state parameters, and then executes the program.

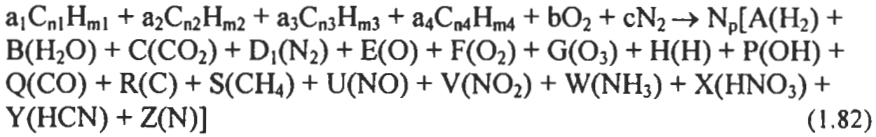
Equilibrium Composition and Temperature

This section presents briefly two computer programs, one was developed by Habik [43] and another was developed by Reynolds [23].

The computer program that was developed by Habik [43] could be used to calculate the equilibrium composition and final state of the products after either constant pressure or constant volume combustion in a mixture of four fuels, C_nH_m , with any proportion of O_2 and N_2 systems; whereas n and m may have any value ≥ 0 [44,45], and one mole of fuel(s) was assumed. Eighteen product species (CO_2 , CO , O_2 , H_2O , H_2 , OH , H , O , N_2 , NO , NO_2 , O_3 , HNO_3 , HCN , CH_4 , C , NH_3 and N) have been considered. These species are similar to those in Ref. 39. The program computes the gas constant of the mixture and the product, as well as, total moles of product, and it is valid for a final temperature of up to 6000 K. The following presents the main equations and solution methods used in the above described program.

Conservation, Energy and Equilibrium Equations

For combustion calculations, if it is assumed that the product consists of eighteen chemical species, then the reaction equation for four hydrocarbon mixture fuels with air may be written as:



where, A, B, C, D₁, E...etc. are the mole fractions of products, N_p is the total number of moles of product, and a, b, c, n, m can take any value.

From the balance of atoms on both sides in Eq. 1.82, the following equations can be obtained:

$$ATOMC/N_p = C+Q+R+S+Y \quad (1.83)$$

$$ATOMH/N_p = 2A+2B+H+P+4S+3W+X+Y \quad (1.84)$$

$$ATOMO/N_p = 2C+Q+B+3X+3G+2F+E+P+2V+U \quad (1.85)$$

$$ATOMN/N_p = 2D_1+U+V+W+X+Y+Z \quad (1.86)$$

The system of equations is as follows:

i) **Mass conservation equations.** From Eqs. 1.82 to 1.86, the followings are obtained:

$$RCO(2C+Q+B+3X+3G+2F+E+P+2V+U) = C+Q+R+S+Y \quad (1.87)$$

$$RHO(2C+Q+B+3X+3G+2F+E+P+2V+U) = 2A+2B+H+P+4S+3W+X+Y \quad (1.88)$$

$$RNO(2C+Q+B+3X+3G+2F+E+P+2V+W) = 2D_1+U+V+W+Y+X+Y+Z \quad (1.89)$$

$$ATOMC+ATOMH+\frac{ATOMO}{\phi} + \frac{ATOMN}{\phi} = N_p[(E+H+R+Z)+ 2(A+D_1+F+P+Q+U)+3(B+C+G+V+Y)+4W+5(S+X)] \quad (1.90)$$

Equation 1.90 represents the conservation of the total number of atoms from reactants to products.

ii) **Concentration conditions.** Let the summation of mole fractions at equilibrium equals unity, then:

$$A+B+C+D_1+E+F+G+H+P+Q+R+S+U+V+W+X+Y+Z=1 \quad (1.91)$$

iii) **Chemical equilibrium equations.** The following equations are considered.

Fourteen chemical equilibrium equations were used in the above-described program, and the values of equilibrium constants (K_1 to K_{14}) for these equations were calculated from Eq. 1.81. The values of A_1 to A_{12} for Eq. 1.81 are given in Table C4 (Appendix C).

iv) **Adiabatic energy conservation for constant pressure P.** From the above discussion in section 1.4.2, it is shown that for an adiabatic process at constant pressure:

$$H_r = H_p \quad (\text{Eq. 1.34a})$$

where,

$$H_r = a_1(H_{f,298K} + \Delta H_{T/298}) + a_2(H_{f,298K} + \Delta H_{T/298}) + a_3(H_{f,298K} + \Delta H_{T/298}) + a_4(H_{f,298K} + \Delta H_{T/298}) + b(H_{f,298K} + \Delta H_{T/298}) + c(H_{f,298K} + \Delta H_{T/298}) \quad (1.92)$$

$$H_p = N_p[A(H_{f,A} + \Delta H_{T/298}) + B(H_{f,B} + \Delta H_{T/298}) + C(H_{f,C} + \Delta H_{T/298}) + D_1(H_{f,D_1} + \Delta H_{T/298}) + E(H_{f,E} + \Delta H_{T/298}) + F(H_{f,F} + \Delta H_{T/298}) + G(H_{f,G} + \Delta H_{T/298}) + H(H_{f,H} + \Delta H_{T/298}) + P(H_{f,P} + \Delta H_{T/298}) + Q(H_{f,Q} + \Delta H_{T/298}) + R(H_{f,R} + \Delta H_{T/298}) + S(H_{f,S} + \Delta H_{T/298}) + U(H_{f,U} + \Delta H_{T/298}) + V(H_{f,V} + \Delta H_{T/298}) + W(H_{f,W} + \Delta H_{T/298}) + X(H_{f,X} + \Delta H_{T/298}) + Y(H_{f,Y} + \Delta H_{T/298}) + Z(H_{f,Z} + \Delta H_{T/298})] \quad (1.93)$$

The above equations are solved simultaneously to determine the equilibrium temperature and composition of products.

v) **Constant volume calculations.** For constant volume combustion calculations it is more convenient to express the various equations in terms of moles rather than mole fractions. In Eqs. 1.87 to 1.89 this is easily done by replacing A, B, C, \dots etc. by $A \times N_p, B \times N_p, C \times N_p, \dots$ etc. Therefore, the equilibrium constant for chemical equation $\text{CO}_2 \leftrightarrow \text{CO} + 0.5 \text{O}_2$ (see Table C4, Appendix C) will be:

$$K_1 = \frac{n_{\text{CO}} n_{\text{O}_2}^{0.5}}{n_{\text{CO}_2}} \left(\frac{P_e}{N_p} \right)^{0.5} \quad (1.94)$$

$$\text{where, } \frac{P_e}{N_p} = \frac{T_{ad}}{T_i} \frac{P_i}{N_R}$$

Equations in Table C4 (Appendix C) are also transformed in the same manner. The energy conservation equation is:

$$E_p = E_r \quad (1.95)$$

where,

$$E_r = a_1(H_{f,298K} + \Delta H_{T/298}) + a_2(H_{f,298K} + \Delta H_{T/298}) + a_3(H_{f,298K} + \Delta H_{T/298}) + a_4(H_{f,298K} + \Delta H_{T/298}) + b(H_{f,298K} + \Delta H_{T/298}) + c(H_{f,298K} + \Delta H_{T/298}) - RT_i N_R$$

$$\text{and, } E_p = H_p - N_p \times RT$$

The above equations are solved in a similar way to that given by Kopa et al [46] and Agrawal and Gupta [39], and the method of solving Eqs. 1.34 (a) and 1.82 to 1.95, together with the data given in Table C4 (Appendix C) is given in Appendix D. Some output results from this model are compared with those in Refs. 39, 47 and 48, and the results from this equilibrium program are given in Tables D1 to D4 (Appendix D).

An alternative program of determining equilibria is that developed by Reynolds [23] and is based on minimization of free energy. In this program, species can be added or removed at will, according to the problem under investigation. This program is used by STANJAN and is included in the widely used CHEMKIN software, and it is freely available on the Internet [23].

For a mixture containing J atom types and I species, it can be shown [23] that minimizing G using J Lagrange multipliers, λ_j (which in this context are called *element potential*) results in the following equations that must be satisfied:

$$X_i = \frac{\exp \left[-\frac{G_i^0}{RT} + \sum_j \lambda_j n_{ji} \right]}{p/p_0} \quad (1.96)$$

$$\text{and } \sum_i X_i = 1$$

where X_i is the mole fraction of species i ($i = 1, \dots, I$), j = atom type, n_{ji} is the number of j atoms in species i , and the constraints of Eq. 1.38 (b) must be hold. The STANJAN program [23] uses this element potential approach to solve chemical equilibrium problems.

When solving for equilibrium products using Eq. 1.76, the reactions to be considered are identified, and the equilibrium constants are evaluated at the specified temperature. Then, the atom balance constraints are specified for the system and an equilibrium equation is written for each of the specified reactions using the form of Eq. 1.77. This set of equations is solved simultaneously to obtain the species mole fractions and other thermodynamic properties of the system.

1.6 Transport Phenomena, and Modeling

1.6.1 Real Gases

The ideal gas equations described before in section 1.3.1 are only valid for gases at low density and where the mean free path is very much larger than the diameter of a molecule. At higher densities and low temperatures, behavior of the gases may deviate substantially from the ideal gas equation of state, and in fact all real gases (or non-ideal gases) are observed to condense to the liquid state. For each gas there is a critical temperature T_c above which condensation does not occur. On the critical isotherm ($T = T_c$), one observes an inflection point at which $(\partial P/\partial V)_T = 0$ and $(\partial^2 P/\partial V^2)_T = 0$. This inflection point is called the critical point for the substance (see Fig.1.12). The volume

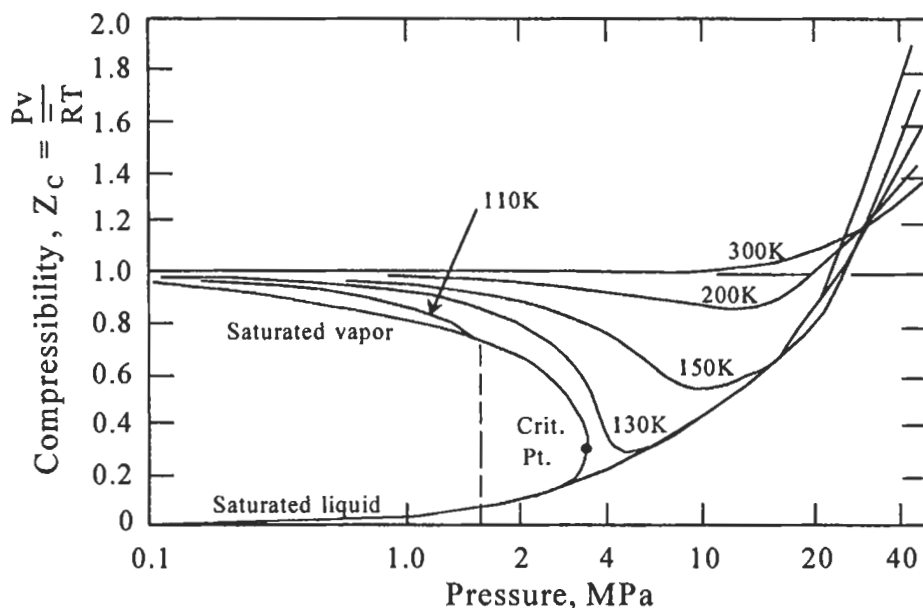


Fig. 1.12: Compressibility of nitrogen [49]. Reproduced by permission of John Wiley and Sons Inc.

and pressure at this point may be measured and are unique constants for each pure substance. At temperatures below the critical temperature, the gas is observed to condense when the pressure reaches its vapor pressure, and to continue to condense at this pressure as the volume is decreased until only the pure liquid phase is present. The principle of corresponding states has led to the development of graphical methods of determining the properties of non-ideal or real gases, and it introduces the concept of the compressibility factor, Z_c which is defined as:

$$Z_c = \frac{Pv}{RT} \quad (1.97)$$

For an ideal gas, $Z_c = 1$, and the deviation of Z_c from unity is a measure of the deviation of the actual relation from the ideal gas equation of state. Figure 1.12 shows a compressibility chart for nitrogen, and it is clear from the figure that, at all temperatures, $Z_c \rightarrow 1$ as $P \rightarrow 0$, this behavior closely approaches that predicted by the ideal gas equation of state. For a constant pressure of 4 MPa, and as we reduce the temperature below 300 K, the value of Z_c becomes less than unity and the actual density is greater than that would be predicted by the ideal gas behavior.

At this condition, the molecules are brought closer together and the attractive force between the molecules increases leading to an increase in the density. Figure 1.12 indicates that, at very low pressures, ideal gas behavior can be assumed with good accuracy [49], regardless of the temperature, while at temperatures that are double the critical temperature or above (the critical temperature of nitrogen is 126K) ideal gas

behavior can be assumed with good accuracy up to pressures of around 10 MPa. When the temperature is less than twice the critical temperature, and the pressure is above the ambient pressure, the deviation from ideal gas behavior may be considerable. In this region it is preferable to use the tables of thermodynamic properties or charts for a particular substance. The critical temperature, pressure and density for some gases are given in Table B1 (Appendix B).

In order to have an equation of state that accurately represents the P-v-T behavior for a particular gas over the entire superheated vapor range, more complicated equations of state have been developed for real gases. Some are empirical; others are deduced from the assumptions regarding molecular properties. Clausius first proposed that the volume term in an equation of state should be the net volume available to the molecules and, therefore, modified the ideal gas law to be:

$$P(v - b) = \bar{R}T \quad (1.98)$$

where b is an effective volume of one gram-mole of molecules. In 1873, van der Waals included a second correction term to account for intermolecular forces, based on the fact that molecules do not actually have to touch to exert forces on one another, and the van der Waals equation is written as:

$$\left(P + \frac{a}{v^2}\right)(v - b) = \bar{R}T \quad (1.99)$$

where P is the externally measured pressure, a is the intermolecular force-of-attraction term, and b is the volume of the molecule. The constant values of a and b are evaluated from experimental data and are listed in Table 1.4, for van der Waals constants [50].

Many other forms of equations of state have been proposed and are given in details with non-ideal gas behavior in Refs. 47, 49 and 50.

Table 1.4: Constants a and b for Eq. (1.99) [49]. Reproduced by permission of John Wiley and Sons Inc.

Gas	A	b
	$N\ m^4\ (kg\ mole)^{-2}$	$m^3\ (kg\ mole)^{-1}$
Air	137,052	0.0366
Ammonia	426,295	0.0373
Carbon dioxide	368,127	0.0428
Carbon monoxide	152,191	0.0400
Freon-12	1,082,470	0.0998
Helium	3,440	0.0232
Hydrogen	24,800	0.0266
Nitrogen	137,450	0.0387
Oxygen	139,044	0.0317
Water vapor	561,753	0.0317

1.6.2 Transport Phenomena of Gases at Low Density

There are three fundamental transport properties, one for each of the properties conserved in the three conservation equations of fluid dynamics. In fact, transport phenomena are only important when the solution to the conservation equations predicts that the fluid must support a large gradient in either concentration, velocity, or temperature. Under these conditions, mass transport, momentum transport, or energy transport will occur and the proportionality constants which relate the quantity transported to the gradient are called the *diffusion coefficient*, the *viscosity coefficient*, and the *coefficient of thermal conductivity*. These properties at low density are presented as follows.

Theory of Viscosity

The viscosity of gases at low density has been extensively studied, both experimentally and theoretically. To simplify the derivation of the viscosity from a molecular point of view, we consider a pure gas composed of rigid, non-attracting spherical molecules of diameter S_i and mass m , and present in a concentration of $[A]$ molecules per unit volume (see Eqs. 1.44 a and b).

Following the results of kinetic theory (section 1.5.1) for a rigid sphere dilute gas in which the temperature, pressure, and velocity gradients are small, Eqs. 1.42, 1.44(b) and 1.46 are used here in the derivation of the viscosity. To determine the viscosity of such a gas in terms of the molecular properties, we consider an imaginary plane in a gas at position y_0 normal to a velocity gradient (Fig. 1.13). Molecules are continually crossing this plane from above and below. The molecules reaching a plane have, on the average, had their last collision at a distance, a , from the plane where:

$$a = (2/3)B_L \tag{1.100}$$

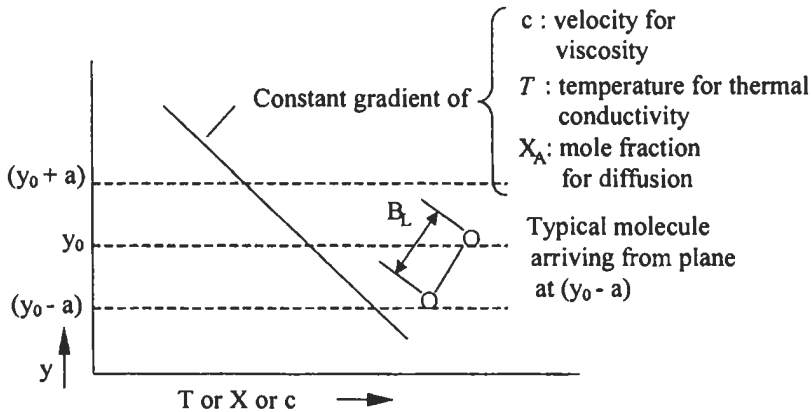


Fig. 1.13: Constant gradient assumed in the kinetic theory derivation of the transport properties, viscosity, thermal conductivity and ordinary diffusion [52]. Reproduced by permission of John Wiley and Sons Inc.

It is assumed that each molecule is carrying an x-momentum characteristic of the x-momentum in the plane of its last collision. The momentum flux across the plane [51] is:

$$\tau_y = Z_a mc|_{y-a} - Z_a mc|_{y+a} \quad (1.101)$$

Equation 1.101 is based on the assumption that all molecules have velocities representatives of the region of their last collision and that the velocity profile $c(y)$ is essentially linear for a distance of several mean free paths (B_L) as shown in Fig.1.13. Thus,

$$c|_{y-a} = c|_y - \frac{2}{3} B_L \frac{dc}{dy} \quad (1.102)$$

$$c|_{y+a} = c|_y + \frac{2}{3} B_L \frac{dc}{dy}$$

By combining Eqs. 1.44 (b), 1.101 and 1.102, then:

$$\tau_y = -\frac{1}{3}[A] m U_m B_L \frac{dc}{dy} \quad (1.103)$$

Equation 1.103 is corresponding to Newton's law of viscosity, therefore the viscosity η is given by:

$$\eta = \frac{1}{3}[A] m_0 U_m B_L = \frac{1}{3}\rho U_m B_L \quad (1.104)$$

This equation was obtained by Maxwell in 1860. By combining Eqs. 1.42, 1.46 and 1.104, then η is:

$$\eta = \frac{2}{3\pi^{3/2}} \frac{\sqrt{m\kappa T}}{S i^2} \quad (1.105)$$

where K is the Boltzmann constant.

The prediction of Eq. 1.105 that η is independent of pressure agrees well with the experimental data up to about 10 atm. [52], while the predicted temperature dependence is less satisfactory. To predict the temperature dependence of η accurately, one has to replace the rigid-sphere model by a more realistic molecular force field as will be discussed in the section 1.6.3.

Theory of Thermal Conductivity

The thermal conductivity of dilute mono-atomic gases is well understood and can be accurately predicted by kinetic theory. The assumptions and equations of kinetic theory described in section 1.5.1 are used here in the calculation of the thermal conductivity, λ .

To determine the thermal conductivity, we consider the behavior of the gas under a temperature gradient dT/dy (see Fig 1.13). The heat flux q_y across any plane of constant y is found by summing the kinetic energies of the molecules that cross the plane per unit time in the positive y -direction and subtracting the kinetic energies of the equal number that cross in the negative y -direction [52]:

$$q_y = Z_a \frac{1}{2} m U_m^2 |_{y-a} - Z_a \frac{1}{2} m U_m^2 |_{y+a} \quad (1.106)$$

The only form of energy that can be exchanged in collision by smooth rigid-sphere is translational energy; the mean translational energy per molecule under equilibrium conditions is:

$$\frac{1}{2} m U_m^2 = \frac{3}{2} kT \quad (1.107)$$

By combining Eqs. 1.106 and 1.107, then

$$q_y = \frac{3}{2} k Z_a (T |_{y-a} - T |_{y+a}) \quad (1.108)$$

Equations 1.106 and 1.108 are based on the assumption that all molecules have velocities representatives of the region of their last collision, and that the temperature profile $T(y)$ is essentially linear for a distance of several mean free paths. Thus;

$$\begin{aligned} T |_{y-a} &= T |_y - \frac{2}{3} B_L \frac{dT}{dy} \\ T |_{y+a} &= T |_y + \frac{2}{3} B_L \frac{dT}{dy} \end{aligned} \quad (1.109)$$

By combining Eqs. 1.44 (b), 1.108 and 1.109, we obtain:

$$q_y = -\frac{1}{2} [A] k U_m B_L \frac{dT}{dy} \quad (1.110)$$

This corresponds to Fourier's law of heat conduction, with the thermal conductivity given by:

$$\lambda = \frac{1}{2} [A] k U_m B_L = \frac{1}{3} \rho C_v U_m B_L \quad (1.111)$$

in which $\rho = [A] m$ is the mass density of the gas.

Evaluation of U_m and B_L from Eqs. 1.42 and 1.46 and using Eq. 1.111 gives the thermal conductivity of a mono-atomic gas as:

$$\lambda_m = \frac{1}{Si^2} \sqrt{\frac{\kappa^3 T}{\pi^3 m}} \quad (1.112)$$

This equation predicts that λ is independent of pressure and the predicted temperature dependence is too weak, just as it was for viscosity, but it is qualitatively correct.

Theory of Ordinary Diffusion

Diffusion of, A species in a binary system of A and B species occurs because of a concentration gradient of A. This phenomena is called *ordinary diffusion* to distinguish it from *pressured diffusion* (motion of A resulting from a pressure gradient), *thermal diffusion* (motion of A resulting from a thermal gradient), and *forced diffusion* (motion forces on A and B).

In this section, the mass diffusivity D_{AB} , for binary mixtures, and non-polar gases is predictable within about 5 percent error by kinetic theory. Here we begin with a simplified derivation to illustrate the mechanisms involved, and then in section 1.6.3, we will present the more accurate results of the Chapman-Enskog theory.

Consider a large body of gas containing two molecular species A and B, both species having the same mass m_A and the same size and shape. To determine the mass diffusivity D_{AB} in terms of the molecular properties, it is assumed that the molecules are rigid spheres of diameter Si_A . The equations of kinetic theory described in the above sections are used here in the calculation of the ordinary diffusion. To determine the diffusivity D_{AB} , we consider the motion of species A in the y-direction under a concentration gradient dX_A/dy (see Fig. 1.13), when the mixture moves at a finite velocity c_y throughout. The temperature T and total molar concentration ρ_m are assumed constant. The molar flux, N_{Ay} , of species A across any plane of constant y is found by counting the molecules of A that cross unit area of the plane in the positive y-direction and subtracting the number that crosses in the negative y-direction [52].

Thus,

$$N_{Ay} = \frac{1}{N_o} \left\{ [A]X_A c_y \Big|_y + \frac{1}{4} [A]X_A U_m \Big|_{y-a} - \frac{1}{4} [A]X_A U_m \Big|_{y+a} \right\} \quad (1.113)$$

With the assumption that the concentration profile $X_A(y)$ is linear (see Fig. 1.13) we may write:

$$X_A \Big|_{y-a} = X_A \Big|_y - \frac{2}{3} B_L \frac{dX_A}{dy} \quad (1.114)$$

$$X_A \Big|_{y+a} = X_A \Big|_y + \frac{2}{3} B_L \frac{dX_A}{dy} \quad (1.115)$$

By combining Eqs. 1.113 to 1.115 and noting that $c\rho_m = N_A + N_B$, we obtain:

$$N_{AY} = X_A(N_{AY} + N_{BY}) - \frac{1}{3}\rho_m U_m B_L \frac{dX_A}{dy} \quad (1.116)$$

where, c is molar average velocity.

This equation corresponds to the y -component of Fick's law with the following approximate value of D_{AB} :

$$D_{AB} = \frac{1}{3}U_m B_L \quad (1.117)$$

Evaluation of U_m and B_L from Eqs. 1.42 and 1.46 and the use of the ideal-gas law $P = \rho RT = [A] K T$, then Eq. 1.117 gives:

$$D_{AA^*} = \frac{2}{3} \left(\frac{\kappa^3}{\pi^3 m_A} \right)^{\frac{1}{2}} \frac{T^{\frac{3}{2}}}{P S i_A^2} \quad (1.118)$$

This equation represents the mass diffusivity of a mixture of two species of rigid spheres of identical mass and diameter. However, for rigid spheres of unequal mass and diameter, the calculated D_{AB} is [52]:

$$D_{AB} = \frac{2}{3} \left(\frac{\kappa^3}{\pi^3} \right)^{\frac{1}{2}} \left(\frac{1}{2m_A} + \frac{1}{2m_B} \right)^{\frac{1}{2}} \frac{T^{\frac{3}{2}}}{P \left(\frac{S i_A + S i_B}{2} \right)^2} \quad (1.119)$$

Equations 1.118 and 1.119 predict that the mass diffusivity varies inversely with pressure; this prediction agrees well with the experimental data up to about 10 atm for many gas mixtures, but the predicted temperature dependence is too weak.

The dimensional similarity of the above three transport properties suggests that their ratios may be used to define a set of convenient dimensionless parameters for discussing the properties of gases. These ratios are:

- 1) Prandtl number, Pr , defined as the ratio of the kinematic viscosity, ν , and the thermal diffusivity, α :

$$Pr = \frac{\nu}{\alpha} = \left(\frac{\eta}{\rho} \right) \left(\frac{\rho C_P}{\lambda} \right) = \frac{\eta C_P}{\lambda} \quad (1.120)$$

- 2) Schmidt number, Sc , defined as the ratio of kinematic viscosity and the self-diffusion coefficient:

$$Sc = \frac{\eta}{\rho D} \quad (1.121)$$

- 3) Lewis number, Le , defined as the thermal diffusivity and the self-diffusion coefficient:

$$Le = \frac{\lambda}{C_p \rho D} \quad (1.122)$$

Selected values of these ratios are given in Table B3 for different gases.

1.6.3 Transport Properties of Multi-Component Mixtures

The above described elementary treatment of transport adequately explains the gross behavior of the transport coefficients of dilute gases, but the results are not useful for estimating the transport coefficient of real gases with reasonable accuracy [22]. The more rigorous Chapman-Enskog theory of transport, however, yields reasonable accurate transport coefficients. It is based on the same hypothesis as the elementary theory, but it includes the effect of an assumed interaction potential during the molecular collision process. Thus, the more rigorous kinetic theory requires that an interaction potential be specified for each molecular encountered. A rigorous kinetic theory of mono-atomic gases at low density was developed before World War I by Chapman in England and independently by Enskog in Sweden [53]. The Chapman-Enskog theory gives expressions for the transport coefficients in terms of the *potential energy of interaction* between a pair of molecules in the gas. This potential energy φ is related to the force of the interaction F_f by the relation $F_f = -d\varphi/dr$, in which r is the distance between the molecules. Now, if one know exactly how the forces between molecules vary as a function of the distance between them, then one could substitute this information into the Chapman-Enskog formulas and calculate the transport coefficients.

The exact functional form of $\varphi(r)$ is not known; fortunately, however, a considerable amount of research has shown that a fairly good empirical potential energy function is the *Lennard-Jones (6-12) potential*:

$$\varphi(r) = 4\varepsilon \left[\left(\frac{S_i}{r} \right)^{12} - \left(\frac{S_i}{r} \right)^6 \right] \quad (1.123)$$

in which S_i is a characteristic diameter of the molecule (the "*collision diameter*") and ε is a characteristic energy of interaction between the molecules (the maximum energy of attraction between a pair of molecules). This function is shown in Fig.1.14, note that it displays the characteristic features of molecular interactions: weak attraction at large separations (very nearly proportional to r^{-6}) and strong repulsion at small separations (roughly proportional to r^{-12}). Equation 1.123 has been shown to be quite useful for many non-polar molecules. Values of S_i and ε are known for many substances; a partial list is given in Table E1, and another list is available in chapter 2. When values of S_i

and ϵ are not known, they may be estimated from the properties of the gas at the critical point (c), liquid at the normal boiling point (b), or the solid at the melting point (m), by means of the following empirical relations.

$$\epsilon / \kappa = 0.777T_c, \quad Si = 0.841 V_c^{\frac{1}{3}} \quad \text{or} \quad 2.44 \left(\frac{T_c}{P_c} \right)^{\frac{1}{3}} \quad (1.124)$$

$$\epsilon / \kappa = 1.15T_b, \quad Si = 1.166 V_{b,liq}^{\frac{1}{3}} \quad (1.125)$$

$$\epsilon / \kappa = 1.92T_m, \quad Si = 1.222 V_{m,sol}^{\frac{1}{3}} \quad (1.126)$$

in which ϵ/K and T are in K, Si is in Angström units, V is in $\text{cm}^3 \text{ g mole}^{-1}$, and P_c is in atmospheres. Between different molecules, the effective values for bimolecular collisions can be calculated by:

$$\epsilon_{12} = \sqrt{\epsilon_1 \epsilon_2} \quad Si_{1,2} = 0.5(Si_1 + Si_2), \quad (1.127)$$

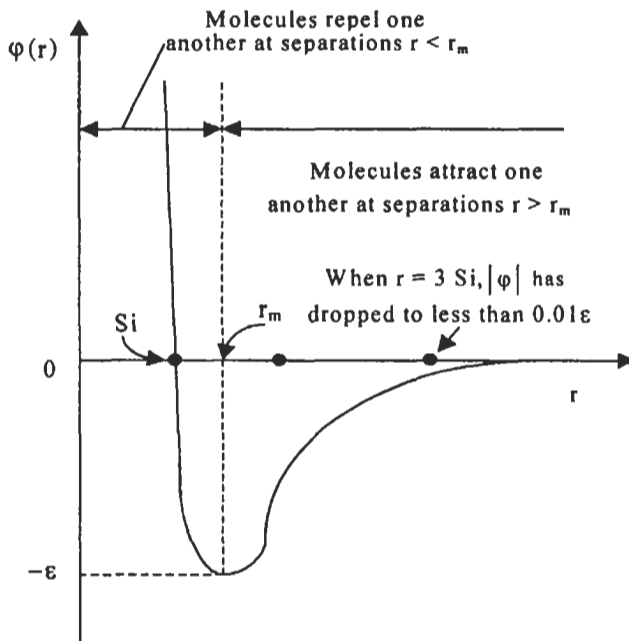


Fig. 1.14: Potential energy function describing the interaction of two spherical non-polar molecules. Equation 1.123 is one of the many empirical equations proposed for fitting this curve [52]. Reproduced by permission of John Wiley and Sons Inc.

To relate this to transport coefficients, it requires both the parameters and the collision integral Ω , which is a function of the temperature and ε/K parameter through a dimensionless function called “*reduced temperature*”, T^* , which is defined as:

$$T^* = \frac{T}{\varepsilon / K} \quad (1.128)$$

where T is the temperature, K , ε / K is the Lennard-Jones, LJ, well depth parameters which are determined by Ref. 54 and tabulated in Table E1. The values of Ω for viscosity are calculated by Ref. 55 from Chapman-Enskog theory, and tabulated in Table E2. Values of Ω_η is equal to those of Ω_λ for thermal conductivity, while Ω_D values are obtained by a slightly different averaging process and are tabulated in Table E2.

The “*collision integrals*” for the LJ potential can be approximated by the Nuffield-Jansen equation [56] to about 1 %.

$$\Omega_o = \frac{A}{T^*B} + \frac{C}{\exp(DT^*)} + \frac{E}{\exp(FT^*)} + \frac{G}{\exp(HT^*)} \quad (1.129)$$

where, T^* is $\kappa T / \varepsilon$, $A=1.06036$, $B=0.15610$, $C=0.19300$, $D=0.47635$, $E=1.03587$, $F=1.52996$, $G=1.76474$ and $H=3.89411$.

For the high-temperature regime of interest in flames, one can often use an approximation due to Westenberg (Eqs. 1.130 and 1.131) good to about 2% providing that T^* exceeds 3. This is usually the case in flames:

$$\Omega^{11} = 1.12 / (T^*)^{0.17} \quad (1.130)$$

$$\Omega^{22} = 1.23 / (T^*)^{0.17} \quad (1.131)$$

where Ω^{11} applies to diffusion and Ω^{22} applies to viscosity and thermal conduction. The coefficient of viscosity at absolute temperature T of a pure monatomic gas of molecular weight M may be written in terms of the parameters S_i and Ω_η as:

$$\eta = 2.6693 \times 10^{-5} \frac{\sqrt{MT}}{S_i^2 \Omega_\eta} \quad (1.132)$$

where η is in $\text{g cm}^{-1} \text{sec}^{-1}$, T in $^\circ\text{K}$, S_i in Å , and Ω_η is given in Table E2. Although this formula was derived for monatomic gases, it has been found to be remarkably good for polyatomic gases as well. If the gases were made up of rigid spheres of diameter S_i (instead of real molecules with attractive and repulsive forces), then Ω_η would be unity. Hence, the function Ω_η may be interpreted as giving the deviation from rigid sphere behavior. The Chapman-Enskog theory has been extended to include multi-component

gas mixtures at low density by Curtiss and Hirschfelder [57]. For most purposes, the semi-empirical formula of Wilke [58] is quite adequate:

$$\eta_{\text{mix}} = \sum_{i=1}^n \frac{X_i \eta_i}{X_i + \sum_{j=1}^n X_j \phi_{ij}} \quad (1.133)$$

$$\text{where, } \phi_{ij} = \frac{1}{\sqrt{8}} \left(1 + \frac{M_i}{M_j} \right)^{-\frac{1}{2}} \left[1 + \left(\frac{\eta_i}{\eta_j} \right)^{\frac{1}{2}} \left(\frac{M_j}{M_i} \right)^{\frac{1}{4}} \right]^2 \quad (1.134)$$

Here n is the number of chemical species in the mixture; X_i and X_j are the mole fractions of species i and j ; η_j η_i are the viscosities of species i and j at the system temperature and pressure; and M_i and M_j are the corresponding molecular weights. Note that ϕ_{ij} is dimensionless and, $\phi_{ij} = 1$ when $i=j$. Equation 1.133 has been shown to reproduce measured values of η_{mix} within an average deviation of about 2 percent. For a more accurate treatment of the monatomic gas and using the rigorous Chapman-Enskog theory, the thermal conductivity equation for monatomic gas will be:

$$\lambda = 8.322 \times 10^{-4} \frac{\sqrt{T/M}}{\text{Si}^2 \Omega_\lambda} \quad (1.135)$$

where $\lambda = \text{W cm}^{-1} \text{K}^{-1}$, Ω_λ and Si are given in Tables E1 and E2 (Appendix E).

The thermal conductivity of a mixture may be determined using an equation given by Mason and Saxena [59].

$$\lambda_{\text{mix}} = \sum_{i=1}^n \frac{X_i \lambda_i}{X_i + 1.065 \sum_{j=1}^n X_j \phi_{ij}} \quad (1.136)$$

Thermal diffusion is not normally considered in approximate treatments of reactive flows unless there are very large differences between the molecular weights of the participating species. However, thermal diffusion of hydrogen atoms can be very important in flames [15].

For accurate results of ordinary diffusion in gases and by using Chapman-Enskog Collision Integral $\Omega_{D_{AB}}$ then:

$$D_{AB} = \frac{2.2646 \times 10^{-5} \sqrt{T \left(\frac{1}{M_A} + \frac{1}{M_B} \right)}}{\rho \text{Si}_{AB}^2 \Omega_{D_{AB}}} \quad (1.137)$$

For ideal gas law, $\rho = \frac{P}{RT}$, then Eq. 1.137 becomes [52]:

$$D_{AB} = 0.0018583 \frac{\sqrt{T^3 \left(\frac{1}{M_A} + \frac{1}{M_B} \right)}}{P \text{Si}_{AB}^2 \Omega_{D_{AB}}} \quad (1.138)$$

where, $D_{AB} = \text{cm}^2 \text{s}^{-1}$, $\rho = \text{g - mole cm}^{-3}$, $T = \text{K}$, $P = 1 \text{ atm}$, $\text{Si}_{AB} = \overset{\circ}{\text{A}}$ units, and $\Omega_{D_{AB}}$ is given in Table E2. For rigid sphere, $\Omega_{D_{AB}}$ would be unity at all temperatures and a result analogous to Eq. 1.119 would be obtained. More details about the modification of the Chapman-Enskog procedure and the subsequent development are given by Dixon-Lewis [15].

1.6.4 Transport Modeling

It is clear from the above discussion that the Chapman-Enskog theory does not yield a simple analytic expression for the transport coefficients. For modeling purposes, it may be convenient to use the approximations: $\eta \propto T$, $\lambda \propto T$ and $D \propto P^{-1}T^2$, and with this approximation, the quantities $\lambda\rho$ and $\eta\rho$ are simple constants in a constant pressure system [14].

In many combustion processes, it is possible to avoid use of the cumbersome multi-component diffusion coefficients in the analysis of flame data by using the Stephen-Maxwell relation. This is the inverse of the generalized Fick equation for diffusion. This formulation is used in Dixon-Lewis's flame theory program [60]. In this method, the concentration gradient is expressed in terms of the ratios of fluxes to concentration and a group of matrices that are related to and as complex as the multi-component diffusion formulation. However, in kinetic flame model, Dixon-Lewis [61] had used rigorous transport formulation including thermal diffusion and more details are given by Dixon-Lewis [15]. Also, for extensive calculations there are a NASA program [62] and the CHEMKIN related program [63]. They can be used in computation on any mixture of species available in the JANAF species list [64].

1.7 Modeling in Combustion Chemistry

Chemistry is the most challenging aspects of calculations of reactive flows, laminar or turbulent. Chemistry is essential in calculating reaction flows, and at the same time it is the hardest part because usually chemistry introduces a large number of non-linear differential equations. With existing computational techniques and computer power, a balance has to be made between including detailed chemistry and complex flow patterns. One can either employ detailed chemistry in very simple flows, like calculations of one-dimensional laminar flames as described in details in chapter 2,

or include complex flows with very simple chemistry as described in chapter 5.

Because kinetic modeling has become an important tool for interpreting and understanding observed combustion phenomena; therefore, a large amount of effort has been done to the development of kinetic mechanisms for fuel combustion. Simplified descriptions of the chemistry, deduced from detailed mechanisms, are called reduced chemical-kinetic mechanisms.

In recent years, there are several review papers and articles for asymptotic analysis and modeling in combustion chemistry such as Dixon-Lewis [15, 65], Gardiner [12], Kee et al [66], Peters and Rogg [67], Seshardri [68], Miller [69], Patnaik et al [70], Fristrom [71], Leung and Lindstedt [72], Zuo and Bulck [73], Yang and Pope [74], Bozzelli and Dean [75], Dupont and Williams [76], Ref. [77], Westbrook and Dryer [78], Oran and Boris [79], and Warnatz [80].

The first quantitative treatments of flames that comprised the nineteenth century thermal theories were developed independently by Mallard and Le Chatelier in France, Haber in Germany, and Mikel'son in Russia (Evans [81]). The period that followed was dominated by a debate between those who believed that combustion was controlled by thermal conduction and those who believed that it was controlled by diffusion. The Russian school of Frank-Kamenetzki [82], Semenov [83], and Zeldovich [84] pointed out that for species of equal molecular weight and diameter the transport contributions were equal and opposite, and could be cancelled.

This is followed by a multi-component kinetic theory developed by Hirschfelder et al [85]. Furthermore, Spalding [86] developed a non stationary technique called the marching method, which was well adapted to computer simulation. Spalding and Stephenson [87] applied it to the hydrogen bromine flame. This was followed by a full synthetic model of the methane flame by Smoot et al [88].

In the late 1960's, Dixon-Lewis began his seminal studies of the hydrogen system, and extended it to carbon monoxide and methane flames. These studies (Dixon-Lewis [89 - 100]) laid the chemical kinetics group-work for the understanding of the general CH_2O flame system and oxygen. More details about kinetic modeling and extending the research in this field are given in chapter 2.

1.8 Combustion Generated Air Pollution

1.8.1 Background

The combustion of hydrocarbon fuel removes O_2 from the atmosphere and releases equivalent amount of H_2O and CO_2 always with trace amounts of numerous other compounds including hydrocarbons (CH_4 , C_2H_2 , C_2H_6 , C_2H_8 , C_6H_6 , CH_2 , CHO , ... etc.), carbon monoxide (CO), nitrogen oxides (NO , N_2O) and reduced nitrogen (NH_3 and HCN), sulfur gases (SO_2 , OCS , CS_2), halo-carbons (CHCl and CH_3Br), and particles. A review of the atmospheric budgets of these gases shows that burning of fossil fuels and recent biomass has led to global alternations in the composition of our atmosphere (Prather and Logan [101]).

Combustion is clearly responsible for most of the enhanced greenhouse forcing to date (through CO_2 , stratospheric O_3 , soot), and also some counteracting effects (through SO_2) and this is presented briefly in the following sections. It has had minimal impact

on stratospheric O_3 (through CH_3Cl , CH_3Br , CH_4), but has likely changed the stratospheric oxidant levels (through CO , NO_x , NMHC), at least over the Northern Hemisphere [101]

The definition of *pollution* is “the introduction by man into the environment of substances or energy liable to cause hazards to human health, harm to living resources and ecological system, damage to structures or amenity, or interference with legitimate uses of the environment” [102]. All pollution events have certain characteristics in common, and all involve (i) the pollutant, (ii) the source of the pollutant (such as combustion which is one of the subjects of this book), (iii) the transport medium (air, water or soil), and (iv) the target (the organisms), ecosystems or items of property affected by the pollutant. Holdgate [102] has divided the pollutants into two types: effect generating properties such as toxicity in living organisms or corrosion of metals, and pathway determining properties which determines the distance and the rate of dispersion of the pollutant in the environment. The air quality and air pollution are presented briefly in section 1.8.2. However, it is increasingly surprising just how resilient global environmental systems are to many of the pollutant burdens imposed upon them. Nevertheless, the instances where ‘chemical time bombs’ have had dramatic ecological effects, such as in the forests of Central Europe where many years of inputs of SO_2 and other atmospheric pollutants eventually led to a widespread die-back in conifers [103] should remind us that we cannot be complacent about environmental pollution. It is therefore, very important for as many people as possible to appreciate the extent of pollution, its causes, the substances involved, their biological and environmental effects, and methods of controlling and rectifying pollution. Legislation of air pollution is presented in sections 1.8.3.

1.8.2 Air Quality and Air Pollution

Air quality is affected by those things that are visible to the eye or under a microscope (dust, pollen, etc.) and those substances that are not (sulfur dioxide, ozone, etc.). Air pollutants in the atmosphere cause concern primarily because of their potential adverse effects on human health.

Air pollutants are either gaseous or particulate in form. Common gaseous pollutants are carbon monoxide, sulfur dioxide, nitrogen oxides, and ozone. Particulate matter can be made up of many different compounds including mineral, metallic, and organic compounds, and can be further differentiated by size (particles, aerosols, and fine particles). Table 1.5 lists the primary industrial air pollutants, with their principal sources. Figures 1.15 and 1.16 show the classification of air pollutants and their effects on human and environment. Another important distinction is the difference between primary and secondary air pollutants (see Fig. 1.15).

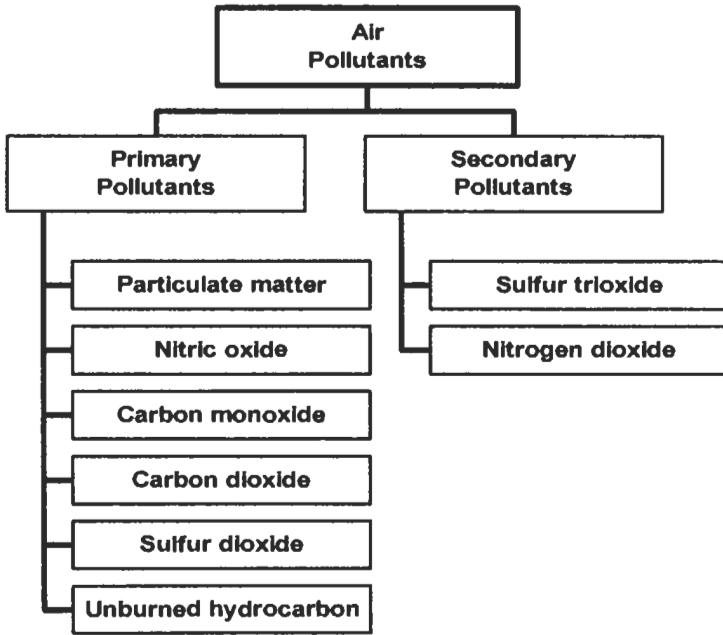
Primary pollutants are those that are directly emitted to the atmosphere. Common examples are carbon monoxide emitted from trucks and automobiles, and sulfur dioxide and nitrogen oxides emitted from factory and power plant smoke-stacks. Secondary pollutants, on the other hand, are formed as the result of chemical reactions with other constituents in the atmosphere. For example, one of the pollutants of most concern in urban areas is ozone. Ozone is a secondary pollutant formed from the photochemical reaction of volatile organic compounds and nitrogen oxides.

Table 1.5: Primary industrial air pollutants.

Air pollutant	Main characteristic	Principal sources	Principal health effects
Carbon monoxide (CO)	Colorless, odorless gas with strong affinity to hemoglobin in blood	Incomplete combustion of fuels and other carbonaceous materials	Absorbed by lungs; impairs physical and mental capacities; affects fetal development
Hydrocarbons (HC)	Organic compounds in gaseous or particulate form (such as methane, ethylene, acetylene); component in forming photochemical smog	Incomplete combustion of fuels and other carbon containing substances	Acute exposure causes eye, nose, and throat irritation; chronic exposure suspected to cause cancer
Lead (Pb)	Heavy, soft, malleable, gray metallic chemical element; often occurs as lead oxide aerosol or dust	Occupational exposure in nonferrous metal smelting, metal fabrication, battery making and from automobiles.	Enters primarily through respiratory tract and wall of digestive system; accumulates in body organs causing serious physical and mental impairment
Nitrogen oxides (NO _x)	Mixture of gases ranging from colorless to reddish brown	Stationary combustion (power plants), mobile sources and atmospheric reactions	Major role as component in creating photochemical smog; evidence linking respiratory problems and cardiovascular illnesses
Particulate matter	Any solid or liquid particles dispersed in the atmosphere, such as dust, ash, soot, metals, and various chemicals; often classified by diameter size-particles in microns, (>50 μm), aerosols <50 μm, particulate, <3 μm	Stationary combustion of solid fuels; industrial process such as cement and steel manufacturing	Toxic effects or aggravation of the effects of gaseous pollutants; aggravation of respiratory or cardio-respiratory symptoms
Sulfur dioxide (SO ₂)	Colorless gas with pungent odor; oxidizes to form sulfur trioxide (SO ₃) and sulfuric acid with water	Combustion of sulfur containing fossil fuels, smelting of sulfur-bearing metal ores, certain industrial processes	Classes as mild respiratory irritant; major cause of acid rain

Adapted from Baumol, W.J. and W.E. Oates. *Economics, Environmental Policy, and the Quality of Life*. Englewood Cliffs, N.J.: Prentice Hall, Inc., 1979

According to pollutant type



According to the degree of dangerous

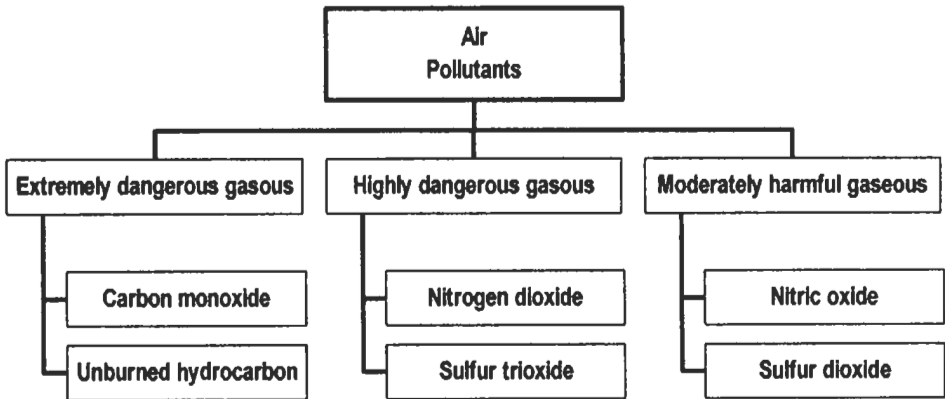


Fig. 1.15: Classification of air pollutants.

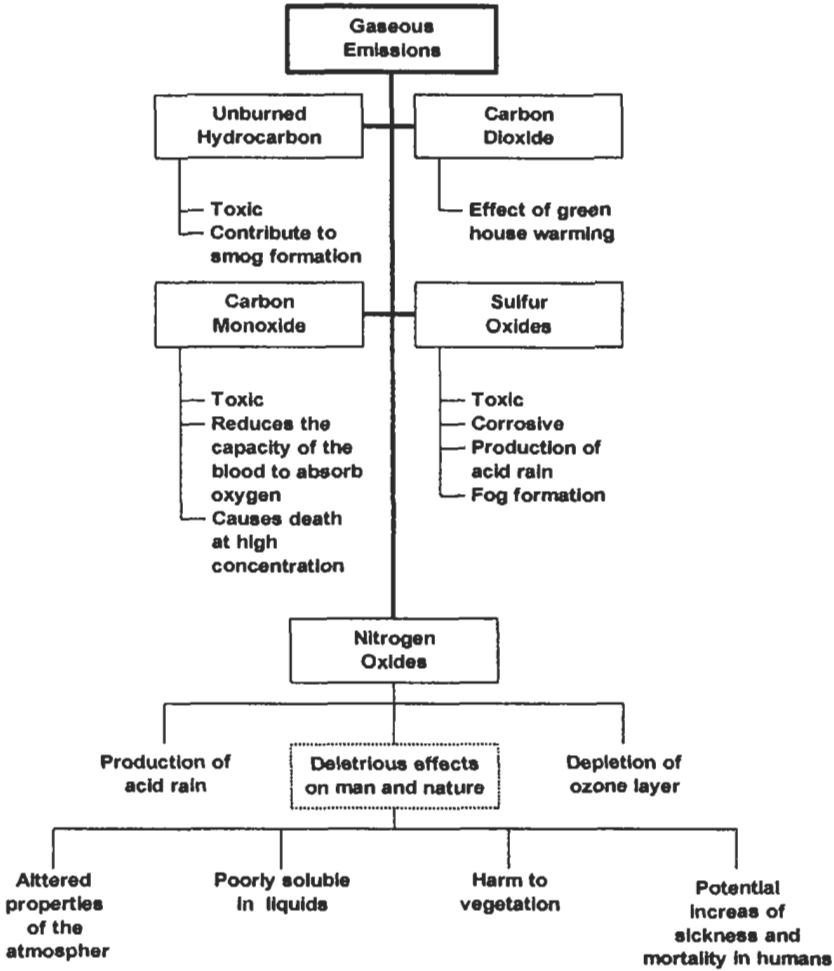


Fig. 1.16: Effect of emissions from combustion equipment on human and environment.

Industrial facilities are referred to as stationary sources of air pollution. Stationary sources can be further classified as either point sources or fugitive sources. Point sources are those that emit air pollutants through a confined vent or stack. The stack of a fossil fuel-fired boiler is a common example. Fugitive emissions, on the other hand, are those emissions that enter the atmosphere from an unconfined area such as leaking pipes, valves, and storage piles.

Stationary source emissions at industrial facilities can result from fuel combustion and various process operations, which is our concern in this book. Common industrial pollutants, depending on their concentrations, can have serious effects on human health and environmental quality. Lead emissions, for example, are linked to mental and physical impairments in children and adults. The impacts of industrial air pollutants are compounded by mobile-source emissions (automobile and truck exhaust). Modern

industrial facilities with significant emissions utilize control devices such as electrostatic precipitators, bag filters, and combustion control systems.

Table 1.6 represents the emissions estimated for the major man-made pollutants for the USA in 1991 [104]. It is clear from the table that some of the pollutants come mostly from transportation (motor vehicles) and others come mostly from industrial sources.

The air pollutant emission situation can be approximated [105], as follows, by :

$$\left(\begin{array}{c} \text{Air pollutant} \\ \text{emissions.} \\ \text{[Impact on environment]} \end{array} \right) = \left(\begin{array}{c} \text{Population economic} \\ \text{activity per person.} \\ \text{[Affluence]} \end{array} \right) \left(\begin{array}{c} \text{Pollutant emissions per} \\ \text{unit of economic activity.} \\ \text{[Technology]} \end{array} \right)$$

The larger the population, the greater the extent of environmental deterioration due to related needs for food production, living space, waste disposal, and communications.

1.8.3 Legislation of Air Pollution

Ultimately, it is concern for the effects of industrial pollution on public health and environmental quality that drives governments to regulate industrial activities, and industry to adopt environmental management practices.

Air pollution standards. The 1970, Clean Air Act Amendments was a major piece of legislation that in many respects first put teeth into air pollution control in the United States. The body of U.S. air pollution law is contained mostly in the Clean Air Act and the regulations (local, state and federal) that implement it. Table 1.7 lists the most

Table 1.6: National emissions estimates for 1991 (values in million ton/yr.) [104]. Reproduced by permission of McGraw-Hill Inc.

Source category	PM ₁₀	SO _x	CO	NO _x	VOC's	Lead (Pb)
Transportation	1.51	0.99	43.49	7.26	5.08	0.00162
Fuel combustion	1.10	16.55	4.67	10.59	0.67	0.00045
Industrial processes	1.84	3.16	4.69	0.60	7.86	0.00221
Solid waste disposal	0.26	0.02	2.06	0.10	0.69	0.00069
Miscellaneous	0.73	0.01	7.18	0.21	2.59	0.00000
Total	5.44	20.73	62.09	18.76	16.89	0.00497
Percentage of 1982 total	97%	101%	69%	92%	87%	9.5%

PM₁₀ = particulate matter, 10 μ or smaller.

important sections of the Clean Air Act of 1970, as amended in 1977 and 1990.

Two types of air pollution standards emerged from the legislation. The first type is ambient air quality standards, those that deal with concentrations of pollutants in the outdoor atmosphere. The second type is source performance standards, those that apply to emissions of pollutants from specific sources. The Occupational Safety and Health Administration (OSHA) and the American Conference of Governmental Industrial Hygienists (ACGIH) regulated industrial exposures to pollutants in the U.S. They have determined permitted occupational exposure concentrations for some of the pollutants listed in Table 1.8 (a).

Motor vehicles did not attract much attention as air pollution sources until about 1950. California began to regulate emissions from autos in 1963. The history of these regulations is shown in Table 1.8 (b). Over time, the permitted emissions have been substantially reduced. A car that meets the 1993 U.S. standards emits about 3 percent as much HC (tailpipe plus crankcase plus evaporative emissions), 4 percent as much CO, and 11 percent as much NO_x as a 1960 car [104].

In Europe for the future, the concentration of SO₂ and NO_x must conform to the EC (European Community) Framework Directive (84/360/EEC) [106], which defines emission limits to be achieved in 3 phases by the year 2003. These limits apply only to power stations and, therefore, exclude about one third of the emitted SO₂ and half of the NO_x for which motor vehicles are largely responsible.

The rate of sulfur deposition in the mountains, most affected by the forest dieback, reached 15 g S m⁻²year⁻¹ which rates it as one of the most severely polluted places in the world [107]. The phenomenon of dieback in trees due to atmospheric pollution is becoming a major cause for concern in many countries.

Air pollutants units. There are two concentration units that are commonly used in reporting atmospheric species abundance, μg m⁻³ and parts per million by volume (ppm). Parts per million by volume is just;

$$\frac{P_i}{P} \times 10^6$$

where ρ_i and ρ are moles per volume of species i and air, respectively, at pressure P and temperature T. Note that in spite of the widespread reference to it as a concentration, parts per million by volume is not really a concentration but a dimensionless volume fraction.

Given a pollutant mass concentration m_i expressed in μg m⁻³,

$$\rho_i = \frac{10^{-6} m_i}{M_i}$$

where M_i is the molecular weight of species i and ρ = P/RT, thus:
 the concentration of species i in ppm = RT / PM_i × concentration in μg m⁻³

If T is in Kelvin and P in Pascal, then:

the concentration of species i in ppm = $\frac{8.314 T}{PM_i}$ × concentration in μg m⁻³

Table 1.7: The most important sections of the Clean Air Act of 1970, as amended in 1977 and 1990 [104]. Reproduced by permission of McGraw-Hill Inc.

Section	Title	Principal provisions
107	Air Quality Control Regions (AQCR)	Divides the country into regions. States must administer air quality in each such region, under federal supervision.
109	NAAQS	Establishes National Ambient Air Quality Standards.
110	Implementation plans (SIP)	Requires states to prepare and enforce State Implementation Plans. Gives details on how it is to be done.
111	NSPS	Establishes the Standards of Performance for New Stationary Sources, commonly called "the new source of performance standards".
112 and 301-306	NESHAP	Establishes National Emission Standards for Hazardous Air Pollutants.
160-169	PSD	Lays out rules and regulations for regions with air cleaner than the NAAQS and for the protection visibility
171-192	Non-attainment areas	Gives detailed descriptions of what must be done in areas where NAAQS are not currently met.
202-235	Mobile sources	Places control of motor vehicle emissions mostly in the hands of the federal government; sets motor vehicle and fuel standards.
401-416	Acid deposition control	Establishes a federal acid deposition control program.
601-618	Stratospheric ozone protection	Establishes programs for protection of the stratospheric ozone layer.

Table 1.8 (a): Comparison of air quality standards and industrial exposure standards [104]. Reproduced by permission of McGraw-Hill Inc.

Substance	Permitted ambient concentrations (NAAQS)	Permitted industrial concentrations
Sulfur dioxide	80 $\mu\text{g m}^{-3}$ (0.03 ppm), annual average.	2 ppm, 8-h average
	365 $\mu\text{g m}^{-3}$ (0.14 ppm), 24-h average	5 ppm, 15 min. peak
Nitrogen dioxide	0.053 ppm (100 $\mu\text{g m}^{-3}$), annual average.	3 ppm, 8-h average
		5 ppm, 15 min. peak
Carbon monoxide	9 ppm (10 mg m^{-3}), 8-h average	50 ppm, 8-h average
	35 ppm (40 mg m^{-3}), 1-h average	400 ppm, 15 min. peak
Ozone	0.12 ppm (235 $\mu\text{g m}^{-3}$), 1-h average	0.1 ppm, 8-h average
		0.3 ppm, 15 min. peak
Fine particles (PM ₁₀)*	50 $\mu\text{g m}^{-3}$, annual average	Standards exist for specific kinds of particle, but not for PM ₁₀
	150 $\mu\text{g m}^{-3}$, 24-h average	
Total Suspended Particulates (TSP)	75 $\mu\text{g m}^{-3}$, annual average	Standards exist for specific kinds of particle, but not for TSP
	260 $\mu\text{g m}^{-3}$, 24-h average	
Lead	1.5 $\mu\text{g m}^{-3}$, quarterly average	150 $\mu\text{g m}^{-3}$, 8-h average
		450 $\mu\text{g m}^{-3}$, 15-min. peak

* PM₁₀ i.e. particulate matter $\leq 10 \mu$

Table 1.8 (b): Selected history of U.S. automobile air pollutant emission regulation [104]. Reproduced by permission of McGraw-Hill Inc.

Year	Permitted emissions in g/mile *				
	Tailpipe emissions			Other HC emissions	
	CO	NO _x	HC	Crankcase	Evaporative
Precontrol, 1960	87	3.6	8.8	3	4
1970	23	-	2.2	0	4
1972	39	-	3.4	0	0.27
1975	15	3.1	1.5	-	-
1978	-	2.0	-	0	0.8
1980	7	-	0.41	-	-
1981	3.4	1.0	-	0	0.27
1993	-	0.4	0.25	-	-
Clean fuel vehicles, 1996	-	0.4	0.125	-	-
Clean fuel vehicles, 2001	-	0.2	0.075	-	-

* Evaporative emissions are in grams per test. The trip length in the current tailpipe emission test is 7.5 miles. To get a comparable basis, one divides the evaporate emissions of 2 g/test by 7.5 miles/test,

1.9 Pollutants Formation and Oxidation Kinetics

This section discusses the mechanism of formation and oxidation of pollutants species such as CO, NO_x (NO+NO₂), N₂O and SO₂. The emissions of NO_x and SO₂ are comparable in most cases, and they are widely recognized as air pollutants. In the atmosphere NO₂ and SO₂ react with water to form nitric and sulfuric acids, which then react with ammonia or any other available cation to form particles of ammonium nitrate or sulfate. These particles, generally in range of 0.1 μm size and are very efficient light-scatterers. However, nitric oxide, NO is a colorless gases that has some harmful effects on health as shown in Table 1.5, but these effects are substantially less than those of an equivalent amount of nitrogen peroxide, NO₂. In the atmosphere and in industrial devices NO reacts with O₂ to form NO₂, a brown colored gas that is a serious respiratory irritant. Nitrous oxide, N₂O has a lifetime of about 100 year owing to its low reactivity and it can react by reaction $N_2O + O \rightarrow 2 NO$, and this reaction reduces ozone formation. Further oxidation of nitric oxide by ozone leads to the peroxide, which may then react with hydroxyl, OH or other free radicals to form nitric acid by reaction, $OH + NO_2 + M \rightarrow HNO_3 + M$.

All fuels contain sulfur and when they burn, sulfur dioxide, SO₂ or SO₃ are formed. Furthermore, sulfur dioxide can react with water to form sulfuric acids which have adverse effects such as: toxicity to humans, acidification of lakes, damage to trees and crops, as well as, damage to buildings. The detection limit of SO₂ by humans is about 0.5 μg / g and exposure at 200 μg / g for 1minute causes great discomfort [103].

1.9.1 Kinetics of Nitrogen Compounds

Nitrogen oxides in the atmosphere contribute to photochemical smog, to the formation of acid rain precursors, to the destruction of ozone in the stratosphere and to global warming. The main source of emissions of nitric oxide, NO and nitrogen dioxide, NO₂ is attributed to increased combustion of biomass and fossil fuels.

Theory and practice of combustion. The chemical reactions of nitrogen compounds that occur in combustion processes have been the subject of intensive study for many years. The expression NO_x (nitrogen oxides) refers to the summation of all oxides of nitrogen. As far as air pollution is concerned nitrogen monoxide, NO and nitrogen dioxide, NO₂ are the most important. The global emission of NO_x and N₂O to the atmosphere is significant, and the understanding of the NO_x emission and its reduction technologies, necessitates the understanding of the reaction mechanism for formation and removal of the various nitrogen oxides. Four mechanisms have been identified for forming nitrogen oxides in combustion processes; thermal-NO, prompt-NO, fuel-NO, and nitrous oxide N₂O, and these mechanisms are given in Fig. 1.17 with some of their rate parameters in Table 1.9 [108] (see chapters 2 and 5). For fuel-NO mechanism, if fuel contains originally bonded nitrogen, then some of this nitrogen eventually forms the so-called fuel-NO. In case of prompt-NO, the formation of NO exceeds that attributable to thermal-NO (assumed equilibrium radical). Such prompt-NO comes from chemical pathways of NO₂ [109], and N₂O [110] reactions (Table 1.9), or in rich fuel flames, where NO is formed by the hydrogen radical-molecular nitrogen reaction [111]. The principal source of thermal nitric oxide, NO is the oxidation of atmospheric molecular nitrogen, N₂. The mechanism of NO formation from

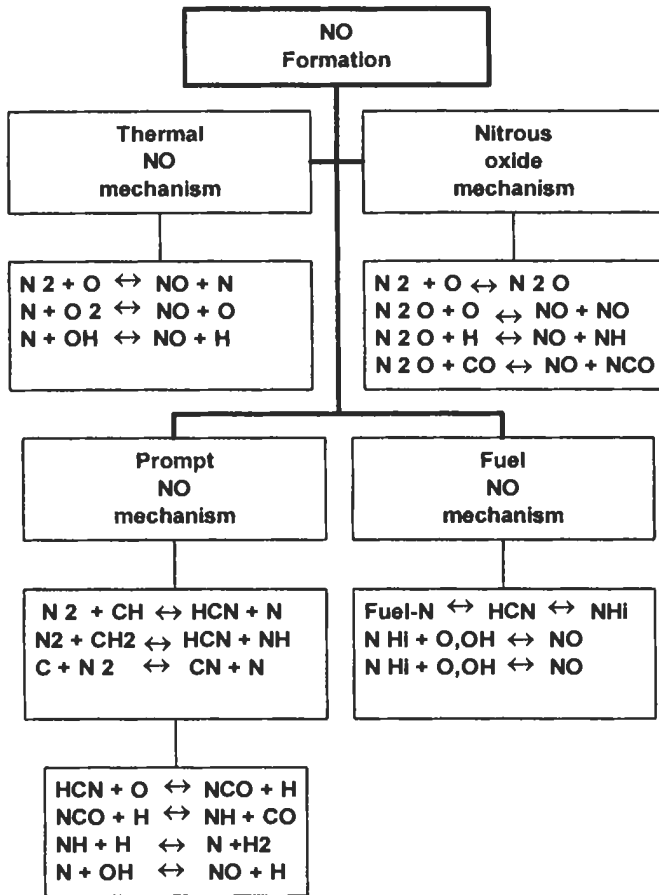


Fig. 1.17: Nitric oxide mechanisms.

atmospheric nitrogen has been studied extensively by Bowman [112], and it is generally accepted that, in the combustion of near stoichiometric fuel-air mixtures, the principal reactions governing the formation of NO from molecular nitrogen are:



This is often called the extended Zeldovich mechanism. Zeldovich was the first to suggest the importance of the first two reactions, and Lavoie et al [113] added the third reaction, which does not contribute significantly. This mechanism is particularly simple because N atoms are the only N-containing intermediate in this mechanism and no knowledge of the fuel oxidation process is required if the O and OH atoms are assumed

Table 1.9: Parameters of forward rate coefficient k for mechanism of nitrogen compounds reactions (Prompt and thermal NO and nitrous oxide, NO_2). Units (cm. mole. s) [108].

No	Reaction	A	B	C/(K)
1	$\text{N}_2 + \text{O} \leftrightarrow \text{N} + \text{NO}$	2.6×10^{14}	0.0	38390
2	$\text{N} + \text{O}_2 \leftrightarrow \text{NO} + \text{O}$	6.4×10^9	1.0	3162
3	$\text{N} + \text{OH} \leftrightarrow \text{H} + \text{NO}$	6.3×10^{11}	0.5	0.0
4	$\text{NO} + \text{HO}_2 \leftrightarrow \text{NO}_2 + \text{OH}$	1.4×10^{15}	0.0	705
5	$\text{NO} + \text{O} + \text{N}_2 \leftrightarrow \text{NO}_2 + \text{N}_2$	1×10^{17}	0.0	0.0
6	$\text{N}_2\text{O} + \text{O} \leftrightarrow \text{NO} + \text{NO}$	7.1×10^{14}	0.0	14100
7	$\text{N}_2 + \text{O} + \text{N}_2 \leftrightarrow \text{N}_2\text{O} + \text{N}_2$	5.5×10^{13}	0.0	10770
8	$\text{NO}_2 + \text{O} \leftrightarrow \text{NO} + \text{O}_2$	5.8×10^{10}	0.5	0.0
9	$\text{N}_2\text{O} + \text{H} \leftrightarrow \text{N}_2 + \text{OH}$	7.6×10^{13}	0.0	7654
10	$\text{CH}_2 + \text{OH} \leftrightarrow \text{CH} + \text{H}_2\text{O}$	4.47×10^{13}	0.0	1511
11	$\text{CH}_2 + \text{NO} \leftrightarrow \text{HCN} + \text{OH}$	1.39×10^{12}	0.0	-554
12	$\text{CH} + \text{N}_2 \leftrightarrow \text{HCN} + \text{N}$	4.4×10^{12}	0.0	11060
13	$\text{CH} + \text{O}_2 \leftrightarrow \text{O} + \text{CHO}$	3.3×10^{13}	0.0	0.0
14	$\text{CH} + \text{OH} \leftrightarrow \text{CHO} + \text{H}$	3.0×10^{13}	0.0	0.0
15	$\text{HCN} + \text{O} \leftrightarrow \text{CN} + \text{OH}$	2.7×10^9	1.58	13394
16	$\text{HCN} + \text{OH} \leftrightarrow \text{CN} + \text{H}_2\text{O}$	4.36×10^{12}	0.0	45171
17	$\text{CN} + \text{OH} \leftrightarrow \text{NCO} + \text{H}$	6.0×10^{13}	0.0	0.0
18	$\text{CN} + \text{O}_2 \leftrightarrow \text{NO} + \text{CO}$	5.6×10^{12}	0.0	0.0
19	$\text{NCO} + \text{OH} \leftrightarrow \text{NO} + \text{CO} + \text{H}$	10^{13}	0.0	0.0
20	$\text{NCO} + \text{NO} \leftrightarrow \text{N}_2\text{O} + \text{CO}$	10^{13}	0.0	-196

to be in equilibrium. The equilibrium O, and OH atom concentrations assumption is often valid in the post flame zone, but not in the flame front where the fast radical formation reactions and the relatively slow radical recombination reactions give rise to large super-equilibrium of O, H and OH atoms concentrations as will be discussed in this section. Thus, detailed fuel oxidation mechanisms, including radical recombination reactions, are necessary to calculate NO formation enhanced by super-equilibrium of O, H and OH atoms concentrations.

The following will describe a simple developed kinetic mechanism for nitrogen compounds (El - Sherif [108]). The kinetic reactions involved in this mechanism for formation and oxidation of NO, NO_2 and N_2O are as follows;

(i) **Nitric oxide, NO reactions (Thermal and prompt NO).** The important thermal-NO (equilibrium) formation reactions are R_1 to R_3 in Table 1.9. These reactions are also important in super-equilibrium conditions.

In the exhaust gases from gas turbines, the concentrations of NO_x are in the region of 60-100 ppm but the gases are greatly diluted with air. For Diesel engines the NO_x concentrations are very dependent upon the load and mode of operation and generally they are about 1000 ppm for idle and 4000 ppm for full load. In both cases the NO_x is produced mainly by the thermal mechanism and the higher pressures.

Furthermore, a considerable quantity of the NO_x produced in spray combustion is produced by the surrounding individual droplets. In particular it has been shown that,

finer fuel sprays produce less nitric oxide than sprays containing considerable quantities of large droplets. The reason for this, is that generally much of the combustion occurs under fuel-rich conditions, i.e. surrounding evaporating droplets. In these cases a certain amount of nitric oxide is produced by the so-called "prompt-NO" route. Here carbon-containing free radicals reacts with molecular nitrogen to form nitric oxide by reactions, which probably involve reactions such as R_{10} to R_{20} in Table 1.9.

(ii) **Nitrogen dioxide, NO_2 reactions.** The important reactions for formation and oxidation of NO_2 are R_4 to R_6 and their rate coefficients are given in Table 1.9. Reactions R_4 and R_5 are the principal reactions for formation of NO_2 . The principal removal step for NO_2 and prompt formation of NO is reaction R_8 .

(iii) **Nitrous oxide, N_2O reactions.** The important reactions for formation and oxidation of N_2O are reactions, R_7 to R_9 and their rate coefficients are given in Table 1.9. The principal reaction for N_2O formation is the third body reaction, R_7 . The principal removal steps of N_2O and prompt formation of NO from N_2O are reactions, R_6 and R_9 .

1.9.2 Kinetics of Pollutants Originating from Sulphur

Sulphur Dioxide Formation

All petroleum products contain organo-sulphur compounds which are present as sulphides, and disulphides. Their nature and concentration are dependent upon the origin of the crude oil, but the highest concentrations are found in residual fuels (0.1 % in kerosene to about 3 % weight in heavy oils), and it is only these fuels that present any problem from the environmental point of view. SO_2 is formed from sulphur by $S + O_2 \rightarrow SO_2$, and its concentrations in the stack gases are in the range of 200-2000 ppm. As discussed above in section 1.8, the sulphur dioxide produced is undesirable for a number of reasons but the principal one is that it reacts to form SO_3 , H_2SO_4 aerosol and acid rain which can damage health, and cause corrosion and acidification of lakes.

Sulphur Trioxide Formation

In dealing with furnaces using residual oils, one must recognize heterogeneous catalysis as a possible route for the conversion of SO_2 to SO_3 . Sulfur dioxide and molecular oxygen will react catalytically on steel surfaces and vanadium pentoxide (deposited from vanadium compounds in the fuel) and at lower temperatures, where the equilibrium represented by: $SO_2 + 0.5 O_2 \rightarrow SO_3$ favors the formation of SO_3 . The equilibrium represented by this reaction is shifted to the left at high temperatures, and one would expect very little SO_3 in a real combustion environment. Sulfur dioxide forms sulfuric acid in its reaction with nitric oxide; $H_2O + NO + SO_2 \rightarrow H_2SO_4 + N$, but in principal route it involves the OH radical. In the presence of water and oxygen, this can be represented as:



Since the acid dewpoint, or temperature at which condensation occurs, may be as high as 150 °C, condensation may occur in economizers and air heaters resulting in the corrosion of metal surfaces and the formation of deposits of sulphates. Generally, the concentration of SO_3 in the flue gases is about 0.2 to 3 % of the total sulphur oxides,

and thus SO_3 concentrations rarely exceed 50 ppm.

Truly, the most interesting finding is that the super-equilibrium concentrations of SO_3 are very sensitive to the original oxygen concentration. Under fuel-rich conditions approaching even stoichiometric conditions practically no SO_3 is found. In proceeding from stoichiometric to 1 % excess air, a sharp increase in the conversion of SO_2 to SO_3 is found. Further addition of air only causes a slight increase; however, the effect of the excess nitrogen in reducing the temperature could be a moderating factor in the rate of increase. If indeed, SO_2 and SO_3 are effective in reducing the super-equilibrium concentration of radicals in flames, then this is apparent that sulphur compounds should play a role in NO formation in flames (as O atom decrease, thus NO formation should be reduced). However, SO_3 may be reduced by its reactions with oxygen and hydrogen atoms via; $\text{O} + \text{SO}_3 \rightarrow \text{SO}_2 + \text{O}_2$ and $\text{H} + \text{SO}_3 \rightarrow \text{SO}_2 + \text{OH}$. Wendt and Ekmann [114] have supported this conclusion.

1.9.3 Kinetics of Carbon Monoxide

Carbon monoxide is found in the combustion products of all carbonaceous fuels and in concentrations above that calculated from equilibrium considerations. In equilibrium the carbon monoxide is given by: $\text{CO}_2 \rightarrow \text{CO} + 0.5 \text{O}_2$, and in this case the CO concentration is dependent on the temperature and excess air. In fuel-rich regions of a flame, the CO levels are necessarily high since there is insufficient oxygen for complete combustion. Only if sufficient air is mixed with such gases at sufficiently high temperature the CO can be oxidized. Thus, imperfect mixing can allow carbon monoxide to escape from combustors that are operated at fuel-lean mixtures. Even in premixed combustion systems, carbon monoxide levels can be relatively high due to the high equilibrium concentrations at the flame temperature, particularly in internal combustion engines where the gases are hot prior to ignition due to compression. As the combustion products are cooled, the equilibrium CO levels decreases.

In flames, the concentration of CO is formed rapid in the reaction zone and is subsequently oxidized to CO_2 by: $\text{CO} + \text{OH} \rightarrow \text{CO}_2 + \text{H}$. If the time available for reaction of CO to CO_2 is short, as in small combustion chambers, thus the CO in the burned gases is higher than that for large units. The CO concentration is about 20 ppm for small combustion chambers compared with 0.3 ppm for large combustion chambers.

1.10 Pollutant Emissions Reduction Techniques

In response to the air pollutant emission regulations described in section 1.8.3, a variety of technologies for controlling pollution from combustion sources has been developed. These development technologies have drawn heavily on the understanding of the chemical pathways for formation and removal of these pollutants as described in some details in section 1.9. In general, the goal of air pollution abatement is the meeting of a set of air quality standards as described in section 1.8.3. Therefore, air pollution abatement programs can be divided into long-term control and short-term control, and these two categories are discussed in details by Flagan and Seinfeld [115]. This section presents some emerging techniques for reducing emissions from combustion sources, such as in industry and power stations as well as vehicle engines.

1.10.1 Reduction Techniques in Combustion Equipment

Over the past 100 years, global emissions of nitrogen oxides into the atmosphere have been increasing steadily. Because of the detrimental effects of nitrogen oxides on the environment and on health as discussed in the previous section, nitrogen oxide emissions from combustion sources are regulated in a number of industrialized countries. In response to these regulations, a variety of technologies for control of NO_x emissions from combustion sources has been developed. The development of these technologies has drawn heavily on our understanding of the chemical pathways of nitrogen oxides. These chemical pathways have been discussed in the previous section. As legislative trends for further reduction in NO_x emissions continue, newer technologies for NO_x emissions reduction will need to be developed, and this may require a more complete understanding of nitrogen chemistry in combustion.

As discussed in section 1.9, the main parameters relevant to the formation reactions of NO_x are combustion temperature, oxidant concentration or its partial pressure, and the length of time spent in the high temperature region, and any reduction of these parameters leads to reduction of NO_x formation. However, reduction in combustion temperature may be achieved by; optimization of fuel introduction system, exhaust gas re-circulation, and water or steam injection. Also, reduction in oxygen partial pressure may be achieved by air staging, fuel staging or exhaust gas re-circulation, while the reduction in residence time can be achieved through the optimization of air distribution, as well as, burner configuration (see Fig. 1.18). Moreover, Poppe et al [116] have confirmed that applied oscillations can reduce emissions of NO_x in premixed, bluff-body stabilized flames. They [116] show that control of naturally occurring oscillations in ducted premixed flames by the oscillation of a spray of water was as effective as that with oscillation of the kerosene spray, and it reduces NO_x concentration by 50 % due to the removal of heat. Furthermore, another alternative approach for the control of NO_x emissions from combustion is NO_x recycle [117]. This approach uses regenerable sorbent to adsorption, producing a highly concentrated NO_x – laden stream containing both NO and NO_2 . This stream is then sent back to the same combustor or to a separate combustor, where the NO_x is reduced in the flame and NO_x formation is inhibited.

Bowman [118] reviewed the existing and some emerging technologies for reducing NO_x emissions from combustion sources, and examined the prospects of these technologies for meeting stricter emissions regulations. The main strategies for reducing NO_x emissions take two forms: (a) modification of the combustion process to control fuel and air mixing and reduce flame temperatures, and (b) post-combustion treatment of the flue gas to remove NO_x (see the applications in chapter 5). Also these strategies can be used to control SO_2 emissions in fluidized-bed combustion. These technologies can be summarized in Fig. 1.18 and discussed as follows.

Combustion Modification Techniques for NO_x Reduction

As discussed in the previous section, there are three main different formation mechanisms of NO . Here, the control of the mechanisms will be discussed briefly as follows.

Thermal NO . In this mechanism, NO is formed by the reaction of molecular nitrogen from the combustion air with atomic oxygen, and the subsequent reactions as

described before. This mechanism is based primarily on the temperature and O₂ concentration. Therefore, any reduction of combustion gas temperature or availability of oxygen or both can produce low NO_x emissions (see Fig. 1.18). In stationary combustion sources, temperature reductions are achieved by diluting combustion air or fuel by flue gas recirculation technology, water injection, and lean combustion. The flue gas recirculation leads to a reduction in the burned gas temperature and O₂ concentration, which, in turn, results in reduction of NO. This in addition to a reduction in the level of HC, thereby decreasing the NO produced by the Fenimore prompt NO species in rich flames. In opposite direction, lower temperatures also may cause increase in CO and unburned hydrocarbon emissions due to quenching of the oxidation reactions. Also, premixed combustion technologies can be used to reduce the gas temperature, and these include porous radiant burners, catalytic combustion, and lean premixed gas turbine combustors. For example, the radiant heat transfer from the porous burner surface results in lower gas temperatures, which, in turn, results in lower NO formation by the thermal mechanism. The concept of catalytic combustors is the stabilization of a lean premixed gaseous fuel-air flame using a catalytic surface.

Controlling the availability of oxygen in stationary combustion devices involves staging the combustion air so that the primary combustion zone operates with an overall rich fuel-air ratio, with the remaining combustion air injected downstream.

Low NO_x burners slow and control the rate of fuel and air mixing, thereby reducing oxygen availability in the ignition and main combustion zones. Low NO_x burners can reduce NO_x emissions by 50 % or more, depending upon the initial conditions. They are of relatively low cost and are applicable to new plants as well as retrofits.

Staged combustion uses low excess air levels in the primary combustion zone with the remaining (overfire) air added at higher levels in the furnace to complete combustion. Significant NO_x reductions are possible with staged combustion.

Flue gas recirculation reduces oxygen concentration and combustion temperatures by recirculating some of the flue gas to the furnace without increasing the total net gas mass flow. Large NO_x reductions are possible with oil and gas firing while moderate reductions are possible with coal firing.

Reburning is a technology used to reduce NO_x emissions from Cyclone furnaces and other selected applications. In reburning, 75 to 80 % of the furnace fuel input is burned in the Cyclone furnace with minimum excess air. The remaining fuel is added to the furnace above the primary combustion zone. This secondary combustion zone is operated substoichiometrically to generate hydrocarbon radicals which reduce NO formed in the Cyclone to N₂. The application of the above methods in combustion systems will be discussed in some details in chapter 5.

Prompt NO. In this mechanism NO is formed at a rate faster than that computed from thermal NO mechanism described above. The sources of prompt NO in hydrocarbon fuel combustion are: first, super-equilibrium O, H, HO₂, and OH concentrations in the reaction zone as described in the previous section, second, reaction of N₂ with hydrocarbon radicals (e.g. CH) in the reaction zone with highly fuel-rich mixtures and finally, from chemical pathways of N₂O and NO₂ as discussed in the previous section. It is clear from this mechanism that, the radical species such as O, H, OH, HO₂, CH₂ and CH play an important part for increasing or decreasing the prompt NO formation (by reactions such as $\text{CH} + \text{N}_2 \leftrightarrow \text{HCN} + \text{N}$ & $\text{CH}_2 + \text{N}_2 \leftrightarrow \text{HCN} + \text{NH}$ [119]).

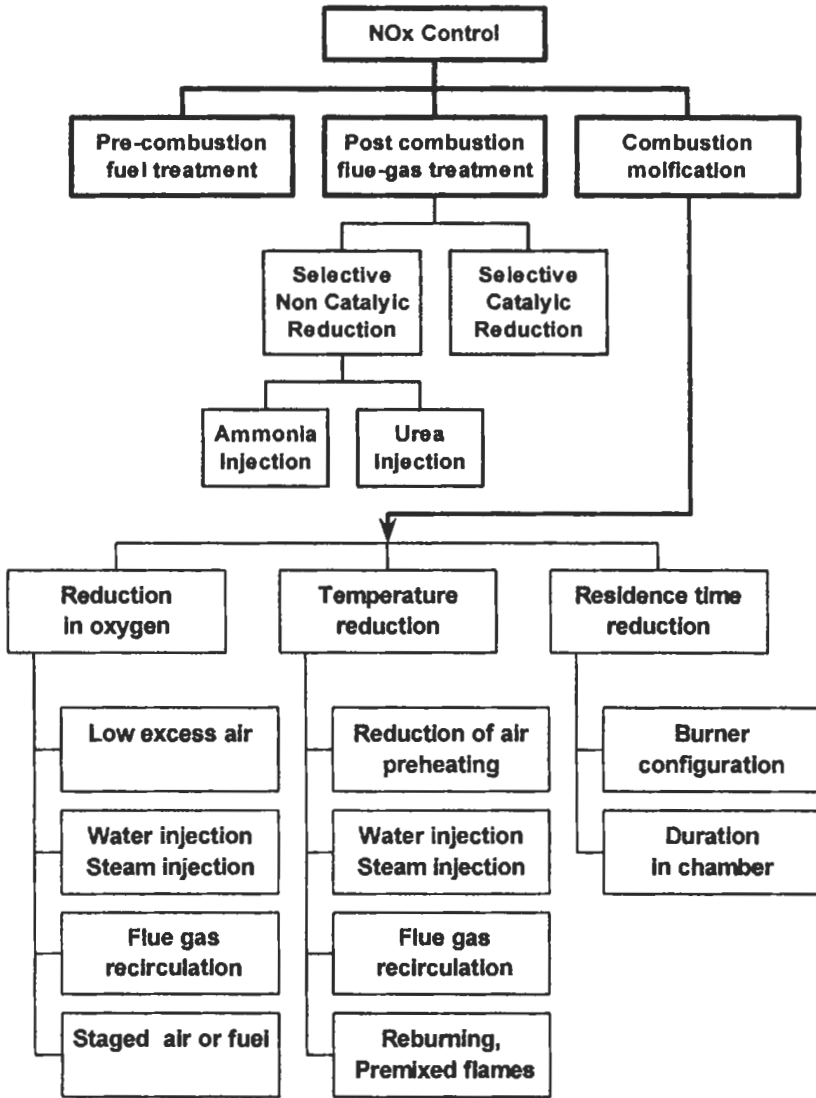


Fig. 1.18: Technical methods of NO_x reduction.

Nitric oxide formation by N₂O mechanism increases in importance as the fuel-air ratio decreases, as the burned gas temperature decreases, or as the pressure increases. The N₂O mechanism is most important under conditions where the total NO formation rate is relatively low. Table 1.10 shows representative contributions of the thermal and prompts NO mechanisms to the total NO formation in different flames. The injection of species that can assist in the production of the radical necessary for the NO-removing reaction sequence to proceed, is expected to be an important method for reducing NO.

Fuel NO. If the fuel contains organically bound nitrogen, as for example in the case of coal and heavy oil, the fuel NO formation must be considered. The extent of

Table 1.10: Representative contributions of thermal and prompt NO mechanisms of total NO formation (Bowman [118]). Reproduced by permission of The Combustion Institute.

Flame	Flame conditions		Total NO _x (ppmv)	Fraction of total NO formation			
				Equilibrium Thermal	Super-equilibrium	HC-N ₂	N ₂ O
Premixed laminar ^a	$\phi = 1$	P=0.1atm	9 @ 5 ms	0.03	0.22	0.73	0.01
CH ₄ -air flames	$\phi = 1$	P=1 atm	111	0.50	0.35	0.10	0.05
Premixed laminar ^b	$\phi = 1$	P=10 atm	315	0.57	0.15	0.21	0.10
Premixed laminar ^b	$\phi = 1.05$	P=1 atm	29@ 5 ms	0.53	0.30	0.17	-
Premixed laminar ^b	$\phi = 1.16$	P=1 atm	20	0.30	0.20	0.50	-
for CH ₄ -air flames	$\phi = 1.27$	P=1 atm	20	0.05	0.05	0.90	-
	$\phi = 1.32$	P=1 atm	23	0.02	0.03	0.95	-
Non-premixed laminar, strained ^c CH ₄ -N ₂ -air flames	$\alpha = 10 \text{ s}^{-1}$	P=1 atm	120 max	-	0.20	0.69	0.11
	$\alpha = 36 \text{ s}^{-1}$	P=1 atm	65	-	0.07	0.86	0.07
	$\alpha = 70 \text{ s}^{-1}$	P=1 atm	43	-	0.05	0.90	0.05
Well stirred reactor	$\phi = 0.7$	P=1 atm	12 @ 3 m s	0.15	0.65	0.05	0.35
CH ₄ -air ^{bd} flames	$\phi = 0.8$	P=1 atm	20	-	0.85	0.10	0.05
	$\phi = 1.0$	P=1 atm	70	-	0.30	0.70	-
	$\phi = 1.2$	P=1 atm	110	-	0.10	0.90	-
	$\phi = 1.4$	P=1 atm	55	-	-	1.00	-
Well stirred reactor ^e CO-moist air	$\phi = 0.6$	P=0.9atm	34 @ 7 m s	0.15	0.75	-	0.10
Non-premixed, Turbulent CO/H ₂ /diluent air	-	P=1 atm	7 peak @ x/d = 100	0.40	0.60	-	-
	-	P=10 atm	-	0.74	0.26	-	-

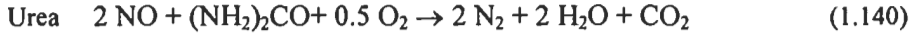
^a Ref. 120 ^b Ref. 121 ^c Ref. 122 ^d Ref. 123 ^e Ref. 124

conversion of nitrogen to NO is strongly dependent on the fuel-air ratio and on the combustion temperature, and slightly dependent on the identity of the parent nitrogen compound. The fuel-rich combustion favors lower conversion of fuel nitrogen to NO.

Post-Combustion Techniques for NO_x Reduction

At the present time, the most effective post-combustion methods for reducing NO_x emissions from stationary sources, including steam boilers, gas turbines, and Diesel engines, are selective non-catalytic reduction (SNCR) and selective catalytic reduction (SCR) [118], which involve injection of a nitrogen-containing additive into the combustion products. In SNCR, ammonia, cyanuric acid and urea (which thermally decomposes to produce ammonia) are injected down-stream of the combustion zone in a temperature region of 760 to 1093 °C. The maximum NO-removal efficiencies, for all

three additives, are comparable and can exceed 90 percent. SCR is being used worldwide where high NO_x removal efficiencies are required in gas, oil or coal-fired industrial and utility boilers. SCR systems remove NO_x from flue gases by reaction with ammonia in the presence of a catalyst. The chemical reactions for ammonia and urea processes can be represented by:



A diagram of an ammonia control and supply system is shown in Fig. 1.19. Ammonia can be anhydrous or aqueous, and due to safety concerns, aqueous NH₃ is required for selected SCR system installations. A controlled amount of ammonia is fed to a vaporizer /mix chamber where it is mixed with air or steam at about a 1:20 volume ratio, and then the mixture is introduced into the flue gas through an injection grid system. The fundamental process control provides ammonia flow at a constant NH₃/NO_x mole ratio. The product of the inlet NO_x concentration and the boiler flue gas flow yields a NO_x flow signal. Ammonia flow control is then established by multiplying the NO_x flow signal by the NH₃/NO_x mole ratio set point (see Fig. 1.20). More details is given in Ref. 126.

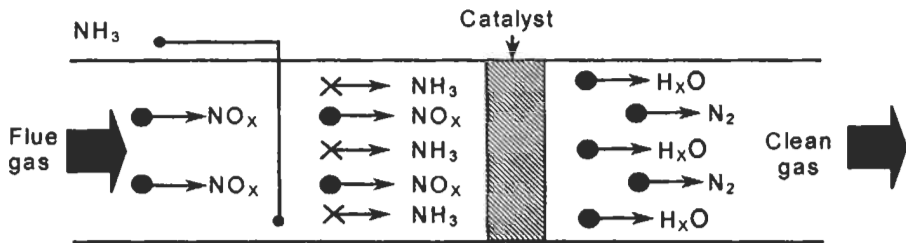


Fig. 1.19: Principles of NO_x removal process for SCR [126]. Reproduced by permission of Babcock and Wilcox Company.

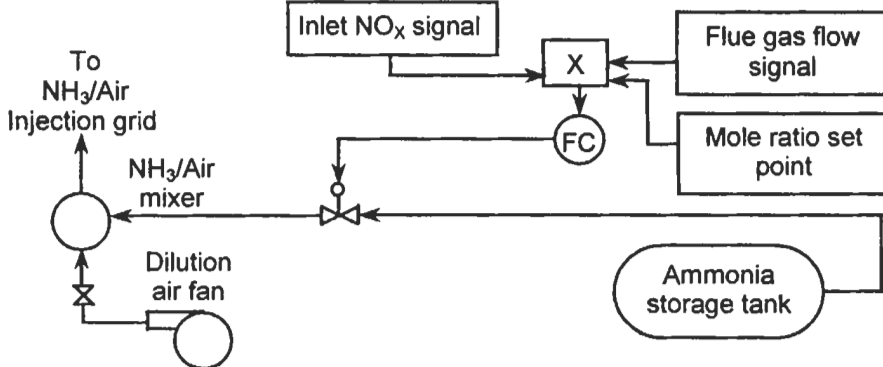


Fig. 1.20: Ammonia (NH₃)/dilution air supply, and control system [126]. Reproduced by permission of Babcock and Wilcox Company.

Many of the above techniques for reduction of NO_x are approaching the limits of their capabilities for reducing NO_x emissions. At the present time, the most effective method for reducing NO_x emissions is by injection of a gaseous fuel or species that can generate or assist in the production of the radicals species (such as HO_2 , O and OH) necessary for reducing NO . Such fuels include hydrogen, carbon monoxide, and various hydrocarbons. Recently, Dagaut et al [125] have investigated the reduction of NO by ethylene in a jet-stirred reactor at 1 atm., and they found that the NO decreases significantly with ethylene additive, and this is due to the increase of atomic hydrogen. These additives can influence not only NO , but also N_2O , NO_2 , temperature, soot formation, residence time and burning velocity. The application of the above methods in combustion systems will be discussed in some details in chapters 2 and 5.

Sulphur Compounds Reduction Techniques

SO_2 emissions from coal-fired boilers can be reduced using pre-combustion techniques, combustion modifications and post-combustion methods.

Pre-combustion. These techniques include the use of oil or gas in new units or the use of cleaned (beneficiated) coal or fuel switching in existing units. By using gas, sulfur emissions can be reduced to almost zero; while the use of low sulfur oil will minimize SO_2 emissions. Switching to oil and gas in existing boilers requires attention be given to receiving equipment, storage facilities, combustion equipment including safety systems, boiler design, and post-combustion FGD unit performance. In the case of new systems, oil or gas firing can significantly reduce steam system capital costs.

Combustion modifications. The above described techniques for reducing NO_x emissions can also be used to control SO_2 emissions in fluidized-bed combustion, where limestone is used as the bed material. The limestone can absorb more than 90% of the sulfur released during the combustion process.

Sorbent injection technologies. Sorbent injection, while not involving modification of the combustion process, is applied in temperature regions ranging from those just outside the combustion zone in the upper furnace to those at the economizer and ductworks following the air heater. Sorbent injection involves adding an alkali compound to the coal combustion gases for eventual reaction with SO_2 . Typical calcium sorbents include limestone (calcium carbonate, CaCO_3), lime (CaO), hydrated lime ($\text{Ca}(\text{OH})_2$) and modifications of these compounds with special additives.

Wet and dry scrubbing technology. Worldwide, wet and dry scrubbing systems are the most commonly used technologies in the coal-fired electric utility industry. Year 1989 indicates that, in the U.S.A., approximately 20 % of the coal-fired utility capacity used wet scrubbing for SO_2 emission control. Both wet and dry scrubbing use slurries of sorbent and water to react with SO_2 in flue gas, producing wet and dry waste products, respectively.

In the wet scrubbing process, a sorbent slurry consisting of water mixed with lime, limestone, magnesium promoted lime or sodium carbonate (Na_2CO_3) is contacted with flue gas in a reactor vessel. Wet scrubbing is a highly efficient (> 90 % at calcium/sulfur molar ratios close to 1.0), well established technology which can produce usable byproducts.

Dry scrubbing involves spraying an aqueous sorbent slurry into a reactor vessel so that the slurry droplets dry as they contact the hot flue gas (149 °C). The SO_2 reaction occurs during the drying process and results in a dry particulate containing reaction

products, and unreacted sorbent entrained in the flue gas, along with flyash. The applications of the above methods in combustion systems will be discussed in chapter 5.

1.10.2 Emission Reduction Techniques in Vehicles

Reducing emissions from vehicle engines may be achieved by [103]:

1. Keeping the compression ratio below the usual 10:1 for petrol engines. This has the effect of reducing the combustion temperature, which is unfavorable to the initial fixation reaction and hence reduces the yield of NO.
2. Enriching the mixture of fuel to bring the post-combustion level of NO as low as possible.
3. NO and unburned fuel can be removed from the exhaust using a catalytic converter. The catalysts are platinum or alloys of platinum/rhodium, which are poisoned by leaded fuels. SO₂ in the emissions is converted to SO₃ and hence to sulfuric acid.

The future use of electric cars will alleviate the problem by dependence on a power source where NO_x and CO emissions can be brought within legal limit [103].

The application of the above described low emission techniques in industry, power stations and vehicles will be described in chapter 5.

1.10.3 Greenhouse Warming and its Reduction Techniques

Solar energy falling on the earth's surface is absorbed and transferred to the atmosphere by evaporation and as heat flux, including infrared radiation. Recently, the energy fall at the surface is about 157 W/m²; rather more than twice this amount enters the stratosphere but is depleted by reflection from clouds and dust and also by absorption by clouds, ozone and water vapor. The infrared energy absorbed by these components is governed by the intensity of infrared emission at the earth's surface and in the lower levels. The emission of energy from the upper levels is reduced as the temperature of the troposphere falls at about 5°C/km, leading to a net energy gain and surface warming [103,127]. Man's activities have introduced additional absorptive molecules, so trapping more heat and disturbing the natural equilibrium [128].

The burning of fossil fuels (coal, oil, and gas) and of recent biomass (savannas, forests, biomass fuels, and agricultural waste) leads to global alteration in the composition of the atmosphere such as the greenhouse effect, depletion of the ozone layer, and the level of tropospheric oxidants. Arrhenius [129] pointed out that CO₂ would act as a greenhouse gas, and recent scientific assessments [130] show that increases in CO₂ and other greenhouse gases (GHGs) will inevitably lead to a warmer climate [101].

The earth's surface temperature has risen by 0.5°C over the last century, and predictions depend on forecasting the likely rate of change in the concentration of greenhouse gases. The earth's atmosphere contains 2.6×10^{15} kg of CO₂ to which man added 5×10^{12} kg in 1985. Computer models, which broadly match conditions in the past, indicate a temperature rise of 3°C on doubling present CO₂ levels [103]. Alloway and

Ayres [103] have pointed out that the consequence of greenhouse warming leads to two important phenomena: firstly, sea levels will rise as a result of expansion of the water body as temperatures increase, and also of its enhancement by melting South Polar ice causing backing up of rivers leading to flooding. Secondly, in the UK the southeast will become drier and growth of arable crops would tend towards the west to secure water supplies. Also, the African desert would move northward and areas of Spain, Italy and Greece would become deserts.

Reduction techniques. The United Nations panel [131] considers that in order to limit temperature rise to within 0.1- 0.2°C/decade, the emissions of CO₂, CFCs (Chlorofluorocarbons) and NO_x must be reduced by 60% and those of methane by 20%. Some desirable measures may be; energy conservation in building design, stricter control of vehicle emissions, overall increase in forestation, taxing inefficient sources such as coal and giving preference to natural gas and removal of CO₂ at power stations by scrubbing emitted gas [103]. Natural gas is an environmentally friendly fuel and when burnt, it produces much lower emissions levels of CO₂ when compared to the other competing fuels as shown in Table 1.11 [132]. Therefore, it is necessary to speed up the natural gas switching policy in the different sectors in order to reduce the liquid fuels consumption, hence improving the balance of payment and to further reduce CO₂ emissions for better environment [133].

In general, pollutant sources removal, modification, or substitution is the most effective and permanent way to solve air quality, if the pollution problem can be identified. Inadequate ventilation design or installation should be corrected, and also the operation and maintenance programs have to be conducted properly. Furthermore, activated charcoal filters are generally effective in removing organic chemicals and particulate [134], and finally, public education can be not only the least costly but also the most effective method of pollution control. Pre-drying of moisture fuels was one of the alternative method for reducing carbon dioxide (Ionel [135]). Thus, by eliminating the water vapors before the fuel is entering the combustion chamber, more stable conditions for the ignition and combustion of the fuel are realized, that is for the benefit of the combustion efficiency. If a suitable recovery of the heat enthalpy of the vapors is organized, and the gained energy is used, being thus a supplementary energy supply alternative, the general power plant efficiency is recovering. Thus, the carbon dioxide emission is reduced for the same used thermal power output of the plant.

Table 1.11: Conversion factors of CO₂ emissions by fuel type [132].

Fuel type	Ton carbon dioxide / ton	Fuel type	Ton carbon dioxide / ton
LPG	2.9837	Diesel	3.2093
Gasoline	3.1046	Fuel oil	3.1094
Kerosene	3.216	Others	2.9473
Gas oil	3.2093	Natural gas	2.615

Chapter

2

Laminar Premixed Flames

2.1 Introduction

It was the hazards of coal mining, rather than problems of engine combustion, that motivated the early development of flame theory. A mining explosion in the North of England in 1815 initiated researches which covered limits of flammability, ignitability of different hot sources, and flame quenching at solid surfaces; all of which led to the development of the safety lamp.

A flame may be described as a reaction zone that moves with respect to the gas supporting it. In practice the term is usually reserved for fast exothermic reactions of this type, and these are often also accompanied by emission of light. Flames may be either stationary flames on a burner and propagating into a flow of gas from a burner tube, or they may be freely propagating flames traveling in an initially quiescent gas mixture. Stationary flames are of two general types:

- (a) Premixed flames where the reactants are mixed before approaching the flame region. These flames can only be obtained if the initial fuel and oxidant mixture lies between certain composition limits called the composition limits of flammability. The characteristic of these flames will be discussed in sections 2.2 and 2.3.
- (b) Diffusion flames where both mixing of fuel and air and the combustion occur at the interface.

The two types of flames are also differentiated physically in that, for defined thermodynamic starting conditions, the premixed system has a defined equilibrium adiabatic flame temperature and for the idealized situation of planar flame in a one-dimensional flow field, it has a defined adiabatic burning velocity or equivalent mass flux in a direction normal to its surface. An unstrained diffusion flame has no such simply defined parameters.

The tasks of combustion flow diagnostics are to increase the fundamentals of combustion and to improve the performance of those engineering devices that utilize it. Many practical combustion problems can be examined most conveniently under the well defined, controlled conditions which the laminar flame provides. In premixed flames, the laminar burning velocity and flame structure data can be extremely useful in the analysis of fundamental processes such as ignition, NO_x and soot formation, and flame quenching. Also, turbulent flame models often prescribe the turbulent burning

velocity as a function of laminar burning velocity. Thus, detailed information describing the dependence of the laminar burning velocity, flame thickness, ignition temperature, heat release rate and flame quenching on various system parameters can be a valuable diagnostic and design aid.

There is a significant discrepancy in measuring burning velocities, which gives an indication of the difficulties and uncertainties often associated with experimental determination of flame properties. In addition to that, the experimental research is very expensive, especially to cover all the factors and conditions affecting the flame propagation. Thus the use of computer modeling techniques could be considered as an alternative method of estimating burning velocity and flame structure over wide ranges of operating conditions. Therefore, mathematical models of laminar flames that incorporate detailed chemical kinetics can reveal the detailed flame structure and predict the burning velocity. The correct prediction of these parameters is a demanding test of the accuracy and completeness of a kinetic reaction mechanism. Once validated by comparison with experimental results, a kinetic flame model can then be used to carry out detailed numerical experiments that provide a great deal of information on physical and chemical processes which occur in laminar flames.

For flame modeling it is necessary to define reaction-rate coefficients over extended ranges of temperature. Rate coefficients are rarely known to be better than $\pm 25\%$ over extended temperature ranges. Thus, when groups of well characterized and not-so-well-characterized reactions are combined into a hydrocarbon-air flame mechanism, there is much room for error. For this reason, it is wise to consider a hydrocarbon-air flame mechanism as three or four groups of reactions, which can be, arranged hierarchically from hydrogen-air through hydrogen-carbon monoxide-air and formaldehyde-air flames to the hydrocarbon system itself. From studies of the intermediate systems, a self-consistent set of rate parameters can be built up for the whole ensemble.

The main objective of the present contribution in this chapter is to present some of our understanding of laminar premixed flame as revealed by detailed numerical kinetic modeling, particularly in relation to interaction between modeling and experiment and to obtain general correlations between the flame propagation parameters for different fuels. It also illustrates the degree of agreement between the experimental and kinetic modeling results. This work is the natural contribution of a set of extensive research by Bradley and Dixon-Lewis over the past thirty years at Leeds University, England, also by Habik and El-Sherif during their research work at Leeds University and further during their work in Suez Canal, Helwan and Cairo Universities.

Section 2.2 in this chapter started with a brief description of some definitions of combustion fundamentals for laminar premixed flame, while section 2.3 describes the basic theory and kinetic of laminar premixed flames through the background of flame propagation, kinetic model with its computational methods. Furthermore, the transport parameters and reaction mechanisms used in this model for different fuels are discussed in this section.

As mentioned above, any hydrocarbon mechanism consists mainly of four sub-mechanisms such as hydrogen, hydrogen-carbon monoxide, formaldehyde and breakdown of the hydrocarbon fuels. Therefore, it is necessary to understand the flame characteristics of such simple fuels. Thus, section 2.4 describes the experimental and computational structure, and characteristics of premixed laminar flames for such simple fuels. Authors of this book and co-workers have done most of these works during the past twenty years. This section is divided into nine sub-sections, which cover most

of the flame characteristics for practical fuels, and involved the experimental systems, techniques of the measurements and results. These are in addition to the computed results from the kinetic model. Sub-sections 2.4.1 and 2.4.2 describes the structure and characteristics of hydrogen and hydrogen-carbon monoxide-air flames. The predicted results for these flames using the kinetic model are compared and discussed with the experimental results.

Because methane and methanol are both chemically simple molecules which have the potential to be widely used as practical fuels, their chemical mechanisms are also examined and validated with the experimental results for both laminar burning velocity and flame structure. Effect of equivalence ratio, initial pressure and temperature on the flame structure, burning velocity, flame thickness, ignition temperature and heat release rate are discussed in sub-sections 2.4.3 and 2.4.4. In addition, the effect of water injected on methanol-air flame, on laminar burning velocity, maximum pressure and temperature, and flame structure is also discussed in sub-section 2.4.5.

The combustion of natural gas is one of the major sources of energy, and a detailed understanding of its combustion behavior is of considerable practical importance. However, composition of commercial natural gas can vary widely with concentration extremes of 75 % - 98 % for methane, 0.5 % - 13 % for ethane and 0 % - 2.6 % for propane. Therefore, it is important to understand the chemistry of each of these individual fuels and then consider how varying levels of these fuels in natural gas affect their performance. Hence, sections 2.4.6 and 2.4.7 describe the chemical kinetics aspects of propane-air and ethane-air flames, respectively as well as the flame characteristics of these flames. Moreover, section 2.4.8 explains kinetically the effect of natural gas composition on the flame characteristics of natural gas-air mixtures.

Because of the importance of laminar burning velocity and volumetric heat release rate in relation to the turbulent flame model, general correlations for such parameters with the heat of reaction per mole mixture for different gaseous and liquid fuels are derived in section 2.5.

The above sections show that, the kinetic mechanisms become complex as the number of carbon atom in hydrocarbon fuels increases, and therefore it is necessary to simplify the kinetic mechanism for the high hydrocarbon fuels. Thus, section 2.6 describes our attempts to develop a reduced kinetic mechanism for practical high hydrocarbon fuels such as n-butane, benzene, n-heptane, gasoline, kerosene and n-hexadecane. The predicted results using these mechanisms have been validated with experimental data. These mechanisms can be used in 2-D or 3-D combustion models to understand the practical combustion and emission problems in engines and furnaces.

Over the past 100 years, global emissions of nitrogen oxides into the atmosphere have been increasing steadily, and the main source of these emissions is attributed to increased combustion of fossil fuels. Because of their detrimental effect on the environment and on health, these emissions are regulated in a number of industrialized countries. This requires a more complete understanding of nitrogen chemistry; therefore, section 2.7 describes the role of gaseous fuel additives (such as hydrogen, ethane and carbon monoxide) on the nitrogen compounds in hydrocarbon flames. Furthermore, section 2.8 describes the effect of using porous burners on the flame characteristics and pollutant emissions.

Finally, the responses of flames to applied stresses are discussed in section 2.9 in the context of flame extinction for premixed flames in both the symmetric back-to-back and the asymmetric unburned-to-burnt configurations.

2.2 Definitions

The premixed flame has a defined *equilibrium adiabatic flame temperature and burning velocity*, the latter may be defined as the velocity of a plane flame front normal to itself and relative to the unburned reactants. Burning velocity, whilst not providing the detailed characterization offered by studies of flame microstructure, is extremely convenient and is used as single-parameter description of a complex phenomenon.

Since a flame travels at a characteristic burning velocity, a stationary flame may be obtained by passing the reactants into the flame at the same velocity in the reverse direction. In practice, flames achieved in this way are unstable and it is necessary to provide a stabilizing device or burner, which locally interacts with the flow and combustion processes. In addition, the premixed flames can only be obtained if the initial fuel and oxidant mixture lies between certain composition limits called the *composition limits of flammability*.

2.2.1 Flammability limits

If small amounts of combustible fuel gas or vapor are added gradually to air, a point will be reached at which the mixture just becomes flammable. The percentage of fuel gas at this point is called the *lower flammable limit or lean limit*. If more fuel is added, another point will eventually be reached at which the mixture will no longer burn. The percentage of fuel gas at this point is called the *upper flammable limit or rich limit*. The range of flammability becomes wider as the temperature of the unburned mixture increases. Also, an increase in pressure above atmospheric usually widens the range of flammability. Most of the widening occurs at the rich end of the range. These flammability limits are presented for different fuels in sections 2.4 to 2.6. Some values of flammability limits of gases are given in Appendix B.

For some fuel and oxidant mixtures, e.g. hydrogen + oxygen or acetylene + oxygen, there is a region within the flammability limits where normal flame propagation may be replaced by a detonation. This inner region, when it occurs, it is surrounded by limits of detonability. One might expect the burning velocity of a mixture is to fall smoothly to zero at the flammability limit, but in fact, the limiting burning velocity is found to be finite at around 0.03 to 0.05 m s⁻¹.

2.2.2 Laminar Flame Stabilization

As indicated above, attempting to establish a flame simply by flowing the gases into it at an equal and opposite velocity to the burning velocity does not produce a stable flame. Instead, it is necessary to attach the flame to a flame-holder or burner, which locally interacts with the flow and combustion processes to provide a stabilizing zone. The burner also mixes the fuel and oxidant, and it will in turn establish a particular flow pattern as will be described in sections 2.4 to 2.6.

The effect of the burner rim on the gas-mixture velocity is to reduce it to zero at the walls due to viscous drag whilst its effect on the burning velocity is to reduce it due to quenching, i.e. the removal of heat and possibly active species in its vicinity. Thus, close to the rim, the flame's position can be determined by the relative magnitudes of the local burning velocity, U_l and flow velocity, U_g . If the burning velocity is greater

than the flow velocity, the flame will move closer to the rim until the burning velocity becomes equal to the local flow velocity. Conversely if the flow velocity exceeds the burning velocity, the flame will move downstream until the two become equal. Thus, within certain flow velocity limits the flame will be stabilized or held in place above the rim as shown in Fig. 2.1 (a). If $U_g > U_l$ and the flame is stabilized at the rim, the flame conforms to the flow pattern such that the burning velocity is balanced by the normal component of gas flow as shown in Fig. 2.1 (b), i.e. $U_l = U_g \sin \alpha$.

Outside the flow velocity limits as mentioned before, various forms of instability are possible such as light back or flashback, tilted flames, blowout and lift. Typically, the stability of the flame against flashback and blowout is achieved by quenching or cooling

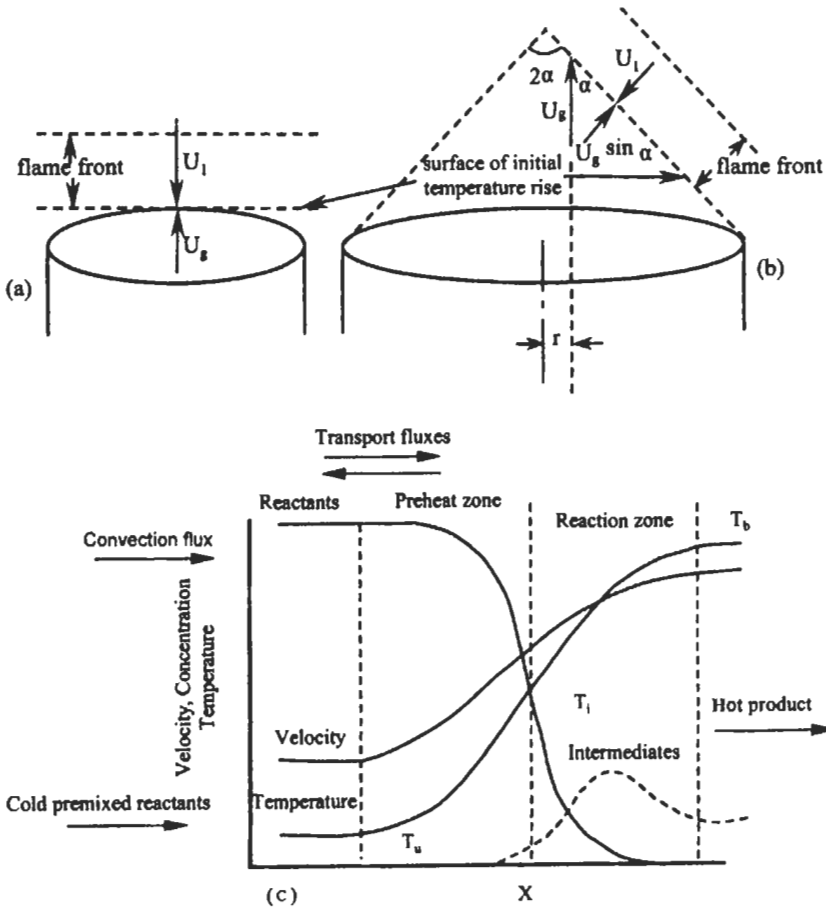


Fig. 2.1: Burning velocity and flow velocity for (a) flat flame and (b) conical flame, (c) is the temperature, concentration and velocity profiles through an idealized one-dimensional stationary premixed flame.

by the burner wall and this in turn reduces the burning velocity in the neighborhood of the wall.

2.2.3 Flame Temperature

This is the temperature of the gases when they leave the reaction zone, T_b (Fig. 2.1(c)). In a diffusion flame, it is difficult to be obtained other than by experiment, since the amounts of the reactants are rather not well-defined. In a premixed flame, a well defined mixture composition enters the flame at a fixed temperature and pressure. It is, therefore, possible to calculate the adiabatic flame temperature from the thermodynamical properties of the original mixture. The equilibrium computer program with 18 chemical product species described in chapter 1 is used in the calculation of adiabatic flame temperature throughout this book. For stoichiometric mixtures of most of the common fuels with air, the flame temperature is about 2000 K. Near the flammability limits, the calculated temperature is lower, about 1400-1500 K. By comparing the calculated and measured flame temperatures it is found that, with few possible exceptions, chemical equilibrium is reached in the product gases.

2.2.4 Burning Velocity of a Premixed Flame

Burning velocity, U_b , is defined as the relative linear velocity with which a planar flame front in a one-dimensional flow system moves normal to its surface through the adjacent unburned gas. Clearly, it is also the volume of combustible mixture, at its own temperature and pressure, consumed in unit time by unit area of flame front. It is independent of flame geometry, burner size and flow rate. As indicated above, the burning velocity is essentially a measure of the overall reaction rate in the flame and is important, both in the stabilization of flames and in determining rates of heat release. The burning velocity of a flame is affected by flame radiation, and hence by flame temperature, by local gas properties such as viscosity, thermal conductivity and diffusion coefficient, and by the imposed variables of pressure, temperature, air-fuel ratio and heat of reaction of mole of mixture. The effect of these parameters on the burning velocity for H_2 , H_2 -CO- H_2O , CH_4 , CH_3OH - H_2O , C_3H_8 , C_2H_6 , natural gas, and high hydrocarbon fuels such as n - C_4H_{10} , C_6H_6 , n - C_7H_{14} , C_8H_{18} , $C_{12}H_{26}$, and $C_{16}H_{34}$ -air flames is given in some details in sections 2.4 to 2.6.

However, although its theoretical definition is straightforward, its practical measurement undoubtedly is not, and there is considerable discrepancies between the results obtained by the various methods. One of the main problems in measuring the normal burning velocity is that a plane flame front can be observed only under very special condition. In nearly all-practical cases, the flame front is either curved or is not normal to the direction of velocity of the gas stream. Broadly speaking there are two types of measurements for burning velocity; one uses flames traveling through stagnant mixtures, whereas the other employs flames that are held stationary in space by a counter flow of fresh mixture. Bradley and his colleagues at the University of Leeds, England, have extensively studied the different experimental techniques for the measuring of burning velocity over many years. They have used the double flame kernel method in a closed vessel, which may offer a simple technique for determinations of the burning velocity for non-stationary flames. Also in stationary

flame methods, those involving a "constant velocity" nozzle or flat flames seem to be preferable, and the most accurate procedure would be to identify the cold gas front and to measure the magnitude and direction of the gas velocity relative to it by using particle tracking or Laser Doppler Velocimetry and allowing for the flow divergence as will be discussed in section 2.4. Recently, techniques for flame observation, probe for flame structure, and measuring burning velocity have been reviewed by Fristrom [71]. The following will describe briefly some of the different techniques for measuring the laminar burning velocity for stationary and non-stationary flames.

Stationary Methods

In these methods, a stream of premixed gas flows into a stationary flame with a velocity equal to the burning velocity. Stability can be achieved by passing the mixture up a tube, at the top of which the annular space separating the flame from the burner edge provides a continuous ignition source and anchors the flame to the burner. The followings are the measurement techniques, which have been used for measuring the laminar burning velocity with stationary flames.

Total area method. When a Bunsen burner is used to measure the normal burning velocity, U_1 , the tube should be sufficiently long for fully developed laminar flow to be achieved (i.e., parabolic velocity distribution). For the nozzle burner, a contraction ratio of at least 5:1 is desirable if a flat velocity profile is to be obtained in the burning region. The main experimental problem is to obtain an accurate photographic record of the location of the flame zone. For most purposes, the line of maximum luminosity, i.e., the line of maximum density on a negative of a film gives the cone boundary with acceptable accuracy. The conditions within an element of the flame front are illustrated in Fig. 2.1 (a).

To determine the normal burning velocity, it is only necessary to measure the gas flow rate and to determine the flame surface area. From these, the burning velocity can be known from V_g/A , where V_g and A are the volume flow rate of gas and total area of flame front, respectively.

Cone angle method. In this method the cone angle of the flame is measured, preferably at a radius equal to 0.7 of the burner radius, where, for a parabolic velocity distribution, the local gas velocity is equal to the average velocity. Then, the burning velocity $U_1 = U_g \sin \alpha$, where U_g and 2α (shown in Fig. 2.1 (b)) are the local gas velocity at radius r and cone angle at radius r , respectively.

Flat flame burner method. Constant velocity profiles of unburned gas issuing from a tube can also be obtained by using flow rectification. At low velocities, with a suitable arrangement of stabilizing screens, a flat stationary flame can be achieved at a short distance above the burner matrix (see section 2.4), whereas at high gas velocities, a conical flame is produced. Burning velocity may be obtained by dividing the gas volume flow rate by the flat flame area, but it is difficult to define the edge of the flame and to measure its area accurately. Because of the foregoing difficulties, particle tracking, total flame electrical conductivity, and change in density techniques have been used to obtain precise results for burning velocity in a flat flame.

Most of the errors involved in the burner method are in the measurement of flame area. To avoid such inaccuracies, the flat flame method with Laser Doppler Velocimetry technique is used by Habik and co-workers as described in sections 2.4.3 and 2.4.4. This is useful for the study of limit mixtures and for investigating low-pressure flames,

where the flame is thicker than that for flame at 1 atm, and this enables accurate measurements of the temperature, velocity and species profiles.

Pressure drop method. The back pressure of a flame due to the acceleration of the flame gases as they pass through the reaction zone, can be related to the burning velocity. Both the pressure differences between the burner and the surrounding atmosphere, and the ratio of densities of the burnt and unburnt gases must be known. Measurement should be made across the flame front, and care should be taken to measure the static pressure rather than the dynamic pressure, as does the pitot probe.

Opposed flames method. Many of the edge problems of the balanced flow methods can be solved by using the opposed double flames method as described in section 2.9. In this method, two flames are produced in opposed flow using a large cylindrical flame or other geometry. Because of the large size, area expansion is minimized, the perturbing effects of external atmospheres are eliminated, and the flow balance point can be accurately established. This method is particularly useful for slow flames near the extinction limit and gives precise results for burning velocity as described in section 2.4.

Propagation Methods

In these methods of measurements, the flame moves through the initially quiescent mixtures. The subsequent spread of such a flame is determined by the nature of the bounding surface between the mixture and its surroundings. These types of bounding surface have been used: rigid cylindrical tubes, either closed at both ends or open at one end or both ends; soap bubble solution or thin elastic membranes; and rigid spherical vessels. Burning velocity measurement can be made by direct measurement of flame propagation. This requires locating the position of the flame front at two (or more) known times. Rapid visualization is required, and it is necessary to know the flame front geometry and the flow constraints, and often the density change across the flame front. The followings are the measurement techniques, which have been used for measuring the laminar burning velocity with non-stationary flames.

Double kernel method. The essence of the method is to oppose a pair of simultaneously ignited flame kernels. As they expand toward one another, the flow of unburned gas is constrained along the line between their centers. The flames flatten and the two approaching flame surfaces approximate the flat flame geometry. Their relative movement asymptotically approaches twice the normal burning velocity. The gas velocity on the axis of centers must be zero at the midpoint, and flame speed along this axis tends to the burning velocity.

Constant explosion method. In this method, a containing envelope surrounds the explosive mixture, which is then ignited centrally, and the rate of propagation of the spherical flame front in space is measured. Close to the point of ignition, the high curvature of the flame causes a reduction in the burning velocity, but if a large vessel is used, approximately of more than 0.25 m diameter, then remote from the spark, the flame front approximates a one-dimensional plane. There are four principal approaches to obtain the burning velocity; first, is the pressure recording during the explosion, second, is the determination of density ratio at constant pressure in a rigid vessel, third, is the determination of density ratio at constant pressure in an elastic envelope, and fourth, is the direct measurement of gas velocity during explosion.

Tube method. This is one of the earliest methods and in this method the mixture is ignited at the open end of a tube and the flame front is photographed as propagating

toward the closed end. The expression for the burning velocity is obtained from the equation of mass conservation for the unburnt gas. There are significant errors in the use of this method for burning velocity measurements.

Because the experimental research is very expensive to cover all the factors and conditions affecting the flame propagation, therefore the modeling techniques can provide an alternative method of estimating the burning velocity and flame structures over wide ranges of operating conditions. Thus in sections 2.3.2 to 2.3.4, a quasi-one-dimensional flame model (treated as a constant pressure) with an interaction solely between chemical events and diffusion of matter and energy is described, and used here to predict the steady, one-dimensional, laminar burning velocity. The predicted burning velocities from the models for H_2 , H_2 -CO- H_2O , CH_4 and CH_3OH - H_2O -air are compared with measurements in sections 2.4.1 to 2.4.5. In section 2.5, a general correlation for burning velocity with the heat of reaction per mole of mixtures for different gaseous and liquid fuels is proposed with an algebraic expression for burning velocity of alkene, alcohol and aromatic in terms of initial pressure, temperature and heat of reaction per mole of mixture.

Finally, the burning velocity of multicomponent mixtures is predicted and given for mixtures of CO- H_2O - O_2 - N_2 and CO- H_2 -air in sections 2.4.1 and 2.4.2. In the literature, there are limited number of experimental measurements for mixtures of hydrogen, methane, carbon monoxide, ethylene and inert gases and there is no general reliable formula to derive the burning velocity of a mixture of fuel gases under different operating conditions. Sections 2.4 to 2.6 cover some of our suggested general correlations for natural gas, propane, n-butane, benzene, n-heptane, gasoline, kerosene and n-hexadecane-air flames.

2.2.5 Ignition

This topic covers the initiation of combustion by a wide variety of means for reactants under a wide range of physical conditions. The ignition phenomena can be divided into two cases: *homogeneous ignition*, in which ignition occurs simultaneously throughout the reactant volume. If the temperature of a vessel containing a homogeneous mixture of reactants is raised, a point is reached at which ignition occurs. This is termed the *self-ignition or auto-ignition*. The criterion for ignition of this kind is related to the net rate of heat loss or gain in a given volume of the reactants. If the heat loss is less than the rate of heat production due to the reaction then ignition will occur. In section 2.4.3, the ignition temperatures are predicted for CH_4 -air flames under different operating conditions. The predicted ignition temperatures from kinetic models and those calculated from thermal theory are compared and generalized with the heat of reaction of mole of mixtures. An algebraic expression is proposed to predict the value of the ignition temperature under different conditions. The second case is instantaneous *point ignition*, in which a flame develops close to the ignition source (e.g. a spark) and then spreads through the reactant volume.

2.3 Theory and Kinetics of Laminar Premixed Flames

2.3.1 Background to Flame Propagation

The propagation mode of laminar flame is expected to govern many properties in the flames. It has been well known that the propagation mode is explained either by means of the "thermal theory" or of the "active-species-diffusion theory". Though these theories are satisfactory for roughly analyzing flame propagation, they are not exact enough to discuss them in details.

The thermal theory neglects the contribution of the chemical reactions in a preheat zone and ascribes the temperature increase in this zone only to thermal conduction. However, at the boundary between a preheat zone and a reaction zone, the increment of thermal energy due to conduction becomes zero and, therefore, conventional heat and heat release through chemical reactions must be equal to each other as indicated by the equation of thermal energy conservation; some chemical reactions must take place at the boundary. Chemical reactions can not start immediately when their environment satisfies certain conditions but are excited gradually.

On the other hand, the flame propagation under the diffusion of active species depends explicitly upon chemical reactions. Chemical reactions should be eventually evaluated accurately for the detailed analyses of both propagation modes. There is a considerable difficulty in expressing analytically the rate of chemical reaction in flames without any experimental data. Moreover, actual flames propagation mode is partly under thermal effects and partly under the diffusion of active species that makes the problem more complicated, and this mode is the one we use throughout this chapter. The flame in this mode is the result of a self-sustaining chemical reactions occurring within a region of space called the flame front where unburned mixture is heated and converted into products. The flame front consists of two regions: a preheat zone and a reaction zone. In the preheat zone, the temperature of the unburned mixture is raised by conductive heat and radicals diffuse from the reaction zone, and there is no significant reaction or energy release occurring in this zone, until reaching a critical temperature, whereas exothermic chemical reaction begins. The region between the temperature where exothermic chemical reaction begins and the hot boundary at the downstream equilibrium burned gas temperature is called the reaction zone. The discussion of this mode will focus mainly on low-velocity laminar premixed flames.

2.3.2 Kinetic Model of Premixed Flames

The study of premixed laminar flame propagation for gaseous and liquid fuels has been long considered as an important subject for experimental and theoretical researches. Thus, the comparison of the measured and predicted flame structure and burning velocity of laminar flame is essential for the successful development of a kinetic model and always demanding test for its accuracy. Recently, the theory and modeling in combustion chemistry has been reviewed by Miller [69].

Here, the basic and comprehensive reaction mechanisms, flame structures, laminar burning velocities, flammability limits, flame thicknesses, ignition temperatures, and heat release rates have been analyzed in section 2.4 through experimental and

theoretical studies of laminar premixed flames for hydrogen, H_2 , carbon-monoxide-hydrogen, $CO-H_2$, methane, CH_4 , methanol, CH_3OH , methanol-water, CH_3OH-H_2O , propane, C_3H_8 , ethane, C_2H_6 , natural gas, n-butane, n- C_4H_{10} , benzene, C_6H_6 , n-heptane, n- C_7H_{14} , n-octane, C_8H_{18} , n-dodecane, $C_{12}H_{26}$, and n-hexadecane, $C_{16}H_{34}$ -air flames. Furthermore, to control the combustion-generated nitrogen oxide emissions, the effect of gaseous additives such as H_2 , CO and C_2H_6 on the formation and oxidation of NO and NO_2 in C_3H_8 -air and CH_4 -air flames as well as the effect of using porous burner on the pollutant emissions are also explained in sections 2.7 and 2.8.

Mathematical models of laminar flames that incorporate detailed chemical kinetics can reveal the detailed flame structure, heat release, and predict the burning velocity. One major difficulty with the comprehensive kinetic models is that they do not readily identify the essential reaction channels and what those to be approximated. This is important because the modeler of more complex aerodynamic system is frequently constrained by computer capabilities and economics when treating simultaneously both the complex chemistry and the aerodynamics. Each new species involved in the model will include an additional differential equation.

In the light of the above remarks, the predicted results from kinetic model for the stated gaseous and liquid fuels will be compared with the experimental data herein. Once the kinetic schemes are validated, the predicted results from kinetic model can be extended to a wide range of conditions and discussed for both fuels.

After studying the burning velocity of H_2 - CO and simple hydrocarbon and alcohol, and the difficulties involved with the chemical kinetics for high hydrocarbons fuels, it was necessary to survey the measured and predicted burning velocity for wide ranges of both conventional and alternative gaseous and liquid fuels. An algebraic expression for the burning velocity of different fuels is suggested in terms of initial pressure, temperature, equivalence ratio, and gaseous fuel and water additives in hydrocarbon and methanol-air flames. The maximum burning velocities of these fuels are evaluated and a degree of generalization of such values is suggested in terms of the heat of reaction per mole of reactants.

Finally, because of the importance of laminar heat release rate in turbulent flamelet model, an algebraic expression in terms of two variables for the profile of normalized heat release rate against fractional temperature increase, is suggested. Effect of the initial temperature and pressure of mixture on these two variables are also explained, but before all of these, it is necessary first to discuss, not in a great details, the mathematical model as in the following parts.

Computational Method

The approach adopted here is that developed over many years by Dixon-Lewis [15, 61, 65, 92-94, 96-98, 136-138] and his colleagues, Isles, Shepherd, Williams, Islam, Missaghi, Cherian, Rhodes, Simpson, Giovangigli, Kee, Miller, Rogg, Smook, Stahl, Warnatz, Bradley, Habik, El-Sherif, Kwa and Mushi [44, 45, 100, 139-156]. This approach is used by the authors and developed further by comparing the predicted results from the model with recent experimental data for methane-methanol-water-air flames. Figure 2.1(c) illustrates the main aerodynamic features of the stationary, premixed one-dimensional flame. In addition to the convective fluxes through the flame, there are molecular transport fluxes along the direction of the temperature and compositional gradients. It is the coupling of these with the combustion chemistry,

which causes the flame to propagate. Conservation equations are set up for flow in the x -direction and these are solved in time dependent form by the implicit method. This implicit solution approach has been used successfully for one-dimensional premixed flame modeling of flames in hydrogen bromine (Spalding and Stephenson [87]), hydrogen-air (Stephenson and Taylor [157], Warnatz [158] and Dixon-Lewis [94, 97, 98]), hydrogen-carbon monoxide-air (Warnatz [159] and Cherian et al [144]), methane-air (Smoot et al [88], Bradley et al [160], Warnatz [80], Dixon-Lewis [96], Dixon-Lewis and Islam [143], Dixon-Lewis et al [146], Bradley et al [149] and El-Sherif [152, 153]), methanol-air (Westbrook and Dryer [161], Dove and Warnatz [162], Bradley et al [44], El-Sherif [152] and Abu-Elenin et al [154]), methanol-water-air by Habik [274], and other lower hydrocarbon-air systems (Habik [156], Bradley et al [45] and Warnatz [80]). An eventual objective of such modeling is the validation of reaction mechanisms and rate parameters, which may ultimately be of service for the solution of more practical flame problems.

Conservation of total mass. In the steady state, the global mass flux, M_x is conserved and it is the adiabatic mass burning velocity. It is also an eigenvalue solution of the physical problem, which equals the product of density and linear velocity of the gas at any position in the flame. Thus:

$$M_x = \rho_u U_u = \rho_b U_b = \text{constant} \quad (2.1)$$

where the subscripts u and b refer to the unburnt and burnt gas, respectively, and U_u is the laminar burning velocity.

In addition, there must be a conservation equation for each chemical species. The concentration of each species i is expressed either as a product of total molar density, ρ_{molar} , and mole fraction X_i , or as a product of density, ρ , and mass fraction Y_i . In an N -component system, mass and mole fractions are related by:

$$Y_i = \frac{m_i X_i}{\sum_{j=1}^N (m_j X_j)} \quad (2.2)$$

$$X_i = \frac{Y_i / m_i}{\sum_{j=1}^N (Y_j / m_j)} \quad (2.3)$$

where m denotes the molecular weight, and the density can be represented as:

$$\rho = \rho_{\text{molar}} \sum_j (m_j X_j) = \frac{\rho_{\text{molar}}}{\sum_j (Y_j / m_j)} \quad (2.4)$$

The species continuity equation then becomes:

$$\frac{\partial}{\partial t}(\rho Y_i) + \frac{\partial}{\partial x}(F_{ix}) = q_i \quad (2.5)$$

where F_{ix} is the flux of the species i in the x -direction and q_i is its mass chemical rate of formation. There is one equation for each species (Eq. 2.5). Computationally, an initial unsteady state is assumed. Ultimate solutions are, of course, for the steady state.

Because of the species concentration gradients in flames, the fluxes F_{ix} consist of two parts; a convective flux ($M_x Y_i$) due to the overall mass flow and a mass diffusive flux j_i . In the one-dimensional case:

$$F_{ix} = M_x Y_i + j_i \quad (2.6a)$$

$$F_{ix} = M_x G_i \quad (2.6b)$$

where G_i is the mass flux fraction. For a stationary, one-dimensional flame and for constant M_x , the mass chemical rate of formation can be presented as:

$$q_i = M_x (dG_i / dx) \quad (2.7)$$

The chemistry is represented in Eq. 2.5 by q_i , which may be expressed as:

$$q_i = m_i R_i \quad (2.8)$$

where R_i is the net molar rate of formation of the species. Particular reactions are discussed in section 2.3.4. The overall rate q_i for each species is obtained by a summation of all the separate rates of its formation in each elementary reaction in which it occurs. For the elementary reaction:



The volumetric molar rate for the creation of C is given by:

$$\begin{aligned} R_c &= k_f \rho_{\text{molar}}^2 X_A X_B - k_r \rho_{\text{molar}}^2 X_C X_D \\ R_c &= k_f \rho_{\text{molar}}^2 (X_A X_B - X_C X_D / K) \\ R_c &= k_f \rho^2 (\sigma_A \sigma_B - \sigma_C \sigma_D / K) \end{aligned} \quad (2.10)$$

where $\sigma_i = Y_i / m_i$, k_f and k_r are forward and reverse rate coefficients and $K = k_f / k_r$ is the equilibrium constant and these are discussed in chapter 1. Both the rate coefficients and equilibrium constant are functions of temperature, and sometimes also of pressure. The dependence on temperature, T , is expressed by:

$$k = AT^B \exp(-C/T) \quad (2.11)$$

or

$$K = DT^E \exp(-F/T) \quad (2.12)$$

The numerical values of the constants, A, B, C, D, E, and F that were used in this work are given in Tables 2.2 to 2.9, 2.14, and 2.15.

In terms of σ_j , Eq. 2.6 becomes:

$$F_{ix} = m_i \sigma_i M_x + j_i \quad (2.13)$$

Substituting from Eqs. 2.8 and 2.13 in Eq. 2.5, leads to:

$$\rho \left[\frac{\partial \sigma_i}{\partial t} \right] + M_x \left[\frac{\partial \sigma_i}{\partial x} \right] = - \frac{\partial}{\partial x} \left[\frac{j_i}{m_i} \right] + R_i \quad (2.14)$$

Evaluation of the diffusion fluxes was conducted by the method evolved by Dixon-Lewis over a number of years (Dixon-Lewis [15]), namely:

$$j_i = - \left\{ \beta_i^h \left[\frac{\partial h}{\partial x} \right] + \sum_{j=1}^N \beta_{ij} m_j \left[\frac{\partial \sigma_j}{\partial x} \right] \right\} \quad (2.15)$$

where:

$$\beta_{ij} = \sum_{k=1}^N [(1 - \delta_{ik}) \rho \sigma_k D_{ik} (m_i m_k / m_j)] - (1 - \delta_{ij}) \rho D_{ij} (m_i / m_G) - \beta_i^h h_j$$

$$(j = 1, 2, \dots, N) \quad (2.16)$$

$$\beta_i^h = D_i^T / C_p T \quad (2.17)$$

Here $[m_G]$ denotes the average molecular mass $\left(\sum_j \sigma_j \right)^{-1}$, δ_{ij} is the Kronecker delta

(Dixon-Lewis [15]), C_p is specific heat per unit mass, D_{ij} and D_i^T are the multicomponent diffusion coefficients and multicomponent thermal diffusion coefficients, respectively. These were computed from the equations of Mason, Monchick and Munn [163, 164] as discussed by Dixon-Lewis [15, 142]. More details and solutions of these equations are given elsewhere (Dixon-Lewis [15]).

The relation between enthalpy and temperature for each chemical species was provided by second order polynomial fits of gaseous specific heats and enthalpies over 300 K temperature range, then:

$$h = \sum_i^N (\sigma_i H_i) \quad (2.18)$$

$$h = \sum_i^N \sigma_i (a_{i,0} + a_{i,1}T + a_{i,2}T^2) \quad (2.19)$$

where H_i is the molar enthalpy, and $a_{i,0}$, $a_{i,1}$ and $a_{i,2}$ are polynomial coefficients for the species. These coefficients are given in chapter 1. The thermal data were taken from JANAF Thermochemical Tables [13] and NASA Thermochemical polynomials Tables [12]. In addition to the above equations, an auxiliary ideal gas equation of state was required:

$$p/\rho = \left(\sum_i \sigma_i \right) RT \quad (2.20)$$

where R is the molar gas constant.

Conservation of energy. For the present conditions, neglecting the small changes in pressure and viscous dissipation, the equation takes the form:

$$\rho(\partial h / \partial t) + M_x (\partial h / \partial x) = - \frac{\partial}{\partial x} [(Q_D + Q_T + Q_R)] \quad (2.21)$$

where h is the mass specific enthalpy, while Q_T , Q_D , and Q_R are the energy fluxes in the x -direction due to conduction, diffusion and radiation, respectively. Only in dust and coal flames the radiation may be significant. However, in the gaseous flame studies it is neglected. A detailed transport flux formulation is used. The transport fluxes in an N -component system are defined (Dixon-Lewis [15]) by:

$$Q_T + Q_D = - \left[\gamma^h \left(\frac{\partial h}{\partial x} \right) + \sum_{j=1}^N \gamma_j m_j \left(\frac{\partial \sigma_j}{\partial x} \right) \right] \quad (2.22)$$

where:

$$\gamma^h = \frac{\lambda_o}{C_p} + \sum_{k=1}^N \beta_k^h h_k, \quad (2.23)$$

and

$$\gamma_j = \frac{RT}{m_j} \left[\frac{D_j^T}{m_j \sigma_j} - \sum_{k=1}^N D_k^T \frac{m_G}{m_k} \right] - \frac{\lambda_o h_j}{C_p} + \sum_{k=1}^N h_k \beta_{ki} \quad (2.24)$$

$$(j = 1, 2, \dots, N)$$

The first term on the right of Eq. 2.22 represents Q_T and the second one for Q_D . The first and second terms in Eq. 2.24 represent the contributions of thermal diffusion. Thermal diffusion of hydrogen atoms can be important in flames (Dixon-Lewis [15]). The notations and other parameters in the equations are defined in this section and λ_o is the thermal conductivity of the mixtures computed from the equations of Mason, Monchick and Munn [163, 164] and discussed in details by Dixon-Lewis [15]. Some more details about λ_o are given in chapter 1 (section 1.6).

Boundary conditions and solution of equations. The complete set of Eqs. 2.14 and 2.21 must be solved subject to the boundary conditions, which define the specific problem. For "free flame" these can be written:

$$\begin{aligned} x_b = -\infty, \quad \frac{\partial \sigma_i}{\partial x} = 0, \quad \frac{\partial h}{\partial x} = 0 \\ x_u = +\infty, \quad \sigma_i = \sigma_{iu}, \quad h = h_u(T_u, \sigma_{iu}), \\ \frac{\partial \sigma_i}{\partial x} = 0, \quad \frac{\partial h}{\partial x} = 0 \end{aligned} \quad (2.25)$$

where the subscripts u and b refer to unburnt and burnt gas, respectively.

As the first step towards a solution of Eqs. 2.14 and 2.21, they are transformed into the von Mises system of coordinates. The details of this are given by Dixon-Lewis [15]. The resulting equations are then integrated forward in time, subject to the boundary conditions. Numerical integrations were performed by means of finite difference techniques with a rectangular grid. Initially, sigmoid-shaped starting profiles of species concentrations and enthalpy were assumed. In order to concentrate the grid spacing at the position where most reactions occur, a total of between 33 and 53 grid points were distributed non-uniformly. The input dependent variables are the mole fraction composition, pressure, and temperature of the initial mixture, together with rough estimates of the hot boundary values. Mole fractions were converted to values of the working composition variables σ_i , and the specific enthalpy of the unburnt mixture was then calculated. The final specific enthalpy assumed the same value. A few grid points near each boundary were given the boundary values of the dependent variables, and a suitable curve generating algorithm was used to initialize values in the central region of the grid (Dixon-Lewis [15]). The object of the calculation is to either observe the evolution of the flame profiles with time or to determine the steady-state value of $(M_x A)$ and the corresponding profiles of the dependent variables. The transport parameters and reaction mechanisms with their rate parameters used in the above model will be discussed next.

2.3.3 Transport Parameters

Molecular interactions for the transport property calculations were represented by the Lennard-Jones (12:6) potential as described in chapter 1, with the use of the force constants given in Table 2.1. This Table involves all the species, which have been used in the kinetic mechanisms described below in sections 2.3.4 and 2.6 to 2.8. Many of the

data for the transport property have been calculated by Dixon-Lewis [97, 15]. For methanol-air mechanism [44, 154] the values of force constants, ϵ_{ij} , S_i and rotational collision number, τ_{ij} for CH_3OH were taken, respectively from Svehla [165] and Monchick and Mason [163]. Because there are no data for ϵ_{ij} , S_i and τ_{ij} available for CH_2OH and CH_3O , they are assumed to be the same as for CH_3OH . For methane-air mechanism, the molecular parameters for C_2H_3 , C_2H_2 and CH_2 species were taken from Warnatz [166]. For propane mechanism, the transport parameters for C_3H_8 , $n\text{-C}_3\text{H}_7$, $i\text{-C}_3\text{H}_7$ and C_3H_6 , were assumed to be the same and were taken from Warnatz [166]. For high hydrocarbon mechanism, the transport parameters of C_4H_{10} , C_6H_6 , C_7H_{16} , C_8H_{18} , $\text{C}_{12}\text{H}_{26}$, and $\text{C}_{16}\text{H}_{34}$ were assumed to be the same and were taken from Warnatz [166]. Also, for the species involved in nitrogen compounds mechanism such NO , NO_2 , N_2O and N , the transport parameters were taken from Svehla [165]. The collision number τ_{ij} assumed for relational relaxation of each polyatomic species on colliding with any other species j is given in the fourth column in Table 2.1. These values are required only for the thermal conductivity and thermal diffusion calculations. The Lennard-Jones parameters (ϵ_{ij}/k) and S_i are the characteristics of the colliding species and thus in the elastic-collision case, all the necessary integrals can be found at any temperature (see chapter 1, section 1.6). All the parameters in Table 2.1 were used to calculate the transport fluxes due to conduction and diffusion. In the interests of computational economy, only OH , O , H , N_2 , O_2 , H_2 , CO , CO_2 , H_2O , CH_3OH , C_3H_8 , C_2H_4 , C_2H_2 , and CH_4 were included in the calculations of the thermal conductivity. Table 2.1 was added to each kinetic scheme of H_2 , $\text{H}_2\text{-CO}$, CH_4 , CH_3OH and $\text{CH}_3\text{OH} + \text{H}_2\text{O}$ -air mixtures throughout the computations in this chapter.

2.3.4 Reaction Mechanisms for Simple Fuels

This section summarizes the important features in the kinetic mechanisms and reaction rate parameters for the combustion of H_2 , CO-H_2 , CH_4 , CH_3OH , C_3H_8 , C_2H_6 , and natural gas fuels. The reaction mechanisms adopted here are those developed over about thirty-five years by Dixon-Lewis and colleagues [15, 44, 45, 61, 65, 92-94, 96-98, 100, 136-156, 160]. These mechanisms were developed further by the authors of this book for high hydrocarbon fuels.

(i) Reaction Mechanism for H_2 -Air Flame

Hydrogen is an important practical fuel. The kinetic modeling of the hydrogen-oxygen-nitrogen flame has been extensively studied and discussed in details by Dixon-Lewis et al [167], Dixon-Lewis and Williams [142], Day et al [168], Snyder and Skinner [169], Dixon-Lewis [65, 94, 96-98, 137], and Warnatz [159]. They showed that, the more important reactions and their rates controlling the burning velocity and flame structures are the reactions R_1 to R_{13} which are given in Table 2.2. In this Table, the rate coefficients are expressed as $k = AT^B \exp(-C/T)$, both in units of $\text{cm}^3 \text{mole}^{-1} \text{s}^{-1}$ and equilibrium constants as $K = DT^E \exp(-F/T) = k_f/k_r$.

The radical species O , H and OH in this mechanism are produced by the chain branching cycle consisting of reactions R_1 to R_3 . In the hotter regions of the flames, they diffuse upstream to meet the incoming oxygen and react with it by the lower activation energy cycles via reaction, R_4 . Then R_4 is followed by reactions, R_5 to R_9 .

Table 2.1: Lennard-Jones (12:6) potential and rotational parameters as well as the rotational collision number.

Species	ϵ_{ij}/k (K)	(Si)/(n/m)	τ_{ij}^a
H	37.0	0.2070	-
O	106.7	0.3050	-
OH	79.8	0.3147	4.5
N ₂	71.4	0.3798	4.5
O ₂	106.7	0.3467	4.5
H ₂	59.7	0.2827	200.0
CO	91.7	0.3690	4.5
CO ₂	195.2	0.3941	2.5
CH ₃ OH	481.8	0.3626	0.9
H ₂ O	260.0	0.2800	4.0
CH ₂ O	312.0	0.3758	2.5
CHO	187.0	0.3465	-
HO ₂	168.0	0.3068	-
CH ₂ OH	481.8	0.3626	0.9
CH ₃ O	481.8	0.3626	0.9
CH ₄	148.6	0.3758	2.5
H ₂ O ₂	289.3	0.4196	-
C ₂ H ₆	215.7	0.4443	2.5
C ₂ H ₄	224.7	0.4163	2.5
CH ₃	312.0	0.3644	-
C ₂ H ₅	220.2	0.4303	-
C ₂ H ₂	209.0	0.4100	-
C ₂ H ₃	209.0	0.4100	-
CH ₂	148.6	0.3760	-
C ₃ H ₆	267.0	0.498	-
C ₄ H ₁₀	357.0	0.5180	1.0
NO	116.7	0.3490	1.0
NO ₂	232.4	0.3830	1.0
N ₂ O	232.4	0.3830	1.0
N	71.40	0.3290	1.0

^a Assumption is made that τ_{ij} depends only on i .

Superimposed on all of these are the effects of the radical recombination steps; R_{10} to R_{12} . But because of the competition with reaction (R_4), these only become dominant in situations where molecular oxygen is more or less absent, for example in the recombination zones of fuel-rich flames.

Because the combined concentrations of H, OH, and O in the flames at atmospheric pressure and below are very much higher than the concentration of HO_2 at all positions except a very small region at the start of the reaction zone, the participation of hydrogen peroxide H_2O_2 is omitted in this mechanism (Dixon-Lewis and Williams [142] and Bradley et al [44]).

The whole series of reverse reactions, R_1 to R_{13} is included in the whole calculations of the flame. Although many of these only become significant in limited regions of the flames, they are nevertheless essential for the representation of the approach to full equilibrium in the hot gases. Reaction ($-R_1$ to $-R_3$ and $-R_{13}$) further play a significant role in the whole of the recombination zone.

In the high temperature combustion of hydrogen, hydrogen-carbon monoxide and hydrocarbons, reaction, R_2 , is the most important chain branching reaction, consuming one H atom and producing two radical species O and OH. In any combustion system, an increase in H atoms production will accelerate the overall rate of combustion by increasing the net amount of chain branching from reaction, R_2 . Conversely, processes, which reduce the H atom concentration, and reactions which compete with, R_2 for H atoms will tend to inhibit the combustion.

Also reaction, R_4 , competes directly with reaction, R_2 , for H atoms, but the rate of the third order reaction, R_4 , is much more pressure dependent than that of, R_2 . Reaction, R_4 begins to compete effectively with reaction, R_2 for H atoms at pressures higher than 1 atm and leads to reduce the burning velocity, but below the atmospheric pressure, reaction, R_4 , does not compete effectively and leads to increase the burning velocity. This exhibits the non-linear dependence of burning velocity on pressure for H_2 , $\text{H}_2\text{-CO}$ and any other hydrocarbon fuels (as it will be shown later in this chapter) or for non-hydrocarbon fuels such as ammonia (NH_3), hydrazine (N_2H_4) and other M-H systems. Moreover, the addition of many halogenated species inhibits the combustion process by removing H atoms from the radical pool, forming H_2 by a catalytic cycle of reaction, thereby reducing the rate of chain branching and slowing the overall rate of combustion process. In addition to the above, nearly all of the elementary reactions rates increase with temperature to accelerate the fuel consumption, heat release rate, and overall combustion process.

Following the above discussion, many hydrocarbon species act as inhibitors for the H_2 -air system (Snyder and Skinner [169]). This is due to the fact that the rates of reaction of breakdown of many hydrocarbon species by H atoms are considered to be larger than the rate of reaction, R_2 , and consequently these reactions will compete effectively with R_2 . Furthermore the reverse of reaction, R_7 , provides a mechanism for initiation of $\text{H}_2\text{-O}_2$ mixture and, R_1 , is responsible for the majority of H_2 consumption.

The extensive comparison between the experimental and predicted results (in this chapter) using the reactions and rate parameters of, R_1 to R_{13} in Table 2.2, confirmed that all the important reactions, R_1 to R_{13} and their rate parameter constants are now well known with good accuracy. The same reactions, R_1 to R_{13} with their rate parameters form an important group of reactions in CO-H_2 , hydrocarbon and alcohol-air flames. Reliable information about these reactions with their rate parameters therefore becomes important as an aid to the elucidation of the more complex hydrocarbon, alcohol and coal-air kinetic mechanism. One last feature is that Dixon-Lewis and his collaborators (Dixon-Lewis et al [170], Dixon-Lewis [97, 98, 136], Dixon-Lewis, and Williams [18], Dixon-Lewis et al [146], and El-Sherif [152]) have devoted a great deal of attention to the problem of third body or Chaperon efficiencies. The Chaperon

efficiency increases with the number of degrees of freedom available to share collisional energy, and water molecules are particularly good Chaperons, with efficiencies 10 to 50 times larger than those of N_2 . The predicted results from the above mechanism and its rate parameters as stated in Table 2.2, in addition with transport properties given in Table 2.1 are compared with recent experimental results and discussed in section 2.4.1.

(ii) Reaction Mechanism for H_2 -CO and CH_2O - O_2 - N_2 Flames

Reactions in the H_2 -CO-air flame are part of the main chain-branching processes maintaining high temperature combustion of hydrocarbon fuels. As described before, the mechanism of the H_2 -air flame and the rate constants of elementary steps involved are well established nowadays. Since carbon monoxide is an important intermediate in hydrocarbon flames, it becomes necessary to develop, as far as possible, kinetic mechanisms with its rate parameters which will satisfactorily predict the experimental data. The CO is the primary product of hydrocarbon oxidation, and is converted to CO_2 in a subsequent slow secondary reactions, and takes place over a more extended region on the hot, burnt gas side of the flame. The responsible reaction for the bulk of the slow oxidation to carbon dioxide is the forward reaction, R_{14} (Table 2.2), and this reaction is important in flames and other systems. Because R_{14} consumes nearly all of the CO with OH, the rate of CO oxidation depends very much on the availability of OH radicals. The presence of any hydrocarbon fuel will effectively inhibit the oxidation of CO until all of the fuel has disappeared, whereupon the OH concentration rises sharply the reaction, R_{14} , and rapidly consumes the CO to produce CO_2 .

Reaction R_{14} and its rate expression has been studied extensively by several workers and well established nowadays as given in Table 2.2 by Dixon-Lewis [65, 96, 97, 137], Baulch and Drysdale [171], Bradley et al [149], and El-Sherif [152]. In addition to reaction R_{14} , carbon monoxide may undergo two further reactions with the chain carriers of the hydrogen-air system. These are, R_{15} and R_{16} in Table 2.2. These two reactions are much slower than reaction R_{14} and they are important as a chain-termination step, which affects the overall concentration of chain carriers. In hydrogen-carbon monoxide-air flame, the formyl radical HCO formed in reaction, R_{16} , will either redissociate by reaction, $-R_{16}$, or undergo one of the forward reactions, R_{17} to R_{20} . All these reactions of the formyl radical are important also in any hydrocarbon flames. The study of carbon monoxide-hydrogen flame mechanism may therefore provide further information on the subgroup mechanism of the reactions involved in the hydrocarbon flames. Such kinetic reactions of this system, R_{14} to R_{20} are given with their rate parameters in Table 2.2. The extensive comparison between the predicted results from such mechanism with the experimental data confirmed the mechanism and its rate parameters. This comparison will be described in the next section [15, 61, 65, 96-98, 100, 137-146].

Formaldehyde, CH_2O , is an intermediate in the oxidation of most hydrocarbon fuels, and modeling of formaldehyde-oxygen supported flames provides an essential link between the H_2 -CO-air and hydrocarbon-air systems. The modeling of these was discussed by Dixon-Lewis [137] in relation to the flame structure measurements of Oldenhove de Guertechin et al [172] and it is established that the CH_2O was consumed primarily by reactions, R_{21} - R_{23} . These reactions with their appropriate rate expressions are also given in Table 2.2. In fuel-rich mixture, reaction R_{21} dominates, while in lean and stoichiometric conditions, R_{22} and R_{23} dominate. The formyl radical HCO will react

Table 2.2: Parameters of expressions of forward rate coefficients, k_f , and equilibrium constants, K used in kinetic mechanisms [44]. Reproduced by permission of Elsevier Science.

No	Reaction	Ref	A	B	C/(K)	D	E	F/(K)
1	$\text{OH}+\text{H}_2\leftrightarrow\text{H}_2\text{O}+\text{H}$	137	1.10×10^9	1.3	1825	0.21	0.0	-7640
2	$\text{H}+\text{O}_2\leftrightarrow\text{OH}+\text{O}$	97,98	1.80×10^{14}	0.0	8450			
3	$\text{O}+\text{H}_2\leftrightarrow\text{OH}+\text{H}$	137	1.80×10^5	2.5	3300			
4	$\text{H}+\text{O}_2+\text{H}_2\leftrightarrow\text{HO}_2+\text{H}_2$	137	2.80×10^{18}	-0.86	0.0	0.745	0.0	-2338
	$\text{H}+\text{O}_2+\text{N}_2\leftrightarrow\text{HO}_2+\text{N}_2$		3.75×10^{20}	-1.72	0.0			
	$\text{H}+\text{O}_2+\text{O}_2\leftrightarrow\text{HO}_2+\text{O}_2$		3.00×10^{20}	-1.72	0.0			
	$\text{H}+\text{O}_2+\text{H}_2\text{O}\leftrightarrow\text{HO}_2+\text{H}_2\text{O}$		9.40×10^{18}	-0.76	0.0			
	$\text{H}+\text{O}_2+\text{CO}\leftrightarrow\text{HO}_2+\text{CO}$		2.10×10^{18}	-0.86	0.0			
	$\text{H}+\text{O}_2+\text{CO}_2\leftrightarrow\text{HO}_2+\text{CO}_2$		4.10×10^{18}	-0.86	0.0			
	$\text{H}+\text{O}_2+\text{CH}_4\leftrightarrow\text{HO}_2+\text{CH}_4$		5.60×10^{18}	-0.86	0.0			
5	$\text{H}+\text{HO}_2\leftrightarrow\text{OH}+\text{OH}$	137	2.20×10^{14}	0.0	710			
6	$\text{H}+\text{HO}_2\leftrightarrow\text{O}+\text{H}_2\text{O}$	137	5.0×10^{12}	0.0	710			
7	$\text{H}+\text{HO}_2\leftrightarrow\text{H}_2+\text{O}_2$	137	2.16×10^{13}	0.0	280			
8	$\text{OH}+\text{HO}_2\leftrightarrow\text{H}_2\text{O}+\text{O}_2$	137	1.80×10^{13}	0.0	0.0			
9	$\text{O}+\text{HO}_2\leftrightarrow\text{OH}+\text{O}_2$	137	2.00×10^{13}	0.0	0.0			
10 ^a	$\text{H}+\text{H}+\text{H}_2\leftrightarrow\text{H}_2+\text{H}_2$	137	9.20×10^{16}	-0.60	0.0	0.24	0.0	-5259
	$\text{H}+\text{H}+\text{N}_2\leftrightarrow\text{H}_2+\text{N}_2$		1.00×10^{18}	-1.00	0.0			
	$\text{H}+\text{H}+\text{O}_2\leftrightarrow\text{H}_2+\text{O}_2$		1.00×10^{18}	-1.00	0.0			
	$\text{H}+\text{H}+\text{H}_2\text{O}\leftrightarrow\text{H}_2+\text{H}_2\text{O}$		6.00×10^{19}	-1.25	0.0			
	$\text{H}+\text{H}+\text{CO}\leftrightarrow\text{H}_2+\text{CO}$		1.00×10^{18}	-1.00	0.0			
	$\text{H}+\text{H}+\text{CO}_2\leftrightarrow\text{H}_2+\text{CO}_2$		5.49×10^{20}	-2.00	0.0			
	$\text{H}+\text{H}+\text{CH}_4\leftrightarrow\text{H}_2+\text{CH}_4$		5.49×10^{20}	-2.00	0.0			
11	$\text{H}+\text{OH}+\text{M}\leftrightarrow\text{H}_2\text{O}+\text{M};$ $\text{M}=\text{H}_2, \text{O}_2, \text{N}_2, \text{CO}, \text{CO}_2,$ $\text{M}=\text{H}_2\text{O}$	137	1.60×10^{22}	-2.00	0.0			
			8.00×10^{22}	-2.00	0.0			
12	$\text{H}+\text{O}+\text{M}\leftrightarrow\text{OH}+\text{M};$ $\text{M}=\text{H}_2, \text{O}_2, \text{N}_2, \text{CO}, \text{CO}_2,$ $\text{M}=\text{H}_2\text{O}$	137	6.20×10^{16}	-0.60	0.0			
			3.10×10^{17}	-0.60	0.0			
13	$\text{OH}+\text{OH}\leftrightarrow\text{O}+\text{H}_2\text{O}$	137	$e(27+1.5 \times 10^{-3}T)$					
14	$\text{OH}+\text{CO}\leftrightarrow\text{CO}_2+\text{H}$	137	1.50×10^7	1.3	-385	3.8×10^{-7}	1.2	-13067
15 ^b	$\text{O}+\text{CO}+\text{M}\leftrightarrow\text{CO}_2+\text{M};$ $\text{M}=\text{H}_2, \text{O}_2, \text{N}_2, \text{CO}, \text{CO}_2,$ $\text{CH}_4 \text{ \& } \text{H}_2\text{O}$	137	5.40×10^{15}	0.0	2300			
16 ^c	$\text{H}+\text{CO}+\text{M}\leftrightarrow\text{CHO}+\text{M};$ $\text{M}=\text{H}_2, \text{O}_2, \text{N}_2, \text{CO}, \text{CO}_2,$ $\text{CH}_4 \text{ \& } \text{H}_2\text{O}$	137	5.00×10^{14}	0.0	755	1.7	0.0	-7080
17	$\text{CHO}+\text{O}_2\leftrightarrow\text{HO}_2+\text{CO}$	137	3.3×10^{13}	-0.4	0.0			
18	$\text{CHO}+\text{H}\leftrightarrow\text{H}_2+\text{CO}$	-	1.2×10^{14}	0.0	0.0			
19	$\text{CHO}+\text{OH}\leftrightarrow\text{CO}+\text{H}_2\text{O}$	137	1.0×10^{14}	0.0	0.0			
20	$\text{CHO}+\text{O}\leftrightarrow\text{OH}+\text{CO}$	-	3.0×10^{13}					
21	$\text{CH}_2\text{O}+\text{H}\leftrightarrow\text{CHO}+\text{H}_2$	137	1.0×10^4	3.0	700	10.6	0.0	-7778
22	$\text{CH}_2\text{O}+\text{OH}\leftrightarrow\text{CHO}+\text{H}_2\text{O}$	137	3.0×10^{13}	0.0	600			
23	$\text{CH}_2\text{O}+\text{O}\leftrightarrow\text{CHO}+\text{OH}$	137	1.8×10^{13}	0.0	1540			

^a Chaperon efficiency relative to H_2 for CO assumed the same as for N_2 ^{b,c} Chaperon efficiencies relative to H_2 are the same as in reaction (R_4) for $\text{N}_2, \text{O}_2, \text{H}_2\text{O}, \text{CO}_2$ and CH_4 .

with other radical species and molecular oxygen by reactions R_{17} to R_{20} . The predicted results from this mechanism for $\text{CO}-\text{H}_2-\text{H}_2\text{O}$ will be discussed in section 2.4.2.

(iii) Reaction Mechanism for Methane, CH₄-Air Flame

Methane is an important practical fuel, constituting approximately 90% of the composition of natural gas. In addition to that methane is chemically simple molecules, extensive kinetic modeling work has been devoted to its oxidation than to all hydrocarbon fuels combined [173]. The earliest such mechanism introduced by Smoot et al [88] and by Tsatsaronis [174], involved 14 species and about 30 reactions with C1 reactions. They compared their predicted and experimental results in lean and near stoichiometric methane-air flames. Warnatz [28] and Westbrook [175] introduced a much more complicated scheme involving 226 species with 74 reactions and 24 species with 74 reactions, respectively. They claimed with Dixon-Lewis [61] and Egolfopoulous et al [176] that C2 species were important for modeling rich or even near stoichiometric flames. During the pyrolysis and oxidation of methane, radical recombination reactions produce significant amounts of C2 hydrocarbons, and species such as ethylene, C₂H₄, ethane, C₂H₆, and acetylene, C₂H₂, which have been observed by methane-air flames (Langley and Burgess [177]). The subsequent consumption reactions of these C2 species must therefore be included in a complete CH₄ mechanism.

Dixon-Lewis [61] attempted to identify the major reaction channels in large mechanisms such as that of Warnatz [28] and Westbrook [175]. He compared two mechanisms, one with 14 species and one with 18 species (including C2, but without C₂H₂ reactions). Both schemes were considered valid for lean or stoichiometric flames; this is because both oxidation bathes include the standard CH₄ → CH₃ → CH₂O → CHO → CO → CO₂.

One of the major difficulty in kinetic model is that, the very comprehensive kinetic schemes do not readily identify the major reaction channels which must be included in specific situations and what approximations can be safely made. These are valid questions from the modeler of more complex chemistry and aerodynamic systems such as turbulent and coal flames, which are frequently constrained by computer capabilities. In this context a reduction in the number of species is more important than a reduction in the number of reactions, since each new species involves the setting up of a fresh differential equation. In the light of these remarks, the adopted kinetic scheme for methane-air flame is based on earlier C1 and C2 kinetic mechanism (called here scheme A and B, respectively) developed by Dixon-Lewis, Islam, Bradley, Habik, and El-Sherif [61, 143, 146, 149], and El-Sherif [152]. Their C2 scheme truncated at the ethylene stage (scheme B). Here scheme B is developed further to include acetylene, C₂H₂ and its subsequent reactions. This is called here scheme C, and is validated against the experimental results in lean and rich flames (El-Sherif [153]) and will be discussed in details in Section 2.4.3.

The established chemical reactions and its rate parameters involved in breakdown of CH₄ to C1 and C2 hydrocarbons are given in Tables 2.3 and 2.4, respectively. Table 2.5 involves breakdown of C₂H₄ to C₂H₃, C₂H₂ and its subsequent reactions. Table 2.3 gives the key reactions involving the attack of CH₄ by radical species, R₂₄ to R₂₆. A major reaction of methyl radical includes, R₂₇ and R₂₈. The subsequent reactions of CH₂O to CHO, CO and CO₂ that are discussed above are given in Table 2.2. Reactions and rate parameters that are given in Table 2.2, together with those in Table 2.3 comprise scheme A. This scheme involves only C1 hydrocarbon and it has a number of reactions of 28 with 14 chemical species (H, O, OH, H₂, O₂, N₂, H₂O, HO₂, CO, CO₂, CH₄, CH₃, CHO and

CH₂O).

Scheme B, involves all reactions, rate coefficients (or parameters) and equilibrium constants of Tables 2.2, 2.3 and 2.4. This scheme involves 44 reactions with 18 species. Reactions R₂₉ to R₃₁ in Table 2.4 show variety of additional attack on CH₃ by CHO and HO₂ to form CH₄ and CH₃O (R₂₉ to R₃₁). Methoxy radical, CH₃O, reacts primarily by means of R₃₂ to R₃₄ as given in Table 2.4. All of these reactions produce CH₂O, which again reacts in subsequent reactions that are given in Table 2.2. In addition to reactions R₂₉ to R₃₁, other methyl recombination reaction includes, R₃₅. The key reactions for C₂H₆ include reactions R₃₆ to R₃₈ as given in Table 2.4. Reaction of the ethyl radical, C₂H₅, include reactions R₃₉ to R₄₂ as presented in Table 2.4.

The importance of reactions R₄₀ and R₄₁ often lies in their roles as chain termination steps rather than their direct effects or the rate of ethyl radical consumption. Ethylene is the product of reaction, R₃₉, and is also produced in large amounts during the combustion of CH₄, C₂H₆ and other higher hydrocarbons. The elementary reactions of C₂H₄ and its product species are R₄₃ and R₄₄ as given in Table 2.4.

The predicted flame properties from scheme B were examined against experimental results by Dixon-Lewis [61], Dixon-Lewis and Islam [143], Dixon-Lewis [65], and El-Sherif [152] and these results will be discussed in section 2.4.3. These results show that scheme B is only valid to lean and near stoichiometric flame and needs to be developed to cover also the rich flames.

Scheme B is developed further here by involving C₂H₂ reactions and the predicted results are validated against the experimental data as will be described in the next section. The developed scheme is called scheme C and it involves all the reactions and rate parameters given in Tables 2.2, 2.3, 2.4 and 2.5. This scheme involves 50 reactions and 21 chemical species. Table 2.5 contains all the reactions involved in the production of C₂H₂ and its subsequent reactions. In addition to reactions R₄₃ and R₄₄, other reactions consisting of H atoms abstraction include, R₄₅ to R₄₆. The two important reactions of the vinyl radical, C₂H₃, are reactions R₄₇ and R₄₈.

Acetylene, C₂H₂ is a practical fuel and is also believed to be an important contributor to the formation and growth of soot. In addition, C₂H₂ and its pyrolysis and oxidation reactions are part of the reaction mechanisms for other hydrocarbon fuels, particularly in fuel-rich conditions. The reaction between C₂H₂ and O atoms is R₄₉. This reaction is predominant under most conditions (Miller et al [178]). The reaction of methylene, CH₂ with O₂ is R₅₀.

Table 2.3: Parameters of expressions for forward rate coefficients and independent equilibrium constant used for CH₄-air mechanism (Scheme A) in addition to Table 2.2. Rate coefficients expressed as in Table 2.2 [21 and 143]. Reproduced by permission of Elsevier Science.

No.	Reaction	Ref.	A	B	C/(K)	D	E	F/(K)
24	CH ₄ +H↔CH ₃ +H ₂	28	2.2×10 ⁴	3.0	4400	29.3	0.0	355
25	CH ₄ +OH↔CH ₃ +H ₂ O	153	1.6×10 ⁷	1.83	1400	6.15	0.0	-7285
26	CH ₄ +O↔CH ₃ +OH	28	1.2×10 ⁷	2.1	3840	66.51	0.0	1293
27	CH ₃ +O↔CH ₂ O+H	28	7.0×10 ¹³	0.0	0.000	0.072	0.0	-35100
28	CH ₃ +O↔CHO+H ₂	28	1.4×10 ¹⁴	0.0	860	0.784	0.0	-42878

Table 2.4: Additional rate parameters for mechanism including methyl radical combination (Scheme B) Rate coefficients expressed as in Tables 2.2 and 2.3. [21]. Reproduced by permission of Elsevier Science.

No	Reaction	Ref.	A	B	C/(K)	D	E	F/(K)
29	$\text{CH}_3+\text{CHO}\leftrightarrow\text{CH}_4+\text{CO}$	61, 143	1.0×10^{12}	0.0	0.0	-	-	-
30	$\text{CH}_3+\text{HO}_2\leftrightarrow\text{CH}_4+\text{O}_2$	61, 143	2.0×10^{12}	0.0	0.0	-	-	-
31	$\text{CH}_3+\text{HO}_2\leftrightarrow\text{CH}_3\text{O}+\text{OH}$	61, 143	2.0×10^{13}	0.0	0.0	-	-	-
32	$\text{CH}_3\text{O}+\text{H}\leftrightarrow\text{CH}_2\text{O}+\text{H}_2$	61, 143	5.0×10^{13}	0.0	0.0	-	-	-
33	$\text{CH}_3\text{O}+\text{OH}\leftrightarrow\text{CH}_2\text{O}+\text{H}_2\text{O}$	61, 143	2.5×10^{13}	0.0	0.0	-	-	-
34	$\text{CH}_3\text{O}+\text{O}\leftrightarrow\text{CH}_2\text{O}+\text{OH}$	61, 143	2.5×10^{13}	0.0	0.0	-	-	-
35	$\text{CH}_3+\text{CH}_3\leftrightarrow\text{C}_2\text{H}_6$	61, 143	2.8×10^{14}	-0.4	0.0	5.33×10^{-7}	0.0	-43880
36	$\text{C}_2\text{H}_6+\text{H}\leftrightarrow\text{C}_2\text{H}_5+\text{H}_2$	61, 143	5.5×10^2	3.5	2620	21.7	0.0	-1140
37	$\text{C}_2\text{H}_6+\text{OH}\leftrightarrow\text{C}_2\text{H}_5+\text{H}_2\text{O}$	153	3.54×10^6	2.12	439.3	-	-	-
38	$\text{C}_2\text{H}_6+\text{O}\leftrightarrow\text{C}_2\text{H}_5+\text{OH}$	153	8.98×10^7	1.92	2864	-	-	-
39	$\text{C}_2\text{H}_5+\text{O}_2\leftrightarrow\text{C}_2\text{H}_4+\text{HO}_2$	61, 143	2.0×10^{12}	0.0	2510	-	-	-
40	$\text{C}_2\text{H}_5+\text{H}\leftrightarrow\text{CH}_3+\text{CH}_3$	61, 143	4.8×10^{13}	0.0	0.0	-	-	-
41	$\text{C}_2\text{H}_5+\text{O}\leftrightarrow\text{CH}_3+\text{CH}_2\text{O}$	61, 143	5.0×10^{13}	0.0	0.0	-	-	-
42	$\text{C}_2\text{H}_5+\text{C}_2\text{H}_5\leftrightarrow\text{C}_2\text{H}_4+\text{C}_2\text{H}_6$	61, 143	1.4×10^{14}	0.0	0.0	-	-	-
43	$\text{C}_2\text{H}_4+\text{O}\leftrightarrow\text{CH}_3+\text{CHO}$	61, 143	2.0×10^{13}	0.0	1300	-	-	-
44	$\text{C}_2\text{H}_4+\text{OH}\leftrightarrow\text{CH}_3+\text{CH}_2\text{O}$	61, 143	4.0×10^{13}	0.0	760	1.9	0.0	-7910

Table 2.5: Reaction mechanism for breakdown C_2H_4 to C_2H_3 and C_2H_2 and its subsequent reactions (Scheme C). Rate coefficients expressed as in Table 2.2 [153].

No.	Reaction	Ref.	A	B	C/(K)	D	E	F/(K)
45	$\text{C}_2\text{H}_4+\text{OH}\leftrightarrow\text{C}_2\text{H}_3+\text{H}_2\text{O}$	166	0.7×10^{14}	0.0	1516	1.99	0.0	-7183
46	$\text{C}_2\text{H}_4+\text{H}\leftrightarrow\text{C}_2\text{H}_3+\text{H}_2$	166	1.5×10^{14}	0.0	513	8.64	0.0	448
47	$\text{C}_2\text{H}_3+\text{H}\leftrightarrow\text{C}_2\text{H}_2+\text{H}_2$	166	2.0×10^{13}	0.0	0.0	0.35	0.0	-33020
48	$\text{C}_2\text{H}_3+\text{O}_2\leftrightarrow\text{C}_2\text{H}_2+\text{HO}_2$	166	1.0×10^{12}	0.0	0.0	1	0.0	-3960
49	$\text{C}_2\text{H}_2+\text{O}\leftrightarrow\text{CH}_3+\text{CO}$	240	41×10^7	1.5	854	5.33	0.0	-25510
50	$\text{CH}_2+\text{O}_2\leftrightarrow\text{CO}_2+\text{H}_2$	238	10×10^{13}	0.0	1864	0.003	0.0	-93262

A schematic representation of the CH_4 oxidation mechanism with scheme C is given in Fig. 2.2. The reactions and rate parameters of Table 2.5 were chosen after an extensive series of computations and comparisons with experimental data (John [179]) as will be described in section 2.4.3.

(iv) Reaction Mechanism for CH_3OH -Air Flame

Methanol is potentially an important fuel, it can be formed by the high-pressure catalytic reaction of CO and H_2 that can be generated from either coal (Heniker [180] and Clark [181]) or natural gas, and also by the fermentation of vegetable products. It is a possible fuel for engines (Bolt [182], Ingamells and Lindquist [183], and Most and Longwell [184]), with the advantages over more conventional fuels of a lower ignition delay (Harrington and Pilot [185] and Gülder [186, 187]), higher burning velocity (Gülder [188]), and reduced propensity to knock (Koenig et al [189], Borisov et al [190]). Because of the absence of emitted particulate, it is contemplated as an alternative fuel for the Diesel engines. However, less effort has been expended on the measurement and prediction of burning velocities and the development of laminar flame mathematical models for methanol-air than for methane-air pre-mixtures.

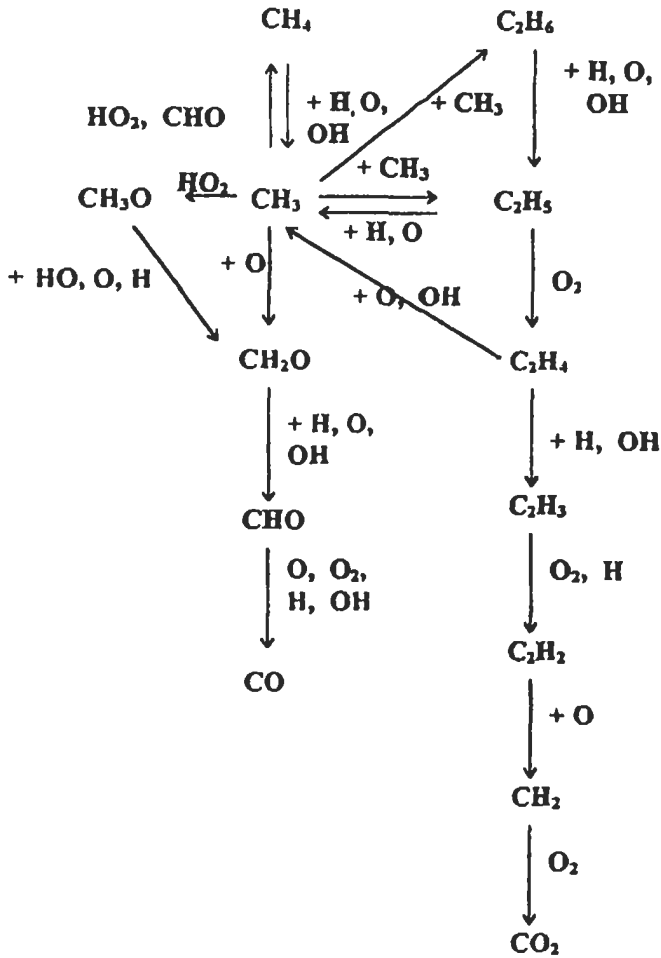


Fig. 2.2: Schematic representation of the CH_4 oxidation mechanism with scheme C.

In addition, methanol is one of the simplest oxygenated organic fuels. Moreover, the intermediate species CHO , CH_2O , CH_3O and CH_2OH which are formed during combustion, also play a significant role in a number of other combustion systems. It is therefore important to develop and verify a mechanism, which accurately represents the combustion kinetics. In the light of these remarks, Westbrook and Dryer [161] and Dove and Warnatz [162] have developed comprehensive kinetic schemes for methanol-air flames. They invoked some 40 to 84 reactions and 15 to 26 chemical species. Olsson et al [191], Andersson et al [192] have compared experimental and computed structures of a low-pressure stoichiometric methanol flame. They reduced the mechanism of Westbrook and Dryer [161] to one involving 18 species and 55 pairs of reaction. Paczko et al [193] have obtained a quasi-global four-steps mechanism for methanol oxidation by using steady state assumptions for some of the intermediates. Bradley et al [44], Abu-Elenin et al [154], and Habik [155] have developed chemical kinetics schemes for methanol-air flames which were validated against extensive experimental measurements

of burning velocities and flame structures. First, they have used two chemical kinetics schemes, A_1 and B_1 [44] to predict the flame properties. The kinetic scheme A_1 involves all the reactions and numerical values of the rate coefficients that are given in Tables 2.2 and 2.6 in which the total number of reactions is 29 with 14 chemical species. This scheme assumes that attack on CH_3OH by H_2O and OH forms CH_2OH , but not CH_3O . The reactions involved in this scheme will be described as follows.

Abstraction of H atoms proceeds primarily by breaking C-H bonds rather than the O-H bond, including, R_{24} to R_{26} as given in Table 2.6. Reaction, R_{24} is responsible for the majority of the CH_3OH consumption, while in rich flame, reaction R_{26} with H atoms is more important. The CH_2OH radicals (hydroxy methyl) which are produced from R_{24} to R_{26} , react with H and O_2 by R_{27} and R_{28} , respectively, or decomposes rapidly to yield H atoms by R_{29} .

In scheme A_1 , the oxidation path for methanol proceeds in a sequential manner through: $\text{CH}_3\text{OH} \rightarrow \text{CH}_2\text{OH} \rightarrow \text{CH}_2\text{O} \rightarrow \text{HCO} \rightarrow \text{CO} \rightarrow \text{CO}_2$. At the low temperature, HO_2 can be produced which, in turn, creates H_2O_2 . Such reactions and their rate coefficients are given in Table 2.7. They have all, with the exception of R_{37} , been discussed in the context of H_2 -CO- CH_2O - O_2 system by Dixon-Lewis and Williams [142]. Computations with scheme A_1 in addition to Table 2.7 showed the effect of reactions in Table 2.7 on the burning velocity to be not more than 1% - 2%.

The hydrogen peroxide, H_2O_2 , is consumed by reactions with radicals and by thermal decomposition, R_{30} to R_{35} . The reaction of HO_2 with itself produces hydrogen peroxide, H_2O_2 , R_{36} . Vandooren et al [200] have found that, the reaction, R_{37} , is important. To correct the underprediction of CO_2 in CH_2O - O_2 flames, this reaction is added to Table 2.7 in order to correct similar mismatches for CO and CO_2 in methanol-air flame, but it has no significant effect as will be described later.

The reactions R_{24} to R_{29} of Table 2.6, postulated as results of experimental studies of (Andersson et al [192], Cooke et al [194] and Vandooren and Van Tiggelen [195]) and computational (Olsson et al [191], Andersson et al [192], Westbrook and Dryer [161], and Aronowitz et al [196]). The rate parameters for these, initially were taken from Dove and Warnatz [162] and subsequently optimized (Bradley et al [44]) to agree with the experimental results which will be described in the next section. It was found that optimization of scheme A_1 coefficients failed to give completely satisfactory agreement with flame compositional profiles of CO and CO_2 or with the pressure dependence of the burning velocity, particularly for lean mixtures. There is, however, the possibility of the primary products formed from CH_3OH being CH_2OH (hydroxy methyl) and CH_3O (methoxy) (Grotheer and Kelm [197] and Hess and Tully [198]), to be followed by reaction, R_{38} in Table 2.8. This possibility has been examined with use of the reactions given in Table 2.8, which together with those in Table 2.2 comprise scheme B_1 . This has a total number of reactions of 32 and 16 chemical species. In addition, reactions of Table 2.7 again have a little effect.

Computations with kinetic scheme B_1 give better agreement with measured concentration profiles, particularly of CO and CO_2 , as well as the burning velocity. In this scheme, there was an appreciable uncertainty in the rate coefficients for hydroxy methyl and methoxy production as well as those for the reaction of methoxy with other species. This scheme will be described now. The breakdown of overall rate coefficients, R_{24} to R_{26} to give CH_2OH and CH_3O (reaction pairs 24 (a) (b) to 26 (a) (b)) are given in Table 2.8.

Reactions of CH_2OH with H, O_2 , and M (reactions R_{27} to R_{29}) are the same as in

scheme A₁ (Table 2.6). Reactions R₂₇ and R₂₉ are important in rich flames and Bradley et al [44] found that the optimized rate coefficients for these rates are 10 and 5 times of those given by Dove and Warnatz [162].

Table 2.6: Reaction mechanism for breakdown of CH₃OH to CH₂OH and its subsequent reactions (used in Scheme A₁). Rate coefficients in Tables 2.6 to 2.8 are expressed as in Table 2.2 [44]. Reproduced by permission of Elsevier Science.

No.	Reaction	Ref.	A	B	C/(K)	D	E	F/(K)
24	CH ₃ OH+OH↔CH ₂ OH+H ₂ O	44	2x10 ¹³	0.0	854	2.14x10 ⁵	-1.66	-1173
25	CH ₃ OH+O↔CH ₂ OH+OH	44	2x10 ¹³	0.0	2353	1.99x10 ⁶	-1.66	-3046
26	CH ₃ OH+H↔CH ₂ OH+H ₂	44	2x10 ¹³	0.0	3067	9.76x10 ⁵	-1.66	-4108
27	CH ₂ OH+H↔H ₂ +CH ₂ O	44	2x10 ¹⁴	0.0	0.0	3.91x10 ⁻²	1.66	-4029
28	CH ₂ OH+O ₂ ↔CH ₂ O+HO ₂	191	1x10 ¹⁴	0.0	3019	1.10x10 ⁻⁴	1.66	-1124
29 ^d	CH ₂ OH+M↔CH ₂ O+H+M	44	5x10 ¹⁴	0.0	12642	5.13x10 ⁻⁴	0.66	10780

M = H₂, O₂, N₂, CO, CO₂, H₂O & CH₃OH

^d M is assumed to have equal collision efficiency for all species.

Table 2.7: Additional rate parameters for mechanism including hydrogen peroxide [44]. Reproduced by permission of Elsevier Science.

No.	Reaction	Ref.	A	B	C/(K)	D	E	F/(K)
30	H+H ₂ O ₂ ↔HO ₂ +H ₂	137	1.4x10 ¹²	0.0	1800	-	-	-
31	H+H ₂ O ₂ ↔H ₂ O+OH	137	1.0x10 ¹³	0.0	1800	-	-	-
32	OH+H ₂ O ₂ ↔H ₂ O+HO ₂	137	6.1x10 ¹²	0.0	720	-	-	-
33	O+H ₂ O ₂ ↔OH+HO ₂	137	1.4x10 ¹³	0.0	3200	-	-	-
34	O+H ₂ O ₂ ↔H ₂ O+O ₂	137	1.4x10 ¹³	0.0	3200	-	-	-
35 [†]	H ₂ O ₂ +M↔OH+OH+M	137	2.7x10 ¹⁷	0.0	22900	1700	-0.37	25055
36	HO ₂ +HO ₂ ↔H ₂ O ₂ +O ₂	137	2.0x10 ¹²	0.0	0.0	0.180	0.0	-21300
37	CO+HO ₂ ↔CO ₂ +OH	200	3.3x10 ¹²	0.0	4125	0.089	0.0	-31140

[†] Chaperon efficiencies relative to H₂ are taken to be the same as in reaction (R₄) in Table 2.2.

Table 2.8: An alternative reaction mechanism (used in Scheme B₁) for R₂₄ to R₂₉ in Table 2.6. Rate coefficients expressed as in Table 2.2 [44]. Reproduced by permission of Elsevier Science.

No	Reaction	Ref.	A	B	C/(K)	D	E	F/(K)
24(a)	CH ₃ OH+OH↔CH ₂ OH+H ₂ O	44	1.2x10 ¹³	0.0	854	2.14x10 ⁵	-1.66	-1173
25(a)	CH ₃ OH+O↔CH ₂ OH+OH	44	1.2x10 ¹³	0.0	2357	1.99x10 ⁶	-1.66	-3046
26(a)	CH ₃ OH+H↔CH ₂ OH+H ₂	44	1.2x10 ¹³	0.0	3067	9.76x10 ⁵	-1.66	-4108
24(b)	CH ₃ OH+OH↔CH ₃ O+H ₂ O	44	0.8x10 ¹³	0.0	854	3.2x10 ⁻²	0.0	-9798
25(b)	CH ₃ OH+O↔CH ₃ O+OH	44	0.8x10 ¹³	0.0	2357	0.310	0.0	-1112
26(b)	CH ₃ OH+H↔CH ₃ O+H ₂	44	0.8x10 ¹³	0.0	3067	0.1366	0.0	-2167
27	CH ₂ OH+H↔H ₂ +CH ₂ O	44	2.0x10 ¹⁴	0.0	0.0	3.9x10 ⁻²	1.66	-4029
28	CH ₂ OH+O ₂ ↔CH ₂ O+HO ₂	199	1.0x10 ¹⁴	0.0	3019	1.1x10 ⁻⁴	1.66	-1124
29 ^{**}	CH ₂ OH+M↔CH ₂ O+H+M	44	5.0x10 ¹⁴	0.0	12642	5.1x10 ⁻⁴	0.66	10780

M = H₂, O₂, N₂, CO, CO₂, H₂O & CH₃OH

38	CH ₃ O+CO↔CO ₂ +CH ₃	199	6.3x10 ¹³	0.0	6697	0.717	0.0	-17365
39	CH ₃ +O↔CH ₂ O+H	28	7.2x10 ¹³	0.0	0.0	0.07228	0.0	-35100
40	CH ₃ +HO ₂ ↔CH ₃ O+OH	143	2.0x10 ¹³	0.0	0.0	0.310	0.0	-12233

** The same as in Table 2.6.

The product of CH_3O from, R_{24} (b), to R_{26} (b), has been studied by Lissi et al [199] and they found that the reaction of CH_3O with CO is important, R_{38} . Then the product, CH_3 reacts with O and HO_2 by R_{39} to R_{40} .

Because of the uncertainty in the rate coefficients mentioned above in scheme B_1 , the scheme has been developed further with the use of most recent recommended values of the rate coefficients for hydroxy methyle and methoxy productions [154]. Also, the rate coefficient of reaction of methoxy and carbon monoxide was optimized to obtain good agreement between computational and experimental results. This developed scheme has been examined in the next section with the use of reactions and rate parameters given in Table 2.9, which together with those in Table 2.2 comprise scheme C_1 . In this scheme, the total number of reactions and chemical species are the same as those for scheme B_1 . A schematic representation of the CH_3OH oxidation with scheme C_1 is given in Fig. 2.3.

Within the kinetic framework developed in scheme C_1 , the rate parameters are established and given in Table 2.9. It was found that the branching ratios of attack on CH_3OH by H , O and OH to form CH_2OH and CH_3O were important in different ranges of pressure, temperature, and equivalence ratio. The optimized ratio of these reactions was found to be; $k_{25}(\text{a}) / k_{25}(\text{b}) = k_{26}(\text{a}) / k_{26}(\text{b}) = 3$ and the pre-exponential factor of reaction R_{30} (Table 2.9), was adopted to be twice that used by Ref. 199. Also reactions, R_{24} and R_{26} are important in consuming CH_3OH in lean and near stoichiometric conditions, while R_{26} is more important in rich flames. The predicted results from scheme C_1 will be discussed in section 2.4.4.

Table 2.9: Reaction mechanism for breakdown CH_3OH to CH_2OH and CH_3O and its subsequent reactions (used in Scheme C_1). Rate coefficients expressed as in Table 2.2 [154].

No	Reaction	Ref	A	B	C/(K)	D	E	F/(K)
24a	$\text{CH}_3\text{OH} + \text{OH} \leftrightarrow \text{CH}_2\text{OH} + \text{H}_2\text{O}$	-	-	-	-	2.14×10^5	-1.66	-1173
24b	$\text{CH}_3\text{OH} + \text{OH} \leftrightarrow \text{CH}_3\text{O} + \text{H}_2\text{O}$	-	-	-	-	3.16×10^{-2}	0.0	-9798
a+b		201	6.67×10^4	2.5	-483	-	-	-
a/b		-	0.27	0.0	-1020	-	-	-
25a	$\text{CH}_3\text{OH} + \text{O} \leftrightarrow \text{CH}_2\text{OH} + \text{OH}$	-	-	-	-	1.99×10^6	-1.66	-3046
25b	$\text{CH}_3\text{OH} + \text{O} \leftrightarrow \text{CH}_3\text{O} + \text{OH}$	-	-	-	-	0.310	0.0	-1112
a+b		201	3.9×10^5	2.5	1550	-	-	-
a/b		-	3	0.0	0.0	-	-	-
26a	$\text{CH}_3\text{OH} + \text{H} \leftrightarrow \text{CH}_2\text{OH} + \text{H}_2$	-	-	-	-	9.76×10^5	-1.66	-4108
26b	$\text{CH}_3\text{OH} + \text{H} \leftrightarrow \text{CH}_3\text{O} + \text{H}_2$	-	-	-	-	0.1366	0.0	-2167
a+b		201	2.13×10^7	2.1	2450	-	-	-
a/b		-	3	0.0	0.0	-	-	-
27	$\text{CH}_2\text{OH} + \text{H} \leftrightarrow \text{H}_2 + \text{CH}_2\text{O}$	44	2×10^{14}	0.0	0.0	3.91×10^{-2}	1.66	-4029
28	$\text{CH}_2\text{OH} + \text{O}_2 \leftrightarrow \text{CH}_2\text{O} + \text{HO}_2$	44	1×10^{14}	0.0	3019	1.1×10^{-4}	1.66	-1112
29 ^a	$\text{CH}_2\text{OH} + \text{M} \leftrightarrow \text{CH}_2\text{O} + \text{H} + \text{M}$ M = H_2 , O_2 , N_2 , CO , CO_2 , H_2O & CH_3OH	44	5×10^{14}	0.0	12642	5.13×10^{-4}	0.66	10780
30	$\text{CH}_3\text{O} + \text{CO} \leftrightarrow \text{CO}_2 + \text{CH}_3$	-	1.26×10^{14}	0.0	6697	0.717	0.0	-17365
31	$\text{CH}_3 + \text{O} \leftrightarrow \text{CH}_2\text{O} + \text{H}$	44	7.0×10^{13}	0.0	0.0	0.07228	0.0	-35100
32	$\text{CH}_3 + \text{HO}_2 \leftrightarrow \text{CH}_3\text{O} + \text{OH}$	44	2.0×10^{13}	0.0	0.0	0.310	0.0	-12233

^a The same as in Table 2.6.

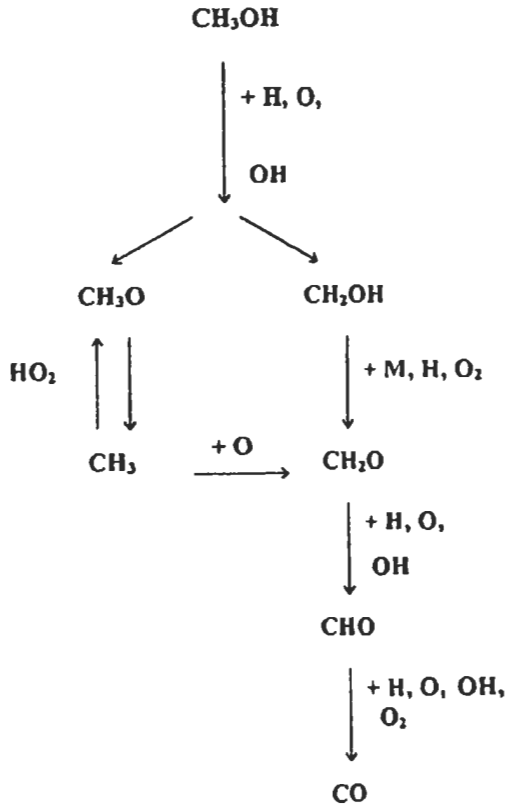


Fig. 2.3: Schematic representation of the CH_3OH oxidation mechanism with scheme C_1 .

Having discussed the kinetic mechanisms for H_2 , CO-H_2 , CH_4 and CH_3OH fuels, we need next to explore this further by use of these kinetic mechanisms in one-dimensional premixed laminar model to predict the flame properties and compare them with the experimental data, and also to discuss them in the context of reaction mechanisms and rate parameters. This will be discussed next.

(v) Reaction Mechanism for Natural Gas-Air Flames

The world's most readily available and abundant gaseous fuel resources are found in natural gas reserves. Its increasing use as the fuel of choice for power generation, industrial process heating, and residential use has been prompted by recently imposed, low-pollutant emission standards, low costs and, in addition, it has a proven safety records.

It is believed that natural gas is formed from the decomposition of petroleum or coal deposits, and it contains principally methane. However, chemical composition of commercial natural gas can vary widely with concentration extremes of 75 % and 98 % for methane, 0.5 % -13 % for ethane and 0 % - 2.6 % for propane and low concentrations of CO , CO_2 , He , N_2 and H_2O . Therefore, it is important to understand the chemistry of each of these individual pure fuels, and then consider how varying levels of these fuels in the natural gas affect their performance (see section 2.4.8).

However, having discussed above the kinetic mechanism of methane, it is necessary in the following sections to discuss the kinetic mechanism of propane and ethane. More details about the flame characteristics of the fuels are given in sections 2.4.6 and 2.4.7. In order to simplify the complexity of the kinetics involved in the natural gas computations, all the compositions of high hydrocarbons which are higher than C_3 were assumed to be C_2H_6 . With this assumption, the natural gas composition will consist of CH_4 , C_2H_6 , CO and N_2 . In this case the kinetic mechanisms and rate parameters of Tables 2.2 to 2.5 can be used for natural gas. This kinetic mechanism with transport parameters in Table 2.1 were used in one-dimensional model in section 2.4.8 to predict the flame structure and burning velocity for natural gas and the results were validated against those measured at atmospheric pressure, room temperature and different equivalence ratios. The effect of different natural gas compositions on the burning velocity and flame structure was also studied in section 2.4.8.

(vi) Reaction Mechanism for Propane-Air Flames

Propane is an important practical fuel and is used in furnaces and internal combustion engines. Generally, propane is the smallest hydrocarbon which has reaction characteristics that are typical of larger hydrocarbons fuels, including jet and ramjet fuels as well as it is one of the components of the natural gas fuel. Therefore, gaining a better understanding of propane combustion mechanism which has been assembled and evaluated against experimental data would be a valuable research tool for analyzing and interpreting the combustion process in furnaces, internal combustion engines and supersonic combustion experiments involving typical hydrocarbon fuels.

Despite the rapid increase in computer capabilities and the emergence of a number of detailed schemes for hydrocarbon combustion as mentioned before; the use of small number of reactions capable of accurately describing major flame features is of considerable importance for a number of practical combustion problems. Kinetic modeling of combustion from 1969 to 2019 has been reviewed by Cathonnet [202]. He concluded that, during the last 25 years, the place of chemistry in combustion modeling increased continuously and this progression is expected to persist in the next 25 years, which would be necessary to improve combustion efficiency and control the pollutant emissions. Therefore, this section describes the attempts, which have been done by the authors as well as the other investigators to develop the kinetic mechanism for propane.

With regards to the modeling background, Westbrook and Pitz [203] have studied the detailed chemical reaction mechanism for propane (163 elementary reactions among 41 chemical species) to describe the experimental results in shock tube and turbulent flow reactor. Numerical simulation of the shock tube experiments has been studied by Jachimowski [204], and he showed that the predicted results for stoichiometric mixtures were in good agreement with the experimental results over the entire temperature range examined (1150-2600 K). The mechanism consists of 27 chemical species and 83 elementary chemical reactions. Details of propane chemistry under jet-stirred flow reactor conditions have been studied by Dagaut et al [205]. Their mechanism consists of 277 reactions among 48 species. Warnatz [166] has published a propane mechanism, which gives good agreement with burning velocity at atmospheric pressure and with species profiles in a low-pressure laminar flame. In addition, an improved chemical mechanism for the combustion of propane has been developed by Sloane [206], which describes experimental results for a broad range of ignition and combustion phenomena. The mechanism consists of 192 reactions.

To identify the important reactions in propane kinetic mechanism, two developed kinetic schemes (A_2 and B_2) were tested against several experimental data for premixed laminar propane-air flames (Habik [20]). These kinetic schemes have been used in one-dimensional model incorporated detailed representation of transport fluxes to predict the burning velocity, flame structure and heat release rate for premixed propane-air flames. Schemes, A_2 , and B_2 , consist of 63 and 74 reactions, respectively, with 25 chemical species each. These mechanisms have been so thoroughly tested in section 2.4.6 by comparing the predicted flame structure (Habik et al [207]) and predicted burning velocity (Habik [20]) with those measured by different investigators under different conditions. The kinetic scheme, A_2 , involved all the reactions with their numerical values of the rate coefficients for CH_4 mechanism (Scheme C, in Tables 2.2 to 2.5) and Table 2.10 which consists of the breakdown of propane fuel. These tables of scheme A_2 , give the simple kinetic mechanism for breakdown propane fuel throughout reactions R_{51} to R_{57} and some of its subsequent reactions such as C_3H_7 and C_3H_6 consumptions in reactions R_{58} to R_{63} as well as the reactions, R_1 to R_{50} to produce final products. The kinetic scheme, B_2 , involved all the reactions with their numerical values of the rate coefficients for scheme A_2 , in addition to data given in Table 2.11. The latter table gives additional reactions for breakdown propane (R_{64} to R_{69}) and its subsequent reactions for C_3H_7 and C_3H_6 consumptions in reactions R_{70} to R_{74} . It was found that optimization of scheme, B_2 coefficients throughout reactions R_{64} to R_{74} in Table 2.11 failed to give completely satisfactory agreement with experimental flame compositional profiles and burning velocity under different conditions. After several attempts it was found that the predicted results when using scheme, A_2 , in the kinetic model gives good agreement with the experimental flame structure and burning velocity (Habik [20]).

Table 2.10: Parameters of expressions for forward rate coefficients and equilibrium constant for mechanism of breakdown propane and its subsequent reactions. Rate coefficients are expressed as in Table 2.2 [20].

No	Reaction	A	B	C/(K)	D	E	F/(K)	Ref.
C ₃ H ₈ Consumption								
51	C ₃ H ₈ +OH \leftrightarrow nC ₃ H ₇ +H ₂ O	4.7x10 ⁵	2.37	196	2x10 ⁻⁶	1.9	-12085	208
52	C ₃ H ₈ +OH \leftrightarrow iC ₃ H ₇ +H ₂ O	3.58x10 ²	3.23	-806	2x10 ⁻⁶	1.9	-12085	208
53	C ₃ H ₈ +O \leftrightarrow nC ₃ H ₇ +OH	5.0x10 ⁶	2.0	1511	15.2	0.0	-2220	203
54	C ₃ H ₈ +O \leftrightarrow iC ₃ H ₇ +OH	5.0x10 ⁶	2.0	1511	15.2	0.0	-2220	203
55	C ₃ H ₈ +H \leftrightarrow nC ₃ H ₇ +H ₂	1.3x10 ¹⁴	0.0	4884	0.15x 10 ⁻³	1.5	-4030	166
56	C ₃ H ₈ +H \leftrightarrow iC ₃ H ₇ +H ₂	2.0x10 ¹⁴	0.0	4179	0.15x 10 ⁻³	1.5	-4030	209
57	C ₃ H ₈ \leftrightarrow C ₂ H ₅ +CH ₃	1.7x10 ¹⁶	0.0	42719	1.13x 10 ⁶	-1	42880	203
C ₃ H ₇ Consumption								
58	nC ₃ H ₇ \leftrightarrow C ₃ H ₆ +H	1.0x10 ¹⁴	0.0	18771	13.0	0.0	17875	28
59	iC ₃ H ₇ \leftrightarrow C ₃ H ₆ +CH ₃	2.0x10 ¹⁰	0.0	14854	4.4x 10 ⁵	-1	12694	210
60	nC ₃ H ₇ +O ₂ \leftrightarrow C ₃ H ₆ +HO ₂	1.0x10 ¹²	0.0	2518	5.0	0.0	-6285	28
61	iC ₃ H ₇ +O ₂ \leftrightarrow C ₃ H ₆ +HO ₂	1.0x10 ¹²	0.0	2518	5.0	0.0	-6285	28
C ₃ H ₆ Consumption								
62	C ₃ H ₆ +O \leftrightarrow C ₂ H ₅ +CHO	3.6x10 ¹²	0.0	0.0	5.014	0.0	-15065	203
63	C ₃ H ₆ +OH \leftrightarrow C ₂ H ₅ +CH ₂ O	1.0x10 ¹³	0.0	0.0	0.17	0.0	-8736	208

Table 2.11: Additional rate parameters for propane mechanism. Rate coefficients expressed as in Table 2.2 [20].

No	Reaction	A	B	C/(K)	D	E	F/(K)	Ref.
64	$C_3H_8+CH_3 \leftrightarrow nC_3H_7+CH_4$	2×10^{12}	0.0	5690	0.252	0.0	-3515	28
65	$C_3H_8+CH_3 \leftrightarrow iC_3H_7+CH_4$	2×10^{12}	0.0	5690	0.252	0.0	-3515	28
66	$C_3H_8+C_2H_3 \leftrightarrow iC_3H_7+C_2H_4$	1×10^{11}	0.0	5237	0.758	0.0	-3726	211
67	$C_3H_8+C_2H_3 \leftrightarrow nC_3H_7+C_2H_4$	1×10^{11}	0.0	5237	0.758	0.0	-3726	211
68	$C_3H_8+C_2H_3 \leftrightarrow C_2H_6+iC_3H_7$	1×10^{11}	0.0	5237	2.76	0.0	237	212
69	$C_3H_8+C_2H_3 \leftrightarrow C_2H_6+nC_3H_7$	1×10^{11}	0.0	5237	2.76	0.0	237	212
70	$iC_3H_7 \leftrightarrow C_3H_6+H$	6.3×10^{13}	0.0	18580	6.31	0.0	17825	206
71	$iC_3H_7+H \leftrightarrow C_3H_8$	2×10^{13}	0.0	0.0	-	-	-	28
72	$nC_3H_7 \leftrightarrow C_2H_6+CH_3$	3×10^{14}	0.0	16721	4.4×10^5	0.0	12694	28
73	$C_3H_6+O \leftrightarrow CH_3+CH_3+CO$	1.17×10^{13}	0.0	302	-	-	-	206
74	$C_3H_6 \leftrightarrow C_2H_3+CH_3$	6.3×10^{15}	0.0	43202	6.3×10^5	-1	43202	206

(vii) Reaction Mechanism for Ethane-Air Flames

Ethane is the second member of the alkane series (C_nH_{2n+2}). It consists of two methyl groups joined through a C-C bond. Ethane as odorless gas, is difficult to liquefy and is considered as one of the important species in the natural gas composition. Ethane has a fast sequence of reactions $C_2H_6-C_2H_5-C_2H_4$, etc which can operate in flame or ignitions. This is the main reason why methane ignites much less easily than ethane, propane, etc, whereas it has similar burning velocity as shown in section 2.4.7. It also explains why methane is hard to detonate. The chemical kinetics mechanism of ethane consists of breakdown ethane by radical species to form ethyl radical (C_2H_5) through reactions R_{36} to R_{38} (Table 2.4). The main reactions for ethyl radical are R_{39} to R_{42} in Table 2.4, while for breakdown C_2H_4 , the reactions are R_{43} and R_{44} in Table 2.4.

2.4 Simple Fuels- N_2 - O_2 Flames

In this section, experimental and computational studies on structure and characteristics of premixed simple fuels- N_2 - O_2 flames are presented. These fuels are: hydrogen, hydrogen+carbon monoxide+water, formaldehyde, methane, and methanol.

2.4.1 Hydrogen-Oxygen-Nitrogen Flames

Experimental Method and Results

The flame measurements considered here are selected from those used by Dixon-Lewis [94, 97, 98] to establish the transport parameters in Table 2.1, and reaction mechanism and rate parameters (R_1 to R_{13}) in Table 2.2, for H_2 - O_2 - N_2 system. In addition to that, the authors also include updated experimental results. These experimental results will cover the properties of low and high temperature fuel lean-rich flames, with the effects of changes of initial composition, temperature, and pressure on the flame structures and burning velocities.

For low temperature hydrogen-rich flame, these measurements are presented as follows:

(i) Temperature profile and profiles of mole fraction ratios X_{H_2} / X_{N_2} , X_{O_2} / X_{N_2} and X_{H_2O} / X_{N_2} measured by Dixon-Lewis et al [213] for hydrogen oxygen-nitrogen flame at 1 atm, with unburnt $H_2/O_2 = 4.09$ and $N_2/O_2 = 16.65$. The measured profiles of temperature and mole fraction ratios are shown by the points in Figs. 2.4 and 2.5.

(ii) Burning velocities of hydrogen flames measured by Day et al [168]. These burning velocities were measured at different values of $X_{H_{2,u}} / X_{N_{2,u}}$ and examined in hydrogen-oxygen-nitrogen flames having $X_{O_{2,u}} = 0.046$ at $T_u = 336$ K and 1 atm pressure. These measured burning velocities are shown by the points in Fig. 2.10.

For high temperature hydrogen lean-rich flames, the measurements are as follows:

(iii) Burning velocities of hydrogen premixed in various proportions with several (oxygen-nitrogen) compositions were measured by Jahn [214], Senior [215] and Edse and Lawrence [216]. These measurements are shown by points in Fig. 2.11.

(iv) Several experimental measurements of burning velocity for hydrogen-air mixtures have been made on burner supported, stationary flame and on the bomb. Two earlier sets of measurements of the burning velocities of hydrogen-air mixture at atmospheric pressure were made by Jahn [214] and Scholte and Vaags [217]. They both found that the maximum burning velocity occurs at about 42 % hydrogen, and lies between 2.7 and 2.8 m s⁻¹. The method of measurement used by Jahn was to divide the area of the Schlieren cone of the flame into the volume flow rate of the gases entering it. Scholte and Vaags [217] burned their flames as straight-sided cones on a constant velocity profile nozzle. They calculated the linear gas velocity, V , from the total volumetric gas flow and the area of the burner port, and then derived the burning velocity by measuring the cone half-angle, α , and using $U_1 = V \sin \alpha$. For a 50% hydrogen-air flame with $T_u = 298$ K, both sets of investigations found a burning velocity of 2.5 (± 0.1) m s⁻¹.

Three more measurements of the same hydrogen-air burning velocities [218-220], again with the use of burner method have given higher results. These measurements have used greater refinement, in that the gas velocities, V , approaching the flames have been measured directly by means of the powder particle tracking technique with stroboscopic illumination. Also, three investigations were carried out using nozzle burners and again Stiller photography was used to define the flame cone half angle, α . By this means, and by using a nozzle of diameter 0.01 m, Edmondson and Heap [218] found $U_1 = 2.96$ m s⁻¹ for the 50 % hydrogen-air flame with $T_u = 295$ K. Using a conical flame of the same composition on a smaller nozzle of 0.004 m diameter, Günther and Janisch [219] found $U_1 = 3.28$ m s⁻¹, from a button-shaped flame having the same initial conditions. These authors (Günther and Janisch [220]) obtained U_1 of 3.05 m s⁻¹. The latter results were preferred because of the reduced curvature in the button-shaped flame.

Strauss and Edse [221] and Agnew and Graiff [222] have used constant volume bomb to study the effect of pressure on the burning velocity of the stoichiometric hydrogen-oxygen flame. Also, Andrews and Bradley [223] have investigated burning velocities of hydrogen-air mixture. They determined the burning velocity from the flame speed measured at 0.025 m radius in a constant volume bomb with single spark

ignition at the center. Their derivation of burning velocities using "thin flame" and "finite flame thickness" are shown by broken curves A and B, respectively in Fig. 2.12. Curve A presents the minimum burning velocities which the hydrogen-air flames can have, and it is consistent with the flame speed observations.

An experimental study on effect of equivalence ratio, temperature and pressure on the burning velocity of hydrogen-air mixture has been conducted by Iijima and Takeno [224] using the spherical bomb technique. The range of measurement covered the equivalence ratio from 0.5 to 4, temperature from 291 to 500 K, and pressure from 0.5 to 25 atm. All the measurement results in (iv) are shown by points in Figs. 2.11 to 2.14.

Computational Results

Flame model computations for hydrogen-oxygen-nitrogen flames were performed by Dixon-Lewis [94, 98, 65] as described in section 2.3. The input data to the model were the reactions R_1 to R_{13} and its rate parameters in Table 2.2 in addition to the transport parameters in Table 2.1. The predicted flame structures and burning velocities from the model were that corresponding to the initial conditions of the above mentioned experimental work. All the computed results are shown by full curves in Figs. 2.4 to 2.14. All of these results will be discussed now in the context of reaction mechanism and its rate parameters.

The flame structure and burning velocity for the above flames are being discussed as follow;

(i) **Flame structure.** Figures 2.4 and 2.5 show that the predicted results from reaction mechanism and its rate parameters (R_1 to R_{13} in Table 2.2) with transport parameters in Table 2.1 give reasonable agreement with experiments. For the same flames in Figs. 2.4 and 2.5, the computed radical species H, O, OH, and HO_2 are shown in Fig. 2.6. The maximum mole fractions of O and OH are about the same and peak before H atoms. The adiabatic temperature for this flame is 1078 K with burning velocity of $0.092 \pm 0.002 \text{ m s}^{-1}$. Having demonstrated the structure of low temperature hydrogen-oxygen-nitrogen flame, it is necessary to discuss the flame structure of hydrogen-air flame. The predicted temperature profile and the mole fraction profiles of atomic hydrogen and the stable molecular species in a premixed hydrogen-air flame, containing 41 percent hydrogen initially are shown in Fig. 2.7. The position of the reaction zone can be seen from the H atom profile, the left-hand toe of which extends almost down to the initial temperature. The figure also shows that the thickness of main flame reaction zone is less than 1 mm.

Figure 2.8 shows the way in which the rate of chemical heat release, which is a measure of the overall reaction rate, changes with temperature in a series of premixed hydrogen-air flames at atmospheric pressure and initial mixture temperature of 298 K. The percentage of hydrogen in each mixture is given by the number above the corresponding line. Each curve terminates at the hot end at the equilibrium flame temperature. At the cold end, the heat release always extends well down towards the initial temperature. The maximum heat release rate is 17.6 GW m^{-3} in the 41% hydrogen and 59 % air flame. In these flames it is clear that the preheating zones is very small. In this zone the transport processes ensure heating of the gases entering the flame. It is, in turn, the increase in reaction rate due to this heating which is the important process in the flames.

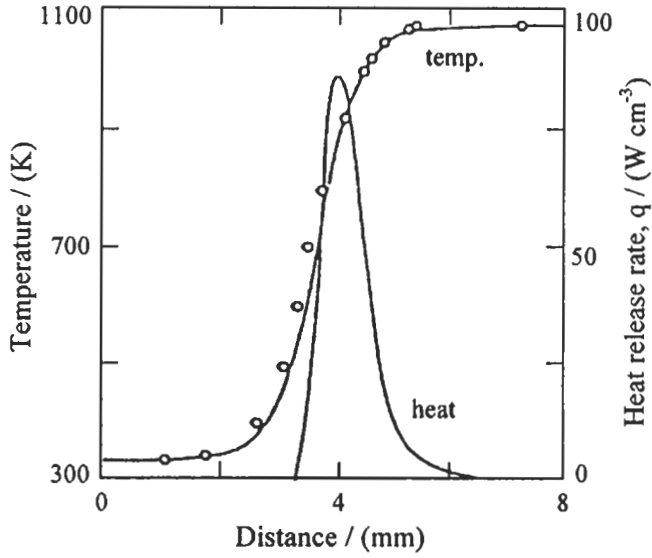


Fig. 2.4: Comparison of computed temperature profile with observation of Dixon-Lewis et al [167] (see text), O, observed points; lines represent temperature profile and heat release rate profile computed by Dixon-Lewis [94]. Reproduced by permission of The Royal Society.

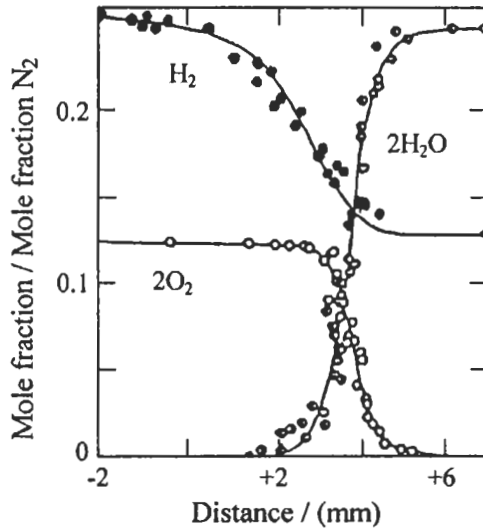


Fig. 2.5: Ratio of mole fractions of hydrogen, oxygen and steam to mole fraction of nitrogen, to compare computed profiles with observations of Dixon-Lewis et al [167] (see text). Points represent observations. Lines computed by Dixon-Lewis [94]. Reproduced by permission of The Royal Society.

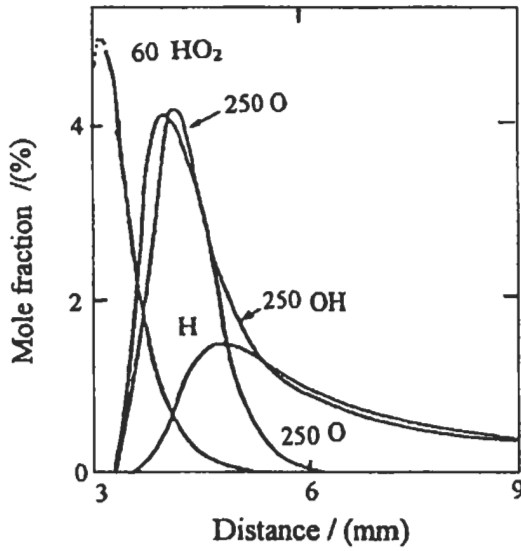


Fig. 2.6: Computed mole fraction profiles of radical species in flame of Fig. 2.5 (Dixon-Lewis [94]). Reproduced by permission of The Royal Society.

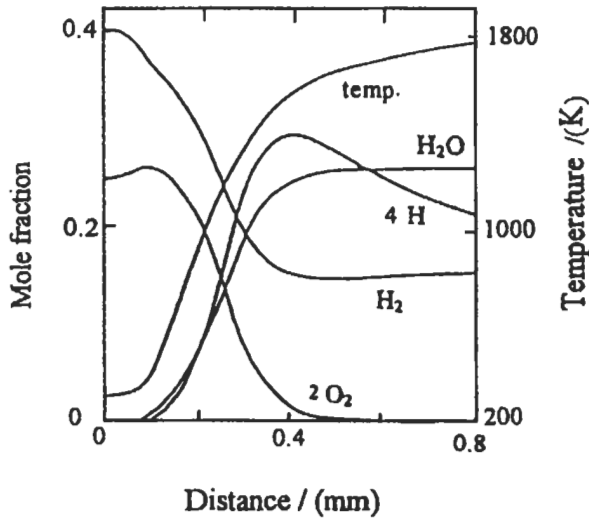


Fig. 2.7: Computed temperature profile and mole fraction profiles for stable species and atomic hydrogen in 41 percent H_2 -59 % air premixed flame at atmospheric pressure, with $T_u = 298$ K (Dixon-Lewis [94]). Reproduced by permission of The Royal Society.

We then look at the net rates of radical production in the flames, as represented by a radical pool consisting of $(H + 2O + OH + HO_2)$. These net rates are given by the difference between, on the one hand, the rate of formation of free valencies by the chain

branching cycle consisting of reactions R_1 , R_2 and R_3 , and on the other, the rate of their removal, principally by reactions, R_7 , R_8 and R_9 . These are shown for several flames in Fig. 2.9. We note immediately that the net rate of formation of free valencies only becomes positive at temperatures in excess of about 900 to 950 K, in any of the flames.

If, for a specific flame, this temperature is denoted by T_i , then the heat release at temperatures below T_i is only due to reactions of radicals which have diffused there from the higher temperature region. The radicals can react by the strongly exothermic reactions of the HO_2 cycle at both high and low temperatures. The rate coefficients of reactions R_4 to R_9 in Table 2.2 do not change much with temperature.

The driving force of the flames, and indeed of all the flames we shall consider, is the chain branching reaction, R_2 , which activates the dormant free valencies or unpaired electron spins present in molecular oxygen, to produce two new, fully active free valencies. As a consequence of the very marked reduction in the rate of the forward reaction, R_2 at lower temperatures, and of the fact that it must also compete with the more or less temperature independent chain termination rates of reactions, R_7 , R_8 and R_9 even at very low radical concentrations, the net formation of new active radicals is restricted to temperatures above T_i . However, the overall system becomes effectively a chain branching, at a rate which increases very rapidly indeed, but which is eventually limited by the consumption of oxygen and the approach of reaction, R_2 to its equilibrium position. This happens when the radical concentration is high, but still finite; and at the same time the rapid reactions, R_1 , R_3 and R_{13} also approach their equilibrium positions, more or less simultaneously. Following this, the free radicals H, O and OH finally decay to full equilibrium at a lower rate which allows reactions R_1 to R_3

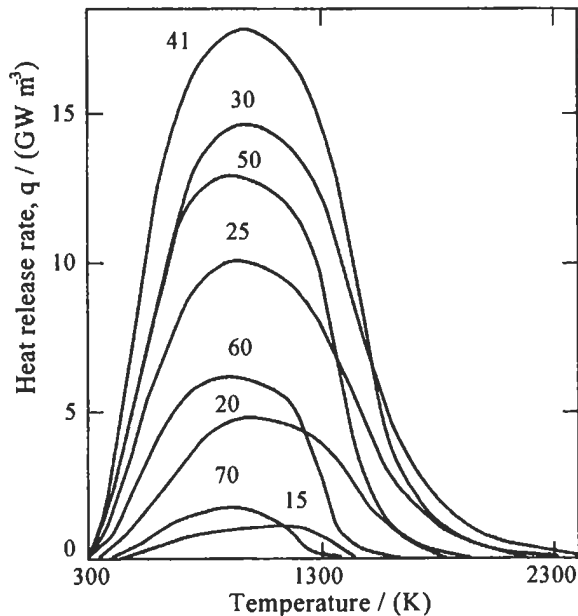


Fig. 2.8: Computed heat release rates in hydrogen-air flames at atmospheric pressure. Number immediately above curves refers to percentage in initial mixture at 298 K (Dixon-Lewis [94]). Reproduced by permission of The Royal Society.

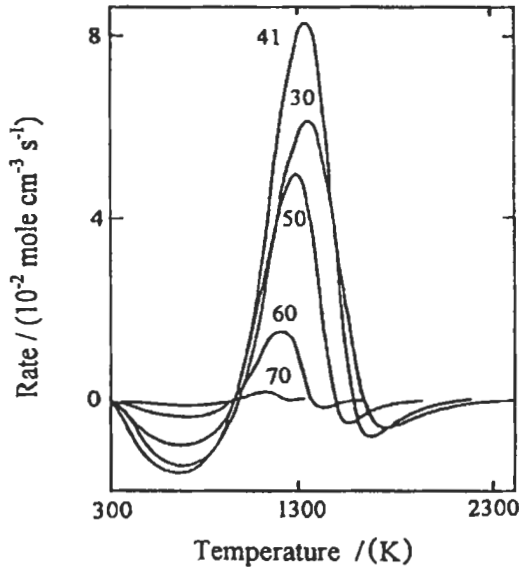


Fig. 2.9: Computed rates of formation of radical pool, defined as $(X_H + 2X_O + X_{OH} + X_{H_2O})$, where X is mole fraction, in fuel-rich hydrogen-air flames at atmospheric pressure. Numbers immediately above curves refer to percentage hydrogen in initial mixture at 298 K (Dixon-Lewis [94]). Reproduced by permission of The Royal Society.

and R_{13} to remain more or less in an equilibrium state throughout the decay region. The decay itself proceeds by way of the termination reactions, R_7 to R_{11} . In the sense that T_i characterizes the start of the very fundamental part of the overall flame process, there is a strong analogy with the ignition temperatures of older thermal theories of flame propagation, and of global asymptotic approaches (Dixon-Lewis [65]).

However, comparing the measuring flame structure with the prediction of the kinetic model, may not be a sufficiently sensitive parameter for assessing all the subtleties of flame oxidation kinetics and for this purpose the experimental burning velocity should also be measured and compared with the predicted one. In the light of this, the next section will deal mainly with the experimental and computational burning velocities at different conditions.

(ii) Laminar burning velocity. This basic physico-chemical parameter is only strictly meaningful in the context of a planar flame in a one-dimensional (1-D) flow system, where it is defined as the speed of cold gas relative to the flame front in a 1-D flow. Clearly, the burning velocity is also the volume of combustible mixture, at its own temperature and pressure, consumed in unit time by unit area of flame front, thus, the burning velocity is essentially a measure of the overall reaction rate in the flame. Accurate determination of this quantity has been discussed by Andrews and Bradley [225] and is still one of the most important aspects of combustion, because of the feedback from the determinations into kinetic mechanisms which come into play in a wide variety of other phenomena, including extinction limits. However, difficulties in the determination of the burning velocity arise when it is applied to real flames. Flow divergence exists in all real flames and causes two problems with burning velocity

measurement. First, the cold gas velocity is no longer constant, so it is not clear which velocity, if any should be used. Second, the divergence always causes some stretch in the flame, which usually affects the burning rate. If true 1-D burning velocities are to be measured then these two effects must be removed. Law and co-workers [226-228] have developed an interesting methodology for measuring burning velocities. In their experiments, a flat flame was stabilized in an axisymmetric stagnation flow and gas velocity measurements were made along the axis using Laser-Doppler Anemometry. The velocity at the cold boundary is U_{is} , and the corresponding stretch rate is given by the slope of the cold gas velocity profile. Measurements of U_{is} are made at various stretch rates and extrapolated to zero stretch to give a 1-D burning velocity, denoted by U_{io} (see section 2.9).

In burner measurements, the gas velocity, V , is used directly to derive the burning velocity as discussed in section 2.2.4. On the basis of computed flame structures, Dixon-Lewis [94] indicated area ratio corrections, which should be applied to such measurements in hydrogen-air flames if the positions of maximum hydrogen atom concentration are used as the reference planes in the flame. For conical flames on very small diameter burners, the appropriate reductions in the burning velocity may be of the order of 30 to 40 %. The reductions will be less on larger burners (Bradley et al [44]).

The non-stationary expanding spherical flame is the most attractive and alternative method for strain-free flame, provided that time-dependent strain effects can be subtracted out from the flame speed measurements ($U_s = dr_f/dt$) [94]. Dixon-Lewis [65, 94, 97, 98] suggested one method of doing this by modeling the planar one-dimensional flame and the expanding spherical flame with use of identical chemical kinetics and transport data. This has been done (Dixon-Lewis [65, 94, 97, 98]) for a series of H₂-air flames (Dixon-Lewis [97]). The correspondence between the flame speed (U_s at $r_f = 0.025$ m) and burning velocities ($U_{i, \text{planar}}$) are shown in Table 2.12 with some values for CO-H₂ and CH₄-air flame which will be discussed next.

It should be noted that the kinetic modeling automatically eliminates the strain effects. The magnitudes of such effects in the H₂-air flames are shown by comparison of the last two columns of Table 2.12. $U_{i, \text{spherical}}$ was computed from the difference between the flame and gas velocities at a single station within the flame [94]. The values were computed at four different stations in each flame, and differed by less than one percent. The flame speed for hydrogen-air flames in Table 2.12 has been measured at a radius of 0.025 m, during the constant pressure period following ignition of gas mixtures in a large spherical bomb by Andrews and Bradley [223, 229]. To explore this further, the measured burning velocities are compared with the predicted values using reactions R₁ to R₁₃ and their rate parameters in Table 2.2 with transport data in Table 2.1. Iijima and Takeno [224] have developed alternative and less arduous method for interpreting expanding spherical flame speed data. They confirmed that the values of $U_{i, \text{spherical}}$ in Table 2.12 are very close to their values, which are also shown in Figs. 2.11 to 2.14.

Figure 2.10 shows the predicted burning velocity of low temperature hydrogen rich flames. These values are in good agreement with experiments, bearing in mind that, divergence correction was applied by Day et al [168] to these experimental results.

a- Variations of burning velocity with compositions. Figures 2.11 and 2.12 show the computed burning velocities of a wide range of hydrogen-oxygen-nitrogen mixture at 1 atm for an initial temperature $T_u = 298$ K. Curves A to E in Fig. 2.11 represent the hydrogen premixed in various proportions with several (oxygen-nitrogen) compositions.

For all ($O_2 + N_2$) compositions, the predictions agree fairly well with Jahn's measurements [214] on the fuel rich side of maximum burning velocity; on the other hand, the predictions agree with the recent measurements of Iijima and Takeno [224] in lean and rich sides and also agree with measurements of Senior [215] on the lean side of stoichiometric, but fall short of his measurements of the maximum burning velocity. At the stoichiometric hydrogen-oxygen composition, the predicted burning velocity agrees closely with the measurement of Edse and Lawrence [216]. If flame E is taken into account, then the agreement between prediction and experiments will cover a hundred-fold change in burning velocity and this in turn shows how chemical kinetics model can be used as a powerful and interpretive tool in experimental research. In Fig. 2.12, the predicted results agree well with most of the experimental data and with curve A [223].

b- Variations of burning velocity with initial temperature. Figure 2.13 shows the predicted effects of variation of initial temperature, T_u on the burning velocities of the stoichiometric hydrogen-oxygen flame (represented by curve A) and the stoichiometric (29.58 % hydrogen) hydrogen-air flame (represented by curve B). Measurements of Edse and Lawrence [216] are only available for the stoichiometric hydrogen-oxygen flame and the recent measurements by Iijima and Takeno [224] are for stoichiometric hydrogen-air flame. The agreement is excellent between the predicted and experimental values.

c- Variations of burning velocity with initial pressure. Figure 2.14 shows the predicted effect of variation of the initial pressure on the burning velocities of stoichiometric hydrogen-oxygen flame (Curve A, by Strauss and Edse [221], Agnew & Graiff [222]) and 20 %, 29.58 % (stoichiometric), 41%, and 70 % hydrogen for

Table 2.12: Computational comparison between speeds of expanding spherical flames at $r_f = 2.5$ cm, and planer one dimensional burning velocities, $U_{l,planar}$ at atmospheric pressure, and that calculated from the spherical flame $U_{l,spherical}$ (Dixon-Lewis [65]). Reproduced by permission of The Combustion Institute.

Initial mole fraction				T_u	U_s	$U_{l,planar}$	$U_{l,spherical}$
H ₂	CO	CH ₄	Air	(K)	(cm s ⁻¹)	(cm s ⁻¹)	(cm s ⁻¹)
-	-	0.095	0.915	298	260	37.5	-
0.7	-	-	0.30	298	297	90.2	75.00
0.6	-	-	0.40	298	894	192.4	184.0
0.5	-	-	0.50	298	1450	271.5	262.0
0.41	-	-	0.59	298	1778	300.0	290.0
0.35	-	-	0.65	298	1758	277.7	273.0
0.30	-	-	0.70	298	1485	232.3	227.0
0.25	-	-	0.75	298	1012	167.9	163.0
0.20	-	-	0.80	298	580	93.00	106.0
0.15	-	-	0.85	298	169	30.20	36.3
0.15	0.45	-	0.40	295	479	95.70	-
0.10	0.30	-	0.60	295	711	113.6	-

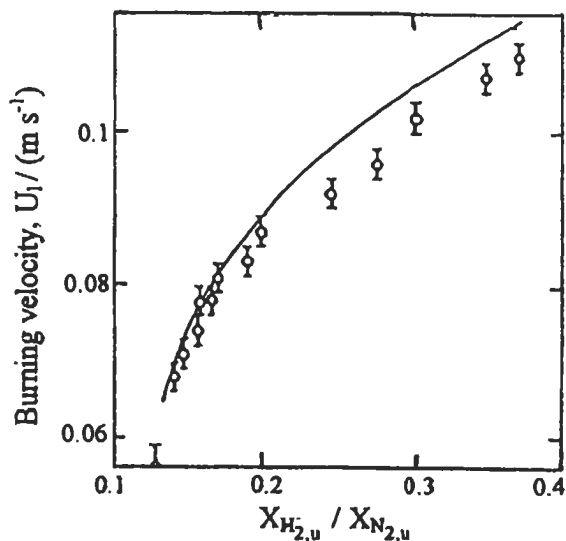


Fig. 2.10: Burning velocities of hydrogen-oxygen-nitrogen flames having $X_{O_{2,u}} = 0.046$ and $T_u = 336$ K, showing dependence on the initial mole fraction ratio $X_{H_{2,u}}/X_{N_{2,u}}$ and comparing observed values of Day et al [168] with line computed using transport and reaction rate parameters from Tables 2.1 and 2.2 [97]. Burning velocities in this figure are on basis of unburnt gas at 291 K and 1 atm. Reproduced by permission of Combustion Science and Technology.

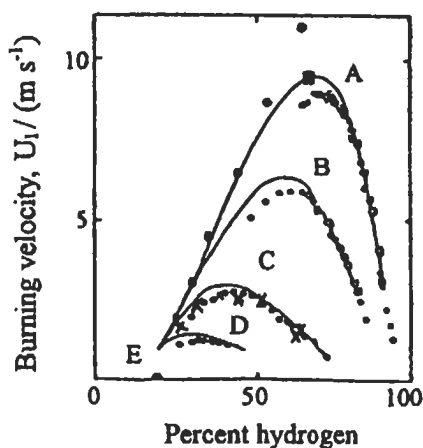


Fig. 2.11: Burning velocities of hydrogen-oxygen-nitrogen mixtures, comparing lines computed from parameters from Tables 2.1 and 2.2 with published measurements. Unburnt compositions: Curves A, $X_{O_{2,u}}/(X_{N_2} + X_{O_2})_u = 1.0$; B, $X_{O_{2,u}}/(X_{N_2} + X_{O_2})_u = 0.51$; C, $X_{O_{2,u}}/(X_{N_2} + X_{O_2})_u = 1.0$; 0.21; D, $X_{O_{2,u}}/(X_{N_2} + X_{O_2})_u = 0.125$; flame E, $X_{H_{2,u}} = 0.1883$, $X_{N_{2,u}} = 0.7657$, $X_{O_{2,u}} = 0.046$. Measurements; O, Jahn [214]; ● Senior [215], ■ Edse and Lawrence [216] (stoichiometric hydrogen-oxygen); X, Iijima and Takeno [224]. Dixon-Lewis [98], reproduced by permission.

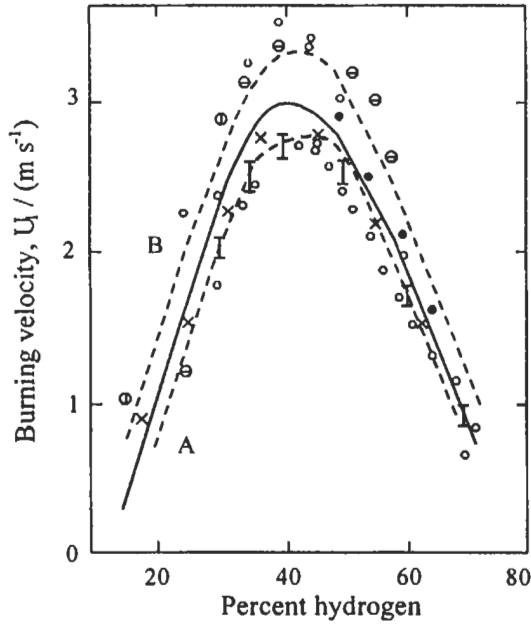


Fig. 2.12: Burning velocities of hydrogen-air mixtures, comparing line computed from parameters of Tables 2.1 and 2.2 [97] with several published measurements by burner methods: O, Jahn [214], I, Scholte and Vaags [217]; ●, Edmondson and Heap [218]; ⊖, Günther and Janisch [219]; ⊕ Günther and Janisch [220], A and B, dashed curves, Andrews and Bradley [223], X, Iijima and Takeno [224]. Reproduced by permission of Combustion Science and Technology.

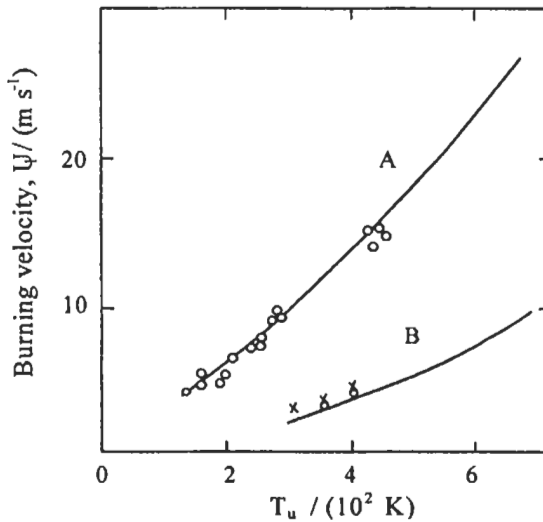


Fig. 2.13: Predicted [98] dependence of burning velocity on initial temperature, T_u . Curve A, stoichiometric hydrogen-oxygen; B, 30 % hydrogen-air. Points for stoichiometric hydrogen-oxygen represent measurements of Edse and Lawrence [216]; X, Iijima and Takeno [224]. Dixon-Lewis [98], reproduced by permission.

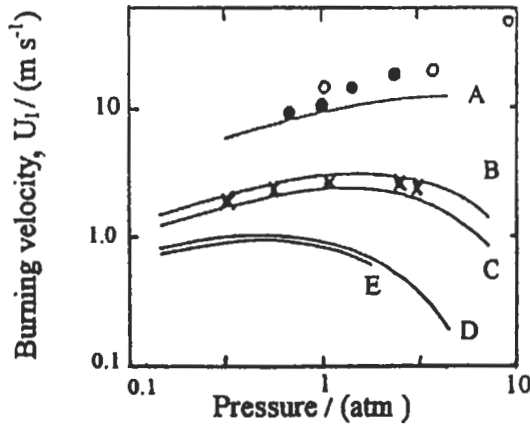


Fig. 2.14: Predicted [98] dependence of burning velocity on pressure; Curve A, stoichiometric hydrogen-oxygen; B, 41 % hydrogen-air; C, 30 % hydrogen-air; D, 20 % hydrogen-air; E, 70 % hydrogen-air. Measurements for $2\text{H}_2 + \text{O}_2$; O, Strauss and Edsc [221]; ●, Agnew and Graiff [222]; X, Iijima and Takeno [224]. Dixon-Lewis [98], reproduced by permission.

hydrogen-air flames (curves D, C, B and E, respectively). In addition to that, the recent measurements by Iijima and Takeno [224] are for 29.58 % stoichiometric hydrogen of hydrogen-air flame. It is clear that the agreement is good between the predicted and experimental values for hydrogen-air flame, but not for the hydrogen-oxygen flame especially above 1 atm.

If the burning velocity is expressed as a function of pressure by $U_f \propto P^n$, then at low pressure the n exponent takes a positive value in the range of 0.2 ± 0.06 . The value of n decreases in all cases as the pressure rises, and becomes negative at around 0.2 to 0.5 atm. The behavior arises from the competition in the flames between the "chain branching" cycle of reactions initiated by reaction, R_2 and the " HO_2 " cycle initiated by reaction, R_4 as described above.

2.4.2 Hydrogen-H₂O-CO-O₂-N₂ Flames

Experimental Method and Results

Again, the considered flame measurements were selected from that used by Dixon-Lewis and co-workers [65, 137, 144] to establish the transport parameters in Table 2.1 and reaction mechanisms and rate parameters (R_{14} to R_{20}) in Table 2.2, for H_2 - H_2O -CO-O₂-N₂ system. These experimental results will cover the flame structures of hydrogen-carbon monoxide-O₂ flame at low pressure and burning velocities of a wide range of premixed H_2 -CO-O₂-N₂, H_2 -CO-air and moist carbon monoxide-air flame.

(i) Vandooren et al [230] measured the temperature and mole fraction profiles in a burner stabilized flame at pressure of 0.053 atm, having a supply stream of mole fraction composition $X_{\text{H}_2} = 0.114$, $X_{\text{CO}} = 0.094$ and $X_{\text{O}_2} = 0.792$. The measured linear fresh gas velocity at the burner was 0.637 m s^{-1} , quoted on the basis of gas at 298 K and 0.053 atm pressure. The measured temperatures and the mole fractions of the stable species versus distance are shown as points in Fig. 2.15. The measured mole

fractions of radicals species for flame of Fig. 2.15 are shown as points in Fig. 2.16. All the mole fractions were measured by molecular beam sampling and mass spectrometry. Temperatures were measured with the aid of a ceramic-coated Pt/Pt-10 % Rh thermocouple.

(ii) A number of flames at atmospheric pressure having the initial mole fraction composition $X_{H_2,u} = 0.1685$, $X_{N_2+CO,u} = 0.7855$ and $X_{O_2,u} = 0.046$, with $T_u = 336$ K, and with the $N_2 + CO$ mixture containing between 0 and 10% carbon monoxide, was supported on an Egerton-Powling type of flat flame burner. Burning velocities were measured by the powder particle tracking technique as described by Dixon-Lewis and Isles [231]. The resulting burning velocities are shown as points in Fig. 2.17.

(iii) It is well known that the oxidation of carbon monoxide is very sensitive to the presence of traces of hydrogen and water vapor. Therefore, the result here is concerned with the burning velocity of complete range of hydrogen-carbon monoxide mixture as fuels, mixtures containing 0.55, 3.0, 10.5, 24.1, 43.3, 69.7 and 100 % hydrogen being used. Burning velocities of mixtures containing between 35 and 65 % of these fuels in air at atmospheric pressure have been measured by Scholte and Vaags [232].

The flames studied by Scholte and Vaags [232] were supported as straight-sided cones on a constant velocity profile nozzle, and the linear unburnt gas velocities V were calculated by dividing the total volumetric gas flow by the area of the burner port.

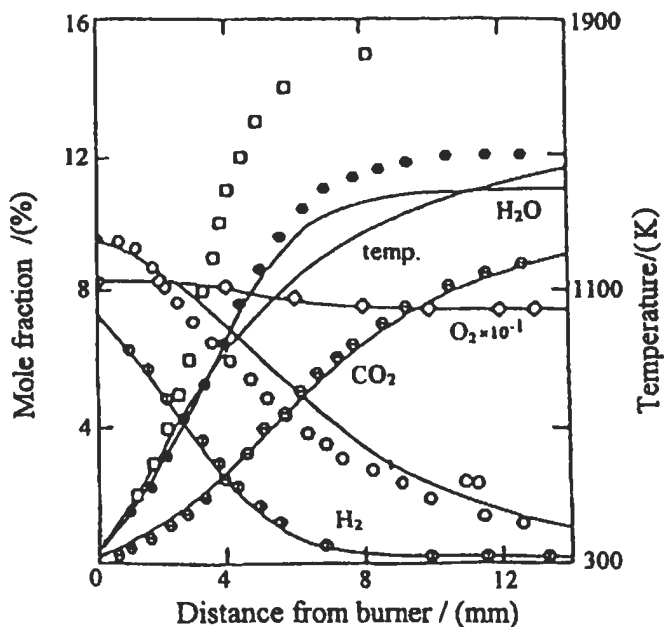


Fig. 2.15: Profiles of temperature and mole fractions of stable species against distance from burner in a lean hydrogen-carbon monoxide-oxygen flame, comparing computed lines [144] with points representing observations of Vandooren et al [230]. Mole fraction composition of supply mixture was; $X_{H_2,u} = 0.114$, $X_{CO,u} = 0.094$ and $X_{O_2,u} = 0.792$, with $P = 0.05$ atm. Flow velocity of free gas was 0.637 m s^{-1} , measured for gas at 298 K and 0.05 atm. Points; \square , temperature; \circ , CO_2 ; \diamond , 0.1 O_2 ; \ominus , CO_2 ; \bullet , H_2O . Reproduced by permission of The Combustion Institute.

The burning velocities were derived by measuring the cone half-angles, α , and using $U_1 = V \sin \alpha$. Because of small boundary layer effects at the edge of the nozzle, this approach of calculating the gas velocity introduces a certain amount of averaging into the experiment, and the precision would have been improved if these velocities had

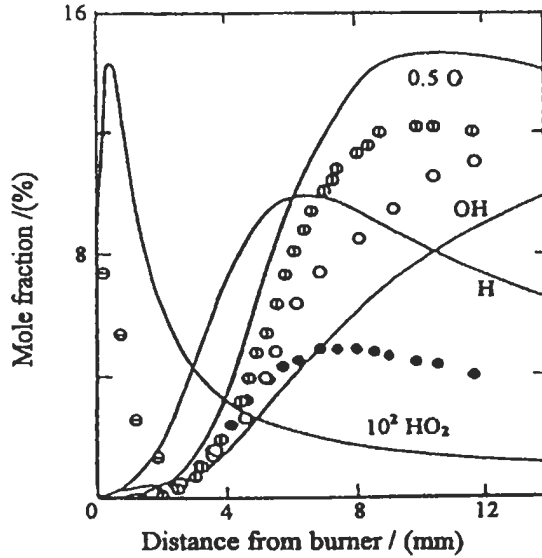


Fig. 2.16: Profiles of mole fractions of radicals against distance from burner for flame of Fig. 2.15, comparing computed lines [144] with points representing observations of Vandooren et al. [230]. Points ●, H; ○, O; ⊖, OH; ⊕, 0.5 O; ⊗, 10² HO₂. Reproduced by permission of The Combustion Institute.

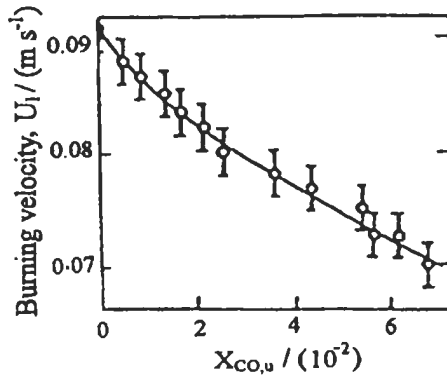


Fig. 2.17: Burning velocities of flames having initial mole fraction compositions: $X_{H_2,u} = 0.1685$, $X_{(N_2+CO)_u} = 0.7855$ and $X_{O_2,u} = 0.0460$ at a pressure of 1 atm, with $T_u = 336$ K. Burning velocities are referred to unburned gas at 291 K and 1 atm [144]. Reproduced by permission of The Combustion Institute.

been directly measured. However, Dixon-Lewis [94] has shown that when such measurements are made for the unburnt gas approaching a flame, flow divergence in the flame zone itself necessitates a correction to the measured velocity to take account of such divergence up to a reference plane at the hot side of the flame. When such corrections had been applied to several hydrogen-air burning velocities which were precisely measured by Edmondson and Heap [218] and Günther and Janisch [219], they led to results of reasonable agreement with theoretical predictions, and with the results of Jahn [214] and Scholte and Vaags [217] for these flames. These are also discussed below. There is a reason, therefore, to suppose that the results of Scholte and Vaags [232] for hydrogen-carbon monoxide-air mixture are adequate to be presented here. Their results for these mixtures are shown in Fig. 2.18. The study by Aung et al [233] on $H_2-O_2-N_2$ flames shows that the effect of flame stretch on laminar burning velocities is substantial, which yields Markstein number, M_a ($M_a = \text{Markstein length}/(\text{characteristic flame thickness, which is defined as the mass diffusivity divided by the burning velocity})$) in the range of -4 to 6 with corresponding variations of U_{∞}/U_1 in the range of 0.5-2.0, where U_{∞} is U_1 at the largest radius observed. This behavior implies significant effects of flame stretch for typical laboratory measurements of U_1 .

(iv) Lastly, burning velocities of carbon monoxide-air mixtures containing traces of hydrogen or water vapor or both are also presented. For a fuel consisting of 0.55 % hydrogen and 99.45 % carbon monoxide, Scholte and Vaags [234] examined the effect of additions of 1.2, 1.87 and 2.3 % water vapor on the burning velocities of fuel-air mixtures containing between 35 % and 65 % fuel. The water concentrations were expressed as percentages of the total mixture. Their results are shown as the points in Fig. 2.19.

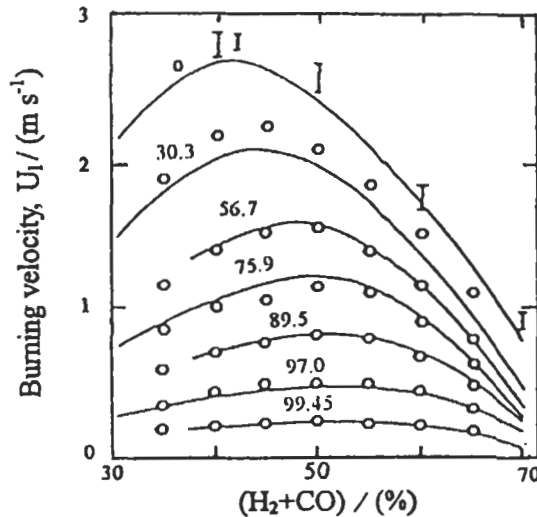


Fig. 2.18: Burning velocities of dry hydrogen-carbon monoxide-air mixtures at atmospheric pressure, with $T_u = 298\ K$, comparing computed lines [144] with points representing observation of Scholte and Vaags [232]. Number above each curve gives percentage of carbon monoxide in the $H_2 + CO$ fuel. Transport and reaction rate parameters were taken from Tables 2.1 and 2.2. Reproduced by permission of The Combustion Institute.

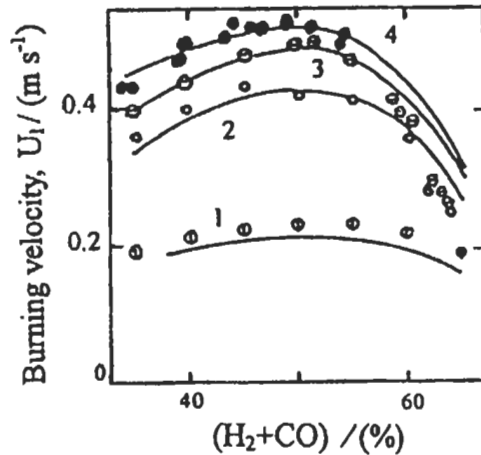


Fig. 2.19: Effect of addition of water vapour on burning velocities of flames of 0.55% hydrogen + 99.45% carbon monoxide in air at atmospheric pressure, with $T_u = 298$ K, comparing computed lines [144] with points representing observations of Scholte and Vaags [234]. Curve 1 and \circ , no. added water, Curve 2 and \circ for 1.2% added water; Curve 3 and \ominus , 1.87% added water, Curve 4 and \bullet , 2.3% added water. Water additions are percentages of the total mixture, and were regarded in computations as replacing nitrogen. Reproduced by permission of The Combustion Institute.

Computational Results

Flame model computations for CO-H₂-H₂O-O₂-N₂ system were performed by Cherian et al [144] and Dixon-Lewis [65, 137] as described in sections 2.3.1 to 2.3.3. The reaction mechanisms R₁ to R₂₀ and their rate parameters in Table 2.2 with transport constants in Table 2.1 were used in these computations. Again the predicted flame structures and burning velocities from the model were that corresponding to the initial conditions of the above experiments. All computed results are shown by full curves in Figs. 2.15 to 2.19. All of these results will be discussed in the context of reaction mechanism and its rate parameters. The flame structure and burning velocity for the above flames are discussed as follow;

(i) **Flame Structure.** Figure 2.15 shows that the agreement between the predicted and measured stable species is very good, except for water vapor, for which the discrepancy between experimental and computational profiles may be due to calibration errors. Further, the predicted maximum rates of formation of carbon dioxide and water are 1.3×10^{-5} and 3.1×10^{-5} mole cm⁻³ s⁻¹, respectively. Both predictions are compared extremely well with the maximum rates of 1.3×10^{-5} and 3.2×10^{-5} mole cm⁻³ s⁻¹ which are deduced directly by Vandoooren et al [230] from their experimental observations. However, there is a large discrepancy between the predicted and measured temperature profiles.

In contrast with the measurements, the computations predict that a temperature of 1800 K will not be reached until a distance of some 0.09-0.1 m from the burner. The difference may be due to some catalytic effect at the surface of the thermocouple used for the measurements. With regard to the radical profiles shown in Fig. 2.16, and for the same flame as in Fig. 2.15, there is again some discrepancies between theory and experiment, which we believe to be too great to be accounted for by the uncertainties in some of the rate parameters used in the computation which may be $\pm 10\%$ in most cases here.

(ii) **Laminar burning velocity.** Figure 2.17 shows that the agreement between the computed and measured results is very good. The flame having mole fractions of $X_{H_2,u} = 0.1685$, $X_{N_2,u} = 0.723$, $X_{CO,u} = 0.0618$, and $X_{O_2,u} = 0.046$, with $T_u = 336$ K and a measured burning velocity of 0.072 ± 0.002 m s⁻¹ referred to gases at 291 K and 1 atm was selected for theoretical investigation. Burning velocities for this flame were initially calculated on the assumption that, in addition to the hydrogen-oxygen-nitrogen flame reactions, R_1 to R_{13} , the flame receives a contribution from the carbon monoxide due, firstly, to reaction, R_{14} alone, secondly, to reactions R_{14} and R_{15} together, and thirdly, to reactions, R_{14} , R_{15} and chain termination mechanism with the reaction of the formyl radical, R_{16} to R_{20} (see Table 2.2). The predicted burning velocity from the third contribution was 0.073 m s⁻¹ which is in excellent agreement with the experimental value. For this, it was found necessary that the reaction rate $k_{18} > k_{17}$. The ratio of k_{18}/k_{17} in Table 2.2 is in good agreement with that found by Mack and Thrush [235] and Washida et al [236]. The predicted burning velocities from the first and second contributions were higher by 40 % and 37 % than the third contribution and this confirmed the importance of the contribution from R_{16} to R_{20} . Reaction R_{14} serves as a dual purpose in oxidizing CO and CO₂, and secondly, in substituting reactions R_1 and R_3 as the partner for reaction R_2 in the chain branching cycles.

Figure 2.18 shows the predicted burning velocity for mixtures of fuel with air containing respectively 60 % and 40 % fuel. The fuels were hydrogen-carbon monoxide mixtures containing 100 %, 69.7 %, 43.3 %, 24.1 %, 10.5 %, 3 %, and 0.55 % hydrogen, respectively. Agreement with the experimental points is satisfactory over the whole composition range. The concentrations of hydroxyl radicals, OH, and oxygen atoms, O, in the 60 % fuel flame are too small for effects of reactions, R_{19} and R_{20} to be significant.

Also, the predicted burning velocities in Fig. 2.19 agree well with the experiments. The effect of water vapor on the burning velocity is small compared to the effect of hydrogen (as shown in Fig. 2.18). This may be due to reduced catalytic efficiency of water vapor compared with that of hydrogen, which is associated with its lower free energy. The chain branching cycle that produces the radical pool in the water-oxygen containing mixtures necessitates an attack of either hydrogen or oxygen atoms on the water vapor, by reaction ($-R_1$) or ($-R_{13}$). Both reactions have activation energies of approximately 75 kJ mole⁻¹, and these makes the radical production to be more difficult than in hydrogen-oxygen containing mixtures. In the latter, the pair of free electron spins associated with the oxygen atom is more easily separated by a direct occurrence of reaction R_3 alone.

Turning back again to the effect of the strain rate on the burning velocity as discussed above; the burning velocity was computed by Dixon-Lewis [137] for two free strain flames of H₂-CO-air. The planar model described above, and the expanding spherical flame with the use of identical chemical kinetics and transport data (Tables 2.1 and 2.2) were used in these calculations and the results are given in Table 2.12.

Although, carbon monoxide and hydrogen are both important as intermediate compounds in the high temperature flame oxidation of hydrocarbon, the modeling of formaldehyde (CH₂O)-oxygen supported flames provides an essential link between the H₂-CO-air and hydrocarbon-air systems. The modeling of these was discussed by Dixon-Lewis [137] in relation to the flame structure measurements of Oldenhove de Guertechin et al [172]. This enabled Dixon-Lewis [137] to establish the reactions and rate parameters for such system, which are included in Table 2.2.

2.4.3 Methane-Oxygen-Nitrogen Flames

Experimental Method and Results

Flame structure and burning velocities were measured at Leeds University for a low-pressure laminar; flat, adiabatic premixed methane-air flames on a matrix burner of 0.076 m diameter as shown in Fig. 2.20 (Bradley et al [150], El-Sherif [153], Bradley et al [160] and John [179]). Flame stability was improved by inserting a vertically adjustable circular asbestos plate, drilled with a large number of small holes and positioned at 0.4 m above the burner matrix. The burner matrix comprised a 0.01 m thick disc of graphite-impregnated copper, supplied by Graphite Technology Ltd. This facilitated the drilling of about 2500 hole centers of 0.0015 m diameter.

The stainless-steel burner tube could be moved vertically within the copper flame tube, to enable axial profiles to be measured through the flame. Burner tube was cooled with water. Radial traversable carriages for thermocouples and gas sampling probes could be attached to two diametrically opposite flanged openings on the flame tube of 0.06 m diameter. A smaller window enabled the flame to be observed and photographed. Glass windows were flange-mounted for Laser optical measurements. Mixtures were ignited by a retractable automobile type igniter. The burned products were exhausted along the water-cooled flame tube and into the atmosphere by a 75-kW water-cooled Reavell rotary exhauster of capacity $0.25 \text{ m}^3 \text{ s}^{-1}$. A needle valve with fine control located in the exhauster line acted as a critical flow orifice and prevented any back transmission of pressure pulses to the flame. In addition, a large gate valve at the exhauster provided coarse control.

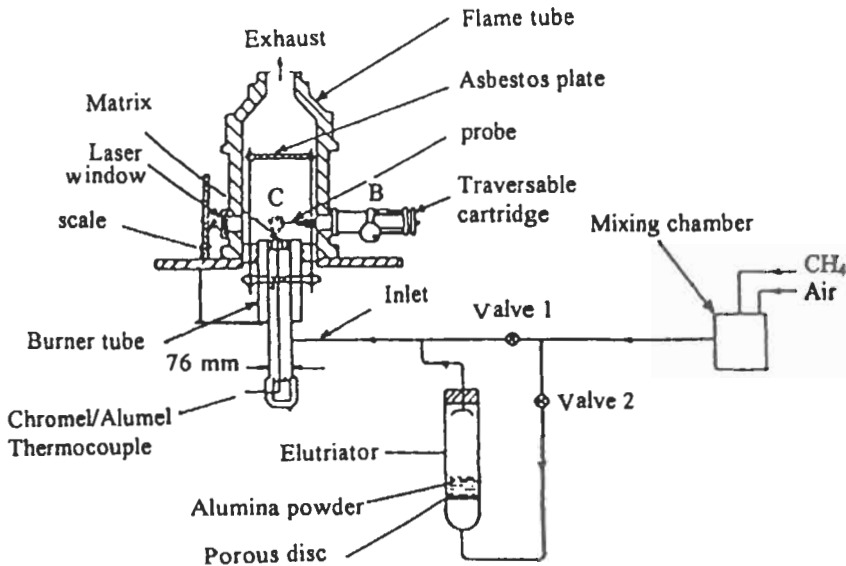


Fig. 2.20: Burner system [160]. Reproduced by permission of Elsevier Science.

a- Fuel and air flow control. Dried air and methane were separately metered through orifices and mixed, after which the mixture divided into two streams finely controlled by needle valves. Approximately 15% of the flow passed through an elutriator consisting of a glass tube and circular porous disc, and containing alumina particle for laser measurement.

b- Gas, burning velocity and temperature measurements. Gas velocities throughout the flame were measured by Laser Doppler Velocimetry. A 5 mW spectra physics helium-neon laser was employed with a Disa Model 55 L01 optical unit. The beam was focused by a lens to give a measuring volume close to the center of the flame. The two opposite windows in the flame tube enabled forward scattering to be employed. Scattered light from the particles was detected by a model 55 L10 photomultiplier, after an optical filter had reduced the radiative emission from the flame. The signal was processed by a Doppler signal processor of model 55 L20. The velocity values were obtained using IBM micro processor at a data rate exceeding 40,000 and was processed using a software that was utilized to compute the velocity from the data which was obtained from the signal processor. The burning velocities were also obtained by correcting the unburnt gas velocities (measured at the position of lowest temperature) for flow divergence (Dixon-Lewis and Islam [143], Bradley et al [44], and Abu-Elenin et al [154]). This was done by reducing the unburnt gas velocity by the area ratio of the unburnt gas to that at luminous zone. These areas were measured from flame photography of each flame.

Gas temperatures were measured by silica coated platinum-20% rhodium versus platinum-40% rhodium thermocouples, formed from wires of 40 μm diameter. The radiation correction for thermocouples was evaluated in the usual way and a typical value for this correction was found to be of about 145 K at the maximum temperature.

c- Gas sampling and analysis. Gas samples were withdrawn isokinetically through a quartz micro probe, situated 0.005 m from the axis, in accordance with the recommendations of Fristrom and Westenberg [237], and did not disturb the flame visibly. The contoured nozzle and large pressure drop effectively quenched the flame reactions in the 30° tapered quartz microprobe, after a small sonic orifice of 80 μm diameter. The sample was compressed from a pressure of 0.0026 atm to atmospheric pressure in a 0.25 m Pyrex vessel by a Neuberger VDE 0530 leak proof gas sampling pump. The entire system was frequently checked for leakage, by evacuating the system and shutting all valves. The probe was carried in the probe carriage, in a similar way to the thermocouple.

Samples from methane-air flat flames at 0.15 atm and 0.25 atm were withdrawn and compressed to the atmospheric pressure into gas analyzers by the leak proof vacuum pump. The samples were then analyzed for CO_2 , CO (low and high range) using Grubb Parsons infrared gas analyzer, and O_2 by a Servomex oxygen analyzer. All the gas analysis equipment was switched on for about half an hour to allow them to stabilize at steady state conditions. After that time, they were settled to zero by using dry air, except in the case of oxygen analyzer which was zeroed using an oxygen free nitrogen gas. The analyzers were calibrated with known mixtures. The gas analyzers measure the concentrations of the species directly in dry molar proportions. The required sample flow rate was about 1-1.5 lit. min^{-1} and the corresponding response time was 3.5 second with accuracy $\pm 1\%$.

d- Experimental results. Mole fractions of the stable species, CO_2 , CO and O_2 , gas temperature and velocity throughout the flame were measured as described above [153]

at equivalence ratios of 0.6, 1.3, and 1.5, with an initial temperature of 300 K, and low pressures. These measured values are shown as points and as a function of height above the burner top in Figs. 2.21 (a) to (d). Also, burning velocities were measured as described above over a range of equivalence ratios of 0.6 to 1.5, at pressures of 0.05, 0.1, 0.15 and 0.25 atm and with an initial temperature of 300 K. The results are shown as points in Figs. 2.22 (a) to (b) and Figs. 2.23. All these measurements are discussed next in the context of reaction mechanism and rate parameters. In all figures, dotted, dashed and solid curves are computed for the above conditions from kinetic model using schemes A, B, and C, respectively (as discussed in section 2.3.4), and these results are discussed now.

Computational Results

The reactions of scheme, A, and the rate coefficient, in Tables 2.2 and 2.3, in addition to the transport parameters in Table 2.1 were used as described in section 2.3.4 to predict the flame structures and burning velocities. A number of 32 CH₄-air flames were computed by El-Sherif [153] with scheme, A, at pressures of 0.05, 0.1, 0.15 and 0.25 atm pressure and over a wide range of equivalence ratios, ϕ , from 0.6 to 1.5 and at an initial temperature of 300 K. For these initial conditions, another 64 runs were also computed, half of these runs were computed by using reactions of scheme, B, rate coefficients and constants in Tables 2.1 to 2.4, and the other half of those runs was done with scheme C, rate coefficients and constants in Tables 2.1 to 2.5. Finally, with scheme C, another seventeen runs for CH₄-air flame were computed, eight of them at 1 atm. pressure and $\phi = 0.6$ to 1.5, and 9 runs at 0.5, 3, 5 and 10 atm pressure for $\phi = 0.6, 1$ and 1.2, all at an initial temperature of 300 K. The results have been obtained using 33 and 53 grid points for each flame, and 1500 to 2000 integration steps to reach the steady

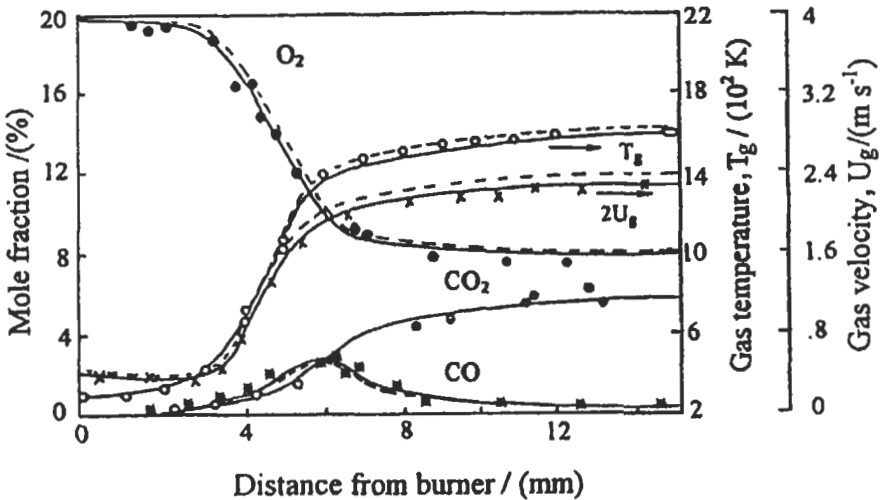


Fig. 2.21(a): Experimental (\bullet , O₂, \otimes , CO and \ominus , CO₂), O, X, gas temperature and velocity, respectively for CH₄-air flame. Dashed and full curves are the computed stable species concentrations, gas temperature and velocity using scheme, B and C, respectively. All results for $P = 0.15$ atm, $T_u = 300$ K and $\phi = 0.6$ [153].

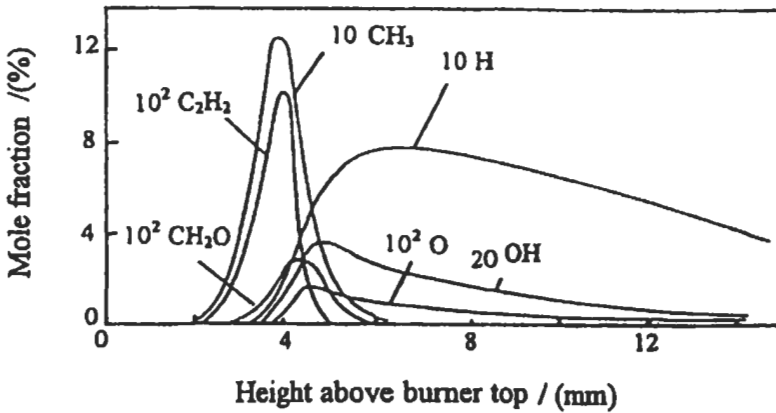


Fig. 2.21(b): Computed radical species concentrations for CH_4 -air flame using scheme, C at $P = 0.25 \text{ atm}$, $T_u = 300 \text{ K}$, and $\phi = 1.5$ [153].

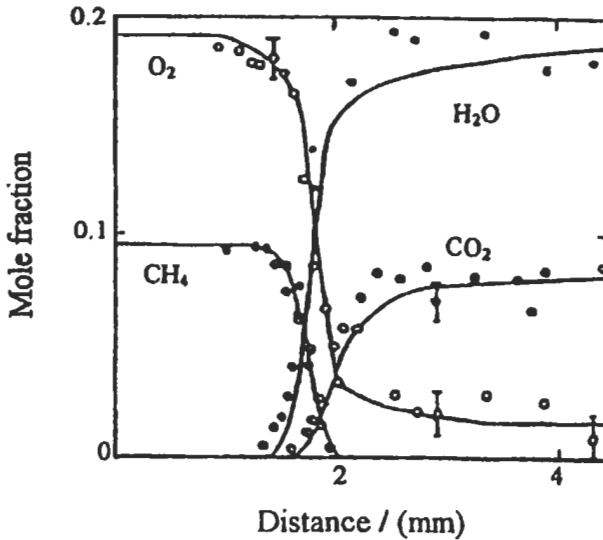


Fig. 2.21(c): Mole fraction profiles of reactants and products in a stoichiometric methane-air flame at atmospheric pressure and $T_u = 298 \text{ K}$, comparing measurements of Bechtel et al [243], represented by points, with line representing computation by El-Sherif [153] using scheme C.

state, depending on the flame. The principal predicted variables include burning velocity, gas temperature and velocity profiles, species profiles (21 species from scheme, C), flame thickness, and volumetric heat release rate. These computed results were performed by El-Sherif [153]. On all Figs. 2.21 to 2.24, the results from schemes, A, B and C are shown, respectively, by dotted, dashed and full curves. Analysis of these results will be presented next.

The flame structure, burning velocity, heat release rate and flame thickness for the

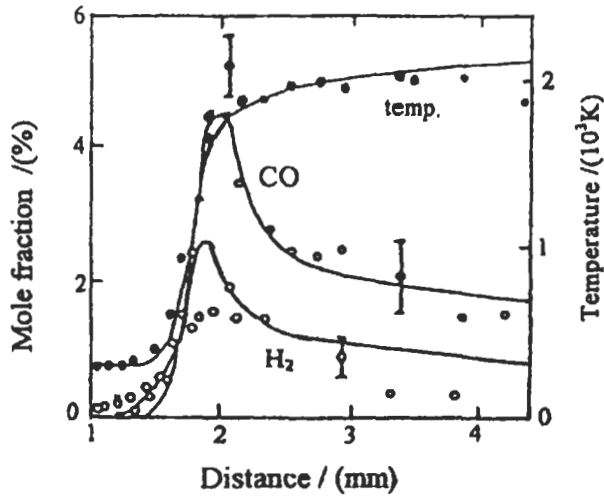


Fig. 2.21(d): Temperature and mole fraction profiles of hydrogen and carbon monoxide in a stoichiometric methane-air flame at atmospheric pressure and $T_u = 298$ K. points represent measurements of Bechtel et al [243] and lines represent computation by El-Sherif [153] using scheme C.

above flames are discussed as follows;

(i) **Flame structure.** The flame structure at low and atmospheric pressures are discussed as follows;

a- Composition profiles at pressures 0.15 and 0.25 atm. The measured CO, CO₂, O₂, gas velocities and temperatures profiles are shown as points in Fig. 2.21 (a), at 0.15 atm, $\phi = 0.6$ and at an initial temperature of 300 K. The predicted profiles for all the above conditions are shown by dashed (scheme B), and full curves (scheme C) in Figs. 2.21 to 2.24. All schemes give nearly identical reasonably good predictions of the measured profiles of oxygen concentrations and gas temperature for all the equivalence ratios. The concentrations of CO and CO₂ are also well and nearly predicted up to ϕ of about 1.3. In contrast, the predicted concentrations of CO and CO₂ are less when scheme B is used. This scheme appears to underpredict and overpredict conversion of CO to CO₂ in the reaction zone and post flame, respectively. Also, scheme B overpredict the gas velocity profiles, especially for $\phi \geq 1.3$. Similar problems for CO and CO₂ have been found by Bradley et al [44] and Abu Elenin et al [154] for CH₃OH-air flames, and it was mainly due to uncertainties in chemical kinetics scheme of breakdown CH₃OH. The combination of circumstances implies that the reaction mechanism needs some revision. The C₂H₂ reactions were found to be important in very rich flames, (Warnatz [166], Langley and Burgess [177], and Coffee [238]). Coffee [238] has included the chemistry of CH₂ in a methane combustion model for the first time and suggested that for an equivalence ratio of $\phi \approx 1.4$, up to 35 % of CH₃ is converted to CH₂ before subsequent oxidation. Warnatz et al [239] did not include this route and estimated that for $\phi \geq 1.6$, virtually all the CH₃ proceeded to C₂-hydrocarbons, implying that the rich combustion of methane becomes essentially the combustion of C₂-hydrocarbons. Following that an attempt was made by El-Sherif [153] to correct the underprediction of CO in the post flame, and CO₂ in the

reaction zone by using the suggested C_2H_2 reactions that are given in Table 2.5 with scheme B (Table 2.1 to 2.4) and this is called scheme C. The reactions R_{45} to R_{48} are responsible for C_2H_2 production, and their rate coefficients were taken from Warnatz [166]. Reactions R_{49} and R_{50} are for the attack of C_2H_2 and CH_2 by O and O_2 , and their rate coefficients were finally taken from Coffee [238] and Westbrook and Dryer [240]. The reactions and rate coefficients in Table 2.5 were chosen after several computed runs to match the predictions with the experiments, not only for flame structures, but also for burning velocities, in both lean and rich flames. The sensitivity analysis for reactions in Table 2.5 shows that reaction R_{49} is responsible for producing of about 12% of CO in the post flame. In addition, reaction R_{45} shares reaction R_{14} for consuming OH, and this will reduce the consumption of CO through reaction R_{14} by about 4 % in the post flame. In reaction zone, reaction R_{50} plays an important role in producing more CO_2 where there is high concentration of O_2 up to a distance of 9 mm.

Clearly, the reactions in Table 2.5 are important for $\phi \geq 1.3$. The absolute value of k_{49} (Table 2.5) at 1800 K is $1.95 \times 10^{13} \text{ cm}^3 \text{ mole}^{-1} \text{ s}^{-1}$ and this agrees with the value of $2.14 \times 10^{13} \text{ cm}^3 \text{ mole}^{-1} \text{ s}^{-1}$ that is found by Vandooren and Van Tiggelen [241]. Also, the value of k_{50} (Table 2.5) at 1800 K is $3.6 \times 10^{13} \text{ cm}^3 \text{ mole}^{-1} \text{ s}^{-1}$, and this agrees with the recent value of $2.2 \times 10^{13} \text{ cm}^3 \text{ mole}^{-1} \text{ s}^{-1}$ that is found by Langley and Burgess [177]. Their results indicated that reaction R_{50} is significant in fuel rich flames and a favorable value for k_{50} towards the higher end of the range of published rate constant of Peeters and Mahnen [242], which is the value used here in Table 2.5, and also by Coffee [238].

Finally, Fig. 2.21 (b) shows the computed profiles of H, O, OH, CH_3 , C_2H_2 , and CH_2O for flame at $\phi = 1.5$, $P = 0.25 \text{ atm}$. and an initial temperature of 300 K. The concentrations of CH_3 and C_2H_2 peak early in the flame. Also, it was found that the concentrations peak of $C_2H_6 \approx C_2H_4$ and C_2H_6 were lower by about 10 and 20 times, than C_2H_2 , respectively. More details about the role of pool radical ($CO + H + OH + CH_3 + C_2H_5 + C_2H_3 + CH_2 + HO_2 + HCO$) will be discussed in the following sections.

b- Composition profiles at atmospheric pressure. Figures 2.21 (c) and (d) show the measurements of Bechtel et al [243], represented by points for stoichiometric CH_4 -air flame at 1 atm, and $T_u = 298 \text{ K}$. The computed results were performed by El-Sherif [153] using scheme C. The predicted results for O_2 , H_2O , CH_4 , and CO_2 shown in Fig. 2.21 (c) and also for CO, H_2 and temperature shown in Fig. 2.21 (d) are in reasonable agreement with the measurements. After the above comparisons, it is necessary to check further the validity of the kinetic mechanism with the laminar burning velocity at different conditions, and this will be discussed now.

(ii) **Burning velocity with equivalence ratio and pressure.** The effect of equivalence ratio, pressure and temperature on the burning velocity is discussed herebelow.

Measurements of burning velocities with its band are shown in Figs. 2.22 (a) and (b) at 0.05 and 0.25 atm pressure, different equivalence ratios, ϕ , and an initial temperature of 300 K. The figures also show the computed burning velocity for the above conditions using schemes A, (dotted curves), B, (dashed curves), and C, (full curves). The comparisons show that scheme C is superior in rich and lean methane-air flames. To explore this further, the computed burning velocity from scheme C at more different pressures and $\phi = 0.8$ is plotted and shown by full curves with some corresponding measurements by different workers [153, 176, 222, 224, 229, 247, 251-253, and 255] (shown as points) in Figs. 2.23. The results of the figure reveal that, in spite of

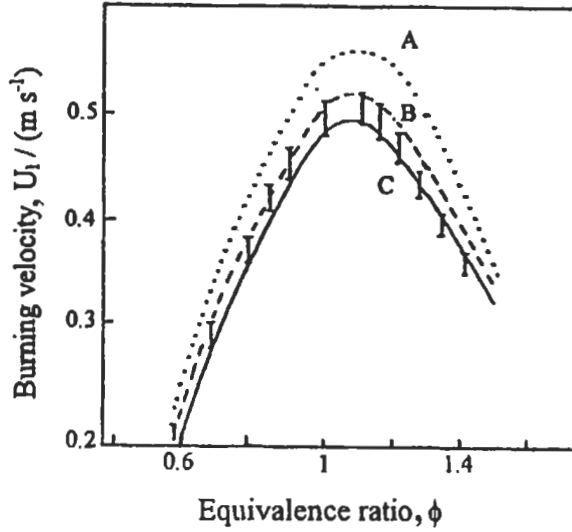


Fig. 2.22(a): Computed and \pm experimental laminar burning velocity for CH₄-air flames vs. equivalence ratio for $P = 0.05$ atm, and $T_u = 300$ K, for scheme A, --- for scheme B and — for scheme C [153].

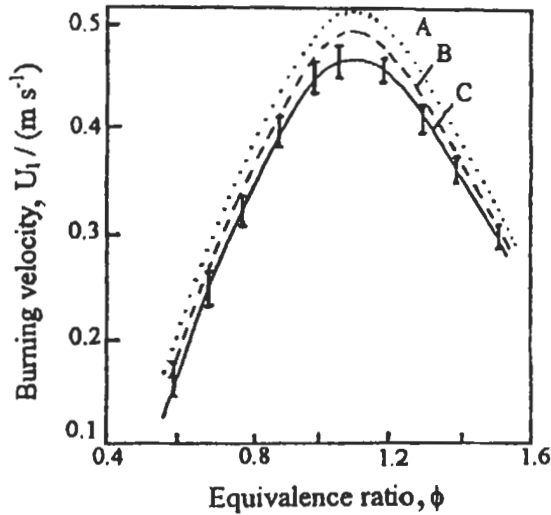


Fig. 2.22(b): Computed and \pm experimental laminar burning velocity for CH₄-air flame vs. equivalence ratio for $P = 0.25$ atm, and $T_u = 300$ K, for scheme A, --- for scheme B and — for scheme C [153].

the extensive effort done to determine accurately the burning velocity, there are still wide spreads in the reported experimental data. The accuracy of different burning velocity measurement techniques has been discussed by Andrews and Bradley [225], and Law [244].

It is clear from Fig. 2.23, that the burning velocity is a pressure dependent, and the computed variation of burning velocity with the pressure indicates that no single pressure law can fit neither the predicted nor the experimental values over the range from 0.1 to 10 atm. This agrees with Habik and co-workers [44, 154] findings for CH_3OH -air flames and also with Refs. 161 and 162. The influence of pressure on HO_2 formation can be paramount. With increase in pressure, reaction R_4 competes directly with the important chain branching reaction, R_2 and decreases the burning velocity.

Figure 2.24 (a) was partly reproduced from Andrews and Bradley [229] and has been updated to include more recent data [176, 220, 224, 245, 247]. The figure again shows a significant spread in experimental data due to the accuracy of different techniques. As mentioned in section 2.4.1, there are two recent and accurate techniques for measuring the burning velocity, and these techniques were used by Egolfopoulos et al [176] and Iijima and Takeno [224] to measure the burning velocity for CH_4 -air flames and their results are shown in Fig. 2.24 (b). These accurate results were used by El-Sherif [153] to optimize the kinetic scheme and predict the burning velocity. The predicted results when using Scheme C are shown in the same figure and gives good agreement with the experimental data. The predicted burning velocity at $\phi = 1$ is 0.365 m s^{-1} , and this agrees well with the recent recommended value of 0.36 m s^{-1} by Dixon-Lewis [65] and this value is shown by black circle in Fig. 2.24 (c).

The predicted burning velocity, U_{10} , using scheme C is correlated with the equivalence ratio, ϕ at 300 K and 1 atm by:

$$U_{10} = 0.38 \phi^{-0.35} \exp [-5.5 (\phi - 1.1)^2] \quad \text{m s}^{-1} \quad (2.26)$$

Also, the variation of predicted burning velocity with the pressure is correlated for CH_4 -air flames at 300 K by:

$$U_1 = U_{10} (P_u/P_0)^{-0.14} \quad \text{m s}^{-1} \quad P_u < 1 \text{ atm} \quad (2.27)$$

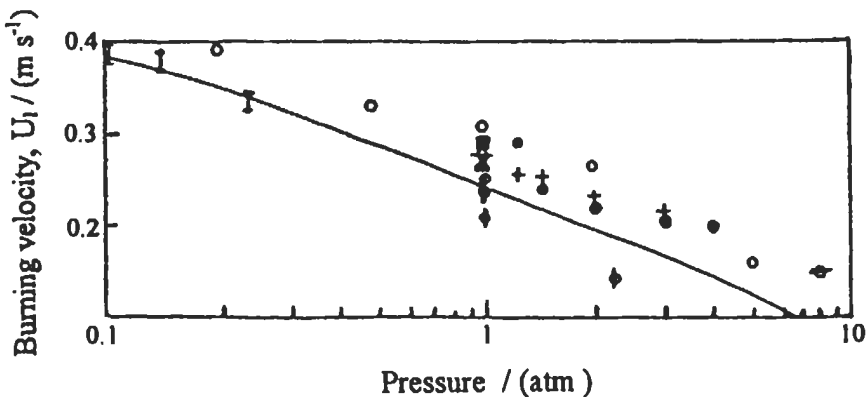


Fig. 2.23: Variation of experimental and computed burning velocity for CH_4 -air flames with different pressures at $\phi = 0.8$, and $T_u = 300 \text{ K}$, I, El-Sherif [153]; O, [254]; ●, [247]; +, [251]; ⊖, [176]; ⊕, [253]; ◆, [222]; ⬤, [255]; ■, [229]; ▲, [224]; Full curve for scheme C.

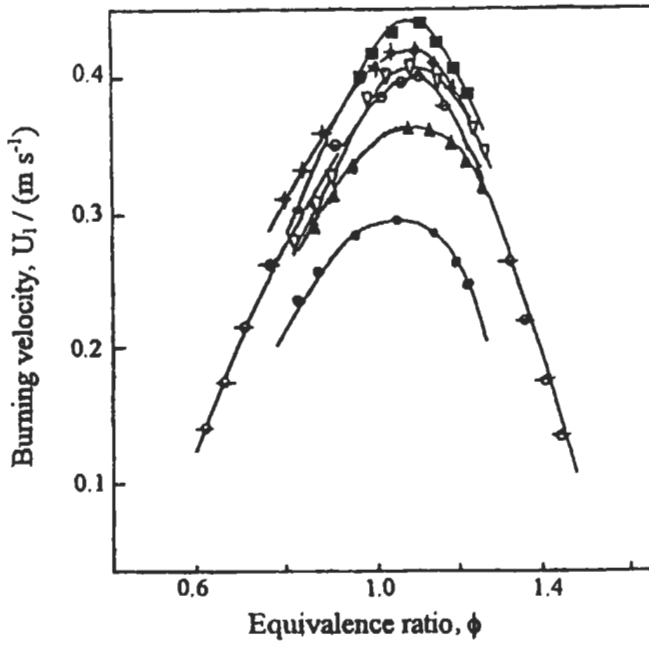


Fig. 2.24(a): Measured burning velocity for CH₄-air flames at $P=1$ atm, and $T_u=300$ K [153], ●, [247]; ▲, [224]; ⊕, [176]; ▽, [245]; ◆, [220]; ■ [225].

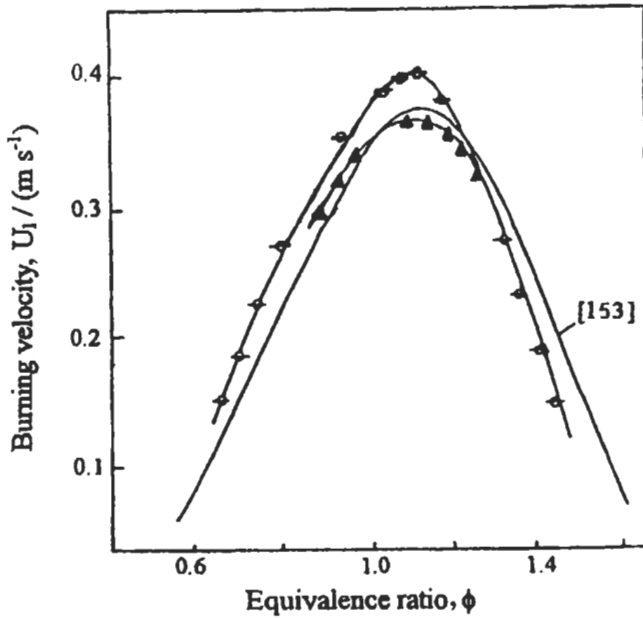


Fig. 2.24(b): Comparison between the computed (Full curve from scheme C [153]) and recent measured burning velocity, ▲, [224]; ⊕, [176] for CH₄-air flames at $P=1$ atm, and $T_u=300$ K.

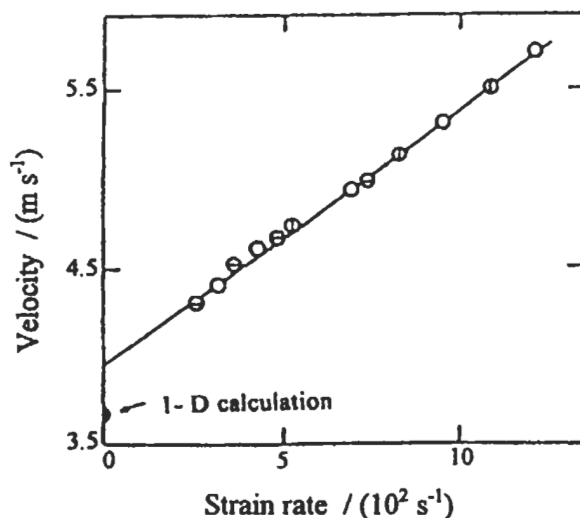


Fig. 2.24(c): Computed effect of immediate preflame strain rate on minima in velocity profiles for CH₄-air flames. Planar axisymmetric configuration. \odot , 2L = 7 mm; \circ , 2L = 16 mm; \ominus , 2L = 20 mm, where 2L is the nozzle separation distance, see also section 2.9 (Dixon-Lewis [65]). Reproduced by permission of The Combustion Institute.

$$\text{and } U_1 = U_{10} (P_u/P_0)^{-0.45} \quad \text{m s}^{-1} \quad P_u > 1 \text{ atm} \quad (2.28)$$

where $P_0 = 1$ atm and P_u is the initial pressure (0.1 to 10 atm).

(iii) **Burning velocity and flame temperature with the ratio of $O_2/(N_2+O_2)$.** Jahn [214] studied experimentally the effect of replacing the nitrogen in the air by oxygen on the burning velocity of mixtures of methane- N_2 - O_2 at atmospheric pressure, room temperature and different volumetric ratios of $O_2/(N_2+O_2)$ (from 21 to 98 %). Some of these results are plotted by points versus equivalence ratio and are shown in Fig. 2.25 (a). It would appear that the burning velocity increases at all range of equivalence ratios as the percentage of volumetric ratio of $O_2/(N_2+O_2)$ increases.

In order to explain kinetically the above results, El-Sherif [246] predicted the burning velocity and flame structure for the corresponding experimental conditions using the kinetic scheme C described above (El-Sherif [153]). These predicted burning velocities are shown by full curves in Fig. 2.25 (a). It is clear from the figure that the predicted results are in satisfactory agreement with the corresponding measured values. The adiabatic flame temperature for the above experimental conditions were calculated using an equilibrium program of 18 species (Habik [155], see chapter 1), and these results are shown by dashed curves in the same figure. The maximum adiabatic flame temperature moves in harmony with the maximum burning velocity towards the rich flame as the ratio of $O_2/(N_2+O_2)$ increases. It was found to be difficult to obtain a predicted stable flame with burning velocity less than 0.05 m s^{-1} . Therefore, the predicted burning velocity was extrapolated by dots to burning velocity less than 0.05 m s^{-1} . The lean limit burning velocity at 1 atm and room temperature was found to be 0.038 m s^{-1} (Bradley et al [147]). Taking this lean limit burning velocity as a reference to determine the lean and rich flammability limits, then the corresponding lean limit adiabatic temperatures were found to be 1400 to 1450 K, while in rich side, the rich limit temperatures were

found to vary from 1450, 1480, 1500 K for O₂/(N₂+O₂) of 21 %, 30 % and 40 %, respectively. The lean limit equivalence ratios were found to be 0.5, 0.36 and 0.26 for 21 %, 30 % and 40 % O₂, respectively, but these equivalence ratios are corresponding to volumetric ratios (F/(F+A)) from 0.049, 0.05, 0.051 (i.e. the lean limit value which is based on the ratio of F/(F+A) is nearly independent of O₂ %). These values are also corresponding to the lean limits mixture heat of reaction range from 41 to 42.6 kJ mole⁻¹ of mixtures. The rich limits equivalence ratio are found to be 1.85, 2.2 and 2.35 for 21 %, 30 % and 40 % O₂. These rich limit of equivalence ratios are corresponding to volumetric ratio of F/(F+A) equal to 0.166, 0.248 and 0.32 (i.e. the rich limit value which is based on the ratio of F/(F+A) is oxygen dependence).

The maximum burning velocities as a function of O₂ % concentrations are found to be correlated by:

$$U_{\text{max}} = 5.55 \times [0.603^{(1/O_2)}] \times O_2^{0.195} \quad \text{m s}^{-1} \quad (2.29)$$

where O₂ is the volumetric ratio of O₂/(N₂+O₂).

For the corresponding flames in Fig. 2.25 (a), the maximum mole fractions of O, H, OH and CO are shown in Fig. 2.25 (b), while the maximum mole fractions of CH₃O, C₂H₆ and C₂H₅ are shown in Fig. 2.25 (c). Both figures show that, these species increase at all equivalence ratios as the ratio of O₂/(N₂+O₂) increase from 21 to 30 %.

From the chemical kinetics point of view, the increase of O₂ % concentrations in the initial mixture will lead to increase in the reactivity of reaction, R₂ which is the most important chain branching reaction and this reaction produces more radical species, O and OH (Fig. 2.25b). Furthermore, the increase of these radicals will lead to increase in the reactivity of reactions, R₂₄ to R₂₆ and consequently increase CH₃ concentration, and this is followed by the increase of C₂H₆ through reaction, R₃₅ (CH₃ + CH₃ → C₂H₆). This leads to increase in ethyl radical, C₂H₅ by reactions, R₃₆ to R₃₈,

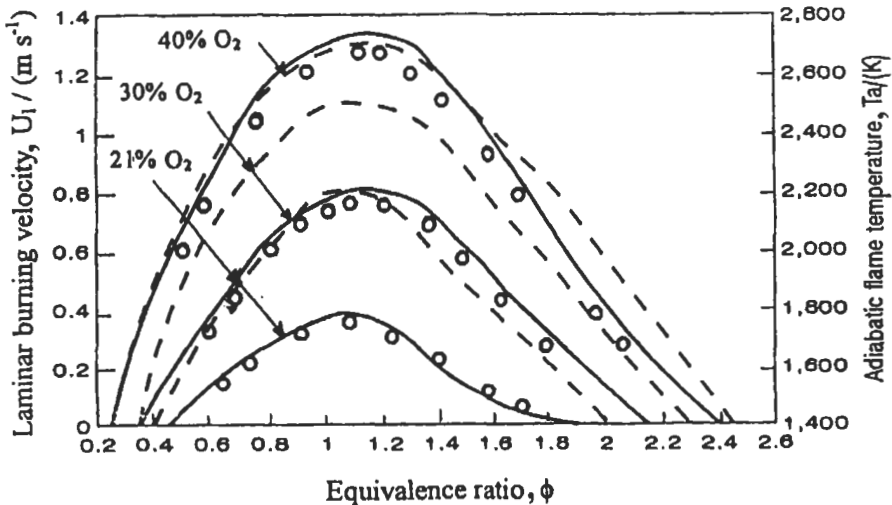


Fig. 2.25(a): Variation of predicted (full curves) and experimental, O, [214] burning velocity and adiabatic flame temperature (dashed curves) with ϕ for CH₄-N₂-O₂ flames, at 1 atm, 300 K [246].

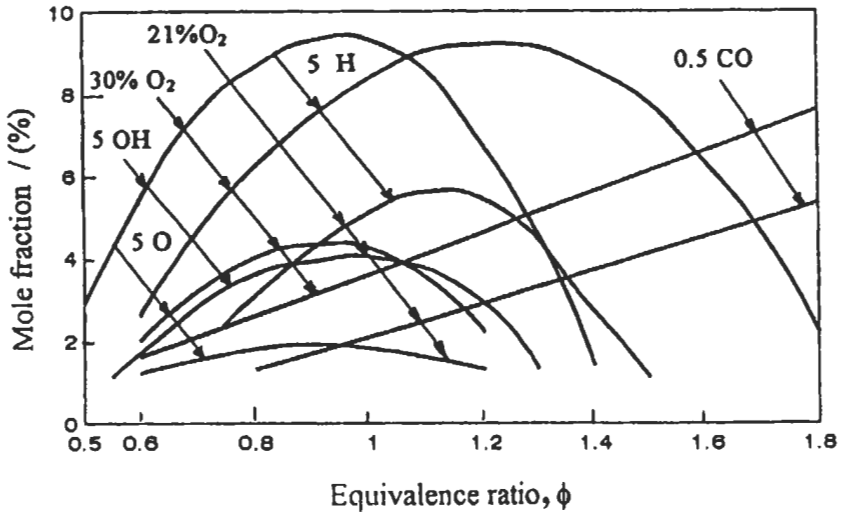


Fig. 2.25(b): Variation of maximum mole fractions of H, O, OH and CO with the equivalence ratio for the same flames as in Fig. 2.25 (a) [246].

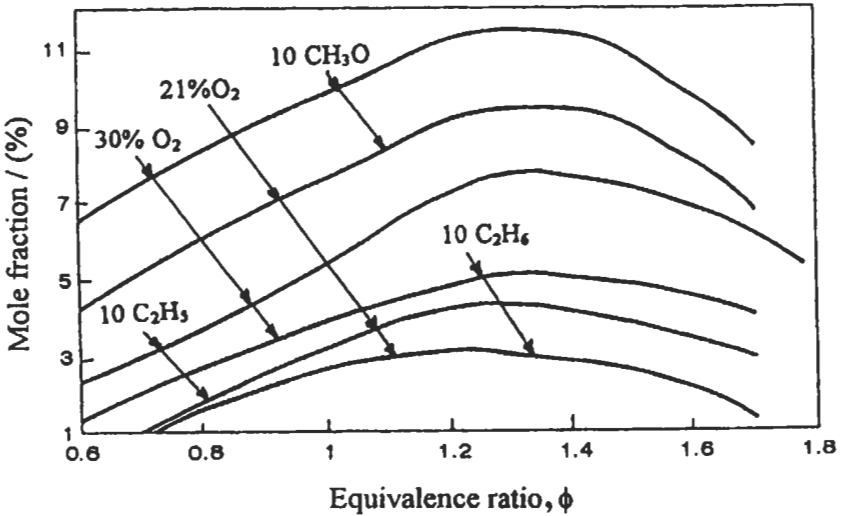


Fig. 2.25(c): Variation of maximum mole fractions of CH₃O, C₂H₆, and C₂H₅ with the equivalence ratio for the same flames as in Fig. 2.25 (a) [246].

which again leads to increase methyl radical, CH₃ through reactions, R₄₀ and R₄₁. The major reactions of methyl radicals are reactions, R₂₇ (CH₃ + O → CH₂O + H), R₂₈ (CH₃ + O → CHO + H₂) and R₃₀ to R₃₁. Reaction, R₂₇ is the major product for H atoms, while reaction, R₃₁ (CH₃ + HO₂ → CH₃O + OH) is the major reaction for producing methoxy radical, CH₃O. All in which H atoms increase in the flame and hence the burning velocities are increased as O₂ % increases, as shown in Fig. 2.25 (a).

(iv) **Variation of heat release rate with pressure and equivalence ratio.** A turbulent flame might be regarded as an array of laminar flamelet, and with this approach, the laminar flame is a sub-model. Then, the volumetric heat release rate in turbulent combustion will be as the laminar heat release rate of laminar flame that is a function of temperature, strain and probability density function (Bradley et al [248], Cant and Bray [249]). It is therefore important to present the laminar heat release rate as a function of temperature, and Fig. 2.26 (a) shows such profiles for four different flames. The effect of equivalence ratio, ϕ , on the heat release rate is shown by three curves (full curves) for $\phi = 0.6, 1.0$ and 1.2 , at 1.0 atm and $T_u = 300$ K. The dotted curve is from scheme A, for $\phi = 1.0, 1$ atm. and $T_u = 300$ K. The figure also shows that the peak of the heat release rate, q_{max} , moves toward high temperature as the equivalence ratio increases. The effect of pressure on the heat release rate is shown by the full curve at 0.05 atm, $\phi = 1.0$ and $T_u = 300$ K. The peak heat release at this pressure is reduced by a factor of about 150 than the peak at 1 atm.

(v) **Variation of flame thickness with equivalence ratio.** Figure 2.26 (b) compares the computed flame thickness (using scheme C) as a function of ϕ with the experimental results. There are two arbitrary definitions of flame thickness suggested by El-Sherif [153],

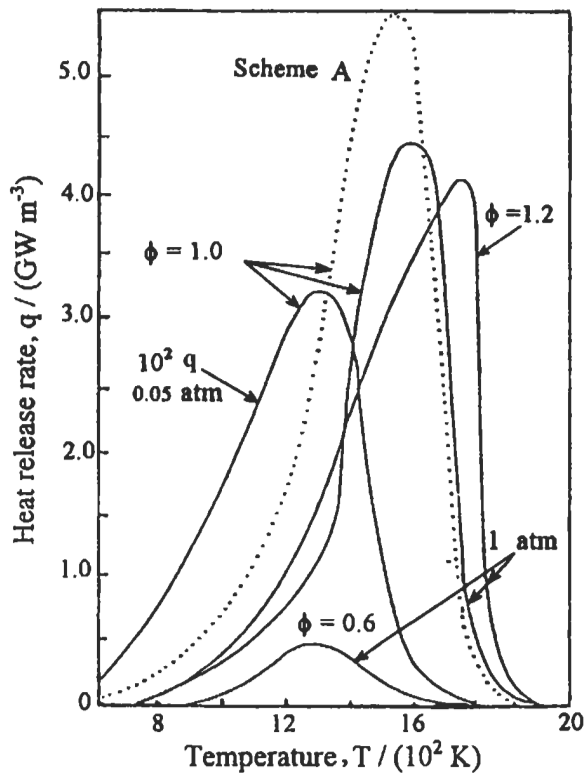


Fig. 2.26(a): Variation of computed heat release rate with temperature at for CH₄-air flames, $P = 1$ atm, $T_u = 300$ K for equivalence ratios of 0.6, 1.0 and 1.2, also shown, the heat release at 0.05 atm and $\phi = 1.0$. Dotted curve for scheme A and full curves for scheme C [153].

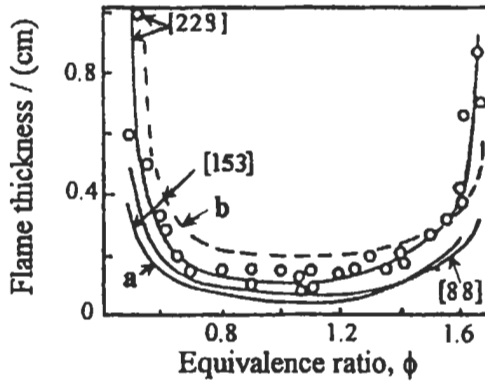


Fig. 2.26(b): Comparison between predicted and experimental CH_4 -air flame thickness at different equivalence ratios at $P = 1$ atm, and $T_u = 300$ K. O, experimental from [229]; curves a and b are calculated from two arbitrary definitions of flame thickness (see text) [153].

the first one is taken from the maximum temperature gradient, starting from T_u to adiabatic temperature, T_b , (curve a) and the second one is taken from the difference between the distance corresponding to $0.9 T_b$ and $T = T_u + 20$, (curve b) and the results from these two assumptions are shown in Fig. 2.26 (b) by full curves a and b, respectively. The figure shows some differences between the results from the two assumptions, which are attributed to the arbitrary definition of the flame thickness. The results from the second definition are generally in agreement with the experiments. The shape of the flame thickness, x , with ϕ is similar to the inverse shape of the burning velocity in Figs. 2.24 (a) and 2.24 (b). Typically, in the simple laminar flame theory [250] the burning velocity, $U_1 \propto 1/x$. A photograph of CH_4 -air flat flame is shown in plate 2.1 for 0.1 atm.

(vi) **Net pool radical and ignition temperature.** The net rate of radical pool production in methane flames are consisting of $\text{H} + 2\text{O} + \text{OH} + \text{HO}_2 + \text{CH}_3 + \text{CH}_3\text{O} + \text{C}_2\text{H}_5 + \text{CHO}$, and are given by the difference between the rate of formation of these radicals and the rate of their removal. The results at T_u of 300 K, ϕ of 0.6, 1.0, and 1.2 for methane-air flames are shown at 1 atm in Fig. 2.26 (c) and the results show that the net rate of radical pool becomes positive at temperature, T_i (defined here as the ignition temperature and marked on the x abscissa) [155].

The main reaction rate, which causes the flame to propagate, is the chain branching reaction, R_2 . This reaction activates unpaired-electron spins present in molecular oxygen, to produce two new full active species, OH and O. As a consequence of the very marked reduction in the rate of the forward reaction, R_2 at low temperatures, and of



Plate 2.1: Direct flame photograph for methane-air flame at $\phi = 1$, 0.1 atm and 300 K.

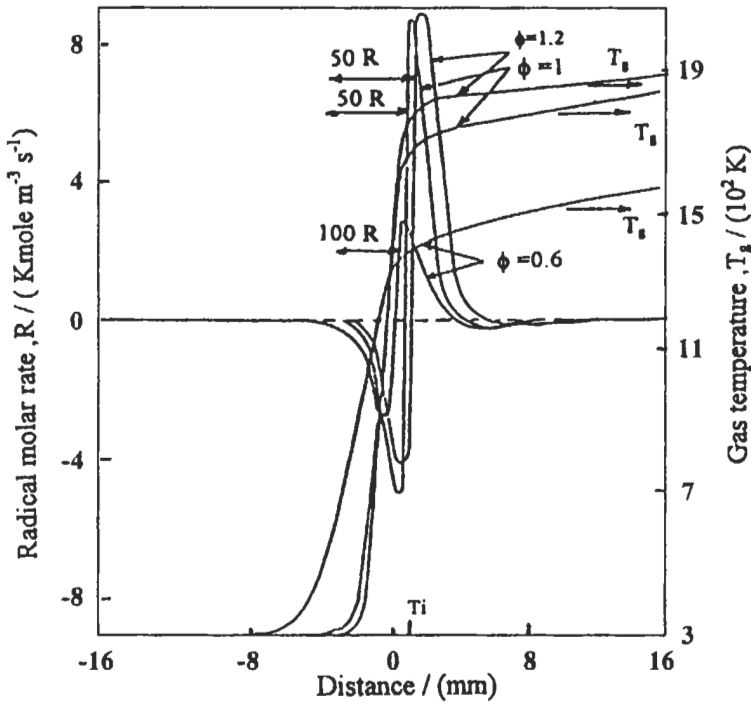


Fig. 2.26(c): Variation of net radical pool rate and gas temperature with distance for CH₄-air mixtures at $\phi = 0.6, 1.0$ and $1.2, 1 \text{ atm}$, and $T_u = 300 \text{ K}$ [155].

the fact that it must also compete with the more or less temperatures independent chain termination rates of reactions, R_7, R_8 and R_9 even at low radical concentrations, the net formation of new active radicals is restricted to temperature above, T_i . Above this temperature, the overall system becomes effectively chain branching, at a rate, which increases very rapidly, but the system is eventually limited by the consumption of oxygen and the approach of R_2 to its equilibrium. At the same time the reactions, R_1, R_3 and R_{14} also approach their equilibrium position. Consequently, the free radicals, O, H, and OH (shown in Fig. 2.21 (b)) finally decay to full equilibrium. The decay itself proceeds by way of the termination reactions, R_7 to R_{11} . It was also found that T_i is coincident with the maximum in the carbon monoxide mole fraction profile where all the methane fuel disappeared. This indicates that, the net radical production only occurs after nearly all the fuels have disappeared (Dixon-Lewis [65]), and the reactions of the hydrocarbon fuel and its initial breakdown products ($\text{CH}_3, \text{CH}_2\text{O}, \text{HO}_2, \text{CH}_3\text{O}, \text{CHO}$, etc.) are supported as a result of radicals species which have diffused from the reaction zone toward the unburnt gases, where about more than 90% by weight of initial attack on the hydrocarbon takes place in a preheat zone.

Figure 2.26 (d) shows the variation of the computed ignition temperatures, T_i , (full curves) with equivalence ratios at 0.1 and 1 atm. The figure shows that, for a given equivalence ratio, the ignition temperature increases as the pressure increases. Also the T_i increases with ϕ until maximum (which correspond to maximum U_i) and then decreases in rich flame. To explain this, the pool radical rate, R is integrated with the distance from x_1 corresponding to $T = T_u + 10$ to x_2 corresponding to $T = T_i$. These

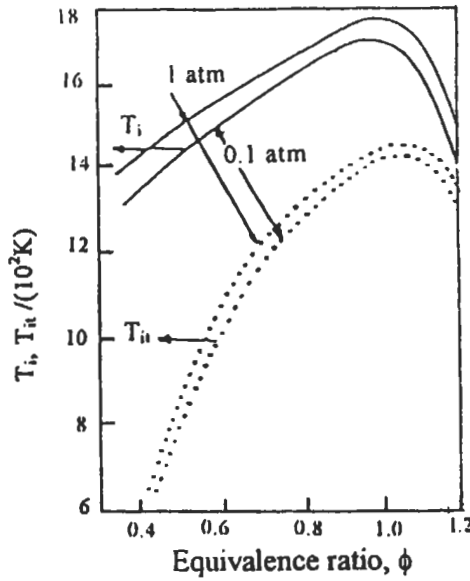


Fig. 2.26 (d): Comparison between the computed ignition temperatures from the kinetic model (full curves) and those computed from thermal theory (dotted curves) for methane-air flames at different equivalence ratios, pressure of 0.1 and 1 atm, and $T_u = 300 K$ [155].

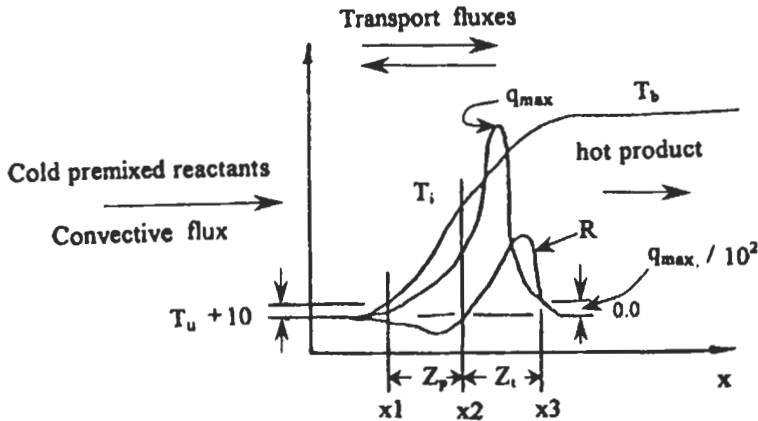


Fig. 2.26 (e): Schematic diagram of flame structure predicted from chemical kinetic model. The graphical definition of the preheating, reaction flame thickness, Z_p , Z_n , and ignition temperature, T_i as a function of heat release rate, q , molar rate of radical pool, R and gas temperature profiles, T , all versus distance, x [155].

distances are defined in Fig. 2.26 (e). The pool flux was calculated by the space integral rate $\int_{x_1}^{x_2} R dx$ and the result shows that the ignition temperature increases as the pool flux increases and vice-versa. The peak of these fluxes always occurs at maximum U_f . The ignition temperatures calculated by Dixon-Lewis [65] using the same way

described above for hydrogen-air flames were 900 to 950 K at different ϕ , T_u of 300 K and 1 atm. The calculated value of the pool flux $\int_{x_1}^{x_2} R dx$ corresponding to these hydrogen-air flames at 1 atm, $\phi = 1$ and T_u of 300 K is found to be 4×10^{-4} kmole $m^{-2} s^{-1}$. This value is lower by three times than that calculated for methane. This means that in flames with less diffusion fluxes the ignition temperature will be small. To explain this more, the ignition temperature, T_{it} , is calculated for flame without diffusion flux as follows.

In thermal flame propagation, the heat flow to the preheating zone is assumed to be only by conduction and the reactions by radical pool which diffuse from the reaction zone are neglected. The simplest representation of the temperature profile in this thermal theory is shown in Fig. 2.26 (f) where the temperature profile is concave upwards. In the figure the preheating zone extends from $x = -\infty$ ($T = T_u$) to $x = 0$ ($T = T_{it}$). This zone is described by a thermal theory as follows:

$$d/dx(kdT/dx) - U_u \rho_u C_p dT/dx = 0 \quad (2.30)$$

where ρ_u and U_u are the unburnt density and velocity of the mixture, respectively.

By introducing mean values for the specific heat \bar{C}_p and the thermal conductivity \bar{k} ,

Eq. 2.30 is solved with the boundary conditions:

$T = T_{it}$ at $x = 0$ and $dT/dx = 0$ at $x = -\infty$ to give:

$$T = T_u + (T_{it} - T_u) \exp(U_u \rho_u \bar{C}_p x / \bar{k}) \quad (2.31)$$

By assuming $T = T_u + 10$ and replacing U_u by U_1 and x by Z_p , then Eq. 2.31 becomes:

$$T_{it} = T_u + \left[\frac{10 \bar{k}}{U_1 \rho_u \bar{C}_p Z_p} \right] \quad (2.32)$$

To calculate T_{it} from Eq. 2.32, the values of \bar{C}_p and \bar{k} are taken as an average of 20 values between T_u and T_{it} . Also Z_p is taken as the distance between x_1 at $T_u + 10$ and x_2 at $T = T_i$ (this distance is considered here as the preheating zone thickness and is shown in Fig. 2.26 (e)), while U_1 is the computed burning velocity. Then the calculated values of T_{it} from Eq. 2.32 are plotted for methane-air flame by dotted curves in Fig. 2.26 (d). The figure shows that there are significant differences between the computed values of T_i from kinetic model and those of T_{it} computed from the thermal theory (dotted curves). The difference between the two values decreases as the equivalence ratio increases. At very rich flame, the two values are close to each other and this is consistent with the lower values of radical pool fluxes of $\int_{x_1}^{x_2} R dx$. This again indicates that the values of T_{it} calculated from thermal theory might be correct when the diffusion molar flux of active species is very small. However, Eq. 2.32 is very sensitive to the average value of specific heat and thermal conductivity [155].

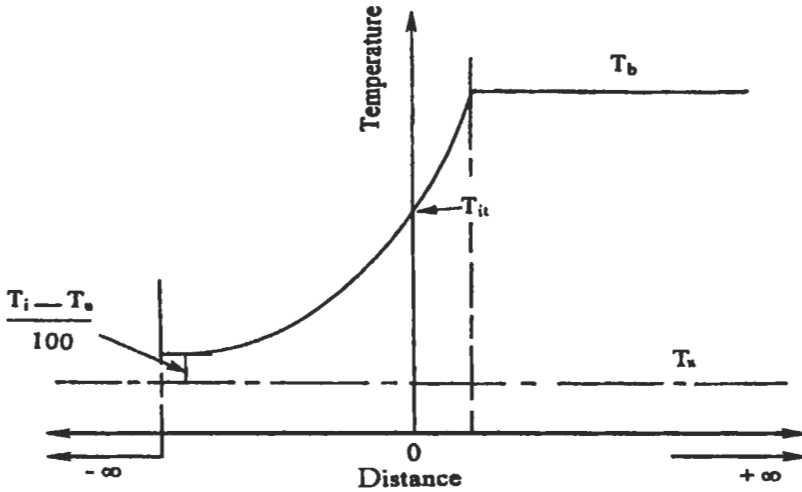


Fig. 2.26 (f): Temperature profile through a thermal propagation of premixed flame [155].

2.4.4 Methanol-Air Flames

Experimental Method and Results

Flame structures and burning velocities were measured (Bradley et al [44]) for low pressure methanol-air laminar, flat, adiabatic flames on a matrix-burner of 0.076 m diameter as shown in Fig. 2.20. Details of the burner were demonstrated in section 2.4.3.

a- Fuel and air flow control. It is not easy to achieve a steady flow of pre-mixture, of constant equivalence ratio, when the fuel is initially liquid. A steady liquid flow must be maintained, followed by evaporation and uniform mixing with air. The system, which is employed and shown only with its essentials in Fig. 2.27, is designed by Habik [257] and Bradley et al [44]. Air flowed at a constant rate from cylinder (1) at an upstream pressure that is maintained constant by a Hela Hamilton regulator (2), through a critical flow orifice (3) into a relatively large air chamber (4) connected to a mercury reservoir (5), all effectively at constant volume. As a result, the pressure increased linearly with time. This caused the mercury to move upwards at a constant rate in the liquid fuel feed tube (6). This was of 0.02 m bore glass, and 2.5 m long. The fuel was introduced into this tube, above the mercury, from the fuel tank (7), and the fuel flowed at a constant rate into the combined evaporator and mixing chamber (8), and maintained at a constant pressure. The flow rate was calibrated against upstream pressure and temperature at the critical flow orifice for three different ruby orifices of 0.08, 0.12, and 0.15 mm diameter. At the top of the feed tube, the methanol was forced through

a stainless-steel hypodermic needle nozzle of 120 μm diameter that was terminated slightly beyond the end of the feed tube. Compressed air entered the annular ring around the end and the flow of this over the liquid at the nozzle tip created a fine spray.

To ensure complete evaporation, the mixing chamber was legged and heated by regulated power heating tapes. The temperature in the chamber was measured by a chromel-alumel thermocouple. Airflow from a compressor was controlled by a fin-needle valve and measured by a mercury manometer and rotameter. The metered air splits into two lines, both controlled by coarse and fine valves. One line fed directly into the annulus of the nozzle holder in the mixing chamber. The other fed directly into the top of the chamber to mix with the remaining mixture. About 15% of this flow was diverted through an elutriator (9). Fine control of the flow leaving the elutriator was provided by a needle valve. The purpose of the elutriator was to seed the gases for the Laser Doppler measurements.

The mixture of vaporized liquid fuel and air left the mixing chamber and was blended with the seeded air from the elutriator before being fed into the burner via a fine control valve (10), which, by throttling the flow rate, improved burner control. This enabled a steady flow rate to be obtained. All airlines were heated by regulated electrical resistance tapes to avoid condensation. Temperatures of the mixture were measured at the mixing chamber, burner tube inlet, the center of the top of the matrix, and above the drilled asbestos plate.

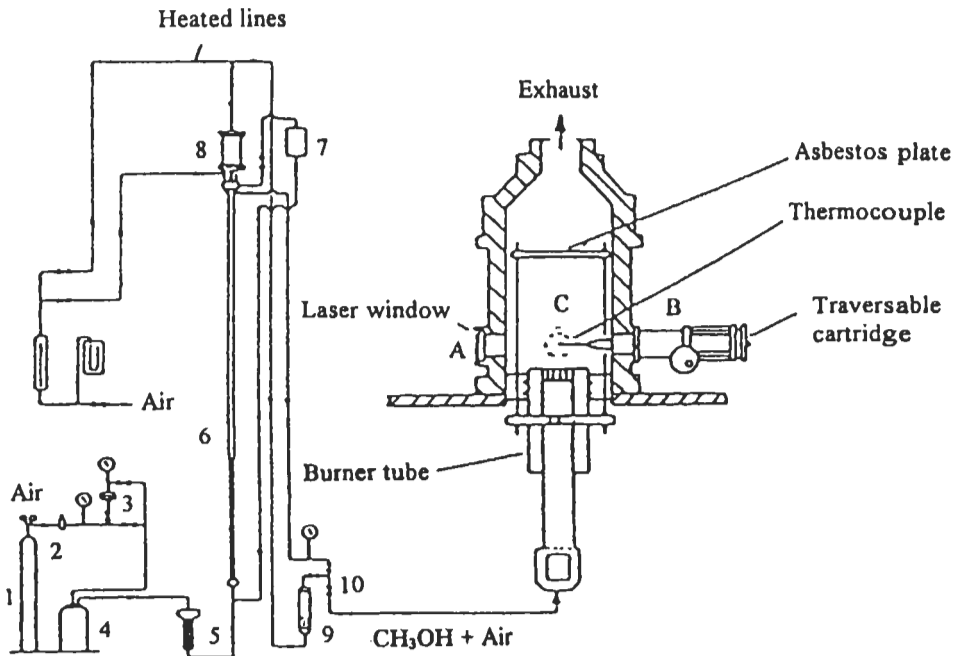


Fig. 2.27: Liquid fuel-air system [44, 257]. Reproduced by permission of Elsevier Science.

b- Gas sampling and analysis. Gas samples were withdrawn through a quartz micro probe as described in section 2.4.3. To avoid condensation of the sample, the lines and vessels were lagged and heated by regulated power heating tapes. The volume of the sample and its rate of injection into the chromatograph are critical for repeatability of the analysis. A 2 ml Hamilton gas tight syringe injected 0.5 ml of sample from the sample vessel into the column through the septum. The syringe was cleaned regularly during use to remove traces of other materials. The flow rate in the system had to be carefully watched and septum renewed when a leak occurred.

Samples from methanol-air flat flames at 0.089 atm were collected, and analyzed for concentrations of CO₂, CO, O₂, H₂ and CH₃OH (Bradley et al [44]). The Pye Unicam 304 gas chromatograph employed a thermal conductivity detector. Two columns in the same oven, one of Porapak R separated CH₃OH and CO₂ and the other of Molecular Sieve 5A separated CO₂, CO, O₂, and H₂. They were connected in parallel to form one outlet to the single detector.

The working temperature for good resolution with both columns was 413 K, with a carrier gas flow rate of 25 ml min⁻¹. The analysis for CO, O₂, and H₂ involved injecting the sample through the Molecular Sieve 5A and using the Porapak R as a reference column. Similarly, the analysis of CO₂ and CH₃OH involved injecting into the Porapak R column with the Molecular Sieve 5A as a reference. The chromatograph was calibrated with known mixtures.

c- Experimental results. Measured mole fraction of the stable species at 0.089 atm and equivalence ratios, ϕ of 1.25 and 0.85 are shown as points in Figs. 2.28 (a) to (b), respectively, for an initial temperature of 323 K (Bradley et al [44]). Measured gas temperatures and velocities are also shown as points in Fig. 2.28 (c) for only ϕ of 1.25. These measurements were used to derive the net reaction rate as described below (Abu-Elenin et al [154]).

The volumetric rate of chemical reaction of each species, R_i , was calculated from the species conservation equation with the assumptions that the flame is in steady state one-dimensional, pressure is uniform, the flame is adiabatic, and thermal diffusion is negligible, and becomes:

$$R_i = \frac{\rho U}{m_i} \frac{dM_i}{dx} \quad (2.33)$$

where, R_i is the net molar rate of species i in kmole m⁻³ s⁻¹, M_i is mass flux fraction of each species which inclusive of diffusion and convective velocity. This is calculated throughout the flame as follows [258]:

$$M_i = \left[\frac{m_i X_i}{\sum m_i X_i} \right] \left[\frac{U + U_i}{U} \right] \quad (2.34)$$

where, U is the mean flow velocity, U_i is the diffusion velocity of species i , and X_i is the species mole fraction. The diffusion velocity of each species i , was calculated by Fick's law with a binary diffusion coefficient, D_{ij} , for the various species in nitrogen. Such coefficients were calculated using the Lennard Jones potential in Ref. 259, and U_i is expressed as:

$$U_i = -\frac{D_{ij} dX_i}{X_i dx} \quad (2.35)$$

The mole fraction of each species X_i over a distance, x , is interpolated into 30 zones with the fixed stepwidth, dx , of 0.25 mm. At each zone, the points are fitted with a linear straight line fit and then differentiated with respect to x . Also the value of C_p was calculated for the different species using data from the JANAF Table [13] and Ref. 260. The neglect in this calculation, of highly diffusive species such as free H, O and OH atoms may result in inaccuracies, but the kinetic mechanism takes into account the diffusion of these species. The differential of the mass flux fraction, $dM_i(x)/dx$, for each species is expressed at each position x by the same way of calculating the mole fraction over the distance x .

Hence, the measured net reaction rate of each species, R_i over the stepwidth, dx , of 0.25 mm, is the multiplication of the differential dM_i/dx and the basic parameters, ρ and U . Figures 2.30 (a) to (c) show the experimental net reaction rate as points for the above species at $\phi = 1.25$. Similar results are found for $\phi = 0.85$ and 1.0.

The unburnt gas velocity was measured by Laser Anemometry at the position of lowest temperature, as indicated by the thermocouple (Bradley et al [44]). However, it must be born in mind [44] and as indicated before, that the burning velocities might more properly be referred to the luminous zone of the flame, and this was used as a correction factor to obtain the burning velocities by using the area ratio of unburnt gas and luminous zone, caused by flow divergence (using flame photography). This leads to 5 % to 15 % reduction in the measured unburnt gas velocity. These measured burning velocities at different equivalence ratios and pressures of 0.089, 0.13, 0.18, 0.2 and 0.25 atm are shown as experimental points in Figs. 2.33 (a) to 2.33 (c). All these measurements will be discussed in the context of reaction mechanism and rate parameters. In all figures, the full, dotted, and dashed curves are the computed results from the kinetic model, which will be discussed now.

Computational Results

The kinetic schemes used in the predicted results for methanol-air flames are discussed in section 2.3.4. The kinetic schemes A_1 , B_1 , and C_1 involved all the reactions and rate coefficients in Tables 2.6, 2.8 and 2.9, respectively, in addition to Tables 2.1 and 2.2. In this section, the predicted results from schemes A_1 , B_1 , and C_1 are shown in all figures by chain dotted, dotted and full curves, respectively. The results have been obtained using 33 grid points for each flame, and 1500 integration steps to reach the steady state. The predicted results from schemes A_1 and B_1 were performed by Bradley et al [44] and those computed from scheme, C_1 were performed by Abu-Elenin et al [154].

The flame structure, net reaction rate, heat release rate and burning velocity will be discussed as follows:

(i) **Flame structure at pressure of 0.089 atm.** Dealing first with scheme A_1 , the rate parameters given in Table 2.6 were chosen after extensive series of computations with this mechanism. In order to match the predicted and experimental burning velocities in rich flames, the pre-exponential factors A_{27} and A_{29} finally adopted were 10 and 5 times higher, respectively, than those of Dove and Warnatz [162]. At 1500 K the rate coefficients themselves were 1.4 and 0.5 times those of Tsuboi and Hashimoto

[261] and Norton and Dryer [262], respectively. These changes in k_{27} and k_{29} had no significant effect on the computed concentrations of stable species. The sensitivities of the burning velocities to these reactions at different equivalence ratios are given by El-Sherif [152].

Olsson et al [263] have found that the measured CH_2OH profile is not correctly predicted by use of the value of k_{28} proposed by Dove and Warnatz [162]. The value of k_{28} suggested by Olsson [263] was used in scheme A_1 , B_1 and C_1 . The resulting burning velocities were all about 3 % lower than those computed with the value of k_{28} used by Dove and Warnatz [162]. At 1500 K the values assigned to k_{24} and k_{26} (Table 2.6) are 23 % and 18 % higher, respectively, than those of Vandooren and Van Tiggelen [195] and Akrich et al [264], but the assigned values of k_{24} are 10 % lower than those of Ref. 198. At no change in composition, the burning velocity was sensitive by more than 3 % to changes in these rate coefficients by up to a factor of two. In Fig. 2.28 (a) to (c), schemes A_1 , B_1 , and C_1 give nearly identical, reasonably good predictions of the measured profiles of methanol and oxygen concentrations, gas temperature, and velocity.

The concentration of H_2 is also well and nearly predicted, but less so are the concentrations of CO and CO_2 when scheme A_1 is used. Scheme A_1 appears to underpredict the conversion of CO to CO_2 in the reaction zone (chain dotted curves). This suggests that the experimental profiles for stable species are effectively independent of the rate constants in Table 2.6. Attempts were made, without success, to correct the underprediction of CO by adjustment of the rate coefficient k_{14} , and by introducing H_2O_2 reactions in Table 2.7. The only reasonable successful attempt involved an increase of k_{37} by two orders of magnitude. Such an increase is not supported by other work on explosion limits [265]. Similar mismatches, with early higher value of CO_2 concentration and lower value of CO concentration, have been observed in other studies of the methanol-air-premixed flame (Andersson et al [192] and Pauwels et al [266]). Such difficulties have not, however, been encountered in studies of lean methane-air flames, where the kinetic scheme of Table 2.2 gives good agreement with the flame profiles including the measured CO and CO_2 profiles (Dixon-Lewis [15], Dixon-Lewis and Islam [143], El-Sherif [152, 153]). The combination of circumstances implies either that there is an experimental problem associated specifically with the methanol-air flame (which is unlikely), or that the reaction mechanism needs a revision.

Scheme B_1 (dotted curves [44]) and its associated coefficients bring the experimental and computed CO and CO_2 profiles in Figs. 2.28 (a) to (b) into better agreement, and as well as the experimental and computed burning velocities. This scheme, however, must be tentative, since it rests on very approximate estimates of the rate coefficients involving CH_2O . Nevertheless, these do appear to be a *prima facie* case for reviewing the part played by CH_2O reactions in methanol oxidation.

Although the overall rate coefficients k_{24} to k_{26} (Table 2.6) appear to be known with reasonable accuracy, the breakdown of such overall rate coefficients to give CH_2OH and CH_3O (reaction pairs 24 (a) and (b) to 26 (a) and (b) in Table 2.8) is less well characterized (Hess and Tully [198] and Vandooren et al [267] and Tsang [201]). For the purpose of exploration and to be very tentatively, the same activation energies have been assumed for the (a) and (b) reaction paths. The sum of the (a) and (b) rate coefficients were equated to the overall rate coefficients for attack on CH_2OH by H , O , and OH as given in Table 2.6. Computations were performed when the ratios

$Z = k_b/(k_a+k_b)$ were assumed to be independent of temperature, and to be the same for all three reaction pairs. The results in Fig. 2.28 (a) show CO and CO₂ profiles calculated for $Z = 0$ (chain-dotted line, scheme A₁), 0.4 (dotted line, scheme B₁), and 0.7 (dotted line, modified of scheme B₁). At temperatures above 1000 K, Hess and Tully [198] estimated the value of Z to be about 0.5 for reactions 24 (a) and (b). They concluded that the H₂O + CH₃O product channel will be important at elevated temperatures. The computed burning velocity is also sensitive to the reaction breakdown between the (a) and (b) routes in Table 2.8, the latter of which leads to CH₃O formation. The sensitivity analysis of k_{27} and k_{29} on the burning velocity of CH₃OH-air flames at 1 atm and 300 K is shown in Fig. 2.29.

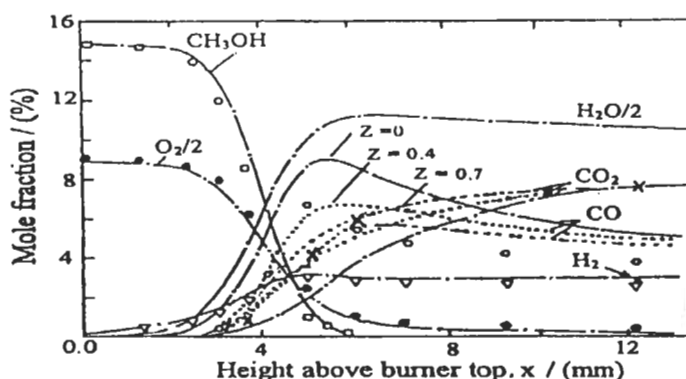


Fig. 2.28(a): Experimental (\bullet , O₂; ∇ , H₂; \square , CH₃OH; \circ , CO, and \times , CO₂) and computed stable species concentrations for CH₃OH-air flame at $P = 0.089$ atm, $T_u = 323$ K and $\phi = 1.25$. Chain dotted curve for scheme A₁, dotted curves for scheme B₁ ($Z = 0.4$ and 0.7) [44]. Reproduced by permission of Elsevier Science.

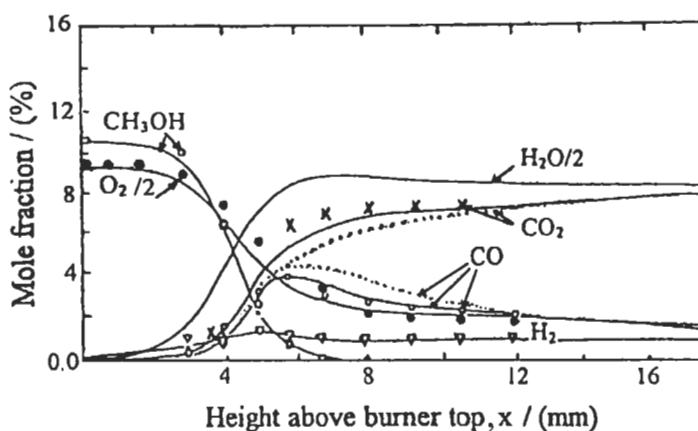


Fig. 2.28(b): Experimental (\bullet , O₂; ∇ , H₂; \square , CH₃OH; \circ , CO, and \times , CO₂) and computed stable species concentrations for CH₃OH-air flame at $P = 0.089$ atm, $T_u = 323$ K and $\phi = 0.85$. Full curve for scheme C₁ [154], dotted curves from [44]. Reproduced by permission of Elsevier Science.

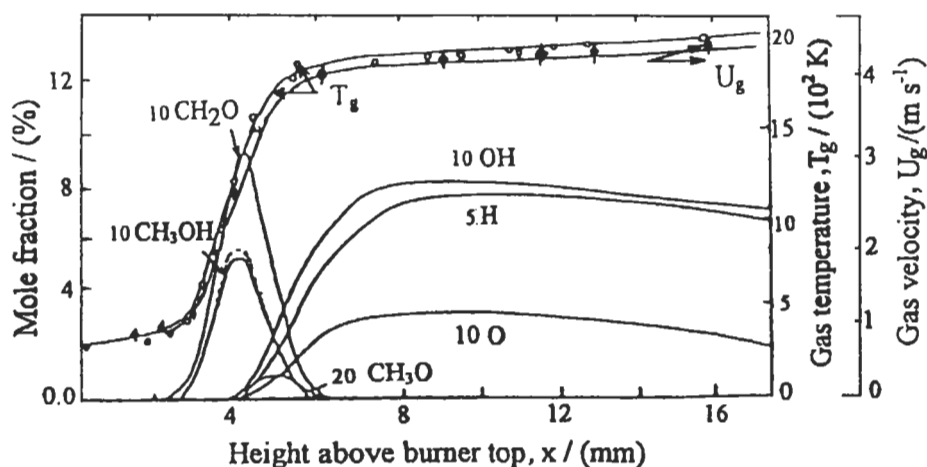


Fig. 2.28(c): Experimental, (O, ϕ) and computed gas velocity, temperature and radical concentrations for CH_3OH -air flame at $P = 0.089$ atm, $T_u = 323$ K and $\phi = 1.25$. Full curves for scheme C_1 [154] and dotted curves from [44]. Reproduced by permission of Elsevier Science.

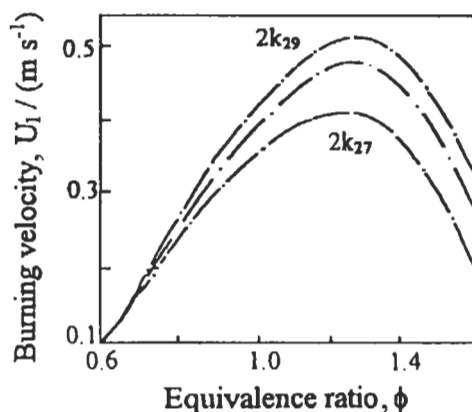


Fig. 2.29: Sensitivity analysis of k_{27} and k_{29} (in Table 2.6) for CH_3OH -air flames at 1 atm and 300 K (using scheme A_1) [44]. Reproduced by permission of Elsevier Science.

An increase in Z above the value of 0.7 eventually resulted in appreciable underprediction of CO. Reaction, R_{38} (Tables 2.8 and 2.9) is important in schemes B_1 and C_1 and has been studied in Ref. 199, but only over the restricted temperature range of 396–426 K. Clearly, more evidence about reaction R_{38} and other reactions of CH_3O is required, particularly in the high-temperature range. Attack on CH_3OH by O, H, and OH is unlikely to be of much significance because of the low concentration of these radicals. The value of the rate coefficient for attack of CH_3O by O_2 was about one twentieth of k_{38} (Norton and Dryer [262]). The appreciable uncertainties of the rate coefficients for hydroxy-methyl [k_{24} (a) to k_{26} (a)] and methoxy production (k_{24} (b) to k_{26} (b)) as well as that for the reaction of methoxy and CO (k_{30}), lead the present author

once again (Habik in Ref.154) to further investigate these rate coefficients by using scheme C₁ (Abu Elenin et al [154] and Tsang [201]).

The rate coefficients given in Table 2.9 were chosen after an extensive series of computations with the mechanism. The ratio of $k_{26}(a)/k_{26}(b)$ and A_{30} initially, were taken from Vandooren et al [267] and Lissi et al [199], respectively and subsequently optimized (within the uncertainty factor) to obtain good agreement between the computed and experimental results. It is also assumed that $k_{25}(a)/k_{25}(b) = k_{26}(a)/k_{26}(b)$. It was found that the ratio of $k_{25}(a)/k_{25}(b)$, which is finally adopted, was 3. Tsang [201] recommended that $k_{25}(a) > k_{25}(b)$, but no value was given. Value of $k_{26}(a)/k_{26}(b) = 4$ with uncertainty factor of three was also recommended by Tsang [201]. In addition to that, the pre-exponential factor A_{30} in Table 2.9, which is finally adopted was two times higher than that of (Lissi et al [199]).

Again, the overall rate coefficient $k_{24}(a+b)$ in Tables 2.8 and 2.9 appears to be known with uncertainty factor of 10 % [44, 198, 201], and also the ratio of $k_{24}(a)/k_{24}(b)$ in Table 2.9 is 0.538 at 1500 K. It agrees well with that suggested by Bradley et al [44], and Hess and Tully [198].

The predicted results from schemes B₁ and C₁ show that reactions R₂₄ and R₂₆ and their channels a and b are dominant methanol consuming path and CH₃O production, respectively, in lean and near stoichiometric flames. While in rich flames, reaction, R₂₆ and its channel b only become important in methanol consuming and CH₃O production.

For $\phi = 0.85$, the computed results from scheme C₁ of Tables 2.1, 2.2, and 2.9 and their associated rate coefficients bring the experimental and predicted CO and CO₂ profiles in Figs. 2.28 (b) (full curves) into better agreement than that predicted by Ref. 44 (dotted curves), as well as the experimental and computed burning velocities. The measured profiles of methanol, oxygen, hydrogen concentrations, gas velocity, and temperature are also well and are close to the predicted values. Similar agreement is also found for flames at $\phi = 1$ and 1.25.

The predicted concentration profiles of O, H, OH, CH₂O, HO₂, CH₂OH, and CH₃O from scheme C₁ and CH₃O from scheme B₁ for $\phi = 1.25$ are shown in Fig. 2.28 (c). Also shown in the same figure, the measured and computed gas temperatures and velocities.

The predicted peak concentration of CH₂OH is in the same order as that found experimentally by Vandooren et al [267] and that computed by Olsson et al [191]. Of the three active radicals, OH has the highest concentration in the lean flame and H has the highest value in the rich flame. Similar results are found for $\phi = 0.85$ and 1.0.

(ii) **Net reaction rate and heat release rate at 0.089 and 1.0 atm.** Although the agreement between experimental and modeled mole fraction profile is acceptable, a new comparison between experimental and modeled net reactions, presents a new interesting step in flame structure analysis. Therefore, Figs. 2.30 (a) to (c) show the experimental net reaction rate as points for the above measured species at $\phi = 1.25$, 0.089 atm and $T_u = 323$ K. The figures show that the agreement in general between the experimental and computed net reaction rate is good for stable species except the computed peak of CO, H, and CH₂OH are slightly higher than the experimental, and this may be due to the highly diffusive species in the model. Similar results were found for $\phi = 0.85$ and 1.0.

Figure 2.30 (a) shows that O₂ chemistry is principally controlled by reactions, R₂, R₁₇, and R₂₈. Figure 2.30 (b) shows that reactions R₁₆ to R₁₈ are the dominant channel for CO formation in the flame zone, and reactions R₁₄ and R₃₀ control its removal; in the

flame zone the production of H_2O is namely controlled by reactions R_1 , R_{22} , R_{24} (a), R_{24} (b), R_{26} (a), R_{26} (b) which are responsible for the major part of the methanol consumption (95 %). However, the relative importance of these reactions changes with equivalence ratio; whereas OH and H attack was the primary way under lean conditions, removal by H dominates under rich conditions. Figure 2.30 (d) shows only the computed net reaction rates for O, H, OH, CH_2O , and CH_2OH for the same flame conditions. Also, the figure shows that the computed peak for H, OH and O decays

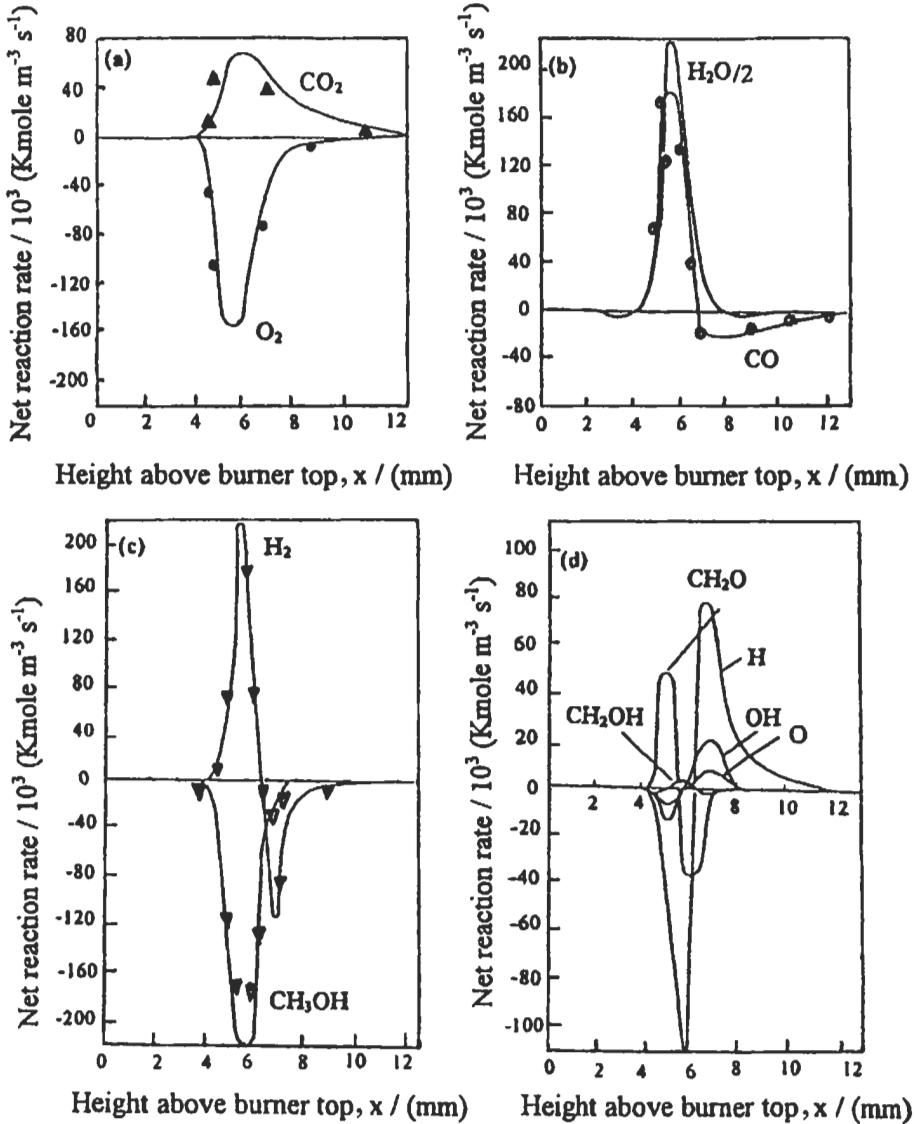


Fig. 2.30: Experimental (points [44]) and computed (full curves [154]) net reaction rates for CH_3OH -air flame at $P = 0.089$ atm, $T_u = 323$ K and $\phi = 1.25$. (a) (\blacktriangle , CO_2 ; \bullet , O_2); (b) (\circ , CO; $H_2O/2$, computed), (c) (\blacktriangledown , H_2 ; ∇ , CH_3OH), (d) computed H, OH, O, CH_2O , CH_2OH [154].

very fast at a distance of about 7 mm above burner top where most of the heat is released. Furthermore, in the post flame zone, reactions R₃ and R₁₄ are important pathways of H production and its removal is by reactions R₁ and R₂. This is true up to the maximum net reaction rate for H, where reaction R₁ occurs in the reverse direction. Also, OH is controlled essentially by the same reaction scheme for H, and reaction R₅ contributes by 93 % of OH production. The rate of chain-branching reaction, R₂ is significantly higher in the early part of the flame, and up to 7 mm above the burner top the formation of O is only balanced by the occurrence of reaction R₁₄ and the importance of this increases until 11 mm distance above the burner top, then the rate of reactions, R₂ and R₁₄ together is greater than the total destruction of O which occurs by reactions R₉, R₁₂, R₁₄, and R₂₃.

Multiplication of the experimental or computed net reaction rate of each species by the actual molar enthalpy yields the heat release rate of each species. The cumulative heat release rate of each species gives the total heat release rate. At 0.089 atm and T_u = 323 K, the heat release rate profiles computed from scheme C₁ and that derived from experimental temperature and concentration profiles (El-Sherif [152]) are compared well. The computed heat release rate profiles at 1 atm, T_u = 300 K and $\phi = 0.8, 1.0$ and 1.2 are shown in Fig. 2.31. Profiles for schemes, A₁, B₁ and C₁ are shown in the figure as a function of the reactendness ($\theta = (T - T_u)/(T_b - T_u)$).

The maximum heat release rate with scheme C₁ for $\phi = 0.8, 1.0,$ and 1.2 occurs at temperatures of 1667, 1676 and 1692 K, respectively. The corresponding adiabatic temperatures are 2010, 2222 and 2048 K. The maximum heat release rate that is predicted by Westbrook and Dryer [161] for a stoichiometric methanol-air flame at 1 atm and T_u = 300 K was found to be 3.6 times higher than that from scheme C₁ (Kwa [268]). A probable explanation is that the transport coefficients of Westbrook and Dryer [161] were about three times higher than those calculated from fundamental diffusion coefficients (Andersson et al [192] and Coffee [269]). Also the peak heat release rates at 1 atm are higher by a factor of about 100 than that at 0.089 atm and T_u = 323 K.

(iii) **Laminar burning velocity.** The effect of equivalence ratio, pressure and temperature on the burning velocity are being discussed as follows:

(a) **Variation of burning velocity with initial pressure.** Figure 2.32 shows the computed burning velocities at pressures of 0.089, 0.2, and 0.25 atm. Although the modeled values of burning velocity and their variations with equivalence ratio shown in Fig. 2.32 are in general agreement with experiments, there is a clear tendency for the measured burning velocities at 0.089 atm to be higher than the predictions.

To explore this further, burning velocities measured in the pressure range 0.1-10 atm are shown in Figs. 2.33 (a) to (c) for three equivalence ratios. The initial temperature is 300 K and the values measured by Bradley et al [44] at 323 K were reduced to 300 K with the experimental temperature dependence law that is found by Kwa [268] for the same burner in Fig. 2.20. Also shown are the computed values of Westbrook and Dryer [161] (dashed curves), Dove and Warnatz [162] (dash dotted curves) and those of the scheme B₁ (dotted curves) and C₁ (full curves). Scheme C₁ again gives very good agreement with experiments particularly for $\phi = 0.8$ and 1.0. However, no model gives burning velocity pressure dependence at low pressure quite as strong as that observed experimentally by Bradley et al [44]. One explanation is unaccounted for pressure effects in the kinetic schemes. Another lies in flow divergence effects as gas flows into the flame and the use of different reference planes to define U₁. These can be different

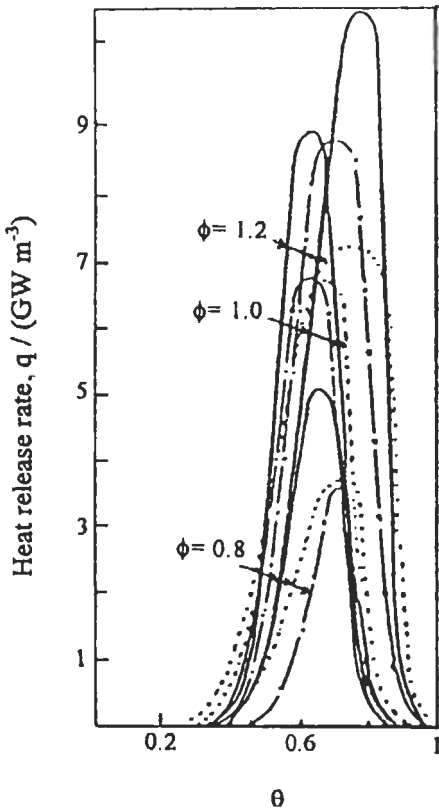


Fig. 2.31: Variation of computed heat release rate for CH₃OH-air flames with reactedness at 1 atm and 300 K for equivalence ratios of 0.8, 1.0 and 1.2. Full curve for scheme C₁, dotted curve for scheme B₁ (Z= 0.4) and chain dotted curves for scheme A₁ [154].

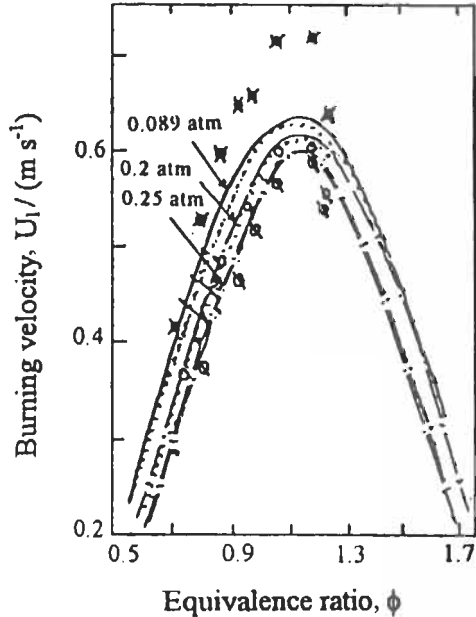


Fig. 2.32: Comparison between computed (full and dotted curves) and experimental values (ringed points \times , O, and \circ at P = 0.089, 0.2 and 0.25 atm, respectively) of laminar burning velocities for CH₃OH -air flames at different equivalence ratios and at T_u = 323 K, chain dotted curves for scheme A₁, dotted curves for scheme B₁ (Z = 0.4) and full curves for scheme C₁ [154].

for various methods of measuring the burning velocity and also the pressure dependence.

The computed variation of burning velocity with pressure from both schemes indicates that no single pressure law can fit neither the predicted nor the experimental values over the range from 0.1 to 10 atm. This agrees with the findings of Westbrook and Dryer [161] and Dove and Warnatz [162]. It was found that four different pressure laws were necessary to give reasonable correlation of the predicted values over the pressure range from 0.1 to 10 atm [44]. The influence of pressure on HO₂ formation can be paramount. With an increase in pressure, reaction R₄ competes directly with the chain branching reaction, R₂ and decreases the burning velocity. Values of pressure power law exponent, n, for burning velocity (using scheme B₁) were given in Ref. 44. They express U₁ in terms of pressure, by U₁ = U₁₀ Pⁿ, where U₁₀ is the burning velocity at atmospheric pressure and 300 K. To account for the density variation with the

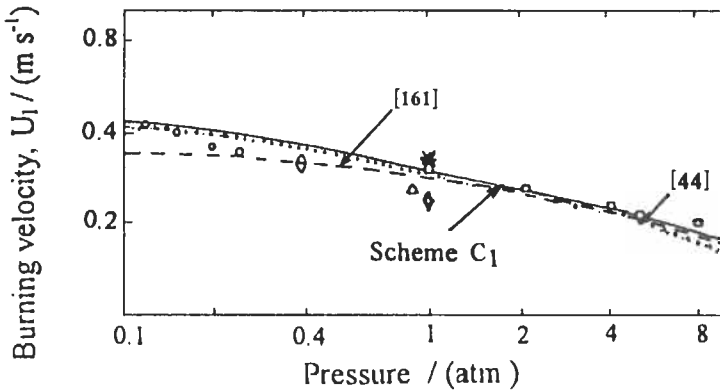


Fig. 2.33(a): Variation of experimental and computed burning velocity for CH₃OH-air flames with different pressures at $\phi = 0.8$ and $T_u = 300$ K. O, [44]; \square , [188], [273]; *, [270]; \diamond , [271]. Full curve for scheme C₁ [154], dotted curve from [44], and dashed curve from [161].

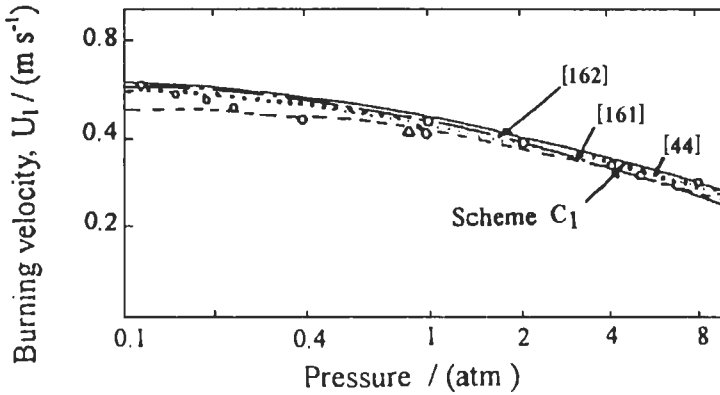


Fig. 2.33(b): Variation of experimental and computed burning velocity for CH₃OH-air flames with different pressures at $\phi = 1$ and $T_u = 300$ K. Symbols and curves are the same as in Fig. 2.33 (a).

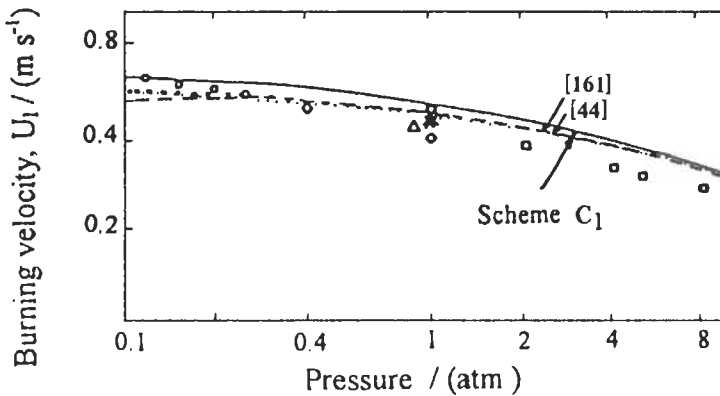


Fig. 2.33(c): Variation of experimental and computed burning velocity for CH₃OH-air flame with different pressures at $\phi = 1.25$ and $T_u = 300$ K. Symbols and curves are the same as in Fig.2.33 (a).

pressure and burning velocity (using scheme C_1), the mass burning rate m_b is calculated by $\rho_u U_b$, where ρ_u is the density of unburnt mixture.

Measured and computed burning velocities at 1 atm and 300 K over a range of equivalence ratios are shown in Fig. 2.34. Another full line curve gives the adiabatic temperatures of the combustion products, T_b . These were calculated using an equilibrium temperature program based on 18 species [43]. The accuracy of different burning velocity measurement techniques has been discussed by Andrews and Bradley [225], Law [228] and here, as elsewhere, there is a significant spread in experimental values. Scheme B_1 tends to give low values on the lean and rich side, but the agreement with the experiments improves with scheme C_1 . The maximum computed burning velocity with scheme C_1 is 0.515, close to the values measured by Gülder [188] and Gibbs and Calcote [270].

b- Variations of burning velocity with initial temperature. Shown in Fig. 2.35 are some measured values of burning velocity at 1 atm but at different initial temperatures. Also shown the computed values from schemes B_1 and C_1 . Again, scheme C_1 gave better agreement with experiments than does scheme B_1 . It was noted that reaction R_{10} becomes less important with increase in temperature. The temperature exponents of Metghalchi and Keck [271], unlike those of Gülder [188], show equivalence ratio dependence. Furthermore, the computed burning velocities by Seshodri [272] for methanol flames are also in reasonable agreement with the corresponding results from scheme C_1 .

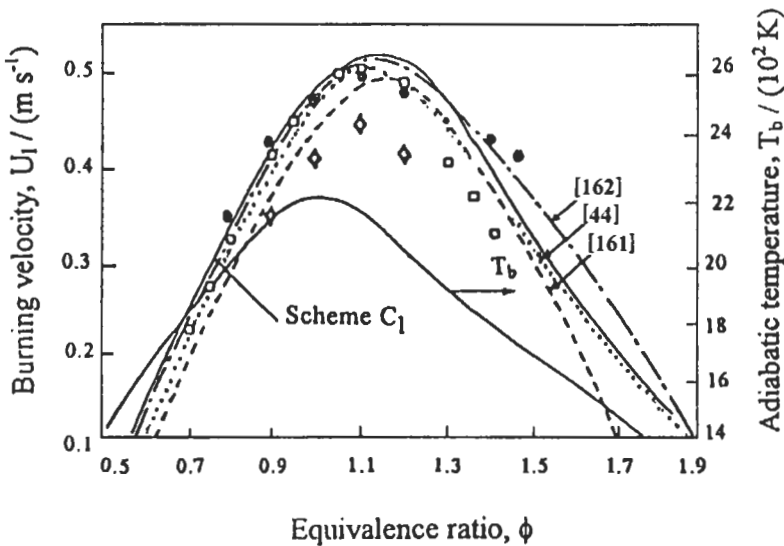


Fig. 2.34: Experimental and computed burning velocity for CH_3OH -air flames at $P = 1$ atm, and $T_u = 300$ K. ●, [270]; □, [188]; ◇, [271]. Full curves for scheme C_1 [154] and dotted curves from Ref. 44.

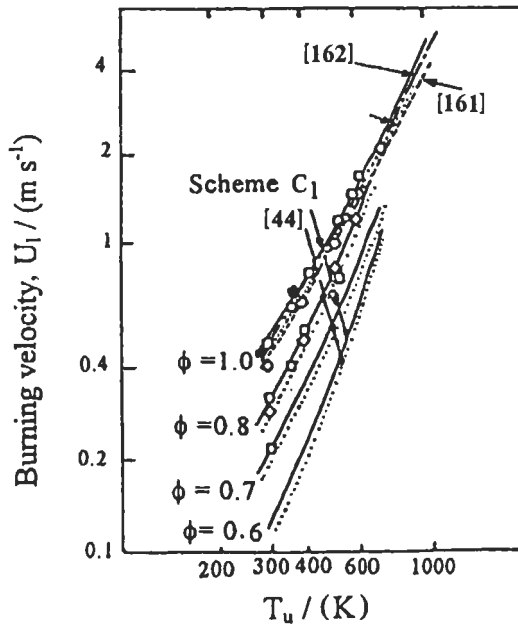


Fig. 2.35: Variation of experimental and computed burning velocity for CH₃OH-air flames at 1 atm, for different equivalence ratios and initial temperatures ●, [270]; □, [188] ($\phi = 0.7, 0.8, 1.0$); ◇, [271] ($\phi = 0.7, 0.8, 1.0$); Full curves for scheme C₁ [154] and dotted curves from Ref. 44.

2.4.5 Methanol-Water-Air Flames

Methanol may be contaminated by water during production and storage; thus if methanol is to be considered as a commercial fuel, effects of contained water on its burning characteristics must be elucidated as well.

Burning velocity, explosion pressure, ignition temperature, and flame structure of methanol-water-air gaseous mixture in burner and constant volume vessel are investigated theoretically in this section. The predicted results from the comprehensive kinetic model for methanol-air mixtures (see section 2.4.4) are compared with the following experimental results (Habik [274]).

Experimental Method and Results

There are three sets of experimental results that were used for comparison with the predicted results from kinetic model. These results are as follows:

a- Burning velocities for laminar methanol-water-air gaseous mixture at atmospheric pressure as a function of equivalence ratio, water content and at initial temperature, $T_u = 413$ K have been measured by Hirano et al [275]. They used flame cone method with a circular nozzle burner. They defined the equivalence ratio, ϕ , as the actual methanol-air ratio/stoichiometric methanol-air ratio, for various methanol-water-air gaseous mixture with the water content C_w as a parameter, where C_w means the water mole fraction in the absolute gaseous mixture. Their results are shown in Fig. 2.36 (a).

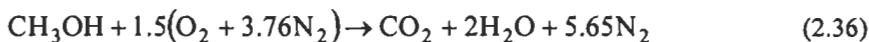
b- Also, Hirano et al [275] have measured the burning velocities as a function of

unburnt mixture temperature, T_u , in the same burner as in (a), and their results are shown in Fig. 2.36 (b).

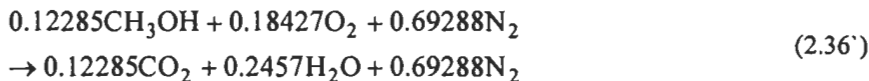
c- Koda et al [276] have measured the explosion pressure, P_m , from combustion of methanol-water-air gaseous mixture in constant volume vessel as a function of equivalence ratio and water content, C_w as described above in (a). When the mixture is ignited, the vessel pressure increases in the usual manner for constant volume explosions from the initial 1 atm up to the peak pressure, P_m that approximately corresponds to the flame arrival at the pressure gauge, and then gradually decreases due to cooling. These results are shown by points in Fig. 2.38 (a) and as a function of equivalence ratio, ϕ for $C_w = 0 - 20\%$ methanol-water-air gaseous mixture. Also shown in Fig. 2.38 (b), the measured explosion peak pressure, P_m , as a function of C_w for stoichiometric methanol-water-air gaseous mixture. The initial pressure and temperature in these experiments were 1 atm and 383 K, respectively.

Computational Results

The chemical kinetics scheme C_1 described in section 2.4.4 is used here. This will explore further the validity of the scheme with another experimental results. The input data were similar to those used with the above experimental results. The equivalence ratio here is defined as described above. The stoichiometric methanol-air ratio is given by:

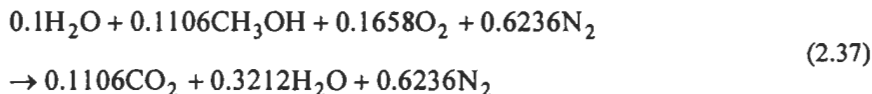


For one mole mixture this equation becomes:



and the ratio of fuel to air is F/A by volume = 14 % or F/A by weight = 15.54 %.

Again, for one mole mixture, stoichiometric methanol-air ratio and water content C_w of 10 % of the mixture, the stoichiometric equation will be:



and F/A by volume = 14% is kept constant.

The amount of water in the methanol+water by mass will be, $\text{H}_2\text{O}/(\text{H}_2\text{O} + \text{CH}_3\text{OH}) = 33.7\%$ or 47 % by volume, and for $C_w = 20\%$, the values will be 53.4 % by mass or 67 % by volume. These values are similar to that of crude methanol containing water. Again the value of C_w is defined here as the mole fraction of water in the gaseous mixture. All the input data in the kinetic program are based on the assumption of one mole of mixture.

The transport constant and kinetic scheme C_1 , in Tables 2.1, 2.2 and 2.9 were used as described in section 2.4.4 to predict the flame structures, burning velocities and to determine the ignition temperatures for methanol-water-air flames.

Eight runs of CH₃OH-air flames were computed at initial temperature, T_u of 413 K and initial pressure, $P_u = 1$ atm over a range of equivalence ratio from 0.7 to 1.6. All of these predicted results for pure methanol-air flame are shown by solid curve in Fig. 2.36 (a).

Another 32 runs of CH₃OH-air flames were computed at T_u from 320 to 413 K and 1 atm at different equivalence ratio to obtain the maximum value at each temperature and the results are shown in Fig. 2.36 (b). Also 16 runs of CH₃OH-water-air flames were computed, 8 of those with $C_w = 10\%$ and the rest with $C_w = 20\%$ at $T_u = 413$ K, 1 atm and over a range of equivalence ratio from 0.7 to 1.6. All the predicted results for CH₃OH-water-air are shown by dashed curves and these results are shown in Fig. 2.36 (a). The results have been obtained using 33 and 53 grid points for each flame, and 1500 to 2000 integration steps to reach the steady state, depending on the flame. These results were performed by Habik [274], and their analyses are given in the next section.

In addition to the above calculations, the adiabatic temperature, T_b , at constant pressure and volume is calculated using the equilibrium temperature program described in chapter 1. The results for pure methanol-air mixture are shown in Fig. 2.36 (c) by full curves and that with $C_w = 10$ and 20 % are shown in the same figure by dashed curves. All at initial pressure 1 atm and temperature of 413 K. The maximum adiabatic pressure at constant volume is shown at different equivalence ratios with full and dashed curves (with $C_w = 0\%$, 10 %, and 20 %, respectively) in Figs. 2.38 (a) and (b). The burning velocity, flame structure, explosion pressure, heat release rate and ignition temperature will be discussed as follows;

i- **Laminar burning velocity.** The kinetic scheme C_1 and its parameters in Tables 2.2 and 2.9 given in section 2.4.4 have been used by Habik [274] to compute the burning velocities for methanol-water-air mixture at 1 atm and 300 to 413 K. These

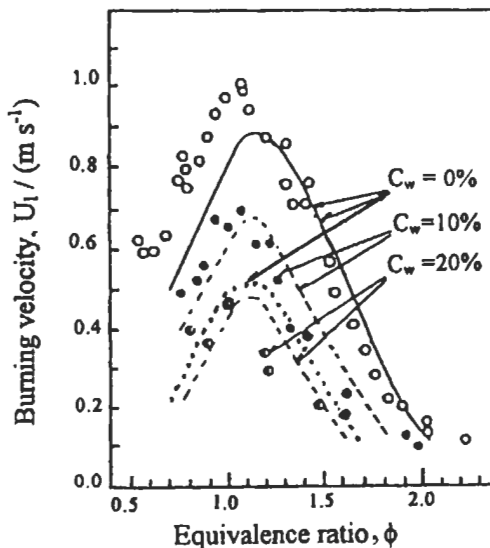


Fig. 2.36(a): Comparison between experimental and predicted burning velocities at 413 K and 1 atm, for $C_w = 0 - 20\%$ methanol-water-air gaseous mixture. Experimental results taken from [275]. The predicted values are shown by full curve ($C_w = 0\%$) and dashed curves ($C_w = 10$ and 20%). Predicted dotted curve at 1 atm, and 300 K with $C_w = 0$ [274].

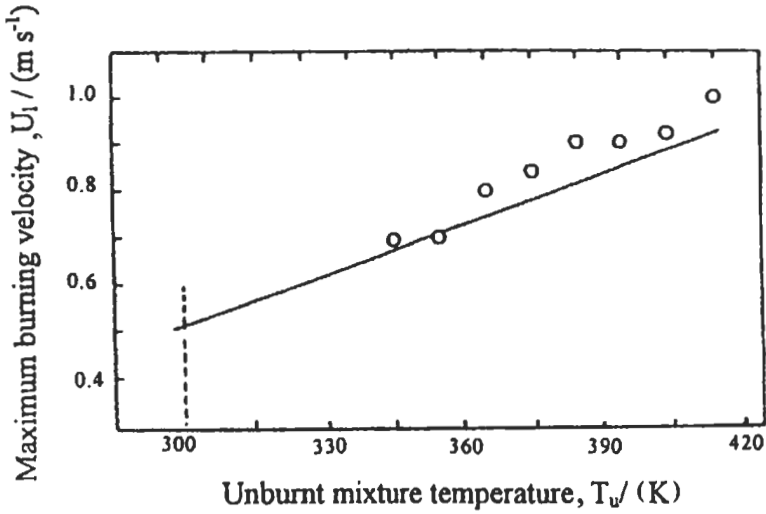


Fig. 2.36(b): Comparison between experimental (shown as points [275]) and predicted (full line) maximum burning velocities as function of unburnt mixture temperature for methanol-air gaseous mixtures, and initial pressure of 1 atm [274].

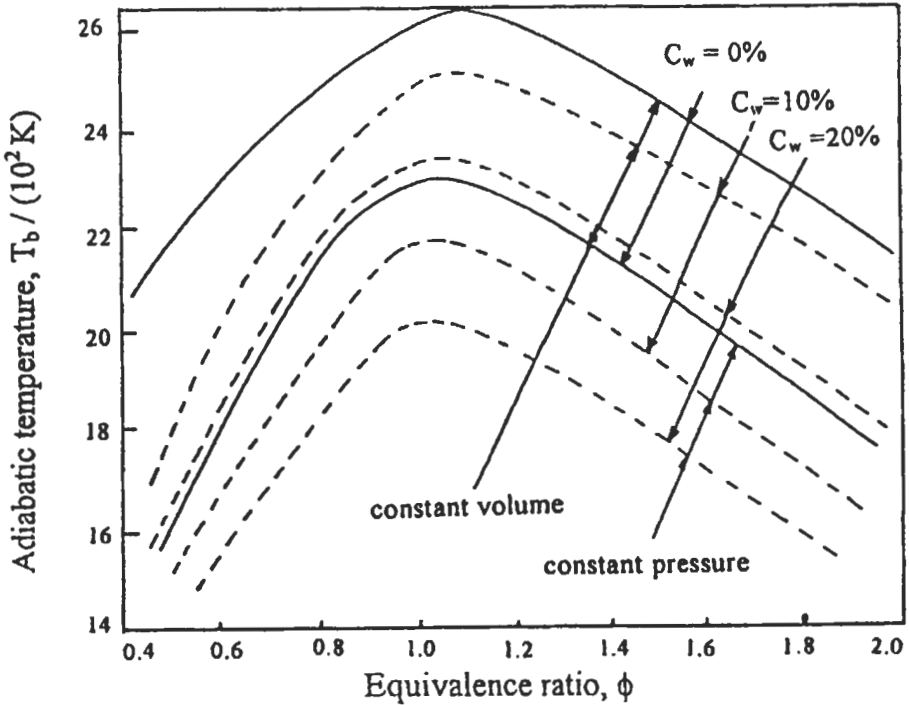


Fig. 2.36(c): Comparison between calculated adiabatic temperature at constant pressure and volume as function of equivalence ratio, ϕ for $C_w = 0$ (full curves) and 10 % and 20 % (dashed curves). Initial pressure and temperature are 1 atm, and 413 K [274].

results are shown in Fig. 2.36 (a) as a function of equivalence ratio, for $C_w = 0$ (full curves) and $C_w = 10$ and 20 % (dashed curves). The accuracy of different burning velocity measurement techniques has been discussed by Andrews and Bradley [225], Law [244] and Dixon-Lewis [65] and here in section 2.4.3.

In Fig. 2.36 (a), as elsewhere, there is some spread in experimental values. As discussed before, one possible explanation lies in flow divergence effects as gas flows into the flame and in the use of different reference planes to define U_1 . In spite of this, the agreement between the computational and experimental results is satisfactory. All solid and dashed curves are at unburnt mixture temperature, $T_u = 413$ K and 1 atm, but dotted curve is computed at 1 atm and 300 K for comparison. The figure shows that when the water vapor concentration was kept constant, the maximum burning velocity occurs at equivalence ratio of 1.2, independent of the water concentrations. It is also clear that, as the water vapor concentration increases, the burning velocity decreases, and at the same time, the range of ϕ for stable flames was narrowed. This is confirmed in the figure theoretically and experimentally. For a mixture with $C_w = 20$ % water vapor or 53.44 % water in fuel (methanol + water) by mass, the burning velocities are slightly lower than that at 1 atm and 300 K for pure methanol-air mixture. This indicated that the crude methanol containing 53.44 % by mass water can be burnt in burner when the mixture is heated to about 413 K. Hirano et al [275] found that no flame could be established on the burner port for a mixture containing more than 20 % water vapor. Although in a closed vessel, a spark ignited flame was found to propagate through a mixture at 383 K containing 30% water vapor [276] as shown in Fig. 2.38 (b). Over the range of ϕ from 0.6 to 1.8, the burning velocities at 1 atm, $C_w = 0.0$, and $T_u = 300$ and 413 K are well represented by the following expressions, with correlation factors of 0.994 and 0.984, respectively:

$$U_1 = -0.9319 + 2.374\phi - 0.9732\phi^2 \text{ m s}^{-1} \text{ at } T_u = 300 \text{ K, } C_w = 0 \% \quad (2.38)$$

$$U_1 = -1.2470 + 3.409\phi - 1.406\phi^2 \text{ m s}^{-1} \text{ at } T_u = 413 \text{ K, } C_w = 0 \% \quad (2.39)$$

For the same initial conditions in Eqs. 2.38 and 2.39, but with $C_w = 10$ % and 20 %, U_1 is also well represented by the following expressions, with correlation factors of 0.981 and 0.997, respectively:

$$U_1 = -1.283 + 3.24\phi - 1.361\phi^2 \text{ m s}^{-1} \text{ at } T_u = 413 \text{ K, } C_w = 10 \% \quad (2.40)$$

$$U_1 = -1.588 + 3.450\phi - 1.441\phi^2 \text{ m s}^{-1} \text{ at } T_u = 413 \text{ K, } C_w = 20 \% \quad (2.41)$$

The Chaperon effect of water is of one order of magnitude more effective than for nitrogen or oxygen molecules. The addition of water will increase the rate of radical recombination steps, R_{10} to R_{12} and reactions R_4 , R_{15} and R_{16} in Table 2.2. This leads to a decrease in H, O and OH atoms and consequently reduces the overall rate of combustion by reducing the net amount of chain branching from reaction R_2 that leads to reduction in the burning velocity.

The effect of initial temperature, T_u on the maximum burning velocities for pure

methanol-air mixtures at 1 atm is shown in Fig. 2.36 (b). The maximum burning velocity decreases linearly as the temperature decreases and this is shown by full computed line which appears to be in reasonable agreement with the experiments. Again at 300 K, the maximum burning velocity was found to be 0.52 m s^{-1} which agrees well with values measured by Gibbs and Calcote [270] and Gülder [188]. The computed line is well represented by the following expression with a correlation factor of 0.995:

$$U_{l_{\max}} = -0.4309 + 0.003129T_u \quad \text{m s}^{-1} \quad (2.42)$$

Most of all the elementary reaction rates in Tables 2.2 and 2.9 increase with increasing the temperature, accelerating the overall combustion processes, and consequently increase the burning velocities.

Figure 2.36 (c) shows also that, as the water vapor concentration was kept constant, the maximum adiabatic temperature was found to be at $\phi = 1.1$ and independent of the water concentration. However, the addition of water to CH_3OH -air mixture will reduce the maximum adiabatic temperature by about 130 K for $C_w = 10\%$ and 300 K for $C_w = 20\%$ (assuming constant volume). Also shown in the same figure, is the calculated adiabatic temperature at constant pressure.

(ii) **Flame structures in burner and explosion pressure in bomb.** Figure 2.37 (a) shows the computed mole fraction of CO , CO_2 , H_2O , CH_3OH and O_2 versus height above the burner top. The full and dashed curves are for $C_w = 0$ and 10% , both at 1 atm, $\phi = 1$, and initial temperature of 413 K. The mole fraction of CO_2 for flame with $C_w = 10\%$ decreases than with $C_w = 0\%$, and this is due to the decrease of OH in reaction, R_{14} . In addition to that, the mole fraction of CO also decreases with addition of water, and this is also due to decreases of radical species in reactions R_{17} to R_{20} . The low CO concentrations from the combustion of the crude methanol will lead to reduction of the atmospheric pollution.

Figure 2.37 (b) shows the computed, O, H, OH and CH_2O with and without water content as a function of height above the burner top. The mole fractions of all of these species decrease as the water is being added. The lower O concentration also reduces the NO formation according to $\text{N}_2 + \text{O} \leftrightarrow \text{NO} + \text{N}$. This reaction is the first and rate determining step of the mechanism of NO formation, which has been first postulated by Zeldovich [277]. This is thought to be the main source of NO in most combustion systems. It is also known that addition of H_2O to a fuel reduces the formation of NO in flame [24]. Also, the rate of NO formation is strongly temperature dependent [278]. As shown in Fig. 2.36 (c), the reduction of maximum temperature by about 300 K (at $C_w = 20\%$) should also decrease NO formation. Figure 2.37 (c) shows the comparison between peak mole fractions of O, OH, H and CO as a function of equivalence ratio for $C_w = 0$ and 10% .

Figure 2.38 (a) shows the explosion peak pressure, P_m (as calculated from the adiabatic equilibrium program at constant volume) versus equivalence ratio, for $C_w = 0 - 20\%$ methanol-water-air gaseous mixture. Although there was inevitable heat loss in practical experiments, the agreement between the computed and experimental results is satisfactory for $C_w = 0\% - 20\%$. Once again the figure shows that the explosion peak pressure decreases as the C_w increases and this is also shown in Fig. 2.38 (b). The computed results in Fig. 2.38 (b) confirmed the experimental results in constant volume vessel by Ref. 276, where methanol with about $C_w = 30\%$ can be burnt if the mixture is heated up to 383 K.

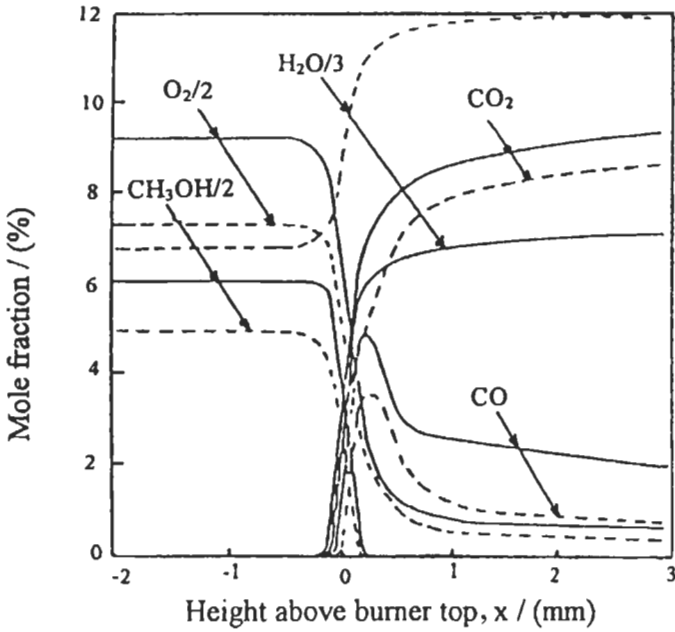


Fig. 2.37(a): Comparison between computed mole fractions of CH₃OH, H₂O, O₂, CO₂ and CO as a function of height above burner top for $C_w = 0\%$ (full curves) and $C_w = 10\%$ (dashed curves) for stoichiometric methanol-water-air gaseous mixture. Initial pressure and temperature are 1 atm, and 413 K [274].

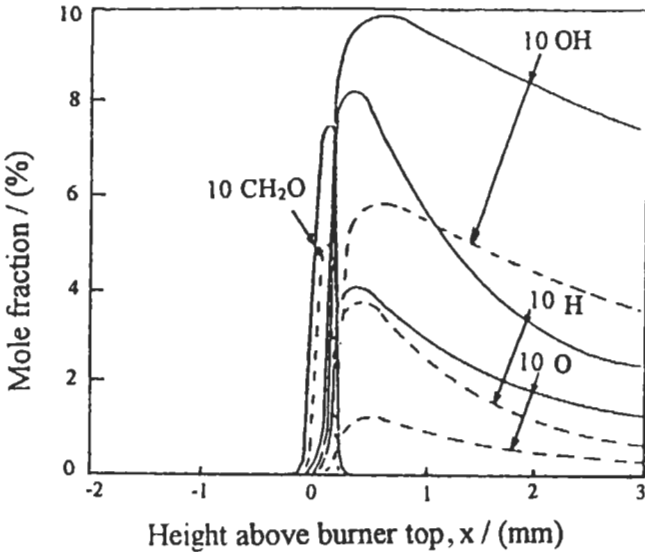


Fig. 2.37(b): Comparison between computed mole fractions of CH₂O, OH, H and O as a function of height above burner top for $C_w = 0\%$ (full curves) and $C_w = 10\%$ (dashed curves) for stoichiometric methanol-water-air gaseous mixture. Initial pressure and temperature are 1 atm, and 413 K [274].

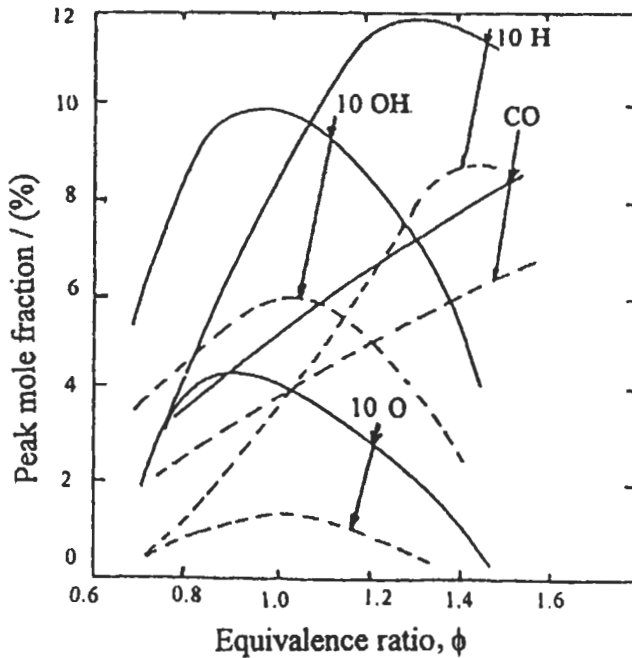


Fig. 2.37(c): Comparison between peak mole fractions of O, OH, H and CO as function of equivalence ratio for $C_w = 0\%$ (full curves) and $C_w = 10\%$ (dashed curves) at 1 atm, and 413 K [274].

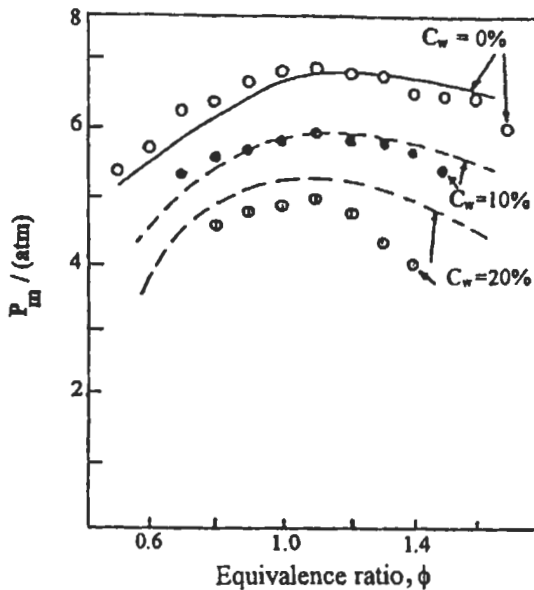


Fig. 2.38(a): Comparison between computed (full and dashed curves) and experimental (shown as points [276]) explosion peak pressure as function of ϕ for $C_w = 0\% - 20\%$ at 1 atm, and $T_u = 383\text{ K}$ [274].

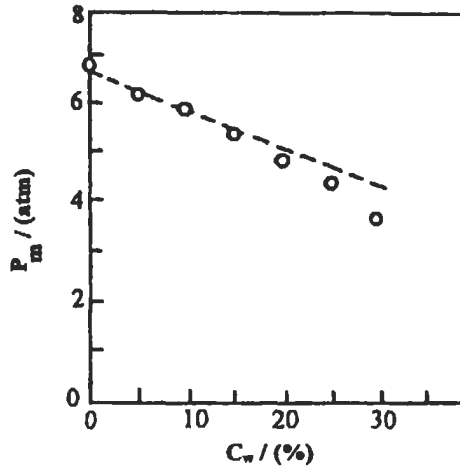


Fig. 2.38(b): Comparison between computed (dashed curves) and experimental (shown as points) [276]) explosion peak pressure as function of C_w ($C_w = 0 - 30\%$) at 1 atm, and $T_u = 383$ K [274].

(iii) **Heat release rate and ignition temperature.** As indicated before, the volumetric heat release rate-temperature profiles are important in laminar flamelet models of turbulent combustion. Another important fundamental parameter in combustion is the knowledge of the ignition temperature, where the risk analyses for transportation and mine safety often depend on the probability attributed to igniting flammable mixture by ignition source.

In connection with that, Fig. 2.39 shows the way in which the rate of chemical heat release (which is a measure of the overall reaction rate) changes with temperature for $\phi = 0.8$ and 1.2, at $C_w = 0 - 10\%$ methanol-water-air gaseous mixtures, at 1 atm and $T_u = 413$ K. Again the full and dashed curves are for $C_w = 0$ and 10%, respectively. Each curve terminates at the hot end at the equilibrium flame temperature. The figure shows that the maximum heat release rate decreases by about 40% for methanol-water-air mixture with $C_w = 10\%$ and this is due to the decrease of the radical concentrations as discussed in (i) and (ii).

We turn now to the net rates of free radical production in these flames, as represented by a radical pool consisting of ($H + 2 O + OH + OH + HO_2 + CHO + CH_2OH + CH_3O + CH_3$). The net rates corresponding to the above conditions are given in the same figure as a function of temperature.

The temperature at which the net rate of formation of free valencies only becomes positive is defined as the ignition temperature, T_i (Dixon-Lewis [65]), then the heat release rate at a temperature below T_i is due only to reaction of radicals which have diffused back from the high temperature region. The radical can react by strongly exothermic reactions of the HO_2 cycle at both high and low temperatures. The rate coefficients of reactions, R_4 to R_9 (Table 2.2) do not change much with temperature. The temperature is determined from Fig. 2.39, marked on the abscissa, and plotted in Fig. 2.40 versus different equivalence ratio, ϕ for $C_w = 0 - 20\%$ methanol-water-air gaseous mixtures. The figure shows that the ignition temperature increases with ϕ until it reaches a maximum value at ϕ about 1.2 and then decreases again. Also the ignition temperature decreases as the water content increases.

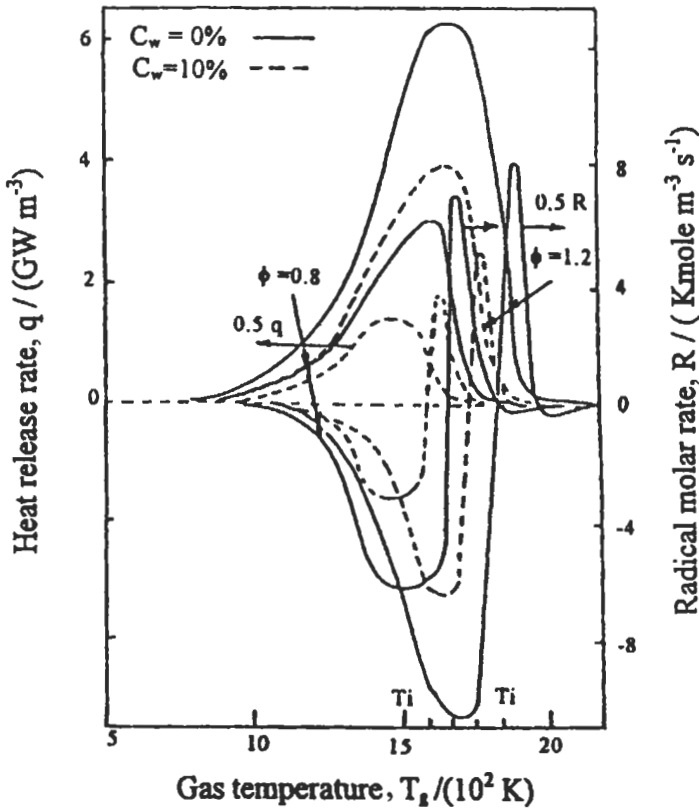


Fig. 2.39: Computed heat release rates and net rate of formation of radical pool (see text), for $\phi = 0.8, 1.2$ and $C_w = 0\%$ (full curves), 10% (dashed curves) at 1 atm, and $T_u = 413 \text{ K}$ [274].

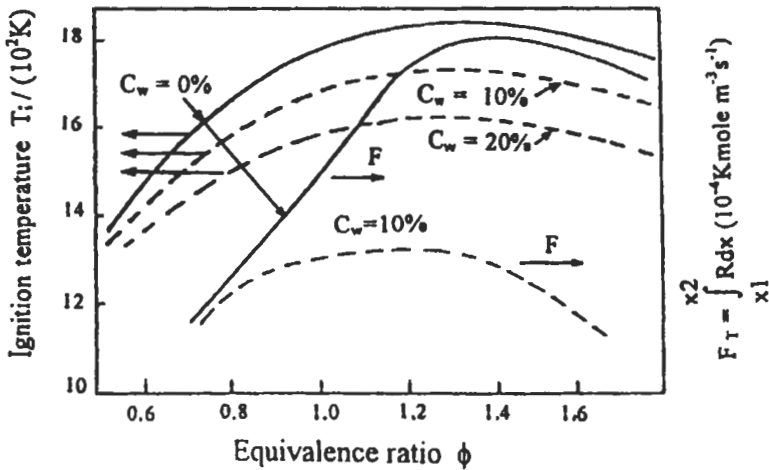


Fig. 2.40: Comparison of ignition temperature and flux of space integral rate (see text) as function of ϕ for $C_w = 0-20\%$ at 1 atm, and 413 K [274].

To explore further the variation of T_i with ϕ and C_w , the flux of free valencies (radical pool) is calculated between two positions, x_1 at $T_u + 10$ and x_2 at T_i , and given by the space integral rate $\int_{x_1}^{x_2} R dx$. The radical pool is plotted versus distance in Fig. 2.41 (a) for equivalence ratios of 0.8, 1.0 1.2 with $C_w = 10\%$, at 1 atm and 413 K. Shown also in the same figures is the gas temperature through the flame. At $x = 0$, the reference temperature of 1450 K was chosen for all the flames. The calculated fluxes by the space integral rate are plotted in Fig. 2.40. The figure shows that, the ignition temperature increases or decreases as the flux $\int_{x_1}^{x_2} R dx$ increases or decreases, respectively. The same can be said when the water content increases or decreases.

Figure 2.41 (b) shows the variations of CH_3OH and CO versus distance for three equivalence ratios. The value of T_i is coincident with the maximum carbon monoxide mole fraction profile, and practically all of the CH_3OH has disappeared at this position. Net radical production thus only occurs after nearly all of the CH_3OH has disappeared, and the reactions of the hydrocarbon fuel and its initial breakdown products (CH_3OH , CH_3O , CHO , HO_2 and CH_3) are supported as a result of H , O and OH radicals which have diffused from the net branching region towards the unburnt gas.

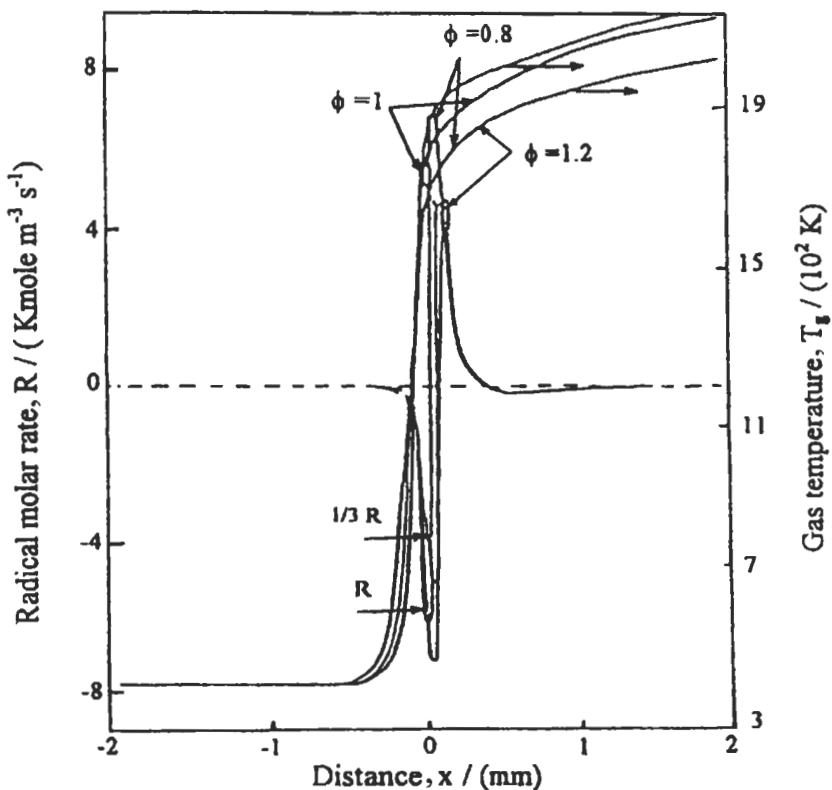


Fig. 2.41(a): Net rate of formation of radical pool and gas temperature as a function of distance for $\phi = 0.8, 1, 1.2$, $C_w = 10\%$ at 1 atm, and $T_u = 413$ K [274].

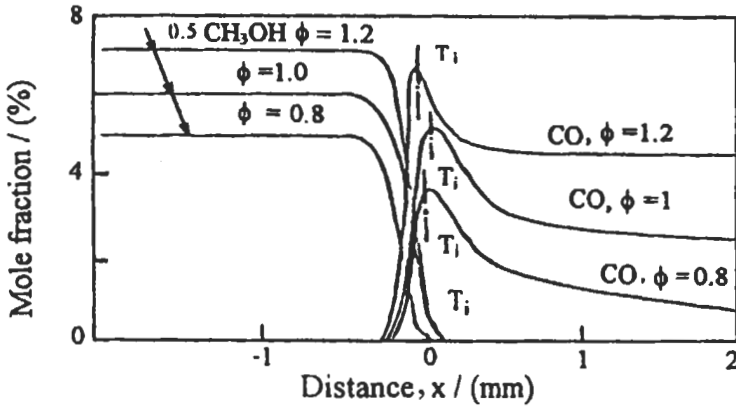
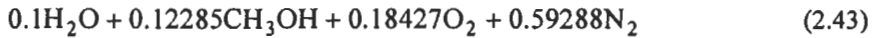


Fig. 2.41(b): Variation of mole fractions of CH₃OH, and CO as a function of distance for C_w = 10 % methanol-water-air gaseous mixture at 1 atm, and T_u = 413 K [274].

One further interesting point is that replacing the number of moles of water by the same number of N₂, therefore, for one mole mixture at C_w = 10 %, Eq. 2.37 becomes:



The simulation of replacing water by nitrogen is similar to the experiment of Olsson et al [263]. The computed species and burning velocity are given in Table 2.13. The results using initial conditions of Eqs. 2.36, 2.37 and 2.43 are defined in the Table by runs 1, 2 and 3.

Table 2.13: Comparison between peak mole fractions for C_w = 0-10 % for methanol-water-air gaseous mixture at 1 atm and T_u = 413K [274].

Species	Run 1* U _l = 0.77 m s ⁻¹	Run 2** U _l = 0.6 m s ⁻¹	Run 3*** U _l = 0.74 m s ⁻¹
	Mole fraction	Mole fraction	Mole fraction
H	0.8 × 10 ⁻²	0.59 × 10 ⁻²	0.73 × 10 ⁻²
O	0.4 × 10 ⁻²	0.25 × 10 ⁻²	3.3 × 10 ⁻²
OH	0.99 × 10 ⁻²	0.80 × 10 ⁻²	1.05 × 10 ⁻²
CO	5.26 × 10 ⁻²	4.5 × 10 ⁻²	5.3 × 10 ⁻²
H ₂	3.01 × 10 ⁻²	2.66 × 10 ⁻²	3.1 × 10 ⁻²
CH ₃ OH	0.024 × 10 ⁻²	0.016 × 10 ⁻²	0.23 × 10 ⁻³
CH ₃ O	0.39 × 10 ⁻²	0.26 × 10 ⁻²	0.33 × 10 ⁻²
CH ₃	0.29 × 10 ⁻²	0.22 × 10 ⁻²	0.24 × 10 ⁻²
HO ₂	0.136 × 10 ⁻²	0.10 × 10 ⁻²	0.14 × 10 ⁻²
CHO	0.115 × 10 ⁻³	0.22 × 10 ⁻⁵	0.78 × 10 ⁻⁴
CH ₂ O	0.76 × 10 ⁻²	0.60 × 10 ⁻²	0.74 × 10 ⁻²

* Stoichiometric methanol-air mixture, φ = 1 (C_w = 0.0, Eq. 2.36)
 ** Stoichiometric methanol-air mixture, φ = 1 (C_w = 10 %, Eq. 2.37, replaced some of CH₃OH by H₂O).
 *** Stoichiometric methanol-air mixture, φ = 1 (C_w = 10 %, Eq. 2.43, replaced some of N₂ by H₂O).

The comparison between runs 3 and 1 shows that, there is a slight increase in H₂ and OH with a slight decrease in all other species, and that the burning velocity decreases by about 4 %. Similar results have been found experimentally and theoretically by Olsson et al [263].

2.4.6 Propane-Air Flames

The combustion process of propane-air mixture can be studied under well defined controlled conditions which the laminar flame provides, thus the comparison of measured and predicted flame structures and burning velocities of laminar propane-air flames under different conditions is essential for the successful development of kinetic model and is demanding tests for its accuracy as discussed before. Such study is lacking because most of the investigations were concentrated on the flame structure while others on the burning velocity. The following sections will cover such lacking through comparison between the predicted results from kinetic model and the experimental flame structure and burning velocity for propane-air flames[20].

Experimental Method and Results

(i) **Flame structure.** There are three sets of experimental results for flame structure at low and atmospheric pressures that were used in this section to validate the kinetic model for propane flames. The experimental test rig for atmospheric flame is shown in Fig. 2.42. These results are:

Low pressure flames. In order to validate the kinetic model, the predicted results should be compared at different pressures. The only experimental results at low pressure were those measured by Fristrom et al [279]. Their flat premixed low pressure flame can give good spatial resolution and they made comprehensive measurements for individual species concentrations, in a propane-air flame at 0.25 atm, $\phi=1$, and 300 K, and these results are shown in Figs. 2.43 (a) and (c).

Atmospheric flames. In this section we will also discuss two sets of experimental data which have been used by Habik [20] and Habik et al [207] to optimize the kinetic mechanism for propane fuel and these data are as follows:

(i) Gas temperature and composition profiles of C₃H₈, O₂, CO, H₂, CO₂, H₂O and OH were measured by Bechtel et al [280], at atmospheric pressure for stoichiometric, premixed, laminar propane-air flame. They have made their measurements on a burner with knife edge flame holder and a focused Laser beam can probe at the center of the flame where the flame geometry was nearly one-dimensional on a scale of few mm flame thickness. Stephenson [281] has measured the gas temperature for propane-air flame at atmospheric pressure and $\phi = 1.0$. These results are shown in Fig. 2.44.

(ii) Flame structure and flammability limits for atmospheric laminar, flat adiabatic premixed propane-air mixtures were measured on a matrix burner by Habik et al [207]. The burner was 0.078 m diameter and is shown in Fig. 2.42, and the matrix comprised 0.01 m thick disc of copper, and this facilitated the drilling of about 2300 holes (0.00065 m diameter) with a distance between the center of the holes of 0.00125 m. The burner tube was cooled with water. Radial and vertical traversable carriage for thermocouple and gas sampling probe enables measurements to be taken accurately throughout the flame. Air and propane were delivered from their main source (1), (2) and metered by the standard orifice-meters (6). These orifices were calibrated using a

rotameter. The air and propane fuel flows were supplied separately into the mixing chamber (9) to ensure a homogeneous mixture. The mixture passed through a flame trap (10), then to a vertical water-cooled burner tube (11), and the flow was distributed uniformly across the matrix (12). The mixture above the matrix was ignited, and a flat stable adiabatic flame was obtained freely above the matrix at different equivalence ratios. Gas samples were withdrawn throughout the flame using a quartz microprobe of 100 μm diameter sonic orifice, made according to the recommendation of Ref. 237, and this did not visibly disturb the flame. The contoured nozzle and large pressure drop effectively quenched the flame reactions in the 30° tapered quartz microprobe, after a small sonic orifice of 100 μm diameter. The sample was sucked through the probe by suction pump and then passed through a filter and dried through a water separator and silica gel as shown in Fig. 2.42. The flow rate in the system had to be carefully checked against leakage.

The gas sample was analyzed for CO, and O₂ concentrations using an electrochemical cells, while for CO₂ an infra-red gas analyzer was used. Gas temperatures were measured in the flame using Pt 13 % Rh-Pt uncoated thermocouple with 100 μm diameter and were corrected for radiation errors. The measured concentrations of CO, CO₂, O₂ and gas temperature profiles are shown in Figs. 2.45 (a), 2.46 and 2.47. Also, the measured maximum flame temperatures at different equivalence ratios and near lean and rich flammability limits for propane-air flames are shown in Fig. 2.49.

(ii) **Burning velocity.** As the flame structure may not be a sufficiently sensitive parameter for assessing all the subtleties of flame oxidation kinetics, and for this purpose, experimental burning velocity for a flat adiabatic premixed laminar flame should also be measured.

Because of the fundamental and practical importance of laminar burning velocity, extensive efforts have been expended over the years towards achieving accurate determination of its value. Some of the early efforts were made in Refs. 282-284 where they measured the burning velocity of propane-air flame by cone angle on nozzle burner, while Gibbs and Calcote [270] have used flame area on a Bunsen burner for their measurements at 1 atm, and Günther and Janisch [219] have made measurements in burner with particle tracking and flame photography at 300 K and 1 atm. Also, burning velocities have been obtained from bomb pressure measurements [285] between 0.4 to 10 atm and temperatures of 298-700 K. These were not confined to the constant pressure period. Similar measurements to those of the latter in bomb [286, 287] were made at 1 atm and 300 K. Recently, one of the efforts to determine the burning velocity accurately is by using the counterflow twin-flame technique and Laser Doppler Velocimetry (LDV). This technique has been used to determine the laminar burning velocity of propane-air flame [227, 245, 288] at 1 atm, 300 K and different equivalence ratios, ϕ . These results are shown in Figs. 2.50 to 2.52. All of these results will be discussed next with the corresponding predicted values.

Computational Results

As mentioned in section 2.3.4, there are two kinetic schemes that were tested by Habik [20] for propane-air flames using one-dimensional kinetic model. The predictions started first with scheme B₂. The predicted results from this scheme are shown by dotted curves in Figs. 2.43 (a) to (c) and 2.50. This scheme consists of 74 chemical reactions

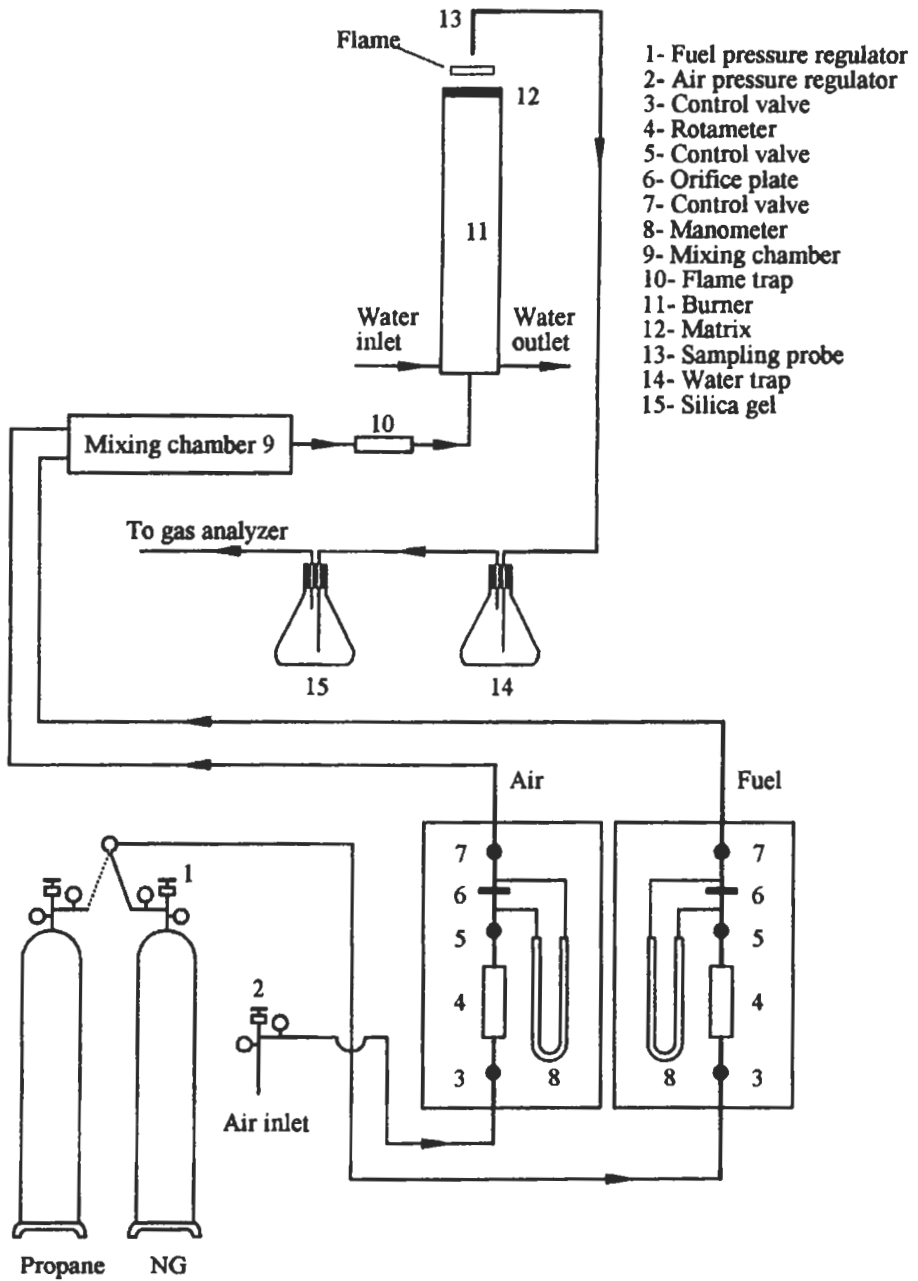


Fig. 2.42: Experimental test set – up [207].

and 25 species. To identify the major reactions in this mechanism, several attempts have been made to optimize these reactions and their rate coefficients to give satisfactory agreement with the experimental data. After these attempts, it was found that the predicted results with scheme A_2 (see section 2.3.4) give good agreement with the experimental flame structure and burning velocity at different conditions (Habik [20]). This scheme consists of 63 reactions among 25 chemical species. The predicted results with this mechanism are shown by full curves in Figs. 2.43 (a) to 2.52 and these results will be discussed with the experimental data. The flame structure, burning velocity, flammability limits and heat release rate will be discussed next as follows;

(i) **Flame structure at low pressure.** Figure 2.43 (a) shows the variation of computed mole fractions of C_3H_8 , O_2 , H_2 , CO , CO_2 , H_2O and gas temperature profiles with distance above the burner top for propane-air flame at 0.25 atm, 300 K and $\phi = 1$. Also, shown in the figure are the corresponding experimental points measured by Fristrom et al [167] for mole fractions of C_3H_8 , O_2 , and CO_2 concentrations. The comparison shows that, the predicted profiles using kinetic scheme, A_2 , give good agreement with measured C_3H_8 , and O_2 profiles compared to the predicted results from scheme, B_2 . Only, the predicted mole fraction of CO is lower than that measured by about 5 % at post flame. Figure 2.43 (b) shows the predicted radical species profiles of H , O , OH , HO_2 , CH_2OH , CHO , CH_3 , CH_2O , and iC_3H_7 from both schemes for the same flame as in Fig. 2.43 (a). It is clear that the results from scheme, B_2 give lower values than those from scheme, A_2 , leading consequently to lowering the burning velocity, as will be described next.

Figure 2.43 (c) shows the predicted profiles of C_2H_4 , C_2H_6 , C_3H_6 , C_2H_2 and CH_4 from both kinetic schemes. These profiles were compared with those species measured by Fristrom et al [279] and predicted profiles by Warnatz [166]. Once again, the predicted profiles from scheme, A_2 , give reasonable agreement with the experimental results compared to those predicted from scheme, B_2 . The maximum discrepancy between the experimental and computed mole fractions of C_2H_4 , and C_2H_6 , is about double, while for C_3H_6 , C_2H_2 and CH_4 species is about 12 %.

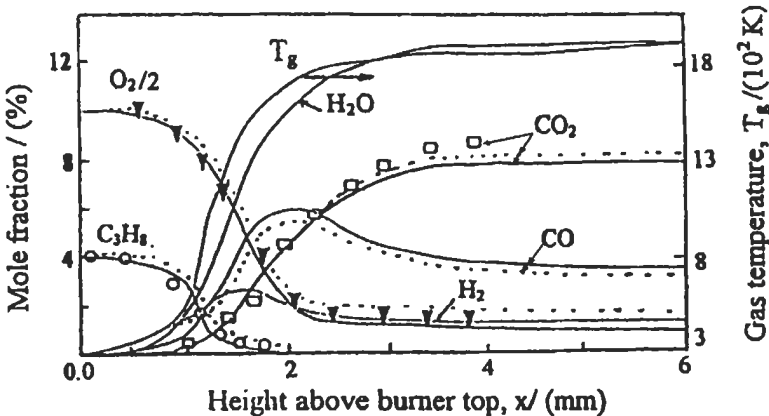


Fig. 2.43 (a): Experimental, \square CO_2 , O C_3H_8 and \blacktriangledown O_2 concentrations [167] and computed gas temperature and stable species against distance for $P_u = 0.25$ atm, $T_u = 300$ K and $\phi = 1$. Full curves (Scheme, A_2) and dotted curves (Scheme, B_2) [20].

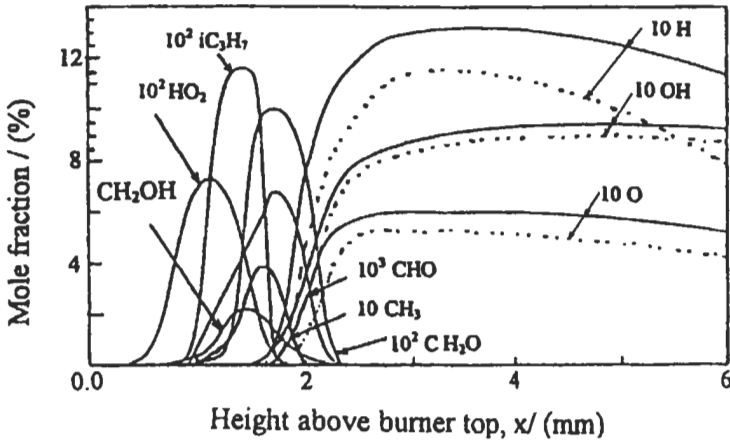


Fig. 2.43 (b): Computed H, O, OH, HO₂, CH₃, CH₃O, CHO, CH₂O and *i* C₃H₇ concentrations against distance for same flame as in Fig. 2.43 (a) [20].

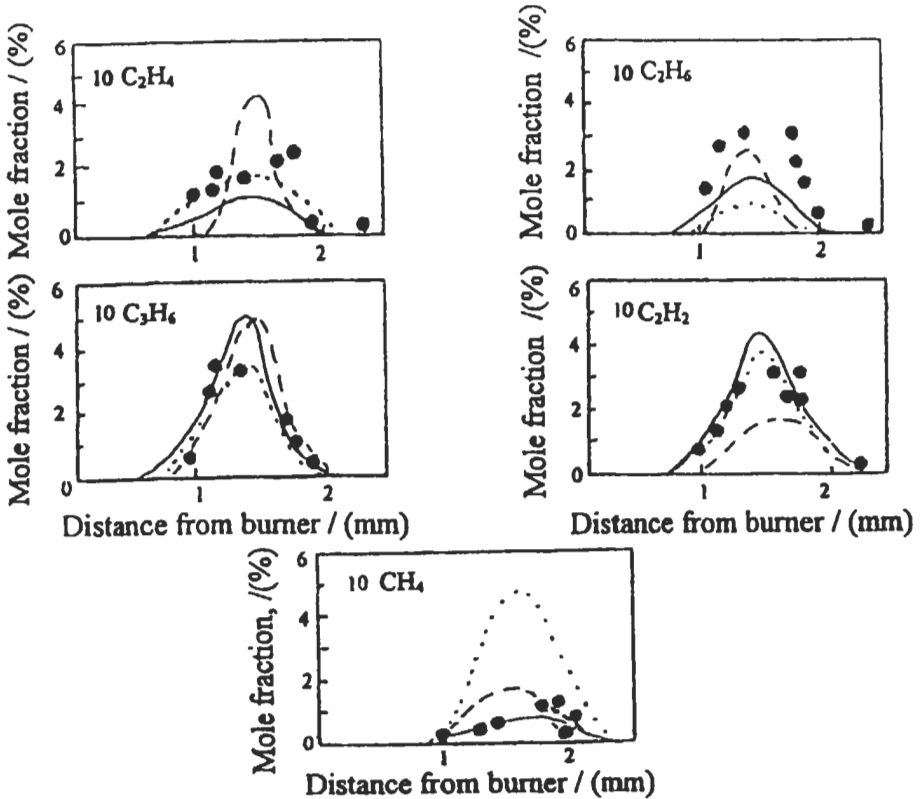
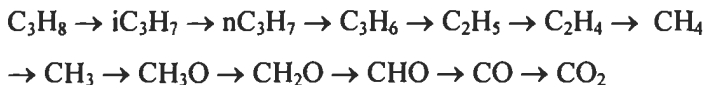


Fig. 2.43 (c): Experimental, • [279] and computed hydrocarbon species for the same flame as in Fig. 2.43 (a). Full curves (Scheme, A₂) and dotted curves (Scheme, B₂) [20] and dashed curves are predicted from [166].

(ii) **Flame structure at atmospheric pressure.** To confirm further the results from scheme, A_2 , two sets of experimental results were used to validate the kinetic model as mentioned above.

Stoichiometric flame. Figure 2.44 shows the comparison between the experimental [280, 281] and predicted [20] (using scheme, A_2) mole fractions of C_3H_8 , O_2 , H_2 , CO_2 , CO , H_2O , and gas temperature profiles for propane-air flame at 1 atm, 300 K and $\phi = 1$. It is clear from the figure that the agreement is good. Also, Fig. 2.45 (a) shows the comparison between the experimental and predicted [207] mole fractions of C_3H_8 , O_2 , H_2 , CO_2 , CO , H_2O , and gas temperature profiles for propane-air flame at 1 atm, 300 K and $\phi = 1$. Again, the comparison confirmed the validation of kinetic scheme, A_2 . The main oxidation path for C_3H_8 includes:



The primary source of H_2 formation is the reactions, R_{55} ($C_3H_8 + H \rightarrow nC_3H_7 + H_2$) and R_{56} ($C_3H_8 + H \rightarrow iC_3H_7 + H_2$). The mole fraction of H_2 peaks at about $x = 0.5$ mm, and then falls down to approximately constant value in the post flame zone where the reverse of reactions, R_1 ($OH + H_2 \rightarrow H_2O + H$) and R_7 ($H + HO_2 \rightarrow H_2 + O_2$) becomes the primary channel for H_2 formation with reaction, R_3 ($O + H_2 \rightarrow OH + H$), the major removal process. The primary source for CO_2 formation is reaction, R_{14} ($OH + CO \rightarrow CO_2 + H$). The water formation occurs exclusively from OH reactions R_{51} , ($C_3H_8 + OH \rightarrow nC_3H_7 + H_2O$) and R_{52} ($C_3H_8 + OH \rightarrow iC_3H_7 + H_2O$) in Table 2.10, but reactions, R_1 , and R_{22} ($CH_2O + OH \rightarrow CHO + H_2O$) are also responsible for H_2O production.

Oxygen chemistry is controlled by reactions, R_{60} , ($nC_3H_7 + O_2 \rightarrow C_3H_6 + HO_2$), and R_{61} , ($iC_3H_7 + O_2 \rightarrow C_3H_6 + HO_2$) in Table 2.10, and R_2 , ($H + O_2 \rightarrow OH + O$) and R_{17} , ($CHO + O_2 \rightarrow H_2O_2 + CO$) in Table 2.2.

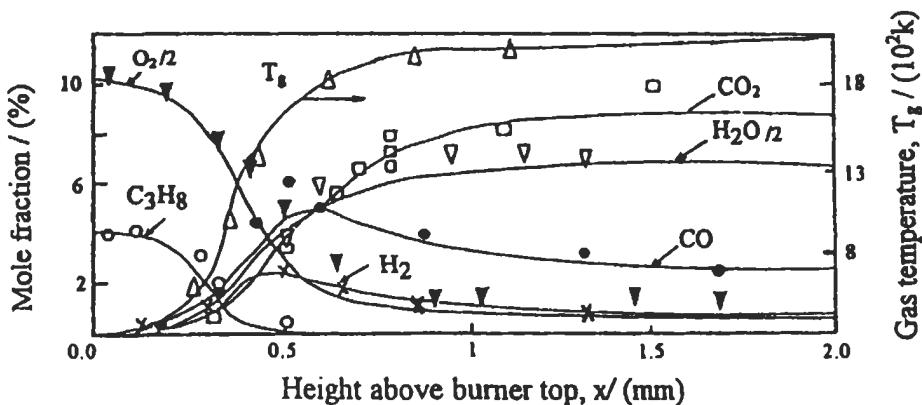


Fig. 2.44: Experimental, \square CO_2 , \bullet CO , \circ C_3H_8 , \blacktriangledown O_2 , ∇ H_2O and \times H_2 concentrations [280], Δ gas temperature [281] and computed gas temperature and species profiles (full curves [20]) against distance for propane-air flame at $P_u = 1$ atm, $T_u = 300$ K and $\phi = 1$.

The net molar rates for the same species shown in Fig. 2.45 (a) are shown in Fig. 2.45 (b). The maximum mole fraction of CO (Fig. 2.45 (a)) is corresponding to the maximum net molar rate of CO (Fig. 2.45 (b)) which occurs at a distance of about 0.5 mm. The same can be said for H₂, H₂O and CO₂ species. The maximum negative net molar rates of C₃H₈ and O₂ occur at distances of about 0.4 and 0.5 mm, respectively.

Figure 2.45 (c) shows the variation of the predicted radical species, OH, O, H, HO₂, and CHO versus distance for the same flame as in Fig. 2.45 (a). It is well recognized that the key to flame propagation is closely tied to the radical balance in each portion of the flame. Radicals are produced in the flame zone (occurring at a distance of about 0.4 to 0.65 mm) and diffuse a head of the flame into the preheat zone (occurring at a distance of about zero to 0.4 mm). In the preheating zone, these radicals (primarily O, H and OH) react with fuel and stable intermediate species molecules; leading eventually to final oxidation in the flame zone.

The main source of O atom is the chain branching, R₂ (H + O₂ → OH + O). At a distance of about 0.45 mm (Fig. 2.45 (c)) the rate of reaction, R₂ is significantly higher than total destruction of O by reactions, R₃, R₉, R₂₃ (Table 2.2), R₂₆ to R₂₈ (Table 2.3), and R₅₃ and R₅₄ (Table 2.10). Up to about 0.6 mm (Fig. 2.45 (c)), the formation of O is balanced by the reaction, R₃ (O + H₂ → OH + H) and then after, the rate of destruction becomes dominant. The peak mole fraction of O is followed by the peak of H atoms at about 0.65 mm. Reaction, R₁, the chain-branching reactions, R₃, R₁₄ (Table 2.2), R₂₇ (Table 2.3) and R₅₈ (nC₃H₇ → C₃H₆ + H in Table 2.10) are the most important pathways of H production, and its removal is by reactions, R₂, R₅, R₇, and R₂₄, R₃₂, R₃₆, R₄₀ (Tables 2.3 and 2.4), and R₅₅ (C₃H₈ + H → nC₃H₇ + H₂) and R₅₆ (C₃H₈ + H → iC₃H₇ + H₂) in Table 2.10. In the post flame after a distance of about 0.65 mm, H is controlled by the equilibrium reaction, R₁₄, and reactions, R₂₄, R₂₇, R₃₂, R₄₆ (Tables 2.3 and 2.4).

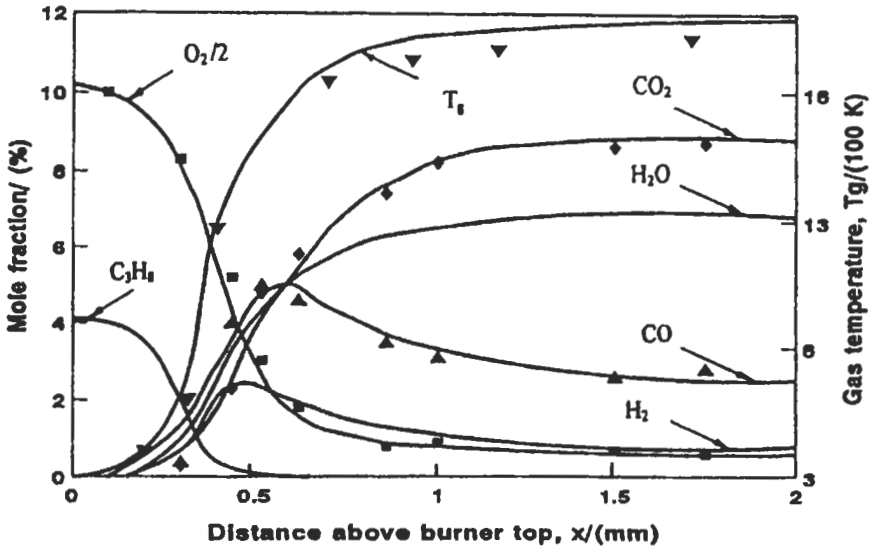


Fig. 2.45(a): Experimental species and gas temperature (■O₂, ▲ CO, ◆ CO₂, and ▼ T_g). Full curves are the computed species and gas temperature for propane-air flame at P_u = 1 atm., T_u = 300 K and $\phi = 1$ [207].

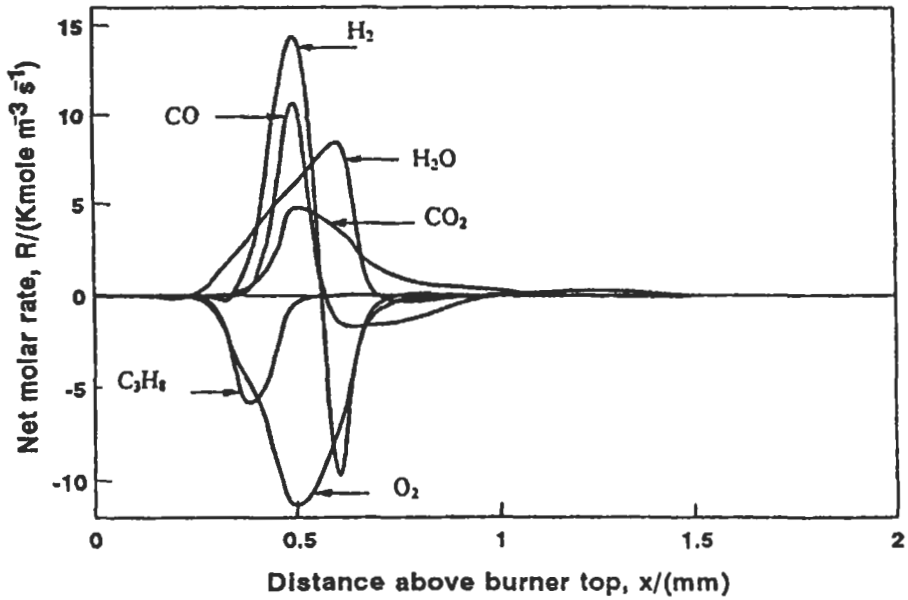


Fig. 2.45(b): Computed molar rate profiles for O_2 , CO , CO_2 , H_2O , C_3H_8 and H_2 for the same flame conditions as shown in Fig. 2.45 (a) [207].

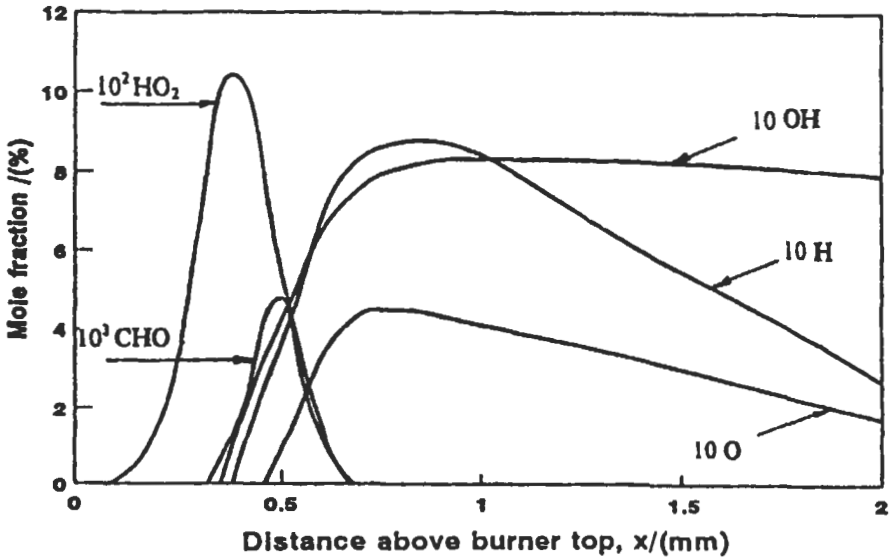


Fig. 2.45(c): Computed mole fraction profiles for radical species of H , OH , O , HO_2 and CHO for the same flame conditions as shown in Fig. 2.45 (a) [207].

Figure 2.45 (c) also shows that, the peak of OH occurs after the peaks of H and O . The OH radical is controlled by $R_1, R_5, R_8, R_{14}, R_{22}$ (Table 2.2), $R_{25}, R_{31}, R_{33}, R_{34}, R_{44}$

(Tables 2.3 and 2.4), and R_{51} , R_{52} and R_{63} (Table 2.10). In addition, the mole fraction of HO_2 peaks first before the peaks of CHO , O , H and OH . This is because, in the hotter regions of the flame, the radicals O , H , and OH , diffuse upstream to meet the incoming oxygen and react with it by the lower activation energy cycles via reaction, R_4 ($\text{H} + \text{O}_2 + \text{M} \rightarrow \text{HO}_2 + \text{M}$) to produce HO_2 . With regard to the mole fraction of CHO it is produced from reactions R_{21} to R_{23} and its removal occurs by reactions R_{17} , to R_{20} (Table 2.2).

The net molar rates for the same species in Fig. 2.45 (c) are shown in Fig. 2.45 (d). These net rates are given by the difference between the rate of formation of these radicals and the rate of their removal. It is clear from both figures that, the formation of the radical species O , H , OH , CHO and HO_2 started at the corresponding positive maximum net molar rates.

The main reaction rate which causes the flame to propagate is the chain branching reaction, R_2 ($\text{H} + \text{O}_2 \rightarrow \text{O} + \text{OH}$). This reaction activates unpaired electron spins present in molecular oxygen, to produce two new, full active species, OH and O . As a consequence of the very marked reduction in the rate of the forward reaction, R_2 at low temperature, and of the fact that it must also compete with the more or less temperature independent chain termination rates of reactions, R_7 , R_8 and R_9 (Table 2.2) even at low radical species, the net formation of new active radicals is restricted to certain temperature (called ignition temperature corresponding to the negative net radical pool rate). Above this temperature, the overall system becomes effectively chain branching, at a rate which increases very rapidly, but the system is eventually limited by the consumption of oxygen and the approach of R_2 to its equilibrium. At the same time the reactions, R_1 , R_3 and R_{14} also approach their equilibrium position. Consequently, the free radicals, O , H , and OH (see Fig. 2.45 (c)) finally decay to full equilibrium. The decay itself is produced by way of the termination reactions, R_7 to R_{11} (Table 2.2).

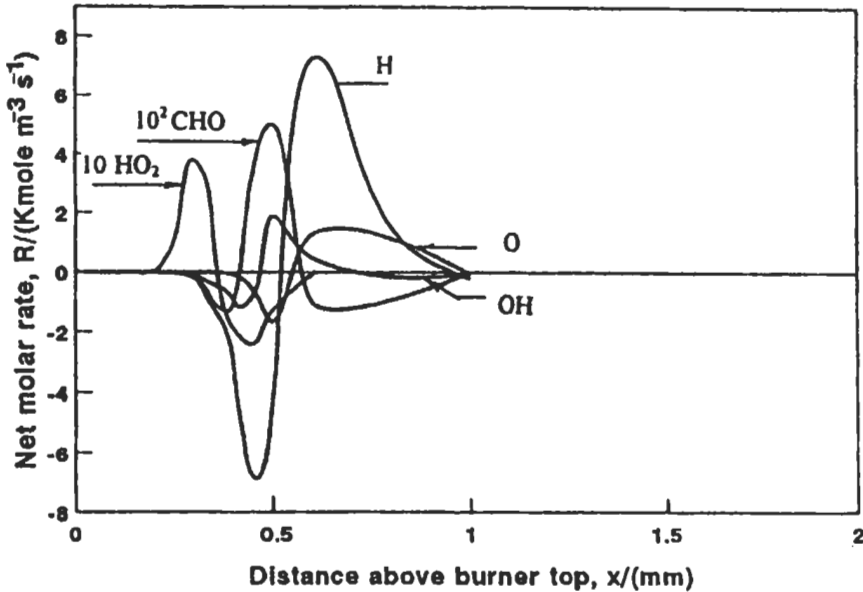


Fig. 2.45(d): Computed molar rate profiles for radical species of H , OH , O , HO_2 and CHO for the same flame condition as shown in Fig. 2.45 (a) [207].

For the same flame conditions in Fig. 2.45 (a), the mole fractions for C_3H_6 , iC_3H_7 , CH_2O , CH_3O and CH_3 are shown in Fig. 2.45 (e), while Fig. 2.45 (f) shows the mole fractions for CH_4 , C_2H_2 , C_2H_4 , C_2H_5 and C_2H_6 . Figure 2.45 (e) shows that, the maximum mole fraction of CH_3O is higher than that of CH_3 , C_3H_6 , C_3H_7 and CH_2O . Methoxy radical, CH_3O , is formed primarily by reaction R_{31} ($CH_3 + HO_2 \rightarrow CH_3O + OH$, in Table 2.3) and then reacts by reactions R_{32} to R_{34} (Table 2.3) to produce CH_2O (formaldehyde) which is the main link between hydrocarbon fuel and $CO-H_2$ reactions in kinetic mechanism. However, the formation of CH_3 species is mainly due to reactions, R_{57} ($C_3H_8 \rightarrow C_2H_5 + CH_3$) and R_{59} ($iC_3H_7 \rightarrow C_2H_4 + CH_3$) in Table 2.10, while C_3H_7 is formed by reactions R_{51} to R_{56} and consumed by R_{58} to R_{61} (Table 2.10) to produce C_3H_6 species which then reacts by O and OH through reactions, R_{62} and R_{63} (Table 2.10) to produce C_2H_5 , CHO and formaldehyde.

Lean flame. Having confirmed the validation of kinetic mechanism for stoichiometric flames, it is necessary next to check further the validation of the predicted results in lean and rich flames. Figure 2.46 shows that, the predicted results from the kinetic model give good predictions through the experimental flame of such leading parameters as CO , CO_2 and O_2 . Also, the gas temperature measurements are well predicted. Again, this comparison confirms the validation of the kinetic model under lean flames. The maximum discrepancy between the experimental and predicted results for most of the measured species is about 4 %, while for gas temperature is about 60 K at the post flame and this may be due to radiation correction calculation of the thermocouple. It is clear from Figs. 2.45 (a) and 2.46 that, the maximum mole fractions of CO and H_2 in lean flame ($\phi = 0.6$) are lower by five times than the corresponding values for flame at $\phi = 1$. The behavior of the species profiles in Fig. 2.46 is similar to that shown in Fig. 2.45 (a) and can be explained kinetically as described in Fig. 2.45 (a).

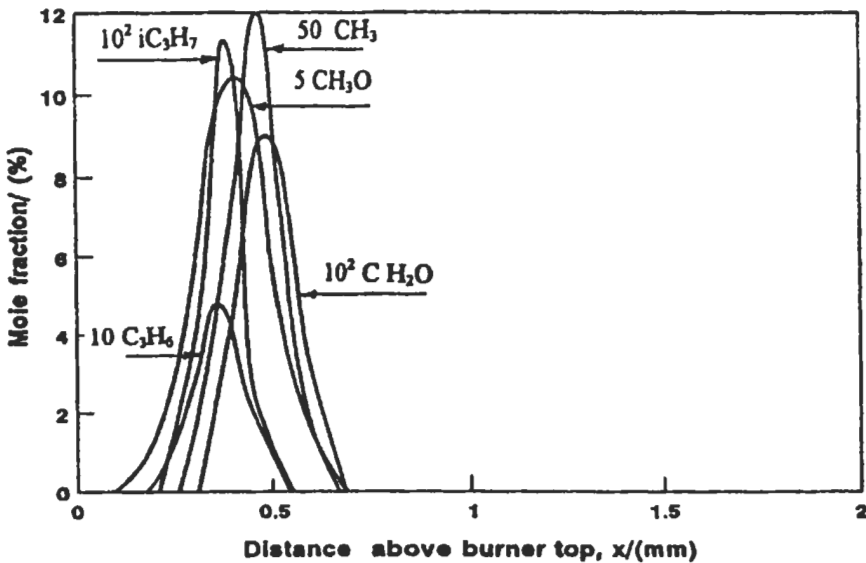


Fig. 2.45(e): Computed mole fraction profiles for C_3H_6 , iC_3H_7 , CH_2O , CH_3O and CH_3 for the same flame conditions as in Fig. 2.45 (a) [207].

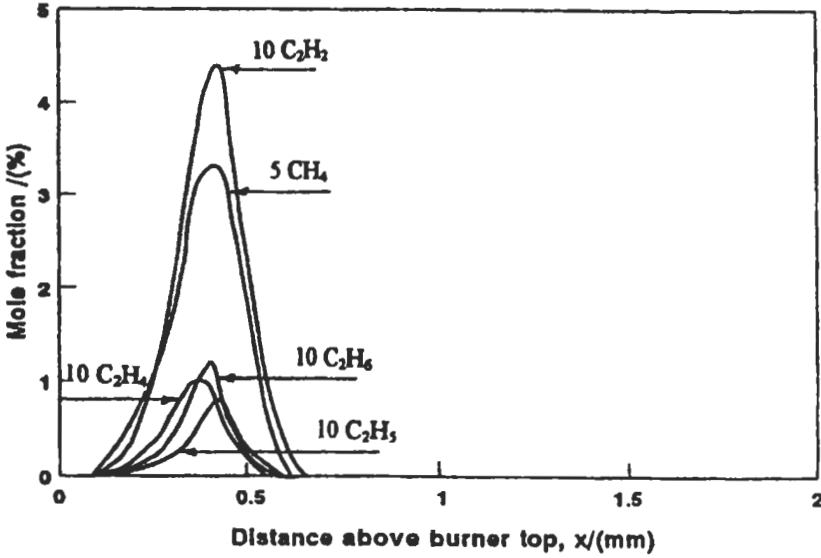


Fig. 2.45(f): Computed mole fraction profiles for CH₄, C₂H₂, C₂H₄, C₂H₅ and C₂H₆ for the same flame conditions as shown in Fig. 2.45 (a) [207].

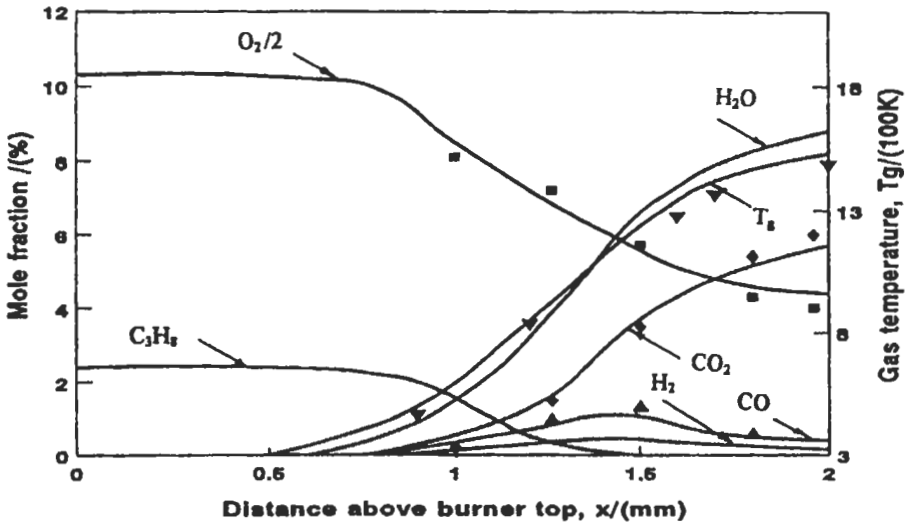


Fig. 2.46: Experimental species and gas temperature (■ O₂, ▲ CO, ◆ CO₂, and ▼ T_g). Full curves are the computed species and gas temperature for propane-air flame at P_u = 1 atm, T_u = 300 K and $\phi = 0.6$ [207].

Rich flame. Figure 2.47 shows the comparison between the computed and experimental results of O₂, CO₂, and CO and gas temperature, and the computed results for H₂ and C₃H₈ versus distance above the burner top. Once again, the agreement

between the experimental and predicted results is good. Also, it could be shown that the maximum mole fractions of CO and H₂ are higher by about 50% than the corresponding values at stoichiometric flames (Fig. 2.45 (a)).

(iii) **Heat release rate.** Figure 2.48 shows the variation of the volumetric heat release rate profiles versus gas temperature for premixed laminar propane-air flames at 1 atm and an initial temperature of 300 K, and equivalence ratios of 0.6, 0.8, 1.0 and 1.2. The maximum heat release rate for different flames occurs at different gas temperatures. The maximum heat release rate for flame at $\phi = 1$ occurs at 1650 K, and is higher than that corresponding value for flame at $\phi = 0.6$. These heat release rates are related to burning velocities or burning rates of the fuel as described in section 2.5.

(vi) **Flammability limits.** Figure 2.49 shows the experimental and calculated maximum flame temperatures for propane-air flames at atmospheric pressure, 300 K and different equivalence ratios. The maximum discrepancy at $\phi = 1$ is about 3%. The blow-out in lean side of the flame occurs at $\phi = 0.47$ and the measured maximum flame temperature just before the flame blow-out is about 1450 ± 20 K. In rich side, the flame blow-out occurs at ϕ of about 2.2 and the measured maximum flame temperature just before the flame blow out is about 1470 K. These limits are shown in Fig. 2.49 by ϕ_r and ϕ_l . At lean limit, the calculated lean limit mixture heat of reaction is found to be $39.8 \text{ kJ mole}^{-1}$ and this value is similar to that suggested by Ref. 289.

(v) **Burning velocity.** The effect of equivalence ratio, pressure and temperature on the burning velocity will be discussed as follows;

Variation of burning velocity with equivalence ratio. Figure 2.50 shows the computed burning velocities, U_b , from the kinetic model at reference conditions (atmospheric pressure, P_0 , initial temperature, $T_u = T_0$, 300 K) and different equivalence ratios. Full and dotted curves are those computed using scheme A₂ and B₂, respectively [20]. Chain dotted and dashed curves were computed from kinetic model by Warnatz [166]

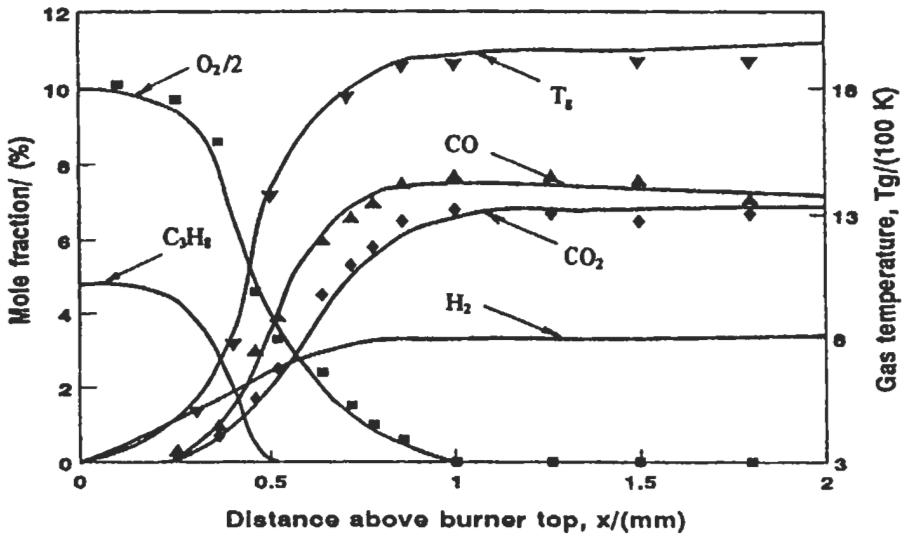


Fig. 2.47: Experimental species and gas temperature (■ O₂, ▲ CO, ◆ CO₂, and ▼ T_g). Full curves are the computed species and gas temperature for propane-air flame at $P_u = 1$ atm, $T_u = 300$ K and $\phi = 1.2$ [207].

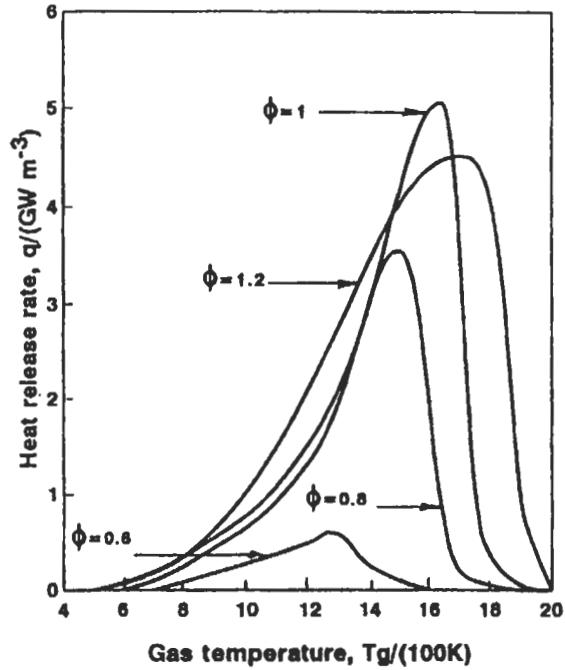


Fig. 2.48: Variation of heat release rate with gas temperature for propane-air flames at $P_u = 1$ atm, $T_u = 300$ K and different equivalence ratios [207].

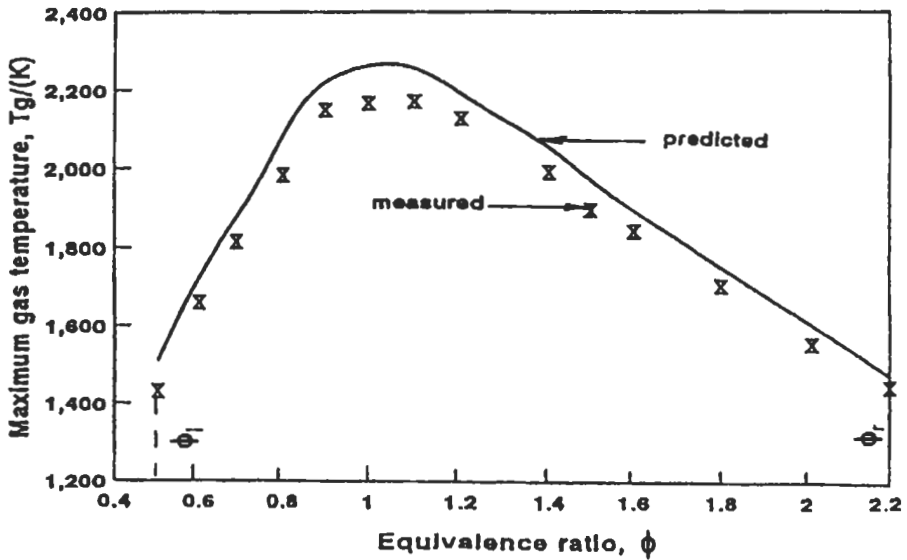


Fig. 2.49: Measured maximum gas temperature for natural gas-air flames at $P_u = 1$ atm and $T_u = 300$ K at different equivalence ratios (0.47 and 2.2 are the lean and rich flammability limits) [207].

and Sloane [206], respectively. Also, experimental burning velocities given by different investigators are shown in the figure. The experimental data in the figure shows that, there is wide spreads in the old experimental data compared to the recent one. This is due to the extensive effort that is expended to determine accurately the burning velocity in recent years. The accuracy of different burning velocity measurement techniques has been discussed by Andrews and Bradley [225]. The comparison between the computed burning velocities [20] using scheme, A₂, and those from other investigators shows that the predicted results [20] are in good agreement with those computed from Sloane [206] and recent experimental values from Refs. 227, 245 and 288. The maximum burning velocity was found to be 0.41 m s⁻¹ and occurring at $\phi = 1.1$. The maximum experimental discrepancy at this ϕ is about 10 %. Scheme, B₂, tends to give low values at different equivalence ratios. This is due to low radical species, O, H, and OH that result in reducing the burning velocity throughout the reaction $\text{H} + \text{O}_2 \leftrightarrow \text{OH} + \text{O}$. The computed burning velocities (full curve in Fig. 2.50) from scheme, A₂, can be correlated (within $\pm 0.01 \text{ m s}^{-1}$) with the equivalence ratio, ϕ , and called U_0 (at standard condition 300 K and 1 atm) by:

$$U_0 = 0.43 \phi^{-0.35} \exp[-4.5 (\phi - 1.1)^2] \quad \text{m s}^{-1} \quad (2.44)$$

Variation of burning velocity with pressure and temperature. Figures 2.51 and 2.52 show the variation of computed ratios of burning velocities, U/U_0 at different pressures and temperatures with equivalence ratios, respectively. The burning velocity, U_1 was computed using scheme, A₂, at different pressures and temperatures for different equivalence ratios.

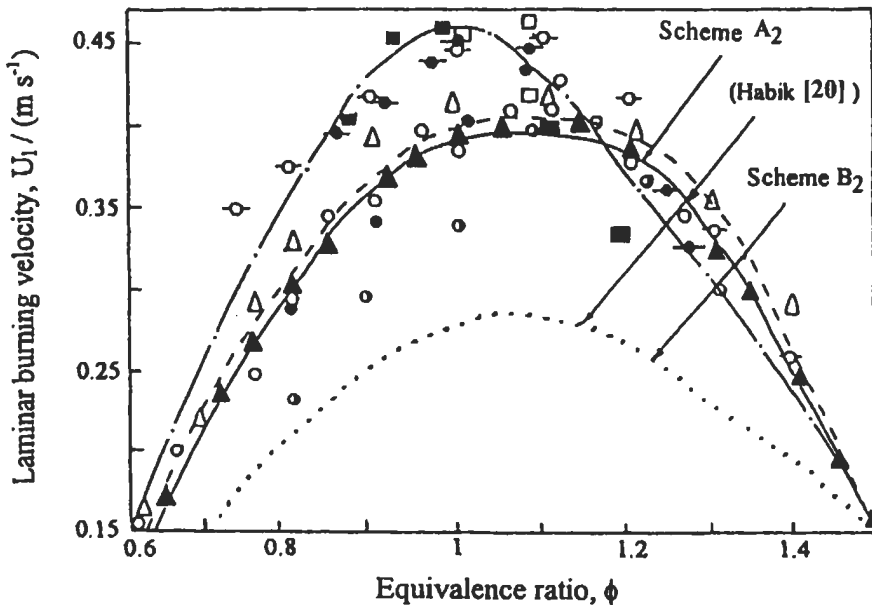


Fig. 2.50: Experimental and computed laminar burning velocity at $P_u = 1 \text{ atm}$ and $T_u = 300 \text{ K}$.
 ●, [285], ○, [245], ---- [206], ◆, [282], △, [227], ○, [270], □, [219], ■, [284], ○, [283],
 --- [166], ○, [287], ▲, [288].

Also, measured ratio, U_f/U_o , of burning velocities given by different investigators are shown by black circle in the figures. For a given pressure or temperature, the ratio of U_f/U_o was found to be the same at different equivalence ratios. Burning velocity, U_o , at different equivalence ratios were computed from Eq. 2.44. At different initial pressures and temperatures, both figures show that the computed [20] and experimental ratios of burning velocity are in agreement within $\pm 5\%$. The computed ratio of burning velocity with initial pressure, P_u (Fig. 2.51) and temperature, T_u (Fig. 2.52) can be correlated by:

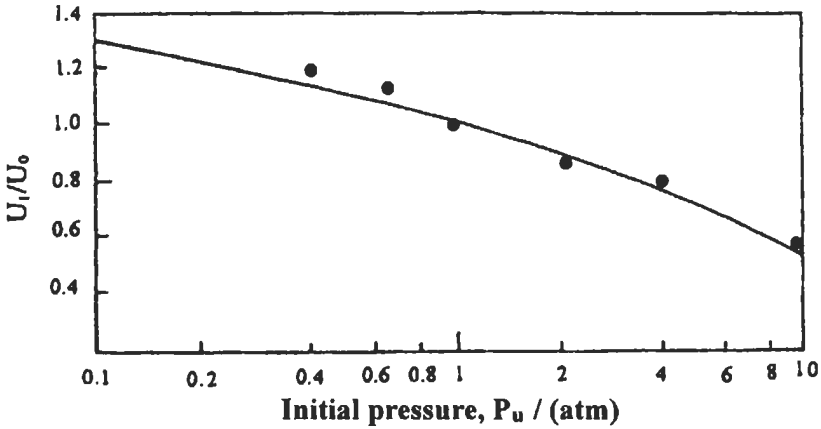


Fig. 2.51: Variation of experimental U_f/U_o (●) [285] and computed U_f/U_o [20] (full curve) for different pressures at $\phi = 0.6, 1.0$ and 1.2 and $T_u = 300$ K. ● is the same for different ϕ .

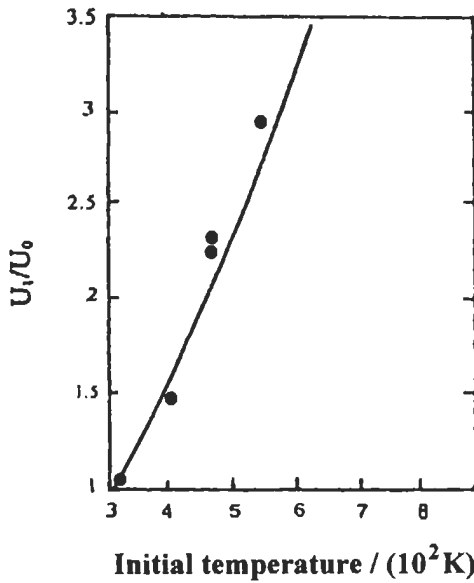


Fig. 2.52: Variation of experimental U_f/U_o (●) [285] and computed U_f/U_o [20] at 1 atm for $\phi = 0.6, 0.8$ and 1.0 and different initial temperatures. Symbol is the same as in Fig. 2.51.

$$U_l/U_o = (T_u/T_o)^{1.7} (P_u/P_o)^{-0.12} \quad \text{for } P_u < 1 \text{ atm} \quad (2.45)$$

$$U_l/U_o = (T_u/T_o)^{1.7} (P_u/P_o)^{-0.25} \quad \text{for } P_u > 1 \text{ atm} \quad (2.46)$$

where U_o is given by Eq. 2.44. These expressions can be used in practical applications and in turbulent modeling [20].

2.4.7 Ethane-Air Flames

Ethane can be broken down by radical species (H, O and OH) to form ethyl radical C_2H_5 through reactions R_{36} to R_{38} in Table 2.4. This ethyl radical is the highest hydrocarbon radical that is thermally stable under flame conditions, but its equilibrium concentrations are negligible except in high-pressure fuel-rich systems. The main subsequent reactions for C_2H_5 are given by R_{39} to R_{50} in Tables 2.4 and 2.5 as explained in section 2.3.4. In rich flames the dominant attack is by H atoms with the O atoms consumed by CH_3 radical and hydrogen, while the attack in lean flames, is dominantly by OH radicals with contributions from O atoms. Water formation is produced from the hydrogen formed by $H + C_2H_6 \leftrightarrow H_2 + C_2H_5$. Also, in lean flames the ethyl radical can be stripped by reaction with H, O, or O_2 (R_{39} to R_{41} in Table 2.4) with the formation of ethylene, C_2H_4 and as a result ethylene chemistry plays an important role in ethane flames. The fast sequence of reactions $C_2H_6 \rightarrow C_2H_5 \rightarrow C_2H_4$, etc makes ethane flames ignites easily as compared with methane and propane flames, while the burning velocity is nearly the same as the methane and propane flames as shown in Fig. 2.53. Since ethyl can recombine with H, CH_3 , and itself to form CH_4 , C_3H_8 , and C_4H_{10} , this requires complex chemistry such as discussed in Tables 2.1 to 2.9.

The first microprobe studies on ethane were made by Fristrom and Westenberg [237]. This was a comparison of lean, low-pressure oxygen C_2H_2 , C_2H_4 , and C_2H_6 flames at matched burning velocities. The next was a study by Fenimore and Jones [290] comparing the attack of ethylene and ethane in flames. The next study was by Singh and Sawyer [291] on the decay of carbon monoxide in comparable ethane

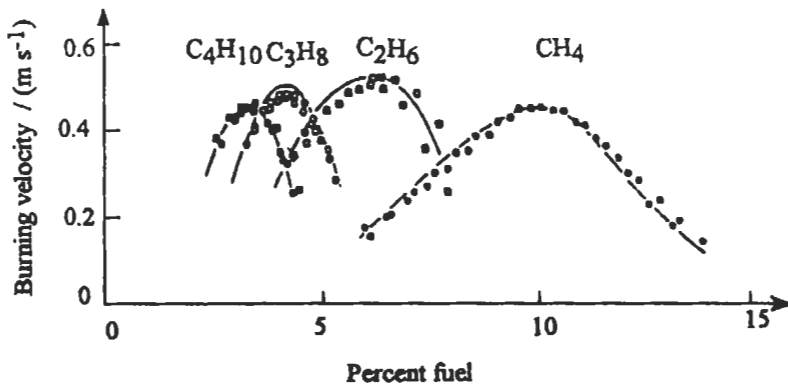


Fig. 2.53: Burning velocities for flames of the lower saturated hydrocarbon-air flames (C1-C4). Experiments by various authors (see Ref. 71). Values corrected as recommended by Günther and Janisch [293]. Lines are calculations by Warnatz [80]. Reproduced by permission of The Combustion Institute.

and ethylene flames. A study by Hennessy et al [292] compared methane and ethane flame chemistry. They used molecular beam sampling coupled with high-resolution mass spectrometry. This allowed resolution of formaldehyde from ethane, ethylene from CO, and their results are shown in Fig. 2.54. They have used 67 reactions to model their experimental for methane and ethane flames. This reproduced the behavior of stable species quite well but showed significant deviations with radicals.

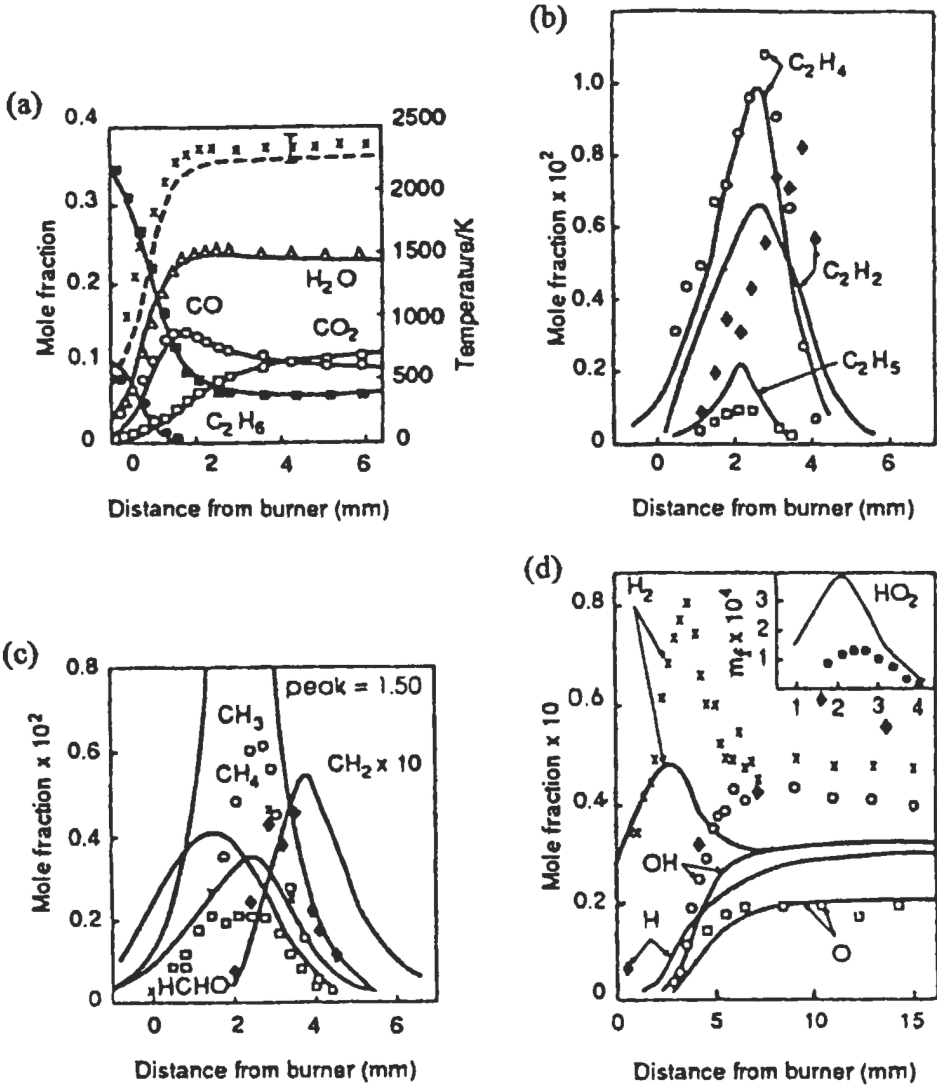


Fig. 2.54: Comparison of experimental structure with detailed modeling of a 20 Torr, ethane 0.118, oxygen 0.415, argon 0.467 flame. (Experiments and modeling by Hennessy et al [292]. Reproduced by permission of The Combustion Institute.

2.4.8 Natural Gas-Air Flames

Technical fuel very often consists of a mixture of several compounds with different physical and chemical properties. A prominent example for a gaseous multicomponent fuel is natural gas. Table 2.14 shows how the composition of natural gas varies from field to field for three fields in Egypt. However, the combustion of natural gas is one of the major sources of energy and a detailed understanding of its combustion behavior is of considerable practical importance. In USA, the natural gas supply industry provides a fuel composition consistent with common uses for natural gas. The local distribution company sells energy in terms of energy content per unit volume of gas, typically 37234 kJ m^{-3} (at 289 K, and 1 atm) as a minimum for most of the country.

While the dominating component of natural gas is always methane (CH_4), the concentrations of additional components vary largely for different sources. The second largest concentration of a reacting species for these sources is ethane (C_2H_6) followed by propane (C_3H_8), and there are large variations of the essentially inert component N_2 . Having discussed in the previous sections the details of the chemical kinetics mechanism and flame characteristic of these individual fuels, it is important for the natural gas to demonstrate how varying levels of these fuels can influence the natural gas characteristics and ignition.

Effect of variations in natural gas composition on the autoignition of natural gas under direct-injection Diesel engine operating conditions were studied experimentally in a constant-volume combustion vessel and computationally using a chemical model (Naber et al [289]). Four fuel blends were investigated: pure methane, a capacity-weighted mean natural gas, a high-ethane-content natural gas, and a natural gas with added propane typical of peak shaving conditions. Experimentally measured ignition delays were the longest for pure methane and became progressively shorter as ethane and propane concentrations are increased. These trends are due to differences in the kinetic processes between methane and high hydrocarbon fuels. In particular, the methyl radical CH_3 , that dominates methane ignition is difficult to oxidize, while alkyl radical, C_2H_5 , produced by high hydrocarbon fuels is easier to be consumed, leading for faster rates of reaction. Measured ignition delays for the four fuels varied from 1.8 ms for the peak shaving and high ethane gases to 2.7 ms for pure methane. Their kinetic model predicts well the measurements of the variations in ignition delay as a function of natural gas composition

Information in the literature about the effect of burning different types of natural gas composition on the emissions, flame structures, burning velocities and flammability limits for laminar premixed flames is lacking. The provision for such information would be beneficial, specially through studying the laminar premixed natural gas flame, since the data thus gained can be extremely useful in the analysis of fundamental processes and design aid.

This section reports measurements of the flame structure and flammability limits for Egyptian natural gas-air laminar premixed flames at atmospheric pressure and room temperature (Habik et al [207]). Explanations of the experimental observations were sought through a developed kinetic model that was described in section 2.3.4. The predicted results were compared well with the experimental data. Another confirmation for the validation of the kinetic model has been done by El-Sherif [18]. She studied the effect of natural gas composition on the nitrogen oxide, flame structure, and burning velocity under laminar premixed flame conditions.

Experimental Method and Results

Flame structure and flammability limits were measured for atmospheric laminar, flat, adiabatic premixed natural gas-air mixtures using the same matrix burner and techniques described in section 2.4.6 and shown in Fig. 2.42 [18, 207]. The actual composition of Egyptian natural gas NG2, is given in the second column in Table 2.15.

Mole fractions of the stable species, CO₂, CO and O₂, and gas temperature profiles were measured as described in section 2.4.6 (Habik et al [207]) at atmospheric pressure, room temperature and equivalence ratios of 1.0, 1.2 and 0.6. These measured values are shown as points and as a function of height above the burner top in Figs. 2.55 (a), 2.56 (a) and Fig. 2.57 (a), respectively. For the preliminary study of flammability limits, the maximum flame temperature was measured at different equivalence ratios and just before the flame blow-out near lean and rich equivalence ratios. Also, El-Sherif [18] has measured the CO, O₂ and gas temperature profiles for laminar premixed flat flame of natural gas (NG2)-air mixture at atmospheric pressure, room temperature and equivalence ratio of 0.5 using similar technique to that described above. These results are also shown in Fig. 2.58 (a). In addition, the maximum mole fraction of carbon monoxide was measured at different equivalence ratios, atmospheric pressure and room temperature. These results are also shown by points in Fig. 2.59 [18]. The measurements of maximum flame temperature were corrected for radiation, and these results are shown in Fig. 2.63 [207].

Computational Results and Discussion

The reactions of scheme, C, and the rate parameters in Tables 2.2 to 2.5 in addition to the transport parameters in Table 2.1 as well as NO_x mechanism in Table 1.23 were used as described in section 2.3.4 to predict the flame structure, burning velocity and

Table 2.14: Composition and heating value of natural gas for three fields in Egypt [18]. Reproduced by permission of Elsevier Science.

	Abu Madi %	Abu Quir %	Abu Ghardig %
Methane	92.766	93.85	83.4-86.4
Ethane	4.117	3.23	10.18-8.13
Propane	1.211	1.22	3.02-0.75
Carbon dioxide	0.688	0.53	2.83-4.00
Nitrogen	0.385	0.17	0.51-0.66
Net heating value, kJ m ⁻³	42212	42208	41630

Table 2.15: Selected natural gas composition [18]. Reproduced by permission of Elsevier Science.

Composition Concentration	NG1 (% vol.)	NG2 (% vol.) Egyptian NG	NG3 (% vol.) Pittsburgh NG	NG4 (% vol.) (CARB)
Methane	100.0	93.80	85.48	88 min.
Ethane (C ₂ H ₆)	0	3.28	13.85	6 max.
Propane(C ₃ H ₈)	0	1.20	0	3 max.
Carbon dioxide(CO ₂)	0	0.53	0	0.0
Nitrogen(N ₂)	0	0.19	0.67	3 max.
The remains	0	1.00	0	0.00

heat release rate for the above experimental conditions. These predicted results are shown in Figs. 2.55 to 2.62 and Figs. 2.64 (a) & (b). Also, Fig. 2.63 shows the computed maximum temperatures at atmospheric pressure and different equivalence ratios. These calculated temperatures were based on an equilibrium program described in chapter 1.

In order to study the effects of natural gas composition on the flame characteristics, four mixtures represent different types of natural gas composition were chosen [18], and these mixtures are shown in Table 2.15. The first column in Table 2.15 is pure methane (NG1) which represents an extreme occurring when LNG is the source delivering a methane content as high as 99.6 % [289]. The second column represents the approximate composition of Egyptian natural gas (NG2) which was used in El-Sherif [18] experimental study. The third column represents the composition of Pittsburgh natural gas (NG3, USA), and the last column represents the composition proposed by California Air Resources Board (NG4, CARB in USA) for natural gas quality standards for commercial and emission certification, and these standards were effective in 1994 to ensure that the natural gas supplied to vehicles is of consistent quality and provides the expected emission benefits. To simplify the complexity of the kinetics involved in the natural gas computations, all the compositions with hydrocarbon higher than C_3 were assumed to be C_2H_6 . With this assumption, and the composition of the natural gas in Table 2.15, the stoichiometric volumetric air-fuel ratios for combustion of NG1, NG2, NG3 and NG4-air mixtures were found to be 10.5, 10.63, 9.51 and 10.54, respectively. These four types of natural gas were used with the developed kinetic scheme, C (see section 2.3.4), to study their effects on the maximum carbon monoxide concentration, flame structure, flammability limits, and burning velocity. These predicted results are shown by dashed, full, dotted-dashed, and dotted curves for NG1, NG2, NG3, and NG4 fuels, respectively. These predicted results are also shown in Figs. 2.58 (a) to 2.60 (b) and 2.62. The results have been obtained using 53 grid points for each flame and 2000 integration steps to reach the steady state. These computed results were performed by El-Sherif [18] and Habik et al [207] using PC machine with 66 MHz (computed time was about 12 hours).

The flame structure, burning velocity, flammability limits and heat release rate will be discussed as follows:

(i) **Flame structure.** Figure 2.55 (a) shows the computed and experimental mole fractions of CO, CO_2 , O_2 , and CH_4 as well as the gas temperature through the Egyptian natural gas (NG2)-air flame at 1 atm, 300 K and $\phi = 1$. It is clear from the figure that, the agreement between both predicted and experimental results is good. This confirms the validation of the kinetic model. The main composition of the Egyptian natural gas is CH_4 and C_2H_6 and the oxidation path for CH_4 fuel includes:



while C_2H_6 includes:



For the same species given in Fig. 2.55 (a), the corresponding net molar rates are shown in Fig. 2.55 (b). Clearly, this figure shows that the methane fuel breaks down, first and is followed by break-down of C_2H_6 . Also, the figure shows that, the position of the maximum positive net molar rates for CO and CO_2 is corresponding to the

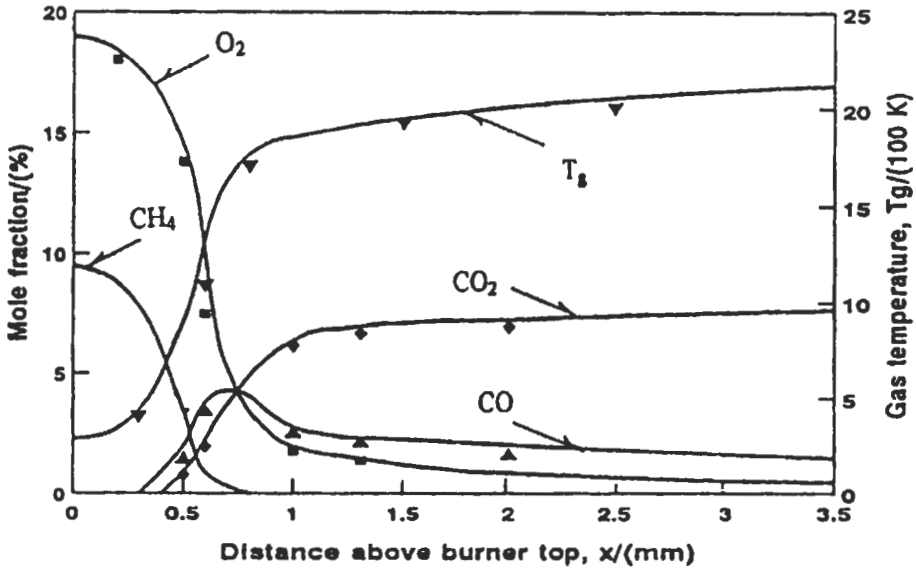


Fig. 2.55(a): Experimental species and gas temperature (\blacksquare O₂, \blacktriangle CO, \blacklozenge CO₂, and \blacktriangledown T_g). Full curves are the computed species and gas temperature for natural gas-air flame at $P = 1$ atm., $T_u = 300$ K and $\phi = 1$ [207].

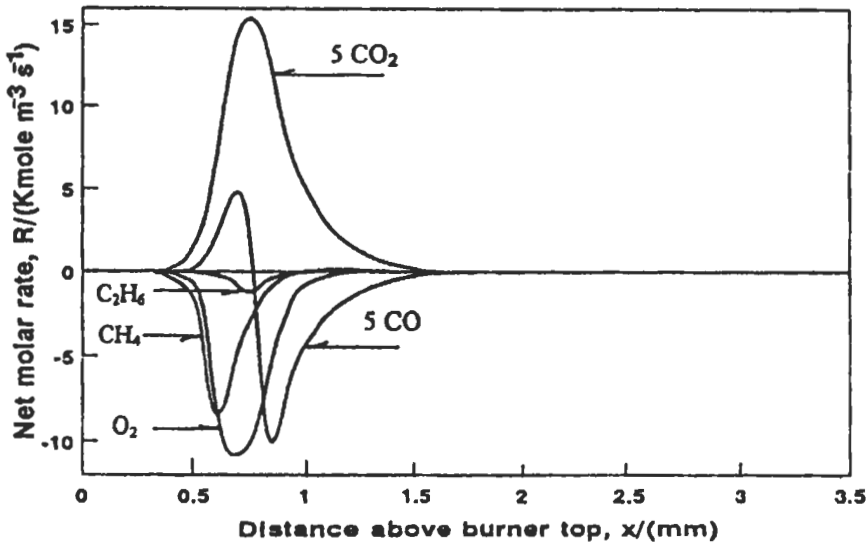


Fig. 2.55(b): Computed molar rate profiles for O₂, CO, CO₂, C₂H₆ and CH₄ for the same flame conditions as shown in Fig. 2.55 (a) [207].

position of the maximum mole fraction of CO, while the position of maximum negative net molar rate of CO is corresponding to the same position of maximum OH (see Figs. 2.56 (a) and (b)), where reaction, R_{14} ($\text{CO} + \text{OH} \rightarrow \text{CO}_2 + \text{H}$) is the major important reaction for producing CO₂ and consuming CO and OH.

Figures 2.56 (a) and 2.57 (a) show the computed and experimental profiles of CO, CO₂, O₂, CH₄ as well as gas temperature for natural gas-air flames at atmospheric pressure, 300 K and equivalence ratios of 1.2 and 0.6, respectively.

Again, the agreement between both computed and experimental results is good. The maximum discrepancy between the experimental and predicted values is about 3 %. The behavior of these species can be explained kinetically by the same way as described above and in section 2.4.3. The corresponding computed mole fractions of H, O, OH, HO₂, and CH₃ are shown in Figs. 2.56 (b) and 2.57 (b).

The effect of natural gas composition on the flame structure is shown in Figs. 2.58 (a), (b) and 2.59. Figure 2.58 (a) shows the discrepancies in CO, CO₂, H₂, O₂, CH₄ and C₂H₆ concentrations and gas temperature throughout the flame for both NG2-air and NG4-air flames near the lean limit of $\phi = 0.5$, $T_u = 300$ K and $P_u = 1$ atm. The agreement between the computed (full curves) and experimental results is good for Egyptian natural gas (NG2). This confirmed again the validation of the kinetic model. The figure also shows an increase in CO, CO₂, H₂ concentrations and T_g as well as a decrease in O₂ concentration for NG4-air flame (dotted curves) as compared to the corresponding values for NG2-air flames (full curves). This is due to high concentration of C₂H₆ in the mixture of the natural gas (NG4) and this consequently leads to difference in the kinetic processes.

For the same flames as in Fig. 2.58 (a), the corresponding radical species, O, H, OH, CH₃, C₂H₅ and N concentrations are shown in Fig. 2.58 (b). It appears from the figure that, as the concentration of C₂H₆ increases in the natural gas composition from 3.28 % (NG2) to 6 % (NG4), then the radical species, O, H, and OH will increase by a factor of about two, and this is due to an increase in CH₃ and C₂H₅ concentrations by factors of 30 and 100 %, respectively. For stoichiometric NG2-air and NG4-air flames at 1 atm, 300 K, there is a slight difference between the above mentioned species. Figure 2.59

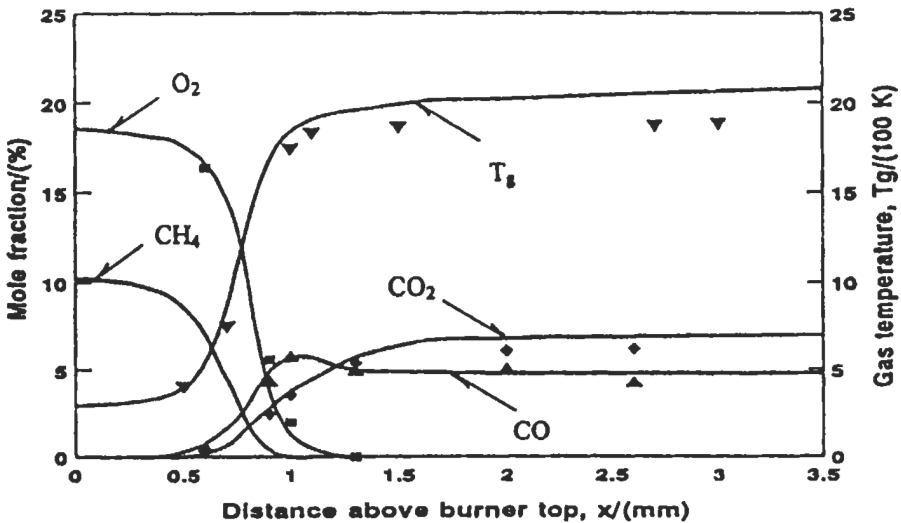


Fig. 2.56(a): Experimental species and gas temperature (■ O₂, ▲ CO, ◆ CO₂, and ▼ T_g). Full curves are the computed species and gas temperature for natural gas-air flame at $P = 1$ atm., $T_u = 300$ K and $\phi = 1.2$ [207].

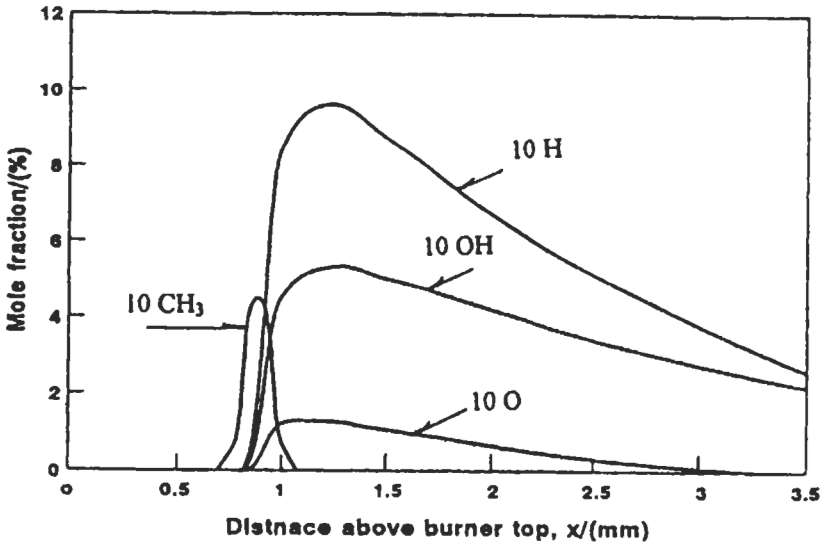


Fig. 2.56(b): Computed mole fraction profiles for radical species of H, OH, O and CH₃ for the same flame conditions as shown in Fig. 2.56 (a) [207].

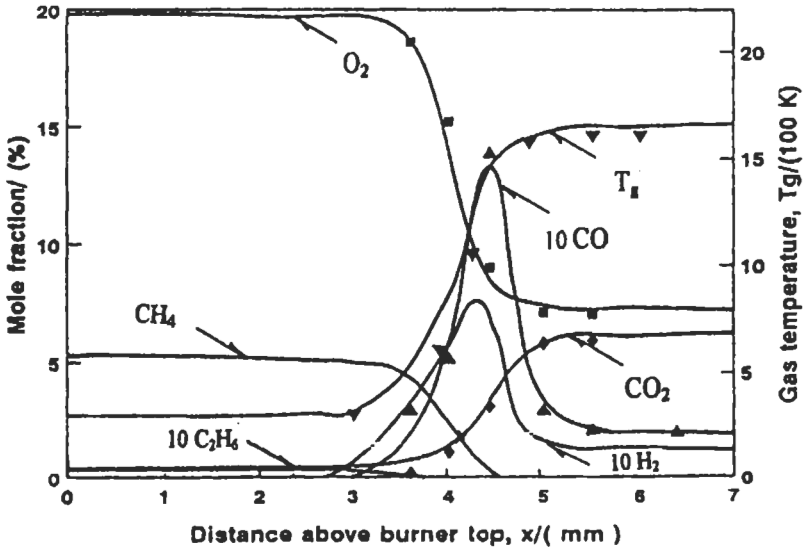


Fig. 2.57(a): Experimental species and gas temperature (■ O₂, ▲ CO, ◆ CO₂, and ▼ T_g). Full curves are the computed species and gas temperature for natural gas-air flame at P = 1 atm., T_u = 300 K and $\phi = 0.6$ [207].

shows the variation of experimental (NG2) and predicted (NG1 to NG4) maximum mole fractions of CO and CHO with the equivalence ratio. There is a good agreement between the computed and experimental results, and both results show that the CO increases with ϕ . In lean flames, the main important reaction for CO

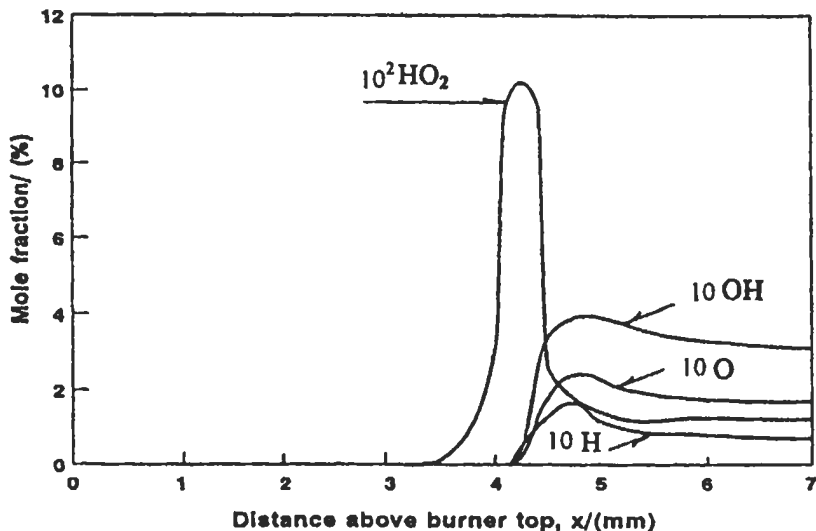


Fig. 2.57(b): Computed mole fraction profiles for radical species of H, OH, O and HO₂ for the same flame conditions as shown in Fig. 2.57 (a) [207].

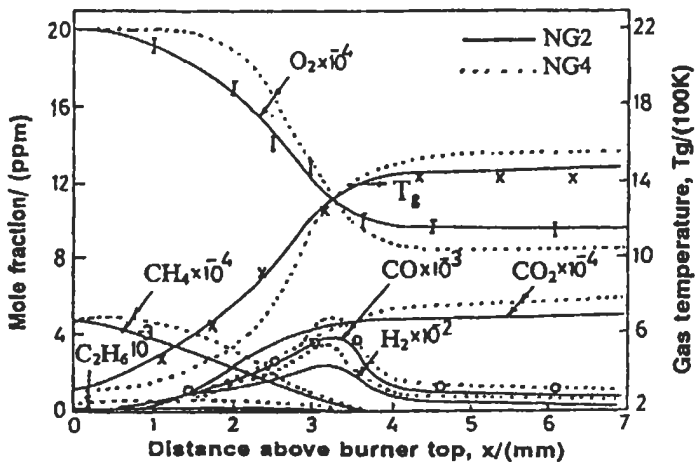


Fig. 2.58(a): Experimental, O_2 , CO species, T_g for NG2-air flame, NG4-air flame and computed profiles of O_2 , CO , CO_2 , H_2 , CH_4 , C_2H_6 and T_g at $P_u = 1$ atm, $T_u = 300$ K and $\phi = 0.5$ [18]. Reproduced by permission of Elsevier Science.

formation is R_{17} ($\text{CHO} + \text{O}_2 \leftrightarrow \text{HO}_2 + \text{CO}$), where CHO increases with ϕ until it reaches its maximum value at $\phi = 1$, and then decreases. For rich flames, the predominant reaction for CO formation is R_{18} ($\text{CHO} + \text{H} \leftrightarrow \text{H}_2 + \text{CO}$) where H is higher than O, OH and CHO.

The effect of natural gas composition on the CO concentration is evident at very lean flame, where $\phi = 0.5$. Again, as the concentration of C_2H_6 in the natural gas

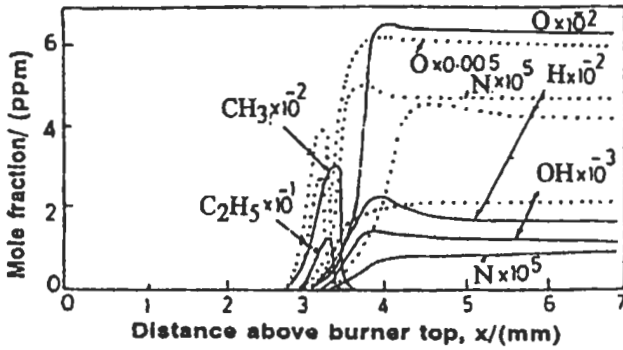


Fig. 2.58(b): Computed mole fraction of N, O, H, OH, CH₃ and C₂H₅ vs. distance above burner top for the same flame conditions as in Fig. 2.58 (a) [18]. Reproduced by permission of Elsevier Science.

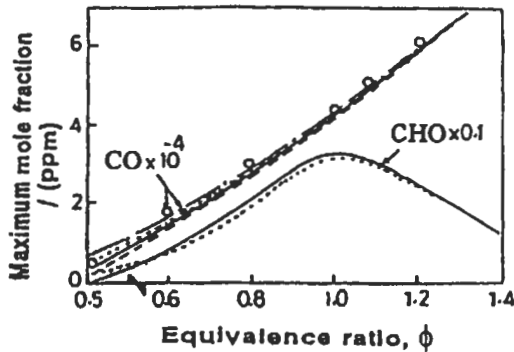


Fig. 2.59: Experimental CO species (O), for NG2-air flame, NG4-air flame and computed mole fractions of CO & CHO with ϕ at 1 atm and 300 K [18]. Dotted and full curves are the same as in Fig. 2.58 (a). Reproduced by permission of Elsevier Science.

increases, then the mole fraction of CO increases. This is due to higher mole fractions of CHO. For example, at $\phi = 0.5$, the mole fractions of CHO for NG2 and NG4 flames are 0.85 and 1.9 ppm, respectively, and this leads to an increase in the mole fraction of CO from 3588 to 4964 ppm, respectively. The mole fraction of C₂H₄, C₂H₅ and CH₃ increase at $\phi = 0.5$ by 45 %, 100 % and 30 %, respectively, compared to their corresponding values at $\phi = 0.6$. These species are important for the formation of CHO species in the flame reaction zone.

The kinetic modeling clearly demonstrates the promoting effect of ethane on methane oxidation by earlier production of H atoms. In this case the production of C₂H₅ radicals is an important step since this species rapidly produces H atoms. Methane consumption is then obtained at much lower temperature than observed for pure methane oxidation in the same condition.

(ii) **Burning velocity.** To further confirm the predicted results, the laminar burning velocities for NG3-air flames were predicted and compared with those measured by Johnston [294] in Fig. 2.60 (a) at different ϕ , $P_u = 1$ atm and $T_u = 331$ K. The agreement between the predicted and experimental results is reasonable, and this

confirms the validity of the kinetic model. Also, shown in the same figure is the predicted burning velocity for the Pittsburgh natural gas-air flame at $P_u = 1$ atm and $T_u = 300$ K. The maximum burning velocity occurs at about $\phi = 1.1$. However, the results show that an increase in the initial temperature by 31°C leads to an increase in the laminar burning velocity by about 16 %. Figure 2.60 (b) shows the variation of computed burning velocity with ϕ for NG1, NG2 and NG4-air flames at $P_u = 1$ atm, $T_u = 300$ K. Also, shown in the same figure are the calculated adiabatic flame temperatures for NG1 fuel. For a range of ϕ from 0.6 to 1.6, and as the concentration of C_2H_6 increases in the composition of the natural gas (NG1 to NG4), the burning velocity decreases slightly, while, in lean flames, where $\phi < 0.6$, the burning velocity increases. This is due to the increase of C_2H_5 and CH_3 radicals and consequential increase of O, H, and OH species which accelerate the combustion process leading to an increase for burning velocity throughout the reaction $\text{R}_2 (\text{O}_2 + \text{H} \leftrightarrow \text{O} + \text{OH})$. This leads to an increase in the lean flammability limit for NG2 to be $\phi = 0.48$ compared to $\phi = 0.5$ for NG1 fuel. The maximum burning velocity for Egyptian natural gas was found to be 0.36 m s^{-1} and occurring at $\phi = 1.1$. The predicted burning velocities for Egyptian natural gas-air flame were correlated at a reference condition of 300 K, 1 atm and different ϕ by:

$$U_l = 0.37 \phi^{-0.35} \exp [-5 (\phi - 1.1)^2] \quad \text{m s}^{-1} \quad (2.47 \text{ a})$$

Burning velocities of SNG mixtures with air were measured by Haniff et al [295] in a stationary flat flame on a burner at atmospheric pressure and 300 K by means of a particle-tracking method. The SNG mixtures were CH_4/H_2 and $\text{CH}_4/\text{H}_2/\text{C}_3\text{H}_8$, with H_2 contents up to 40 % mol and propane contents up to 19 % mol (mole fraction). Their results show that the maximum burning velocity as a function of hydrogen content can be replaced by:

$$U_l = 0.4285 + 0.001192 [\text{H}_2] + 0.000134 [\text{H}_2]^2 \quad \text{m s}^{-1} \quad (2.47 \text{ b})$$

where $[\text{H}_2]$ is the mol % hydrogen in fuel (H_2 from 0 to 38 %).

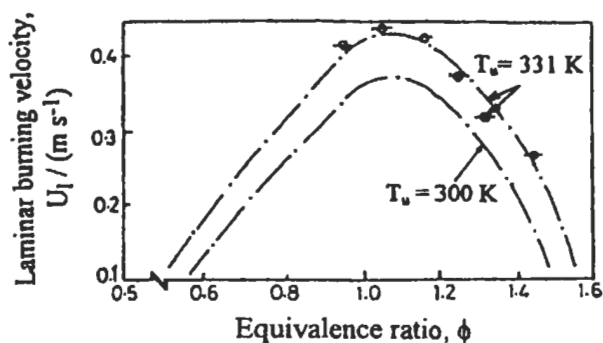


Fig. 2.60(a): Experimental, \ominus [296] and computed burning velocity with equivalence ratio for Pittsburgh natural gas (NG3)-air flame at $P_u = 1$ atm, $T_u = 331$ K and 300 K [18]. Reproduced by permission of Elsevier Science.

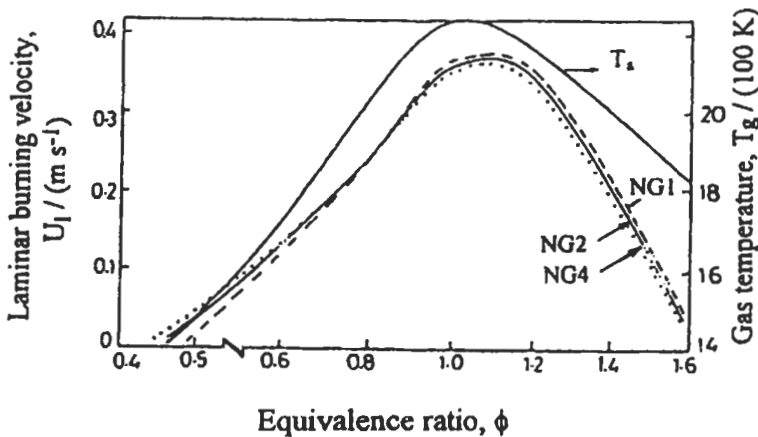


Fig. 2.60(b): Variation of computed burning velocity and adiabatic temperature with equivalence ratio for NG1, NG2, and NG4-air flames at $P_u = 1$ atm, and $T_u = 300$ K [18]. Reproduced by permission of Elsevier Science.

(iii) **Heat release rate.** Heat release rate-temperature profiles are important in laminar flamelet models of turbulent combustion as discussed before. Therefore, such profiles are shown in Figs. 2.61 (a) to 2.62. Figure 2.61 (a) shows the computed heat release rate for stable species of CO, CO₂, O₂, H₂O, H₂ and CH₄ versus gas temperature for the same flame as in Fig. 2.55 (a), and these values are shown by full curves, while the summation of all stable species is shown by dashed curve. The heat release rate for H₂O is the highest one; followed by O₂, CO₂, CO, CH₄ and H₂. Figure 2.61 (b) shows the computed heat release rates for radical species of H, O, OH, CH₃ and CH₃O for the same flame as in Fig. 2.55 (a). These results are shown by full and dashed curves. The summation of the total heat release rate for the stable and radical species is shown by full curve in Fig. 2.61 (c) and compared with that of total heat release rate of stable species (dashed curve in Fig. 2.61 (a)) and that for radical species (full curve in Fig. 2.61 (b)). It is clear from the figure that the heat release rate of stable species represents about 68 % of the total heat release; while for radical species it represents about 32 % of the total heat release rate. This indicates the importance of heat release rate from the radical species. The effect of natural gas composition on the heat release rate is shown in Fig. 2.62 for three equivalence ratios, and NG1 and NG2. At $\phi = 1$, the heat release rate for NG2 fuel decreases slightly than that for NG1 and its peak occurs at about 1640 K; while for $\phi = 0.6$, its peak occurs at 1440 K. For NG1 and NG2-air flames, the effects of natural gas composition on the heat release is clear at $\phi = 0.5$. The maximum heat release rate for NG2 fuel increases by about twice than that for NG1 fuel. Again as discussed above, this is due to an increase of the C₂H₆ in the natural gas composition and consequently an increase of C₂H₅ and H atom.

(iv) **Flammability limits.** Figure 2.63 shows the experimental and calculated maximum flame temperatures for natural gas (NG2)-air mixtures at atmospheric pressure, 300 K and different equivalence ratios. The maximum discrepancy at $\phi = 1$ is about 3 %. The blow-out in lean side of the flame occurs at $\phi_L = 0.48$ and this is corresponding to adiabatic flame temperature of 1420 ± 20 K, and also corresponds to

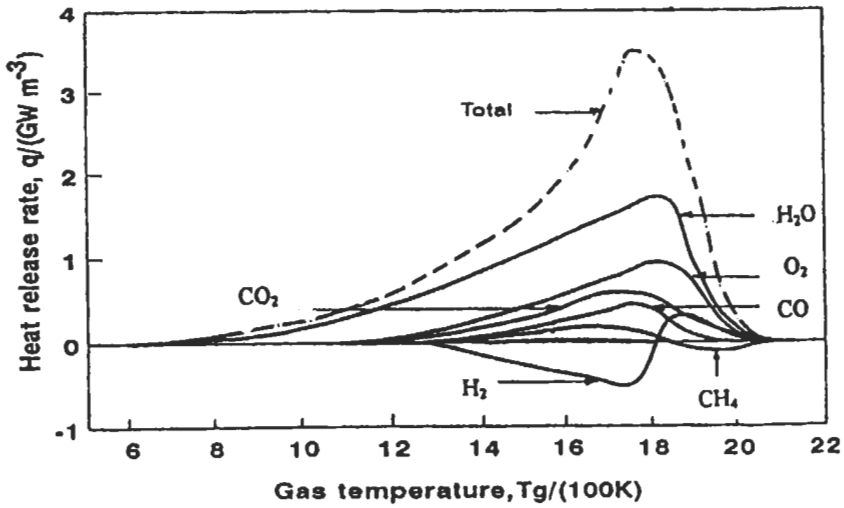


Fig. 2.61(a): Variation of computed heat release rates of O_2 , CO , CO_2 , CH_4 , H_2 and H_2O with temperature for the same flame conditions as shown in Fig. 2.55 (a) [207].

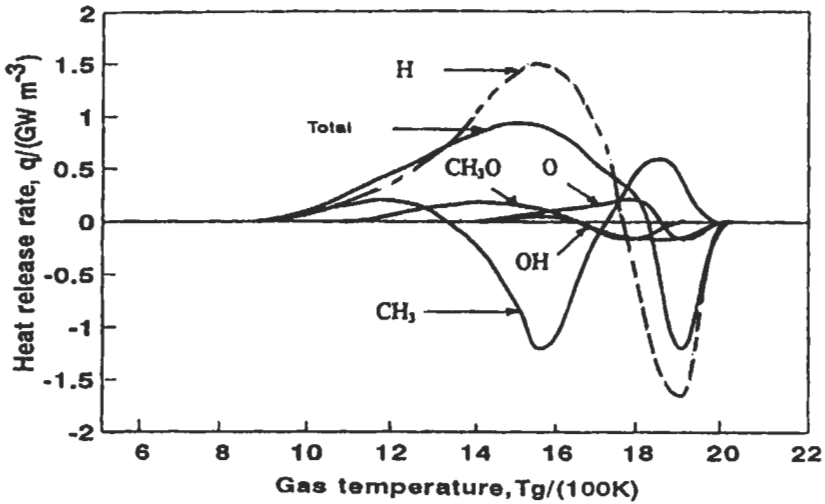


Fig. 2.61(b): Variation of computed heat release rates of H , OH , O , CH_3O and CH_3 with temperature for the same flame conditions as shown in Fig. 2.55 (a) [207].

the lean limit mixture heat of reaction of 41 kJ mole^{-1} . This value is within the limit of $42\text{-}54 \text{ kJ mole}^{-1}$ of flammable mixture, which suggested by Burgess and Hertzberg [296]. This confirms further that the lean limit of natural gas occurs at about $\phi_L = 0.48$ which is less than the corresponding value for CH_4 -air flame. In rich side, the flame blow-out at $\phi_R = 1.8$ and this is corresponding to an adiabatic flame temperature of about 1450 K . These limits are shown in the figure by ϕ_L and ϕ_R . This narrow range

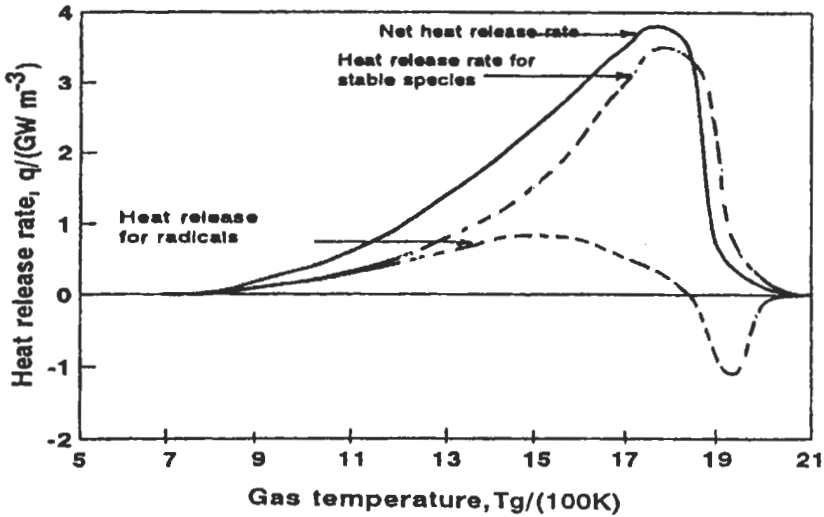


Fig. 2.61(c): Variation of computed net heat release rate with temperature for natural gas-air flame at the same flame conditions as shown in Fig. 2.55 (a) [207].

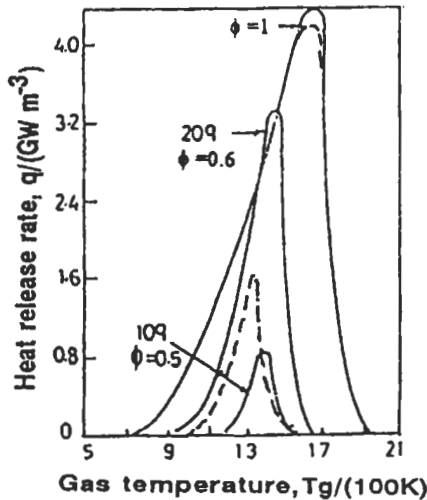


Fig. 2.62: Comparison between computed heat release rates for NG1 (dashed curves) and NG2 (full curves) at $P_u = 1$ atm, $T_u = 300$ K and $\phi = 0.5, 0.6,$ and 1.0 [18]. Reproduced by permission of Elsevier Science.

of flammability limits for natural gas compared to other fuels such as propane indicated that the natural gas is more safe than other fuels to probable accidental combustion.

(v) **Effects of natural gas composition on the nitrogen oxide.** Figures 2.64 (a) and (b) show the computed [18] variation of maximum mole fractions for NO_x , NO ,

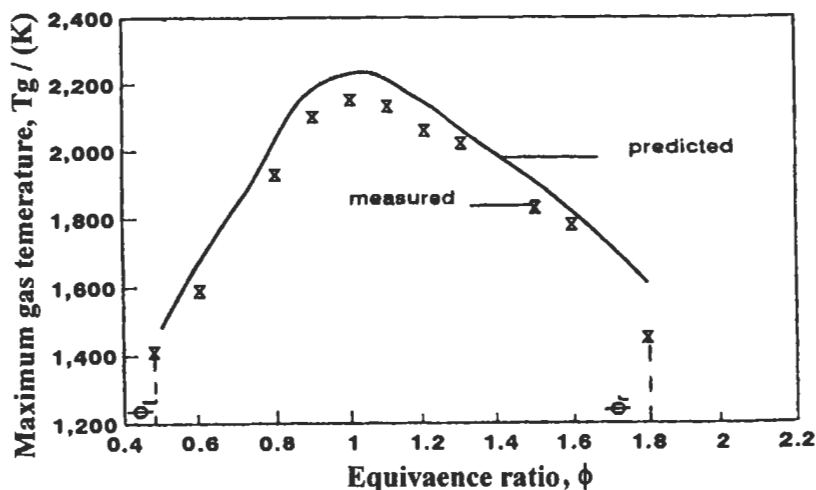


Fig. 2.63: Measured maximum gas temperature for natural gas-air flame at $P = 1$ and $T_u = 300$ K at different equivalence ratios (0.48 and 1.8 are the lean and rich flammability limits) [207].

NO_2 , N_2O , and N with ϕ for different types of natural gas (Table 2.15). Figure 2.64 (a) shows that the mole fractions of NO , NO_x and N increase with ϕ , until they reach their maximum values at $\phi = 1$, and then they decrease in rich flames. This is consistent with the profiles of radical species, O , H and OH shown in Fig. 2.58 (b). These radical species as well as the adiabatic flame temperature are important in producing and consuming NO , NO_2 , and N species throughout reactions, R_1 to R_{20} (Table 1.9). For Egyptian natural gas-air mixture, the experimental and computed results of NO_x are in general agreement within maximum discrepancy of about 11 % at $\phi = 1$.

Figure 2.64 (b) shows that the mole fraction of N_2O decreases as ϕ increases. This is due to reaction, R_6 in lean flames, followed by reaction, R_9 in rich flames (Table 1.9). However, in lean flames, the concentrations of radical species, O and H increase with ϕ , while in rich flame O atom decreases rapidly compared to H atom. Also, Fig. 2.64 (b) shows that the mole fraction of hydroperoxyl, HO_2 increases by a factor of 2.5 for $\phi = 0.5$ to 1, while in rich flame, there is a very small increase. This radical species is very important in lean flames for producing NO_2 through reaction, R_4 , this in addition to reaction, R_5 (Table 1.9). The effect of these reactions (R_4 to R_5) becomes less in rich flames where O and HO_2 radicals decrease at post flame. This explained the reason for the increase and decrease of NO_2 in lean and rich flames at $\phi = 0.6$ to 1.5.

The effects of natural gas composition on NO_x , NO and NO_2 are evident in Figs. 2.64 (a) and (b), especially in very lean flame. As the concentration of C_2H_6 increases in the natural gas mixture (NG3 and NG4 in Table 2.15), and for a given ϕ (ϕ between 0.6 to 1) the NO_x , NO and NO_2 increase slightly, while at $\phi = 0.5$, the NO_x increases rapidly compared to that at $\phi = 0.6$. This latter increase is due to the increase of N_2O , HO_2 , and N_2 concentrations. For the range of ϕ from 0.47 to 0.6, the mole fractions of NO_x , NO and NO_2 increase rapidly as the mole fraction of C_2H_6 in the NG3 and NG4 fuels increases. This is due to reactions, R_4 and R_8 (Table 1.9). At $\phi = 0.5$, the rate of formation for NO_2 (R_4) is higher than the rate of its consumption (R_5); while at $\phi = 0.6$, the rate of consumption of NO_2 (R_5) is higher than the rate of its formation (R_4).

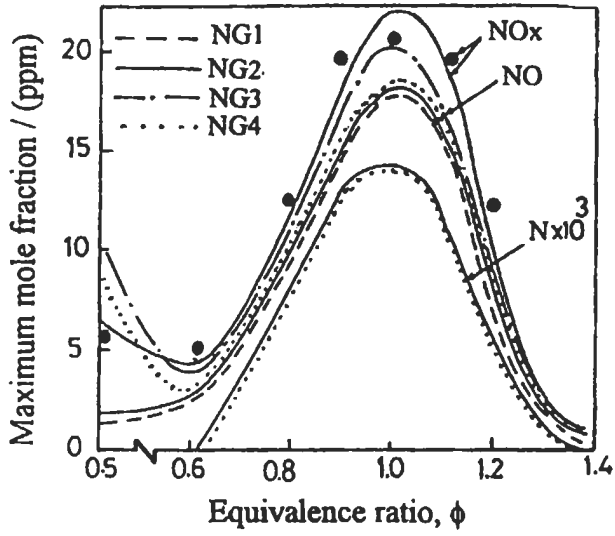


Fig. 2.64(a): Experimental, $\bullet \text{NO}_x$ for NG2-air flames and computed mole fractions of NO_x , NO and N with ϕ at $P_u = 1$ atm, and $T_u = 300\text{K}$ [18]. Reproduced by permission of Elsevier Science.

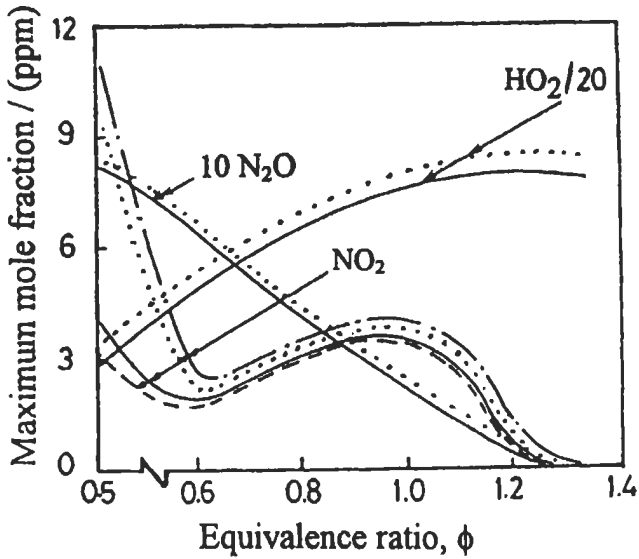


Fig. 2.64(b): Computed maximum mole fractions of N_2O , HO_2 and NO_2 with ϕ for the same flame as in Fig. 2.64 (a) [18]. Reproduced by permission of Elsevier Science.

2.5 Generalization of Flame Characteristics

2.5.1 Laminar Burning Velocity

The maximum measured values of burning velocities of gaseous and liquid fuels with air are surveyed. A degree of generalization of these values is suggested in terms of the chemical structure of the fuel. It is also shown that for lean mixtures and different classes of gaseous and liquid fuels, the burning velocity varies approximately linearly with the heat of reaction of a mole of the premixture. The classical expressions for laminar burning velocity help to explain the relationship observed between both the integral of the normalized computed volumetric heat release rate, q (with respect to fractional temperature increases and the position of the centroid of this integral, θ_c) and the product of the molar heat of reaction, and the burning velocity. A generalized correlation is shown to exist between the burning velocity eigenvalue, and θ_c . Moreover, an algebraic expression is suggested, in terms of two variables, for the profile of the normalized heat release rate against the fractional temperature increase. Finally, an algebraic expression is proposed for the burning velocity for alkanes fuels in terms of initial pressure, temperature, water content (in methanol), and heat of reaction.

General Background

The rate of laminar burning of premixtures are expressed by the physical and chemical parameters of both the laminar burning velocity, U_l , and the profile of volumetric heat release rate against temperature. The two are interrelated in the classical theories of laminar burning velocity, and also in the more recent chemical kinetics computations of flame structure. Furthermore, the importance of these parameters extends into the regime of turbulent combustion, through the application of laminar flamelet concepts to turbulent burning velocities and turbulent heat release rates.

Practical combustion involves a variety of fuels burning under different conditions. Furthermore, the laminar burning velocities and heat release rates are not always known. Sections 2.3.4 and 2.4.1 to 2.4.8 show how the chemical kinetics are complex to predict these parameters specially for high hydrocarbon fuels, and the need for obtaining general correlations of these parameters to be used in practical applications and turbulent complex models.

The purpose of this section is to attempt the maximum generalization of the available laminar burning velocity data for lean to stoichiometric fuel-air mixtures. Such a generalization of burning velocities provides the basis for one of the heat release rate-temperature profiles.

First, maximum burning velocities under atmospheric conditions of a variety of gaseous and liquid hydrocarbon, alcohol, and hydrogen-air mixtures are surveyed. These show that the burning velocities of lean mixtures of alkanes, alcohols, olefines, and hydrogen can be correlated, for each category of fuel, with the heat of reaction of a kmole of the original mixture, Q . It is also shown, with rather more theoretical justification, that for a particular fuel the area under the dimensionless heat release rate-temperature profile and the location of the centroid of that area correlate with QU_l . If a two-variable mathematical form is assumed for the heat release rate-temperature

relationship, then that expression can be generated explicitly from the product QU_1 for different fuels.

Review of Burning Velocity Data

There are much data in sections 2.4.3-2.4.8 as well as in the literature on the burning velocities of gaseous fuels with air, but rather less on liquid fuels. The different measurement techniques that have been used to measure U_1 have been discussed briefly in sections 2.2.4 and 2.4.1 to 2.4.8, and were summarized and described in details by Andrews and Bradley [225]. They also gave maximum values, U_{\max} , for the more common gaseous fuels. The values of U_{\max} for methane-air flame which were obtained by different investigators are selected and shown in Fig. 2.65. The figure is taken partly from Ref. 225 and then updated to include some recent data that measured through 1972 to 1990. However, in spite of the extensive effort expended to accurately determine their values (especially those of the conventional hydrocarbon-air mixture), wide systematic spreads in the reported experimental data still exist [297-346]. In recent years, the spreads became much less, where the experiments appear to have been carefully executed [44, 153, 176, 224-246].

Bradley et al [45] have reviewed the maximum burning velocities for liquid-air mixture [152, 161, 162, 188, 217, 237, 270-275, 305, 316, 346-364]. They suggested a general correlation between U_1 and q with Q . The maximum values of the laminar burning velocities of various liquid fuels with air at 1 atm and 300 K are shown in Figs. 2.66 (a) to (d), as categorized in terms of the molecular structures. Some predicted values from chemical kinetic models are also given in these figures. The numbers on the figures are those of the references.

The figures reveal those values of maximum burning velocities ranging from 0.3 to 0.8 m s⁻¹. Examination of the data for generalized trends shows that the maximum burning velocities of alkanes and aromatics to be similar, but somewhat less than those of alkenes and alkyl alcohols. Alkyl oxides have significantly higher burning velocities than their parent alkenes, whereas the nitrogen compounds and chloro alkanes have the lowest burning velocities.

General Correlations of Burning Velocity

(i) **Correlation of burning velocities with molar heat of reaction.** In the quest for generalization, earlier workers have correlated burning velocities with the adiabatic temperature of the mixture [365, 366]. Here, a somewhat more convenient correlation with the heat of reaction of a kmole of mixture is proposed. The correlation covers not only liquid but also gaseous fuels, which are not tabulated in Figs. 2.66 (a) to (d).

The heat of reaction, Q , is defined here as the difference between the enthalpy of the products and the enthalpy of 1 kmole of the initial mixture for complete combustion at a given temperature and pressure. Thus:

$$Q = H_P - H_R$$

$$Q = \sum_P n(h_f + \Delta h) - \sum_R n(h_f + \Delta h) \quad (2.48)$$

where, the subscripts R and P refer to the reactants and products, respectively, n is the number of kilo moles, and h_f is the enthalpy of formation at 298 K at 1 atm. The lower heating value is used with H₂O vapor in the products.

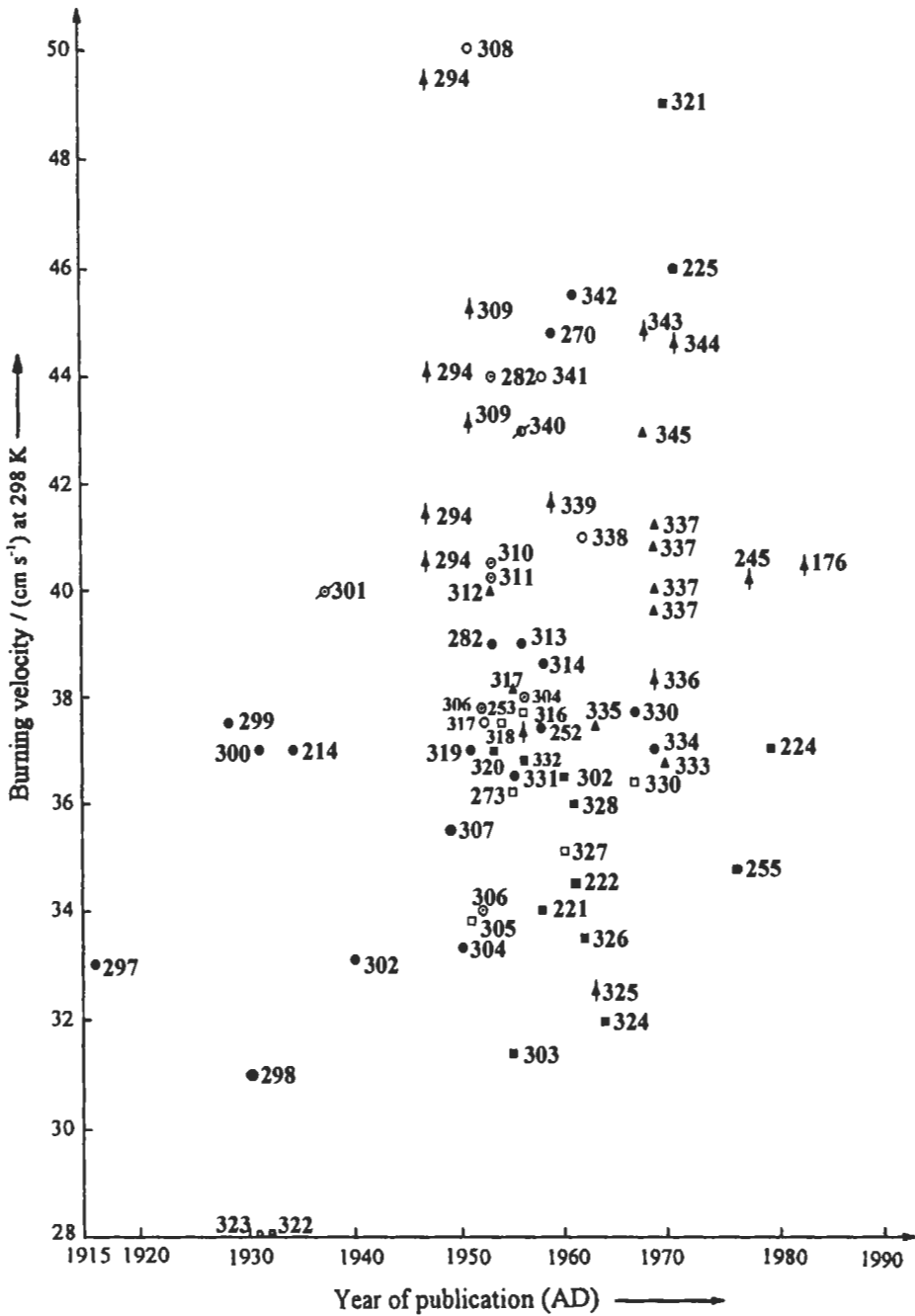


Fig. 2.65: Maximum burning velocities for methane-air, at 1 atm and $T_u = 300$ K [225]. Reproduced by permission of Elsevier Science.

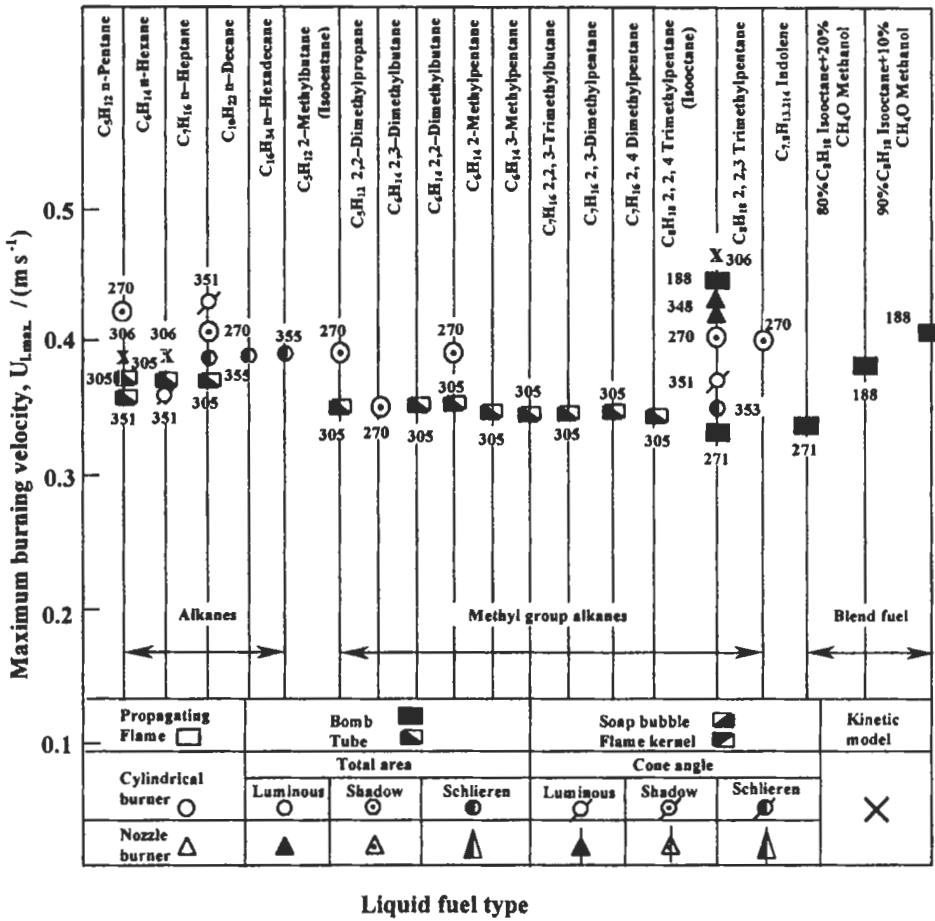


Fig. 2.66 (a): Measured and computed maximum burning velocities of liquid fuels at 1 atm, and 300 K [45]. Reproduced by permission of Elsevier Science.

Usually, heat of reaction is expressed per unit mass or per kmole of fuel. Here, the mixture heat of reaction, Q , is expressed from JANAF data per kilo mole of reactants, at 1 atm and 298 K: for product gaseous CO_2 , $h_f = -393,522$ kJ kmole⁻¹, and for product H_2O vapor, $h_f = -241,827$ kJ kmole⁻¹ [13]. Heat of formation of most of the liquid and gaseous fuels were taken from Ref. 12, except for C_3H_4 and C_5H_{10} , where values were taken from Refs. 14 and 25, respectively.

Because it is difficult to estimate accurately the heat of reaction for rich flames, and because of the increasing complexity of chemical kinetics for such flames as the equivalence ratio increases, only heat of reaction of different fuels for equivalence ratios between 0.6 and 1.0 are presented. These values and their corresponding burning velocities for different fuel-air mixtures are shown for an initial temperature of 300 K in Fig. 2.67.

Figure 2.67 further confirms the way in which the fuels fall into different families, or categories. The straight lines A_1 , A_2 and A_3 are computed for pressures of 0.1, 1, and 10 atm., respectively, from the kinetic models for CH_4 [152, 153, 156] and CH_3OH -air

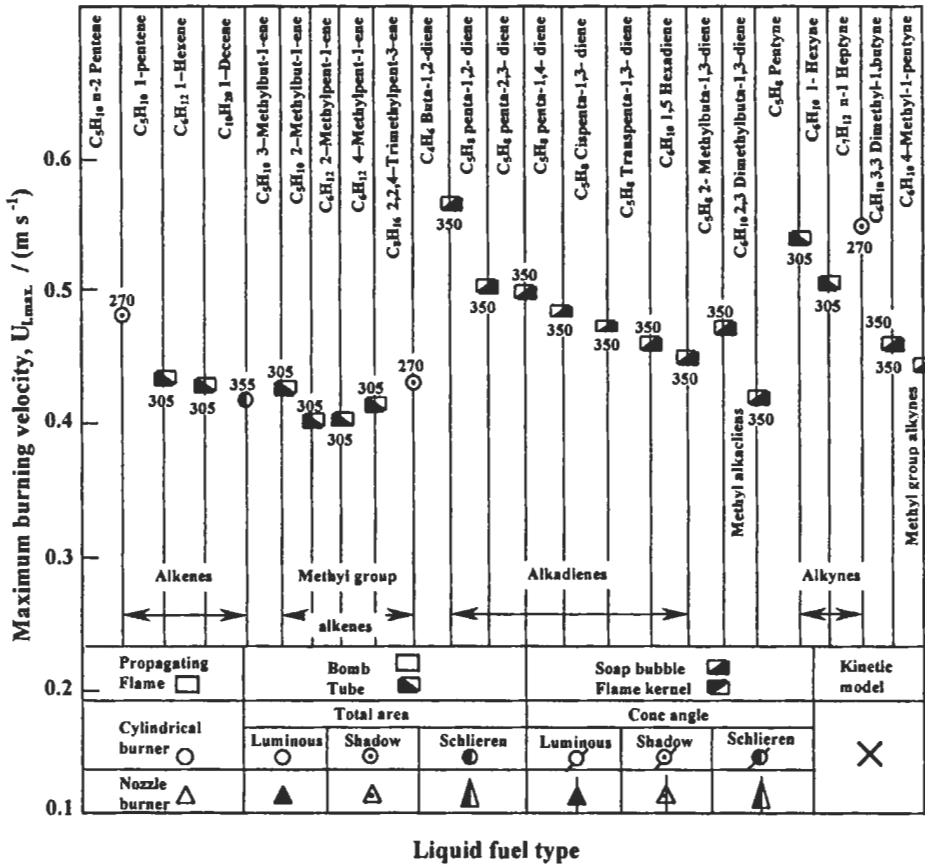


Fig. 2.66 (b): Measured and computed maximum burning velocities of liquid fuels at 1 atm, and 300 K [45]. Reproduced by permission of Elsevier Science.

[44, 154, 156] flames. Around these lines are grouped experimental values for alkanes, aromatics, cyclanes, and alcohols. The line B is through values for alkenes and acetylenes, save for C₂H₄ and C₂H₂, which are covered by lines C and D [361], whereas E1 [361] and E2 [94, 97] are computed values for hydrogen-air mixtures.

There are many scatters, and a linear relationship between U_l and Q can only be an approximation. Experimental values of U_l are notoriously susceptible to a variety of errors [225], whereas computed values are dependent upon the chemical kinetics and values of rate coefficients, as well as the oft-imposed one-dimensionality. The significance of Fig. 2.67 then lies not so much in the precise relationship between U_l and the molar heat of reaction, but in the different families of fuels it reveals. This suggests, for example, that the reaction schemes for alkanes and alcohols, and even aromatics and cyclanes, may not be so dissimilar, particularly when compared with acetylene or hydrogen; a not altogether surprising conclusion in the light of the degree of generality suggested in the reaction schemes for high paraffinic hydrocarbons of Warnatz [357] and Westbrook et al [367]. The data in Fig. 2.67 might also be used in the estimation of volumetric heat release rate-temperature profiles, as described in the following section.

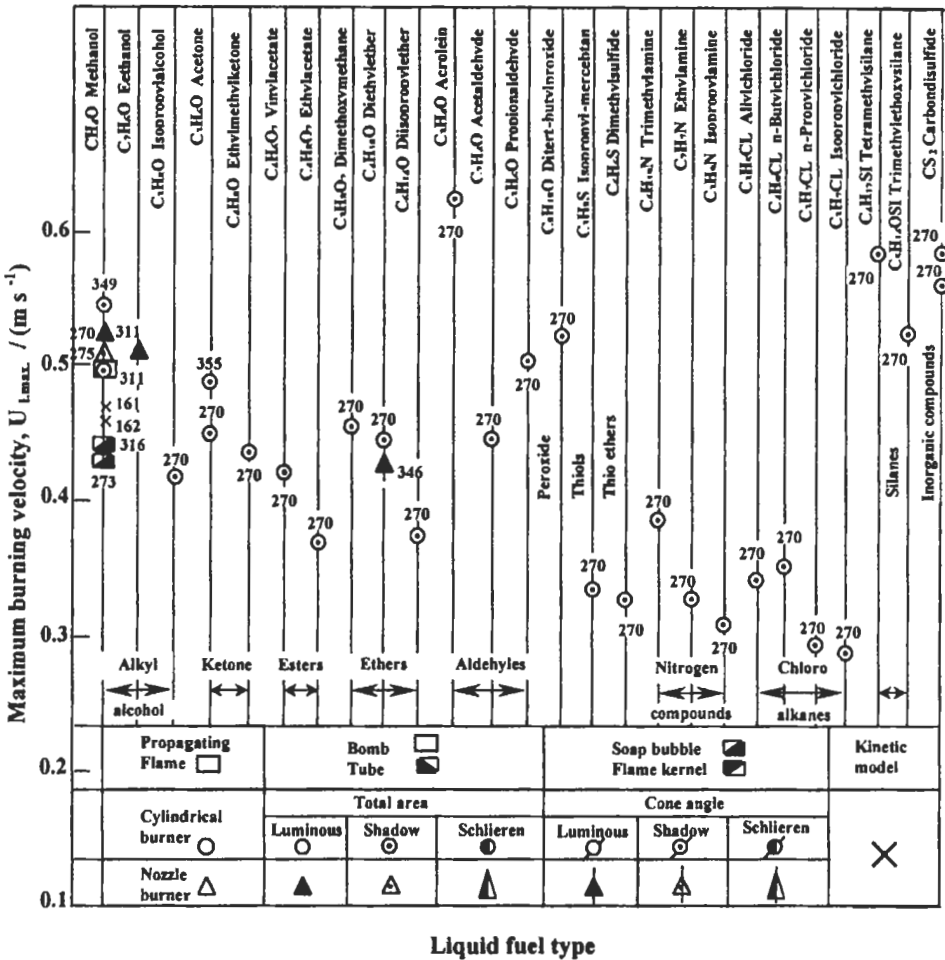


Fig. 2.66 (c): Measured and computed maximum burning velocities of liquid fuels at 1 atm, and 300 K [45]. Reproduced by permission of Elsevier Science.

The data for H₂, CH₄, and CH₃OH-air flames at 1 atm, and an initial temperature of 300 K are shown in Fig. 2.68. The black circled points, which close to the full lines, are those computed from laminar flame models, with detailed chemical kinetics, by Dixon-Lewis, Bradley, Habik and El-Sherif [94, 97, 44, 152, 153, 155, 156]. Throughout this section recourse will be made to these data at equivalence ratios ranging from 0.6 to 1.0. In addition, for CH₃OH-air mixture the computed data cover pressures of 0.1, 1, and 10 atm at temperatures of 400 K and 500 K.

(ii) **General algebraic form of the burning velocity.** Figure 2.69 shows the predicted burning velocity with (C_w) and without water content (Habik [274]) against the corresponding heat of reaction per mole of mixture. The circle, o, and cross, x, points in the figure represent the computed values from kinetic models for CH₃OH-air and CH₃OH-H₂O-air flames, respectively. The full and chain-dashed lines represent the mean value of these points. The initial pressure, temperature and

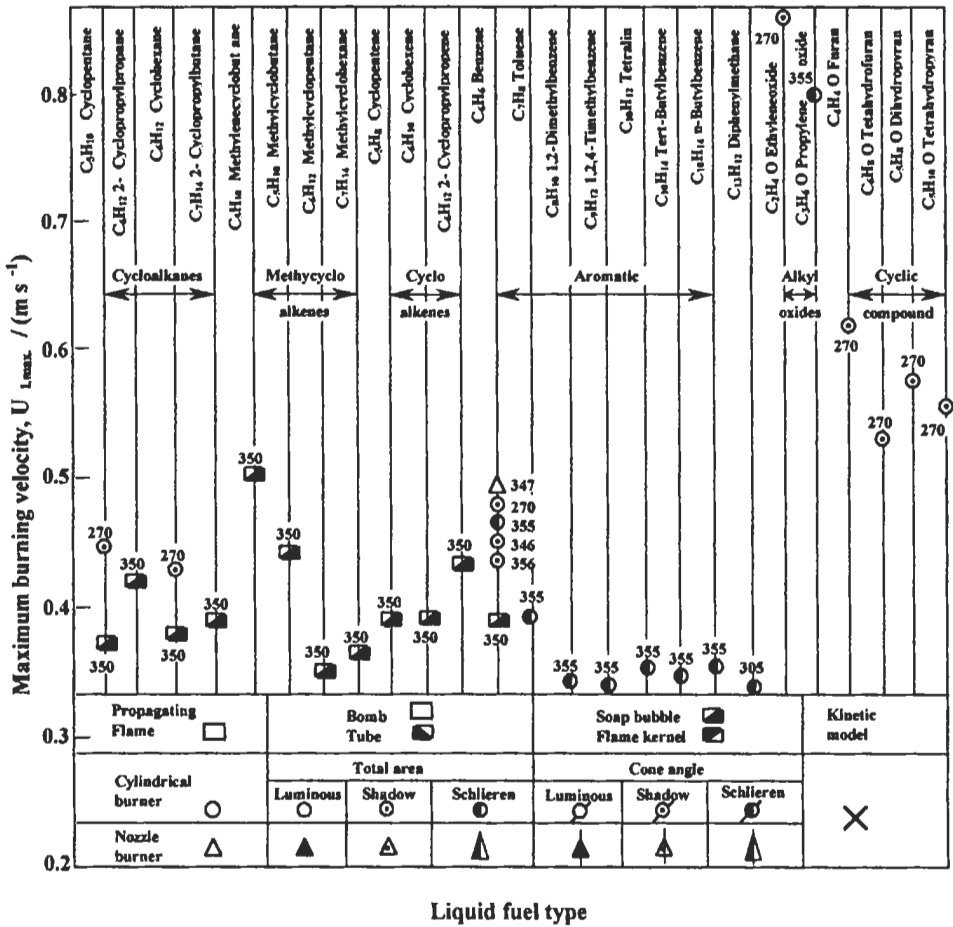


Fig. 2.66 (d): Measured and computed maximum burning velocities of liquid fuels at 1 atm, and 300 K [45]. Reproduced by permission of Elsevier Science.

equivalence ratio, ϕ are 0.1, 1.0, 10 atm, 300, 500 K and ϕ of 0.6 to 1.0. The water content represented by C_w is 0.0, 0.1 and 0.2.

For the above initial conditions (with $C_w = 0.0$), the corresponding predicted burning velocity for CH₄ - air (El-Sherif [153]) is shown in the same figure by black circle. The mean full lines for all of these points are lower by about 0.01 m s⁻¹ than those corresponding to pure methanol-air flames. This value is within the uncertainties in the reaction mechanism and rate parameters, and confirmed again the experimental findings in Fig. 2.67 and 2.68 in that the reaction scheme for alkanes, alcohols and even aromatics and cyclanes, may not be so dissimilar, particularly when compared with acetylene or hydrogen. The figure also shows that for a given heat of reaction, the burning velocity decreases as the water content, C_w in methanol increases. The burning velocities for methanol-air flames with and without water content are correlated (with correlation factor of 0.98) with the following expression in terms of initial pressure, temperature, water content, C_w , and heat of reaction.

$$U_l = (-0.324 + 0.0096Q)(P/P_u)^{-12/Q} (T/T_u)^{(125/Q)} (1 + C_w)^{-120/Q} \quad (2.49)$$

where, $P_u = 1 \text{ atm}$, $T_u = 300 \text{ K}$, Q in Mj kmole^{-1} , $C_w = 0.0$ to 20% , and U_l in m s^{-1} . This equation may be applied for alkanes, alcohols and aromatic-air flames within $\pm 0.01 \text{ m s}^{-1}$. The equation can also be used in turbulent models where the turbulent burning velocity is correlated with the laminar burning velocity.

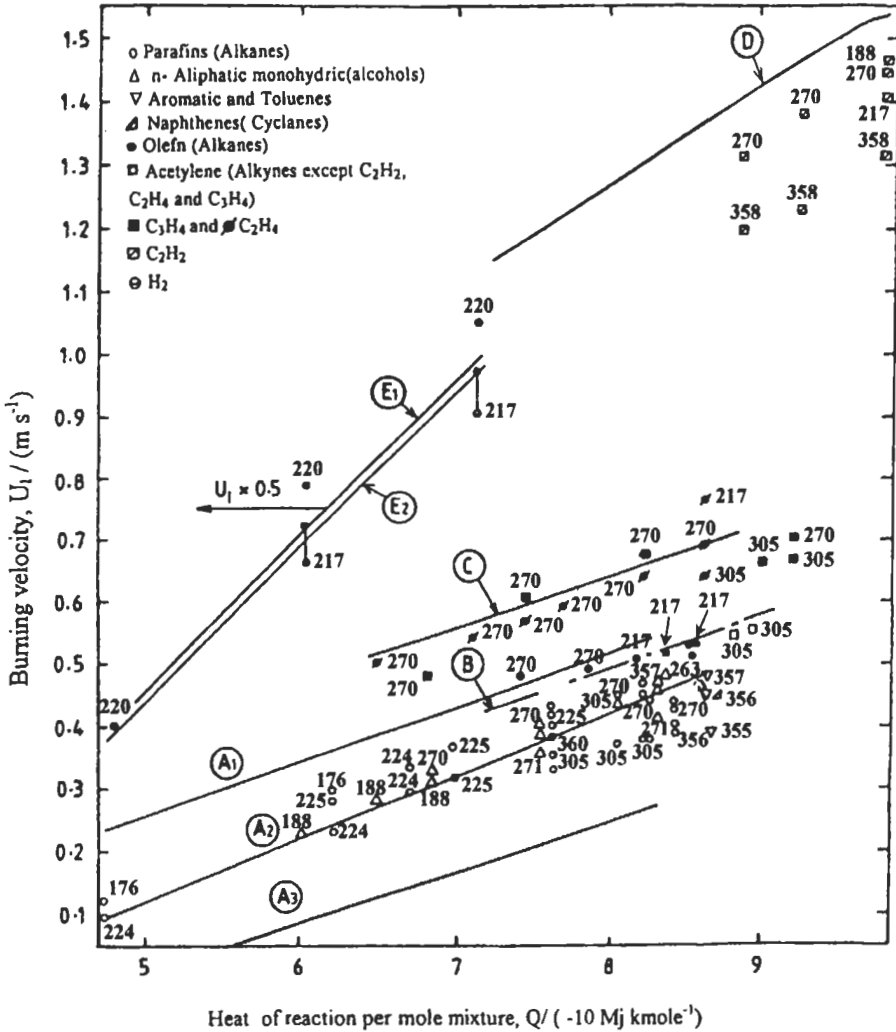


Fig. 2.67: Burning velocities of lean mixtures of different fuels at 300 K. Full lines are computed A1: CH_4 and CH_3OH at 0.1 atm [44, 153, 154 & 156], A2: CH_4 and CH_3OH at 1 atm [44, 153 & 156] and A3: CH_4 and CH_3OH at 10 atm [44, 153 & 156], C: C_2H_4 at 1 atm [537], D: C_2H_2 at 1 atm [537], E1: H_2 at 1 atm [537], E2: H_2 at 1 atm [94, 97]. Experimental points references are given. B is through alkene experimental points at 1 atm, but not C_2H_2 and C_2H_4 [45]. Reproduced by permission of Elsevier Science.

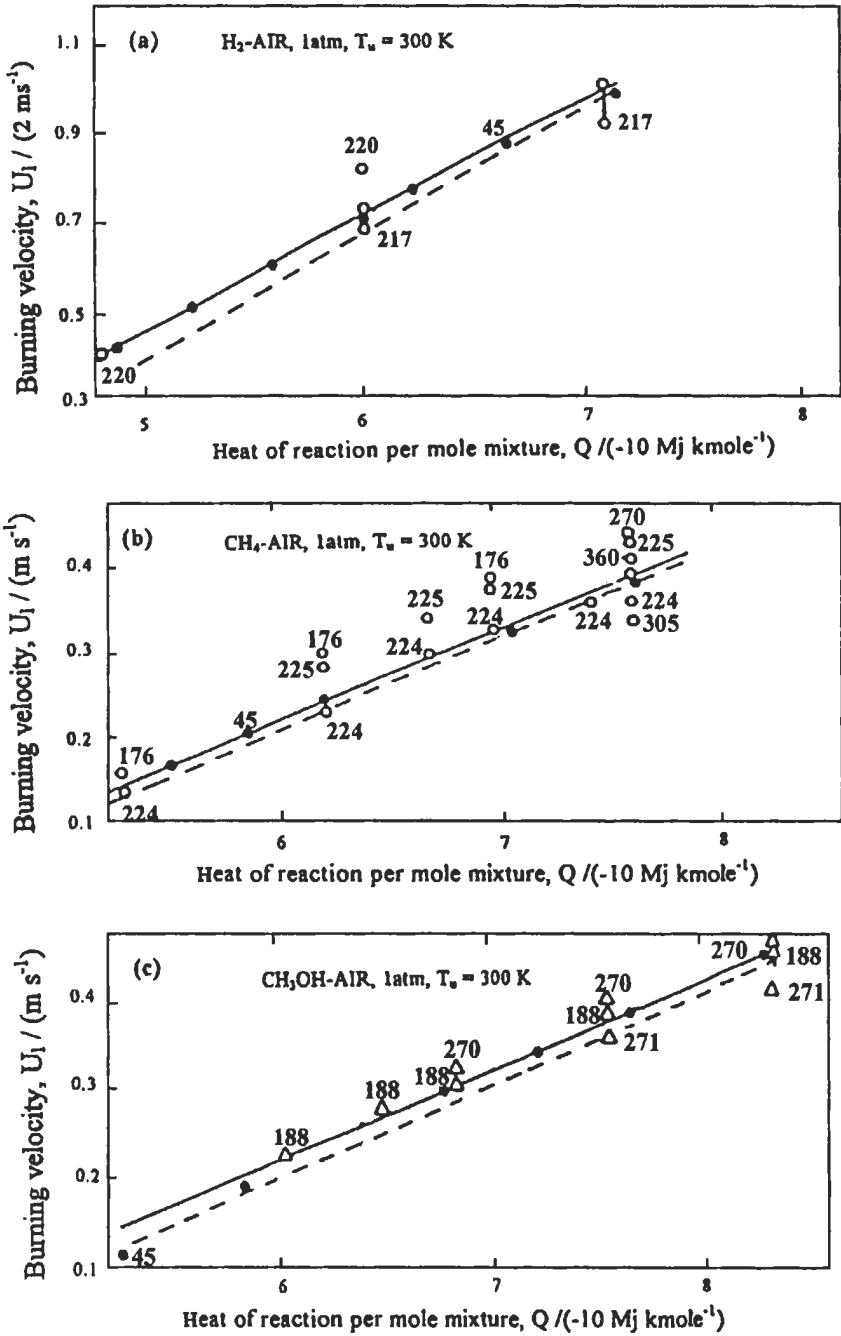


Fig. 2.68: Burning velocities of (a) H_2 -air, (b) lean CH_4 -air, and (c) lean CH_3OH -air. Computed points indicated by black circles, dashed lines based on Eq. 2.50 [45]. Reproduced by permission of Elsevier Science.

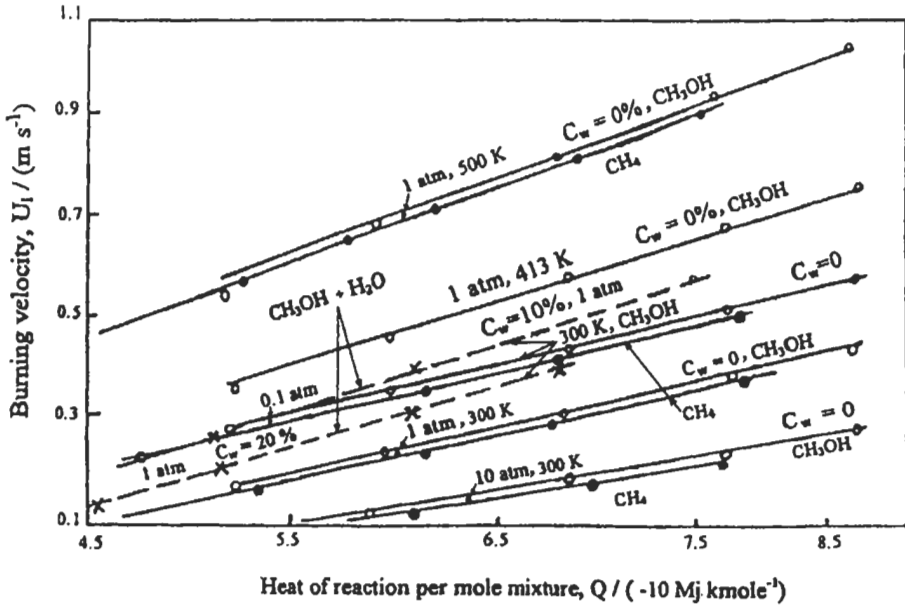


Fig. 2.69: Variation of burning velocity of methanol-water, methane-air flames with heat of reaction per mole of mixture. The points are those computed from chemical kinetic model and the lines are the mean value of these points. O (—) Habik and co-workers [44, 154, 156] for CH_3OH -air, X (-----) Habik [274] for CH_3OH - H_2O -air, ● (—) El-Sherif [153] and Habik [156] for CH_4 -air flames. The initial conditions vary from 0.1, 1 to 10 atm, 300 to 500 K, and equivalence ratio of 0.6 to 1.0.

2.5.2 General Correlations of Heat Release Rate

(i) **Volumetric heat release rate-temperature profiles.** Laminar flamelet modeling concepts extend the use of laminar data into the turbulent regime as will be described in chapters 3 and 4. For example, turbulent burning velocities are correlated with laminar burning velocities, U_1 [368, 369], and spatial distributions of mean turbulent heat release rate-temperature profiles [370]. Therefore, it is appropriate to examine the possibility of correlating the heat release rate-temperature profile with U_1 and Q . A relatively simple theoretical guide to a possible correlation is provided by classical theories of laminar burning velocity [371-373], that express this parameter in terms of Q and an integration of the volumetric heat release rate through the flame, q , with respect to temperature. The formulation of Spalding [374] can be rewritten as:

$$QU_1 = \frac{1}{\bar{m}_M} \left[\frac{q_{\max} (\tau_b - \tau_u) \int_0^1 k(q/q_{\max}) d\theta}{\Omega} \right]^{0.5} \quad (2.50)$$

where \bar{m}_M is the molar density of the unburnt mixtures, at a temperature, T_u , and T_b is

the burned gas adiabatic temperature. A reaction progress variable is defined in terms of dimensionless temperature, θ , such that $\theta = (T - T_u)/(T_b - T_u)$, where T is the temperature, at which point the thermal conductivity is k . The maximum value of the heat release rate is q_{max} , and Ω is the burning velocity eigenvalue, which in the original theory of Zeldovich and Frank-Kamenetski is 0.5 [371].

Equation 2.50 rests upon a bimolecular reaction between fuel and oxidant, and a Lewis number of unity. The dashed lines in Fig. 2.68 were derived by substituting values for the parameters on the right of the equation that were obtained from the computed heat release rate by the kinetic models. That solid and dashed lines are not coincident is due to the assumptions inherent in the equation.

Despite these limitations, the relationships implied by Eq. 2.50, between QU_1 and $\int_0^1 (q/q_{max}) d\theta$ were explored, using the computed heat release rate, with the results shown in Fig. 2.70. A further influence upon U_1 is that of the eigenvalues, which as suggested by Spalding [374] correlates with the centroid of the heat release rate integral θ_c . This is given by:

$$\theta_c = \frac{\int_0^1 \theta (q/q_{max}) d\theta}{\int_0^1 (q/q_{max}) d\theta} \tag{2.51}$$

and values of θ_c computed from this expression are shown in Fig. 2.70. The two sets of curves in Fig. 2.70 reveal a degree of generality in the behavior of different fuels. This is shown particularly well by the coincidence of the curves for CH_4 , CH_3OH , and perhaps surprisingly, H_2 at 1 atm. and 300 K. A change in pressure and temperature alters these relationships, as is shown by the CH_3OH curves for two different temperatures and one different pressure. The eigenvalues were evaluated for the kinetically modeled flames and, in the light of Spalding's correlation, plotted against θ_c in Fig. 2.71. This has revealed a particularly gratifying generality in that, within 3 %, all

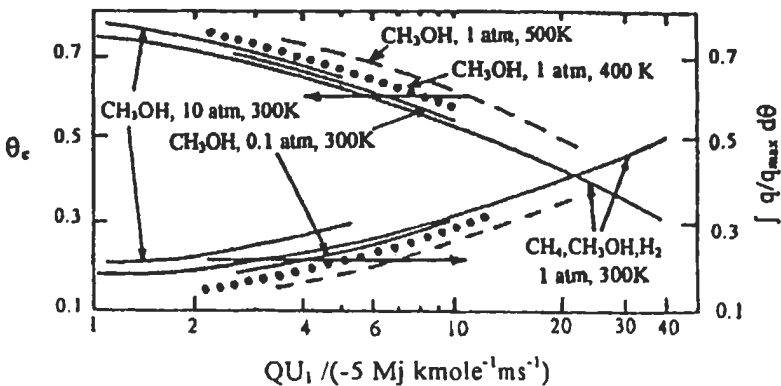


Fig. 2.70: Heat release rate integral and location of its centroid for different fuels and different pressures and temperatures [45]. Reproduced by permission of Elsevier Science.

the computed data lay on the single solid line represented by:

$$\Omega = 0.43\theta_c^2 \tag{2.52}$$

The dotted curve shows Spalding's centroid rule, for $\theta_c \geq 0.6$. The limit condition of $\theta_c = 1$ recovers the Zedovich and Franek - Kametski value of 0.5. This curve is for the centroid distance as defined by Spalding [374]; this is slightly different from Eq. 2.51, in that both the numerator and denominator terms inside the integral are multiplied by k .

Shown by the dotted curves in Fig. 2.72 are computed profiles of q/q_{max} versus θ for four different mixtures. Of these, the CH₄-air flame, $\phi = 0.8$, has the highest value of θ of 0.68, whereas the stoichiometric H₂-air flame has the lowest value of 0.37. The profile of the latter is of particular interest, in that the distribution of the heat release is so different from that of the classical assumption that the peak heat release rate occurs close to T_b [94].

In addition to such data, as are embodied in Fig. 2.72, any turbulent flow field computations of mean heat release rate using the flamelet assumption [370, 375] would require absolute values of the volumetric heat release rate, and hence that of q_{max} for the mixture. The computed values of the latter are presented, plotted against QU_1 , for different mixtures in Fig. 2.73. Because these cover different pressures and because bimolecular reactions are important, the data are reduced partially by plotting, q_{max} / \bar{m}_M^2 .

(ii) **Algebraic forms of heat release rate-temperature profiles.** For computational convenience it is desirable to express heat release profiles algebraically, and a two-parameter expression that was found to be useful in Ref. 375, is:

$$\frac{q}{q_{max}} = \frac{(a + b)^{a+b}}{a^a b^b} \theta^a (1 - \theta)^b \tag{2.53}$$

in which a and b are numerical constants. This yields:

$$\int_0^1 \frac{q}{q_{max}} d\theta = \frac{(a + b)^{a+b} \Gamma(a + 1) \Gamma(b + 1)}{a^a b^b \Gamma(a + b + 2)} \tag{2.54}$$

where, Γ is the Gamma function, and

$$\theta_c = \frac{a + 1}{a + b + 2} \tag{2.55}$$

To find the profile for a particular mixture, QU_1 must first be evaluated either from direct knowledge, or from the heat of reaction of the mixture and the data on Figs. 2.67 and 2.68. From Fig. 2.70 both $\int_0^1 (q/q_{max}) d\theta$ and θ_c are found, and a and b are evaluated numerically from Eqs. 2.54 and 2.55. This enables the algebraic generalization of Eq. 2.53 to be used. How close an approximation this two-parameter expression might be, is indicated by a comparison of the full line curves with the kinetically computed dotted curves in Fig. 2.72. The area under the dotted curves and

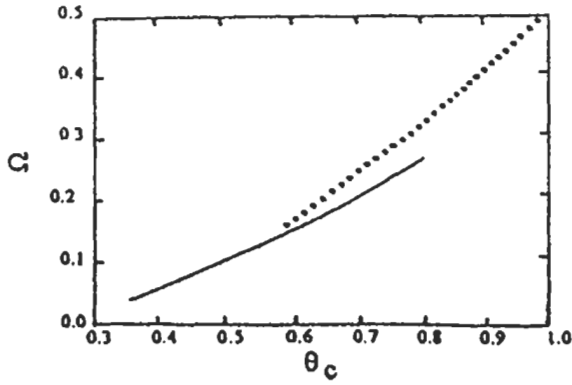


Fig. 2.71: Burning velocity eigenvalue, Ω , relationship to centroid of heat release rate integral, θ_c . Full line curve computed relationship [45] and dotted line Spalding's centroid expression [374]. Reproduced by permission of Elsevier Science.

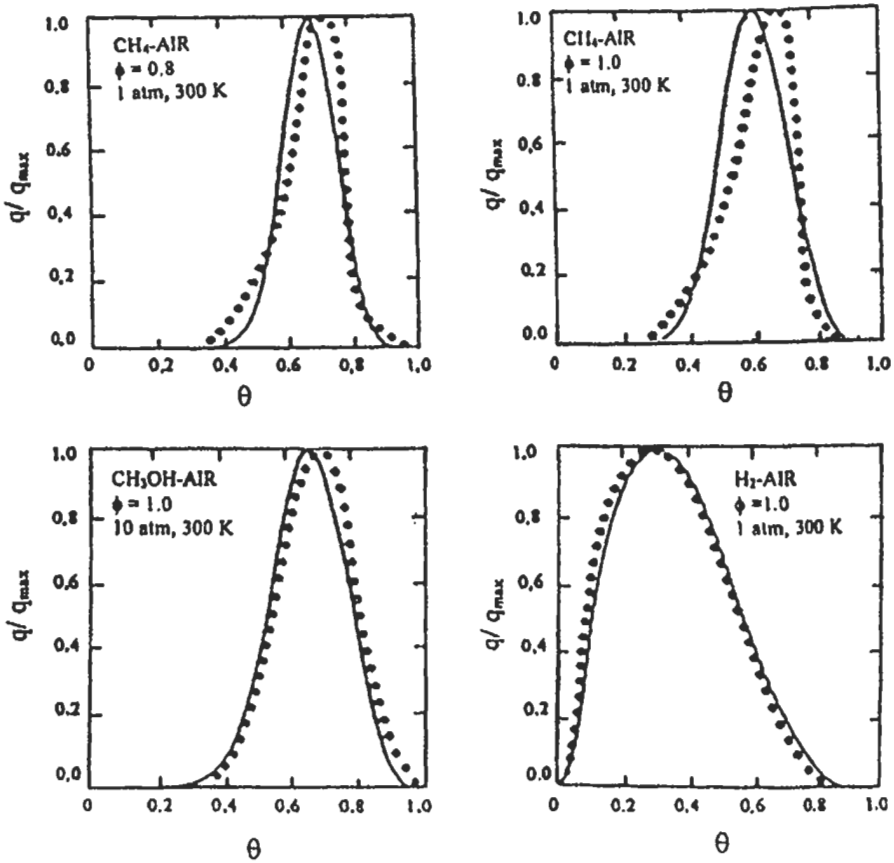


Fig. 2.72: Heat release rate profiles for different mixtures. Full line curves from Eq. 2.53, and dotted curves from mathematical models [45]. Reproduced by permission of Elsevier Science.

their respective centroid distances were evaluated and the values of a and b were found, by the procedure just outlined, to generate the full line curves from Eq. 2.53. Apart from the case of the stoichiometric methane profiles, the ability of Eq. 2.53 to express the profile is quite good. Although it is not perfect, the curve fit approximation might be within the accuracy currently to be expected of the chemical kinetic models. Shown in Fig. 2.74 are values of a and b evaluated as described for these lean and stoichiometric mixtures. To obtain an absolute (as distinct from a dimensionless) heat release rate profile, q_{\max} might be evaluated from Fig. 2.73.

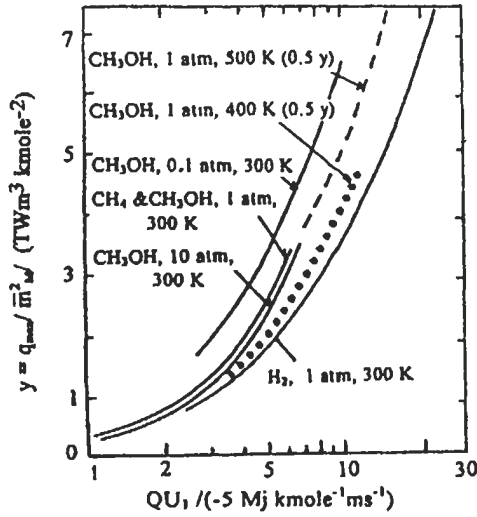


Fig. 2.73: Values of q_{\max} for different fuel-air mixtures [45]. Reproduced by permission of Elsevier Science.

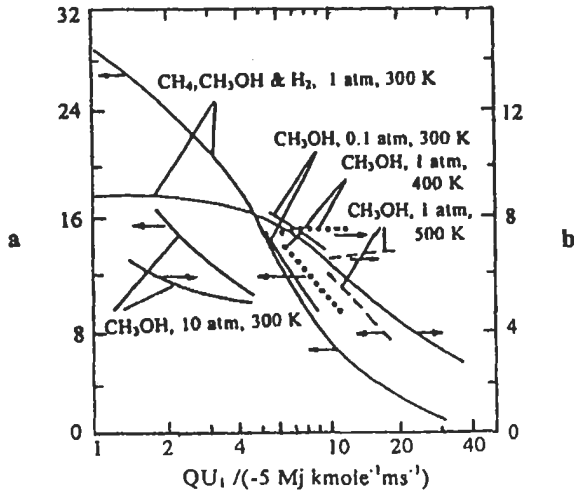


Fig. 2.74: Values of a and b in Eq. 2.53 for different fuels with air [45]. Reproduced by permission of Elsevier Science.

2.6 High Hydrocarbon Fuels-Air Flames

In this section reduced kinetic models have been developed to describe the combustion fundamentals for practical high hydrocarbon fuels over a wide range of experimental conditions. The fuels include n-Butane, Benzene, n-Heptane, Gasoline, Kerosene (JP-8), and n-Hexadecane. The mechanism for each fuel includes a single reaction expression for fuel and oxygen to form formaldehyde (CH_2O) and hydrogen (H_2) or carbon monoxide (CO), together with a detailed reaction mechanism for CH_2O - CHO - CO - H_2 oxidation (Table 2.2 in section 2.3.4). These kinetic mechanisms will be as generally applicable as possible and can be used in 2-D or 3-D combustion models to understand the practical combustion and emission problems in engines and furnaces. Each mechanism consists of 13 chemical species with 22 elementary reactions.

The proposed reduced kinetic mechanisms were used in one-dimensional laminar premixed flame model and incorporated detailed representation of transport fluxes to predict laminar burning velocity and flame structure for the above fuels. To validate these kinetic models, the predicted results were compared satisfactorily with the experimental data for each fuel over a wide range of equivalence ratios, pressures, and temperatures. In addition, the flammability limits for different types of fuels were also examined. A single reaction expression for breakdown each of the above fuels has been derived, and can be used with CH_2O - CHO - CO - H_2 mechanism to predict satisfactorily the experimental combustion fundamentals for these practical fuels, and all of that will be discussed hereunder.

2.6.1 Background to Reduced Kinetic Models

The evaluation of combustion science in the last decades is characterized by the mutual comparison between experimental, computation, and theory (Williams [376]). Concerning the status of chemistry in combustion, Dryer [377] observed that while early combustion modeling virtually ignored chemistry, in recent years, the inclusion of detailed chemical mechanisms in combustion models has been accelerated.

Many combustion scientists consider that large mechanisms which typically involve several tens of species and several hundreds of reactions will remain too complex for many years to be included in practical 2-D or 3-D combustion code because the computing time would be much too great. For these reasons, efforts have been made to extract simplified kinetic schemes from these large systems of elementary reactions [377]. Systematic approaches have been developed for the construction of simple or reduced kinetic mechanisms (2 to 100 steps) for small hydrocarbon fuels (Dixon-Lewis and Islam [143], Bradley et al [44], El-Sherif [18, 153], Habik [16, 20], Paczko et al [193], Peters and Rogg [378], Lam and Goussis [379], Mass and Pope [380], Kennel et al [381], Westbrook and Dryer [382], Warnatz [383], Edelman and Fortune [384], Ranzi et al [385], and iso-octane fuel by Pitsch et al [386]).

One of the attempts to simplify the kinetic mechanism for methane to n-decane (CH_4 to $\text{C}_{10}\text{H}_{22}$) was made by Westbrook and Dryer [382]. Their mechanisms included one and two reaction steps as well as quasi-global mechanisms. The latter combines a single reaction of fuel and oxygen to form CO and H_2 , together with a detailed reaction mechanism for CO and H_2 oxidation, and consists of 12 chemical species and 22 reactions. Their results show that the addition of intermediate species such as CO and

H₂, together with further refinement of the reaction mechanism into several steps, makes the predicted product temperature and compositions more accurate. Consequently, it will improve the prediction of NO_x and CO emission in complex combustion modeling.

High hydrocarbon fuels are important in practical applications such as furnaces, combustion chambers and engines. Therefore, understanding the combustion fundamentals of these fuels is necessary to improve the efficiency of the combustion system and reduce pollutant emissions. The chemical structure of these fuels is complex. However, there is no available detailed chemical mechanism for practical high hydrocarbon fuel because the mechanism would be too large, in addition to its unknown breakdown compositions (such as kerosene and n-Hexadecane fuels).

This section represents further development of previous attempts by Westbrook and Dryer [382] to simplify the kinetic mechanism for high hydrocarbon fuels such as n-butane, benzene, n-heptane, gasoline, kerosene, and n-hexadecane. Habik et al [17] have developed reduced reaction mechanisms for these fuels that combine a single reaction of fuel and oxygen to form formaldehyde (CH₂O) and hydrogen (H₂) or carbon monoxide (CO), together with detailed reactions for CH₂O-CHO-CO-H₂ mechanism as described in section 2.3.4. The mechanism for each fuel was used in one-dimensional laminar premixed flame model incorporating detailed representation of the transport fluxes to predict the laminar burning velocity, flame structure, and heat release rate. In the following sub-sections, the predicted laminar burning velocities for these fuels were compared satisfactorily with the available experimental data over a wide range of equivalence ratios, pressures, and temperatures, as well as with the flammability limits. These developed reduced mechanisms can be used in 2-D or 3-D combustion models such as KIVA-II [387].

2.6.2 Computational Methods and Reaction Mechanisms

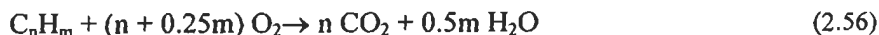
Computational Approach

The laminar flame properties for different types of fuels have been calculated by Habik et al [17] using one-dimensional model that was described in section 2.3.2. The data for enthalpy and gaseous specific heat for kerosene, gasoline, n-butane, n-heptane, benzene and n-hexadecane were taken from KIVA-II code [387] and Gardiner [12], and for other species were taken from JANAF Table [13]. Detailed transport property formulation employed in these calculations was described in section 2.3.3. In the interest of computation economy, only H, N₂, O₂, H₂, CO, CO₂, H₂O, and fuels were included in the calculation of thermal conductivity.

Reduced Reaction Mechanisms

In any reaction mechanism, the first important reaction is the fuel breakdown reaction, which broadly determines the shape of the primary reaction zone. It is well-known that the initial attack on the fuel is made predominant by hydroxyl, OH, hydrogen, and oxygen atoms, and in higher alkenes, thermal decomposition is of major importance [28].

In most of the simplest one-step reaction for oxidation of a hydrocarbon fuel, the overall reaction is represented as:



The rate for this reaction must therefore represent an appropriate average of all of the individual reaction rates involved. This rate is usually expressed as:

$$k_0 = A_0 T^n \exp(-E_0 / R T) [\text{fuel}]^a [\text{O}_2]^b \quad (2.57)$$

where, A_0 is the pre-exponential factor, and E_0 is the effective or overall activation energy. This one-step reaction can lead to serious errors in the predicted burning velocity and emission as will be discussed next. Therefore, detailed reaction mechanisms for hydrocarbon fuels are necessary to predict accurate results. These mechanisms are built in a hierarchical manner with sub-mechanisms for H_2 and CO oxidation forming the core of the overall reaction mechanism. These sub-mechanisms were tested independently as described in the above sections, and additional reactions and chemical species are incorporated as the complexity of the fuels dictates. For practical high hydrocarbon fuels, the breakdown of these fuels is unknown and is very complex, in addition, the computing time would be much too great. For these reasons, the attempt in this section will include the breakdown of different practical high hydrocarbon fuels by oxygen to form intermediate species which represent the core of the overall reaction mechanism [17].

To simplify the breakdown of above mentioned fuels, it is assumed that the above fuels breakdown by oxygen molecules to form formaldehyde, CH_2O (which is a short lived intermediate in the oxidation of most of the hydrocarbon fuels) and hydrogen, H_2 , or carbon monoxide (CO) is as follows [17]:



It is well known that the kerosene and gasoline fuels are complex in their compositions. However, for reasons of simplicity, the kerosene (JP-8) and gasoline fuels are assumed to be n-dodecane, $\text{C}_{12}\text{H}_{26}$ (Hardalupas et al. [388]) and n-octane, C_8H_{18} (Metghalchi and Keck [271]), respectively.



Then, the formaldehyde will breakdown by radical attack (reactions R_{21} to R_{23} in Table 2.2) to form formyl radical, CHO , and hydrogen, H_2 . Consequently, the formed CHO will be redissociated and will undergo one of the forward reactions R_{17} to R_{20} to form CO and H_2 . The reactions for CO-H_2 mechanism (R_1 to R_5 and R_8 to R_{16}) with their rate parameters were given in Table 2.2. The developed reduced mechanisms will include Eqs. 2.58 to 2.63 for breakdown of the fuels with their rate expressions similar to that given by Eq. 2.57, together with the transport parameters (Table 2.1), and $\text{CH}_2\text{O-CHO-CO-H}_2$ mechanism with their rate parameters (R_1 to R_5 and R_8 to R_{23} in Table 2.2).

Computational Procedure

For each fuel, the corresponding breakdown reaction (Eqs. 2.57 to 2.63) and its rate expression of Eq. 2.57 together with the reaction mechanism described above have been used to predict the burning velocity and flame structure. The parameters for the rate expression of Eq. 2.57 can be adjusted to provide agreement between computed and experimental results. First, we have assumed constant values for n and activation energy E_0 . Then, they [17] have evaluated the remaining parameters a , b , and A_0 in the rate expression of Eq. 2.57. The concentration exponents a and b were assumed, and then the pre-exponential A_0 was varied until the model correctly predicted the experimental laminar burning velocity, U_l at atmospheric pressure, P , initial temperature, $T_u = 300$ K, and stoichiometric equivalence ratio $\phi = 1$. In this computational procedure, the parameter of rate expression (Eq. 2.57) at $\phi = 1$, $P = 1$ atm, $T_u = 300$ K was used together with kinetic mechanism (Table 2.2) and the transport fluxes to predict the laminar burning velocity and flame structure at different equivalence ratios, temperatures, and pressures. If the predicted results are not in a good agreement with the experimental data over the above wide range of conditions, the values of a and b should be readjusted again. Then, a new value of A_0 must be determined for each fuel separately relative to one calibration point at $\phi = 1$, $P = 1$ atm, and $T_u = 300$ K [17].

2.6.3 Experimental and Computational Results

Experimental Results

This section describes the experimental data, which will be used to validate the reduced kinetic mechanisms as well as to derive the parameters of the rate expression of Eq. 2.57 for each fuel. The review of the laminar burning velocities for different liquid fuels described in section 2.5 (Bradley et al [45]) shows that the laminar burning velocity, U_l for C_8H_{18} is 0.4 m s^{-1} at $P = 1$ atm, $T_u = 300$ K and $\phi = 1$, and maximum U_l is about 0.42 m s^{-1} at $\phi = 1.15$. The experimental flammability limit for lean mixture occurs at equivalence ratio of $\phi_l = 0.5$ and rich limit at $\phi_r = 4.3$ (Dugger et al [389]). These values are also used by Westbrook and Dryer [382] to derive the one- and two-step reaction for *n*-octane. These experimental results were used first as a calibration point to derive the parameters of the rate expression of Eq. 2.57. Then, additional experimental results from different investigators were used to validate the final predicted results over a wide range of conditions. These experimental results of laminar burning velocities for C_8H_{18} were measured at $P = 1$ atm, $T_u = 300$ K, and over a wide range of equivalence ratios [270, 271, 274, 348, 353, 355, 390, 391]. Also, the effect of the initial temperature on U_l was investigated by Heimel and Weast [356], Metghalchi and Keck [271], and Gülder [390]. More details for all of these measurements have been reviewed by James [392], and these measurements are shown in Figs. 2.75 to 2.79.

The only available experimental results for flame structure of *n*-octane were that measured at Leeds University by Benkoussan [393]. He measured O_2 , CO , CO_2 and H_2 concentrations on a burner for a flat premixed *n*-octane-air flame at 320 K, 0.2 atm and different equivalence ratios. These results are shown in Figs. 2.80 (a) and (b) and were used to validate the kinetic model.

Unfortunately, for aviation kerosene (JP-8) fuel, there are no available

measurements for laminar burning velocities. The survey for burning velocities shows that there is only one measured value for maximum laminar burning velocity for n-decane of 0.4 m s^{-1} at 1 atm and $T_u = 300 \text{ K}$ [355]. They [17] have assumed that the kerosene is similar to n-dodecane $\text{C}_{12}\text{H}_{26}$. Hence, this measured value for n-decane is lower by 0.02 m s^{-1} than the maximum U_1 for C_8H_{18} , and therefore, it can be assumed that the burning velocity for kerosene at 1 atm, $\phi = 1$, and $T_u = 300 \text{ K}$ is 0.38 m s^{-1} . The measured flammability limits for kerosene are $\phi_l = 0.50$ (lean limit) and $\phi_r = 4.3$ (rich limit) [394]. Hence, the laminar burning velocity of 0.38 m s^{-1} for kerosene, together with lean and rich flammability limits were used as calibration points to validate the reduced mechanism and to derive the parameters for the rate expression of Eq. 2.57.

The experimental burning velocity data at 1 atm and different equivalence ratios for n-butane and benzene fuels were taken from Gibbs and Calcote [270], while for n-hexadecane fuel, the data were taken from Gerstein et al [350]. These data are shown in Fig. 2.81 and are used to validate the reduced mechanism for these types of fuels. In 1998, Bradley et al [396] have measured the laminar burning velocities and Marhstein numbers for iso-octane-air and iso-octane-n-heptane-air mixtures at elevated temperatures and pressures in an explosion bomb. Extrapolating their results for iso-octane to 1 atm and 300 K gives a maximum burning velocity, which agreed with that determined previously by Bradley et al [45]. Also in 1996, Davis et al [397] have measured the laminar burning velocities of benzene-air and toluene-air flames at atmospheric pressure, room temperature and different equivalence ratios using the counterflow twin-flame technique and these results are also used to validate the reduced mechanism.

Computational Results and Discussion

For all fuels mentioned above, the reaction mechanism and their rate parameters (Table 2.2) incorporated with the transport parameters (Table 2.1), together with Eqs. 2.57 to 2.63 (using different values of n , a , b , A_0 , and E_0) were used by Habik et al [17] to predict the laminar burning velocity and structure for different flames. The initial parameters for these flames were taken over a wide range of equivalence ratios (0.5 to 1.5), temperatures ($T_u = 300$ to 800 K), and pressures ($P = 0.1$ to 10 atm).

Most of the assumptions in the combustion literature for the concentration exponents are that the rate expression of Eq. 2.57 is first order in fuel and oxygen (i-e $a = b = 1$). Following the above procedure, and with the experimental data described above, and the assumption that, $a = b = 1$, $n = 0$, and $E_0 = 30 \text{ kcal mole}^{-1}$ (in Eq. 2.57) [382], the resulting rate expression for n-octane is found to be:

$$k_0 = 2.3 \cdot 10^{14} e^{-15106/T} [\text{O}_2] [\text{C}_8\text{H}_{18}] \quad \text{mole cm}^{-3} \text{ s}^{-1} \quad (2.64)$$

This rate, together with the kinetic mechanism in Table 2.2 and transport parameters in Table 2.1, correctly predicted the measured laminar burning velocity of 0.4 m s^{-1} at $\phi = 1$, 1 atm, and 300 K. For the same parameters, the predicted laminar burning velocities at different equivalence ratios are shown by curve 1 in Fig. 2.75. Another attempt was thought, by assuming $a = b = 1$ and changing n and E to be different than that of Eq. 2.64. Following the same above procedure, the rate expression for breakdown of the n-octane which is used with kinetic mechanisms to give a burning velocity of 0.4 m s^{-1} at $\phi = 1$, 1 atm and 300 K is found to be ($n = 4$, $E_0 = 16 \text{ kcal mole}^{-1}$):

$$k_0 = 0.34 T^4 e^{-8000/T} [\text{O}_2] [\text{C}_8\text{H}_{18}] \quad \text{mole cm}^{-3} \text{ s}^{-1} \quad (2.65)$$

The predicted burning velocities at different equivalence ratios using this rate expression with kinetic mechanism in Table 2.2 give nearly the same values as in curve 1 shown in Fig. 2.75. These results again, did not correctly predict the experimental data. In order to match correctly the predicted and experimental burning velocity, several attempts have been made by changing n , E_0 , a , b , and A_0 in Eq. 2.64.

The first attempt was made, by assuming $n = 0$, $E_0 = 30 \text{ kcal mole}^{-1}$ and changing a and b to be different than 1. The most satisfactory rate expression, which is capable of reproducing the experimental results over a wide range of initial conditions of the flames is found to be:

$$k_0 = 2 \cdot 10^{12} e^{-15106/T} [\text{O}_2]^{1.7} [\text{C}_8\text{H}_{18}]^{0.1} \quad (2.66)$$

The second attempt was made, by assuming $n = 4$, $E_0 = 16 \text{ kcal mole}^{-1}$ and changing a and b to be different than 1. The most satisfactory rate expression, which is capable of reproducing the experimental results over a wide range of initial conditions of the flames is found to be:

$$k_0 = 3.2 \cdot 10^{-3} T^4 e^{-8000/T} [\text{O}_2]^{1.7} [\text{C}_8\text{H}_{18}]^{0.1} \quad (2.67)$$

This expression again gives nearly the same results as the expression in Eq. 2.66. Using rate expressions of Eqs. 2.66 and 2.67 together with kinetic mechanisms described above, the predicted values of U_1 are shown in Fig. 2.75 (by curves 3 and 4) and in Fig. 2.76 over a wide range of equivalence ratios and at 1 atm and $T_u = 300 \text{ K}$. Also, the prediction of the laminar burning velocity at different initial temperatures and pressures over a wide range of equivalence ratios were calculated using Eq. 2.66 together with Table 2.2. These results are shown in Figs. 2.77 to 2.79, respectively. The flame structures for C_8H_{18} -air flames at $\phi = 1$ and 1.24, 0.2 atm, and $T_u = 320 \text{ K}$ are shown in Figs. 2.80 (a) and (b).

For the above fuels and by following the above procedure by varying a , b and assuming $n = 0$, $E_0 = 30 \text{ kcal mole}^{-1}$, the burning velocities were predicted and tested to match correctly the experimental results. These predicted results are shown in Fig. 2.81, and the rate expressions, k_0 (units in $\text{cm} \cdot \text{mole} \cdot \text{s}$) for breakdown of these types of fuels are given in Table 2.16.

Burning velocity and flame structure for these fuels will be discussed as follows.

(i) **Burning velocity of gasoline-air flames.** Rate expressions for breakdown of gasoline fuel, effects of pressure, temperature and equivalence ratio on the burning velocity will be discussed as follows.

Effect of using different rate expressions for breakdown of gasoline on burning velocity. Figure 2.75 shows the variation of the computed laminar burning velocity for gasoline-air flame with equivalence ratio at 1 atm, and $T_u = 300 \text{ K}$. The result of using rate expression of Eq. 2.64 is shown by dashed curve (curve 1). It is clear that, when this rate expression is used with kinetic mechanisms in Table 2.2, the predicted burning velocity does not reproduce the experimental data of rich flammability limit, particularly for fuel rich mixtures. In addition, the maximum burning velocity occurs at $\phi = 2.5$, which again does not agree with the experimental value (see Figs. 2.75 and 2.76). The same results have been found when the reaction rate expression of Eq. 2.65

was also used.

These computed results show that, the assumption of a reaction rate expression that

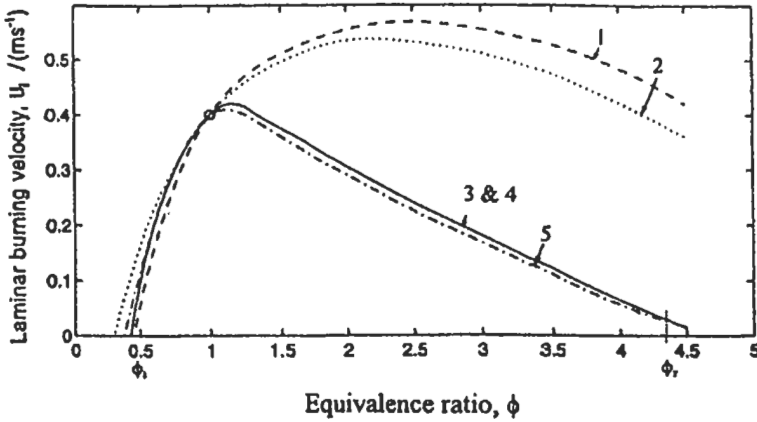


Fig. 2.75: Variation of laminar burning velocity with equivalence ratio for n-octane-air flame at 1 atm, and $T_u=300$ K. Experimental values for $\phi_l = 0.5$ and $\phi_r = 4.3$ from Ref. 389 and burning velocity at $\phi = 1$ from [45, 389] (open circle). Curve 2 and curve 5 from [382] and curves 1, 3 and 4 are the computed values using the kinetic mechanism see Table 2.17 in text [17]. Reproduced by permission of Combustion Science and Technology.

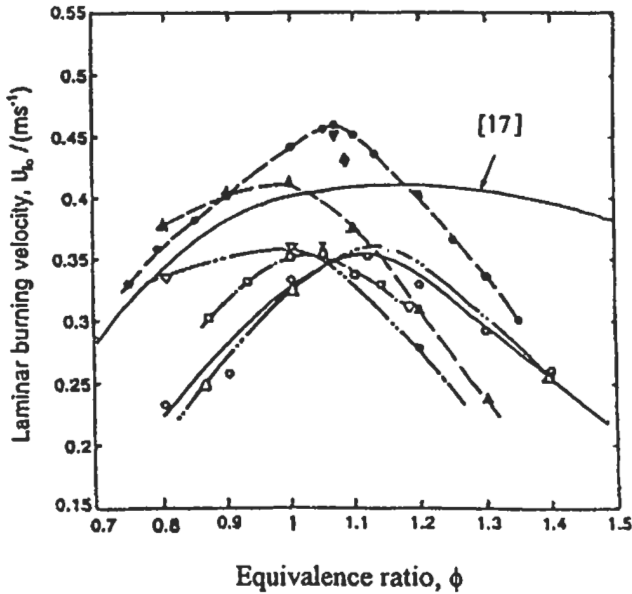


Fig. 2.76: Comparison between the computed [383] laminar burning velocity [17] with different experimental data for n-octane-air flame at 1 atm and $T_u= 300$ K. \bullet [390], \circ [271], Δ [270], \square [355], ∇ [348], \times [353], \diamond [274], ∇ [391], \blacktriangle [271] for Indolene fuel. Reproduced by permission of Combustion Science and Technology.

is first order in both fuel and oxidizer concentrations leads to serious errors in computed burning velocities, even with different values of n and E_0 in Eq. 2.57, particularly for fuel rich mixtures. Only for the case of stoichiometric fuel-air mixture, the reaction rate of Eqs. 2.64 and 2.65 predicts the proper value of burning velocity, which originally was used as a calibration point to obtain these rate expressions. The same problem has been found for kerosene and other fuels when $a = b = 1$. Also, Westbrook and Dryer [382] have found similar results and their predicted burning velocities are shown by dotted curve (curve 2) in Fig. 2.75 (see Table 2.17). These results have used only single step reaction. This confirmed that, the reaction rate expression with $a = b = 1$ should not be used in any combustion model. For large hydrocarbon fuel molecules like gasoline, kerosene, and n-hexadecane, an increase in the equivalence ratio from $\phi = 1$ to $\phi = 2$ increases the fuel concentration by about 100 %, while the O_2 concentration increases by less than 2 %. Therefore, Eqs. 2.64 and 2.65, as well as the Westbrook and Dryer equation with $a = b = 1$, predict that the reaction rate is roughly proportional to ϕ to cover the range ($1 < \phi < 10$) [382]. This rapid increase is more than to compensate for the gradual decrease in flame temperature, and leads to the observed over-estimate of the reaction rate when $a = b = 1$. The following will correct this assumption.

After several attempts, by varying a , b , n , and E_0 of Eq. 2.57, it was found that the values of a and b have most significant improvements in predicting the burning velocity. In rich flames, the burning velocity depends strongly on the fuel concentration exponent, a , and in lean flames, on the air concentration exponent b . Similar conclusion has also been found by Westbrook and Dryer [382] when they assumed constant values for n and E_0 . The best agreement between the computed and experimental results was obtained when the rate expression of Eqs. 2.66 or 2.67 was used together with the kinetic mechanism in Table 2.2. The results from using both expressions (see Table 2.17) with kinetic mechanism (Table 2.2) are shown by curves 3 and 4 in Fig. 2.75. By using these expressions, the flammability limits corresponding to 0.03 m s^{-1} [147] at lean and rich flame were found to be $\phi_l = 0.48$ and $\phi_r = 4.6$.

The predicted results from Westbrook and Dryer [382] for one-step reaction are shown by dotted-dashed curve 5 in Fig. 2.75, and the expression of this curve is given in Table 2.17. In this reaction, they have used the proper values of exponents a and b , and they assumed that the fuel and oxygen are burnt only to CO_2 and H_2O , but this one-step reaction is not useful for studying the emission and combustion problems, because the only product species are CO_2 and H_2O .

To further confirm the above predicted results, the results from curve 3 were compared with the available experimental data at 1 atm and $T_0 = 300 \text{ K}$ of Fig. 2.76. The predicted results are in the middle of the experimental data and are in good agreement in the lean side with Gülder [390] and Gibbs and Calcote [270], but are higher than Gülder [390] in the rich side. The predicted maximum burning velocity is also in agreement with Gibbs and Calcote [270] and occurs at $\phi = 1.2$, which is in agreement with Metghalchi and Keck [271, 391]. The predicted results of curve 3 were found to be correlated (at $\phi = 0.6$ to 1.2 within maximum discrepancy of $\pm 0.005 \text{ m s}^{-1}$) by:

$$U_{10} = 0.42 \phi^{-0.35} e^{-(2.5(\phi - 1.15)^2)} \quad \text{m s}^{-1} \quad (2.68)$$

where, U_{10} is the burning velocity at a reference condition, $P_0 = 1 \text{ atm}$, and $T_0 = 300 \text{ K}$.

Effect of equivalence ratio and temperature on burning velocity. Figure 2.77 shows a collection of the available experimental data from the literature. The figure was taken from James [392], and the above computed burning velocity is plotted in this figure by full curves (using Eq. 2.66 and kinetic mechanism in Table 2.2) at different initial temperatures and equivalence ratios. The figure shows that, the predicted burning velocities are in a reasonable agreement in the lean side and near stoichiometric ($\phi = 1.2$) at different temperatures with Gülder results [390]. The maximum computed burning velocity occurs at about $\phi = 1.2$ for different initial temperatures. Again, the spread in the experimental data is attributed to the accuracy of different burning velocity measurement techniques. One of the recent accurate techniques is that used by Egolopoulos et al [176], which gives good agreement in the lean and rich sides with the previous study for CH₄-air flame described in section 2.4.3

Also, shown in Fig. 2.78 is the variation of the predicted burning velocity with initial temperature at 1 atm and $\phi = 1$. Again, the predicted results were compared with the experimental data and were found to be in a reasonable agreement with that calculated from Gülder [390], and Metghalchi and Keck [391] using their derived power law equation. The predicted results [17] shown in Fig. 2.78 were found to be correlated (at $\phi = 0.6$ to 1.2 within maximum discrepancy of $\pm 0.005 \text{ m s}^{-1}$) by:

$$U_1 = U_{1,0} (T_u / T_0)^{1.65} \quad (2.69)$$

Effect of pressure on burning velocity. The variation of burning velocity with pressure is important in many combustion application processes. Thus, comparing the results from the kinetic model with the experimental data at different pressures will help to validate the model to be used at different conditions. Figure 2.79 shows these comparisons. In sections 2.4.3, 2.4.4 and 2.4.6, the results have shown that, the variation of burning velocity with the pressure can be expressed by simple relation in the form:

$$U_1 = U_{1,0} (P_u / P_0)^{-x} \quad (2.70)$$

The predicted results in Fig. 2.79 show the same behavior for pressure dependence, but are approximately independent of ϕ . This pressure dependence is attributed to the effects of radical recombination reaction R_2 , which competes with chain branching reaction R_4 (Table 2.2), and decreases the burning velocity at high pressure. Similar behaviors of the pressure dependence have been found by Westbrook and Dryer [382]. They show that, the value of $x = -0.05$ at low pressure and -0.125 at high pressure, for n-octane-air flames. The values of x for n-octane-air flames at low ($0.1 < P < 1 \text{ atm}$) and high pressures ($1 < P < 10 \text{ atm}$) were found to be -0.04 and -0.06 , respectively, for different equivalence ratios, and 300 K (see Fig. 2.79).

In order to reproduce the pressure dependence at low pressure, the predicted results show that, the value of exponent b for oxygen concentration must be approximately equal to 1.7 or less. Also, the concentration exponents a and b were found to be nearly independent of the value of E_0 and n of Eq. 2.57.

(ii) **Flame Structure of gasoline-air flames.** Further attempt to validate the kinetic mechanism for n-octane (Eq. 2.66 and Table 2.2) is to compare the predicted flame structure from the kinetic model with the available experimental data [393]. This comparison is shown in Figs. 2.80 (a) and (b) for n-octane-air flames at 0.2 atm, 320 K,

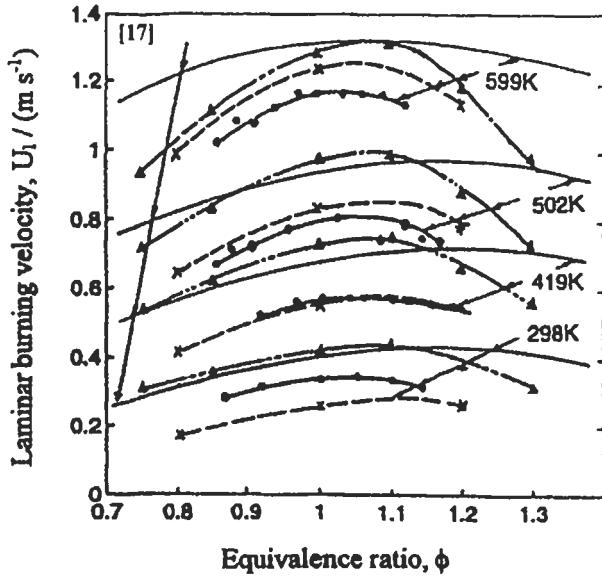


Fig. 2.77: Comparison between the predicted burning velocity [17] with experimental data for n-octane-air flame at 1 atm, different initial temperatures, and equivalence ratios. ● [355], x [271] and ▲ [390]. Reproduced by permission of Combustion Science and Technology.

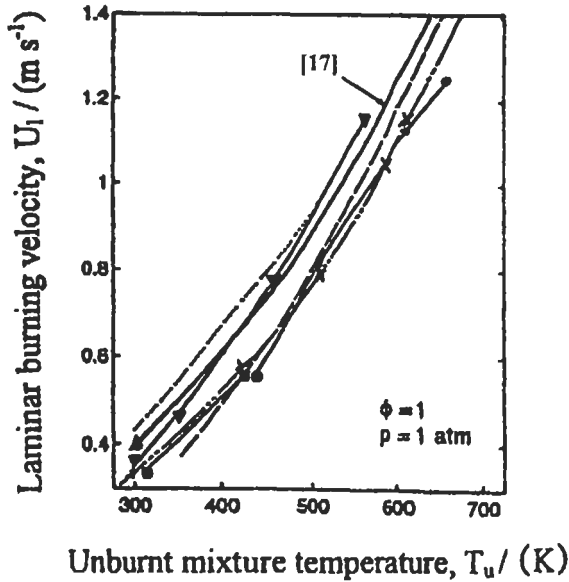


Fig. 2.78: Comparison between the predicted [17] burning velocity with experimental data for n-octane-air flame at 1 atm, stoichiometric condition, and different initial temperatures. X [355], ---- [271], power law equation, ■ [353], ▼ [391], power law equation, ▲ [270], [390], power law equation, and ● [395]. Reproduced by permission of Combustion Science and Technology.

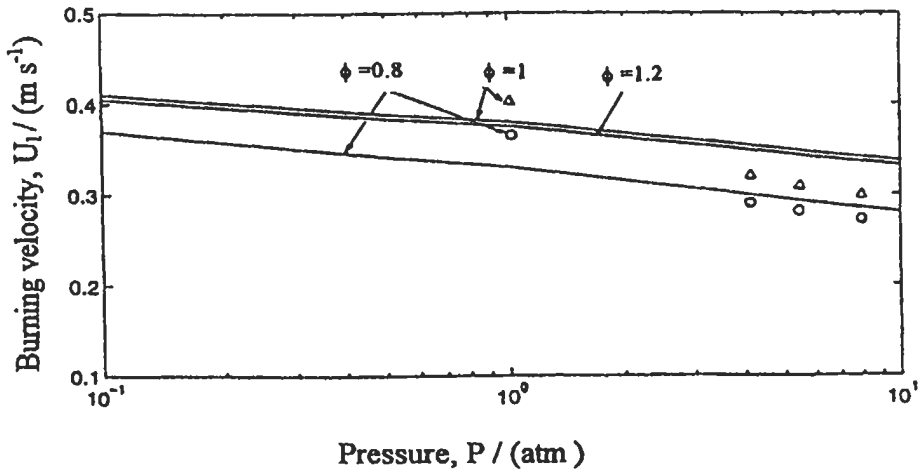


Fig. 2.79: Comparison between the present predicted burning velocity [17] and experimental data (O at $\phi = 0.8$, Δ at $\phi = 1$ from Gülder [390]) for n-octane-air flame at $T_u = 300$ K, different pressures (0.1 to 10 atm,) and equivalence ratios, $\phi = 0.8$, 1 and 1.2. Reproduced by permission of Combustion Science and Technology.

and $\phi = 1$ and 1.24, respectively. Both figures show that, the predicted mole fractions of CO and CO₂ are over and under-predicted, than the corresponding experimental values, respectively (with maximum discrepancy of about 12 %). This may be due to the proposed breakdown of the fuel to one-step reaction. However, the comparison between the predicted and experimental mole fractions of H₂ and O₂ is satisfactory.

By using the kinetic mechanism described above with k_0 of Eqs. 2.66 and 2.67, the computed mole fractions of stable, radical species and gas temperature profiles for n-octane-air flame at 1 atm, $T_u = 300$ K, and $\phi = 1$, show that there is no significant difference between these results (Habik [17]).

(iii) **General correlations for burning velocity of n-butane, benzene, n-heptane, gasoline, kerosene and n-hexadecane-air flames.** Having discussed above, the gasoline-air flames in some details, and to provide further validation of the reduced mechanism, it is necessary now in this section to compare the predicted burning velocity from the kinetic model with available experimental data for different practical high hydrocarbon fuels such as n-butane (C₄H₁₀), benzene (C₆H₆), n-heptane (C₇H₁₆), kerosene (C₁₂H₂₆), and n-hexadecane (C₁₆H₃₄). The variation of the predicted burning velocity from the kinetic model for these fuels with the mole fraction of fuel (fuel/(fuel+air)) is shown by full curves in Fig. 2.81 at 1 atm and 300 K. Also, the experimental burning velocities for these types of fuels are shown by marks in the same figure. The predicted burning velocities for n-butane, benzene, n-heptane, and n-hexadecane were calculated by the same procedure described. The rate parameters for breakdown of these fuels are given in Table 2.16. It is clear from Fig. 2.81 that, the comparison between the predicted and experimental values is satisfactory. There is some slight evidence of the over prediction of burning velocity for very rich flames after $\phi = 1.2$. Therefore, the kinetic mechanisms are only valid for lean to near stoichiometric flames.

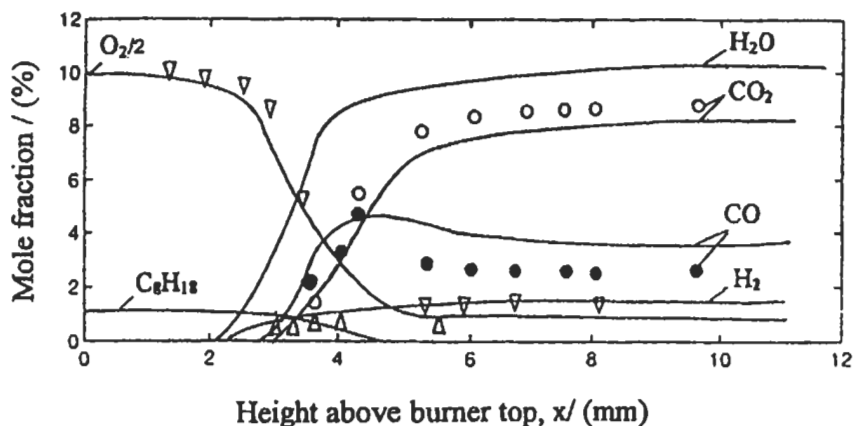


Fig. 2.80 (a): Measured (marks) [393] and predicted mole fractions (full curves [17]) of stable species versus distance above burner top for n-octane-air flame at $\phi = 1$ and 0.2 atm, and 320 K. Reproduced by permission of Combustion Science and Technology.

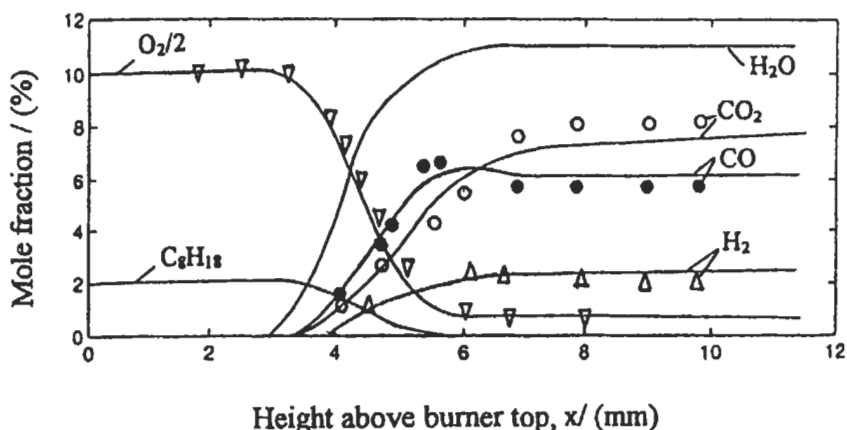


Fig. 2.80 (b): Measured (marks) [393] and predicted mole fractions (full curves [17]) of stable species versus distance above burner top for n-octane-air flame at $\phi = 1.24$ and 0.2 atm, and 320 K. Reproduced by permission of Combustion Science and Technology.

Figure 2.81 shows that, for the fuel with high carbon content, the maximum burning velocity moves towards low value of mole fraction of fuel, and this is due to the high volumetric air-fuel ratio as shown in Table 2.16. The volumetric air-fuel ratio and fuel mole fraction, for each stoichiometric combustion of these fuels with air are also given in Table 2.16. The mass air-fuel ratios for most of alkane fuels (C_nH_{2n+2}) are nearly the same (~ 15) but the ratio for benzene fuel is 13.2, because the latter has different molecular structures (Aromatic compounds). It was also found that, the burning velocity dependence of both pressure and temperature for these fuel is similar to that described above. The predicted results for benzene fuel are in general agreement with those measured recently by Davis et al [397].

Table 2.16: Predicted rate expressions, k_0 , for breakdown of practical high hydrocarbon fuels, calculated air-fuel ratio and mole fraction of fuels [17]. Reproduced by permission of Combustion Science and Technology.

Fuel type	Formula	k_0 (Units in cm.mole.s)	Stoichiometric fuel mole fraction, %	Stoichiometric volume air-fuel ratio
n-Butane	C_4H_{10}	$7.1 \times 10^{12} e^{-15105/T} [C_4H_{10}]^{0.1} [O_2]^{1.6}$	3.130	31.25
Benzene	C_6H_6	$4.1 \times 10^{12} e^{-15105/T} [C_6H_6]^{0.1} [O_2]^{1.6}$	2.723	35.71
n-Heptane	C_7H_{16}	$1.65 \times 10^{12} e^{-15105/T} [C_7H_{16}]^{0.1} [O_2]^{1.6}$	1.874	52.36
n-Octane	C_8H_{18}	$2.0 \times 10^{12} e^{-15105/T} [C_8H_{18}]^{0.1} [O_2]^{1.7}$	1.653	59.52
n-Dodecane	$C_{12}H_{26}$	$5.3 \times 10^{11} e^{-15105/T} [C_{12}H_{26}]^{0.1} [O_2]^{1.7}$	1.123	88.03
n-Hexadecane	$C_{16}H_{34}$	$1.9 \times 10^{11} e^{-15105/T} [C_{16}H_{34}]^{0.1} [O_2]^{1.6}$	0.850	116.62

Table 2.17: Rate expressions for gasoline breakdown, which were used with kinetic mechanism in Table 2.2 (see Fig. 2.75) [17]. Reproduced by permission of Combustion Science and Technology.

No.	k_0 (Units in cm.mole.s)	Note
1	$2.3 \times 10^{14} e^{-15105/T} [C_8H_{18}] [O_2]$ or $0.34 \times T^4 e^{-8000/T} [C_8H_{18}] [O_2]$	Habik et al [17]
2	$1.15 \times 10^{14} e^{-15105/T} [C_8H_{18}] [O_2]$	single step reaction [382]
3	$2.0 \times 10^{12} e^{-15105/T} [C_8H_{18}]^{0.1} [O_2]^{1.7}$	Habik et al [17]
4	$3.2 \times 10^3 T^4 e^{-8000/T} [C_8H_{18}]^{0.1} [O_2]^{1.7}$	Habik et al [17]
5	$4.6 \times 10^{11} e^{-15106/T} [C_8H_{18}]^{0.25} [O_2]^{1.5}$	single step reaction [382]

For practical applications and complex modeling, a simple expression for burning velocity for the above fuels is necessary. Therefore, in this section a general correlation to calculate the burning velocity for each of the above hydrocarbon fuels is proposed as a function of equivalence ratio, ϕ , temperature, T_u , and pressure, P_u . These correlations are given in Table 2.18. The calculated burning velocities from each expression at different T_u , P_u , and ϕ are in good agreement with that predicted from the reduced kinetic models at $\phi = 0.6$ to 1.2 (with maximum discrepancy of $\pm 0.005 \text{ m s}^{-1}$).

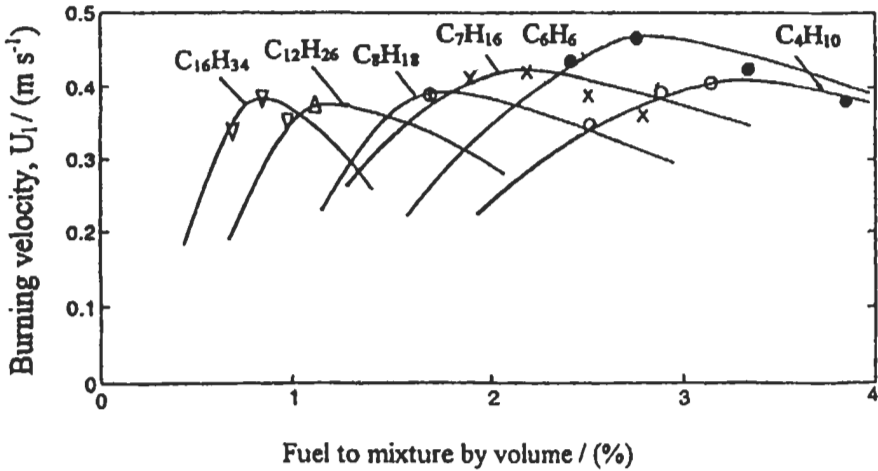


Fig. 2.81: Variation of the computed (full curves) [17] and experimental burning velocity (shown by marks) with mole fraction of fuel for different types of practical high hydrocarbon fuel. O C₄H₁₀, ● C₆H₆, x C₇H₁₆ [270], ⊕ C₈H₁₈ [see Figs. 2.75 to 2.77], Δ C₁₂H₂₆, ∇ C₁₆H₃₄[350]. Reproduced by permission of Combustion Science and Technology.

Table 2.18: General correlation for burning velocity as a function of equivalence ratio, ϕ , initial pressure, P_u , and temperature, T_u for different types of practical high hydrocarbon fuel [17]. Reproduced by permission of Combustion Science and Technology.

Fuel type	Formula	U_{10} (function of ϕ , at $P_0 = 1$ atm, and $T_0 = 300$ K), (m s ⁻¹)	U_1 (function of ϕ , P_u and T_u) (m s ⁻¹)
n-Butane	C ₄ H ₁₀	$0.43 \phi^{-0.35} e^{-2.2(\phi-1.15)^2}$	$U_{10}(P_u/P_0)^{-0.065} (T_u/T_0)^{1.65}$ P<1 atm $U_{10}(P_u/P_0)^{-0.090} (T_u/T_0)^{1.65}$ P>1 atm
Benzene	C ₆ H ₆	$0.50 \phi^{-0.35} e^{-2.2(\phi-1.20)^2}$	$U_{10}(P_u/P_0)^{-0.070} (T_u/T_0)^{1.65}$ P<1 atm $U_{10}(P_u/P_0)^{-0.100} (T_u/T_0)^{1.65}$ P>1 atm
n-Heptane	C ₇ H ₁₆	$0.43 \phi^{-0.35} e^{-2.2(\phi-1.15)^2}$	$U_{10}(P_u/P_0)^{-0.070} (T_u/T_0)^{1.65}$ P<1 atm $U_{10}(P_u/P_0)^{-0.090} (T_u/T_0)^{1.65}$ P>1 atm
n-Octane	C ₈ H ₁₈	$0.42 \phi^{-0.35} e^{-2.5(\phi-1.15)^2}$	$U_{10}(P_u/P_0)^{-0.040} (T_u/T_0)^{1.65}$ P<1 atm $U_{10}(P_u/P_0)^{-0.060} (T_u/T_0)^{1.65}$ P>1 atm
n-Dodecane	C ₁₂ H ₂₆	$0.40 \phi^{-0.35} e^{-2.3(\phi-1.15)^2}$	$U_{10}(P_u/P_0)^{-0.040} (T_u/T_0)^{1.60}$ P<1 atm $U_{10}(P_u/P_0)^{-0.060} (T_u/T_0)^{1.60}$ P>1 atm
n-Hexadecane	C ₁₆ H ₃₄	$0.40 \phi^{-0.35} e^{-2.3(\phi-1.15)^2}$	$U_{10}(P_u/P_0)^{-0.065} (T_u/T_0)^{1.60}$ P<1 atm $U_{10}(P_u/P_0)^{-0.090} (T_u/T_0)^{1.60}$ P>1 atm

2.7 Effect of Fuel Type and Additives on Emissions and Flame Characteristics

2.7.1 Effect of Fuel Type on Nitrogen Compounds

Kinetic mechanism for nitrogen compounds has been used by Habik [19, 20] to study the effect of fuel type (such as CH_4 and C_3H_8) on the pollutant emissions and flame characteristics. These results were compared in Figs. 2.82 (a) and (b) at 1 atm, $\phi = 1$ and 300 K. Nitrogen compounds for methane-air flames were computed in similar way to that described in section 2.4.3, and these results are shown by dashed curves as well as the computed mole fractions of CO and HO_2 in Fig. 2.82 (a). Figure 2.82 (b) shows the corresponding radical species, O, H, and OH for the same flame of Fig. 2.82 (a).

The nitrogen compounds for propane-air flame were computed using the same kinetic mechanism described in section 2.3.2 in addition to the kinetic mechanism for NO_x given in Table 1.9. These computed values are shown by full curves in Fig. 2.82 (a) as well as CO and HO_2 at $\phi = 1$ and 300 K. For this flame, the computed O, H, and OH are also shown by full curves in Fig. 2.82 (b). In Fig. 2.82 (a), the comparison

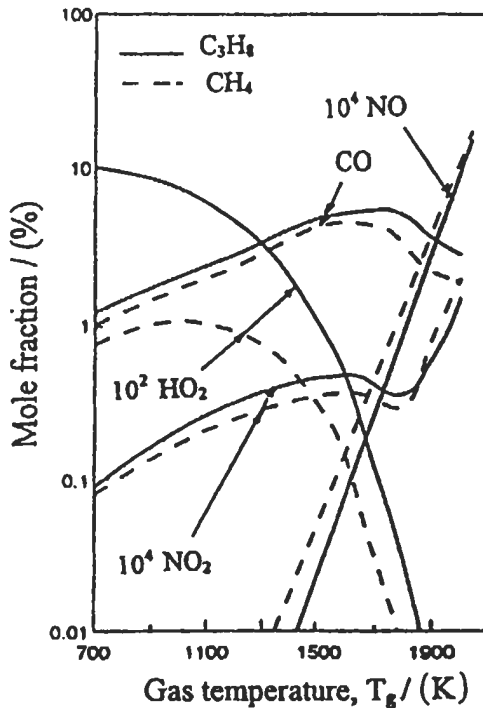


Fig. 2.82 (a): Comparison between the maximum mole fractions of NO, NO_2 , CO and HO_2 for both CH_4 -air and C_3H_8 -air flames, at $\phi = 1$, 300 K and 1 atm [19].

between the mole fraction of NO from both flames shows that, for a given gas temperature, the NO from methane flame is higher than the corresponding value for propane flame, even though there is a difference in combustion time due to the difference in the burning velocity. For a gas temperature less than 1850 K, the increase of NO and the decrease of NO₂ for CH₄-air flame as compared to the corresponding values for C₃H₈-air flame are due to the decrease of HO₂ which in turn decreases the reactivity of R₄ ($\text{NO} + \text{HO}_2 \leftrightarrow \text{NO}_2 + \text{OH}$ in Table 1.9). This is followed by the increase of the reactivity of reaction, R₈ ($\text{NO}_2 + \text{O} \leftrightarrow \text{NO} + \text{O}_2$ in Table 1.9) due to high concentration of O atoms. After this temperature, the O atoms (see Fig. 2.82 (b)) are responsible for the increase of NO through reaction R₅ ($\text{NO} + \text{O} + \text{M} \leftrightarrow \text{NO}_2 + \text{N}_2$ in Table 1.9).

For a gas temperature higher than 1850 K, the sudden increase in NO₂ is due to the decrease of O atoms, which in turn reduce the reactivity of reaction, R₈. The increase of O atoms in propane-air flame as compared to the corresponding value in methane-air flame is mainly due to high reactivity of reaction $\text{H} + \text{O}_2 \leftrightarrow \text{O} + \text{OH}$. Also shown in the same figure, that the mole fraction of CO from methane flame is lower than that from propane flame at all temperatures. This is mainly due to the decrease of OH concentration as shown in Fig. 2.82 (b).

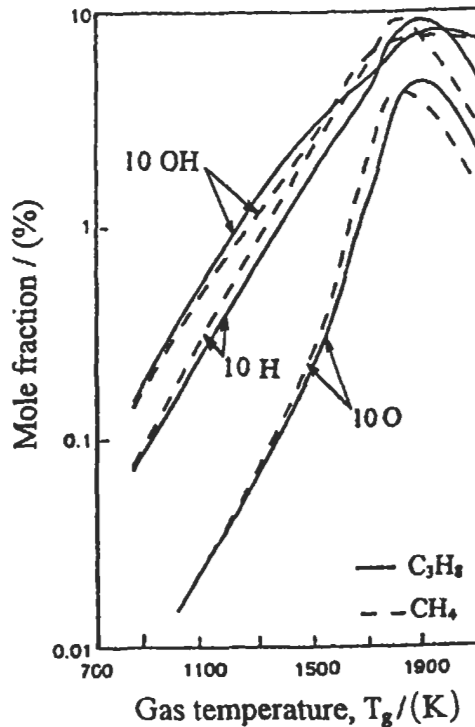


Fig. 2.82 (b): Comparison between the maximum mole fractions of O, H and OH for both flames as in Fig. 2.82 (a) [19].

2.7.2 H₂ and C₂H₆ Addition to C₃H₈-Air Flames

As we have discussed in section 1.10 (chapter 1), the burning of lean hydrocarbon is one of the important methods for reducing the NO_x and CO emissions. In addition, the lean burning offers the potential of enhanced fuel economy, and improves thermal stress characteristics of the combustor hardware. However, lean mixtures are hard to ignite and more susceptible to extinguish. Thus, their utilization imposes more stringent criteria on the operational reliability of the combustor.

A promising approach to enhance the combustion intensity of the lean mixtures and reduce pollutant emissions is thought through the addition of gaseous fuels (which has high burning intensity) to liquid-air flames. This will increase the concentrations of the radical species, which control the pollutant emissions and otherwise would be supplied through back diffusion from the reaction zone to heat up the incoming lean mixture.

Yu et al [227] have used hydrogen as an additive to hydrocarbon-air flames and their results showed that the burning velocity is substantially increased with hydrogen addition. Habik [19] studied the effect of H₂ and C₂H₆ as an additive on the characteristics of the propane-air flames. Moreover, Hori et al [398] have studied the effect of low-concentration fuels addition on the conversion of nitric oxide to nitrogen dioxide and they suggested that the presence of fuel in the cool region of the flow in a combustion system should be prevented in order to reduce NO_x exhaust emission. Such additives exert an enormous effect on NO₂ levels in practical combustion. Furthermore, the addition of hydrogen has significant effect on the suppressing soot inception in strained flame [399].

This section will discuss the effect of gaseous additives (such as H₂ and C₂H₆) on the characteristics of propane-air flame [19]. In order to investigate this approach, it was necessary to validate the predicted results with the experimental results. The only experimental data available are those measured by Yu et al [227]. They have used the symmetrical, adiabatic, counterflow arrangement to measure the burning velocity for propane-air flame at atmospheric pressure, room temperature, with and without the addition of stoichiometrically small amounts of hydrogen. They determined the burning velocity firstly, by measuring the flame speed with stretch, and secondly, by linearly extrapolating these values to zero stretch. Such results are shown by circles in Fig. 2.83. These experimental results will be discussed with the corresponding predicted values as given by Habik [19], in the following sub-sections.

(i) **Effect of H₂ and C₂H₆ as additives on the burning velocity.** Yu et al [227] have shown that, the concentration of H₂ additives has to be present only in small quantity, and there should be enough air to facilitate its complete oxidation. Thus, if the mole fractions of the propane fuel, hydrogen, and air are, C_F, C_H, and C_A, respectively, with C_F+C_H+C_A=1, then in order to oxidize totally the C_H amount of H₂, it will need C_H/(C_H/C_A)_{st.} amount of air, where (C_H/C_A)_{st.} = 0.418 is the stoichiometric hydrogen-to-air molar ratio. If the remaining air is used to oxidize the propane fuel, then an effective fuel/air equivalence ratio, φ_F can be defined as:

$$\phi_F = \frac{C_F / [C_A - C_H / (C_H / C_A)_{st.}]}{(C_F / C_A)_{st.}} \quad (2.71)$$

where, (C_F/C_A)_{st.} is the stoichiometric fuel-to-air molar ratio, which is 0.0418 for propane-air mixture.

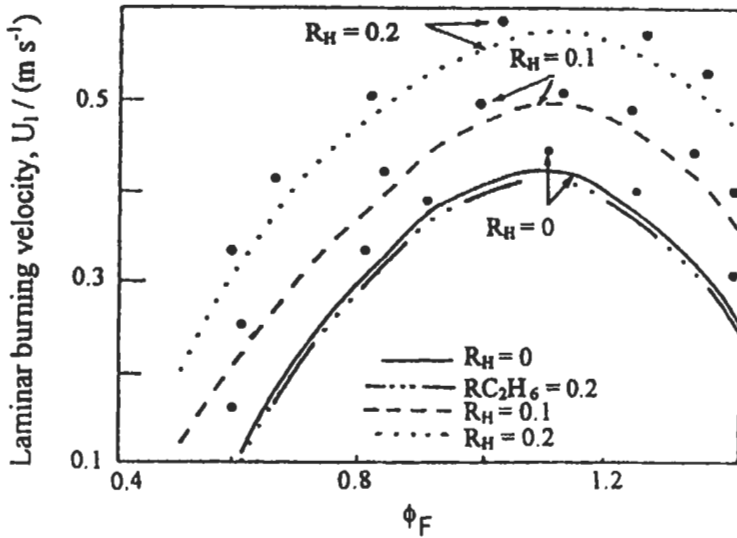


Fig. 2.83: Predicted (curves) and experimental, ● [227] laminar burning velocity of propane-hydrogen-air mixture as a function of ϕ_F with R_{H_2} and $R_{C_2H_6}$ at 1 atm and 300 K [19].

To indicate the relative amount of hydrogen addition, Yu et al [227] have defined the ratio of R_H as:

$$R_H = \frac{C_H + C_H / (C_H / C_A)_{st.}}{C_F + [C_A - C_H / (C_H / C_A)_{st.}]} \quad (2.72)$$

The numerator of R_H is the amount of hydrogen plus the amount of air needed to oxidize it totally, while the denominator is the amount of hydrocarbon fuel plus the amount of air available for its oxidation.

Thus ϕ_F and R_H are the two parameters to be used to indicate the concentrations of propane and hydrogen. Following the procedures described in section 2.4.6, and Eqs. 2.71 and 2.72, the computed burning velocity and nitrogen compounds for propane-air flames at different values of ϕ_F and R_H , 1 atm and 300 K are shown in Figs. 2.83 to 2.86 (b).

Figure 2.83 shows the measured (circles) and computed (full, dashed and dotted curves) burning velocity as a function of ϕ_F , with R_H as a parameter. For $R_H = 0$, we have the reference propane-air flame without any additives. With hydrogen addition and therefore, increasing R_H , the burning velocity increases. For different R_H , the variation of burning velocity with ϕ_F remains qualitatively the same, with the maxima occurring around a narrow range of ϕ_F .

Yu et al [227] have found that the experimental upper limit in R_H was constrained by the propensity of the flame to flashback, but for the leanest propane case ($\phi_F = 0.5$), and with great caution they were able to extend their investigation to $R_H = 1.0$. Figure 2.83 shows that, the agreement between the experimental and the computed results are good. This validates the kinetic model with hydrogen addition and gives more confidence to study the effect of addition stoichiometrically small amounts of ethane species (C_2H_6) to

propane-air flames. In this case, the stoichiometric ethane-to-air molar ratio is represented by $(C_{C_2H_6}/C_A)_{st.} = 0.06$ and can be replaced by the term $(C_H/C_A)_{st.}$ in Eqs. 2.71 and 2.72. The predicted burning velocity with $R_{C_2H_6} = 0.2$ is shown by dashed dotted curve in Fig. 2.83. The figure shows that, for a given value of ϕ_F with the value of $R_{C_2H_6} = 0.2$ or $R_H = 0.2$, there is a significant change in the burning velocity with R_H , while with $R_{C_2H_6}$ there is no significant difference. This is due to the significant increase of H atoms with R_H compared to the corresponding value with $R_{C_2H_6}$ as shown in Fig. 2.84 (d). The increase or decrease of H atom has a significant effect on the burning velocity through reaction R_2 ($H + O_2 \rightarrow OH + O$) as it has been explained in the previous sections.

In section 2.4.6, it has been shown that the burning velocity for propane-air, U_o , can be correlated as a function of ϕ by Eq. 2.44, while the burning velocity, U_i , shown in Fig. 2.83 can be linearly correlated with the hydrogen concentration parameter, R_H by:

$$U_i(\phi_F, R_H) \approx U_o(\phi = \phi_F) + 0.82 R_H \quad \text{m s}^{-1} \quad (2.73)$$

This equation is in excellent agreement with that proposed by Yu et al [227]. Therefore, Eqs. 2.44 and 2.73 can be used to calculate the burning velocity for propane-air flame without and with the addition of stoichiometric small amounts of hydrogen. Such a relation is expected to be useful from practical considerations for the case of adding hydrogen only, but with addition of ethane, the second term of Eq. 2.73 can be neglected.

Having thus validated the kinetic model with the addition of hydrogen and ethane to propane-air flame through the above comparisons, we can now turn to continue our study on how these additions affect the nitrogen oxides and carbon monoxide emissions in propane-air flames, and this will be explained next.

(ii) **Effect of H_2 and C_2H_6 as additives on the maximum nitrogen oxides and carbon monoxide.** Habik [19] studied the effect of addition of stoichiometric small amounts of hydrogen or ethane on the nitrogen oxides and carbon monoxide for propane-air flames at 1 atm, 300 K, and for different equivalence ratios. These flames were the same as those described in the above section (Fig. 2.83) in which their computed burning velocities were validated with the experimental data. The computed nitrogen oxides, carbon monoxide and radical species for these flames are shown in Figs. 2.84 (a) to (e). Fig. 2.84 (a) shows the variation of the computed maximum value of NO_x (ppm) with ϕ_F and for different R_H and $R_{C_2H_6}$ parameters. The figure shows that the NO_x decreases at $\phi_F = 1$ by about 45 % as the R_H increases from 0.0 to 0.2. This large reduction of NO_x is due to the decrease of NO_2 by about 55 % as shown in Fig. 2.84 (b). This decrease is consistent with the decrease of HO_2 by about 60 % as shown in Fig. 2.84 (e). The main reaction responsible for decreasing NO_2 in the reaction zone is R_4 ($NO + HO_2 \rightarrow NO_2 + OH$ in Table 1.9). Consequently, the reduction of NO_2 will lead to another reduction of NO through reaction R_8 ($NO_2 + O \rightarrow NO + O_2$ in Table 1.9), which contributes significantly to NO production. Although the O atom concentration increases as shown in Fig. 2.84 (d), but this increase is small compared to the reduction of NO_2 and does not contribute significantly to an increase of the reaction, R_8 compared to NO_2 species. This is in addition to the reduction of combustion time for the flame with $R_H = 0.2$ compared to the flame with $R_H = 0.0$.

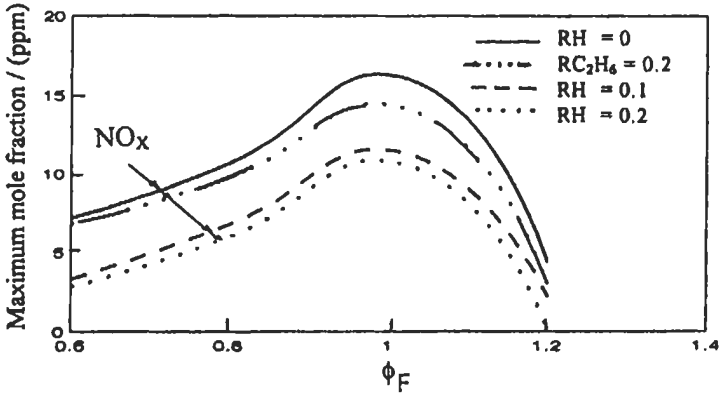


Fig. 2.84 (a): Effect of H₂ and C₂H₆ additives on the maximum mole fraction of NO_x for the same flames as in Fig. 2.83 [19].

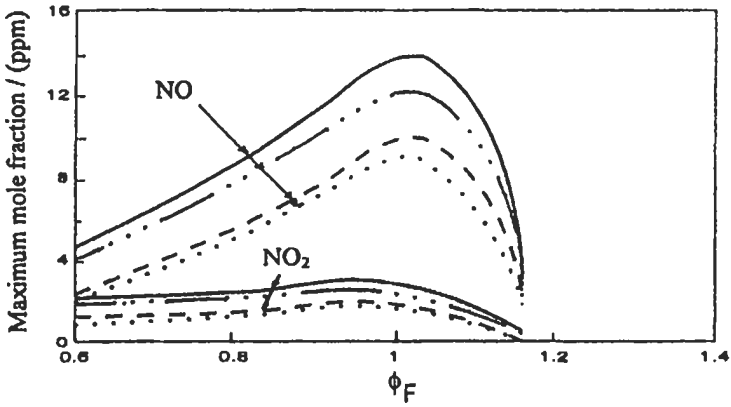


Fig. 2.84 (b): Effect of H₂ and C₂H₆ additives on the maximum mole fractions of NO, NO₂ for the same flames as in Fig. 2.83 [19].

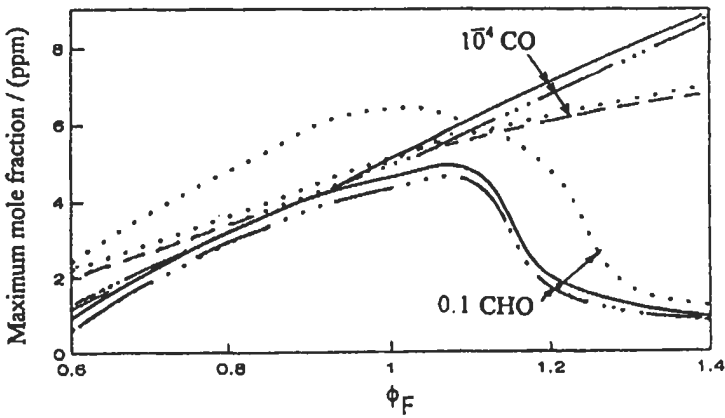


Fig. 2.84 (c): Effect of H₂ and C₂H₆ additives on the maximum mole fractions of CO and CHO for the same flames as in Fig. 2.83 [19].

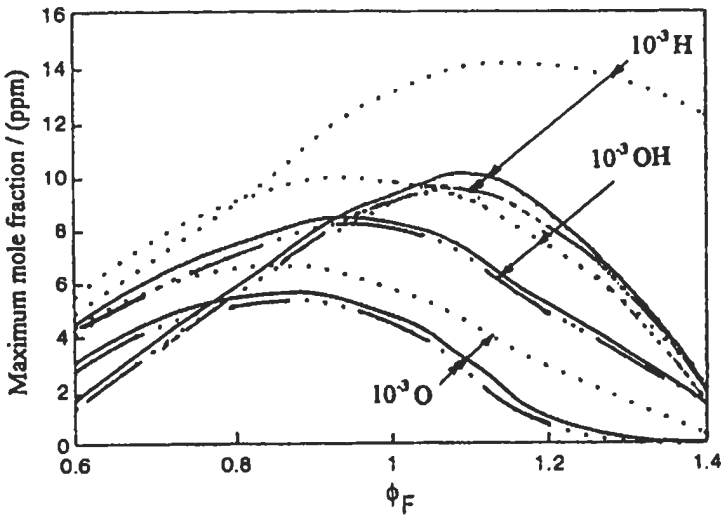


Fig. 2.84 (d): Effect of H_2 and C_2H_6 additives on the maximum mole fractions of H, O and OH for the same flames as in Fig. 2.83 [19].

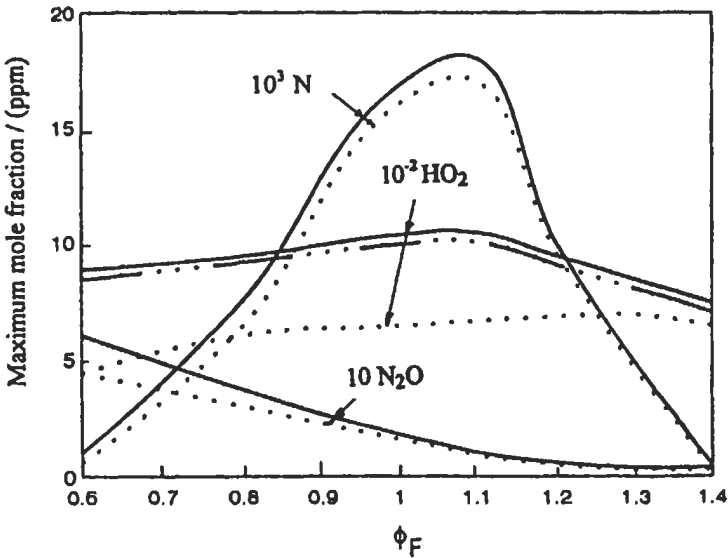


Fig. 2.84 (e): Effect of H_2 and C_2H_6 additives on the maximum mole fractions of N, HO_2 and N_2O for the same flames as in Fig. 2.83 [19].

Figures 2.84 (a) to (e) show that there is a significant change of NO_x , NO, NO_2 , O, H, OH and HO_2 species when hydrogen fuel is added to the propane-air flame, compared to the corresponding species when ethane fuel is added. This significant change due to hydrogen addition, occurs only for lean and near stoichiometric flames, while in rich flames, there is a slight change for all the above species.

Figure 2.84 (c) shows the variation of the maximum mole fractions of CO and CHO with ϕ_F . In lean flames of $\phi_F < 0.8$, and as the R_H increases, the CO increases twice due to the increase of CHO, H, O, OH and O_2 species, and consequently increases the reactivity of reaction R_{17} to R_{20} resulting in more CO production, while in rich flames $\phi_F > 1$, and as R_H increases, the mole fraction of CO decreases. This is due to high reactivity of reaction R_{14} ($CO + OH \rightarrow CO_2 + H$) where OH increases as R_H increases and this is shown in Fig. 2.84 (d).

Also shown in Fig. 2.84 (e) the variation of N, HO_2 and N_2O species with ϕ_F . It is clear from the figure that the mole fraction (ppm) of N_2O increases as the value of ϕ_F decreases for the two cases with and without the addition of stoichiometric small amounts of hydrogen. Flames with $R_H = 0.2$ result in a reduction of N_2O and this reduction increases as ϕ_F decreases. This latter reduction is due to high H atoms, which result in increasing the reactivity of reactions R_6 and R_9 in Table 1.9.

(iii) **Effect of R_H and $R_{C_2H_6}$ on NO_x and CO throughout the flame.** For propane-air-hydrogen flame at $\phi_F = 1$, 1 atm and 300 K, with $R_H = 0.0$ and 0.2, the computed mole fractions of NO, NO_2 , CO and HO_2 as a function of gas temperature are shown by full (for $R_H = 0.0$) and dotted (for $R_H = 0.2$) curves in Fig. 2.85 (a), while Fig. 2.85 (b) shows the variations of the computed mole fractions of O, H, and OH with the gas temperature for the same flame as in Fig. 2.85 (a). Figure 2.85 (a) shows that the concentration of HO_2 decreases throughout the flame with $R_H = 0.2$ compared to that corresponding to $R_H = 0.0$. This leads to low concentrations of NO_2 and NO through the reactions R_4 and R_8 (in Table 1.9) even when the concentrations of O, H and OH increase with R_H as shown in Fig. 2.85 (b). This indicates that, it is possible to reduce nitrogen oxides with fuel additives even though the increase of the radical species, O, H and OH. This is due to the high level of HO_2 concentration, which has predominant effect through reactions R_4 and R_9 compared to the reactions involved with O, H, and OH (see Table 1.9).

The low mole fraction of HO_2 as R_H increases is due to low reactivity of reaction R_4 ($H + O_2 + M \rightarrow HO_2 + M$) which competes with R_2 ($H + O_2 \rightarrow OH + O$), however, the reaction R_2 is very reactive in this flame due to high concentration of H atoms. The maximum HO_2 occurs at about 700 K. Also, the concentration of CO decreases throughout the flame as R_H increases. This is due to the increase of OH concentration with R_H , which in turn increases the reactivity of R_{14} ($OH + CO \rightarrow CO_2 + H$) and hence reduces CO. Figure 2.85 (b) shows that, the radical species of O, H, and OH increase as R_H increases throughout the flame.

(iv) **Effect of pressure on NO_x and CO with R_H and $R_{C_2H_6}$.** Figures 2.86 (a) and (b) show the effect of pressure on the mole fractions of NO, NO_2 , N_2O , N, CO, H, O, OH and HO_2 for propane-air flames with addition of small stoichiometric amounts of hydrogen (R_H) at 300 K and $\phi_F = 1$. Figure 2.86 (a) shows that the mole fractions of NO and NO_2 increase with the pressure, while O, and H atoms decrease. However, as R_H increases from 0.0 to 0.2, the NO and NO_2 decrease, while O and H increase at all pressures. It is clear from the figure that, at a pressure of 0.1 atm, the volumetric ratio of NO_2 (at $R_H = 0.2$)/ NO_2 (at $R_H = 0.0$) is found to be about 0.5 and this ratio increases as the pressure increases. This is due to the decrease of the volumetric ratio of HO_2 (at $R_H = 0.2$)/ HO_2 (at $R_H = 0.0$) as the pressure increases. This ratio is about 0.45 at 0.1 atm and it becomes about 0.9 at 10 atm (see Fig. 2.85 (b)). This again indicates the importance of HO_2 formation. The increase of H atoms with R_H at all

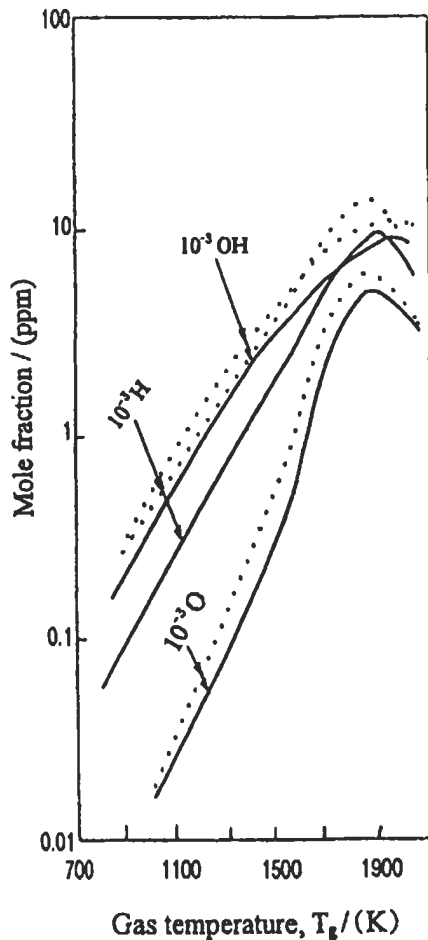
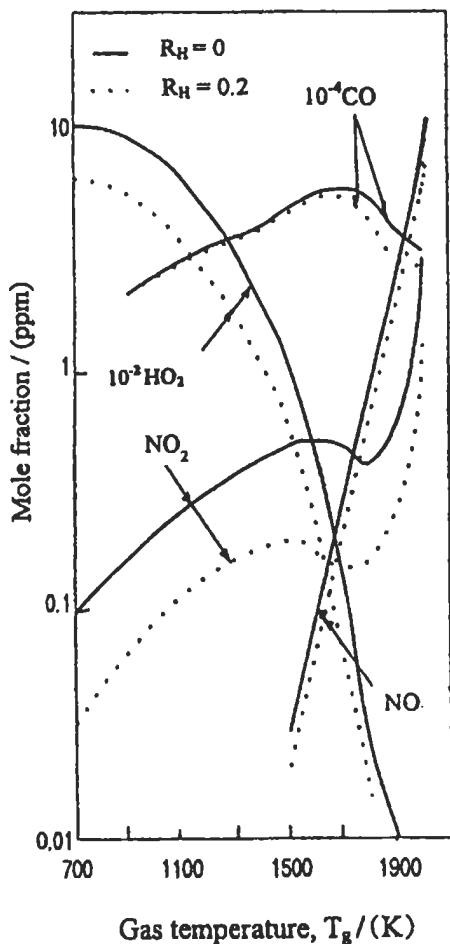


Fig. 2.85 (a): Predicted maximum mole fractions of HO_2 , NO , CO , and NO_2 versus gas temperature for $\text{C}_3\text{H}_8\text{-H}_2\text{-air}$ flame with $R_H = 0$ and 0.2 , 1 atm and 300 K and $\phi_F = 1$ [19].

Fig. 2.85 (b): Predicted maximum mole fractions of O , H and OH versus gas temperature for the same flame as in Fig. 2.85 (a) [19].

pressures indicates that the burning velocity will increase with R_H at all pressures.

Figure 2.86 (b) shows that, the decrease of N_2O , N , and CO with R_H is approximately constant at all pressures. The decrease of N_2O with R_H is due to the increase of O and H atoms in reactions R_6 and R_9 (Table 1.9).

2.7.3 H_2 and CO Addition to $\text{CH}_4\text{-Air}$ Flames

This section represents another investigation of the effect of gaseous additives on the pollutant emissions in $\text{CH}_4\text{-air}$ flames (El-Sherif [400]). She [400] investigated the effect of H_2 and CO addition on nitrogen oxides and carbon monoxide in $\text{CH}_4\text{-air}$ flames. These flames were simulated by the one-dimensional model described before.

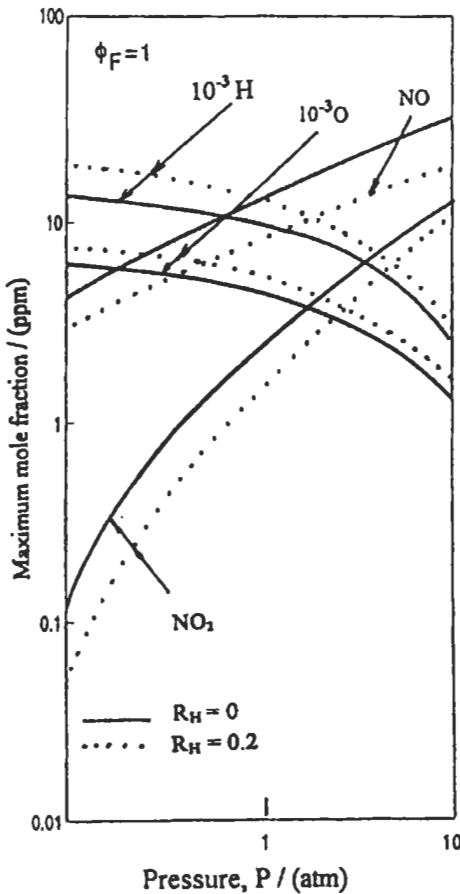


Fig. 2.86 (a): Variation of predicted maximum mole fractions of NO, NO₂, O and H with pressure and R_H for propane-H₂-air flames at 300 K and $\phi_F = 1$ [19].

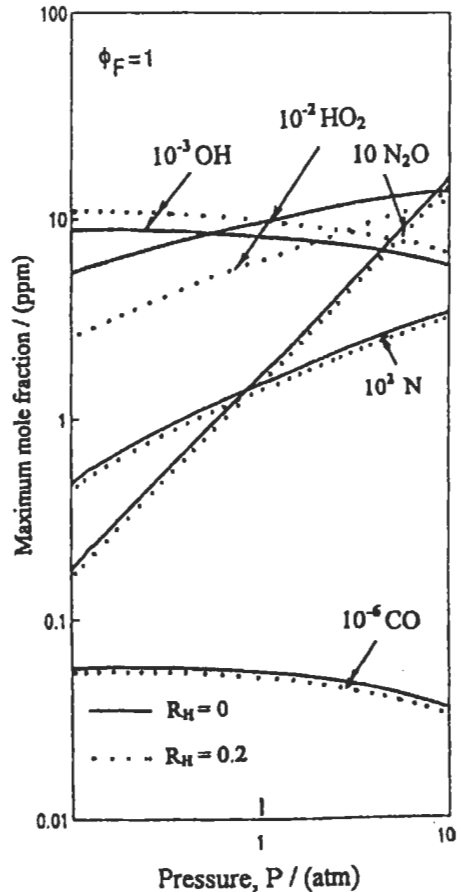


Fig. 2.86 (b): Variation of predicted maximum mole fractions of N₂O, HO₂, HO, N and CO with pressure and R_H for the same flames as in Fig. 2.86 (a) [19].

A set of experimental data given by Yu et al [227] were used to be compared with the corresponding predicted results from the kinetic model [400]. They [227] have measured the laminar flame speed of methane-air at 1 atm and 300 K with and without the addition of stoichiometric small amounts of hydrogen. They used symmetrical, adiabatic, counterflow arrangement, and their results are shown by circles in Figs. 2.87 and 2.88.

For methane-air flames with hydrogen addition, the mole fractions of the methane fuel, hydrogen, and air are represented in the total mixture by C_F , C_H , and C_A , respectively, with $C_F + C_H + C_A = 1$, while the hydrogen addition is represented by the parameter, R_H , and the effective fuel equivalence ratio, ϕ_F . These are defined by Eqs. 2.71 and 2.72. In case of carbon monoxide addition to the CH₄-air flame, the molar stoichiometric CO-air is represented by $(C_{CO}/C_A)_{st.} = 0.42$, and can replace the term $(C_H/C_A)_{st.}$ in Eqs. 2.71 and 2.72. Furthermore, the mole fraction of hydrogen, C_H , and

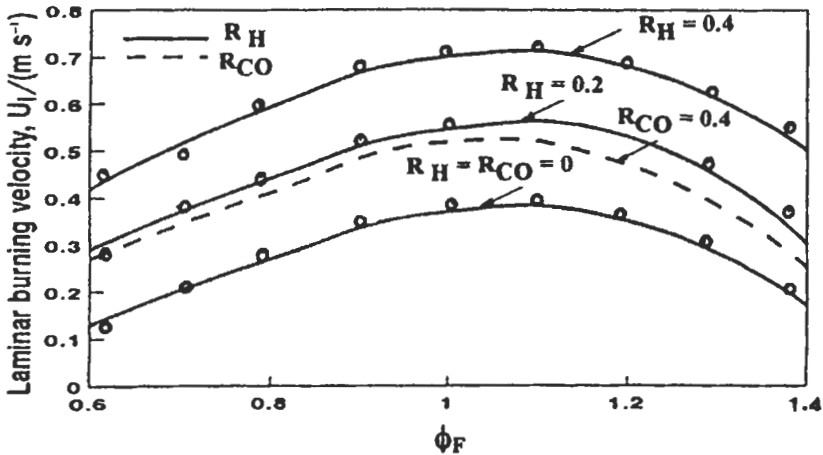


Fig. 2.87: Predicted laminar burning velocity of methane + hydrogen + air and methane + carbon monoxide + air flames [400] as a function of ϕ_F with R_H and R_{CO} as parameters at 1 atm and 300 K, O, Experimental [227] for methane + hydrogen + air flames. Reproduced by permission of Elsevier Science.

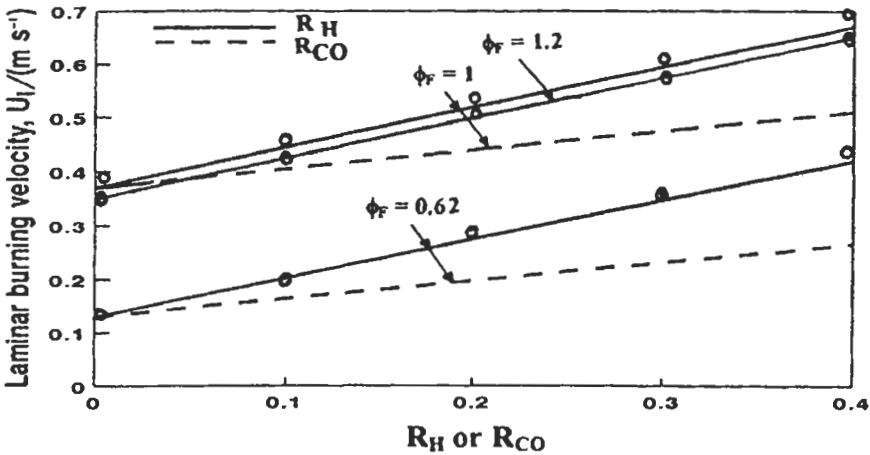


Fig. 2.88: Predicted laminar burning velocity of methane + hydrogen + air and methane + carbon monoxide + air flames [400] as a function of R_H and R_{CO} with ϕ_F as parameters, for lean and rich ϕ_F at 1 atm and 300 K, O, Experimental [227] for methane + hydrogen + air flames. Reproduced by permission of Elsevier Science.

parameter, R_H in Eqs. 2.71 and 2.72 can be replaced by C_{CO} , and R_{CO} . The predicted results by El-Sherif [400] are shown by full (for $R_H = 0$ to 0.4) and dashed curves (for $R_{CO} = 0$ to 0.4) in Figs. 2.87-2.88, while the computed mole fractions of NO_x , NO_2 , HO_2 , H, CO, OH and O for flames of Fig. 2.87 are shown in Figs. 2.89 (a) to 2.89 (d). The variations of N_2O , NO_x , HO_2 , CO, as a function of R_H , R_{CO} at $\phi_F = 1$ are shown in Fig. 2.90. The computed mole fractions of NO_x , NO_2 , NO, HO_2 , H, O and OH at $\phi_F = 1$, 1 atm, and 300 K as a function of the burned gas temperature throughout the flame are shown in Figs. 2.91 (a) and (b). The above results will be discussed as follows:

(i) **Variation of burning velocity with ϕ_F , R_H and R_{CO} for CH_4 -air flames.** Figure 2.87 shows the comparison between the experimental and computed [400] (full and dashed curves) burning velocity, U_1 , as a function of ϕ_F with R_H and R_{CO} as parameters. With $R_H = R_{CO} = 0$, the full curve shown in the figure represents the reference CH_4 -air flames without any additives. The agreement between the computed and experimental value of U_1 , is good (maximum discrepancy of about 3 %) and this validates the kinetic model. With H_2 , R_H , or CO , R_{CO} addition, the burning velocity increases at all ϕ_F . This is due to the increase of H atoms and consequently the increase in the chain branching reaction, $H + O_2 \leftrightarrow OH + O$, which play a significant role for increasing U_1 . At $\phi_F = 1$, $R_H = 0.4$ and $R_{CO} = 0.4$, the U_1 increases by a factor of about 2 and 1.5 (Fig. 2.87), while the maximum H atoms increase by about 1.9 and 1.3, respectively (Fig. 2.89 c). In Fig. 2.88, the increase of the U_1 with R_H and R_{CO} at different ϕ_F varies linearly over a wide range of R_H and R_{CO} , but the slope with R_{CO} is less than the slope with R_H . These slopes do not vary too much from each other at different ϕ_F . It was found that the linear slope of burning velocity with R_H is 0.84 m s^{-1} , while with R_{CO} is 0.4 m s^{-1} for ϕ_F of 0.6 to 1.2. Yu et al [227] have assumed a value of 0.83 m s^{-1} for their experimental results of $C_3H_8 + H_2 + \text{air}$ and $CH_4 + H_2 + \text{air}$ flames. The linear slope is in a good agreement with that proposed by Habik [19] for $C_3H_8 + H_2 + \text{air}$ flames. This indicates that the linear slope of U_1 with R_H may be the same for hydrocarbon fuels, but it varies for different gaseous additives. Based on the behavior of Fig. 2.88, it is possible to correlate U_1 with R_H by Eq. 2.73' and with R_{CO} by Eq. 2.74 as follows:

$$U_1 = 0.38 \phi_F^{-0.35} \exp[-5.5 (\phi_F - 1.1)^2] + 0.82 R_H \quad \text{m s}^{-1} \quad (2.73')$$

$$U_1 = 0.38 \phi_F^{-0.35} \exp[-5.5 (\phi_F - 1.1)^2] + 0.4 R_{CO} \quad \text{m s}^{-1} \quad (2.74)$$

These equations are of practical utility. Having thus validated the kinetic model with the addition of hydrogen and CO, it is now important to study the effect of these additives on the NO_x and CO emitted from the flame, and this will be discussed next.

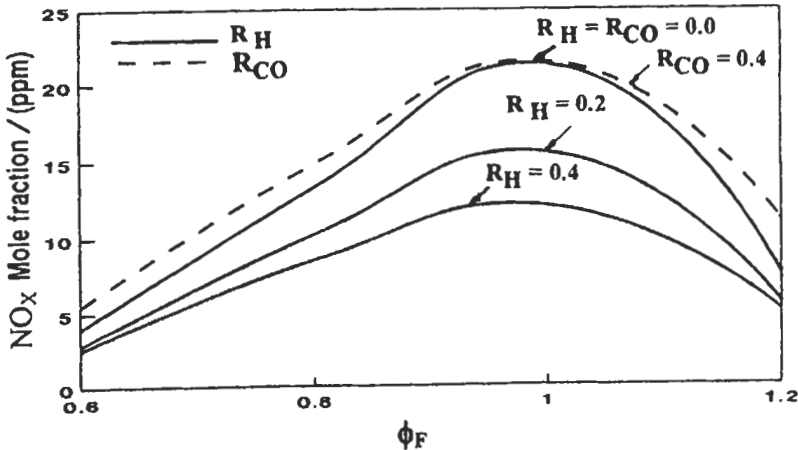


Fig. 2.89 (a): Variation of maximum mole fraction of NO_x with ϕ_F for the same flames as in Fig. 2.87 [400]. Reproduced by permission of Elsevier Science.

(ii) **Variation of NO_x and CO with R_H and R_{CO} for CH_4 -air flames.** In Fig. 2.89 (a), the decrease of NO_x species with the increase of R_H is significant at all ϕ_F , while with R_{CO} , the NO_x species increase slightly compared to the case without additives. At $\phi_F = 1$, and $R_H = 0.4$, the NO_x species decrease by about 56 %. This is due to the increase of O atoms (see Fig. 2.89 c) and consequently the increase of the reactivity of reactions R_8 ($\text{NO}_2 + \text{O} \rightarrow \text{NO} + \text{O}_2$ in Table 1.9) and R_5 ($\text{NO} + \text{O} + \text{N}_2 \rightarrow \text{NO}_2 + \text{N}_2$ in Table 1.9) leading to a reduction of NO and NO_2 . Figure 2.89 (b) shows that the decrease of NO_2 is accompanied by the decrease of HO_2 . The main reaction responsible for decreasing NO_2 with HO_2 in the reaction zone is reaction R_4 ($\text{NO} + \text{HO}_2 \rightarrow \text{NO}_2 + \text{OH}$ in Table 1.9). Also, the increase of NO_x with the increase of R_{CO} , is due to the increase of HO_2 (see Fig. 2.89 (b)).

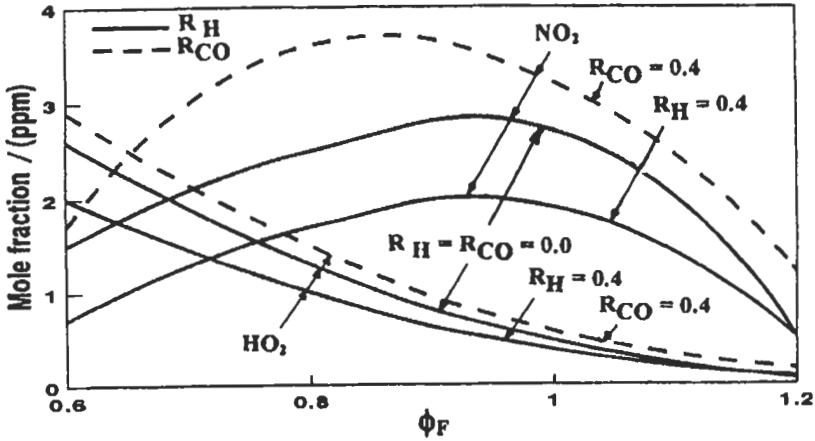


Fig. 2.89 (b): Variation of maximum mole fractions of NO_2 and HO_2 with ϕ_F for the same flames as in Fig. 2.87 [400]. Reproduced by permission of Elsevier Science.

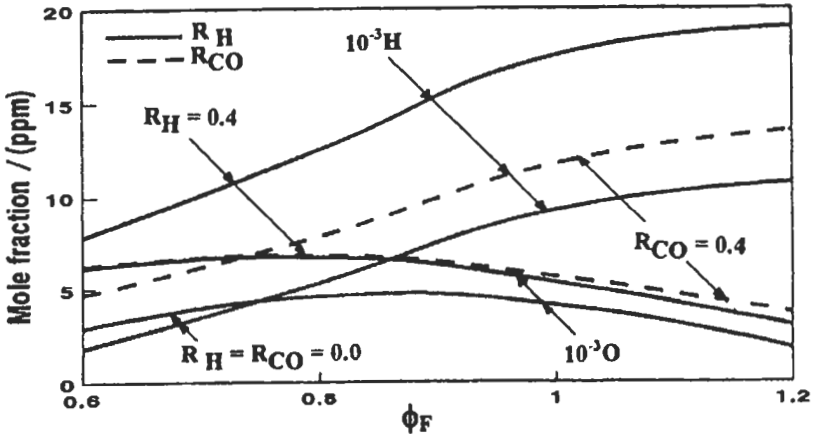


Fig. 2.89 (c): Variation of maximum mole fractions of O and H with ϕ_F for the same flames as in Fig. 2.87 [400]. Reproduced by permission of Elsevier Science.

In Fig. 2.89 (d), the increase of the mole fraction of CO with $R_H = 0.4$ at lean values of ϕ_F , is due to the increase of the mole fraction of CHO and consequently its subsequent reactions which lead to a production more CO, while for rich values of ϕ_F , the decrease of CO is due to the high reactivity of reaction $\text{OH} + \text{CO} \rightarrow \text{CO}_2 + \text{H}$, where OH increases with R_H . Figure 2.90 summarizes the effect of different values of R_H and R_{CO} on NO_x , N_2O , HO_2 , and CO at $\phi_F = 1$. The figure shows that NO_x and HO_2 decrease linearly with R_H , while CO decreases with R_H until $R_H = 0.2$ and then increases again. With CO addition, there is a slight increase in NO_x and HO_2 , while CO increases by about twice as R_{CO} increases from 0 to 0.4. Also, the figure shows that, N_2O decreases by about half its value at $R_H = 0.4$. This is due to the reaction $\text{N}_2\text{O} + \text{H} \rightarrow \text{N}_2 + \text{OH}$, which is the key reaction to convert N_2O into N_2 , thus avoiding the production of undesirable nitrogen oxides. Having discussed the variations of maximum NO, NO_2 , and N_2O with ϕ_F , R_H and R_{CO} , it is necessary to discuss next the distribution of these

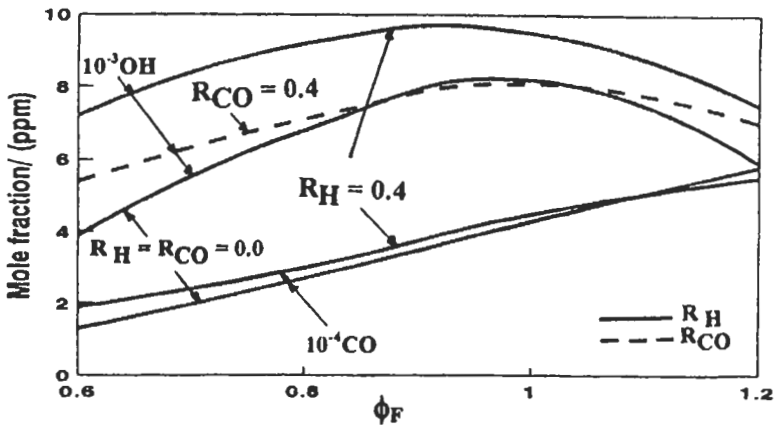


Fig. 2.89 (d): Variation of maximum mole fractions of OH and CO with ϕ_F for the same flames as in Fig. 2.87 [400]. Reproduced by permission of Elsevier Science.

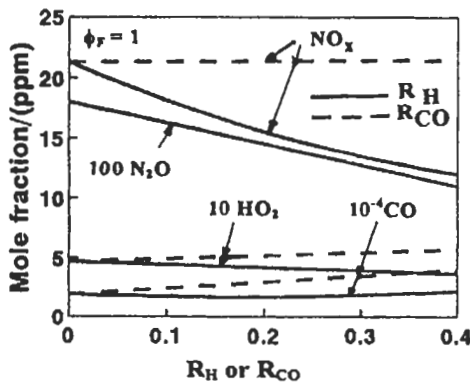


Fig. 2.90: Variation of maximum mole fractions of N_2O , NO_x , CO and HO_2 for methane + hydrogen + air and methane + carbon monoxide + air flames with R_H and R_{CO} at 1 atm and 300 K, and $\phi_F = 1$ [400]. Reproduced by permission of Elsevier Science.

species throughout the flames at a given burned gas temperature. Figure 2.91 (a) shows that, NO_2 species is predominant in NO_x species for CH_4 -air flame with and without hydrogen addition until a temperature of 1700 K and 1600 K, respectively. Thereafter, NO becomes predominant. Before these temperatures, the main reaction, which is responsible for producing NO_2 is reaction R_4 given in Table 1.9. After these temperatures, reaction R_8 (in Table 1.9) becomes the main removal of NO_2 due to high concentration of O atoms until the latter species reaches its maximum value at about 1800 K. This is the reason for decreasing NO_2 in this region. Thereafter, the NO_2 species increases rapidly again due to decreasing of O and H atoms which leads to a decrease in the reactivity of R_3 and R_8 in Table 1.9. At temperature less than 1700 K with $R_H = 0.4$, and $\phi_F = 1$, the NO_2 decreases to about 11 % of its initial value, while HO_2 decreases by about 50 %. This latter decrease will lead to a decrease in the reactivity of reaction, R_4 and consequently to a decrease in NO_2 . The reduction of HO_2 is due to that the reaction $\text{H} + \text{O}_2 \rightarrow \text{HO} + \text{O}$ competes with the reaction $\text{H} + \text{O}_2 + \text{M} \rightarrow \text{HO}_2 + \text{M}$ and reduces its reactivity. The early peak of HO_2 , which occurs at 500 K with hydrogen addition, has no significant effect on NO_2 at this temperature. Figure 2.91 (b) shows that, the increase of O, H and OH with hydrogen addition is significant at low temperature. Also, at post flame, O atoms increase by about 20 % with $R_H = 0.4$, while N_2O decreases by about 55 %, and this leads to a reduction in the reactivity of reaction $\text{N}_2\text{O} + \text{O} \rightarrow \text{NO} + \text{NO}$ and consequently to a decrease of NO.

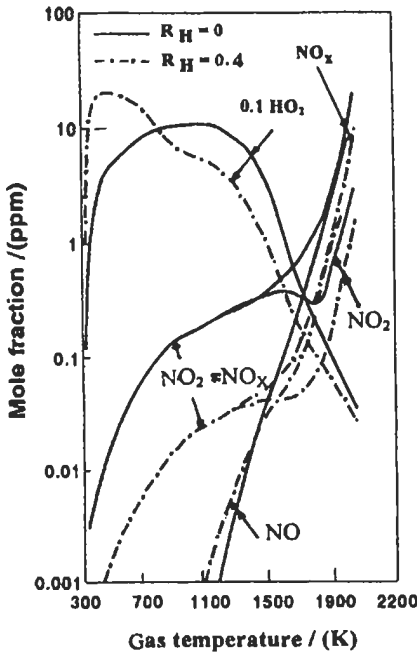


Fig. 2.91 (a): Variation of mole fractions of HO_2 , NO_2 , NO_x , and NO with burnt gas temperature and as a function of R_H for methane + hydrogen + air at 1 atm and 300 K, and $\phi_F = 1$ [400]. Reproduced by permission of Elsevier Science.

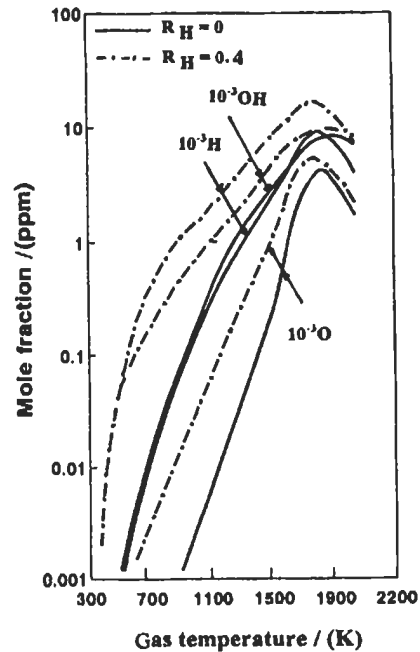


Fig. 2.91 (b): Variation of mole fractions of H, O, and OH with burnt gas temperature for the same flame as in Fig. 2.91 (a) [400]. Reproduced by permission of Elsevier Science.

2.8 Porous Burners

There is an increasing demand by air-quality regulation to reduce pollutant emissions from combustion systems to extremely low levels, while economic interests demand high radiant efficiency equipment for a wide range of applications. To achieve such aims, a variety of direct-fired porous radiant burners have been developed. These burners emit fewer pollutants and delivers radiant heat with high efficiency than standard burners, and this offers significant advantages over conventional flame burners. Several investigators [108, 401-403] have reviewed the combustion research in porous media.

In radiant burners, the premixed flame stabilizes inside a porous ceramic or fibrous metal flame holder, and the combustion occurs within or near the porous metal which causes the metal to radiate much heat, thus lowering the flame temperature and consequently reducing NO_x formation rate [403]. The heat transfer from the gas to the solid is nearly 50 % higher than that in conventional burners.

Several studies of gas-fired radiant burners and submerged flame reactions have been reported [404-407]. Measurements of flame speed, radiation efficiency, and solid matrix temperature for a lean premixed methane-air flame ($\phi < 0.6$) embedded in 5.1 cm long cylinder of lithium aluminum silicate ceramic foam were studied by Hsu et al [404]. In addition, Hsu et al [405] have measured the flame speed and stability range for a burner with two 5.1 cm long partially stabilized zirconia cylinders stacked together. Species measurements over a Pyrocore (metal fiber) burner [406] showed that, although around 90 % of methane reacted within the porous medium, the maximum heat release and the peak temperature were found immediately downstream of the burner surface. The model revealed that the vast majority of NO was formed by the prompt-NO mechanism. Other investigators [407-409] have experimentally measured pollutant emissions from ceramic radiant burners. Bouma et al [410] have found that the prompt NO emitted from ceramic radiant burner has the same order of magnitude as the thermal NO.

Measurements of solid and gas phase temperatures obtained by inserting a thermocouple through a slit cut in the burner matrix have been reported [411]. Mital et al [412] have measured the temperature and species distribution within the submerged reaction zone stabilized inside radiant burners made of reticulated ceramic matrices. Their temperature and species profiles show that the reaction zone is very broad, and that the tendency to flashback results from high preheating of the unburned mixture. Williams et al [406] have reported experimental results for premixed methane-air mixtures within and near the downstream surface of a porous matrix burner. They measured the radiant flux, surface and gas temperatures, and stable species concentrations. Rumminger et al [413] have developed a radiant burner model. This model includes multi-step chemistry, radiative heat transfer in the porous medium, and separate gas and solid energy equations. Their model over-predicts the observed gas temperature above the burner and they attributed that deviation to the uncertainty in the porous medium properties and the possibility that the chemistry is affected by the solid surface in the porous medium.

Recently, El-Sherif [108] has reported experimental measurements of surface and gas temperatures, as well as the stable species concentrations of CO, CO_2 , O_2 , and NO_x in radiant burner. These results provide the fundamental information concerning the flame structure in porous radiant burner for deeper understanding and future model

validation. Her work [108] presents a developed one-dimensional kinetic model of bi-layered ceramic radiant burner to simulate the experimental results. The followings present the experimental and computational results.

2.8.1 Experimental Study

A schematic diagram of the experimental apparatus including some details of the radiant burner construction is shown in Fig. 2.92 [108]. The porous radiant ceramic tile (or burner) has a rectangular cross section of 9 x 6.5 cm (1). This burner or ceramic tile consists of two parts; the first one is the upper part, which represents the flame support layer, and the second one is the lower part, which represents the diffusion layer. These two layers are mounted on the gasket (2) inside a rectangular metal housing (6), and they are sealed with high temperature cement. The porous ceramic tile housing is half-filled with stone bead (4) to obtain homogenous mixtures of air and natural gas fuel and to ensure an even flow of mixtures into the ceramic tile. Bottled Egyptian natural gas is passed through a fine control valve (12), rotameter (10) and an orifice plate (9), and dried air is passed through similar system. Both air and natural gas volume flow rates were metered separately by air rotameters and calibrated orifices (9). The air and natural gas were mixed in a mixing chamber (8). Thereafter, the mixture is passed through a sintered steel plate (as a safety device to prevent any flashback) and then to the burner housing. The mixture is ignited above the porous ceramic tile at atmospheric pressure, and stable flames inside the flame support layers are obtained at different equivalence ratios, ϕ . The volumetric composition of natural gas used is given in section 2.4.8.

The porous ceramic tile consists of about 2.3 cm thick (L), with two-layers reticulated ceramic structure. The first one is the upper layer with large pores, called "flame support layer", and the second one is the lower layer with small pores that prevents the flame from moving upstream, called "diffusion layers". The diffusion layer is 1.9 cm thick and 25-ppc, while the flame support layer, is 0.4 cm thick and 4 ppc. The properties of the diffuser (25 ppc) layer are: porosity, $\psi = 0.65$, bulk thermal conductivity, $\lambda_s = 1 \text{ W m}^{-1} \text{ K}^{-1}$, pore diameter, $d = 0.022 \text{ cm}$, scattering albedo, $\varpi = 0.77$ and extinction coefficient, $\sigma_e = 10 \text{ cm}^{-1}$. While for the flame support (4 ppc) layer, the properties are; porosity, $\psi = 0.8$, bulk thermal conductivity, $\lambda_s = 1 \text{ W m}^{-1} \text{ K}^{-1}$, pore diameter, $d = 0.22 \text{ cm}$, scattering albedo, $\varpi = 0.72$ extinction coefficient, $\sigma_e = 1.1 \text{ cm}^{-1}$, and forward scattering fraction, $f = 0.5$ [413].

The convection coefficient correlation for gas flow in reticulated ceramics was taken from Ref. 309. The volumetric convection coefficient is in the order of $107 \text{ W m}^{-3} \text{ K}^{-1}$ in the diffuser layer and $105 \text{ W m}^{-3} \text{ K}^{-1}$ in the flame support layer. The relation between the bulk thermal conductivity, λ_s to the effective thermal conductivity, $\lambda_{s,e}$ for the solid is $\lambda_{s,e} = (1 - \psi) \lambda_s$ and for the gas $\lambda_{g,e} = \psi \lambda_g$, where $\lambda_{g,e}$ is the effective thermal conductivity of the gas and ψ is the porosity of the solid [413].

The experimental measurements were carried out with a thermal loading of 250 to 460 kW m^{-2} based on the external surface area. Equivalence ratio varied from 0.6 to 1.2, the initial pressure and temperature of the mixture were 1 atm and 300 K, respectively. For a fixed firing rate, the equivalence ratio was varied by changing the airflow rate (monitored by rotameter and calibrated orifice), and for a fixed equivalence ratio, the firing rate was varied by changing both the air and the fuel flow rate in small steps simultaneously. The flame stabilized within the radiant porous

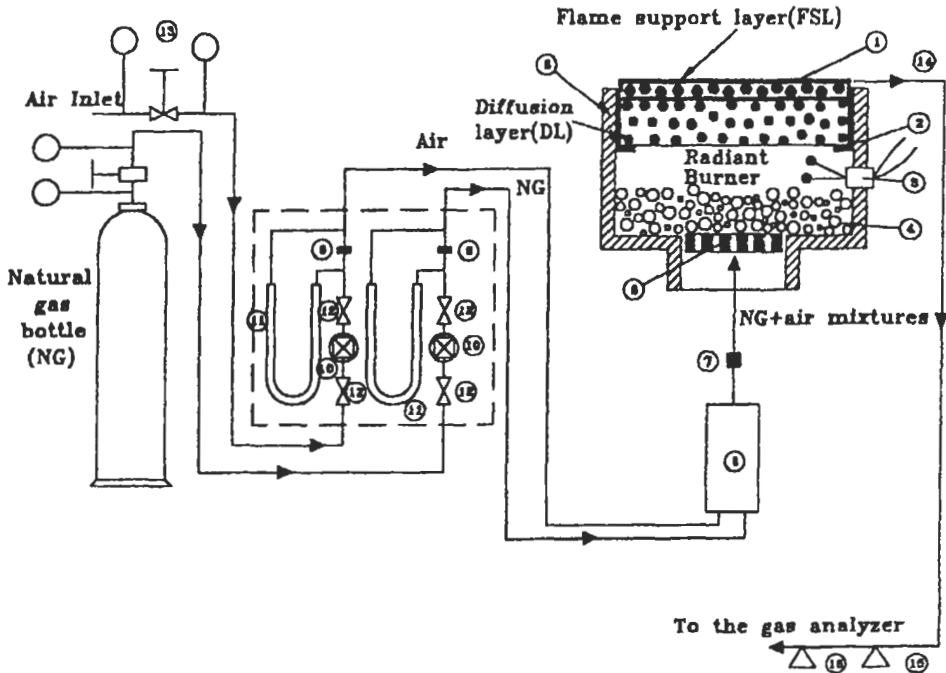


Fig. 2.92: Experimental apparatus [108]

- | | | |
|----------------------------|---------------------|---------------------------------|
| 1. Porous ceramic tiles | 2. Gasket | 3. Chromel-alumel thermocouples |
| 4. Stone beads | 5. Sintered steel | 6. Burner housing |
| 7. Flame trap | 8. Mixing chamber | 9. Orifice plate |
| 10. Flow rotameter | 11. Water manometer | 12. Control valves |
| 13. Air pressure regulator | 14. Sampling probe | 15. Water trap, |
| | | 16. Silica gel |

burner is characterized in terms of stability limits. For firing rates above 460 kW m^{-2} , flame flashback occurs and is defined as the undesirable movement of the premixed flame upstream into the diffusion layer. The lift-off limit for the flames was determined when the flame starts to lift from the edge of burner and becomes non-uniform.

For temperature measurements, three uncoated thermocouples are used, two are made of Pt 13 % Rh-Pt wires of $100 \mu\text{m}$ diameter, one in Y-shaped supporting wires and is used to measure the gas temperature along a pore centerline of the flame support layer, and the other is attached to the upstream edge of the burner tile to give an estimate of the upstream solid surface temperature, while the third one is made of chromal-alumel and is attached to the burner housing for detection of the onset of flashback, as well as to measure the inlet temperature.

For species concentration measurements, gas samples are withdrawn from above and along a pore centerline of the flame support layer using a quartz microprobe of $100 \mu\text{m}$ inner diameter and 2.0 mm outer diameter. The sample is analyzed for CO , O_2 , and NO_x by means of a gas analyzer with electrochemical cells, and prior to entering the analyzer the gases are passed through a water trap and silica gel to dry the sample. The probe and thermocouple are carried separately by a mechanical traversing mechanism

with 0.2 mm positioning accuracy. Care has to be taken when inserting the thermocouple and the probe inside the pore of the flame support layer to avoid any damage. In all measurements, an average of three readings from different places in the burner center was taken. The variation between the three readings for the probe and thermocouple measurements was found to be within $\pm 3.5\%$ to 5% . Because of complex radiative field around the thermocouple when the thermocouple is inside the pore matrix or burner, further work still need to be done. Therefore, the radiation correction for the thermocouple was made here by solving the balance equation between energy received by convection from the gases and that lost by radiation from the thermocouple junction, and the estimated error by this method is around 40 to 60 K [413]. The experimental results are shown by points in Figs. 2.93 – 2.95 and 2.99 (a) and (b), and these will be discussed in the next section together with the corresponding predictions.

2.8.2 Computational Method and Discussion

Computational Method

The flow in and out of the reticulated ceramic burner is assumed to be one-dimensional in the x direction. This model represents further development over the model described in section 2.3.2, because it includes separate gas and solid energy equations as well as the radiatively participating porous solid medium. The fuel and air mixture is assumed to enter an adiabatic infinitely wide duct, $x = x_{in}$, then it flows into upstream of the porous medium, $x = 0$, to downstream of the porous medium, $x = L$, and exits at $x = x_{out}$ after reacting. The boundary conditions for the gas are evaluated at the inlet and exit of the system, x_{in} and x_{out} , and the solid energy and radiative heat transfer boundary conditions are evaluated at $x = 0$ and at $x = L$. Two-flux approximation method is used for the radiative heat transfer as well as multi-step kinetic mechanism. In the following, the governing equations, method of solution, kinetic model and transport parameters, used in this model are presented and discussed as follows:

The radiant burner combustion zone is assumed as one-dimensional laminar flame with a radiating surface as the initial boundary conditions. It is assumed that, the combustion occurs at constant pressure, and the porous medium is spectrally gray. The governing equations are Eqs. 2.1 to 2.13 in addition to the following equations:

Gas phase energy equation:

$$\rho_t \psi \left(\frac{\partial h_i}{\partial t} \right) + M \psi \left(\frac{\partial h_i}{\partial x} \right) - \frac{\partial (\lambda_g \psi \partial T_g / \partial x)}{\partial x} + \sum_i \frac{\partial (j_i \psi h_i)}{\partial x} + H_v (T_g - T_s) = - \sum_{i=1}^S (\psi R_i h_i) \quad (2.75)$$

where, h_i is the specific enthalpy of species i , T_g and T_s are the gas and solid temperatures, respectively, ψ is the porosity of the porous solid burner; which is equal to one for gas only, H_v is the volumetric heat transfer coefficient, and $\lambda_{g,e}$ is effective gas thermal conductivity. The equation of j_i has been described in details in section 2.3.2.

Solid energy equation:

$$\frac{\partial}{\partial x} \left(\lambda_s \frac{\partial T_s}{\partial x} \right) + H_v (T_g - T_s) = \frac{\partial q_r}{\partial x} \tag{2.76}$$

where λ_s is the thermal conductivity of the solid burner, and q_r is the net radiative heat flux which represents the difference between forward radiative flux (q_r^+) and backward radiative flux (q_r^-) and these are given by:

$$\frac{\partial q_r}{\partial x} = \frac{\partial q_r^+}{\partial x} - \frac{\partial q_r^-}{\partial x} \tag{2.77}$$

where $\frac{\partial q_r^+}{\partial x} = -2\sigma_e q_r^+ + 2\sigma_e \omega (f q_r^+ + b q_r^-) + 2\sigma_e (1 - \omega) \sigma T_s^4$ (2.78)

$$- \frac{\partial q_r^-}{\partial x} = -2\sigma_e q_r^- + 2\sigma_e \omega (f q_r^- + b q_r^+) + 2\sigma_e (1 - \omega) \sigma T_s^4 \tag{2.79}$$

where ω is the single scattering albedo, σ_e is the extinction coefficient, σ is the Stefan-Boltzmann constant, f is the forward-scattering fraction, and b is the backward-scattering fraction.

The input data for the model are: at the inlet ($x = x_{in}$) the mixture boundary conditions are $T_g = T_{initial}$ (300 K), $\sigma_{ig} = \sigma_{ig, initial}$, and $P = 1$ atm. The boundary condition at the upstream of the porous medium ($x = 0$) is given by:

$$- \lambda_s \frac{\partial T_s}{\partial x} \Big|_{x=0} = H_0 (T_g - T_s) - (q_r^-(0) - q_r^+(0)) \tag{2.80}$$

$$q_r^+(0) = \epsilon Q^+ + \upsilon q_r^-(0) \tag{2.81}$$

where H_0 is the convective heat transfer coefficient, Q^+ is the ambient radiant flux from burner housing, υ is the reflectivity of the porous medium and ϵ is the average emissivity of the surface.

At the downstream surface of the porous medium ($x = L$), the radiant losses from the burner is assumed to be equal to the convective heat loss from the gas, therefore, the boundary condition is given by [413]:

$$\lambda_s \frac{\partial T_s}{\partial x} \Big|_{x=L} = H_0 (T_g - T_s) - (q_r^+(L) - q_r^-(L)) \tag{2.82}$$

$$q_r^-(L) = \epsilon Q^- + \upsilon q_r^+(L) \tag{2.83}$$

where Q^- is the ambient radiant flux from the firing rate. At the gas outlet ($x = x_{out}$), the

boundary conditions are: $\frac{\partial T_g}{\partial x} = 0, \frac{\partial \sigma_{ig}}{\partial x} = 0.$

The gas-phase chemical reactions, with their rate parameters are those given in section 2.4.8 in addition to Table 1.9.

Results and Discussions

The followings are the discussions of the above results.

(i) **Stability limits.** To obtain operating conditions where the burner glows and the flames within the porous burner become extremely stable, several attempts were made by changing the equivalence ratio and firing rate as described above, and these results are shown in Fig. 2.93. For steady state condition, the upstream and housing temperature remained constant. The operating conditions are 250 to 460 kW m^{-2} for the firing rate, and 0.6 to 1.2 for the equivalence ratio. The figure shows that below the lower limit of 250 kW m^{-2} it was difficult to obtain a stable flame within the porous burner. Complete extinguishment of the flame occurs at equivalence ratio of 0.61 and it increases to 0.64 as the firing rate increase from 325 to 460 kW m^{-2} . As the equivalence ratio increases from 0.65 to 0.72 at firing rates higher than 250 kW m^{-2} , the flame starts to lift from the surface of the burner. As the firing rate increases over 375 kW m^{-2} and at equivalence ratio higher than 0.9, the flashback occurs, and this is attributed to the increase in the radiative-convective preheating of the mixture and leads the reaction zone to move upstream. There is no flashback observed for firing rate below 375 kW m^{-2} .

(ii) **NO_x , CO concentrations and surface temperature.** Figures 2.94 and 2.95 show the effect of the equivalence ratio on the NO_x and CO concentrations in radiant burner under different firing rates. Figure 2.96 shows the variation of total NO_x (thermal + prompt) and prompt NO versus the firing rate at constant equivalence ratio. Also, Fig. 2.97 shows the effect of equivalence ratio and firing rate on the porous surface temperature. In all the figures, the predicted results [108] are shown by full curves, while the experimental results by El-Sherif [108] and other investigators are shown by symbols. Furthermore, the dashed curves of Figs. 2.94 and 2.95 present the predicted values of NO_x and CO for conventional natural gas burner [18].

In most practical combustion systems, NO_x forms via the thermal- NO_x and prompt-NO mechanisms. The thermal- NO_x mechanism involves conversion of molecular nitrogen

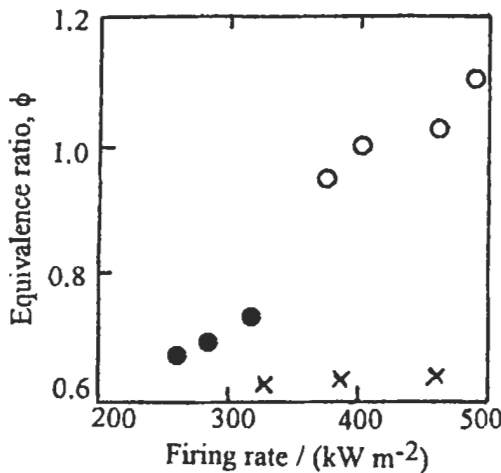


Fig. 2.93: Stability limits; x lean limit, ● lift-off limit and ○ flashback limit [108].

to NO at high temperatures, and involves reactions R_5 to R_8 (in Table 1.9), while prompt-NO mechanism leads to NO formation in the flame front versus reactions R_{10} to R_{20} (in Table 1.9). The predicted results of maximum NO_x shown in Fig. 2.94 for three firing rates are computed using thermal- NO_x and prompt-NO mechanisms. The experimental values of NO_x [108] are for firing rates of 250 kW m^{-2} and 350 kW m^{-2} , while the other experimental data for a firing rate of 366 kW m^{-2} were taken from Ref. 406, and were used here to validate the computed NO_x . Figure 2.94 shows that the concentration of NO_x increases with the increase in both the firing rate and the equivalence ratio in the lean side only, because the gas temperature in the reaction zone increases under these conditions. Experimental and predicted results show the same trend and are in satisfactory agreement, and thus validating the kinetic radiant burner model.

The experimental results are similar to those obtained in Ref. 406. Maximum NO_x concentration is reduced by about 55 % when using radiant burner instead of conventional burner at equivalence ratio, $\phi = 1$ and firing rate of 250 kW m^{-2} . This indicates that the radiant burner can give NO_x concentration as low as 10 ppm when using natural gas, which can meet the strict NO_x emissions standard.

Figure 2.96 indicates that the prompt-NO mechanism is more important than the thermal NO mechanism for lean flame ($\phi = 0.85$) at different firing rates. The difference between total NO_x and prompt NO concentrations is attributed to thermal-NO. Prompt-NO formed early in the flame zone from reactions of molecular nitrogen with hydrocarbon radicals. It was found that in lean radiant burner, reactions R_{12} ($\text{CH} + \text{N}_2 \leftrightarrow \text{HCN} + \text{N}$, initial reaction of the Fenimore mechanism), R_{11} ($\text{CH}_2 + \text{NO} \leftrightarrow \text{HCN} + \text{OH}$) and R_{13} ($\text{CH}_2 + \text{OH} \leftrightarrow \text{CH} + \text{H}_2\text{O}$) are more important than reactions R_1 ($\text{N}_2 + \text{O} \leftrightarrow \text{NO} + \text{N}$), R_4 ($\text{NO} + \text{HO}_2 \leftrightarrow \text{NO}_2 + \text{OH}$), and R_6 ($\text{N}_2\text{O} + \text{O} \leftrightarrow \text{NO} + \text{NO}$). The

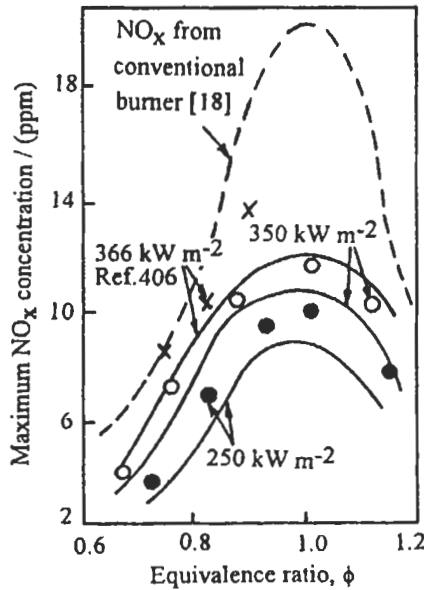


Fig. 2.94: Experimental (●, ○) and predicted (full curves) [108], maximum NO_x concentration versus equivalence ratio at two firing rates. Experimental values, x, were taken from Ref. 406.

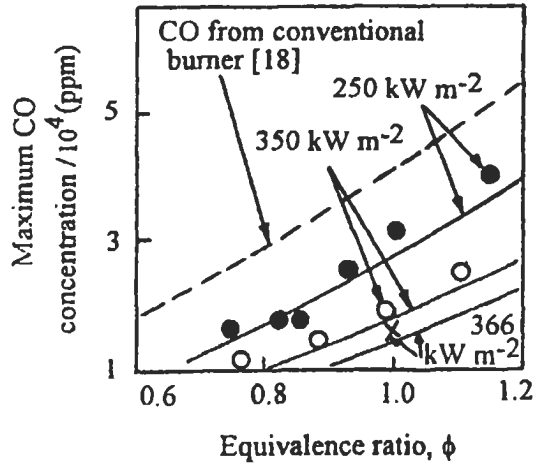


Fig. 2.95: Experimental, O, ● and computed (full curves) [108], maximum CO concentration versus equivalence ratio for the same flames as in Fig. 2.94. Experimental, x, were taken from Ref. 406.

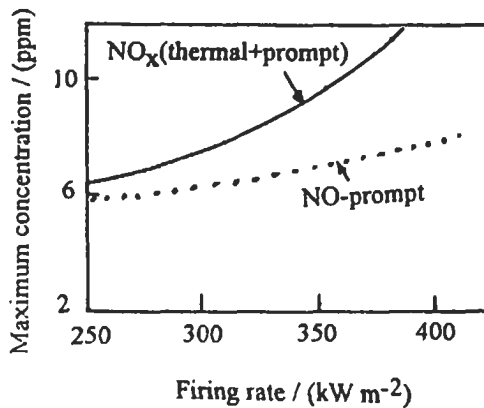


Fig. 2.96: Variation of the predicted NO_x (thermal + prompt) and NO (prompt) with firing rates at equivalence ratio of 0.85 [108].

results indicate that the prompt-NO is most sensitive to reaction R_{12} , that CH radicals are formed mainly by reaction R_{10} , and that the reaction R_{13} ($\text{CH} + \text{O}_2 \leftrightarrow \text{O} + \text{CHO}$) is the main reaction in lean flame that removes CH radical. The figure also shows that NO_x increases as the firing rate increases. This again is due to the increase of the gas temperature. The predicted NO_2 and N_2O concentrations were quite low at different firing rates.

Figure 2.95 shows that CO concentration increases with the equivalence ratio at all firing rates. It is clear from the figure that there is a satisfactory agreement between the experimental and predicted CO concentration [108]. Also, the predicted results are similar to those obtained in Ref. 406. Maximum reduction of CO from the radiant burner compared to the conventional one is found to be about 30 % at $\phi = 1$ and

250 kW m⁻². The figure also shows that the concentration of CO decreases with the increase of firing rate and this is due to the higher energy release per unit area as well as the increase in the preheating zone, which leads to the increase of the gas temperature.

Figure 2.97 shows the variation of the predicted and experimental surface temperatures with the equivalence ratio for two firing rates [108]. The surface temperature increases with the equivalence ratio having its peak at $\phi = 1$, and then decreases with ϕ . The maximum discrepancy between measured and predicted values is about 60 K and this is due to uncertainties in the radiation correction as described before. The surface temperature also increases with the firing rate, and as the firing rate increases, the range of equivalence ratio for stable flame decreases until eventually the flame lifts off the surface. Furthermore, Fig. 2.97 shows that the surface temperature drops by about 70 K for a change in the equivalence ratio from 1 to 0.85, while the adiabatic temperature drops from 2220 to 2080 K, and this indicates that there is a high thermal contact with the radiant burner.

(iii) **Radiant efficiency.** In normal operating conditions, the burner glows and the flame stabilized within the porous burner results in an efficient energy transfer by convection to the solid, and this appears as a high radiative heat flux. Therefore, the effectiveness of this burner can be expressed by the radiant efficiency (ratio of the radiant heat to the chemical heat input) and these results are shown in Fig. 2.98. The predicted results by El-Sherif [108] are shown by full curves for three different firing rates. The predicted radiant efficiency for a firing rate of 366 kW m⁻² is compared with the experimental data from Ref. 406. There is a satisfactory agreement between the experimental and predicted results with maximum discrepancy of about 6 %, and this may be due to uncertainties in the properties of porous burner as well as the catalytic surface effect.

Maximum radiant efficiency of 28 % is predicted at $\phi = 1$ and a firing rate of 250 kW m⁻². As the firing rate increases, the radiant efficiency decreases and its peak occurs at $\phi = 1$, where the gas and surface temperatures are the highest as shown in Figs. 2.97

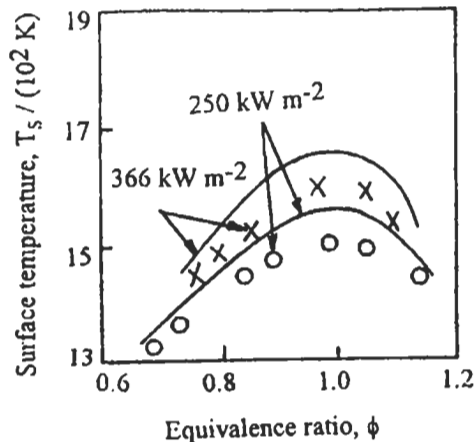


Fig. 2.97: Variation of surface temperature with equivalence ratio at two firing rates. Full curves and O are the predicted and experimental values from Ref. 108. The experimental values, x, are taken from Ref. 406.

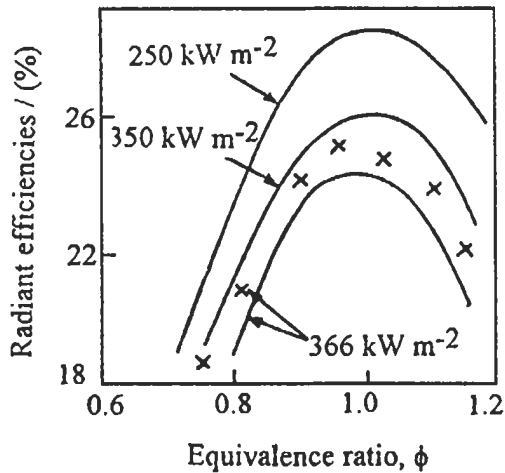


Fig. 2.98: Variation of radiant efficiency with equivalence ratio at different firing rates. Full curves are the predicted values [108] and, the experimental values, x, were taken from Ref. 406.

and 2.99 (a) and (b). For low firing rate the radiant efficiency increases because the flame is stabilized deeper in the burner pore. As the firing rate increases, the radiative and conductive heat feedback rate increases and leads to a nonlinear enhancement in the burning velocity. This causes the flame to move upstream until a balance between the rate at which the unburned mixture is supplied to the preheated mixture and reaction zone and the rate at which the mixture can be consumed is established. However, if the firing rate is excessive, the flashback occurs as discussed in section (i).

(iv) **Flame structure.** The measured carbon monoxide, and gas and surface temperatures are compared with the corresponding predicted results as shown in Fig. 2.99 (a), while the measured and predicted NO_x are compared in Fig. 2.99 (b). Results in both figures are at a firing rate of 250 kW m⁻², and $\phi = 0.85$. Figure 2.99 (a) shows the measurements along the pore centerline of the flame support layer, FSL, while the predicted results for CH_4 , CO_2 , CO , T_g and T_s are shown through the diffusion layer, DL, and FSL, as well as, above the FSL. Before the combustion gases reach the surface of the flame support layer, most of CH_4 and CO is already consumed within about 3 mm in the FSL. The results show that about 94 % of CH_4 are consumed in DL, and carbon monoxide is formed mostly in the diffusion layer. The figure shows that there is a reasonable agreement between the predicted and experimental results and there is a similarity in the flame structure for different firing rates.

Also, the predicted results [108] in Fig. 2.99 (b) show the concentrations of the radical species such as OH, O, and H, and they are consumed inside the pore of the flame support layer. The figure shows also the variation of NO_x with the distance from the burner surface. The prompt- NO represents about 80 % of the NO_x -total (thermal + prompt) and its peak corresponding to the peak of CH which represents the main important species in prompt NO mechanism (see Table 1.9). Most of NO formation occurs in the flame front where the gas loses enough heat to the porous of FSL to suppress the thermal- NO_x reactions.

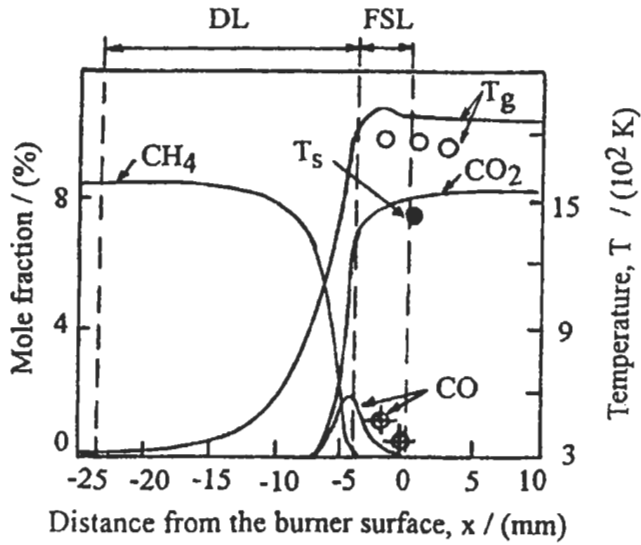


Fig. 2.99 (a): Variation of the predicted stable species versus distance at firing rate of 250 kW m^{-2} and $\phi = 0.85$, DL and FSL are the diffusion and flame support layers. O, ● are the measured surface and gas temperature, respectively [108].

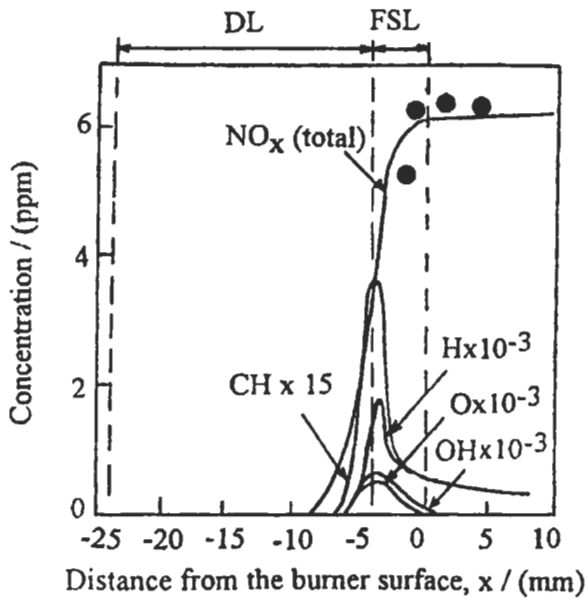


Fig. 2.99 (b): Variation of the predicted concentration of NO_x , O, OH, CH and H for the same flame as in Fig. 2.99 (a). ● is the average measured value of NO_x [108].

2.9 Flame Extinction Pattern

Flames propagate at subsonic velocities, usually sufficiently low for the small Mach number, constant pressure assumption to apply. A natural consequence of this circumstance has been that, until comparatively recently, the detailed modeling of laminar premixed flames has been confined to idealized system, which can be analyzed without explicit consideration of the momentum conservation equations. Such systems include (a) one-dimensional flows having constant stream tube area, in Cartesian coordinates (b) flows which are always normal to the cylinder axis, in cylindrical coordinates or (c) flows with spherical symmetry. However, case (a) demands the concept of a one-dimensional adiabatic laminar burning velocity, as already described in the previous sections; while for cylindrical and spherical flames of fixed radius, the cases (b) and (c) demand corresponding mass flows from a line source of unit length at the cylinder axis, or from a point source at the center of the sphere [65].

The flows in all the above cases are uniform; and all the stationary flames, as well as the corresponding non-stationary planer flame, are unstrained. In practice, however, nearly all flames are strained. In general terms, the strain rate K_s at any point on a flame surface is defined as the fractional rate of change of area A of an infinitesimal element of the surface at that point:

$$K_s = (1/A)dA/dt \quad (2.84)$$

with the element itself moving with the fluid in a Lagrangian manner; and with the area changes confined to those caused by flow non-uniformities, or by a combination of flame motion and flame curvature. Strain has its origin in flow non-uniformities and curvature effects. Its units are inverse seconds. It should be noted that strain is normally not uniform over a flame surface, but is defined both locally at a point, and instantaneously [65]. Nevertheless, there are three well-known examples, where the strain rate is uniform over the whole of any isothermal surface in the flame, the first is the counterflow or stagnation point flow configuration, which will be discussed in this section, and of which two planer flame examples are shown in Figs. 2.100 (a) and (b). The others are the non-stationary cylindrical and spherical flames. For the variable density stagnation point flows of Figs. 2.100 (a) and (b), where ρuA remains constant inside a streamtube, the strain rate K_s is given by:

$$K_s = -(1/\rho)d/dx(\rho u) \quad (2.85)$$

where ρ is the fluid density. Constant density, stagnation point potential flow, known as Hiemenz flow, is characterized by a constant radial velocity gradient a , such that in the axisymmetric configurations of Figs. 2.100 (a) and (b), $u = -2ax$. The strain rate in this situation is simply the negative of the axial velocity gradient, that is, $K_s = 2a$. Dixon-Lewis [65] have used eigenvalue velocity gradient a_e which relates his formulation with potential flow gradient a , and this is given by $a_e = (-J/\rho_e)$, where ρ_e is the density of the unburned gas entering the flame and J is the eigenvalue [65]. The method of characterization of flame stretch by way of the velocity gradient, a_e is frequently used in discussions relating to turbulent combustion. Also, although this may seem attractive in terms of mental imagery, it must be clearly recognized that the contribution of a_e is by

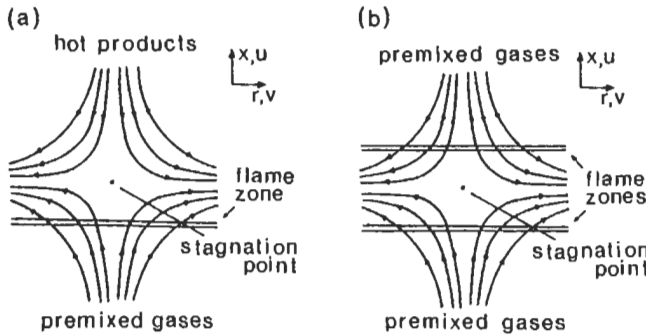


Fig. 2.100: Stagnation point flow configuration: (a) strained premixed flame formed by opposed flows of fresh mixture and hot combustion products; (b) strained premixed flame formed by opposed flows of fresh gases [65]. Reproduced by permission of The Combustion Institute.

way of defining something a kin to applied stress, rather than a strain rate in the system (Dixon-Lewis [65]).

Historically, the concept of flame stretch is introduced by Karlovitz [415]. In the past twenty years, the topic of flame strain or stretch has been discussed by many authors and was the subject of an invited lecture by Law [244] and Dixon-Lewis [65] at the Twenty-Second and Twenty-Third Combustion Symposium.

However, counter flow flame configurations, that may be established in the stagnation region between two opposed gaseous streams (Tsuji [416, 417]) are of particular interest for the study of flame extinction phenomena and of flame behavior near flammability limits. The flow through such flames is characterized by a velocity gradient across the flame front, and the flames themselves are therefore suitable for the study of aerodynamic quenching or "flame stretch" phenomena. Figures 2.100 (a) and (b) illustrate possible counterflow premixed flame arrangements. The flows illustrated schematically in Figs. 2.100 (a) and (b) will have an inlet nozzle situated above and below the stagnation plane of finite distances. In the figure two axisymmetric premixed gas streams of identical composition, and with uniform and equal velocities, impinge normally on the stagnation plane between them, and premixed flames are established back-to-back on either side of the stagnation region. Despite the uniqueness of the controlling chemistry for a given fuel-oxidizer combination, each of the opposed flow configurations shown in the figure has its own pattern of response to increasing applied stress.

The mathematical formulation of counterflow flame problem has been done and reviewed by Dixon-Lewis [65], and extinction limits were subsequently determined by arc-length continuation methods [66, 418, 419]. Details will not be given here. Apart from purely geometric effects, opposed flow premixed flames offer a range of configuration possibilities depending on the compositions of the two input streams. Figure 2.100 (a) illustrates a single planer flame formed in an "unburnt-to-products" or "unburnt-to-burnt" configuration, while Fig. 2.100 (b) shows back-to-back premixed flames, formed in counter flowing streams of fresh combustible mixture. It is likely that the first of these configurations is the more relevant to the flamelet models of premixed turbulent combustion which were mentioned in chapter 3. On the other hand, the second configuration lends itself the more readily to laboratory investigations. The back-to-back system may also be either symmetric or asymmetric; we shall consider only the symmetric configuration with identical input streams.

Theoretical analyses of the extinction and ignition phenomena for premixed flames are due mostly to Libby and co-workers [420-423]. They [421, 423] have considered the unburnt-to-burnt system formed by fresh mixture and its equilibrium combustion products at temperature T_b . The temperature T_b may be above, equal to, or below the adiabatic equilibrium temperature for the corresponding unstrained flame. Extinction limits were found for sufficiently subadiabatic conditions ($T_b < T_{ad}$).

Darabiha et al [424] numerically examined the extinction behavior of a lean propane-air flame in this same configuration, at a series of hot stream temperatures. They presented the results as curves of space integral heat release rate Q_h against applied stress, for each T_b . The space integral heat release across the whole flame is given by:

$$Q_h = \int_{-\infty}^{+\infty} q dx \tag{2.86}$$

Figure 2.101 shows a series of such curves for the propane-air flame with equivalence ratio $\phi = 0.75$, and adiabatic flame temperature of 1965 K.

At sufficiently large T_b , the space integral rates vary monotonically with applied stress. However, for sufficiently cool product streams, that is, sufficiently low T_b , there are abrupt extinction and ignition transitions at the points of vertical tangency on the S-shaped curves. The upper branches of these curves correspond to standard flame structures, the lower to extinguished solutions, and the intermediate branches to unstable solutions. The transition from monotonic to S-shaped behavior occur when $T_b = 1530$ K.

In the back-to-back systems, the maximum temperature achieved, at the stagnation plane, may be used as ordinate for the extinction curves, in place of the space integral heat release rate. With this temperature as the characterizing parameter, Fig. 2.102 shows the computed upper branches of the extinction curves for a series of methane-air flames in the planer axisymmetric configuration (Kee et al [66]). Note that a_e here represents a radial stress. The temperature at the extinction limits is all close to, but somewhat higher than the T_i for the appropriate flame (see section 2.4.3). The limits are again determined by the necessity for the formation of a radical pool sufficient to maintain the flame.

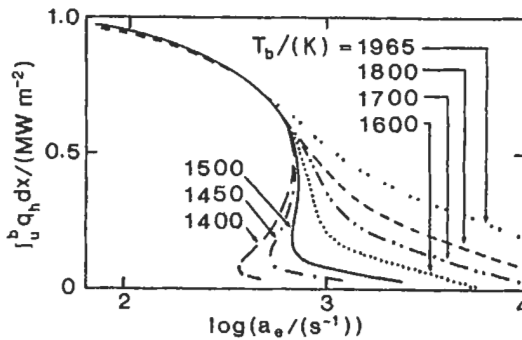


Fig. 2.101: Space integral heat release rates plotted as a function of applied stress for different hot stream temperatures T_b , for propane-air premixed flame, $\phi = 0.75$, in asymmetric unburnt-to burnt configuration (Fig. 2.100 (a) [424]). Curves are monotonic when $T_b > 1530$ K, S-shaped below that value. Unstrained equilibrium flame temperature, $T_{ad} = 1965$ K [65]. Reproduced by permission of The Combustion Institute.

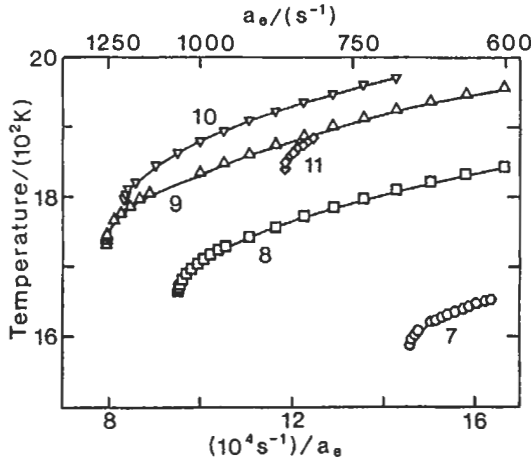


Fig. 2.102: Maximum flame temperatures as a function of applied stress in planar axisymmetric opposed flow methane-air premixed flame [66]. Extinction limit is at point of tangency on each curve [65]. Reproduced by permission of The Combustion Institute.

Heat release rate profiles, in the back-to-back and unburnt-to-burnt configurations have been computed by Dixon-Lewis [65], for a planar, premixed methane-air flame (Cartesian coordinates), equivalence ratio 0.84, and $T_u = 295$ K and the results are shown in Figs. 2.103 and 2.104. The back-to-back configuration leads to an extinction limit at $a_e = 2080$ s^{-1} . As already indicated, the major effect of increasing the applied stress is the curtailment of the profiles at the hot end, accompanied by the decrease in maximum temperature. By contrast, the unburnt-to-burnt configuration shows a reaction rate which decreases continuously with increasing stress, though the flame never extinguishes completely. The situations are further illustrated by the space integral heat release rates shown in Fig. 2.105. The unburnt-to-burnt configuration shows only a pseudo-extinction limit, at $a_e = 4000$ s^{-1} [65].

A comparison between Figs. 1.101 and 1.102 yields one further note-worthy feature. The sub-adiabatic extinction curves ($T_b < T_{ad}$) of Fig. 2.101 all lie below and to the left of the "monotonic" curves, that is, they lie at lower stresses. In Fig. 2.105, on the other hand, the back-to-back extinction curve A lies at higher stress rates. Since the symmetry condition in the back-to-back configuration prevents diffusive loss of H, O and OH across the stagnation plane, the behavior illustrates the beneficial effect, on the combustion, of realigning the radical pool intact, once it is formed, rather than trading some of it for thermal energy. A similar effect has been observed in spark ignition simulation [425].

In spite of fair shape of our understanding of both the chemistry and the physics of laminar flame propagation, there are still important quantitative questions to be settled. In addition, the theory of premixed flame extinction and flammability limits is not yet fully developed. Extinction limits are a consequence of the need for a flame to develop a radical pool of sufficient size to propagate itself. In the fact of progressively reduced residence time caused by increasing strain, the radical pool must be large enough to provide, by upstream diffusion, sufficient active material so that exothermic reactions there, aided by thermal conduction, allow the achievement of T_i . Once appreciable

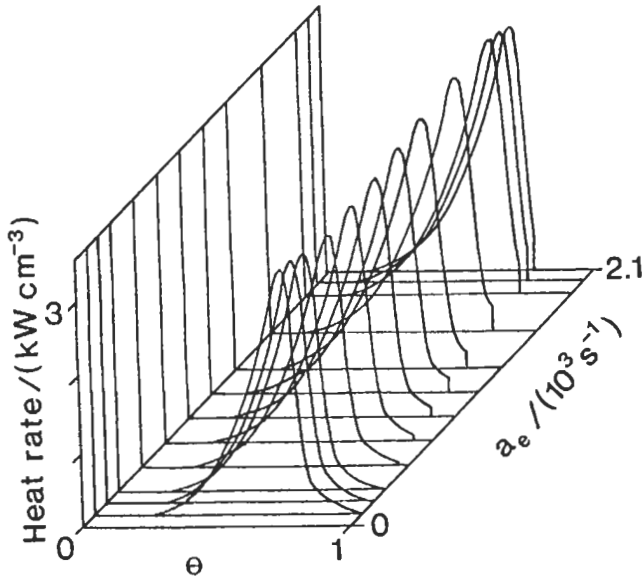


Fig. 2.103: Heat release rate profiles for premixed methane-air flames, $\phi = 0.84$, $T_u = 295$ K, in symmetric back-to-back configuration Hiemenz flow formation, cartesian coordinates. $\theta = (T - T_u)/(T_u - T_b)$, where T_b is the adiabatic, unstrained equilibrium flame temperature (Dixon-Lewis [65]). Reproduced by permission of The Combustion Institute.

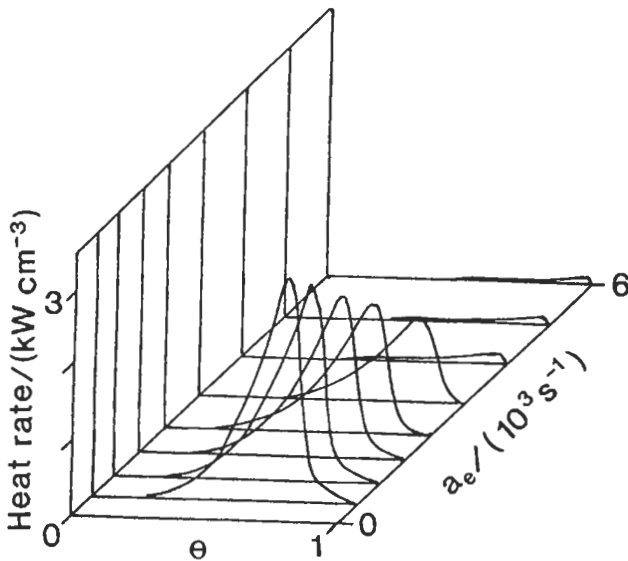


Fig. 2.104: Heat release rate profiles for flame of Fig. 2.103, but in adiabatic unburnt-to-burnt configuration [65]. Reproduced by permission of The Combustion Institute.

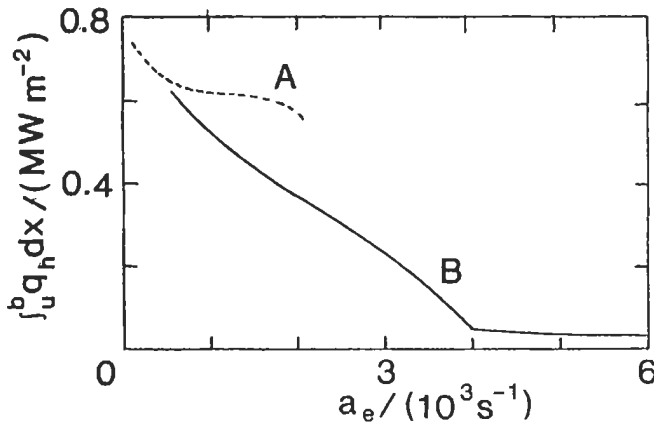


Fig. 2.105: Space integral heat release rates for flames of Figs. 2.103 (curve A) and 2.104 (curve B) [65]. Reproduced by permission of The Combustion Institute.

break through of the deficient component of the initial mixture occurs, the achievement of this temperature becomes much less likely, until eventually the flame extinguishes [65].

Flammability limits, on the other hand, are composition limits, which are closely associated with some value of T_i . A flame just inside such a limit might well be regarded as belonging to the unburnt-to-burnt configuration, but with the transition from monotonic to S-shaped behavior occurring at the adiabatic flame temperature. An effect of weakly stressing such a flame would be to reduce slightly its space integral heat release and thereby to trigger an abrupt extinction following a small heat loss from the combustion products. In opposed flow systems of fixed geometry and finite dimensions, the behavior of the symmetric back-to-back flames which are not too close to the inlet nozzles are for practical purposes characterized entirely by the applied stress.

In 1998, Kalamatianos et al. [426] have developed a two-parameter continuation algorithm for combustion processes which can calculate ignition and extinction conditions and illustrate the effect of any parameter (e. g., pressure, composition, residence time, hydrodynamic strain rate, surface heterogeneities, etc.) on ignition and extinction. When they applied this methodology to premixed hydrogen-air mixture in a jet-stirred reactor, they found that some of the fast reactions do not necessarily affect ignition and extinction temperatures. Two minimal reaction schemes of six reactions have been identified which lead to flame multiplicity.

The lack of initiation reactions in stationary simulations leads to a transcritical bifurcation. It has been found that on the second ignition branch of the P-T diagram, H, O, and OH are in quasi-steady-state. Significant deviation from quasi-steady-state occurs on the first ignition branch of the P-T diagram, specially for H atoms at fuel rich conditions and O atoms at fuel lean conditions. At extinction, HO_2 , O, H, and OH are in quasi-steady-state along the entire P-T diagram.

Chapter

3

Turbulent Premixed and Diffusion Flames

3.1 Introduction

There has been an appreciable improvement in the understanding of turbulent flames in recent years, but much work aided by advanced experimental techniques remains to be done. Where laminar flamelet models are applicable (Bradley et al [248] and Al-Masseeh et al [427]), the considerable data on laminar flames which has been discussed in chapter 2 can be utilized in the turbulent regime. In the mathematical modeling of turbulent combustion, formidable problems arise in the development of acceptable closure procedures (Rhine and Tucker [428]).

The flow field and turbulence parameters can be computed from the mass and momentum conservation equations, in conjunction with an appropriate model of turbulence. The coupling of these with the chemistry is difficult. Ideally, a conservation equation is required for each chemical species, and the computational task can be formidable (as shown in chapter 2). Furthermore, the computational effort to solve coupled chemical reactions and flows within complex geometries is overwhelming. There are no exact correct turbulence models for turbulence in recirculating flows. The detailed chemistry is unknown for the practical higher hydrocarbon fuels, and even partial success with global reactions necessitates a high degree of complexity as well as a detailed knowledge of the chemical kinetics. Errors in numerical analysis must not be underestimated and these have received increased attention, with the formulation of more accurate numerical schemes [429-431]. The complexity of the calculation is simplified and reduced by assuming that, the turbulent combustion is comprised of an array of laminar flamelets [248, 427] (see also chapter 2). This simplification is achieved through the use of experimentally measured or empirically estimated parameters that embody the chemical reaction rates. Two of such parameters in premixed flames are the laminar burning velocity and the profile of volumetric heat release rate against temperature for a laminar flame.

At higher levels of turbulence when the laminar flame becomes stretched, fragmented, and eventually extinguished, the reality is more complex and not fully understood. The turbulent flow field of premixed gases with simplified concept of a laminar flamelet model, enables the heat release rate source in the energy equation to be expressed in terms of the laminar flame profiles of heat release rate versus temperature

and a probability density function of the fluctuating temperature [430]. Whilst such a modeling approach is attractive for complex recirculating turbulent flows in which there is no readily discernible flame front, in the case of explosions with a propagating front, the concept of a turbulent burning velocity can be more so. This modeling approach is briefly described in this chapter.

In his invited lecture entitled "How Fast can we Burn ?", at the Twenty-Fourth Symposium on Combustion, Bradley [432] had presented the roots of understanding of turbulence, flame chemistry and their interaction. His attention was focused on premixed turbulent combustion and the different analyses of stretch-free theories of turbulent burning velocity. Furthermore, the problems of appropriate probability density functions of both stretch and temperature as well as some of the concepts applied to spherical explosions and continuous swirling combustion were discussed. He compared in Table 3.1 a variety of mean energy release rate, and answering the question posed by his paper's title he said "it all depends"; it depends on how fast we want to burn, where and why?, on whether combustion is required for heat transfer or power production. Probably the fluidized-bed gives the best reconciliation of burning and heat transfer rates. Is combustion steady or time varying? What are the material properties of the containing wall? What are the environmental limitations?. To respond to the wide range of possible requirements demands a high degree of control of diverse processes, the complexities of which require accurate, computer-based, mathematical models. These rest upon the fundamental understandings revealed by comparatively simple burners, explosion bombs, shock tubes and clear minds [432].

Bray [433] have described a number of models of turbulent combustion, identifying common features and differences between them. Turbulence simulations reveal the intense vorticity structure as filaments, and simulations of passive flamelet propagation show how this vorticity creates flame area and defines the shape of the expected chemical reaction surface [434].

This chapter describes mainly the characteristics of turbulent free premixed and diffusion flames. The effect of some parameters on the turbulent burning velocity, flame structure, heat release rate, flame height and flame stability under different conditions is introduced. Furthermore, laminar flamelet model for turbulent combustion process as well as an extensive theoretical and experimental study of the characteristics of free flames are described. The determinations of these characteristics as well as the experimental methods and techniques form the principal objective of this chapter. Therefore, the material of this chapter are complementary and necessary to enhance the understanding of the flow, mixing, chemistry, heat liberation and heat transfer in confined flames which will be described in chapters 4 and 5.

Table 3.1: Energy release intensities (GW m^{-3}) [432]

Electric spark	10
Hydrocarbon atmospheric laminar flame (peak)	6
Dissipation in vehicle brake	5
Aero gas turbine (take off)	
primary zone	4
whole combustor	1.5
Gas central heating boiler	0.2
Gasoline engine	0.1
Pressurized water nuclear reactor	0.1
Gas-fired fluidized bed (atmospheric)	0.04
Pulverized coal (cyclone combustor)	0.01

3.2 Characteristics of Diffusion Flames

As described briefly in chapter 2, the fuel and oxygen in the diffusion flames meet to form a combustible mixture, and once ignition has taken place, burning starts immediately upon creation of such mixture. In this case, the flame appears at the border between the fuel and oxygen zones. Combustion products created by the flame spread to both side, and fuel and oxygen have to diffuse against those streams in order to mix and react. This overall description fits the laminar diffusion flame in which mixing is brought about by molecular diffusion, as well as the turbulent diffusion flame in which the rapid creation of a coarse mixture through large scale transport processes greatly accelerates the formation of the final mixture which is combustible.

It is seen from the above that, the laminar diffusion flames occur in boundary layer flow. The more commonly encountered flow configurations which support such flames are (a) initially parallel flows, or co-flowing jets, of the unmixed reactants, and (b) initially opposed jets, leading to stagnation points. The former flame is held stationary on a burner by a small premixed flame region, which attaches the flame to the burner port (Fig. 3.1). Downstream of the stabilizing region, mixing and reaction occur in the developing boundary layer, the thickness of which increases in the downstream direction. The subsequent system may be considered in principle as an unsteady one-dimensional problem in the cross-stream direction, with time represented by the streamwise coordinate [65].

Theoretical treatment of diffusion flames has been developed early by several investigators [435-438]. A reasonable measure of the progress of burning of a diffusion flame is its height. A jet of fuel is assumed to issue from a burner of known diameter in a vertical direction upward into an ambient medium containing an oxidant. For a given fuel and burner, beginning at low flow rate, the flame height increases with increasing flow rate, reaches a maximum, and then shortens. Shortly before the maximum height is reached, the flame begins to flicker (becomes turbulent) at the top. This occurrence separates "Laminar diffusion" from flames of "Transitional" type. With further increase of the flow rate, flickering spreads in a downward direction. This spreading stops rather suddenly when only few diameters above the port are left free of fluctuations. At this point, the flame height becomes independent of flow rate, and the "Transition flame" passes over into the "Turbulent flame", Fig. 3.2. Further increase of jet velocity will maintain the break point a fairly constant distance above the rim, and the flame length changes little accompanied with an increase in the turbulence level or the rate of mixing.

The simplest case of a laminar diffusion flame resulting from a fuel jet flowing from a small diameter tube into air flowing at the same velocity in a wider concentric tube is shown in Fig. 3.3 [435]. Two flames are possible. When the cross-sectional area of the tubes are such that there is more air than required to burn the fuel to completion, an over-ventilated flame type is formed. The flame boundary is defined as the surface at which combustion is complete. Since chemical reaction is very rapid, the boundary corresponds essentially to the surface in which air and fuel are in stoichiometric ratio. This surface closes towards the axis as the diffusion process progress. The length L_1 of the flame is determined by the condition that at the point $x = L_1$ above the burner rim, sufficient air has arrived at the stream axis to burn the fuel to completion. Above this point no further combustion takes place, but the process of mixing continues between combustion products and air. When the fuel gas is in excess, a flame of the under-ventilated type is formed. The flame boundary moved outward,

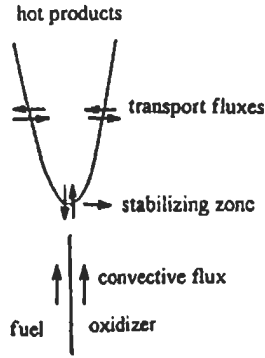


Fig. 3.1: Diffusion flame formed at co-flowing jets [65]. Reproduced by permission of The Combustion Institute.

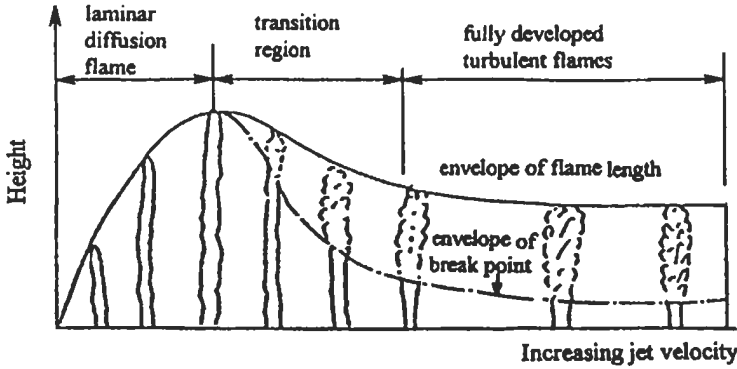


Fig. 3.2: Progressive change in flame type with increasing jet velocity [436]. Reproduced by permission of The Combustion Institute.

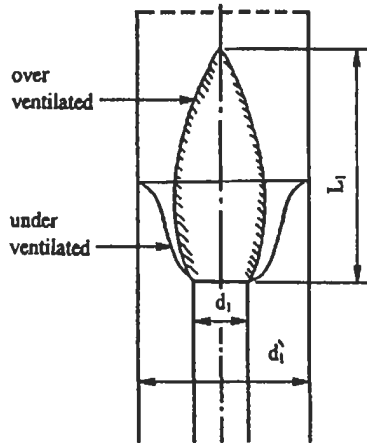


Fig. 3.3: Over-ventilated and under-ventilated diffusion flames [435].

and the length of the flame is determined by the arrival of fuel gas at the wall of the tube.

The diffusion flame structure is shown in Fig. 3.4. The concentration of fuel is highest on the axis and decreases to zero at the flame boundary. The concentration of oxygen is a maximum at the wall and decreases to zero at the flame boundary.

3.2.1 Diffusion Flame Length

The characteristics of turbulent mixing are radically different from mixing by molecular diffusion. This is illustrated in Fig. 3.5, as an example, for mixing of two streams, A and B, in a tube of diameter d_1 and length L_1 . If we change the scale having the dimensions d_2 , d_2 and L_2 , with the assumption that for both tubes stream A initially occupies the same portion of the total area and L_1 and L_2 are so chosen that the center line concentration is the same in both tubes. In each tube the rate of mixing of the two streams in any region is proportional to the area taken normal to the direction of mixing, and to a concentration gradient normal to this area (proportional to $1/d$). The proportionality constant is the diffusion coefficient D . It follows that the ratio of mixing rates in the two tubes out to the corresponding points L_1 and L_2 is [438]:

$$\frac{d_1 L_1}{d_2 L_2} \times \frac{(1/d_1)}{(1/d_2)} \times \frac{D_1}{D_2} \text{ or } \frac{L_1 D_1}{L_2 D_2}$$

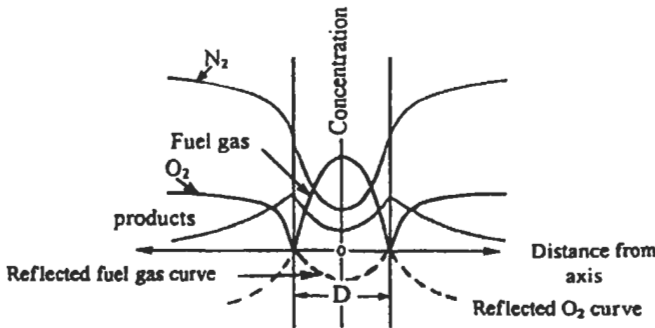


Fig. 3.4: Concentration profiles in cross-section of a laminar diffusion flame [436]. Reproduced by permission of The Combustion Institute.

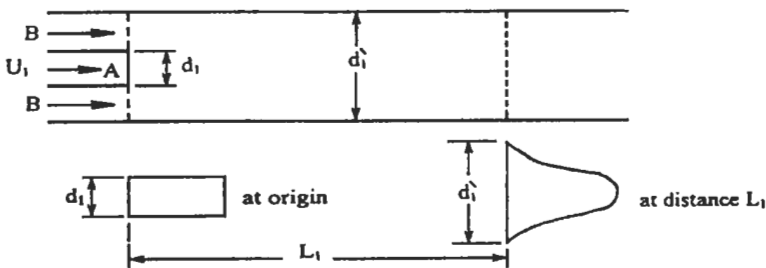


Fig. 3.5: Mixing of an inner stream of gas A with an outer stream of gas B [438]. Reproduced by permission of The Combustion Institute.

The ratio of the amounts of gas A to be mixed in unit time in the system is the ratio of the quantities flowing, i.e. $d_1^2 U_1 / d_2^2 U_2$. To achieve the equality of the centerline concentration at points L_1 and L_2 , the ratio of the amounts to be mixed must equal the ratio of the mixing rates. Then:

$$L_1 D_1 / L_2 D_2 = d_1^2 U_1 / d_2^2 U_2$$

or

$$L \propto d^2 U / D \quad (3.1)$$

In the case of laminar flames, the diffusion coefficient is independent of the tube dimensions and velocity. It then follows that the length required to achieve a specified degree of mixing is proportional to the volumetric rate $d^2 U$. But in turbulent flames, the coefficient D represents a turbulent mixing coefficient or eddy diffusivity. This eddy diffusivity was found to be the product of scale and intensity of turbulence. For a tube the scale is proportional to the diameter d and the intensity is proportional to the average velocity U . Thus:

$$L \propto U d^2 / U d \quad \text{or} \quad L \propto d \quad (3.2)$$

This relation shows that flame length is only proportional to the port diameter d .

A mathematical development of the diffusion problem has been given by Burke and Schumann [435]. Since a rigorous analysis of the diffusion process in the flame is extremely complicated, the simplifying assumptions are made that: the combustion takes place without change in the number of moles, the temperature and diffusivities of the gases are everywhere constant and equal, the inter-diffusion is entirely radial, and the velocities of the gas and air streams are the same.

If C is the concentration of any component in the gas mixture, the diffusion equation for a flame of cylindrical symmetry is:

$$\frac{\partial C}{\partial t} = D \left(\frac{\partial^2 C}{\partial y^2} + \left(\frac{1}{y} \right) \frac{\partial C}{\partial y} \right) \quad (3.3)$$

where y is the radial distance from the stream axis. The concentration of oxygen is a maximum at the wall of the outer duct and zero at the flame boundary.

The solution of the diffusion equation would give the oxygen concentration. If the terms of the diffusion equation are divided by some constant factor i , the resulting curve of O_2 concentration (shown in Fig. 3.4) is the same except that its scale is changed along the ordinate in the ratio 1 to i . If i is the number of moles of oxygen required to burn 1 mole of fuel to complete combustion, the curve represents the equivalent fuel concentration. Since at the flame boundary fuel and oxygen are in stoichiometric ratio and since the diffusivities are assumed to be the same for all gases, it follows that at the flame boundary:

$$\frac{dC_{\text{fuel}}}{dy} = -\left(\frac{1}{i}\right)\left(\frac{dC_{O_2}}{dy}\right) \quad (3.4)$$

where C_{fuel} and C_{O_2} are the fuel and oxygen concentrations, respectively. Thus in Fig. 3.4, the reflected or mirror image curve $-C_{O_2}/i$ connects smoothly with the fuel curve and the two curves are both determined by the same diffusion equation. The reflected curve may be considered, for mathematical purposes, to represent negative concentrations of the fuel having a maximum value (largest negative value) at the wall of the outer duct and a value of zero at the flame boundary. The diffusion problem then reduces to the diffusion of a single gas, namely the fuel. From the assumptions considered, it follows that the velocity U is constant everywhere, so that Eq. 3.3 becomes:

$$\frac{\partial C}{\partial x} = (D/U)\left(\frac{\partial^2 C}{\partial y^2} + \left(\frac{1}{y}\right)\frac{\partial C}{\partial y}\right) \quad (3.5)$$

where x is the distance from the burner rim. The boundary conditions are $\partial C/\partial y = 0$, when $y = 0$ and $y = d'/2$ where d' is the diameter of the outer tube. For $x = 0$, $C = C_1$ from $y = 0$ to $y = d/2$, and also $C = -C_2/i$ from $y = d/2$ to $y = d'/2$, where C_1 and C_2 are the initial fuel and oxygen concentrations, respectively.

The solution of Eq. 3.5 that satisfies the given conditions is:

$$C = C_o \frac{d^2}{d'^2} - \frac{C_2}{i} + \frac{4dC_o}{d'^2} \sum \frac{1}{\phi} \frac{J_1(\phi d/2)J_o(\phi y)}{[J_o(\phi d'/2)]^2} \exp(-D\phi^2 x/U) \quad (3.6)$$

where $C_o = C_1 + C_2/i$ and ϕ is a constant that assumes all the positive roots of the equation $J_1(\phi d'/2) = 0$ and J_o and J_1 are Bessel functions of the first kind. The equation for the flame boundary is obtained by putting $C = 0$ and $y = y_f$ where y_f is the radial distance of the flame boundary from the axis, hence,

$$\sum \frac{1}{\phi} \frac{J_1(\phi d/2)J_o(\phi y_f)}{[J_o(\phi d'/2)]^2} \exp(-D\phi^2 x/U) = \frac{d'^2 C_2}{4diC_o} - \frac{d}{4} \quad (3.7)$$

This equation allows the calculation of the shape of the flame boundary, which is given by the values of y_f and x that satisfy the equation. The height of an under-ventilated flame is obtained from the value of x corresponding to $y_f = d'/2$, and the height of an over-ventilated flame is obtained from the value of x corresponding to $y_f = 0$. Fig. 3.6 shows an example of the calculated flame boundary for an over-ventilated and under-ventilated flame for a burner of $d = 0.0254$ m, $d' = 0.0508$ m, $D = 0.489 \times 10^{-4}$ m² s⁻¹, which corresponds to the diffusivity of methane, and $U = 0.0155$ m s⁻¹, corresponding to

a flow of $0.0283 \text{ m}^3 \text{ h}^{-1}$, in the inner tube.

The above theoretical treatment of the flame boundary should be modified by empirical or semi-empirical relationships which compensate for the effect of the factors such as change of temperature along the jet with its many concomitant effects; gravitational, buoyancy and others. The following part is the treatment given by Refs. 436 and 437 for free flames and following the treatment of Burke and Schumann in that the diffusion equation is formulated for a single gas.

A sample of gas taken from some points in the stream consists of combustion products and either excess air or fuel. The sample originates from a mixture of the fluid from the burner port (nozzle fluid) which may contain primary air and the surrounding atmosphere. If one calculates the composition of the mixture in the unburnt state from the sample composition, one may determine what portion came from the nozzle. The mole fraction of the nozzle fluid in the sample is called C .

$$C = m_{\text{fuel}}(1 + a_o) \tag{3.8}$$

where m_{fuel} is the mole fraction of fuel in the sample and a_o is the ratio of moles of air/fuel in the nozzle fluid. At the flame boundary, the nozzle fluid and the surrounding air are in stoichiometric ratio. If a_t denotes the number of moles of air required for theoretical combustion of one mole of fuel, then the value of C at the flame boundary is:

$$C_f = (1 + a_o)/(1 + a_t) \tag{3.9}$$

because at the flame boundary $m_{\text{air}}/m_{\text{fuel}} = a_t$. The values of C at any point along the axis are C_m and it is noted that $C_m = C_f$ at the flame tip. The value of C or C_m at nozzle is 1, and at infinite distance from the port it is zero.

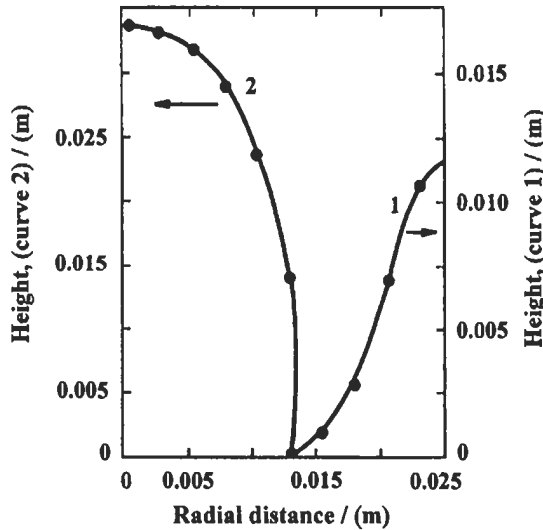


Fig. 3.6: Curve 1 under-ventilated flame, curve 2 over-ventilated flame [435].

From the diffusion equation one obtains a relation between C_m and the generalized time W defined as:

$$W = 4Dt/d^2 \tag{3.10}$$

where t is the time for gas to flow from the nozzle to point where $C = C_m$. The relation is:

$$C_m = 1 - C^{-0.25W} \tag{3.11}$$

The value of W at the flame tip is W_f , corresponding to C_f . From the above equations, W_f can be given by:

$$W_f = 4 \ln[(1 + a_o)/(1 + a_t)] \tag{3.12}$$

W_f , or the actual time of flow, t_f , to the flame tip, is correlated with the flame length L by the following equation:

$$W_f = 4Dt_f/d^2 = (4D/d^2) \int_0^{t_f} dt = (4D/d^2) \int_0^L dx/U \tag{3.13}$$

where U is the gas velocity at the distance x from the nozzle. The solution of Eq. 3.13 involves the determination of a relationship between U and x . If U is considered to be constant, Eq. 3.13 can be easily integrated and the flame length becomes:

$$L = \frac{Ud^2W_f}{4D} = \frac{VW_f}{\pi D} \tag{3.14}$$

This relation is in accordance with the experimental results for small flames. The non-applicability of this relation to longer flames implies that the assumption of consistency of U is unsatisfactory. Further relations for the flame length were obtained with non-uniform distribution of the velocity. Also empirical relations were obtained for the flame length and the flow rate. Whol et al [437] gave the following empirical relation relating the flame length and the volumetric flow rate:

$$L = 1/(0.206/\sqrt{V} + 0.354/V) \tag{3.15}$$

where L is in cm and V in cm^3s^{-1} . This equation is compared with the theoretical Eq. 3.14 and is approximated further as follows. Series expansion of Eq. 3.11 for the condition at the flame tip ($C_m = C_f$, $W = W_f$) and neglect of higher terms lead to:

$$C_f = \frac{1}{4W_f} \tag{3.16}$$

so that Eq. 3.14 becomes approximately:

$$L = V / 4\pi C_f D \quad (3.17)$$

In the above equation, it was assumed that the diffusion coefficient D and the average velocity U are constants over the whole flame length. In reality both increase with increasing height because of the increase of average temperature, which increases more rapidly than U so that the total change of conditions with increasing height may be accounted for in the above equation as an increase in D . The simplest form to describe this increase is:

$$D = D_0 + k L$$

where D_0 is the diffusivity at room temperature. The second term is always considerably larger than the first. If D_0 is considered small compared with $k L$, from the above equation we have:

$$L = 1 / [2\sqrt{\pi k C_f / V(1 - C_f / 2)} + 2\pi D_0 C_f / V(1 - C_f / 2)] \quad (3.18)$$

A comparison of Eqs. 3.15 and 3.18 gives with $C_f = 0.187$ the following numerical values for the constants of the equation; $D_0 = 0.27 \text{ cm}^2 \text{ s}^{-1}$, $k = 0.033 \text{ cm s}^{-1}$.

3.2.2 Opposed Diffusion Flames

The opposed jet or counterflow diffusion flame is the more suitable for most aspects of the investigation of diffusion flame reaction zone structure and properties. In this configuration, the thickness of the boundary layer remains constant. Furthermore, studies of strained laminar diffusion flames have proven useful, both for developing a fundamental understanding of the flame structure and extinction, and for application in the flamelet model of turbulent combustion. Flame extinction resulting from excessive strain is of particular importance and has received considerable attention.

The combustion in opposed flow diffusion flame, shown in Fig. 3.7 takes place in a single thin flame zone near the stagnation plane, and around the location of the stoichiometric mixture. Normally, either the fuel or the oxidizer reaches the flame by diffusion from the stagnation plane in a direction counter to the convective flow, and the products of the combustion are convected back towards the stagnation plane. Figure 3.8 shows the response of the heat release rate profile to increasing applied stress, for the diffusion flame of an equimolar H_2/N_2 fuel with air [100]. The flame becomes thinner, and moves towards the stagnation plane, while the heat release rate increases and the maximum temperature achieved in the flame falls until eventually the flame is extinguished.

The higher stress rates are accompanied by decreased residence times in the reaction zone, and the concomitant fall in temperature is a direct consequence of increased breakthrough of both fuel and oxidizer past the stoichiometric position. The flame departs from its low stress, near equilibrium structure, and is able to support higher reaction rate [100], this time without freezing on the fuel side. The situation continues until the temperature effect on reaction overtakes the effect of increase in concentration of reactant, in which case extinction occurs. The system under consideration

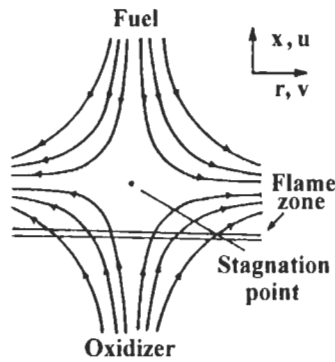


Fig. 3.7: Strained diffusion flames [65]. Reproduced by permission of The Combustion Institute.

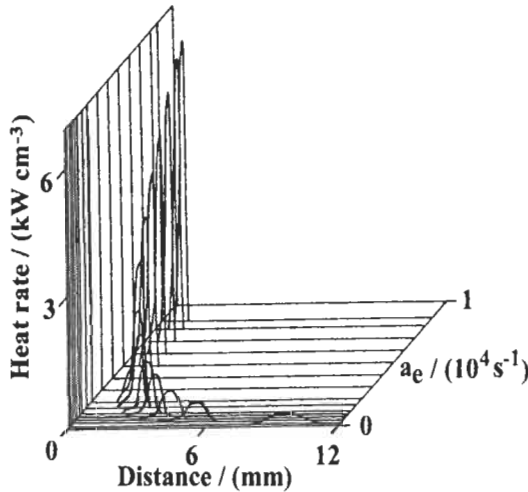


Fig. 3.8: Computed heat release profiles in counter flow diffusion flame of equimolar H₂/N₂ with air at applied stresses of 100, 300, 500, 750, 1000, 1500, 2000, 3000, 4000, 5000, 6000, 7000, 8000 and 8600 s⁻¹ (extinction limit, Dixon-Lewis and Missaghi [100]) [65]. Reproduced by permission of The Combustion Institute.

has a maximum temperature of 1308 K at extinction, with $T_i = 1030$ and 1130 K on the fuel and air sides, respectively [65]. The extinction temperature is consistent with the decisive role of net radical production in its origin [100].

The effect of flame structure on the extinction limits of CH₄-O₂-N₂ counter flow diffusion flames is investigated by Du and Axelbaum [439]. The stoichiometric mixture fraction is varied by varying free-stream concentrations, while the adiabatic flame temperature is held constant by maintaining a fixed amount of nitrogen at the flame. The experimental results yielded an extinction strain rate of 375 s⁻¹ for the methane-air flame, increasing monotonically to 1042 s⁻¹ for the diluted-methane-oxygen flame. For the CH₄-O₂-N₂ system at a given adiabatic flame temperature, the extinction limits increase with stoichiometric mixture fraction. They found that this increase is due to shift in the oxygen profiles into regions of higher temperature, which raises the OH

and O production rates and concentrations in this region, yielding stronger flames. This also results in difference of up to 200 °C in extinction temperature for the same fuel and the same adiabatic flame temperature. Their study [439] is relevant to practical flames where the fuel is diluted and/or the oxidizer is enriched. There is a number of applications where enriched oxygen is presently used, notably in blast furnaces. Enriched oxygen combustion has also been proposed to reduce particulate in diesel engine and emissions as described in chapters 1 and 2.

3.3 Turbulent Burning

Because flames propagate through molecular processes such as species diffusion, conduction and chemical reaction, which are much more rapid than turbulent rate processes, a turbulent flame might be regarded as an array of laminar flamelets. Computationally, with this approach, the laminar flame is a sub-model and a library of laminar flame structures may be compiled for different initial mixtures and strain rates, although problems arise in seeking a correspondence between straining in laminar and turbulent flames (Abdel-Gayed et al [440]). In the latter, there is a distribution of strain rates, so that in parts of the flow field the strain rates might be so high that a flamelet cannot be sustained.

If A is the elemental surface area of a material normal to the flow into the flame, the strain rate is given by $A^{-1} dA/dt$, in which t is the time. The key of turbulent flow parameter is the mean strain rate [441]:

$$\frac{1}{A} \frac{dA}{dt} = \left[\frac{\varepsilon}{\nu} \right]^{0.5} \quad (3.19)$$

where ε is rate of turbulent energy dissipation per unit mass and ν is the kinematics viscosity. For isotropic turbulence [442]:

$$\left[\frac{\varepsilon}{\nu} \right]^{0.5} = 15^{0.5} \left[\frac{u'}{\lambda} \right] \quad (3.20)$$

where u' is the r.m.s. turbulent velocity and λ is the Taylor microscale.

The dimensionless Karlovitz stretch factor, K' , can be regarded as the mean Eulerian aerodynamic strain rate, u'/λ , normalized by a chemical strain rate, U_1/δ_1 in which δ_1 is the laminar flame thickness and U_1 is the laminar burning velocity:

$$K' = \frac{u' \delta_1}{\lambda U_1} \quad (3.21)$$

For homogeneous and isotropic turbulence, with $\delta_1 = \nu/U_1$, Abdel-Gayed et al [440] derived:

$$K' = 0.157 \left[\frac{u'}{U_1} \right]^2 R_L^{-0.5} \tag{3.22}$$

where R_L is the turbulent Reynolds number ($u'L/\nu$), with L as the integral length scale.

It is convenient to express the regimes of premixed turbulent combustion diagrammatically. The Borghi [443] diagram has u'/U_1 and L/δ_1 as axes, whilst that of Abraham et al [444] has Damkohler number ($(L/u')(U_1/\delta_1)$) and R_L as axes. Figure 3.9 shows the modified Borghi diagram of Abdel-Gayed et al [445] in which values of constant K' are straight lines on the logarithmic plot.

The different regimes that are identified are based upon experimental observations. In explosions with a low rate of flame straining, Schlieren cine' films showed a continuous wrinkled laminar flame sheet. Those with a progressively higher strain rate showed the sheet to break up at values of $K'L_e$ of about 0.15 (L_e is the Lewis number = α/D where D is diffusion coefficient and α is the premixture gaseous thermal diffusivity). This process continued up to a value of $K'L_e$, in the region, of 0.3. In explosions at high values of this product, prior to complete flame quenching, partial quenching was observed in a fragmented reaction zone. Theoretically, when the value of K' exceeds 0.26 the chemical time is greater than the Kolmogorov time and the laminar flame thickness exceeds the Kolmogorov microscale. Because of the distribution of strain rates, quenching is a statistical phenomenon. Abdel-Gayed and Bradley [446] suggested flame quenching occurred when:

$$K' R_L^{-0.5} > 0.079 \text{ for } R_L < 300 \tag{3.23}$$

$$K' L_e > 1.5 \text{ for } R_L > 300 \tag{3.24}$$

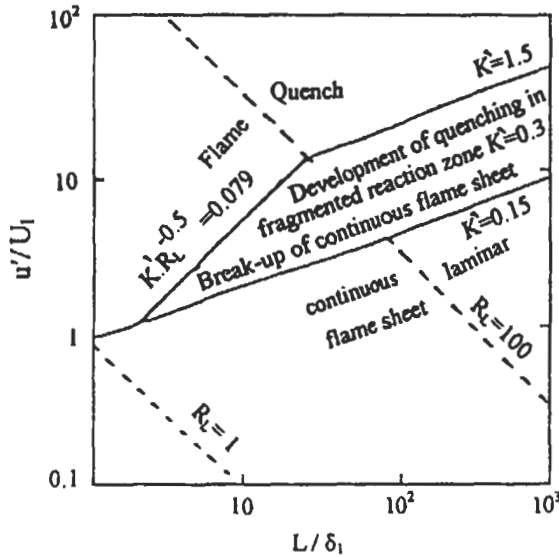


Fig. 3.9: Turbulent flame regimes [511]. Reproduced by permission of the Pure and Applied Chemistry.

3.4 Turbulence Models

The turbulent motion, which is highly random, unsteady and three-dimensional, is difficult to describe and predict. The exact instantaneous equations, which describe this flow, are known and the numerical procedures to solve these equations are available. But the storage capacity and speed of computers are still need to be developed to allow this exact solution. The prediction of turbulent flow is based on the time-averaged partial differential equations which have introduced statistical correlations involving fluctuating velocities, temperatures and scalar quantities whose magnitudes are not known. Further differential equations could be added for this turbulent correlation. The process of approximating these unknown correlations in terms of known quantities is known as "Turbulence modeling".

The hydrodynamic field is described by the k - ϵ model [447] with Favre averaging [448] of the dependent variables in this model. Reynolds stresses and scalar fluxes, in Cartesian tensor notation, are modeled by [449,450]:

$$-\bar{\rho} \tilde{u}_i'' \tilde{u}_j'' = \mu_t \left(\frac{\partial \tilde{u}_i}{\partial x_i} + \frac{\partial \tilde{u}_j}{\partial x_j} \right) - \frac{2}{3} \delta_{ij} \left(\bar{\rho} \tilde{k} + \mu_t \frac{\partial \tilde{u}_m}{\partial x_m} \right) \quad (3.25)$$

$$-\bar{\rho} \tilde{u}_i'' \tilde{\Phi}'' = \frac{\mu_t}{\sigma_\Phi} \frac{\partial \Phi}{\partial x_i} \quad (3.26)$$

where the turbulent viscosity, μ_t is given by:

$$\mu_t = C_\mu \bar{\rho} \frac{\tilde{k}^2}{\tilde{\epsilon}} \quad (3.27)$$

The symbols ρ , u_i , k , ϵ , Φ , and δ_{ij} represent the gas density, velocity in the x_i coordinate, turbulent kinetic energy, the dissipation rate of this energy, a scalar quantity, and the Kronecker delta function, respectively. The superscripts $''$, $\bar{}$, and $\tilde{}$ indicate fluctuating, time average, and Favre average quantities, respectively, while C_μ and σ_Φ are empirical constants.

Two additional pressure-containing terms were introduced [248] to the standard k - ϵ model [447]. These arise naturally as source terms in the exact k transport equation from compressibility effects [449] and were modeled as follows:

$$\overline{\rho' \frac{\partial u_i''}{\partial x_i}} = -\frac{9}{55} \bar{\rho} \tilde{k} \frac{\partial \tilde{u}_i}{\partial x_i} \quad (3.28)$$

$$-\bar{u}_i'' \frac{\partial \bar{P}}{\partial x_i} = \frac{\overline{\rho' u_i''}}{\bar{\rho}} \frac{\partial \bar{P}}{\partial x_i} = -\frac{\mu_t}{\sigma_\rho} \frac{1}{\bar{\rho}} \frac{\partial \bar{\rho}}{\partial x_i} \frac{\partial \bar{P}}{\partial x_i} \quad (3.29)$$

where P is the pressure and superscript ' denotes a time fluctuating component. Equation 3.28 follows the modeling by Launder et al [451] of the pressure-strain correlation;

$$\left(\frac{P' \partial u_i^n}{\partial x_j} + \frac{P' \partial u_j^n}{\partial x_i} \right),$$

In the Reynolds stress equations, the indices i and j are contracted and the term divided by 2 in their model. In Eq. 3.29, the gradient transport approximation, Eq. 3.26, has been used to model the nonzero Favre mean fluctuating velocity, $\overline{u_m^n}$. The Prandtl number, σ_p , for density transport is set equal to unity. Equations 3.28 and 3.29 are usually neglected when the k - ϵ model is applied to reacting flows. When included, they reduce the magnitude of the source term in the k -equation and lead to smaller values of k . They become important in the reaction zone where density gradients are greatest [248].

3.5 Interaction Between Turbulence and Chemical Kinetics

The interaction of turbulence and chemical reactions occurs in turbulent reacting flows over a wide range of flow conditions. Various degrees of interaction between turbulence and chemical reactions can lead to different phenomena. Weak interactions between turbulence and chemical reactions may simply modify the flame slightly causing wrinkles of flame surface [452]. Strong interactions could cause a significant modification in both the chemical reactions and the turbulence.

The interaction of turbulence and chemical reactions is a complex phenomenon that can cause significant modification in both the turbulence and chemical reactions. For chemical reactions with negligible heat release, this interaction has only one direction, that is, turbulence will modify the chemical rates, but the reactions have no influence on the flow field. The purpose of combustion is generating heat; therefore, one expects large density variations which can alter the fluid dynamics. Hence, the turbulence will experience strong influence by the chemical processes and vice versa.

It has been observed experimentally that the entertainment process in mixing layers has been significantly altered by the heat release leading for different growth rates than those expected in constant density flows (Hermanson et al [453] and Dimotakis [454]). On the other hand, strong turbulence can strain the flames to a point that chemical reactions can no longer keep up with mixing process causing the flame to extinguish. Experiments by Masri et al [455] have revealed that local flame extinction can occur prior to the flame blowout limit indicating a strong interaction between turbulence and chemistry.

To understand and quantify the complex interactions between turbulence and chemistry, it is useful to identify the relevant length and time scales in turbulent reacting flows. An overall characterization of the interactions between turbulence and chemical reactions can be obtained by plotting the Damkohler number (i.e., the ratio of flow time scale and reaction time scale) versus the Reynolds number over the whole range of length scales (Williams [452]). Based on the length scales of flames and turbulence, two extreme regimes are identified. One extreme with the flame thickness much smaller than the smallest length of turbulence is identified as the flamelet regime. The other opposite extreme with thick flames compared to the smallest turbulence length is

identified as the distributed reaction regime. The nature of the intermediate regimes between these two extremes is rather complex, and is yet to be explored. Unfortunately, many practical combustion systems involve a wide range of operation conditions including the intermediate regimes. (Kollmann and Chen [456])

3.5.1 The Influence of Turbulence on the Chemical Reactions

Kollmann and Chen [456] provided a valuable review of the interaction of the fluid mechanical and chemical processes involved in turbulent reacting flows. In their work, the basic governing equations of the dynamics in turbulent combustion are outlined in the Eulerian frame. The corresponding transformation to the Lagrangian frame has been presented with the aid of the Lagrangian position field. It was shown that in the Lagrangian frame, the transport equation for a thermo-chemical variable does not contain the nonlinearity due to convection, but the diffusive flux appears as a highly nonlinear process depending on the time histories of the Lagrangian strain rate.

The influence of turbulence on the chemical processes is expressed by the statistical moments that appear in the mean reaction rate. Upper and lower bounds for the mean reaction rate were obtained for a binary mixture. It was shown that the mean reaction rate could have values radically different from the quasi-laminar values (reaction rate at the mean properties). The influence of temperature fluctuations on the mean chemical-reaction rate was shown to be significant for reactions with large activation energies at a low mean temperature. Furthermore, it was shown that the PDF equation (probability density function) for a single reactive scalar could be solved for a homogeneous turbulence. The solution indicates that for bounded scalar variables, the scalar and its dissipation rate must be correlated in order to satisfy the realizability conditions.

The analysis of non-premixed flames illustrates the important role of mixing in determining the progress of chemical reactions. Kollmann and Cheng [456] have used nonpremixed turbulent methane-air jet flames to illustrate the mixing properties predicted by a PDF method. Mixedness parameters were introduced and the mixed models for the single point PDF methods were discussed. The main conclusions drawn from their [456] studies of non-premixed reacting systems are that the mixing models must satisfy realizability conditions and that they must represent the effect of turbulent mixing correctly at least for lower order moments. It was also shown that the mean reaction rates could be larger or smaller than the quasi-laminar rates by different orders of magnitude due to the effect of turbulence. From their [456] computation results, the predicted mixedness parameters were examined showing that they are not positive-definite as in binary systems. The treatment of premixed systems was restricted to the flame sheet regime. In this regime, the effect of turbulence is essentially through the distortion of the thin flame sheet leading to increased flame surface.

The interaction of turbulence and chemical reactions in nonpremixed and premixed combustion can also be described in terms of the effects of turbulence on surfaces, in particular, the flame surfaces. Hence, the basic dynamical and topological properties of surfaces were introduced. It was shown that for flame surfaces, both the diffusive flux and the chemical sources could alter the relative progression velocity of such surfaces.

3.5.2 Fantasy Versus Realism in Chemical Kinetics Description

In high-speed combustion, the matter of the interaction of turbulence and chemical kinetics is of great importance because in high-speed flows the usual assumptions of relatively small chemical times become suspect and ignition and extinction phenomena are of crucial importance. Therefore, the knowledge about the interaction between turbulent mixing and chemical kinetics is crucial to the successful development and optimization of the scramjet (Swithenbank et al [457]). Thus the clear presentation by Kollmann and Chen [456] of the well-known but frequently neglected influence of turbulence on the effective chemical kinetics of the system is highly appropriate. The fluctuations in temperature and species concentrations associated with the turbulence can either increase or decrease by orders of magnitude of the mean rate of creation of products from that given by the assumption of mean values in the applicable kinetic equations, i.e., by the "quasi-linear" description [458]. A review of the literature on high speed combustion in turbulent flows indicates that, considerable progress on the computational aspects of these flows has been achieved, but that the equations being solved frequently lack realism, in particular the assumption of quasi-laminar chemistry is often used with the consequence that unconvincing results are obtained despite the computational sophistication brought to bear. There may be other shortcomings of the equations being treated as well, for example, due to the fluid mechanical descriptions employed.

While it is clear that the quasi-laminar model for chemical kinetics is inapplicable to the flows of applied interest, the practical alternative to be brought to bear when ignition and extinction phenomena are important is unclear. The most convincing calculations of turbulent reacting flows are those based on the conserved scalar approach of Bilger [459], and Libby and Williams [460] which applies for flows either in complete or nearly complete chemical equilibrium. As suggested by Kollmann and Chen [456] it is unrealistic to apply to turbulent flows the full kinetics descriptions currently available for various chemical systems with their multiplicity of chemical reactions and species. In PDF methods the number of independent variables and the complexity of the computations would be overwhelming while in moment methods there would be an overwhelming number of correlations of species, temperature and density to be taken into account in reliable calculations. Thus the development of reduced mechanisms by several research workers (as described in chapter 2) is important for the development of turbulent combustion models. Kollmann and Chen [456] emphasize the PDF approach to the exploitation of this development, an approach to which they and their co-workers have made significant contributions [461]. Comments on the interaction of turbulence and chemical kinetics were suggested by Libby [458]. He discussed briefly an alternative means of exploitation, one with which some might be more comfortable since it is based on moment methods and it represents an extension of widely used techniques for the description of turbulent flows. He [458] referred to the laminar flamelet theory of Bray and co-workers [462-463] and to an admirable review of flamelet concepts in both nonpremixed and premixed systems [464]. The relevance of the laminar flamelet to turbulent combustion was examined by Correa [465]. Data on NO_x and temperature in laboratory flames were reviewed. Turbulence and chemical

time-scales are compared with one another in a hypothetical scramjet and gas turbine combustor. The results indicate that, contrary to the situation required for the existence of laminar flamelets in turbulent flames, chemical time-scales are often much larger than turbulence scales. Due to the wide disparity in chemical time-scales associated with the phenomena of potential interest: ignition and extinction, combustion efficiency, NO_x , CO, and so on, it is not possible to universally classify all flames, or even all the reactions in a given flame, as being entirely inside or outside the flamelet regime.

The laminar flamelet library approach has been applied by Nilsson and Bai [466] for modeling of a lean premixed propane-air turbulent flame stabilized by a bluff body. In this approach the mean flame location and mean flame thickness were modeled by a level-set G-equation and the variance of G, along with empirical expressions. The detailed species, temperature and density were calculated using a presumed probability density function together with the laminar flamelet library. The flamelet library approach generally simulated a better distribution of species and temperature field, compared to fast-reaction models such as the Eddy Dissipation Concept (EDC). In particular the maximal values of major species and temperature were found to be not sensitive to the model parameter [466]. The mean flame location was also found to be fairly sensitive to the modeling of turbulent flame speed. The intermediate species were also found to be more sensitive to the turbulent flame thickness model.

The reason for using combustion models such as EDC in industrial applications is that such models are inexpensive and can be applied to both diffusion and premixed flames. However, they do not naturally allow extensions to the detailed chemistry that is necessary for emissions calculations and neglect many of the processes related to the dynamics of turbulence. For example, for thermal NO according to the simplified Zeldovich mechanism, information on the O radical is required. In commonly used NO prediction procedures, based on EDC type combustion modeling, typically, equilibrium is assumed between O and O_2 . However, this does not allow for the radical overshoot in the flame zone, and therefore, leads to an underprediction of the NO formation rates within flame zones.

Nilsson and Bai's [466] experimental setup is shown in Fig. 3.10 (a). The fuel propane supplied at the inlet (left), mixes with air. Before the position for ignition, a perfect mixture is obtained. The combustion chamber is a rectangular channel with height of 0.12 m (y-direction) and width of 0.24 m (z-direction). The premixed combustion is stabilized in the channel by a triangular prism shaped flame holder. The velocity, temperature and some species are measured by LDA and gas analysis equipment (a chemiluminescence analyzer for NO_x , two non-dispersive infrared instruments for CO and CO_2 , a paramagnetic analyzer for O_2 and flame ionization detector for unburned hydrocarbons). The experimental conditions studied are that the equivalence ratio is 0.6, the unburned mixture temperature is 600 K and pressure of 1 bar.

Species mole fraction and temperature distribution measured by Nilsson and Bai [466] using the above described experimental setup are shown in Fig. 3.10 (b). The calculations are performed using the turbulent flame speed model of Damkohler (S-1) and by a level-set G-equation model (G-1, G-2 and G-3). Several flame-thickness models are tested. The figure shows that at $x = 0.15$ m, the major species CO_2 and O_2 as well as the temperature are well predicted by these models. In particular, the peak species mole fractions of CO_2 and O_2 and the peak of temperature in the centre of the channel are well predicted by all the models, as compared to the experimental data. The minor species such as CO are more sensitive to the flame-thickness model. A thinner

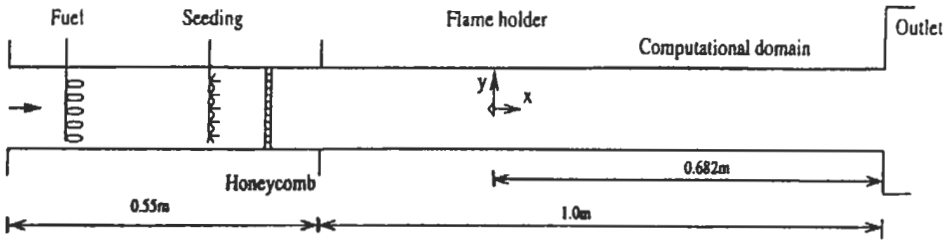


Fig. 3.10 (a): The experimental setup and the computational domain [466]. Reproduced by permission of Elsevier Science.

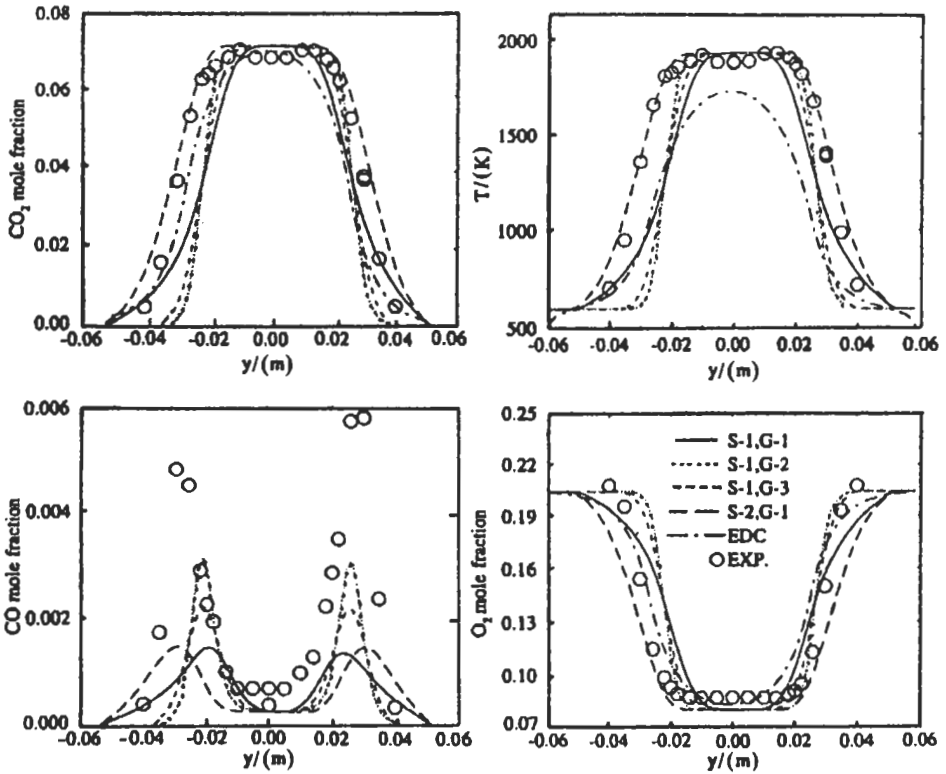


Fig. 3.10(b): Comparison of computed mean species mole fractions and temperature to the experimental data, along the vertical direction at 0.15 m downstream of the flame holder. EDC denotes results calculated using Magnussen's EDC model with model constant $C_s = 8.5$ [466]. Reproduced by permission of Elsevier Science.

flame has a higher peak value of CO and vice versa. The reason for this, is that in the laminar flamelet of lean fuel combustion, CO is only seen in the flame zone. In the post flame zone, because of the excess of oxygen, the CO formed in the flame inner layer is quickly oxidized.

Calculations using a direct phenomenological approach, the EDC model, are also performed. One step irreversible global reaction of propane and air to form final product CO_2 and H_2O is presumed. It is possible to include intermediate fuel such as CO in the model. However, it has been shown that the model constant for mean CO reaction rate would have to be different for different fuels to obtain a realistic CO distribution. The EDC model constant used is $C_a = 8.5$. This value is adjusted to have a best match with the measurements in O_2 and CO_2 as shown in Fig. 3.10 (b). However, the temperature calculated is lower than the experimental value.

An alternative to the EDC type of modeling is the Laminar Flamelet Method (LFM) [464]. This offers very detailed information on the chemistry, where concentrations of a great number species are computed from elementary chemical kinetics and their interaction with the turbulence is treated explicitly. Although, once flamelet libraries are generated, the LFM is not much more computationally expensive than the EDC, it is still far from being state-of-the-art, as its use in industrial applications such as gas turbines seems to have remained extremely restricted. This may be due to the argument that the LFM is valid for high Damkohler numbers, which is designated by the wrinkled and corrugated flame zone in the Borghi diagram [467], whereas many practical combustion devices including gas turbines fall into the distributed reaction regime. However, there have been arguments encouraging an increased validity of LFM in many applications. More details about LFM are given in section 3.7.2. Recently, Benim and Syed [468] have used the LFM for turbulent premixed combustion, and they investigated two different approaches. In both approaches, the treatment of NO formation as postprocessing is retained. Since NO reactions are very slow compared to the main combustion reactions, the extraction of NO concentrations out of the flamelet data is inappropriate. Therefore, they [468] computed the NO concentrations by solving its mean transport equation. The critical issue of obtaining the oxygen radicals is treated by using the flamelet data for the oxygen radicals instead of the equilibrium assumptions. In the first approach, which is easier to implement, the LFM is adopted only as a part of the NO post-processing for predicting the oxygen radical concentrations, where the main heat release process is modeled by the conventional EDC. The second approach is the full implementation of the LFM as the turbulent combustion model. Their predicted results [468] were compared with experiments of Moreau and Borghi [469-470]. The experiments have been done on a ducted turbulent premixed methane-air laboratory flame at atmospheric pressure, and the flow is everywhere uni-directional. The geometry of the test section is illustrated in Fig. 3.11 (a). The combustor has a rectangular cross section. The burnable methane-air stream (Stream A) passes through a turbulator before entering the test section. The flame is stabilized by a co-flowing stream of high temperature exhaust gases (Stream B) of a complete methane-air combustion from an auxiliary burner. Measured equivalence ratio, velocity and temperature of the stream A are 0.83, 57 m s^{-1} and 600 K, respectively, while for the stream B are 1, 112 m s^{-1} and 2000 K, respectively, at the combustor inlet (Fig. 3.11 (a)). The pilot flame (Stream B) introduces NO into the combustor. The NO concentration of stream B is estimated as 65 vppm (wet) [470], which has been set as a boundary condition.

Computed transverse profiles of axial velocity are compared with experiments in Fig. 3.11 (b). The sharp gradient at $x = 0.039 \text{ m}$ is due to the different inlet velocities of the streams A and B. Along the combustor length, gradients smear out and velocities increase due to expansion of combustion gases. The shear layer between the streams is

well produced. Comparisons of predicted and measured temperature profiles are presented in Fig. 3.11 (c), at two axial stations. At $x = 0.322$ m, a sharp gradient is observed. This results from the inlet temperature difference of streams, and the combustion of stream A, stabilized by the stream B. Computations overpredict the temperature over much of the profile. Despite this, a satisfactory qualitative agreement is observed. Near the outlet ($x = 0.922$ m), Fig. 3.11 (c) shows that both prediction and experiment indicate rather flat temperature profiles. Profiles of NO concentrations are shown in Fig. 3.11 (d), where flamelet and equilibrium approaches are compared with experiments. Near the inlet ($x = 0.122$ m), both predictions agree well with each other and with experiments. This is because the NO prediction in the chamber by this station is quite small, and the NO is dominated by that introduced by the pilot flame, causing high values for $0 < y < 0.02$ m. Further downstream, one observes that sharp gradients flatten, and the NO level increases. Equilibrium results show an increasing deviation from experiments, and from flamelet predictions, along the combustor length. The maximum deviation is seen near the combustor exit ($x = 0.992$ m). The flamelet-based NO predictions are seen to reproduce much better the experimental increase in NO concentrations along the combustor length. NO levels near the upper wall ($y = 0.1$ m) are underpredicted. A possible cause of this can be the local dominance of NO formation mechanisms other than the Zeldovich one (e.g., prompt NO, N_2O path), since temperature near the upper wall remains low for much of the combustor length.

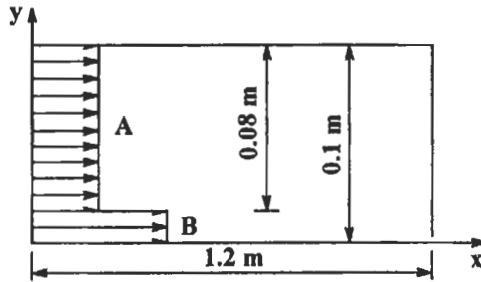


Fig. 3.11 (a): Geometry of combustor, Benim and Syed [468], reproduced by permission.

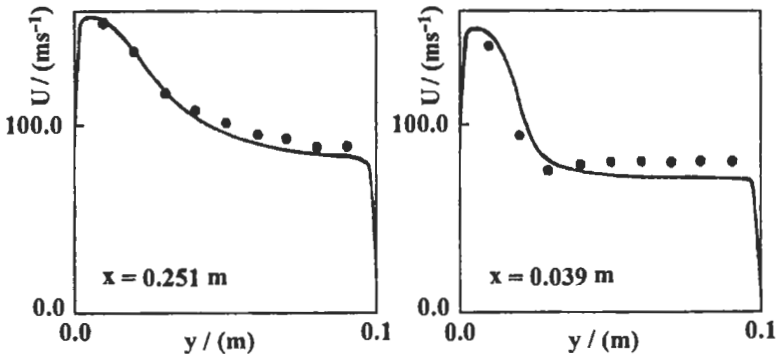


Fig. 3.11 (b): Axial velocity profiles, ●: Experiments [470], — Prediction, Benim and Syed [468], reproduced by permission.

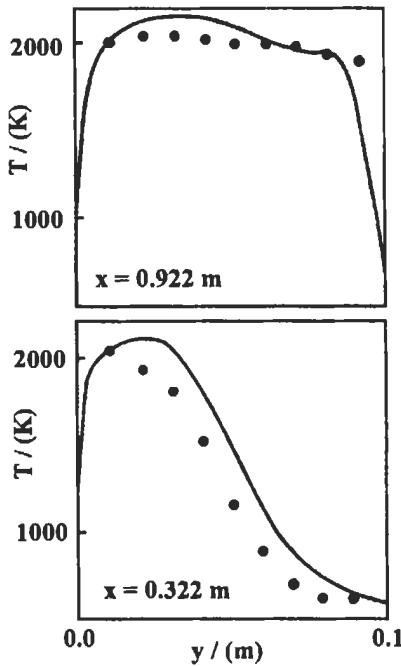


Fig. 3.11 (c): Temperature profiles,
 ●, Experiments [470], — Prediction, Benim and Syed [468], reproduced by permission.

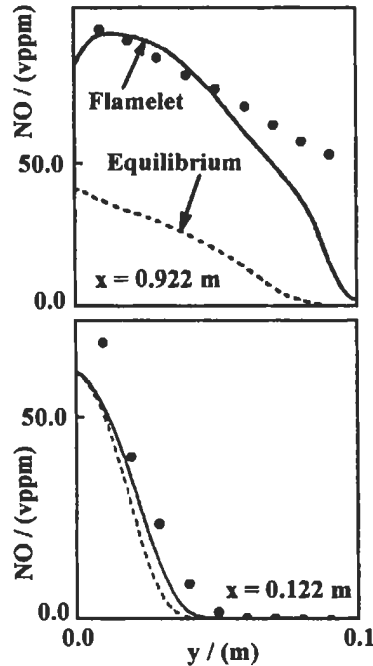


Fig. 3.11 (d): Profiles of NO concentration,
 ●, Experiments [470], — Prediction, Benim and Syed [468], reproduced by permission.

3.6 Flame Stabilization

3.6.1 Introduction

To obtain high volumetric combustion rates from a jet engine, it is required to feed its burner with high velocity streams. Burner must be capable to stabilize the produced flame. The flame stability limits is the most important controlling factor in the design of such burners. Thus, burner design would be greatly facilitated by knowing the effect of the input parameters such as fuel-air ratio, average velocity and its distribution, burning velocity and its distribution, and the intensity of swirl, on the stability of the flame.

It was found that the Bunsen burner could not stabilize turbulent flames with high flow velocity due to the impossibility of self-propagation of the combustion wave. Many previous investigators tried to improve the stability of premixed turbulent flames by creating a recirculation zone which affects the transfer of mass and energy from the burned gases to the unburned ones, or by using a pilot flame which works as a continuous ignition source.

It was found that, the blow off velocity, (which is the average velocity of gas and air streams), when flame propagation stops as the flame ceases, and the critical boundary velocity gradient at blow off, (which is the slope of gas velocity curve at the blow off limit), are reasonable criteria for flame stability.

With the application of swirl, a central recirculation zone may be established, hence, high combustion intensities and wide operating limits could be achieved. The process of flame stabilization varies widely with the variation in swirler design and its position. Flame stabilization was the objective of many theoretical and experimental studies. In the following sections, different flame stability theories and the effect of different parameters on flame stability are presented with some related studies by El-Mahallawy et al [471].

It is generally appreciated that the continuous propagation of a burner flame requires raising temperature and /or providing sufficient chain carriers to a portion of the unburned combustible flow up to the initiation of the chemical reaction. This portion itself becomes the source of heat and chain carriers and is capable of initiating the reaction in the next layer.

The first successful attempt, to explain the flame stability limits and their mechanisms, has been made by Lewis and Von Elbe [472, 473]. They considered a laminar-premixed jet of an explosive gas issuing from a tube into the open atmosphere. They assumed Poiseuille flow, the gas velocity is zero at the stream boundary and increases to a maximum in the center of the stream. They proposed that the increase of the distance from the solid rim reduces the loss of heat and chain carriers. This causes the burning velocity to increase except at the outermost fringe where the mixture is diluted by the atmosphere. At one point, gas velocity and burning velocity are equal, that indicates the equilibrium position. They considered the gas velocity profile at the wave fringe, U_n , is linear, and its equation could be written as:

$$U_n = g'y \quad (3.30)$$

where y is the distance from the stream boundary and g' is a constant which will be referred to as the boundary velocity gradient. When the gas velocity decreases, a condition is reached at which the gas velocity at some points becomes smaller than the burning velocity and the combustion wave propagates against the gas stream into the tube. This refers to the flash-back condition. The critical value of g' at which this condition is first realized is denoted by g'_F . The another critical value of the boundary velocity gradient refers to the conditions of blow-off and is denoted by g'_B .

When the gas flow is increased, the equilibrium position shifts away from the burner rim. It is noted that, as increasing the distance from the rim, the explosive gas becomes progressively diluted by inter-diffusion with the surrounding atmosphere. The burning velocity in the outermost stream lines decreases correspondingly. Thus, an ultimate equilibrium position of the wave exists beyond which the effect of the burning velocity as increased from the burner rim is overbalanced by the effect of dilution. If the boundary velocity gradient is so large that the combustion wave is driven beyond this position, the gas velocity exceeds the burning velocity in every streamline and the combustion wave blows off.

It has been shown also by Lewis and Von Elbe [473] that the critical boundary velocity gradient can be calculated. Assuming fully developed laminar pipe flow, and applying Poiseuille equation, yield:

$$U = n(R^2 - r^2) \quad (3.31)$$

and the definition of the boundary velocity gradient as,

$$g' = \left| \frac{dU}{dr} \right|_{r \rightarrow R} \quad (3.32)$$

where U is the velocity at radius r , R is the pipe radius, r is the radial co-ordinate, $n = \Delta p / 4\mu L$, Δp is the pressure difference over length L and μ is the dynamic viscosity. Differentiating Eq. 3.31 and setting $r = R$, the velocity gradient g' can be given as:

$$g' = -2nR \quad (3.33)$$

The boundary velocity gradient for a given pipe diameter can also be obtained from the volumetric flow rate. In a cylindrical tube, the volume flow rate can be given as:

$$V = 2\pi \int_0^R U r dr \quad (3.34)$$

Substituting $U = n(R^2 - r^2)$ and integrating we have:

$$V = \frac{\pi}{2} nR^4 \quad (3.35)$$

and by combining Eqs. 3.33 and 3.35 we have:

$$g' = -\frac{4V}{\pi R^3} \quad (3.36)$$

Lewis and Von Elbe [472] reached an expression which indicates the effect of tube diameter on the flash back velocity of a given gas mixture as:

$$g'_F = -8U_f / D = -U_{bu} / X \quad (3.37)$$

where g'_F is the velocity gradient at the tube wall below which flash-back can occur, U_f is the flash-back velocity, i.e. average velocity in the tube below which flash-back can occur. D is the inner diameter of tube, U_{bu} is the normal burning velocity and X is the penetration distance, i.e. the distance at which quenching of combustion becomes noticeable and at which the burning velocity curve and the gas velocity curve for the flash-back limit touch each other.

Von Elbe and Mentser [474] used Eq. 3.37 of laminar flow to draw the stability curves of turbulent hydrogen air flames. They obtained different curves for the different burners. They concluded that the laminar equation could not be applied for the turbulent flames.

3.6.2 Stability of Premixed Flames

Wohl et al [475] had studied the stability of premixed butane-air flames burning from tubes and nozzles in laminar and turbulent flow. They found that the turbulent flames are much less stable than would follow from extrapolation of the blow-off velocity curve valid for laminar flames. Furthermore, with laminar flames, the blow-off velocity is proportional to the tube diameter (Eq. 3.37) while turbulent flames blow-off velocity is practically independent of the tube diameter over a considerable range. It has been found, however, that the reason for this difference is the different relation which exists between the velocity gradient at the tube wall and the average velocity in laminar and turbulent flow. Hence, the velocity gradient at the tube wall, in case of turbulent flow, can be approximately given between the Reynolds numbers of 5000 and 200, 000 by the equation:

$$g' = 0.023 \text{Re}^{0.8} U / D \quad (3.38)$$

where U is the average velocity of the flow, and D is the inner diameter of the tube. According to this equation, the velocity gradient g' of a given mixture depends on the ratio $U^{1.8} / D^{0.2}$. In other words, the average velocity that corresponds to a certain velocity gradient is proportional to $D^{(0.2/1.8)} = D^{0.11}$. Thus the critical boundary velocity gradient in turbulent flow is nearly independent of diameter.

Van Krevelen and Chermin [476] studied the premixed flames, and they determined the two stability limits; flash-back limit and blow-off limit, for the methane and hydrogen gases, which more or less can be considered as extremes. These two stability limits were plotted on the same scale and are shown in Figure 3.12 (a). The large difference in behavior between the two gases becomes very obvious. It is clear from the figure that the hydrogen with its extremely high combustion rate may flash-back already at a boundary velocity gradient of $10,500 \text{ s}^{-1}$ but can hardly be blown off; methane on the other hand can flash-back only when the boundary velocity gradient has fallen to the low value of 400 s^{-1} , whereas blow-off already occurs at $2,000 \text{ s}^{-1}$ at the stoichiometric gas concentration.

Van Krevelen and Chermin [476] had characterized the flame stability diagram by the following data:

1. The coordinates of the peak (T) of the flashback curve g'_m, F_m .
2. A quantity provides a measure of the width of the flashback curve.
3. The distance of the blow off curve from the peak of the flash back curve characterized, for example, by the distance TP and TQ, and this data is represented in Fig 3.12 (b).

They [476] represented a generalized stability diagram in Fig 3.12 (c). This comprises a bundle of blow off curves, which are exclusively determined by the percentage of hydrogen in the mixture. They concluded that the critical boundary velocity gradient at blow off (g'_B) increases with the increase in hydrogen percentage in the mixture.

Also, Reed [477] had challenged the classical theory of Lewis and Von Elbe on the stabilization of aerated flames on a burner rim. He suggested that blow-off might result from a reduction in the reaction rate caused by the enthalpy loss from the stabilizer. This is due to shear flow, rather than from the fact that the gas velocity exceeds the local burning velocity throughout the whole flow field. Reed recommended the

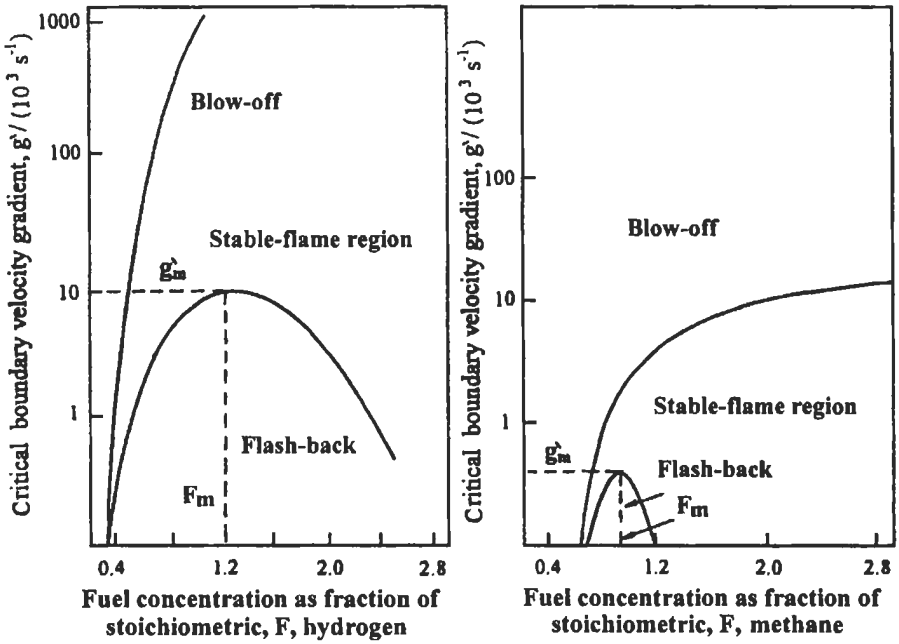


Fig. 3.12 (a): Flame stability diagram [476]. Reproduced by permission of The Combustion Institute.

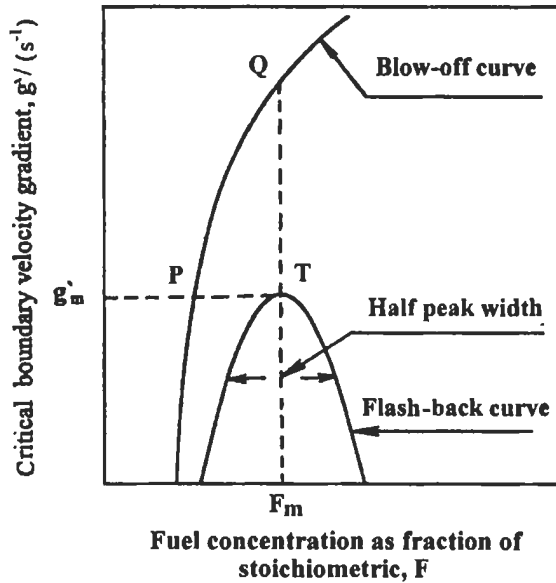


Fig. 3.12 (b): Generalized stability diagram [476]. Reproduced by permission of The Combustion Institute.

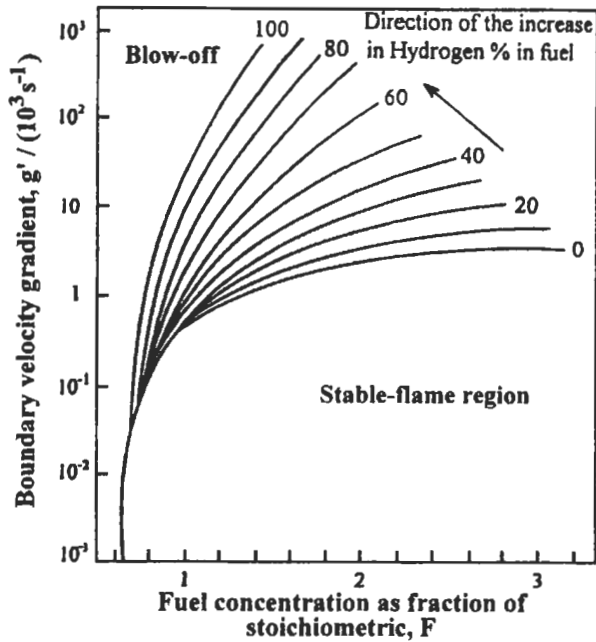


Fig. 3.12 (c): Different fuels stability diagram [476]. Reproduced by permission of The Combustion Institute.

following expression to determine the boundary velocity gradient at blow-off [477].

$$g'_b = (0.23\rho C_p S_u^2 / K) \left[1 - (1 - X_v^{6.4}) \alpha \right] \quad (3.39)$$

where S_u is the laminar flame speed, K is the thermal conductivity of the gas, X_v is the volume of fuel gas in the mixture expressed as a fraction of stoichiometric, and α is a constant; $\alpha = 0$ for premixed flames and $= 1$ for flames with secondary combustion. This equation is valid for $X_v < 1.36$.

Many attempts had been made to improve the flame stability especially in turbulent flames. Turbulent flames may be stabilized by pilot flames, bluff bodies, deflected jets, and swirl jets. The pilot flame may be outside or inside the main high velocity flow, and provides continuous sources of ignition. Jensen and Shipman [478] studied the stabilization of flames in high-speed flow by pilot flames. The main stream was propane air mixture, while the pilot stream was hydrogen-air mixture. They found that, the pilot heat would be sufficient to raise the average temperature of 19 mm diameter core of the main stream from its initial temperature 288 K to the required preheat temperature 414 K, and the thermal energy generated is sufficient to supply the required preheat to the remainder stream.

Bespalov [479] had studied the effect of bluff bodies on the stability of turbulent premixed flames. He concluded that, when the main stream velocity around a bluff body stabilizer is progressively increased, a critical value is reached at which the flame blows off. Furthermore, the maximum blow-off velocities generally occur with stoichiometric

mixture ratios and blow-off velocities decrease as mixtures are made richer or leaner. He showed that, stability limits are widened under the conditions of increase in stabilizer dimensions and increase of final and initial temperatures of the mixture.

Those who have studied bluff-body, reflected jets and swirl jets, agree that the recirculation zone occurs immediately downstream of each of them and works as a pilot. Energy and mass are transferred from the burned gases of this zone to the unburned portion in the main stream. Failure of flame propagation is due to quenching effect of hot gases due to rapid mixing with the cold unburned combustible main flow.

Beltagui and Maccallum [480], had studied the effect of swirl on the stability of premixed town gas-air flames in a furnace. They used vane generated type, with vanes placed at 15°, 30°, 45° and 60° to jet axis. They found that the central recirculation zone (CRZ) is established with swirlers, 45°, 60°, but not with either the 15° or 30° swirlers. They also found that in the case of creating the CRZ the spread of the jet is more rapid than in the free case, hence, the flame is more stable.

Bafuwa and Maccallum [481] studied the mechanism of flame stabilization in premixed town gas-air jets. They used vane swirlers having angles of 30°, 45° and 60° to the axis of the jet, for generating swirl in air jets entering furnaces. They found that the central recirculation zone controlled only the weak stability limits. The stability of the rich flames depended on secondary combustion with entrained air. They found that the stabilization of flames in the central recirculation zone of swirling free jets is very much influenced by entrainment of ambient air into the central zone. This entrainment increases with the increase in the degree of swirl, and amounts to just over 50% of the recirculation flow for the 60° vane swirler.

Rao and Sriramulu [482] made an investigation on a coaxial swirl burner to determine the improvement in stability due to using swirl with the premixed mixture. Fuel and air as a premixed mixture was conducted through the inner tube of the burner which concentric with it, a swirl generator. The premixed flame is thus surrounded by a swirling secondary stream. The two streams come into contact with each other just at the exit of the burner. The blow-off velocity is the average velocity of the mixture of gas and air through the central tube when flame propagation has ceased. The schematic diagram for the variation in intensity of the recirculation zone is shown in Fig. 3.13. In the absence of the central jet, the annular swirling stream creates a recirculation region (1), the size of the region increases with the increase in the flow rate of swirling stream. With the introduction of the central jet, this zone is penetrated; the depth of penetration being naturally dependent upon its momentum at the burner exit. For a given swirling flow rate, as the mixture velocity increases the region of recirculation confined to the burner periphery (2) contracts, and when it becomes so small (3) that it can't ignite the fresh mixture any longer, the flame propagation ceases.

A unified reaction model, being valid in all turbulent combustion regimes, has been developed and tested by Schmid et al [483]. Based on a thoroughly validated model for the turbulent burning velocity, the Kolmogorov, Petruvski and Piskunov (KPP) theorem was applied, thus leading to the formulation of the mean reaction rate as a function of local turbulence and kinetic parameters in the flow. Numerical calculations, comprising all flame structures of premixed flames were performed and compared with experimental data. Their [483] predictions of stability limits of unconfined, strongly swirling flames show satisfying agreement with experiments, supporting the earlier formulated opinion [484] that the blow-off limits of strongly swirling flames were determined by chemical kinetics limitation of the mean reaction rate.

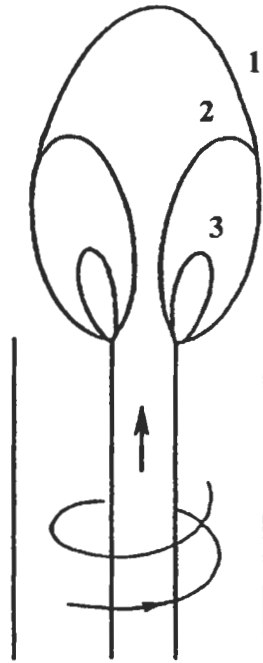


Fig. 3.13: A schematic diagram for the variation in intensity of the recirculation zone.

3.6.3 Stability of Diffusion Flames

The effect of fuel volatility on the blow off limit and the flame stability in spray combustion were investigated by Farag, et al [485]. The fuels used were gasoline, kerosene, and heavy oil. Every spray from an air blast atomizer used in their experiment had the same initial thrust and also had the same mean droplet diameter. They measured the axial temperature distributions on the flame centerline at the conditions with and without swirl. For all fuels used, the fuel flow rate of blow-off limit decreased with increasing swirl strength. At weak swirl, the fuel volatility had higher effect on the blow-off limit than at strong swirl where the recirculation zone had a higher effect on flame stability, whereas the maximum temperature gradient decreased and the peak temperature position shifted downstream.

Also, Yuasa [486] studied the effect of swirl on the stability of jet diffusion flames by using a double swirl burner (for air and fuel). The degrees of swirl of both fuel jet and air stream were varied continuously by varying the axial and tangential flow rates. The experimental variables were the air stream velocity, the hydrogen fuel injection, the swirl intensity of fuel jet, and the swirl intensity of air stream. It was concluded that the flame stability is improved by swirling both the fuel and air in the same direction.

It is clear from the above that, most of the investigators stressed their works on studying the stability and the structure of the premixed flames. Very few investigations were directed towards the studying of the stability of the turbulent free diffusion flames. There is also a lack of knowledge as far as the effect of swirl on the stability of the turbulent free diffusion flames is concerned.

Furthermore, to obtain high volumetric combustion rates from jets engines, it is required, as described above, to feed its burners with high velocity streams provided that this burner would be capable of stabilizing the produced flame. Thus, flame stability limits are the most important controlling factor in the design of such burners. With regards to this point, El-Mahallawy et al [471] have investigated the effect of swirl and the swirler position on the stability of turbulent free diffusion flames. They have used a vertical burner, which consists of two jets, inner jet for air and annular jet for commercial butane fuel. Four swirlers of 0° , 30° , 45° and 60° were used with the air jet. The position of the swirler inside the air jet (z) was varied between $z = 0$ and $z = 7$ mm.

Blow-off velocities for different swirlers are shown against the equivalence ratio, ϕ in Fig 3.14. The figure shows that, swirling the air jet increases blow-off velocities due to the creation of a recirculation zone. The intensity of this zone is very much influenced by changing the swirl angle, thus achieving good mixing between hot products and fuel and air streams, which subsequently leads to an increase in the burning velocity, and blow-off velocities. This effect is clear for low and medium degrees of swirl (0° , 30° , and 45°) as shown in Fig. 3.15. For high degree of swirl, 60° , it was found that there is a decrease in blow-off velocities which is attributed to the air motion when leaving the swirler. Air issuing from the swirler is spread in the radial direction and takes most of the fuel with it, therefore, the combustion and mixing will be concentrated more in the periphery than in the flame core where small amounts of air and fuel could mix and burn. The combustion in the core declines under the effect of quenching, which results due to high-entrained atmospheric air in the recirculated mass as the intensity of the recirculation zone is increased. Hence we expect that there is an optimum value of swirl angle, where the maximum flame stability could be achieved. Results in Fig. 3.15 show that this optimum value is corresponding to 45° of swirl.

As regards to the effect of the swirler position, it was found that when the swirlers were lowered inside the air jet, flame stability improved and the blow-off velocity increased as shown in Fig. 3.16. The best position, z , for all swirlers was found to be 7 mm between the burner rim and the swirler surface. The increase in blow-off velocities at this position is due to two effects. The first one is the decrease of the cooling effect, which in turn leads to an increase in the burning velocity. The second effect is the decrease of the effective degree of swirl, due to the friction losses with the inner jet

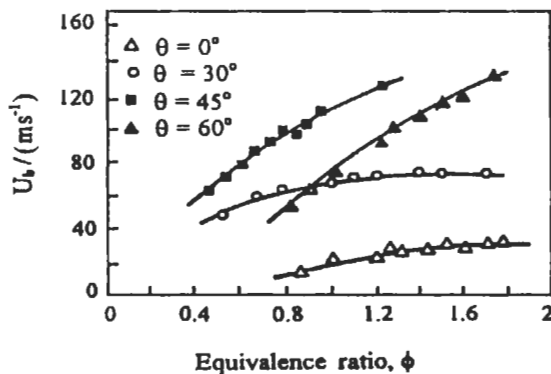


Fig. 3.14: Effect of equivalence ratio on the blow-off velocity ($z = 0$ mm) for different degrees of swirl [471].

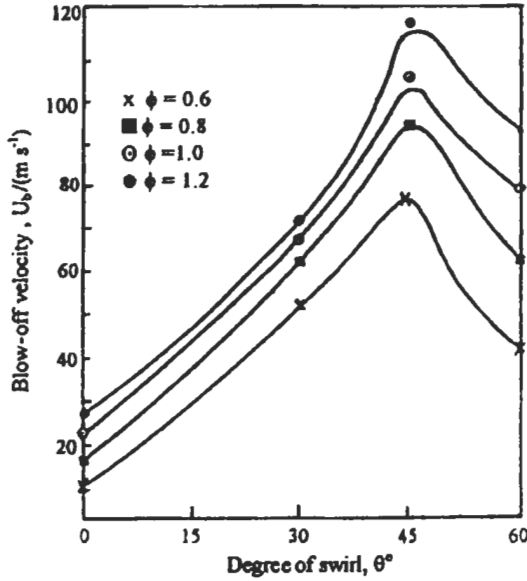


Fig. 3.15: Effect of the degree of swirl on the blow-off velocity ($z = 0$ mm) for different equivalence ratios [471].

surface. Generally, the combination of the effect of cooling and the change in the effective degree of swirl gives an improvement to all swirlers except the 45° of swirl, where these two effects nearly cancel each other. It was found that, 60° of swirl gives the maximum value of blow off velocity (Fig. 3.16) at $z = 7$ mm.

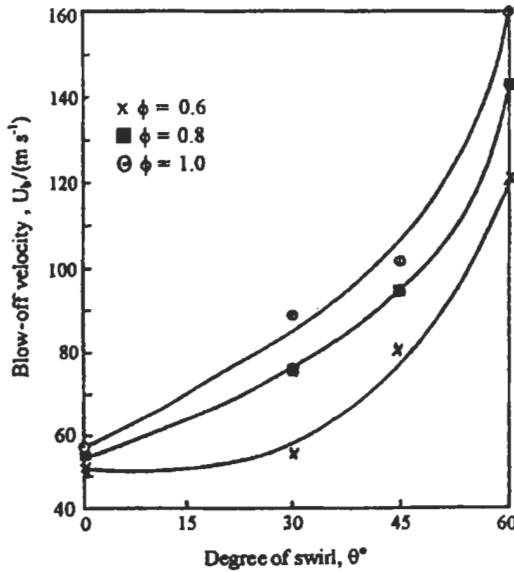


Fig. 3.16: Effect of the degree of swirl on the blow-off velocity at $z = 7$ mm [471].

3.6.4 Flame Stabilization by Non-Streamlined Bodies

The bluff body is a basic device to stabilize double concentric jet diffusion flames in industrial burners, for reasons of safety, providing excellent turbulent mixing characteristics, improvement in flame stability, and ease of combustion control. The flow and flame structure produced in bluff-body burners are complex and dominant by time-varying large-scale mixing structures.

If a badly streamlined body is inserted into the air stream, for example a circular plate, as shown in Fig. 3.17, then a zone having a reduced static pressure is created behind it. As a consequence of the reduced pressure, the air will flow into the zone from a space situated some distance behind the bluff body. The direction of this motion will be opposed to the direction of the main flow, thus a reversal zone is formed by the bluff body. The dimensions of the reversal zone in a given case will be determined by the dimensions of the badly streamlined body (the stabilizer).

Furthermore, modern high performance jet engines frequently incorporate after-burners to provide an increase in thrust for short periods, e.g. take-off and climb out, with a comparatively low increase in the weight and frontal area of the engine. In after-burners, more fuel is burned between the turbine exit and the jet propelling nozzle using unreacted oxygen in the turbine exhaust. Since the flow velocity in the after-burner combustion zone greatly exceeds the flame speed, the flame must be stabilized in a region of low velocity such as in the wake of bluff bodies [487-490].

The investigation of the flame structure in the vicinity of bluff bodies was the subject of some other works [491-493]. The flow pattern in the wake of bluff bodies with different geometries was studied in a model furnace involving no chemical reactions (Beér and Chigier [491]). Also, measurements of unsteady parameters in a model test rig (Smart et al [492]) were carried out to simulate after-burner instabilities. Axisymmetric centerbody stabilized diffusion flames have been studied by several investigators [493-495], which have highlighted the advantages of this arrangement over simple and coflowing jet flames in terms of improved mixing rates, reduced flame lengths and enhanced burner stability and efficiency.

Lightman et al [494] have used Laser Doppler Velocimetry to measure the mean locations of the recirculation zone stagnation points and establish the variations in their locations with changes in operating conditions. The instantaneous mixing and reactive scalar fields have been measured by Masri et al [495] in the recirculation zones of turbulent non-premixed flames stabilized on a bluff body, using the spontaneous Raman scattering technique. They measured means and r.m.s fluctuations of mixture fraction,

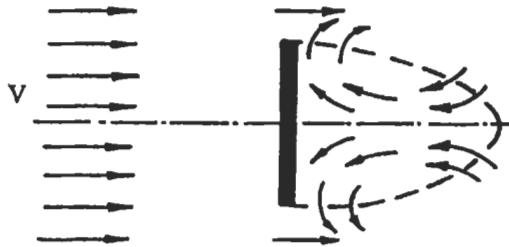


Fig. 3.17: Flow downstream of a non-streamlined body.

temperature, and the mass fractions of stable species for various axial locations in the recirculation zone of CH_4/CO and CH_4/H_2 flames. They identified two regions of almost homogenous mixture within the recirculation zone: a large outer region, which on average is fuel lean, and an inner region, which is smaller and closer to the central fuel jet. Combustion is more intense in the inner region, where mean mixture fraction is stoichiometric and the peak values for temperature and mass fractions of combustion products are reached.

Recently, a detailed regime diagram for bluff-body stabilized flames is proposed by Cheng et al [496] for the flame lift-off and stabilization limits. At low fuel velocities, the flame structure is classified into three stable modes: recirculation zone flame, jet-dominated flame and jet-like flame according to the velocity ratio of annular to central jets. They also showed that, at high fuel velocities the annular air flow has little effect on the lift-off heights, and premixed flame propagation becomes dominating. Furthermore, Bradley et al [497] have studied the premixed turbulent flame instability in a lean-burn swirl burner. Computed results are presented from a Reynolds stress, stretched laminar flamelet model, for premixed swirling combustion rotating matrix burner. They found a good agreement with flame photography and Coherent Anti-Stokes Raman Spectroscopy (CARS) temperature measurements. They also found that, at higher equivalence ratios, the flame is stabilized by hot gas in both the inner and outer recirculation zones. As the equivalence ratio is reduced below 0.6 another steady state solution appears, in which the flame is stabilized only by the hot gas in the inner zone.

The flame stabilization and flow field characteristics of premixed flame in an axisymmetric curved-wall jet utilizing the Coanda effect are investigated experimentally by Gil et al [498]. Their results show that the blow-off velocity is much higher and the flame height is reduced significantly as compared to a tube jet burner. The condition of maximum blow-off velocity occurs when the mixture is rich and the equivalence ratio increases as the nozzle exit area decreases. Along these lines of investigation, Bailly et al [499] have studied numerically and experimentally a turbulent reactive zone stabilized by a rectangular cross-section cylinder positioned in a fully developed turbulent channel flow of a propane-air mixture. The flow is experimentally investigated with a two-dimensional laser Doppler velocimeter and thin compensated thermocouples. The modeling of the reactive flow is based on a modified Bray-Moss-Libby combustion model associated with a Reynolds stress turbulence model. The resulting set of equations is solved by a finite difference Navier-Stokes code on a rectilinear mesh. The comparison between numerical and experimental results shows that the use of a full second-order model with dedicated equations for both the Reynolds stresses and the scalar turbulent flux does not lead to a significant improvement of the numerical results. Additional measurements and calculations are required to find the exact range of mass flow rate, equivalence ratio, and obstacle bluffness over which such a tendency can be observed.

The above measurements, as well as, the following studies provide an important diagnostics in support of developing and validating turbulent flow models. Of equal importance is the study of stability margin for such burner configuration under a wide range of operating conditions.

Effect of the Stabilizer Geometry

El-Mahallawy et al [490] have studied the effect of the stabilizer geometry and operating conditions on the flame structure. The structure of premixed and diffusion

flames downstream of flame stabilizers was studied in a cylindrical water-cooled model combustion chamber fired by commercial LPG. The firing conditions at the lowest noise level were also investigated. The shape of the central recirculation zone of each stabilizer under non-reacting and firing conditions was determined.

The concentrations of oxygen, carbon dioxide, and carbon monoxide, the mean gas temperature, and the noise level at several sections along the model combustion chamber and in the vicinity of flame stabilizers were measured. The test rig used in their experimental study was a cylindrical combustion chamber model of 0.075 m inner diameter and 1.1 m length. The chamber was water-cooled and was fitted with 21 equidistant measuring tappings as shown in Fig. 3.18. The shape and dimensions of the used stabilizers in this investigation are shown in Fig. 3.19. The noise level was determined using a microphone noise meter at a distance of 1 m facing the combustion chamber exit section. A 3-hole water-cooled probe was used to determine the boundary of the central recirculation zone. The local time-average temperature of the flame gases was measured using fine water-cooled suction pyrometer having thermocouple wires of platinum – versus - Platinum 10 % Rhodium. The local time-average gas concentrations of carbon dioxide, carbon monoxide and oxygen in the flame gases were measured using infrared and paramagnetic gas analyzers.

Their results [490] for the effects of the blockage ratio on mass recirculation, as well as, stabilization limits are shown in Figs. 3.20 and 3.21. Figure 3.20 shows the distribution of the recirculated mass as a percentage of the input mass flow for a thin disc stabilizer with different blockage ratios, while the influence of the stabilizer shape on the flame stability limits for both lean and rich mixtures is shown in Fig. 3.21. It is established that the stabilization limits expand on passing from 90° (solid cone), 90° (hollow cone) to thin disc flame holders. It is noted that thin disc and 90° (hollow cone) give similar results for a leaner mixture, and the stability limits (rich and lean limits) are wider for

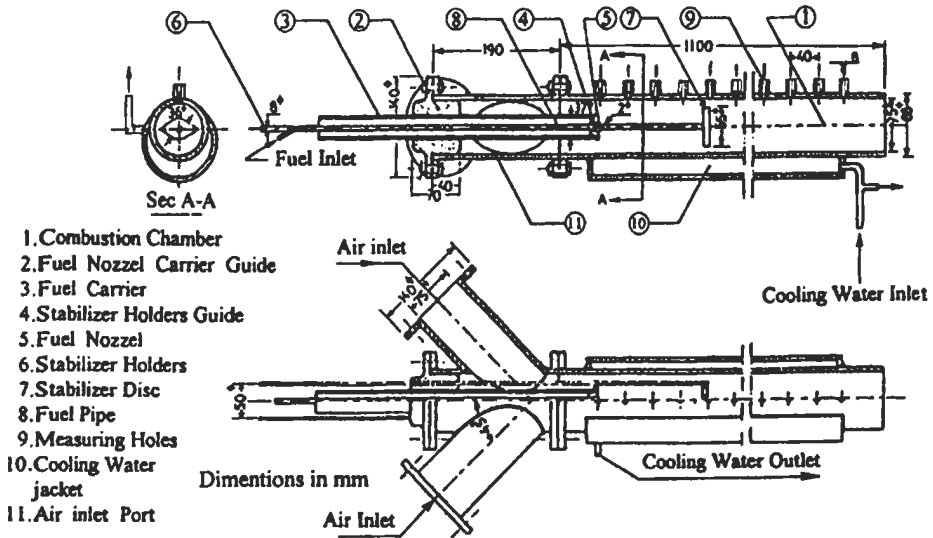


Fig. 3.18: Model combustion chamber [490].

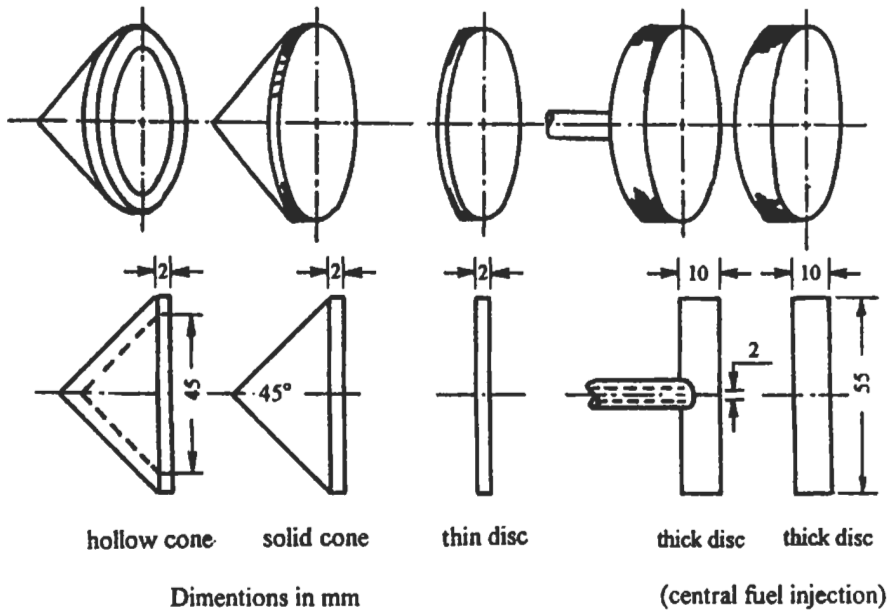


Fig. 3.19: Flame stabilizers [490].

lower values of the mixture velocity. Also, the figure shows that the maximum value of the mixture velocity at which stability occurs corresponds to a slightly rich mixture for all stabilizers.

Bakrozis et al [500] have investigated experimentally confined turbulent reaction wake flow past a 2D square cylinder with planer fuel-jet injection into the vortex formation region. They [500] measured the mean and turbulent velocities and temperatures with Laser Doppler Velocimetry and thin digitally compensated thermocouples throughout the wake region for two Reynolds numbers and for a range of fuel-to-air velocity ratios (FAVR). Their results show that 2D slender bluff-body stabilized diffusion flames differ from their axisymmetric counterpart in that they produce longer recirculation zones and flame lengths. Peak temperature and turbulence levels are located at the forward stagnation point, away from the burner face. In contrast to axisymmetric geometries, large-scale activity and periodic shedding were drastically suppressed at medium and low FAVR operation. These intensify as the flame length shortens and global extinction conditions are approached, in a fashion similar to premixed bluff-body stabilized flames. On the basis of vortex shedding, suppression is suggested for the reacting wake. Vortex strengths, the double vortex structure, and the linear flame length dependence on FAVR were found to be more similar for both geometries. The following presents a brief description of their experimental method and results [500].

The combustion rig is shown in Fig. 3.22. It consists of a 0.042 x 0.208 x 0.81 m rectangular cross-section duct in which a two-dimensional flow is attained, followed by a constant cross-section area axial distorting duct. The cross-section area of the duct is maintained constant while allowing for an exponential reduction of its height and increase of its span [501]. A settling chamber and a series of grids followed by a nozzle

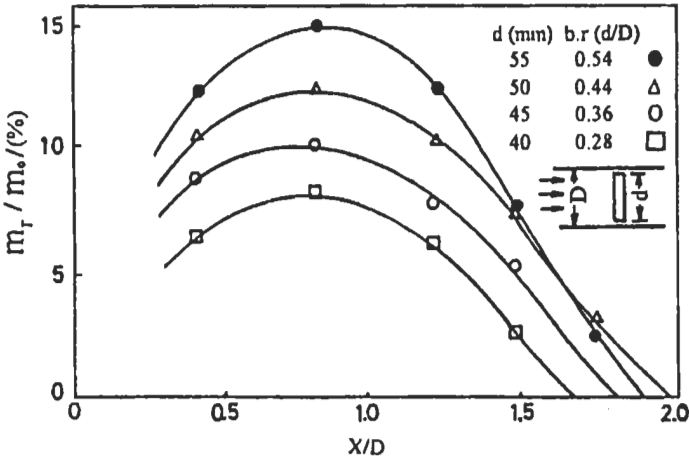


Fig. 3.20: Effect of blockage ratio of a thin disc on the reversed mass flow rate along the chamber axis, $A/F = 19.5$, $m_f = 2.8 \text{ kg h}^{-1}$ [490].

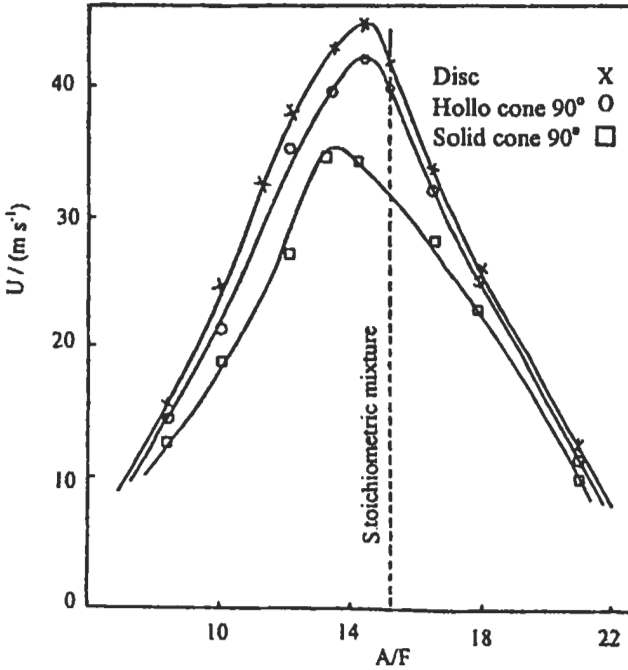


Fig. 3.21: The stabilization limits of the flame for different shapes of the bluff-body and for a blockage ratio 0.36 [490].

with a 6:1 contraction are installed upstream of the test section. A uniform mean flow distribution, over 87 % of the span, with less than 0.5 % turbulent intensity (U_{rms}/U_a) was produced at the test section entrance where U_a is the inlet axial air velocity.

The square cross-sectional area burner, with side of 8 mm, was inserted into the

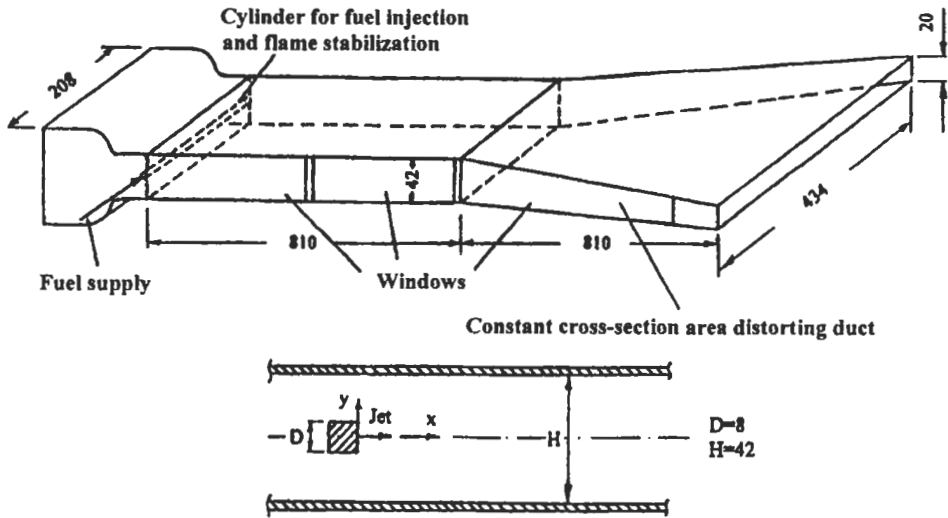


Fig. 3.22: Schematic diagram of the experimental facility and the test section. All dimensions in mm [500]. Reproduced by permission of Elsevier Science.

0.042 m height duct, producing a blockage of 19 %. Two Reynolds numbers of 8520 and 14285 based on approach air velocity and cylinder diameter were investigated [500]. Propane was fed through the hollow cylinder ends and then injected into the wake through 125 holes closely spaced along a width of 0.155 m and lying on horizontal symmetry plane. Spanwise uniformity of fuel injection was achieved by suitably tapering the hollow of the cylinder to adjust the injection pressure according to inviscid manifold theory and this was checked by LDV. Details of the rig and its operational characteristics may be found in Ref. 501.

Initially the burner was investigated under iso-thermal operation. Subsequently, a selected number of flames that was within the stability limits of the combustor and with fuel-air velocity ratio (FAVR) ranging from 0.189 to 0.631. Ultralean overall equivalence ratios ranged from 0.0159 to 0.093. Transverse profiles of mean axial and cross-stream velocities, turbulent intensities and related statistics were measured within the main flame-stabilizing region and in the developing hot wake with a single component LDV. Temperatures were measured with Pt-Pt/10 % Rh uncoated butt-welded thermocouples (S-type) of 76 μm diameter wire. Further details of the thermocouple signal procedure are in Ref. 502.

For the reacting wakes, a number of flames have been studied operating at overall fuel-air mass flow rates (FAR) in the range 10^{-3} to 6×10^{-3} and the overall equivalence ratio Φ_0 in the range of 0.0156 to 0.093. The overall development of the reacting flows is displayed as center-plane distributions of the mean streamwise velocity, the two turbulence intensities (normal V_{rms}/U_a and axial U_{rms}/U_a) and measured vector plots in Figs. 3.23 and 3.24, for three investigated FAVRs and two Reynolds numbers. A four-vortex system (two on each side of the symmetry plane) is established downstream of the burner head. The primary recirculation, driven by combustion products, opposes the fuel jet which, in part, recirculates close to the cylinder base. The remainder splits into two parts, one of which moves upstream along the square burner's sides, while the other

continuously supplies the flanks of the main recirculation where the flame zone is located (see Fig. 3.24 a).

The length of this composite recirculation zone is now 5 times longer than for the isothermal case (injected air-jet to "blocked" air velocity ratio, $IR = 0$, Fig. 3.24), in line with a fourfold decrease in the recirculating zone density. Over the investigated FAVR range, within the non-penetrating regime, there is only a moderate influence of FAVR in the mean and turbulence fields, localized in the fuel-jet injection, impingement and deflection region. Differences in the axial turbulence intensity in the near injection region are mainly due to variable impingement depth and strength as the FAVR changes (Fig. 3.24 b).

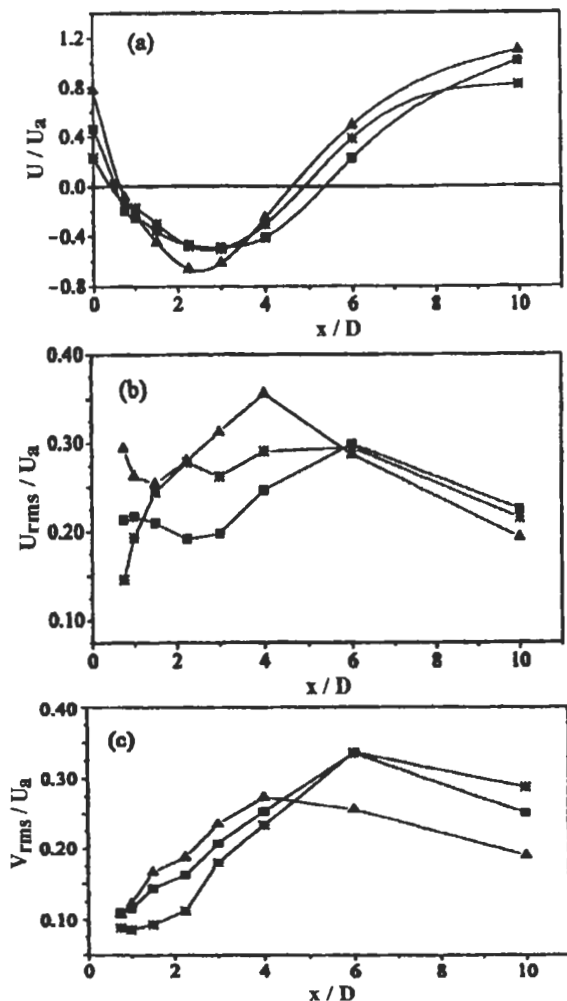


Fig. 3.23: Center-plane distributions of (a) streamwise mean velocity, (b) and (c) turbulent intensity for reacting flow: \blacksquare , $Re = 14285$, $FAVR = 0.375$, \blacktriangle , $Re = 8520$, $FAVR = 0.631$, $*$, $Re = 8520$, $FAVR = 0.189$ [500]. Reproduced by permission of Elsevier Science.

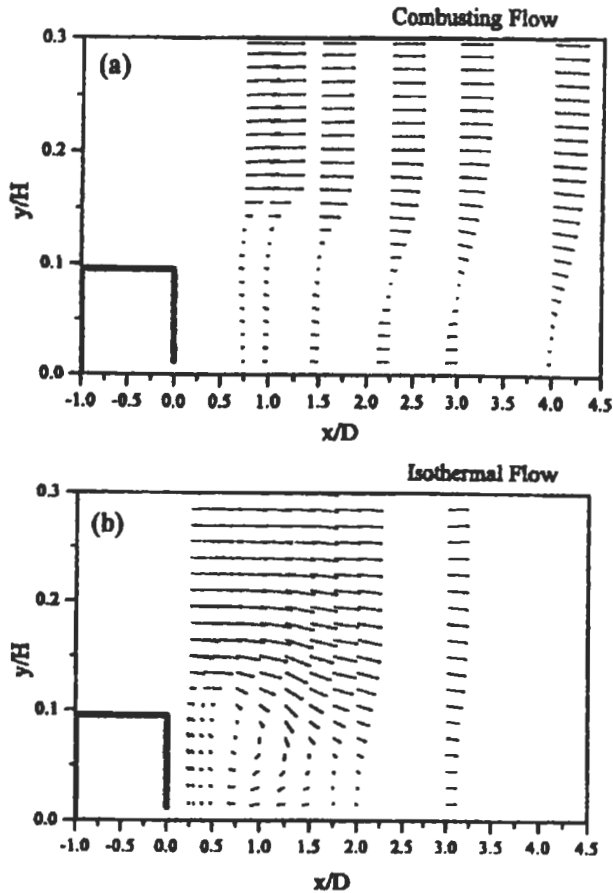


Fig. 3.24: Measured velocity vectors in (a) reacting flow, $Re = 8520$, $FAVR = 0.631$, (b) isothermal flow, $Re = 8520$, $IR = 0.53$ [500]. Reproduced by permission of Elsevier Science.

Mean isotherms in the reacting wakes are presented in Fig. 3.25 for values of $FAVR$ of 0.631 and 0.189 and Re of 8520. Low temperatures of about 400-500 °C are encountered near the nozzle exit and are consistent with a fuel-rich condition ($x/D = 0.5$, Fig. 3.25 a). Overall maximum values of about 1600-1700 °C are located slightly upstream of the forward stagnation point and occupy a significant width of the wake. Contours of about 1100 °C extend upstream of the trailing edge of the square, in support of the pattern of flame stabilization alongside the flanks. As the $FAVR$ decreases toward the overall lean blow-off limit, the isotherms at $FAVR = 0.189$ (see Fig 3.25 b) reveal that the flame length shortens in the vicinity of the primary recirculation region.

Using estimates of the turbulent Damköhler and Reynolds numbers to characterize the flame on a combustion diagram [503] indicates that both turbulent mixing and chemical time scales control the behavior of the low $FAVR$ flames in the regime of perturbed flamelets, overlapping the regime of homogeneous combustion. The entrainment characteristics of the burner are shown in Fig. 3.26. These were evaluated for plane, air-injected and reacting wakes. These are important as they control

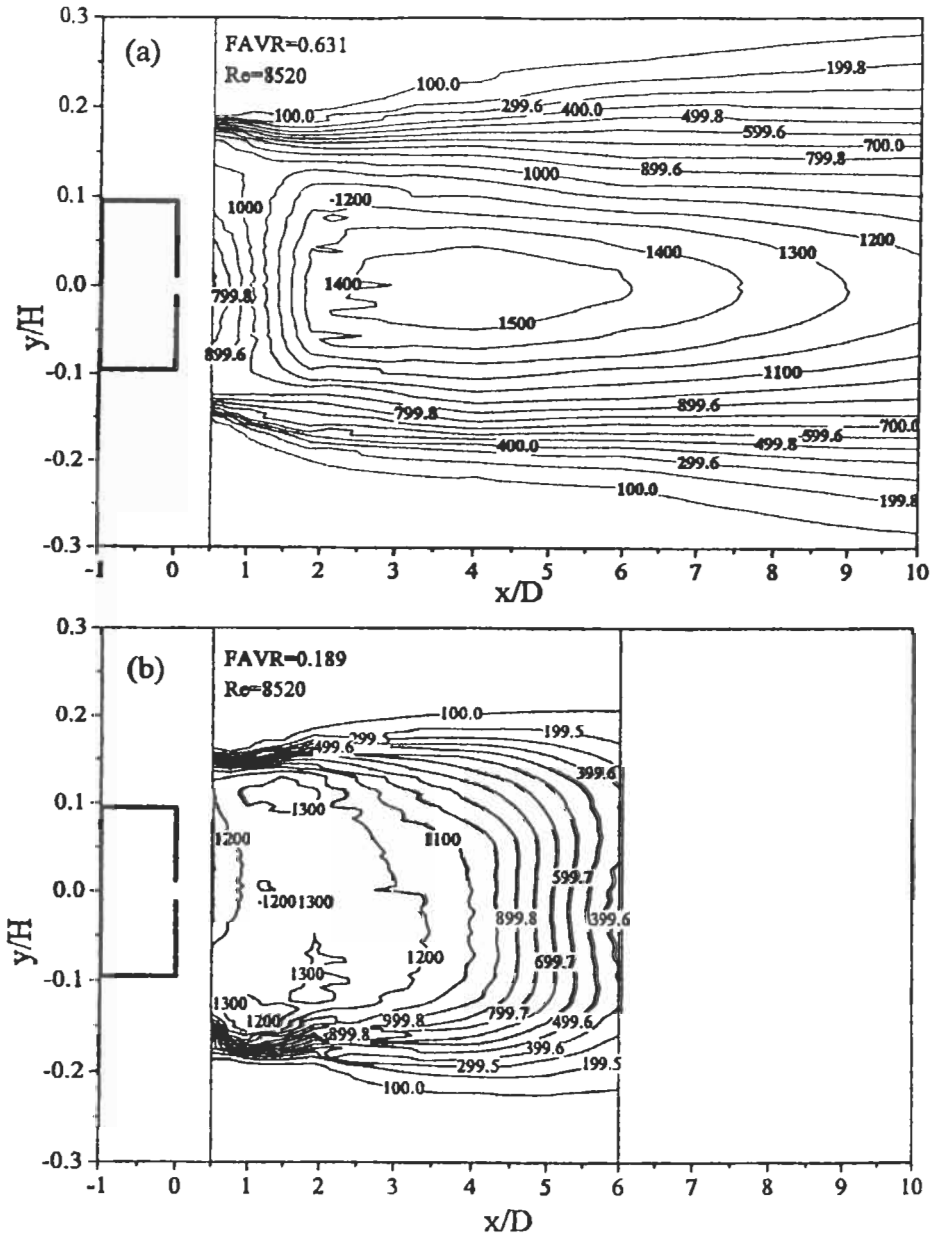


Fig. 3.25: Mean isotherms ($^{\circ}\text{C}$) for (a) FAVR = 0.631 and (b) FAVR = 0.189, Re = 8520 [500]. Reproduced by permission of Elsevier Science.

the forward stagnation point location and the flame length. The figure also shows the maximum value of the normalized reverse-flow, obtained by integration of the measured velocity profiles, within the vortex zone. Downstream of the reattachment, entrainment rates were calculated by integration of the axial velocity profiles, relating

densities through temperature distributions. With fuel or air injection the recirculating mass is seen to increase initially up to FAVR = 0.75, but thereafter entrainment into the composite vortex zone is disrupted and gradually reduced.

The flame stability of the burner is shown in Fig. 3.27 together with the “overall lean” and “stoichiometric” lines. The plot is similar to those reported by Feikema et al [504] for swirl burners, and Cheng et al [496] for axisymmetric centerbody burners.

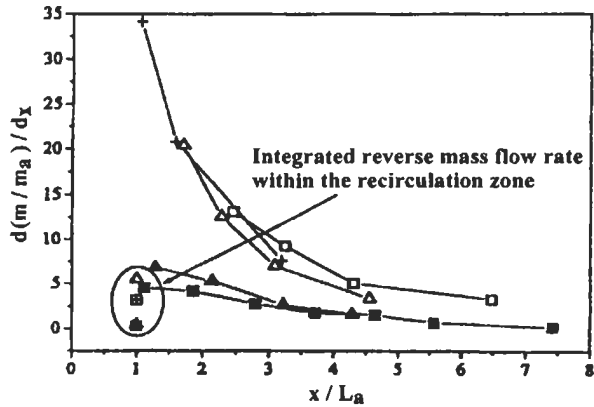


Fig. 3.26: Entrainment rates $[d(m/m_a)/dx]$, of isothermal and reacting flows. Reacting flow: \blacksquare , $Re = 14285$, $FAVR = 0.375$; \blacktriangle , $Re = 8520$, $FAVR = 0.631$; Isothermal flow: \square , $Re = 14285$, $IR = 0$; \triangle , $Re = 8520$, $IR = 0$; $+$ $Re = 8520$, $IR = 0.53$ [500]. Reproduced by permission of Elsevier Science.

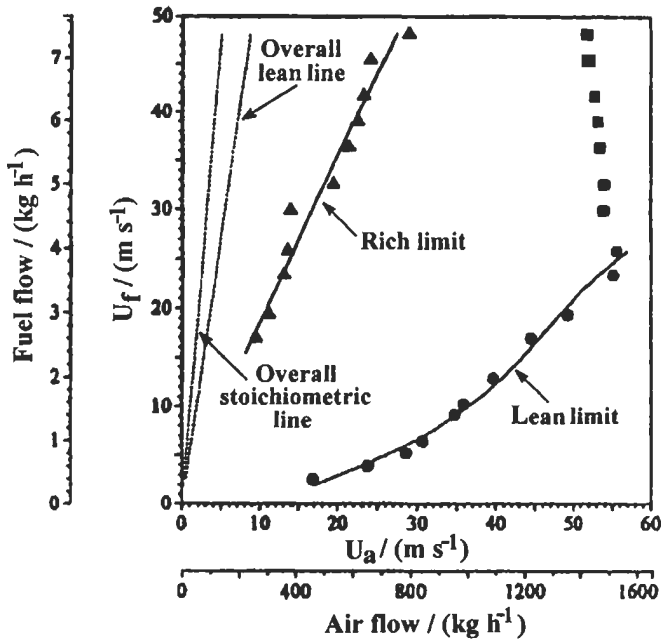


Fig. 3.27: Blow-out limits of burner [500]. Reproduced by permission of Elsevier Science.

One of the major considerations in burner design is the improvement of flame stabilization: the lift-off and blowout limits. Three distinct types of lifting mechanisms have been observed for burner-rim-attached flames in a double concentric burner [505]: I. direct lifting from burner exit, II. Local flame extinction lifting, and III. Lean-limit extinction lifting. Types II and III are found to dominate for a straight fuel tube with a thick wall. This type of burner configuration is analogous to the bluff-body burner with a large blockage ratio at the annulus exit. The flow field in the near burner zone is characterized by large-scale structures in a recirculation bubble. Following the work of Cheng et al [496] regrading the bluff body stabilized flames, they have shown that, at low fuel velocities, the flame structure is classified into three stable modes: recirculation zone flame, jet-dominated flame, and jet-like flame according to the velocity ratio of annular to central jets. Two different flame stability limits can be identified between cold and combusting recirculation zones. For the former case, local flame extinction dominates lifting of the jet-like flame due to a strong interaction between the recirculating airflows and the jet flame front. A critical annulus Reynolds number is found at which the jet-like flame is least probable to lift off, whereas, for the latter case, partial quenching of the blue neck flame in jet-dominated flame is retarded due to the presence of a reignition source, the combusting recirculation zone. Thus, flame stability can be improved. It is further shown that stabilization of lifted flame is more sensitive to the co-flow air than the fuel jet velocity at the inception of flame lift-off, indicating the importance of diffusion flamelet quenching. At high fuel velocities, the annular airflows have little effect on the lift-off heights and premixed flame propagation becomes dominating. When the flame approaching the maximum lift-off height, the flame base consists mainly of separated, broken flamelets, suggesting an inhomogeneous fuel/air premixing, due to interaction with large-scale vertical structures. The following presents brief description of Cheng et al [496] experimental method and results.

The configuration of the double concentric burner employed is shown schematically in Fig. 3.28. At the burner exit, a 5 mm thick circular disc around the central fuel tube was used as the bluff body. The disc diameter D_b is variable between 30, 35, 40, and 45 mm, while the inner diameter of the annular air tube D_a is kept constant at 55.1 mm. The corresponding air flow blockage ratios, defined as $(D_b/D_a)^2$, are 0.296, 0.403, 0.527, and 0.667, respectively. Three layers of stainless steel mesh upstream in the annulus inlet straightened the airflow. The central tube is 60 cm long and 3.5 mm in inner diameter ($l/D_f \sim 170$) to ensure a fully developed turbulent pipe flow at the burner exit. The fuel supply was connected directly to a commercial liquefied petroleum gas cylinder. Downstream flow velocities were measured with a two-component backward-scattering Laser Doppler Velocimetry, mounted on a precision-traversing table.

The mean and instantaneous structure at the base of lifted flames were registered with color slides (exposure time 1 to 4 s) and video tapes, respectively. The mean lift-off heights are determined from the time-averaged slide images. Instantaneous lift-off heights are examined by the individual video images. Comparison of the mean lift-off heights with those from the (Laser-Induced Fluorescence) LIF = OH images of Ref. 506 shows good agreements.

Figure 3.29 shows the different regimes for bluff-body stabilized nonpremixed flames with an annulus blockage ratio of 0.667. The regime diagrams for the other three bluff bodies are qualitatively the same. Three characteristics stable flame modes can be found in Fig. 3.29 by varying the average velocity ratio between the air and fuel

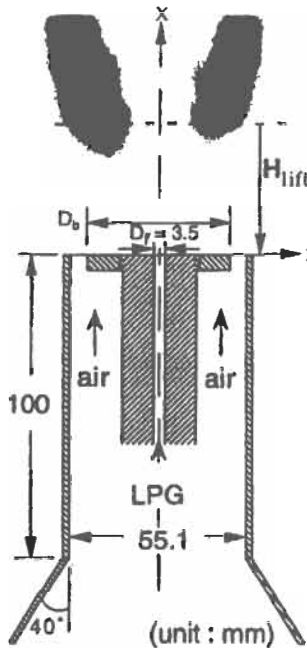


Fig. 3.28: Double concentric burner. Diameters D_b varied between 45, 40, 35 and 30 mm. Mean OH image of a lifted nonpremixed jet flame shows lift-off height, H_{lift} [496]. Reproduced by permission of Elsevier Science.

streams, γ , recirculation zone flames, central-jet dominated flames, and jet-like flames. Figure 3.30 shows the variation of the lift-off height with fuel velocity for pure jet flame and jet-like flame. The figure shows that H_{lift} , of a jet-like flame becomes greater than $D_b = 45$ mm (disc diameter) when the fuel velocity slightly exceeds the corresponding value of U_{lift} . In contrast, the pure jet flame created by shutting off the air stream shows an almost linear relationship between H_{lift}/D_b and U_f , as expected.

The argument of a strong interaction between the entrained air flow and the flame front also provides reasonable explanations for the existence of the optimal operating point. Since the flame base of the lifted flame immediately after the sudden jump can be correlated with the recirculation zone length, L_r , Cheng et al [496] defined a critical lift-off height, H_c , at the inception of flame lift-off. In Fig. 3.30, it is the lift-off height where the solid and open squares join. The dependency of H_c on the annular air exit velocity is plotted in Fig. 3.31 to examine how L_r varies with U_a . The linear increase of H_c with U_a at a constant bluff-body diameter $D_b = 45$ mm supports the view that the dimensionless recirculation zone length L_r/D_b of a jet-like flame increases with Re_a for $Re_a < Re_{a,c}$. At higher air velocities, however, H_c still increases with U_a , but is independent of U_f . This suggests that the stabilization of a lifted flame is more subject to the co-flow air rather than the fuel velocity. Both premixed flame propagation and diffusion flamelet quenching could be responsible for lifted flame stabilization at such elevated axial position [507]. The early shift of the lifting velocity for the pure jet flame ($U_a = 0$ m s⁻¹) from 13 m s⁻¹ to 7 m s⁻¹ can be attributed to the ultrasensitivity of flame lift-off behavior to the small-scale turbulence at the burner exit.

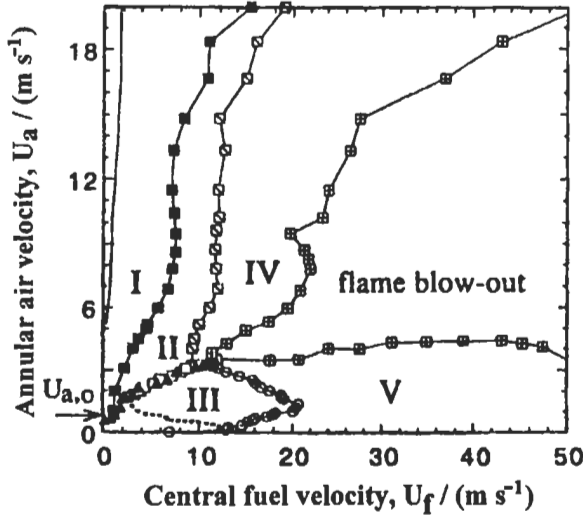


Fig. 3.29: Combustion diagram for bluff-body burner at annulus blockage ratio of 0.667. Regime I: recirculation zone flame. Regime II: central-jet dominated flame. Regime III: jet-like flame. Regime IV: partially quenched flame. Regime V: lifted flame. Dashed line and open squares represent reattachment and blow-out limits of lifted flames in hysteresis region. Off-set air velocity U_a indicated by arrow [496]. Reproduced by permission of Elsevier Science.

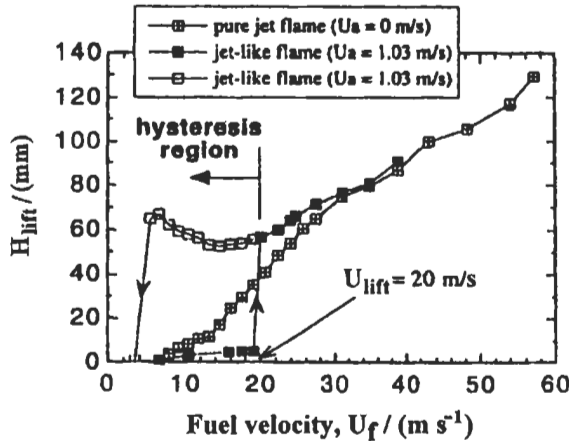


Fig. 3.30: Lift-off heights, H_{lift} . For pure jet flame ($U_a = 0 \text{ m s}^{-1}$) and jet-like flame ($U_a = 1.03 \text{ m s}^{-1}$) with $D_b = 45 \text{ mm}$. Open squares represent lift-off height in hysteresis region. Fuel lift-off velocity of this jet-like flame is 20 m s^{-1} [496]. Reproduced by permission of Elsevier Science.

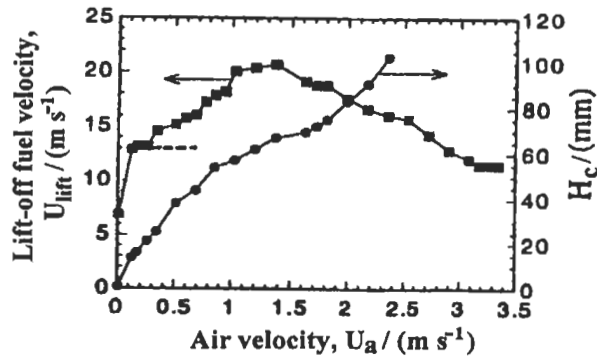


Fig. 3.31: Dependence of the critical lift-off height, H_c , on air velocity, U_a , with bluff-body diameter $D_b = 45$ mm. Corresponding fuel lift-off velocity U_{lift} is also plotted. Dashed line indicates lift-off velocity of pure jet flame at 13 m s^{-1} [496]. Reproduced by permission of Elsevier Science.

Stabilization of Free Diffusion Flames

El-Mahallawy et al [508] have investigated the stability characteristics of free diffusion flames produced by the injection of gaseous fuel into the center of a reverse flow zone induced by a bluff body placed in the air stream at a burner mouth. This burner configuration offers a simple method to stabilize a diffusion flame which in ordinary circumstances seems to be difficult, if not impossible, to stabilize without the use of swirler or any other flame stabilization techniques. The aerodynamic situation created by the bluff body leads to a long diffusion flame anchored to the burner by an intense primary flame at its root. Such flame stabilization technique is practically effective for gaseous and oil fuels and it is believed that this stabilization technique, when used for confined flames, the stability margin will range from very lean to very rich mixtures without the loss of flame stability. Flames, which are produced in a very wealthy oxygen environment, are relevant to several practical applications such as afterburners of aircraft engines or in industry where hot gases, at moderate temperatures and minimal percentages of exhaust polluted gases, are required.

The fuel residence time, heating rates and the availability of oxygen in the near-burner field should be maximized in order to achieve good flame stability under a wide range of burner operating conditions. This is usually achieved by creating a strong recirculation zone near the burner, which carries the hot combustion products back towards the burner exit to establish a temperature high enough to ignite the fuel. When immersing a non-streamlined bluff body into the air stream, the annular air will converge towards the centerline down-stream of the centerbody and forms a wake region. A toroidal recirculation zone is formed within the wake region by the interacting of the outer annular air with the central jet flow. The structure of this recirculation region has been found to vary significantly with the relative flow rates of fuel and air. Two counter-rotating vortices can be identified in the recirculation zone. One is located adjacent to the upstream portion of the fuel jet and is bounded on the upstream side by center body surface. This vortex rotates in a counterclockwise direction and is driven primarily by the central fuel jet. A second vortex, rotating in clockwise direction, is located adjacent to the shear layer established along the outer

annular airflow. This vortex is driven by the annular air in a direction counter to the vortex created by the fuel jet.

The burner used by El-Mahallawy et al [508] is horizontally oriented, Fig. 3.32; the air is fed through two pipes at 45° inclination to the burner axis. The bluff body is mounted flush to the burner mouth; LPG gas (90 % propane and 10 % butane) is injected co-axially through the center of the bluff body from a nozzle of 2 mm diameter. The Reynolds number of the annular air is allowed to change in the range of 5000 to 30,000 (correspond to air velocity of 2-11 m s⁻¹); a range adequately ensures turbulent flow and represents practical applications. Different bluff body shapes including hollow and solid cones as well as discs are used with different tip angles (30°, 60°, 90°). The blockage ratio, BR, (ranges between 28% and 87%) is defined as d^2/D^2 where d and D are the bluff body and burner diameter respectively. Plate 3.1 presents a series of successive direct photographs of the above described flames, and reveals how the flame progress when the fuel jet is initiated.

The flow field is portrayed in Fig. 3.33, Leuckel and Fricker [509] and Schmid et al [510]. At first, when the fuel enters in very small quantity, the recirculation zone formed behind the bluff body prevents the forward progress of the fuel jet and causes it to spread radially away from the flame axis within the main air stream generating an intense flame with rapid mixing. As the fuel rate is raised, the core of the fuel jet partially penetrates the recirculation zone but is quickly entrained completely by the reverse flow prevailing in the region. With further progressive increase of fuel, the central fuel jet becomes able to penetrate the recirculation zone, leaving relatively small annular region of reverse flow between the gas jet and the main combustion air. Part of the fuel is recirculated within this reverse flow zone together with hot combustion gases and then mixes with the combustion air to give the first reaction zone (primary flame) which stabilizes the flame at the burner. The rest of fuel is preheated in passage through this oxygen-deficient zone, and subsequently mixes and burns with the entrained air giving comparatively a long diffusion flame tail (secondary flame), connected to the intense primary combustion zone through a region of neck-like shape. This necking phenomena becomes more severe and narrow as fuel velocity (i.e. the fuel flow rate) is elevated with its subsequent augmented amount of entertainment until the secondary

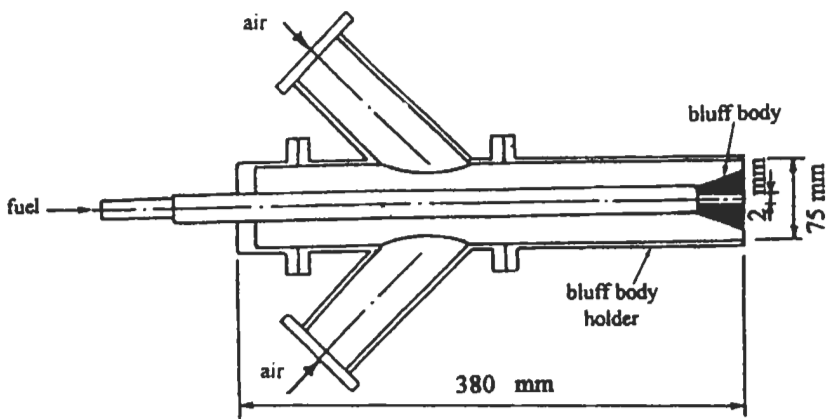


Fig. 3.32: The burner [508].

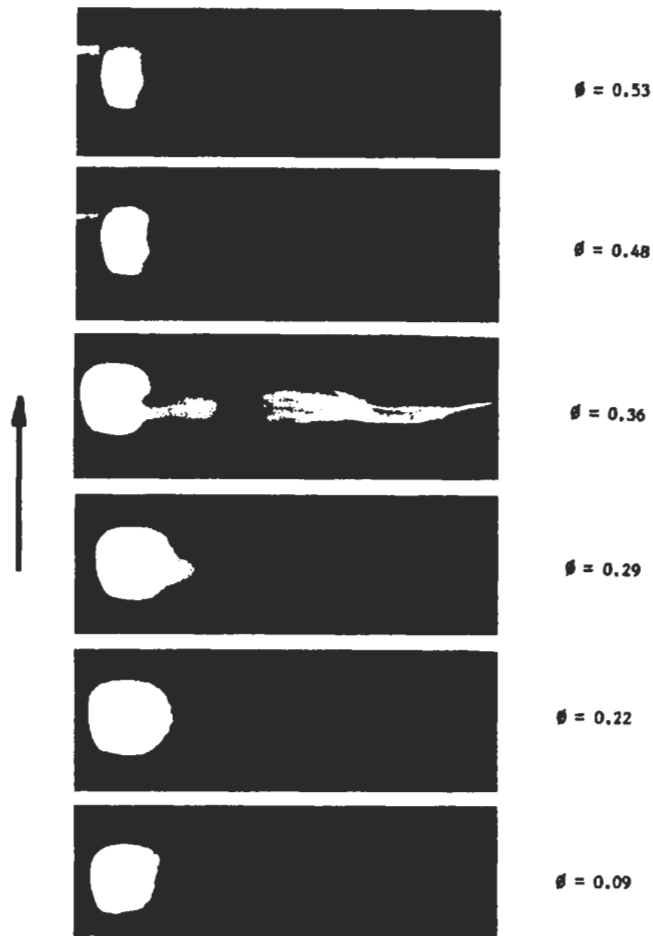


Plate 3.1: A series of photographs at successive equivalence ratios prior to blow-off (hollow cone, $\theta = 60^\circ$, BR = 87 %, $V_a = 8 \text{ m s}^{-1}$) [508].

flame exhibits exactly the same features of a lifted flame and loses its attachment to the ignition source (i.e. primary flame) at the burner. Soon afterwards, the secondary flame blows off while the primary flame stays lit at all times.

The input equivalence ratio, ϕ , is used to express the mixture strength as a function of the fuel and air mass flow rates upstream of the burner mouth as ratio of the stoichiometric one. Lean extinction limit, ϕ_e , is the equivalence ratio when the secondary flame disappears. The anticipated values of the lean blow off limits are expected to be rather dissident from that result in the case of a confined flame since not all the input air from the burner is directly involved into the flame zone reaction; a considerable amount of air is diverted by the presence of the bluff body away from the reaction region. This air, which escapes the primary reaction zone, even works as a shield or envelope to the primary flame zone and diminishes the entertainment influence of the surrounding atmospheric air.

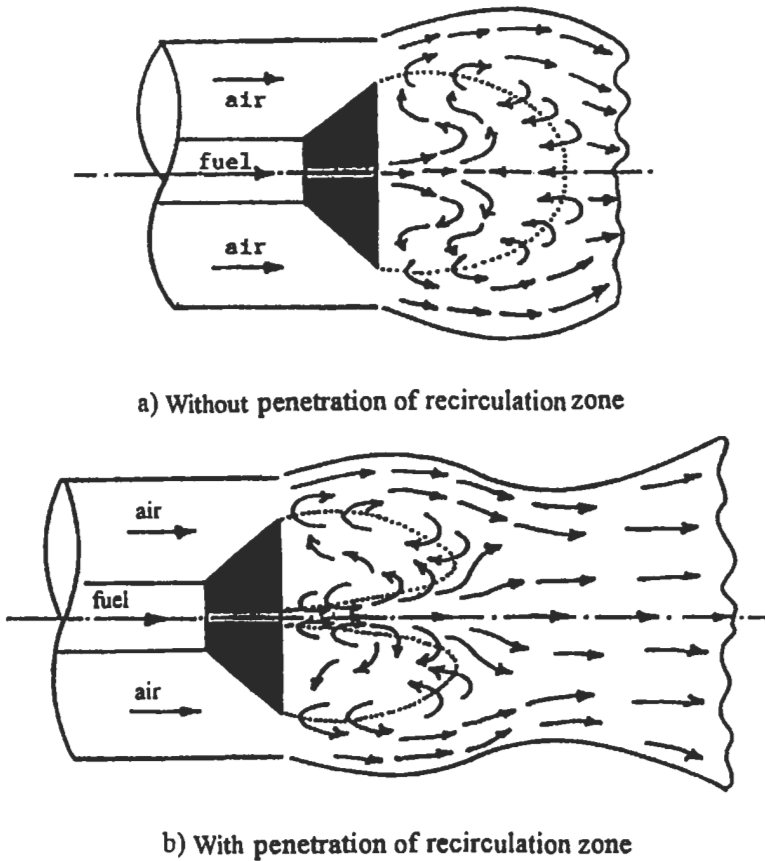


Fig. 3.33: The detail of the flow fields [508-510]. (a) without penetration of recirculation zone, and (b) with penetration of recirculation zone [508].

The stability curves are plotted in terms of the burner equivalence ratio at blow off (ϕ_c) as a function of the air approach velocity (V_a , m s^{-1}), Fig. 3.34 for discs, Fig. 3.35 and 3.36 for solid and hollow cone respectively. The stability range is the area bounded between the blow off characteristic curves and vertical velocity axis. The blow off limit, equivalence ratio at which the flame extinct, is determined by increasing the fuel flow rate keeping the air approach, and hence the air mass flow rate, constant until the secondary flame blows off. The data shows that a stable primary flame exists when the fuel flow rate, corresponds to equivalence ratio as low as 0.02 of the air flow. This value can be safely assumed constant irrespective of the geometrical characteristics of the bluff body. The stability ranges, as shown in Figs. 3.34 to 3.36, for different cone angles increase as the blockage ratio is increased. As the area blockage is extended, the annular area between the bluff body and burner tube is reduced which causes the air velocity at the burner exit plane to increase. This increases the reverse airflow, which in turn augments the mixing with the incoming fuel in the early part of the flame and consequently enhances flame stability. Figures 3.37 and 3.38, which delineate the blow off limit as a function of the cone angle for both solid and hollow cones, reflect a

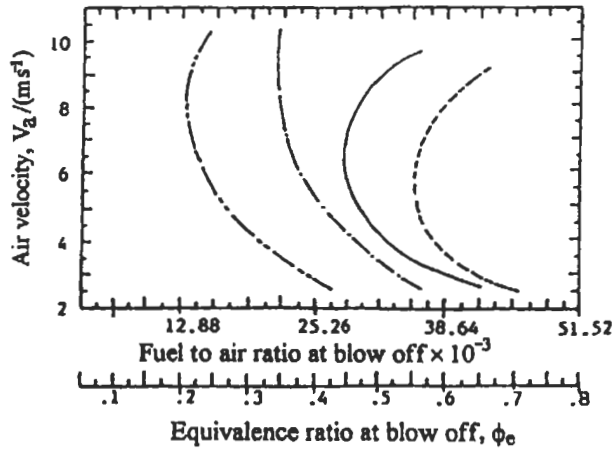


Fig. 3.34: Blow-off limits at various area blockage in the case of discs [508].
 (— · — · — BR = 28 %, — — — BR = 44 %, — BR = 64 %, - - - BR = 87 %)

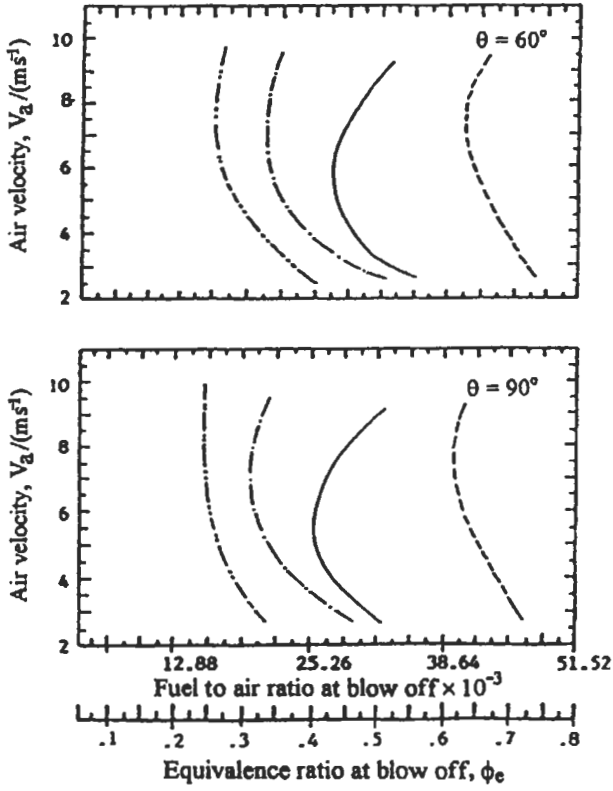


Fig. 3.35: Blow-off limits at various area blockage in the case of solid cones [508].
 (— · — · — BR = 28 %, — — — BR = 44 %, — BR = 64 %, - - - BR = 87 %)

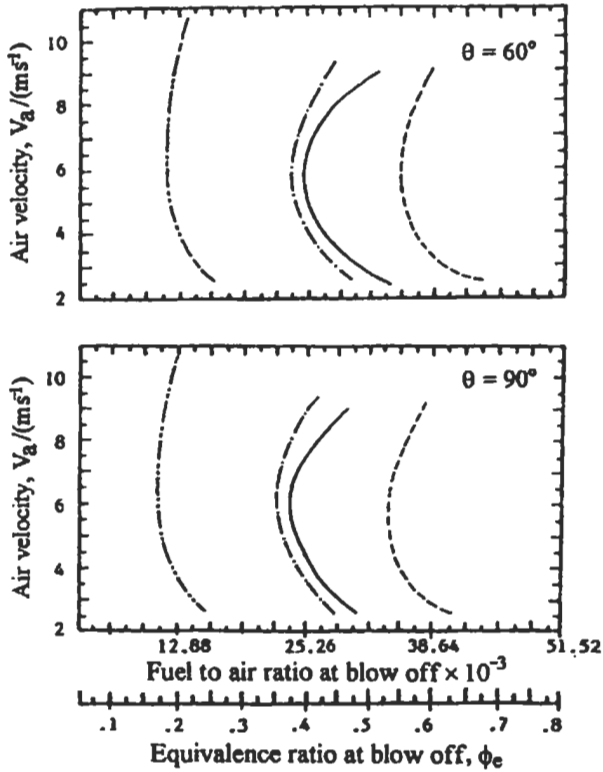


Fig. 3.36: Blow-off limits at various area blockage in the case of hollow cones [508].
 (--- BR = 28 %, -.- BR = 44 %, — BR = 64 %, --- BR = 87 %).

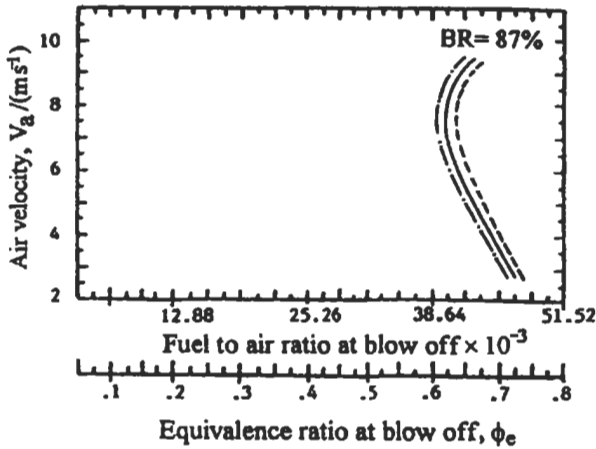


Fig. 3.37: Blow-off limits at various cone angles in the case of solid cones [508].
 (-.- $\theta = 30^\circ$, — $\theta = 60^\circ$, --- $\theta = 90^\circ$).

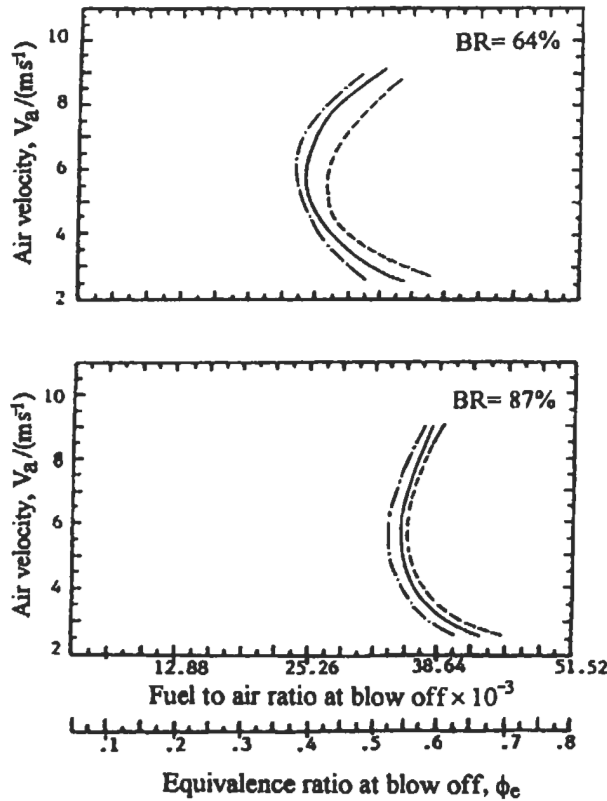


Fig. 3.38: Blow-off limits at various cone angles in the case of hollow cones [508]. (--- $\theta = 30^\circ$, — $\theta = 60^\circ$, -.- $\theta = 90^\circ$).

diminished effect of the cone angle on the extinction values. This result leaves the area blockage to be the solely dominant geometrical factor affecting the stability performance.

In all the experiments involving the hollow cones, the fuel nozzle was normally located at the base of the bluff body (position I). In order to investigate the effect of fuel relative position on the lean blow off limit, two more positions of the fuel nozzle are arbitrarily selected, namely: - position II where the fuel nozzle is pushed 10 mm inwards from the front surface of the bluff body and position III in which the fuel nozzle is pushed forward by 15 mm from the cone base deep into the recirculation zone (Fig. 3.39). For these three fuels positions, the blow off limits for two hollow cones (cone angles 60° , 90° and area blockage 64% and 87%) are given in Fig. 3.40. The blow off limits are significantly augmented by pushing the fuel nozzle inside the hollow cone (position II). On the other hand, those limits seem to be unaffected by the area blockage when the nozzle is located outwards into recirculation zone (position III). Nevertheless, the area blockage effect is pronounced when the nozzle is located inside the hollow cone (position II). The reason behind these observations could be related to the alteration of the fuel residence time, its heating rate and the mixing rate between the fuel jet and air reverse flow.

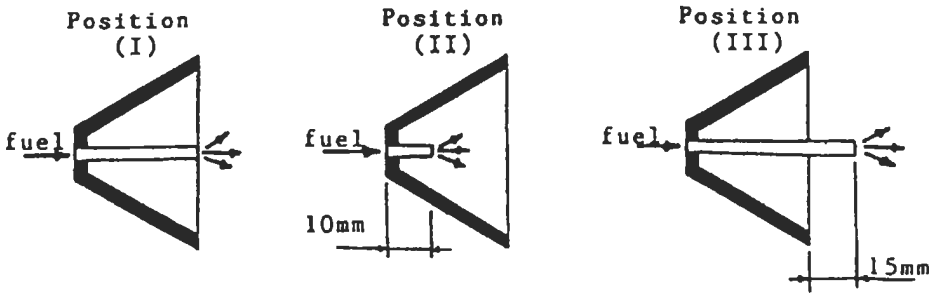


Fig. 3.39: The different positions of the fuel nozzle for the case of hollow cones [508].

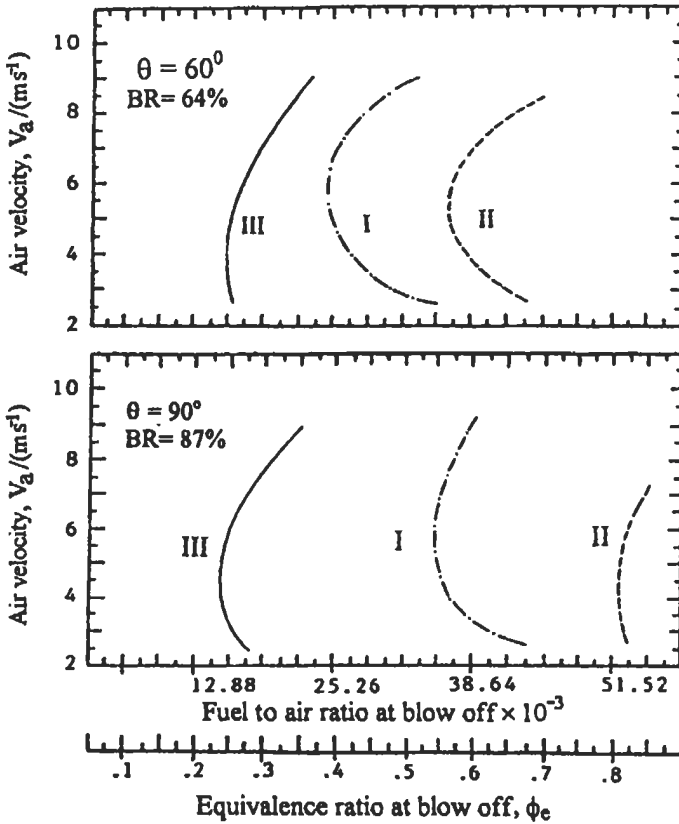


Fig. 3.40: Effect of the fuel nozzle position on blow-off limits (see Fig. 3.39) [508].

3.7 Turbulent Premixed Flames

3.7.1 Introduction

The discovery of the premixed flames was essentially completed in 1855 by Bunsen's invention of a burner, which allowed the stabilization of a premixed flame in a flow system. The most common type of turbulent premixed flame that has been studied in the laboratory is the rim-stabilized burner flame for which the approach-flow is turbulent. Usually, this is accomplished by either placing a turbulence-generating grid upstream of the rim or by generating fully developed turbulent pipe flow at Reynolds numbers above 2300. When the intensity of the approach-flow turbulence is low, the flame becomes a wrinkled laminar flame, but when the intensity is high, small individual flamelets are formed in the neighborhood of the tip. Since each flame element has a longer lifetime on a larger burner, there is more time available for the flame to become wrinkled and, therefore, to exhibit a higher effective turbulent burning velocity.

The probability density function (PDF) of the temperature fluctuations in a premixed turbulent burner flame verifies that the flame is simply a wrinkled laminar flame. The characteristics of the laminar premixed flame have been discussed in chapter 2. In this section, the laminar flamelet model will be briefly described as well as the experimental and computational analysis of flame structure and heat release rate for premixed turbulent flames. Furthermore, the turbulent burning velocity will be discussed with its determination for closed systems and flat premixed turbulent flames as well as its relation to the gasoline engine.

3.7.2 Laminar Flamelet Model (LFM)

In premixed flames, chemical processes are strongly dependent upon temperature. The mean volumetric heat release rate in turbulent combustion on the basis of the flamelet approach will depend upon the variation of heat release rate with both temperature and strain rate, S_r , for the corresponding laminar flame. The variation of normalized volumetric heat release $q_1(\theta)$ through a premixed, atmospheric, laminar, and strain-free methane-air flame of equivalence ratio, ϕ , of 0.64 is shown by full line curve as a function of θ in Fig. 3.41. The gas temperature, T , is expressed by the dimensionless reaction progress variable $\theta = (T - T_u)/(T_b - T_u)$, where, T_u is that of the cold reactants and T_b is the adiabatic gas temperature. If $q_1(S_r, \theta)$ is the laminar heat release rate as a function of S_r and θ and $P(S_r, \theta)$ is the joint probability density function (PDF) of S_r and θ , then the mean turbulent volumetric heat release rate is given by [511, 512]:

$$\bar{q}_t = \int_{-\infty}^{+\infty} \int_0^1 q_1(S_r, \theta) P(S_r, \theta) d\theta dS_r \quad (3.40)$$

For non-strain turbulent flame, the normalized turbulent mean heat-release rate and covariance are given by:

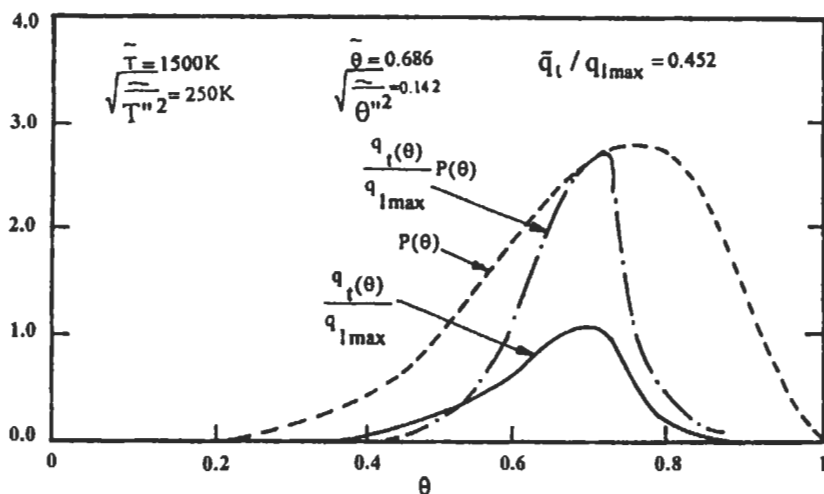


Fig. 3.41: Heat release rate through laminar flame and PDF, $P(\theta)$. Bradley [512], reproduced by permission.

$$\frac{\bar{q}_l}{q_{lmax}} = \int_0^1 \frac{q_l(\theta)}{q_{lmax}} P(\theta) d\theta \quad (3.41)$$

$$\frac{\overline{T'' q''}}{(T_b - T_u) q_{lmax}} = \int_0^1 (\theta - \bar{\theta}) \frac{q_l(\theta)}{q_{lmax}} P(\theta) d\theta \quad (3.42)$$

where, $\overline{T'' q''}$ is the thermo-chemical correlation and q_{lmax} is the maximum heat release rate.

At present, the $P(S_r, \theta)$ function is unknown. Perhaps, not unreasonably at this stage, it can be taken as the product of the separated PDFs, $P(S_r)$ and $P(\theta)$. For the symmetric, counter flow laminar flame, $q_l(S_r, \theta)$ is invariant with S_r , and is expressed by $q_l(\theta)$, when $S_r \leq S_q$. When $S_r > S_q$ then $q_l(S_r, \theta)$ falls to zero. To a first approximation, q_l is unaffected by strain until a limit strain rate, S_q , is attained, above which no heat release occurs. For these conditions:

$$\bar{q}_l = \int_{-\infty}^{S_q} P(S_r) dS_r \int_0^1 q_l(\theta) P(\theta) d\theta \quad (3.43)$$

Distribution of temperature. Both $P(\theta)$ and $P(S_r)$ are currently unknown and have to be assumed. In the Bray et al [513] flame model, $P(\theta)$ is dominated by values at $\theta = 0$ and $\theta = 1$: at any point in the turbulent flame, the gases are either completely unburnt or burnt [513]. This is most valid with relatively fast reaction and when the value of K' is low. The two delta functions at $\theta = 0$ and $\theta = 1$ are related to the first moment of $\bar{\theta}$.

Such functions in Eq. 3.43 would give $\tilde{q}_t = 0$ and, as an alternative, the reaction rate at a point is expressed in terms of a flamelet crossing frequency. This frequency depends upon the time auto-correlation of $P(\theta)$ and a related integral time scale that can be generated experimentally (Bray et al [514, 515]).

An alternative is to make an “a priori” assumption about the form of $P(\theta)$. The beta function has been widely used for this and other distributions in combustion. It is based upon the first and second moments of, in this case, θ . It has the form [511]:

$$P(\theta) = \frac{\theta^{\alpha-1}(1-\theta)^{\beta-1}}{\int_b^d \theta^{\alpha-1}(1-\theta)^{\beta-1} d\theta} \tag{3.44}$$

In which:

$$\alpha = \tilde{\theta} \left[\frac{\tilde{\theta}(1-\tilde{\theta})}{\tilde{\theta}'^2} - 1 \right] \tag{3.45}$$

$$\beta = \frac{(1-\tilde{\theta})\alpha}{\tilde{\theta}} \tag{3.46}$$

The integral in Eq. 2.44 can be expressed by a gamma function as:

$$\frac{\Gamma(\alpha)\Gamma(\beta)}{\Gamma(\alpha + \beta)}$$

where $\tilde{\theta}$ is the first moment and $\tilde{\theta}'^2$ is the second moment about the mean.

The more precisely to represent the fluctuations in temperature, a higher order function is desirable, but the closure limitations on the modeled energy equation are such that only first and second moments are modeled satisfactorily; nor is the matter resolved by experiments, due to the dearth of reliable experimental temperature PDFS. The thermal inertia of thermocouples renders them unreliable, even when compensated, (Heitor et al [516] and Bradley et al [517]); whilst even laser techniques have difficulty in attaining the requisite spatial resolution. Although it is a flexible function, the beta function is unable to capture strong bimodality at $\theta = 0$ and 1.

Values of $\tilde{\theta}$ and $\tilde{\theta}'^2$ are obtained from equations for the first and second moments of temperature, derived from the energy equation. These are given in Favre, or mass averaged, forms as (Bradley et al [248])

$$\frac{\partial}{\partial x_m} (\rho \tilde{u}_m \tilde{T}) = \frac{\partial}{\partial x_m} \left(\frac{\mu_{eff} \partial \tilde{T}}{\sigma_T \partial x_m} \right) + \frac{\tilde{q}}{C_p} \tag{3.47}$$

$$\frac{\partial}{\partial x_m} (\rho \tilde{u}_m \tilde{T}'^2) = \frac{\partial}{\partial x_m} \left(\frac{\mu_{eff} \partial \tilde{T}'^2}{\sigma_{T^2} \partial x_m} \right) + \frac{2\mu_t}{\sigma_T} \left(\frac{\partial \tilde{T}}{\partial x_m} \right)^2 - C_T \rho \frac{\tilde{\epsilon}}{k} \tilde{T}'^2 + \frac{2\tilde{T}'' q''}{C_p} \tag{3.48}$$

where $\mu_{\text{eff}} = \mu_t + \mu_1$

These equations embody the $k - \epsilon$ model of turbulent closure, with μ_t as the turbulent viscosity and μ_1 as the dynamic viscosity. The specific heat at constant pressure is C_p and C_T is a modeling constant, while q_1 is the volumetric heat release rate which is an algebraic expression in terms of two variables and it is suggested in chapter 2 to calculate its normalized profile against fractional temperature. Gas properties such as ρ , μ_1 , and C_p are functions of T , and can be taken from laminar kinetic model in chapter 2 which also gives the heat release profiles as a function of T , and hence of θ .

Flow field computations, in which \tilde{u}_m is a mean velocity would also use the $k - \epsilon$ model. The modeling assumptions in Eqs. 3.47 and 3.48 are well known [441, 450, 518] despite the equations are not always in this form, particularly with regard to heat release rate terms. Briefly, any turbulent fluxes are assumed to follow a gradient transport, i-e.

Eq. 3.26 and the time scale of the dissipation rate of \tilde{T}''^2 is taken to be proportional to $\tilde{k} / \tilde{\epsilon}$. In this section, attention is restricted to the modeling of the mean reaction rate

\tilde{q}_1 , and the covariance $\overline{\tilde{T}''q''}$.

Shown by the dashed curve in Fig. 3.41 is $P(\theta)$ the beta function for the given conditions at a point in the turbulent flame brush. The product of this and the $q_1(\theta)$ curve yields the chain dotted which, when integrated, gives the second integral in Eq. 3.43.

The covariance $\overline{\tilde{T}''q''}$, the mean product of two fluctuating quantities is given by:

$$\overline{\tilde{T}''q''} = (T_b - T_u) \int_{-\infty}^{\infty} P(S_r) dS_r \int_b^1 (\theta - \tilde{\theta}) q_1(\theta) P(\theta) d\theta \tag{3.49}$$

Distribution of strain rate. Neither the mean Lagrangian strain rate acting on the material surface elements moving into a laminar flamelet nor the distribution of such rates is known with precision in turbulent combustion. It is to be anticipated that it is related to the mean Eulerian strain rate, u'/λ . Girimaji and Pope [519] have shown how such Lagrangian PDFS, can be computed in the absence of reaction. These might be applicable for high values of K' , and they found that positive strain rates to be significantly more probable than negative ones. Abdel-Gayed et al [439] have obtained Lagrangian PDFS on the assumption that material line elements of the flame surface tend towards the axis of maximum positive principal strain and have attempted to check this assumption with high speed Schlieren photographs of partially quenching explosion flames.

One possible Lagrangian distribution is the quasi-gaussian, with $0 \leq S_r \leq \infty$:

$$P(S_r) = \frac{2}{(2\pi)^{0.5} \sigma} \exp\left[\frac{-S_r^2}{2\sigma^2}\right] \tag{3.50}$$

where $\sigma = \left[\frac{\epsilon}{12\nu}\right]^{0.5}$ and $\overline{S_r} = \left[\frac{\epsilon}{6\pi\nu}\right]^{0.5} = 0.89 \frac{u'}{\lambda}$ (3.51)

The mean strain rate \bar{S}_r , is not so different from the mean Eulerian aerodynamic strain rate, u'/λ . With such a distribution, the first integral in Eq. 3.43 is given by:

$$\int_{-\infty}^{S_q} P(S_r) dS_r = \text{erf} \left[\frac{S_q}{2^{0.5} \sigma} \right] = \text{erf} \left[\frac{S_q}{\bar{S}_r \pi^{0.5}} \right] \quad (3.52)$$

$$\text{as } \sigma = \left(\frac{\pi}{2} \right)^{0.5} \bar{S}_r$$

This integral represents the proportion of the material surface elements that can support a flame, and erf is the error function. Bradley and Lau [511] and Bradley [512] have tentatively suggested an interim expression of $\bar{S}_r = 0.07 \left(\frac{\epsilon}{\nu} \right)^{0.5}$.

Even without combustion, there is a need to measure the Lagrangian distribution of strain rates, initially for isotropic turbulence. This is a particularly challenging area of velocimetry. With combustion, the problems are even greater. Again the distribution law is uncertain, as are the appropriate values to be assigned to S_q and \bar{S}_r and the effect of curvature. It is not known whether the symmetric or asymmetric strain rate, which was discussed in chapter 2 is more appropriate. Perhaps the heat release-strain rate relationship for a turbulent flame is somewhere between those for these two conditions. This, however, would lead to an expression that is more complex than Eq. 3.43. With regard to the mean strain rate actually acting on the flame, there is some evidence that it might be about a quarter of \bar{S}_r (Bradley and Lau [511]).

3.7.3 Structure and Heat Release Rate

A turbulence model is required to reveal the turbulent flow field in which the reaction zone resides. In Eqs. 3.47 and 3.48, for the purposes of illustration, the well-known $k - \epsilon$ formulation was adopted. This first order scheme rests upon the Boussinesq isotropic eddy viscosity, gradient transport, and concept to determine second moment correlation such as Reynolds stresses and turbulent scalar fluxes from first moment quantities. For example, the first term on the right of Eq. 3.47 expresses the energy flux in terms of μ_{eff} and the gradient of the first moment of temperature. More accurate second order schemes eschew isotropy and use second moment transport equation to determine the second moment correlation.

Great care must be taken with the associated numerical methods. Unless a higher order numerical discretization is employed for the convective terms in the conservation equations to reduce numerical diffusion, the full advantages of higher order Reynolds stress closure will not be realized (Bradley et al. [430], Correa and Shyy [520]). However, higher order numerical schemes are often associated with unboundedness characteristics with over and under shoot solution oscillations and a boundedness-preserving scheme becomes necessary [521].

Reynolds stress modeling, which still retains the ϵ equation, is particularly important for recirculating and swirling flows. Without it, some recirculation may be undetected

(Bradley et al [430]) and predicted swirling velocities are over-attenuated with axial distance [522]. Flame blow-off characteristics can be particularly sensitive to the detailed structure of recirculation zones and hence careful modeling is required. More differential equations are required for Reynolds stress modeling and particularly for reacting flow; converged solutions require time and patience.

Jet-Stirred Conical Reactor

Bradley et al [248] have applied a laminar flamelet model to turbulent, recirculating CH_4 , C_3H_8 -air premixed combustion in a jet-stirred conical reactor. The complete statistical description of the thermochemistry is obtained from a one point probability density function (PDF) and detailed chemical kinetics of laminar flame structure. The normalized heat release rate $\tilde{q}_t / q_{l\max}$ in Eq. 3.41, at a given point in the flow field, depends upon the profile of $q_l / q_{l\max}$ against θ , the assumed form of $P(\theta)$, and the moments of θ necessarily associated with it. Their results from Eq. 3.41 are illustrated in Fig. 3.42 (a) where contours of $\tilde{q}_t / q_{l\max}$ are shown when $P(\theta)$ is a beta function operating on the q_l profile of a CH_4 -air flame of equivalence ratio, ϕ of 0.8 at atmospheric temperature and pressure. The value of $q_{l\max}$ is about 4 GW m^{-3} (see chapter 2). The first moment of θ is $\tilde{\theta}$ and the second moment is $\tilde{\theta}^2$, the square root of which is indicated by \bar{g} . Similarly, Fig. 3.42 (b) shows the associated contours of

$\frac{\overline{(\tilde{T}''q'')}}{(T_b - T_u)q_{l\max}}$ in Eq. 3.42. Such evaluation for a particular mixture was necessary precursors to the operation of the full computed program, for which they provided necessary inputs. When infinitely fast chemistry is assumed at a given point, the gas composition fluctuates between wholly burnt and wholly unburnt, and both terms on the left side of Eqs. 3.41 and 3.42 are zero, and is indicated by the semicircular envelope in both figures.

At the large values of \bar{g} , Fig. 3.42 (a) shows values of $\tilde{q}_t / q_{l\max}$ to be low and almost invariant over an appreciable range of \bar{g} . When g is zero, the heat release rate as a function of the reaction progress variable is that of a laminar flame.

The $\frac{\overline{\tilde{T}''q''}}{(T_b - T_u)q_{l\max}}$ contours in Fig. 3.42 (b) show the covariance to be largely

positive when $\tilde{\theta}$ is less than 0.7.

The Favre mean species concentration, \tilde{m} , with neglecting the strain effect, can be found from a similar relationship to Eq. 3.41:

$$\tilde{m} = \int_0^1 m_1(\theta)P(\theta)d\theta \quad (3.53)$$

where $m_1(\theta)$ is the concentration of the particular species in the laminar flame. The laminar profiles of concentrations for each species and heat release rate are included in the input data supplied by Dixon-Lewis [143] (for CH_4 fuel) and Westbrook and Pitz [523] (for C_3H_8 fuel).

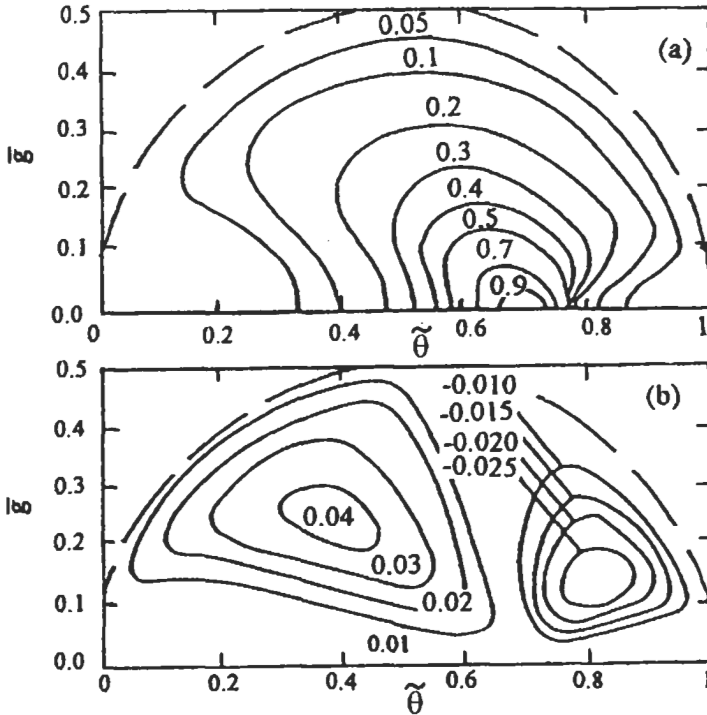


Fig. 3.42: CH₄-air mixture, $\phi = 0.84$: (a) normalized volumetric turbulent heat release rate, Eq. 3.41; (b) normalized heat rate correlation term, Eq. 3.42 [248]. Reproduced by permission of Elsevier Science.

In addition to the laminar flame data, the complete solution of their two-dimensional steady state turbulent combustion model involves seven coupled partial differential equations in terms of the two velocity components, pressure, \bar{k} , $\bar{\epsilon}$, \bar{T} , and \bar{T}''^2 . The conical reactor used in their work is shown in Fig. 3.43 and complete details of the reactor and the numerical methods were given in Ref. 248. The computed and measured profiles of temperature and species concentrations in the conical reactor (Fig. 3.43) are shown in Fig. 3.44 (a) and (b) for traverses at port B for a CH₄-air mixture, $\phi = 0.84$, with a mean entry jet velocity, U , of 60 m s^{-1} . Figure 3.44 (a) shows the computed Favre mean and r.m.s. fluctuating temperature are in good agreement with those measured. A more exacting test of the model lies in the prediction of species concentrations. Figure 3.44 (b) shows that the major species of CH₄ and CO₂ are well predicted; while those for CO, although satisfactory are less good. There are discrepancies occur between the computed and measured species concentrations close to the wall for both CH₄ and C₃H₈ fuels. This can be attributed qualitatively to the principal theoretical limitations, such as; the distribution of strain rate in the turbulent field is unknown, the relationship between laminar flame straining and turbulent strain is not fully understood, no allowance has been made for strong pressure field and lastly the $k - \epsilon$ model assumes Reynolds stress isotropy.

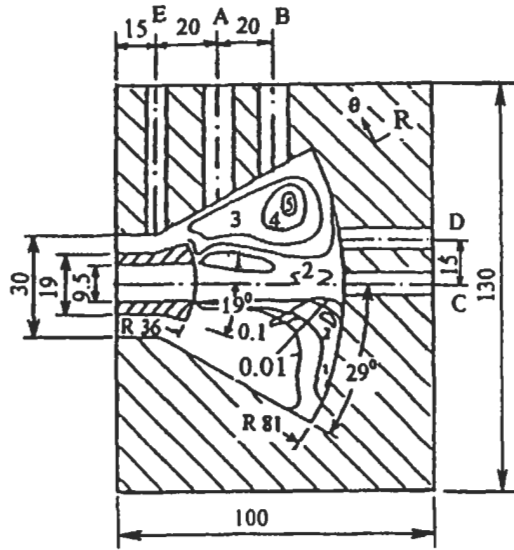


Fig. 3.43: Reactor details, with computed eddy lifetime 10^{-4} s (top contours) and turbulent heat release rate GW m^{-3} (bottom contours) for CH_4 -air mixture, $\phi = 0.84$ and $U = 60 \text{ m s}^{-1}$. Dimensions in mm [248]. Reproduced by permission of Elsevier Science.

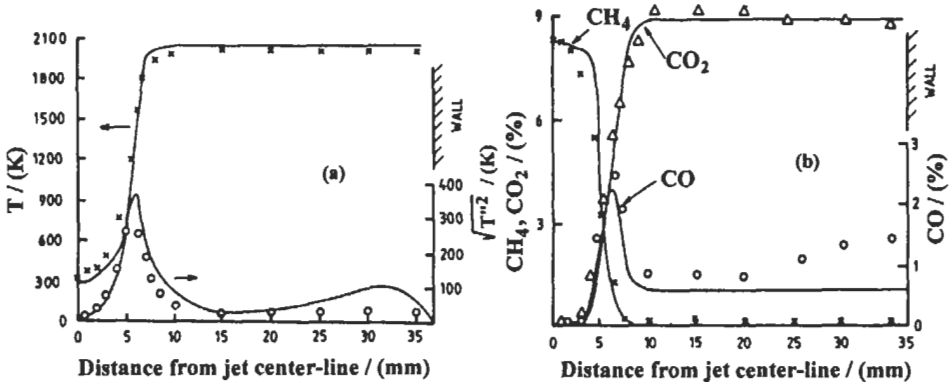


Fig. 3.44: CH_4 -air mixture, $\phi = 0.84$ and $U = 60 \text{ m s}^{-1}$. Traverse B ($K = 0.43$). (a) mean and fluctuating temperatures; (b) mole fractions of CH_4 , CO_2 and CO ; full line curves are computed values; Symbols show the measurements from Ref. 248. Reproduced by permission of Elsevier Science.

Tunnel Burner with Annular Entry of a Pre-Mixture

The strained laminar flamelet model described above in section 3.4.2 is presented in this section for turbulent swirling and combustion (Abd El-Masseeh et al [524]). Their [524] model predictions are compared for three entry velocities and three swirl numbers, with those from the $k-\epsilon$ model and with measurements in a laboratory burner with the facility for the annular entry of swirling pre-mixture. Figure 3.45 shows measured and computed temperature contours for non-swirling gases, with an annular

axial jet velocity of 60 m s^{-1} . The theoretical prediction employed both the direct stress (D.S.) and the $k-\epsilon$. Both the predicted and measured contours reveal a cone-like turbulent flame and the velocity vectors, shown at the left of the figure, clearly demonstrate flame stabilization by recirculation of hot combustion products at the outer annular corner. Unburnt gaseous premixture is trapped in a central recirculation zone, which has no role in flame stabilization. The agreement between the predicted and measured flame length of approximately 80 mm is satisfactory, particularly with the direct stress model. The theoretical flame length is that to a point with a temperature of 1700 K on the centerline, and this is where the maximum heat release usually occurs.

However, the temperature contours reveal significant differences between theory and measurement. Both sets of predicted contours suggest a thinner flame brush than is revealed by the measurements. A partial explanation is the flow disturbance due to the presence of the thermocouple. The measured maximum temperature close to the flame is about 400 K less than the adiabatic temperature of the premixture, a consequence of heat losses to the burner tube. Where there might be some cooling of reacting gases, a non-adiabatic flamelet model becomes necessary. This can be a formidable requirement.

Figure 3.46 shows measured and predicted temperatures for similar conditions but with a lower mean annular jet entry velocity, U , of 30 m s^{-1} . Reduction of the mean entry velocity to 30 m s^{-1} reveals an interesting sensitivity to the details of the mathematical model. At the lower velocity, thermocouple measurements and the Reynolds stress model isotherms revealed an annular, rather than a conical flame, as shown in Fig. 3.46. On the other hand, the $k-\epsilon$ model showed a shortened flame but, incorrectly, still in a conical form. This important difference can be attributed to the difference in the modeling of the two recirculations of either side of the flame. For

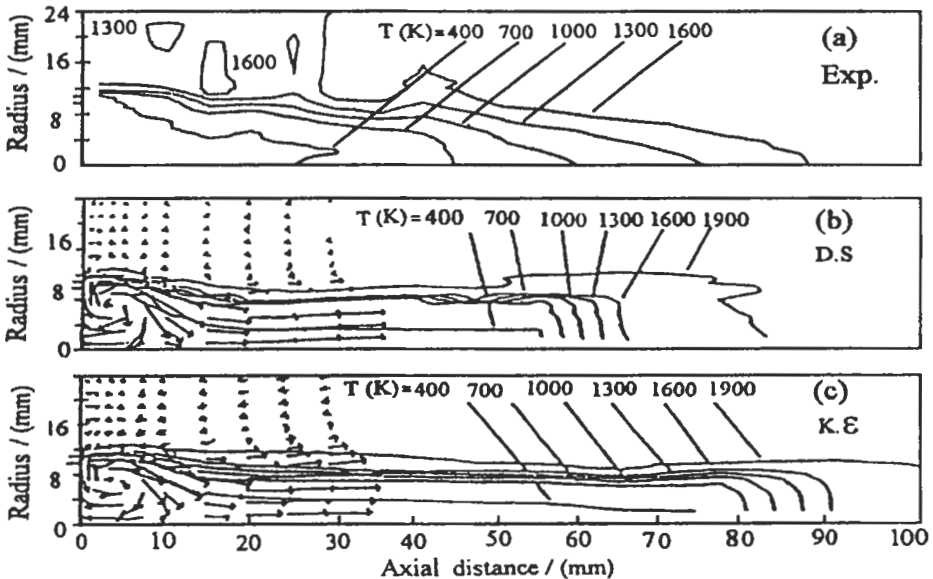


Fig. 3.45: Temperature contours for tunnel burner, CH_4 -air, $\phi = 0.84$, $S = 0$ and $U = 60 \text{ m s}^{-1}$. (a) Measured, (b) Direct stress and (c) $k-\epsilon$ models [524]. Reproduced by permission of The Combustion Institute.

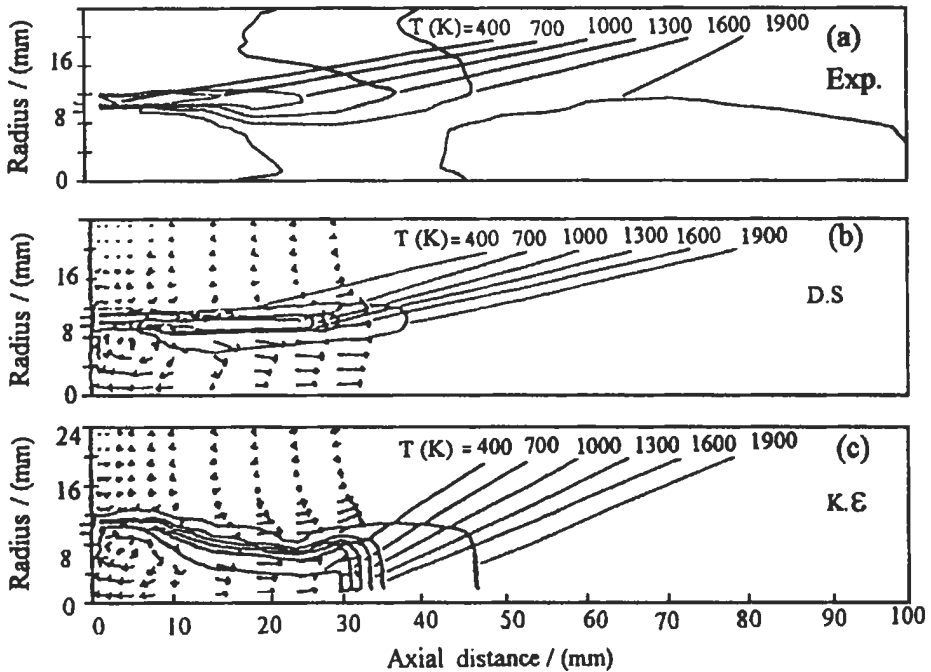


Fig. 3.46: Temperature contours for tunnel burner, CH_4 -air, $\phi = 0.84$, $S = 0$ and $U = 30 \text{ m s}^{-1}$. (a) Measured, (b) Direct stress and (c) k - ϵ models [524]. Reproduced by permission of The Combustion Institute.

swirling flows, both models correctly predicted annular flames, but with the k - ϵ model flame thicknesses were somewhat greater than those measured.

Turbulent Vertical Free Flames

In chapter 2, it was shown how the laminar heat release rate, q_l can be determined from the measured gas temperature, velocity, and species concentrations, and is compared with the corresponding values from the laminar kinetic model. In this chapter as we discussed above, the mean heat release rate and co-variance of heat release rate and temperature are derived from the computed PDF and heat release rate for the laminar flame using laminar flamelet model of turbulent combustion. Therefore, it is important now to show how the turbulent heat release rate can be determined from the measured species concentrations, velocity, and temperature profiles in premixed flame. Furthermore, the knowledge of the heat release rate at different points in flames will help in defining the flame envelope.

Another two attempts to obtain the experimental heat release rate of premixed flames have been investigated for turbulent vertical free flames by Megahed et al [525] and for turbulent horizontal flames by El-Mahallawy et al [526]. The first attempt will be described now and then followed by the second attempt. In both attempts, it is required to calculate the different modes of energy transfer, and from an energy balance the heat release rate can be obtained.

In the first attempt [525], it was shown how the heat release is affected by the geometry of the burner and the fuel-air ratio. The burner used in their study is shown in Fig. 3.47 (a) and is consisted of a copper tube 0.038 m diameter, D_o , with a central rod of 0.017 m diameter, d . Sleeves of different diameter were used to change the inner diameter of the burner tube, and a mixture of 0.6 butane and 0.4 propane by mass was used as a fuel (LPG). Tests were carried out for the temperature measurements under different conditions of burner geometry (burner diameter ratio, D_o/d) and fuel air ratio. The relative A/F represents the ratio between the actual and theoretical air-fuel ratio.

The calculation of the heat release rate requires the knowledge of both the temperature and velocity distributions. Temperature distribution with the required precision was obtained by measurement while the velocity distribution was obtained by solving the equations of motion using the computational procedure of Gosman et al [527], with effective viscosity of the turbulent flow, μ_t , proposed by Schlichting [528]. In the following, the calculation procedure of different modes of energy transfer in the flame (namely, thermal conduction, internal convection, thermal radiation, and viscous dissipation) is given.

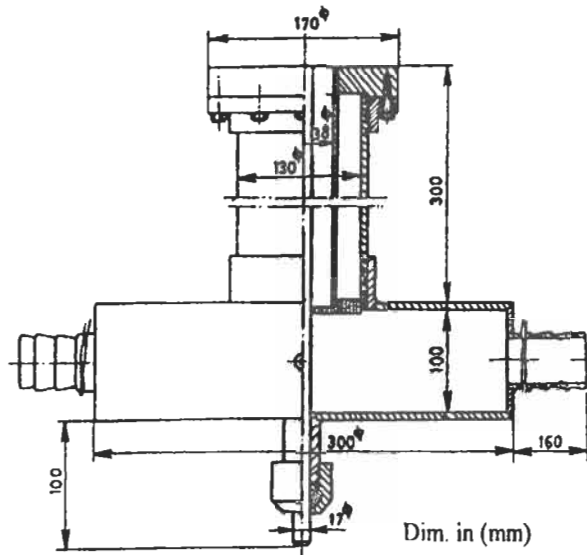


Fig. 3.47(a): Burner and mixing chamber [525].

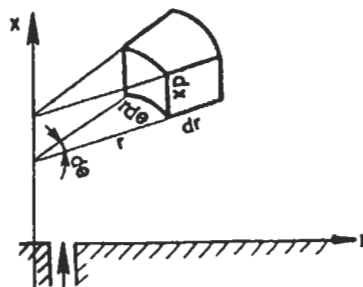


Fig. 3.47(b): Element of volume [525].

i- Thermal Conduction. It could be shown that the time average of the heat gained by conduction for an isotropic element in the radial, r , and axial, x , directions is given by:

$$Q_{\text{cond}} = \frac{1}{r} \frac{\partial}{\partial r} \left(rk \frac{\partial \bar{T}}{\partial r} \right) + \frac{\partial}{\partial x} \left(k \frac{\partial \bar{T}}{\partial x} \right) \quad (3.54)$$

where r is the radius, k is the thermal conductivity, \bar{T} is the mean temperature, and x is the axial distance along the flame. The elemental control volume is shown in Fig. 3.47 (b). The thermal conductivity is taken as that of the combustion products and the data given by Mikheyev [529] is fitted by the following straight line relation:

$$k = 0.0227 + 8.58 \cdot 10^{-5} t \quad \text{W/m K} \quad (3.55)$$

where t is temperature in °C.

ii- Internal Convection. The time average of the heat loss by the element in both radial and axial directions is given by:

$$Q_{\text{conv.}} = \frac{1}{r} \frac{\partial}{\partial r} (\rho C_p r \bar{V} \bar{T}) + \frac{\partial}{\partial x} (\rho C_p \bar{U} \bar{T}) + \frac{1}{r} \frac{\partial}{\partial r} (\rho C_p r \overline{V'T'}) + \frac{\partial}{\partial x} (\rho C_p \overline{U'T'}) \quad (3.56)$$

where \bar{U} , and \bar{V} are the mean components of the axial and radial velocities, respectively. While ρ , C_p are the density and specific heat at constant pressure, U' , V' are the fluctuating components of the axial and radial velocities, and T' is the fluctuating component of the temperature.

Using the continuity equation:

$$\frac{1}{r} \frac{\partial}{\partial r} (r \rho \bar{V}) + \frac{\partial}{\partial x} (\rho \bar{U}) = 0 \quad (3.57)$$

From the above two equations:

$$Q_{\text{conv.}} = \rho \bar{V} \frac{\partial}{\partial r} (C_p \bar{T}) + \rho \bar{U} \frac{\partial}{\partial x} (C_p \bar{T}) + \frac{1}{r} \frac{\partial}{\partial r} (\bar{q}_r^t) + \frac{\partial}{\partial x} (\bar{q}_x^t) \quad (3.58)$$

where $\bar{q}_r^t = \rho C_p \overline{V'T'}$, $\bar{q}_x^t = \rho C_p \overline{U'T'}$

The last two terms in the above equation are similar to the terms of the thermal conduction, so they represent the following substitution:

$$\bar{q}_r^t = -k_t \frac{\partial \bar{T}}{\partial r}, \quad \bar{q}_x^t = -k_t \frac{\partial \bar{T}}{\partial x} \quad (3.59)$$

where k_t is called "the turbulent coefficient of thermal conductivity".

Since we have the eddy kinematic viscosity $\nu_t = \mu_t / \rho$, the eddy thermal diffusivity

$\alpha_t = k_t / \rho C_p$ and for free jet $v_t / \alpha_t = 0.5$, then:

$$k_t = 2C_p \mu_t \quad (3.60)$$

This relation between k_t and μ_t permits to use the above described model for μ_t to calculate k_t . The convective term is divided into two parts. In the first part, the convection by mean stream is given by:

$$Q_{\text{conv.}} = \rho \bar{V} \frac{\partial}{\partial r} (C_p \bar{T}) + \rho \bar{U} \frac{\partial}{\partial x} (C_p \bar{T}) \quad (3.61)$$

In the second part, the convection by turbulent fluctuations is given by:

$$Q_{\text{turb}} = - \left[\frac{1}{r} \frac{\partial}{\partial r} \left(r k_t \frac{\partial \bar{T}}{\partial r} \right) + \frac{\partial}{\partial x} \left(k_t \frac{\partial \bar{T}}{\partial x} \right) \right] \quad (3.62)$$

Sometimes Q_{turb} is called "turbulent diffusion". The specific heat at constant pressure is assumed to be a linear function of temperature and is given by the following:

$$C_p = 1.043 + 2.76 \times 10^{-4} t \quad \text{kJ kg}^{-1} \text{K}^{-1} \quad \text{for } t < 900 \text{ }^\circ\text{C}$$

$$C_p = 1.147 + 1.59 \times 10^{-4} t \quad \text{kJ kg}^{-1} \text{K}^{-1} \quad \text{for } t > 900 \text{ }^\circ\text{C}$$

iii- Thermal Radiation. In order to express the thermal radiation per unit volume at a point in element, a volume element of unity m^3 was assumed to be geometrically similar to the original volume element at that point, and to be filled by gases of the same temperature and composition. Therefore, the heat transfer by radiation per unit volume at that point will be equal to the total heat radiation from the surface of the unity m^3 element. Neglecting the re-radiation from the surroundings, the thermal radiation will be given by:

$$Q_{\text{rad}} = \sigma A \epsilon_f T_f^4 \quad (3.63)$$

where ϵ_f is the nonluminous flame emissivity and is calculated from Ref. 530, and T_f , A and σ are the maximum flame temperature, area and Stefan-Boltzman constant.

iv- Viscous Dissipation. Due to the viscous shear, there will be a dissipation source term which has the following form for axisymmetrical problems [52]:

$$Q_{\text{dissip}} = 2\mu_t \left[\left(\frac{\partial \bar{V}}{\partial r} \right)^2 + \left(\frac{\bar{V}}{r} \right)^2 + \left(\frac{\partial \bar{U}}{\partial x} \right)^2 \right] + \mu_t \left(\frac{\partial \bar{U}}{\partial r} + \frac{\partial \bar{V}}{\partial x} \right)^2 \quad (3.64)$$

After calculating all of these terms, energy balance can be made to obtain the heat release rate:

$$Q = Q_{\text{conv.}} + Q_{\text{turb.}} - Q_{\text{cond.}} - Q_{\text{dissip.}} + Q_{\text{rad.}} \quad (3.65)$$

From the above analysis, the heat release rate under different operating conditions was obtained [525] using the above equations and the computer program of Gosman et al [527]. For nearly all the experimental conditions, it was found that for any cross section of the flame, the point of maximum temperature did not coincide with the point of maximum heat release rate. Figures 3.48 and 3.50 show the contours of maximum temperature and maximum heat release rates. The deviation between the two is explained by the fact that the maximum heat release rate occurs at a temperature less than the maximum flame temperature where at the former temperature most of the important active species started to decline due to the recombination reactions (see also chapter 2). The flame envelope was defined as that surface which bounds the zone inside which most of the chemical energy is released. From the distribution of the heat release across the flame as shown in Fig. 3.49, it can be seen that, the surface of the peak points of heat release rate profiles is a good representation of the flame envelope. The heat release rate outside this surface is very small, as the profiles are steep with sharp peaks.

The flame envelopes for different operating conditions were obtained. Figures 3.50 and 3.51 show a comparison between these envelopes. From these figures, it can be concluded that, increasing the air-fuel ratio towards the theoretical mixture leads to a decrease in the size of the premixed zone. The maximum diameter and flame length were decreased (the flame length was defined by the point of intersection of the flame

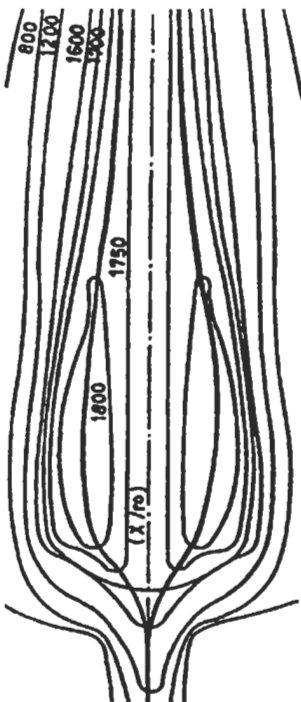


Fig. 3.48: Isothermal contours, burner diameter ratio of 25/17, relative A/F = 0.45 [525].

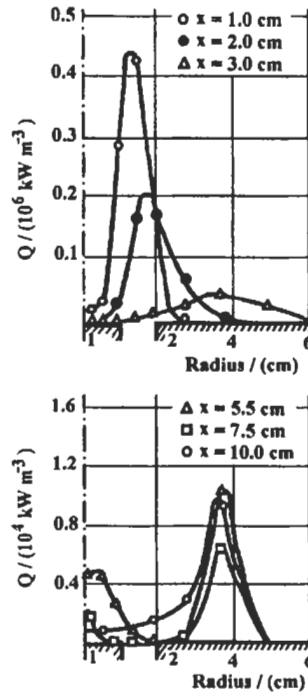


Fig. 3.49: Heat release rate distribution, burner diameter ratio of 38/17, relative A/F = 0.7 [525].

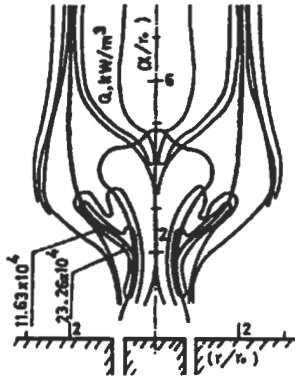


Fig. 3.50: Heat release rate contours, burner diameter ratio of 25/17, Relative A/F = 0.45 [525].

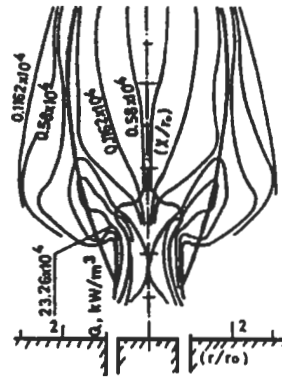


Fig. 3.51: Heat release rate contours, burner diameter ratio of 25/17, relative A/F = 0.7 [525].

envelope with the flame axis). As regards to the effect of the burner geometry which is expressed by the ratio of the outer diameter to the inner diameter, D_o/d , it is shown by Figs. 3.51 and 3.52 that, increasing this ratio leads to an increase in the size of the premixed flames.

As regards to the total fuel burned, it was defined as the volume integration of the heat release along the flame and is given as a fraction of the total chemical energy of the fuel in the fresh mixture. This fraction E_v is calculated by:

$$E_v = \int_0^V Q dV / m_f C.V \tag{3.66}$$

where m_f and $C.V$ are the fuel mass flow rate and calorific value of fuel, respectively. The calculated value of E_v against the axial distance of the flame is shown for different

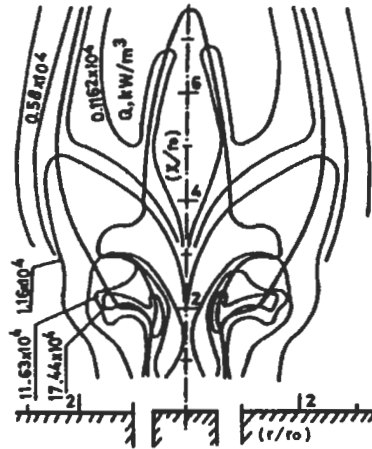


Fig. 3.52: Heat release rate contours, burner diameter ratio of 30/17, relative A/F = 0.7 [525].

conditions in Fig. 3.53. The value of E_v at the downstream section gives the efficiency of combustion of the flame. If all the fuel is completely burned, the integration of the profiles over the whole volume of the flame will be equal to the chemical energy of the fuel. At any cross section, the heat release per unit length of the flame is equal to:

$$\int_0^{\infty} Q 2\pi r dr \tag{3.67}$$

and the heat release from the centerline up to a radius, r is:

$$\int_0^r Q 2\pi r dr \tag{3.68}$$

Thus, a new variable can be defined as:

$$E_A = \frac{\int_0^r Q 2\pi r dr}{\int_0^{\infty} Q 2\pi r dr} \tag{3.69}$$

Figure 3.54 shows the constant (E_A) contours. The importance of this variable is showing that most of the heat is released in a thin layer surrounding the contour of maximum heat release leaving the core of the flame nearly without heat release.

Turbulent Horizontal Flat Flames

As shown above, the study of the heat release rate in turbulent premixed flames is of a considerable value, because it shows the regions of high and low combustion intensity and this will finally lead to the optimum design of furnaces and combustion chambers. In addition, such study will also develop and increase the knowledge about the chemical kinetics of reaction and validate its kinetic mechanism. This section is concerned with the study of the characteristics of heat release rate in flat, axisymmetric, turbulent, horizontal, and free premixed flames. El-Mahallawy et al [526] have obtained the heat release rate for such flames by calculating the different modes of energy transfer in the flame and by making an energy balance on the basis of the first law of

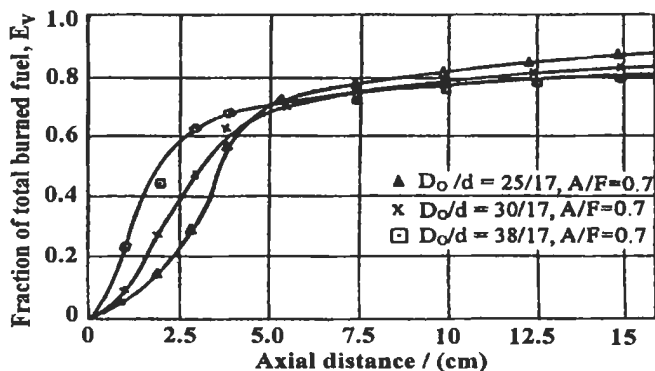


Fig. 3.53: Effect of burner geometry on total burned fuel [525].

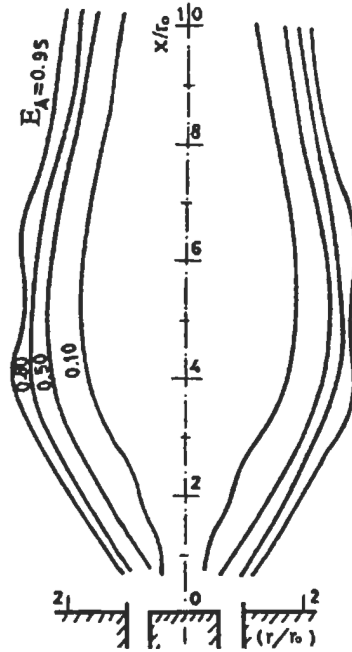


Fig. 3.54: Burned fuel contours, burner diameter ratio of 30/17, relative $A/F = 0.6$ [525].

thermodynamics. The temperature and velocity at different points in the flame were measured and used in the calculations. This removed the necessity to specify a combustion model and to solve the momentum equations like the above work in vertical flame. The turbulent viscosity was obtained from the turbulent kinetic energy and its dissipation rate model of turbulence. This work has contributed new data on the characteristics of heat release rate in premixed flames. It includes the effect of gap width and Reynolds number as well as the fuel-air ratio on the heat release rate, and the fraction of the fuel burned in the premixed zone. The burner used in this work consisted of two horizontal discs as shown in Fig. 3.55, and the general shape of flame under consideration is shown in plate 3.2. Furthermore, El-Mahallawy et al [531] have used the same burner to obtain the turbulent flat flame burning velocity.

The burner tube was made of copper with 0.038 m diameter, a central rod on which an upper disc was tapped and a sleeve of 0.03 m inner diameter. The mixture flows vertically in the annular space formed between the sleeve and the central rod and then horizontally into the gap formed between the upper disc and horizontal flat surface of the sleeve, considered as a lower disc. The fuel used is a mixture of butane and propane with gravimetric analysis of 0.6 and 0.4, respectively. Temperature and velocity measurements were conducted only in the premixed zone where the flow could be safely considered as a one-dimensional flow in the radial direction. The main parameters considered are the Reynolds number, relative fuel-air ratio and gap width. The Reynolds number, Re , was varied between 648 and 1188 and it was calculated as based on the gap width, δ , and the velocity of the mixture at burner exit and at 25 °C. The relative fuel-air ratio, F_r , is defined as the ratio between the fuel-air ratio of the mixture and the stoichiometric ratio, and it was varied between 1.67 and 2.22.

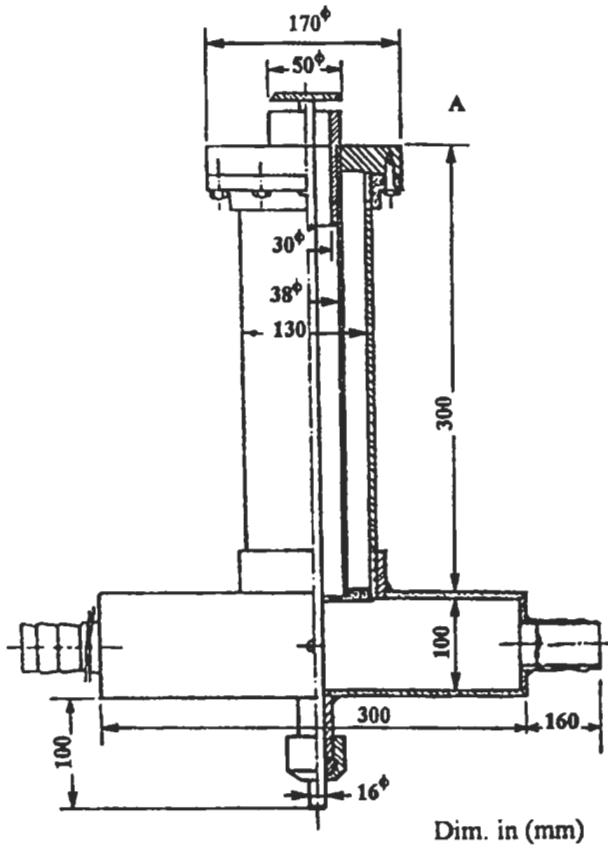


Fig. 3.55: Burner and mixing chamber [526].

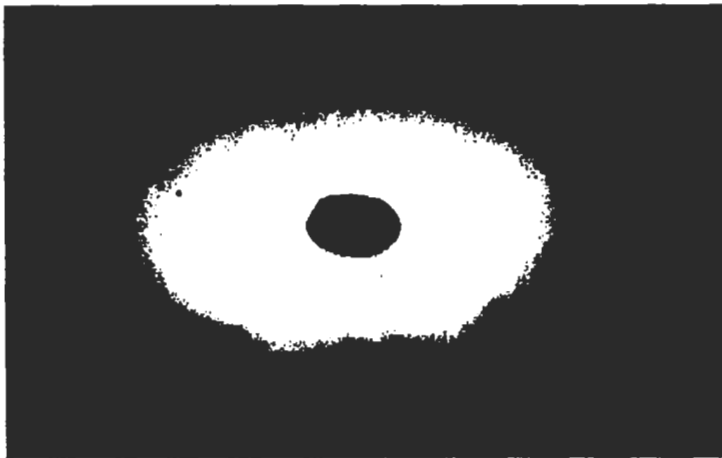


Plate 3.2: Direct flame photograph [526].

Furthermore, two gap widths were considered, namely: 3 and 5 mm gaps. Figures 3.56 and 3.57 show the measured profiles of gas velocity and temperature, respectively. The temperatures were corrected for radiation errors. The heat release rate at different points was obtained using the same procedure described above by Eqs. 3.54 to 3.65 as well as the experimental data of velocity and temperature, except that a cylindrical-polar coordinates were used here, and the flow within the flame brush was assumed as a steady one-dimensional flow.

Figure 3.58 shows the distribution of the heat release rate versus the vertical height (x) at different radii, r. For the gap width of 5 mm, the heat release rate distribution is generally characterized by high rates close to the burner rim, and relatively low rates as it proceeds in the radial direction. For the 3 mm gap, the heat release rate attains its maximum value at further downstream distances as compared with the 5 mm gap. This shows that the flame is stabilized at the burner rim for large gaps and at downstream sections for small gaps.

The average heat release rate at a certain radius, r, is calculated by summing up the heat released at different nodes on this radius, sweeping from point to point in x-direction. This amount of heat released is divided by the total control volumes along the considered constant radius grid line. This is expressed by:

$$Q_{j,avr} = \frac{\sum_i Q_{ij} V_{ij}}{\sum_i V_{ij}} \tag{3.70}$$

The above steps are repeated at different radii to get the distribution of the average heat release rate in radial direction. This is shown in Fig. 3.59 for different conditions of gap

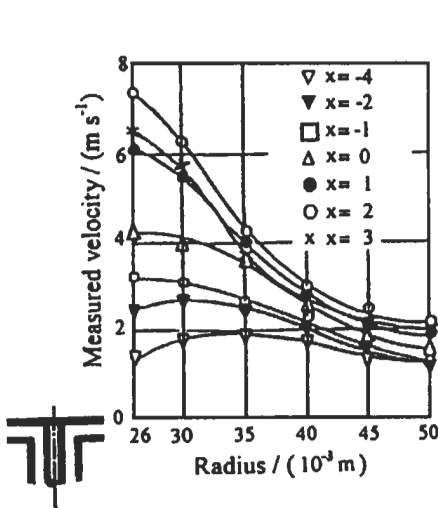


Fig. 3.56: Measured velocity $\delta = 5$ mm, $R_e = 733$, and $F_r = 1.67$ [526].

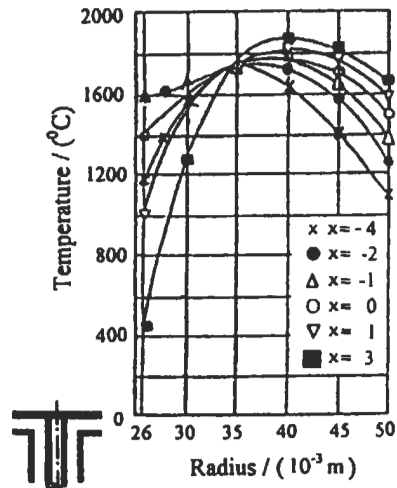


Fig. 3.57: Measured temperature $\delta = 5$ mm, $R_e = 733$, and $F_r = 1.67$ [526].

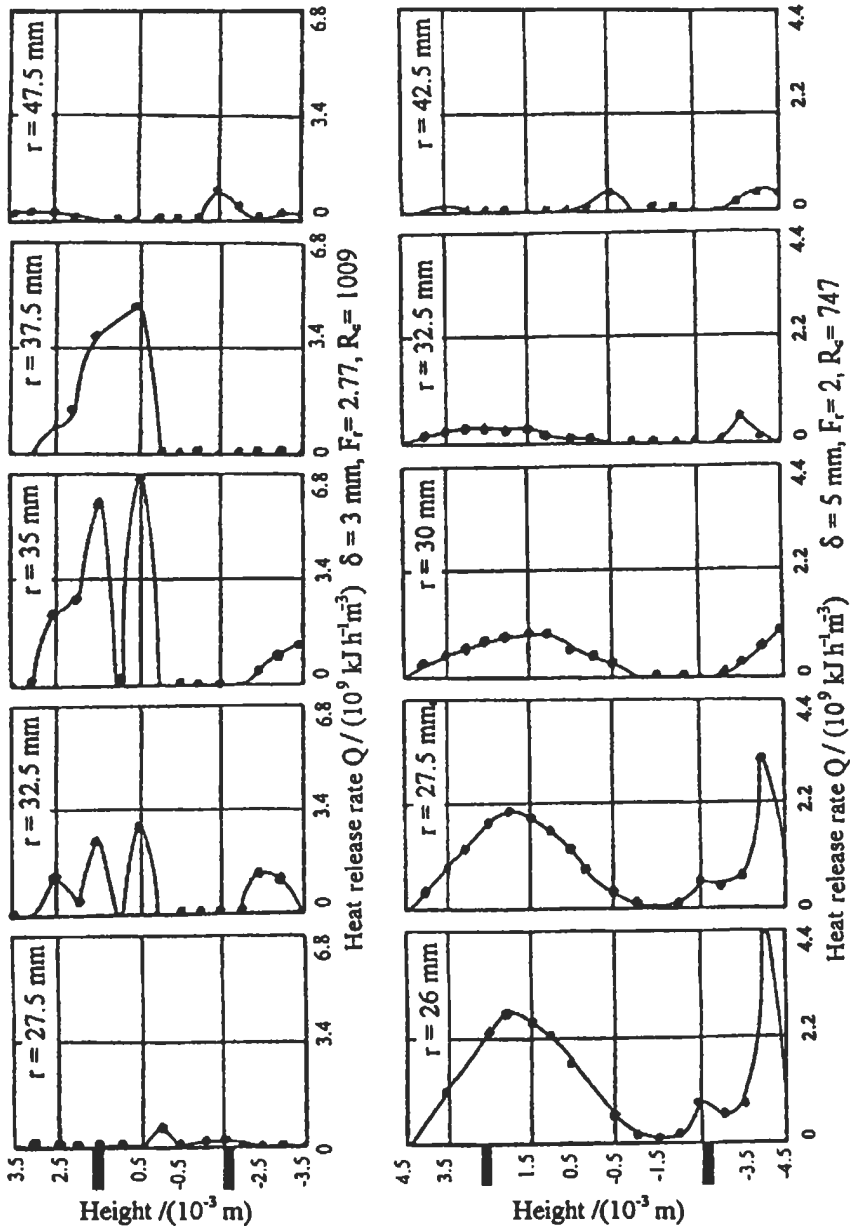


Fig. 3.58: Axial distribution of the heat release rate for 5 mm and 3 mm gaps [526].

widths, Reynolds numbers, and fuel-air ratios. By using the same procedure of Eq. 3.66, it was possible to calculate the fraction of the fuel burned up to a certain radius (η_r) which is a measure of the efficiency of combustion in the premixed zone. These results are shown in Fig. 3.60 for different conditions. The figure shows to what extent the fuel is burned as it proceeds along that zone.

Figure 3.61 shows the different modes of energy transfer, it is clear from the figure that, in gaseous flame, the only two types which can be safely dealt with are the internal convection, Q_c and the turbulent diffusion, Q_t . The thermal conduction Q_n is less important than those two modes. The thermal radiation and viscous dissipation are very small as compared to the other terms.

Having discussed the turbulent heat release rate and flame structure, we next look to the turbulent burning velocity as one of the important characteristics of premixed turbulent combustion.

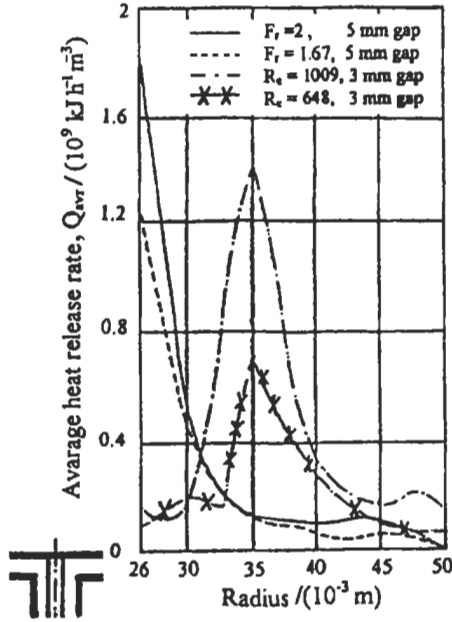


Fig. 3.59: Variation of the radial distribution. of the average heat release rate with δ , R_e and F_r [526].

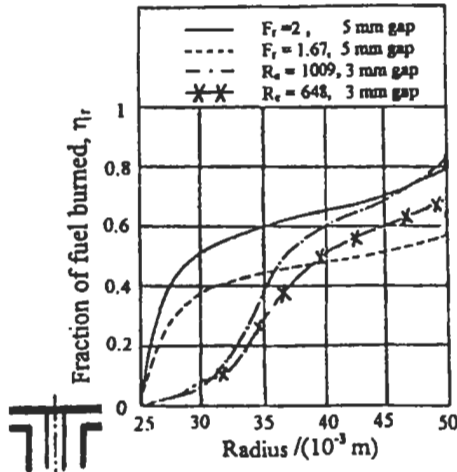


Fig. 3.60: Variation of the fraction of fuel burned with δ , R_e and F_r [526].

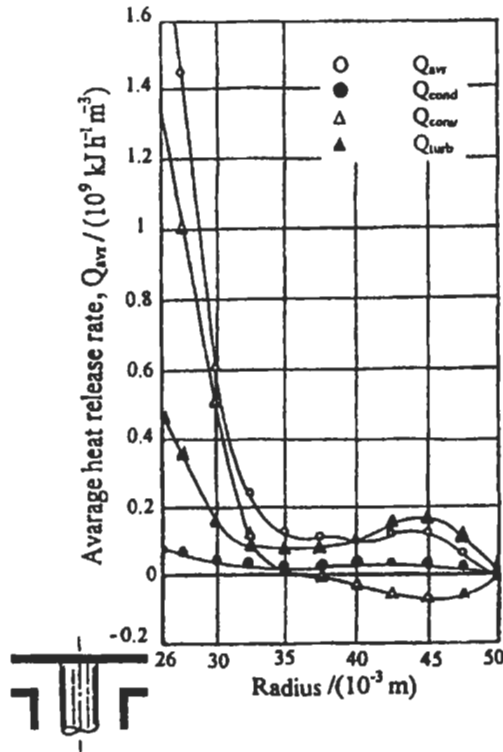


Fig. 3.61: The distribution of the different modes of energy transfer in flame ($\delta = 5 \text{ mm}$, $R_e = 747$ and $F_r = 2$) [526].

3.7.4 Turbulent Burning Velocity

The study of turbulent burning velocity is of great importance in most of heat producing devices, because an increase in the turbulent burning velocity will result in an increase of heat release rate. The result will be the reduction of the volume of combustion chamber, which is a most favorable case in the design of jet engines.

In 1883, Mallard and Le Chatelier [532] noted that turbulence increased both energy transfer and flame surface area and also formed new centers of inflammation. Significant further advance had to await the work of Damköhler [533] who introduced a duality into the understanding of planar turbulent flame propagation. If the integral length scale of the turbulence, L , was greater than the laminar flame thickness, then the only effect of the turbulence would be to wrinkle the flame front, without altering the internal structure of an essentially laminar flame. If the length scale was less than the laminar flame thickness, a rather uncommon regime for practical flames, changes in transport processes due to the turbulence would create a localized flame structure which was different from that of a laminar flame. Both Damköhler [533] and Shchelkin [534] developed turbulent burning velocity expressions for the two regimes, with the latter recognizing that the wrinkled front could be split into separate islands. Several workers have suggested that at higher levels of turbulence the reaction zone can become

fragmented and extended, and yet separate regions might maintain essentially laminar flame characteristics.

Many of early measurements of turbulent burning velocities were carried out for Bunsen-type flames burning different fuels and subject to different scales and intensities of turbulence. The turbulence parameters were varied by using burners of different geometries and placing grid in the approach flow. Turbulent burning velocity was estimated from flame zone. Some of early investigators simply chose the mean area between the inner border observed and the outer one. Others took the point of maximum flame intensity. So, the burning velocity was estimated by dividing the volume rate of flow, at 25 °C, by the proposed flame surface which gives a mean burning velocity over-all the flame surface. Moreover, some investigators studied turbulent burning velocity in explosion vessels, which is specially applied for petrol engines.

In this section, an attempt is made to review, in very brief, the work of some investigators concerning turbulent burning velocity.

Shchelkin [534] extended Damköhler's work and gave a correlated formula between turbulent, U_t , and laminar burning velocity, U_l , for fine scale turbulence:

$$U_t / U_l = \sqrt{1 + \varepsilon / \nu} \quad (3.71)$$

which takes into account the molecular transport besides the turbulent transport process, ε and ν are eddy diffusivity and kinematic viscosity, respectively. For strong large-scale turbulence, Shchelkin demonstrated that the flame surface is distorted so much that islands of flame start to break away and are swept away by the flow. Shchelkin assumed that the area of the combustion wave is increased by turbulent fluctuations in the ratio of u'/U_l , and from this assumption he reached the conclusion that, for strong turbulence, the resulting turbulent burning velocity should be equal to r.m.s. of fluctuating component, u' :

$$U_t = u' \quad (3.72)$$

and be independent of scale of turbulence and of normal burning velocity of explosive mixture.

For weak turbulence, Shchelkin followed Damköhler's argument but he calculated the surface area of the small cones carefully and arrived at the following formula:

$$U_t = U_l \sqrt{1 + b \left(\frac{u'}{U_l} \right)^2} \quad (3.73)$$

where, b is a coefficient equal unity for weak turbulence.

For strong turbulence, this formula reduces to $U_t = u'$, so it can be considered as the general formula in this case. Karlovitz [535] proposed that the stretching of a flame surface can reduce the burning velocity.

In order to test rather surprising results of Shchelkin and clear up the disagreement between various theories, Bollinger and Williams [536], measured the turbulent burning velocity on Bunsen-type flames, realizing that the inner and outer boundaries of turbulent flames are more or less arbitrary. Bollinger and Williams have used an

intermediate surface drawn approximately halfway between the inner and outer boundaries for determining the average turbulent burning velocity. Figure 3.62 shows this intermediate flame surface.

The burning velocity was calculated from the following formula:

$$U_t = \dot{V} / A \quad (3.74)$$

where, \dot{V} is the volume rate of flow and A is the area of the medium flame surface. The experimental work was carried out for acetylene-air, ethylene-air and propane-air mixtures. The resultant formula is :

$$U_t = 0.1761U_1d^{0.256} Re^{0.238} \quad (3.75)$$

where Re is the pipe Reynolds number and d is the burner diameter.

The strong influence of U_1 found by these investigators is in accordance with Demköhler. However, the large effect of, d , which might be interpreted as an effect of turbulence scale in the approach flow known to be proportional to d , was not previously predicted, and the influence of, U , the mean velocity, which might be interpreted as the effect of u' in the approach stream known to be proportional to U , was lower than expected.

Bollinger and Williams concluded that the theory of Damköhler of the effect of large scale turbulence on the flame speed in a Bunsen-type flame is found to be correct as to the dependence of laminar flame speed, but in error as to the dependence on Reynolds number. At about the same time, experiments were carried out by Hottel et al [537], at the fuel Research Laboratory of M.I.T. on turbulent flames in confined channels. Measurements of turbulent burning velocity gave the surprising results that the approach flow turbulence had little effect on the burning velocity, which also was much larger than the value calculated from the formula by Shchelkin. It was concluded from these results that very strong additional turbulence must have been produced by some disturbances, which did overshadow the turbulence of approach flow. This was the first case in the study of turbulent flames where turbulence production by the flame was recognized from careful measurements.

Karlovitz et al [538] studied Bunsen flames, disturbed by pipe turbulence. Two relations were derived for U_t in the presence of large-scale turbulence. The first of these was proposed for use in the presence of weak turbulence, where $u'/U_t \ll 1$, is:

$$U_t = U_1 + u' \quad (3.76)$$

The second was proposed for strong turbulence where $u'/U_t \gg 1$,

$$U_t = U_1 + \sqrt{2U_1u'} \quad (3.77)$$

According to the theoretical results, the effect of turbulence should be independent of scales, and U_1 should remain the important controlling factor even at very high u' .

Bradley and Abdel Gayed [539] studied the turbulent burning velocity for hydrogen-air

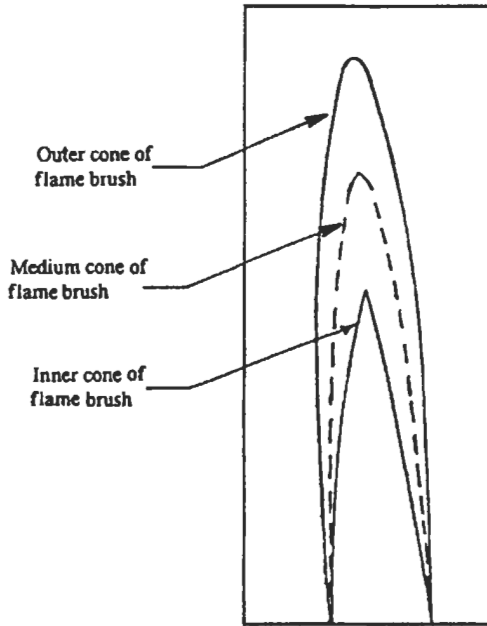


Fig. 3.62: Construction of medium flame surface for the measurements of turbulent burning velocity [526].

in an explosion vessel equipped with four fans driven by air-turbines. This arrangement created a central region of isotropic turbulence in which measurements were made. They [539] measured u' and L (integral length scale) at room temperature using hot wire anemometer (see section 3.3). The apparatus is capable of giving high turbulent Reynolds numbers R_L , where turbulent Reynolds number is given by:

$$R_L = \frac{u'L}{\nu} \tag{3.78}$$

They [539] plotted U_t/U_1 versus U_1/u' for different turbulent Reynolds numbers. The use of hydrogen-air mixtures has extended the data on premixed turbulent combustion to a regime with high values of U_t/u' . In comparison of the correlation between U_t/U_1 and U_1/u' , they have used an alternative method for finding R_L in the work of others who have not measured the turbulent scale. This method was adopted in such cases, when circular tube and flat slot burners had been employed.

At half the radius of the tube it was estimated that,

$$R_L = 5.927 \times 10^{-8} (Re)^{1.84} \tag{3.79}$$

Halfway between the central plane and a plate

$$R_L = 6.121 \times 10^{-6} (Re_p)^{1.593} \tag{3.80}$$

for $R_L > 50$, and with Re_p based upon the distance apart of the plates.

For values of R_L which are less than the limiting value, the values of u'/U were obtained by other means.

$$\frac{u'}{U} = 0.1676(Re)^{-0.119} \quad (3.81)$$

and

$$\frac{u'}{U} = 0.1151(Re_p)^{-0.118} \quad (3.82)$$

where U is the mean velocity, Re is the pipe Reynolds number and Re_p is the Reynolds number for flow issuing between two plates.

In spite of the difficulties in accurately measuring burning velocity and turbulent parameters, the exhibited correlations are still significant. As U_t/u' tends to large values, the molecular transport overwhelms transport process, and in the limit where U_t/u' tends to infinity, U_t/U_1 is unity. Andrews et al [540], Libby and Williams [541], Bray [542] and Bradley [543] have reviewed turbulent burning.

Kobayashi et al [544] have investigated the effect of ambient pressures on the turbulent burning velocity in a high-pressure environment, turbulent premixed flames of lean methane-air mixtures stabilized with a nozzle-type burner in high-pressure chamber. Their results show that the effect of elevated pressure on turbulent burning velocity are significant and that the ratio of turbulent to laminar burning velocity, U_t/U_1 increases with both turbulence intensity u' and pressure, reaching a value of 30 at 3 MPa. Also, in 1998, Furukawa et al [545] have investigated burning velocities in a vertically oriented, burner-stabilized turbulent premixed propane-air flame in the reaction-sheet regime using a microelectrostatic probe and a Laser-Doppler Velocimetry, that give components in a vertical plane of the flame front velocity and the gas velocity, respectively. They concluded from their observations that the turbulence may exert substantial influences on the flamelets.

Some workers who postulate an influence of turbulent transport processes on flame propagation emphasize the large scale eddies whilst others, such as Magnussen and Hjertager [546], have emphasized the role of dissipative eddies. Spalding [547], in his eddy break-up theory, expressed the rate of decay of large eddies as a rate determining step, and Ballal and Lefebvre [548] related burning to eddy structure. In the two-eddy theory of Abdel-Gayed and Bradley [549], the rate of burning is expressed by the product of the rate of eddy decay and the amount of mixture chemically reacted during the eddy lifetime. The turbulent Reynolds number, R_L , expresses dimensionless eddy lifetime. Dimensionless chemical life time for both large and dissipative eddies involves this, as well as the ratio of turbulent velocity, U_t , to laminar burning velocity, U_1 . The Karlovitz [538] stretch factor, K' , can be obtained from the same dimensionless groups.

When the flame develops from a point source the reaction front is affected first by the higher frequencies of the turbulence spectrum and then, progressively, by the lower ones. Initially, the laminar flame is subject to geometric strain whilst the full turbulent strain is developing. At any instant, the effective r.m.s. turbulent velocity for the propagation of the flame front, u'_k is given by the integral of the P.S.D. (power spectral

density) function against the frequency, from the highest frequency to the reciprocal of the elapsed time t_k . The experimental P.S.D. function values were obtained from four different reciprocating engine configurations and from the results of Abdel-Gayed et al [550] from a stirred bomb.

A total of 1650 measurements of U_t for gaseous premixtures for Lewis number, $L_e \leq 1.3$ have been correlated in this way by Abdel-Gayed et al [550] and are shown in Fig. 3.63 with the different combustion regimes. Figure 3.64 is taken from the same reference [550] and shows how the turbulent burning velocity U_{tk} develops with time. Here τ_a is the integral time scale, given by $L/(\text{mean velocity})$.

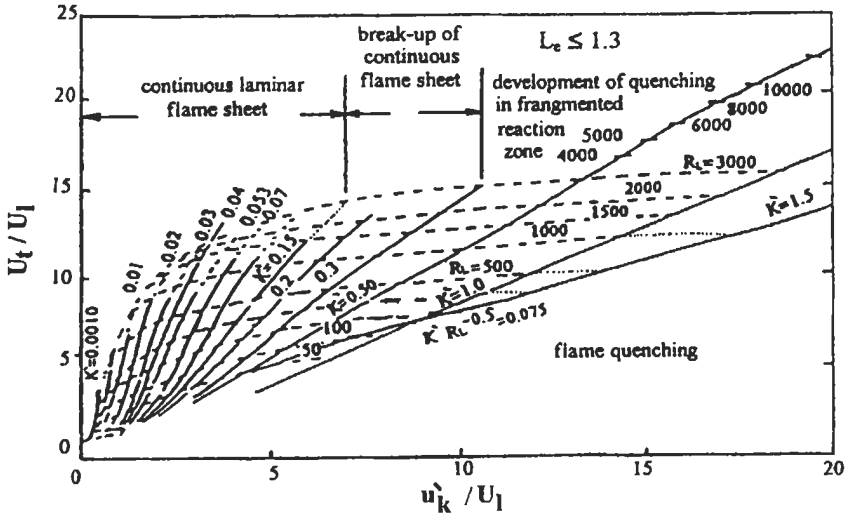


Fig. 3.63: Correlation of turbulent burning velocities, $L_e \leq 1.3$ [550]. Reproduced by permission of The Royal Society.

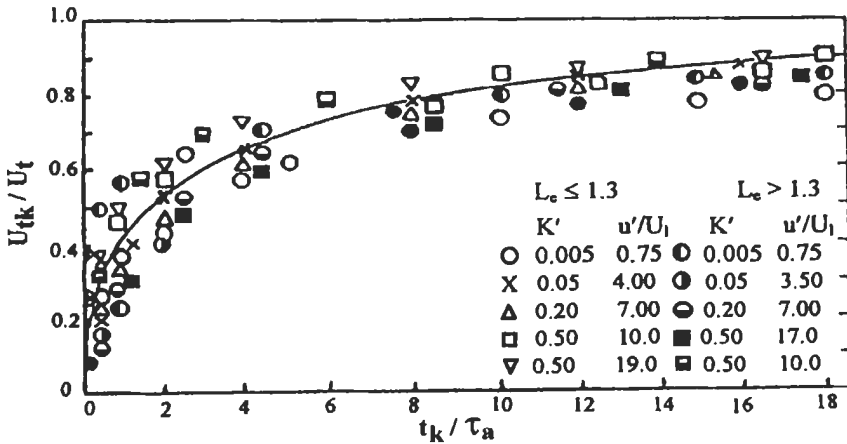


Fig. 3.64: Development of turbulent burning velocity with time [550]. Reproduced by permission of The Royal Society.

There are principle theoretical limitations which are: (i) Detailed chemical kinetics have been eschewed except in laminar burning velocity, chemistry is embodied in its measured values (ii) Effects of straining of laminar flamelet have only been embodied by the use of approximate asymptotic analyses. (iii) The distribution of strain rates in the turbulent field is unknown and no allowance has been made for strong pressure fields.

Burning Velocity in Closed Systems

The rate of burning in the cylinder exercises a considerable influence upon the power and efficiency of the engine. Combustion should occur close to top center and be rapid enough to utilize the fullest possible extent of the maximum compression, and yet not so rapid as to induce strong shock waves in the gas or intolerable impact loading on bearings and other mechanical components.

The combustion characteristics for a gasoline engine may be described in terms of the characteristic curves in Fig. 3.63. This requires knowledge of the aerodynamic and turbulent characteristics of the charge flow in the engine during combustion. This may be obtained by mathematical modeling or experimental measurements. Accurate laminar burning velocities of the fuel-air mixture are required over the appropriate ranges of temperature and pressure and this is discussed in details in chapter 2. Shown by the bold curves in Fig. 3.65 are the modeled loci of performance for a high turbulence combustion chamber, different engine speeds and equivalence ratios, ϕ , of octane-air mixtures of 0.8 and 1.0 (Bradley et al [551]). On the curve for a speed of 3400 r.p.m. and $\phi = 0.8$ are shown flame front radii from the spark gap. Initially, u'_k develops with time, to be followed by an appreciable increase in U_1 as the unburnt gases are adiabatically compressed. The result is that the highest values of K' occur in the early stages of flame propagation, and particularly with lean mixtures, it is here that the flames are closest to being quenched. This tendency can be encountered by greater spark energy or by charge stratification that increases U_1 in the initial stages. A lean mixture, high turbulence, and high engine speed, all increase the value of K' . This can lead to performance deterioration due to excessive flame quenching by straining.

Figure 3.66 shows the effects of engine speed for a flame radius of 10 mm [551]. Both u' and u'_k increase linearly with engine speed and speeds of 2000 and 3000 r.p.m. are marked on the curves for low and high turbulence chambers and two equivalence ratios. As the engine speed increases so does the value of K' and partial flame quenching develops. The rate of increase of U_1 with engine speed diminishes with that speed. Although increased turbulence increases, U_1 , this is at the expense of greater pumping losses. However, there are diminishing returns from an increase in u' or engine speed and, ultimately, quenching might become excessive.

Exhaust gas recirculation is often a mean of reducing burnt gas temperature and NO_x production. However, this reduces the burning velocity, which consequently increases the value of K' . Excessive flame quenching reduces efficiency, power and derivability, and increases emission of carbon monoxide and unburnt hydrocarbons. The magnitude of U_1 determines the rate at which the flame front propagates into the unburnt mixture. As the value of K' increases, because of partial flame quenching, the volume fraction of completely burnt gas behind the visible front can be as low as 60% in an engine [552]

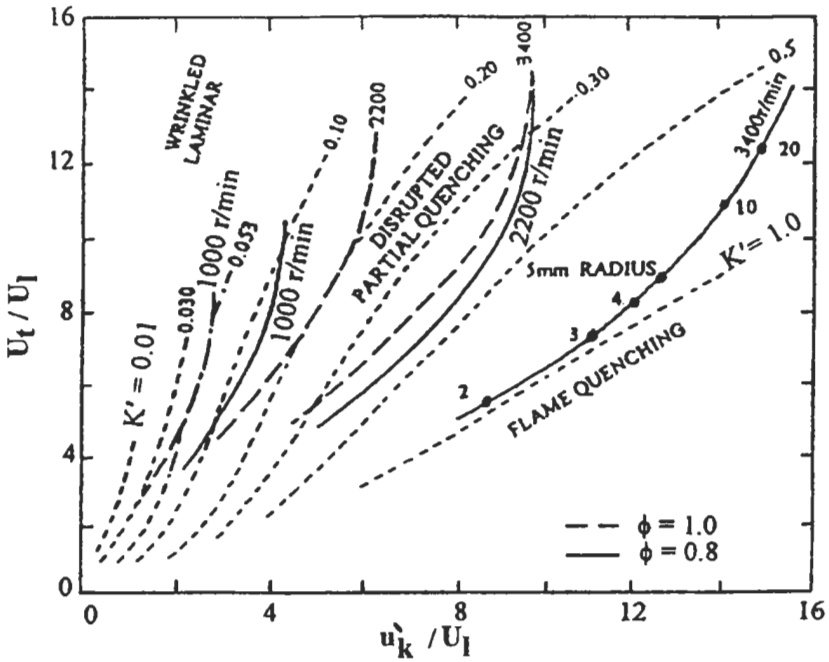


Fig. 3.65: Variation of K' and U_t/U_1 during combustion, at different engine speeds [551]. Reproduced by permission of Institution of Mechanical Engineers.

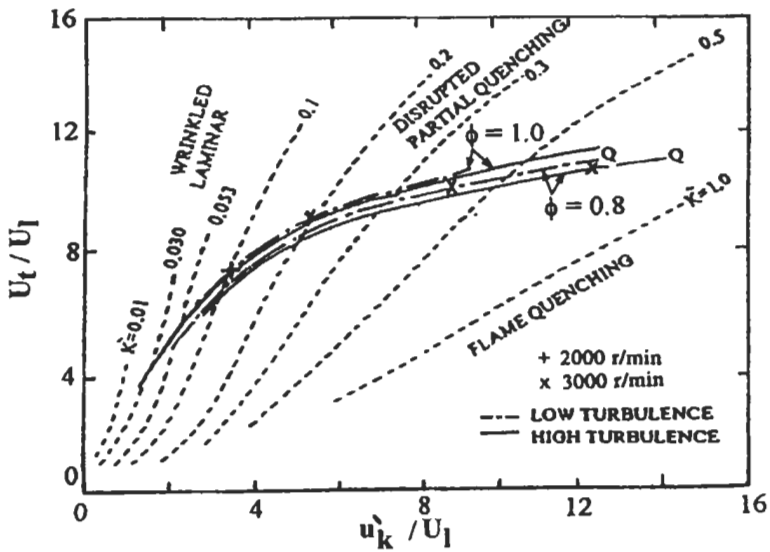


Fig. 3.66: Variation of K' and U_t/U_1 with engine speed and equivalence ratio [551]. Reproduced by permission of Institution of Mechanical Engineers.

and even less in a fan-stirred bomb [553]. Because of the adiabatic compression concomitant with combustion, unburnt gas might auto-ignite. This can be beneficial for the completion of the combustion process close to top center. On the other hand, a high chemical heat release rate at auto-ignition creates strong pressure waves which might reinforce with those from other auto-igniting centers to create yet further such centers, soot formation, excessive heat transfer, and material damage. Also, the pressure waves might react with flames to generate vorticity there and increase further the rate of burning.

Greater appreciation of all these processes will emerge from optical techniques with much improved temporal and spatial resolutions. This will enhance understanding of how aerodynamics and chemistry might interact to increase the burn-up rate without the deleterious consequences of knock.

Effect of global flame curvature on the burning velocity. Lipatnikov and Chomiak [554] have investigated the effect of global flame curvature on the burning velocity. They considered the simplified case of an adiabatic premixed flame propagating in frozen uniform turbulence under a constant pressure. Statistically spherical and planer one-dimensional expanding flames are simulated by solving the balance equations for the mean progress variable [555] (Eqs. 3.83 to 3.85) supplemented with the mass conservation equation.

$$\frac{\partial \bar{\rho} \tilde{c}}{\partial t} + \frac{\partial}{\partial x_j} (\bar{\rho} \tilde{u}_j \tilde{c}) = \frac{\partial}{\partial x_j} \left[\bar{\rho} (\kappa + D_t) \frac{\partial \tilde{c}}{\partial x_j} \right] + \frac{\bar{\rho} (1 - \tilde{c})}{\tau_r (1 + D_t / \kappa_b)} \exp\left(-\frac{\Theta}{\tilde{T}}\right) + A \rho_u u' \left[\frac{L}{u' \tau_c} \right]^{1/4} \left\{ 1 + \frac{\tau'}{t} \left[\exp\left(-\frac{t}{\tau'}\right) - 1 \right] \right\}^{1/2} \left\{ \sum_{j=1}^3 \left(\frac{\partial \tilde{c}}{\partial x_j} \right)^2 \right\}^{1/2} \quad (3.83)$$

where the time dependence of turbulent diffusivity D_t [556] is approximated by:

$$D_t(t) = D_{t,\infty} \left[1 - \exp\left(-\frac{t}{\tau'}\right) \right] \quad (3.84)$$

Here, t is time counted beginning with ignition; x_j and u_j are the coordinates and flow velocity components, respectively; ρ is the gas density; $\tau_c = \kappa_u / U_1^2$ and $\tau' = D_{t,\infty} / u'^2$ are the chemical and turbulent time scales, respectively. Subscript u and b label the unburned and burnt gas, respectively; the Reynolds averages are denoted by overbars and the Favre averages, such as $\bar{\rho} \tilde{c} = \overline{\rho c}$, are used. The r.m.s. turbulent velocity $u' = \sqrt{2k/3}$, integral turbulent length scale $L = C_D u'^3 / \tilde{\epsilon}$, and the asymptotic turbulent diffusivity $D_{t,\infty} = C_\mu k^2 / (\epsilon \sigma_c)$ are evaluated using, for example, the standard k - ϵ turbulence model, where C_D , C_μ , and σ_c are constants, k and ϵ are the turbulent kinetic energy and its dissipation rate, respectively. The Favre averaged temperature is linked with the progress variable as follows [555]:

$$\tilde{T} = T_u (1 - \tilde{c} + \gamma \tilde{c}) \quad (3.85)$$

where $\gamma = \rho_u/\rho_b$ is the heat release parameter. In addition to the two turbulence characteristics (k and ϵ or u' and L), the TFSCM (Turbulent Flame Speed Closure Model) includes a single constant A and a set of physico-chemical characteristics, such as the laminar flame speed U_l , the molecular heat diffusivity κ of the mixture, and the activation temperature Θ of a single global combustion reaction. The time scale τ_r of this reaction is calculated so that it yields the known value of U_l for the planer steadily propagating flame at $u' = 0$.

The initial conditions correspond to a small kernel filled with combustion products. Some results of such simulations are presented in Fig. 3.67 where the flame speeds $U_t = d\bar{r}_f/dt$, computed at different flame radii \bar{r}_f and various integral turbulence length scales L , are plotted against u' . The flame radius corresponds to the spherical surface on which $\bar{c} = 0.1$. The results of the simulations of the developed planer turbulent flames are also presented for comparison. Figure 3.67 distinctly shows the bending or even the decrease in U_t by u' (curves 1 and 4) for the spherical flames. It is worth emphasizing that the effect has been predicted without any submodel of flamelet stretching and quenching.

Since the decrease does not happen for the planer flames (see data 5 and 6), the effect appears to be controlled by the global flame curvature. Two mechanisms of the influence of global flame curvature on the flame speed are worth emphasizing. First, the expansion of hot combustion products induces gas flow and increases the flame speed as compared with the constant density case [554].

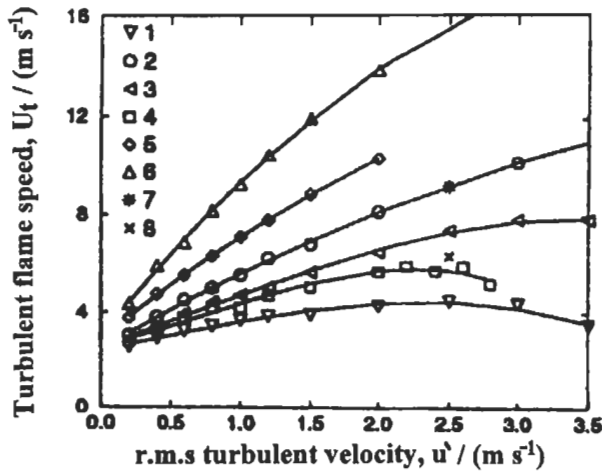


Fig. 3.67: Turbulent flame speed $U_t = d\bar{r}_f/dt$ vs. u' , computed at various flame radii \bar{r}_f and integral turbulence length scales L . Iso-octane / air mixture, $F = 1.0$, $T_o = 358$ K, $P = 1$ bar, Lipatnikov and Chomiak [554], reproduce by permission.

1- $L = 20$ mm, $\bar{r}_f = 20$ mm; 2- $L = 8$ mm, $\bar{r}_f = 40$ mm;

3- 7, and 8- $L = 20$ mm, $\bar{r}_f = 40$ mm; 4- $L = 30$ mm, $\bar{r}_f = 40$ mm;

5- $L = 2$ mm, developed planer flame; 6- $L = 20$ mm, developed planer flame;

7- D_t is multiplied by 0.5; 8- D_t is multiplied by 1.2.

Due to the finite thickness of the flame, the ratio of $\langle \rho \rangle$ (gas density averaged over the enflamed area) / ρ_u is higher than $\gamma^{-1} = \rho_b / \rho_u$. As a result, the speed of the spherical flame, $U_{t,u} \rho_u / \langle \rho \rangle$, is slower than the speed of the planar flame, $\gamma U_{t,u}$, if the values of $U_{t,u}$ are the same. The effect is controlled by the ratio of the flame thickness to its radius. For turbulent flame kernels, the importance of this effect has been emphasized by Ashurst [557].

Second, for the planar one-dimensional and for the spherical flames, Eq. 3.83 can be rewritten as follow [373]:

$$\bar{\rho} \frac{\partial \tilde{c}}{\partial t} + \bar{\rho} \left(\tilde{u} - a \frac{\kappa + D_t}{r} \right) \frac{\partial \tilde{c}}{\partial r} = \frac{\partial}{\partial r} \left[\bar{\rho} (\kappa + D_t) \frac{\partial \tilde{c}}{\partial r} \right] + \bar{W} \quad (3.86)$$

where symbol \bar{W} combines the two last source terms on the right hand side (RHS) of Eq. 3.83. Thus, in the spherical case ($a = 2$), the flame speed is slower than in the planar one ($a = 0$) due to the last term on the left-hand side (LHS) of the above equation. The effect is controlled by the ratio of $(\kappa + D_t) / (r U_t)$, characterizing the magnitude of the curvature term as compared to the convection one.

The two geometrical effects mentioned above are well known to control the difference between γU_t and dr_f / dt for spherical laminar flames [373]. However, for typical laminar flames, the ratio of $\kappa / (r U_t) \sim \delta_l / r_f \ll 1$, where δ_l is the laminar flame thickness; hence, the effect are of minor importance and the difference is much smaller than γU_t . Hence, in the turbulent case, $\delta_t \gg \delta_l$ and $D_t \gg \kappa$, both the effects can be substantial and they reduce the flame speed as compared with the planar case. This has been confirmed by Ibrahim et al [558] who simulated propagation of planar, cylindrical, and spherical turbulent flames and reported that the global curvature markedly reduced the flame speed, other things being equal.

Another interesting manifestation of the effect of global flame curvature consists in the fact that the dependencies of U_t on L , computed in the spherical case, reverse as the flame grows. The results computed for planar flames (see data 5 and 6 in Fig. 3.67) and for large spherical flames (not shown) indicate that U_t is increased by L , whereas the flame speeds computed for relatively small kernels ($\bar{r}_f = 40$ mm) show the opposite behavior (see data 2-4). Higher values of L are associated with a stronger reduction of the spherical flame speed due to the curvature. For relatively small flame kernels, the effect dominates and controls the dependence of U_t on L . As the flame kernel grows, the effect relaxes and the dependence reverses because the TFSCM predicts $U_t \sim L^{1/4}$ for the developed planar flames. This phenomenon is discussed, in details elsewhere [559].

Burning Velocity in Horizontal Flat Flames

This section represents some contributions in the field of turbulent burning velocity which has been done by El-Mahallawy et al [531]. In this work, a special burner was designed to give an axisymmetric premixed, flat, turbulent free flame. The burner was fed with commercial butane as fuel and atmospheric air as oxidant. The burner and the fuel composition were described in section 3.7.3. The burner is shown in Fig. 3.55 and the general shape of the flame is shown in plate 3.2.

As the flame studied is axisymmetric and flat one, the flow could be considered as one-dimensional flow. This gives nearly uniform value of turbulent burning velocity for

all points on the same radius through the flame brush. Also, the flame studied satisfies the condition that the flow parameters at burner exit are those approaching the flame front. So, the simple geometry of the flame under consideration gives an easy method to determine the turbulent burning velocity. The main parameters studied are the turbulence intensity, as expressed by Reynolds number, and scale of turbulence as expressed by burner-gap width.

To determine the turbulent burning velocity, temperature and velocity distributions were measured by the same way as described in section 3.7.3. Because the flame under consideration is brushy, it is required to determine the mean radius of the flame brush at which turbulent burning velocity is considered. The mean radius of flame brush was taken as the mean radius of maximum temperature gradient through the flame brush.

Three gap widths are used, namely 3, 4 and 5 mm. With these gaps, eleven experimental tests are conducted at different excess air factors α (Actual air-fuel / theoretical air-fuel ratio) and Reynolds numbers, and these results are shown in Figs. 3.68 to 3.71.

Figure 3.68 shows the average temperature distribution for different conditions and Fig. 3.69 depicts a sample of the average temperature distribution, where:

R_1 : radius at the start of temperature rise,

R_2 : radius at maximum attained temperature, and

R_m : mean radius at maximum temperature gradient, $= 0.5 (R_1 + R_2)$.

The velocity at different heights and different radii is shown in Fig. 3.70 for gap width of 5 mm, $\alpha = 0.5$, and $Re_p = 658$. Because the velocity is not uniform over the gap width, an average velocity is obtained after integration, using Simpson's rule, at the mean radius of flame brush. The average turbulent burning velocity at different Reynolds numbers for different geometries is plotted in Fig. 3.71.

The Reynolds number for flow issuing from the gap between the two plates is given here as:

$$Re_p = \frac{U_o \delta}{\nu}$$

where:

U_o : mean flow velocity at burner exit.

δ : gap width.

ν : kinematic viscosity.

The results in Fig. 3.71 show that the turbulent burning velocity is significantly affected by the Reynolds number and the gap width. The results of this figure are used to find the variation of U_t in the form:

$$U_t = C \delta^a Re_p^b \quad (3.87)$$

where a and b are exponents, and C is a constant; all being empirically determined from the data. The exponent of (δ) is found by cross plotting the data of Fig. 3.71 of U_t for different gap widths at a given Reynolds number, and the results show that the exponent a , equals unity.

The values of the exponent b of Re_p in Eq. 3.87 are found by making log-arithmetic plot of the quantity U_t/δ , as a function of Re_p . The results are shown in Fig. 3.72.

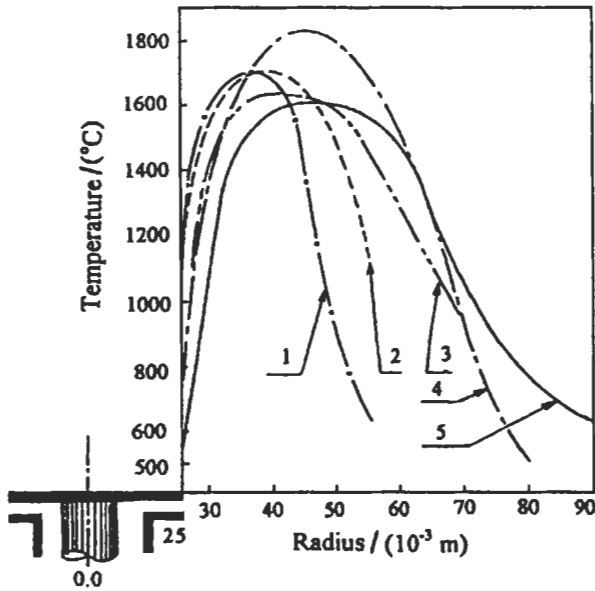


Fig. 3.68: Average temperature distribution (gap width, $\delta = 5$ mm and $\alpha = 0.5$) [531]. Curves (1), (2), (3), (4), and (5) for $U_o = 2.1$ m s⁻¹, 2.7 m s⁻¹, 3.4 m s⁻¹, 3.7 m s⁻¹, and 3.8 m s⁻¹, respectively.

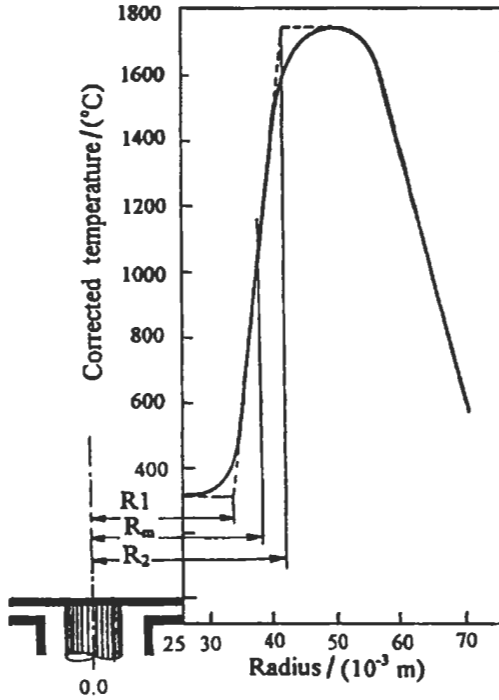


Fig. 3.69: Average temperature distribution. (gap width, $\delta = 3$ mm, $\alpha = 0.45$ and $U_o = 3.7$ m s⁻¹) [531].

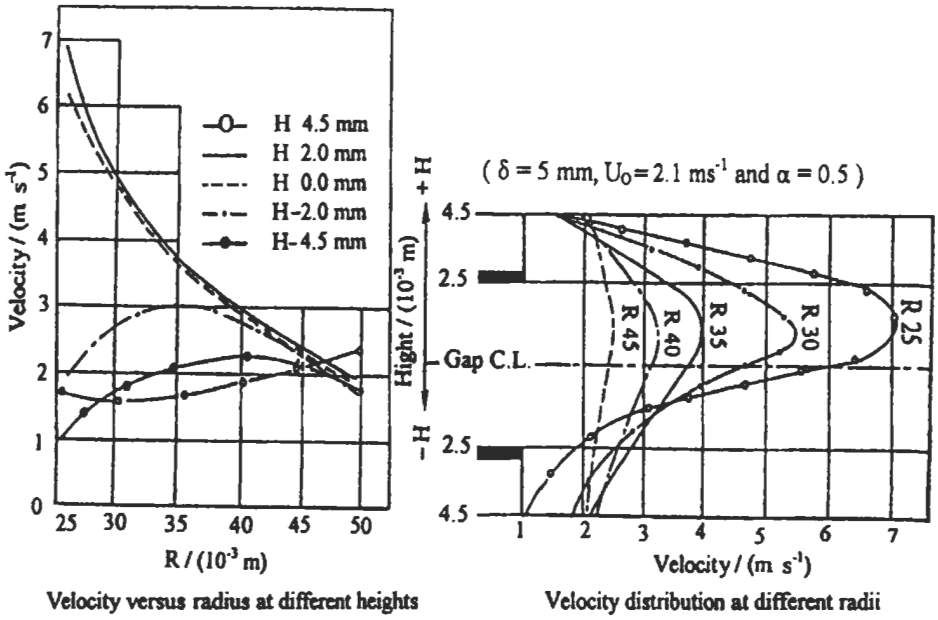


Fig. 3.70: Velocity distribution [531].

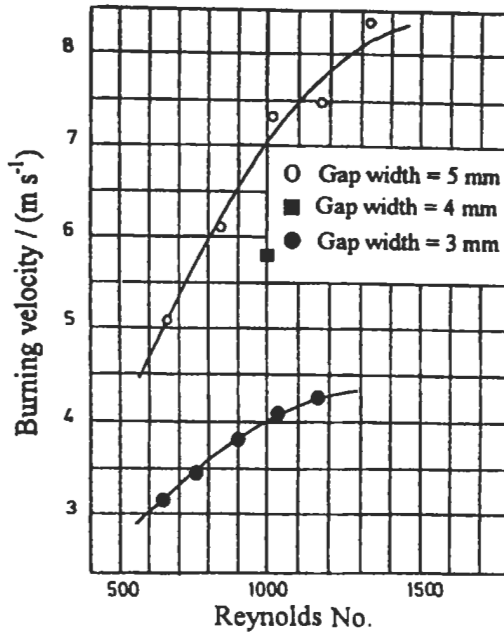


Fig. 3.71: Measured turbulent burning velocity [531].

The equation of the line in the figure is given by:

$$U_t / \delta = 0.01283 Re_p^{0.6769} \tag{3.88}$$

This leads to a turbulent burning velocity relation given by:

$$U_t = 0.01283\delta Re_p^{0.6769} \tag{3.89}$$

where δ is the gap width in mm and U_t in $m\ s^{-1}$.

Equation 3.89 shows that the turbulent burning velocity increases with increasing Reynolds number and, therefore, with increase of the intensity of turbulence, but not linearly. Also, the relation shows that the turbulent burning velocity increases with increasing gap width, and therefore with increase of mixing length.

The above results are compared with Damköhler [533] and Bollinger and Williams [536]. Damkohler studied turbulent burning velocity for open Bunsen type flames, and identified the ratio of U_t/U_1 with the ratio of the outer and inner surface areas of the turbulent flame by an argument which may not be valid as mentioned by Karlovitz [535]. The flame speed ratio was shown, by somewhat limited data, to vary linearly with the square root of Reynolds number for smaller tubes and linearly with large burner diameters. By the procedure adopted by Damköhler, U_t/U_1 reaches a value of 6, while El-Mahallawy et al [531] found that the value of U_t/U_1 is about 20 or more. However, the latter value is in general agreement with that given in Fig. 3.64 by Abdel-Gayed et al [550], and also with U_t/U_1 reaching a value of 30 given by Kobayashi et al [544].

The burning velocity of Eq. 3.89 agrees, qualitatively, with Bollinger work, i.e. U_t depends mainly on the intensity of turbulence represented by Reynolds number and on the scale of turbulence which is represented by the geometry of the burner (gap width or pipe diameter).

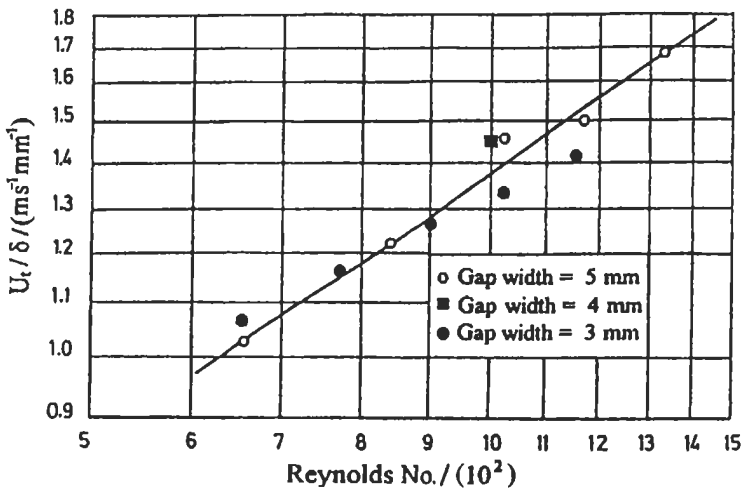


Fig. 3.72 : Variation of (U_t/δ) with Reynolds number [531].

3.8 Turbulent Free Diffusion Flames

3.8.1 Introduction

As noted in the discussion of laminar flame in chapter 2, when the velocity of the jet from a given burner reaches a certain value, the flame length remains essentially constant as the velocity is increased further. This behavior is one of the characteristics of turbulent diffusion flames.

The fact that the flame height is independent of volumetric flow rate means that the higher the jet velocity, the faster the oxygen from the surroundings is mixed with the fuel, so that the distance along the jet axis required for mixing of sufficient air to burn the fuel is more or less constant. This can be explained by assuming that the rate-determining process is the mixing of the reactants or eddy diffusion, since normally the eddy diffusivity is proportional to the jet velocity. It has been also found that the flame length measured in port diameter remains nearly constant for turbulent flames burning from ports of varying diameter. This can be considered a consequence of the fact that normally the eddy diffusivity is proportional to the characteristic dimensions of the flow system.

Turbulence of either combustion air or fuel is an important parameter that affects the mixing in furnaces and combustion chambers, and consequently improves the combustion efficiency and reduces pollution emission, and hence short flames can be achieved, as in the case of jet engine combustion chambers. Thus, the investigations of the flame length and flame structure of practical diffusion flames are important, and can be used to illustrate the completeness of combustion and flow field in which the reaction zone resides.

The following parts of this section present the theoretical calculation of flame height, and the effect of some parameters on the flame structure and height of turbulent diffusion flames. These parameters will involve the effect of buoyancy, relative angle between fuel and air jets, air swirl, and fuel-air ratio as well as the effect of some other operating parameters on turbulent diffusion flames. In addition, the flame structure of the lifted turbulent jet flame will be described using the laminar flamelet model approach.

3.8.2 Structure and Height of Diffusion Flames

Theoretical Calculation of Flame Height

Hawthorne et al [438] gave a summary of observations of various authors on the structure of turbulent jets emerging into a medium of similar density and viscosity. Three characteristics are emphasized:

1. The concentration of fluid from the jet at any point is independent of port diameter and velocity, if the coordinates are measured in port diameter (r/d , H/d), where r , d , and H are the radius, diameter, and height of the flame, respectively.
2. The ratio of concentration of jet fluid to the concentration of jet fluid on the axis of the jet at the same height varies with radial position in nearly the same way for all values of height, port diameter, and initial jet velocity.

3. The boundary of the jet, defined as the point where the concentration is a small constant fraction of the axial concentration at the same height, is an inverted circular cone.

For the treatment of the turbulent diffusion flame, i.e. of a fuel jet which undergoes a chemical reaction and produces heat as a result of mixing with the surrounding air, the above three characteristics have been retained, and the situation has been simplified further by assuming that the velocity and composition are constant over any cross-section of the flame jet, and change abruptly into the constant velocity and composition of the surrounding air. The flame height is then obtained by applying the laws of conservation of mass and momentum and equation of state as follows:

1. **Continuity.** The moles of port fluid leaving the burner equal the moles of port fluid which pass through any cross section of the jet, if moles of constituents, irrespective of chemical transformation, are always counted as unreacted. Therefore:

$$\pi r^2 U \rho \chi_N = \frac{\pi r^2 U M_0 P X_N \gamma}{RT} = \frac{\pi r^2 U M_0 P X \gamma}{RT X_0} = \pi r_0^2 U_0 \rho_0 = \frac{\pi r_0^2 U_0 M_0 P}{RT_0} \quad (3.90)$$

where r is radius of the jet at some height H , U is velocity, ρ is density, T is the temperature, χ_N is the mass fraction of jet port fluid, X_N , is the mole fraction of port fluid counted as unreacted (χ_N , X_N are equal to 1 at the burner port), M_0 is molecular weight of port fluid in the unreacted state, X is mole fraction of fuel, counted as unreacted, and γ is moles of reactants per moles of product; all values without subscript are averages at the height H ; while the subscript 0 refers to burner port conditions.

2. **Momentum law.** No forces acting, i.e. the momentum of the jet is constant:

$$\pi r^2 U^2 \rho = \pi r_0^2 U_0^2 \rho_0 \quad (3.91)$$

3. **Equation of state.** The ideal gas law is written for the varying composition as,

$$\frac{\rho}{\rho_0} = \left[\frac{X}{X_0} + \frac{M_\infty}{M_0} \left(1 - \frac{X}{X_0} \right) \right] \frac{\gamma T_0}{T} \quad (3.92)$$

where M_∞ is the molecular weight of the surrounding air.

At the height where the combustion is just completed, it is assumed that the temperature, T , is the adiabatic flame temperature, T_s , the mole fraction that of the stoichiometric mixture is X_s , and the density that of the stoichiometric mixture at T_s is ρ_s . Equations 3.90 and 3.91 can each be solved for $(U/U_0)^2$ and equated to each other to yield an expression for the jet radius. The maximum radius r_s , occurring at the height of completion of combustion is obtained as,

$$\frac{r_s}{r_0} = \frac{1}{X_s} \sqrt{\frac{\rho_0}{\rho_s}} = \frac{X_0}{X_s} \sqrt{\frac{\rho_s}{\rho_0} \left(\frac{T_s}{\gamma T_0} \right)} \quad (3.93)$$

$$\frac{r_s}{r_0} = \frac{X_0}{X_s} \sqrt{\left[\frac{X_s}{X_0} + \frac{M_\infty}{M_0} \left(1 - \frac{X_s}{X_0} \right) \right] \frac{T_s}{\gamma T_0}} \quad (3.94)$$

where X_s is the mass fraction of port fluid at this height.

The height H is obtained with the help of the assumption that the angle of spread of a flame jet is the same for all flames, i.e. $H = k_1 (2r)$, where k_1 is a constant, then:

$$\frac{H_s}{d} = k_1 \frac{X_0}{X_s} \sqrt{\left[\frac{X_s}{X_0} + \frac{M_\infty}{M_0} \left(1 - \frac{X_s}{X_0} \right) \right] \frac{T_s}{\gamma T_0}} \quad (3.95)$$

There is always some distance S above the port for which the flame appears free of turbulence. Since in that region, mixing probably occurs by molecular diffusion, and since molecular diffusion is a slower mixing process than eddy diffusion, it is assumed that little combustion occurs in this region, and Eq. 3.95 thus takes the following form:

$$\frac{H_s - S}{d} = \frac{k_1 X_0}{X_s} \sqrt{\left[\frac{X_s}{X_0} + \frac{M_\infty}{M_0} \left(1 - \frac{X_s}{X_0} \right) \right] \frac{T_s}{T_0 \gamma}} \quad (3.96)$$

The value of k_1 has been determined empirically from a graph in which the measured height of several flames was plotted versus the maximum flame radius calculated for the flames according to Eq. 3.94. The best value of the constant k_1 is 5.3. The assumed half angle of spread of the flames can be 5.4° . A more detailed comparison of Eq. 3.96 with experimental data is given in Table 3.2. Sawai et al [560] agreed that if air and fuel jets impinge on one another at right angles, the mixing is most efficient and the flame is very short in an open hearth furnace.

Another treatment of turbulent flames is based on the concept of eddy diffusivity ϵ which is defined as the product of mixing length and the intensity of turbulence, the latter being the root mean square of the velocity fluctuations. For fully developed turbulent flow inside the burner tube, the maximum value of the mixing length occurs at the axis and is approximately equal to $0.085 d$. The value of the intensity of turbulence at the axis of the tube is approximately equal to $0.03 U$. Thus the eddy diffusivity at the axis is given by [561]:

Table 3.2: Experimental and theoretical flame length for different fuels.

	H ₂	City gas	C ₃ H ₈	C ₂ H ₂
$[(H_s - S) / d]_{\text{cal}}$	152	101	300	205
$(H_s / d)_{\text{exp}}$	147	136	296	188
$(S / d)_{\text{exp}}$	2	6	-	11
$[(H_s - S) / d]_{\text{exp}}$	145	130	-	177
$[(H_s - S)_{\text{cal}} / (H_s - S)_{\text{exp}}]$	1.05	0.78	1	1.09

$$\varepsilon_e = 0.00255 U_0 d \quad (3.97)$$

Although this value is not in general applicable to a jet, a representative value for the turbulent flame may not be greatly different because as was shown from photographs, the burning zone forms a regular inverted cone and the main stream of fuel gas remains cylindrical in the flame for a longer distance from the nozzle than in an unignited jet. Therefore, the following expression is used:

$$\varepsilon_e = 0.00255 f U_0 d \quad (3.98)$$

where f is an arbitrary constant factor not greatly different from unity, and U_0 is the average gas velocity at the nozzle of the burner tube. Introduction of ε instead of D into Eq. 3.17 and substituting $(\pi d^2 U_0 / 4)$ for V results in:

$$L/d = 1/16(0.00255) f C_f \quad (3.99)$$

For city gas the equation becomes:

$$L/d = 1/0.00837 f \quad (3.100)$$

and for a mixture of 50% city gas in air it becomes:

$$L/d = 1/0.0187 f \quad (3.101)$$

Empirically, the data for the two gases are approximately represented by the following equations:

$$L/d = 1/(0.00775 + 3.8/U_0) \quad (3.102)$$

and

$$L/d = 1/(0.0132 + 3.23/U_0) \quad (3.103)$$

where U_0 is expressed in centimeters per second. In order to make the derived equations conform to the empirical equations, the following terms are introduced:

$$L/d = 1/[0.00837 f (1 + U_L/U_0)] \quad (3.104)$$

$$L/d = 1/[0.0187 f (1 + U_L/U_0)] \quad (3.105)$$

where U_L is an empirical constant. For the two gases (city gas and a mixture of 50 % city gas in air) f is 0.93 and 0.71, respectively, and U_L is very small, being 0.16 and 0.18 m s^{-1} , respectively.

The foregoing treatments are applicable to fuel jets discharged into an unlimited supply of air. They are therefore not immediately related to problems of combustion in furnaces. In common with the approach to the free jet problem, it is necessary to identify the origin of the mixed gas at any station in the furnace by calculating from the chemical analysis the fraction that came from the fuel port. In addition, the sample

should be evaluated in terms of completeness of mixing and combustion. In this way, it is possible to study experimentally the progress of mixing and combustion of the air and fuel streams throughout the volume of the furnace.

In the above study and early investigations [562-563] attempts were made of the simultaneous effects of jet momentum and buoyancy on mixing and combustion in turbulent jet diffusion flames, but no equations for the flame heights of either buoyancy controlled or buoyant jet momentum controlled flames were developed. Other studies utilized the simple diffusion model that is applied to laminar flames, and is developed by Hottel and Hawthorne [436] and Wohl et al [437]. They have developed an equation for the height of turbulent diffusion flames. Again, these theories neglected the effect of buoyancy. Becker and Liang [565] have developed an overall flame height model for the whole range of forced and natural convection conditions, taking into consideration the effect of buoyancy.

The effect of buoyancy, air swirl, relative angle between fuel and air as well as the effect of some other different parameters on the structure and height of turbulent diffusion flames will be described in the following parts.

Effect of Buoyancy

From the above discussion it could be noticed that the previous investigations have often supposed conditions to be very nearly the forced convection limit, while in fact they were quite far away. El-Mahallawy et al [566] have studied experimentally and theoretically the effect of different parameters on the turbulent free diffusion flame height, taking into account the effect of buoyancy in a region near the forced convection limit. In their calculation procedure, the equation of the flame height was obtained by combining the law of conservation of mass and the equation of momentum balance, taking the effect of buoyancy into consideration with the equation of state of gases. These calculations required the temperature profiles, obtained experimentally, and velocity profiles, obtained by applying the entrainment law. The main parameters which were thought to have significant effects on the flame height were considered as, the fuel-air ratio, burner geometry, and initial jet momentum. Also, they compared the calculated flame height with the visible flame height obtained by direct photography as well as the thermal height to the stoichiometric height.

The studied flame by El-Mahallawy [566] was issued from a small vertical burner with central air jet surrounded by a co-axial gaseous fuel jet. This burner is shown in Fig. 3.47 (a). The inner air tube diameter, d_1 , is 11.4, 9 mm and outside diameter d_2 of 16 mm, and the outer tube is a copper tube of inside diameter of 38 mm.

The inside diameter of the outer tube was changed by using sleeves of diameters (d_3) 20 and 30 mm. The fuel used is a mixture of butane and propane with ratios of 0.6 and 0.4 by mass, respectively.

The air jet and fuel jet combine, and the behavior of the compound jet can be predicted with good approximation from the combined mass flow rates and jet momenta. The value of the equivalent burner diameter d_0 for the compound jet was calculated by [491]:

$$d_0 = \frac{2(\dot{m}_c + \dot{m}_a)}{[\pi\rho(\dot{G}_c + \dot{G}_a)]^{0.5}} \quad (3.106)$$

where \dot{m}_c and \dot{m}_a are the mass flow rates of the central jet and the annular jet, respectively, while \dot{G}_c and \dot{G}_a are the respective momentum fluxes. The temperatures were measured by using a fine wire thermocouple and were corrected for radiation losses. These temperatures are shown in Fig. 3.73 for different burner geometries, F/A , and Reynolds numbers.

Flame height. To develop the equation for the height of the turbulent diffusion flame, in a region near the forced convection one ($1 < \xi_H < 4$, where ξ_H is the flame-zone Richardson ratio), the same procedure of Hawthorne et al [560], which was described in the previous section, was followed, but taking into account the effect of the buoyancy force and the variation of temperature and velocity in both radial and axial directions.

The parameter which serves as a measure of the importance of buoyancy is the Richardson number, $R_i = (\text{buoyancy})/(\text{input momentum flux})$. A characteristic measure of buoyancy in a flame as a whole is the value [567-568] of $g y^3 (\rho_\infty - \bar{\rho})$ at the flame tip, $y = H$, where g , y , ρ_∞ , and $\bar{\rho}$ are the gravitational acceleration, axial position, local density and average jet density, respectively, and H is the visible flame height. Since at the flame tip $\bar{\rho} \approx 0.2 \rho_\infty$, one can consider that $\rho_\infty - \bar{\rho} \approx \rho_\infty$. Thus, the buoyancy in a flame is reasonably represented by $g H^3 \rho_\infty$. The characteristic source momentum flux is exactly \dot{G}_0 . Thus, the flame Richardson ratio pertinent to the theory of flame height is appropriately defined as [565] $R_{iH} \approx \pi g \rho_\infty H^3 / 4 \dot{G}_0$. It was found, however, more convenient to use the cubic root of R_{iH} , denoted by ξ_H , which is a dimensionless representation of the flame height. Thus; $\xi_H = (\pi g \rho_\infty / 4 \dot{G}_0)^{1/3} H$, and consequently $\xi = (\pi g \rho_\infty / 4 \dot{G}_0)^{1/3} y$.

To get the temperature and velocity profiles at any axial distance, y , the temperature T at any radius r is divided by the temperature at centerline, T_c , and by plotting $\ln(T_c/T)$ against (r/y) for each run, as shown in Fig. 3.73, it was found that:

$$T/T_c = \exp(-30 (r/y)^{1.65})$$

This form is a good representation for the temperature distribution for of this study.

Because the mechanisms of transfer of momentum and mass are the same, there is always a similarity between radial profiles for the jet properties [491, 567] for both cold and burned jets such as temperature or concentration, velocity and momentum flux. So one can put the radial velocity profiles in the form:

$$U/U_c = \exp(-K_u (r/y)^{1.65})$$

where, U is y component of gas velocity and U_c is its value at the centerline. K_u is a profile shape factor, and it was determined by applying the entrainment law, which reads [565]:

$$\dot{m} = C_e \dot{m}_0 (\rho_\infty/\rho_0)^{0.5} y/d_0$$

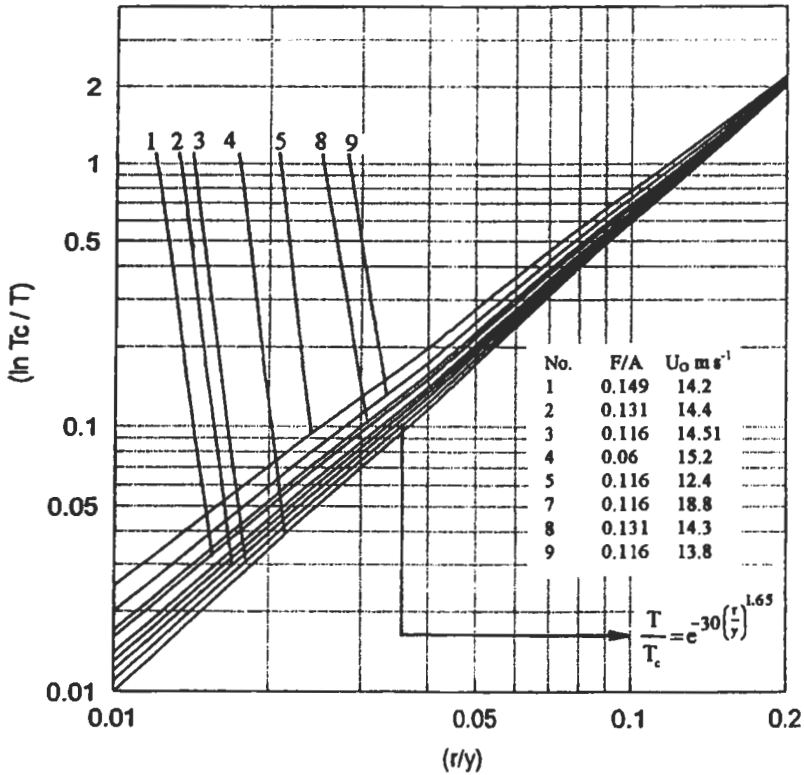


Fig. 3.73 : Temperature profile for a turbulent free diffusion flame ($1 < \xi_H < 4$). The numbers from 1 to 9 represent different conditions of the experimental runs [566].

where, the subscript 0 refers to the value at the burner exit and C_e is the mass entrained coefficient, and it is a function of (ξ), as was shown by Becker and Yamazaki [567].

The mass crossing the plane y, \dot{m} , is given by:

$$\dot{m} = \int_0^{r_j} 2\pi r \rho U dr$$

where, r is the radial position and r_j is a characteristic jet radius.

From the above equations and for the range of this study, it could be shown that K_u equals 31.2 and 47.5 for ξ equals 1.5 and 4, respectively.

The flame height equation is obtained by applying the continuity equation and making a local momentum balance with the equation of state of gases.

The continuity equation at the burner port and at a plane y, gives:

$$\int_0^{r_j} 2\pi r \rho U W dr = \pi r_0^2 U_0 \rho_0 \tag{3.107}$$

where, W is the mass fraction of the jet port fluid and U_0 is the equivalent burner velocity. With some substitutions, Eq. 3.107 could be solved to give:

$$U_j/U_0 = \frac{r_0^2}{2\phi_1 y^2} \frac{X_0}{X_c} \frac{T_c}{\gamma T_0} \quad (3.108)$$

where, γ is the mole of reactants per mole of products, ϕ_1 is a factor resulting from solving the integration of Eq. 3.107 against the different values of ξ , and X is the mole fraction of fuel counted as unreacted.

Equating the change in momentum from plane y to plane $y + dy$ to the force of buoyancy acting on the slice of jet of thickness, dy yields:

$$d\dot{G} = \pi r_j^2 (\rho_\infty - \rho_j) g dy \quad (3.109)$$

It was found, for $1 < \xi < 6$, that [542]

$$r_j/y = 0.16 \xi^{0.36} \quad \text{and} \quad \rho_j/\rho_\infty \approx 0.084 \xi$$

and since, by definition, $\zeta^3 = (\pi g \rho_\infty / 4 \dot{G}_0) y^3$, then $\zeta^2 d\zeta = (\pi g \rho_\infty / 4 \dot{G}_0) y^2 dy$ with these substitutions in Eq. 3.109, and by integrating both sides with $\dot{G} = \dot{G}_0$ at $\zeta = 0$ (i.e. $y = 0$), the following relation is obtained:

$$\dot{G} / \dot{G}_0 = 1 + 0.0275 \zeta^{3.72} (1 - 0.066 \zeta) \quad (3.110)$$

But the jet momentum (\dot{G}) can be calculated as:

$$\dot{G} = \int_0^{r_j} 2\pi r \rho U^2 dr \quad (3.111)$$

The solution of Eq. 3.111 gives:

$$\dot{G} = 2 \pi \phi_2 \rho_c U_c^2 y^2 \quad (3.112)$$

where, ϕ_2 is also a factor resulting from the integration of Eq. 3.111, against the different values of ζ .

Substituting for \dot{G} from Eq. 3.112 and for $\dot{G}_0 = \pi \rho_0 U_0^2 r_0^2$ into Eq. 3.110, gives:

$$\frac{U_c^2}{U_0^2} = \frac{r_0^2 \rho_0}{2\phi_2 \rho_c y^2} \left[1 + 0.0275 \xi^{3.72} (1 - 0.066 \xi) \right] \quad (3.113)$$

Through Eqs. 3.108 and 3.113, the following equation is obtained:

$$\frac{y}{d_0} = (5.3 - 0.89\xi) \frac{X_0}{X_c} \frac{T_c}{\gamma T_0} \left(\frac{\rho_c}{\rho_0} \right)^{0.5} \quad (3.114)$$

Putting $y = H_s$, $X_c = X_s$, $T_c = T_s$, $\rho_c = \rho_s$ and $\xi = \xi_{H_s}$ yield the following equation:

$$\frac{H_s}{d_0} = (5.3 - 0.89\xi_{H_s}) \frac{X_0}{X_s} \frac{T_s}{\gamma T_0} \left(\frac{\rho_s}{\rho_0} \right)^{0.5} \quad (3.115)$$

where, subscript, s , refers to the stoichiometric mixture and H_s is a chemical measure for the flame height based on considering the stoichiometric contour as the flame boundary.

Since from the equation of state:

$$\frac{\rho_s}{\rho_0} = \left[\frac{X_s}{X_0} + \frac{M_\infty}{M_0} \left(1 - \frac{X_s}{X_0} \right) \right] \frac{\gamma T_0}{T_s}, \quad \text{Then, Eq. 3.115 becomes:}$$

$$\frac{H_s}{d_0} = (5.3 - 0.89\xi_{H_s}) \frac{X_0}{X_s} \left[\left(\frac{X_s}{X_0} + \frac{M_\infty}{M_0} \left(1 - \frac{X_s}{X_0} \right) \right) \frac{T_s}{\gamma T_0} \right]^{0.5} \quad (3.116)$$

Neglecting the effect of buoyancy, Eq. 3.116 becomes:

$$\frac{H_s}{d_0} = 5.3 \frac{X_0}{X_s} \left[\left(\frac{X_s}{X_0} + \frac{M_\infty}{M_0} \left(1 - \frac{X_s}{X_0} \right) \right) \frac{T_s}{\gamma T_0} \right]^{0.5} \quad (3.117)$$

where the constant 5.3 is identical to that of Hawthorne et al [560] and this equation becomes the same as Eq. 3.96, while values of 5.2 and 5.13 were given by Refs. 561 and 562, respectively.

There is also a well-defined thermal measure to the flame height H_t . This thermal flame height is determined by the point at which the radial maxima of the mean temperature converge on the axis as shown in Fig. 3.74. Comparing this height H_t with the height H_s , indicated that the two quantities are quite identical.

In reality, the visible flame heights are, as might be expected, greater than H_s or H_t , and this is due to effects of turbulent eddying, billowing and undulation. Because of these erratic motions, the gases are everywhere imperfectly mixed, and so flaming gas is still observed at positions considerably further down-stream. So, the visible flame tip, as judged by photographs, is then the furthest down-stream point in the flame jet at which flame elements are seen with a significant frequency. The visible flame height, H_v , is thus inexactly defined.

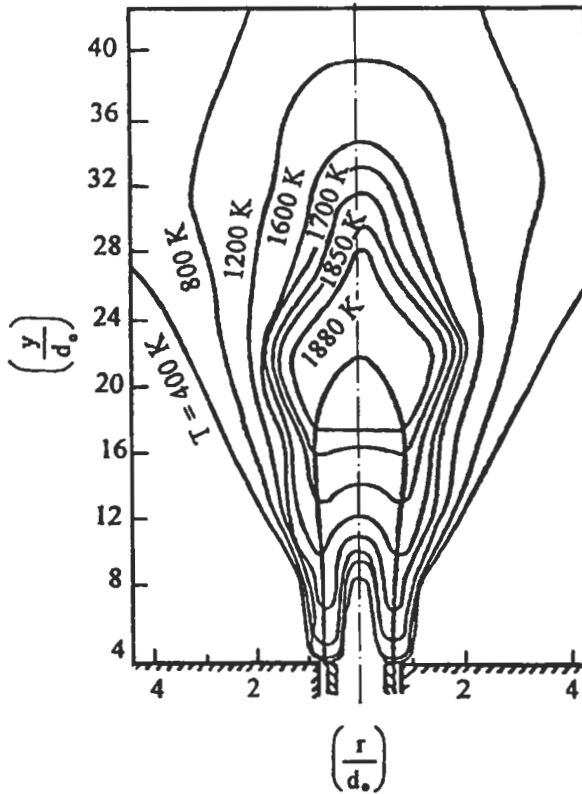


Fig. 3.74: Isothermal contours, $d_0 = 12.65$ mm. $Re = 12130$, and $F/A = 0.149$ [566].

For the relation between the flame heights H_v and H_s or H_t , another investigation [567] suggested that to a good approximation for flames in an atmosphere of cold air, $H_t/H_v = h(\xi_{H_t})$, where, $h \approx 1$ in the forced-convection limit, $\xi_{H_t} = 0$ and $h \approx 0.45$ when natural convection prevails, $\xi_{H_t} > 15$.

It was found that, the ratio of H_s/H_v is nearly constant ≈ 0.565 for the range of ξ_{H_t} studied here, i.e. $H_v/H_s \approx 1.77$ and consequently $\xi_{H_v}/\xi_{H_t} \approx 1.77$.

With the above substitution into Eq. 3.116, the equation for the visible flame height, H_v , is then:

$$\frac{H_v}{d_0} = (9.4 - 0.89\xi_{H_v}) \frac{X_0}{X_s} \left[\left(\frac{X_s}{X_0} + \frac{M_\infty}{M_0} \left(1 - \frac{X_s}{X_0} \right) \right) \frac{T_s}{\gamma T_0} \right]^{0.5} \tag{3.118}$$

Comparing the visible flame height calculated from Eq. 3.118 with the corresponding photographs, it can be concluded that this equation is a very good representation of the visible flame height. Figure 3.75 shows this comparison.

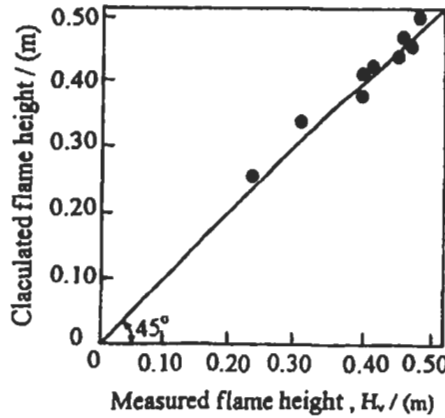


Fig. 3.75: Comparison between calculated and experimental flame heights [566].

Now, comparing Eq. 3.117 with Eq. 3.118, it could be noticed that the constant in Eq. 3.117, in fact, represents an average for experimental data in a range of ξ_H going well outside the neighbourhood of $\xi_H = 0$. A value of $\xi_H = 4.6$ makes Eq. 3.118 coincide with Eq. 3.117.

Flame envelope. An equation for the stoichiometric envelope was derived by dividing Eq. 3.115 by Eq. 3.114 and substituting for $X_c/X_s = T_c/T_s$ and $\rho_s/\rho_c = \exp(-30(r/y)^{1.65})$. This equation gives:

$$r_s = 0.19 y \left[\ln \left(\frac{5.3 - 0.89\xi}{5.3 - 0.89\xi_{H_s}} \right) \left(\frac{H_s}{y} \right) \right]^{0.61} \tag{3.119}$$

Equation 3.119 for the stoichiometric contour can be used to determine the visible flame envelope by putting r_v , H_v and ξ_{H_v} instead of r_s , H_s and ξ_{H_s} , respectively, thus:

$$r_v = 0.19 y \left[\ln \left(\frac{5.3 - 0.89\xi}{5.3 - 0.89\xi_{H_v}} \right) \left(\frac{H_v}{y} \right) \right]^{0.61} \tag{3.120}$$

A comparison between the flame envelope obtained by applying this equation and the corresponding photographs, shows that the two envelopes are similar in shape with some enlargement in the calculated one as shown in Fig. 3.76.

Effect of different parameters. For the effect of the different parameters on the flame height, it can be concluded that the flame height is proportional to both the fuel-air ratio and to the equivalent burner diameter while the Reynolds number has insignificant effect.

As shown in Fig. 3.77, the relation between the flame height and fuel-air ratio is linear. This is in accordance with the results on confined diffusion gaseous flame by

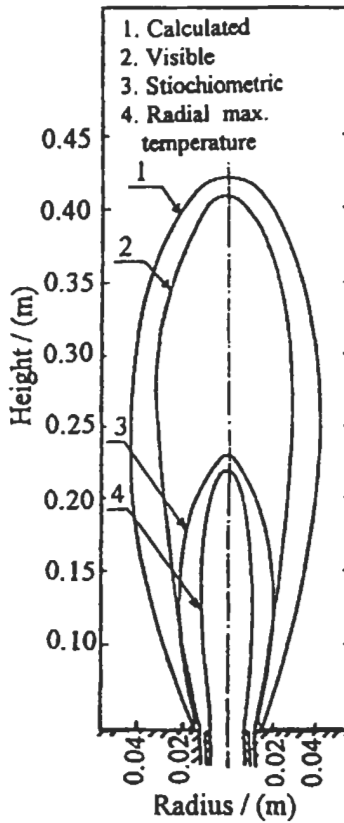


Fig. 3.76: Comparison between different flame envelopes, $Re = 12130$, and $F/A = 0.116$ [566].

Lockwood et al [569]. The results obtained in Fig. 3.78 show the insensitiveness of the flame height to a change in burner port velocity (or Reynolds number). A change in burner velocity from 8.5 to 19 m s^{-1} (or Reynolds number from 7200 to 15700) results in an increase in flame height from 0.38 to 0.43 m which is a relatively small change compared with the effect of other parameters. As concerns the effect of burner dimensions, Fig. 3.79 shows that increasing the equivalent burner diameter leads to a significant increase in the flame height.

Effect of Relative Angle Between Fuel and Air Jets

Ibrahim and EL-Mahallawy [570] have investigated experimentally and computationally the structure and height of a turbulent free diffusion flame issued from a vertical burner. The main parameters considered are the relative angle between fuel and air jets, air-fuel ratio, burner-geometry, and fuel and air momenta. Both temperature distributions and concentrations of CO_2 and O_2 were measured. The above mentioned theory [566] of the flame height was developed further to include the relative angle between fuel and air jets, taking into account the effect of buoyancy force near the forced convection region.

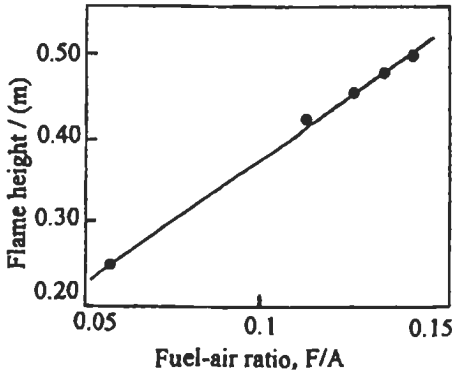


Fig. 3.77: Effect of fuel-air ratio on flame height [566].

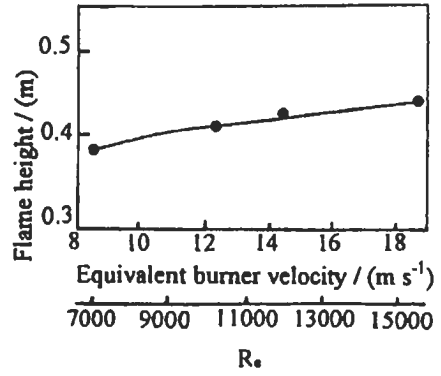


Fig. 3.78: Effect of equivalent burner velocity (or Reynolds number) on the flame height [566].

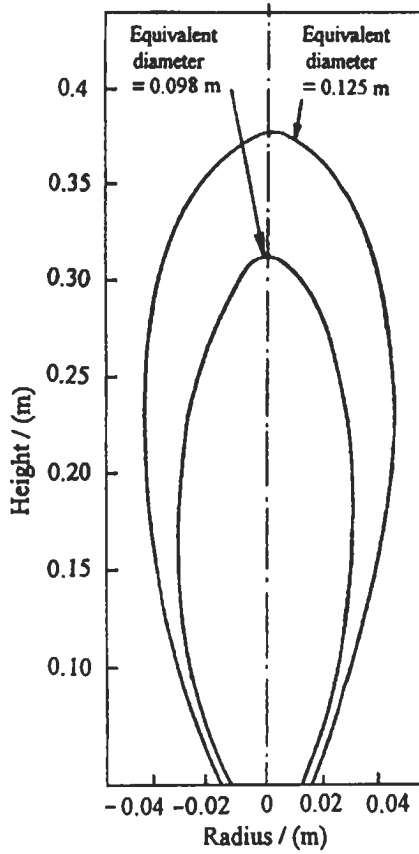


Fig. 3.79: Effect of the equivalent burner diameter on the flame height [566].

Their experiments were conducted on three vertical burners with angles, θ , between the fuel and air jets, of 0° , 30° , and 60° . Figure 3.80 shows the burner heads for $\theta = 0^\circ$ and 60° . Each burner has two parts, a fixed inner part, which has a concentric inner air jet and a movable outer part which has an annular fuel jet. The fuel was a commercial butane which is a mixture of butane and propane of volumetric analysis of 0.9 and 0.1, respectively. The value of the compound jet diameter, d_0 , for the compound jet was calculated by Eq. 3.106. Gas temperatures were measured by fine wire thermocouple and were corrected for radiation errors. The visible flame height, H_v , was obtained as an average value of a number of photographs taken for the flame, while, the thermal flame height, H_t , was determined from the maximum temperature at the flame centerline. Also, the chemical flame height (H_{ch}) was obtained from the position of maximum centerline CO_2 concentration. The mean measured temperatures at the flame centerline are plotted at different axial distances in Fig. 3.81. Shown also on Fig. 3.81 are the corresponding values of H_t and H_v/H_t .

Figure 3.82 shows the effect of θ on the axial distance for maximum temperature. It is shown that as θ increases, the location of the centerline maximum temperature moves towards the burner exit due to good mixing between the reactants. Measured isothermal contours are shown in Fig. 3.83. The measured concentrations of CO_2 on centerline for different axial distances are shown in Fig. 3.84. In this figure, the chemical flame height, H_{ch} , is also shown and it was found from the position of maximum CO_2 concentration on centerline.

The stoichiometric flame height, H_s , for coaxial flow ($\theta = 0^\circ$) may be calculated from Eq. 3.116 and can be related to the chemical flame height, H_{ch} , as obtained experimentally for different values of θ . From Fig. 3.82 the relation between H_{ch}/H_s and θ could be represented by the following straight line equation [570]:

$$H_{ch}/H_s = 1 - 0.052 \theta \quad (3.121)$$

Substitution of Eq. 3.117 into Eq. 3.121 gives:

$$\frac{H_{ch}}{d_0} = [5.3 - \xi_{H_t} (0.89 - 0.0463\theta) - 0.276\theta] \frac{X_0}{X_s} \left[\left(\frac{X_s}{X_0} + \frac{M_\infty}{M_0} \left(1 - \frac{X_s}{X_0} \right) \right) \frac{T_s}{\gamma T_0} \right]^{0.5} \quad (3.122)$$

When values of H_{ch} plotted against H_t for the different experimental conditions, it was found that the two values are identical.

Following the same procedure described previously by EL-Mahallawy et al [566], the visible flame height can be calculated by [570]:

$$\frac{H_v}{d_0} = [10.6 - \xi_{H_v} (0.89 - 0.0463\theta) - 0.552\theta] \frac{X_0}{X_s} \left[\left(\frac{X_s}{X_0} + \frac{M_\infty}{M_0} \left(1 - \frac{X_s}{X_0} \right) \right) \frac{T_s}{\gamma T_0} \right]^{0.5} \quad (3.123)$$

A comparison between the calculated visible flame height from Eq. 3.123 with that measured, is shown in Fig. 3.85. This figure indicates clearly that the above equation is a good representation of H_v .

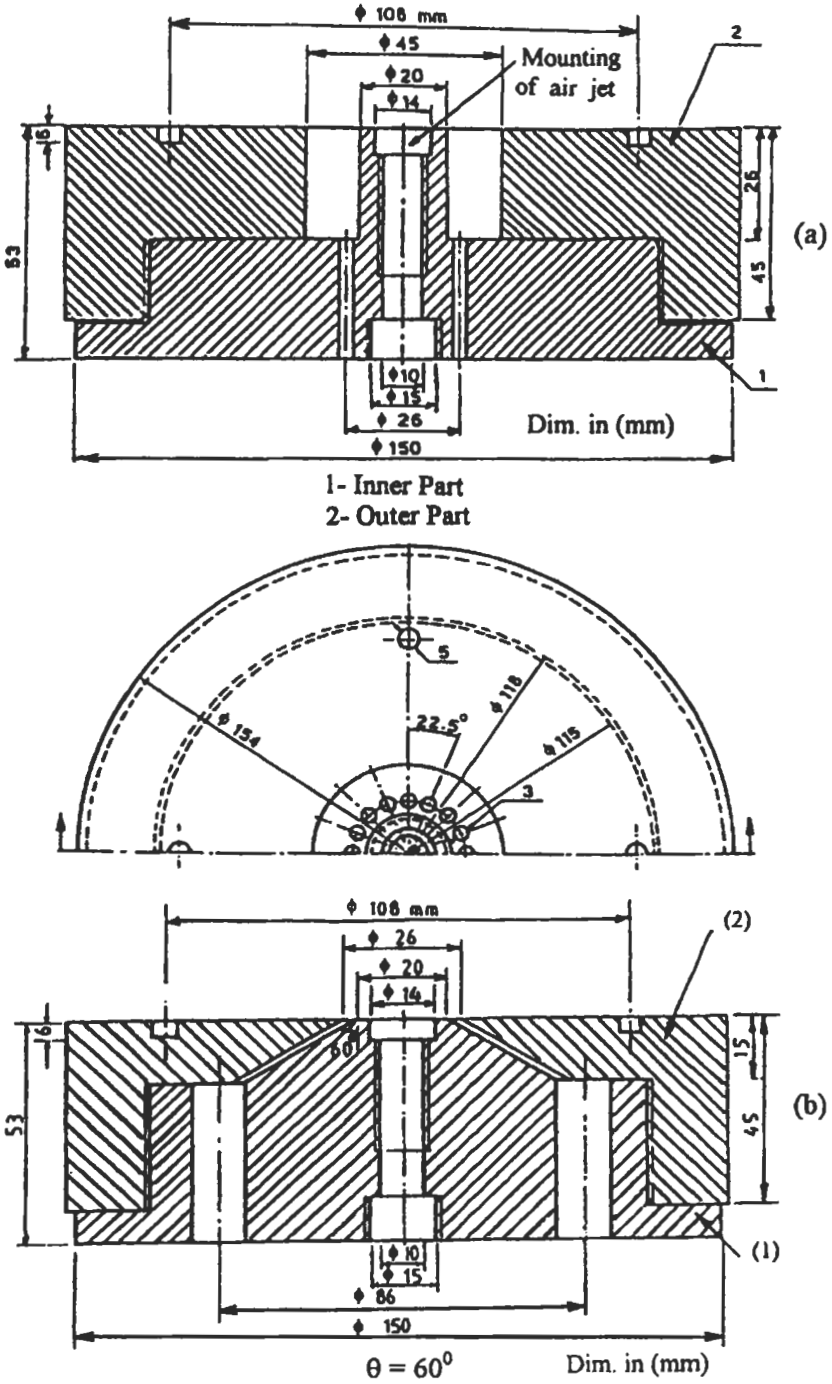


Fig. 3.80: Burner head (a) for $\theta = 0^\circ$ and (b) for $\theta = 60^\circ$ [570]. Reproduced by permission of Elsevier Science.

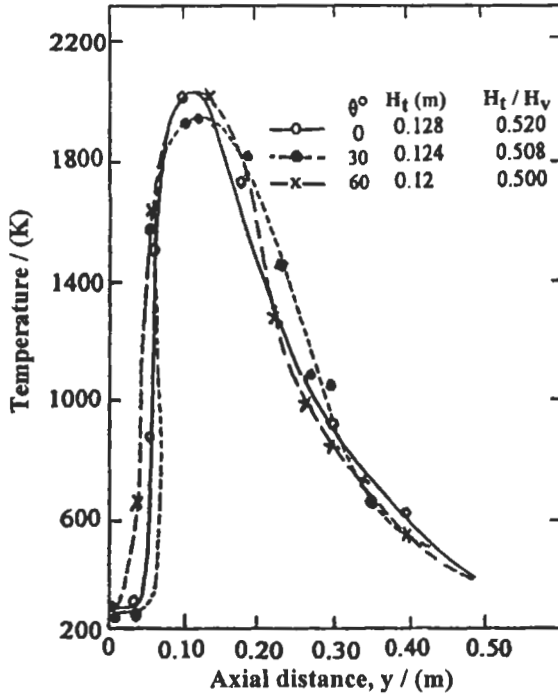


Fig. 3.81: Effect of θ on the temperature distribution on centerline, $A/F = 11.67$ and $U_o = 11.95 \text{ m s}^{-1}$ [570]. Reproduced by permission of Elsevier Science.

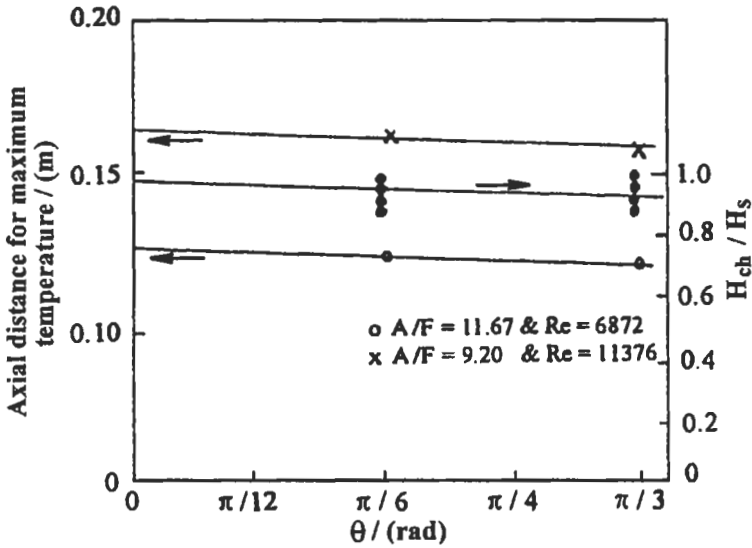


Fig. 3.82: Effect of θ on axial maximum temperature position and on H_{ch}/H_s [570]. Reproduced by permission of Elsevier Science.

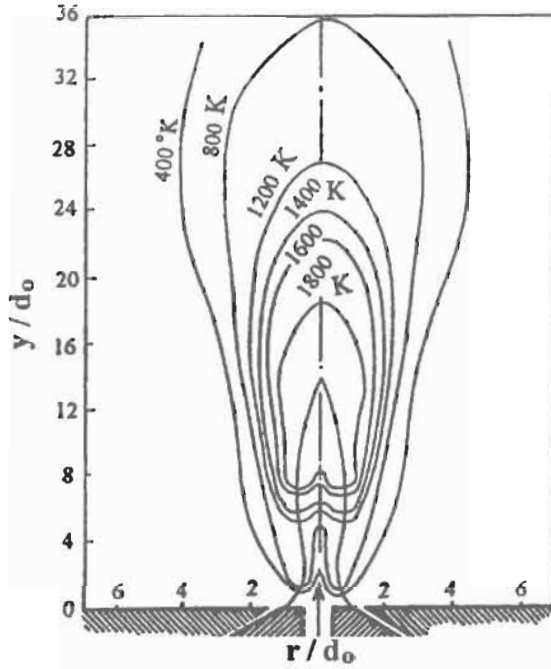


Fig. 3.83: Isothermal contours for $A/F = 11.67$, $U_o = 11.95 \text{ m s}^{-1}$ and $\theta = 60^\circ$ [570]. Reproduced by permission of Elsevier Science.

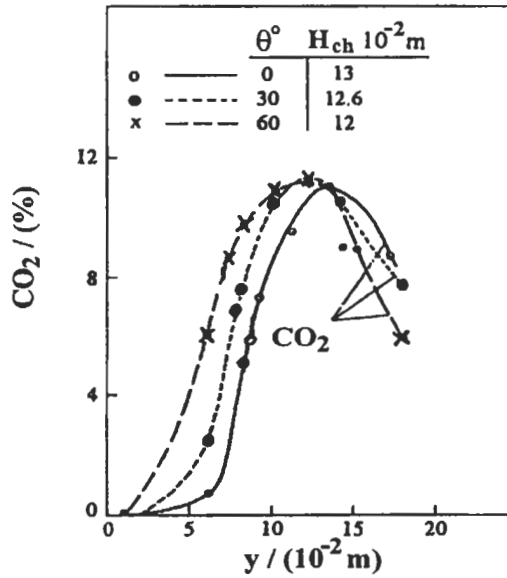


Fig. 3.84: Concentration of CO_2 on centerline for different axial distances, $A/F = 11.67$ and $U_o = 11.95 \text{ m s}^{-1}$ [570]. Reproduced by permission of Elsevier Science.

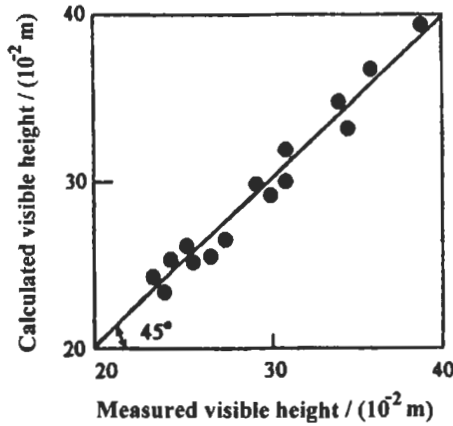


Fig. 3.85: Comparison between predicted and measured H_v [570]. Reproduced by permission of Elsevier Science.

The above results show that the flame height decreases as θ increases. This occurs as a result of the good mixing of fuel and air streams issuing from the intersecting jets of the burner. However, θ has a little effect on H_{ch} and H_v . This may be due to the small momentum of the fuel stream from the inclined annular space as compared with the momentum of the air stream from the inner jet. Figure 3.86 shows the effect of air-fuel ratio on both H_{ch} , and H_v , it is seen that the relation is linear. The results show that the flame height decreases significantly as the air-fuel ratio increases. This confirms the previous finding by EL-Mahallawy et al [566].

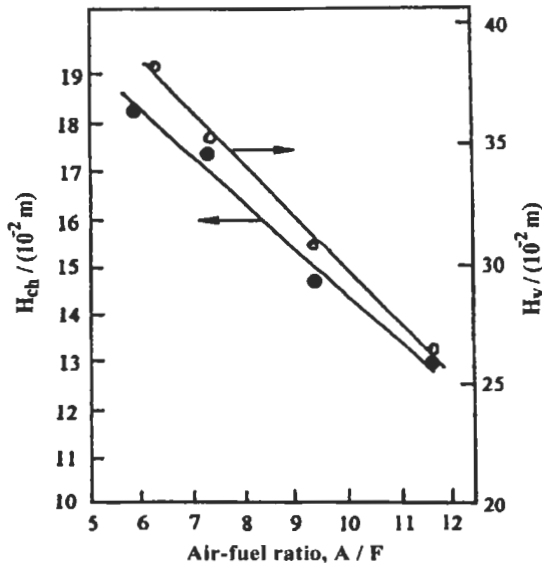


Fig. 3.86: Effect of air-fuel ratio on H_v and H_{ch} [570]. Reproduced by permission of Elsevier Science.

Figure 3.87 shows the comparison between the above results and those from Becker and Liang [565]. In this figure the value of ψ is plotted against ξ_{H_v} , where the flame height equation of Becker and Liang [565] reads:

$$\psi = 0.18 + 0.022 \xi_{H_v} \tag{3.124}$$

where $\psi = d_c \beta / (H_v W_s)$, d_c is the effective jet diameter which equals $d_0 (M/M_\infty)^{0.5}$, $\beta = (M_\infty T_s / M_s T_\infty)^{0.5}$ and W_s is the mass fraction of the jet port fluid. The values of ψ obtained by El-Mahallawy et al [570] is represented by:

$$\psi = (1 / (10.6 - 0.89 \xi_{H_v}))^{2/3} \tag{3.125}$$

The results from Eqs. 3.124 and 3.125 are compared and shown in Fig. 3.87. This comparison indicates satisfactory agreement between the results.

Effect of Air Swirl

As mentioned before, the swirl imparted to combustion air is one of the most important parameters that affect mixing and flow patterns in furnaces to enhance the performance of combustion systems. Also, the swirl can induce recirculation and so control the length of the flame. Therefore, EL-Mahallawy et al [571] have investigated the effect of the intensity of swirl of combustion air on the structure of turbulent free diffusion flames. They used a small vertical burner similar to that used by Ref. 471. It consists of a central air jet surrounded by co-axial fuel jet. Four degrees of swirl namely 0° , 30° , 45° and 60° which correspond to swirl number, S , 0, 0.57, 1 and 1.73, respectively were applied to the central combustion air jet. Measurements of temperature and concentration of CO_2 , CO and O_2 , were carried out at different points in the flame with and without swirl.

The effect of swirl on the thermal and chemical flame height and flame boundary was investigated. General relations based on the theoretical study and experimental data were obtained between the flame height, the swirl number of combustion air, and the equivalent burner diameter.

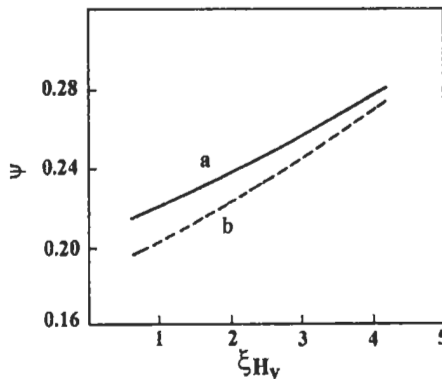


Fig. 3.87: Comparison between the flame height (curve a from Eq. 3.125) [570] and that of Becker and Liang [565] (curve b, Eq. 3.124). Reproduced by permission of Elsevier Science.

Results of temperature distributions, with swirl number $S = 1.73$, in the radial direction for different axial distances, are shown in Fig. 3.88. The figure shows that, the maximum temperature of the flame occurs at/or near the centerline. For sections close to the burner rim, the temperature drops suddenly from high values at centerline to relatively low values at radial distances close to the centerline. Higher temperatures occurring near the burner rim in these flames are attributed to recirculation of hot gases to the entry of fuel and air streams which has a marked effect on mixing and heating of these streams and hence on the characteristics of heat liberated by combustion.

Results of the isothermal contours are shown in Figs. 3.89 and 3.90. Immediately downstream from the burner, for zero swirl, there is a potential core, of length about 4 to 5 equivalent jet diameter. For swirling flames, there is no potential core due to the fast chemical reaction and good mixing occurring on the burner rim. Experimental results were obtained for the concentration profiles of CO_2 , CO , and O_2 across the flame at different axial distances. Profiles of CO_2 are only considered in this discussion. The chemical contours for zero and 60 degrees of swirl are shown in Figs. 3.91 and 3.92, respectively.

For zero swirl and for sections close to the burner exit, the concentration of CO_2 inside the flame surface increases from zero value on the centerline to a certain maximum value, and then decreases to zero again. For swirling flames, the concentration of CO_2 , for $S = 1.73$, is higher as compared to the zero swirl flame and takes place in cross sections close to the burner rim due to high reaction intensity in this region. For cross sections very near to the burner exit the concentration of CO_2 is rapidly decreased as moving from the flame axis, but for higher cross sections, slight changes are observed. The two photographs in Plate 3.3 for the same swirl numbers, $S = 0$ and $S = 1.73$, show how the flame shape and dimensions are significantly affected by swirl applied to combustion air.



(a) $S = 0$, $A / F = 15.5$



(b) $S = 1.73$, $A / F = 15.5$

Plate 3.3: Direct flame photograph [571].

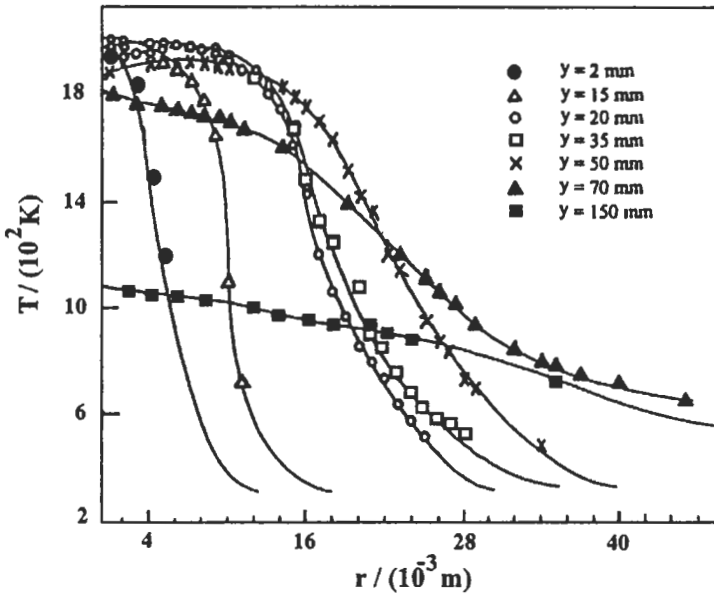


Fig. 3.88: Temperature distribution for different axial distances, $S = 1.73$ [571].

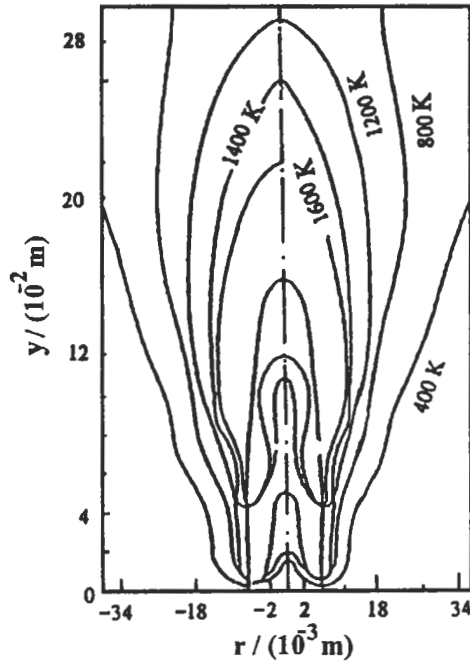


Fig. 3.89: Isothermal contours for $S = 0$ [571].

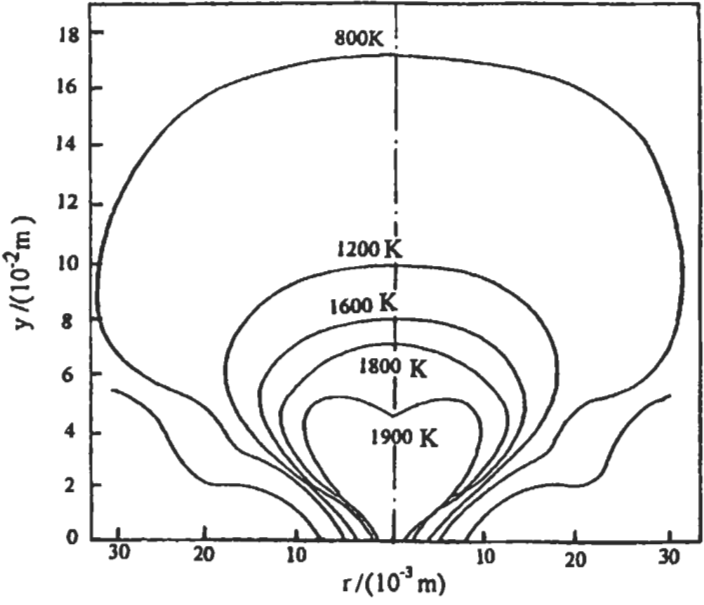


Fig. 3.90: Isothermal contours for $S = 1.73$ [571].

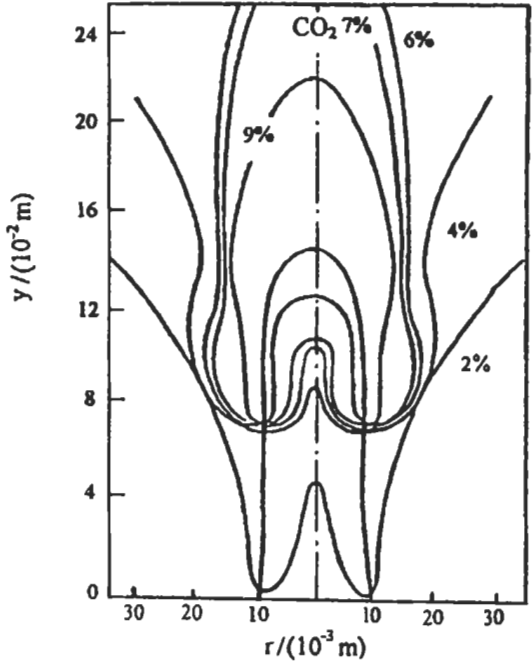


Fig. 3.91: Chemical contours of CO_2 for $S = 0$ [571].

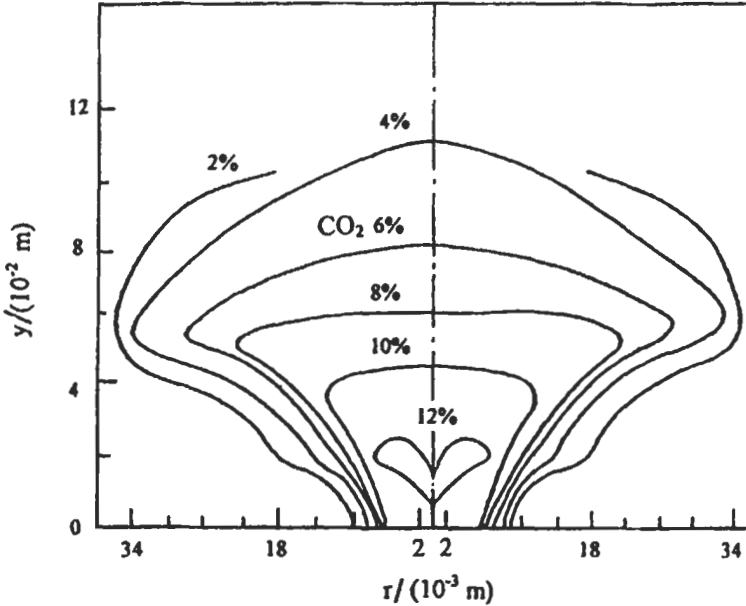


Fig. 3.92: Chemical contours of CO₂ for S = 1.73 [571].

Figure 3.93 shows the effect of swirl number on both thermal and chemical flame heights. The thermal flame height is defined as the distance from the burner exit to the point of maximum temperature on the centerline, while the chemical flame height is determined by the point of maximum CO₂ on the centerline. From Fig. 3.93, it is clear that with increasing the swirl number, the flame height significantly decreases. It is clear from this figure that the two heights are nearly the same. The following relations between the flame height and swirl number are obtained:

$$H_{ch_s}/H_{ch_0} = \exp(-2.25 S) \quad \text{for } 0 < S < 1 \quad (3.126)$$

where, H_{ch₀} is the chemical height for S = 0

$$H_{ch_s}/H_{ch_0} = 0.128 - 0.023 S \quad \text{for } S > 1 \quad (3.127)$$

Figure 3.94 shows the thermal and chemical boundaries are nearly the same. It was also found that the flame size decreases with increase of swirl intensity. To obtain general equations for the flame height taking into consideration the effect of degree of swirl or the swirl number, the flame height obtained experimentally for 30°, 45°, and 60° swirl is related to that height for zero swirl.

From Eq. 3.117 (for zero swirl) and Eqs. 3.126 and 3.127 given before, the following general flame height equations are obtained:

$$\frac{H_{ch_s}}{d_0} = 5.3 \exp(-2.25S) \frac{X_0}{X_s} \left[\left(\frac{X_s}{X_0} + \frac{M_\infty}{M_0} \left(1 - \frac{X_s}{X_0} \right) \right) \frac{T_s}{\gamma T_0} \right]^{0.5} \quad \text{for } 0 < S < 1 \quad (3.128)$$

$$\frac{H_{chs}}{d_0} = (0.68 - 0.122S) \frac{X_0}{X_s} \left[\left(\frac{X_s}{X_0} + \frac{M_\infty}{M_0} \left(1 - \frac{X_s}{X_0} \right) \right) \frac{T_s}{\gamma T_0} \right]^{0.5} \text{ for } S > 1 \quad (3.129)$$

The above relations could also be applied for the thermal flame height.

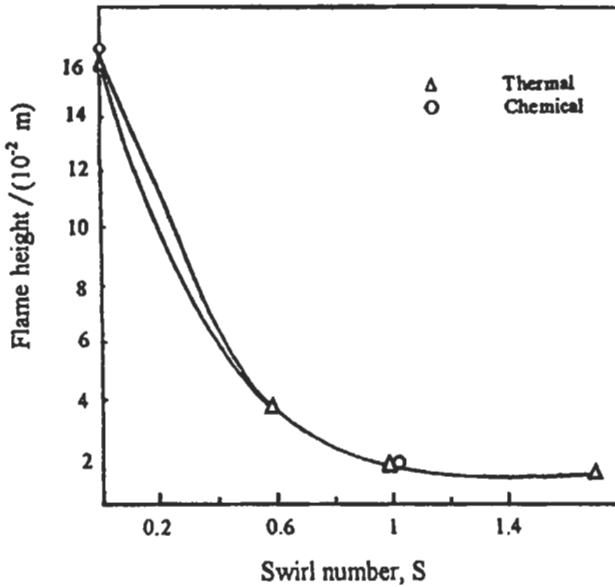


Fig. 3.93: The effect of swirl on chemical and thermal flame heights [571].

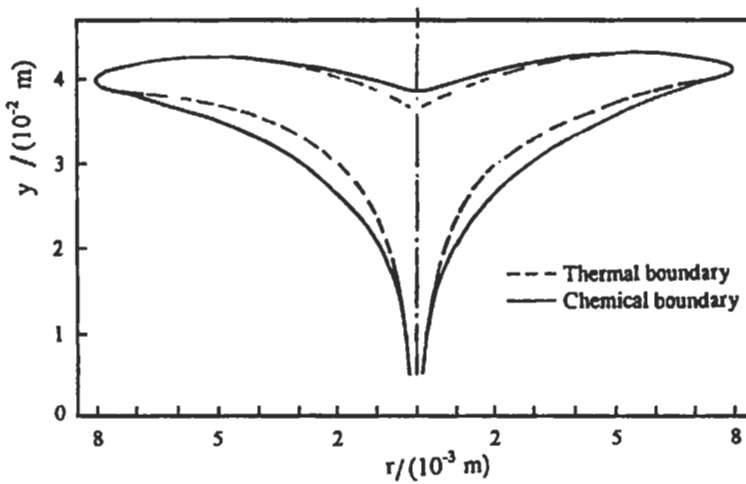


Fig. 3.94: Comparison between thermal and chemical boundaries for $S = 0.57$ [571].

Structure of Vertical Flat Free Flames

Although flat diffusion flames are quite technically important (most of the domestic gas water heaters use such flames), very few experiments exist which report on this type of flames [572-575]. Mahdi Ali et al [576] have carried out experimental tests on a vertical flat free diffusion flame. In their investigation the main parameter considered was the input air-fuel ratio to the burner. The effect of this parameter on the flame characteristics, shape and height was investigated. The test burner, shown in Fig. 3.95, consists mainly of three vertical ducts separated by thin septa for passing air and fuel to atmosphere. Commercial butane (L.P.G) as a fuel is fed as single or double jet from the outer ducts and the combustion air is fed from the middle duct, and a double flat flame is shown in Plate 3.4. The composition of the flame gases within the flame zone was measured using a tapered quartz micro probe, and the sampling probe is connected to infrared gas analyzers for measuring carbon dioxide and carbon monoxide concentration and to a paramagnetic oxygen analyzer for measuring oxygen concentration. The flame temperature was measured using a fine wire thermocouple.

It should be noted that the flat burner geometry allows most of the air issuing from the burner rim not to take place in the reaction when fired in free atmosphere. This clarifies the very high values of the input air-fuel ratio used in this study compared with conventional confined diffusion flames. This has the advantage of using this type of burners as a hot air generator for the industrial drying processes.

Results are presented here for the time average flame temperature and the time average concentration of the flame gases. The results include also a comparison between different flames, which are characterized by the flame height.

In all tests reported here, the air-fuel ratio was varied through the variation of the mass flow rate of the fuel jet keeping the mass flow rate of the air jet constant. This was done in order to keep approximately constant total jet momentum of the burner.

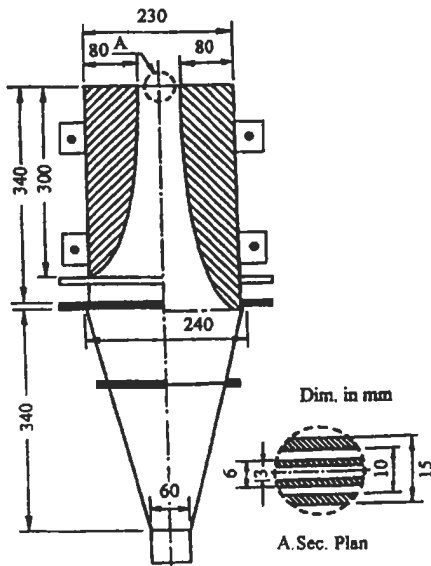


Fig. 3.95: Test burner [576].



Plate 3.4: Direct flame photograph [576].

Samples of the time average temperature distribution and the isothermal contours in the flame for single and double fuel jet arrangements are shown in Figs. 3.96 and 3.97, respectively. The maximum flame temperature in all tests was found to be slightly above 1600 °C. The height above the burner rim at which this maximum temperature occurs is quite different and depends on the input air-fuel ratio as it is clear from the isothermal contours. The comparison of the isothermal contours with the direct flame photograph, Plate 3.4, shows a good similarity in shape between the two.

Samples of the oxygen distribution and its constant concentration contours in the flame for the case of single fuel jet arrangement are shown in Fig. 3.98. The constant concentration contours are nearly of similar character and shape as the isothermal contours and the direct flame photographs. The results show that the core of the oxygen contours corresponds to low concentration values.

The comparison between the isothermal contours, the constant concentration contours and the direct flames photographs shows for both single and double fuel jet arrangements that there is a proportionality relation between the visible flame height, the thermal flame height and the chemical flame height. The ratio between chemical and thermal flame heights is about 0.88 at all input air-fuel ratios for both arrangements.

A comparison between visible, thermal and chemical flame heights at different input air-fuel ratios and for the different arrangements is shown in Fig. 3.99. In the case of single fuel jet, the ratio of visible flame height to thermal flame height varies between 1.39 to 1.15 as the air-fuel ratio increases from 66.7 to 170. The ratio of visible flame height to chemical flame height in this case varies between 1.59 to 1.28. In case of double fuel jet arrangement, the ratio of visible flame height to the thermal flame height varies between 1.15 to 1.07 as the air-fuel ratio increases from 33.3 to 85. The ratio of visible flame height to chemical flame height in this case varies between 1.44 to 1.2.

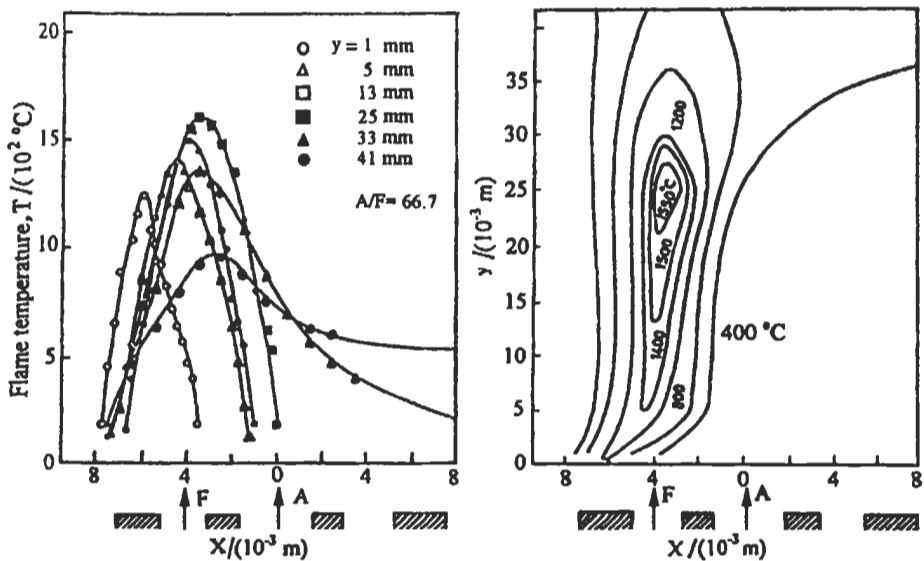


Fig. 3.96: Temperature distribution and isothermal contours for single fuel jet arrangement. Input air-fuel ratio= 66.7 [576].

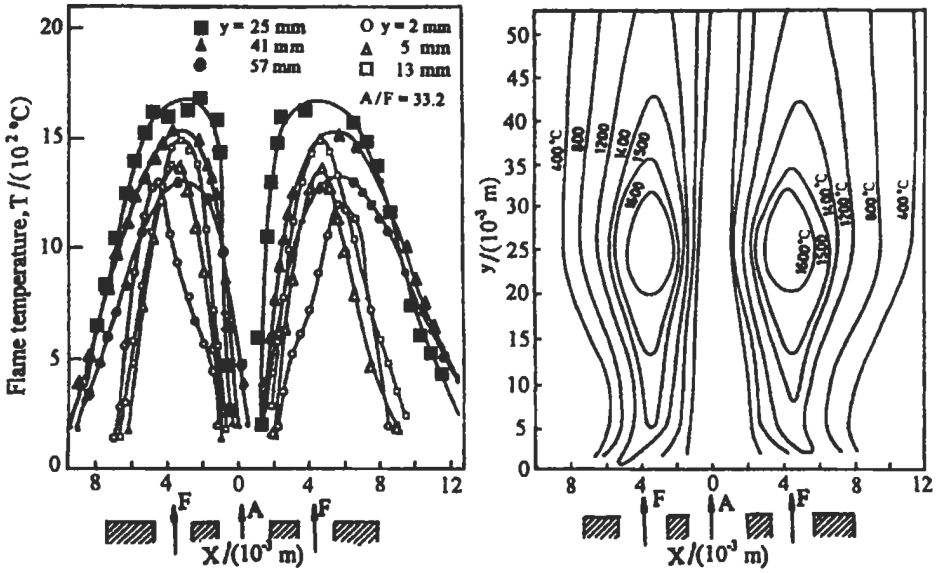


Fig. 3.97: Temperature distribution and isothermal contours for double fuel jet arrangement. Input air-fuel ratio = 33.2 [576].

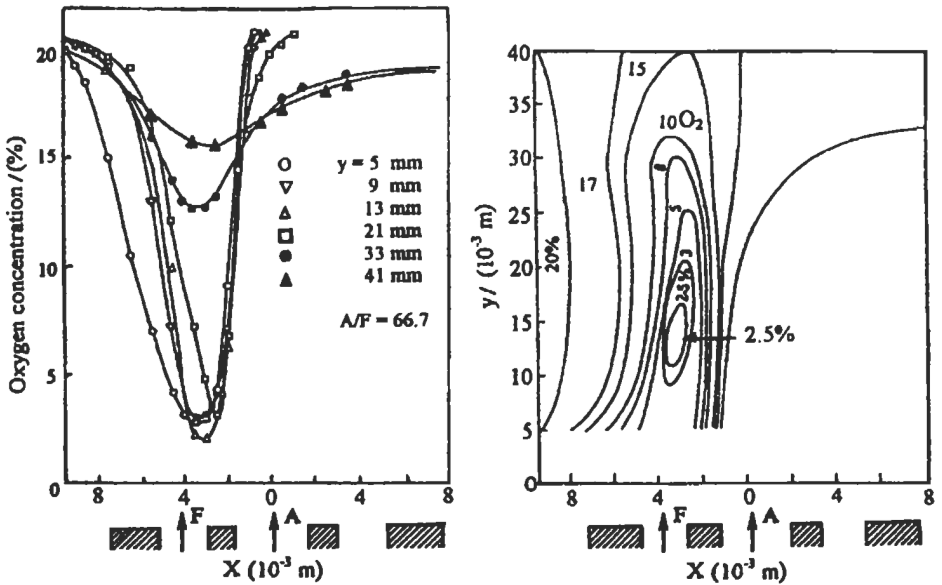


Fig. 3.98: Distribution and constant concentration contours of oxygen in the flame for single fuel jet arrangement ($A/F=66.7$) [576].

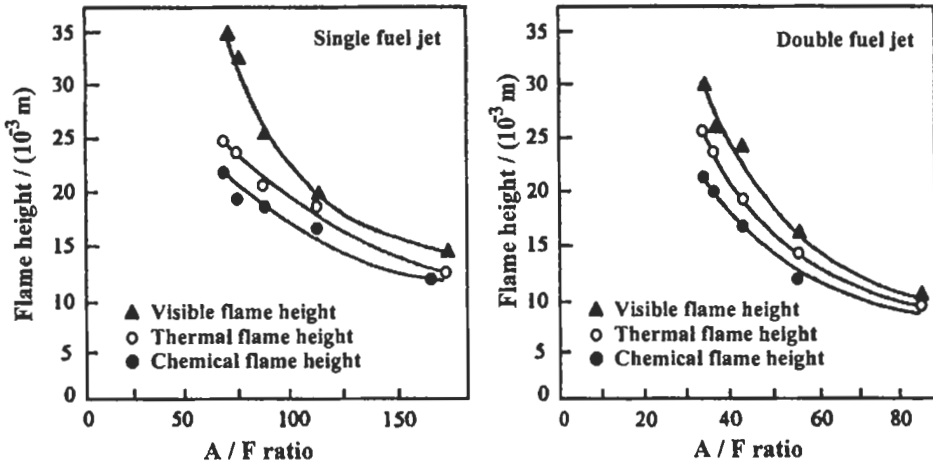


Fig. 3.99: Comparison between visible, thermal and chemical flame heights at different input air-fuel ratios [576].

Structure of Lifted Turbulent Jet Flames

Another approach of predicted turbulent diffusion flame structure is that based on laminar flamelet model (Bradley et al [375]) which is discussed in section 3.4.2 in this chapter. As discussed before, the diffusion flame has the merit of preventing flash back, and also the rate of straining during such mixing can be sufficiently high to prevent flame propagation through the mixture. During convection of the flow, appreciable premixing can occur and the strain rate can be reduced to a level at which flame propagation becomes possible. A model based upon premixed rather than diffusion flamelets is appropriate. Various degrees of premixing may occur and when combustion occurs the compositional changes due to reaction are more rapid due to non-reactive mixing. Turbulent modeling of the flow field enables a mixing progress variable, C , to be evaluated in terms of a conserved scalar. This expresses the mixture fraction from which an equivalence ratio, ϕ , can be found for the localized premixed flamelet. With this approach, when allowance is made for the variation in C , Eq. 3.43 becomes:

$$\tilde{q}_t = \int_{C_{min}}^{C_{max}} \left[\int_{-\infty}^{S_q(C)} P(S) dS \int_0^1 q_{l1}(C, \theta) P(C, \theta) d\theta \right] P(C) dC \tag{3.130}$$

In general, S_q is a function of (C) and C_{min} and C_{max} are lower and upper limits of flammability. Simplification is achieved if C and θ are assumed to be statistically independent, such that $P(C, \theta) = P(C) P(\theta)$. This can only be an interim approximation, because the value of C influences that of θ through the effect of C on T_b . The mean volumetric heat release rate is now given by:

$$\tilde{q}_t = \int_{C_{min}}^{C_{max}} \left[\int_{-\infty}^{S_q(C)} P(S) dS \int_0^1 q_{l1}(C, \theta) P(\theta) d\theta \right] P(C) dC \tag{3.131}$$

Bradley et al [375] have applied this method to model lifted turbulent jet-diffusion flames of methane in air. In the absence of swirl and recirculation, the $k-\epsilon$ model gave acceptable accuracy. As with $P(\theta)$, it was assumed that $P(C)$ was a beta function, but more experiments are needed to test this assumption. There was good agreement between predicted and measured lift-off heights as a function of jet velocity. A quasi-Gaussian distribution of strain rates was assumed and it was found to be sufficiently accurate to take a constant value of $S_q(C)$, equal to 3000 s^{-1} . A value of $0.25 \bar{S}$ was taken to represent the mean flame strain rate. Shown in Fig. 3.100 for a mean jet exit velocity of 60 m s^{-1} , are the velocity vectors, Favre average value of $\tilde{T}, \tilde{C}, \tilde{q}_t$ and $\bar{S}_q = S_q(\epsilon/\nu)^{-0.5}$. Although, initially, the strain rate can quench a potential flame, a value of \bar{S}_q of 0.1 would be too high to do this. Their study [375] suggested that flame quenching is not a principle determinant of lift-off height. This depends, in a complex way, upon the interaction of convection, turbulent mixing, heat release under strain and thermal expansion.

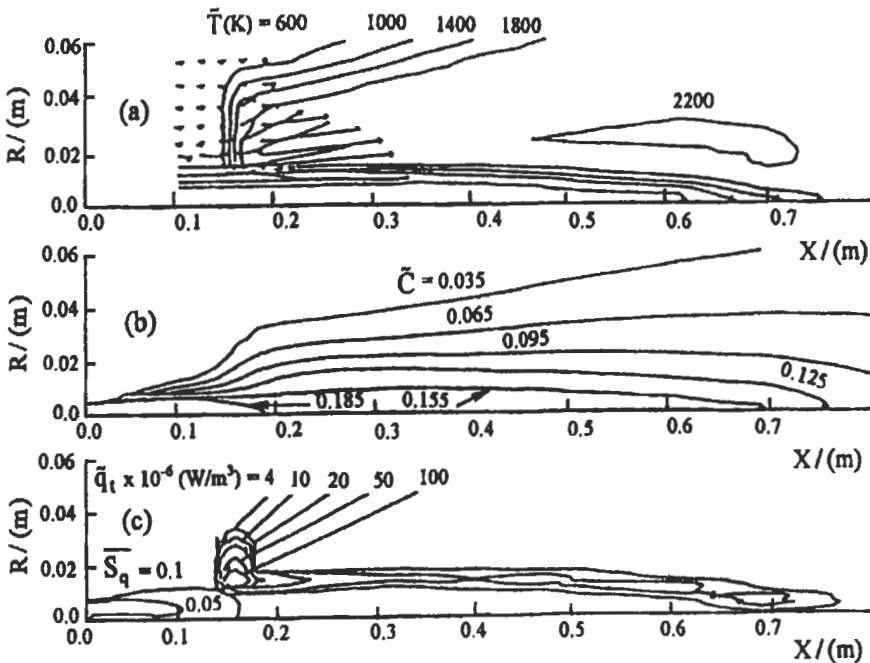


Fig. 3.100: Computed jet-diffusion flame fields of (a) temperature and velocity (b) mixedness (c) \tilde{q}_t and \tilde{S}_t [375]. Reproduced by permission of The Combustion Institute.

Chapter

4

Characteristics of Turbulent Confined Diffusion Flames

4.1 Introduction

In practical combustion systems, the length and shape of the flame depend to a large extent on the mixing process between the fuel and air, which enter the furnace separately. The rate of mixing depends on the flow characteristics such as the turbulence level, the swirl imparted to the combustion air, strain rate, burner and furnace geometries, forced flow reversal, non-streamlined bodies, and the air-fuel ratio.

Direct attacks on comprehensive modeling of real practical combustors are unlikely to succeed due to the extreme complexity of the phenomena, and the insufficient control of the vast number of variables. Here is an attempt to simplify these complicated approaches. Therefore, modeling studies and the measurement of time mean average properties of temperature, three velocity components, static pressure and concentrations of CO_2 , CO , and O_2 in flame enabled description of flame to be made in terms of flow patterns, and stream lines distributions.

Isothermal models can be very valuable in yielding concrete and detailed information on the basic flow and mixing processes and on general tendencies of the effect of the experimental variables on these processes. Moreover, measurements conducted on isothermal models with high accuracy can be used to test the validity of the theories encountered in the prediction methods. Some of the important parameters that affect flow and mixing in furnaces under cold and hot conditions are discussed in this chapter.

Thus, most of the work presented in this chapter is devoted to study such parameters on the aerodynamic flow and mixing patterns, both in cold and hot conditions, as well as the heat liberation in the later condition. The fundamentals of earlier chapters such as chemical mechanisms, velocity-composition, probability density function (PDF) model coupled with a k - ϵ based mean flow computational fluid dynamics (CFD) model, are used here to describe the effect of such parameters on the characteristics of the combustion systems. These will help the designer to select the suitable burner and furnace geometry in addition to the different operating conditions. Furthermore, understanding the effect of such parameters on the combustion systems is important for providing a bridge between fundamentals and applications which will be discussed here and in chapter 5.

4.2 Mixing and Flow Fields of Jets

Usually the streams of fuel and air issuing from the burner into furnace volume are both in the form of a jet, i.e. flows fully separated from walls. The jet momentum of the fuel and air streams is utilized for directing the flame and for controlling mixing process. Round jets are formed by fluid issuing from pipes or nozzles of circular cross-section. Because of their symmetry about the jet axis, round jets may be considered as two dimensional, for purpose of analysis, in a cylindrical co-ordinate system. Above a Reynolds number of 10^3 the round jet may be treated as turbulent.

Annular jets frequently serve for the introduction of secondary air around the primary jet that carries the fuel. Non-streamlined bodies, so called "bluff bodies" are often placed in the center of round nozzles. The flow is then issuing from an annular nozzle and a region of reverse flow forms in the wake of the bluff body, which is considered as an instrument to flame stabilization.

Double concentric jets are compound jets of a central and a coaxial jet. At a distance of several nozzle diameters downstream the burner, the two jets combine together and the behavior of the compound jet in this region can be predicted with good approximation from the combined mass flow rates and jet momenta. When jets are confined, there is a limited supply of fluid for entrainment. As a result, an adverse pressure gradient is set up along the jet associated with a recirculating flow outside the jet stream. Jet characteristics and swirl flows [586] have been studied by several investigators [491, 577-581].

4.2.1 Free Jets

When fluid emerges from a nozzle it interacts with fluid from the surroundings to form a jet. Immediately downstream from the nozzle, there is a region, the potential core, within which the velocity and concentration of nozzle fluid remain unchanged. Outside this region, a free boundary layer develops in which momentum and mass are transferred perpendicular to the direction of flow. The fully developed region is preceded by the transition region as indicated in Fig. 4.1. The length of the potential core and the transition region is about 4-5 and 8-10 d_o (from the nozzle), respectively.

The fully developed regions of turbulent jets are similar with general relationships for the velocities and concentration distribution. Figure 4.2 shows the variation of the reciprocal of the normalized axial velocity as a function of distance, X , from the nozzle exit. The normalized axial centerline velocity is inversely proportional to $(X+a)$ by:

$$\frac{U_m}{U_o} = A \frac{d_o}{(X + a)} \quad (4.1)$$

where U_o is the velocity at the nozzle exit, U_m is the axial component of the centerline velocity, d_o is the nozzle diameter, a is the jet virtual origin, and A is constant.

Because the mechanism of transfer of momentum and that of mass are the same, a similar relation can be given for the axial distribution of concentration:

$$\frac{F_m}{F_o} = B \frac{d_o}{(X + a)} \quad (4.2)$$

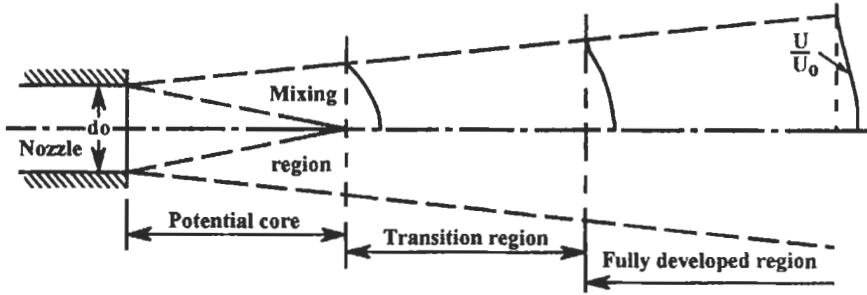


Fig. 4.1: Regions of jet.

where F_0 and F_m are the concentration of the jet fluid at the nozzle exit and on the centerline at a distance X , respectively.

In Fig. 4.2, the horizontal part of the curve represents the distribution within the potential core and the difference in slopes as given by the above equations is due to the difference in the value of the coefficients for the turbulent transfer of momentum and mass, respectively. Because of the similarity of velocity profiles, the ratio of the axial velocity at any point to that on the axis at the same axial distance from the nozzle, U/U_m is the same when given as a function of r/X . This is true also for concentration distributions. The normalized velocity and concentration profiles follow a Gaussian distribution, and the corresponding equations are:

$$\frac{U}{U_m} = \exp\left[-K_u\left(\frac{r}{X}\right)^2\right] \tag{4.3}$$

where K_u has a value between 82 and 92 and, for concentration profiles,

$$\frac{F}{F_m} = \exp\left[-K_f\left(\frac{r}{X}\right)^2\right] \tag{4.4}$$

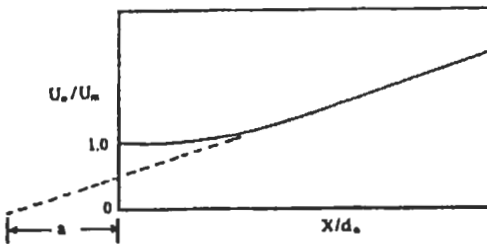


Fig. 4.2: Determination of the origin of a round jet. Beér and Chigier [491], reproduced by permission.

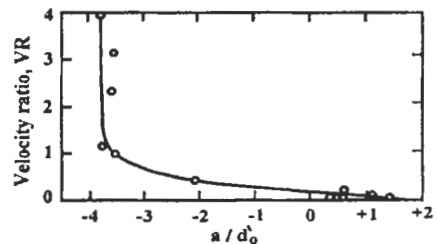


Fig. 4.3: The displacement of effective origin as a function of the velocity ratio for combined jet. Beér and Chigier [491], reproduced by permission.

where K_f has a value between 54 and 57 (Beèr and Chigier [491]).

Entrainment. As a consequence of momentum exchange between the jet and surroundings, fluid is entrained from the surroundings across the boundaries of the jet. The magnitude of entrainment can be illustrated by the fact that, a turbulent jet entrains fluid equivalent to the nozzle fluid mass flow rate about every three-nozzle diameter distance along the jet axis. For a constant density system, entrained mass is given by [491]:

$$\frac{\dot{m}_e}{\dot{m}_o} = 0.32 \frac{X}{d_o} - 1 \quad (4.5)$$

where \dot{m}_e and \dot{m}_o are the entrained and jet mass flow rates, respectively. The more general relationship for non-constant density system is given by:

$$\frac{\dot{m}_e}{\dot{m}_o} = 0.32 \left(\frac{\rho_a}{\rho_o} \right)^{0.5} \frac{X}{d_o} - 1 \quad (4.6)$$

where ρ_o and ρ_a are the densities of the jet fluid and surrounding fluid, respectively.

4.2.2 Annular and Coaxial Jets

A circular jet with an annular coaxial stream shows patterns similar to that of a round jet in the fully developed regions (8-10 nozzle diameters downstream). There is, however, a displacement of the origin, i.e. the axial distance X must be replaced by $(X + a)$ in the equations giving velocity, concentration and entrainment along the jet. Close to the nozzle, the annular jet sets up a region of under-pressure with an associated closed ring vortex in the central region of the jet. Such vortices are also found in the wake of the annular interfaces between co-axial jets [491]. Chigier and Beèr [577] have determined experimentally the values of the displacement of the origin of the jet for a wide range of values of the annular to central jet velocity ratio, VR, of coaxial jets and their results are shown in Fig. 4.3. The value of the equivalent nozzle diameter d_o' for a double concentric jet was calculated as [491]:

$$d_o' = \frac{2(\dot{m}_c + \dot{m}_a)}{\pi \rho (\dot{G}_c + \dot{G}_a)^{0.5}} \quad (4.7)$$

where \dot{m}_c and \dot{m}_a are the mass flow rates of the central jet and the annular jet, respectively, and \dot{G}_c and \dot{G}_a are the respective momentum fluxes.

For the central jet alone, the characteristic velocity is the mean exit velocity, U_{co} , through the central nozzle diameter, d_o . The length of the potential core is dependent upon the shape of the nozzle and the intensity of turbulence generated before the exit from the nozzle. For $VR = 0.08$ as indicated in Fig. 4.4, the velocity of the centerline is constant for a distance of four central nozzle diameters. Thereafter, the axial velocity distribution tends towards the hyperbolic decay of [491]:

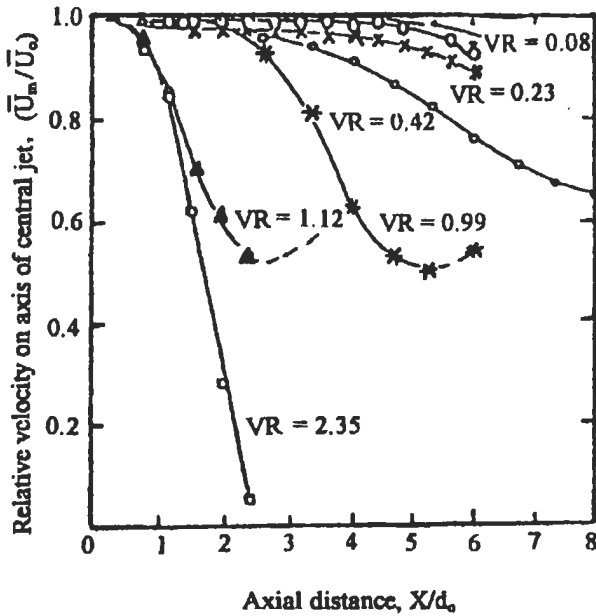


Fig. 4.4: Influence of the annular jet on the potential core and decay of the central jet. Beér and Chigier [491], reproduced by permission.

$$\frac{U_m}{U_{co}} = 6.4 \left(\frac{d'_o}{X + a} \right) \quad (4.8)$$

As the annular velocity is increased, the length of the central potential core decreases and the decay of the velocity is faster, until for $VR = 2.35$ the central jet is completely absorbed by the annular jet so that at a distance of $3 d_o$, reverse velocity is measured on the center line.

4.2.3 Wall Jets

The flow structure in the developing region of the jet is important in many applications especially in combustion. Therefore, EL-Mahallawy et al [578] have experimentally investigated the near field characteristics of a free jet issued from a circular exit mounted in the center of a large flat plate. The study includes all the three regions (up to $15 d_o$) of both cold and heated jet fluids (air). Two basic flow conditions were considered:

- i) Isothermal mixing of an air jet (cold jet) with the ambient air.
- ii) Non-isothermal mixing of a heated air jet with the ambient air.

The characteristics investigated through this work were:

The radial distributions of the axial and radial velocity components, the radial distributions of the mean temperature, decay of both centerline velocity and temperature, the half width of the isothermal and hot jets, momentum and heat spread, and entrainment distribution throughout jet zones.

The following describes the characteristics of cold round wall jet.

Jet zones. Figure 4.5 is a logarithmic representation of the dimensionless centerline velocity against the dimensionless distances downstream the jet exit for different Reynolds numbers. From this figure, three distinct zones can be remarked. The first one represents the potential core region through which the centerline velocity remains constant. It extends from the jet exit up to $4.6 d_o$.

The second one is the transition region in which [578]:

$$U_m / U_o = 2(X / d_o)^{-0.46} \quad 4.6 \leq X / d_o \leq 8 \quad (4.9)$$

where U_m is the centerline velocity, and U_o is the velocity at the jet exit.

The third one is the fully developed region, which is characterized by a greater rate of decay of the centerline velocity. In this region [578]:

$$U_m / U_o = 5.64(X / d_o)^{-0.96} \quad X / d_o \geq 8 \quad (4.10)$$

The rate of centerline velocity decay, through the fully developed region, decreases as moving downstream along the jet axis. The existence of the transition and the fully developed regions may be explained by what has been found by Boguslawski and Popiel [579], that is within a distance of $4 d_o$ to $9 d_o$ from the jet exit a rapid increase in turbulence intensity is observed due to the extension of the mixing layer over the whole cross-section of the jet. Beyond a distance of $9 d_o$ the turbulence intensity still grows up but at a slower rate. Figure 4.5 also shows that Reynolds number in the range investigated (14620-77460) has no effect on the division and lengths of the jet zones.

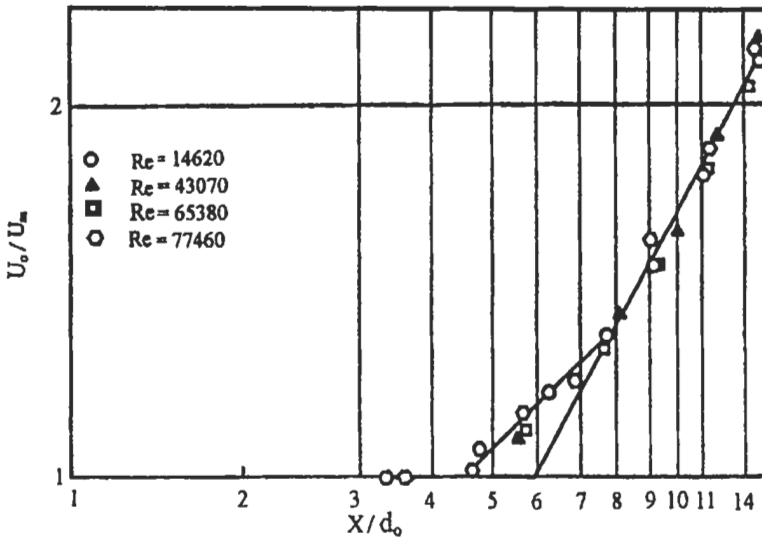


Fig. 4.5: Jet zones and centre-line velocity decay [578].

Jet angle. This angle is taken as a measure of the momentum spread. The method of determining the value of the radius $r_{0.5U}$ at which the axial velocity is half the value of the centerline axial velocity is used in this work as a measure of the jet spread. The results show that the jet begins to diverge after the potential core region. In the transition region [578]:

$$r_{0.5U}/d_o = 0.21 (X/d_o)^{0.59} \quad 4.6 \leq X/d_o \leq 8 \quad (4.11)$$

In the fully developed region, the experimental results can be represented by a mean straight line. In this region the jet angle of divergence is equal to 4.8° , which means that [578]:

$$r_{0.5U}/d_o = 0.084 (X/d_o) \quad X/d_o \geq 8 \quad (4.12)$$

which is in agreement with that found by Hinze [556].

Radial distribution of the axial velocity. The radial distribution of the axial velocity, U_x at any section can be described by the following formula [578]:

$$U_x / U_m = \exp(-0.73 (r/r_{0.5U})^{1.75}) \quad (4.13)$$

Figure 4.6 shows the comparison between the results obtained from (Eq. 4.13) and some previously proposed relations [491, 556]. The figure shows that the experimental results, represented by small circles, are closer to the results from Eq. 4.13 than those of Refs. 491 and 556. The noticeable deviation between the experimental results and the previously proposed relations, especially in the transition region arises from the assumption that the jet diverges linearly with the distance X which is not true especially in proximity of the jet exit. From the above-obtained relations, it can be shown that the constant axial velocity lines expressed as fixed ratios of the jet exit velocity can be implicitly represented by [578]:

$$2r/d_o = 0.805 (X/d_o)^{0.59} \left[\log \left(\frac{U_o}{U_x} \right) + \log 2 - 0.46 \log (X/d_o) \right]^{0.57}$$

for $X/d_o < 8$ (4.14)

and

$$2r/d_o = 0.324 (X/d_o + 0.5) \left[\log \left(\frac{U_o}{U_x} \right) + \log 5.64 - 0.96 (X/d_o) \right]^{0.57}$$

for $X/d_o > 8$ (4.15)

Radial distribution of the radial velocity. Figure 4.7 shows the radial distribution of the radial velocity component, U_r , throughout the jet zones. These results show that the radial velocity component increases from its zero value at the jet axis to a certain maximum value and then decreases. This figure shows also that the value of the maximum radial velocity has a general decreasing tendency as one moves in the downstream direction.

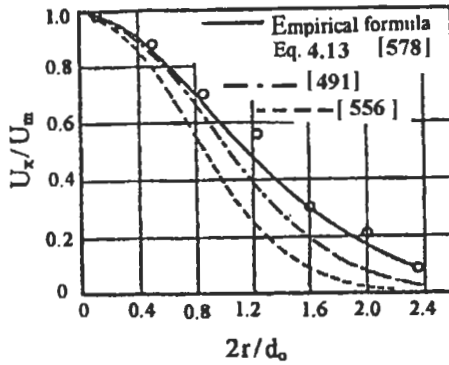


Fig. 4.6: Comparison between the experimental results, O, and empirical formula ($X/d_0 = 5.08$) for the radial distribution of the axial velocity.

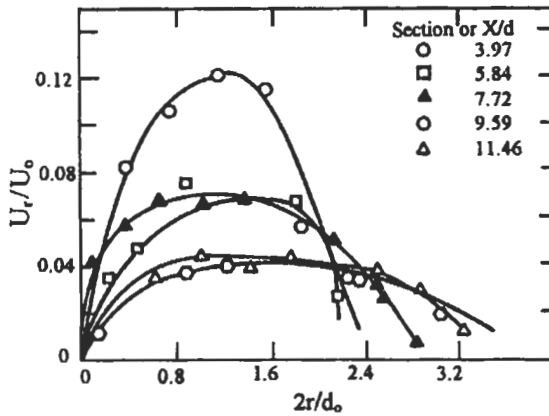


Fig. 4.7: Radial distribution of radial velocity, U_r , for different sections along the jet axis [578].

Entrainment. Figure 4.8 gives the variation of the dimensionless entrained mass related to the mass at the jet exit with the dimensionless distance downstream the jet exit. From this figure it can be seen that the experimental results can be represented by a mean straight line [578] as:

$$m_e/m_0 = 0.242 (X/d_0 - 0.6) \quad X/d \geq 0.6 \quad (4.16)$$

where m_e is the entrained mass and m_0 is the mass at the jet exit.

The values of m_e obtained from the above equation are lower than those found by some previous investigators due to the existence of a large wall, from which the jet is issuing and hinders the entrainment.

For hot jets, the centerline velocity in the transition and full developed regions can be represented by [578]:

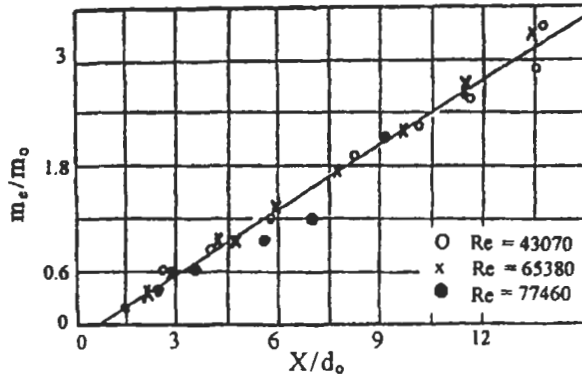


Fig. 4.8: Entrained mass throughout jet zones [578].

$$U_m/U_o = 1.38(X/d_e)^{-0.27} \quad 3.3 \leq X/d_e \leq 7.9 \quad (4.17)$$

$$U_m/U_o = 6.4(X/d_e)^{-1} \quad X/d_o \geq 7.9 \quad (4.18)$$

where d_e is the equivalent nozzle diameter ($d_e = d_o (\rho_o/\rho_a)$) [581].

Figure 4.9 shows the comparison between the centerline velocity decay for both cold (Eqs. 4.9 and 4.10) and hot (Eqs. 4.17 and 4.18) round jets, in which the distance downstream the jet exit has been expressed as X/d_e . The figure shows that the concept of equivalent exit diameter introduced by Thring and Newby [581] failed to eliminate the deviation of jets (hot and cold) in proximity of the jet exit, but it succeeded to eliminate this deviation throughout the fully developed region.

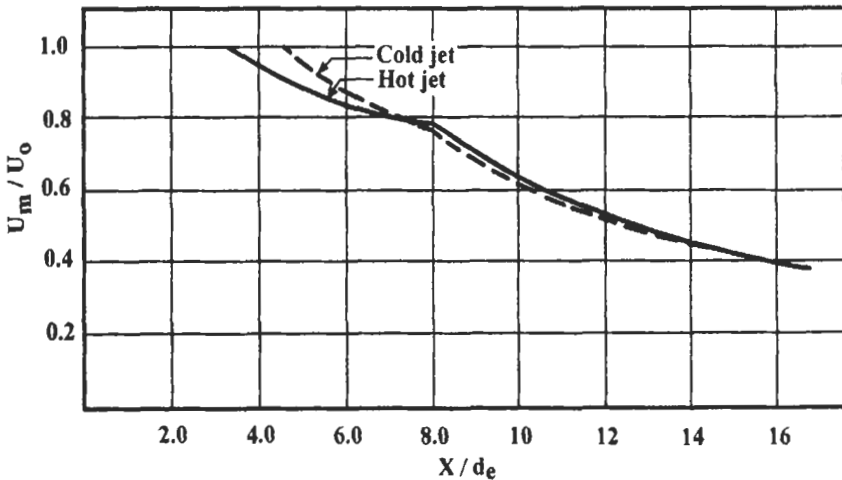


Fig. 4.9: Comparison between the centerline velocity decay for both cold and hot jets [578].

4.2.4 Swirling Jets

Swirling jets are used as a mean of controlling flames in combustion chambers. The aerodynamics of swirling turbulent jets combine the characteristics of rotating motion and the free turbulence phenomena encountered in jets and wake flows.

When rotating motion is imparted to a fluid upstream of an orifice, the fluid flow emerging from the orifice has a tangential velocity component in addition to the axial and radial components of velocity encountered in non-swirling jets. The presence of swirl results in the setting up of radial and axial pressure gradients, which, in turn, influence the flow field. In the case of strong swirl, the adverse axial pressure gradient is sufficiently large to result in reverse flow along the axis and the setting up of an internal recirculation zone.

The swirl number. In swirling free jets or flames, both axial flux of the angular momentum G_t and the axial thrust G_x are conserved. These can be written as [491]:

$$G_t = \int_0^R 2\pi U_x U_t \rho r^2 dr = \text{const.} \quad (4.19)$$

$$G_x = \int_0^R 2\pi U_x^2 \rho r dr + \int_0^R 2\pi P r dr = \text{const.} \quad (4.20)$$

where U_x , U_t , and P are the axial and tangential components of the velocity and static pressure, respectively in any cross-section of the jet. Since both these momentum fluxes can be considered as characteristics of the aerodynamic behavior of the jet, a non-dimensional criterion based on these quantities was recommended [577] as a criterion of swirl intensity as:

$$S = \frac{G_t}{G_x R} \quad (4.21)$$

where R is the exit radius of the nozzle.

Subsequent experiments have shown that the swirl number S was the significant similarity criterion of swirling jets produced by geometrically similar swirl generators. In general the swirl may be generated by the tangential entry of the fluid stream, or a part of it, into a cylindrical duct or by the use of guide vanes swirlers or by swirl generators. The calculation of the swirl number for the guide vane swirler is shown in the following part. Figure 4.10 shows a sketch of the swirler, the angular momentum can generally be given as:

$$G_t = \int_{R_h}^R 2\pi U_x U_t \rho r^2 dr \quad (4.22)$$

For very thin vanes of constant chord and swirl angle θ , and provided that the axial velocity distribution is uniform over the tube cross-section, this equation reduces to:

$$G_t = 2\pi\rho U_0^2 \tan \theta \frac{R^3 - R_h^3}{3} \quad (4.23)$$

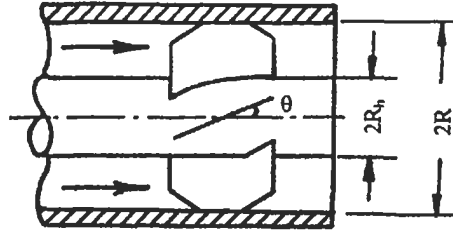


Fig. 4.10: Vane air swirler [586]. Cited by Beèr and Chigier [491].

Introducing the linear momentum:

$$G_x = \pi \rho U_0^2 (R^2 - R_h^2) \quad (4.24)$$

One may further write:

$$G_t = G_x \tan \theta R \frac{2}{3} \frac{1 - \left(\frac{R_h}{R}\right)^3}{1 - \left(\frac{R_h}{R}\right)^2} \quad (4.25)$$

Thus, the swirl number of an annular swirler with constant vane swirl angle θ can be given as:

$$S = \frac{G_t}{G_x R} = \frac{2}{3} \left(\frac{1 - (R_h/R)^3}{1 - (R_h/R)^2} \right) \tan \theta \quad (4.26 a)$$

In the case of a hubless swirler (i.e. R_h/R is very small), Eq. 4.26 (a) can be simplified to:

$$S = 2/3 \tan \theta \quad (4.26 b)$$

so that vane angles of 15, 45, and 80 degrees, for example, correspond to S values of 0.2, 0.7, and 4, respectively.

4.2.5 Confined Jets

For an enclosed jet, such as a jet in a duct, and in case when the surrounding secondary flow is less than that which the jet can entrain, a recirculation flow is set up i.e. some of the mean streamlines take the form of a closed loop as shown in Fig. 4.11. The details of the recirculating flow are of great interest to combustion engineers as the strength and size of the recirculation eddy affect both the stability and the length of turbulent diffusion flames. As shown in the figure, the secondary fluid is entrained upstream of point N and the recirculation eddy extends from the downstream boundary at point P to its upstream limit N. The rate of the reverse flow, defined as the integral of the negative velocities across the cross-section, varies between these two points. It reaches its maximum value at cross-section C between P and N [580].

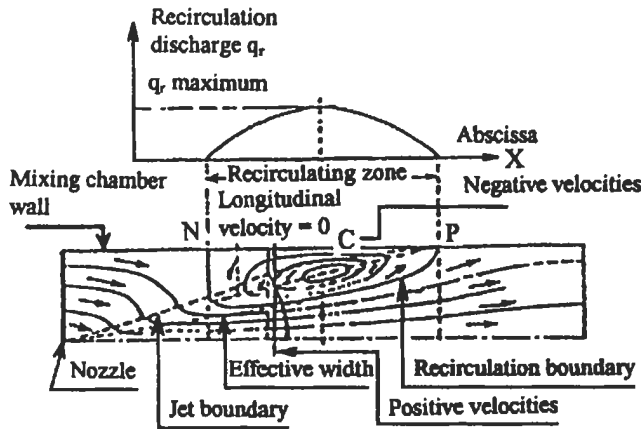


Fig. 4.11: Recirculation map for a ducted axisymmetric jet [580].Cited by Beér and Chigier [491].

The ratio of the entrained mass to the nozzle mass is given by Eq. 4.6. Now, by treating the primary and secondary flows as a single jet (i.e. $X_N = 0$), the distance from the nozzle to point C in Fig. 4.11 can be given as:

$$X_1 = 0.5 \left[X_p + \frac{d'_o}{0.32} \left(\frac{\rho_o}{\rho_a} \right)^{0.5} \right] \tag{4.27}$$

where X_p is the distance from the jet origin to the point P where the jet extends to the wall and by assuming a jet angle of 9.7° , then $X_p = 5.85 L$, where $2 L$ is the duct diameter.

By introducing a parameter $\theta_a = \frac{d'_o}{2L} \left(\frac{\rho_o}{\rho_a} \right)^{0.5}$

$$\text{Then, } X_1 = 0.5 \left[X_p + \frac{2L\theta_a}{0.32} \right] = L \left[2.925 + \frac{\theta_a}{0.32} \right] \tag{4.28}$$

For the case where $\dot{m}_e = \dot{m}_r$, the fluid entrained between the nozzle and point C is given by:

$$\frac{\dot{m}_e}{\dot{m}_o} = \frac{0.32X_1}{\theta_a 2L} - 1 = \frac{0.16}{\theta_a} \left[2.925 + \frac{\theta_a}{0.32} \right] - 1 = \frac{0.47}{\theta_a} - 0.5 \tag{4.29}$$

For the case where all the secondary flow is entrained by the jet before recirculation starts, $\dot{m}_e = (\dot{m}_a + \dot{m}_r)$, and the proportion of recirculated mass flow is given as:

$$\dot{m}_r / (\dot{m}_o + \dot{m}_a) \tag{4.30}$$

and the modified Thring and Newby [581] parameter as:

$$\theta'_a = \frac{\dot{m}_a + \dot{m}_o}{\dot{m}_o} \frac{d_o}{2L} \left(\frac{\rho_o}{\rho_a} \right)^{0.5} \quad (4.31)$$

From the above equations we have:

$$\frac{\dot{m}_r}{\dot{m}_o + \dot{m}_a} = \frac{0.47}{\theta'_a} - 0.5 \quad (4.32)$$

Equations 4.29, 4.30 and 4.31 gave the position of points N and C in Fig. 4.11 as:

$$X_N = 6.25\theta'_a L \quad (4.33)$$

$$\text{and } X_1 = 3.12(\theta'_a + 0.94) L \quad (4.34)$$

4.3 Swirling Flows in Combustion Systems

4.3.1 Introduction

As described above, the main aspect in furnaces, boilers and gas turbines design, is to obtain an efficient, stable and quite flame, with higher combustion efficiency and minimal noise level that is associated with such flame. The higher combustion efficiency would allow for more energy savings and for lower environmental pollution of carbon monoxide and nitrogen oxides. On the other hand, stable flame would also allow for safe operation under a wide range of air to fuel ratios; especially for aircraft gas turbines during wind gusts, foreign object ingestion into engine that might cause engine compressor surge.

In order to achieve the above aims, manufacturers of burners incorporate into the design the physical and chemical factors that govern burning, which are known as the classic "Three T's of combustion" Time, Temperature and Turbulence. As there had been a progress in burning speed, the designers of gas turbine were quick to take advantage by reducing furnace volume and increasing furnace temperature. As a corollary of the shorter flames, the length of combustion chamber is reduced, which has been a great gain for aircraft gas turbines manufactures. Such reduction in combustor length has led to reducing the engine weight, and minimizing the engine specific fuel consumption, and thereby reducing the engine cost. The burner designers thus find that two of the above mentioned precious three T's have been pre-empted and have only the final "T" at turbulence, to benefit of.

Turbulence is demanded in the two zones, where the fuel and air are being mixed, and where the fuel is being burnt. High turbulence can be achieved either by bluff bodies, which have been mainly used for premixed flames, or by swirlers for diffusion flame burners. On the other hand, high turbulence may cause high noise level during combustion. Therefore, it has been favored to optimize between high turbulence,

which is required for improvement of combustion efficiency, and the associated noise. Methods of swirl generation and characterization have been discussed in details by Beèr and Chigier [491], and by Gupta et al [582]. The most commonly used methods of swirl generation are the multi-jet tangential entries and different types of swirlers. Recirculation zones are formed in flows when adverse axial pressure gradient exceeds the kinetic energy of fluid particles, whereas stagnation points are formed. This can be brought about by imparting strong swirl to jets. This kind of recirculation zone is called "Central Toroidal Recirculation Zone". Also, sudden expansion of flow entrained into combustor creates another kind of recirculation zone called "Corner Recirculation Zone". The main factors that affect the existence of recirculation zone and its size and shape are the swirl strength, the swirler vane angle, and the chamber to burner diameter ratio.

Significant relationships exist between the size and strength of the recirculation vortex, and the flame stability characteristics and the combustion efficiency. The combustion efficiency and stability are improved by good mixing between fuel and air and re-ingestion of the combustion products as hot gases into the combustion zone. The injection of liquid fuel into a strong toroidal flow would cause a short axial travel distance of fuel droplets downstream of burner exit. Also the recirculation of combustion products into the burning zone, improves and assists the fuel evaporation, which affects the flame characteristics such as shape, length, maximum temperature, and concentrations of carbon monoxide and nitrogen oxides.

The splitting of combustion air into primary and secondary streams, especially for diffusion flames, is favored for flame stability and safety. It also enables higher preheat temperature to be used in the secondary air, which in turn, improves the thermodynamic efficiency of the system. The splitting of the combustion air is commonly carried out by double concentric jets, which are compound jets consisting of a central and coaxial annular jet. Swirling of either primary air and/or secondary air by using any method of swirl generation would thus create an adequate toroidal vortex and the associated recirculation zone. It has been concluded [582] that, when a swirled flow is confined by divergent exit or quarl, the size and shape of the created recirculation zone are significantly affected.

Furthermore, conditions of the air entry (with or without swirl) to the combustion zone have a great effect on the flame length, flame diameter, and the distribution of the constant concentration contours. A characteristic special feature of the gas-dynamic flow pattern for combustion zones is the presence of a zone of reversal flow near the axis of the flame.

It can be seen from Fig. 4.12 (a), that along the axis of combustion zone, reversal of the direction of flow occurs. As a consequence of this, a part of the combustion products, possessing high temperature, returns upstream to heat the fuel and air entering the combustion zone. By these means, ignition of fresh mixture is ensured with subsequent development of the combustion process.

4.3.2 Methods of Combustion Air Swirling

The swirl can be generated by three main methods [582]:

- Tangential entry (axial-plus-tangential entry swirl generator).
- Guided vanes swirlers.
- Direct rotation (rotating pipe).

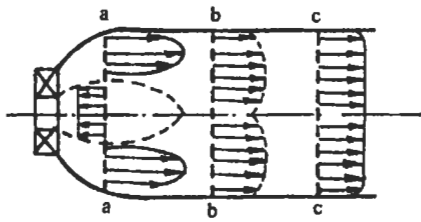
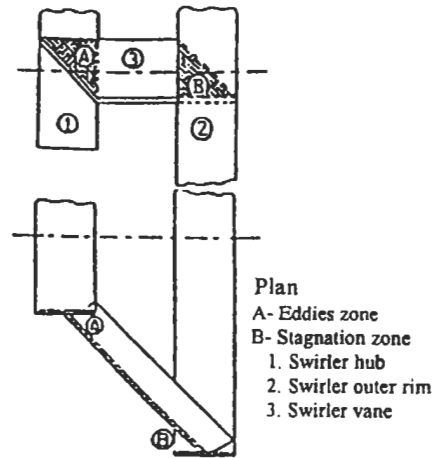
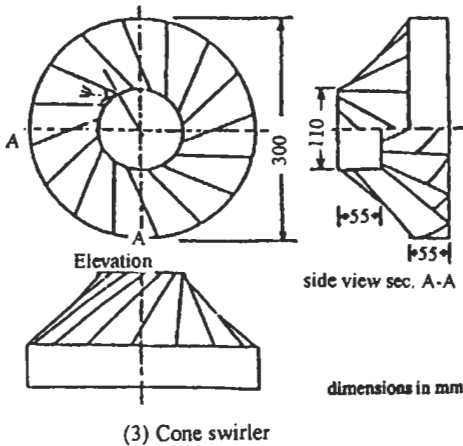


Fig. 4.12(a): Distribution of the axial velocity in the combustion chamber.

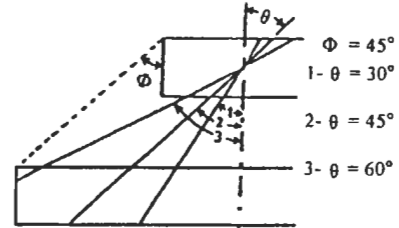
(a) Upstream section (b) & (c) Downstream sections



(1) Demonstration of first concept of cone swirler design.



(3) Cone swirler



(2) Relation between cone angle Φ and vane angle θ .

Fig. 4.12(b): Cone type swirler [583].

The first method is used extensively for providing uniform stable jets, and the quantities of air can be controlled and metered separately so that simply by adjusting the air flow rates, the degree of swirl can be varied from zero swirl to that of a strongly swirling jet with reverse flow. This system is extremely efficient at low swirl strengths, but inefficient for producing high swirl intensities. Total pressure requirements of this system are relatively high, and commercial burners have tended to adopt the guided vane system (the second method), where vanes are so positioned that they deflect the flow direction. In axial pipe flow, a swirler or swirl vane pack consists of a fixed set of vanes at angle, θ , (called swirl angle) to the mainstream direction, which deflects the stream into rotation. This technique is common in furnaces and gas-turbine combustors, because it is relatively efficient, and in this technique the vanes are usually mounted on a central hub and the vanes occupy the space in the annular regions. In the last method, a rotating cylinder may be used to induce a swirl motion solely by frictional drag of the cylinder wall upon the air stream passing through it. Because of the relatively low viscosity of air, it is possible to generate only weak swirl by this method.

In addition to the most commonly vane type swirlers there is another type of swirlers, that has a cone shape and is called a cone type swirler, Fig. 4.12 (b). The basic

concept of this type of swirlers is to give the vanes a tilt angle with respect to the horizontal plane in order to construct the cone shape. This cone swirler is designed by El-Mahallawy et al [583] to swirl the secondary part of combustion air of double concentric jets burners. The effect of this cone-type swirler on the flow characteristics and the structure of confined oil fired diffusion flame will be discussed in section 4.5.3. This cone air swirler is a new type of swirlers whereas its vanes have two angles. The angle, θ , is similar to that related to the conventional swirler. The other, is the swirler cone angle (2Φ), which is formed by tilting the vanes outer tip outward of swirler hub, by a way, that the vanes mean lines having the half cone angle (Φ).

For this type of swirlers, there are two concepts for manufacturing, to form the cone shape:

- a. By tilting the vanes of the prevalent shape swirler by an angle equals the half cone angle while the vanes positioned at the swirl angle. As shown in Fig. 4.12 (b) (1), it is evident that there are eddies-generating zones in the cavities created between the vanes and the inner hub (zone A); while there are flow stagnation zones between the vanes and the outer rim of swirler (zone B). This shape will make the swirler acts as bluff body more than as swirler, where the vanes are facing the airflow rather being aligned with flow stream lines. This concept of swirler construction is not favored due to the above mentioned disadvantages.
- b. The second concept of cone swirler design is to make the vane tip tilted forward at the same plane of swirl angle till it reaches the outer rim. This design offsets the disadvantages of the previous design, whereas the vanes become in streamline with the airflow. It is worth noting to mention that such design concept has a disadvantage of making the maximum swirl angle, which may be given to vanes, strongly dependent on the cone angle. Figure 4.12 (b) (2) illustrates how the vane swirl angle is inversely proportion with the cone half angle.

The latter mentioned cone swirler design concept has been incorporated for the construction of the used cone swirlers for swirling the secondary air jet of the designed burner. A cone swirler having half cone angle (Φ) of 45° and vane swirl angle (θ) of 45° , is illustrated in Fig. 4.12 (b) (3). This figure illustrates that there is another angle between the vane edge and a line tangential to the inner hub at the same point, this angle is designated by the helic angle (ψ).

A set of cone swirlers are manufactured with different half cone angles (of 45° and 60°) and vane swirl angles (of 0° , 30° , 45° and 55°) has been used to investigate the effect of cone swirler on flow characteristics for cold and hot conditions, as well as the characteristics of the created confined diffusion flame [583].

4.3.3 Effect of Combustion Air Swirling

When actively induced to promote mixing and combustion, the design of swirling motion is generally faced with two requirements. On one hand, it is desirable to have high swirl to achieve adequate mixing between oxidizer and fuel; on the other hand, the associated strain rates must not be so large to cause extinction of the reaction. Thus, the following is a background, which mainly concentrates on the research in the field of the effect of swirling the combustion air on flow, mixing and flame characteristics in combustion systems.

The swirling air jets issuing from annular and divergent nozzles had been investigated by Chigier and Beèr [491] from the point of view of velocity and static pressure distributions. The swirl was generated by means of tangential entry of part of air, while the other part was issued axially. The measurements were carried out for three different nozzles, short divergent, long divergent and convergent divergent, for isothermal conditions. They concluded that with increasing the degree of swirl, the spread angle of the jet is increased, and correspondingly, the decay of the maximum values of axial, tangential and radial components of velocity along the lengths of the jets is faster. The measurements showed that the maximum tangential velocity is found very close to the outer wall, indicating that the type of flow approaches that of a solid-body rotation.

The effect of swirl on axi-symmetrical turbulent jets had been investigated by Kerr and Fraser [584] through measurement of velocity by means of three-dimensional pitot probe on full size furnace burner, where the combustion air was divided into primary and secondary flows. The primary flow swirled by constant cord vanes swirler, while the secondary flow passed through angled slots in the burner head. The theoretical calculation based on swirling jet theory, where swirl number is defined as:

$$S = 2/3 [(1-Z^3)/(1-Z^2)] \tan \theta$$

where Z is the hub ratio d_h/d , θ is the vane angle, and the jet spread half angle is defined as:

$$\alpha_s = \tan^{-1} [y_{1/2}/X]$$

where $y_{1/2}$ is the half velocity radius ($U = 1/2 U_m$), U_m is the maximum value. A relation between spread angle of swirl to spread angle of zero swirl is:

$$\tan \alpha_s / \tan \alpha_{s=0} = 1 + (K_2/K_1) S$$

where K_1 and K_2 are experimental constants. They concluded that, the constants for entrainment (K_1) and swirl (K_2) are evaluated as 0.35 and 1.7, respectively, and that the flux of angular momentum is constant within the jet and is independent of the distance from the nozzle. This means that the swirl number does not change with the axial distance downstream of the nozzle exit, which is logic.

The effect of swirl on flame performance had been studied by Kerr [585] by using a full size boiler furnace. The measurements had been carried out through a wide range of swirl number (0.0 to 0.6) and of excess air (5 to 10%) by using a twin air-stream oil burner. A combined swirl number ranging from 0.1 to 0.3 was found to give optimum mixing of the two nozzle streams. The velocity distribution, pressure and CO_2 concentration had been measured through the flame, while the smoke level had been measured by water-cooled soot pyrometer. The primary and secondary parts of oxidizing air were swirled by variable angle flat vanes swirlers. The discussion of the experimental results was concentrated on the effect of swirl on maximum axial velocity, radial temperature profile, position of maximum temperature contour line, mass ratio, and smoke meter reading. They found that, the swirl helps the flame stability by dropping the air velocities more rapidly, and as the swirl increases, the flame front

approaches the burner. In addition, with low combined swirl, the flame was found to be long and thin, while with high combined swirl it was found to be short and flat. These conclusions are in agreement with those found by Refs. 581 and 583.

Knio et al [587] have constructed and applied a low Mach-number, vorticity-based combustion model to examine effects of partial mixing in an idealized swirl chamber. The results indicate that incomplete mixing may have a dramatic impact on rates of burning and pressure rise, and this leads to a loss in combustion efficiency that, in some cases exceeds 20 %.

Efficiency and pollutant formation studies in a swirling flow combustor had been carried out by Research Office of Aerospace of France [588]. Experiments were conducted in order to determine the effect of the swirl on combustion and carbon monoxide and nitrogen oxides production. A combustor with inlet flow injected from variable direction nozzle was used for this study. Results obtained with zero swirl angle were compared to those obtained with 37° swirl angle. The fuel used was kerosene, and injected through 16 radial tubes with 0.6 mm injection holes. Mass flow rate, temperature and gas composition measurements had been made in two reference test stations. The results show that, an increase of 200 K in combustion temperature leads to an increase of 37 % and 19 % for CO₂ content and combustion efficiency, respectively, while CO, NO, NO_x content decrease by 65 %, 67 %, and 55 %, respectively.

Beltagui and MacCallum [589] studied the aerodynamics of vane-swirled flame in furnaces. Detailed measurements of the three components of velocity, static pressure, temperature, and carbon dioxide concentration, for annular and hubless vane swirlers having vane angle in the range of 15°-60° had been carried out. They concluded that, with sufficiently strong, swirl, a central recirculation zone is established, and its maximum diameter is primarily a function of the furnace diameter (about 0.65 D). Also, the central recirculation zone is proportional to the furnace diameter, but is somewhat reduced by combustion.

El-Banhawy [590] studied the confined spray flame with combustion air swirled by vane swirler. The fuel was injected to combustor by rotating atomizer. The measurements of local flame properties, including droplet velocity, temperature and species concentrations were presented for a range of unconfined and confined kerosene spray flames. Isothermal airflow velocity measurements within the combustion chamber were also obtained to aid understanding of the main aerodynamics features of the flow. The velocity measurements were carried out by the L.D.A. method. For the effect of degree of swirl on confined flame, it was concluded that, with increasing of swirl, the maximum centerline mean velocity, evaporation rate, the flame jet spreading rate and the combustion intensity were increased. The experimental results were compared with the predicted values, which indicate good qualitative agreement with finite discrepancies. The main deficiencies in the calculation method were related to the assumptions of the turbulence, combustion and spray models. This confirms once again the unreliable prediction by modeling of spray flames.

Ahmed et al [591] carried out a work to investigate the significance of the centrifugal forces in enclosed swirling flames that simulate practical gas turbine primary zone conditions. A flat bladed axial swirler was investigated with the downstream combustion confined in a circular uncooled duct. Three different methods of propane fuel injection (central, radial injection into each swirler vane passage and wall injection inclined by 30°) were used to study the effect of centrifugal force on the flame propagation. In addition, NO_x, unburned hydrocarbon (UHC), CO, and, CO₂ were

measured. Equivalence ratio, radial gas temperature profiles and radial gas analysis of UHC, CO, CO₂, and NO_x were compared for the three methods of fuel injection. It was concluded that, in the enclosed swirling flow combustion system, the centrifugal forces have an important influence on the flame propagation and mixing of fuel and air. Also, it was found that the flame characteristics were significantly affected by the method of fuel injection.

The retardation of mixing and counter-gradient diffusion in a swirling flame had been studied by Toshimi et al [592]. Simultaneous measurements of velocity and temperature have been made with a two-colour Laser Doppler Velocimeter and a compensated thermocouple in swirling and non-swirling turbulent diffusion flames confined in a tube. The results were compared for the flames with and without swirl to determine the effect of swirl. A gaseous fuel was injected at the center of a Pyrex tube in which the flame was formed at the atmospheric pressure. The air was then swirled by an annular variable swirler. Profiles of time-averaged velocity and turbulence intensity of swirled flame at 30° (swirl number was 0.26) were compared with that of 0° swirl. Their results indicated that: the suppression of the radial momentum flux and counter gradient diffusion in the swirling flame were dominated by the interaction of the fluctuation of velocity or temperature and radial gradient of pressure induced by the circumferential velocity due to swirl.

Gouldin et al [593] studied the velocity field characteristics of a swirling flow combustor consisting of two confined and concentric swirling jets. The central flow was premixed methane and air while the annular jet flow was air. Both co-swirl and counter swirl flow were investigated. Visual observations and measurements of temperature and compositions inside and at exit of the chamber have been made for methane-air combustion under different flow conditions. A single-channel Laser Doppler Anemometer system operated in the dual-beam was employed to measure axial and tangential velocities in the combustor. They observed stable central recirculation zone of finite length in the vortex core, and at large axial distance along combustor, the axial velocity profiles were found to be relatively flat except for the combustor case where a fast, hot core flow is evident.

A manifestation of vortex break down in swirling flows had been investigated by Keller and Escudier [594]. LDA measurements of the swirl and axial velocity components as well as, the corresponding streamline pattern were presented for water flow in a model based upon the geometry of a swirl combustor. The effect of exit contraction on the characteristics of flow was studied. They introduced a swirl number, which is defined to be the rate of the azimuthal and axial velocity components at the surface of the cylinder within the annular cylinder section. It was argued that a cold flow was likely to be totally representative of the reacting flow through the same geometry, and great care has to be taken over the boundary conditions to be imposed for the numerical computation of subcritical flows. They concluded that; free and confined flames produced by the same swirl burner, may significantly produce different properties because of the reaction zone can be decoupled from the downstream flow field by a suitable confinement of the vortex flow.

Sturgess and Sayed [595] gave a calculation model of confined swirling flows. The calculation procedures used for the mathematical simulation of internal viscous flows with recirculation were derived from the so-called TEACH generic solution procedure. The used procedure computer codes provide stationary-static solutions of Reynolds

averaged Navier-Stokes equations. The experimental results were carried out by a bench mark-quality experiment to represent the front of a gas turbine engine combustor. A comparison between calculations of mean axial velocities along the centerline and the LDV measurements was illustrated. They concluded that, swirling jets with internal recirculation couldn't be calculated reliably and accurately with existing CFD (Computational Fluid Dynamics) codes of the TEACH-type. Also, further physical understanding is required to know exactly how a swirling jet forms an internal recirculation zone, and how this depends on swirl strength, jet expansion ratio, central ventilation, back-pressure, and stream turbulence.

The effect of swirl on the development of recirculation flow patterns in a swirl combustor had been studied by Choi and Lyvzkowski [596] by using a cylindrical combustor of, Argonne National Laboratory (ANL). The primary air was swirled by means of guide vanes in the annular nozzle of burner. The primary air was introduced axially through two symmetrically spaced inlets into a large swirl chamber, and injected tangentially through eight diffusers into the combustion chamber. The primary purpose of their study was to model a swirl combustor with complex air inlet louvers. It is also concerned with determining how the recirculation flow patterns developed in a swirl combustor as the swirl ratio varies from zero (no swirl) to infinity (pure swirl). The flow patterns under cold flow conditions were simulated with a three-dimensional computer program, COMMIX-1A. Since the swirl number can't be calculated from the current version of the used program, they have used the swirl ratio (maximum tangential velocity in the combustor / maximum axial velocity in the nozzle) as a parameter to study the effect of swirl on the development of recirculation flow patterns. Computer simulation of the cold flow patterns of a swirl combustor was done for swirl ratios of 0, 3, 8 and ∞ at single Reynolds number of 50000. Their results showed how recirculation flow patterns developed in a swirl combustor as the degree of swirl increased.

Kawaguchi and Akiyama [597] studied the jet diffusion flame behavior in a coaxial swirling air flow, and made clear the effects of swirl strength of air flow. Detailed measurements of temperature, gas composition and velocity had been carried out for the interpretation of the flame behavior. The exhaust gas emissions and radiant heat energy were also measured, and the relations to air swirl strength were obtained. They found that, the length of jet diffusion flames in a ducted coaxial air flow increases due to swirling motion of air flow, but excess swirl reduces the flame length. Also, the effect of air swirl on flame length changes by shifting the injection position or the fuel jet momentum, which comes from the interaction of fuel flow and swirling air flow.

Ramavajjala and Gupta [598] carried out the measurement of NO, NO₂, CO, and UHC concentrations to evaluate combustion efficiency of the variable geometry swirl combustor. The design of this combustor was based on the concept of issuing the combustion air from multiannular swirler shifted downstream from the fuel nozzle. The measurements had been carried out on three geometries, central fuel rich, central fuel lean, and partial premixing of fuel and air. The burner was equipped with an extension tube of the same internal diameter as the outer most annulus, in order to eliminate the entrainment of air into the flame. They found that, the creation of large recirculation zone is essential for enhanced flame stability in variable geometry combustors. Also, the residence time, turbulent mixing and radial temperature profile across the exit of combustor influence the NO_x emission levels.

The aerodynamic effect of combustion in a swirl type combustor was studied by Arai et al [599]. The reverse flow region inside the recirculation zone was found by a flow

direction detector. The velocity and the velocity fluctuation were measured by a Laser Doppler Velocimeter and compared with that of without combustion. They concluded that, when the swirl number of the flow was higher than 0.5, the reverse flow zone was increased by the thermal expansion due to the combustion occurred in this zone. The axial velocity in this zone was also increased by combustion. On the contrary, when the swirl number was 0.23, the reverse flow zone was decreased by the combustion. The large-scale fluctuation of the velocity is increased by combustion but the small-scale fluctuation is decreased. Also, the flow photographs taken for flow visualization by a spark tracing technique showed that the small turbulence in the flow was diminished by the combustion.

4.4 Flow and Mixing in Cold Models

Combustion in turbulent diffusion flames is a physically controlled process in which the chemical reaction proceeds so rapidly that the process is entirely determined by the finite rates at which mixing of the reactants takes place. The rates at which this mixing occurs are controlled in the first place by aerodynamic turbulent transport processes of mass, momentum, and heat. Hence, in the study of diffusion flames, interest lies mainly in the establishment of these turbulent transport processes. Direct measurements in flames can provide a wealth of the data necessary for such procedure in the form of spatial distribution of velocity, pressure, temperature, concentration of gases, and turbulence parameters.

The shortage of detailed and accurate experimental data on fuel-air mixing in furnaces is due to the difficulty and complexity of measurements in flames. For this reason, some previous workers carried their studies on cold model furnaces or isothermal models (no chemical reactions). This cold model can provide quantitative results, which can be very valuable in yielding concrete and detailed information on the basic flow and mixing processes and on general tendencies of the effect of the experimental variables in these processes. Moreover, measurements conducted on isothermal models with ease and high accuracy can be used to test the validity of the theories and hypotheses encountered in the prediction methods.

The difference between the mixing pattern with chemical reactions and that without chemical reactions may arise from the fact that the combustion process is accompanied by high temperature and density gradients across and along the furnace, and consequently the mixing pattern might be affected to some extent.

There are numbers of tracer techniques used for modeling of hot combustion systems as well as cold isothermal models. One of these techniques is the flow visualization for isothermal modeling with air or water. Fine balsa dust or smoke can be used as a tracer in the air models, while polystyrene particles, air bubbles or aluminum powder are used in the water models, and the flow is then photographed. Also, light refraction techniques and flash vaporization of kerosene are used.

El-Mahallawy et al [600] and Khalil et al [601] have tested experimentally the validity of the similarity criterion in a cylindrical furnace equipped with a double concentric jet burner. The size of the cold model burner was kept undistorted, while the swirling fuel jet, was replaced by an equivalent air jet. This jet provided the same input mass flow rate, axial momentum flux and the swirl number as that of the hot test. The work revealed that although the general shapes of the radial distribution curves of axial and tangential velocities are slightly affected by combustion (Fig. 4.13), kinematics

similarity could not be achieved between the hot and cold tests. Kerr [585] suggested that dynamic similarity could be achieved if both the burner size and the swirler vane angle, under cold conditions, were suitably altered. The concept of constant flow rates, constant axial momentum fluxes along the furnace and the equality of the flow swirl numbers at equivalent furnace and model sections provide the criteria for this alteration.

The effects of main important parameters on the flow and mixing in cold conditions have been investigated extensively by El-Mahallawy and co-workers [602-609], and will be discussed in the following parts.

4.4.1 Co-Axial Confined Jets

The mixing of two co-axial confined jets is of special importance to fuel-air mixing in furnaces. The phenomenon of flame in furnaces is a result of complex interaction of physical and chemical processes. The knowledge of how to control and predict the major properties of the flame has become essential to furnace design engineers for obtaining optimum design and to achieve maximum economy.

As an intermediate step to understand the mixing pattern in furnaces, which depends on the rate of molecular and turbulent transfer, it is necessary to study the aerodynamic mixing pattern without chemical reactions. This study besides having the advantage of simplicity and accuracy in flow measurements, it provides the necessary experimental data in order to develop the prediction methods and finally to understand the actual mixing process accompanied by chemical reactions.

In this section, an experimental and theoretical investigation of the aerodynamic mixing pattern of two co-axial confined jets, with special reference to fuel-air mixing in

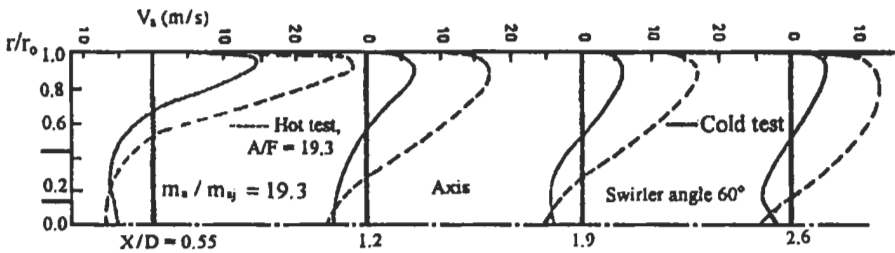


Fig. 4.13 (a): Effect of combustion on the radial distributions of axial velocity along the furnace [600, 601].

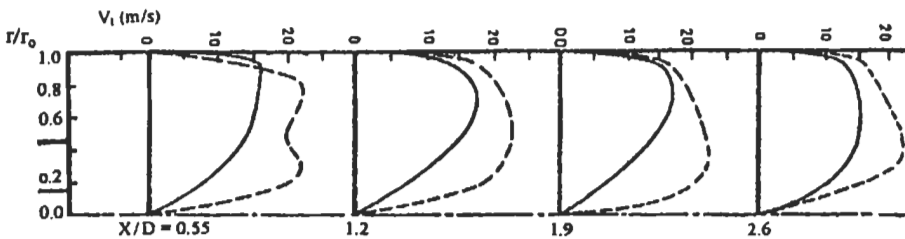


Fig. 4.13 (b): Effect of combustion on the radial distributions of tangential velocity along the furnace, $A/F = 19.3$ and swirl angle = 60° [600, 601]. ---- Hot — Cold.

furnaces, was carried out by Khalil et al [602]. Data were obtained for the following parameters: mass ratio of the two jets, the annular thickness separating the two jets, the Reynolds number and the degree of swirl or the swirl number of the annular jet. A comprehensive study was made on the effect of these parameters on mixing and distribution of constant concentration contours.

The test rig used consists of a cylindrical model furnace provided with a double concentric jet burner. The dimensions of the furnace cylinder are $D = 0.2$ m diameter, 2.15 m long and 6 mm thickness. The primary air is supplied through the central jet and its temperature is controlled by an electric heater. The secondary air is supplied through an air distributor to the annular space surrounding the primary jet.

The tracer technique used was the temperature tracer technique. The local concentration at any point was calculated as follows:

$$F = \frac{t - t_s}{t_p - t_s} = \frac{1}{(1 + m_s / m_p)} \quad (4.35)$$

where F is the mixture fraction or the concentration of the primary jet, t_s and t_p are the temperature of the secondary and primary streams respectively, m_s and m_p are the corresponding mass flow rates.

The mixing pattern is predicted using computational procedure of Gosman et al [610], which solves the conservation elliptic partial differential equations. The experimental and predicted results will be discussed as follows:

Effect of the mass ratio of the two streams. One of the important parameters that affects the mixing in furnaces and determines the dimensions of the flame is the fuel-air ratio in combustion systems or the mass ratio of the primary and secondary air jets in the cold system. The distribution of the mixture fraction across the furnace for two mass ratios was found to be of an exponential form;

$$F/F_m = K_1 \exp (-K_2(r/X)) \quad (4.36)$$

where F is the mixture fraction at a radius r , F_m is the mixture fraction on the centerline at a distance, X , from the burner, K_1 and K_2 are constant.

Figure 4.14 shows the constant concentration contours for two mass ratios, MR. It is clear that increasing the mass ratio of the secondary air stream to the primary air stream, results in an increase in the rate of decay of center line concentration, i.e. the flame length in the hot system will get shorter.

Effect of Reynolds number. As regards to the effect of Reynolds number of the input streams on mixing under cold conditions, it was shown that its effect is small but not insignificant. This is clear from the comparison of the measured center line concentration of the primary air stream, for three values of Reynolds number of input streams, as shown in Fig. 4.15. The three values of Reynolds number correspond to secondary air mass flow rates of 405, 320 and 185 kg h⁻¹.

Effect of swirl on mixing. Concentration measurements were carried out on four degrees of swirl (0, 30, 45 and 60°) to study their effect on the mixing pattern and these results are shown in Fig. 4.16. It is clear from this figure that increasing the swirl intensity increases the rate of decay of the primary stream centerline concentrations. This is because the application of swirl to the secondary stream results in a region of

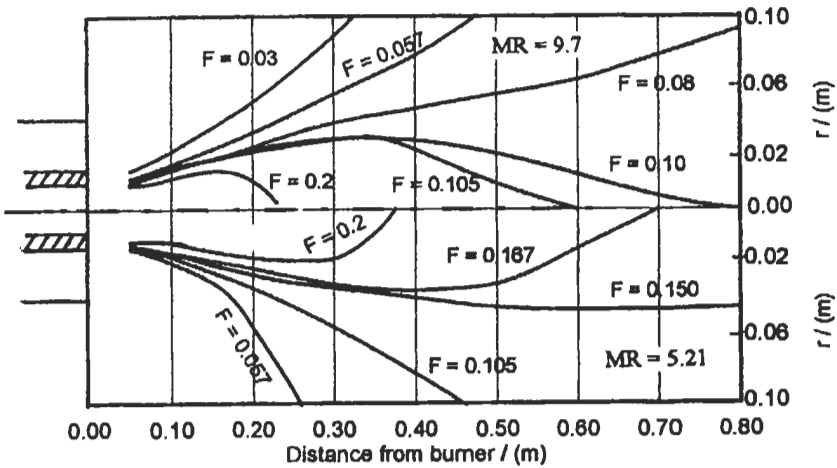


Fig. 4.14: Effect of the mass ratio of the two streams on the constant concentration contours at zero° swirl ($m_s = 405 \text{ kg h}^{-1}$) [602].

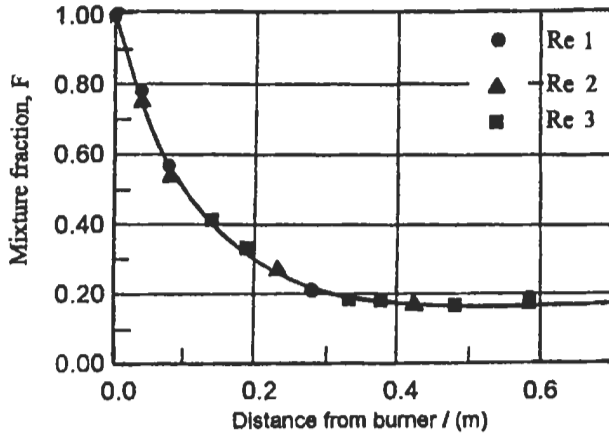


Fig. 4.15: Effect of the Reynolds number on centre line concentration at 45° swirl (MR = 5.21) [602].

static under pressure just after the burner as a consequence of the centrifugal force applied to the flow. In furnaces, this region has an important effect on flame stabilization as it constitutes a well-mixed zone of combustion products and acts as storage of heat and of chemically active species located in the center of the jet near the burner.

For mass ratio, MR = 5.21, it was found that the radial distribution of the mixture fraction across the furnace can be correlated by:

$$F/F_m = \exp(-4.4 (r/X)) \quad \text{for zero}^\circ \text{ swirl} \quad (4.37)$$

and

$$F/F_m = 1.395 \exp(-2.9 (r/X)) \quad \text{for } 45^\circ \text{ swirl and } r/X > 0.15 \quad (4.38)$$

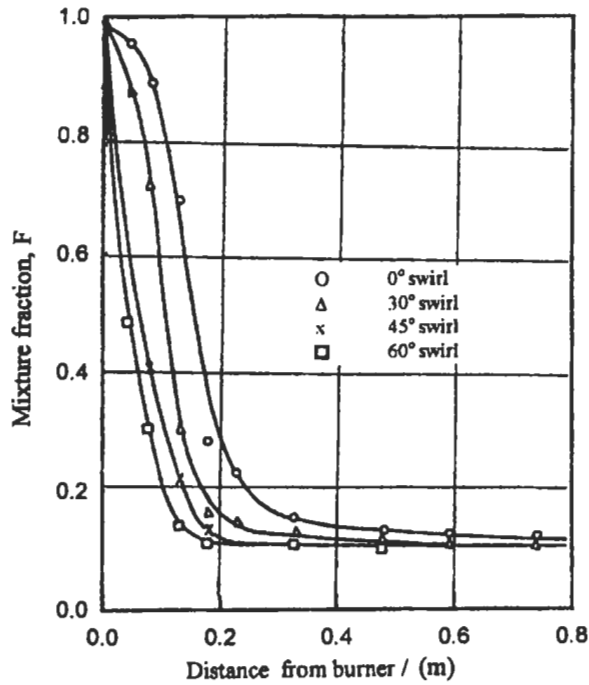


Fig. 4.16: Effect of the degree of swirl on the centre line concentration ($m_s = 320 \text{ kg h}^{-1}$, $MR = 9$).

From the plot of the mixing length (L), determined by the point of intersection of the concentration contour with the center line against the swirl number S , the following relations were obtained for three values of the initial concentration of the primary jet and for the range of S between 0 and 0.85:

$$L = 0.33 \exp(-1.206 S) \quad \text{for } F_i = 0.15 \quad (4.39)$$

$$L = 0.55 \exp(-1.485 S) \quad \text{for } F_i = 0.125 \quad (4.40)$$

$$L = 0.75 \exp(-1.800 S) \quad \text{for } F_i = 0.115 \quad (4.41)$$

where F_i is the initial concentration of the primary jet. In general, $L = A \exp(-nS)$, where A and n are functions of F_i .

Figure 4.17 shows the effect of swirl of the secondary jet on the constant concentration contours. It is clear from this figure that increasing the swirl intensity imparted to the secondary air stream increases the maximum diameter of the constant concentration contours and shortens their lengths. Figure 4.18 shows a comparison between the experimental and predicted concentration contours. It is clear from this figure that at high values of the primary stream concentration, the predicted mixing length is nearly the same as the experimental one. The difference between the two is in the range from 0 to 5 %.

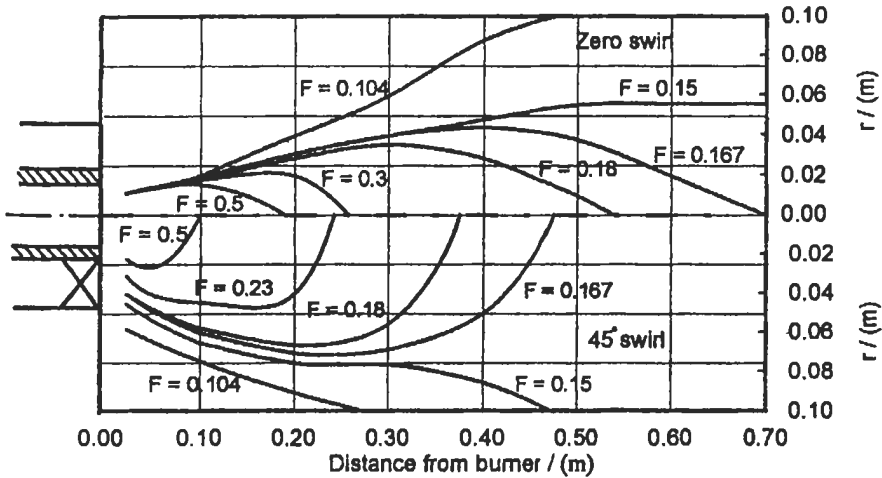


Fig. 4.17: Effect of swirl degree on concentration patterns ($MR = 5.21$, $m_f = 320 \text{ kg h}^{-1}$) [602].

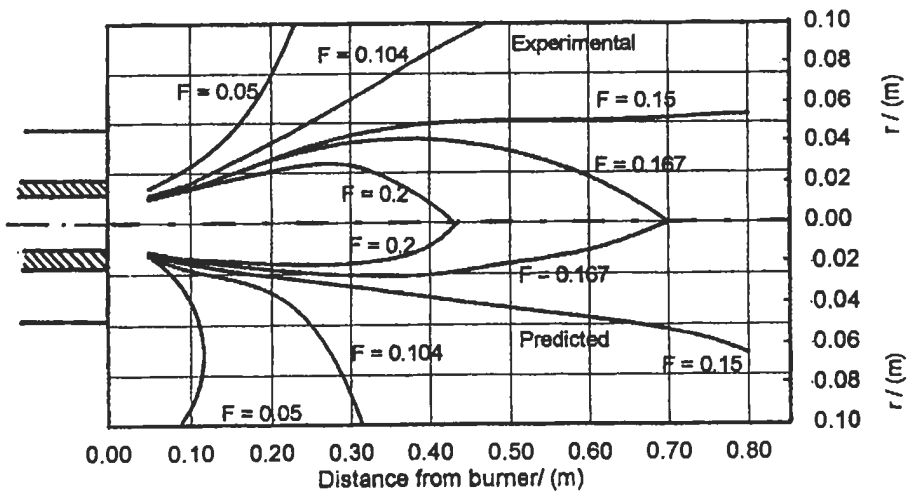


Fig. 4.18: Experimental and predicted concentration contours at zero° swirl ($MR = 5.21$) [602].

4.4.2 Asymmetric Confined Jets

In the last few years, there has been considerable interest to burn fuel with low combustion quality such as: low-grade coals and biomass fuel. Such fuels are relatively difficult to burn and stabilize, therefore, the possibilities of flame failure are rather high. This has led to increased efforts to improve the performance of industrial burners to handle the problems associated with the combustion and stability of these difficult to burn fuels, Cogoli et al [611]. The poor flame stability of such type of fuel is mainly due to two predominate reasons: (i) high axial momentum of the incoming primary jet of

fuel, high enough to carry the fuel parcel, which can result in their fast travel and penetration of the near-burner zone and (ii) a significant heat addition is required to evolve the gas phase of such fuels and the volatile release may not occur soon enough for the disengaged gases to enter the near-burner region.

These types of fuels require that aerodynamics of the near burner region is such that the fuel particles residence time, its heating rate and the availability of oxygen be maximized in the primary reaction zone in order to achieve good flame stability, Abbas et al [612]. This is usually accomplished by creating a strong recirculation zone near the burner, which carries the hot combustion product back towards the burner exit to establish temperatures high enough to ignite the incoming fuel. This recirculation zone is commonly achieved by means of either imparting swirling motion to the incoming air or by placing a bluff body into the air stream to create wake eddies in the near-burner zone as discussed in chapter 3 and section 4.3.

El-Mahallawy et al [603] have investigated the principles of an asymmetrical jet stablization technique, which is used to creat a natural 3-D flow field with a large recirculation zone. Figure 4.19 (a) shows the typical flow of asymmetric (non-symmetric) jet. The behavior of the flow is described by a set of non-linear partial differential equations. These equations express the conservation of different properties characterizing the flow. All equations are cast into a standard equation format, which allows a single finite differencing and greatly simplifies the solution technique and model coding. The standard differential equation form governing the fluid dynamic and heat transfer for the three dimensional flow is presented in Cartesian coordinates:

$$\begin{aligned} \partial/\partial X(\rho u\phi) + \partial/\partial Y(\rho v\phi) + \partial/\partial Z(\rho w\phi) - \partial/\partial X(\Gamma_\phi \partial\phi/\partial X) - \\ \partial/\partial Y(\Gamma_\phi \partial\phi/\partial Y) - \partial/\partial Z(\Gamma_\phi \partial\phi/\partial Z) = S_\phi \end{aligned} \tag{4.42}$$



Fig. 4.19(a): Schematic diagram of an asymmetric jet air [603]. Reproduced by permission of ASME.

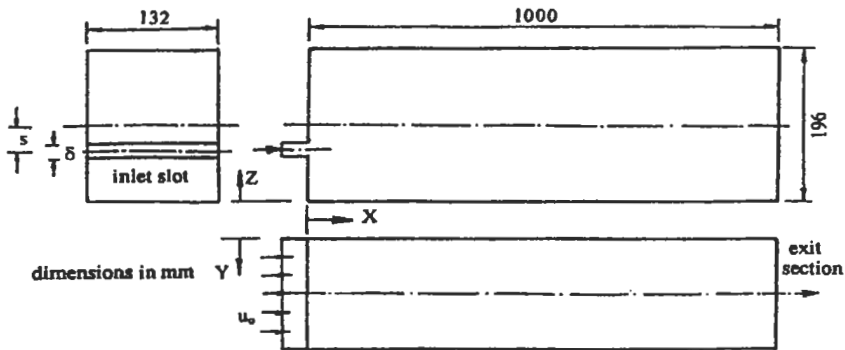


Fig. 4.19(b): Basic configuration of the test section [603]. Reproduced by permission of ASME.

Table 4.1 specifies the values of the representative variable (ϕ) and the corresponding exchange coefficient (Γ_ϕ) as well as the source term (S_ϕ) that allow the standard equation to represent each differential equation, where ρ is the density, p is the total pressure, μ_t is the turbulent viscosity, and g_z is the component of gravity in Z -direction. The term, G , which expresses the shear production of turbulent kinetic energy, is given as:

$$G = \mu_t \left\{ \begin{aligned} &2\left[(\partial u / \partial X)^2 + (\partial v / \partial Y)^2 + (\partial w / \partial Z)^2\right] + \\ &(\partial u / \partial Y + \partial v / \partial X)^2 + \\ &(\partial u / \partial Z + \partial w / \partial X)^2 + (\partial v / \partial Z + \partial w / \partial Y)^2 \end{aligned} \right\} \quad (4.43)$$

The eddy viscosity (μ_t) is calculated from the Prandtl-Kolmogorov relationship:

$$\mu_t = C_\mu \rho k^2 / \epsilon \quad (4.44)$$

The values of the constants appearing in k and ϵ equations are given, as follows:

$$c_1 = 1.44, c_2 = 1.92, \sigma_k = 1.0, \sigma_\epsilon = 1.2, C_\mu = 0.09.$$

A detailed treatment of the boundary conditions for the k - ϵ model as well as the turbulence intensity which is specified for the inlet stream in order to get Dirichlet boundary conditions for k [613]. The dissipation level (ϵ) is estimated at the inlet from an empirical correlation [614]. The boundary conditions at the inlet for the velocity components are given by the following formulation:

$$u = u_0, v_0 = 14 \text{ m s}^{-1}, w_0 = 0$$

Finite difference method based on the finite control volume [615] is adapted for the numerical solution of the flow field. The forementioned differential equations are integrated over each control volume to form a finite-difference set of algebraic equations which are written for each control volume with due care to preserve the correct representation of the physical phenomena and ensure computational stability. These finite difference set equations are solved by Gauss-Seidel iterative procedure. The SIMPLE algorithm, described by Gosman et al [616] is employed to couple the pressure with momentum equations. A staggered grid is used for velocity components (u, v, w).

Table 4.1: Cartesian differential equation set [603]. Reproduced by permission of ASME.

ϕ	Γ_ϕ	S_ϕ
I	0	0
U	μ_t	$\partial / \partial X(\mu_t \partial u / \partial X) + \partial / \partial Y(\mu_t \partial v / \partial X) + \partial / \partial Z(\mu_t \partial w / \partial X) - \partial p / \partial X - 2 / 3 \rho k$
V	μ_t	$\partial / \partial X(\mu_t \partial u / \partial Y) + \partial / \partial Y(\mu_t \partial v / \partial Y) + \partial / \partial Z(\mu_t \partial w / \partial Y) - \partial p / \partial Y - 2 / 3 \rho k$
w	μ_t	$\partial / \partial X(\mu_t \partial u / \partial Z) + \partial / \partial Y(\mu_t \partial v / \partial Z) + \partial / \partial Z(\mu_t \partial w / \partial Z) - \partial p / \partial Z - 2 / 3 \rho k - \rho g_z$
K	μ_t / σ_k	$G - \rho \epsilon$
ϵ	μ_t / σ_ϵ	$(\epsilon / k)(c_1 G + c_2 \rho \epsilon)$

Initially it should be mentioned that the flow under consideration possesses three velocity components, namely: the axial velocity (u) in the longitudinal X-direction, the azimuthal velocity (w) in the vertical Z-direction and a cross-sectional flow velocity (v) in the Y-direction, see Fig. 4.19 (b). In order to validate the predictive model, the predicted profiles [612] of the axial flow velocity (u/u_0) at different axial stations, and at the middle vertical plane of symmetry are compared in Fig. 4.20 with the corresponding experimental ones reported at zero off-axis distance (s) by Wu et al [617]; u_0 stands for the velocity at entrance.

Figure 4.21 presents the predicted streamlines and velocity contours [612] at different consecutive vertical planes. A streamline is a hypothetical continuous line of massless particle traces drawn through the flow field to show the direction of the velocity vector for every particle. The figure indicates the formation of a large recirculation zone, which is attached to the upper wall and extends to at least five times the furnace height. The jet tilts to the opposite side as a natural result of the conservation of mass. The reverse flow zones are attributed to the pressure difference created in the furnace by the incoming air stream. One should anticipate that the large recirculation zone formed on the top wall immediately after entrance would act as the main source of ignition for the incoming fuel. This is due to the long heating time which would be offered by this extended reverse flow zone; heavy particles will tend to follow deterministic trajectories as imposed by their original direction of injection while the lighter ones will follow the gas phase and hence it turns more easily and captured by the recirculating flow, Lockwood et al [618].

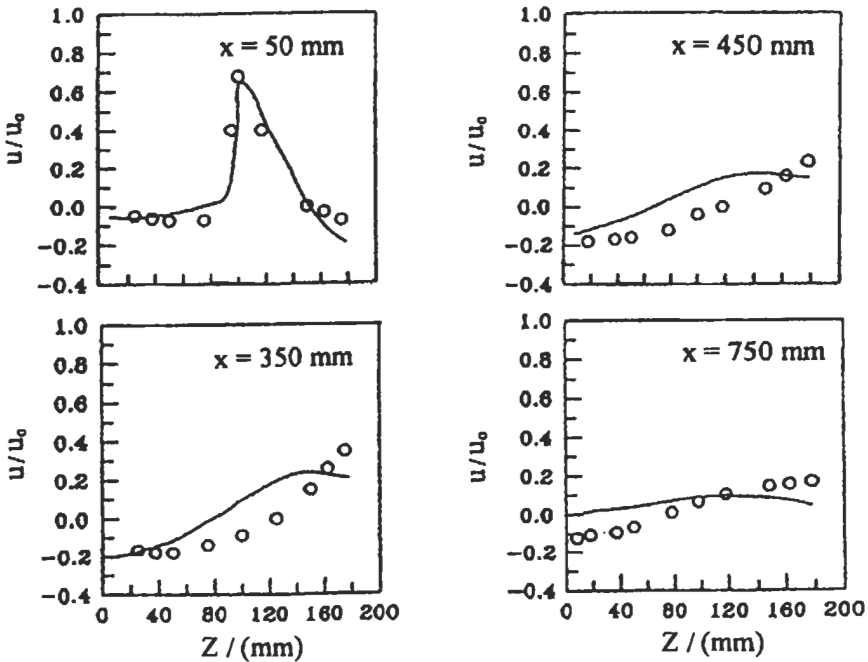


Fig. 4.20: Comparison between predicted and measured velocity profiles [603]. Reproduced by permission of ASME.

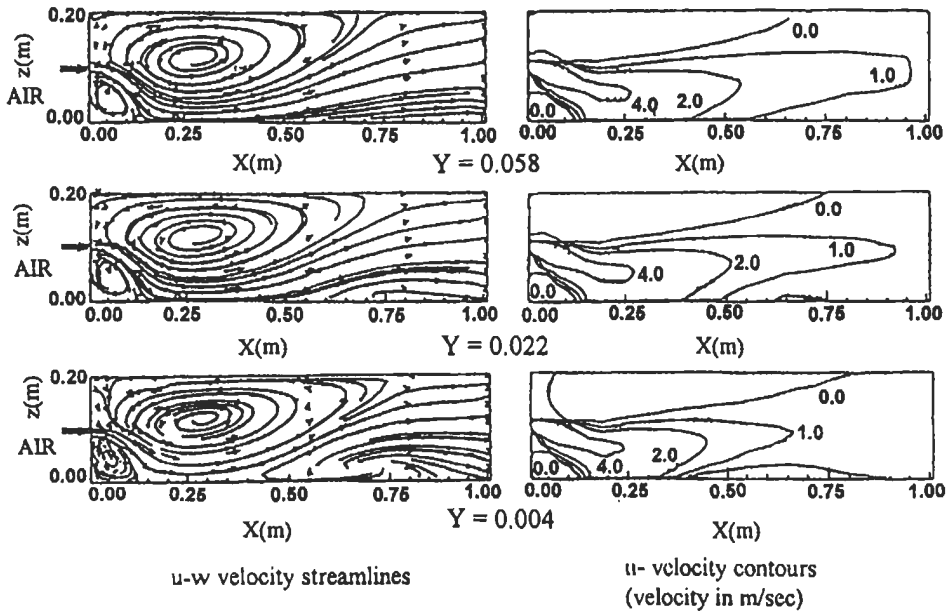


Fig. 4.21: The velocity fields at various X-Z planes [603]. Reproduced by permission of ASME.

Figure 4.22 represents comparative typical predictive results [612], at the vertical middle plane of symmetry, indicating the effect of varied off-axis distance on the flow field and the size of produced recirculation zone. The shift of the inlet air jet downward from the horizontal centerline of the furnace model produces a change in the size of the recirculation zone. Both the length and the width of the torroidal recirculation zone are increased as the off-axis gap (s) is increased. However, as the off-axis gap exceeds 6 times the inlet slot thickness, it seems that the size of the recirculation zone is slightly affected. The figure also shows that the size of recirculation zone affects the exit velocity behavior. The control of the recirculation zone length by the alteration of the off-axis distances can be utilized to control the flame length and intensity.

4.4.3 Co-Flowing Jets with Large Velocity Difference

In certain combustion applications it is desirable to promote heat exchange between the flame and the receiving media (charge) without perceptibly increase the temperature of the furnace walls to the advantages of its mechanical resistance, corrosion and furnace pollution control. In these applications, the enhanced mixing in jet streams and fuel streams, as well as the extent of mixing between recirculated hot product gases and remaining air streams will enhance the heat transfer to the required media. Advancing technologies are required for the development of jet mixing schemes [619], in order to achieve such objective.

Oriented heat transfer can be achieved by using flames of non-uniform thermal gradients where the hot part of the flame is directed towards the heated media which results in less heat and radiation received by the walls. Furnaces of the arched type, open hearth steel furnaces, cement kiln and smelting furnaces are some examples of

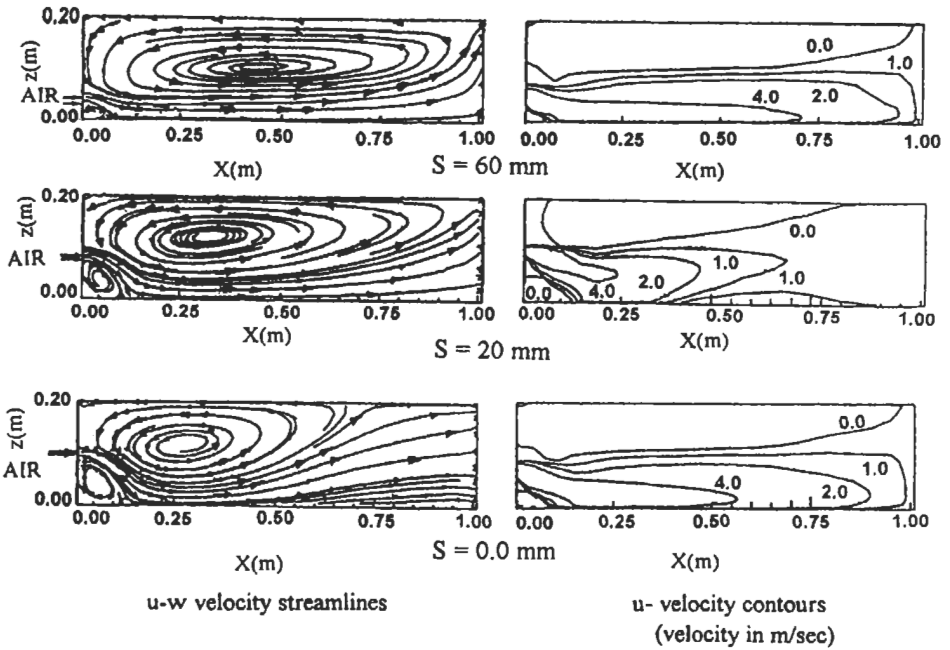


Fig. 4.22: The effect of the off-axis distance on the flow velocity field [603]. Reproduced by permission of ASME.

such industrial devices [620]. In most of these industrial applications, multi-jet burners are usually used. However, despite the practical motivation for detailed investigation of multi-jet applications, there remains only a handful of studies in the literature [621].

EL-Mahallawy et al [604] have predicted cold flow results in a 3-dimensional furnace jets having a burner with co-flowing jets of large velocity ratios. The burner comprises a main jet, which enters the combustor along the axis and few small nozzles, which are located at a given radius from the axis. Air is injected through the auxiliary jets at relatively high velocities. Due to the strong action of the high-velocity jets in the furnace, the low-velocity primary air will be sucked into the high-velocity jets causing it to flow away from the axis. The pressure field thus created causes a large recirculation zone to be formed downstream of the primary air inlet, even though the pressure differential are quite small [622]. The study covers many parameters such as velocity ratio, number of co-flowing jets and the relative distance between the small secondary jets and the central main jet.

As drawn in Fig 4.23, the furnace dimensions are $W = 0.5$ m, $H = 0.55$ m and $L = 0.8$ m. The burner consists of a primary central air jet located at the furnace axis and two jets with equal high-velocity flow of air placed at a given distance of the furnace axis. The predicted results from the model were validated against the relevant experimental data reported by Fu et al [622]. The experimental conditions are as follows:

The velocity ratio $(VR) = V_j/V_m = 15.0$

The flow rate ratio $= Q_j/Q_m = 0.05$

$$\delta y = \Delta Y / W = 0.60$$

$$\delta z = \Delta Z / 0.5 H = 0.82$$

where V and Q represents the velocity and the flow rate respectively, while the suffix (s) stands for the small "secondary" high-velocity jets and the suffix (m) stands for the "main" central jet. δy and δz varying from 0 to unity, Fig. 4.23. ΔY is the horizontal gap between the two secondary jets and W is the furnace width; ΔZ is the vertical distance between the center of the main jet and the common horizontal axis passing through the secondary jets while H is the height of the furnace.

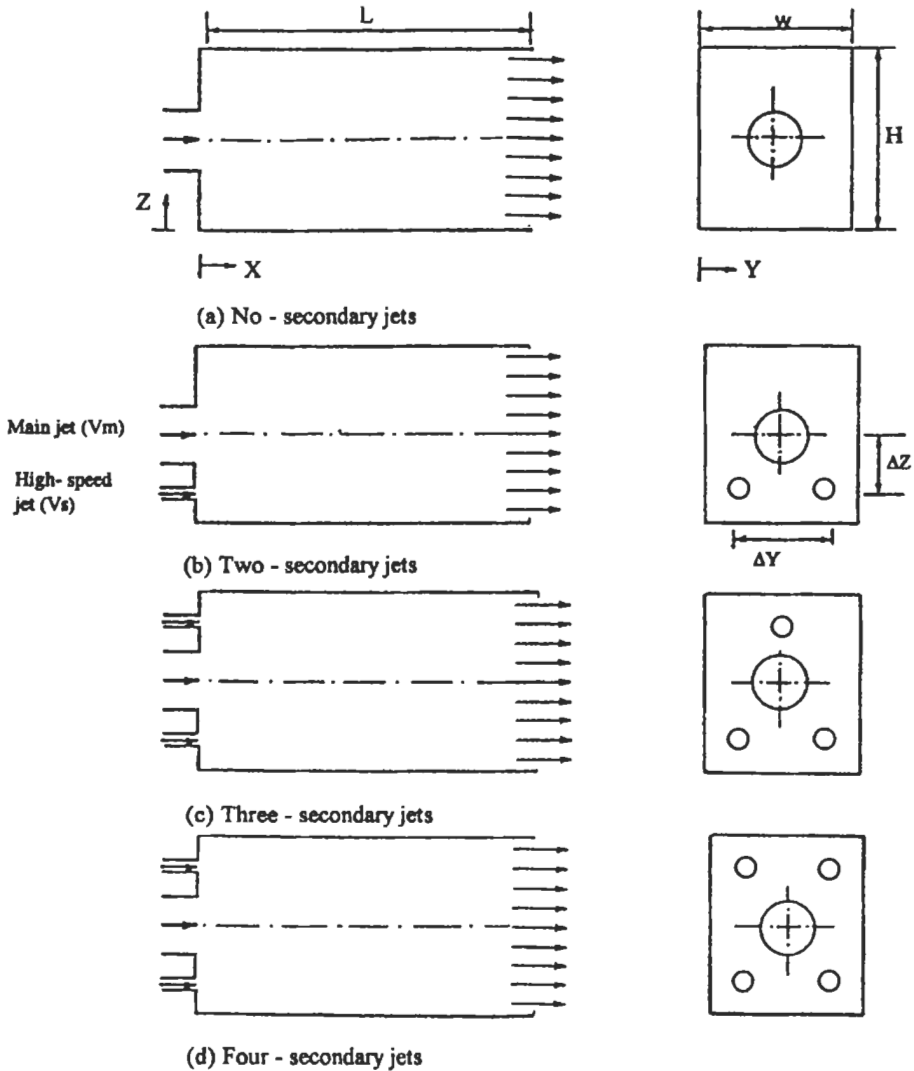


Fig. 4.23: The test furnace and burner arrangements [604].

The flow behavior in three-dimensional furnaces can be described by a set of standard differential equations expressing the conservation of different flow properties; presented hereinafter in Cartesian coordinates as described in section 4.4. The numerical solution of the flow field adopts the finite difference method based on the finite control volume [615], together with the SIMPLE algorithm, described by Gosman et al [616]. Cartesian grid size of $22 \times 23 \times 23$ was used for the present calculations. Adequate grid refinement study was performed to ensure the grid independence of the solution. Figure 4.24 demonstrates the predicted axial flow velocity at two axial locations along the furnace length [604], as compared with the experimental results of Fu et al [622], for two cases: with and without the high-velocity secondary air jets.

The principal objective of the co-flowing jets is to control the combustion zone, which control the combustion by acting as a source for heating, ignition and prolonging the residence time. Such recirculation zone (RZ) can generally be characterized by its size and strength. The size is expressed by the zero axial velocity contour [491], while the strength, denoted herein by β , at any axial station can be determined by the mass of the reverse flow as a percentage of the forward flow mass. Both the forward and backward flow masses, at any axial station (X), are calculated by integrating the mass influx through the faces of each control volume over the Y-Z cross-sectional plane.

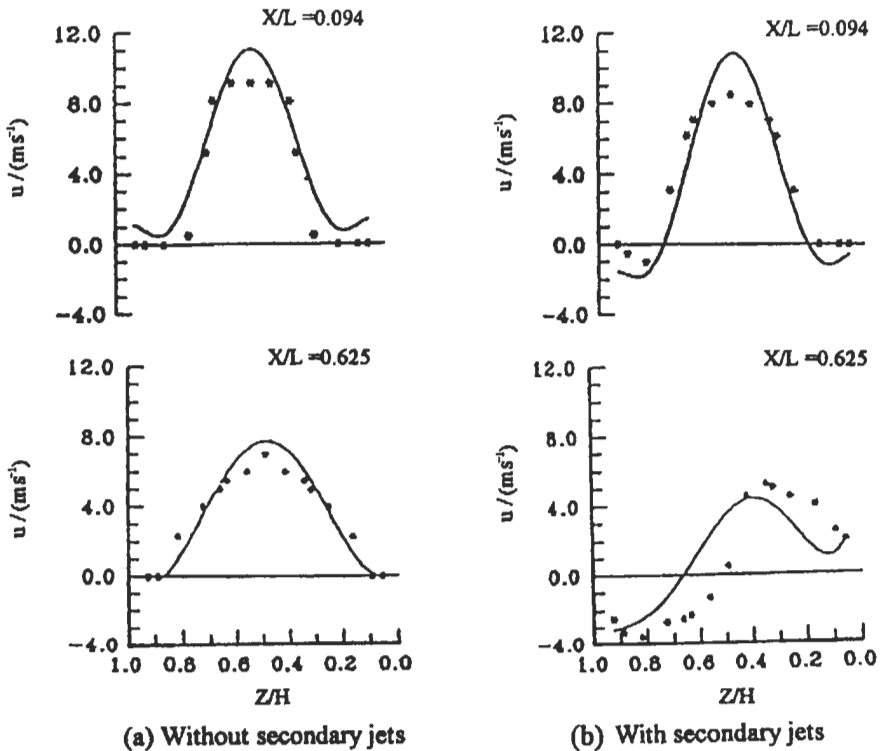


Fig. 4.24: The comparison between the measured and the predicted axial velocity along the middle plane [604]. * Measurements from Fu et al [622].

Figure 4.25 illustrates the influence of the number of secondary jets on the strength of the recirculation zone for two velocity ratios of 15 and 35 ($\delta y = 0.60$, $\delta z = 0.82$) [604]. The strength is augmented as the velocity of the secondary jets is increased. The dominance of the two jets configuration is strongly pronounced and its recirculated flow exhibits more strength and larger size. In summary, the results strengthen the belief that the flow field is optimized by using two secondary jets and the recirculated flow is controlled by adjusting the velocity of these jets. Flow pattern for different co-flowing jets on the axi-symmetrical central plane of the furnace is presented in Fig. 4.26. El-Mahallawy et al [604] have concluded that the size and strength of the recirculation zone produced by the co-flowing jets are quite large. This recirculation zone indicating good mixing between the recirculated flow and the forward flow.

Finally, the results indicate that the size and strength of the recirculation zone produced by the two small secondary jets is relatively large. There are also strong cross-flow components of the high-velocity, indicating good mixing between the forward and reverse flows. Such large recirculation zone with strong mixing would prolong the contact time of the fuel with hot gases and provide enough high temperature gases to heat the combustible fuel and air. Moreover, since the basic principle is quite simple and mainly aerodynamic, the combustors are easily scaled-up.

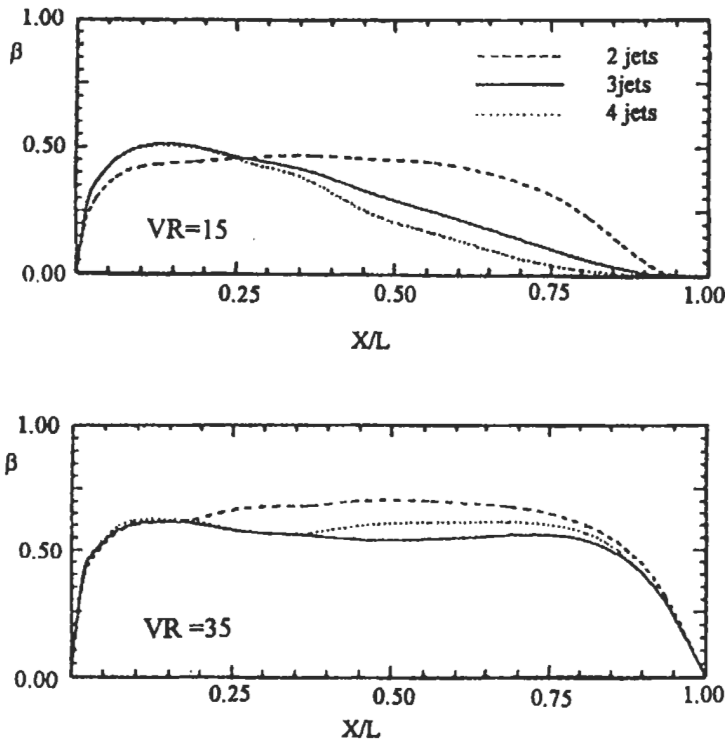


Fig. 4.25: The effect of the velocity ratio on the strength of the recirculation zone for different burner configurations [604].

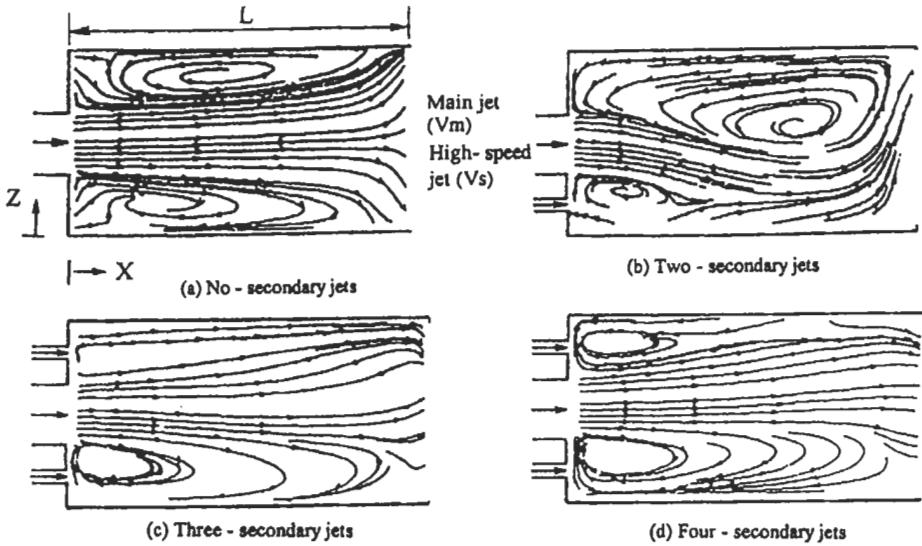


Fig. 4.26: Flow pattern of different coflowing jets arrangement [604].

4.4.4 Two Swirling Confined Jets

In this section, an experimental and theoretical investigation of the effect of swirling both the two streams in the same and opposite direction on the aerodynamic mixing pattern was carried out by El-Mahallawy and Habib [605]. They have used a cylindrical model furnace involving no chemical reactions, and is similar to that used in Ref. 602. The aim of this investigation is to provide experimental data on mixing between two axi-symmetrical jets to simulate the actual mixing process in furnaces.

Secondary and/or primary streams are given tangential momentum at inlet by using thin bladed vane type swirlers. The swirl number for different swirlers is calculated according to the procedure described in section 4.2. The temperature tracer technique (see section 4.4.1) is used for the measurement of the concentration of the primary stream and the local concentration at any point is calculated using Eq. 4.35. The conditions considered are: swirling the secondary stream only, swirling the primary stream only, swirling the two streams simultaneously and the relative direction of swirl (same or opposite direction). A comparison of center line concentration for the case of swirling the two streams in the same direction with that of swirling the secondary stream only is shown in Fig. 4.27. The figure reveals that the addition of swirl to the primary stream, besides the swirl of the secondary stream, has the effect of improving mixing. This is because, the addition of swirl in this case results in a region of static under-pressure just after the burner and this will constitute a well mixed zone of the primary and secondary streams. The effect of the relative direction of swirl of the two streams on the constant concentration contours is given in Fig. 4.28. The opposite direction of swirl is shown to result in better mixing. The main conclusion obtained is that the best condition of mixing is when swirling the two streams at the same time and in opposite direction.

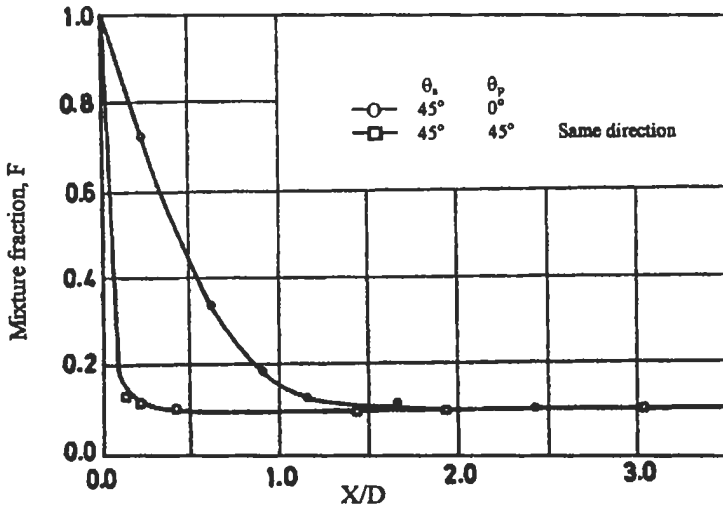


Fig. 4.27: Effect of swirling two streams and one stream only on the distribution of mixture fraction along the centre line ($m_s = 250 \text{ kg h}^{-1}$, $MR = 9$) [605].

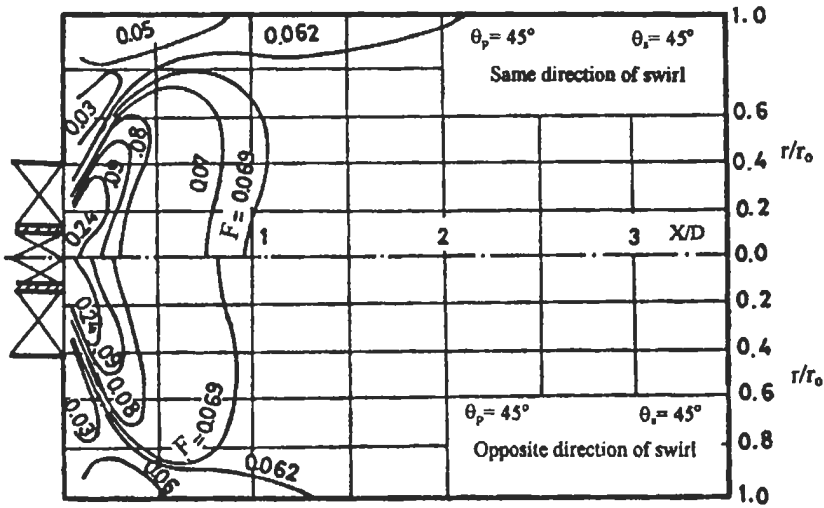


Fig. 4.28: Effect of the relative direction of swirl on the constant concentration contours ($m_s = 250 \text{ kg h}^{-1}$, $MR = 13.5$) [605].

4.4.5 Forced Flow Reversal

The technique of reversing back the combustion products to the entry of fuel and air stream introduces an effective method to obtain the flame over a wide range of operating conditions with an improvement in the flame stability and combustion efficiency. This technique has been used by El-Mahallawy et al [606] to study the mixing processes in a cold model furnace. The main parameters considered are the mass ratio of the two input streams and the length-diameter ratio of the reversed flow model .

The test rig used in this study is shown in Fig. 4.29 and is similar in principle to that used in Ref. 602. It consists of a horizontal cylindrical mixing chamber of 0.20 m diameter and 2.1 m length. The mixing chamber is well insulated. A double concentric jet burner is mounted co-axially with the chamber to achieve axi-symmetrical flow. The far end of the chamber is fitted with an insulated piston. The position of the piston can be varied using a controlling mechanism whose stroke permits the piston to traverse the whole length of the chamber.

The electrically heated primary air and the secondary air issue from the double concentric burner in the mixing chamber. The two air streams flow in the downstream direction to the end of the chamber, where they are reversed back and leave the chamber from the annular space surrounding the burner.

For temperature measurements, three calibrated fine wire thermocouples are used. The adopted technique for mixing studies is the temperature tracer technique described in the previous sections. The mixture fraction (F) which is taken as a measure for local mixedness is defined by Eq. 4.35. For the study of the flow pattern, the boundary of the reversal zone is determined by a directional velocity probe.

Mixing studies are carried out by investigating the decay of centre-line concentration, the wall concentration, the constant concentration contours and the mixing lengths. The mixing length, for a certain concentration of the primary stream, is defined as the distance from the burner at which its corresponding constant concentration contour intersects either the centerline or the wall of the furnace.

Figures 4.30 and 4.31 show a comparison of the centerline concentration for the reversed flow and tunnel type furnaces for mass ratios of 10.5 and 7.25, respectively. The decay of centerline concentration for the reversed flow furnace is faster. After a certain distance X/D , the trend is altered because the effect of the stagnation region

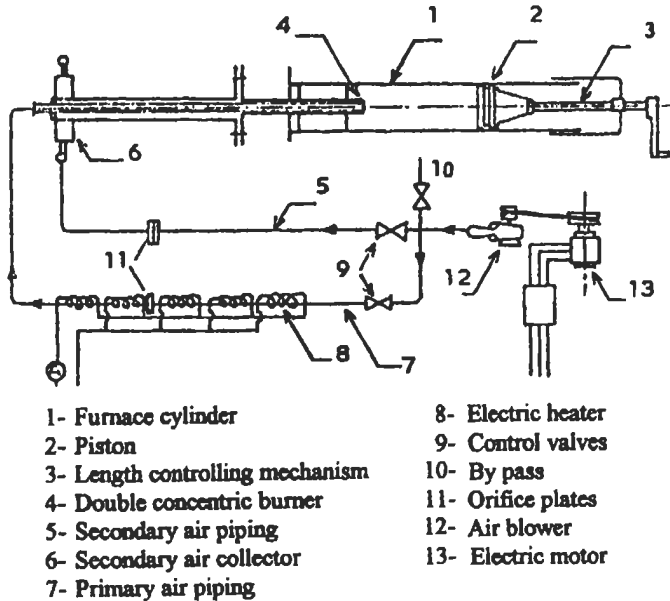


Fig. 4.29: General layout of the test rig [606].

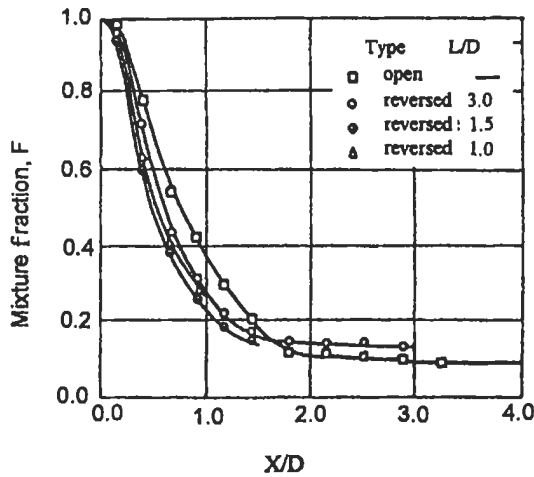


Fig. 4.30: Decay of the centre line concentration for different reversed flow furnace lengths and different furnace types ($MR = 10.5$, $F_i = 0.087$, and $m_s = 315 \text{ kg h}^{-1}$) [606].

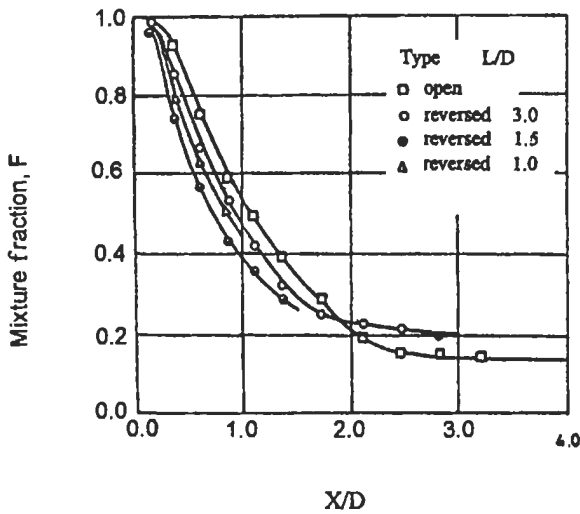


Fig. 4.31: Decay of the centre line concentration for different reversed flow furnace lengths and different furnace types ($MR = 7.25$, $F_i = 0.121$, and $m_s = 315 \text{ kg h}^{-1}$) [606].

created near the piston in long reversed flow furnaces. In the reversed flow type, the mixing continues in the backward flow and completeness of mixing is brought before exit. Figure 4.32 shows the effect of reversing the flow on the mixture fraction contours. The lengths of these contours become shorter in the first stages of mixing.

Finally, it could be concluded that for the same length of the reversed flow and tunnel type furnaces, better mixing is obtained in the reversed flow one, or for the same degree of completeness of mixing at the furnace exit, shorter furnace lengths are required for the reversed flow furnace.

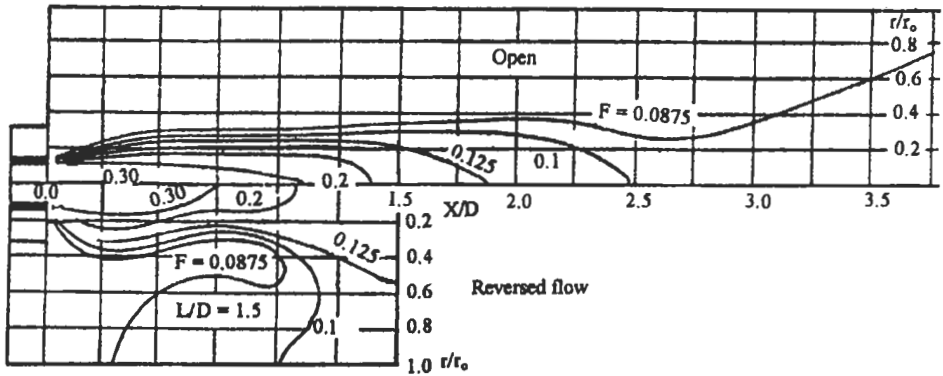


Fig. 4.32: Distribution of the constant concentration contours for two different furnace types (reversed flow of $L/D = 1.5$, $MR = 10.5$, $F_1 = 0.087$, and $m_1 = 315 \text{ kg h}^{-1}$) [606].

4.4.6 Furnace and Burner Geometry

The aim of this section is to complete the information obtained by Khalil et al [602], and El-Mahallawy et al [603-606] in the previous sections (4.4.1 to 4.4.5) through studying the effect of other parameters such as furnace and burner geometry which are thought to have significant effect on flow and mixing. Therefore, three points are investigated in this field (El-Mahallawy et al [607-609]); Firstly, is the effect of the exit section geometry and furnace length, secondly, is the effect of burner geometry, and thirdly, is the effect of combustion zone shape, and these three points will be discussed herein:

Effect of exit section geometry and furnace length. El-Mahallawy and Hassan [608] have investigated the effect of the exit section geometry and the furnace length on mixing and flow patterns in a cold model industrial furnace. The model furnace used is of a cylindrical cross section, similar to that used by Ref. 602, to achieve two-dimensional flow and its size is sufficient to ensure turbulent flow. The exit section diameter of the model furnace is varied by using pistons of different inner diameters, d , and mounted at the model downstream end. Different furnace lengths were obtained by adjusting the piston at the appropriate distances from the model inlet. The model furnace is also provided with a double concentric jet burner at its inlet-section. The secondary air is supplied through an air distributor to the annular space surrounding the primary stream. The location of the model furnace exit restriction inside the test section (representing the required exit section geometry) is shown in Fig. 4.33.

The temperature tracer technique is used to detect the concentration of the primary stream at different points inside the model furnace. The primary air stream is preheated to a temperature up to 145°C , while the temperature of the secondary stream is kept at the ambient air temperature.

The distribution of the centerline concentration for two exit section geometries at zero swirls is shown in Fig. 4.34. It is clear from the figure that decreasing the exit section diameter has a significant effect on increasing the rate of decay of the primary stream concentration along the model furnace length. This is attributed to the increase of the size of the wall reverse flow region existing near the exit section as a consequence of reducing the exit section diameter.

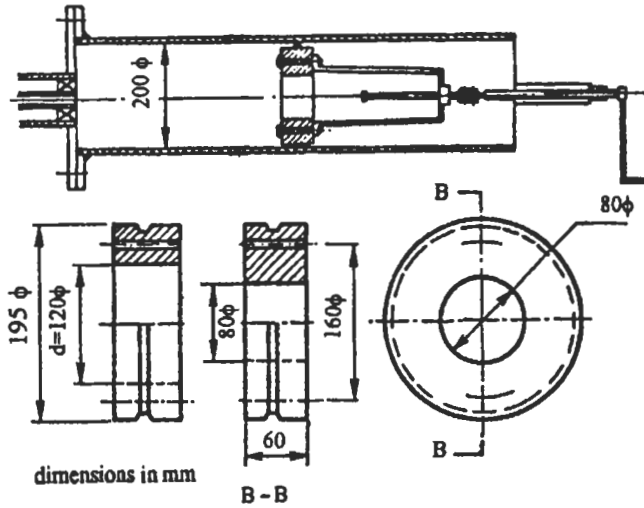


Fig. 4.33: Construction details of piston and piston mechanism [608].

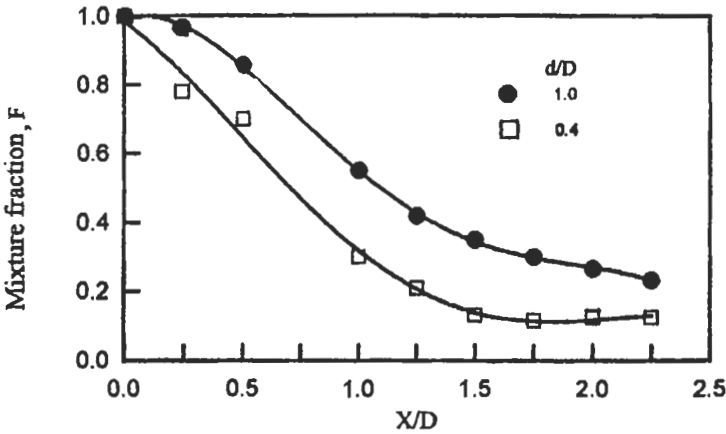


Fig. 4.34: Centre line concentration for different exit section geometries at 0° swirl ($L = 0.5$ m, $m_s = 272$ kg h^{-1} , and $MR = 6.6$) [608].

Figure 4.35 shows the distribution of the constant concentration contours for two exit section geometries at zero swirl. It is clear that reducing the exit section diameter has a combined effect of reducing the radii of the constant concentration contours and decreasing the mixing length (which is defined as the distance between the model furnace inlet and the point of intersection of a constant concentration contour with the model axis). Results obtained for different swirl intensities and furnace lengths confirmed the effect of the exit section geometry on the mixing process.

The exit section of the model is restricted when studying the effect of the model furnace length. It is noticed that reducing the model furnace length has an effect on increasing the rate of decay of the primary stream concentration along the furnace

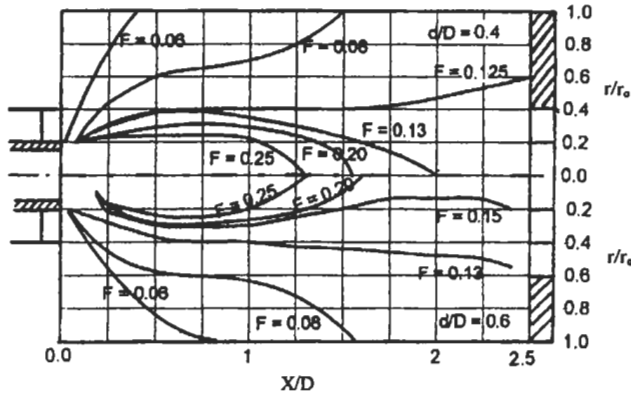


Fig. 4.35: Constant contours for different exit section geometries at 0° swirl ($L = 0.50$ m, $m_a = 272$ kg h^{-1} , and $MR = 6.6$) [608].

length. The effect of reducing the model furnace length on the aerodynamic mixing pattern is shown in Fig. 4.36. It can be noticed that reducing the model furnace length has an effect on decreasing the length of the constant concentration contours, which means increasing the mixing between the two streams. As shown in Fig. 4.37 (a) there is a similarity in the wall recirculation zone for the two model furnace lengths, and the difference in mixing downstream may be attributed to the longer residence time of the recirculated mass with the increase of the model length. Figure 4.37 (b) as compared to Fig. 4.37 (a) shows how the wall recirculation zone is significantly affected by applying swirl to the secondary air stream.

From the above discussion it can be concluded that restricting the model furnace exit section increases the rate of decay of the primary stream concentration along the model length. This results in decreasing the mixing length for a certain degree of mixing which may obviously leads to shorter flames in an actual combustion system. Also the results showed that reducing the model furnace length affects the decay rate of the primary stream concentration along the model furnace length especially in the upstream region.

Effect of burner geometry. El-Mahallawy and Ghali [607] studied the effect of burner geometry on the aerodynamic mixing pattern in a cold model furnace. The test rig and the technique used in this study are similar to those in Ref. 602. The geometries used in this study are; the diameter ratio of the two jets (d_s/d_p), the conduit thickness

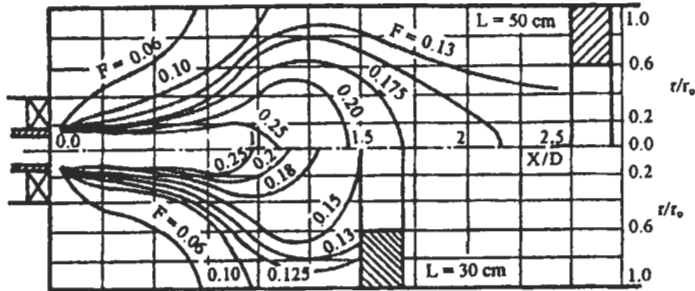


Fig. 4.36: Constant concentration contours for different furnace Lengths at 30° swirl ($d/D = 0.6$, $m_a = 272$ kg h^{-1} , and $MR = 6$) [608].

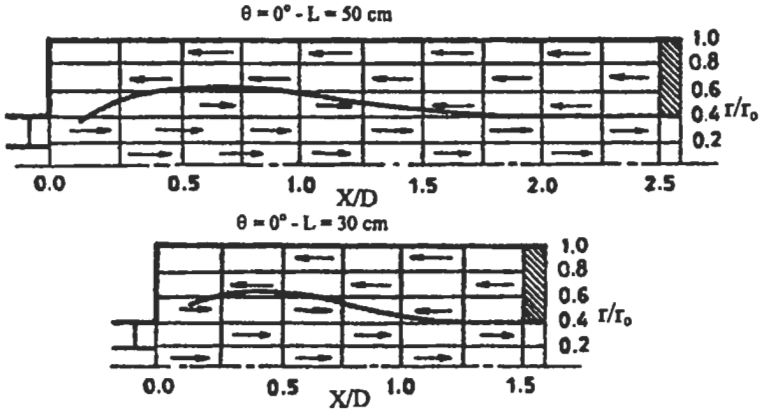


Fig. 4.37(a): Effect of the furnace length on the shape and size of the recirculation zones ($d/D = 0.4$, $m_s = 272 \text{ kg h}^{-1}$, and $MR = 6.6$) [608].

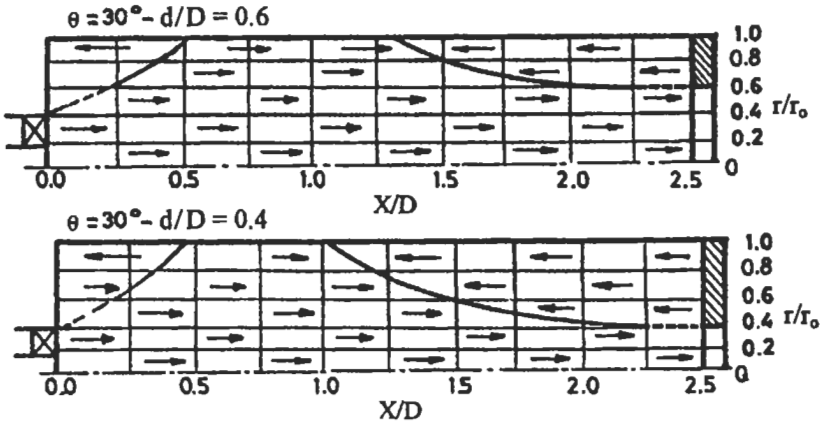


Fig. 4.37(b): Effect of the exit section restriction on the shape and size of the recirculation zones ($L = 50 \text{ cm}$, $m_s = 272 \text{ kg h}^{-1}$, and $MR = 6.6$) [608].

separating the two jets, the height of rings fitted on the outer surface of the primary air pipe and convergency and divergency of the two jets.

Figure 4.38 shows a comparison between the constant concentration contours for 3.6 and 2.8 diameter ratios. It is clear that high rates of mixing correspond to the small diameter ratios. For a given certain constant mixture fraction contour, say $F = 0.2$, as representing the flame boundary under hot conditions, then it could be shown from the figure that the flame length gets shorter as the diameter ratio is decreased. This is a result of the increase of the momentum of the secondary air stream as the diameter of the secondary air pipe is decreased.

Figure 4.39 shows the constant concentration contours for different conduit thicknesses. The mixing improved by increasing the thickness. This is due to the increase in the momentum of the secondary stream and the internal recirculation created due to the increased thickness of the wall separating the two streams.

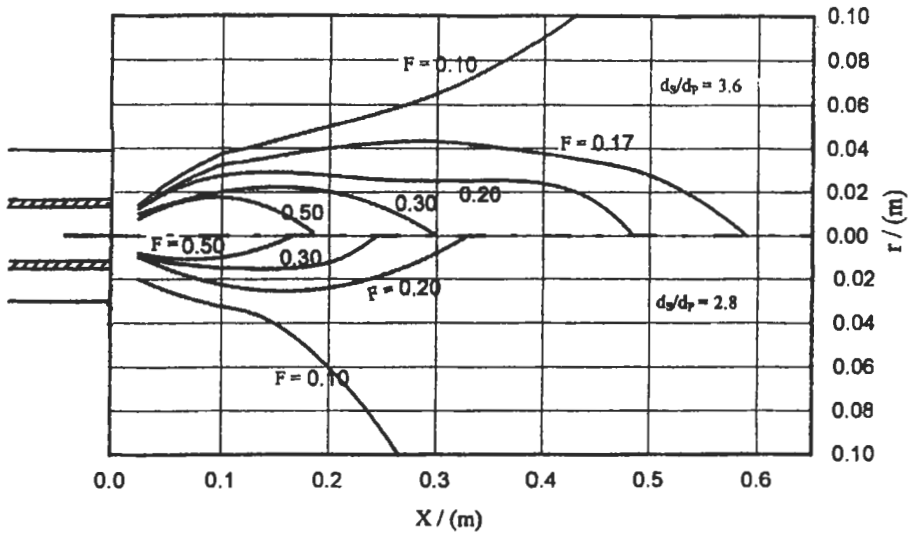


Fig. 4.38: Distribution of the concentration contours for two diameter ratios [607].

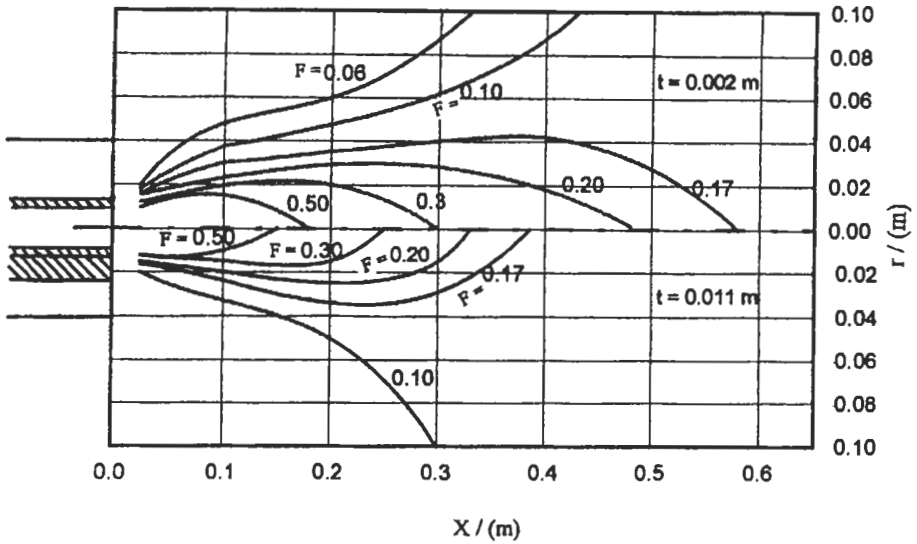


Fig. 4.39: Distribution of the concentration contours for two conduit thicknesses [607].

The effect of a lip fitted on the outer surface of the central air pipe is shown in Fig. 4.40. It is clear that the increase in the lip height results in an increase in the rate of mixing. The development in the mixing is due to the disturbance and internal recirculation formed by the lip, this is beside the increase of momentum of the secondary air in this case.

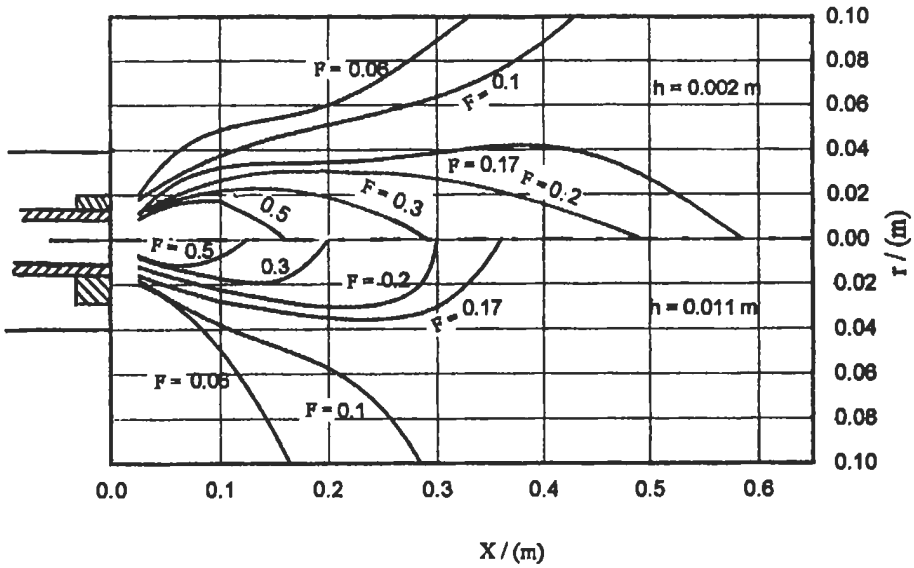


Fig. 4.40: Distribution of the concentration contours for two lip heights [607].

To study the effect of divergence of the secondary air, the experiments were carried out with 0° , 15° , 25° and 45° divergence angles. It is found that the highest rate of mixing corresponds to 15° divergence angle. Figure 4.41 shows a comparison of the constant concentration contours for divergence angles of 15° and 25° . The increase in the rate of mixing and hence the expected decrease in flame length under hot conditions,

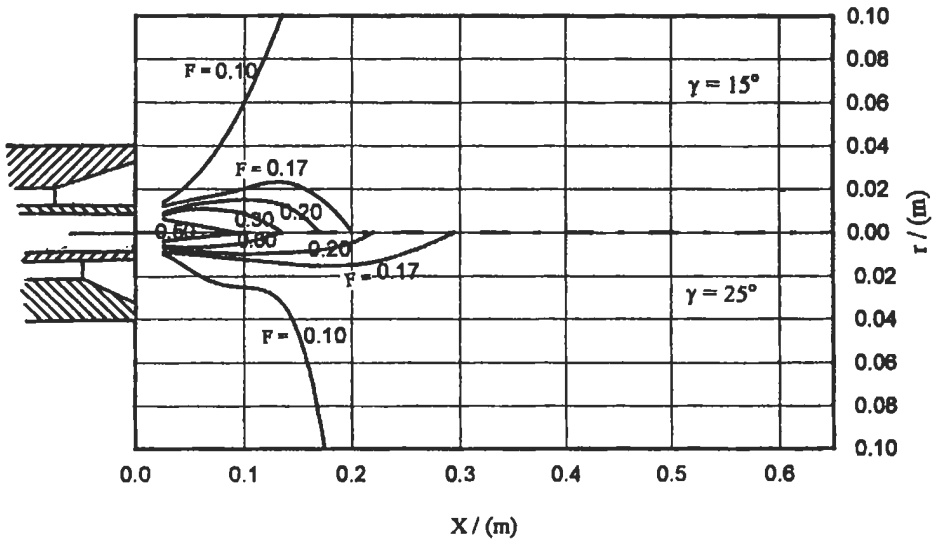


Fig. 4.41: Distribution of the concentration contours for two divergence angles given to the secondary air jet ($\gamma = 15^\circ$ and 25°) [607].

caused by the divergence of the secondary air jet, is due to the internal recirculation created. This effect is more clear for small angles because the flow is completely guided with no separation and divergence of the secondary flow inlet, in this case, will have a significant effect on increasing the internal recirculation.

Convergence angles of 0° , 15° and 25° are given to the secondary air jet. A comparison of the constant concentration contours for convergence angles of 0° and 25° is shown in Fig. 4.42. By comparing the contours of nearly complete mixing ($F = 0.17$), it could be shown that the highest rate of mixing is at 25° . A small improvement was also shown at 15° , as compared to zero degree. The increase in the rate of mixing by increasing the convergence of the secondary air jet is due to the quick interaction between the two streams.

Divergence angles of 0° , 15° and 25° are given to the primary air jet. Figure 4.43 shows a comparison of the constant concentration contours for divergence angles of 0° and 25° . It is generally shown that there is a slight improvement in the mixing process by increasing the divergence angle. Another tests were also carried out for convergence angles of 0° , 15° and 25° to the primary air. The 25° convergence angle gives better mixing as compared with other angles.

Effect of combustion zone shape. El-Mahallawy et al [609] have studied the aerodynamic flow pattern under isothermal condition in three different model combustion zones, one cylindrical and the other two are of conical shape with 45° , 30° cone angle. Figure 4.44 shows the combustion zone of a conical shape. For the calculation of reversed mass flow rate from the measured values of the axial velocity, the cross section of the furnace is divided into a number of equi-area rings to ensure that each ring has nearly uniform value of axial velocity. The reversed mass flow rate, \dot{m}_r , is calculated by Eq. 4.9. This reversed mass flow rate is given as a percentage of the input mass flow

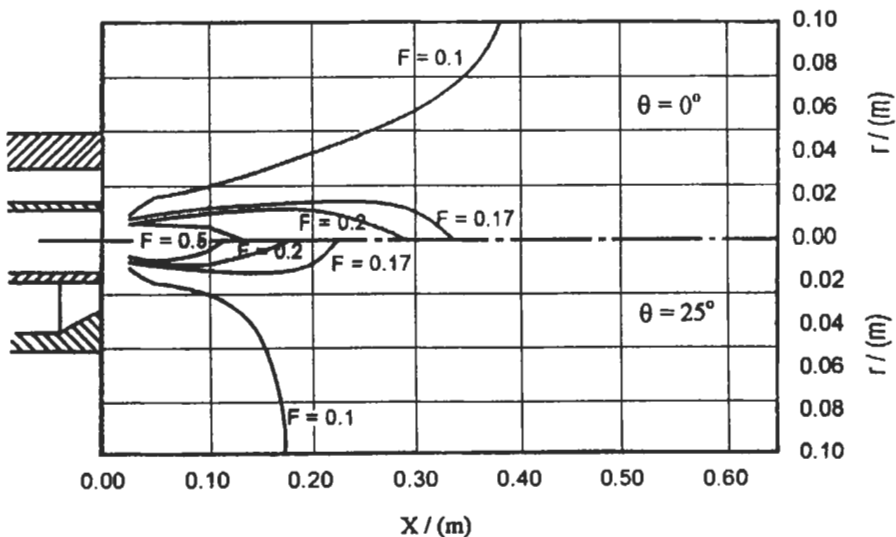


Fig. 4.42: Distribution of the concentration contours for two convergence angles given to the secondary air jet ($\theta = 0^\circ$ and 25°) [607].

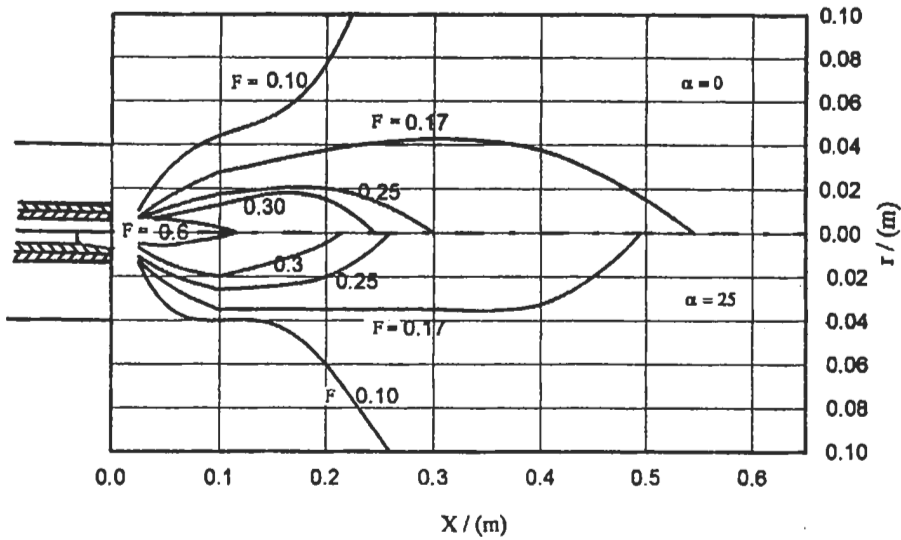


Fig. 4.43: Distribution of the concentration contours for two divergence angles of the primary air jet ($\alpha = 0^\circ$ and 25°) [607].

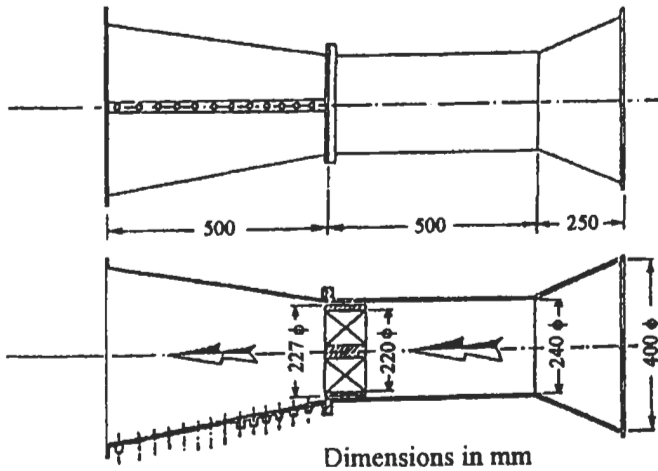


Fig. 4.44: The conical combustion zone [609].

Rate, \dot{m}_0 . The effect of the degree of swirl on the reversed mass flow rate along the model is shown in Fig. 4.45 for the 45° combustion zone and the 30° combustion zone.

It is clear from this figure that for the divergent combustion zones, the reversed mass flow rate increases as moving in the downstream direction of the combustion zone. It is also shown that, the reversed mass increases with the increase of the degree of swirl applied to the air. The results show also that, the reversed mass flow rate and the dimensions of the central recirculation zone are increased with increase of the angle of divergence of the combustion zone.

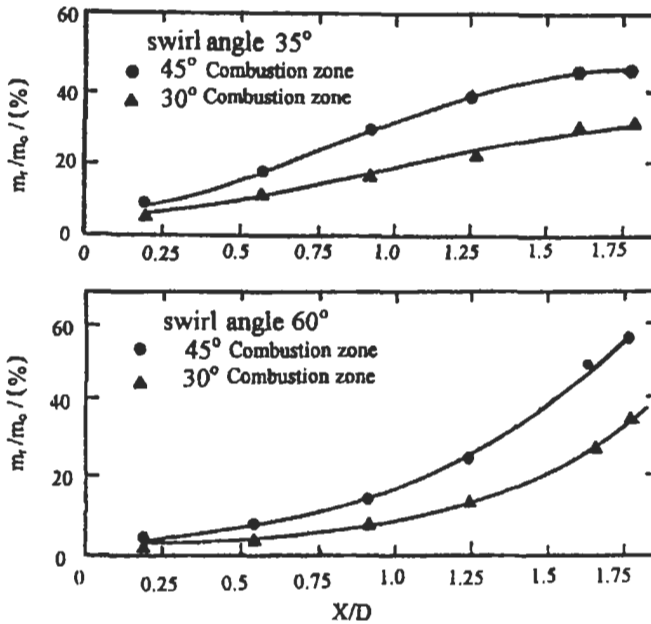


Fig. 4.45: Effect of combustion zone shape on the reversed mass flow rate for the 45° combustion zone and the 30° combustion zone for two different degrees of swirl [609].

4.5 Characteristics of Confined Flames

In most practical cases, the fuel and air enter the furnace as two separate streams and the length and shape of flames produced depend to a large extent on the mixing process between those two streams. The rate of mixing between the fuel and air streams depends on the flow characteristics such as the turbulence level, the swirl imparted to combustion air and the mass ratio of the two streams. It depends also on the burner and furnace geometries.

Due to the considerable increase in the rate of transport under turbulent conditions, aerodynamic effects are more prevalent; and when the fuel and oxidant are not premixed prior to ignition, aerodynamics become the rate-determining factor. This means that the most important characteristics of turbulent diffusion flames, such as spatial distribution of concentration and temperature in the flame as well as its physical dimensions, can be determined from the flow characteristics alone. The effect of these flow characteristics on the flow and rate of mixing between the fuel and air streams will be discussed in sections 4.5.1 and 4.5.3.

Furthermore, some applications require that the heat liberated due to combustion to be continued for long distances as in boilers and most industrial furnaces. In this case the flame is long with high heat transfer by radiation. In some other applications, as in jet engines and gas turbines combustion chambers, high heat liberation rates are required with the combustion to be completed at a short distance (short flame) from the fuel and air entry. This shows the importance of knowing the extent to which the flame characteristics are affected by the different geometrical and operating conditions. Some of these characteristics will be discussed in section 4.5.2.

4.5.1 Aerodynamics and Turbulent Mixing

As we mentioned before, combustion between two separate jets of fuel and air (as a diffusion flame) is a physically controlled process in which the chemical reaction proceeds so rapidly that the process is entirely determined by the finite rates at which mixing of the reactants takes place. A review of the knowledge required for successful scaling of small-scale flames into industrial ones has been carried out by Weber [623] from the point of view of fluid flow (aerodynamics), heat transfer, and pollutant emissions. Constant velocity and constant residence time scaling criteria have been scrutinized for their applicability in engineering of gaseous, spray-oil and pulverized coal flames. He demonstrated that both have limitations and in particular when applying to two-phase combustion, there appear to be considerable difficulties in scaling of the interactions between the gaseous and solid (liquid) phases.

In order to achieve the suitable dimensions of the flame and combustion zone, studies should be directed towards the factors that may affect the rate of mixing between the fuel and air in furnaces. The factors which are thought to have significant effects on mixing in furnaces are: the fuel-air mass ratio, the swirl imparted to the combustion air, fuel atomization, air momentum, the Reynolds number, and the burner geometry. These factors have been investigated by Khalil et al [624], Lockwood et al [569], and El-Mahallawy et al [625-626] and will be given in the following subsections.

Flow Pattern

Rotating flows with central recirculation are found in many engineering applications such as gas turbine combustion chambers, industrial furnaces, and boilers, etc. The swirling of combustion air acts on the flow field by creating radial and axial pressure gradients. [627]. In the case of strong swirl, the adverse axial pressure gradient is sufficiently large to create an internal recirculation zone along the furnace axis and at the same time reduces the outer recirculation zone near the walls [628]. It is well known from all past works in the field of diffusion flames that application of swirl to the combustion air stream is an effective means of flame stabilization. The use of swirl always leads to an increase in the maximum burner load without reducing the ignition stability [627, 629]. Shorter and bigger diameter flames are also obtained in this way [585, 625].

Khalil et al [624] have investigated theoretically and experimentally the mean structure of flow pattern due to the interaction of swirling combustion air and a spray of kerosene fuel issuing from a swirl atomizer in a cylindrical water-cooled furnace (0.2 m diameter and 2 m length). The study was carried out with special reference to the velocity and temperature patterns, the characteristics of the central recirculation zone and the angular momentum flux. The experiments were carried out with four swirl numbers (1.98, 1.247, 0.939 and 0.721) imparted to the combustion air through the use of guide vane cascade swirlers. The axial and tangential components of velocity were measured throughout the furnace with a water-cooled pitot probe while temperature was measured with a suction pyrometer.

The radial distributions of tangential and axial velocity components for two chosen swirl numbers of 1.98 and 0.721 are given in Fig. 4.46. The patterns of tangential velocity are seen generally to take the same shape of forced vortex inside the central recirculation zone and nearly free vortex outside it. The irregular patterns observed at earlier axial distances may be attributed to the existence of large portions of recirculated

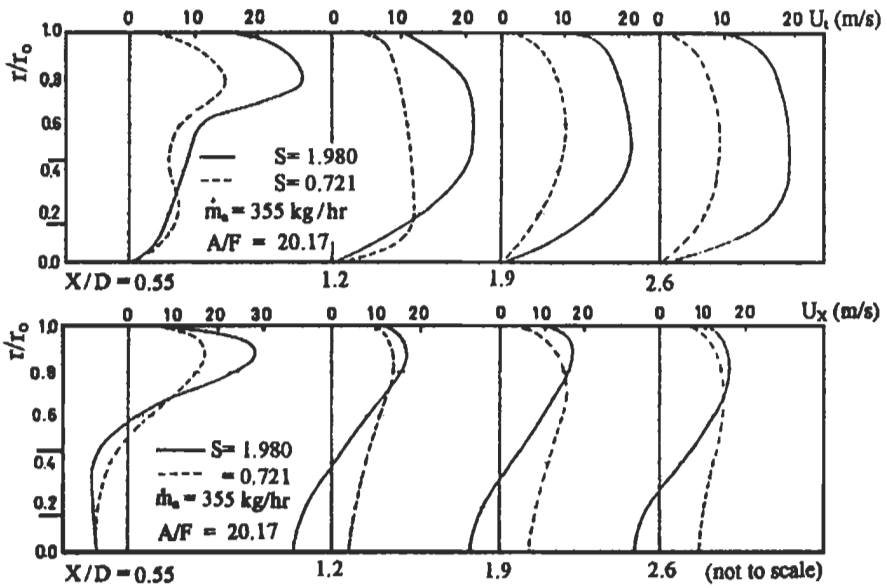


Fig. 4.46: Measured profiles of axial and tangential velocities for two swirl numbers [624]. Reproduced by permission of The Combustion Institute.

flow and the sudden expansion of the swirling jet at these sections. High values of tangential velocity, especially at the outer forward flow, are seen to be associated with high swirl numbers.

It is seen that for different swirl numbers, the axial components of velocity attain a maximum value near the furnace wall, which gradually decreases, moving inward, and drops quickly near the axis. Increasing the swirl number is shown to increase the maximum forward and reversed velocities.

The boundary of the central recirculation zone was obtained from the points where the flow starts to reverse its direction. For low degrees of swirl, the readings took a relatively longer time to get the flow direction. In this case, any point on the boundary of the central recirculation zone was checked by taking the flow direction at two points located at small radial distances above and below this point. In spite of the difficulty in getting the points of flow reversal, the resulting errors are not serious enough to affect the conclusions concerning the characteristics of the central recirculation zone.

The contours of the central recirculation zone, given in Fig. 4.47, show that although swirl affects the shape and length of the central recirculation zone to a large extent, the maximum diameter only changes slightly and has an average value of 0.6 times the furnace diameter.

The recirculated mass flow rate was calculated by Eq. 4.9. To confirm the accuracy of the measurements, the net mass flow rate through any cross section was obtained graphically from the equation:

$$\dot{m}_{\text{net}} = \int_{r_c}^{r_0} \rho U_x 2\pi r dr - \int_0^{r_c} \rho U_x 2\pi r dr \tag{4.45}$$

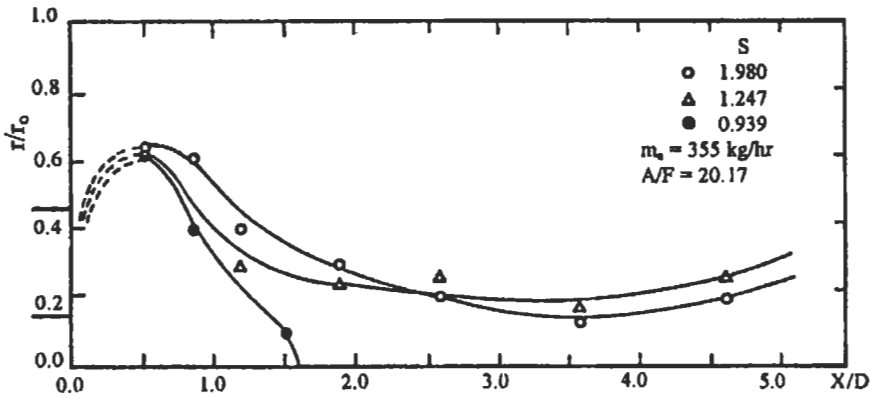


Fig. 4.47: Measured central recirculation contours for different swirl numbers [624]. Reproduced by permission of The Combustion Institute.

In most cases the difference between the net and the input mass flow rate was within 5 % of the input value. Figure 4.48 shows that although the value of the maximum recirculated mass flow rate depends on the intensity of swirl imparted to the combustion air, its location along the furnace is only slightly affected and has an average value of 0.5 times the furnace diameter. As the intensity of swirl affects the stability and dimensions of the flames, the maximum recirculated mass is considered here as a measure of the strength of the central recirculation zone.

Figure 4.49 is a sample of temperature profiles for two different swirl numbers of 1.98 and 0.721. The profiles show a remarkable uniformity throughout the reverse flow zone. The peaks, as well as the uniformity of the temperature distribution, are shown to exist at earlier axial distance for high swirl numbers, which is obviously attributable to the rapid mixing of fuel and air in this case.

In the theoretical study, efforts were made to obtain the relation between the intensity of swirl and the size of the central recirculation zone. To achieve reality and

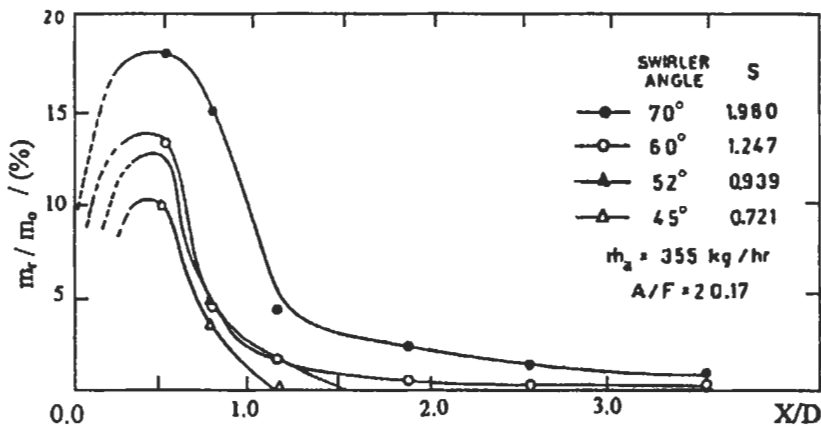


Fig. 4.48: Effect of swirl on the distribution of reversed mass flow rate [624]. Reproduced by permission of The Combustion Institute.

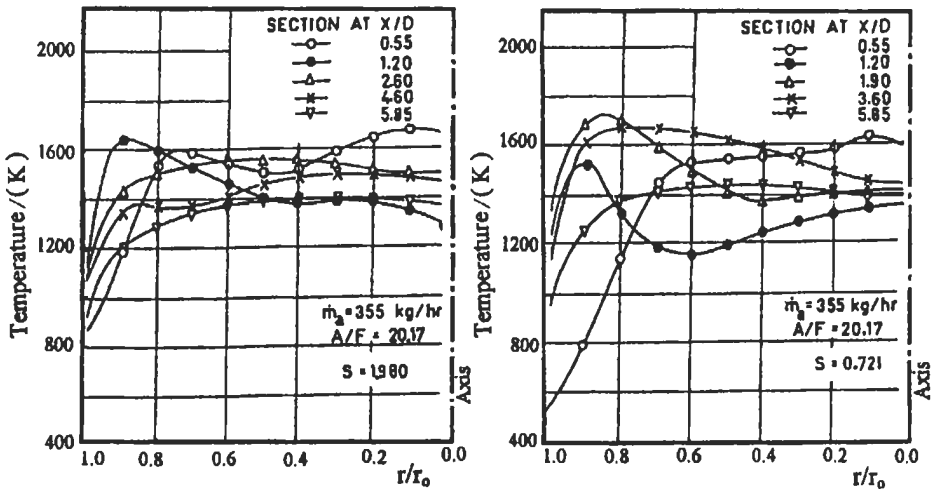


Fig. 4.49: Measured temperature profiles for two swirl numbers [624]. Reproduced by permission of The Combustion Institute.

simplicity in this study, simplified patterns of axial and tangential components of the velocity are chosen on the basis of the actual measured patterns. These simplified patterns are as follows.

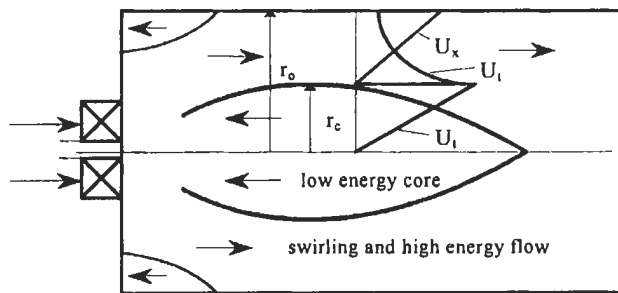
(a) The tangential velocity distribution is of a forced vortex type inside the central recirculation zone, and of a nearly free vortex type outside it:

$$U_t = C_1 r \quad 0 < r < r_c \quad (4.46)$$

$$U_t r^n = C_2 \quad r_c < r < r_0 \quad (4.47)$$

where n is a constant.

(b) A linear distribution for the axial velocity component outside the central recirculation zone is chosen. The simplified patterns are shown in Fig. 50 (a).



Main regions of flow in the model furnace

Fig. 4.50 (a): Simplified patterns in the model furnace [624]. Reproduced by permission of The Combustion Institute.

The combustion gases density is taken to be uniform over a given cross-section. In addition, due to the comparatively small values of reversed velocities throughout the central recirculation zone, neglecting the mass flow, angular momentum, and kinetic energy in this region is assumed.

From the adopted pattern of axial velocity outside the central recirculation zone:

$$U_x = U_{x0} \frac{r - r_c}{r_0 - r_c} = U_{x0} \frac{\frac{r}{r_0} - R_c}{1 - R_c}$$

where U_{x0} is the value of axial velocity at the furnace wall, $R_c = r_c/r_0$. From the definition:

$$\bar{U}_x = \frac{\dot{V}}{\pi r_0^2}$$

where, \dot{V} is the volumetric flow rate.

$$U_x = \frac{3}{2} \bar{U}_x \frac{\frac{r}{r_0} - R_c}{1 - \frac{3}{2} R_c + \frac{1}{2} R_c^3} \quad (4.48)$$

For the axial flux of angular momentum of the flow (G_ϕ) we have:

$$G_\phi = \int_{r_c}^{r_0} 2\pi\rho U_x U_t r^2 dr \quad (4.49)$$

For which we have: $U_t = \frac{1}{k_t} \frac{G_\phi}{\rho \dot{V} r^n}$

$$\text{where } K_t = \frac{3r_0^{1-n}}{(4-n)(3-n)} \times \frac{(3-n)(1 - R_c^{4-n}) - (4-n)(R_c - R_c^{4-n})}{\left(1 - \frac{3}{2} R_c + \frac{1}{2} R_c^3\right)}$$

The axial fluxes of tangential and axial kinetic energy, $K.E_t$ and $K.E_x$, respectively are given by:

$$K.E_t = \int_{r_c}^{r_0} \pi\rho r U_x U_t^2 dr$$

$$K.E_t = \frac{3G_\phi^2}{2\rho\dot{V}(1 - 1.5R_c + 0.5R_c^3)} \times \frac{1}{K_f^2} \times \frac{1}{r_0^{2n}} \times \frac{R_c^{3-2n} - (3 - 2n)R_c + (2 - 2n)}{(3 - 2n)(2 - 2n)} \tag{4.50}$$

$$K.E_x = \int_{r_c}^0 \pi\rho r U_x^3 dr$$

$$= \frac{27}{160} \pi\rho \bar{U}_x^3 r_0^2 \frac{4 - 15R_c + 20R_c^2 - 10R_c^3 + R_c^5}{(1 - 1.5R_c + 0.5R_c^3)^3} \tag{4.51}$$

Applying the hypothesis of minimum kinetic energy flux, then the value of (R_c), which corresponds to the minimum kinetic energy flowing through is given by the condition:

$$\frac{\partial(K.E)}{\partial R_c} = \frac{\partial(K.E)_x}{\partial R_c} + \frac{\partial(K.E)_t}{\partial R_c} = 0$$

and the following relation is obtained:

$$K_f^2 = \frac{G_\phi^2 r_0^2}{\rho^2 \dot{V}^4} = \frac{81}{80\pi^2} \frac{(3 - 2n)(2 - 2n)}{[(4 - n)(3 - n)]^2} \times \frac{f_1 f_2^2}{f_2 f_3 - f_4 f_5} \tag{4.52}$$

where K_f is the dimensionless flow parameter, which depends on the swirler vane angle, $f_1, f_2, f_3, f_4,$ and f_5 are functions of R_c and the exponent (n). Depending upon the exponent (n), different relations between the core radius (R_c) and K_f are obtained as shown in Fig. 4.50 (b). The value of R_c used for comparison with the theoretical results, is that obtained experimentally at the given cross section where K_f is calculated. The study of the figure will clarify the following points:

1. The experimental plot shows that for a certain minimum angular momentum, there is no central recirculation. This result is also obtained when using a constant tangential velocity ($n = 0$), and a nearly free vortex distribution ($n = 0.75$).
2. At high values of the flow characteristic dimensionless parameter (K_f), which means high swirl conditions, the aerodynamic forces are so dominant that a little change occurs to the flow field, and a nearly unvaried core radii are obtained. This conclusion is seen to be in a good agreement with the experimental plot.
3. The calculated plot for a nearly free vortex ($n = 0.75$) is seen to be quite close to the experimental plot for normal range of the swirl number, but there exists a discrepancy between the two plots in the range of higher or lower values of the flow characteristic dimensionless parameter. These deviations are obviously attributed to the assumptions of constant density of the combustion gases for a given cross section and of the simplified velocity patterns.

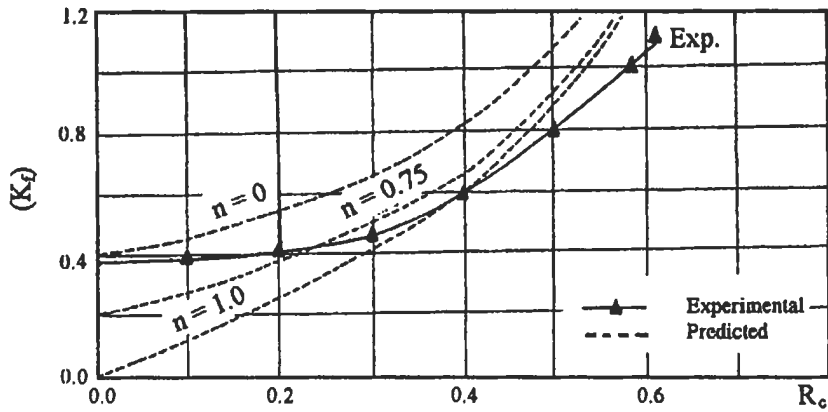


Fig. 4.50 (b): Relation between flow characteristic parameter (K_f) and dimensionless recirculation zone radius (R_c) [624]. Reproduced by permission of The Combustion Institute.

Turbulent Mixing

The design and development of combustion equipment is still based to a large extent on the empirical data and modeling techniques. Computational techniques are, however, now available for the prediction of turbulent reacting flows in furnaces of arbitrary geometry. Therefore, accurate experimental data would be useful for the validation of furnace prediction procedures. Accordingly El-Mahallawy et al [625] and Lockwood et al [569] have studied experimentally and theoretically the mixing process in a cylindrical furnace axially fired with a gaseous fuel. Data have been obtained for four fuel/air ratios, two burner geometries, two Reynolds numbers, and four swirl numbers imparted to the incoming air stream. The data are intended to assist the validation of prediction procedures.

Figure 4.51 shows the experimental furnace. The cylindrical combustion chamber consisted of an air-cooled, stainless-steel tube 0.21 m in internal diameter by 1.9 m in length. A double concentric-tube jet burner was secured, axially aligned, to one end of the chamber.

Two burners were employed; the annular air delivery tube of both of these had inner and outer diameters of 0.0445 m and 0.0781 m, respectively; but the diameter of the fuel-delivery tube was 0.0195 m in the one case (geometry 1) and 0.0123 m in the other (geometry 2), the change being effected by altering the thickness of the solid annulus separating the fuel and air streams. Three vane systems were constructed for the purpose of imparting a swirl velocity to the air stream. These had vane angles of: 30°, 45°, and 60°; and they were placed in the air-delivery annulus at the burner exit plane.

Measurements of mixture fraction were made within the furnace. Samples of the combustion products were withdrawn by a water-cooled probe mounted on a traversing gear. The sample was first enriched with oxygen from a metered oxygen supply and then burned to completion in a stainless steel tube situated in the flow of combustion products at the furnace exit. The resulting sample, containing O_2 , CO_2 , N_2 , H_2O , and a small amount of CO was dried and analyzed for CO_2 and CO concentrations using an infrared analyzer, and for O_2 concentration, using a paramagnetic analyzer; the concentration of N_2 was determined by differences. The concentration of CO_2 at upstream locations near the furnace axis frequently exceeded the maximum range of the CO_2 analyzer (i.e., 15% by volume). When this happened the sample was diluted by the addition of a metered flow of N_2 .

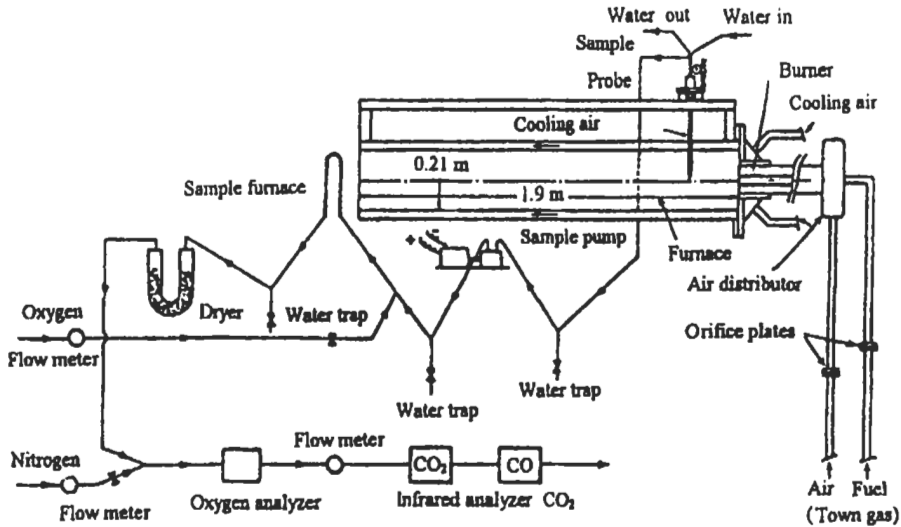


Fig. 4.51: Sketch of the test rig [569]. Reproduced by permission of Elsevier Science.

The air/fuel mass ratio at the sampling location was obtained by balancing the measured concentrations of C and N₂ in the sample with the concentrations of these species in the incoming fuel and air streams (and the stream of nitrogen dilutes when employed). The mixture fraction, F, was then obtained from:

$$F = \frac{1}{1 + (\text{air/fuel mass ratio})} \quad (4.53)$$

Very simple physical model is used for predictions and it was based on the computational procedure of Gosman et al [610] which solves elliptic partial differential equations of the form of Eq. 4.42 in radial, r and axial, X coordinates.

The effective viscosity of the turbulent flow was determined from Ref. 610. The fuel and oxidant were presumed to unite always in their stoichiometric proportions, intermediate species being ignored. Equal turbulent exchange coefficients were assumed for the fuel, oxidant, and enthalpy. Further, thermal radiation, kinetic-heating, and shear-work effects were ignored. In consequence, the specific enthalpy h could be determined from the values of mixture fraction via the simple algebraic relation. Temperature was evaluated from the specific enthalpy. The concentrations of the fuel, and air mixture were determined from the value of the mixture fraction assuming chemical equilibrium to prevail throughout the flow. Density was calculated from the ideal gas law for the fuel, air and product mixture.

Measured radial profiles of mixture fraction for the fuel/air ratio 0.0786 are shown in Fig. 4.52. Figure 4.53 displays the corresponding contour plots of F. Note that the contour of their stoichiometric mixture fraction $F_{st} = 0.087$, characterizing the time-mean flame location, is shown in Fig. 4.53.

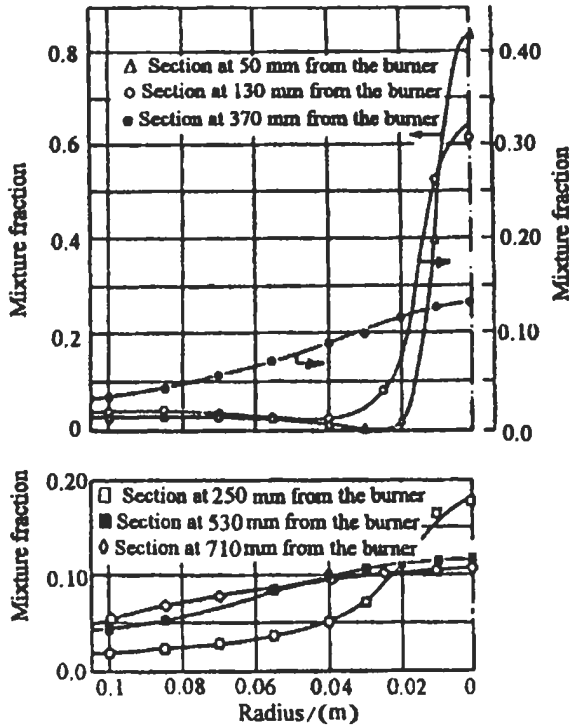


Fig. 4.52: Measured mixture-fraction profiles for $F/A = 0.0786$, zero swirl, and $Re = 16,300$ [569]. Reproduced by permission of Elsevier Science.

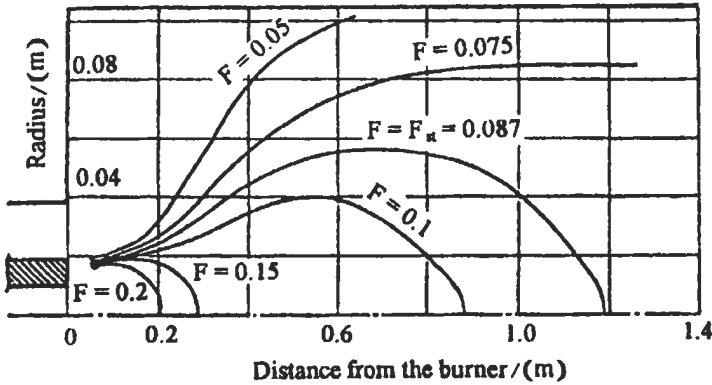


Fig. 4.53: Measured mixture-fraction contours for $F/A = 0.0786$, zero swirl, and $Re = 16,300$ [569]. Reproduced by permission of Elsevier Science.

Figure 4.54 shows a comparison between the predictions and measurements of the fall-off in F along the furnace axis for the fuel/air ratios 0.0635 and 0.072; the agreement in the important region of steep fall-off near the burner is only fair.

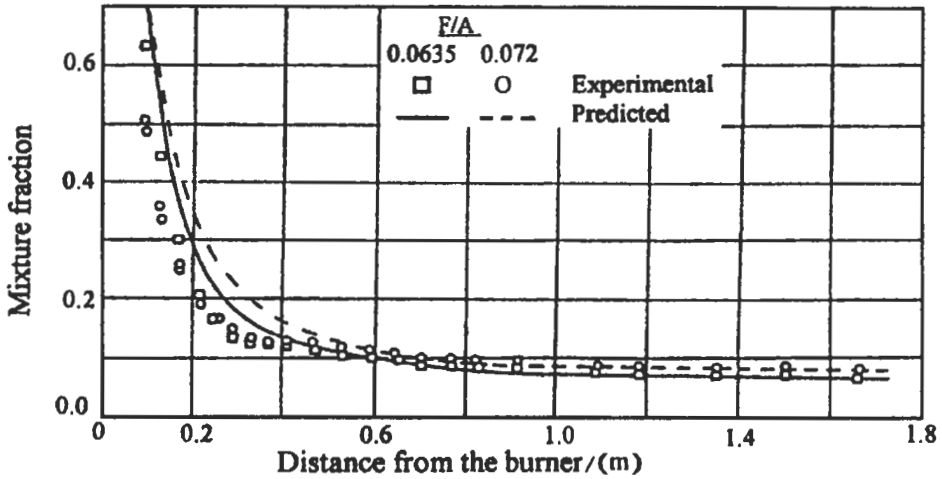


Fig. 4.54: Comparison of the predicted and measured mixture-fraction distributions along the axis for $F/A = 0.0635$, $Re = 16,030$, and for $F/A = 0.072$, $Re = 16,300$; both for zero° swirl [569]. Reproduced by permission of Elsevier Science.

Having discussed the above measuring technique for mixture fraction in turbulent gaseous flame, it is important to use this technique in oil fuel combustion. Therefore, El-Mahallawy et al [626] have developed the sampling technique to measure the local mixture fraction and gaseous species concentrations in a water-cooled, oil-fired flame tube having similar features as a practical fire-tube boiler. The flame tube is 0.6 m diameter and 3.75 m length fired with light diesel oil using an industrial type burner equipped with a pressure jet atomizer. The effect of different operating parameters such as: the Sauter mean diameter of the spray droplets (SMD), the combustion air momentum (AM) and the excess air level (EA) are investigated. The soot concentration is quantified by the “Bosch Number”, and the temperature is mapped using a suction pyrometer.

A sampling probe is newly developed to measure the local fuel mixture fraction; the sampling system and the probe are sketched in Fig. 4.55 (a). At each measurement location, the sample is enriched with pure oxygen as soon as it enters the probe head; the sample is forced to pass through a lengthy helical passage close to the probe outer surface where the reaction is completed with the aid of the heat from the flame engulfing the probe head. The dimensions of the helical passage are chosen in order to keep the sample for a residence time of about 130 ms, a time long enough to ensure complete reaction of the unburnt fuel (Kuo [630]). Practically, the rate of oxygen addition to the sample is controlled at every measuring point to be a little more than the value, which gives the maximum concentration of carbon dioxide in the sample indicating complete combustion. The sample leaving the probe is directed via coolers and dryers to separate calibrated analyzers in order to determine its composition (CO_2 , CO and O_2 , the remaining percentage of the sample is considered to be nitrogen and sulphur dioxide).

The mixture fraction is calculated by balancing the measured carbon and nitrogen concentrations in the sample with the corresponding concentrations of these species in the inlet streams, assuming, for the fuel composition in use, that sulphur dioxide represents 0.7 % of the sum ($CO_2 + CO$). The fuel mixture fraction (F) is defined by Eq. 4.53.

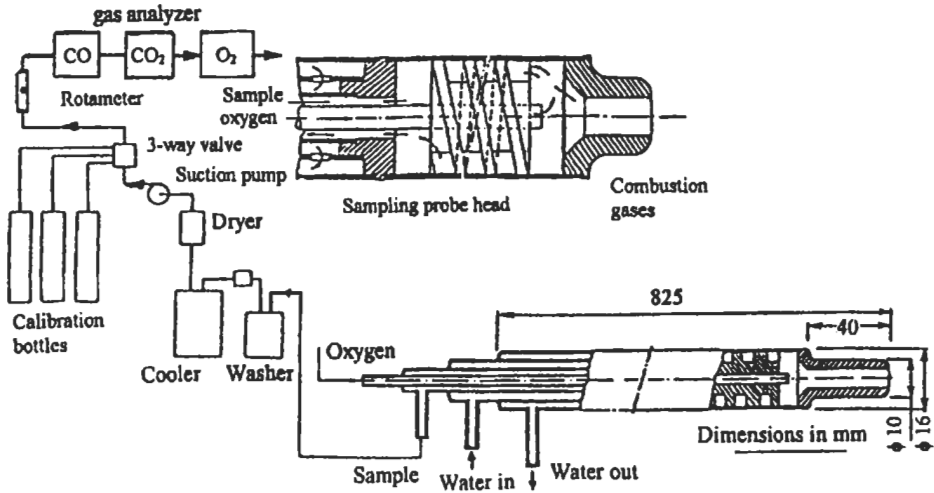


Fig. 4.55(a): Sampling system and sampling probe [626]. Reproduced by permission of John Wiley and Sons Limited.

In case of the presence of sulphur content in the fuel, then the mass air/fuel ratio (A/F) at the sampling location is calculated as:

$$A / F = [1 - O_2 - 1.0067(CO_2 + CO)] / [0.3948 (CO_2 + CO)] \quad (4.54)$$

In case of neglecting the sulphur content, (A/F) can be calculated by:

$$A/F = 3.04 C N_2 / (CO_2 + CO) \quad (4.55)$$

where C is the carbon content by mass in the fuel, CO and CO_2 are the measured volume concentrations.

The volume concentrations of carbon dioxide, carbon monoxide and oxygen are measured using a water-cooled probe coupled to a dedicated sampling system (Infrared CO and CO_2 analyzers, a paramagnetic O_2 analyzer). The time-average flame temperature is measured using a suction pyrometer fitted with type-B Platinum-Rhodium thermocouple wires. The output voltage of the thermocouple is measured using a digital integrator and a voltmeter which gives the time mean voltage.

The test conditions are chosen to simulate industrial practice. The air flow rate (M_a) was kept constant at 940 kg h^{-1} in all experiments and the air-fuel mass ratios were 16 and 20. The droplet size is commonly quantified by the Sauter mean diameter (SMD) which is more suitable to quantify the droplet size in combustion process [631]. The Sauter mean diameter is calculated using the experimental empirical formula defined by Jasuja [632] for pressure jet atomizers. Two identical fuel atomizers with different orifice sizes have been employed to change the quality of the spray atomization from fine to coarse droplets. The input air momentum is changed at the same flow rates of both fuel and air by changing the burner stabilizing disc diameter. The excess air level was changed by altering the fuel mass flow rate.

Figure 4.55(b) schematically portrays the combustion zones of the spray flames [633]. The spray emerges from the fuel gun at the center of the stabilizing disc. The fuel leaves

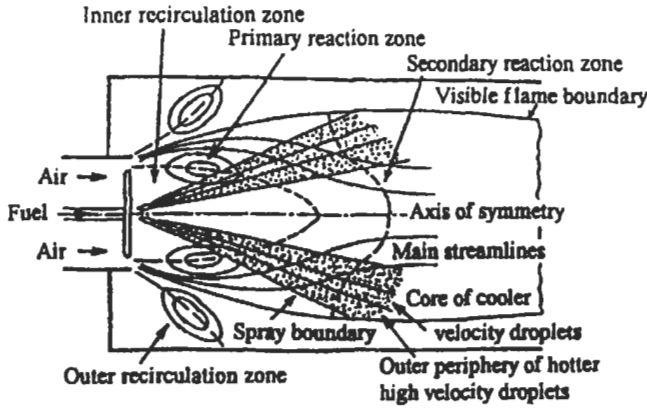


Fig. 4.55(b): The flow and combustion zones of a hollow cone pressure jet spray burning in the wake of a stabilizer disc [633]. Reproduced by permission of Elsevier Science.

the atomizer in the form of a hollow conical spray (at half angle of 28° approximately) with a central air core. The flow field is divided into three zones: inner recirculation zone formed by the air flow in the wake of the disc bluff body, an outer recirculation zone and a free shear zone. The reaction takes place in two zones namely: the primary and secondary zones. The former zone is effected near the edge of the disc by the fuel vapor and the small droplets transported by the recirculating gas flow towards the outer air stream. This zone provides an ignition source acting as a pilot flame, introducing hot products into the main air flow stream which ignites the vapor mixture further downstream in the secondary reaction zone. The latter zone is formed at greater axial distance where the coarser fuel droplets, escaping the primary zone and the main air come together and react.

Figure 4.56 shows the contours of fuel mixture fraction, and it indicates that the reaction zone occupied only the upstream region of the flame tube. In the early stage of flames ($X/D = 0.5$), the two expected regions may be identified; (i) a central core containing the reaction zone ($0.0 < R/D < 0.3$) and (ii) an outer wall recirculation ($R/D > 0.3$). The central region follows the trends of free jet flames. The turbulent

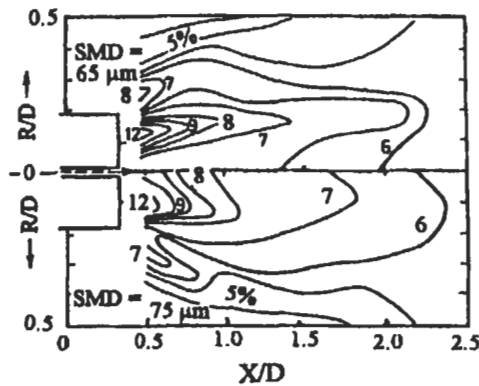


Fig. 4.56(a): Contours of fuel mixture fraction for different Sauter mean diameters (SMD) [626]. Reproduced by permission of John Wiley and Sons Limited.

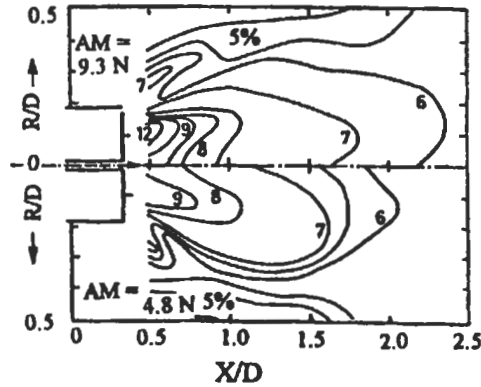


Fig. 4.56(b): Contours of fuel mixture fraction for different air momenta (AM.) [626]. Reproduced by permission of John Wiley and Sons Limited.

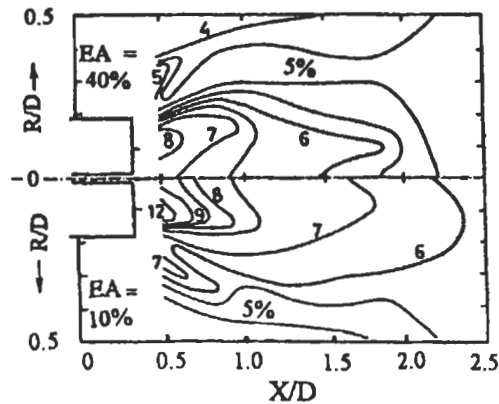


Fig. 4.56(c): Contours of fuel mixture fraction for different excess air (EA.) [626]. Reproduced by permission of John Wiley and Sons Limited.

reaction zone is typically thick, occupying roughly the radial locations $0.2 < R/D < 0.4$. The fuel mixture fraction has maximum values in between the boundaries of the hollow cone spray. The peaks of the (F) flatten and approach the centerline values at further axial distance.

The axial variations of the sectional-average flame temperature at different values of SMD is illustrated in Panel (a) of Fig. 4.57. The larger SMD produced lower temperatures up to axial distance $X/D < 2.0$, thereafter the trends is inverted. Smaller droplets (i.e. less SMD) are fastly evaporated as soon as they are injected into the primary combustion zone resulting in early faster reaction rate and hence higher rates of heat release which consequently produce elevated temperature levels. However, larger droplets (bigger SMD) have longer life time and their evaporation is slower and therefore they travel longer past the primary zone and into the secondary reaction zone where they react and releasing their heat producing higher temperatures at downstream locations ($X/D > 1.5$) and more than those produced by smaller droplets, see panel (a) in Fig. 4.57.

The axial variation of the sectional-average flame temperature at two values of combustion air momentum are shown in Fig. 4.57 (panel (b)). The flame with higher air momentum produced higher temperature levels at upstream sections due to augmentation of mixing and hence enhanced combustion. Lower momentum onsets the combustion further downstream, which shows relatively higher temperature levels.

The axial variation of the sectional-average temperature at different excess air ratios is shown in Fig. 4.57 (panel c). As expected the average temperature is lower everywhere when the excess air is excessively raised to 40 % due to dilution of the combustion gases.

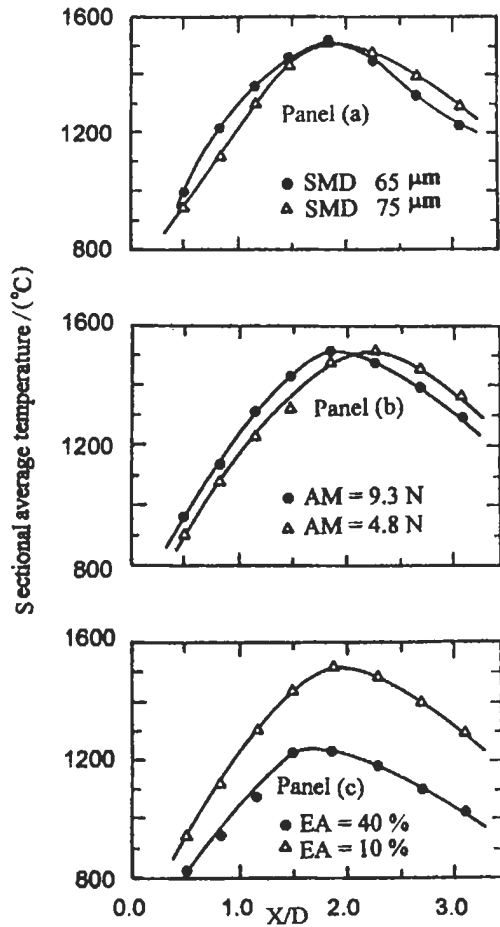


Fig. 4.57 : Influence of the operating parameters on the axial distribution of the sectional average temperature [626]. Reproduced by permission of John Wiley and Sons Limited.
 (a) Effect of Sauter mean diameter SMD.
 (b) Effect of air momentum AM.
 (c) Effect of excess air EA.

4.5.2 Heat Liberation in Confined Flames

Introduction

Most of confined flames are physically controlled and the combustion heat liberated depends mainly on the process of mixing between the fuel and air streams. Therefore, it is necessary to know how to determine the heat liberated along the flame tubes.

Realistic prediction of heat liberation and heat transfer accompanying combustion processes necessitates the use of highly complicated and lengthy methods which need long computer time. Also, these complicated methods can not be easily manipulated by industrial engineers. Therefore, there is a strong necessity for developing simplified calculation procedures with sufficient accuracy, which could be easily applied in practical furnace design. Accordingly, El-Mahallawy et al [634] have developed a simplified analytical calculation procedure for the heat liberation and heat transfer in flame tubes. The following is the developed simplified theoretical determination of heat liberation:

The heat liberated up to a certain section (H_i) of the flame tube is equal to the increase in enthalpy of gases (ΔI_i) and the heat transfer to furnace wall up to this section (Q_i) as shown in Fig. 4.58 and is given by.

$$H_i = \Delta I_i + Q_i \quad (4.56)$$

The values of the H , I and Q are usually represented in dimensionless forms: $\bar{H}_i = H_i / \dot{m}_f \cdot \text{C.V.}$, $\bar{\Delta I} = \Delta I / \dot{m}_f \cdot \text{C.V.}$ and $\bar{Q}_i = Q_i / \dot{m}_f \cdot \text{C.V.}$, where \dot{m}_f and C.V. are the mass flow rate of fuel and its calorific value, respectively.

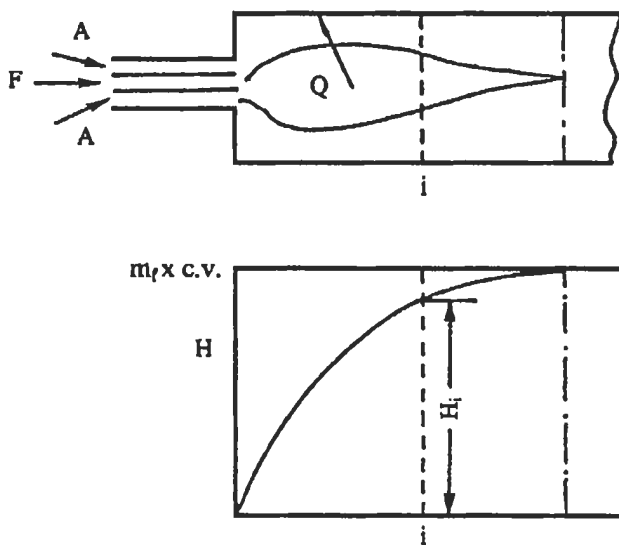


Fig. 4.58 : Heat liberation in flame tubes [634].

Also, the axial variation of the dimensionless heat liberated \bar{H}_i up to the section i in the flame tube may be written in the following general form [634]:

$$\bar{H}_i = 1 - \exp(-(X_i / L_{ec})^2) \tag{4.57}$$

where X_i is the axial distance of section i from the entrance and L_{ec} is a characteristic distance depending on the flame length. Knowing the distribution of H and Q , the increases of the enthalpy of gases at any section i is given by:

$$\Delta I_i = H_i - Q_i \tag{4.58}$$

The gases flowing at a certain section are assumed to be a mixture of two components. The first component is the gases resulting from the stoichiometric combustion reaction of the fuel that is consumed up to this section, while the second one is the non-reacted combustion air, which is represented by the difference between the total air supplied to the flame tube and the air used in the reaction. Hence, the mass fraction of air (G_a) at any section i is given by:

$$G_{a,i} = \frac{m_{a,e} - m_{a,r}}{m_{f,e} + m_{a,e}} \tag{4.59}$$

where subscripts a , f , e and r referred to air, fuel, entering, and reacting:

$$m_{a,e} = m_{f,e} (A/F)_e, \quad \text{and} \quad m_{a,r} = m_{f,r} (A/F)_{th}$$

The values of $(A/F)_e$ and $(A/F)_{th}$ are the inlet and theoretical air-fuel ratios, respectively.

Thus, Eq. 4.59 becomes:

$$G_{a,i} = \frac{(A/F)_e - \bar{H}_i (A/F)_{th}}{1 + (A/F)_e} \tag{4.60}$$

Now, the specific heat of the mixture, $C_{p,g}$ can be calculated in terms of the specific heats of the air and theoretical combustion gases, $C_{p,a}$ and $C_{p,tg}$, respectively. Thus:

$$C_{p,g} = G_a C_{p,a} + (1 - G_a) C_{p,tg} \tag{4.61}$$

$C_{p,a}$ and $C_{p,tg}$ can be calculated using the values given by Chernov and Bessrebrennikov [635]. It was found that in the range of temperature of practical interest, the dependence of these specific heats on temperature, T , could be expressed to a good approximation by straight-line relation, i.e.:

$$C_{p,a} = A_a + B_a T \tag{4.62}$$

$$C_{p,tg} = A_g + B_g T \tag{4.63}$$

where A_a , B_a , A_g and B_g are constants.

Thus,

$$C_{p,g} = G_a (A_a + B_a T) + (1 - G_a) (A_g + B_g T) \quad (4.64)(a)$$

or

$$C_{p,g,i} = A_g + B_g T_i + \frac{(A/F)_e - \bar{H}_i (A/F)_{th}}{1 + (A/F)_e} [(A_a - A_g) + (B_a - B_g) T_i] \quad (4.64)(b)$$

The composition of the gases at any section i is calculated from the fuel composition and the mass fraction of air and theoretical products at this section i .

Neglecting the mass of unreacted fuel, the dimensionless enthalpy, at section i , is \bar{I}_i could be given in the form:

$$\bar{I}_i = \bar{I}_e + \left[\frac{m_{tg,i} + m_{a,i}}{m_{f,e} C.V.} \right] \int_{T_e}^{T_i} C_{p,g} dT \quad (4.65)$$

where, $m_{a,i}$ and $m_{tg,i}$ are the mass flow rates of air and theoretical gases at section i , respectively, and could be given by:

$$m_{a,i} = m_{f,e} (A/F)_e - m_{f,i} (A/F)_{th} \quad (4.66)$$

$$\text{and} \quad m_{tg,i} = m_{f,i} [(A/F)_{th} + 1] \quad (4.67)$$

Substituting Eqs. 4.66 and 4.67 into Eq. 4.65 yields:

$$\bar{I}_i = \bar{I}_e + \left[\frac{\bar{H}_i + (A/F)_e}{C.V.} \right] \int_{T_e}^{T_i} C_{p,g} dT \quad (4.68)$$

Equation 4.68 is a second order equation in the temperature, T , which can be solved for T_i if \bar{I}_i is known. It can be seen from Eq. 4.68 that the dimensionless enthalpy \bar{I}_i can be obtained from \bar{H}_i if the total dimensionless heat transferred to the furnace wall \bar{Q}_i is known. This heat which is transferred by radiation and convection will be discussed in details in chapter 5, and will be briefly explained below.

Heat Liberation in Flame Tubes

For the experimental determination of heat liberation, El-Mahallawy [636] studied the effect of some parameters on the distribution of the combustion heat liberated along a cylindrical (0.205 m diameter and 2.1 long), water-cooled, oil fired flame tube. The main parameters considered are the intensity of combustion expressed by the air-fuel mass ratio, varied through varying the fuel mass flow rate, and the intensity of swirl expressed by the swirl number of combustion air. These results will be discussed in the next section 4.5.3.

El-Mahallawy et al [637] have obtained some empirical relations for the distribution of heat liberation and soot concentration along the flame tube. These relations were based on the experimental data for practical range of operating conditions such as air fuel ratio and degree of swirl of combustion air. These experimental data were obtained on a horizontal; segmented, water-cooled flame tube (0.6 m diameter and 3.5 m long) fired with light oil fuel. Measurements of gas temperature and velocity were made by a water-cooled suction pyrometer and a 3-hole pitot probe, respectively. The measurement of soot concentration was carried out discontinuously using a Bosch soot tester.

The heat liberated up to a certain section of the flame tube is calculated from the increase in enthalpy and the total heat transfer to the wall up to this section. First, the total heat transfer, Q_i , is obtained from the rate and average temperature of the cooling water flowing through the different segments of the flame tube up to the section i . Thus, the total heat transfer to the furnace walls up to a section i is calculated by:

$$Q_i = C_w \sum_{n_i} \dot{m}_{w_n} \Delta T_{w_n} \quad (4.69)$$

where C_w is the specific heat of water, n_i is the number of water cooled segments upstream the section i , \dot{m}_{w_n} , ΔT_{w_n} are the mass flow rate and temperature rise of water for each segment n , respectively. Here, there are some approximations, as the flame radiates to points on the wall downstream of the section considered, and at the same time the upstream sections receive radiation from the downstream parts of the flame and gases, which is thought to have small effect on the distribution of the heat transfer by radiation along the flame tube.

The increase in the enthalpy of the gases, ΔI_i , due to the heat liberated from the fuel combustion is obtained by subtracting the sensible enthalpy of the input fuel and air from the value of the enthalpy at T_i . The measured axial velocity and temperature distributions are used in the following equation to calculate the increase in the enthalpy:

$$\Delta I_i = \sum_{j=1}^n \rho_{ij} A U_{ij} C_{p_{p,j}} T_{ij} - (m_a C_{p,a} T_{a,e} + m_f C_{p,f} T_{f,e}) \quad (4.70)$$

where i is the section number and j is the ring number. For the accurate calculation of the enthalpy, each section is divided into (n) equi-area rings (A), each is considered of uniform axial velocity, U and temperature, T . The value of ρ_{ij} and U_{ij} are taken at the mean radius of the ring considered and $C_{p_{p,j}}$ is the mean specific heat of combustion gases (a mixture of air and theoretical gases) at the section considered.

Using the above calculation procedure and the experimental data of Ref. 638 of the segmented water cooled flame tube, the following correlation for the dimensionless heat liberation, Fig. 4.59, is obtained:

$$\bar{H}_i = 1 - \exp(-2.3 X_i/D) \quad (4.71)$$

where \bar{H}_i is the heat liberation expressed as a fraction of the fuel chemical energy input, X_i is the axial distance of the section i measured from the entrance, and D is the tube diameter.

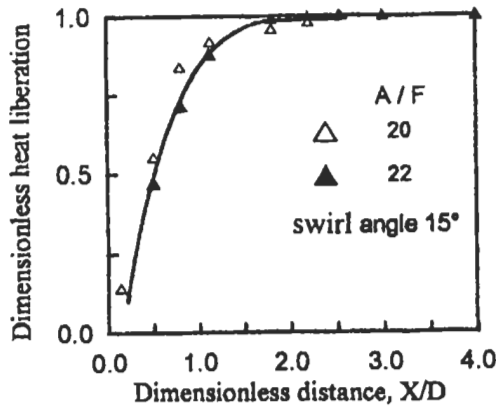


Fig. 4.59: Distribution of heat liberation along the flame tube [637]. Reproduced by permission of Taylor and Francis Books, Inc.

Calculation trials and heat transfer to walls. The calculation is started by assuming a linear distribution of the cumulative dimensionless total heat transfer \bar{Q}_i to the walls along the flame tube. The dimensionless heat liberation is calculated from Eq. 4.71. At any distance X_i from the tube inlet, the increase in the enthalpy of gases is calculated as the difference between the heat liberation and the heat transfer up to that section i as given by the following relation:

$$\bar{I}_i - \bar{I}_e = \bar{H}_i - \bar{Q}_i \tag{4.72}$$

where \bar{I}_i and \bar{I}_e are the dimensionless enthalpies at the section i and at the entry, respectively. Then the mean gas temperature at the section i can be obtained from the following relation:

$$\bar{I}_i - \bar{I}_e = \left[\frac{\bar{H}_i + (A/F)_e}{C.V.} \right] \int_{T_e}^{T_i} C_{p,g} dT + \left[\frac{1 - \bar{H}_i}{C.V.} \right] \int_{T_e}^{T_i} C_{p,f} dT \tag{4.73}$$

This equation is similar to Eq. 4.68 except the increase of the enthalpy of unreacted fuel is considered in the Eq. 4.73, and $C_{p,f}$ is the specific heat of the unreacted fuel.

The mean specific heat of mixture, $C_{p,g}$ at a certain temperature T_i is calculated from:

$$(C_{p,g})_{T_i} = G_{a,i} (C_{p,a})_{T_i} + (1 - G_{a,i}) (C_{p,tg})_{T_i} \tag{4.74}$$

A second calculation trial is then started by calculating the radiative and convective heat transfer to the flame tube wall and thus a new distribution of the cumulative total heat transfer is obtained. From the enthalpy distribution in this case, the temperature distribution for the second trial is obtained. These trials are repeated until the sum of the enthalpy at the tube exit and the total heat transfer to the wall (as deduced from the proceeding enthalpy distribution) is equal to the total heat liberated, within the accuracy required. The details of the heat transfer by radiation and convection are given in the following parts.

Heat is transferred to the tube walls by radiation and convection. The net radiation falling on a cylindrical wall slice, *i*, situated at a distance X_i from the tube inlet is composed of two parts. The first part is the normal radiation falling on it from the gases enclosed in the cylindrical slice, *i*, itself, while the second part is the summation of the inclined radiation coming from other gas slices, *j*, each having a radiating area A_j , equal to the tube cross-sectional area. In the following calculations, all combustion gases are divided into 30 equal cylindrical slices, each is considered to have uniform temperature and composition, i.e. variation of gas properties is considered in the axial direction only.

The net radiant heat flux density gained by the cylindrical wall slice shown in Fig. 4.60 can be found to be:

$$q_{r,i} = \sigma \epsilon_i \epsilon_w (T_i^4 - T_w^4) + \sum_j \left(\cos \beta / 2\pi R_{ij}^2 \right) \epsilon_j A_j (T_j^4 - T_w^4) \sigma \epsilon_w \tau_{ij} \tag{4.75}$$

where σ is the Stefan-Boltzmann's constant, ϵ_i is the emissivity of the gas layer *i* enclosed by its cylindrical surface, ϵ_j is the emissivity of the gas layer *j*, ϵ_w is the wall emissivity, and τ_{ij} is the average transmittance. τ_{ij} is calculated from:

$$\tau_{ji} = 1 - \epsilon_{ji} \tag{4.76}$$

where ϵ_{ji} is the emissivity of the gas layers between *j* and *i* (the emissivity is taken equal to the absorptivity), based on average values of gas temperature, soot concentration and partial pressures of gases in these layers.

The emissivity of the gas mixture is considered to be due to luminous (soot) and non-luminous contributions. The emissivity of a mixture of gases and soot ϵ can be calculated using the method outlined by Beér [639] as:

$$\epsilon = \sum_n a_{g,n} (1 - \exp(-k_n B_L)) \tag{4.77}$$

where *n* corresponds to the radiating components: CO₂, H₂O, and soot, B_L is the mean

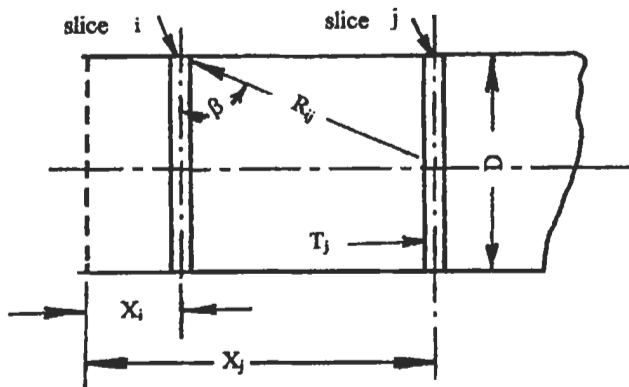


Fig. 4.60: Radiation exchange [637]. Reproduced by permission of Taylor and Francis Books, Inc.

beam length, $a_{g,n}$ is a weighting factor linearly related to the temperature, and k_n is given by:

$$k_n = k_{c,n} \rho_c + k_{g,n} (P_{CO_2} + P_{H_2O}) \quad (4.78)$$

where $k_{c,n}$ and $k_{g,n}$ are the soot and gas absorption coefficients, respectively, P_{CO_2} and P_{H_2O} are the partial pressures of carbon dioxide and water vapour in the mixture, respectively. At any section, the partial pressures of non-luminous radiating components CO_2 and H_2O could be calculated as a function of fuel chemical composition, the excess air factor, and the heat liberation up to this section [634]. The soot concentration, ρ_c , is obtained experimentally for two different air-fuel ratios and for medium degree of swirl. The results are shown in Fig. 4.61 and expressed by the following equation:

$$\rho_c = 0.00065 \exp[-2.25 (X/D)^2] \quad \text{kg m}^{-3} \quad (4.79)$$

This relation is valid for $X/D \geq 0.1$, and it can be seen from Fig. 4.61 that the values of the soot concentration in the downstream sections are too low to be detected.

The dimensionless total radiant heat transfer to the wall up to a section i is by:

$$\bar{Q}_{r,i} = \frac{1}{\dot{m}_f C.V.} \sum_i q_{r,i} A_i \quad (4.80)$$

The convective part of the heat transfer to the flame tube wall can be expressed in the following dimensionless form:

$$\bar{Q}_{c,i} = \frac{1}{\dot{m}_f C.V.} \sum_i q_{c,i} A_i \quad (4.81)$$

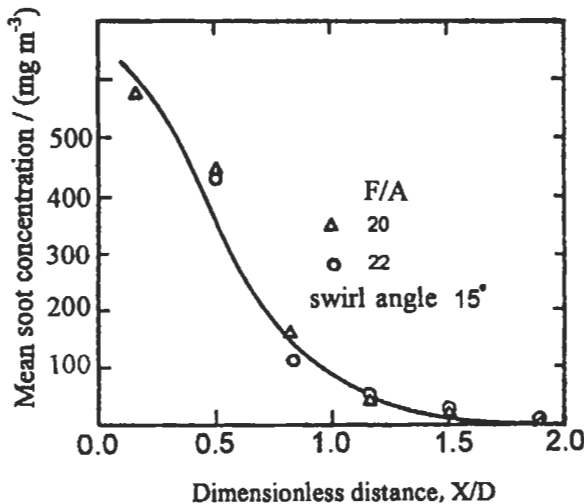


Fig. 4.61: Distribution of mean soot concentration along the flame tube [637]. Reproduced by permission of Taylor and Francis Books, Inc.

where $q_{c,i}$ is the convective heat flux density at section i , given by:

$$q_{c,i} = h_i (T_i - T_w) \tag{4.82}$$

where h_i is the local convective heat transfer coefficient at section i ; calculated from [640] as:

$$Nu_i = 0.0261 \frac{Re_i^{0.8}}{(X_i/D)^{0.12}} \tag{4.83}$$

where Re is the Reynolds number.

The total dimensionless heat transfer up to a section i is then:

$$\bar{Q}_{1,i} = \bar{Q}_{r,i} + \bar{Q}_{c,i} \tag{4.84}$$

As mentioned before the calculation trials are repeated until we get convenient results for two successive trials.

The results of the final trial are shown in Figs. 4.62 to 4.66. These results apply to an oil fuel having gravimetric analysis of 86 % C and 14 % H₂, and calorific value of 42000 kJ kg⁻¹. The mass flow rate of fuel is 0.0139 kg s⁻¹.

Figure 4.62 shows the values of the calculated emissivity ϵ and the local coefficient of convective heat transfer, h , along the flame tube. The decrease of h is due to the increase of the distance X and its effect is shown by Eq. 4.83.

The flame emissivity consists of luminous and non-luminous parts. High values shown in the upstream sections are due to high values of soot concentrations, which are responsible for the luminous part. It could be shown that the flame emissivity follows the same trend as that of the soot concentration up to $X/D = 1.5$, where the soot

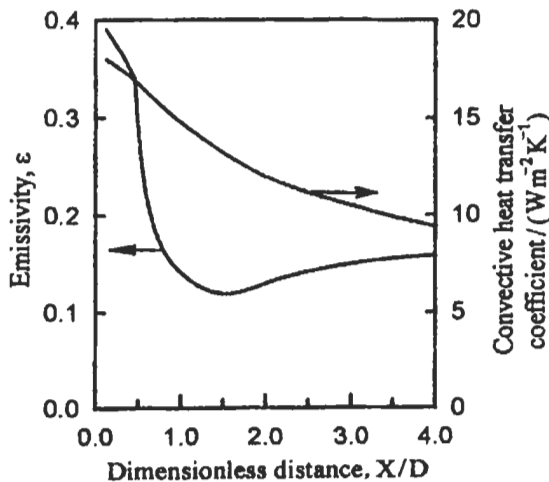


Fig. 4.62: Emissivity and heat transfer coefficient [637]. Reproduced by permission of Taylor and Francis Books, Inc.

concentration is very small. The magnitude of the emissivity decreases from nearly 0.4 to a minimum and then increases slightly due to the increase of the non-luminous part with falling temperature.

Figure 4.63 shows the distribution of the radiation heat flux falling on different wall segments from the gases enclosed by these segments (normal radiation) and inclined radiation from other slices. As shown normal radiation and inclined radiation from adjacent gas slices represent most of the radiation energy falling on a certain wall segment. This could be recognized from the characteristics of radiation flux given by Fig. 4.64, which is the summation of the distribution given by Fig. 4.63 and this almost follows the same trend of the normal radiation flux. The high values of the radiant flux correspond to the range of elevated temperatures and emissivities.

The dimensionless cumulative total heat transfer to walls is given in Fig. 4.65 with its radiant and convective components. The experimental results of the total heat transfer are also given on the same figure. The comparison with the results of calculations shows close agreement. The total heat transfer to the walls represents about 48 % of the total heat released due to combustion, of which nearly 38 % by radiation and 10 % by convection.

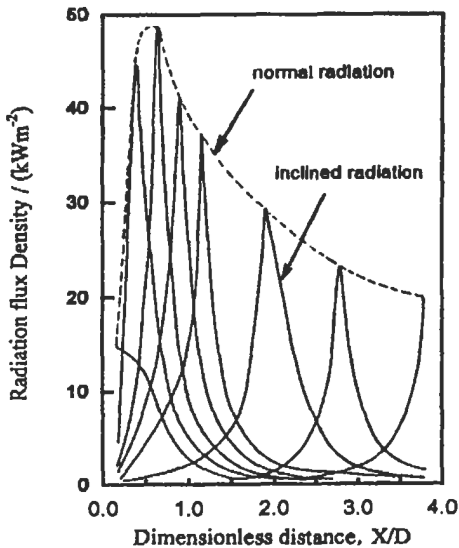


Fig. 4.63: Radiation distribution [637].
Reproduced by permission of Taylor and Francis Books, Inc.

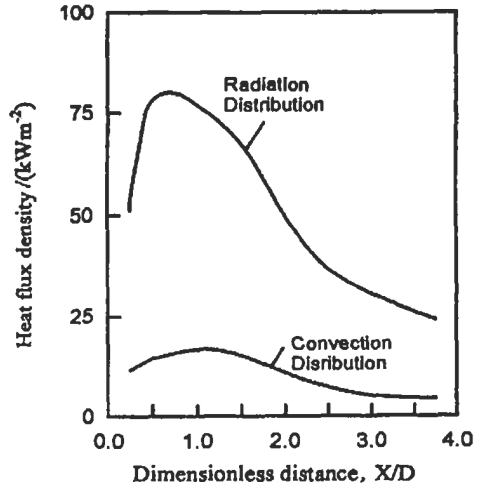


Fig. 4.64: Radiant and convective heat flux density distributions [637].
Reproduced by permission of Taylor and Francis Books, Inc.

Figure 4.66 shows the mean temperature distribution along the tube length as given by calculation and experiment. The comparison between the two sets of results shows good agreement for most sections of the tube with a maximum deviation of about 5 %.

In the following section, the effect of different parameters on mixing, heat liberation and flame stability will be discussed.

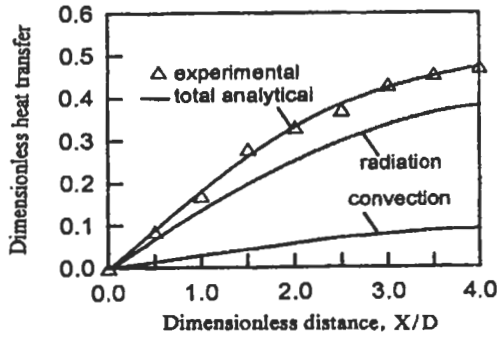


Fig. 4.65: Cumulative heat transfer [637]. Reproduced by permission of Taylor and Francis Books, Inc.

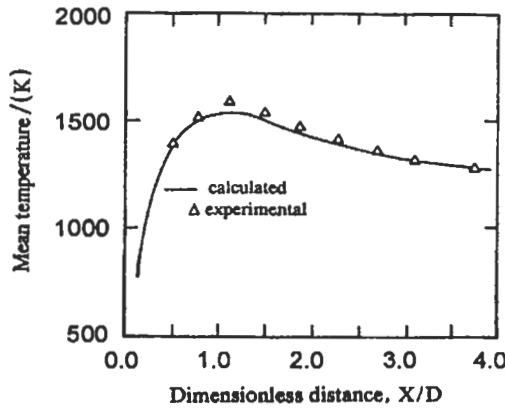


Fig. 4.66: Experimental and calculated temperature distribution [637]. Reproduced by permission of Taylor and Francis Books, Inc.

4.5.3 Effect of Different Parameters

This part is concerned with the effect of different parameters on the flow, mixing and heat liberation in confined and free flames. The parameters considered are: air and fuel swirl, fuel-air ratio, forced flow reversal, furnace and burner geometries, and bluff bodies. However, understanding of the effect of such parameters on the combustion systems is important for providing a bridge between fundamentals and applications as will be described here and in chapter 5. These parameters are frequently employed in combustion chambers and burners to improve fuel-air-mixing rates and to promote stable efficient operation of the main reaction zone and reduce pollutant emissions in some cases. The fundamentals of earlier chapters such as chemical mechanisms, velocity-composition probability density function (PDF) model coupled with a k-ε based mean flow computational fluid dynamics (CFD) model are used here to describe the effect of such parameters on the characteristics of the combustion systems.

In combustion systems such as furnaces, gas turbines, and afterburners, flame can be stabilized by bluff bodies (as will be described below), step expansion [641] and, aerodynamically, by swirl [504] or interacting jets [642], together with any other flow or geometry variation that locally reduces the air velocity to the level of the flame propagation velocity. Burner performance is then related to the distribution of local stoichiometry as dictated by two processes, the active role played by turbulence entrainment, and the resulting fine scale mixing down to the molecular level necessary to initiate chemical reactions. In bluff-body systems the aerodynamic interaction between the injected fuel (in jet or other form) and the primary recirculation was conducive to flame stabilization over a wide range of air velocities and fuel injection rates [643, 500].

Effect of Air Swirl on Flow and Mixing

It is well known from all past works carried out in the field of diffusion flames that the application of swirl to the combustion air stream is an effective tool of flame stabilization. The use of swirl leads always to an increase of the maximum possible burner load without losing ignition stability. On the other hand, swirl is a much more valuable aid to combustion than a mere stabilizing device, since it permits more effective use of all the combustion volume by eliminating dead spaces.

As regards to the effect of the intensity of swirl of the combustion air and the forward momentum of the fuel jet on the flame structure and ignition zone, two important cases can be distinguished.

In the **first case**, the swirl intensity and the forward momentum are high. As shown in Fig. 4.67 (a), the central jet penetrates straight through the reverse flow core, which is thus modified into an annular, closed zone between the central jet and the outer forward flow. Mass exchange between central jet and reverse flow takes place by the entrainment of a portion of recirculation by the central jet. Also some of the central jet matter is sealed off from the central jet boundary, gets mixed with and is transported back by the recirculating matter. Thus, hot fuel is mixed with the incoming combustion air and burns in a quiet manner, which is controlled by the gradual mixing of fuel and air. Also, the hot combustion products are entrained from the reverse flow into the fuel jet, which also becomes heated before it mixes with the remaining air in the second combustion zone. This situation leads to long and comparatively quite flames.

In the **second case**, the swirl intensity is high and the forward momentum is very low. In this case, the central (fuel) jet is divided away from the axis immediately after leaving its nozzle, i.e. the fuel jet fails to penetrate the central recirculation zone. Thus mixing of cold air and cold fuel takes place prior to the warming of the fuel by the combustion products. Subsequent mixing of the hot combustion products then apparently leads to an explosive type of ignition of the turbulent pockets of air/fuel mixture; this is shown in Fig. 4.67 (b).

El-Mahallawy et al [625] carried out an experimental study on the effect of combustion air swirl on mixing in a cylindrical gas-fired furnace as described in section 4.5.1. Data were obtained for different values of swirl number imparted to the combustion air. Three vane systems were constructed for imparting a swirl velocity to the air stream. These had vane angles of 30°, 45° and 60°, and were placed in the air-delivery annuls at the burner exit plane. The experimental data for a 30° swirl and a fuel-air ratio of 0.0652 are presented as contours of mixture fraction in Fig. 4.68. The

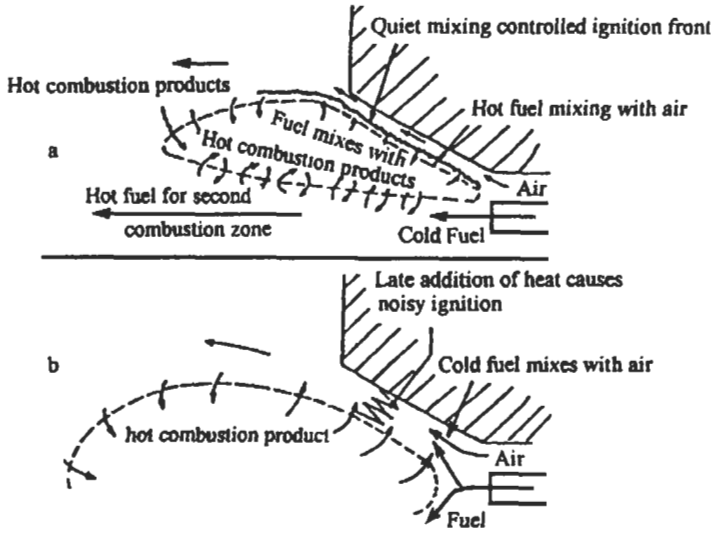


Fig. 4.67: Mixing between fuel, air and combustion products in confined diffusion flames [627].

experimental contours for a 60° swirl have been added to Fig. 4.68 for comparison with the 30° contours, the fuel-air ratio being the same in both cases. The increased rate of decay of mixture fraction with axial distance resulting from the increased swirl is apparent. They concluded that increasing the swirl number of the combustion air leads to an increase in the maximum flame diameter and shortens its length.

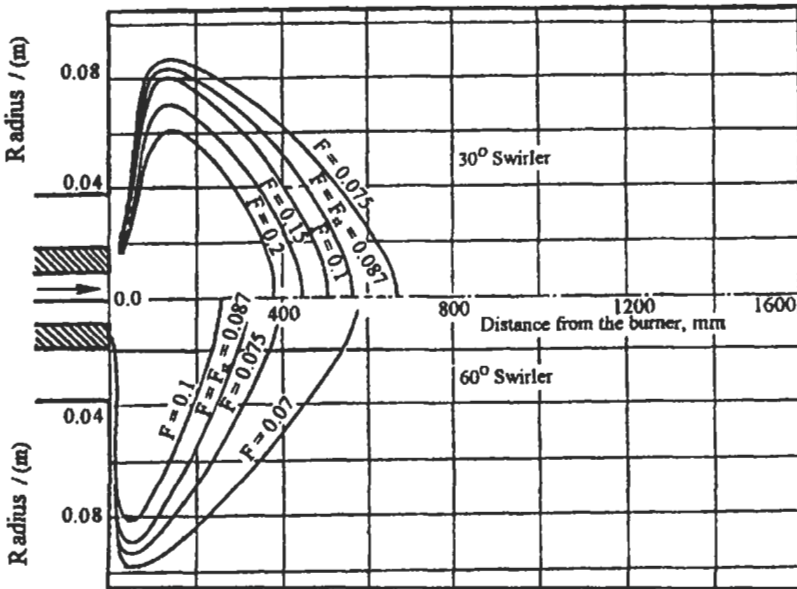


Fig. 4.68: Comparison of the measured mixture-fraction contours for the 30° and 60° swirlers, $F/A = 0.0652$, and $Re = 20,520$ [569]. Reproduced by permission of Elsevier Science.

Khalil et al [624] studied the effect of intensity of swirl on the flow pattern in a cylindrical oil-fired furnace as described in section 4.5.1. Different swirl intensities were imparted to combustion air by vane type swirlers. The variation of maximum and average recirculated mass flow rates with the swirl number are shown in Fig. 4.69. These are fitted by the following straight-line relations:

$$\frac{\dot{m}_r \text{ max.}}{\dot{m}_o} = 0.06S + 0.07 \quad 0.7 \leq S \leq 2.0 \quad (4.85(a))$$

$$\frac{\dot{m}_r \text{ av.}}{\dot{m}_o} = 0.031S + 0.006 \quad 0.7 \leq S \leq 2.0 \quad (4.85 (b))$$

Figure 4.69 shows that the intensity of swirl has significant effect on the value of recirculated mass and its distribution along the furnace.

Desoky et al [644] studied the influence of the swirling angle of the primary air, secondary air ratio and equivalence ratio on combustion performance in a can-type gas turbine combustor shown in Fig. 4.70. They used hydrogen, ammonia and liquefied petroleum gaseous fuels with four different swirl angles 0° , 32° , 52° and 72° . The secondary air ratios are varied from 10 to 50% from the total air supplied. They [644] have found that the change in primary air swirl angle, equivalence ratio and secondary air ratio cause significant changes in combustion performance. The results obtained were similar for all fuels used. The effect of swirl angle on exit gas temperature, oxygen and NO concentrations are shown in Figs. 4.71 (a) to (c) at different swirl angles. Figure 4.71 shows that the exit gas temperature increases and the oxygen concentration decreases and NO increases with the increase of the swirling angle of the primary air. This can be explained by better mixing and high burning rate as the primary air swirl is increased.

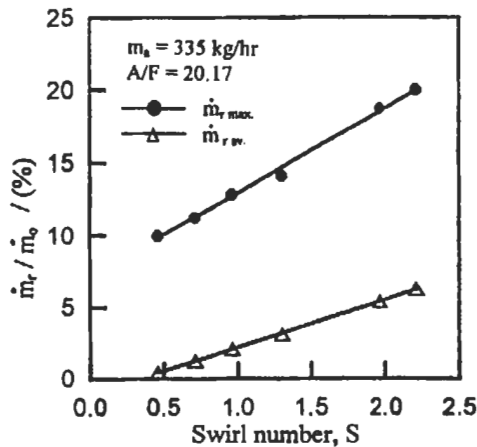


Fig. 4.69: Variation of maximum and average recirculated masses flow rate with the swirl number [624]. Reproduced by permission of The Combustion Institute.

El-Mahallawy et al [583] studied the effect of cone type swirler (described in section 4.3.2) on the characteristics and structure of confined oil diffusion flame. The cone swirler is designed to swirl the secondary part of combustion air of double concentric jet burner. A liquid fuel is sprayed from an atomizer into the center of primary air variable cord vane-swirler. The burner is fitted to a water-cooled flame tube (0.6 m diameter and 3.75 m long, as will be described in chapter 5). Four cone swirlers having vane angle 0°, 30°, 45° and 55° with half cone angle 45°, and one cone swirler having vane angle 45° with half cone angle 60°, have been constructed and used in their work. The results using the cone swirler are compared with that using the prevalent type swirler, which has a vane angle of 45°. Three dimensional velocity measurements are carried during both cold and firing conditions by means of a special water-cooled pitot probe. The flame chemical and thermal structures are investigated through the measurements of oxygen concentration using paramagnetic oxygen analyzer, and gas temperature, using

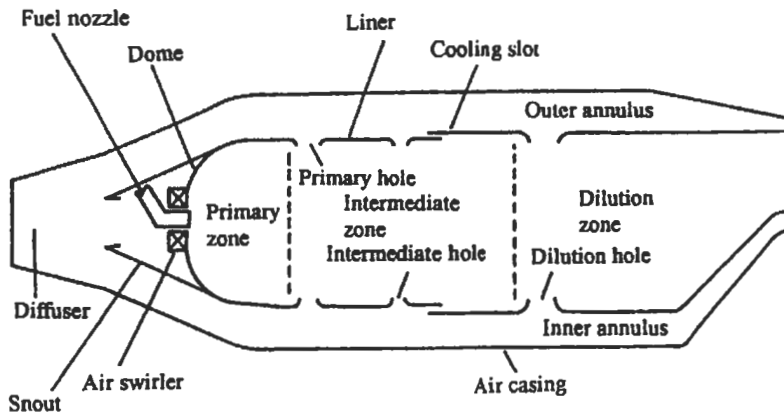


Fig. 4.70: Main components of a gas turbine combustor [644].

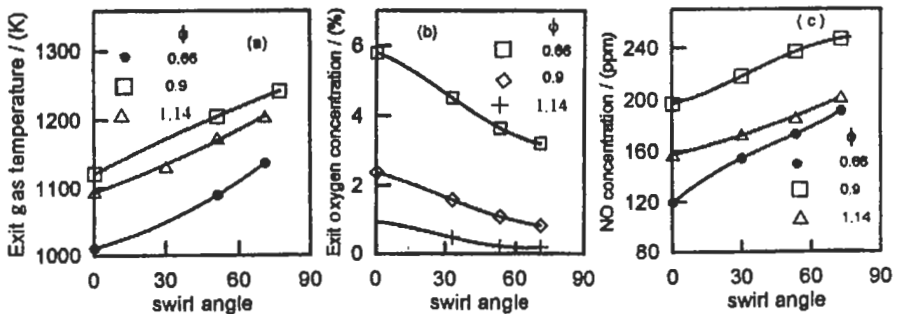


Fig. 4.71: Effect of swirl angle and equivalence ratio on exit gaseous temperature, exit oxygen concentration and NO concentration (ppm) for fuel H_2 [644].

fine bare wire thermocouple with the necessary corrections made for the radiation errors.

The results show that, the cone swirler has a significant effect on both the flow characteristics, shape and size of the central recirculation zone, as this type of swirlers could be considered as a swirl augmentation device. Furthermore, the cone swirler, combined with prevalent type for double concentric flow burner, improves the efficiency and the stability of created confined diffusion spray flame.

Figure 4.72 shows the central recirculation zone (CRZ) for isothermal condition as being compared with the hot condition for cone swirler $45^\circ/55^\circ$. The figure reveals that, the CRZ shape and size are extremely changed under hot condition. It is shown that, under hot conditions the maximum diameter is decreased by 20-30 %, while the length is decreased by 50 %.

Figure 4.73 shows the plotting of CRZ for primary flow only, secondary flow only and combined flow for cone swirler $45^\circ/45^\circ$. It is evident that, the CRZ for the combined flow is affected by the primary flow during the earlier distance downstream of the burner exit, whereas its maximum diameter is shifted by $0.25 D$ downstream relative to the case of primary flow. Also, the length of the recirculation zone is different for these cases which means that the shape and dimensions of the central recirculation zone is significantly affected by both the primary and secondary streams.

Figure 4.74 shows the comparison of the CRZ generated by cone swirlers $45^\circ/45^\circ$, $60^\circ/45^\circ$, and $90^\circ/45^\circ$. It is clear that the maximum diameter of CRZ for cases $45^\circ/45^\circ$ and $60^\circ/45^\circ$ has approximately the same value, but it increases by $0.18D$ compared with

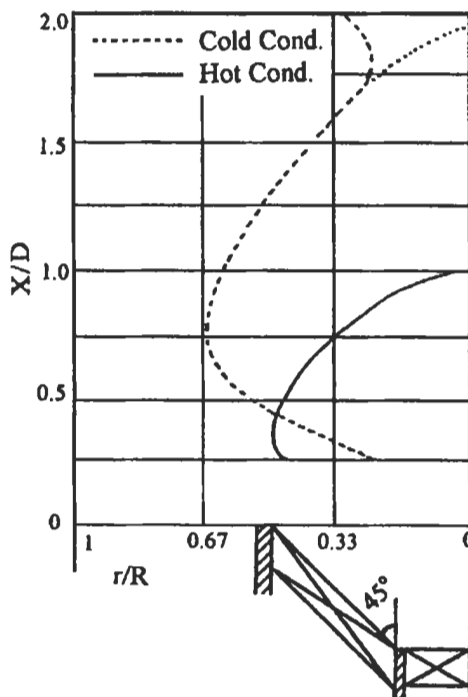


Fig. 4.72: Effect of combustion on C.R.Z. size for cone swirler $45^\circ/55^\circ$ [583].

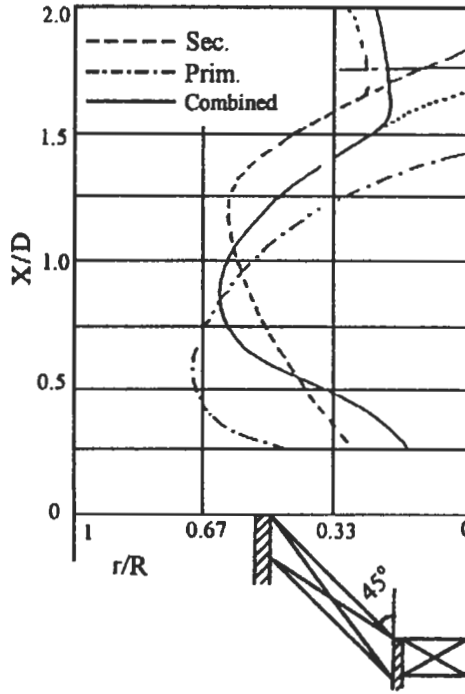


Fig. 4.73: Effect of primary and secondary swirlers on C.R.Z. for cone swirler $45^\circ/45^\circ$ [583].

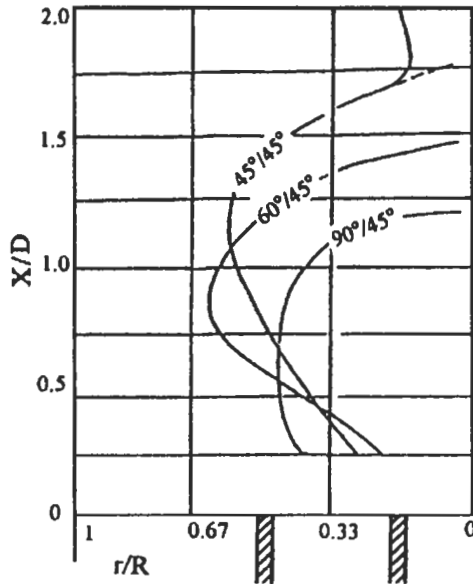


Fig. 4.74: Effect of half cone angle (Φ) on cone swirler C.R.Z. [583].

the case of cone swirler 90°/45°. It is evident that the axial distance for the onset of CRZ maximum diameter decreases with the increase of cone angle.

Generally, it could be concluded that the shape and dimensions of C.R.Z. is greatly affected by the cone angle of the cone type swirler.

Furthermore, the following empirical formula is being suggested by El-Mahallawy et al [583] to calculate the swirl number of the cone swirler, S^* :

$$S^* = (1 + \sin \psi \cos \Phi) S [1/(1 - k)] \tag{4.86}$$

Due to vanes number (N), thickness (s), and length (L), the calculated swirl number has to be increased by a factor called blockage factor (1/(1-k)), where:

$$k = [N \cdot s \cdot L] / [\pi(R^2 - R_h^2)]$$

and R_h is hub radius, R is outer radius, Φ is half cone angle, ψ is helic angle, θ is vane angle and S is prevalent swirl number = $2/3 (1 - f^3) / (1 - f^2) \tan \theta$ where $f = R_h / R$ (see also section 4.3.2).

Effect of Air Swirl on Heat Liberation

El-Mahallawy [636] studied the effect of combustion air swirl on the characteristics of combustion heat liberated along a cylindrical, water cooled, oil fired furnace with 0.205 m diameter and 2.1 m long as described before in section 4.5.1. The experimental results are shown in Figs. 4.75 and 4.76. The distribution of the heat liberated given in Fig. 4.75 is shown to be significantly affected by the degree of swirl. For the range of swirl angle from 45° to 60°, increasing the swirl leads to higher rates of heat liberation at the upstream sections. The results in this figure can be correlated by:

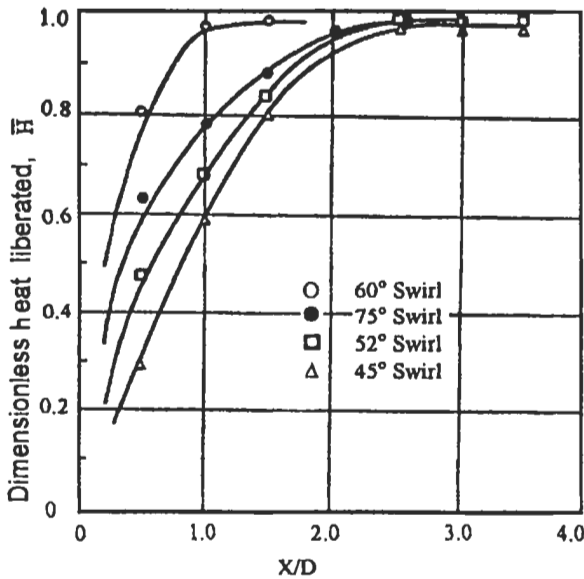


Fig. 4.75: Distribution of the total heat liberated along the furnace for different degrees of swirl [636].

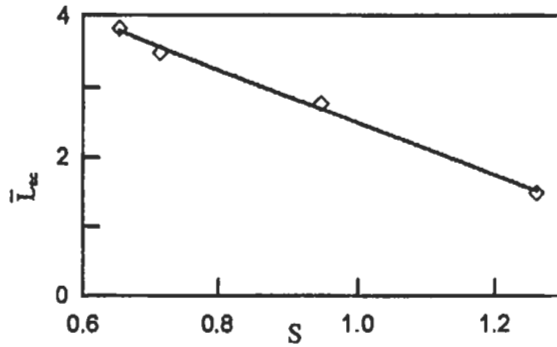


Fig. 4.76: Variation of \bar{L}_{ec} with the swirl number [636].

$$\bar{H} = 1 - \exp\left[-\frac{(\bar{X})^{(2.078-0.9467 S)}}{2.18-1.493 S}\right] \quad (4.87)$$

The variation of \bar{L}_{ec} (the dimensionless distance, X/D , corresponding to zero value of $d\bar{H}/d\bar{X}$) and the swirl number is shown in Fig. 4.76. This dimensionless length (\bar{L}_{ec}) of the full heat liberation can be considered as the flame length, and can be correlated with the swirl number (S) as follows:

$$\bar{L}_{ec} = 6.5 - 4 S \quad (4.88)$$

Furthermore, El-Mahallawy and Abbas [645] have investigated the effect of swirling the fuel and air jets on the heat liberation in a cylindrical gas-fired furnace (0.168 m diameter and 0.68 m long). The furnace is water-cooled by cooling rings fitted on the outer surface of the furnace cylinder. They obtained the distribution of the total heat liberated along the furnace for different conditions of swirl and the results are shown in Figs. 4.77 (a) and (b). The figure shows that the distribution of the heat liberated is affected by the degree of swirl imparted to the combustion air, while the degree of swirl of fuel is kept constant. It can be seen from Fig. 4.77 (a) that, swirling the two stream in opposite direction leads to a reduction in flame length and increases the rate of mixing as compared with the case of swirling the two streams in the same direction. The variation of (\bar{L}_{ec}), corresponding to the zero value of $d\bar{H}/d\bar{X}$ with the degree of swirl of air can be expressed by the following:

$$\bar{L}_{ec} = 2.25 - 0.028 \theta_a \quad \text{at } 30^\circ \leq \theta_a \leq 60^\circ, \theta_f = 60^\circ \quad (4.89 a)$$

where θ_a and θ_f are the degree of swirl of air and fuel, respectively. Also, when changing the degree of fuel swirl keeping the air swirl constant, they found the following relation for \bar{L}_{ec} :

$$\bar{L}_{ec} = 1.8 - 0.015 \theta_f \quad \text{at } 30^\circ \leq \theta_f \leq 60^\circ, \theta_a = 45^\circ \quad (4.89 b)$$

Shown in Fig. 4.77 (b) the effect of changing the degree of swirl of fuel, for constant degree of air swirl, on the distribution of the dimensionless heat liberation. It could be concluded that swirling the fuel and air streams at the same time and in the same direction leads to an increase in the rate of mixing and hence the rate of heat liberation as compared to the case of swirling the air stream or fuel stream only.

In addition, the effect of the intensity of swirling the combustion air on the total heat liberation characteristics along a cylindrical water-cooled oil fired flame tube (0.6 m diameter and 3.75 m long) has been also investigated by El-Mahallawy et al [646, 647].

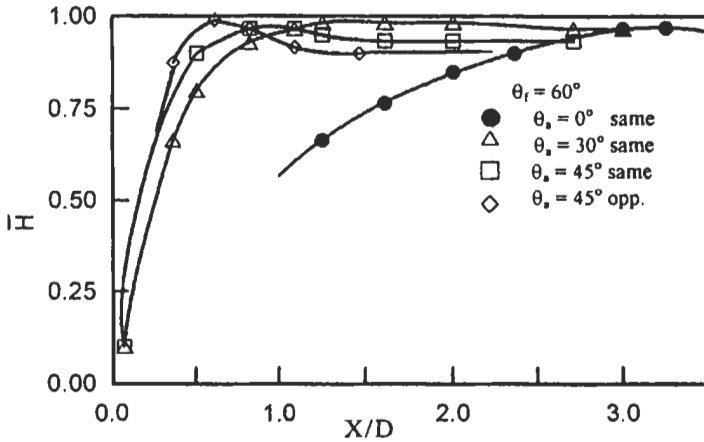


Fig. 4.77(a): Distribution of the total heat liberation along the furnace for different degrees of swirl of air, ($\theta_r = 60^\circ$) and for swirling the two streams in same and opposite directions [645].

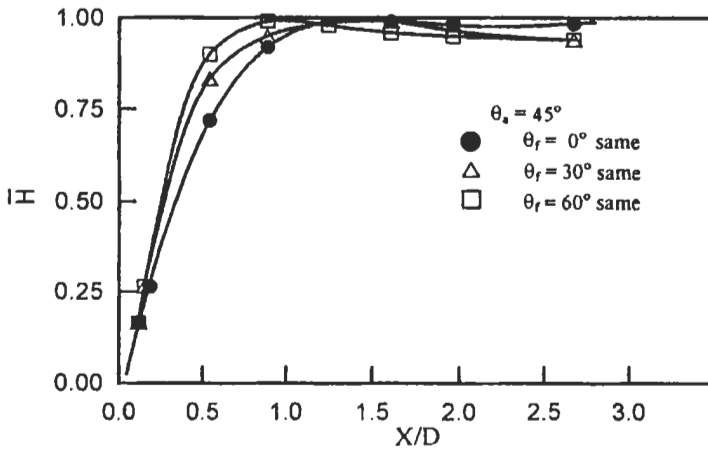


Fig. 4.77(b): Distribution of the total heat liberation along the furnace for different degrees of swirl of fuel, $\theta_s = 45^\circ$ [645].

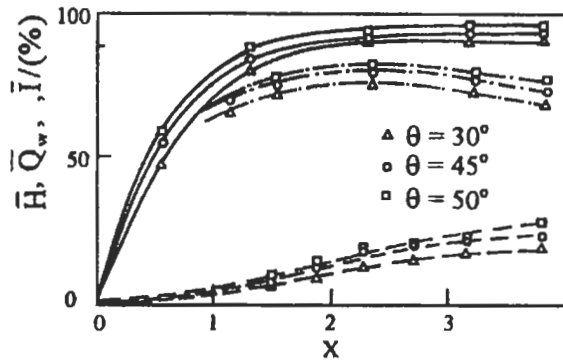


Fig. 4.78: Distribution of dimensionless heat along the flame tube for different degrees of swirl and for air-fuel ratio of 21 [647]. X in m. — heat liberation
 - - - enthalpy of gases
 - · - heat transfer to walls

The test rig in both investigations will be described in chapter 5. A swirl motion was imparted to the air with the use of simple cascaded vane swirlers. Three swirlers with angles 0, 15, and 30 degrees were employed [646].

Shown in Fig. 4.78, the experimental results [647] of the dimensionless heat liberation, \bar{H} , dimensionless enthalpy, \bar{I} and dimensionless heat transfer to the flame tube walls, \bar{Q}_w . The figure reveals that the increase in swirl angle (θ) leads to an increase in the total heat liberation (\bar{H}) especially at upstream sections of the flame tube. The dimensionless heat liberated, \bar{H} , is expressed by:

$$\bar{H} = 1 - \exp(-b \bar{X}^a) \quad (4.90)$$

where $a = 0.6885 + 0.0029\theta - 7.74 \times 10^{-5} \theta^2$

and $b = 1.1505 + 0.0035\theta + 1.25 \times 10^{-5} \theta^2$ for $30^\circ \leq \theta \leq 50^\circ$

Effect of Fuel-Air Ratio

The effect of fuel-air mass ratio on mixing and flame length has been studied in a cylindrical gas-fired furnace by El-Mahallawy et al. [625] and Lockwood et al [659]. The results are shown in Fig. 4.79 where the flame length increases with the increase of fuel-air ratio. It was also shown that the effect of Reynolds number on the flame length is very small.

The experimental results by Khalil et al [624] show that varying the air-fuel ratio for a wide range does not affect the characteristics of central recirculation zone and only the values of the recirculated mass flow rate are changed. Figure 4.80 (a) shows these results where the maximum recirculated mass flow rate increases with the increase of air-fuel ratio, while Fig. 4.80 (b) shows the effect of air-fuel ratio on the distribution of the recirculated mass flow rate along the furnace. These effects on the recirculation zone are due to the temperature and density gradients with the change in the air-fuel ratio.

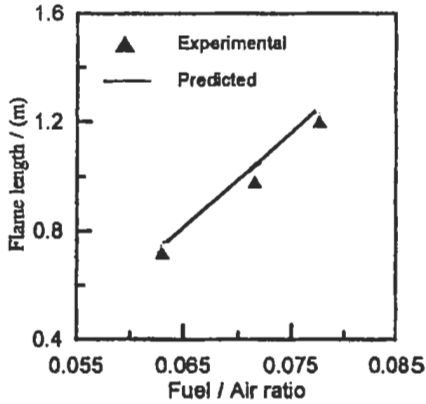


Fig. 4.79: Variation of the flame length with the fuel-air ratio [569]. Reproduced by permission of Elsevier Science.

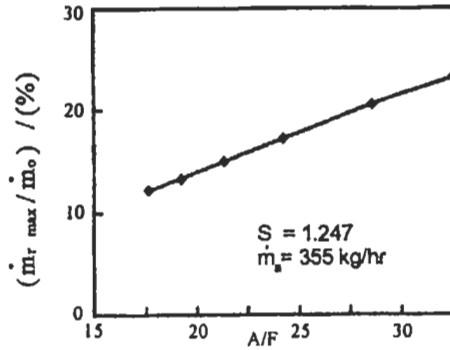


Fig. 4.80 (a): Variation of maximum recirculated mass flow rate with the A/F ratio [624]. Reproduced by permission of The Combustion Institute.

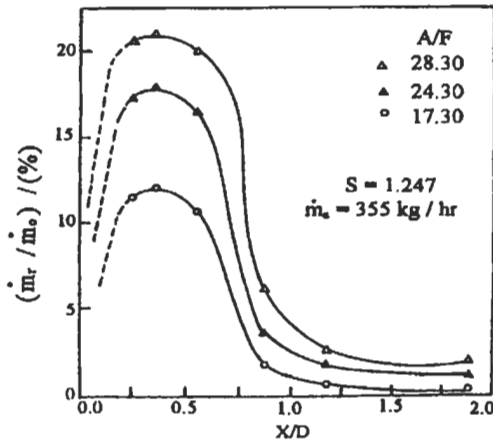


Fig. 4.80 (b): Distribution of recirculated mass flow rate along the furnace for different A/F ratios [624]. Reproduced by permission of The Combustion Institute.

Desoky et al [644] studied the effect of the secondary air ratio and equivalence ratio on combustion performance of can-type gas turbine combustor. Some of their results for H_2 fuel are shown in Figs. 4.81. The figures show that the exit temperature increases with increasing the overall equivalence ratio, ϕ , until it reaches a maximum value at $\phi = 1.2$. It is shown also that the exit oxygen decreases with the increase in the equivalence ratio and that the maximum NO concentration corresponds to a slightly lean mixture.

As regards the effect of air-fuel ratio on the heat liberation, El-Mahallawy [636] investigated this effect along a cylindrical, water-cooled, light oil fuel fired-furnace. The distribution of the total dimensionless heat liberated along the furnace for two air-fuel ratios is shown in Fig. 4.82. Generally, higher rates of heat liberation at upstream are shown corresponding to higher air-fuel ratios. This confirmed the results in Fig. 4.79 in which the flame length decreases as the air-fuel ratio increases.

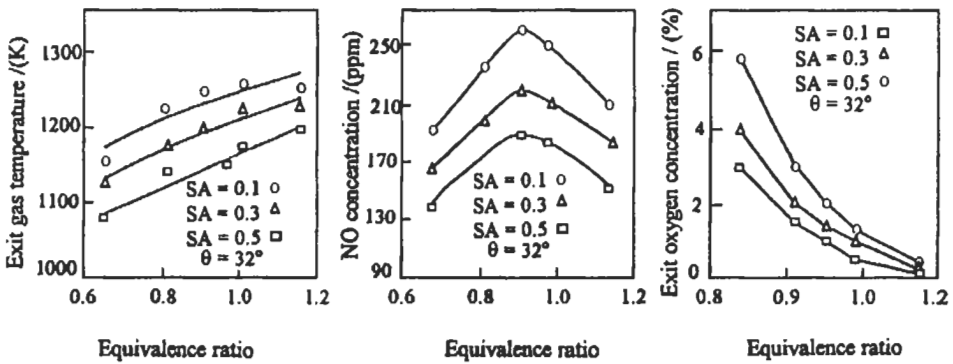


Fig. 4. 81: Effect of equivalence ratio on, NO, O_2 concentration and exit gaseous temperature for fuel H_2 . SA is the secondary air ratio [644].

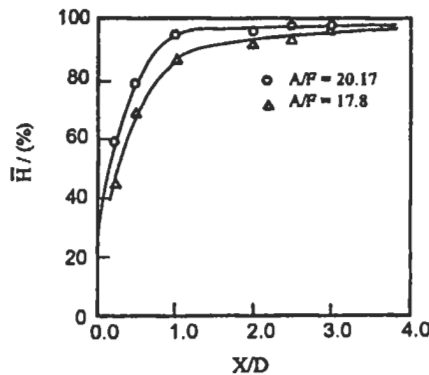


Fig. 4. 82 : Distribution of the total heat liberation along the furnace for two air-fuel ratios [636].

Forced Flow Reversal

The work of Ref. 606 on mixing in a cylindrical, cold model reversed flow furnace was extended further by Mahdi Ali et al [648] to include the combustion conditions. The test rig was that used in Ref. 32, but was fired by two co-axial streams of commercial butane (60 % C_4H_{10} and 40 % C_3H_8) and combustion air. They compared the results of the reversed flow furnaces with those of the normal open tunnel type ones. The main parameters considered are the reversed flow furnace length and the mass ratio of the two input streams. The results show that the reversed flow furnaces have generally better mixing patterns and higher rates of total heat transfer to the walls as compared with the tunnel type ones.

The effect of the reversed flow furnace length on the temperature at the exit section of the furnace is shown in Fig. 4.83 (a). The results show that the short reversed furnaces are characterized by high temperature value i.e. high enthalpy of the combustion gases at the exit section. This may be due to the increase of heat transfer area in the case of longer furnace lengths.

The effect of furnace length on the total heat transfer flux to the walls is shown in Fig. 4.83 (b). A high heat flux is transmitted to the furnace walls at small furnace length. However, the total heat transfer to the walls increases with increasing the furnace length, due to the relatively greater heat transfer surface area in this case. Generally, these types of furnaces as compared with the open tunnel type ones are characterized by good mixing, and short and high heat transfer flames.

An experimental study on the characteristics of combustion heat liberated in a model cylindrical gas fired reversed flow furnace has been carried out by El-Mahallawy et al [649], and Khalil et al [650]. The furnace (0.168 m diameter and 0.68 m long) is fed by two jets of commercial butane and air at one end and closed by a movable piston at the other end. The main parameters considered are the furnace length and the intensity of combustion, expressed by the fuel-air ratio, keeping the air mass flow rate constant. Comparisons are also made between this type of furnaces and the open tunnel type one. The heat liberated due to combustion is calculated from the enthalpy of the gases and the heat losses to the walls as described before. The results of the distribution of the dimensionless heat liberated along the furnace for different furnace lengths are shown in Fig. 4.84. High rates of heat liberation along the furnace are shown corresponding to

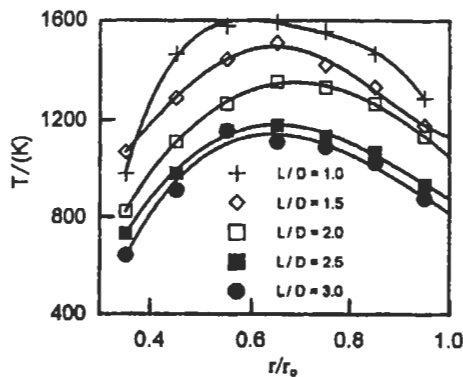


Fig. 4.83 (a): Temperature distribution at the exit section for different reversed flow furnace lengths [648].

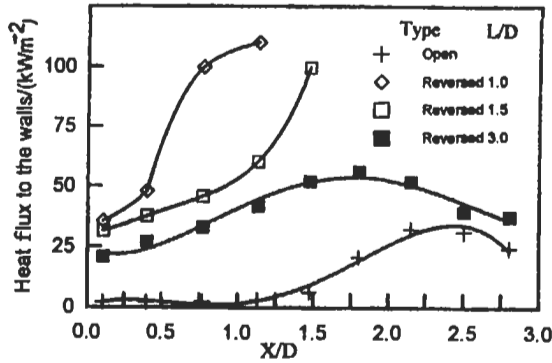


Fig. 4. 83 (b): Distribution of the total heat flux to the furnace walls for different reversed flow furnace lengths [648].

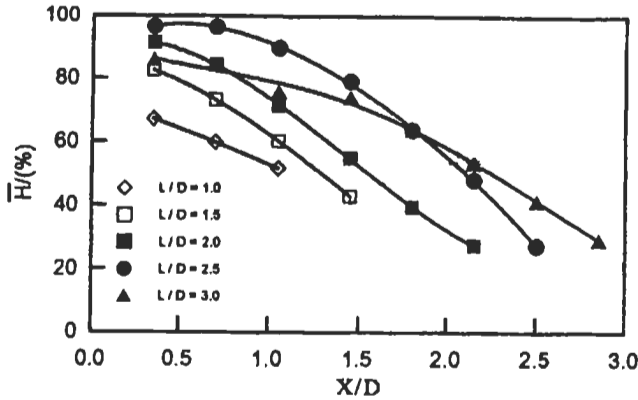


Fig. 4. 84 : The distribution of the heat liberation along the furnace for different furnace lengths (A/F = 23.08) [649, 650].

medium furnace lengths. This may be due to the high mixing rates as a result of the high turbulence level in this case as the gases flowing in the downstream direction should be reversed in relatively short distance. If considering the flame length as corresponding to a certain percentage of the heat liberated from the input heat (say 95%), this means that the furnace length of $L/D = 2.5$, has the shortest and efficient flame as compared to other lengths as shown in Fig. 4.85. The results of the distribution of the heat liberation in the open tunnel furnace and in the forward and backward directions for the reversed flow furnace are shown in Fig. 4.86. The figure reveals that the reversed flow furnace is characterized by high heat liberation (combustion efficiency) and short flame as compared to the open tunnel type one.

Furnace and Burner Geometry

El-Mahallawy et al [651] have investigated experimentally the effect of exit section geometry and furnace length on the characteristics of combustion heat liberated in a cylindrical gas fired model furnace of 0.168 m diameter. At the inlet section of the furnace, two jets of gaseous fuel and air were fed. The model furnace exit is restricted

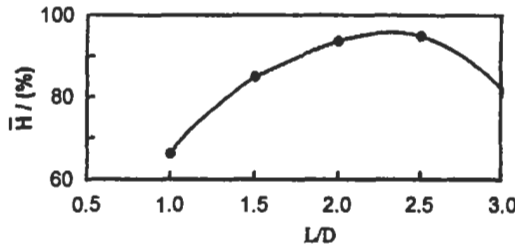


Fig. 4. 85 : Variation of the combustion efficiency with different furnace lengths ($A/F = 23.08$) [649, 650].

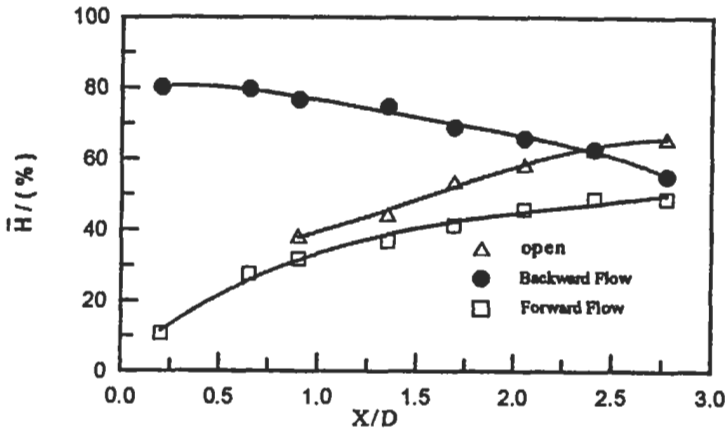


Fig. 4. 86: Distribution of dimensionless heat liberation along the furnace for the open and reversed flow furnaces ($L/D = 3.0$, $A/F = 20.13$) [649, 650].

by means of two water-cooled pistons having diameter ratios of 0.6 and 0.4 relative to the furnace diameter. Different model furnace lengths are obtained by changing the location of the piston inside the furnace.

The heat liberated due to combustion up to a certain section is calculated from the increase in the enthalpy of gases and the heat transfer to the furnace walls up to this section as described by the procedure given before. Measurements of velocity and temperature were carried out and the heat transfer to the walls was obtained from the rate and temperature rise of cooling water flowing through cooling rings fitted on the outer surface of the furnace. The results of the effect of exit section restriction on the dimensionless heat liberated \bar{H} are shown in Fig. 4.87. The figure shows that, restricting the exit section will have a significant effect on improving the heat liberation or the degree of completeness of combustion. A similar conclusion was obtained by El-Mahallawy and Hassan [608].

The interest in the study of industrial-type furnaces has grown enormously in the recent years to improve design features and optimize the operating conditions. Therefore, El-Mahallawy et al [652] have studied an elbow-shaped flame tube. This type of flame tubes makes use of the heat generated in the tube, which is orientated vertically, to introduce air required for combustion under the effect of buoyancy lifting forces. Therefore, the need for a forced draught fan is eliminated and this is

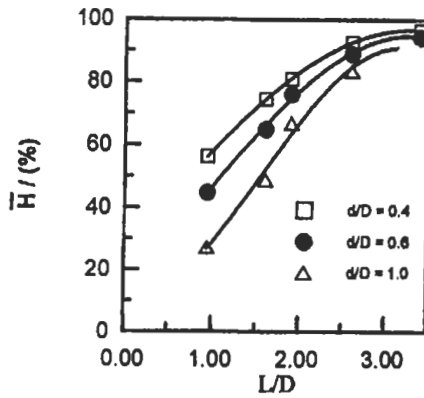


Fig. 4. 87: Effect of exit section restriction on the dimensionless heat liberated \bar{H} for 0° swirl [651].

advantageous in the applications where supply of electrical power is a difficulty. A 90 degree sharp bend at entrance section provides a direct and efficient method for fast mixing and flame stabilization. The body forces impose a secondary flow in the plane perpendicular to the centerline. This results in non-symmetrical axial velocity and temperature profiles, which modify the flow behavior so as to increase the flow resistance and the rate of heat transfer.

A recirculation zone is produced at the entrance of the flame tube (the right-hand side corner of the L tube) which again plays an important role in flame stabilization. This kind of flame tubes can be used for producing steam for water distillation or food processing. The tube is shown with fuel nozzle position in Fig. 4.88 (a and b) and consists essentially from an elbow-shaped tube and a fuel supply system. The fuel nozzle (shown in Fig. 4.88 (c)) is made of brass and comprises four holes each of 1 mm in diameter. This multi-hole nozzle assures symmetry of fuel distribution and promotes stability. The fuel used is a mixture of butane, C_4H_{10} and propane, C_3H_8 with a ratio of 0.9 and 0.1 by volume, respectively. Measurements of temperature contours on the symmetrical plane (A-A) in this furnace for different nozzle positions are carried out and a sample of these measurements is shown in Fig. 4.89. It is clear that the temperature of the flame is a function of the nozzle position. The nozzle position generally affects the visible flame length. The reason being that the flame length depends on the quantity of the fuel, which penetrates the reversed-flow zone.

The average oxygen percent at exit is calculated by summation over the flame tube cross-sectional area and the results are shown against m_f in Fig. 4.90. Excess air factor (λ), air to fuel ratio (A/F), air inlet velocity (U_a), air mass flow rate (m_a) and Reynolds number (Re) are also given versus m_f in the same figure. Figure 4.90 shows that as fuel rate increases, the excess air leaving the furnace decreases despite the apparent increase of the amount of air needed for complete combustion. Consequently, both buoyancy effect and the resistance to the flow increase. There exist a region for m_f where O_2 % declines to a minimum value. This is attributed to the occurrence of natural resonance in the tube medium. This resonance causes lateral motion of the combustion mixture and hence increases mixing which subsequently results in enhanced flame stability and efficient combustion.

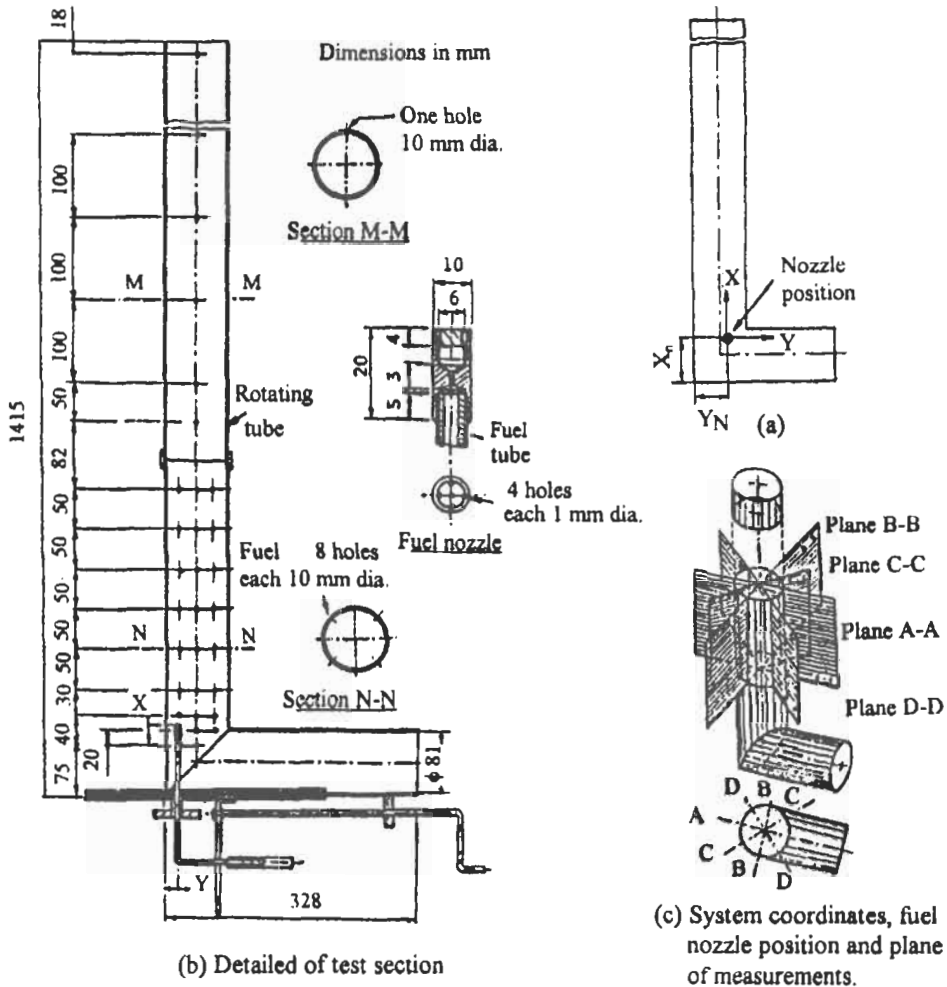


Fig. 4. 88: Elbow-shaped furnace [652].

El-Mahallawy et al [625] and Lockwood et al [569] also investigated the effect of burner geometry on the fuel mixture fraction in a cylindrical furnace axially fired by gaseous fuel as described before in section 4.5.1. Measured axial profiles of mixture fraction for two burner geometries are compared in Fig. 4.91. The more rapid decay of, F , on the axis of geometry 1, reflects the more intense mixing of fuel and air due to the greater inlet velocity differential between the fuel and air streams for this case.

Effect of the Direction of Air and Fuel Entries

Abdel Hafez and Taha [653] studied experimentally the case of two opposite gaseous fuel jets, injected normally onto a confined circular air stream. Two input parameters are investigated: the momentum ratio between fuel and air streams (MR) and the equivalence ratio. The study is conducted on a cylindrical water - cooled horizontal

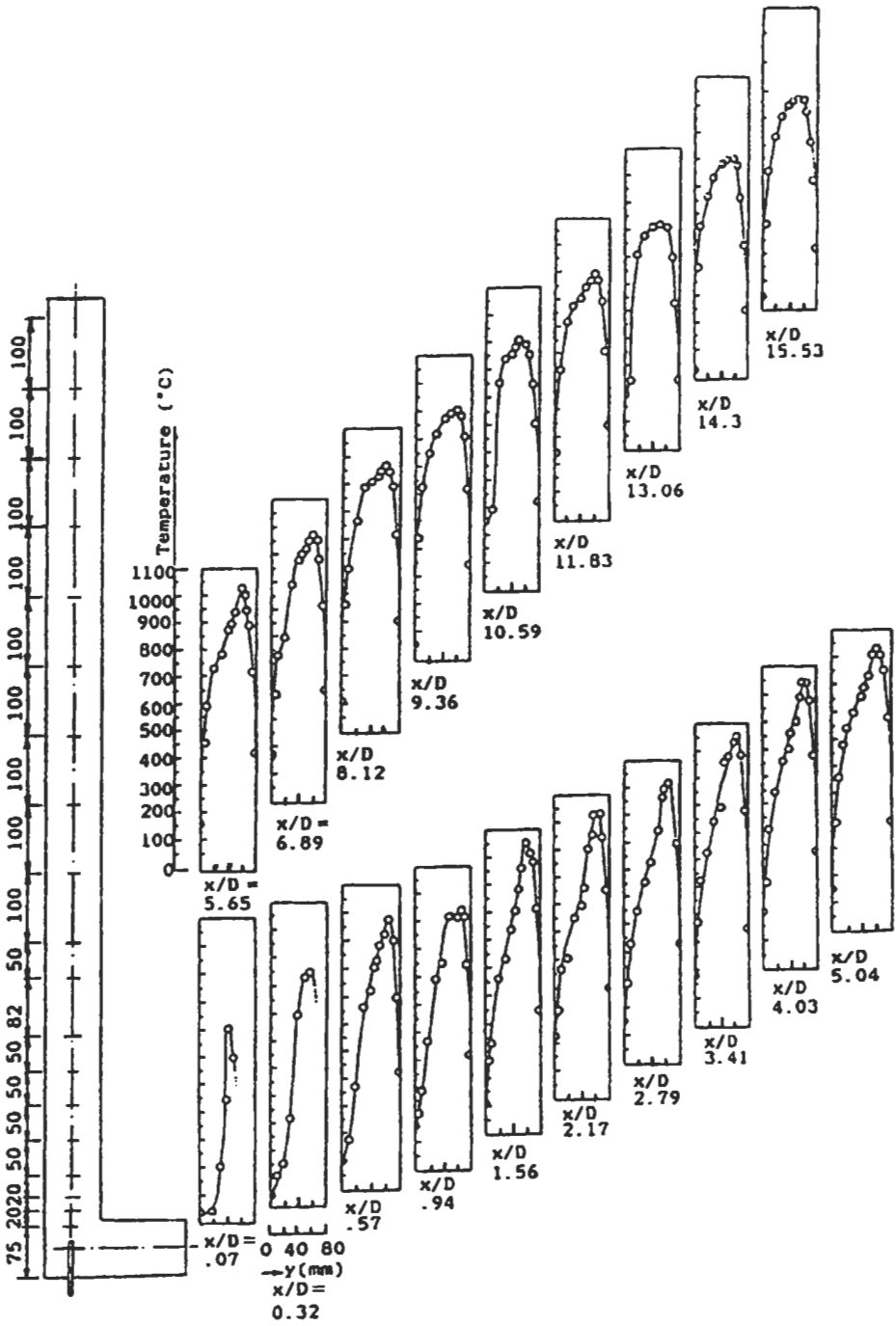


Fig. 4.89: Temperature distribution in flame tube in section A-A for $m_f = 2.18 \text{ kg h}^{-1}$, $\lambda = 1.4$, $A/F = 22$, $u = 2 \text{ m s}^{-1}$, and $Re = 23000$ (see Fig. 4.88) [652].

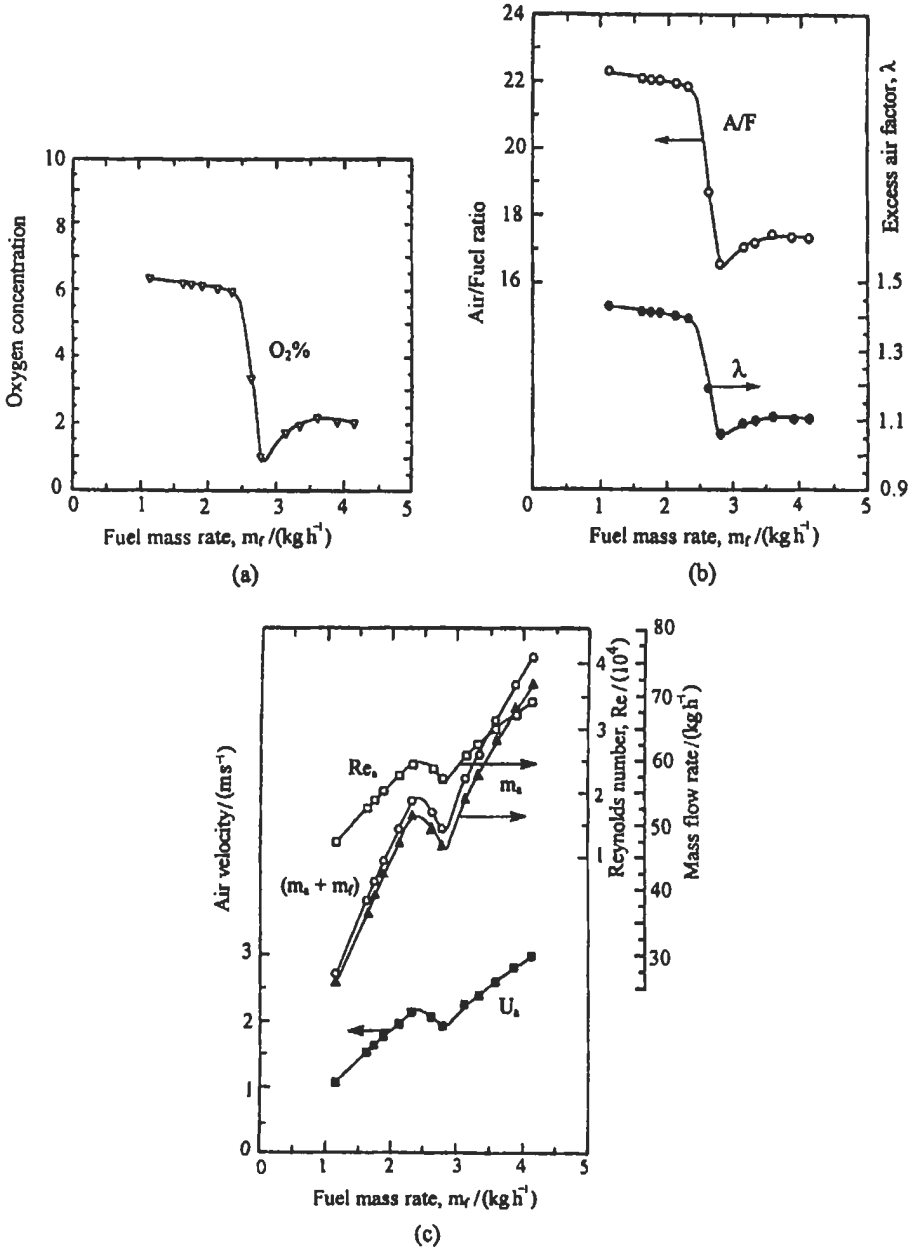


Fig. 4.90: Variation of different operating conditions with the fuel mass flow rate [652].

combustor, 0.102 m inner diameter and 0.95 m length. The test rig section is shown in Fig. 4.92. The combustor is equipped with the suitable fuel and air systems. The momentum ratio is changed by replacing the fuel jet nozzle diameter, d_n and/or varying the fuel mass flow rate m_f .

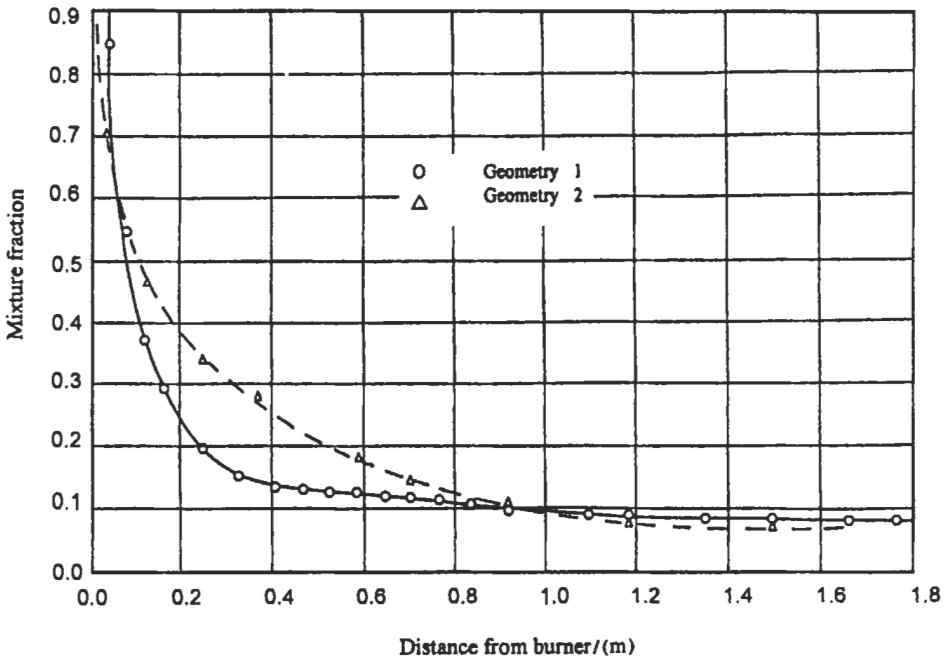


Fig. 4.91: Comparison of the measured mixture-fraction distribution along the axis for geometries 1 and 2, $F/A = 0.0786$, and $Re = 10,810$ [569]. Reproduced by permission of Elsevier Science.

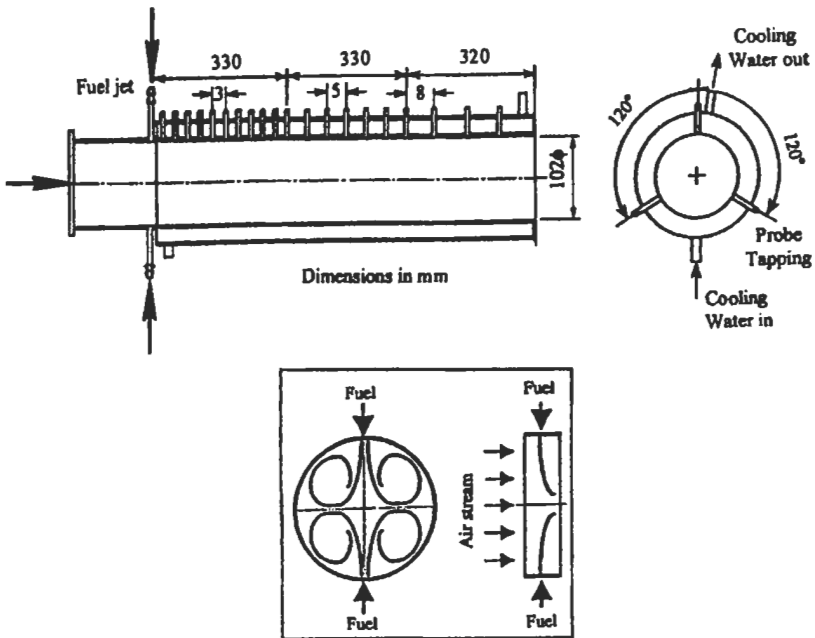


Fig. 4.92: Test section and fuel jets flow field [653].

Figures 4.93 (a), (b), and (c) show the transverse contour regions of temperature, CO_2 , and O_2 . The results show that the flame in the earlier sections is lapping over the inner surface of the cylindrical combustor, and this is quite clear in section 1 ($X/D = 0.3$). The high impingement of the two opposite fuel jets causes the formation of four toroidal vortices occupying the entire upstream sections, Fig. 4.93 (b). Moreover, the two fuel jets obstruct and decelerate the air stream at their upstream front creating a region of negative pressure in the downstream part of the fuel jets section. The combined effect of the fuel jets impingement and obstructed air stream yields a deceleration of the flow velocity to the levels so they can compete with the burning velocities. The flame is, therefore, initiated and stabilized in the early section. It is known that the rate of reaction can be examined through the oxidant concentration in the combustion zone. As an evidence of the lapping-over and the presence of the aforementioned vortices, O_2 at section 1, $X/D = 0.3$ has been consumed to the concentration of 2% near the wall and to 10% - 20% in the core of the section, Fig. 4.93 (c). At section 3, $X/D = 0.9$, O_2 has been consumed to the concentration of 2% on the vortex boundaries and 14% in its core. The persistence of the vortices is confirmed by investigating section 7, $X/D = 2.1$. The transverse contour regions of temperature, Fig. 4.93 (a) confirms the presence of lapping-over phenomenon. Temperature near the wall is 1500 K with corresponding value of $\text{CO}_2 = 8\%$. This local high value of CO_2 indicates a high rate of reaction at this region. At the core of the section, however, $T = 600 - 1000$ K with corresponding value of CO_2 of $< 4.0\%$. The longitudinal contour maps for the same experimental conditions of Fig. 4.93 are shown in Fig. 4.94.

Finally, it was concluded that, the transverse admission of two opposite fuel jets onto a stream of air in a confined combustor is a successful method to attain a stable highly turbulent flame. Also, the flame is characterized by a complicated three-dimensional flow pattern where four toroidal vortices are generated and lasted in the upstream part of the combustor.

As shown above, the transverse admission of fuel into the stream of combustion air is a successful method for flame stabilization. Therefore, Abdel Hafez et al [654] continued their studies on the same subject but taking into consideration the effects of the fuel admission angle and the air-fuel ratio on the flame characteristics and the total heat transfer to the wall. The fuel admission angle (θ) is designated as the angle between the direction of each fuel gun and the radial direction of the burner. Three values of (θ), namely, 0° , 45° and 90° are investigated. The coaxial conventional admission of fuel has been also considered for the sake of comparison. Slightly rich, lean, and over lean flames, expressed by the three air-fuel ratios 15, 20 and 25, respectively, have been studied together with those fuel admission angles. Air is swirled (45° swirler) in the same direction of fuel whirling. The study shows that using a burner of a transverse-flow with fuel to be admitted with an angle of 45° would result in a flame of highest values of total heat transfer. It also shows that an angle of 0° would offer a flame of shorter length and relatively lower heat transfer to the surrounding walls.

The burner configuration and the test section are shown in Fig. 4.95. Fuel is let in from four circumferential nozzles, 90 degrees apart. Three replaceable parts each of which allows the fuel to be admitted with a different angle (θ), namely, 0° , 45° and 90° . The fuel nozzles are located 12.5 mm downstream of the combustor swirler. The horizontal cylinder is 0.14 m ID and 1.7 m long surrounded by 15 cooling rings fitted at equi-distances. The local gas mean temperatures at the different points inside the chamber

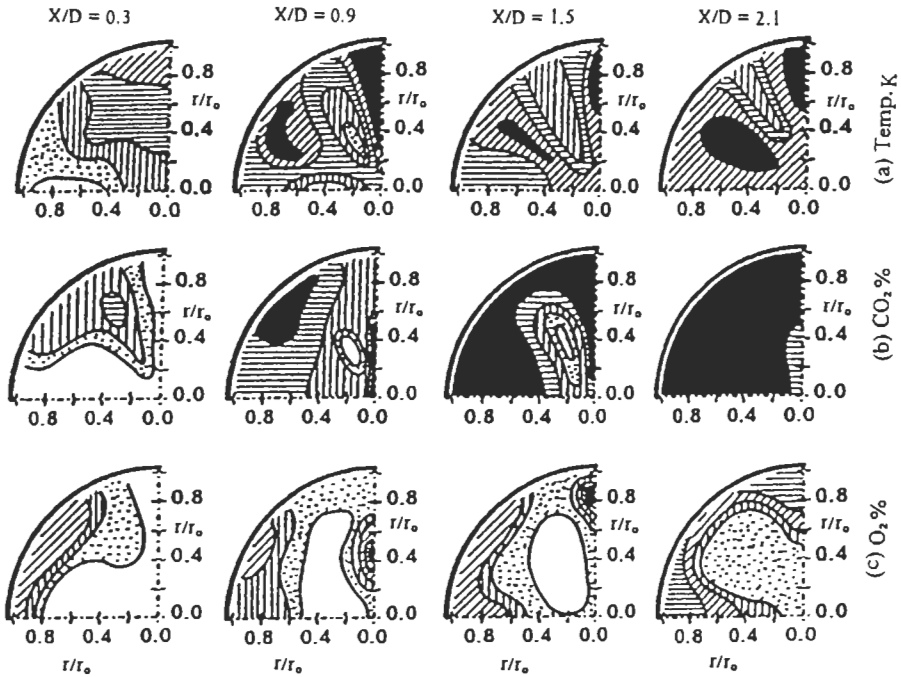


Fig. 4.93: Transverse contour regions, nozzle diameter (d_n) = 1.25 mm, fuel rate (m_f) = 5 kg h⁻¹, and momentum ratio (MR) = 1.5, and $\phi = 0.71$ [653].

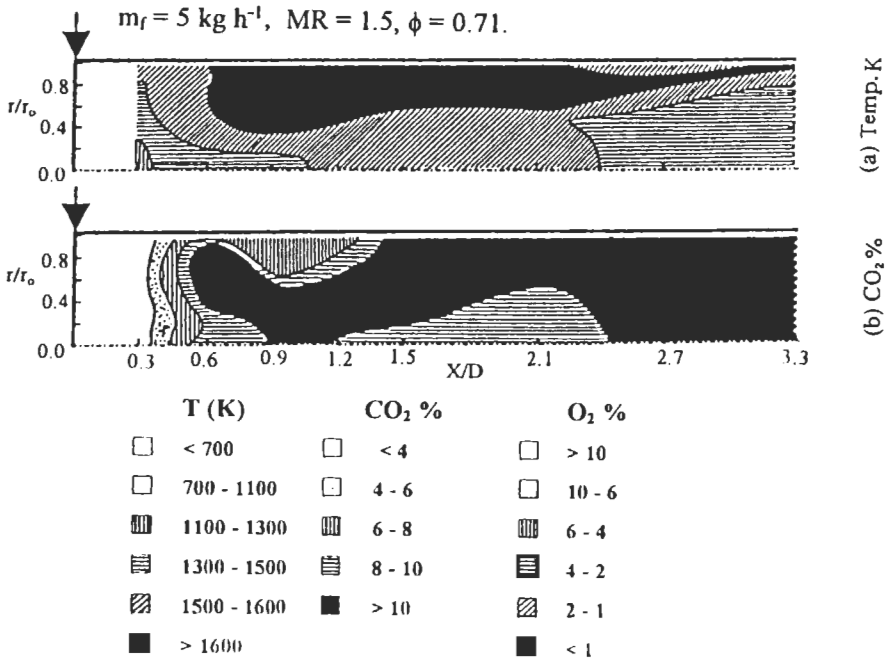


Fig. 4.94: Longitudinal contour maps. Same data as in Fig. 4.93 [653].

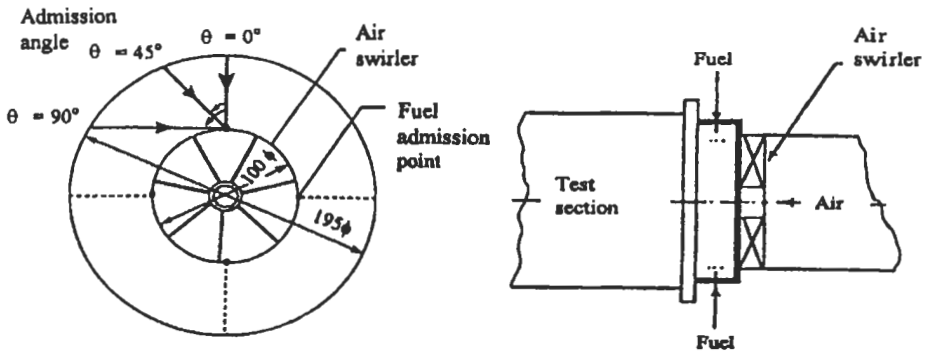


Fig. 4.95: Layout of the test rig and burner configuration [654]. Reproduced by permission of ASME.

were measured using a bare fine-wire thermocouple. The total heat transfer is obtained through measuring water mass flow rate and its temperature-rise in each of the cooling segments.

The temperature radial profiles across some sections, for different fuel admission angles (θ) and same air-fuel ratio, are shown in Fig. 4.96. The figure reveals that the smaller the angle (radial admission) the shorter the flame. The intensity of turbulence is relatively high, in the upstream sections of the combustor, when the fuel is admitted perpendicular to the air stream. The rate of mixing is also remarkable near the chamber centerline; the flame has reached a temperature of 1500 K in a short distance (less than twice the diameter). This is attributed to the characteristics of the flow field

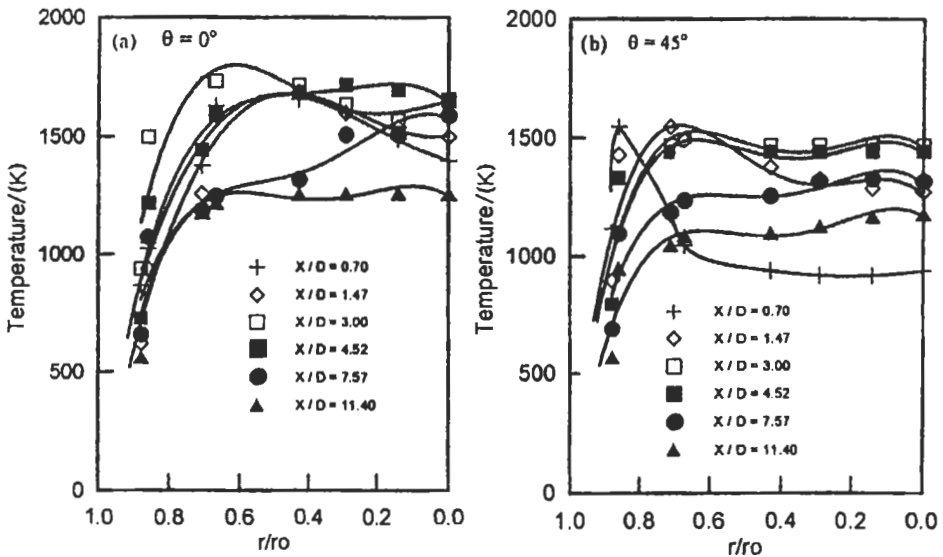


Fig. 4.96: Temperature radial profiles across some sections along the chamber for different θ [654]. Reproduced by permission of ASME.

when a jet with high momentum is injected normal to another main stream of less momentum. The interaction between the two streams yields a counter rotating vortex pair, which is a characteristic of the jets and plumes in cross-flows, (Kamotani and Gerber [655]).

Figure 4.97 shows, quantitatively, the distribution of the dimensionless cumulative total heat transfer, q' , along the chamber for different fuel admission angles. The high values associated with $\theta = 45^\circ$ are attributed to the fact that the flame is occupying entirely the combustion space and the mean temperature level, therefore, is higher. For $\theta = 90^\circ$ (tangential admission of fuel) the flame is adjacent to the wall and the heat transfer should be of the highest distribution. Nevertheless, the core of the flame, as it was mentioned before, is completely consisting of air and combustion gases, i.e. a mixture of relatively lower temperature. This would lower the average flame temperature, which, in turn, affects the heat transfer from the flame to the wall (in particular heat transfer by radiation).

At $\theta = 0^\circ$, (pure radial admission of fuel), the flame is centered in the core of the combustor and surrounded by air and/or combustion gases. The intensity of turbulence is high along the central part of the upstream, unlike the region near the wall whose levels of turbulence and temperature are lower. That has yielded lower values of heat transfer in comparison with case of $\theta = 45^\circ$. In this regard, the fuel angle $\theta = 0^\circ$ would be reasonable to be used in the burner of the gas turbine combustion chamber. The angle $\theta = 45^\circ$ should be used in burners attached to furnaces and boiler flame tubes.

Regarding the case of conventional coaxial admission of fuel, lower values of heat transfer to the wall are then obtained. Figure 4.98 shows the distribution of total heat flux, q'' , along the chamber, for air swirling in the same and opposite directions of fuel. When air is swirled in the same direction of fuel, the heat flux distribution is higher. The phenomenon is ascribed to the thought that with air swirl in the direction of fuel,

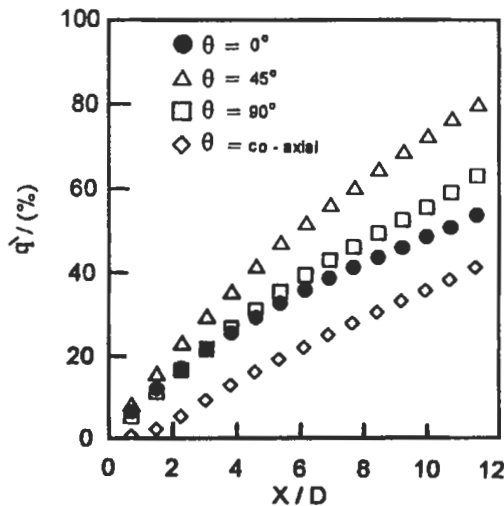


Fig. 4.97: Distribution of dimensionless cumulative heat transfer for different values of θ , ($A/F = 20$) [654]. Reproduced by permission of ASME.

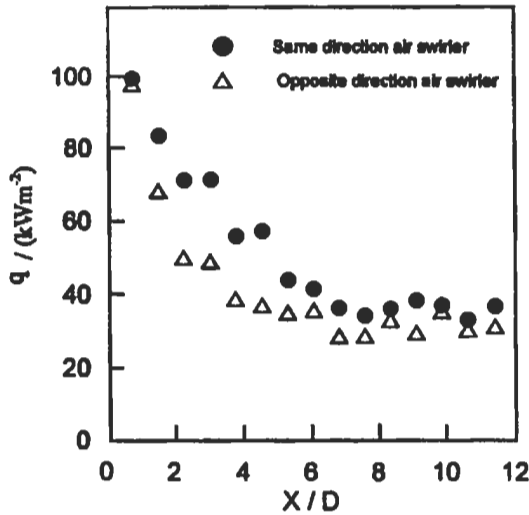


Fig. 4.98: Distribution of total heat flux for same and opposite directions of air swirling. ($\theta = 45^\circ$, $A/F = 25$) [654]. Reproduced by permission of ASME.

the resultant tangential velocity in the vicinity of the wall is relatively higher. This, in turn, will enhance the heat transfer by convection to the wall. With an opposite direction of swirl, the resultant tangential gas velocity near the wall is relatively lower and so is the heat transfer.

The effect of the transverse flow of the fuel on the behavior of heat liberation and heat transfer along the axial direction of a horizontal flame tube was also investigated by Abdel Hafez [656]. A simplified computational technique has been developed based on the gas and radiation properties. The technique uses an iterative procedure which describes the heat liberation through Eq. 4.90, and the polynomial fitted constants a, and b for this equation are found to be:

$$a = \left(-6.173 \times 10^{-7} \theta^2 - 8.333 \times 10^{-5} \theta + 0.05 \right) A/F$$

$$b = \left(2.469 \times 10^{-6} \theta^2 - 3.555 \times 10^{-4} \theta + 0.06 \right) A/F$$

Figure 4.99 shows the calculated distribution of the dimensionless heat liberation along the flame tube. The figure displays the effect of fuel injection angles for the same air-fuel ratio and the effect of the air-fuel ratio for the same fuel injection angle. The resulting behavior matches well with the argument given by Ref. 654, regarding the effect of fuel injection angle and combustion intensity on the flame structure.

Heat is transferred from the flame body and the flue gases to the tube walls by radiation and convection modes. The net radiant heat flux falling on a unit cylindrical wall area located at a distance X_i from the tube inlet, refer to Fig. 4.100, is the summation of the net radiant flux exchanged with all the cylindrical slices j within the flame tube. The summation can be written as given by Eq. 4.75 except that the view factor is found to be:

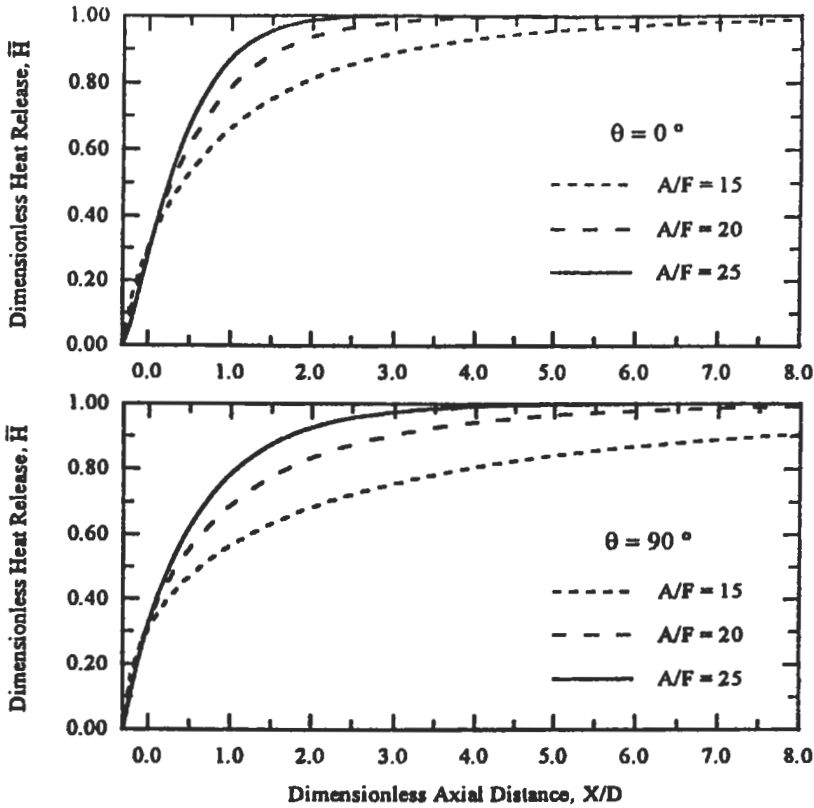


Fig. 4.99: Effect of fuel injection angle and air-fuel ratio on the behavior of heat release [656].

$$\frac{4\delta}{D} \left[\frac{Y^2 + 0.5}{\sqrt{Y^2 + 1}} - Y \right] \quad \text{with:} \quad Y = \frac{X_j - X_i}{D} \quad \text{and} \quad X_j \neq X_i$$

The dimensionless heat transfer by radiation from the flame to the wall is given by Eq. 4.80. The convective part of the heat transfer to the wall of the flame tube is given by Eq. 4.83, while the total dimensionless total heat transfer is calculated by Eq. 4.84.

Figure 4.101 shows the values of calculated total cumulative heat transfer, from the flame body and gases, to the tube wall as compared to the experimental values. The approach yields a reasonable agreement between the calculated values of total cumulative heat transfer and the experimental ones. Figure 4.101 also shows the radiative and convective components of heat transfer. In a similar study [637], where oil fuel was used to fire a test rig of 0.6 m in diameter, the convective part \bar{Q}_c reached a value of $\approx 18\%$ of the total heat transfer \bar{Q} . In this work, however, \bar{Q}_c has reached a value of $\approx (25 - 30 \%)$ of \bar{Q} . This is explainable in view of the geometry of the burner and the test rig. As it was mentioned earlier, the circumferential admission of the gaseous fuel results in shear layer of relatively high level of turbulence in the vicinity of the wall. Moreover, the zones of high temperature will move towards the wall. Heat and mass transfer is then enhanced and the convective part of heat transfer is higher.

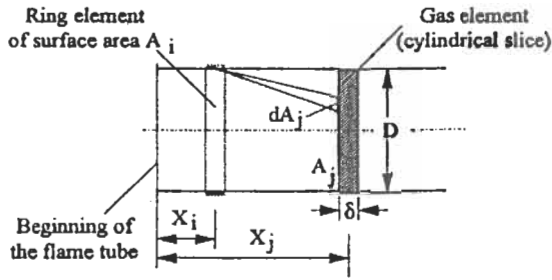


Fig. 4.100: Schematic presentation to ease obtaining the view factor [656].

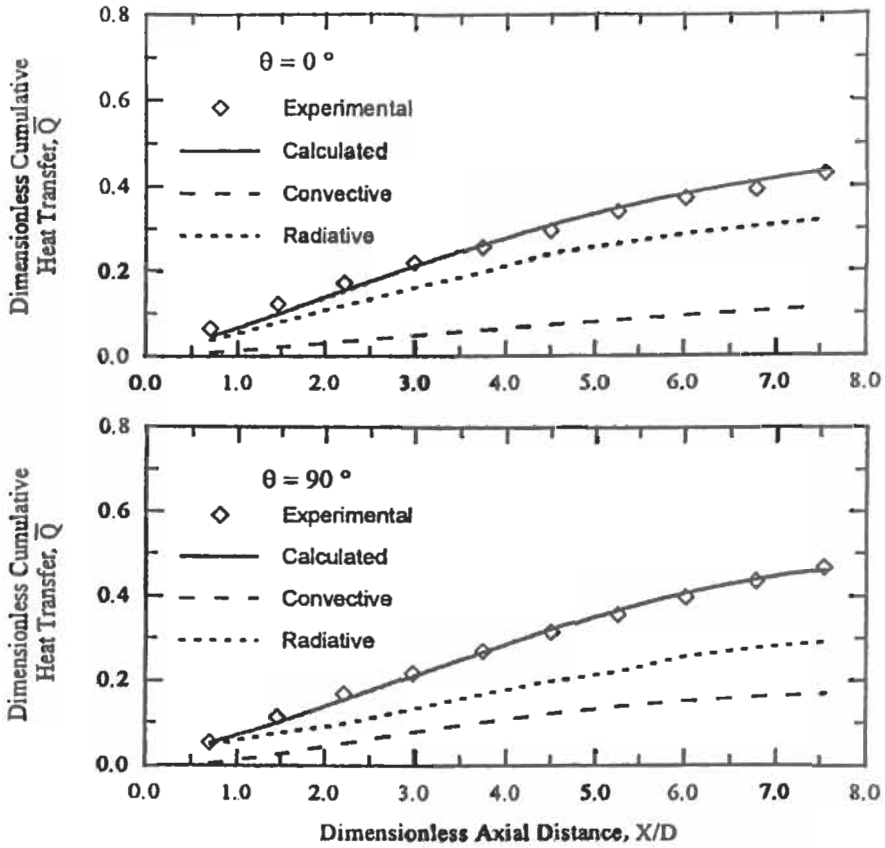


Fig. 4.101: Cumulative heat transfer for different fuel injection angles and $A/F=20$ [656].

Furthermore, very little work has been so far done on the effect of the entry profiles, specially radial entry of the air to the combustion zone. Therefore, El-Mahallawy et al [657] have studied experimentally the effect of combustion air direction on the flow and heat liberation in cylindrical furnaces. The experiments were carried out on two test rigs (cold and hot). The cold rig was for the investigation of recirculation down-stream of circular flat plates located near the inlet section of a cylindrical cold model furnace of

0.4 m diameter as shown in Fig. 4.102 (a). Four discs were located at the upstream end of the furnace with a small gap left between these discs and the furnace inlet section to allow radial admission of combustion air. The radial momentum of air was varied by varying the width of the formed gap. Three of these discs were smaller in diameter than the inlet pipe, while the fourth one was bigger than the diameter of the inlet pipe. Three air swirlers were also used for creating a tangential component to air plus the radial and axial components. The hot rig was used for the investigation of flow and heat liberation characteristics under firing conditions. This test section is shown in Fig. 4.102 (b) and it consists of a horizontal water-cooled, stainless steel pipe of 0.168 m diameter and 0.68 m long (El-Mahallawy et al [658]). Again, the radial entry of the combustion air to the furnace was achieved by discs mounted at the upstream end of the test section. Four discs were used and the gap between the disc and the inlet section could be easily varied. The fuel used was a mixture of butane and propane with gravimetric analysis of 0.6 and 0.4, respectively. Under cold conditions, the experimental results showed that the discs of diameter smaller than the diameter of the inlet pipe failed to create a considerable central recirculation. Thus, the analysis of central recirculation under cold conditions will be concerned with the effect of swirl and radial air entry.

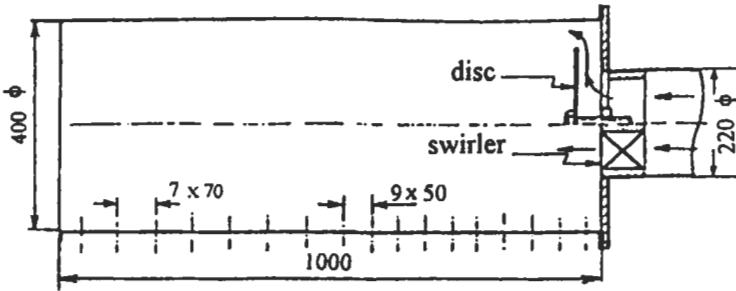


Fig. 4.102 (a): The chamber entrance [657].

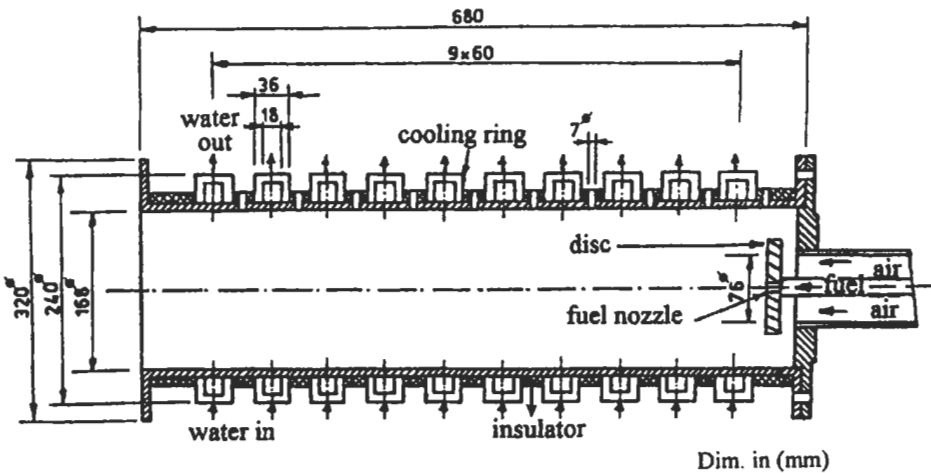


Fig. 4.102 (b): Hot model test section [657, 658].

The boundary of the central recirculation zone is obtained from points of zero axial velocity where the flow starts to reverse its direction. This boundary is shown in Fig. 4.103 for different degrees of swirl. For high and intermediate intensities of swirl ($S = 1.195$ and $S = 0.753$) an open ended central recirculation zone is obtained. Generally, the volume occupied by the recirculation zone increases with the increase in the intensity of swirl.

The boundary of the central recirculation zone for different gaps, or radial momentum of air, is shown in Fig. 4.104 (a). The diameter of this zone is shown to be mainly affected by the dimensions of the disc and of nearly the same volume for different gaps. For the calculation of the reversed mass flow rate, every cross section of the furnace was divided into a number of equi-area rings to ensure that each ring has nearly uniform axial velocity. Therefore, the reversed mass flow rate was calculated by:

$$\dot{m}_{rj} = \sum_{i=1}^n \rho_{ij} U_{ij} A \tag{4.91}$$

where i and j are the ring and section number, respectively, while n is the number of rings in the recirculation zone and A is the area of the ring.

Figure 4.104 (b) shows the distribution of the reversed mass flow rate along the furnace for the cases of swirl and radial air entry. It is clear that relatively high-recirculated mass is obtained in case of radial air entry as compared with air swirl. Under firing conditions, Fig. 4.105 shows the boundary of the central recirculation zone for different gaps. It is clear that, increasing the radial momentum results in a significant increase in the size of the recirculation zone. While the maximum diameter is slightly

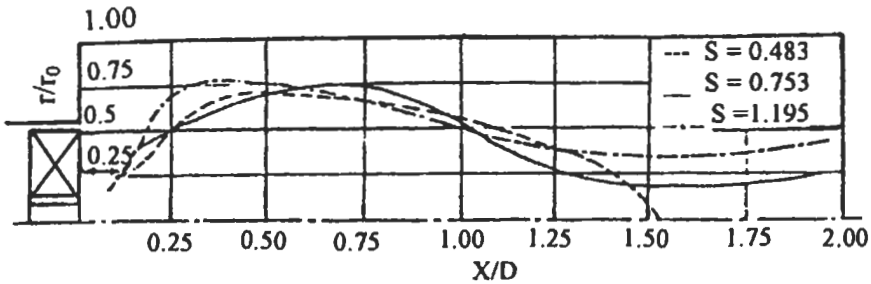


Fig. 4.103: Boundary of the central recirculation zone for different intensities of swirl-cold [657].

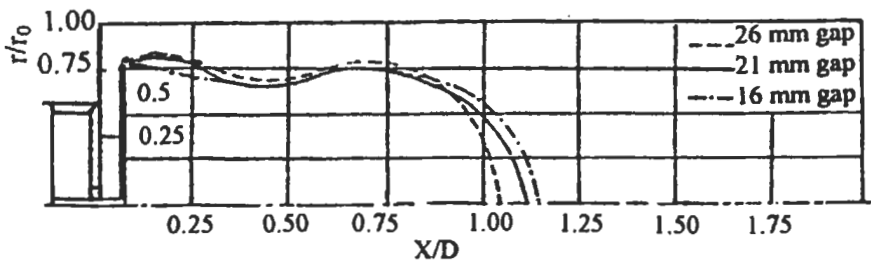


Fig. 4.104 (a): Boundary of the central recirculation zone for different gaps (cold conditions) [657].

changed as it is affected by the diameter of the disc, the length of the zone is shown to be strongly affected. The slight change in the dimensions of the recirculation zone, which is observed under cold conditions (see Fig. 4.103), may be attributed to the relatively narrow range of the radial momentum change in this case compared with the hot tests. Also, the characteristics of the central recirculation are affected by the high temperature and density gradients existing under hot conditions. For all conditions given in Fig. 4.105, a narrow forward flow zone, around the furnace centerline and down-stream of the fuel jet, is shown in the figure. This zone closes to the center line for high values of radial momentum due to the high momentum of the reserved flow as compared with that of fuel jet. For low values of radial momentum the recirculation zone is in the form of a closed loop touching the disc and shifted from the centerline.

The effect of changing the gap width for a certain disc on the reversed mass flow rate as a fraction of the input mass flow rate is shown Fig. 4.106. The reversed mass is shown to be strongly affected by the radial momentum of combustion air. The figure also shows that, for high values of radial momentum, the maximum reversed mass is about 50% of the input mass. Finally, the above results indicate that, the characteristics of central recirculation are mainly affected by the value of radial momentum inspite of the method used to generate it.

The degree of completeness of combustion is defined as: $\eta_c = H_{\max} / H_f$, where H_{\max} is the maximum value of the heat liberated, and H_f is the chemical energy of the fuel input. Figure 4.107 shows the variation of η_c and the flame length with the radial momentum of combustion air. The flame length is considered as the distance from the upstream end of the furnace to the points of maximum heat liberation (H_{\max}).

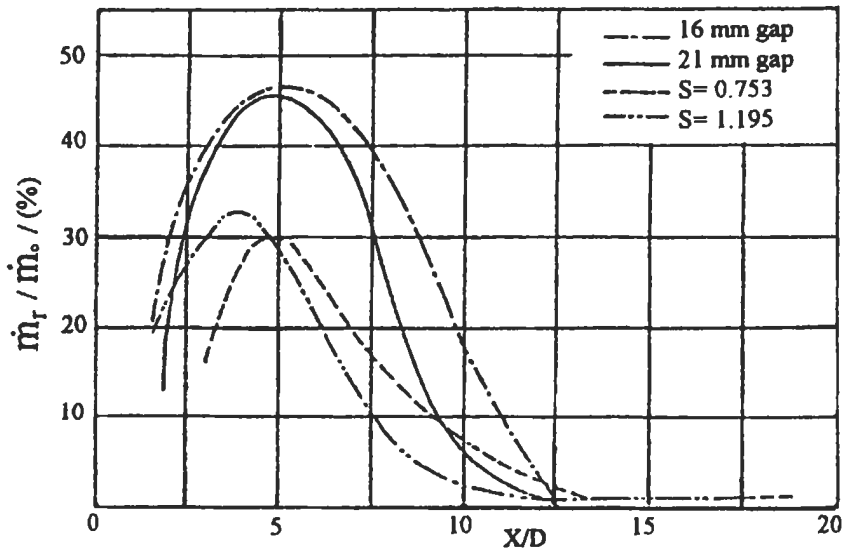


Fig. 4.104 (b): Reversed mass flow rate for different intensities of swirl and different gaps [657].

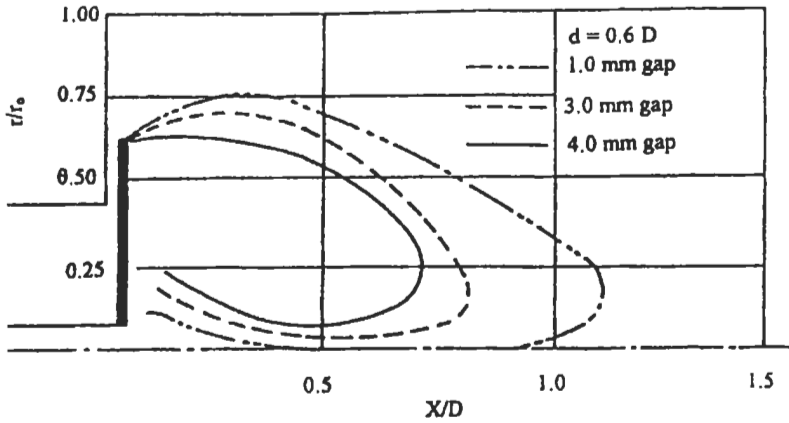


Fig. 4.105: Boundary of the central recirculation zone for different gaps (hot conditions). ($d/D = 0.6$, $\dot{m}_a = 79.4 \text{ kg h}^{-1}$, and $\dot{m}_f = 3.97 \text{ kg h}^{-1}$) [657].

Again, these two quantities were found to depend mainly on the value of radial momentum and are independent of the method used to create this momentum.

The effect of different gap widths on the heat liberated is shown in Fig. 4.108 [658]. It can be seen that, the increase of the radial momentum through decreasing the gap width results in shortening the flame. This is explained by the increase in the rate of mixing between the fuel and air streams in the upstream section as a result of increasing the turbulence level and the recirculated hot gases. The results show also that decreasing the diameter of radial air entry (but not less than the diameter of combustion air pipe) results in a slight improvement in the rate of heat liberation.

Bluff Bodies

The bluff body is a basic device to stabilize double concentric jet diffusion flames in industrial burners, for reasons of safety and easy implementation. It is desirable that the

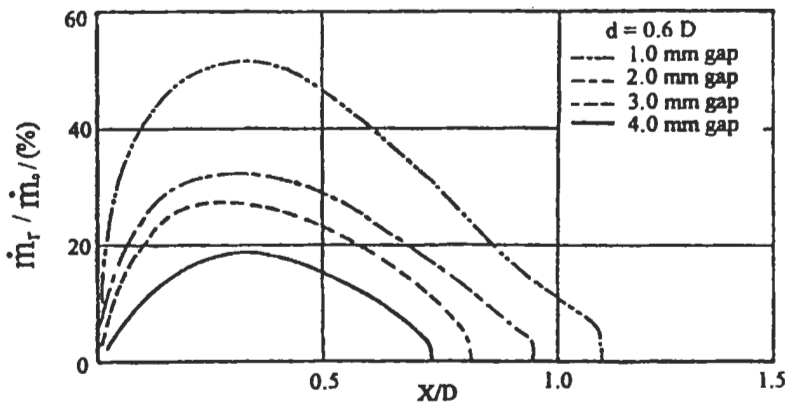


Fig. 4.106: Reversed mass flow rate for different gaps (hot conditions) ($d/D = 0.6$, $\dot{m}_a = 79.4 \text{ kg h}^{-1}$, and $\dot{m}_f = 3.97 \text{ kg h}^{-1}$) [657].

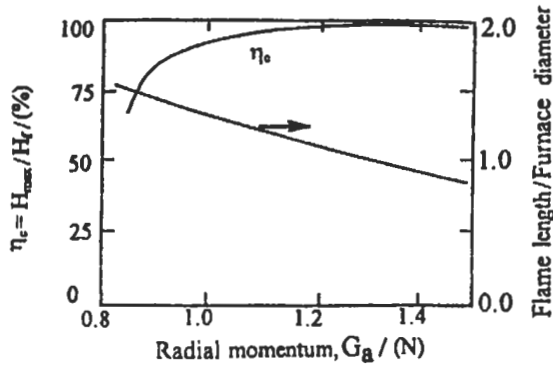


Fig. 4.107: Variation of the combustion efficiency and flame length with the radial momentum of combustion air [658].

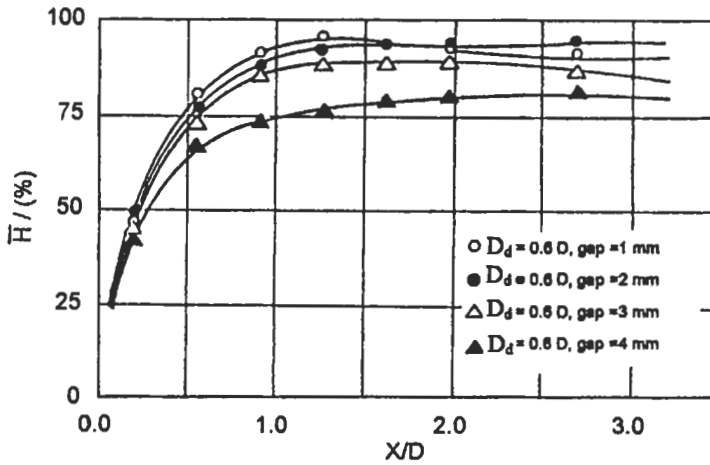


Fig. 4.108: Distribution of the heat liberation along the furnace for different gaps ($D_d = 0.6 D$, and $m_a = 97.4 \text{ kg h}^{-1}$) [658].

annular airflow entrains part of the central fuel jet into a low-speed recirculation region in the wake of the bluff body to form a well-stirred combustible mixture for flame stabilization purpose. Thus, a stable pilot flame is created near the burner exit and serves as a continual ignition source to prevent the downstream stoichiometric, or even lean, nonpremixed flames from direct blow-out. Previous investigations on double concentric jet burners with a circular bluff body at the annulus exit [505-659] have shown the flame structure to be very complex and of various patterns. The underlying combustion mechanisms depend strongly on the hydrodynamic interactions between the fuel jet and the annular air streams. The basic modes of bluff-body stabilized flames based on the air-to-jet velocity ratios have been studied recently by Yang et al [506] and Chen [660]. This section describes the flame structure; stabilization mechanisms as well as the heat liberation of confined turbulent reacting wake flows and nonpremixed jet flame on bluff-body burner.

Following the experimental work described in chapter 3, El-Mahallawy et al [661] have investigated the effect of stabilizer geometry on the size and shape of the central recirculation zone under cold and firing conditions, and their results are given in Fig. 4.109. The figure shows that the size of the recirculation zone for cold flow is much larger than that under firing conditions. For the given test conditions, the length of the recirculation zone of the 90° hollow cone stabilizer under reacting and non-reacting conditions is $X/D = 1.3$ and $X/D = 2.3$, respectively. Furthermore, Fig. 4.109 shows that under firing conditions the thick disc stabilizer creates the smallest central recirculation zone while the 90° hollow cone stabilizer creates the largest. The zone belonging to the hollow cone stabilizer is shown to extend to a relatively larger distance downstream of the stabilizer as compared with the other zones. On the other hand, it is noted that the central recirculation zones created by the thin disc and the 90° solid cone are nearly of similar shape and size. The flame shape could be represented by either the maximum concentration contour of carbon dioxide or the minimum concentration contour of oxygen. Figure 4.110 shows the effect of stabilizer geometry on carbon dioxide contours. The chemical flame boundary of the hollow cone is represented by the contour of 12.5% CO_2 and as shown it ends at $X/D = 1.7$. The measured radial carbon monoxide concentration profiles at the exit of the combustion chamber are used to illustrate the completeness of combustion. Figure 4.111 shows that the best combustion efficiency is obtained for the case of hollow cone stabilizer.

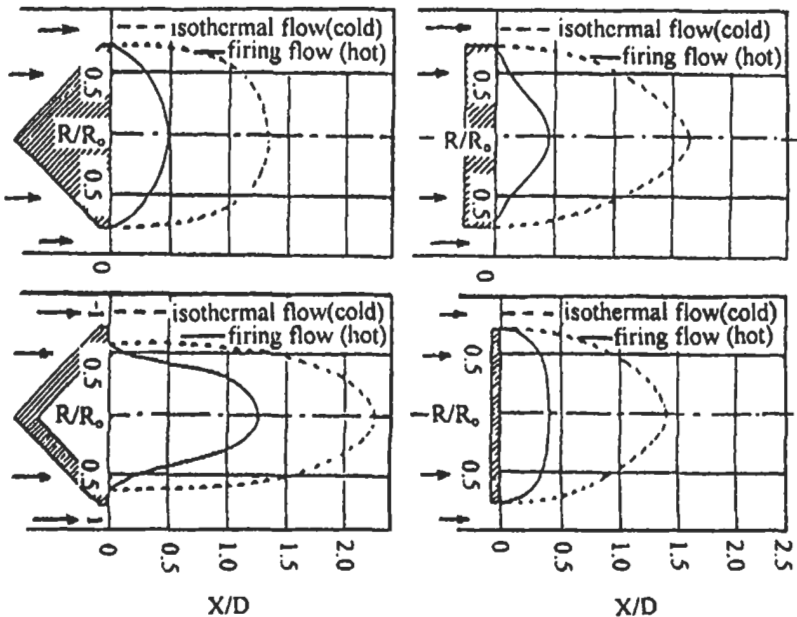


Fig. 4.109: Effect of stabilizer geometry on size and shape of central recirculation zone under non-reacting and firing conditions for premixed flames. (fuel flow rate of 2.75 kg h^{-1} , air fuel ratio is 19.5) [661]. Reproduced by permission of ASME.

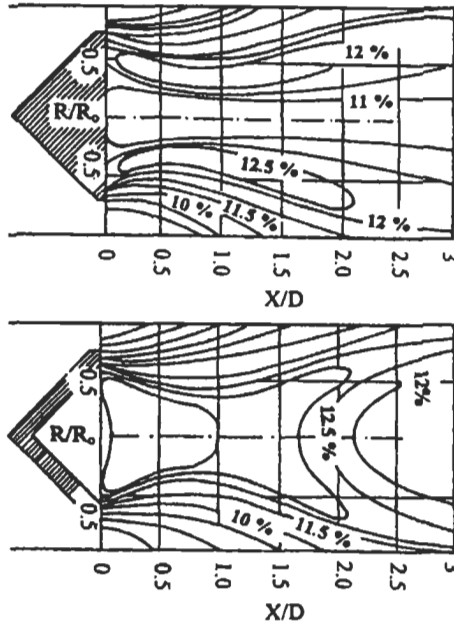


Fig. 4.110: Effect of stabilizer geometry on carbon dioxide contours for premixed flames (fuel flow rate of 2.75 kg h^{-1} , and air fuel ratio is 19.5) [661]. Reproduced by permission of ASME.

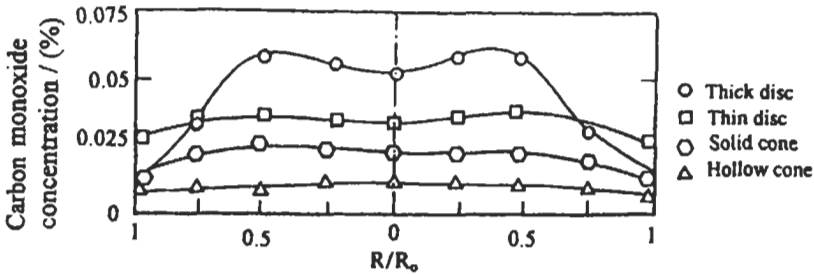


Fig. 4.111: Effect of stabilizer geometry on the emission of carbon monoxide in exhaust [661]. Reproduced by permission of ASME.

A thick disc with central fuel injection was used to form the diffusion flame and the stabilizer was located at the same distance as in the case of premixed tests. Two experimental runs were carried out for the structure of diffusion and premixed flames and the results are shown in Fig. 4.112. The diffusion flame is compared with the premixed flame created downstream of the same disc under air-fuel ratio of 19.5 and fuel flow rate of 2.75 kg h^{-1} .

It is clear that the diffusion flame is stabilized at a far distance from the disc compared with the premixed flame, which is attached to the stabilizer. It was found that, the noise level is slightly affected by the air-fuel ratio and significantly affected by both the mass flow rate and the distance between the fuel nozzle and the stabilizer.

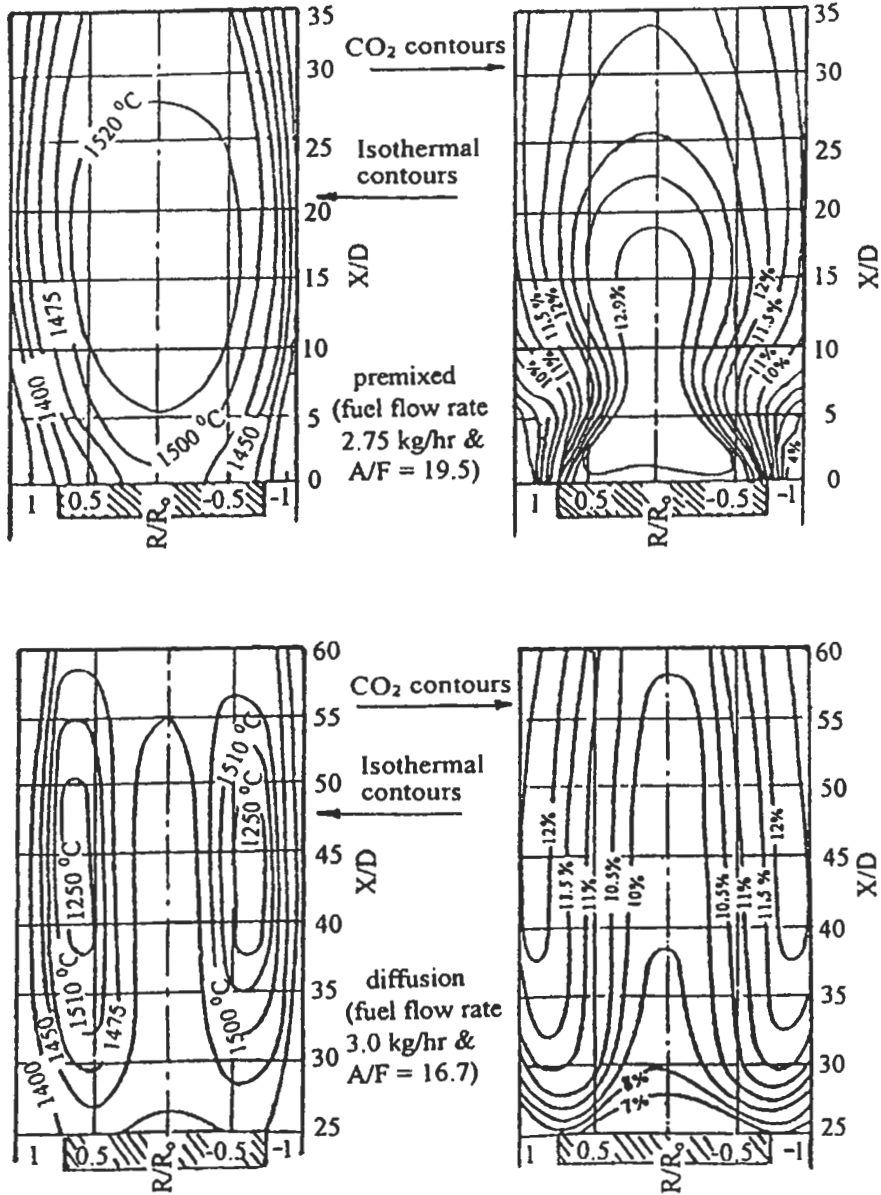


Fig. 4.112: Structure of premixed and diffusion flames (thick disc) [661]. Reproduced by permission of ASME.

Finally, the diffusion flame has a tube shape and its length is extended beyond the exit section of the combustion chamber. The main conclusion is that the flame shape and dimensions are greatly affected by the stabilizer geometry, and that the shortest and the smallest size flame correspond to the hollow cone stabilizer.

4.6 Emission and Combustion Modeling in Flames

The turbulent flame study with the prediction of pollutant species formed mainly in the near flame zones necessitates a best comprehension of the nature of all physical and chemical phenomena that appear during the combustion process. That constitutes a big interest to improve combustion performance and more to decrease the impact of hydrocarbon combustion on environment. On the other hand, the costs and delay improvement to develop domestic and industrial burners require some physical models describing perfectly the complex combustion mechanism [662]. In real combustion systems these mechanisms occur in a turbulent flow, three dimensional, often multiphase flow and are closely coupled. Implementation of these physical models in numerical simulation codes is one of most important parts to determine and predict the flame structure, the efficiency of burning, heat transfer and also pollutants formation like CO and NO. This problem poses a scientific challenge because the standard fast reaction assumption generally made in turbulent combustion modelling is no longer valid for pollutant prediction (see chapter 2). Therefore, a new formulation is necessary to take into account chemical species such as CO and NO because the characteristic chemical time of oxidation of these species is longer than the one of hydrocarbon oxidation [663].

Several investigators [664-667] have recently concentrated their work on the study of pollutant emissions in the flames, and the followings present some of their computational methods for predicting emissions.

4.6.1 PDF Model Using In-Situ Tabulation Chemistry Method

Lean premixed combustion offers a practical way of restricting NO_x emissions to less than 10 ppm. In order to efficiently design and optimize such combustors, a reliable comprehensive model that can treat the turbulent fluid flow, heat transfer, chemistry and their interactions is needed. Therefore, Cannon et al [664] have developed a comprehensive model for describing the turbulent fluid flow, heat transfer, chemistry, and their interactions in a bluff-body, lean, premixed, methane-air combustor. The model consists of the velocity-composition probability density function (PDF) model coupled with a k - ϵ -based mean flow computational fluid dynamics (CFD) model using in-situ tabulation method for describing 5 step reduced chemistry. Measured data [668] including velocity, temperature, and chemical species concentrations were used to evaluate the model. The chemistry calculations were performed with an in-situ look-up tabulation method [669]. A reduced, 5-step chemical mechanism [670] for describing fuel oxidation, CO, and NO chemistry was used in the model. NO formation from thermal, N_2O -intermediate, and prompt pathways was included in the 5-step mechanism (see chapters 1 and 2). An axisymmetric, unstructured grid was used for solving the Eulerian, mean flow equations (see chapter 3) and the vertices were used to store mean statistics for solving the Lagrangian, fluid particle equations. Predicted velocity and composition mean statistics were compared to measurements in the bluff-body combustor for a lean equivalence ratio of 0.59. The predictions of the major species are matched with measured and calculated equilibrium values in the recirculation zone. Comparisons of mean CO throughout the combustor were always within an order of magnitude and showed marked improvements

over past predictions. Maximum discrepancies between measured and predicted NO concentrations were between 5 and 7 ppm (~ 50 %).

The experimental data in a bluff-body-stabilized combustor at lean premixed conditions were obtained by Nandula et al [668]. The Laser-Doppler Anemometry (LDA) measurements of velocity and a combination of Rayleigh scattering, spontaneous Raman scattering, and Laser-induced fluorescence (LIF) measurements of chemical species and temperature were obtained to provide a source of information with which to evaluate models. The combustor chamber, shown in Fig. 4.113, was configured such that a stainless steel conical bluff-body of base diameter 0.04455 m and apex angle 45° was mounted coaxially at the center of the combustor and served as a flame holder. The burner enclosure is consisted of a square cross-section with filled round corners. The model assumed an axisymmetric geometry. The mass flow rate for the bluff-body combustor model was specified by using the measured values reported for the air (3960 standard liters per minute [slpm]) and the CH_4 fuel (244 slpm). This corresponded to a CH_4 -air equivalence ratio of 0.59. A turbulence grid was placed at the entrance of the combustor section, up-stream of the bluff body. The corresponding uniform velocity and free stream turbulence at the inlet to the combustor, just downstream of the turbulence grid, were 15 m s^{-1} and 24 %, respectively. An inlet temperature of 300 K and a combustor pressure of 1 atm were also specified in the model. A combustor wall temperature of 500 K was used in the simulations.

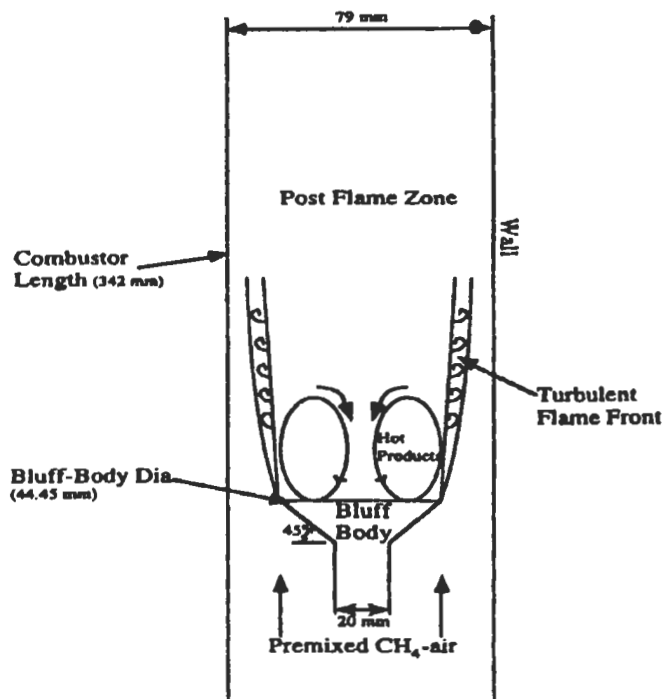


Fig. 4.113: Schematic and turbulent flame structure of bluff-body-stabilized lean premixed combustor [668].

Figure 4.114 (a) shows the predicted radial profiles of mean axial velocities compared with experimental data at x/d locations of 0.1 and 1.0. The recirculation zone behind the bluff-body allowed hot combustion products with radicals to mix and subsequently react with the incoming, cold CH_4 -air mixture and stable combustion was obtained without the use of a pilot flame. The location of the shear layer, indicated by the steep gradient in axial velocity was well described by the model. Despite the correct prediction of centerline velocity trends, the magnitude of the negative centerline velocities was overpredicted (by $5\text{--}14\text{ m s}^{-1}$). This overprediction of negative centerline velocities has been observed previously for confined, swirling flows [671].

Figure 4.114 (b) shows comparisons between the measurements and predictions for the mean temperature at x/d axial location 0.1 and 1.0. The mean temperatures in the recirculation zone region ($r/d < 0.4$) were, at most, only 6.7 % (100 K) higher than the measurements. The adiabatic equilibrium temperature for these conditions is 1640 K, only 40 K higher than the predicted recirculation zone temperature. The locations of temperature gradients, where cold and hot gases mixed, were predicted accurately, especially at x/d locations of 0.1, 0.3, and 0.6. Only the mean temperature gradient in the shear layer region at $x/d = 1.0$ was underpredicted, and thus mean temperatures at the edge of the recirculation zone and in the shear layer ($0.3 < r/d < 0.5$) were underpredicted by about 40 %. This underprediction of mean temperature at the shear layer indicates either an underprediction of heat release due to the chemical model, an overprediction of fluid mixing between the reactant and product streams due to the $k\text{-}\epsilon$ model, or some coupling between these processes.

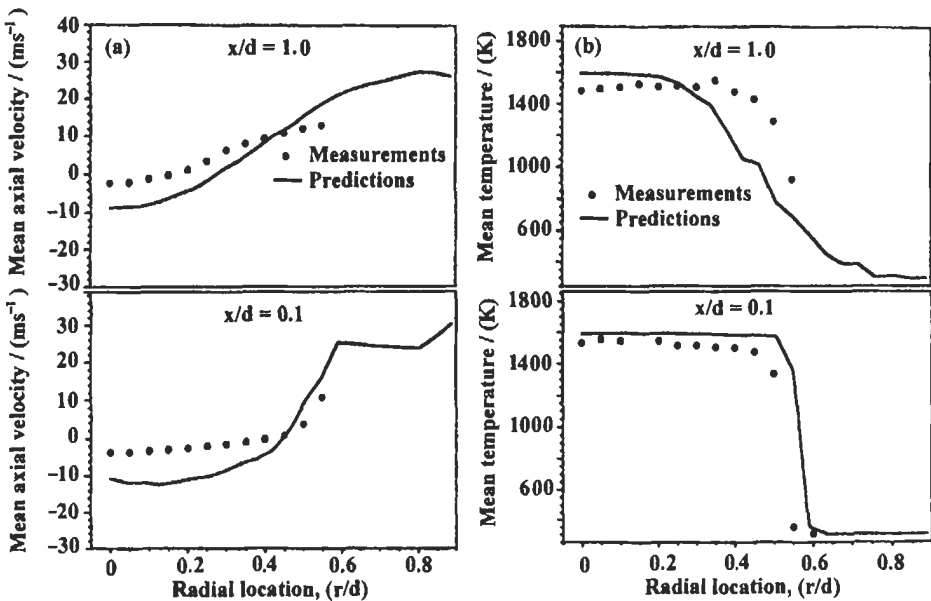


Fig. 4.114: Measured and predicted radial profiles of (a) mean axial velocity and (b) mean temperature profiles in bluff-body-stabilized combustor. $\phi = 0.586$, $T_{in} = 300\text{ K}$, $P = 1\text{ atm}$, 5-step mechanism. [664]. Reproduced by permission of Elsevier Science.

Figure 4.115 (a) shows comparisons between the measured and predicted radial profiles of mean CO mole fractions at two axial locations in the bluff-body combustor. When fluid reaches the centerline and base of the bluff-body, the CO has oxidized to CO_2 before mixing again with incoming reactants. The equilibrium value of CO is 7 ppm, much lower than the concentrations that were predicted and measured in the recirculation zone and shear layer region. At the lower axial location of $x/d = 0.1$, the model showed underpredicted level of CO in the recirculation zone and shear layer region. These results indicate that the model underpredicts the initial CO formation in the shear layer and then overpredicts the CO oxidation in the recirculation zone. Also, at $x/d = 1.0$, the CO was overpredicted in the shear layer region and compared well at the centerline along the recirculation zone.

Despite the noticeable discrepancies between the measurements and predictions, the comparisons were reasonably good. A previous modeling study [672], using an assumed shape PDF model and detailed PSR chemistry, obtained reasonable agreement for CO in the shear layer and overpredictions by a factor of 4 along the centerline. Figure 4.115 (b) shows comparisons between the measured and predicted radial profiles of mean NO mole fractions at two axial locations in the bluff-body combustor. At the lowest axial location of $x/d = 0.1$, the model showed underpredicted levels of NO in the recirculation zone. The measurements were as high as 11 ppm, while the predictions reached maximum level of 5 ppm. The model underpredicted the overall formation of NO in this lean premixed system. At $x/d = 1.0$, the measurements and predictions compared well at the centerline, where both showed values near 5 ppm.

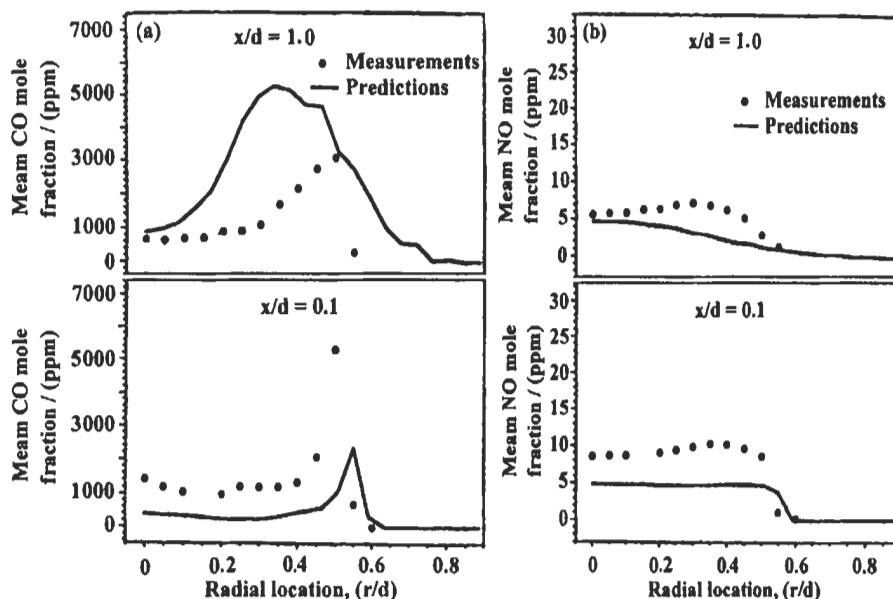


Fig. 4.115: Measured and predicted radial profiles of mean (a) CO mole fraction (ppm) and (b) NO mole fraction (ppm) in the bluff-body-stabilized combustor. $\phi = 0.586$, $T_{in} = 300$ K, $P = 1$ atm, 5-step mechanism. [664]. Reproduced by permission of Elsevier Science.

4.6.2 Coherent Flame Model

Coherent flame model is used by Bentebbiche et al [665] for modeling of methane combustion in premixed turbulent flame [673, 674]. This model allows to analyze the flame front and provides a mathematical formulation for coupling the chemical kinetics of combustion reactions and the turbulent flow description [675]. Also, an extended model of the flame surface density designated as CFM has been used to analyze the pollutant formation. They [665] have used kinetic mechanism of methane-air taking into account combined two-step reaction mechanism for methane-air combustion [676], and a one step thermal-NO reaction to predict the formation of NO. Interaction of turbulence with chemical reactions is one of the most interesting factors, which has to be taken into account. They have used k- ϵ turbulence model in their work to predict flow field, temperature and different species concentrations.

The coherent flame model is put for the eddy interaction presented in the mixing layer zone where the flame is produced [674, 677], Fig. 4.116. In this model the flame is described as a collection of laminar flames convected and stretched by the turbulent flow keeping coherent structure in the zone of reaction [673]. This consideration allows closing the production rates, namely:

$$W_k = -V_{Dj} \sum \quad (4.92)$$

with $V_{Dj} = \rho S_l Y_{fo}$ as the local reaction rate, \sum the flame surface density, ρ is the density of the gas mixture and Y is the mass fraction of species concentrations.

The balance equation for flame surface density was described like;

$$\frac{\partial \bar{\sum}}{\partial t} + \text{Convection} = \text{Diffusion} + E_S \bar{\sum} - \text{Annihilation} \quad (4.93)$$

and, $E_S = \alpha \epsilon/k$, where ϵ is the dissipation rate of turbulent kinetic energy, k .

Using the strain rate E_S and the laminar propagation flame speed S_l permits to consider as analytical formulation for the local reaction rates calculation, where $S_l = f(\phi)$ and $\phi = s \frac{Y_F(\infty)}{Y_O(\infty)}$ is the global equivalence ratio, and s is mass stoichiometric coefficient.

With regard to the reaction mechanism used in the model, a two-step mechanism for methane combustion was used based on the following two equations:



The following reaction rates for methane CH_4 and CO are used,

$$\dot{\omega}_{\text{CH}_4} = \rho S_l Y_{fo} \sum \quad (4.96)$$

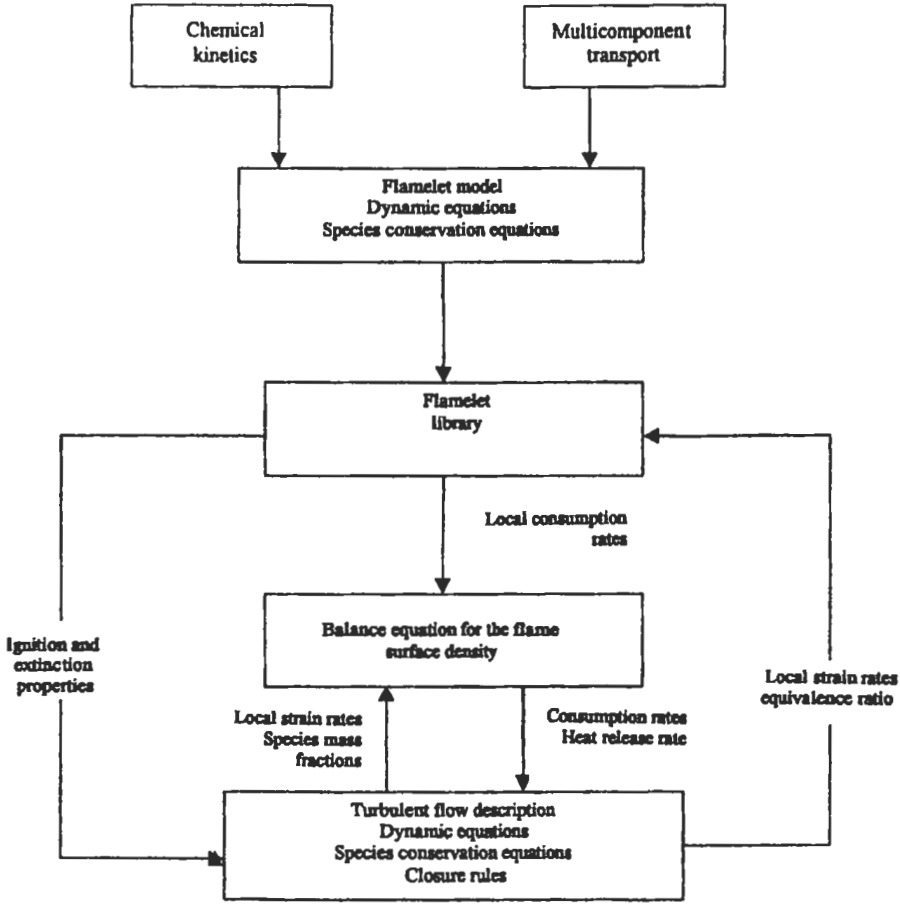


Fig. 4.116: Coherent flame concept. Bentebbiche et al [665], reproduced by permission.

$$\dot{\omega}_{CO} = 5.4 \times 10^9 e^{-15125K/T} \rho^2 Y_{CO} Y_{O_2}^{0.5} Y_{H_2O}^{0.5} \tag{4.97}$$

An extended Zeldovich mechanism based on the chemical kinetics was applied in order to model the formation of nitric oxide NO from molecular nitrogen N₂ in combustion air.

The reaction equations are;



where, the reaction rate of formation is:

$$\dot{\omega}_{NO} = 1.35 \times 10^{16} T^{-1} e^{-69160K/T} \rho Y_{N_2} Y_{O_2}^{0.5} \tag{4.99}$$

The numerical method used for solving the Navier Stokes equations is the finites volumes difference. The phenomena that can be modeled include effect of turbulence, heat transfer, and combustion process for compressible subsonic flows. They [665] have adopted SIMPLE method (Semi implicit Method for Pressure Linked Equation) procedure of Patankar [678]. The proposed model is tested by numerical simulation for ducted turbulent methane-air flame stabilized behind a rod flame holder. The combustor is 0.3 m long and 0.05 high. The blockage ratio and equivalence ratio are 6 % (see Fig. 4.117) and 0.75, respectively.

The predicted results from the above model show that the CO mass fraction qualitatively and quantitatively is well reproduced and it formed near the flame front. The maximum value of CO is in order of 3 % in the reaction zone and 0.3 % at the chamber exit. The NO emission is observed with maximum value in the burned gas zone and it increases with temperature. Dynamic parameters are also investigated and the results provide a good approach for numerical simulation for turbulent combustion process comparing with experimental results [665].

4.6.3 Stochastic Model

A stochastic model of combustion and NO_x formation in premixed turbulent methane flames is developed by Vicente et al [668]. The model is based on the combination of Computational Fluid Dynamics and Monte Carlo methods for the solution of the joint scalar Probability Density Function. A GRI-derived reduced-chemistry model is used and it allows for the consideration of finite chemical rates. This model is that reported by Mallampalli et al [679], which was derived from the full GRI mechanism 2.11 [680] using the automated reduction software of Chen [681]. The reduced mechanism is an update to an earlier version of the same mechanism [682] (see chapter 2), and it consists of a 5-step, 9-species, given by the following reactions:

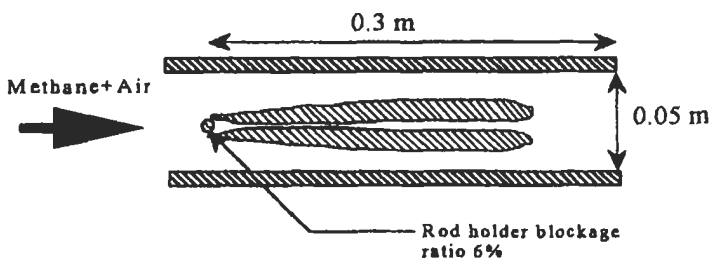
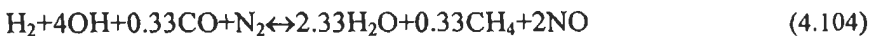


Fig. 4.117: Combustor geometry and calculation domain [665]. Bentebbiche et al [665], reproduced by permission.

The flame aerodynamics is modeled via Favre-averaged continuity and momentum equations. Thus, a closure is needed for the turbulent-convection term arising out of the averaging of the convection term in the conservation equations. Two different closure approaches have been used: one is based on the widely-used $k-\epsilon$ turbulent model (described in chapter 3), of which several variants are tested in their model [666]; and the other is a Reynolds-Stress-Transport closure, with the Isotropisation-of-Production pressure-strain model [683-684], and with the coefficients proposed by Younis [685].

The case simulated by Vicente et al [666] is the methane-air, turbulent flame of Nandula et al [668]. The test rig is shown in Fig. 4.113. The simulation domain states at the bluff body, and extends for 4.6 diameters in the axial direction. The aerodynamic equations are solved using a finite-volume method, with a SIMPLE-type algorithm for solving the pressure-velocity coupling. A 40×45 (radial-times-axial) mesh is used. In grid-refinement tests carried out using Eddy-Break-UP model [547], the results proved to be grid-independent on this mesh. The joint multi-scalar PDF equation is solved using a cell-based, Monte Carlo particle method [686], in which the PDF is represented locally (i.e. at each computational cell) by an ensemble of stochastic particles. Typically, 100 stochastic particles are used per cell. Steady-state accumulation of particles was implemented to avoid stochastic fluctuations when computing mean values. The number of particles was doubled to 200 (per cell) in the course of test runs, with no noticeable change in the average values, while the CPU times are around 28 hours on a Pentium II PC at 300 MHz running Linux.

The predicted results from the above-described model are compared with experimental data reported by Nandula et al [668]. The predicted results of NO formation is very challenging, both because of the very low values, and because all NO formation-routes are relevant. The results obtained show good accuracy for velocities, main species, and temperature, and are very encouraging in respect of minor species, including NO. The results for some key minor species are shown in Fig. 4.118. These are CO, OH, and NO. CO is predicted to be fully burned in the recirculation zone, which is not consistent with experimental data. However, the peak values of CO, OH and NO in the shear layer are rather well reproduced. The profiles of OH show considerable agreement on the centerline, where the OH concentration is close to its equilibrium value of 200 ppm, while the trend towards super-equilibrium values is correctly predicted in the shear layer, albeit the computed peak values are in excess of the measured ones. The overall shape of the NO profile is also well captured, although values in early part of the recirculation zone are under predicted by 5 ppm.

4.6.4 Three Dimensions CRFD Model

The need to better understanding the NO_x formation mechanism inside industrial furnaces and to evaluate the NO_x emission with different combustion systems, leads to carry out a new design approach "hybrid model" [687-689] which couples the use of 3D CRFD codes with a detailed kinetic scheme for simulating hydrocarbon combustion and NO_x formation. Regarding this approach, a preliminary study has been carried out to identify the parameters which mainly influence the NO_x formation in the different combustion zones (main, reburning and post-combustion zones in boilers). The effects of temperature and residence time at different stoichiometrics of the main combustion and reburning zone have been investigated with a detailed kinetic model on a simplified three-reactor scheme of the boiler [690]. On the other hand, the reburning efficiency is affected

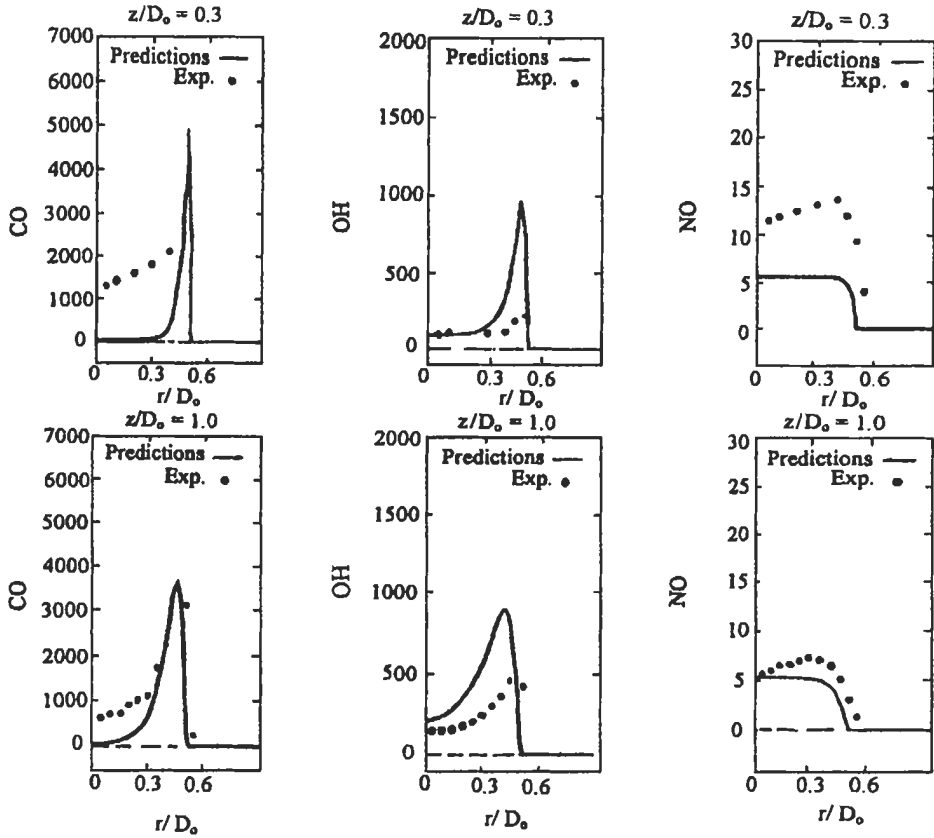


Fig. 4.118: Radial evolution of minor species in ppm at two axial locations (top: $z/D_o = 0.3$, bottom: $z/D_o = 1.0$). Comparison with experimental data [666]. Reproduced by permission of Combustion Science and Technology and Taylor & Francis.

both by temperature and by the degree of mixing between the reburning fuel and the main gas flow [691, 692].

The analysis of the flow field and the local temperature maps provided by the CRFD codes allow to identify uniform zones, in terms of temperature, stoichiometry and/or degree of mixing of different streams, which can be modeled as isothermal perfectly stirred reactors and/or plug flow reactors. Recently, Benedetto et al [667] have developed 3D CRFD model and applied it to the design of industrial furnaces. The objective is to predict the emission of pollutants, such as nitrogen oxides, in combustion flue gases. The following presents the procedure analysis and their applications on the Monfalcone # 3 steam generator [667]. The detailed steps of the procedure used to analyze and extract a reactor network from 3D data are the following (see Fig. 4.119).

1. CRFD 3D codes are used to evaluate the flow field, the temperature and residence time distributions in furnaces, together with the concentrations of the major species (O_2 , CO , CO_2 , H_2O etc.) and the local stoichiometry. The CRFD 3D codes calculate self-consistently the flow field, the heat release and the heat exchange, using iterative procedure [693].

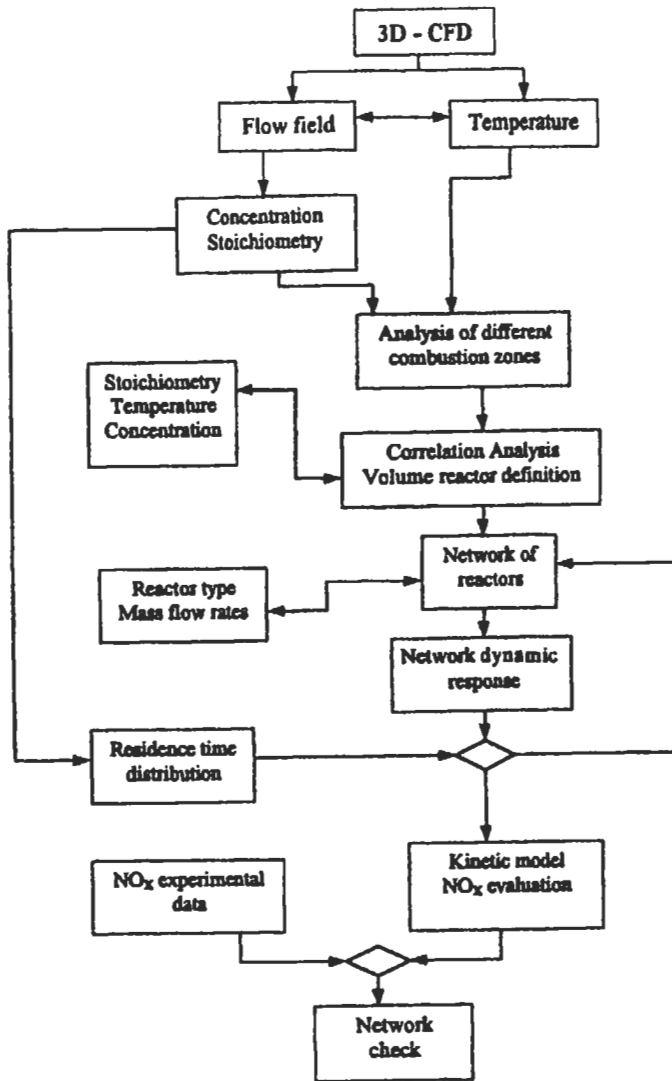


Fig. 4.119: Procedure of 3D CRFD model [667]. Reproduced by permission of Combustion Science and Technology and Taylor & Francis.

2. Temperature, and stoichiometry values are associated to each cell: cells are then grouped into homogenous zones according to the values of the above parameters using Temperature/Stoichiometry correlation. Each region is modeled as an ideal reactor.
3. The volume of each reactor is taken as the sum of the corresponding cell volumes and the effective stoichiometry and temperature are obtained as proper weight averages of the cell values.
4. The mass inlet and outlet of each reactor are computed as the sum of the mass flows between cells belonging to different homogeneous zones.

5. The homogeneous zones are modeled as perfectly stirred or plug flow reactors on the basis of the velocity vector distribution.
6. The correspondence of the reactor network with the real flow field is verified by comparing the residence time distributions of the different streams obtained from CRFD analysis with the dynamic response of the network of reactors to the introduction of a finite pulse of tracer (0.1 second) of amplitude proportional to the mass ratio between the injected gas and the total flow.
7. The detailed kinetic model is used for the reactor scheme. The NO_x emissions predicted by the model are compared with the values obtained in the combustion tests. The detailed kinetic model, used on the reactor scheme to predict NO_x emissions, counts about three thousands reactions involving about two hundreds species (molecules and radicals). The main oxidation mechanism, for the simulation of hydrocarbon mixtures containing up to eight carbon atoms, is the core of the overall kinetic scheme [694, 385]. The nitrogen sub-mechanism involves 203 reactions and 25 species.

The above described approach has been applied by Benedetto et al [667] to different furnaces geometries, as pilot-scale and full scale boilers, low- NO_x burner flames and glass furnaces. Combustion tests performed on the Monfalcone #3 boiler were used to test the procedure and to improve the analysis tools. The Monfalcone #3 boiler is a 320 MWe, oil and opposite wall fired steam generator, supercritical, once-through, with simple super-heating and single reheating; the furnace is $10 \times 10 \text{ m}^2$, measuring 30 m from the hopper bottom to the arch narrowest section. The boiler was modified in 1993, with the installation of new low- NO_x ENEL/ANSALDO burners, capable of reducing NO_x emissions down to 50 %; after, oil-reburning with OFA (see chapter 1) was set up in the furnace (see Fig. 4.120). The two cases described below are characterized by the same main combustion conditions and differ for the reburning configuration. A 5 % reburning fuel and 43 % over-firing air configuration is applied to both the cases, while the flue gas recycle (FGR) and the number of reburning injectors are different: case #1 is a 12 reburning injectors configuration and 16 % of FGR; case #2 is a 6 reburning injector configuration and 23 % of FGR. Although the main combustion conditions are identical and the difference in the reburning zone is very small, case #2 showed NO_x emission lower than the limit of the National law (200 mg m^{-3}).

In the following, the simplified flow field of each plant condition is defined and the results of the kinetic simulation are shown. The CRFD flow field of the main combustion zone shows large gradients (Fig. 4.121): flames generated by low NO_x burners are characterized by internal fuel and air staging as the correlation Temperature/Stoichiometry shows large variability of the value of the two parameters of each cell due to the volumetric section of the second burner level (Fig. 4.122). The homogeneous zones are defined by clustering the cell according to their stoichiometric and temperature values. The distribution shows cells characterized by a low temperature and a stoichiometric value approximately equal to the stoichiometric ratio of the fuel and combustion air entering the boiler ($\text{SR} \cong 0.75$). A similar analysis has been performed on the other volumetric section of the main combustion zone. The reactor scheme extracted from the temperature and flow field is that the flames of each burner level are described with a fuel-rich and a fuel-lean volume and a following mixing zone, while perfectly stirred reactors better describe the high turbulence and the large velocity gradients of the jet flows [667].

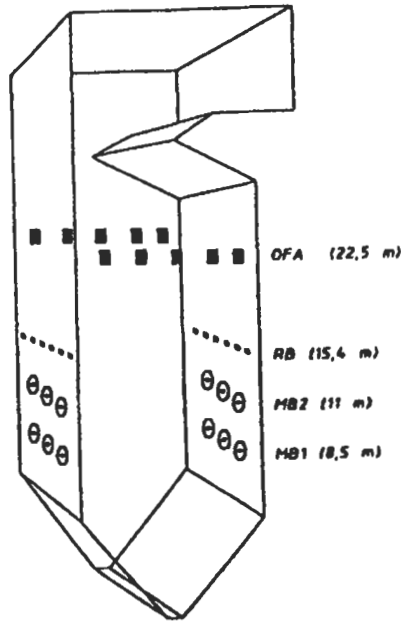


Fig. 4.120: The Monfalcone # 3 boiler [667]. Reproduced by permission of Combustion Science and Technology and Taylor & Francis.

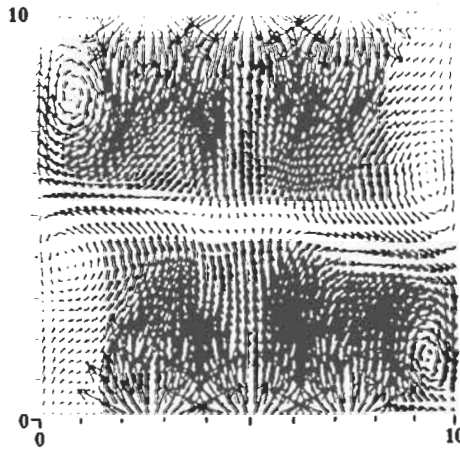


Fig. 4.121: 2⁰ level burner with flow field [667]. Reproduced by permission of Combustion Science and Technology and Taylor & Francis.

Also, the predicted results [667] show that the upper part of the main combustion zone is characterized by the mixing of the mass flows coming from the two burner levels, even if, at first look, a single plug flow reactor would seem sufficient: in this way a much better agreement with the complete CRFD analysis is reached in terms of the residence time distribution (see Fig. 4.123). As the main combustion zone does not differ in the

two cases, it is simulated with the same reactor network. As far as the reburning zone is concerned, the flow field and temperature distribution are strongly affected by the flue gas recirculated stream and, most of all, by the number of injectors used to introduce the reburning fuel (Fig. 4.124). In case #2, the higher mass flow and lower number of injectors (6 instead of 12) cause high stream velocity, while the injector configuration is responsible for the non-zero angular momentum of the mass flow. The difference between the flow fields affects both the mixing between the reburning and main combustion streams and the temperature distribution. The degree of mixing is evaluated by the concentration of the reburning fluid, introduced as an inert species in the 3D CRFD simulation.

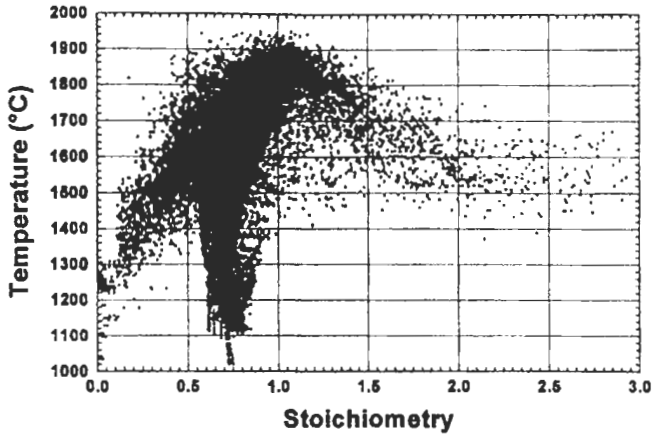


Fig. 4.122: Temperature/stoichiometry distribution 2⁰ level burner section (10.5-11.5 m elevation) [667]. Reproduced by permission of Combustion Science and Technology and Taylor & Francis.

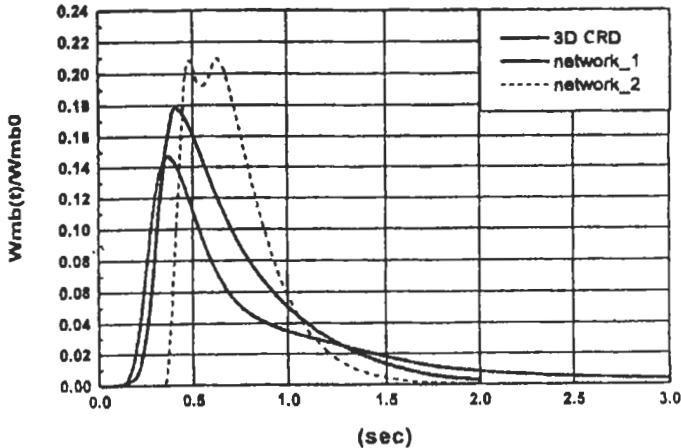


Fig. 4.123: Residence time distribution [667]. Reproduced by permission of Combustion Science and Technology and Taylor & Francis.

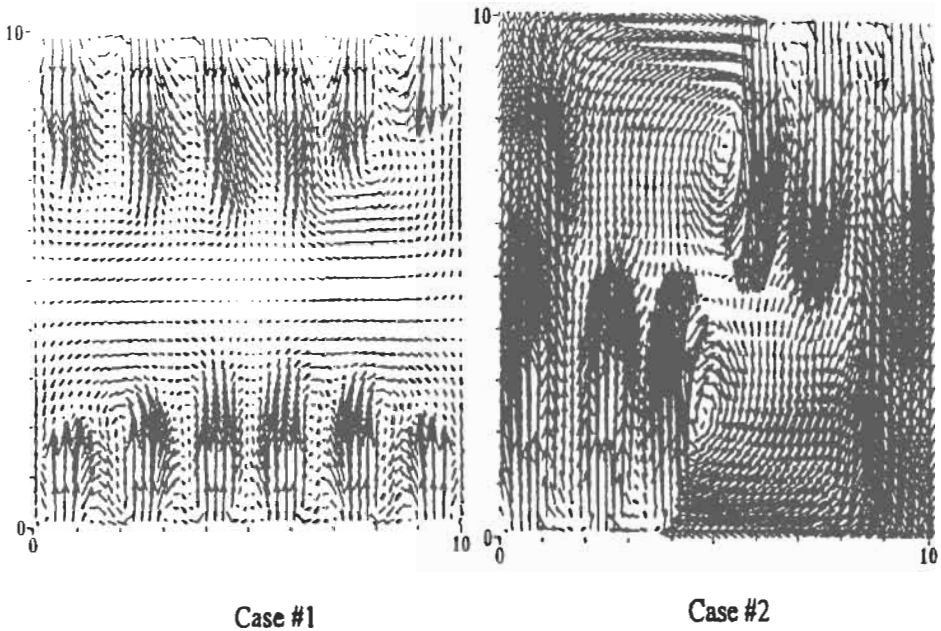


Fig. 4.124: Flow field in the re-burning section [667]. Reproduced by permission of Combustion Science and Technology and Taylor & Francis.

Case # 1) 12 injectors, FGR = 180 kg h⁻¹;

Case # 2) 6 injector, FGR = 260 kg h⁻¹.

Faster mixing and higher local temperature characterize the second plant condition: the correlation Temperature/Concentration-of-reburning-fluid showed that mass flow entering each cells of the upper volumetric section of the reburning zone has been partially mixed; in the other configuration (case # 1), the main gas flow localized in the middle part of the boiler does not mix with the reburning fluid at all [667].

In the post-combustion zone, the analysis shows that the calculated NO_x concentration, out of the post-combustion zone, agrees with the experimental data, confirming the correct characterization and simulation of the two reburning zones. In case #1 and 2 the calculated NO at post-combustion output are 204 and 180 mg Nm⁻³ (3 % O₂) compared to the experimental data of 200 and 175 mg Nm⁻³ (3 % O₂).

From the above analysis and discussion of the four approaches we can have the following comments:

- 1- The in-situ tabulation approach allows for practical kinetic calculations using more detailed chemical mechanisms in multidimensional, Monte Carlo PDF, combustor modeling than the standard prior tabulation approaches.
- 2- The coherent flame model allows surpassing difficulties of the turbulent reactive flow modeling. The model provides reasonably accurate values of CO and NO formation and can be used with very various and complex geometries using turbulent reactive flow modeling, like the direct numerical simulation and a large eddy simulation that provided good results.
- 3- A stochastic model of combustion and NO_x formation in premixed turbulent

methane flames is based on the combination of Computational Fluid Dynamics and Monte Carlo methods as well as a GRI-derived reduced chemistry. The results obtained from this model show good accuracy for velocities, main species and temperature and are very encouraging in respect of minor species including NO.

- 4- The CRFD-3D with a detailed kinetic scheme modelling represent promising tools for the design of low-NO_x installations. This approach has been successfully applied to different scales of furnaces such as pilot plants and industrial boilers, low-NO_x burners and glass furnaces.

Chapter

5

Combustion, Heat Transfer, and Emission in Boilers and Furnaces

The responsibility of the combustion engineers should mainly be devoted towards the utilization of the energy sources in more efficient and economical mode. The efficient combustion of fuel in combustion chambers and the efficient transfer of heat to water and steam in steam generators are essential for the economical operation of power plants. Tangentially-fired and fluidized-bed furnaces are considered as one of the modified modes of the conventional furnaces which are constructed to fulfill the requirements of recent years and become more attractive in the field of power stations firing systems.

Heat transfer problems pertaining to the combustion in industrial furnaces, gas turbine combustors, boilers, internal combustion engines, and open flames, burning gaseous, liquid and solid fuels are of great importance to the engineering designer of such devices. In most industrial flame applications, the achievement of high heat transfer rates is a target and is desirable.

In this chapter, combustion and heat transfer are considered in three main combustion equipment: Firstly, the conventional flame tube of the fire-tube boilers and the furnace of the water-tube boilers (sections 5.1) , secondly, the furnace of the tangentially-fired boilers (section 5.2), and thirdly, the combustor of fluidized-bed boilers and furnaces (section 5.3). The first section of this chapter begins with a general background and classification of the fire and water tube boilers (section 5.1.1), then followed by the radiative heat transfer (section 5.1.2) and convective heat transfer (section 5.1.3). Section 5.1.4 explains the experimental and computational results of combustion and heat transfer in horizontal and vertical flame tubes of circular cross section, as well as, horizontal flame tubes of square cross section and real boilers. Furthermore, the experimental and computational flame structure and heat transfer in water-tube boilers' furnaces, as well as from flame impingement are also considered in some details in section 5.1.5. This is followed by the emission and emission control in such equipment (section 5.1.6).

The next section of this chapter involves a background to the tangentially-fired furnaces (section 5.2), followed by the experimental study of flame stability in such furnaces. Moreover, the combustion characteristics as well as heat transfer in such furnaces are discussed experimentally and computationally.

The final section of this chapter describes the fluidized-bed furnaces and boilers

(section 5.3), which starts with the background to their applications, followed by the phenomenon of fluidization, and solid fuel combustion and heat transfer in fluidized-bed. It also involves experimental and analytical studies of heat transfer to the distributor plate, the surrounding walls, and immersed bodies as well as to tube bundles in the free board.

The link between the fundamentals, given in chapters 1 to 4, and the applications discussed herein is presented for different combustion equipment. In response to the air pollutant emissions regulations, a variety of techniques for controlling pollution from combustion sources has been developed, as described in chapter 1. The applications of these techniques in flame tubes and water tube boilers, tangentially-fired and fluidized-bed furnaces are also described in some details in this chapter.

5.1 Steam Boilers

5.1.1 Fire and Water Tube Boilers

This section presents a background to the fire and water tube boilers (steam generators), as well as their classifications, and applications.

5.1.1.1 Background

A boiler is a closed pressure vessel in which a fluid is heated for use external to itself by the direct application of heat resulting from the combustion of fuel, or by the use of electricity or nuclear energy. Steam generators, or steam boilers, use heat to convert water into steam for a variety of applications. Primary among these are electric power generation and industrial process heating. Steam has become a key resource because of its wide availability, advantageous properties and nontoxic nature. The steam flow rates and operating conditions can vary dramatically. The flow rate can vary from 0.36 ton h^{-1} in one process to more than 4540 ton h^{-1} in large electric power plants, while the pressure and temperature may vary from about 1 bar and 100°C in some heating applications to more than 310 bar and 593°C in advanced cycle power plants.

Fuel use and handling add to the complexity and variety of steam generating systems. In addition to the use of coal, natural gas and oil fuel (see chapter 1) as well as nuclear energy in most of steam generators, the biomass materials and process by product have also become heat sources for steam generation. These include peat, wood and wood wastes, bagass, straw, coffee grounds, cornhusks, coal mine wastes, waste heat from steel-making furnaces and even solar energy.

The main job of the boiler designer in any application is to combine fundamental science, technology, empirical data, and practical experience to produce a steam generating system which meets the steam supply requirements in the most economical package. Other factors in the design process include fuel characteristics, environmental protection, thermal efficiency, operation, maintenance and operating costs. For example, the reduction of pollutants such as nitrogen oxides (NO_x) may require a large boiler volume, increasing capital cost and potentially increasing maintenance costs. Such a design activity is based upon the physical and thermal science such as solid mechanics, thermodynamics, heat transfer, fluid mechanics, and material science.

5.1.1.2 Boiler Types and Classifications

There are two general types of boilers: fire-tube and water-tube. In addition, boilers are classified as “high” or “low” pressure and as “steam” boilers or “hot water” boilers.

By definition, high-pressure boilers are steam boilers that operate at a pressure greater than 1 bar. An advantage of using higher pressure is a reduction in physical size of the boiler and steam piping for the same heat-carrying capacity. This is due to the increased density of the higher-pressure steam. The advantage is particularly important if the boiler is some distance away from the heat load. A low-pressure boiler is one that is operated at a pressure lower than 1 bar. Almost all low-pressure boilers are used for space heating. Low-pressure boiler systems are simpler since pressure-reducing valves are seldom required and the water chemistry of the boiler is simpler to maintain. Another boiler classification is the hot water boiler. It is essentially a fuel-fired hot water heater in which sensible heat is added to increase the temperature to some level below the boiling point.

Fire-Tube Boilers

Fire-tube boilers constitute the largest share of small to medium sized industrial units. In fire-tube boilers the flue gas products of combustion flow through boiler tubes surrounded by water as shown in Fig. 5.1 (a). The flue gases are cooled as they flow through the tubes, transferring their heat to the water. Cooling of the flue gas is a function of, the heat conductivity of the tube and its surfaces, the temperature difference between the flue gases and the water in the boiler, the heat transfer area, the time of contact between the flue gases and the boiler tube surface, flame characteristics, and other factors [695].

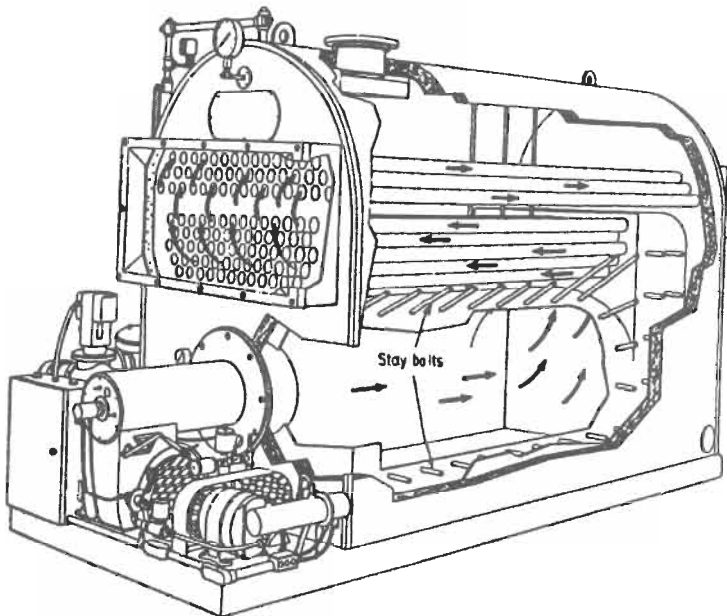


Fig. 5.1(a): Economic-type fire-tube boiler consists of three passes with arched crown sheet and stayed surfaces [696]. Reproduced by permission of McGraw Hill Inc.

The number of boiler passes for a fire-tube boiler refers to the number of horizontal runs the flue gases take between the furnace and the flue gas outlet. The combustion chamber or furnace is considered as the first pass and each separate set of fire tube provides additional pass. The increase in gas velocity in some cases will lead to the improvement of heat transfer by increasing the turbulence of the gases as they travel through the tubes. The maximum pressure of fire-tube boilers ranges between 10 bar to 15 bar with steam flow rate of 0.03 ton h^{-1} to 20 ton h^{-1} . These types of boilers are the most prevalent boilers used for heating, commercial and industrial process applications.

Water-Tube Boilers

The main difference between the water-tube boiler and the fire-tube boiler is that in the former the water circulates through the tubes instead of around them as shown in Fig. 5.1 (b). The hot gases pass around the tubes. There are two advantages for the

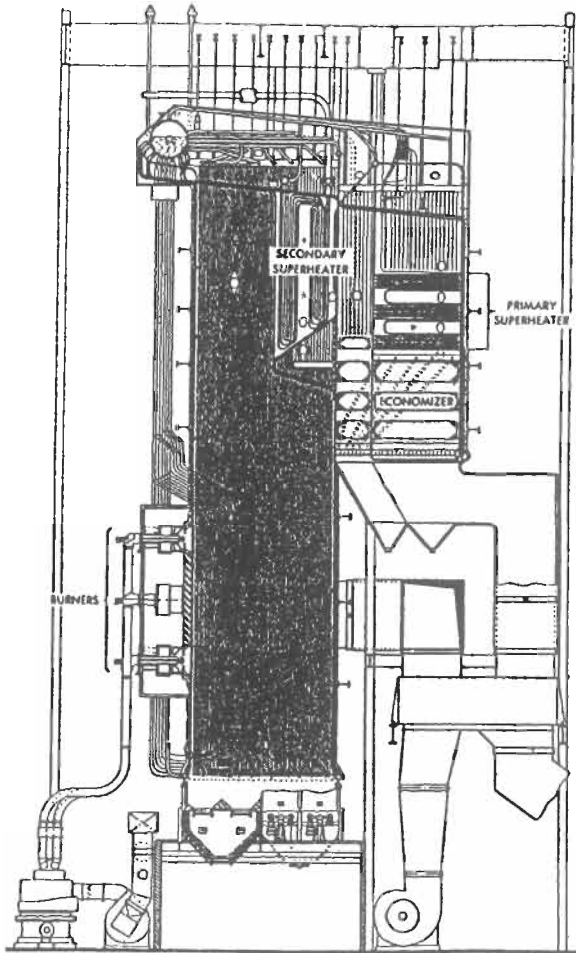


Fig. 5.1 (b): Pulverized coal-fired utility boiler [126]. Reproduced by permission of Babcock and Wilcox Company.

water-tube boiler: (1) higher capacity may be obtained by increasing the number of tubes independent of shell or drum diameter, and (2) the shell or drum is not exposed to the radiant heat of the fire. In fire-tube boilers, the thick shells and other structural requirements become prohibitive over 22 ton/h of steam and over 20 bar. The large capacities and pressures of the water-tube boiler have made possible the modern, large utility-type steam generators.

Because water-tube boilers can be easily designed for greater or lesser furnace volume using the same boiler convection heating surface, water-tube boilers are particularly applicable to solid fuel firing. They are also applicable for a full range of sizes and for pressures from about 3.5 bar to 350 bar. The present readily available minimum size of industrial water-tube boilers is approximately 9 ton h⁻¹ to 12 ton h⁻¹ of steam. A typical industrial water-tube boiler for gas and oil firing is the packaged boilers which generally have a single burner with up to approximately 55 ton h⁻¹ steam flow but are available in size up to approximately 110 ton h⁻¹ with more than one burner.

Water-tube boilers generally have gas baffles for directing flue gases and to assure contact between the hot gases and the maximum amount of the tube-heating surface. The baffle design determines the number of gas passes and which tubes act as “risers” and “downcomers”. This evolution in the design of boilers came about because of the economical benefits resulting from the lower cost of the required radiant heat transfer surface as compared with convection heating surface. The net result was a reduction in the physical size and cost of the boilers and changes in water volume, heat storage, and an improvement in response characteristics. Other effects of the water-cooled furnaces were reduced furnace temperatures and the resulting reduction in nitrous oxides (NO_x) production as will be discussed in section 5.7.

As industrial boilers increase in size for liquid and gaseous fuel, the balance between radiant and convection heat transfer surface remains approximately the same as for the package boiler for oil and gas firing. For solid fuel, however, coal, wood, or waste material-fired boilers usually require greater spacing between the boiler tubes. In addition, the furnace volume must be increased. A large industrial boiler for solid fuel is shown in Fig. 5.1 (b). These differences make it difficult to convert a gas or oil fired boiler to coal and obtain full steam capacity, while a conversion from coal to gas or oil firing can be much more easily accomplished.

As stated earlier, boilers used in electric utility generating plants are generally considerably larger than their industrial counterparts. The steam generating capacity of the largest electric utility boiler is approximately 10 times the capacity of the largest industrial steam boiler. The maximum size of electric utility water-tube boilers is approximately 5000 ton h⁻¹ of steam. In industrial use the largest are in the approximate range of 500 to 800 ton h⁻¹. More details about boilers and new developments in boiler energy systems are given elsewhere [126, 696].

5.1.1.3 Applications of Steam Generators

Most applications of steam generators involve the production of electricity or the supply of process steam. In some cases, a combination of the two applications, called co-generation, is used. In each application, the steam generator is a major part of a larger system that has many subsystems and components. Figure 5.2 identifies the major subsystems. Key subsystems include fuel receiving and preparation, steam generator and combustion, environmental protection, turbine-generator, and heat rejection

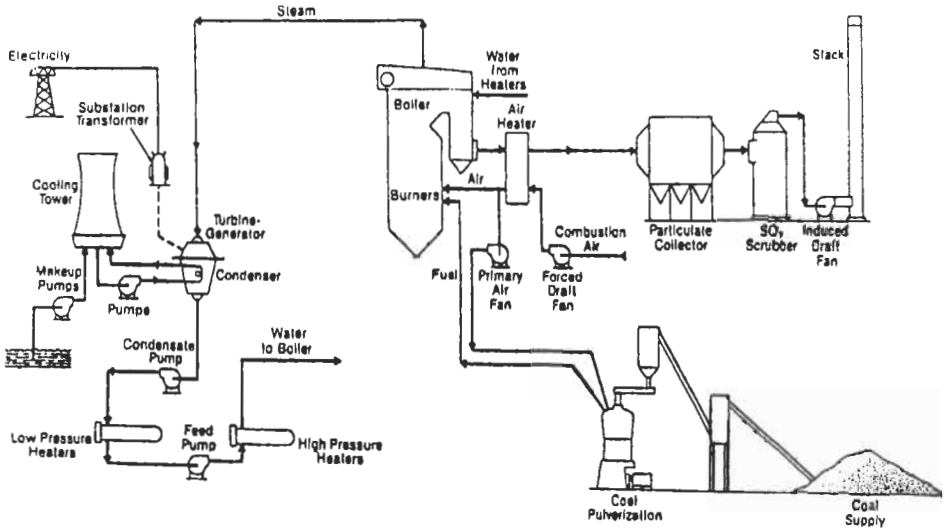


Fig. 5.2: Coal-fired utility power plant schematic [126]. Reproduced by permission of Babcock and Wilcox Company.

including cooling tower. The fuel handling system stores the fuel supply, prepares the fuel for combustion and transports it to the steam generator. The associated air system supplies air to the burners through a forced draft fan. The flue gases leave the air heater and pass through particulate collection and sulfur dioxide (SO₂) scrubbing systems, where pollutants are collected and the ash and solid scrubber residue are removed. Ultimately, the steam is passed from the turbine to the condenser where the remaining waste heat is rejected. The heat absorbed by the condenser is eventually rejected to the atmosphere by one or more cooling towers. For the industrial power system, many of the same features are needed, but the turbine-generator and heat rejected portions are replaced by the process applications.

The steam-water components are arranged for the most economical system to provide a continuous supply of steam. The circulation system (excluding re-heater) for a natural circulation, sub-critical pressure, drum-type steam generator is shown in Fig. 5.3. Feed water enters the bottom header (A) of the economizer and passes upward in the opposite direction to the flue gases. It is collected in the outlet header (B). The water then flows through a number of pipes, which connect the economizer outlet header to the steam drum. It is sometimes appropriate to run these tubes vertically (B-C) through the convection pass to economizer outlet headers located at the top of the boiler [126]. The feed water is injected into the steam drum (D). The water flows through the down comer pipes (D-E) to the bottom of the furnace where supply tube (E-F) route the circulating water to the individual lower furnace panel wall headers (F). The water arises through the furnace wall to an outlet header (G), absorbing energy to become a steam-water mixture that leaves the furnace wall outlet headers by means of riser tubes (G-D) to be discharged into the drum and steam-water separators. The residual moisture in the steam that leaves the primary steam separation devices is removed in secondary steam separators and dry steam is discharged to the superheater through a number of drum outlet connections (H-I and H-J). Steam flow then rises through the primary superheater and discharges through the outlet header (N) and spray attemperator (O).

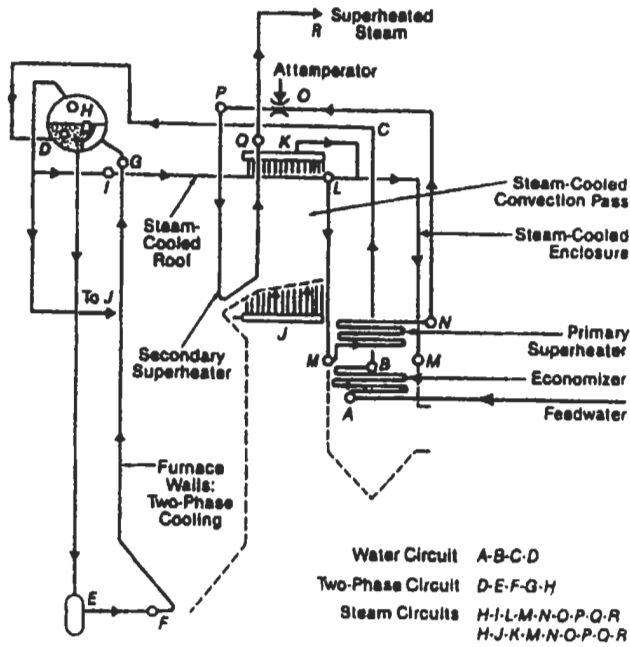


Fig. 5.3: Coal-fired boiler steam-water circulation system [126]. Reproduced by permission of Babcock and Wilcox Company.

It then enters the secondary superheater inlet header (P), flowing through the superheater section to an outlet header (Q), and then to the main steam line (R).

The following sections, give some general details for the calculation of the radiative and convective heat transfer, the combustion and heat transfer in fire and water tube boilers as well as the emission from these boilers.

5.1.2 Radiative Heat Transfer

This section presents a historical citation of radiative heat transfer, its methodology, as well as computational bases for zonal, flux and discrete ordinates methods for radiation exchange.

5.1.2.1 Historical Citation

The theory of radiant energy propagation can be considered from two points of view: classical electromagnetic wave theory and quantum mechanics. Thermal radiation may be viewed as a phenomenon based on the classical concept of the transport of energy by electromagnetic waves. The spectral distribution of emitted energy and the radiative properties of gases can only be explained and derived on the basis of quantum effects in which the energy is assumed to be carried by discrete particles (photons). However, the "true" nature of electromagnetic energy (that is waves or quanta) is not yet known.

The study of energy transfer through media that can absorb, emit, and scatter radiation has received more attention in the past three decades. This interest stems from the complicated and interesting phenomena associated with nuclear explosions, hypersonic shock layers, rocket propulsion, and combustion chambers at high pressure and temperature. Although some of these applications are fairly recent, the study of radiation in gases has been of continuing interest for over 100 years. One of the early considerations was the absorption and scattering of radiation in the earth's atmosphere. This has always plagued astronomers when observing on earth the light from the sun and more distant stars. The arriving form of the solar spectrum was recorded by Langley [697] over a period of years beginning in 1880. Extensive discussions of absorption in the atmosphere are given later by Goody [698].

In industry, the importance of gas radiation was recognized in the 1920s in connection with heat transfer inside furnaces. The carbon dioxide and water vapor formed as products of combustion were found to be significant emitters and absorbers of radiant energy, as well as the heated carbon (soot) particles formed within the flame being found to contribute with emitted energy.

Upon tackling the problem of radiative heat, the so-called configuration factors have to be evaluated in most applications. The first published statement that the geometrical factors in the radiant interchange equations could be separated from the energy factors has proven to be elusive. One of the first calculations of the radiant exchange between two surfaces was carried out by Christiansen [699]. He applied a ray-tracing technique, and found a relation for diffuse cylinders exchange. The concept of configuration factors, however, did not apply.

Sumpner [700] discussed the validity of Lambert's cosine law in relation to some experiments in photometry. He came near to defining a configuration factor, but didn't quite make the final step. As late as 1907, Hyde [701] discussed the geometrical theory of radiation. He didn't separate the geometry terms and explicitly define a configuration factor, even though he proceeded to evaluate the integrals appearing in the interchange equations.

Saunders [702] extended Christiansen's work, and defined a factor in the period of 1928-1929. This factor was considered as the fraction of energy leaving a surface that returns to it by reflections from all other surfaces and is then reabsorbed by the surface. This is equivalent to Gebhart's factor [703]. It is in the period of 1920 to 1930 that the concept of configuration factors appears in many references. Nusselt's paper [704] on his derivation of the unit-sphere technique, referred to the "angle-factor" had defined the factor as the fraction of radiant energy leaving one surface that is incident upon another. The several techniques developed for solving the radiant-interchange problem are surveyed below.

One of the methods which is based upon the experimental mathematics is the so-called Monte Carlo approach. Hammersley and Handscomb [705], gave reference to many works dealing with Monte Carlo and closely related material. However, the great bulk of the literature has appeared since 1950. Credit for development of Monte Carlo techniques as they are presently used in engineering and science goes to the competent group of physicists and mathematicians who gathered at Los Alamos during early work on nuclear weapons, including especially John von Neumann and Stanislaw Ulam. Available early outline was given by Metropolis and Ulam in 1949 [706], which was the first work to use the term Monte Carlo for such approach. One of the scientists who explicitly gave a definition to the Monte Carlo method was Khan [707]. Extension of

Monte Carlo methods to thermal analysis problems with radiation and conduction, including property uncertainties, was made later by Howell [708] and Zigrang [709]. Various mathematical manipulations of the general equation of radiative transfer have been carried out, which yielded different radiation models still being developed.

An integrated form for the first-order linear integro-differential equation of heat transfer, could be effected by the use of an integrating factor. The application of singular eigenvalue expansions (also called Case's method) and the related method of Ambarzumian in Ref. 710, to certain homogeneous medium plane-geometry problems with simple source configurations could provide exact solutions for a gray medium. Singular eigenvalue expansions were also used by Gritton and Leonard [711], for the gray case. Yener et al [712] have expanded further the method to a non-gray medium, including isotropic scattering and specularly reflecting boundaries; whereas mathematically exact solutions were presented. The Wiener-Hopf technique presented by Williams [713], could be applied to certain multi-dimensional problems.

The general radiation diffusion equation, following the outline given by Deissler [714], has been adopted by various researchers. Howell and Perlmutter [715] applied the diffusion solution to a real gas and compared results to those from exact formulation by the Monte Carlo method. The agreement was, however, rather unsatisfactory. Later in 1967, Bobco [716], had used a modified diffusion solution to find the directional emissivity for radiation from a semi-infinite slab of isothermal gray scattering-absorbing medium with isotropic scattering. In order to avoid having to carry detailed spectral calculations, certain approximations are often made. The most common is that the gray gas equations can be applied for a real gas by substituting an appropriate mean absorption coefficient in place of that of the gray gas. Amongst these is the Rosseland mean absorption coefficient, named after Rosseland, who first made use of diffusion theory in studying radiation effects in astrophysics [717]. Sampson [718], synthesized a coefficient that varies from the Planck mean to the Rosseland mean as the optical depth increases along a path. Abu-Romia and Tien [719], applied a weighted Rosseland mean over optically thick portions of the spectrum, and a Planck mean over optically thin regions, while Patch [720] defined an effective mean absorption coefficient.

The astrophysical approximations based on the mathematical properties of the equation of transfer and developed by astrophysicists for non-dimensional layers of an atmosphere, are still being adopted and extended to multi-dimensional thermal radiation problems. Chandrasekhar [721], has extended the two-flux method as originally developed by Schuster [722], and Carlson [723], by dividing the intensity of radiation into mean portions from discrete directions, terming this the discrete-ordinates method. A comparison of the discrete-ordinates method with the two-flux and six-flux methods has been given by Daniel et al [724]. With respect to the intensity of radiation, the approximation made independently by Eddington [725] and Milne [727], was the same as that of Schuster [722].

Another way of handling the equation of transfer in its integro-differential form, is the differential approximations. However, this is a generalization of the method of Milne and Eddington [725, 726] and termed as the moment method. An equivalent method called spherical-harmonics has been also developed [727]. Krook [728], has shown that the moment method, the spherical-harmonic method, and the discrete-ordinates method are all equivalent. Higher-order differential approximations had been derived by Bayazitoglu and Higenyi [729].

Building upon the extensive foundations established for the simple case of radiation

exchange between surfaces with no intervening absorbing-emitting and scattering medium, an engineering treatment of gas radiation in enclosures has been scientifically and physically evolved. The Curtis-Godson technique is the basis for one engineering treatment. This approximation has been discussed and applied for non-uniform gases by Karkow et al [730], and by Edwards and Weiner [731].

Another interesting engineering treatment, due chiefly to Hottel [732] is the zoning method of analysis. Multi-dimensional consideration had been presented by Hottel and Cohen [733], and by Einstein [734]. Extensions of the method to include other modes of heat transfer, had been adopted by El-Mahallawy [735], who incorporated this method for extensive study in combustion chambers. The method is practical, powerful, and exact; Hottel and Sarofim [736], discussed it at some length in 1967.

5.1.2.2 Equation of Radiant Energy Transfer

It has been tacitly assumed that opaque solids emit energy based solely on the temperature and physical properties of the body. The spectrum of the emitted energy is therefore assumed unaffected by the characteristics of an incident radiation. This is generally true because all the absorbed parts of the energy incident on an opaque body are quickly redistributed into internal energy states in an equilibrium distribution at the temperature of the body.

In gas, the redistribution of absorbed energy occurs by various types of collisions between the atoms, molecules, electrons, and ions that comprise the gas. Under most engineering conditions, this redistribution occurs quite rapidly, and the energy states of the gas will be populated in equilibrium distributions at any given locality. Accordingly, the Planck spectral distribution correctly describes the emission from a black body, and correctly describes the emission from a gas volume element. The assumption that a gas will emit according to Planck spectral distribution of intensity passing through and being absorbed by a gas volume element is a consequence of the prevailing condition of "local thermodynamic equilibrium". Radiative heat transfer problems would become much more complex, when this condition breaks down.

The equation of radiant energy transfer is based upon considering the radiation of directional intensity, i'_λ (s) within wave length, λ , along a certain path length, s , within a volume of absorbing, emitting, and scattering medium. Attention is directed to the change of intensity as the radiation passes through a distance ds . The change of radiation intensity along the path length, ds , would be due to the following:

- Decrease due to absorption.
- Emission contribution by the medium.
- Loss by scattering.
- Gain by incoming scattering into s-direction.

Summing up the above changes of radiation intensity, with certain deductions, the equation of transfer becomes, for an isotropic scattering:

$$di'_\lambda / dk_\lambda = -i'_\lambda (k_\lambda) + I'_\lambda (k_\lambda, \omega) \quad (5.1)$$

where, I'_λ is called the source function, which forms both local emission and scattering, k_λ is the optical differential thickness along path (s), and ω is the solid angle subtends path (s).

Equation 5.1 is an integro-differential equation, since i'_λ , is within the integral of the source function. Consequently, this integro-differential equation of transfer needs to be subjected to certain assumptions and simplifications in order to be solvable.

The intensity as given by the equation of transfer gives the radiation that is locally traveling in a single direction per unit solid angle and wavelength, and that is crossing a unit area normal to the direction of travel. To obtain the net energy crossing an area requires integrations that include the contribution of the intensities crossing in all directions and at all wavelengths. This results in an equation for local radiative flux that is used in forming energy balances within the medium. The energy balance is needed to obtain the temperature distribution within the medium.

When scattering is present, a source-function equation must be solved simultaneously with the energy equation to determine both the temperature distribution and the source-function distribution, which contains the distribution of scattered energy. For an emitting, absorbing, non-scattering medium, the equation of transfer reduces to:

$$\frac{di'_\lambda}{dk_\lambda} + i'_\lambda(k_\lambda) = i'_{\lambda b}(k_\lambda) \tag{5.2}$$

where subscript b refers to black body radiation, and the optical depth, k_λ , defined along the path, s, as $k_\lambda = \int_0^s \alpha_\lambda ds$.

The optical thickness could be defined along the x-coordinate as:

$$k_\lambda(x) = \int_0^x \alpha_\lambda dx \tag{5.3}$$

where α is the absorption coefficient and the relation between optical positions along the s and x directions, having an angle θ , is given by:

$$k_\lambda = \frac{k_\lambda(x)}{\cos \theta} \tag{5.4}$$

5.1.2.3 Methodology

In this section, several mathematical models and methods evolved for the prediction of radiative heat transfer are generally outlined. Analytical or numerical solutions to the equations of radiative transfer and energy conservation to yield temperature distributions and heat flows in an absorbing, emitting, and scattering medium require considerable effort in most cases in practice. Various approximate techniques can be usefully applied in some instances. One technique is to neglect one or more terms in the transfer equations, when only justified. Another technique is to examine limiting cases. For example, for an optically thick medium, a diffusion approximation could be effected.

Other types of approximations involve using the complete transfer equations and then using various devices to obtain approximate solutions. In one method, the exponential integral functions in the radiative equations are approximated by simple exponential functions. This enables the integral equations to be transformed into

differential equations that can be readily solved. In other methods such as the Schuster-Schwarzchild approximation, the radiation is assumed to be diffuse in each coordinate direction. This section consists of three parts, the first part represents a general background on these different methods, while the second and last parts discuss in some details the two-flux model and the last one is the zonal method.

The various techniques adopted for establishing models for predicting the radiant heat transfer, are basically discussed, hereafter:

Integrating by Use of an Integrating Factor

The equation of transfer is a first-order linear integro-differential equation, and an integrated form can be obtained by use of integrating factor. Multiplying through the equation of transfer by the factor, $\exp(k_\lambda)$, and integrating over an optical thickness from $k_\lambda = 0$ to $k_\lambda(s)$, would yield the integrated form of the equation of transfer. However, the integrated form cannot be used by itself to obtain the local intensity of radiation because it contains the unknown temperature and scattering distributions that are in the source function. In some cases, the energy equation could be solved in conjunction with a source function to yield compatible temperature and scattering distributions. In general, the yielded equations are sufficiently complex so that numerical solutions are essential, and closed-form solutions are very limited.

Diffusion Method

In this method, the medium is considered as being optically dense, whereas the radiation can travel only a short distance before being absorbed. The radiation penetration distance is small compared with the distance over which significant temperature changes occur. Then a local intensity will be the result of radiation coming from only nearby locations, where the temperature is close to that of the location under consideration.

Radiation emitted by locations where the temperature is appreciably different will be greatly attenuated before reaching the location being considered. For these conditions, it is possible to transform the integral type equations that result from the radiative energy balance into a diffusion equation like that of heat conduction. The energy transfer depends only on the conditions in the immediate vicinity of the position being considered and can be described in terms of the gradient of the conditions at that position. Thus, the local energy flux could be related to local conditions in the form of the following equation:

$$q(x) = -(4/(3K_\lambda(x)))(de_{\lambda b} / dx) \quad (5.5)$$

where, $K_\lambda =$ extinction coefficient $= \alpha_\lambda + \sigma_{s\lambda}$, and $e_{\lambda b}$ is the emissive power for blackbody radiation and $\sigma_{s\lambda}$ is the scattering coefficient.

This equation is known as the Rosseland diffusion equation. It does not involve integrals of contributions from other regions and thus provides a considerable simplification over the exact formulation of the equation of transfer. If the medium is moreover considered as a gray gas, the following simple equation could be found:

$$q(x) = -(4\sigma/(3(\alpha + \sigma_s)))(dT^4 / dx) \quad (5.6)$$

The diffusion method is a useful tool for the use of standard finite-differences schemes to solve the resulting diffusion differential equations. However, this method of analysis is limited to the cases where the assumptions used for its derivation are justified. Care must be taken when evaluating absorption coefficient. There are several applicable mean absorption coefficient models, such as Planck mean, incident mean, and Rosseland mean. To apply diffusion methods at certain interfaces where there is a pronounced temperature gradient, "radiation slip" or "jump" boundary conditions are to be employed.

Approximate Solutions

These methods analytically account for all terms in the equation of transfer. However, only approximate solutions will be sought, so that while some accuracy may be lost, the ability will be gained to obtain closed-form analytical solutions in some cases.

(i) **The astrophysical approximations.** It has been cited from literature that much work has been done in the study of stellar structure by analysis of the observed radiation. Quite early in the twentieth century, astrophysicists considered the mathematical properties of the equation of transfer and applied some approximations that remain useful today. Such approximations have been also extended to multidimensional problems. The most common two approximations are given here below:

The Schuster-Schwarzschild approximation. The simplest approximation is to assume that for one-dimensional energy transfer, the intensity in the positive direction is isotropic and that in the negative (opposite) direction has a different value but is also isotropic. This is known as a two-flux model (see Fig. 5.4). Without scattering, the equation of transfer for the intensity of radiation in each hemisphere is given as:

$$\begin{aligned}
 -\frac{\cos \theta}{\alpha_{\lambda}} \frac{di_{\lambda}^{+}(x)}{dx} &= i_{\lambda}^{+}(x) - i'_{\lambda,b}(x) & ; 0 \leq \theta \leq \pi/2 \\
 -\frac{\cos \theta}{\alpha_{\lambda}} \frac{di_{\lambda}^{-}(x)}{dx} &= i_{\lambda}^{-}(x) - i'_{\lambda,b}(x) & ; \pi/2 \leq \theta \leq \pi
 \end{aligned}
 \tag{5.7}$$

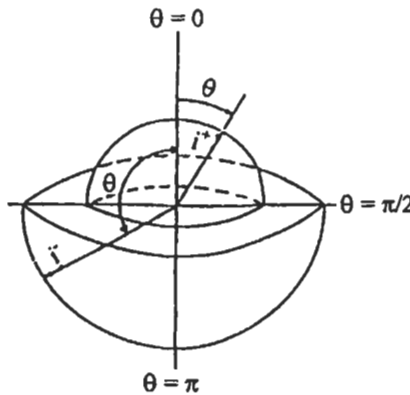


Fig. 5.4: Representation of the two-flux model.

These equations could be solved with certain mathematical manipulations and using integrating factors, and with appropriate boundary conditions. The following equation, known as the diffusion type relation for the Schuster-Schwarzschild approximation, is obtained:

$$q = -\frac{d(\sigma T)^4}{dk} \quad (5.8)$$

This method has been extended, by dividing the intensity into mean portions or directional streams from discrete directions, terming this the discrete-ordinates method. The *discrete-ordinates* method is equivalent to the differential-approximation or moment method.

In general, the flux methods are developed so as to divide the angle surrounding a point into a small number (2N) of equal solid angles, in each of which the intensity of radiant energy is assumed to be independent of direction (isotropic). Thus, the integro-differential equation of transfer can be then replaced by (2N) simultaneous differential equations in the (2N) unknown average intensities (or flux intensities) of radiant energy. This would be called a 2N-flux method of representation of the radiative transfer. These flux methods are favored, because the differential equations in the unknown flux densities are similar in form to those which describe mass, momentum and energy transfer at a point, and can therefore be conveniently linked with them and solved numerically by utilizing the techniques developed for solution of the flow field. Four, six, multi-flux methods were formed to provide a compromise between accuracy and convenience of use.

The Milne-Eddington approximation. With respect to the intensity, the approximation is the same as that of the Schuster and Schwarzschild. For radiation crossing a unit area oriented normal to the x-direction, all intensities with positive components in x-direction have a constant value independent of angle, and all intensities with a negative x-component can be considered isotropic. However, in comparison with the Schuster-Schwarzschild method, the approximation is made one step later, and with regard to computing heat fluxes rather than intensities. The equation of transfer, Eq. 5.2 rearranged in the x-directions without scattering, is multiplied by $d\omega$ and by $\cos\theta d\omega$. Then, the assumption of isotropic intensities is made to the two resulting equations which compute heat fluxes rather than intensities. Integrating over all solid angles, would yield:

$$\begin{aligned} -\frac{1}{\alpha_\lambda} \frac{d^2 q_\lambda}{d\lambda \cdot dx} &= 4\pi \left(\frac{i_\lambda^+ + i_\lambda^-}{2} - i'_{\lambda b} \right) \\ \frac{dq_\lambda}{d\lambda} &= -\frac{2\pi}{\alpha_\lambda} \frac{d}{dx} \left(\frac{i_\lambda^+ + i_\lambda^-}{3} \right) \end{aligned} \quad (5.9)$$

When gray medium is considered, the equations would yield a solution similar to the diffusion approximation, without scattering:

$$q(k) = \frac{-4}{3} \frac{de_b(k)}{dk} \quad (5.10)$$

(ii) **The differential approximation.** The differential approximation reduces the integral equations of radiative transfer in absorbing-emitting media to differential equations by approximating the equation of transfer with a finite set of moment equations. The moments are generated by multiplying the equation of transfer by powers of cosine between the coordinates direction and the direction of intensity. This is a generalization of the method of Milne and Eddington as their equations are the equation of transfer multiplied by $(\cos\theta)^0$ and $(\cos\theta)^1$. The moments of i' are generated by multiplying i' by powers of directional cosines and integrating over all solid angles. This method is favored for having some physical basis. The zero-order moment, $i'^{(0)}$, has the physical significance that dividing it by speed of light gives the radiation energy density. The first moment, $i'_j{}^{(1)}$, is the radiative energy flux in the J-coordinates direction. The second moment, $i'_{jk}{}^{(2)}$, divided by the speed of light can be shown to be the radiation stress and pressure tensor. The higher moments equations have no specific physical significance and are generated by analogy with the first three moments.

An infinite set of moment equations could be generated. Accordingly, approximation should be made to replace and approximate the infinite set of moments equations by a finite set. When such truncation is carried out, there are (n) equations in (n+1) unknowns. The additional equation needed to relate the moments and provides a determinate set is obtained by representing the unknown angular distribution of, (i') , as a series of Legendre polynomials, P_n , then applying the orthogonality relations for spherical harmonics, and truncating this series after a finite number of terms. This procedure, known as *spherical harmonic method* is quite complicated. If truncation is carried out by retaining only the direction cosines equal zero and unity, the result is known as P_1 -approximation, and so forth.

The Monte Carlo Technique

Monte Carlo technique is a statistical numerical method. Herman Kahn [707], has given the following definition of the Monte Carlo method which seems to incorporate the salient ideas: "The expected score of a player in any reasonable game of chance, however complicated, can in principle be estimated by averaging the results of a large number of plays of the game. Such estimation can be rendered more efficient by various devices which replace the game with another known to have the expected score. The new game may leads to a more efficient estimate by being less erratic, that is, having a score of lower variance, or by being cheaper to play with the equipment on hand. There are obviously many problems about probability that can be viewed as problems of calculating the expected score of a game. Still more, there are problems that do not concern probability but are nonetheless equivalent for some purposes to the calculation of an expected score. The Monte Carlo method refers simply to the exploitation of these remarks". The above definition reveals, as well, a good outline for use of the method.

The Eq. 5.1 of heat transfer is integro-differential which is quite difficult to solve and is a consequence of using a macroscopic viewpoint when deriving the heat flow quantities. By invoking a probabilistic model of radiative-exchange process and applying Monte Carlo sampling techniques, it is possible to utilize a microscopic approach and avoid many of the difficulties inherent in the averaging processes of the integral formulations. In this way, actions of small parts of the total energy could be examined on an individual basis, in place of an attempt to solve simultaneously for the

entire behavior of all the energy involved. The radiative exchange process of discrete amounts, (bundles) of energy since local energy flux is computed as the number of these energy bundles arriving per unit area and time at a position. The obvious bundle to visualize is the photon, but the photon has a disadvantage as a basis for a model; its energy depends on its wavelength, which would introduce a needless complication. Therefore, a model particle is devised that is more convenient. This is the photon bundle, which is a bundle carrying a given amount of energy; it can be thought of as a group of photons bounded together. For spectral dependency where the wavelength of the bundle is specified, enough photons of that wavelength are grouped together to make the energy of the bundle.

By assigning equal energies to all photon bundles, local energy flux is computed by counting the number of bundles arriving at a position per unit time and per unit area and multiplying by the energy of the bundle. The bundle paths and histories are computed by the Monte Carlo method of a statistical and probabilistic basis. An additional factor pertaining to the participating intervening medium is the path length traveled in the medium by the bundle before it is absorbed or leaves the system. The required relations would be related to a random number. It would be possible to allow for variations in medium properties along the bundle path, indeed, it is in principle possible to account for variations in the refractive index of the medium by causing the bundles to travel through curved paths. For radiative equilibrium, whenever a bundle is absorbed in the medium, a new bundle must be emitted from the same point in the medium to ensure no accumulation of energy. The functions required for determination of the angles and wavelengths of emission are tabulated in literature, e.g., (Ref. 737). The new emitted bundle in the medium might be considered as merely the continuation of the history of the absorbed bundle, and the history is continued until the energy reaches a bounding surface.

Monte Carlo computations give results that fluctuate around the real answer; for the technique being a repetitive experiment using a mathematical model in place of the actual physical situation. The uncertainty can be found by applying standard statistical tests; the uncertainty can also be reduced as experimental error, that is, by averaging over more tests (bundle histories), and/or by reducing the variance of individual tests.

The Engineering Treatment of Gas Radiation

Such a treatment could be regarded as an extension of the surface-to-surface energy exchange methods. An earlier type of this treatment was the well-stirred reactor model in which the gas is considered isothermal. This is, however, a realistic assumption; as in many instances the products of combustion are well mixed. The great simplification associated with such a model, is that the temperature distribution need not be computed to obtain the radiative behavior. But, this model must not be applied straightforward in furnaces where there are pronounced gradients of gas temperature and gas entities, such as the regions of flame/flames propagation which might represent a reasonable volume of the enclosure. This limitation could be overcome by dividing the furnace volume into several isothermal gas zones, and applying the zoning technique [738].

The mean radiative beam length is introduced as an engineering approximation to account for the geometry of a gas radiating to its boundary. The beam length is found to be relatively insensitive to the wavelength dependency of the absorption coefficient. This insensitivity enables the effects of the geometry to be separated from the effects of spectral property variations.

Removing the isothermal gas restriction introduces considerable additional complication. In a non-isothermal case, the band absorption may vary strongly with position in the gas. Then, a linear absorption law may be valid in one portion of a gas, but a power law might be necessary in another portion. The Curtis-Godson technique is the basis for one engineering treatment of non-isothermal gases. Another engineering treatment is the zoning method.

An accurate and useful method of thermal radiation in non-uniform gases is the *Curtis-Godson technique*. A method for computing radiative transfer through gases that makes use of the limiting absorption characteristics of weakly and strongly absorbing bands to compute absorption in all spectral regions. In this method, the transmittance of a given path through a non-isothermal gas is related to the transmittance through an equivalent isothermal gas. Then, the solution can be obtained by using isothermal-gas methods. The relation between the non-isothermal and isothermal gas is carried out by assigning an equivalent amount of isothermal absorbing material to act in place of the non-isothermal gas. The amount is based upon a scaling temperature and a mean density or pressure that is obtained in the analysis. These mean quantities are to be found by specifying that the transmittance of the uniform gas be equal to the transmittance of the non-uniform gas in the weak and strong absorption limits.

The model of *zonal method analysis* could be defined as a method of computing radiant exchange in enclosures containing absorbing-emitting media that is based on dividing the boundary into finite areas, and the medium into finite volumes. Consequently, the areas and volumes are assumed to be individually uniform and energy exchanges among all elements and volumes is then calculated. The method is capable of predicting both gas temperature and wall heat flux distribution and is suited to computer solution. An energy balance is written for each division of area and volume. This leads to a set of simultaneous equations for the unknown heat fluxes and temperatures. Typically, the zonal method is practical and powerful, and the algorithm is considered as an exact solution. However, the furnace volume and walls surface should be divided with care in order to account for the gas property gradient in an economical fashion.

Having discussed above briefly about methodology of radiative heat transfer, it is necessary now to discuss in some details about some of these methods, flux discrete ordinates, and zonal methods. The latter method is extensively used in sections 5.5 and 5.6 to calculate the heat transfer by radiation in flame tubes and water tube boilers' furnaces.

Flux and Discrete Ordinates Methods

This section presents the two-flux method, which has been used to calculate the radiation from the two phases in one dimensional laminar flame kinetic model. This method is developed recently by Bradley et al [160]. First, the flame model, which includes radiation is briefly discussed, then the radiation model itself using two-flux model is presented.

Flame model. For simplicity, the flame is assumed to be one dimensional in the x direction, and the time dependent conservation equations for the two phases are:

(i) Gaseous species (molar rates):

$$\rho_t \frac{\partial(F' \sigma_{ig})}{\partial t} + M \frac{\partial(F' \sigma_{ig})}{\partial x} = - \frac{\partial(J_i / m_i)}{\partial x} + R_i \tag{5.11}$$

(ii) Solid Graphite particles (mass rates):

$$\rho_t \frac{\partial Y_c}{\partial t} + M \frac{\partial Y_c}{\partial x} = R_c m_c \quad (5.12)$$

(iii) Energy:

$$\rho_t \frac{\partial h}{\partial t} + M \frac{\partial h}{\partial x} = -\frac{\partial(q_c + q_d + q_r)}{\partial x} \quad (5.13)$$

It is assumed that the gaseous transport fluxes are unaffected by the presence of the solid, and diffusion of the solid particles can be neglected. The value of Y_c is defined as mass fraction of solid in the overall mixture, and gaseous compositions by mass or mole fractions in the gas phase. More information about these equations is given in chapter 2. The subscript, g, denotes as mass fraction in the gas phase alone, the subscript, c, graphite particles and subscript, t, a value for the overall mixture. Y_i represents a species mass fraction and $\sigma_{ig} = Y_{ig}/m_i$ is a gaseous species molar fraction. $F' = 1 - Y_c$ and $\rho_g = F'\rho_t$, where ρ is the local density. M is the total mass flux, J_i is the mass diffusive flux of species, i , R_i is its volumetric molar rate of formation and m_i its molecular mass (all described before in chapter 2). Energy fluxes, q_c , q_d , and q_r are due to thermal conduction, diffusion, and radiation, respectively.

The volumetric molar rate of graphite oxidation, R_c , in Eq. 5.12 is given by:

$$R_c = N_n \frac{\sum_{i=1}^n Fx_i}{m_c} A_p \quad (5.14)$$

where $\sum_{i=1}^n Fx_i$ in $\text{kg m}^{-2}\text{s}^{-1}$, is the total rate of oxidation per unit external surface area of

the particles. N_n is the graphite particle number density and A_p is the external surface area of a single spherical particle. Since ρ_t and ρ_g are the mass of mixture and gas in unit volume, respectively, then $(\rho_t - \rho_g)$ is the mass of particles in the same unit volume, and if m_p is the mass of a particle, $(\rho_t - \rho_g)/m_p$ becomes the particle number density.

The particles were assumed to be less than 20 μm diameter and gaseous specific heats and enthalpies were expressed as polynomial functions of temperature as described in chapter 2. The equations were solved by a fully implicit finite domain method (see chapter 2) that used the time - dependent equations to secure entry into the steady state. Evaluations of gaseous specific heats, enthalpies, and transport properties associated with q_c and q_d are described in chapter 2.

Now the treatment of the radiative energy flux q_r is presented in some detail using two-flux method;

Radiative flux model. When monochromatic radiation of wavelength λ and intensity i'_λ ($\text{W m}^{-2} \mu\text{m}^{-1} \text{Sr}^{-1}$) along a distance ϑ , the local intensity in this direction is attenuated by absorption and scattering according to the exponential attenuation law. The radiative heat transfer equation [[722], for the distance ϑ in the solid angle $d\omega$, becomes:

$$\frac{di'_\lambda}{d\vartheta} = -K_{e\lambda} i'_\lambda(\vartheta) + K_{a\lambda} i'_{\lambda b}(\vartheta) + \frac{K_{s\lambda}}{4\pi} \int_{\omega_i=4\pi} i'_\lambda(\vartheta, \omega_i) \phi(\lambda, \omega, \omega_i) d\omega_i \quad (5.15)$$

(i) (ii) (iii)

values $K_{e\lambda}$, $K_{a\lambda}$, and $K_{s\lambda}$, (m^{-1}) are monochromatic extinction, absorption, and scattering coefficients of the medium, respectively, over the solid angle $d\omega$ in the direction of ϑ , $K_{e\lambda} = K_{a\lambda} + K_{s\lambda}$, and $i_{\lambda b}$ is the black body spectral intensity given by:

$$i_{\lambda b} = \frac{2h'c_0^2}{\lambda^5 (\exp(h'c_0 / \beta'T\lambda) - 1)} \quad (5.16)$$

where, h' is Planck's constant, β' the Boltzmann constant ($1.38066 \times 10^{-23} \text{ j molecule}^{-1} \text{K}^{-1}$), and c_0 the speed of light. The three terms on the right of Eq. 5.15 are (i) loss by absorption (including induced emission) and scattering, (ii) gain by emission (not including induced emission) and (iii) gain by scattering into the ϑ direction from the surroundings. The scattering phase function, $\phi(\lambda, \omega, \omega_i)$ within scattering integral, is unity for isotropic scattering.

Because the required intensity, i'_λ appears inside the integral term, the equation can not be solved directly. Flux methods, which assume i'_λ to be invariant over a finite number of solid angle intervals, are widely used to do this. In astrophysical, calculations on dimensionality can be assumed and a two-flux model was developed, first by Schuster [722] and Schwarzschild [739]. This approach [428] involves transfer equations for intensity in both positive, i^+ , and negative, i^- , directions and is the one presently adopted. It assumes that the flat laminar flame is a plane of infinite extent. In numerical solutions incremental distances normal to it, corresponding to the adopted mesh size, are small enough to justify a scattering phase function of unity.

In Fig. 5.5, x is the direction of gas flow normal to the flame and the intensity in the direction of x increasing, is i^+ , and of x decreasing, is i^- [160]. The gain in radiation intensity by scattering from the surroundings arises from i^+ and i^- . Figure 5.5 shows for the integral in Eq. 5.15 $d\omega_i = \sin \theta d\theta d\phi$. With a scattering phase function of unity this integral becomes:

$$\int_0^{2\pi} \int_0^{\pi/2} i^+ \sin \theta d\theta d\phi + \int_0^{2\pi} \int_{\pi/2}^\pi i^- \sin \theta d\theta d\phi = 2\pi(i^+ + i^-) \quad (5.17)$$

As θ no longer appears in the integral, for the convenience of using Fig. 5.5, let the general direction of ϑ be at an angle θ to the x axis and $x = \vartheta \cos\theta$. In the direction of x

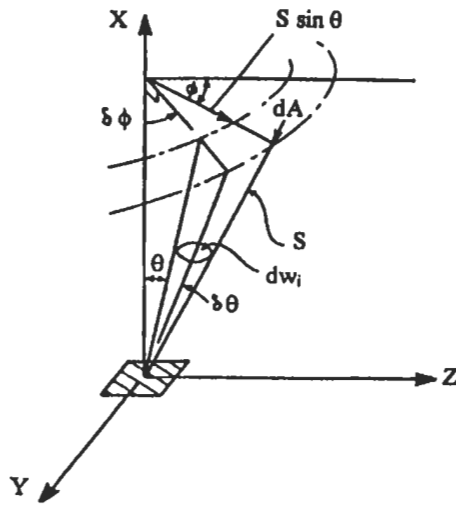


Fig. 5.5: Diagram of angular radiation intensity contribution to the flux vector [160]. Reproduced by permission of Elsevier Science.

increasing, Eq. 5.15 gives;

$$\cos \theta \frac{di_{\lambda}^{+}}{dx} = -K_{e\lambda} i_{\lambda}^{+} + K_{a\lambda} i_{\lambda b}^{+} + \frac{K_{s\lambda}}{2} (i_{\lambda}^{+} + i_{\lambda}^{-}) \quad (5.18)$$

For $0 \leq \theta \leq \pi/2$, and for the opposite direction;

$$\cos \theta \frac{di_{\lambda}^{-}}{dx} = -K_{e\lambda} i_{\lambda}^{-} + K_{a\lambda} i_{\lambda b}^{+} + \frac{K_{s\lambda}}{2} (i_{\lambda}^{+} + i_{\lambda}^{-}) \quad (5.19)$$

For $\pi/2 \leq \theta \leq \pi$

The radiative energy flux in the x direction, q_{λ}^{+} , arising from i_{λ}^{+} is given by:

$$q_{\lambda}^{+} = \int_{\omega_i=2\pi} i_{\lambda}^{+} \cos \theta d\omega_i = \int_0^{2\pi} \int_0^{\pi/2} i_{\lambda}^{+} \cos \theta \sin \theta d\theta d\phi = \pi i_{\lambda}^{+} \quad (5.20)$$

Similarly, $q_{\lambda}^{-} = \pi i_{\lambda}^{-} \quad (5.21)$

When Eqs. 5.18 and 5.19 are multiplied by $2 \sin \theta$ and integrated with respect to θ , between the given limits, and when q_{λ} is substituted for i_{λ} from Eqs. 5.20 and 5.21, then:

$$\frac{dq_{\lambda}^{+}}{dx} = (-2K_{e\lambda} + K_{s\lambda})q_{\lambda}^{+} + K_{s\lambda}q_{\lambda}^{-} + 2(K_{e\lambda} - K_{s\lambda})e_{\lambda b} \quad (5.22)$$

and

$$-\frac{dq_{\lambda}^-}{dx} = (-2K_{e\lambda} + K_{s\lambda})q_{\lambda}^- + K_{s\lambda}q_{\lambda}^+ + 2(K_{e\lambda} - K_{s\lambda})e_{\lambda b} \tag{5.23}$$

where $e_{\lambda b} = \pi i_{\lambda b}^-$ is the hemispherical spectral emissive power of unit area of a black surface. The net radiative energy flux in the direction of x increasing is:

$$q_{\lambda} = q_{\lambda}^+ - q_{\lambda}^- \tag{5.24}$$

Taking account of the contributions from all wavelengths the total net flux is given by:

$$q_r = \int_0^{\infty} q_{\lambda} d\lambda \tag{5.25}$$

Values of radiative physical constants and computational method. Now, the radiative physical constants which are used in the above two-flux method is discussed. The principal gaseous absorbers and emitters are CO₂ and H₂O. The exponential wide-band model of Edwards and Balakrishnan [740] groups the absorption spectra into discrete absorption bands. This procedure was followed and the computed values were validated against those of Skocypec et al [741] for homogenous dust-gas suspensions. Detailed computations showed that the gaseous contribution to radiative energy exchange was negligible compared to that of the particles. The extinction and scattering coefficients for monosize particles, both indicated here by the K_{λ} prefix, are related to the particle macro cross section by a corresponding dimensionless efficiency, η_{λ} :

$$K_{\lambda} = \eta_{\lambda} \pi r^2 N \tag{5.26}$$

Both efficiencies are a function of a particle size parameter, $\chi = 2\pi r / \lambda$ and the complex refractive index, $m = n - ik$, with n and k as the real and imaginary parts. The use of Mie theory to estimate these parameters is complex but the simplifications of Van de Hulst [742] were used. These give:

$$\eta_{e\lambda} = 2 - \frac{4}{u} \cos v \sin(u - v) \exp[-u \tan v] - \frac{4}{u^2} \cos^2 v \cos(u - 2v) \exp[-u \tan v] + \frac{4}{u^2} \cos^2(2v) \tag{5.27}$$

$$\text{and } \eta_{a\lambda} = 2K'(w)(4\chi k) \tag{5.28}$$

where

$$K'(w) = \frac{1}{2} + \frac{\exp(-w)}{w} + \frac{\exp(-w) - 1}{w^2} \tag{5.29}$$

and $u = 2\chi(n-1)$, $v = \arctan(k/n-1)$, and $w = 4\chi k = 2u \tan v$. These are valid for $\chi \geq 0.2\pi$. Note that $\eta_{s\lambda} = \eta_{e\lambda} - \eta_{a\lambda}$.

For soot, the investigations by Lee and Tien [743] have shown optical properties to be rather insensitive to temperature changes at elevated temperature and they suggested values of n and k agreed well with those obtained by Chippet and Gray [744]. Goodwin and Mitchner [745] reported a much larger variation of k than of n with λ for coal ashes, with a maximum value when λ was about $9 \mu\text{m}$. Twitty and Weinman [746], after reviewing values for graphite, coal and soot recommended values of $n = 1.8$ and $k = 0.5$ for $0.25 \mu\text{m} \leq \lambda \leq 15.0 \mu\text{m}$, and these were used in the radiation model.

Even with values of n and k and are invariant with wavelength, $\eta_{e\lambda}$ and $\eta_{s\lambda}$ become functions of λ through their dependence on χ . Bradley et al [160] have found that the value of $\eta_{s\lambda}$ ranged between about 1 and 1.6. Beér and Clause [747] and Jones [748] have shown that, in this regard, a good approximation for the emissivity of soot is obtained when a spectral emissivity is evaluated at the wavelength above which half the energy of the blackbody spectrum lies. This was adopted for the evaluation of the two efficiencies and rendered values of $K_{s\lambda}$ and $K_{e\lambda}$ independent of λ . Simple integration of q_{λ}^{+} and q_{λ}^{-} over all wavelengths as indicated by Eq. 5.25 and Eqs. 5.22 and 5.23 to give q_r^{+} and q_r^{-} , respectively, yields:

$$\frac{dq_r^{+}}{dx} = (-2K_e + K_s)q_r^{+} + K_s q_r^{-} + 2(K_e - K_s)e_b \quad (5.30)$$

$$-\frac{dq_r^{-}}{dx} = (-2K_e + K_s)q_r^{-} + K_s q_r^{+} + 2(K_e - K_s)e_b \quad (5.31)$$

Here K_e and K_s indicate values valid over all wavelengths, with $\int_0^{\infty} e_{\lambda b} d\lambda = e_b = \sigma T^4$, where σ is the Stefan-Boltzmann constant ($5.669 \times 10^{-8} \text{ W m}^{-2} \text{ K}^{-4}$). These equations were solved and:

$$\frac{dq_r}{dx} = \frac{dq_r^{+}}{dx} - \frac{dq_r^{-}}{dx} \quad (5.32)$$

gave the radiative flux term which has been used by Bradley et al [160] in energy equation (see also chapter 2).

The two radiative fluxes in Eqs. 5.30 and 5.31 are found numerically by the fourth order Runge-Kutta method. The flame is assumed flat and of infinite extent in both the y and z directions. The length of the burnt gas zone is L_b , taken to be 0.1 m [160], with no radiation originating from the space beyond L_b , where $q_r^{-} = 0$. In this zone, the x coordinate is discretised into 30 grid points and into 33 nonuniformly distributed grid points through the reaction zone, such that intervals were small in regions of rapid change. These mesh points were used for simultaneous solutions of the conservation Eqs. 5.11 to 5.13 and the radiation Eqs. 5.30 to 5.31 with the following boundary conditions

$$\frac{\partial \sigma_{ig}}{\partial x} = 0, \quad \frac{\partial h}{\partial \pi} = 0, \quad \text{at } x = +\infty \text{ and } x = -\infty \quad (5.33)$$

As a first step towards a solution to these equations, the coordinates are transformed into the Von Mises system of coordinates as detailed by Dixon-Lewis [15]. The resulting equations are integrated forward in time, subject to the boundary conditions. Numerical integration are performed by means of implicit, finite difference techniques in order to secure entry into the steady state. The input dependent variables are the mole fraction composition, pressure, temperature and mass fraction of graphite of the initial mixture, together with rough estimates of the hot boundary values. Mole fractions were converted to values of the working composition variables σ_{ig} and the specific enthalpy of the unburnt mixture calculated. The final specific enthalpy assumed the same value. A few grid points near each boundary were given the boundary values of the dependent variables, and a suitable curve-generating algorithm was used to initialize values in the central region of the grid, where most reactions occurred. The predicted results from the flame model which included the above radiation treatment gives good agreement with the experimental results and this has been discussed in details by Bradley et al [160].

The flux and discrete transfer methods can be easily integrated into computational fluid dynamic models and also in the kinetic model as described above, since solution of the radiation field can be carried out using the same numerical techniques used to solve the conservation equations for the temperature, flow and composition fields.

Lockwood and Shah [749] developed an improved flux model for the calculation of radiation heat transfer of so called "flux" or differential approximation. They used a six-term Taylor's series expansion to represent the directional dependency of intensity. Extension of this method to allow for non-homogeneous, non-gray combustion products is described by Docherty and Fairweather [750].

Gosman and Lockwood [751], have calculated the radiation in furnaces. Their calculation involves two dimensional, and turbulent transport properties of flows with a procedure similar to that suggested by Spalding [752]. Mass transfer and chemical reactions were calculated from a model that assumes a single-step chemical reaction and physical control. Experiments were carried out on a furnace at the International Flame Research Foundation, and some sort of agreement was obtained between the predicted and radiant heat transfer along the furnace walls. However, they attributed the unsatisfactory agreement within the flow, to the negligence of the effect of the unmixedness phenomenon. It is evident that the deviation in the predicted quantities is mainly due to the errors that might arise with the subsidiary models of flow and chemical reaction.

Selcuk and Siddall [753] have written several papers on prediction of the thermal behavior of furnaces employing different models. One of these papers dealt with two-flux harmonic modeling of two-dimensional radiative transfer in a large-scale experimental furnace, having length to diameter ratio of 5.5. Predicting the thermal behavior of the large-scale water-cooled furnace extensively tested the accuracy of the radiation model. The deviation errors in the predicted values could be attributed to approximations employed in the mathematical modeling of the flow and concentration patterns in the furnace, rather than to the simplifications employed in deriving the two-flux model.

Truelove [754] used the discrete ordinates approximation to obtain solutions for radiative transfer through absorbing-emitting non-isothermal gray media confined between parallel planes, concentric spheres, and infinite coaxial cylinders. His principal objective of the investigation was to assess the accuracy of the approximation by comparing approximate solutions with known exact solutions for the simple problems. The comparison indicated deficiencies in the lowest order approximation for curved

geometries, and significantly better solutions to be obtained with the next higher order of approximation for all three geometries.

However, the interactive simulation of radiation and turbulent reacting flows remains a fully open research subject. Several years ago, interesting studies appeared, estimating the global effect of turbulence on radiation-heat transfer and illustrating that this phenomenon is significant. It was shown that in flames, the radiant intensity can be easily increased by 24 % because of turbulent fluctuations [755]. From Ref. 756, time-consuming ensemble averaging over a large number of path realizations was circumvented by a new method based on discrete probability functions. However, with each additional stochastic variable, the number of calculations necessary is multiplied by the number of discrete steps for the distribution of this new variable. For engineering applications, such stochastic or discrete probability density function (PDF) approaches seem difficult when considering a complete turbulence/chemistry/radiation simulation. In 1996, Hartick et al [757] extended of such an approach to an enclosed diffusion flame, for which a double Dirac PDF model is not suitable. Mainly, mixing process drives diffusion flames, and a continuous PDF is required for the mixture fraction. Because of radiation-heat loss in confined combustion systems, there is no fixed relation between mixture fraction and enthalpy. Thus, local properties are described by at least two variables, the mixture fraction and the heat-release rate, and a two-dimensional PDF is necessary for statistical description. Their study [757] demonstrated that for middle-sized enclosed diffusion flames, the complex phenomenon of turbulence-radiation interaction can be simulated efficiently without use of tedious stochastic approaches.

Also, Abbas and Lockwood [758] described a fully three-dimensional mathematical model to the combustors of two large power station boilers: one front wall-fired and the other corner-fired. Predictions for the flow aerodynamics are compared with experimental data obtained in cold models. The Eulerian partial differential equations governing the transport of mass, momentum, energy and turbulent mixing are cast into finite-difference form and solved by an iterative procedure. Closure of the time-averaged equations of the mean flow is obtained with assistance of the k - ϵ turbulence model. The radiation transfer is handled by the flexible and economical "discrete transfer" technique; special grids and computational procedures are employed to handle the burner inlet, hopper and nose boundary conditions. The isothermal velocity predictions are in fairly good agreement with the model data.

Zonal Method of Analysis

Combustion is a very complicated process. It is often consisting of chemical reactions in series and in parallel involving a variety of intermediate species. The composition and concentration of these species cannot be predicted very well unless complete knowledge is available about the reaction kinetics of the flame, such as described in chapters 1 and 2. Because the radiation properties of the flame depend on the distribution of temperature, species, and soot, a detailed prediction of radiation from flames and combustion gases is not often possible from knowledge only of the original combustible constituents, and the flame geometry and conditions.

Because of these difficulties and the shorthand on combustion phenomena insight, it is reasoned enough to incorporate measured profiles of gas temperature, species and soot concentrations as the input data for the computational algorithms, rather than relying on empirical formulae. Doing so, the errors associated with models for

predicting radiating properties would be put aside, otherwise the accuracy of the model should be vague. In the meantime, the model with its reliable data could be used as a judgment for the accuracy of other models for prediction of both radiative flux and radiating properties distributions. Furthermore, the zonal method is one of practical and powerful tool to calculate the radiative heat in enclosures. These are the initiatives for the method of analysis used by El-Mahallawy and Rezk [759] for radiation model in large models of fire-tube and water tube boiler furnaces as will be described in details in sections 5.1.4 and 5.1.5.

The basis for this model relies on the zoning method of subdividing the furnace filled with absorbing-emitting gas into areas and volumes that can be essentially considered isothermal with uniform properties. The furnace division takes into account the various changes and gradients of gas temperature and properties, all over the furnace volume in an economical manner. It is also worthy to note that this concept is being excelled as the exploitation of the techniques initiated by El-Mahallawy [530, 760, 761], and primarily applied by him and co-workers [762-775], in combustion chambers.

Each gas volume zone is considered to be radiating with a uniform temperature and an averaged spectral emissivity through its bounding surface. The local thermodynamic equilibrium is assumed to be prevailing. Then, each gas volume zone is said to exchange radiant energy with each of the wall surface elements; according to the geometrical view factors and the transmissivity of the intervening gas layer. The gas mixture is considered as only an absorbing-emitting medium with no scattering. The multi-scatter/reflection at the furnace wall is taken into account.

The gas is not considered to be gray but it is used as a real gas and is represented by a one-clear two-gray gas. The emissivity of gas/soot mixture is defined by the three-term equation of Beér [776] which has been found successful for a practical range of combustion in oil-fired furnaces.

The luminous emissivity of flames is usually ascribed to hot carbon (soot) particles that are formed because of incomplete combustion in hydrocarbon flames. Some other researchers, however, have advanced the hypothesis, supported by some experimental facts, that the luminous emission from some flames is due to the emission from vibrational-rotational bands of chemical species that appear during the combustion process prior to soot particles formation. Nevertheless, the soot formation is yet being the accepted view. Some information is available on soot formation and radiative properties, but the amount is insufficient. Determining the soot concentration is a serious difficulty in flame radiation computations. The concentration depends on the particular fuel, the flame geometry, and the mixing phenomena within the flame. At present, there is no way of computing soot concentration from basic parameters, such as burner geometry, fuel-air ratio and the particular fuel.

Richer and Bauersfeld [777] have investigated mathematical radiation models to be used in complete mathematical furnace models. The two types which has been investigated are; (1) the semi-empirical models that only include the energy balance based on the zonal method of analysis, and (2) the more comprehensive models which solve the convective transport equations of momentum, mass, and energy. It is obvious that the possibility of predicting realistic distributions of local heat flux densities at the furnace walls shall depend on the reliability of the input data. However, the complete mathematical furnace models usually incorporating the Spalding's prediction technique need only few input data. It should also be noted that the accuracy would depend on the individual accuracy of the subsidiary models substituted for the required input data.

In that investigation, the radiative heat exchange had been evaluated by a four-flux method allowing for net radiant heat fluxes only in radial and axial directions. Also, a potential coupling of the zonal method of analysis with the solution procedure of the convective transport equation was shown. A program was developed to evaluate the interchange areas between annular zone-pairs of any size, and two different computational techniques as used in the evaluation were compared. The classical integration technique is considered to be only approximate when the absorption coefficient varies between the zone pair under consideration. The matrix-inversion technique were then found to be rather sophisticated; while the so-called Monte Carlo method is being in demand of much computer time.

Beér [776] discussed the recent advances in methods for predicting radiative heat flux distributions in furnaces and combustors. He suggested special reference to the zone methods of analysis and the flux methods. He found that the mathematical formulation of the zone method could be much simplified if absorbing medium could be treated as gray gas. To achieve this simplification, the emissivity of the real gas as well as the emissivity of soot cloud might be considered as the sum of the emissivities of a number of gray gases. He also conducted extensive testing on a proposed model of emissivity as sum of three terms. The constants for that model showed an excellent agreement between the measured and predicted emissivity, over a wide range of practical applications.

Stewart and Gürüz [778] developed a mathematical simulation of the heat transfer in a large modern boiler using the zonal method of analysis. They evaluated the input data for that method from the data available in an operating plant, theoretical consideration found in related literature, and certain simplifying assumptions. Their prediction of heat flux distribution was found to be in qualitative agreement with experimental measurements. Assumption was made that a single volume zone is perfectly mixed within itself and thus having a single temperature to be determined by a system of steady state energy balance on each surface and volume zone in the system. The energy balances produced a set of simultaneous equations equal in number to the total number of volume and surface zones in the system. Two flow patterns were compared; one based on data of Beér et al [779], and the second used as a pseudo plug flow which does not involve any recirculation. It must be pointed out that both flow patterns should only be considered as rough estimates of those in practice. From the presentation of Stewart and Gürüz [778], it could be concluded that a significant amount of computation effort had been involved in the calculation of the total radiative interchange in an enclosure with an irregular geometry such as the boiler studied by El-Mahallawy and his research teams in Section 5.1.5. Their simulation is considered to be exact, except the assumptions made for the input data and the crude division of the furnace volume/walls, as well as the incorporation of uncertain models for flow patterns and convective heat formulae.

Radiation Calculation in Boiler Furnaces

The zone method of analysis has provided the basis for a wide range of flame tube and furnace mathematical models, ranging from one-dimensional division algorithm (gas discs division of varying temperature and composition in axial direction), two-dimensional division algorithm (gas rings division with varying temperature and composition in both axial and radial directions) and finally, the three-dimensional

division algorithm. Data for the mass flow rates, temperature, composition and heat release in each gas element must be specified as input to these divisions. The later two methods of division algorithms will be discussed in this part:

General case. Let us consider a gas volume dv radiating to a small element of the surface dA . This radiation consists of radiation from dv itself to dA and also radiative scattering by dv of energy from whatever source or gas. If we denote the total flux leaving dv due to its emission and scatter by \overline{W} and if the part leaving dv is multiplied by the transmittance of the intervening gas, the result will give the net flux leaving dv and reaching dA . Thus the incident flux can be expressed by:

$$(GS.\overline{W})_{dv-dA} \tag{5.34}$$

where $GS = VF_{gs} \tau_{gs}$, and represents the fraction of the total flux leaving the gas volume dv due to its emission and scatter and which is intercepted by the surface element dA , VF_{gs} is the view factor between gas and surface and τ_{gs} is the intervening gas layer transmittance.

If we divide the combustion zone into zones small enough to make each substantially uniform in temperature and composition and if we denote the flux leaving a surface w by W_w and that leaving a gas volume zone j by \overline{W}_j , the total flux incident on the surface (i) is the sum of the energy incident from, n surface zones and m gas zones; all constituting the whole combustion zone (see Fig. 5.6). This is given by:

$$\sum_{l-n} S_w S_i W_w + \sum_{l-m} G_j S_i \overline{W}_j \tag{5.35}$$

If we consider the part of this incident energy reflected by the surface (i) and the emission from the surface (i) itself, then the net energy absorbed will be:

$$\left[\sum_{l-n} S_w S_i W_w + \sum_{l-m} G_j S_i \overline{W}_j \right] (1 - \rho_i) - A_i \epsilon_i E_{bi} \tag{5.36}$$

ρ_i and E_{bi} are the reflectance and the black body emissive power (σT_i^4) of surface (i),

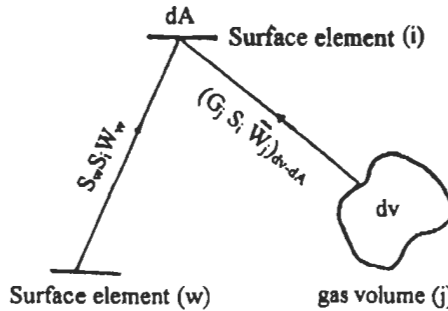


Fig. 5.6: Radiation from gas volume, J, and surface element, w, to surface element, i [530].

respectively. $W_w = A_w \epsilon_w E_{bw}$ and $\overline{W}_j = A_j \epsilon_j E_{bj}$, and ϵ_j is the emissivity of gas volume zone j .

In order to be able to apply the above analysis for the one-dimensional model, El-Mahallawy [530] suggested the following points:

- Variations of gas temperature and composition in the radial direction are neglected and variations are considered in the axial direction only.
- Radiant heat exchange between different surfaces is neglected as it is usually small compared with the radiation from gases.
- Multi-gas scatter and surface reflections are neglected.
- Any gas segment is considered to be radiating uniform in all directions.
- Average gas absorptivity is assumed for all radiation reaching any surface.

Case (1): Two-dimensional division algorithm. This model is a modification of the one-dimensional model. Here the temperature and composition variations are considered in both axial and radial directions. For this purpose, each gas disc (j) is divided into a number of gas rings (m_r) and each ring (k) is considered substantially uniform in temperature and composition. The net radiation from all gas rings to the surface element (i) is given by:

$$\sum_{\text{all}(j)} \sum_{\text{all}(k)} G_{kj} S_i \overline{W}_{kj} \tag{5.37}$$

where j and k are disc and ring numbers, respectively, and kj means that of a ring k lying in a gas disc j . \overline{W}_{kj} is the total radiation flux leaving the gas ring, k , in gas segment, (disc) j (in Fig. 5.7). The flame emissivity with its luminous and non-luminous parts, view

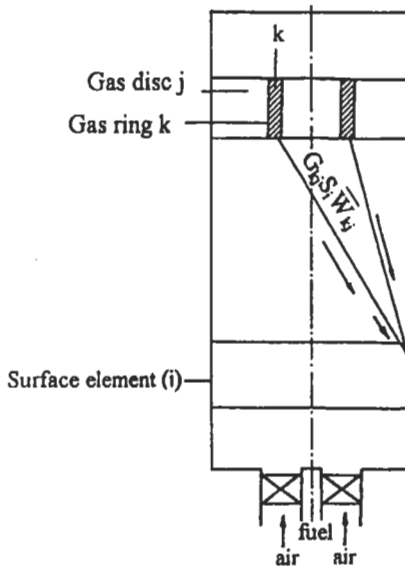


Fig. 5.7: Radiation from a gas ring to a cylindrical surface element [530].

factor and transmissivity will be discussed in the next sections. However, if the average gas temperature and absorption strength are known for any gas segment or any gas ring, the luminous component of flame emissivity could be calculated from Refs. 780 and 640. For the calculation of the absorption strength for each gas ring, the soot concentration is considered roughly to be proportional to the mass concentration of the unburnt fuel [610].

Case (2): Three-dimensional division algorithm. El-Mahallawy and Rezk [759] have developed a mathematical model for predicting wall radiative heat transfer distribution in boiler furnaces. This model lends itself towards the engineering treatment of radiation problem. The complications arose for the account of having an intervening absorbing-emitting and/or scattering gas between the surfaces of the combustion chamber enclosure, can be accounted by building upon the foundation established for the simpler case where no gas is present. The used technique in this model is based upon the zonal method of analysis. In this technique, the furnace gas volume as well as the enclosure surfaces are divided into small gas/wall elements. Each of these elements are considered to have uniform radiative properties. The surface element is assumed to have a uniform emissivity, ϵ_s , and a uniform temperature, T_s . The gas volume element is considered of having a uniform temperature, T_g , as well as the species concentration of oxygen, O_2 , carbon monoxide, CO and carbon dioxide, CO_2 , water vapour H_2O , and a soot concentration of, ρ_c . The gas element is regarded as radiating in all directions from its bounding surface, with an emissivity of ϵ_g .

Typically, the gas volume is considered as an absorbing-emitting medium with no-scattering. The transmissivity of radiation incident upon a surface wall element is therefore evaluated as unity minus the emissivity of the intervening gas volume between the pair of gas/wall element under consideration. The multi-reflection/scatter at surface wall element is estimated to be as, $(1+\epsilon_s)/2$. Accordingly, the radiative net heat flux exchange between any of the wall elements, and a gas volume element (radiating through its bounding area, A_g), could be expressed by:

$$q_{R_{gs}} = \sigma A_g V F_{gs} \epsilon_g (\bar{T}_g^4 - T_s^4) \tau_{gs} (1 + \epsilon_s) / 2 \tag{5.38}$$

As discussed earlier, the mathematical model relies rather on the measured profiles of gas temperature and species concentrations of oxygen, carbon monoxide, and carbon dioxide, and soot concentrations, as the required input data. Consequently, the errors that might arise due to the models to be incorporated for estimating such input data, are put aside. The main scheme of this computational algorithm is illustrated in Fig. 5.8.

Input data to the model. The input data of gas temperature, species and soot concentrations for each gas volume element should be extracted from thoroughly measured profiles as averaged over the three dimensions such as given in Refs. 781 and 782.

The temperature is averaged according to the following expression:

$$\bar{T}_g = \left(\sum_{i=1}^N T_{gi}^4 / N \right)^{0.25} \tag{5.39}$$

Gas emissivity model. The mathematical formulation of the zoning method is much simplified, if the absorbing medium can be treated as a gray gas. Real gases, such as

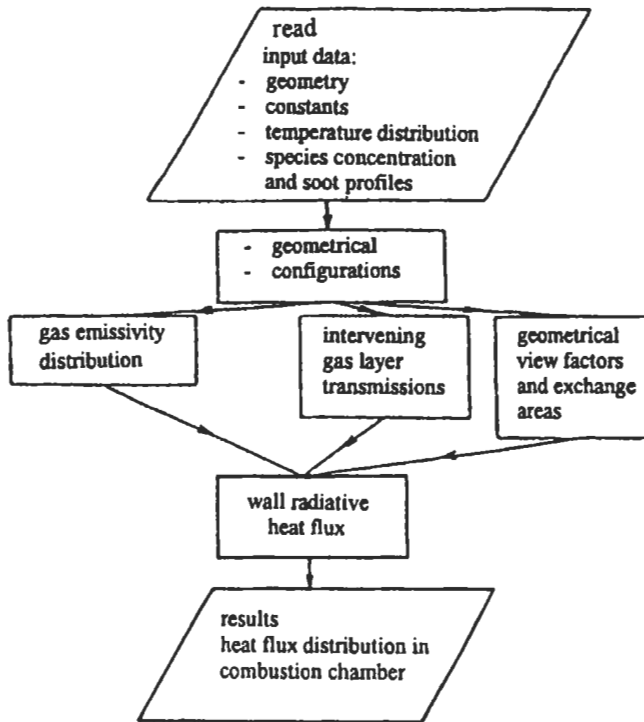


Fig. 5.8: Organization map of the computational algorithm [759].

water vapor and carbon dioxide, do not behave as gray gases, because of the discrete nature of their absorption bands. However, it is possible to retain the simplicity of the mathematical formulation of the zonal method of analysis, by representing the emissivity of the combined real gas-soot mixture as the weighed sum of the emissivities of a number of gray gases, e. g. Ref. 776.

Geometrical view factors. In order to gain as much accuracy as possible and to assess the mathematical model correctly, a closed form solution of the established geometrical view factor is used. Hence, the error would be minimized to zero for this quantity calculation. Whenever, the view factor is not found directly in the literature as a closed form solution, the view factor algebra and rules are applied to find the desired factor from other pertaining factors.

The application of this zonal method will be discussed in relation to the flame tube in section 5.1.4 and to the water-tube boilers' furnace in section 5.1.5.

5.1.3 Convective Heat Transfer

Convective heat transfer from flame to flame tube is difficult to be estimated accurately. For example in the primary zone of combustion chamber, the gases involved in heat transfer are at high temperature and are undergoing rapid physical and chemical changes. Further difficulty is introduced by the existence within the primary zone of

steep gradients of temperature, velocity, and composition. Uncertainties regarding the air flow pattern, the state of boundary-layer development, and the effective gas temperature make the choice of a realistic model almost arbitrary.

It will be found convenient in most cases to define a convection heat transfer such that the heat flux from the flame to the flame tube is the product of the heat transfer coefficient by convection, h_c and a temperature difference between gas, T_g and wall, T_s [782]. Thus:

$$q_c = h_c(T_g - T_s) \quad (5.40)$$

The coefficient, h_c is essentially an aerodynamic property of the system, whereas the temperature difference is of course a thermodynamic quantity. The usefulness of Eq 5.40 lies largely in the fact that in many technical application, q_c is close to being directly proportional to $(T_g - T_s)$, as the linearity of the applicable differential equation reveals. Nevertheless, numerous nonlinear problems will be encountered where h_c itself is a function of the temperature difference and other parameters, as it will be described in sections 5.1.4 and 5.1.5. For example, the heat transfer coefficient by convection for a cylindrical combustion zone is given by the following relation [610]:

$$Nu = \frac{h_c d}{\lambda_c} = 0.0207 Re^{0.8} \quad (5.41)$$

where Nu is the Nusselt number, d , λ_c and Re are the diameter, gas conductivity and Reynolds numbers, respectively. $Re = Ud\rho/\mu$, where U , d , ρ and μ are the velocity, tube diameter, density and viscosity of gases. For a certain combustion zone geometry and certain gas temperature and composition, d , λ_c , and μ will be constant. Then, $h_c = KU^{0.8}$ where K is a constant which depends on the values of d , λ_c , and μ . This shows that the heat transfer by convection in this case depends mainly on the gas velocities. In some cases at low values of the gas temperature and gas emissivities, the heat transfer by radiation will be very small as compared with that by convection.

The convective heat transfer of gases sweeping the walls of a furnace is well established. In most of the water-tube boilers, the convective heat transfer by impingement is the main cause of overheating or the failure of the tubes in boilers. This problem was treated by many investigators [783-789], and the details of this type of convective heat transfer will be given in section 5.1.5.3 Therefore, it is important to gain more information on this type of convective heat transfer, and the following section will discuss this subject.

The general conclusion from the above background is that, the realistic prediction of heat flux and heat transfer characteristics for furnaces and combustion chambers requires rather too complicated and lengthy procedures and methods as well as the use of long computer time. Thus, further investigations are needed strongly towards the development of more simplified methods with more accuracy which can be easily manipulated by industrial engineers and designers of furnaces and combustion chambers in various applications and this will be discussed next in sections 5.1.4 and 5.1.5.

5.1.4 Combustion and Heat Transfer in Flame Tubes

The problems of wall heating of the gas turbine combustion chamber or industrial furnaces are of special importance since a long flame tube life, measured in thousands of hours, can not be expected unless the design metal temperature is limited to a maximum value. The wall heating depends on the air velocity in the cooling annulus, the design and construction of the flame tube and on the total heat transfer from the flame to the flame tube wall. One example of these problems is the overheating or the failure of the furnace tubes in boilers which is considered as an indication of a non-uniform heat flux distribution resulting from an inappropriate choice of the burner system and flame size.

This section will be devoted to investigate mainly the combustion and heat transfer by radiation and convection in flame tubes such as horizontal and vertical circular cross sectional flame tubes as well as the horizontal flame tube of square cross section.

The total heat transfer from the flame to the combustion zone wall consists of two parts, namely the heat transfer by radiation and the heat transfer by convection. The heat transfer by radiation increases with the increase of the combustion zone size and fuel viscosity as in industrial and marine applications. The heat transfer by convection increases with the decrease of the flame tube size and the increase of the combustion intensity as in aircraft applications.

Confined turbulent diffusion flames always impose a number of important scientific and practical features, they are complex, and three-dimensional turbulent flows, which combine the characteristics of jets and co-axial confined flames. Many investigators have devoted their work to study the turbulent confined diffusion flames in furnaces among which Becker et al [790], Baker et al [791], Wu [792], Hoogendoorn et al [793], Elgobashi and Pun [794], Wu and Fricker [795], Lewis, and Smoot [796], Lenze [797], Hassan et al [798] and by El-Mahallawy and co-workers [626, 759, 769, 771-774, 779-807].

The performance of existing industrial fire tube boilers as well as furnaces is dependent to a great extent on the control of the developed heating flame. In such diffusion flames, the combustion process is mainly mixing controlled, i.e., one has to ensure aerodynamically the best possible mixing to obtain higher combustion efficiency. The study of the mixing patterns inside these flames under different operating conditions (which was discussed in chapter 4) is evidently important in the studies of the heat transfer characteristics along the flame length. These mixing patterns or flame structure are affected by different parameters such as the fuel-air ratio, burner design, degree of swirl of combustion air (see also chapter 4), degree of atomization of fuel when burning liquid and heavy fuel oils, and preheating of the oxidant and/or the fuel.

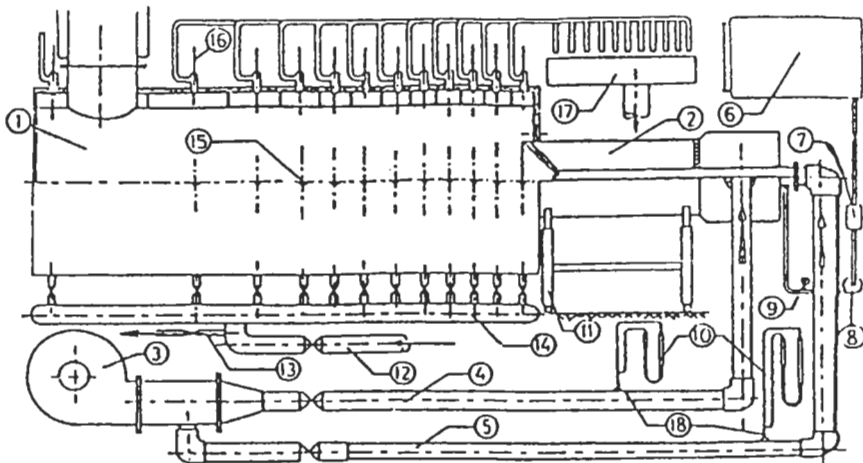
Because the realistic prediction of heat transfer and release during combustion processes necessitates the use of rigorous and lengthy methods as described in previous chapters, therefore the work in this chapter presents relatively simplified analytical computation procedures for predicting the heat transfer characteristic in flame tubes of combustion systems. This involves the measurements of gas temperature, species concentrations of CO, CO₂, O₂, and soot particles using specially designed water-cooled probes. The development of this analysis is based on the application of the zonal method of modeling radiative heat flux and the establishment of accurate mathematical

models. These methods are applied and tested against experimental data.

Also, in this section, the effect of operating parameters such as fuel-air ratio, swirl angle of the combustion air, the swirler to furnace diameter ratio, shape of combustion zone and burner loading on the flame structure and heat transfer is demonstrated.

5.1.4.1 Horizontal Flame Tube of Circular Cross Section

The flame tube (FT) of circular cross section is one of simplest combustion equipment usually used to study such above parameters. Therefore, El-Mahallawy and his research team [759, 769, 772, 773, 799-803, 807] have studied the combustion characteristics and heat transfer on laboratory cylindrical fire tube of 0.6 m inner diameter and 3.7 m long. It is water cooled by a segmented jacket. Each segment is provided with a measuring tapping as shown in Fig. 5.9. The flame tube is equipped with an industrial oil burner with low and high firing conditions. Full details of FT and the burner were given in Refs. 769, 773, 779 and 780. The fuel used was light Diesel fuel, which has a calorific value of 43116 kJ kg⁻¹. They investigated the effect of loading on the flame structure, heat transfer and hence on the overall tube performance. The experimental work covers, the low and high firing operating conditions. In the low firing case (when one of the burner nozzles was working), the fuel flow rate was 74.5 kg h⁻¹ and the mass air-fuel ratio was about 15.75. In case of high firing (when two nozzles were working), the fuel flow rate was 114.7 kg h⁻¹, and the mass air-fuel ratio was about 15.5. The effect of different operating parameters on the flame structure, combustion characteristics and heat transfer will be discussed in the following parts.



- | | | | |
|------------------|-------------------------|-------------------------------|------------------------|
| 1- U.T.R | 6- Fuel tank | 11- Burner carrier | 15- Measuring tappings |
| 2- Burner | 7- Fuel filter | 12-Cooling water supply | 16- Thermometers |
| 3- Blower | 8- Fuel pump | 13-Probe cooling water header | 17- Sink |
| 4- Sec.air line | 9- Fuel press.indicator | 14-Cooling water header | 18- Pilot probc |
| 5- Prim.air line | 10- U-tube monometer | | |

Fig. 5.9 Flame tube test rig layout [773, 799].

Flame Structure

Gas temperature, volume concentration of CO_2 , CO , O_2 , and soot are measured in the above described flame tube. Figures 5.10 to 5.13 show the radial distributions of temperature, CO_2 , CO and O_2 along the flame tube for the high-firing condition [773, 800].

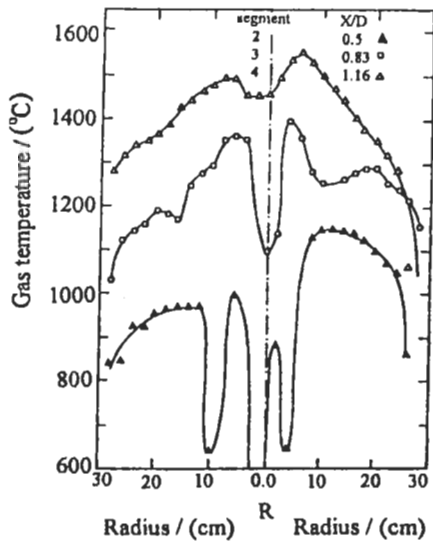


Fig. 5.10: Radial distribution of gas temperature at different segments of the FT at high firing conditions [773, 800].

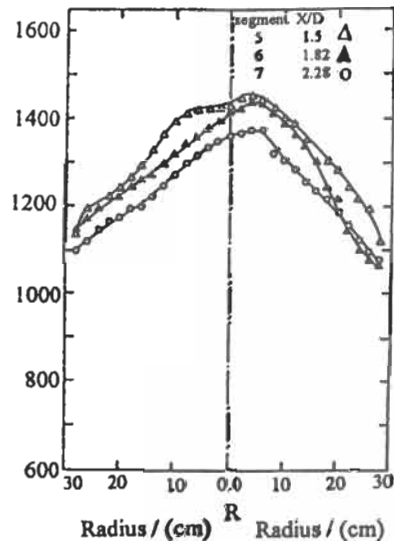


Fig. 5.10: (cont.).

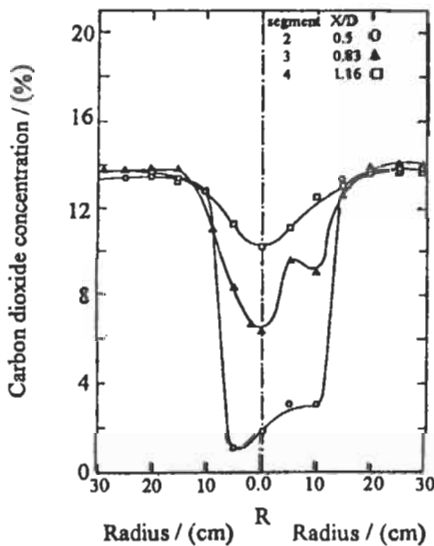


Fig. 5.11: Radial distribution of carbon dioxide concentration at different segments of the FT at high firing conditions [773, 800].

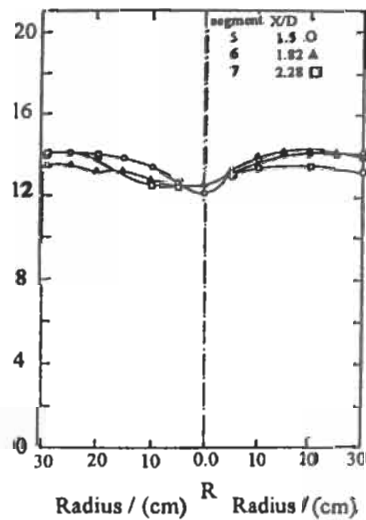


Fig. 5.11: (cont.).

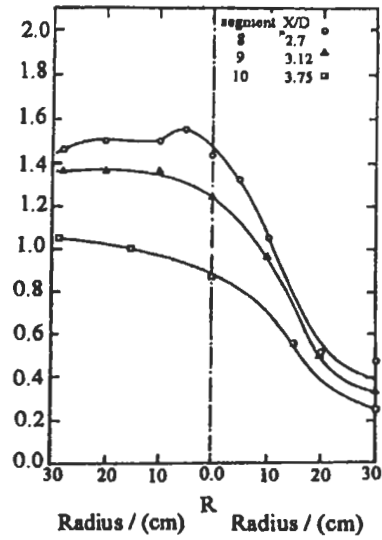
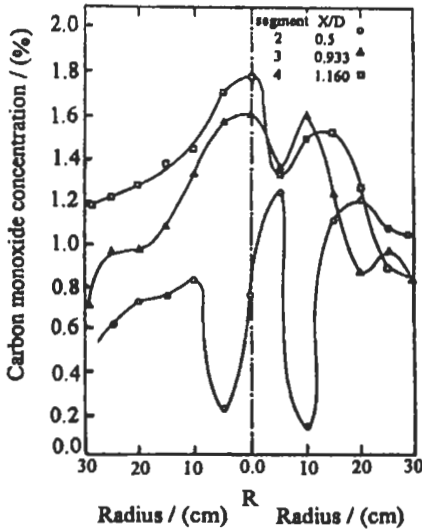


Fig. 5.12: Radial distribution of carbon monoxide at different segments of the FT at high firing conditions [773, 800].

Fig. 5.12: (cont.).

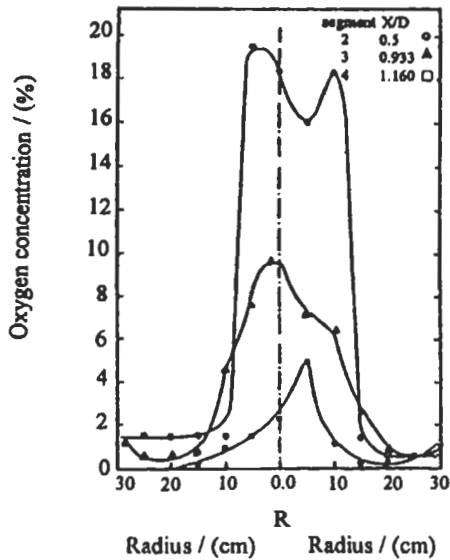


Fig. 5.13: Radial distribution of oxygen concentration at different segments of the FT at high firing conditions [773, 800].

Most of the features found in the low-firing case [799] are also evident in high firing case. As expected the distributions exhibited severe gradients in the early developing stages of the flame ($X/D = 0.5$). The core zone ($R/D < 0.166$) of the flame in this early stage, is characterized by poor mixing as shown by low CO_2 values coupled with low

gas temperature, where partial reaction certainly occurs in this zone as some production of CO is observed. The irregularities observed in the upstream distributions can be attributed to the non-uniformities in fuel and air streams. The former is caused by the interaction of the two fuel sprays, which are different in intensities, while the latter is caused by the finite number of vanes in the burner stabilizer disc. At a further downstream distance ($X/D = 0.833$), the highest temperature in the flame is around 1523 K. There are two off center temperature peaks identifying the reaction zone. It can be seen that the rate of reaction increased significantly between X/D of 0.5 and that at $X/D = 0.833$. This is also evident from the large increase of CO_2 concentrations particularly in the core zone, where $R/D < 0.166$. At this location, CO traces are still high, which indicate the still incomplete combustion, the O_2 concentrations decreased in the core region down to 10%.

At further distance X/D of 1.16, the temperature profiles exhibited higher values and still off center peaks can be identified. This leads to the conclusion that the reaction zone is still persistent at this location. The temperature off center peaks moved however towards the chamber walls indicating the flame spread. The corresponding CO_2 profile shows a trough in the core due to the low rate of reaction, but increases gradually towards the edges of the reaction zone. The CO_2 levels maintain their high value till the wall due to the effect of wall recirculation zone that recirculated hot products of combustion to the upstream sections. The O_2 profiles indicates very low concentration in the outer region with a small peak along the flame centerline. The peaks of the profiles, previously observed at upstream locations disappear and are smoothed out to fully developed temperature profiles. The temperature profiles at these locations exhibit a parabolic shape, the corresponding CO_2 profiles are shown to be flattened out at a value of 14%.

Figure 5.14 shows the radial profiles of soot concentrations, which is represented by the Bacharach soot number, BN. At the early stages $X/D = 0.5$, the observed soot concentrations were high in the center of the flame, where the fuel burns under rich conditions, and decrease at the outer zone. At $X/D = 4.62$, no peaks in soot distribution were observed and the reduction of soot levels is attributed to a reduction of its formation rate caused by disappearance of fuel and the increase of the oxidation reaction rate of soot particles due to expected high radical concentration in reaction zone (Bradley, Dixon-Lewis, Habik, El-Sherif and co-workers [43, 146-153, 807-813]). The peak values

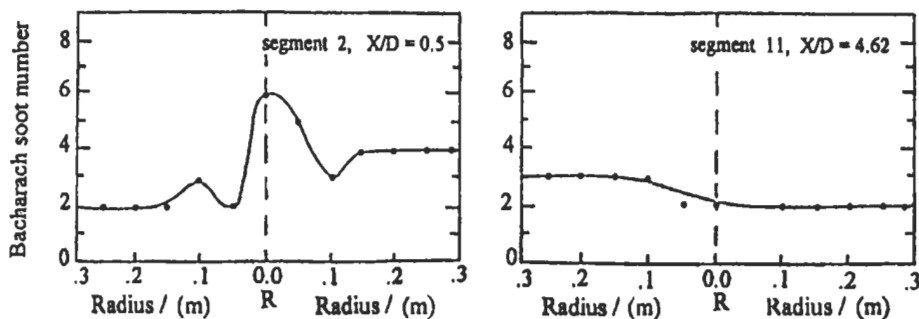


Fig. 5.14: Radial distribution of soot concentration for different segments of the FT at high firing conditions [773, 800].

of soot concentration coincided with those of CO (see Fig. 5.12) as would be anticipated. The comparison of soot profiles for low and high burner firing [800] conditions shows that the levels of soot for high firing are generally higher than for low firing condition. This can be attributed to the fact that the high firing flame is actually consisting of two interacting flames and the region of interaction is always suffering from oxygen deficiency and it takes too long time for oxygen to diffuse to this region. This will reduce the reactivity of one of the important chain branching reaction ($H + O_2 \rightarrow OH + O$) in kinetic mechanism, and consequently reduce the radical concentrations, H, O, and OH and hence reduce the reactivity of soot oxidation and increase its concentrations (El-Sherif [153] and Habik [155, 156, 813], see also chapter 2).

Radial velocity, temperature and CO_2 concentrations have been measured along the same flame tube, FT, by El-Mahallawy et al [801]. The fuel used was Diesel fuel (86.3% carbon, 12.8% hydrogen and 0.8-1.1% sulphur). An industrial burner type has been used in this experiment. The fuel mass flow rate was 90 kg hr^{-1} and mass air-fuel ratio was varied between 19 to 25. The measured axial velocity contours were constructed showing lines of constant velocity along the flame tube as shown in Fig. 5.15. They also found that the flame length, diameter, CO_2 concentrations, and temperature were decreased along the flame tube as the air-fuel ratio increased. In general, the results confirmed the finding in Refs. 799 and 800.

Also, El-Mahallawy [802] have investigated the effect of water-in-oil emulsion on the soot, CO_2 concentrations, gas temperature, flame length, and the total heat transferred to the walls and combustion efficiency in the same, FT, which was described before. Different percentages of water in oil emulsions namely zero, 10, 15, 18 and 21% were used during the test. These results show that the gas properties and the soot concentrations are significantly affected by the water-in-oil emulsions. Figure 5.16 shows the measured soot concentration in Bacharach scale, flame length, combustion efficiency, and the maximum temperature versus water-in-oil emulsion, w_{em} , all of which decreases as the water-in-oil emulsion increases. This indicated that it is possible to burn oil fuel with very low excess air, which may assure complete combustion of soot particles. Also, the results show that up to a certain value of w_{em} , the CO_2 concentration increases as the water-in-oil emulsion increases.

Heat Transfer

The effect of different operating conditions on the total heat transfer from the flame was studied on the tube described above by El-Mahallawy et al [772]. The total heat transfer is obtained from the measured values of the enthalpy rise of the cooling water flowing through the different cooling jackets. Figure 5.17 shows the measured total heat

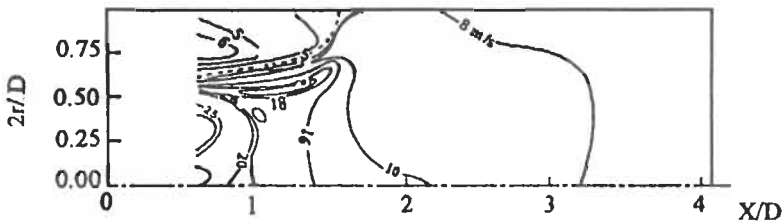


Fig. 5.15: The axial velocity contours for $A/F = 19$ and air swirl angle of 30 degrees [801].

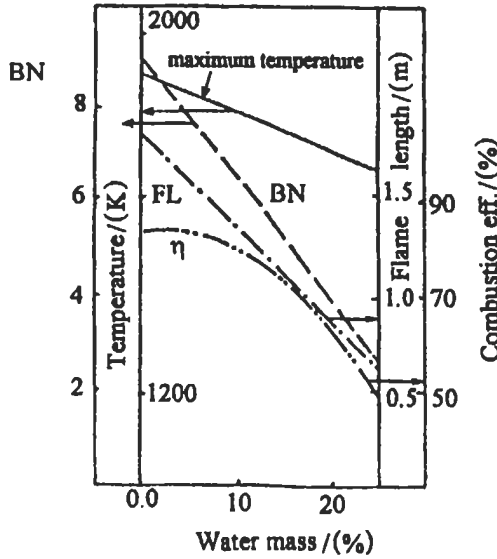


Fig. 5.16: The combustion characteristics curves of water in-oil fuel-emulsion .BN: Bacharach number, FL: Flame length, m [802].

flux to the flame tube wall for the flames of different input air-fuel ratios at constant air flow rate. Figure 5.18 shows the results for the case of constant fuel flow rate and for the same range of air-fuel ratio.

In Figs. 5.17 and 5.18, the distributions indicate that the variation of the air-fuel ratio has a slight effect on the location of maximum total heat flux, $X/D = 2.0$. This suggests

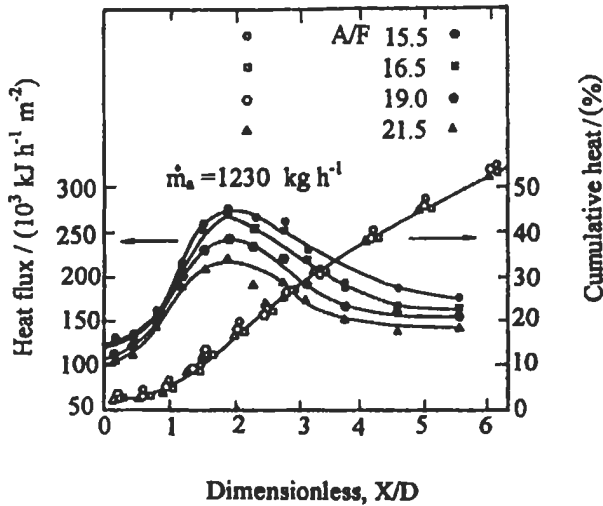


Fig. 5.17: Distribution of the total heat flux and cumulative total heat transfer along the flame tube at constant air flow rate and for different air-fuel ratios [772].

that the changes in the local flame properties associated with this range of air-fuel ratio are not significant to alter the general trend of the total heat flux distributions. In Fig. 5.17, constant air flow rate, the results indicated that the increase in the air-fuel ratio has a small effect on the observed total heat flux values at upstream distances of the flame tube. However, the change in heat flux is more significant at further downstream locations, $X/D > 1.5$. This reveals that at upstream sections, the variation in the input fuel flow rate (air-fuel ratio) is not linearly related to the expected variation in the reaction rate, and hence, to the resulting temperature and radiation emitting species which influence the heat transfer process. The distribution of cumulative total heat transfer corresponding to the results in Fig. 5.17 is shown in the same figure. The observed independence of the cumulative total heat transfer on air-fuel ratio is partly attributed to the changes in the thermal energy loading of the flame tube and to the small variations in heat flux at upstream sections.

The results of Fig. 5.18 reveals that constant fuel flow rate has a much stronger effect of the air-fuel ratio on the total heat flux values at upstream locations of the flame as compared to the previous case. This suggests that the local flame properties at the early stages of the flame are more sensitive to changes in the air flow rate than to changes in the fuel flow rate. The dimensionless cumulative total heat transfer distributions for this case are shown in Fig. 5.18. Here, the changes in air-fuel ratio are shown to alter the cumulative distributions.

Figure 5.19 shows the heat flux and dimensionless cumulative heat transfer distributions which are obtained with different air and fuel flow rates, at mass air fuel-ratio of 16.8. As expected, the results show an increase in the heat flux with the increase in the thermal loading of the combustor. The cumulative distribution suggests that a higher percentage of the input energy can be utilized in the flame tube when using a lower fuel flow rate.

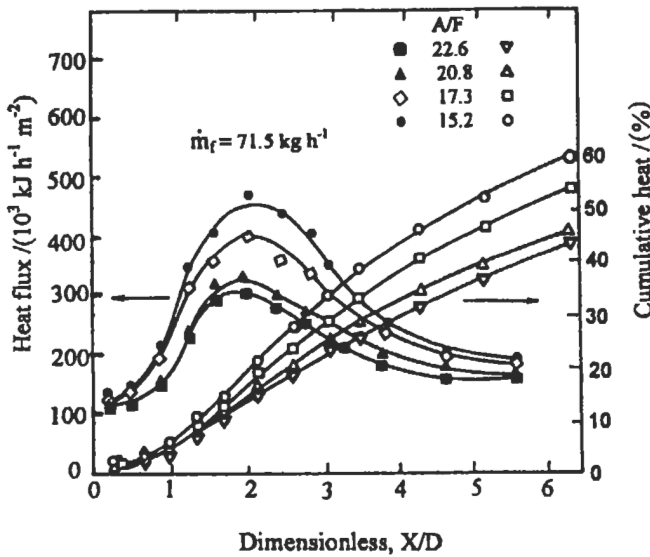


Fig. 5.18: Distribution of the total heat flux and cumulative total heat transfer along the FT at constant fuel flow rate and for different air-fuel ratios [772].

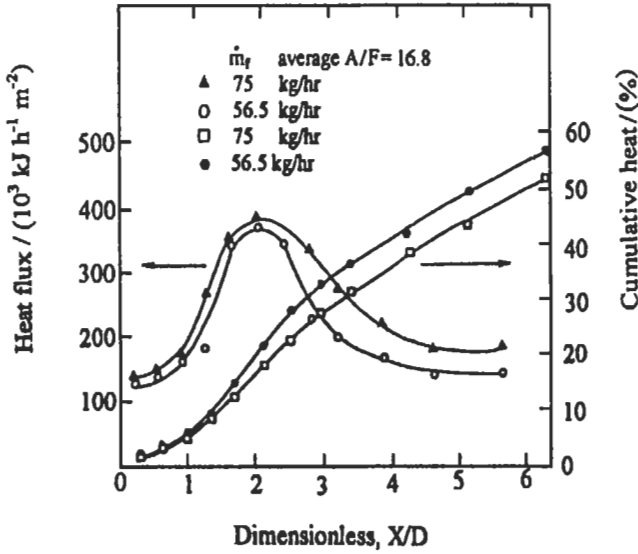


Fig. 5.19: Distribution of the total heat flux and cumulative total heat along the FT at an average air-fuel ratio of 16.8 [772].

El-Mahallawy et al [583] investigated the effect of cone swirler (see chapter 4) on the thermal efficiency and heat transfer in the above described flame tube. Their results are shown in Fig. 5.20, and it shows the heat flux distribution along the flame tube for cone swirler $45^\circ/55^\circ$ compared with that related to the conventional swirler [583]. It is evident that the cone swirler gives relatively uniform heat flux along the flame tube, which can be considered as an advantage, for most industrial applications like boilers, industrial furnaces and gas turbine combustion chambers.

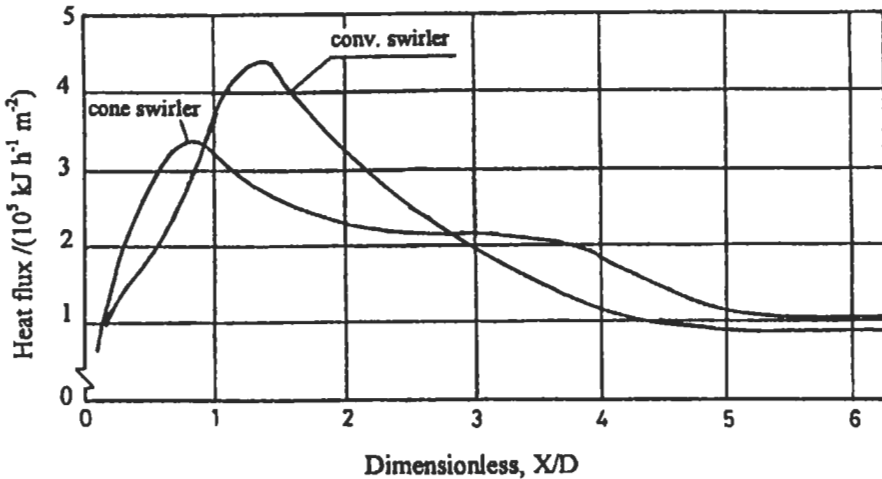


Fig. 5.20: Distribution of heat flux for cone swirler $45^\circ/55^\circ$ and the conventional swirler [583].

Computational Analysis and Results

The zonal method of analysis, which will be used in this section to predict the radiative heat has been already described in section 5.1.2. In order to apply this procedure to the flame tube described above, further computational analysis is presented with the predicted results in the following section:

Computational analysis. There are two ways of dividing the flame tube volume into gas elements. The first one is the annular division algorithm, while the second is the spherical division algorithm. The latter has proven to be faster on computing machines [759].

The annular division algorithm. The flame tube volume is divided into (IN) cylindrical segments, each having a width of DX(I). This gives a corresponding division of furnace wall into (KN) cylindrical surface elements, Fig. 5.21. Each of the cylindrical gas segments is divided into equi-area annular volume elements (JN).

Calculations are carried out for the view factors between a gas element (I, J) and its enclosing wall element K (K = I), and between this gas element and other wall elements (I ≠ K). Finally, the distribution of radiative heat along the furnace wall $q_{gs}(K)$ is given by:

$$q_{gs}(K) = \sum_I^{IN} \sum_J^{JN} \sigma A_g(I, J) VF_{I, J-K} \epsilon_g(I, J) \times (\bar{T}_g^4(I, J) - T_s^4(K)) \tau_{I, J-K} \left(\frac{1 + \epsilon_s(K)}{2} \right) \tag{5.42}$$

where $A_g(I, J)$ is the radiating area of the annular gas ring, VF is the view factor, ϵ_g is the gas emissivity, ϵ_s is the wall emissivity, τ is the gas transmissivity, T_g is the gas element temperature, and T_s is the wall element temperature.

The gas element emissivity is calculated from:

$$\epsilon_g(I, J) = \sum_{n=1}^3 a_{g,n} (1 - \exp(-\alpha_n B_L(I, J))) \tag{5.43}$$

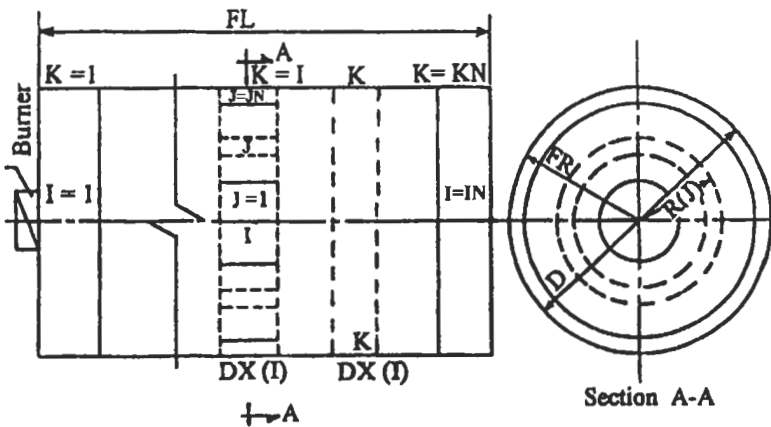


Fig. 5.21: The annular division of the flame tube [759].

where $B_L(I,J)$ is the beam length for finite optical thickness and is calculated by:

$$B_L(I,J) = \frac{0.9D}{JN \left(\sqrt{J/JN} + \sqrt{(J-1)/JN} + \frac{D}{DX(I) * 2JN} \right)}$$

The gas/soot weighting factors, $a_{g,n}$, are found to vary linearly with gases temperature, such that [782];

$$a_{g,n} = b_{1,n} + b_{2,n} \overline{T_g}(I,J) \tag{5.44}$$

The absorption coefficients, α_n , are found by adding the absorption coefficients for gas and soot in each spectral region, as follows:

$$\alpha_n = \alpha'_{c,n} \rho_c + \alpha'_{g,n} (P_{CO_2} + P_{H_2O}) \tag{5.45}$$

The values of the constants $b_{1,n}$ and $b_{2,n}$, and the specific absorption coefficients $\alpha'_{c,n}$ and $\alpha'_{g,n}$, are given by Ref. 776, and ρ_c is the soot concentration.

Full details of this calculation procedure are given by Ref. 759.

The spherical division algorithm. The flame tube volume is divided into gas segments each having a width of $DX(I)$. This gives a corresponding division of tube wall into (KN) cylindrical elements. The segment mid cross-sectional area is divided into equi-area rings (JN) . Then, the volume of the gas segment is transferred into spherical coinciding shells with the same radii of divisions $R(J)$, concentric and coaxial with the gas element. The division should be considered with care, that is, having small deviation between the volume of furnace and the spherical shells. The spherical division is illustrated in Fig. 5.22.

The view factor for normal radiation between the spherical gas element (I, J) and the cylindrical wall element $(K = I)$ and the view factor for inclined radiation and wall element $(K \neq I)$ are given by Ref. 759.

The gas emissivity, $\epsilon_g(I,J)$ is calculated as described above in Eqs. 5.43, 5.44 and 5.45,

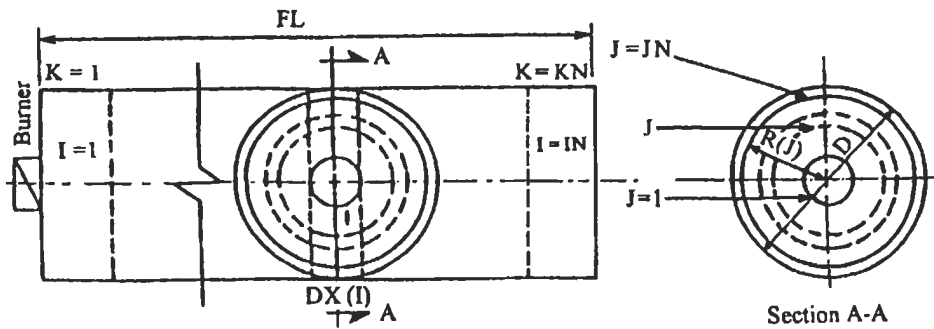


Fig. 5.22: The spherical division of the flame tube [759].

while the gas radiation mean beam length of a spherical element is given by:

$$B_L(I, J) = \frac{0.65D(J^{1.5} - (J - 1)^{1.5})}{\sqrt{JN}(2J - 1)} \tag{5.46}$$

The distribution of radiative heat along the furnace wall is calculated as described above by Eq. 5.42.

Computational results. The developed computer program based on the computational algorithm described above in section 5.1.2.3 has been fed with the adequate data [781, 799-800] for FT using different configurations of computational grids for both types of annular and spherical division algorithms. The computational grid geometry and specifications for the spherical division algorithm and the annular division algorithm are shown in Figs. 5.23 and 5.24, respectively. One test case of study was implemented here for the fired-tube boiler, which is firing 114.7 kg h⁻¹ of light oil fuel with air-fuel mass ratio of 15.5. The predicted profiles of radiative heat flux distributions along the flame tube (FT) and the measured data [772, 773, 781, 799, and 800], are shown in Fig. 5.25 for the annular division algorithm, and in Fig. 5.26 for the spherical division one. Both profiles reveal an increase in the heat flux values in the axial direction to a peak value at a location around X/D = 2, after which a decrease is enhanced towards the end of the furnace where the heat flux tends to flatten. The shape of profiles is quite matching with measured data profiles. Comparison with the measured total heat flux values along the furnace reveals that the radiant energy contributes with the major part of flux on furnace wall. The convective heat shares with small amount not higher than 12 kW m⁻². The values of convective heat would correspond to a value of heat transfer coefficient in the order of 12 W m⁻² C⁻¹, which is experienced in such types of combustion chambers where no impingement takes place. The agreement between the predictions and the measured data is quite obvious. This

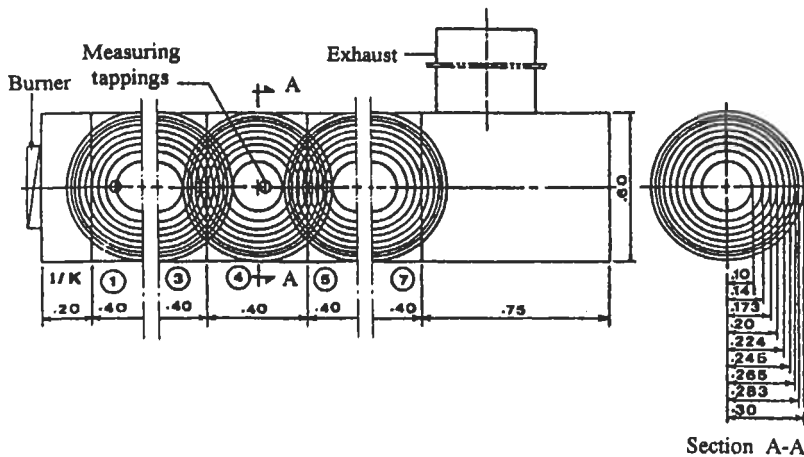


Fig. 5.23: Details of the computational grid for the spherical division algorithm of the flame tube [759].

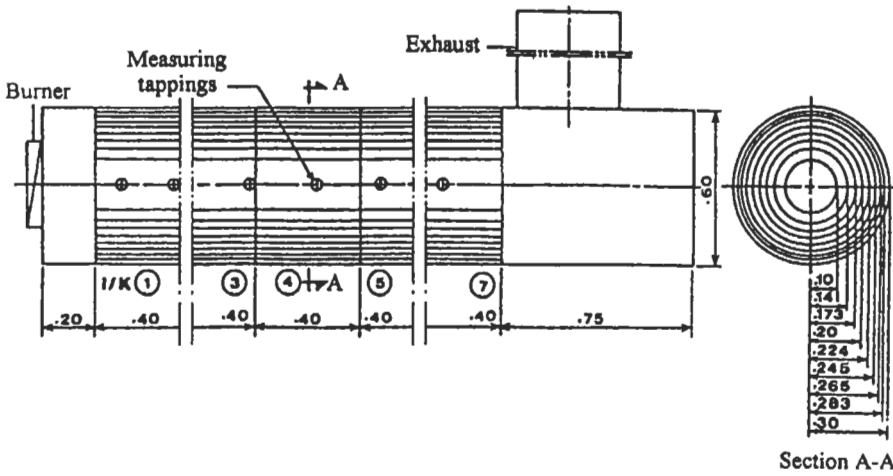


Fig. 5.24: Details of the computational grid for the annular division algorithm of the flame tube [759].

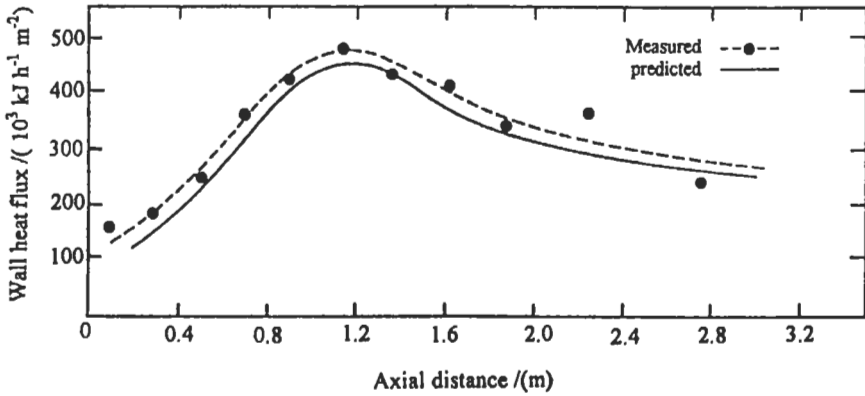


Fig. 5.25: Axial distribution of the measured total heat flux and the predicted profile of radiative heat flux along the wall of flame tube using annular division algorithm [759].

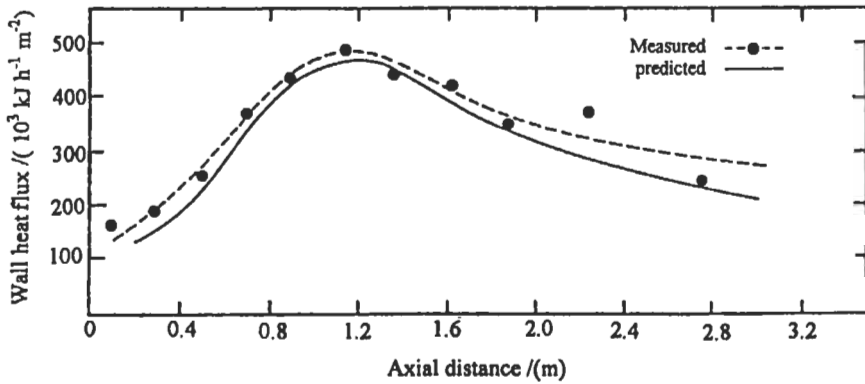


Fig. 5.26: Axial distribution of the measured wall heat flux and the predicted profile of wall radiative heat flux along the wall of flame tube using spherical division algorithm [759].

also concludes that in the case where the enclosed volume and wall is being divided has no influence on the predicted results as long as the division is handled properly and relevant input data is being fed. On the other hand, the profile of gas emissivity along the flame tube is shown in Fig. 5.27, while the radial distributions of gas elements emissivity using both furnace divisions is shown in Fig. 5.28. The results in both figures are quite in correspondence with the radiative heat flux profile.

El-Mahallawy et al [769] have continued their theoretical investigation of the flow pattern, temperature contours and heat transfer by radiation in the above described FT. They measured the velocity, temperature and heat transfer rates along the flame tube. A prediction procedure, that solves the conservation equations of the various entities, was successfully used to produce computed velocities, temperatures and heat flux distributions. A two-equation turbulence model, a combustion model and a discrete ordinates radiation model were used to approximate the various characteristics of the flow. The combustion model solved the Eulerian equations of the gas phase, and the Lagrangian equations of the droplet motion, heating, evaporation and combustion are

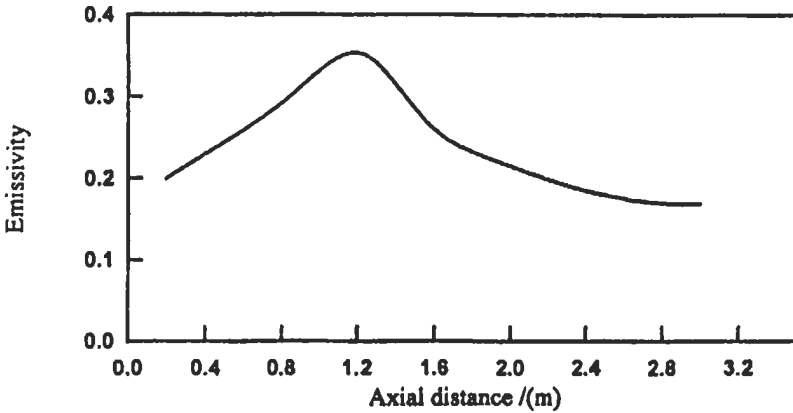


Fig. 5.27: Predicted distribution of gas segments emissivity along the flame tube [759].

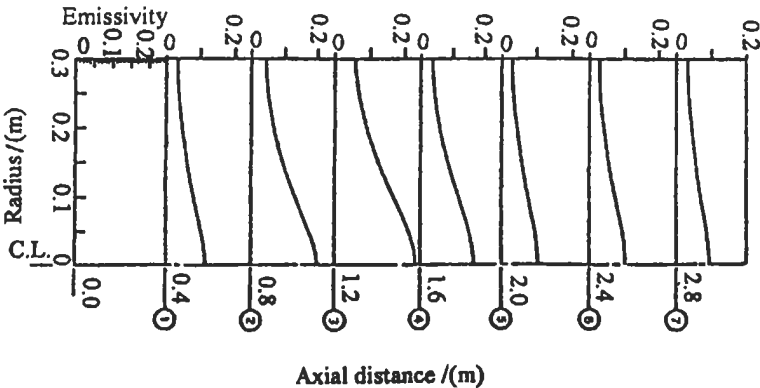


Fig. 5.28: Radial distribution of predicted gas emissivity along the axis of the flame tube [759].

used. Figures 5.29 and 5.30 show the measured and calculated distributions of total, q_t , and radiative, q_r , wall heat flux for various swirl numbers. The effect of changing the combustion air swirl number was significant; the wall heat flux increases as the swirl intensity increases. The reason is due to enhancement of swirl, turbulence and mixing, hence, more heat is transferred to the wall. However, the heat flux increases along the wall to a peak value which coincided with the location of the reattachment point (end of corner recirculation zone). At this stagnation point, high values of kinetic energy of turbulence, and consequently high turbulent diffusion of heat occurs. At the low swirl number, characterized by a larger corner recirculation zone, the location of peak wall radiative heat flux is shifted downstream and the value of this peak decreases. These observations suggest that, as the swirl number increases, the furnace can be shortened to achieve the same thermal loading. Both measured and calculated total and radiative wall heat flux distributions as shown in Fig. 5.29, are in reasonable agreement with discrepancies of the order of 10 %.

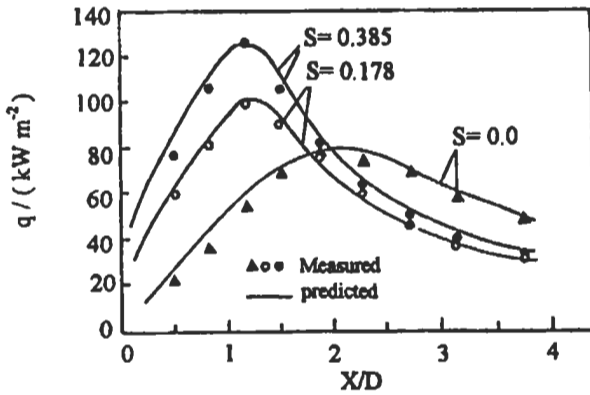


Fig. 5.29: Measured and calculated wall heat flux distribution, for air to fuel ratio of 20 and different values of swirl number (S) [769]. Reproduced by permission of ASME.

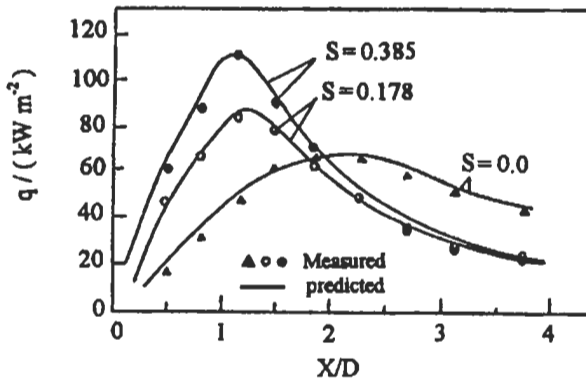


Fig. 5.30: Measured and calculated radiative heat flux distributions for air to fuel ratio of 20 and different values of swirl number (S) [769]. Reproduced by permission of ASME.

Discrete Ordinates Method (DOM) has been the most widely used technique for obtaining numerical solutions to radiative transfer equation (RTE). The DOM has many important advantages that account for its popularity. Apart from the obvious ease with which the method can be incorporated into Computational Fluid Dynamics (CFD) calculations due to its compatibility with the solutions of differential equations for turbulent, reacting and radiating flows, it is computationally efficient [814] and relatively easy to code, and requires single formulation to invoke higher order approximation. Selcuk and Kayakol [815, 816] investigated the solution accuracy of DOM by predicting the distributions of radiative flux density and source term of a rectangular enclosure problem and comparing the results with exact solution produced previously for the same problem. The problem was based on data taken from a large-scale experimental furnace with steep temperature gradient typical of operating furnaces.

The DOM has been used recently by Kayakol et al [817] to predict the incident radiative heat fluxes at the walls of a gas turbine combustor simulator (GTCS), and the predicted results are compared with the measurements. More details about these results will be discussed in section 5.1.5.2.

5.1.4.2 Vertical Flame Tube of Circular Cross Section

Experimental Study

Having discussed above about the flame structure and heat transfer in horizontal flame tubes, it is necessary now to study such characteristics for vertical flame tubes. This will eliminate the effect of gravity on having an unaxisymmetrical flame. Hence, El-Mahallawy et al [766] have investigated the effect of the swirl angle of combustion air, the swirler to furnace diameter ratio, and the air-fuel ratio on the flame radiation in a vertical cylindrical oil-fired furnace. The test rig for this study is shown in Fig. 5.31, and it consists of seven water-cooled axial segments, each of 0.4 m inner diameter and 0.14 m height. It is fired by a kerosene fuel jet emerging from a swirl atomizer surrounded by a swirling jet of combustion air. Swirlers of different diameters and swirl angles are used. Three swirler to tube diameter ratios of 0.25, 0.3 and 0.45 (D_s/D_1) were tested at different air-fuel ratios of 18 to 24.

The gas temperature was measured by a water-cooled one shield suction pyrometer described in Ref. 768 and the red brightness temperature was measured by a filament pyrometer. The measurement of flame radiation was carried out by a total radiation pyrometer. The flame radiation is collected and focused upon the hot junction of a thermopile such that, a temperature difference and hence a voltage difference exists between the hot and cold junctions. The pyrometer was calibrated against spherical black body furnace at different temperatures. The experimental values of the gas temperature and the red brightness temperature are used in the calculation procedure mentioned above in section 5.1.2.3 to get the flame emissivity and radiation to the furnace wall segments for the different parameters considered. The general trend of the mean effective radiating temperature (\bar{T}_g) is given by Eq. 5.39.

Figure 5.32 shows that the value of \bar{T}_g increases with the increase of combustion air swirl. For 30° swirl, long type flames are formed where the fuel jet is able to penetrate the internal reversal flow zone set up by the swirling of combustion air. Also, the mixing of fuel and air is not complete and unfavorable regions of high fuel-air ratio

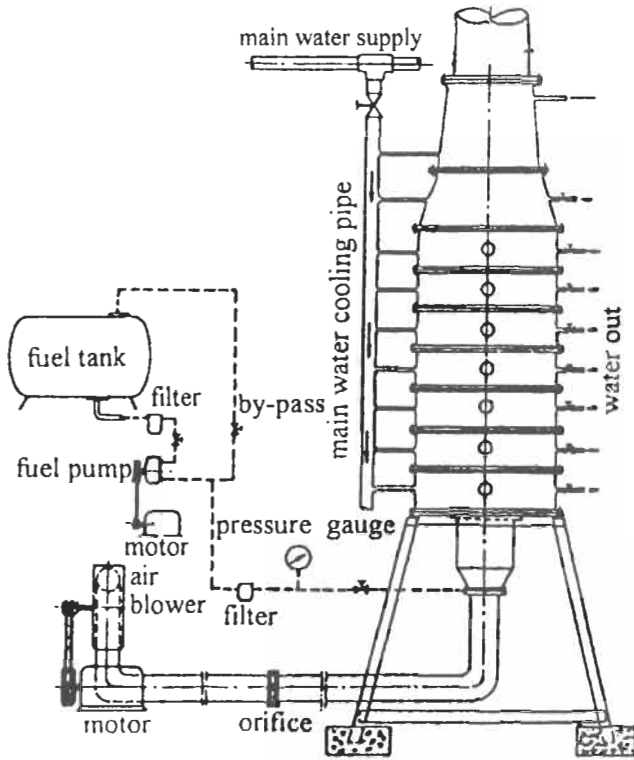


Fig. 5.31: Vertical flame-tube test rig [766].

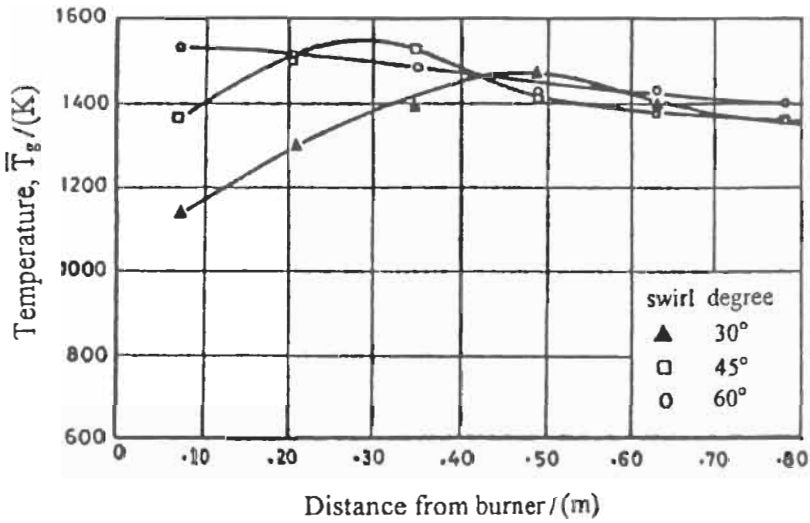


Fig. 5.32: Effect of degree of swirl on the distribution of mean effective temperature along the flame tube ($A/F=19$) [766].

exist where unreacted combustible mixture is formed. Moreover, for 60° swirl, hot combustion products are entrained from the reverse flow into the fuel jet which becomes heated before it mixes with the remaining combustion air and this leads to a short and efficient flame in this case. It is generally noticed that, the soot concentration is markedly increased for 30° swirl and leads to an observable increase in total flame emissivity as shown in Fig. 5.33.

Figure 5.34 shows that the flame radiation is higher for low values of air-fuel ratio, and this is expected due to the increase of flame temperature and emissivity with the decrease of air-fuel ratio as shown in Fig. 5.35. Also, Fig. 5.36 shows that the

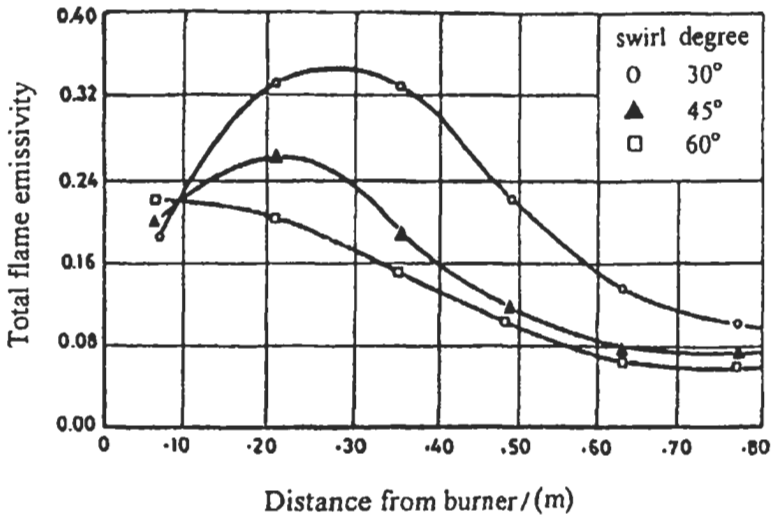


Fig. 5.33: Effect of degree of swirl on total emissivity distribution along the flame tube (A/F = 19) [766].

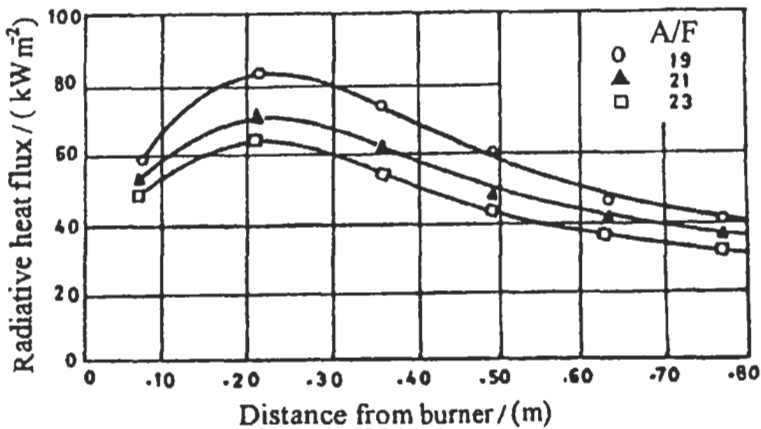


Fig. 5.34: Effect of A/F ratio on the distribution of radiative heat flux along the flame tube (45° swirl and $D_1/D_t = 0.35$) [766].

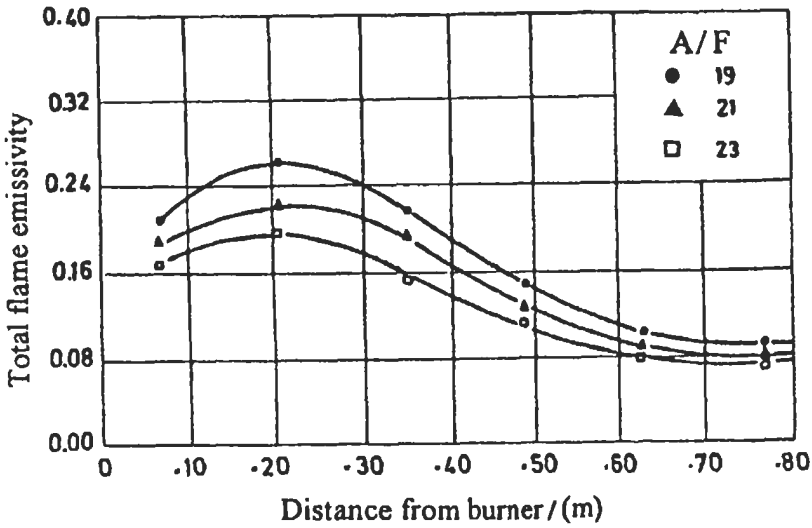


Fig. 5.35: Effect of A/F ratio on the total emissivity distribution along the flame tube (45° swirl and $D_s/D_t = 0.35$) [766].

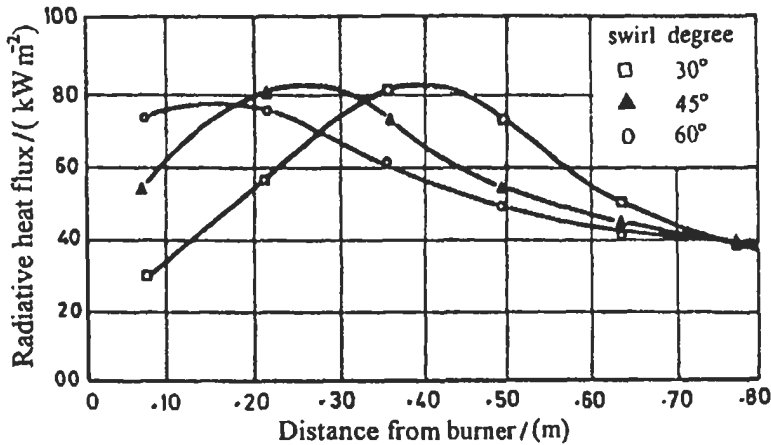


Fig. 5.36: Effect of degree of swirl on the distribution of radiative heat flux along the flame tube ($A/F = 19$) [766].

distribution of flame radiation intensity is greatly affected by the swirler angle [766]. At the upstream section, the higher values of flame radiation are for 60° swirl due to high temperature level, while less values are for 30° swirl. Also, at $X/D = 1.125$, the 30° swirl had the highest temperature and emissivity and hence the highest radiation. At down-stream sections, as the combustion is completed and non-luminous gases dominate, therefore, the differences in temperature and emissivity are small and thus the values of flame radiation get close for different degrees of swirl. The results of Fig. 5.37 show that the increase of the swirler to furnace diameter ratio (D_s/D_t) has insignificant effect on the radiation intensity to the flame tube wall.

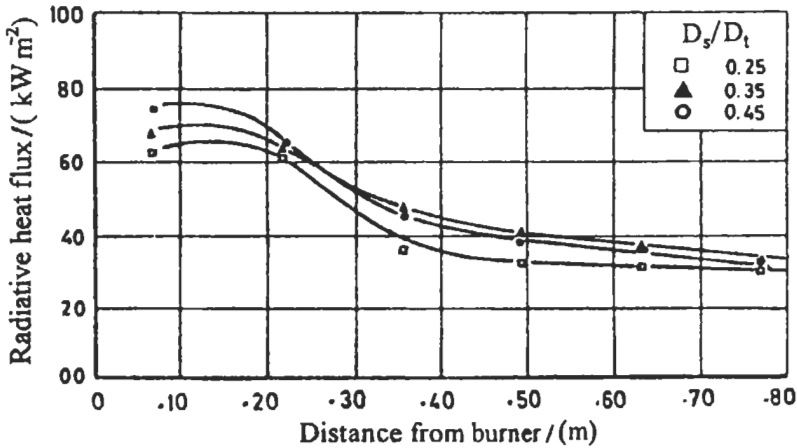


Fig. 5.37: Effect of D_s/D_t on the distribution of radiative heat flux along the flame tube ($A/F = 23$ and 60° swirl) [766].

Computational Analysis

The method of calculation is described before in section 5.1.2.3 (case 1) and is based on the zonal exchange method; in which the furnace or the flame tube is divided into several gas rings in the radial direction. The luminous part of the flame emissivity is calculated from the above measured flame temperature and flame red brightness temperature, while the non-luminous part is determined from the values of gas temperature and the partial pressure of both carbon dioxide and water vapour.

Figures 5.38 (a) and (b) show sketches, which represent the radiative heat exchange between different gas rings and wall segments as described before in section 5.1.2.3. In order to avoid complexity and make the problem easier to be approached, the following simplifying assumptions were suggested and used by Yowakim et al [762] to calculate the radiative flux in vertical flame tube:

- i. Each gas ring is considered of uniform temperature, composition and emissivity.
- ii. Multi gas scatter and surfaces reflections are neglected and the radiation reaching any surface segment is considered due to the emission of different gas zones. This is strictly true for perfect black surfaces only. However, for surfaces of high emissivities the error is usually negligible.
- iii. The surface of each wall segment is considered of uniform temperature.
- iv. Consider a cylindrical wall segment receiving radiant energy from different gas rings in the furnace, and according to assumption (ii), the radiant heat transmitted to this surface, q_{R_i} , consists of radiation to the wall segment, i from its enclosed gas rings, $q_{R_{ei}}$, and radiation from other gas rings, $q_{R_{oi}}$ as:

$$q_{R_i} = q_{R_{ei}} + q_{R_{oi}} \quad (5.47)$$

The following part represents the methods of calculations of these two parts ($q_{R_{ei}}$ and $q_{R_{oi}}$):

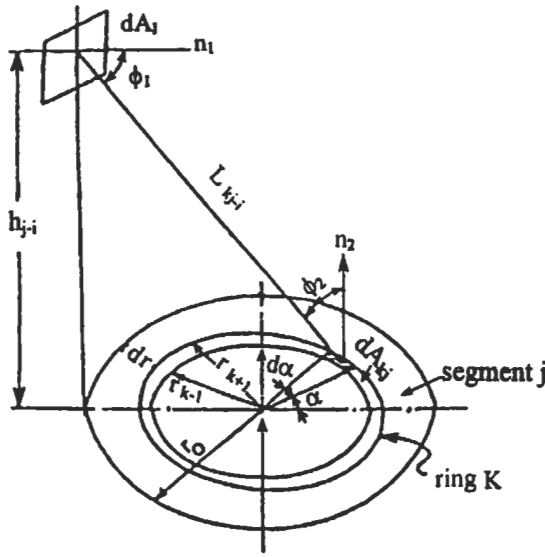


Fig. 5.38 (a): Determination of the view factor between a gas ring K enclosed in a gas segment j and a wall element dAi [762].

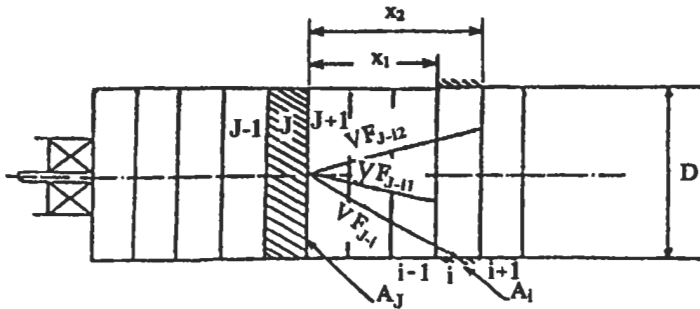


Fig. 5.38 (b): View factor between gas segment and surface area, j for gas segment and i for the cylindrical surface area [762].

(a) Radiation to wall segment i, from its enclosed gas rings. If a certain gas segment j, enclosed by a wall segment, i (j = i in this case), is divided into m_r gas rings, then the radiation to wall segment, i, is given by:

$$q_{R_{oi}} = \sum_{\substack{k=1 \\ j=i}}^{k=m_r} q_{R_{kj}} \tau_{kj-i} \quad (j = i) \tag{5.48}$$

when $\lambda_{k,j-i}$ is the intervening gas layer transmittance between gas ring K, enclosed in gas segment J, and the surface segment i.

where the value of $q_{R_{kj}}$ is given by:

$$q_{R_{kj}} = \sigma V F_{kj-i} \left(\frac{\epsilon_i + 1}{2} \right) \epsilon_{kj} \bar{T}_{kj}^{1.5} \left(\bar{T}_{kj}^{2.5} - T_i^{2.5} \right) \quad (5.49)$$

This equation is based on the assumption that the ratio of α_g/ϵ_g (absorptivity/emissivity) is equal to $(\bar{T}_g/T_i)^{1.5}$ [818] for low values of gas emissivity.

(b) Radiation from other gas rings. The radiation from a gas segment, j , divided into a number of gas rings, k , to a wall segment, i ($j \neq i$), is given by:

$$q_{R_{j-i}} = \sum_{\substack{k=1 \\ j \neq i}}^{k=m_r} G_{kj} S_i \bar{W}_{kj} \quad (j \neq i) \quad (5.50)$$

where $G_{kj} S_i = V F_{kj-i} \tau_{kj-i}$, and $\bar{W}_{kj} = \sigma \left(\frac{\epsilon_i + 1}{2} \right) \epsilon_{kj} \bar{T}_{kj}^{1.5} \left(\bar{T}_{kj}^{2.5} - T_i^{2.5} \right)$

Calculation of flame emissivity. The radiation from oil flames is due to soot particles formed by thermal cracking of hydrocarbons, which causes the luminous part of flame emissivity, while water vapor and carbon dioxide cause the non-luminous part. Hence the total emissivity is given by:

$$\epsilon_{tot} = \epsilon_{NL} + \epsilon_L \quad (5.51)$$

and

$$\epsilon_{NL} = \epsilon_{CO_2} + \epsilon_{H_2O} - \epsilon_{CO_2} \epsilon_{H_2O} \quad (5.52)$$

Each component of the total flame emissivity is treated separately in the following analysis.

Luminous flame emissivity. The red brightness temperature, T_r , and the average gas temperature, T_g , are sufficient for the determination of the absorption strength, KL . However, it was found that the relationship between luminous flame emissivity, gas temperature and the absorption strength could be expressed by [640, 772]:

$$\epsilon_L = 1 - \exp\left(-0.236(KL)(\bar{T}_g/1000)^{1.39}\right) \quad (5.53)$$

and also the absorption strength could be given by:

$$KL = 0.232 \left(\frac{T_r}{1000} \right)^{2.92} \left(\frac{T_r}{T_g} \right)^{15.88} \quad (5.54)$$

This formula is correct for emissivity ranging from 0.0 to 0.8 and gives values within $\pm (2-3)\%$ difference from those obtained by Ref. 780. These equations are more suitable for the computational procedures. It should be noted that the red brightness

temperature that is required must be determined experimentally and could be considered as an average value for each gas segment.

Details of the calculation of the absorption strength, the non luminous emissivity and the mean beam length for each gas ring is given by Ref. 762.

The sum of the radiation from all rings, except the enclosed ones, will be:

$$q_{R_{oi}} = \sum_{\substack{j=1 \\ j \neq i}}^{j=m} \sum_{k=1}^{k=m_r} G_{kj} S_i \bar{W}_{kj} \tag{5.55}$$

where m is the number of gas segments (surface wall elements). Therefore the radiant heat intercepted by surface, i , from all gas rings is given by:

$$q_{R_i} = \sum_{\substack{k=1 \\ j=i}}^{k=m_r} q_{R_{kj}} \tau_{j-i} + \sum_{\substack{j=1 \\ j \neq i}}^m \sum_{k=1}^{m_r} G_{kj} S_i \bar{W}_{kj} \tag{5.56}$$

The differential value of the view factor of the elemental surface wall area dA_i with respect to the annular area of the gas ring k in a gas segment j ($j \neq i$) (see Fig. 5.38) is given by Yowakim et al [762].

A computer program was used to predict different terms in Eq. 5.56 as well as of equations in section 5.1.2.3, and the predicted radiant heat is shown in Fig. 5.39. This figure shows a comparison between the results of this computational procedure and the experimental results as applied to the above vertical cylindrical oil-fired flame tube [766].

5.1.4.3 Horizontal Flame Tube of Square Cross Section

The above investigations were limited to the cylindrical flame tubes, while the tubes of square cross-section, which simulate the geometry of some industrial furnaces, have been the subject of some studies such as by Wahid et al [804]. The test rig used is a segmented water-cooled flame tube of square cross section 0.4 m x 0.4 m and 1.8 m in

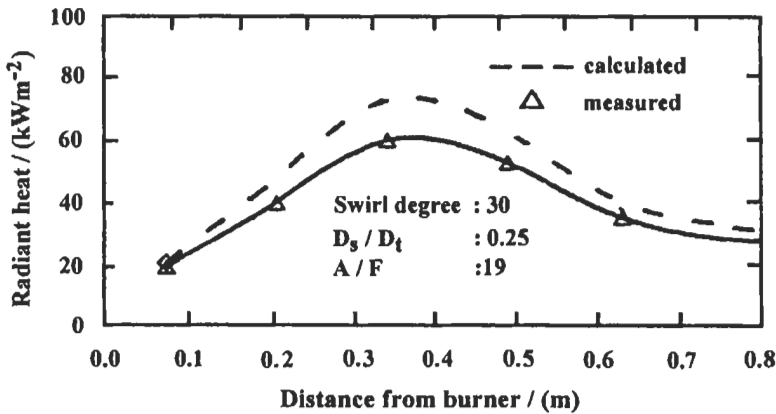


Fig. 5.39: Comparison between experimental and calculated values of the heat transfer by radiation in a vertical cylindrical flame tube [762, 766].

length fired by light Diesel fuel industrial burner. The fuel mass flow rate was 30.6 kg h^{-1} and the air-fuel mass ratio was varied between 14.93 to 20.73. The study of the flame structure includes temperature, CO_2 , CO , O_2 , and soot concentrations measurements.

Figure 5.40 shows the effect of variation of air-fuel ratio on the distribution of heat transfer along the tube. The figure shows that the influence of air-fuel ratio is more pronounced by keeping constant air flow rate and varying the fuel flow rate. This is attributed to the increase of the thermal energy loading of the tube. Figure 5.41 shows the axial distribution of the total heat flux to the wall at different swirl angles. It is seen that increasing swirl angle leads to an increase of the total heat flux and reduction in the flame length. This in turn shifts the peak of the curve towards the upstream sections of the tube. The axial distributions of the increase of enthalpy of gases, the heat transferred to the tube wall, and the total heat liberation, represented in a non-dimensional form, are shown in Fig. 5.42. Details of the calculation of the enthalpy of gases and heat liberation along the furnace are given in chapter 4. It can be seen that most of the enthalpy increase occurs in the upstream sections.

From the axial distribution of the heat liberation along the tube, it can be seen that the rate of the total heat liberation highly increases at the upstream sections of the tube. The distance from the burner tip to the location where the slope of the heat liberation distribution curve is zero represents the flame length, although it may be slightly different from the visible length of the flame. The figure also shows that the maximum total heat liberation is always less than the input chemical energy, this may be attributed to incomplete combustion of the fuel, and the unaccounted for losses.

Following the above experimental results, Wahid et al [806] continued their work to predict the radiative heat from the gases to the inner surface of the tube described above. They have used the zone method in similar way to that used by El-Mahallawy

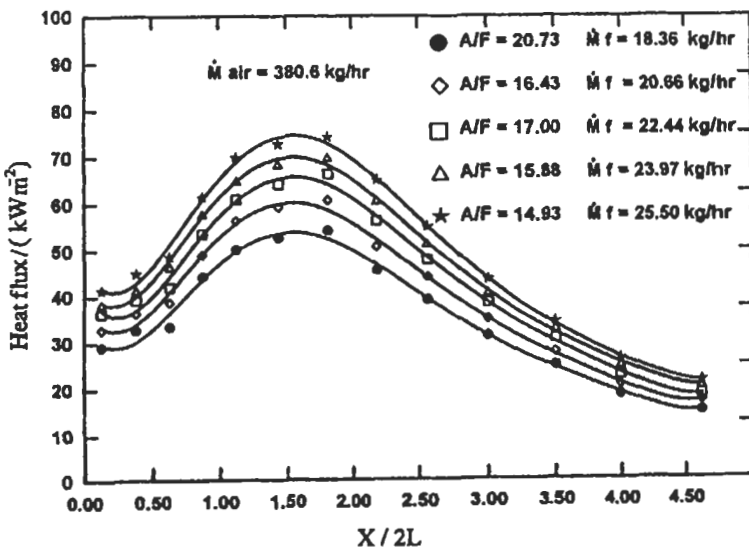


Fig. 5.40: Effect of variation of air-to- fuel ratio keeping air flow rate constant on the distribution of heat transfer along the flame tube, $2L = 0.4 \text{ m}$ [804].

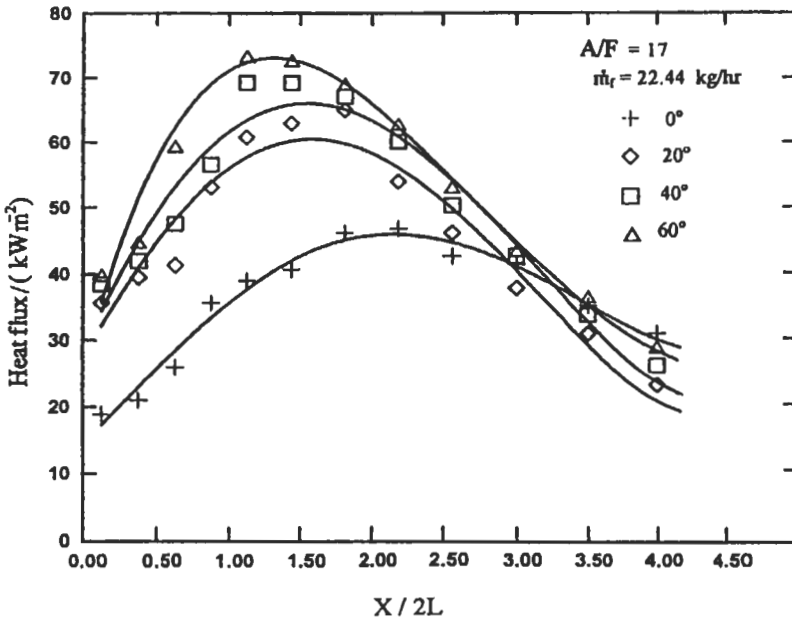


Fig. 5.41: Effect of variation of swirl angle on the distribution of the total heat transfer along the flame tube, 2L = 0.4 m [804].

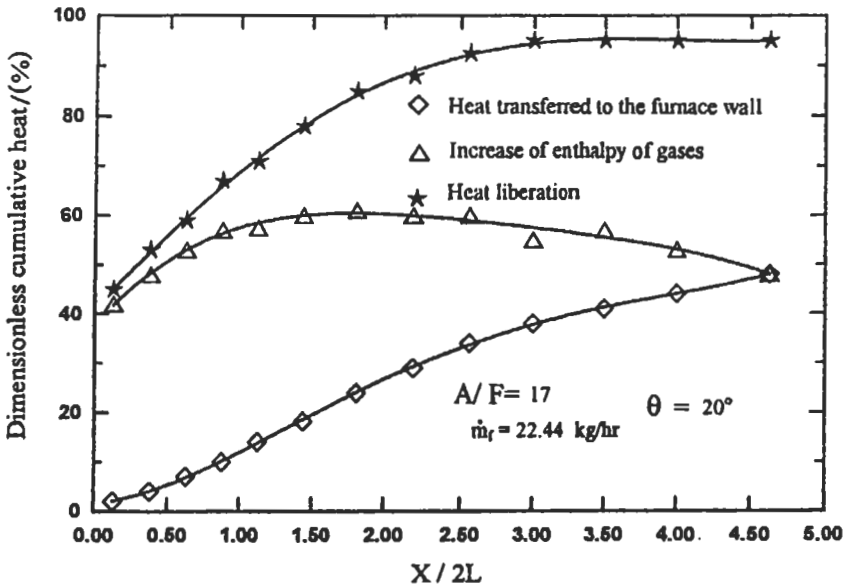


Fig. 5.42: Axial distribution of increase of enthalpy of gases, heat transferred to the flame tube wall, and heat liberation along the flame tube, 2L = 0.4 [804].

and Rezk [759] as described in section 5.1.2.3. The mathematical modeling of the “zone method” for the tube has been developed by dividing the furnace volume into rectangular parallelepipeds. The radiative heat is calculated in terms of gas temperature, emissivity, transmissivity and the view factor. The gas emissivity is calculated as a function of the gas temperature, soot concentration and partial pressure of the emitting gases. The convective coefficient of heat transfer is taken from Eq. 5.57 [760], where it increases with the increase of the swirl angle θ :

$$h_{c\theta} = h_{c0} (1 + 0.014 \theta) \tag{5.57}$$

where $h_{c\theta}$ and h_{c0} are the coefficient of heat transfer by convection with and without swirl, respectively. The predicted radiative heat flux profiles are shown in Fig. 5.43 and comparison with the corresponding measured profiles of total heat flux is given in Fig. 5.44. In this figure, the measured total heat flux values along the tube are compared with the summation of predicted radiative and convective heat flux values. The agreement between the predictions and the measurements is shown to be fairly good, either qualitative or quantitative.

5.1.5 Combustion and Heat Transfer in Water-Tube Boilers

In power stations boilers, some combustion-generated problems are known to have undesirable effects and can probably cause failure of some parts of the boiler. Particularly with severe loading variations, such problems stem mainly from, among others, poor burners design (e.g. number of burners, their relative positions and burner type), incorrect choice of boiler operating conditions including type of fuel, air to fuel

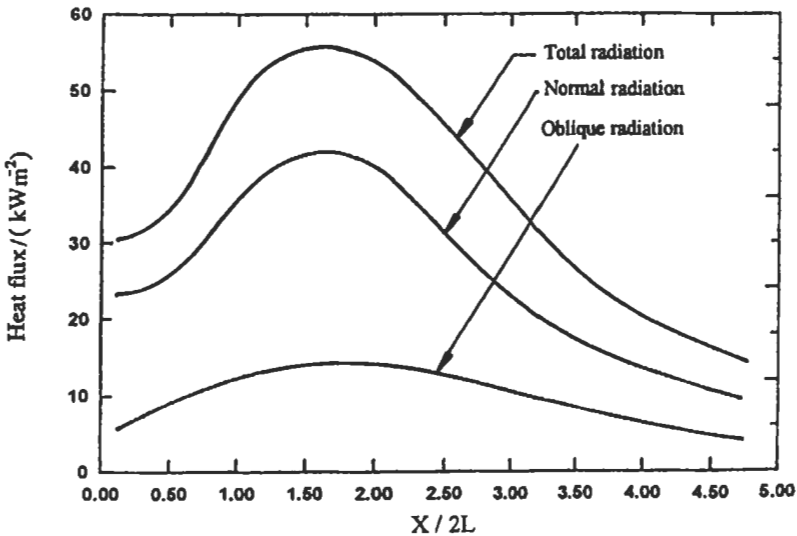


Fig. 5.43: Predicted profiles of radiative heat flux along the flame tube for fuel flow rate 22.4 kg h^{-1} , air-fuel ratio 17 and 20° air swirl [806].

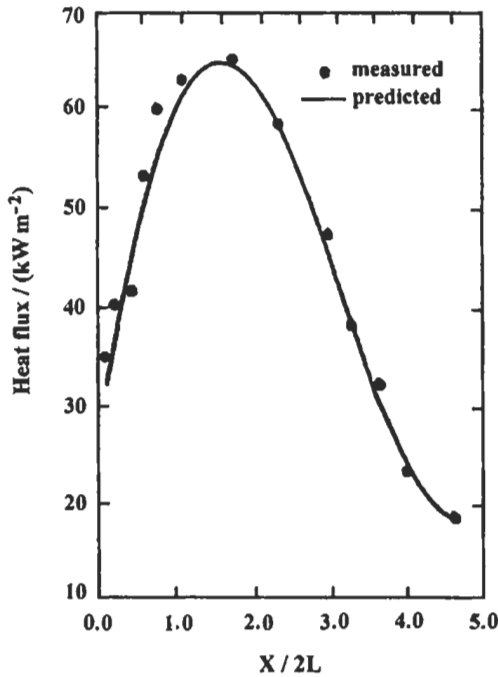


Fig. 5.44: Axial distribution of predicted and measured total heat flux along the flame tube for the same data of Fig. 5.43 [806].

ratio, and burner loading. In addition to those, if the excess air factor is incorrectly adjusted, it causes a reduction in boiler efficiency and increased pollutant formation levels and high levels of SO_3 at higher excess air factors. This is in turn coupled with a decrease in the dew point temperature, which promotes the formation of sulphuric acids that enhance the corrosion of air preheaters and exhaust ducts [771, 805]. Measurements of mean velocities, gas temperature and species concentrations as well as wall heat flux distribution have been performed at IFRF [819, 820] in a horizontal squared sectioned furnace of $2 \times 2 \times 6.5$ m length. The effects of burner arrangement and fuel type on the flame characteristics are also investigated [821]. Some investigations were also reported on actual boiler furnaces, such as those reported by Godridge [822], Lamb [823], Arscott et al [824] and Anson et al [825]. The reported data were incomplete to enable an overall flow pattern, combustion analysis to be build up and further experimental data is still needed to cover the multi-burner arrangements in the sense of practical boiler furnaces. To cover this lack of information, El-Mahallawy et al [761, 771, 799, 800, 805] had designed an experimental test facility as a model of water-tube boiler (MWB) to investigate the heat transfer characteristics under different operating conditions as well as configuration of a multi-flame system. Furthermore, the heat transfer characteristics of the impingement of a single and multi-flame was also investigated experimentally and theoretically. This study is motivated by the need to rationalize the fuel consumption in water-tube boiler furnace through a better understanding of the aerodynamic, combustion and heat transfer. This section will cover such investigations.

The model of water-tube boiler test rig (MWB) [759, 781, 799, 800] is shown in Fig. 4.45. The model dimensions were determined to represent average value of the ratio between depth/width of most of the water-tube boilers in existing steam power stations. The test section is of the vertical type chamber having a square cross section of 2×2 m, with a height 4 m. The furnace water-tube walls (53 mm inside diameter) have 27 tubes, each. The burner wall has only a 2 m height of water tubes at the top section.

To allow for convenient measurement facilities, measuring tappings are furnished in each wall for the measurements of wall heat flux, and for the insertion of probes for temperature, velocity, species and soot concentrations measurements. The tappings were made in the same level and position in the two opposite side-wall to allow for probe insertion from both sides, and thus reducing the length of different probes traverses. The available number of tappings on the right hand side-wall was 85, while on the left and rear walls were 108 and on the burner wall was 36. Nine burners were accommodated in the burner wall in an arrangement of three rows by three columns. The burners have the main features of industrial type burners. They comprise a fuel nozzle and a stabilizer disc with a built-in vane-swirler and a holder with a number of radial holes for air admission. Exhaust gases from the furnace flow through a duct of 0.25 reduction ratio. This followed by two segments chimney stack of a total height of 6 m. As a cooling water system is considered to be the safety relief of the furnace, wall temperatures were to be kept well below a prescribed value in order to prevent overheating and water evaporation or dry-out. The experimental test runs on MWB, which have been conducted, are given in Table 5.1.

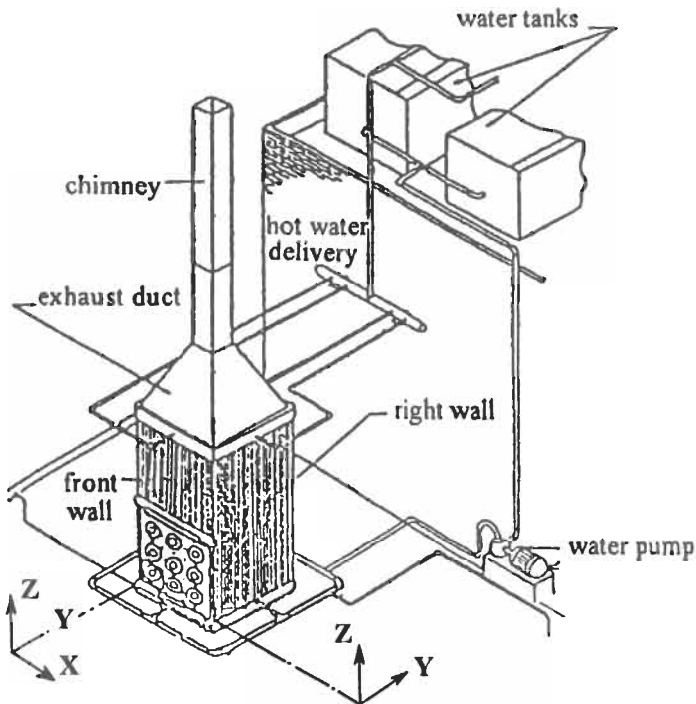


Fig. 5.45: The model of water-tube boiler furnace, MWB [759, 781].

Table 5.1: Experimental sets adopted for the MWB Test Facility [759].

Test Set	Designation	Test Conditions	Fuel Supplied kg h ⁻¹	Input Energy, 10 ³ kJ h ⁻¹
1	1F X	Single central flame, with high firing intensity	114.7	4625
2	3HF XXX	Three horizontally arranged flames, each with low firing intensity.	3 × 70.0	3 × 2822
3	3VF X X X	Three vertically arranged flames, each with low firing intensity.	3 × 70.0	3 × 2822
4	5F X X X X X	Five burners arrangement, each with low firing intensity.	5 × 70.0	5 × 2822
5	6F X X X X X X	Six horizontally arranged flames in two rows.	6 × 70.0	6 × 2822

5.1.5.1 Experimental Study

Flame Structure

Two cases are considered for the MWB described above, the first is a single central burner (0.9 MW) which has been used to provide information on the basic flame structure in the absence of multi-flame interactions.

In the second case, the burner system comprises the central and two adjacent burners in the same horizontal plane (2.6 MW) and the experimental results are considered from the point of view of quantifying the influence of flame interactions on combustion and heat transfer characteristics within the model. Local flame structures including gas temperature, species and soot concentrations have been obtained for the two sets of burner arrangements and the results will be discussed as follows:

Single flame results. Figure 5.46 shows the measured profiles of temperature, species concentrations, and soot levels for the single-flame case [771, 774, 781, 790, 800, 805], while the corresponding temperature and CO₂ contours are shown in Figs. 5.47 and 5.48, respectively. These results together with visual observation allowed the formulation of a physical description of the flame structure. A recirculation zone is formed behind the stabilizer disc, and the spray sheet is penetrated through this reverse flow zone and, as a result, small droplets and fuel vapour are recirculated towards the combustion air exit. At the boundaries of the recirculation zone, the high turbulent mixing rates and the recirculated combustion products allowed chemical reaction to proceed with a high intensity. This region extends to the fuel spray region whereas the resulting high temperature increases the fuel droplet evaporation and tends to stabilize the main diffusion-like flame, which extends downstream.

The measured values of temperatures, soot, CO₂, CO and O₂ (Figs. 5.46 to 5.48), confirm this description of the flame structure. For example, the temperature profiles, at upstream locations, show the expected double-peak shape coupled with steep gradients at locations corresponding roughly to the boundaries of the recirculation zone, X = 0.15 m and Y = 0.22 m (see Fig. 5.46). The upstream flame region is also characterized by comparatively high soot, CO₂ and CO values and low O₂ concentration close to the

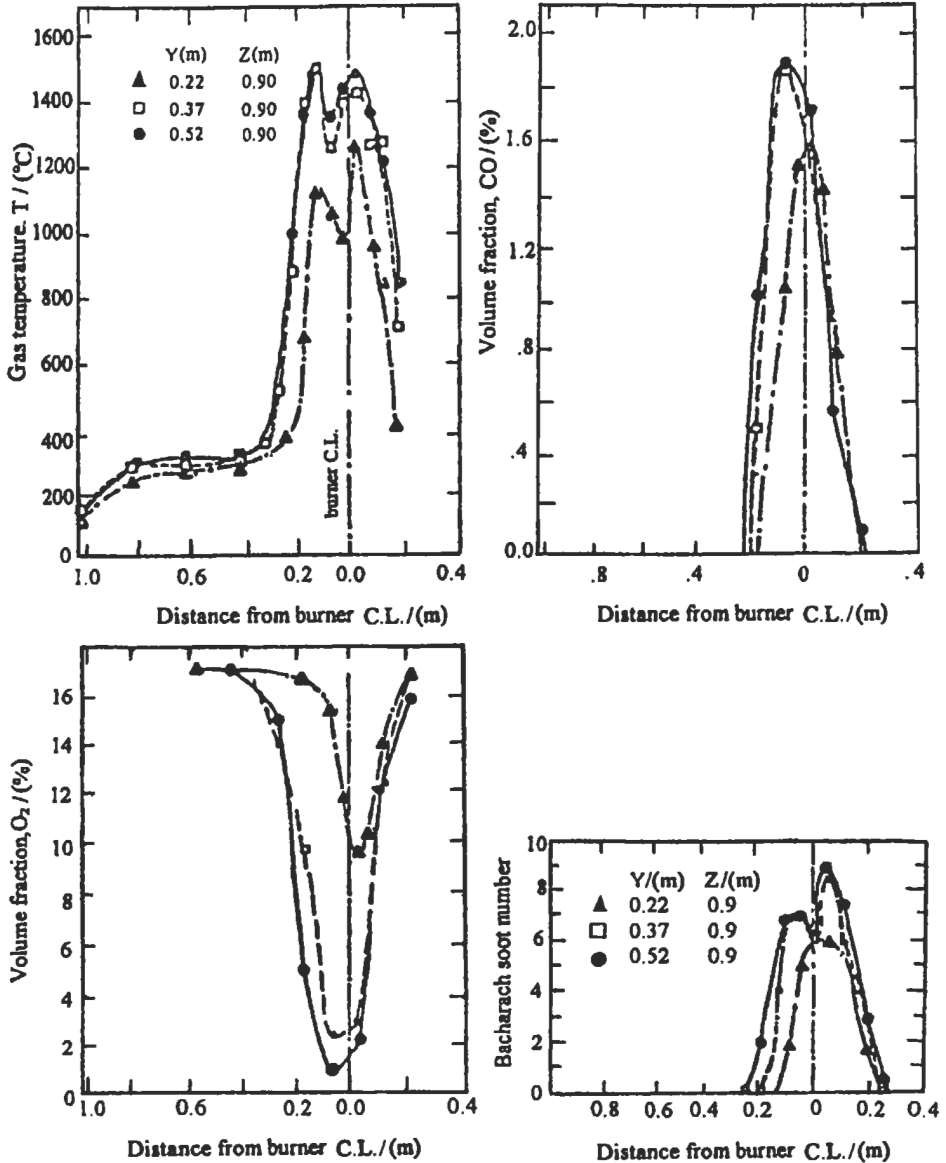


Fig. 5.46: Distributions of gas temperature and percentage volume fraction of CO, O₂ and soot for the single flame case in the MWB furnace [781].

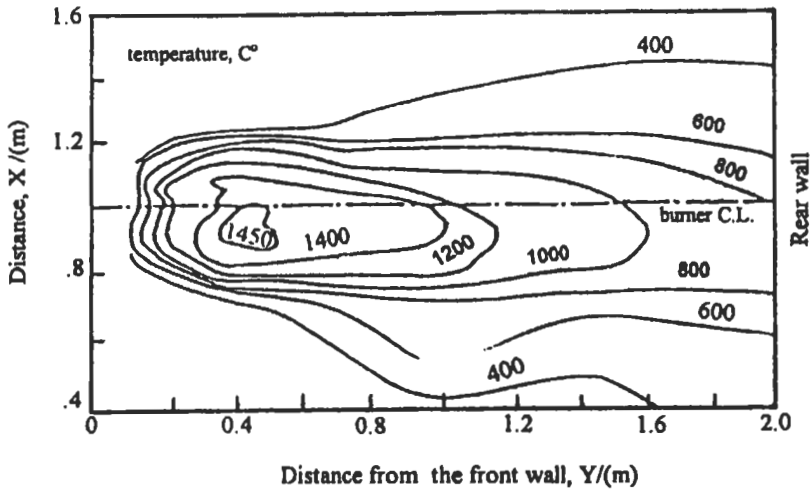


Fig. 5.47: Temperature contours for the single flame case in the MWB furnace [781].

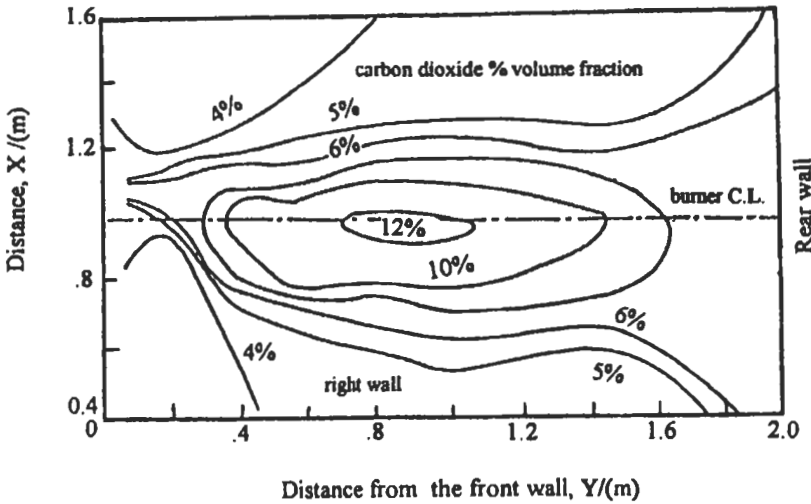


Fig. 5.48: CO₂ contours for the single flame case in the MWB furnace [781].

flame center-line, the maximum CO and soot values suggest that the flame core is characterized by fuel-rich mixture. This implies that large quantities of the fuel vapor that evaporate close to spray are swept towards the flame core.

The development of the main diffusion-like flame region is clearly indicated in the temperature and CO₂ contours of Figs. 5.47 and 5.48 and has general features consistent with the development of gaseous diffusion flames. The contours show that, due to the increasing rate of chemical reaction, both temperature and CO₂ increase along the flame center-line and take-up maximum values of around 1723 K and 12%, respectively.

The measured values of CO₂ decrease away from the flame centerline and towards the rear wall of the model with higher gradients at the upstream locations of the flame. The flame properties, particularly at the downstream region, are influenced by the

entrainment and mixing of the air with the flame gases. For example, the observed high CO value there indicates quenching of its oxidation reaction which is attributed to air dilution and the associated low temperature in this downstream region.

Three-flame results. Measured values of temperature, species and soot concentrations of the three-flame test case, are shown in Fig. 5.49 at selected upstream

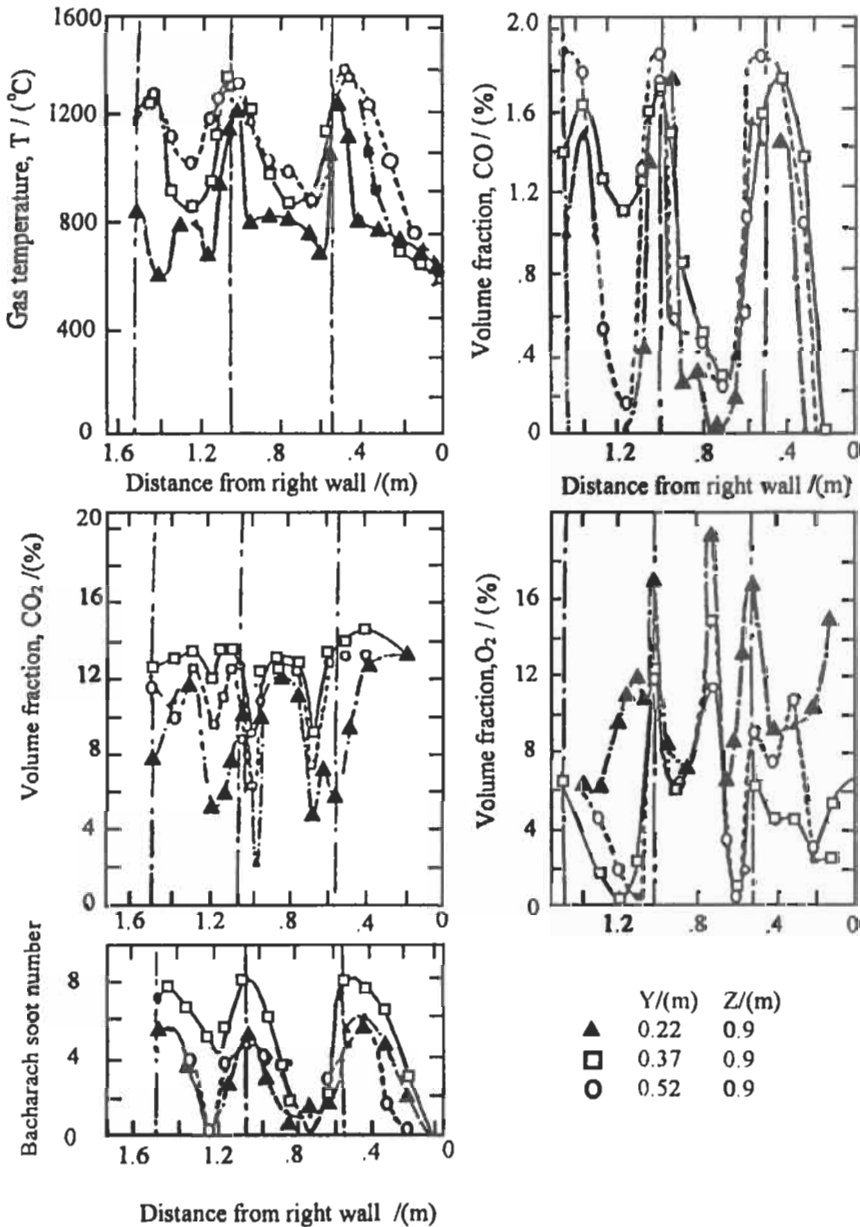


Fig. 5.49: Distribution of temperature; percentage volume fraction of CO₂, CO, O₂ and soot for the three-flame case in the MWB furnace [781].

locations and the corresponding contour plots of temperature, CO₂ and O₂ are shown in Figs. 5.50, 5.51 and 5.52, respectively. The three flames are easily identified by the regions of maximum temperature, soot, CO and minimum O₂ values which as indicated in the single-flame results, characterize the flame core. The flame properties within each flame region (X around 0.5, 1.0 and 1.5 m and Y < 0.8 m) are shown not to be largely influenced by flame interaction. For example, temperature values in the range of 1473-1673 K are observed in the single and three-flame cases. Soot levels, O₂, CO and CO₂ concentrations indicated similar trend with values of 5-8, 9-0.5%, 1.4-1.9% and 6-13%, respectively.

The burning of three flames in this case, with a relatively higher flame to furnace volume ratio, has significantly reduced the slightly diluted air which was observed in the single flame results to surround the flame. Accordingly, air dilution by entrainment and cross-stream diffusion rates are reduced and as a result the combustion products at downstream locations exhibit high CO₂ and low O₂ values. The downstream region is also influenced by the increased rate of CO oxidation reactions (see chapter 2 for these

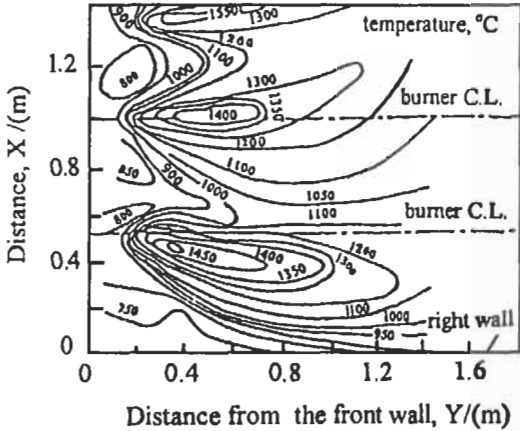


Fig. 5.50: Temperature contours for the three-flame case in the MWB furnace [781].

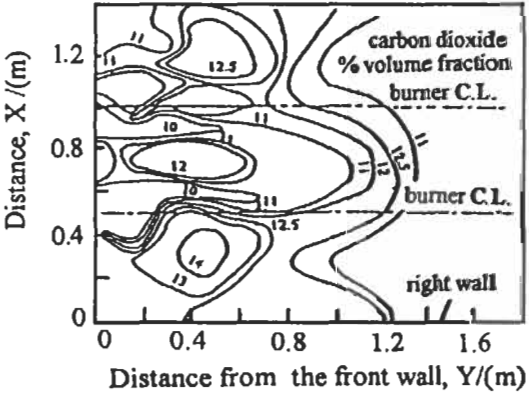


Fig. 5.51: Carbon dioxide contours for the three-flame case in the MWB furnace [781].

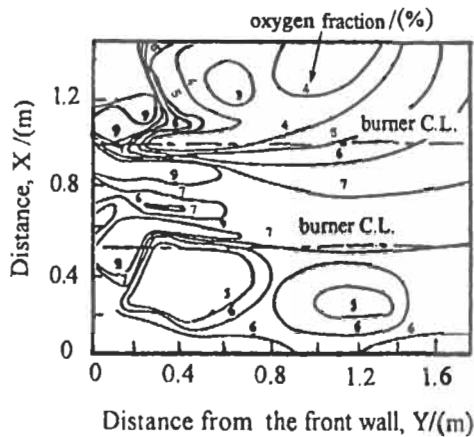


Fig. 5.52: Oxygen contours of the three-flame case in the MWB furnace [781].

reactions) which was evident from the negligible CO values detected in this region.

The main observed differences between the single and three-flame cases are emphasized in the inter-flame regions ($X = 0.75$ and 1.25 m) and at higher planes of the furnace where significant changes in the measured flame properties were detected. The results at locations in the immediate vicinity of the flame boundaries ($X \approx 0.6, 0.9, 1.1$ and 1.4 m and $Y \leq 0.052$ m) showed comparatively high O_2 values, 8-14%, and indicated that part of the combustion air supplied to each burner has penetrated through the inter-flame region.

The previous effect extends only up to an axial distance of around $Y = 0.65$ m and suggests that the initial flame development is not influenced by the surrounding combustion products. Close inspection of the profiles in Fig. 5.49 and the contour plots of Figs. 5.50 to 5.52 showed that the two left hand-side flames interfere with each other. The merging of the two flames, particularly with the comparatively higher values of temperature, CO_2 , CO, and soot observed in their cores, caused a noticeable increase in the corresponding measured values in the inter-flame region. The presence of reacting species in the inter-flame region ($X = 1.2$ m, $Y < 0.6$ m) allowed chemical reaction to proceed further downstream and as a result the two left hand side flames are not clearly distinguished at downstream locations.

The interference of the two left side flames is likely to be a result of slight geometrical or flow pattern imperfection in one of the burners which is probably augmented by aerodynamic or thermal effects stemming from the presence of surrounding flames.

Finally, we conclude that in a single-flame case, the flame properties, particularly at downstream locations, are influenced by the presence of a large quantity of a nearly stagnant air in the furnace volume. However, this was not observed in the three-flame case as a result of higher larger flame to furnace volume ratio and consequently, the downstream region of the flames was characterized by the presence of undiluted combustion products. These were found to be recirculated upstream towards the inter-flame regions. In addition, part of the combustion air supplied to each burner penetrated through the inter-flame region in the close vicinity of the flame boundaries, and minimized the influence of recirculated combustion products on the flame development.

Heat Transfer

Measurements of total heat flux to the furnace walls have been carried out using the heat flux meter described in Ref. 771. Figure 5.53 presents the heat flux distribution along the rear wall of MWB using single flame where flame impingement is evidently resulting in peak heat flux. It is clear that the heat flux values for the side walls vicinity are lower than the central portion of the rear wall. The maximum values occur at the center and decrease to both sides. The regions of maximum heat flux are those facing the flame and are attributed to the large convective heat transfer at these locations. The peak heat flux increases from 105 kW m^{-2} at the lower measuring level at $Z = 0.55 \text{ m}$ to a peak value of 256 kW m^{-2} at $Z = 1.05 \text{ m}$ which is slightly above the burner centerline.

Integrating the measured heat flux values over all the walls showed that about 32% of the total heat is transferred through the rear wall and about 19% to each of the side walls. That means 75% of the total heat (assuming 5% contribution from the front wall) is transferred to water walls. This value is much larger than that occurring in large boiler furnaces and may be attributed to the fact that the model size is very large relative to the present single flame. Simple calculations that are based on the exhaust gas analysis and temperature showed that around 20-25% of the total heat escaped with exhaust gases.

The experimental results obtained for the two burner arrangements comprising cases 4 and 5 in Table 5.1 are shown in Figs. 5.54 and 5.55 [781]. The heat flux contours on the rear wall of MWB using five flames are shown in Fig. 5.54. It is clearly shown that there are five distinct regions of maximum heat flux with steep gradients in between. These five regions coincide with the impingement regions of the hot gases resulting from the five flames. The steep heat flux gradients between these regions reflect the lower

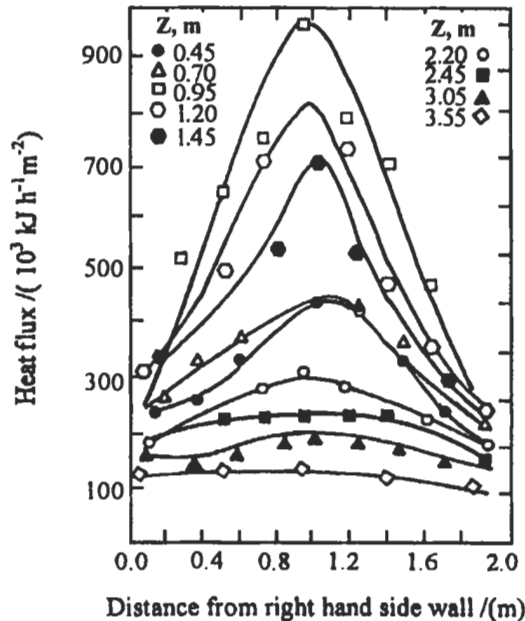


Fig. 5.53: Heat flux distribution on the rear wall at different heights (Z) for the case of a single flame [781].

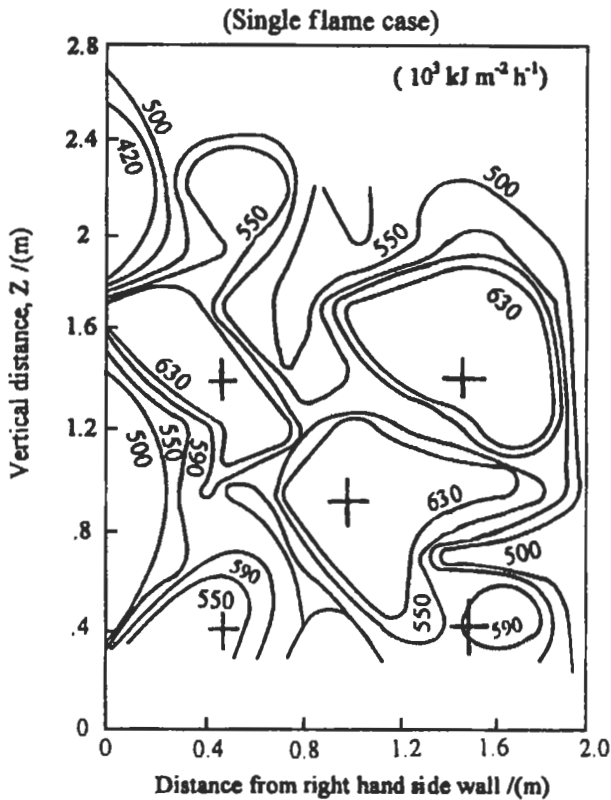


Fig. 5.54: Heat flux contours on the rear wall of the MWB furnace for the case of five flames [781].

degree of interaction between flames in this arrangement due to the larger centerline distances between flames. Mixing between reflected gases after impingement results in a more homogenous heat flux distribution at the upper regions of the rear wall.

The heat flux values on the side walls increase with the distance from the burners wall to a peak value which is consistent with the flame development. The heat flux decreases at further down stream distances due to the decrease of the flame radiation caused by soot burn-up. In general the maximum heat flux values are recorded at levels lying on the same horizontal planes passing through the centerlines of the different flames.

Figure 5.55 shows the heat flux contours on the rear wall of MWB using six flames. It is clear that there are two regions of high heat flux resulting from the impingement of the hot flame gases. Although, the hot gases in each region are issuing from three different flames, the heat flux gradients within the two regions are not too large due to the interaction between the hot flame jets close to the rear wall. On the other hand, in the areas between these regions the heat flux values are smaller and the gradients are steeper in the vertical direction. This reflects the fact that the distance between the two flame rows is large enough that no interaction occurs between the flames of the two rows. Interaction between the flame jets seems to play an important role in the homogeneity

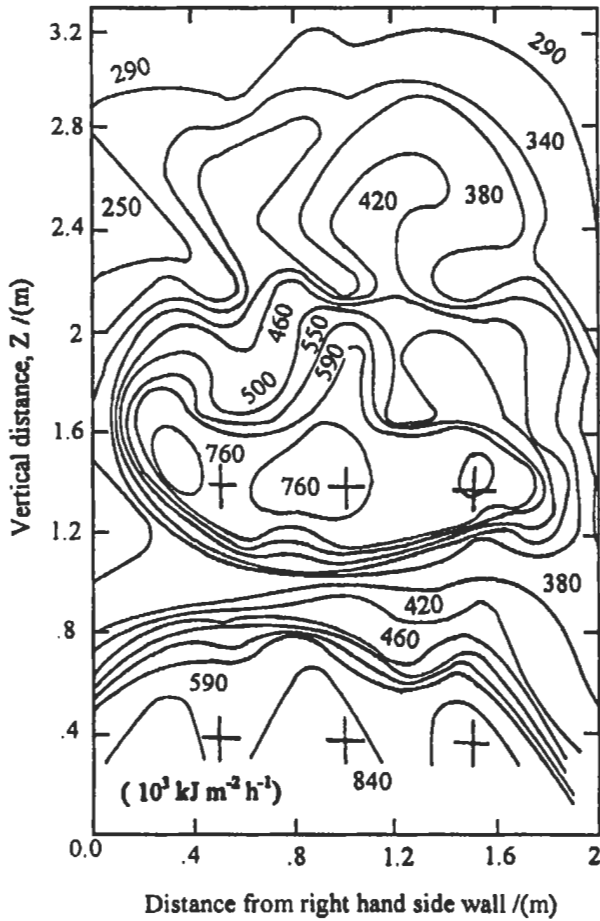


Fig. 5.55: Heat flux contours on the rear wall of the MWB furnace for the case of six flames [781].

of heat flux distribution. Heat flux profiles on the side walls follow the same trend where maximum values are measured at levels coinciding with the horizontal planes passing through the centerlines of the flames. However, the heat flux increases with the distance from the burner wall to a maximum value where the flame temperature is high and soot concentration is maximum. The heat flux then decreases near the rear wall due to soot burn-up and decrease in flame radiation.

5.1.5.2 Computational Analysis of Heat Transfer

Zonal Method

The main procedure of the computational analysis described in section 5.1.2.3 (case 3) with the assumption of steady state condition is used in this section to predict the radiative heat flux for MWB. The analysis in such type of furnaces (MWB) would be tackled as a three-dimensional problem, unlike the cylindrical furnaces where the

analysis could be treated as a two-dimensional axisymmetrical case. The enclosed furnace volume and its surrounding walls are divided into gas layers/wall slices. The wall slices are divided into rectangular surface elements. The gas layers are either divided into rectangular parallelepipeds or spheres [738]. The latter division is being more economical regarding computations [738], and is being outlined hereafter. This is basically because, for the case of spheres, the radiation is handled as emitted from one continuous surface; while upon dealing with rectangular parallelepipeds, the emitted energy from an element is decomposed as radiation from its six faces. In order to monitor both gas and wall elements, the indices (IG), (JG) and (KG) are used for gas elements, and (I), (J) and (K) for wall elements in the three dimensions (x, y, z); respectively. The details of furnace configuration and division are illustrated in Fig. 5.56.

The elemental gas spheres exchange normal and inclined radiation with rectangular wall elements coaxial and non-coaxial with them. Referring to Fig. 5.56, the view factor between the gas sphere (IG, JG, KG) and the coaxial wall element (J,K) which will be used in Eq. 5.38 is given by [766]:

$$VF_{IG,JG,KG \rightarrow J,K} = (1/2\pi) \left[\sin^{-1} \left\{ \frac{2A^2 - (1 - A^2)(A^2 + B^2)}{(1 + A^2)(A^2 + B^2)} \right\} + \sin^{-1} \left\{ \frac{2B^2 - (1 - B^2)(A^2 + B^2)}{(1 + B^2)(A^2 + B^2)} \right\} \right] \quad (5.58)$$

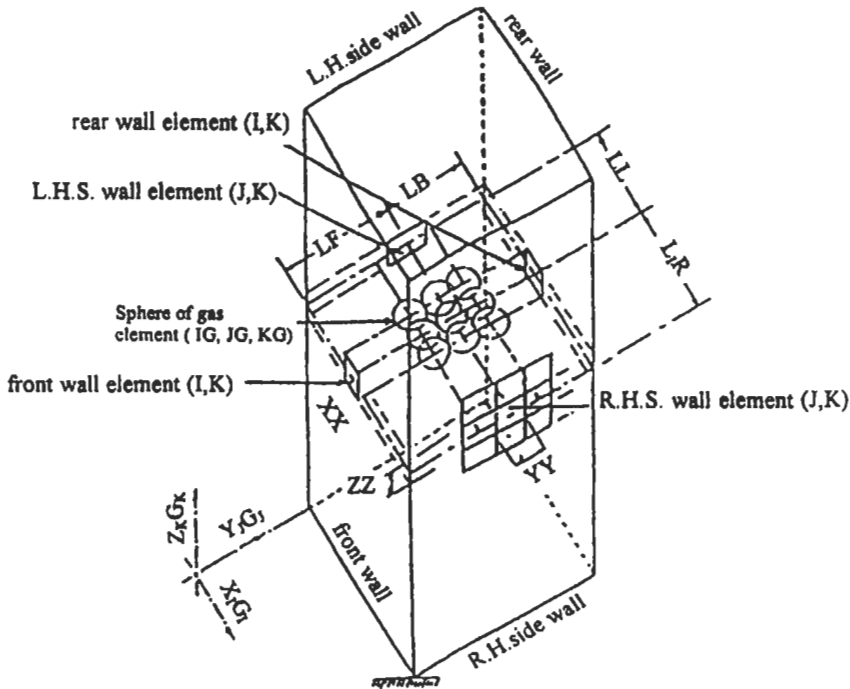


Fig. 5.56: The spherical division of the water-tube boiler furnace, MWB [738, 759].

where $A' = 0.5 \times ZZ(K) / (L1R(IG, JG, KG) + 0.5D(IG, JG, KG))$ & $B' = 0.5 \times YY(J, K) / (L1R(IG, JG, KG) + 0.5D(IG, JG, KG))$.

For the other non-coaxial wall elements, Figs. 5.57 and 5.58, the following view factors can be deduced [759]:

$$VF_{IG, JG, KG - J-1, K} = 0.5 \times (VF_{IG, JG, KG - (J-1 \& J \& J-1), K} - VF_{IG, JG, KG - J, K}) \tag{5.59}$$

$$VF_{IG, JG, KG - 1256} = 0.25 \times (VF_{IG, JG, KG - 123456789} + VF_{IG, JG, KG - 456} + VF_{IG, JG, KG - 258} + F_{IG, JG, KG - 5}) \tag{5.60}$$

For example $VF_{IG, JG, KG - 258}$ means the view factor between the gas element (IG, JG, KG) and the wall element composed of the numbered rectangles 2, 5, and 8.

The gas emissivity, ϵ (IG, JG, KG) is calculated as described by Eqs. 5.43, 5.44, 5.45, and the radiation mean beam length of the sphere gas element having a diameter $D_{IG, JG, KG}$ is calculated using the following formula:

$$B_L = 0.65 \times D_{IG, JG, KG} \tag{5.61}$$

The distribution of radiative heat along the furnace walls, $q_{gs}(I, J, K)$, is calculated as:

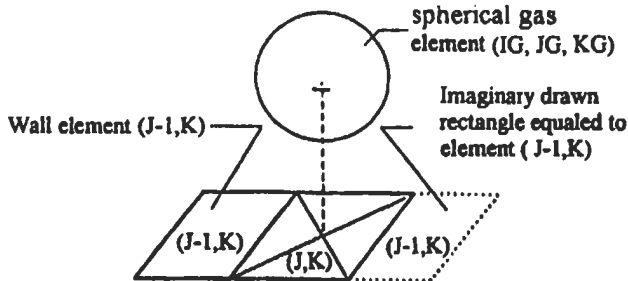


Fig. 5.57: Synthesis of the view factor between a sphere and a non-coaxial rectangle [738, 759].

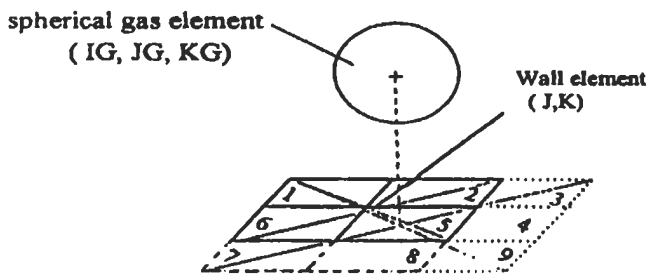


Fig. 5.58: Synthesis of the view factor between a sphere and a displaced rectangle [738, 759].

$$q_{gs}(I, J, K) = \sum_{IG, JG, KG}^{IGN, JGN, KGN} \sigma A_g(IG, JG, KG) V F_{IG, JG, KG-I, J, K} \times \epsilon_g(IG, JG, KG) \left(\bar{T}_g^4(IG, JG, KG) - T_s^4(I, J, K) \right) \tau_{IG, JG, KG-I, J, K} \left(\frac{1 + \epsilon_s(I, J, K)}{2} \right) \tag{5.62}$$

A proper selection of divisions for the furnace volume and walls would yield reliable results, regardless of grid geometrical configurations, as long as it correctly resembles the gas data profiles. Accordingly, the furnace volume is divided into gas layers and the division is traced so as to match, wherever possible, the levels of measurements specified in [781]. Thereupon, each gas layer is divided duely into spheres filling adequately the whole of the furnace volume. The arrangements of spheres and wall elements are considered so as to resemble the profiles of all gas input data. The specifications of the computational grids used for each case of this investigation, as well as the burners locations are described in Ref. 738. The deviation in furnace volume division is found to be 0.17% for both test cases (1, 2), described in Table 5.1, -0.08% for test case (3) and 0.01% for test case (4) (see Table 5.1). The predicted profiles of radiant heat flux incident on the rear wall of the furnace model, for test case (1) in Table 5.1, are traced in Fig. 5.59. The profiles on the rear wall show a symmetry around the flame centerline, which was evident in the experimental profiles [781], due to the symmetry in radiating gas properties. The radiative heat flux profiles could be regarded as if it were scaled down from the measured total heat flux profiles. The heat flux peak values coincide, to a great extent, with those of experiments, Fig. 5.60. This is anticipated due to such flow patterns for single flame operation, whereas there are no flame interactions that would appreciably alter the average convective heat transfer coefficients. The peaks of heat flux profiles are pronounced around the flame centerline where the input data peaks, while at distant localities the trend of profiles is smoothed according to input data behavior. The comparison between the predicted wall heat flux and the extracted values of radiative heat flux from measured wall total heat flux, using empirical correlation for the convective part of heat transfer by impingement [738], is shown in Fig. 5.60. Quite good agreements prevailed and this reveals that the zonal analysis technique for radiative heat is quite satisfactory.

Discrete Ordinates Transfer Method

The design of industrial furnaces has traditionally been based on a combination of experience and experiment supplemented by a very limited amount of analysis. This approach has hardly been unsuccessful, but it is limited by the fact that experiments on full scale furnaces are either extremely difficult or costly, or both, and by the complexity of the many interacting physical and chemical processes which occur in furnaces which encumber the analysis of data.

Widely used computational techniques [758, 826, 827] have the potential to be of considerable assistance to designers. This section describes the computation procedure of flow pattern in furnaces, which will be used in this section. This procedure is similar to that used for other Imperial College studies [827]. The prediction procedure incorporates the standard k-ε turbulence model, fast “flame sheet” chemistry and the discrete

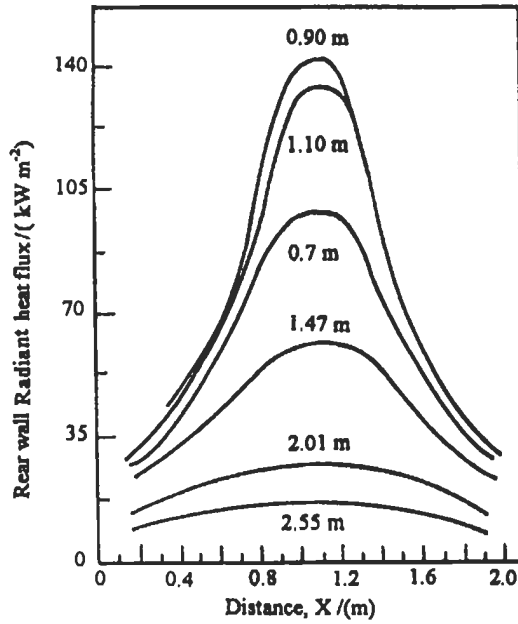


Fig. 5.59: Predicted profiles of rear wall radiant heat flux at different levels (meters), of the water-tube boiler furnace model MWB [738, 759].

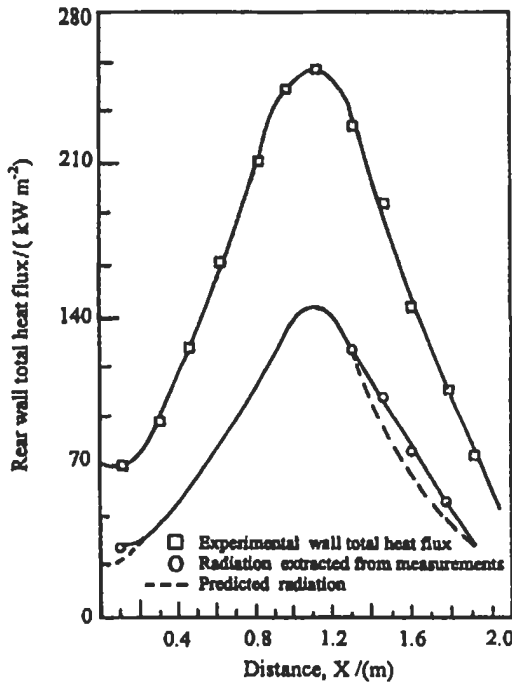


Fig. 5.60: Comparison between the predicted and measured profiles of rear wall heat flux, at the burner level, of the water-tube boiler furnace model MWB [738, 759].

transfer formulation for the radiation heat transfer. The description herein is necessarily brief and further details may be sought elsewhere [758, 827].

The governing equations. A turbulent reacting recirculating flow system of the type under consideration can be mathematically described by a set of elliptic non-linear partial differential equations. These equations can be written in a generalized vector form for the steady state as:

$$\operatorname{div}(\rho \bar{u} \phi) = \operatorname{div}(\Gamma_{\phi} \operatorname{grad} \phi) + S_{\phi} \quad (5.63)$$

where ρ is the density, \bar{u} is the velocity vector, ϕ is the dependent variable, Γ_{ϕ} is the "effective" diffusion coefficient for that quantity and S_{ϕ} is the source term. The dependent variable ϕ may stand for a variety of different quantities such as: the mass fraction of chemical species, the enthalpy, a velocity component, the turbulence kinetic energy, or a turbulence length scale. For each of these variables, the diffusion coefficient Γ_{ϕ} and the source term S_{ϕ} should be appropriately specified.

The flow field must satisfy an additional constraint imposed by the continuity equation which for the steady state is:

$$\operatorname{div}(\rho \bar{u}) = 0 \quad (5.64)$$

The turbulence model. A turbulence model is required to relate the solved-for time-averaged main flow variables to the turbulence properties of the flow. The usual two-equation model of turbulence [828] (see also chapter 3) is employed here in which equations are solved for the turbulence kinetic energy, k , and its dissipation rate, ϵ . The $k-\epsilon$ model has acquired an established position for furnace prediction due to the computational efficiency resulting from the solution of just two equations. It is an adequate simulation of high-swirl flow.

The combustion model. The often-termed "Simple Chemically Reacting System" (SCRS) has been used in this study [697]. Its principal feature is to ignore all intermediate reactions so that pure fuel and pure oxidant are imagined always to unite in fixed proportion. This is satisfactory in respect of the prediction of the combustion aerodynamics and heat transfer. In addition the effective mass exchange coefficients for the fuel and oxygen are equated, which is an acceptable practice for turbulent flows. With these two assumptions, the quantity ϕ which is denoted by:

$$\hat{\phi} = S \hat{m}_{fu} - \hat{m}_{ox} \quad (5.65)$$

becomes a conserved scalar property of the flow where m_{fu} and m_{ox} are, respectively, the mass fractions of fuel and oxidant and S is the stoichiometric oxidant requirement to burn 1 kg fuel. A conserved scalar ϕ_n obeys the instantaneous differential equation:

$$\rho \bar{u} \cdot \operatorname{grad} \phi_n - \operatorname{div}(\Gamma_{\phi_n} \operatorname{grad} \phi_n) = 0 \quad (5.66)$$

which is distinguished by the lack of a source term.

The mixture fraction, a useful variable related to the fuel-air ratio, and measuring the extent to which fuel and oxidant have been mixed is defined by:

$$\hat{F} = \frac{\hat{\phi} - \phi_0}{\phi_1 - \phi_0} \quad (5.67)$$

where the subscripts 0, 1 designate the oxidant and fuel streams, respectively.

Time-averaged secondary scalar properties. The turbulence results in fluctuations of all fluid properties, including the mixture fraction, about their time-averaged values. The effect of these fluctuations on important properties of the flow is very significant. Spalding [518] characterized the fluctuations in a modeled equation for the time-average of the square of mixture fraction fluctuations, $\overline{g}_f \cong (F - \overline{F})^2$. Now, for the SCRS other important variables of the flow such as the mass concentration and temperature depend on F alone. In order to calculate the time average of these variables, $\overline{\phi}(F)$ say, an assumption about the temporal nature of the F fluctuations must be made. By assuming the probability density function, $P(F)$, we can employ the definition [829]:

$$\overline{\phi}(F) = \int_0^1 \phi(F)P(F)dF \quad (5.68)$$

where the overbar indicates the time-averaged value, and \wedge is the instantaneous value.

A Beta function [830] for the shape of the $P(F)dF$ has been assumed. This distribution is mathematically simple and computationally economical. It is expressed by:

$$P(\hat{F}) = \frac{\hat{F}^{a-1}(1-\hat{F})^{b-1}}{\int_0^1 \hat{F}^{a-1}(1-\hat{F})^{b-1} d\hat{F}} \quad 0 \leq \hat{F} \leq 1 \quad (5.69)$$

where $a \cong \overline{F} \left[\frac{\overline{F}(1-\overline{F})}{\overline{g}_f} - 1 \right]$, $b \cong \frac{1-\overline{F}}{\overline{F}}$, a , and \overline{F} is the solved for time-averaged F .

The radiation model. The fraction of heat exchange due to radiation in furnaces is particularly large. The "Discrete Transfer" (DT) method of Lockwood and Shah [831] has been employed in these predictions. This method possesses several advantages among which are: ease of use, the provision of a numerically exact solution, and computational economy. Space restrictions do not permit a satisfactory description of the DT techniques and the reader is necessarily referred to [817, 831].

Solution of governing differential equations. Time-averaged differential equations having the common form of Eq. 5.63 have been solved for the three velocity components, k , ε , \overline{F} , \overline{g}_f , and stagnation enthalpy using the finite-difference procedure described in Ref. 832 and embodied in a version of the TEACH-3E computer code. This procedure is used in this section to predict the flow pattern and performance of practical furnaces.

Predicted results. The procedure of computational analysis of k- ϵ turbulence model described above has been used by Abdel-Rahman et al [833] to predict the flow pattern and performance of the practical MWB furnace. The total number of grids employed in these computations is 896 nodes with the assumption of instant vaporization of the oil fuel. This mesh size is not particularly fine, but fine grids are not always an affordable luxury. Fortunately, the good calculations of the radiation heat transfer, the dominant process affecting furnace performance except very near the burners, does not always necessitate the use of expensive grids. In order to validate the predicted flow pattern with the above procedure, the predicted results are compared by Abdel-Rahman et al [833] with the corresponding experimental one for water tube boiler' furnace (MWB) in Figs. 5.61 to 5.63. The inlet condition for the computational analysis are: fuel and air flow rates are 90 and 1620 kg h⁻¹, fuel vapour, air, and wall temperatures are 383 K, 313 K, and 400 K, respectively, with turbulent intensity of 0.03. The predicted results show that the flow is dominated by a strong jet like movement from the burner towards the opposite wall. This supports the view that the fluid flow dependent processes are dominant near the burner region. Also, the maximum heat flux occurs at the impingement location of the burner jet. Figure 5.61 shows a comparison between the predicted and measured gas temperature. The agreement is reasonable. Figure 5.62 shows a similar comparison for carbon dioxide concentration, the agreement is fair. Wall heat flux, which is most often the quantity of greatest interest to engineers, is well predicted and is shown in Fig. 5.63. Similar results are obtained at low firing conditions and this validates the model under different conditions.

Recently, predictive accuracy of discrete ordinate method (DOM) was assessed by applying it to the prediction of incident radiative fluxes on the walls of a gas turbine combustor simulators (GTCS), and comparing its prediction with measurements [817].

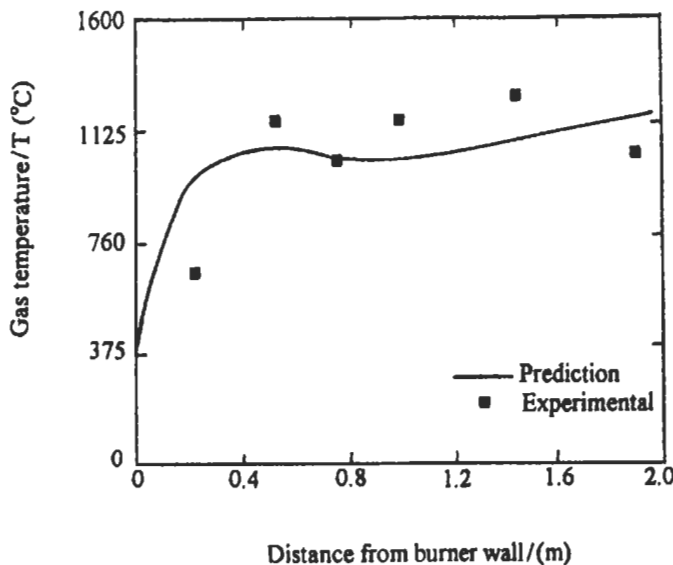


Fig. 5.61: Comparison between predictions and experimental data for gas temperature along the flame center line for the case of single flame in MWB furnace ($Z = 0.9$ m) [833].

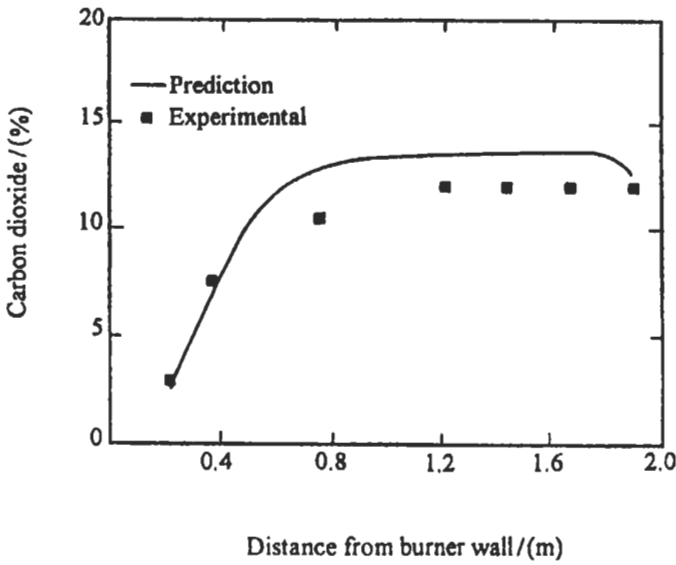


Fig. 5.62: Comparison between predictions and experimental data for carbon dioxide along the flame center line for the case of a single flame in the MWB furnace ($Z = 0.9$ m) [833].

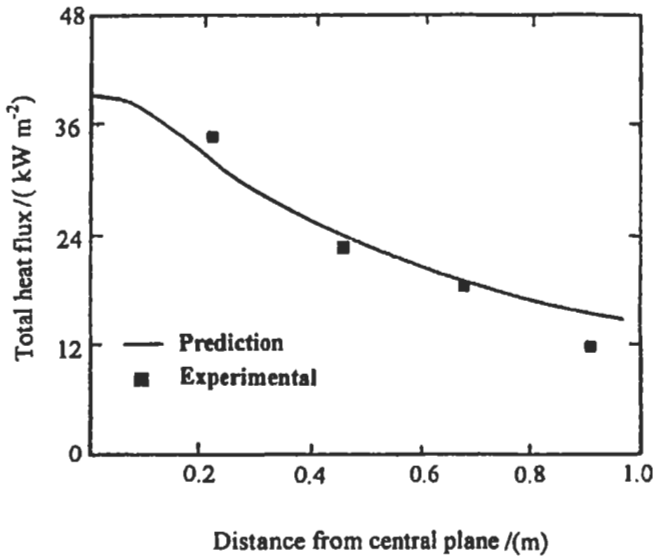


Fig. 5.63: Comparison between prediction and experimental data of the total heat flux distribution on the rear wall for the case of a single flame in the MWB [833].

Input data utilized for the DOM were measured gas concentration and temperature profiles and inner wall temperatures of the GTCS which is a cylindrical enclosure containing a turbulent diffusion flame of propane and air. Effects of order of approximation (S_4 and S_6) and using uniform and non-uniform gas absorption

coefficients for the non-homogeneous medium on the accuracy of the predicted heat fluxes were also investigated [817]. Comparisons show that S_4 approximation is adequate for the prediction of incident wall heat fluxes and the use of an absorption coefficient profile based on measured gas concentrations and temperatures improves the accuracy significantly. These results [817] are shown in Fig. 5.64. The figure illustrates the comparison between the incident heat fluxes predicted by S_4 with uniform and non-uniform absorption coefficient and the measurements. As can be seen from the figure, the use of non-uniform absorption coefficient leads to considerable improvement in the accuracy of the predicted fluxes. In order to show the effect of using higher order approximation on accuracy, incident fluxes determined by S_6 for non-uniform absorption coefficient have also been plotted on the same diagram. When the profiles of S_4 and S_6 predictions for a uniform absorption coefficient are compared with the measured values, the effect of higher order approximation on the accuracy of the predicted fluxes seems insignificant.

Boiler Heat Transfer Modeling

Energy for steam production is derived from a combustion process, which takes place within the boiler furnaces as described in section 5.2. The heat transfer from the hot gases to the sink surface is the heart of such boiler. Therefore, several investigators [834-851] have concentrated their research on this field and the following present's brief description of some of their research on the boiler heat transfer modeling.

Patel [834] has developed a generalized computer program for modeling the characteristics of boiler furnaces and compared the results obtained from the model with the experimental data of the same furnace. He [834] investigated the effects of various

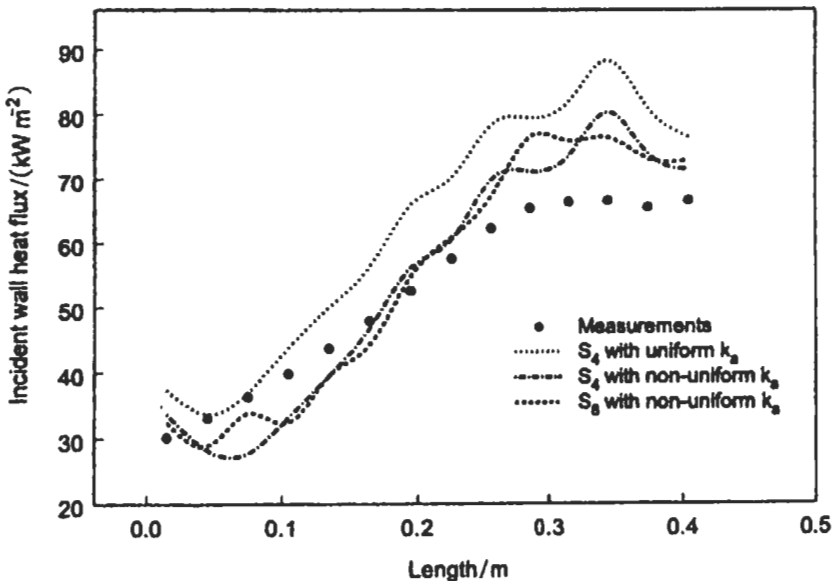


Fig. 5.64: Comparison between S_4 and S_6 prediction of incident heat fluxes along the side wall of GTCS and measurements [817]. Reproduced by permission of Elsevier Science.

radiative properties on the performance of the model. In this type of model the effective length of the furnace is divided into suitable number of zones. The number of zones and dimensions of each one depend upon the accuracy required and relative position of the zone in the furnace. Patel [835] has derived from first principles the nonlinear equations which provide values of the radiosity of an i^{th} surface of a given zone- m consisting of such N surfaces. The radiation passing from one surface to another is attenuated by the medium; and the medium itself also radiates energy. In his model [834] all the surfaces forming a given zone are grouped as source, sink and radiatively adiabatic surfaces. The heat absorbed by furnace walls can be computed when gas properties are known. For the first and the last zone in the long furnace model, it is preferable to include the bottom and top surfaces of the zone respectively, in sink. Furthermore, to simplify the model, the following assumptions are made, (i) Energy interaction between the zones is neglected and this equivalent to dividing the furnace into a cascade of well stirred model, (ii) Sink surfaces are assumed to be black.

The salient points of the computational procedure are as follows:

- 1- Read furnace dimensions and air fuel data.
- 2- Compute mass of products of combustion.
- 3- Evaluate useful heat released.
- 4- Determine average specific heat of product of combustion and hence adiabatic flame temperature.
- 5- Evaluate flame emissivity.
- 6- Compute appropriately flame surface area, sink area, tube wall temperature and furnace emissivity.
- 7- Divide effective length of the furnace in a suitable number of zones. Treat each zone as well-stirred zone.
- 8- Compute various shape factors.
- 9- Using radiosity equations and equation for enthalpy balance of furnace gas determine average gas temperature.
- 10- Evaluate radiation heat transfer.
- 11- Repeat the procedure for all the zones.
- 12- For investigating parametric influence, change the data card of that particular parameter and obtain necessary computer runs.

In order to validate the furnace model, the experimental furnace internationally reported by Anson et al [836] has been selected. The test conditions with furnace, air and fuel data are given in Table 5.2. Also, they [836] have reported the measurements on flame emissivity and its wall temperature and wall emissivity (see Table 5.2). The total heat flow rates to various walls have been computed from heat balance measurements on waterside and also by zone method of analysis (see Table 5.3). The total heat transfer to the various walls of the Anson furnace is 129 MW by zone method of measurement and 121 MW by heat balance on waterside. The predicted results by Patel [834] using the model described above are given in Table 5.4. These results show the influence of various furnaces parameters on the radiative heat transfer and these parameters are the equivalence ratio, ϕ , flame emissivity, ϵ_f , wall temperature, T_w , wall emissivity, ϵ_w and sink area, A_w .

Another mathematical boiler heat transfer simulation for coal-fired plant is developed by Zibas and Idem [837]. Required model input includes boiler geometry, fuel composition, and limited CEMS data that are typically available. Radiation heat transfer in the furnace is calculated using curve-fits to the Hottel charts. The model

Table 5.2: Experimental data of furnace [834].

(a) Furnace data	
Furnace dimension	24.5 x 9 x 5 m
Steam output	75 kg s ⁻¹ , 66 bar and 763 K
Fuel oil pressure	4060 Kn m ⁻²
Fuel flow rate per burner (16 burners)	0.35 kg s ⁻¹
Oil temperature	403 K
Air temperature	513 K
Average temperature of furnace wall	753 K
Average gas temperature	1820 K
Wall emissivity	0.82
Average flame emissivity	0.612
(b) Fuel data:	
C	85.2 %
H	11.3 %
S	3.3 %
Ash	0.05%
Moisture	0.1 %
Excess O ₂	0.8 %
Heating value of fuel	43000 kJ kg ⁻¹

Table 5.3: Data for heat flow [834].

Position	Zone method, MW	Heat balance, MW	Heat flux, kW m ⁻²
Left	23	22	278
Right	24	22	268
Back	31	31	201
Front	36	31	320
Roof	02	03	-
Floor	13	12	186
Total	129 MW	121 MW	

Table 5.4: Parametric influence [834].

 $\epsilon_f = 0.647$, $\epsilon_w = 0.85$, $A_w = 843 \text{ m}^2$, and $T_w = 753 \text{ K}$.

ϕ	Zone-1 T_g (K)	Zone-1 Q_r (MW)	Zone-3 T_g (K)	Zone-3 Q_r (MW)
0.98	2124	41.0	1512	23.98
1.05	2092	38.5	1504	23.78
1.10	2068	36.7	1500	23.68
1.15	2048	35.3	1492	23.48
1.20	2028	33.9	1480	23.05
ϵ_f	0.647	0.647	0.697	0.747
Q_r (MW)	129.67	129.67	133.15	136.22
T_w (K)	753	753	1250	1450
Q_r (MW)	129.67	129.67	117.38	106.83
ϵ_w	0.80	0.80	0.82	0.85
Q_r (MW)	121.6	121.6	124.8	129.67
A_w (m ²)	777	777	800	843
Q_r (MW)	124.2	124.2	126.5	129.67

employs empirical heat transfer coefficient correlation to evaluate convection heat transfer to various boiler component surfaces. In order to solve for the component heat transfer rate, it is assumed that the steam temperature remains constant in the steam generator components where a saturation process is occurring, i.e., the furnace tubes, screen, and boiler bank. In these cases, the convection heat transfer rate is calculated by the log-mean temperature approach. Figure 5.65 shows the schematic diagram of steam generator. It is assumed that there is no steam-side temperature gradients transverse to the gas flow direction. In solving for the component heat transfer rate, the calculations are iterative. The gas-side temperature is guessed, and convergence is obtained when the guessed temperature equals the calculated temperature, based on the gas-side energy balance. Temperature gradients exist transverse to the gas flow direction in the superheater, air heater, and the economizer. Gas radiation is modeled using curve fits to the Hottel charts presented in Ref. 838. The empirically determined radiation heat transfer coefficient is a function of partial pressure of CO_2 and H_2O , which are the only radiating species. In solving for the gas radiation, it is assumed that the gas is well mixed with a uniform temperature. It is also proposed that the average gas temperature is employed in the correlation and the walls are black. Turbulence/radiation interaction is not accounted for. It is assumed that gas radiation incident on the screen is completely absorbed, or in effect does not pass through to subsequent components.

In order to test the boiler performance model described above, base line operating conditions as described in Ref. 839 are selected, and the predicted results [837] are shown in Fig. 5.66, and the figure depicts temperature variations on the gas-side and

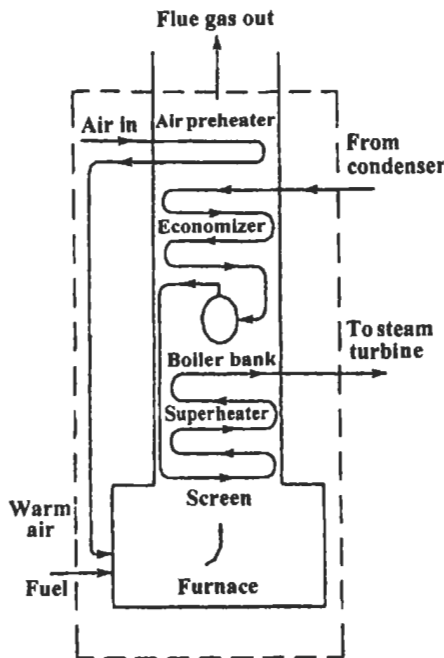


Fig. 5.65: Schematic diagram of steam generator [837]. Reproduced by permission of ASME.

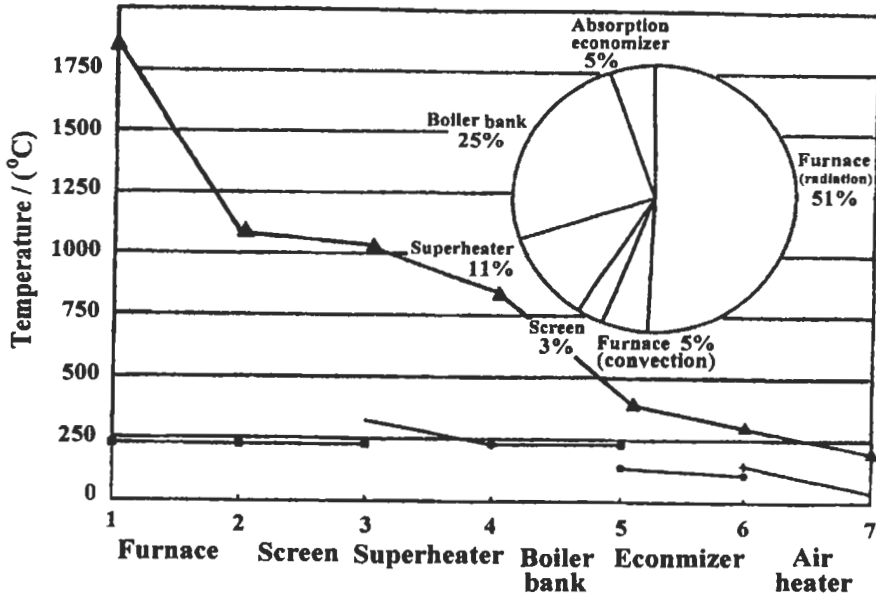


Fig. 5.66: Boiler thermal performance summary [837]. Reproduced by permission of ASME.

steam-side. Also the figure inset displays the relative percentage of steam heat transfer associated with each boiler component. In general the boiler performance predicted by the above model does not agree with the results presented in Ref. 839 despite the similar input data. For example, the flue gas temperature predicted by the model is 421 K, whereas the value indicated by Ref. 839 is 472 K. It is noted that steam-side and gas-side heat transfer rates calculated by a graphical approach in Ref. 839 are not equal, in apparent violation of the first law of thermodynamics, whereas the boiler model yields same gas-side/steam-side heat transfer rates. This discrepancy cannot be accounted for by infiltration, radiation losses, etc.

Comparison Between Different Methods

As discussed above there are several models for thermal radiation, which is the predominant mode for heat transfer in furnaces and boilers. Thus an accurate prediction of radiation is essential for the design of these systems. Recently, Schneider [852] and Knaus et al [853] have compared several radiation models for cartesian grids (e.g. moment method [854], flux model [855], discrete ordinates method [856], finite volume method [857], discrete transfer method [830], and Mont-Carlo method [858]). They [852, 853] found that the discrete ordinates method is the optimum choice considering accuracy and computational effort. The following presents some of these comparisons:

Ströhle et al [849] have applied the discrete ordinates method [859] and moment method for body-fitted coordinates and tested the results from these models at an idealized squared combustion chamber. The computed radiative source terms and wall heat fluxes are in very good agreement with the exact solution. The computational effort strongly depends on the grid with its symmetry conditions and the marching order of the solver. The discrete ordinates method was further investigated at a coal-fired test

facility. Apart from the near burner region the computed temperature distribution agrees well with the measurements. These results show that the discrete ordinates method in combination with a weighted-sum-of-grey-gases model for the gas absorption coefficient and an appropriate model for the particle radiative properties yield an efficient and accurate model for the prediction of radiative heat transfer in coal-fired furnaces.

In the discrete ordinates method the radiative transfer equation is solved for a set of discrete directions. According to its solid angle sector each direction is associated with a weight factor that is determined by numerical quadrature. The sum of all numerical weights is equal to the total solid angle of 4π . The S_4 -approximation of Fiveland [860] with 24 directions is applied in their study [849]. For coal flames a higher number of directions does not improve the accuracy significantly while the computational effort increases proportionally with the number of rays.

The results of the discrete ordinates method are compared with the moment method which is based on a Milne-Eddington approximation using a Taylor series expansion, truncated after terms of first order, for the radiative intensity. The intensity is independent on direction and therefore scattering cannot be accounted for. The computational effort of this model is low but the behavior of convergence is very pure compared to the discrete ordinates method [853]. Apart from an accurate models to solve the radiative transfer equation it is also essential to calculate the radiative properties of the combustion products. The assumption of a constant absorption coefficient is often too crude as it strongly depends on temperature and concentrations of combustion gases and particles. More details about an appropriate method for the computation of solid and gas phase properties are given elsewhere in Ref. 849.

The radiation model is introduced into a computer code named AIOLOS for predicting steady, three-dimensional, turbulent reacting flows in coal-fired utility boilers. In submodels for fluid flow, turbulence and combustion conservation equations of mass, momentum and energy are solved to compute the flow, temperature and concentration fields. Coupling between velocity and pressure is achieved by the SIMPLEC method [861]. The turbulence closure is done by a standard k- ϵ model according to Launder and Spalding [447]. Coal combustion is described by a four-step reaction scheme covering two heterogeneous reactions for coal pyrolysis and char combustion and two gas-phase reactions for the oxidation of hydrocarbons and carbon monoxide. The gaseous reactions are assumed to be mixing limited which is modeled by the Eddy-Dissipation Concept (Magnussen and Hjertager [546]). The procedure is based on a fully conservative, structured finite-volume formulation employing Cartesian vector and tensor components with a non-staggered variable arrangement [862]. The advantages of using a body-fitted grid for the simulation of an industrial furnace are described by Knaus et al [863]. The code is adopted for vector and parallel computers to reduce the computational time [864]. A detailed description of the simulation program AIOLOS is presented by Schnell et al [865].

The first test case for the above model is an idealized rectangular combustion chamber described by Selcuk [866]. The combustion chamber has a squared cross section, cooled side walls and uncooled front and rear walls. The burner is located in the centre of the front wall so that an axisymmetric temperature distribution can be assumed. Due to several simplifications an exact solution of the radiative intensity distribution exists for this problem. All walls are assumed to be black, a constant absorption coefficient is set, and scattering is neglected. The radiative intensity is

calculated using the discrete ordinates method and the moment method in body-fitted coordinates. Four grids with non-orthogonal cells are generated for this geometry. Grid A and B are both H-grid, the latter discretized only one half of the furnace using a symmetric boundary. The other two are O-grid with periodic boundaries and an axis, where grid D discretized a 90° sector of the furnace. Normalized radiation source terms and wall heat fluxes are computed as described above and compared to exact values along two lines parallel to the axis inside the combustion chamber and on the side wall, respectively. The computed values on all four grid differ negligibly, so that only the results for grid D are shown in Fig. 5.67. The figure shows that both radiation source terms and wall heat fluxes calculated by the discrete ordinates method agree well with the exact solution, whereas the results of the moment method clearly deviate from those values.

In order to elucidate the influence of the radiative properties on the accuracy of the radiative heat transfer predictions, they [849] applied the entire radiation model to a swirled 400 kW dry brown coal flame in a cylindrical test facility. The burner is located on top of the vertical tube, which is 0.75 m in diameter and 6 m in length. The coal-air-mixture and the swirled secondary air enter the furnace through an inner and an outer annulus, respectively, expanding into a swirl. The walls at the upper part of the combustion chamber are bricked and water-cooled. For the computations, a quarter section of the combustion chamber with periodic boundaries is discretized by a 36 x 11 x 97 grid leading to approximately 24000 computed cells. The upper part of this grid is shown in Fig. 5.68. Measurements of temperature and gas concentrations have been carried out using suction probes along radial lines on several measuring levels. In Fig. 5.69 the radial measured temperature profiles are compared to the computed results, where z is the distance from the burner. At the first level (z = 0.63 m) the penetration of the secondary air jet is predicted as a distinct minimum about 0.1 m from the axis. This effect cannot be reproduced by the experiment as irradiation from the hot surrounding strongly heats the measuring system.

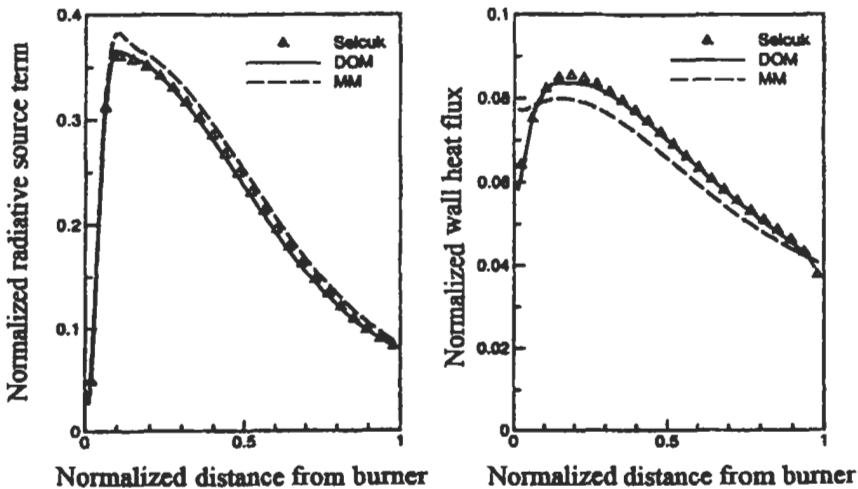


Fig. 5.67: Comparison of computed normalized radiative source terms (left) and wall heat fluxes (right) by the discrete ordinates method (DOM) and moment method (MM) [849] with the exact solution of Selcuk (symbols) [866]. Reproduced by permission of Combustion Science and Technology and Taylor & Francis.

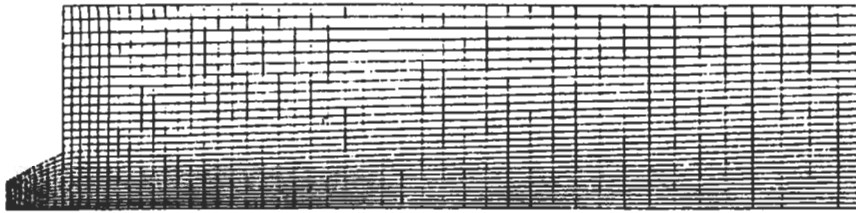


Fig. 5.68: Body-fitted grid for the coal-fired test facility (rotated by 90°) [849]. Reproduced by permission of Combustion Science and Technology and Taylor & Francis.

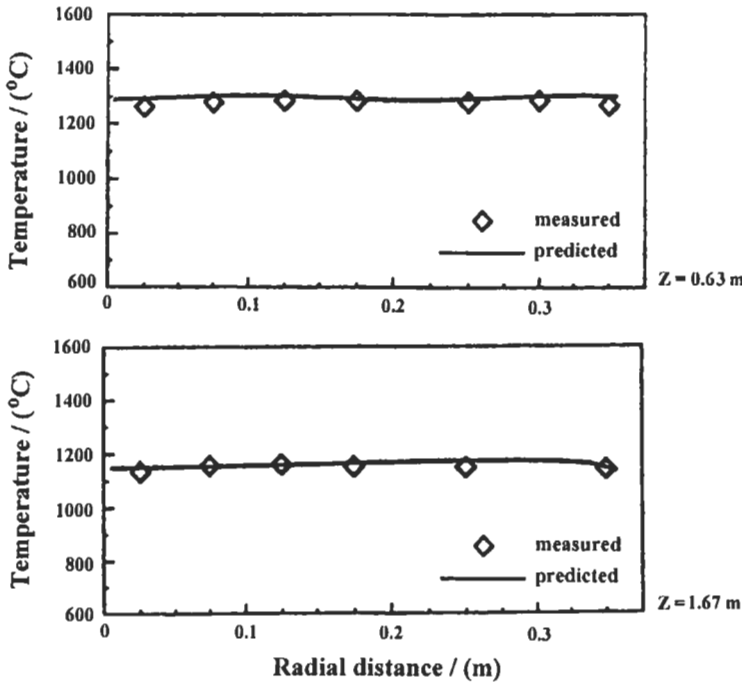


Fig. 5.69: Comparison of computed temperature profiles with measured values on two measuring levels of the coal-fired test facility [849]. Reproduced by permission of Combustion Science and Technology and Taylor & Francis.

Radiation models suitable for incorporation in reactive fluid flow codes are extended by Coelho et al [850] to calculate radiation in enclosures containing obstacles of very small thickness. The discrete transfer (DTM), the discrete ordinates (DOM) and the finite volume method (FVM) are employed to predict the heat transfer in two-dimensional enclosures and the results are compared with zone method calculations, with the total exchange areas determined by the Monte-Carlo method. All the methods predict similar heat fluxes, but the computational requirements are different. The discrete ordinates and finite volume method are the most economical ones.

Also, a three-dimensional enclosure resembling the combustion chamber of a utility boiler was modeled by Coelho et al [850]. The enclosure contains five baffles, as shown

in Fig. 5.70, which simulate the panels of superheaters that may be suspended from the top of the combustion chamber. The temperature and the emissivity of the boundaries, including the surface of the baffles, were taken as 800 K and 0.65, respectively, except at $x = 10$ m and for $22 < z < 30$ m, where the temperature was set equal to 1200 K and a black body surface was assumed. An emitting-absorbing medium was assumed. The calculations were performed using a grid with $20 \times 60 \times 60$ control volumes, and the inclined walls were simulated in a stepwise fashion. An angular discretization with $N_0 = N_\varphi = 5$ was employed both in the FVM and DTM calculations, while the S_8 approximation was used in the DOM. The predicted net heat flux contours for the front wall, side wall and back wall boiler using these three methods are presented in Fig. 5.71. This figure shows that the maximum heat fluxes occur at the level where the temperature and absorption coefficient of the medium are higher, i.e. at the burners level of an actual boiler, and decrease progressively towards the top, the bottom and the vertical edges. The contour of 100 kW m^{-2} on the front wall exhibits a wavy shape due to the influence of the baffles. The local heat fluxes are larger in vertical planes equidistant from the baffles, and decrease towards the baffles. The contours are almost identical regardless of the radiation model. It has been observed that the DTM sometimes produces oscillatory solutions [867]. In this problem the DTM has also required less iterations, but about 1.5 times more CPU time to attain convergence than the DOM and the FVM.

Furthermore, Guo and Maruyama [851] have used the radiation element method by ray emission method (REM^2) to predict radiative heat transfer in three-dimensional arbitrary participating media with nongray and anisotropically scattering properties surrounded by opaque surfaces. The method was verified by bench mark comparisons with the existing several radiation methods (such as generalized zonal method (GZM) [868], and YIX method [869]) in rectangular three-dimensional media composed of a gas mixture of carbon dioxide and nitrogen and suspended carbon particles.

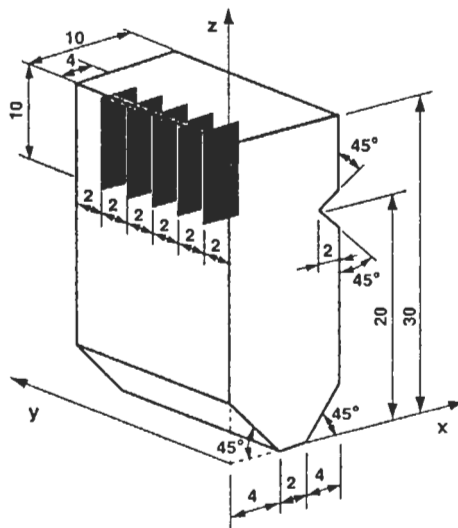


Fig. 5.70: Schematic of the enclosure studied in test case 3. Dimensions in m [850]. Reproduced by permission of Elsevier Science.

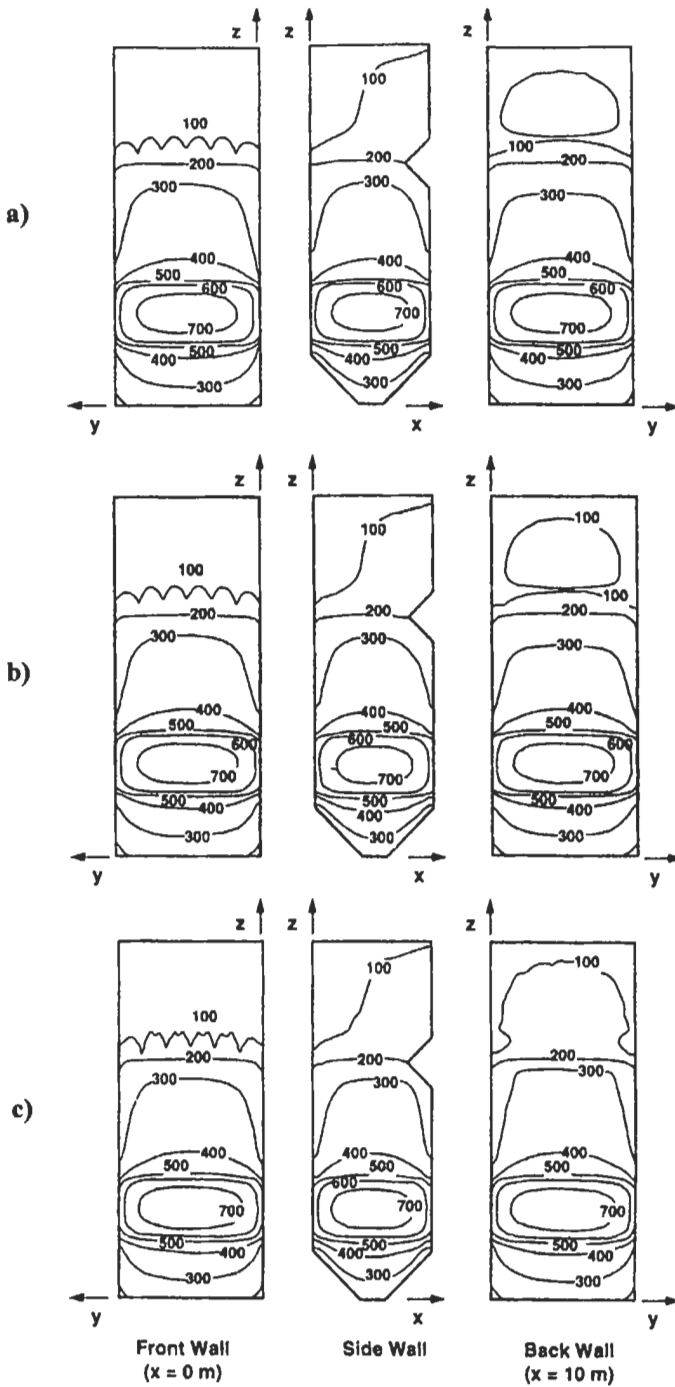


Fig. 5.71: Predicted net heat flux (kW m^{-2}) contours on the walls of the boiler: (a) DOM; (b) FVM; (c) DTM [850]. Reproduced by permission of Elsevier Science.

Good agreements between this method and the Monte Carlo method were found with several particle density variations, in which participating media of optical thin, medium and thick were included. As a numerical example, the method [851] is applied to predict radiative heat transfer in a boiler model with non-isothermal combustion gas and carbon particles and diffuse surface wall. The distributions of heat flux and heat flux divergence in the boiler furnace are obtained. Figure 5.72 (a) presents the geometry of a rectangular medium, and the participating medium is a mixture of CO_2 and N_2 gases and carbon particles. The total mixture pressure is 1 atm, with a volume fraction of CO_2 of 0.21. The temperature of the medium is constant and uniform at 1000 K. The calculations by Guo and Maruyama [851] are compared with the results of several other solution methods for several carbon particle densities of $N_c = 2.0 \times 10^7$, 2.0×10^8 , and 2.0×10^9 particles per cubic meter, which represent participating media of optical thin, medium and thick, respectively. The bench mark comparison of radiative heat flux is shown in Fig. 5.72 (b). The results of the Monte Carlo method, the YIX method and GZM method are from Ref. 870, 869 and 868, respectively. Good agreements are found among the simulations of the Monte Carlo, the YIX and the REM^2 methods. The divergence of radiative heat flux is displayed in Fig. 5.72 (c), in which comparisons are performed between the REM^2 method and the Monte Carlo method [870] in the same conditions of Fig. 5.72 (b). In all the cases of three particle densities, the results agree well with those of Monte Carlo.

The REM^2 method [851] has advantages over other solutions except the Monte Carlo method in dealing with radiation transfer in arbitrary geometry. As a numerical example of complicated configuration, radiative heat transfer in a boiler furnace was also investigated by Guo and Maruyama [851]. A practical boiler configuration of 125 MWe is used with ASTM No. 6 heavy oil is fed from two opposite side walls. The boiler is operated in atmospheric pressure. The temperature of the boiler wall is 623 K. The combustion gas is composed of CO_2 , H_2O and N_2 with the mole fractions of CO_2 and H_2O are 0.119 and 0.085, respectively. The profile of the combustion gas is assumed to be uniform all over the boiler. According to the measurement of Smyth et al [872], the soot inception region in flame is found to occur at the high temperature edge with maximum intensity in a region at 1300-1650 K. The predicted [851] heat flux distributions on the wall and the divergence of heat flux at the center plane of the boiler are illustrated in Figs. 5.73 (a) and (b), respectively, for anisotropic scattering. The heat flux and the divergence of heat flux in the figures are normalized by $-\sigma T^4$ with $T = 2000$ K. The negative value of heat flux represents that the heat is from participating medium transfer into wall surface. As for the divergence of heat flux, a

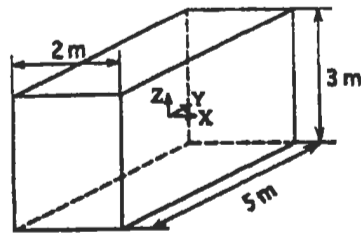


Fig. 5.72 (a): Geometry of a rectangular medium [851]. Reproduced by permission of ASME.

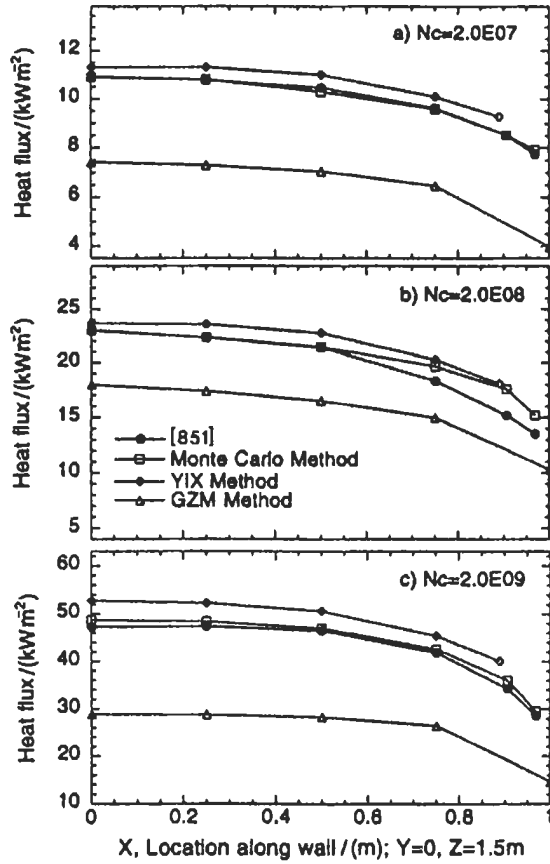


Fig. 5.72 (b): Comparison of heat flux at Y = 0 and Z = 1.5 m [851]. Reproduced by permission of ASME.

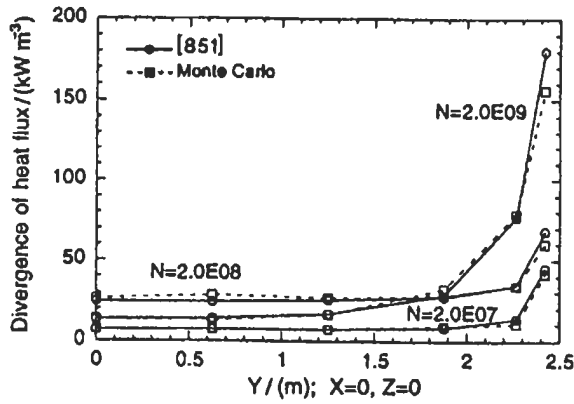
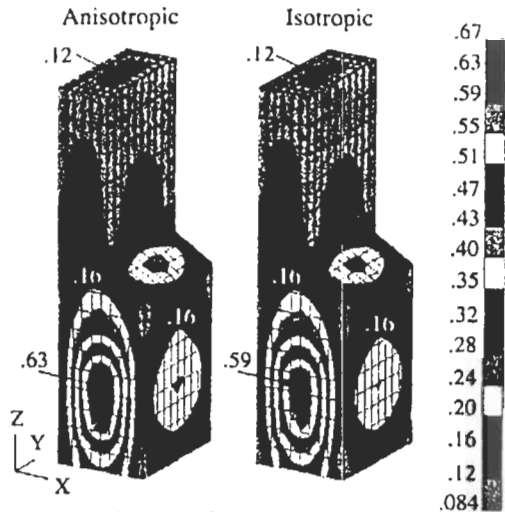
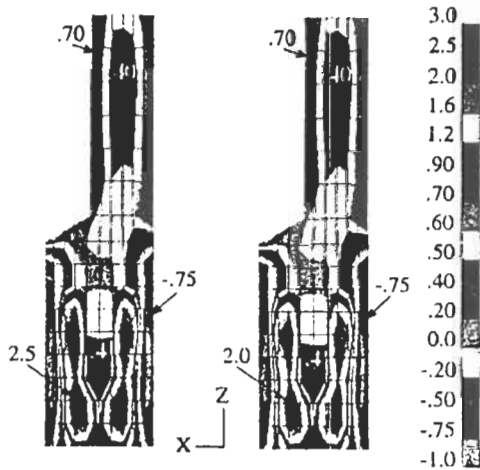


Fig. 5.72 (c): Comparison of divergence of heat flux [851]. Reproduced by permission of ASME.

negative value means absorbing heat, while a positive value stands for heat generation. The larger the absolute value is, the larger is the heat flux or heat flux divergence. It is seen that larger heat flux is distributed in the wall surfaces near the fire region, while the heat flux on the surfaces in pure combustion gas and gas exit regions is very low. This reveals that the radiation from high temperature particles is much stronger than that from high temperature combustion gas, especially for the case of larger number density of the particles. The comparison between Figs. 5.73 (a) and (b) shows that the heat flux as well as the divergence of heat flux increased when the anisotropic property was accounted for. The difference of the results between the anisotropic and isotropic scattering is generally 15 %.



(a) Distribution of normalized heat flux.



(b) Normalized heat flux divergence at $Y=L/2$

Fig. 5.73: Comparison between anisotropic scattering and isotropic scattering with $N_c = 2.0 \times 10^9$ [851]. Reproduced by permission of ASME.

Moreover, a three-dimensional comprehensive furnace model capable of predicting gas flow, coal combustion, and radiative heat transfer has been developed by Boyd and Kent [873]. The model uses fundamental data as input, including the furnace geometry, the operating flow rates of coal and air, the coal type, and the particle size distribution of the coal. Numerical solutions of the gas-phase time-averaged transport equations for mass; momentum, enthalpy, and mixture fraction are obtained using the standard k - ϵ turbulence model. Average major species concentrations using fast chemistry assumption in the gas phase are predicted from mixture fraction fluctuations. Particles motion and combustion are described in a Lagrangian fashion with a stochastic treatment for particle dispersion. Radiant heat transfer is modeled by the discrete transfer method [873].

The Bayswater units which are used as validation test with the above model [873] are 660-MWe opposed wall swirl burner-fired boilers having furnace plan dimensions of 25 m x 13 m. Each boiler is fired by four levels of four burners on the front wall and three levels of four burners on the rear wall. Five of the seven-burner level is necessary for maximum output. Elevational views of the boiler are illustrated in Fig. 5.74. Three operating cases were considered. In the base case, mills A and C were inactive and low swirl in the inlet air to the burners was used. This represents a typical operating condition. The variations on this base case investigated in this study were (a) high swirl mills A and C again out of service and (b) high swirl, with mills A and C in service and mills E and G out of service. Particle trajectories for these three different conditions are presented in elevation views in Figs. 5.75 [873]. The elevation views in these figures show that the particle impactation on the walls is occurring over the region of the furnace near and above the burners. The high-swirl case shows lesser penetration of the burner jets, a higher particle concentration in the center of the furnace, and fewer resultant collisions with the boiler front and rear walls. As expected, comparison of the high-swirl conditions for the two different burner level configurations shows significant differences. A greater degree of particle-wall interaction is evident for the case with E and G level burners out of service. The elevation views reveal that most of this interaction is caused by the unopposed B level, C level, and F level burner jets reached the opposite wall. This effect is not evident with the level A and level C burners being out of service as only the level D is unopposed. Since levels A and C are the highest burners in service with this case, the bulk gas flow in the furnace is quite strong and predominantly vertical. This feature reduces the penetration of the jets. Calculations were performed using first-order finite differences with hybrid upwind differencing.

5.1.5.3 Heat Transfer from Flame Impingement

Overview

In certain industrial processes such as steel and glass making, high rates of heat transfer are obtained by causing the flame to impinge directly on the surfaces. The increase of heat transfer is caused by the higher heat transfer coefficient in the impinging region and the high gas temperature of the flame. Milson and Chigier [874] investigated experimentally the characteristics of heat transfer rates from a coke-oven gas flame impinging at angle of 20 degrees on the hearth of a furnace. El-Askary [875] studied the influence of varying the momentum flux at the burner exit on the convective heat transfer to the impinging surface. Also, Anderson and Streisno [876] have

studied the heat transfer from both the premixed and diffusion flames impinging on water-cooled surfaces. Average heat transfer coefficient for a perpendicular and oblique impinging flame on a water-cooled flat plate has been investigated experimentally by Schulte [877].

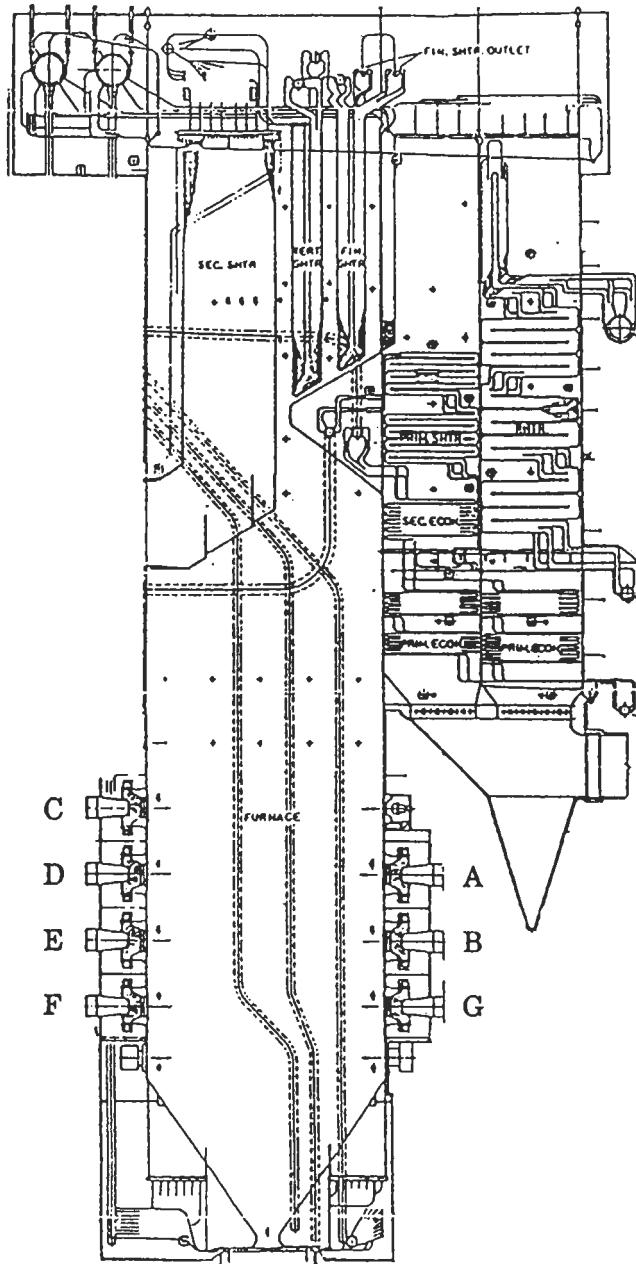


Fig. 5. 74: Bayswater boiler elevation. [873]. Reproduced by permission of ACS.

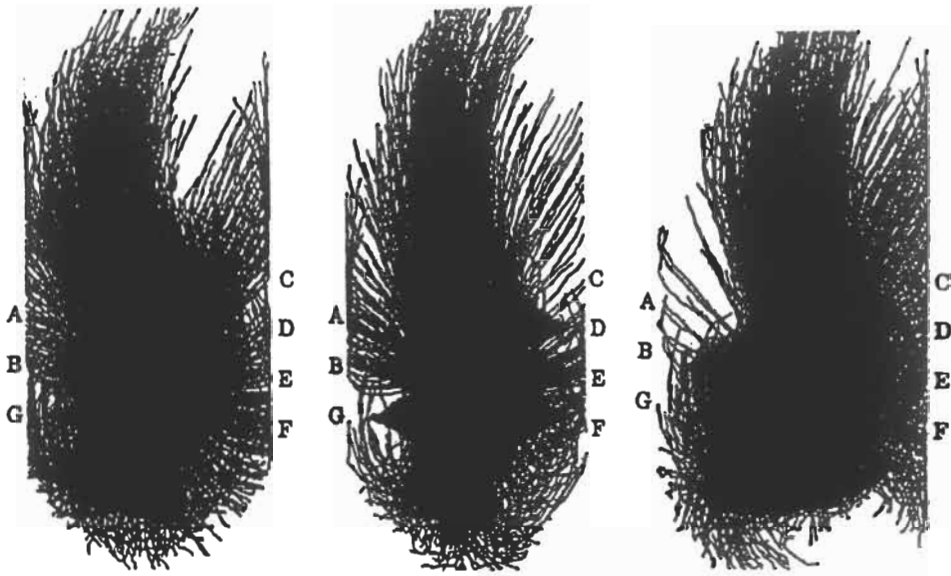


Fig. 5.75: Elevation views of particle trajectories in the Bayswater furnace for the three cases: (a, left) low swirl, mills A and C out of service, all other mills in service, (b, middle) high swirl, mills A and C out of service, (c, right) high swirl, mills E and G out of service, all other mills in service [873]. Reproduced by permission of ACS.

This section describes briefly the flow characteristics concerned with the case of a jet impinging on a solid surface. This will be followed by a background research on the convective heat transfer by impingement.

Considering a circular jet impinging normally on a plane smooth surface, three distinct regions of flow could be recognized, see Fig. 5.76, and are defined as follows:

- **Region 1**, where the flow characteristics are identical to those of the free jet and it is referred to "Free jet region".
- **Region 2**, where the jet is deflected from the axial direction, and it is referred to "Impingement region".
- **Region 3**, where the flow becomes almost parallel to the wall, and it is known as the "wall jet region". Of fundamental importance in the study of impinging jet is the distinction between laminar and turbulent jets.

McNaughton and Sinclair [783] defined four types of free jets, namely:

- Dissipated laminar jet, $Re < 300$. In this case, the viscous forces are larger as compared to the inertia forces, and the jet diffuses rapidly into the surrounding fluid.
- Fully laminar jet, $300 < Re < 1000$. In this case, there is no noticeable diffusion of the jet into the surrounding fluid.
- Transition or semi-turbulent jet, $1000 < Re < 3000$.
- Fully turbulent jet, $Re > 3000$.

In the year 1954, Perry [784] studied the influence of convective heat transfer on the total heat transfer in fuel spray furnaces. Attention was directed to the investigation of heat transfer at the jet streamline of a plate in the narrow range of outflow rates for

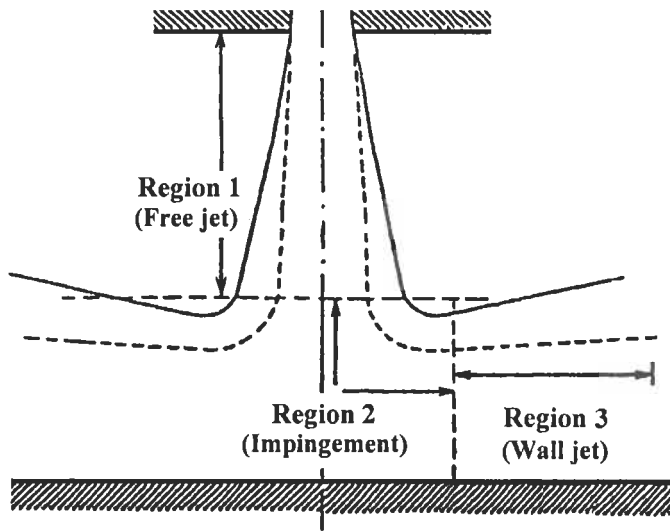


Fig. 5.76: Characteristic regions in impinging jet.

various angles of attack. The Reynolds number related to the outflow rate at the nozzle throat and its diameter varied from 11000 to 30000. A shortcoming of Perry’s experiments is laid in the fact that the distance from the nozzle to the plate was kept constant in all experiments, (the distance equaled eight times the nozzle diameter). This implies that Perry’s rated formulae, however still useful, do not show the influence of the relative distance-to nozzle diameter on the intensity of heat transfer, though physically this influence is emphasized. The experiments of Perry were carried out with a nozzle having a diameter of 16.5 mm, using hot air of temperature varied from 573 K to 873 K. The surface receiving heat had the form of a round plate with a diameter of 344 mm. The rated formula of the heat transfer coefficient for an angle of attack measuring 90°, is the following form:

$$Nu = 0.181 Re^{0.7} Pr^{1/3} \tag{5.70}$$

In the same year, Thurlow [785], investigated in his experiments the influences of the relative jet length-to-nozzle diameter on the heat transfer coefficient for a plate normal to air flow. In these experiments, the relative length varied from ten and higher. The Reynolds number related to the nozzle diameter fluctuated between 22000 to 60000 and the air temperature at the nozzle throat varied from 323 K to 473 K. A copper plate measuring 0.61x 0.152 m served as the heat receiving surface. He also studied the effect of natural convection but gave no indications as to the range of values of Reynolds number and relative length for which the heat transfer by natural convection would predominate.

Thurlow [785] concluded the following formula for an angle of 90° as:

$$Nu = C Re \exp(-0.037X/d) \tag{5.71}$$

where X is the distance between nozzle and plate, and d is the nozzle diameter.

The coefficient, C , in Eq. 5.71, was taken as 1.06 for a nozzle diameter of 25.4 mm and 0.33 for a nozzle of 12.7 mm. The characteristic dimension is the nozzle diameter and air properties was taken at the temperature at nozzle throat, while the velocity for Reynolds number was related to the nozzle cross-section. Yet, the equation given by Thurlow needs further evaluations for the constant, C , as a function of nozzle diameter.

Smirnov et al [786], extended the work of heat transfer from impinging jet. They studied experimentally the heat transfer between a submerged jet of liquid (water) and a plate held normal to the flow. Different nozzles were used having a diameter ranging from 2.5 mm up to 36.6 mm. The plate was circular with a diameter of 48 mm. The experiments were conducted for a range of Reynolds number ranging from 50 to 31000, whereas the velocity was referred to the flow at nozzle throat. The characteristic diameter was considered as the nozzle diameter. The distance between the nozzle and the plate was being varied.

Three heat transfer regions varying in relative to length-to-nozzle diameter were established. The Nusselt number was related as a function of Reynolds and Prandtl numbers as well as the relative distance-to-nozzle diameter:

$$\text{For } X/d \leq 0.5 \quad Nu = 0.55 Re^{0.5} Pr^{1/3} \quad (5.72)$$

$$\text{For } 0.5 < X/d < 10.0 \quad Nu = C Re^{0.64} Pr^{1/3} \exp(-0.037X/d) \quad (5.73)$$

where,

$$C = 0.034 + d^{0.9} \quad (5.74)$$

Noting that d is in mm.

$$\text{For } X/d > 10.0 \quad Nu = C_1 (Re Pr_r)^{1.3} \exp(-0.037X/d) \quad (5.75)$$

where,

$$C_1 = 0.034d^{1.3} \quad (5.76)$$

The rated formula satisfactorily agreed with the experimental data of Thurlow [786]. Later, Gordon and Akfirat [787] presented a paper for the local as well as the average heat transfer coefficients between an isothermal flat plate and impinging two-dimensional jets, for both cases of single and arrays of jets. For the measurement of heat flow, a heat flow transducer mounted in the hot plate was used. The nozzles incorporated for the experiments were 0.153 m. long slots having openings of 4.2, and 6.4 mm wide. The nozzle-to-plate spacing was varied. The plate was kept at 275 K above the temperature of ambient air and the incoming jets. They correlated a formula for fully developed turbulent slot jets, for the stagnation-point heat transfer coefficient with accuracy of $\pm 5\%$:

$$Nu = 1.2 Re^{0.58} (Z_n/B)^{-0.62} \quad (5.77)$$

where, the Reynolds number at nozzle exit condition is in range ($2000 < Re \leq 5000$), B is the nozzle width, Z_n is the nozzle-to-plate spacing and Nu is the Nusselt number at

stagnation point. The characteristic dimension was taken as the nozzle width. The parameter (Z_n/B) is greater than 14 for their above mentioned formula. They also studied as well the lateral variations of local heat transfer coefficients, which were evident to have the shape of bell. For the arrays of jets, they concluded a formula for the average heat transfer coefficient:

$$Nu = 0.36Re^{0.62} \quad (5.78)$$

The Reynolds number was based upon the nozzles spacing as the characteristic dimension, and the arrival velocity. The nozzles spacing was also used for Nusselt number. Their work [787] indicates important rules for heat transfer from impinging jets. However, the formulae need to be tested more extensively, and the arrival velocity has to be accurately estimated.

Kataoka and Mizushina [788] studied the effect of free-stream turbulence on the local heat transfer in an impinging round jet. For large Prandtl numbers, they used the so-called electrochemical method. The rate of heat transfer for large Prandtl numbers was much more enhanced by the amplified turbulence of free-stream rather than skin friction in the impingement region. The enhancement of heat transfer could be explained with two contributions: (1) the penetration of mixing-induced turbulence across the laminar boundary layer in the presence of negative pressure gradients, and (2) the subsequent transition from laminar to turbulent boundary layer by the disappearance of pressure gradients. They deduced a formula based on theoretical calculation for the Nusselt number, as follows:

$$Nu(X) = k_2 Re^{3/4} Pr^{1/3} (X/d)^{-5/4} \quad (5.79)$$

where X is the radial distance from stagnation point and Re is the Reynolds number based on the jet velocity at nozzle exit. The characteristic diameter was taken as that of nozzle. Their formula had been correlated experimentally, and showed good agreement. The coefficient k_2 is not obtainable directly by means of a single equation. However, their work is considered a success because of the theoretical background, which diverts the work on such study away from being only empirical or semi-empirical.

El-Mahallawy et al [789] extrapolated the study of heat transfer by impingement of flames to circular plates, and more details about the heat transfer characteristics resulting from the impingement of reacting jets on cold and hot solid surfaces will be discussed next.

Experimental and Computational Analysis

El-Mahallawy et al [878] have investigated the heat transfer characteristics resulting from the impingement of a single as well as multiple flames fired inside the model of water-tube boiler (MWB) described above. In the impingement region, the measured pressure at the stagnation point reaches its maximum value and the measured velocity has a zero value at this point. The total heat fluxes on the impinging wall were measured by means of calibrated heat flux meters (conductivity type). The same instrument has been used to measure the radiative heat fluxes, but in this case, the sensing element of the instrument was covered with a glass cub. The measured temperature, total heat flux,

and convective heat flux are shown respectively in Figs. 5.77 (a) to (c) with the distance from central plane of the rear wall. These results are compared with the corresponding predicted values for a single flame. The model used in predicting the flame properties and heat transfer fluxes [165] comprises the continuity, momentum and energy equations, the k - ϵ turbulence model, fast flame sheet chemistry and the discrete transfer formulation for radiative heat. General description of the model is given in section 5.1.5.2. The inlet conditions to the model are the experimental fuel and air flow rates, fuel vapor temperature of 1000 K, oxidant temperature of 700 K, wall temperature of 400 K, and turbulent intensity of 0.03.

Their results [838] show that the maximum convective heat flux occurs at the stagnation point in the impingement region as the results of higher gas temperature as well as the effects of impingement which cause the distortion of viscous sub-layer and augment the turbulence at the impingement region and consequently increases the heat transfer coefficients. Integrating the heat flux values over the impinging wall for single flame showed that about 31.6 % of total heat is transferred by convection. Also in the impingement region the intensity of the maximum convective heat flux is 42% of the total heat transfer; while without impingement, the convection percentage is between 5 % to 10 % of the total heat transfer. This observation shows the severe effect of the impingement.

For single flame case, it was found [878] also that changing momentum flux at the burner exit from 29.7 to 13.2 kg m s⁻² ($A/F = \text{constant}$) leads to a decrease in the maximum convective heat flux by about 50%. This is attributed to the decrease of the heat transfer coefficients on the wall as the results of decreasing the gas velocity, turbulence level, and the gas temperature. In addition to that, the changing of A/F from 18 to 21 (with constant momentum flux at the burner exit) leads to a decrease in the maximum convective heat flux intensity by about 16.6%. This can be attributed to the decrease in the gas temperature on the impinging wall. In case of two and three flames, about 27.3 % and 26.88 % of the total heat is transferred by convection to the impinging wall. This indicated that the multi-flame impingement has a relatively lower influence on the convective heat transfer intensities especially in the impingement region.

Figures 5.77 (a) to (c) show the comparison between the experimental and predicted results for gas temperature, total heat flux, and convective heat flux, respectively. The comparison shows that there is a fairly good agreement from the qualitative point of view, but from the quantitative point of view, the figures show noticeable differences between the predicted and experimental values, especially for the convective heat flux, Fig. 5.77 (c). It could be concluded from this work that the prediction of flame properties and heat transfer resulting from the impingement of oil flames on heat transfer surfaces in three dimensional furnaces is still a difficult problem which requires further trials and modifications.

Recently, Keramida et al [879] have studied the heat transfer by radiation in impinging jet flows on granite plates. Two different eddy viscosity turbulence models, namely the standard k - ϵ (described in chapter 3) and the RNG k - ϵ model with and without radiation (discrete transfer model) were assessed. The results indicate that the main effect of radiation is the decrease of temperature values near the jet stagnation point and along the plate surface. Radiation increases temperature gradients and affects predicted turbulence level independently of the used closure model. Also, the RNG k - ϵ model predicts higher temperature towards the solid plate, with and without radiative heat transfer. Some of these results [879] are shown in Figs. 5.78 and 5.79.

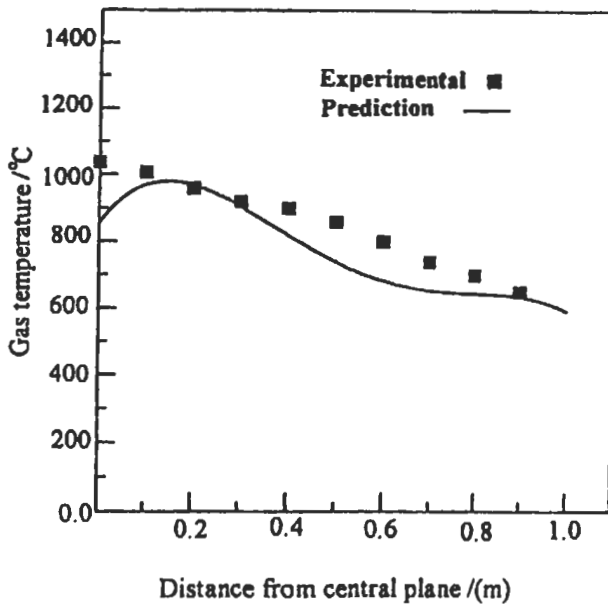


Fig. 5.77 (a): Comparison between prediction and experimental data of the gas temperature distribution on the impinging rear wall of MWB [878].

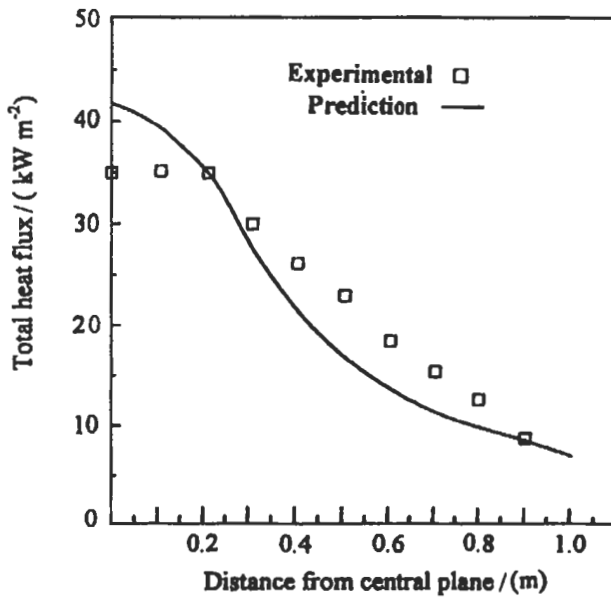


Fig. 5.77 (b): Comparison between prediction and experimental data of the heat flux distribution on the impinging rear wall of MWB [878].

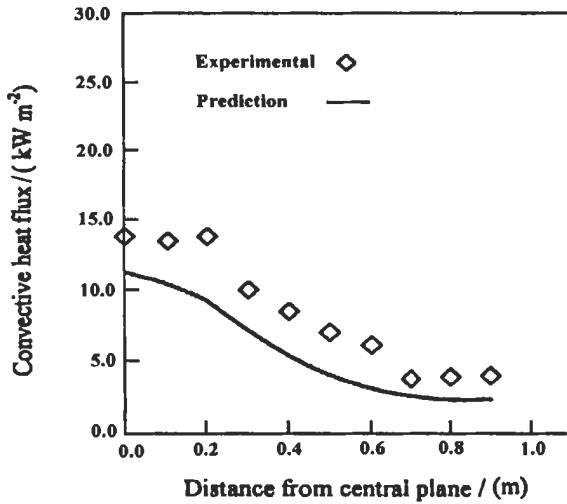


Fig. 5.77 (c): Comparison between prediction and experimental data of the heat flux distribution on the impinging rear wall of MWB [878].

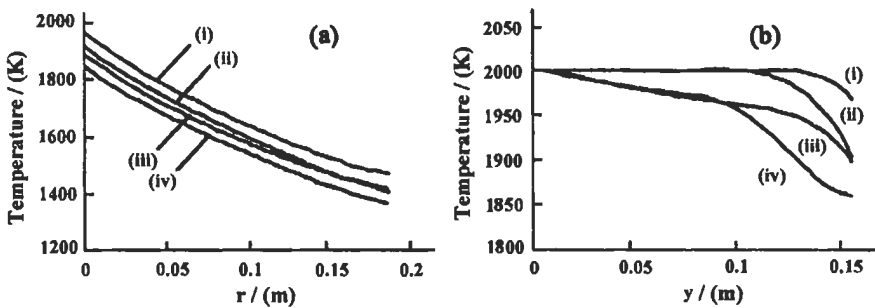


Fig. 5.78: Temperature profiles a) along the granite plate outer surface and b) along the centerline of the heated impinging jet. Here, y is the distance from jet exit and r is the plate radius. (i) No radiation RNG $k-\epsilon$, (ii) No radiation standard $k-\epsilon$, (iii) Radiation RNG $k-\epsilon$, and (iv) Radiation standard $k-\epsilon$. Keramida and Liakos [879], reproduced by permission.

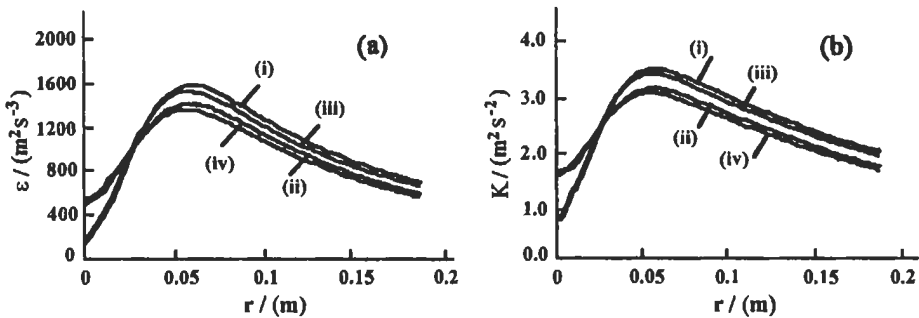


Fig. 5.79: a) Energy dissipation profiles and b) turbulence kinetic energy profiles along the plate surface. (i), (ii), (iii), and (iv) are the same as in Fig. 5.78. Keramida and Liakos [879], reproduced by permission.

Figure 5.78 shows temperature profiles along the granite plate outer surface (a) and along the centerline of the jet (b). Four cases have been studied. Two cases do not take into account the radiative heat transfer and use the standard k- ϵ turbulence model and the RNG k- ϵ model, while the other two use the same turbulence models including the effect of radiation. It is clear that without consideration of radiation effects the calculated temperature values are higher along the surface (see Fig. 5.78 a). The predicted temperature difference (with and without radiation) is about 50 K independently of the used turbulence model. At $y = 0.125$ m, the temperature gradients (Fig. 5.78 b) start to become steeper towards the plate when radiation is taken into account. Close to the stagnation point, predicted temperatures are higher with the RNG k- ϵ than with the standard k- ϵ turbulence model. The predicted temperature gradients are different with the two turbulence models while are the same for each turbulence model with and without the radiation effect. Again, predicted temperatures without radiation effects are higher. Figure 5.79 shows that the predicted dissipation of turbulence (a) and the variation of turbulence kinetic energy (b) along the plate surface exhibit lower values when radiation is taken into account. The maximum predicted values of the turbulence kinetic energy and dissipation rate of turbulence are higher with RNG k- ϵ model, because it can capture better the characteristics of the developing shear flow [880].

Keramida et al [879] have concluded that the temperature predictions are intrinsically different when radiation heat-transfer is taken into account and the difference is larger near the surface and specifically within the stagnation area which is the most important region where intense heat-transfer occurs. The application of the standard k- ϵ and the RNG k- ϵ models yielded different temperature profiles.

5.1.6 Emission and Emission Control

An understanding of the mechanisms and chemical reactions that produce pollutant emissions (such as CO, SO_x, NO_x and particulate matter as discussed in chapter 1-4) have enabled engineers and scientists to develop techniques for reducing emissions of these pollutants. Along with carbon-monoxide (CO), sulfur oxides (SO_x) and particulate matter, NO_x emissions have been identified as contributors to acid rain and ozone formation, visibility degradation and human health cancers as discussed in chapter 1. As a result, CO, SO_x, NO_x emissions from most combustion sources are regulated and required some techniques of control as discussed in chapter 1. Several investigators [881-890] have investigated the application of these techniques to the boiler equipment. In chapter I we have discussed the pollutant emission and its control. In industrial boilers, the most common control techniques include:

1. Application of combustion control systems capable of maintaining low levels of excess air with safe limits for CO.
2. Upgrading of airflow distribution systems for stoker fired boilers.
3. Reduction of fuel bound nitrogen in residual fuels by blending distillate oil.
4. Use of modified oil gun nozzle tips for residual oil combustion.
5. Application of diluents for gaseous fuel combustion, including air, steam and flue gas.
6. Reduction in the boilers maximum continuous rating (MCR) for the purpose of lowering the furnace heat release rate.

7. Replacement of an air preheater with an economizer.
8. Installation of burners designed to combust fuel at low NO_x generation rates.

Regarding the modeling of NO_x and CO in boilers and related combustion equipment, Joseph [889] has developed a semi-empirical model, which may be used to correlate NO_x as a function of boiler load, oxygen concentration and degree of flue gas recirculation (FGR), water, steam, or diluent injection, burner out of service, air staging, nitrogen content in the fuel, and selective non-catalytic reduction (SNCR) or selective catalytic reduction (SCR).

The following describes some applications for the techniques in industrial boilers.

5.1.6.1 Combustion Modification Techniques

This section presents the application of low emission combustion modification techniques in boilers and furnaces.

Flue Gas Re-circulation (FGR)

Flue gas re-circulation (FGR) is a well-known technique for oxides of nitrogen (NO_x) control in industrial boiler or burner applications. This control technique reduces both oxygen partial pressure and flame temperature. This is due to increasing the proportion of inert gas in the combustion zone, and this reduction has its greatest effect on reducing the thermal NO formation. It has been demonstrated in a small-scale boiler [891] and in laminar diffusion flame [892] that introducing the recirculated flue gas with the fuel results in a much greater reduction in NO_x per unit mass of recirculated gas, when compared to mixing the flue gas with air. This technique is referred to as fuel injection recirculation (FIR). For example, NO_x emissions were reduced from 90 to 30 ppm with 5 % FIR, while 23 % conventional windbox FGR was required to achieve the same reduction [891]. Large water-tube boilers would require considerable auxiliary power consumption for larger amounts of re-circulation, nevertheless small re-circulation rates (up to 10 %) give useful improvements in overall NO_x emissions. Figure 5.80 (a) shows the practical technique of the external exhaust gas re-circulation using a separate fan, where the principle of this technique is to re-circulate controlled quantities of exhaust gases from the boiler into the combustion air [105]. However, in this case care is taken to maximize the heterogeneity of the mixing to ensure maximum temperature suppression in the flame. The practical feasibility of the exhaust flue gas re-circulation has been investigated by Wiles and Gerhold [893] who found that significant reduction of NO_x (50 %) could be achieved if 20 % or less of the total external exhaust gases is re-circulated at base load conditions. The degree of reduction, which can be achieved, is dependent on the fuel, the concentration of nitrogen oxide at the boiler exit and the degree of re-circulation. Representative reductions in NO_x emissions that can be achieved in utility boilers burning natural gas using flue gas re-circulation are shown in Fig. 5.80 (b). Nitrogen oxide emissions reductions up to 70 %, corresponding to NO_x emissions in the range 50-100 ppmv (at 3 % O_2) have been achieved in large-scale utility boilers [894-896].

Recently, the internal flue gas re-circulation gives an advantage over the external gas re-circulation, where the cost for installation and controls associated with the external re-circulation technique are eliminated. An example of the internal gas recirculation is the

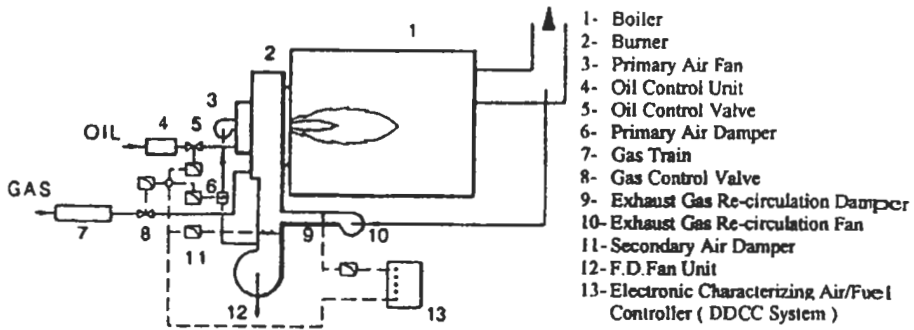


Fig. 5.80 (a): Exhaust gas re-circulation using a separate fan [903]. Reproduced by permission of Saacke Limited.

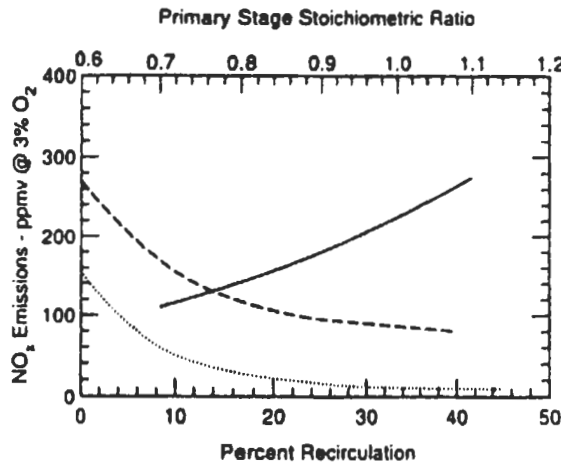


Fig. 5.80 (b): The effect of fuel-air staging (solid line) and flue gas re-circulation (dashed line) on NO_x emissions from a corner-fired 320 MW_e utility boiler [894] and from a 1.5 MW_e simulated fire-tube boiler [896] (dotted line) with natural gas firing [118]. Reproduced by permission of The Combustion Institute.

Delta burner head, where some of the exhaust gases behind the burner head region strongly drawn very rapid in the flame root by the present Delta vanes in the burner head. This ensures that the fuel, combustion air and drawn-in exhaust gas are predominantly mixed and produce very rapid and uniform mixing of the three material flows. The re-circulated exhaust gas as “thermal ballast” flows through the main reaction zone, leading to a decrease of maximum flame temperature and consequently reduces the thermal NO. El-Sherif and Ismail [897] have investigated the effect of internal re-circulation of exhaust gases on the emissions using commercial oil Delta burner head (see Fig. 5.81 (a)). They have found a significant reduction of NO_x (60 %), while CO increases by about 28 % when using a Delta vane angle of 30° (see Figs. 5.81 (b) and (c)).

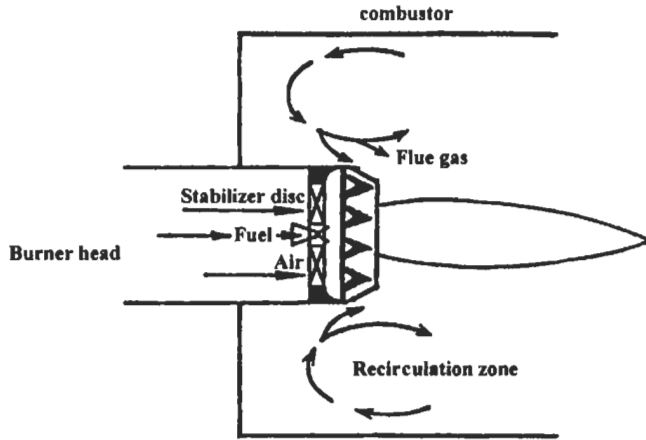


Fig. 5.81 (a): Delta burner with internal re-circulation zone [897].

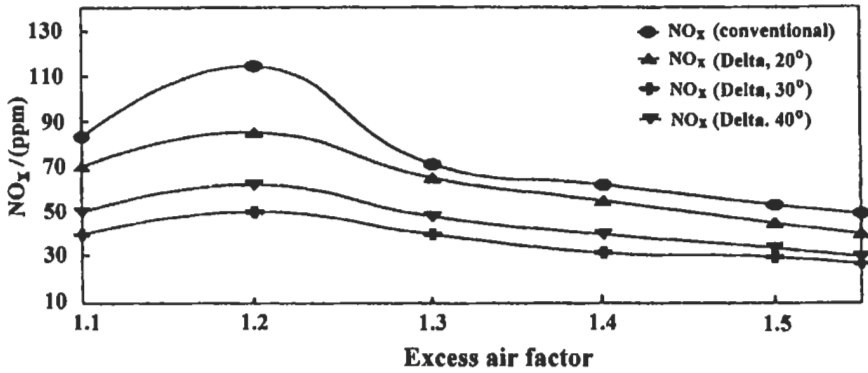


Fig. 5.81 (b): Effect of excess air and burner head geometry on nitrogen oxides in the exhaust gases (with conventional and Delta burner heads) [897].

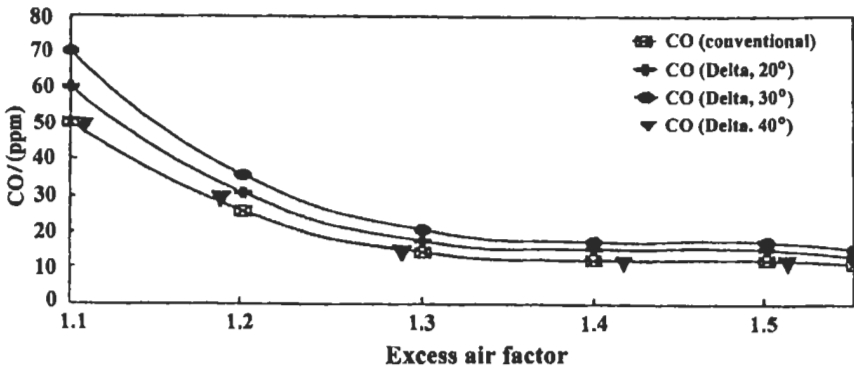


Fig. 5.81 (c): Effect of excess air and burner head geometry on carbon monoxide in the exhaust gases (with conventional and Delta burner heads) [897].

Water and Steam Injection

Addition of water or steam as a diluent through burnt-gas recirculation can be beneficial method (see chapter 1) for reducing NO_x in industrial boilers [885]. However, injection of water or steam into the combustion zone has a similar physical effect to that of combustion gas re-circulation. In some cases the water or steam is injected directly into the flame, either through a number of separate nozzles located at the head end of the combustor or through holes that are integrated into the fuel nozzle. In conventional combustors, and by using water injection system shown in Fig. 5.82 (a), a reduction of NO_x (25 %) has been achieved by El-Mahallawy et al [898] with mass ratio of water/fuel (m_r) injection of 0.95 (see Fig. 5.82 (b)), and this was associated with the increase of CO concentration. When steam is used to reduce NO_x emissions, it may also be injected directly into the combustion zone or into air, which subsequently flows into the combustion zone. In some installations the steam is injected into the compressor discharge air. This method is simple but inherently wasteful, because only about 40 % of the steam actually flow into the combustion zone. By introducing steam through the

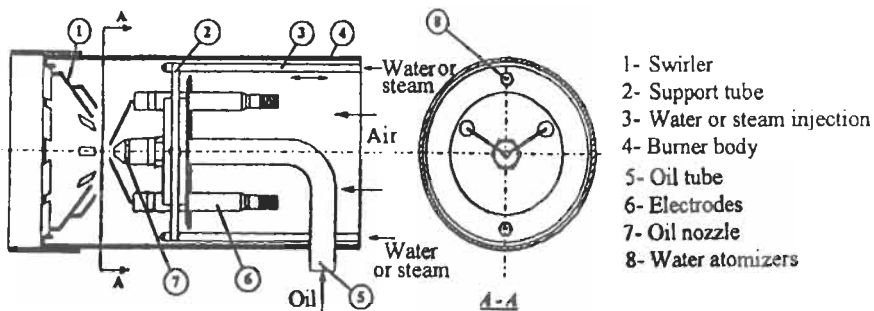


Fig. 5.82 (a): Burner head with water and steam injection [898].

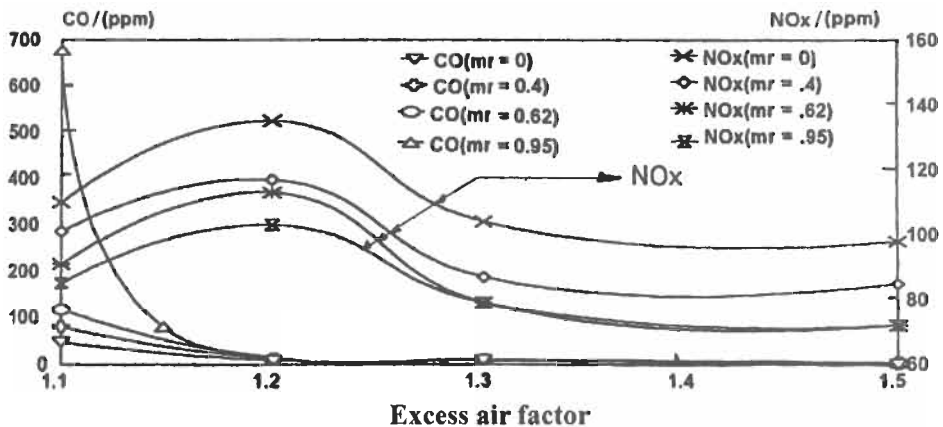


Fig. 5.82 (b): Effect of excess air and water addition on carbon monoxide and nitrogen oxides concentrations at exhaust gases [898].

atomizing circuit of the oil gun, NO_x reductions of up to 25 % can be achieved [885]. Also, a reduction up to 50 % of NO_x has been observed in two-stage methane-air flames when 5 % water by mass was added to the air stream [899].

Air and Fuel Staging

Air and fuel staging means the division of combustion zones into areas of sub-stoichiometric and over-stoichiometric combustion. The purpose of this measure is to effect combustion under conditions of insufficient air, which has the results of a low nitrogen oxide concentration, and then to transfer the products of this incomplete combustion to a subsequent over-stoichiometric stage. The principles of air and fuel staging are applied to heavy oil and coal combustion systems, but are most applicable to water-tube boilers which have a lower furnace heat release rate and the resultant greater volume in which to achieve complete combustion. Different burner geometries to achieve staging in boilers and furnaces, termed low- NO_x burners, have been developed. A common characteristic of most low- NO_x burners is that the primary combustion zone is fuel-rich, with staged introduction of additional air (see Fig. 5.83). Representative reduction in NO_x emissions from utility boilers achieved by staging is shown in Fig. 5.80 (b) for natural gas firing and in Fig. 5.84 for pulverized coal firing [900-901]. Reduction of NO_x emissions by staging in the range of 50-70 % has been achieved in practice.

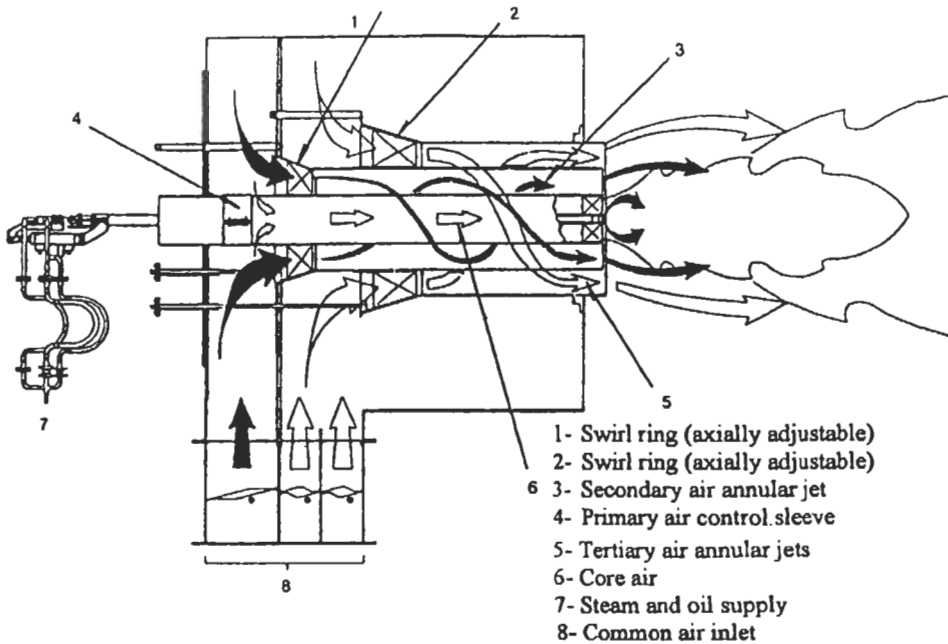


Fig. 5.83: Low NO_x axial swirl staged combustion burner [903]. Reproduced by permission of Saacke Limited.

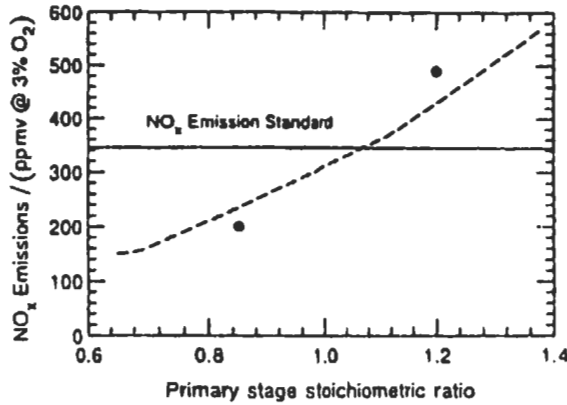


Fig. 5.84: The effect of fuel-air staging on NO_x emissions from a 160 MWe tangentially fired pulverized coal boiler for a bituminous coal (1.7 wt % N daf) [900] solid circles. The dashed line shows pilot-scale data for a bituminous coal (1.4 wt % N daf) [901]. Also shown is the current U.S. NO_x emissions standard for tangential firing [118]. Reproduced by permission of The Combustion Institute.

Burner Configuration and Duration

The principle of rotary cup atomization, which utilizes mechanical means supplemented with high velocity primary air, together with thermal assistance from the flame, are considered to form a particularly suitable technology for progressive emission reduction and energy optimization. The complimentary gas ring burner, which uses circumferential staging with fuel rich and fuel weak zones, is equally effective.

A unique method of NO_x reduction for oil combustion has been through the application of oil gun nozzle tips, which have been modified for the purpose of reducing NO_x. The installation of these tips requires some trial and error adjustments. These tips concentrate on:

1. Spray angle changes.
2. Fuel atomization characteristics
3. Increasing atomization steam flow.

NO_x reductions in the range of 10 to 20 % is feasible with this application [885].

Application of Round Burner with Tilted Air Supply (RoBTAS' burner) to the Northside NO. 3 boiler is described by Joe et al [890]. This low NO_x oil/gas burner originally supplied to Jacksonville Electric Authority, Northside No. 3, 500 MW unit, were based on a duplex air register design with lobed spray oil atomizers providing additional fuel staging. Although the burners could meet the targeted NO_x levels of 0.113 and .075 kg 10⁻⁶ kJ⁻¹ on oil and gas respectively, these were insufficient margin on these NO_x levels to enable continuous low NO_x operation to be achieved. Future burner development was undertaken based on improved aerodynamic control within the burner design to give an approximate 25 % improvement in NO_x emission reduction thus providing an adequate operating margin. This burner (RoBTAS) design based on techniques developed successfully for front wall coal firing applications achieved the required NO_x reduction in full scale firing demonstrations on both heavy fuel oil and natural gas firing.

A general analytical approach for scaling NO_x emissions from burners and furnaces has been suggested by Hsieh et al [902], together with the scaling model for NO_x emissions performance that results when this approach is applied to a broad class of swirl-stabilized industrial gas burners. This approach provides the first NO_x scaling data over the range of thermal scales from 30 kW to 12 MW (represent a factor of 400 in thermal scale, and called SCALING 400 test), including input-output measurements as well as detailed in-flame measurements of NO , NO_2 , CO , O_2 , unburned hydrocarbons, temperature, and velocities at each scale. The scaling model permits design trade-off assessments for a broad class of burners and furnaces, and allows performance of full industrial-scale burners and furnaces of this type to be inferred from results of small-scale tests.

Burner performance scaling of NO_x emissions is shown in Figs. 5.85 (a) to (d). Figure 5.85 (a) compares the predictions obtained from the scaling model [902] under the assumption of perfect similarity (solid symbols) with the measured NO_x emissions (presented as emission indexed NO_x , $\text{EI NO}_x = \dot{m}_{\text{NO}_x} / \dot{m}_{\text{fuel}}$) for burner performance with turndown at all five primary burner scales. Also shown are results for the 300 kW performance in the BERL test under both hot-wall and cold-wall conditions. Figure 5.85 (b) compared the scaling model prediction, again under the assumption of perfect similarity (solid symbols), with the measured NO_x emissions over the entire range of air dilution level. The model appears to capture many of the trends in the data, though there are clear differences at the 12-MW scale. Figure 5.85 (c) shows the variation in NO_x emissions with combustion air preheat as obtained from the measurements (open symbols) over all burner scales, and as predicted by the scaling model under the assumption of perfect similarity (solid symbols). Figure 5.85 (d) shows corresponding comparisons between the scaling

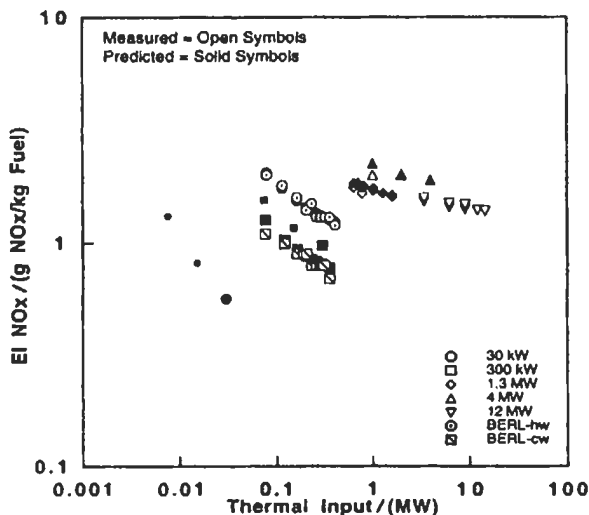


Fig. 5.85 (a): Turndown scaling. Comparison between measured NO_x emission levels versus thermal input (open symbols) and predicted NO_x emission levels from the scaling model [902] assuming perfect aerodynamic and thermal similarity (solid symbols). Reproduced by permission of Elsevier Science.

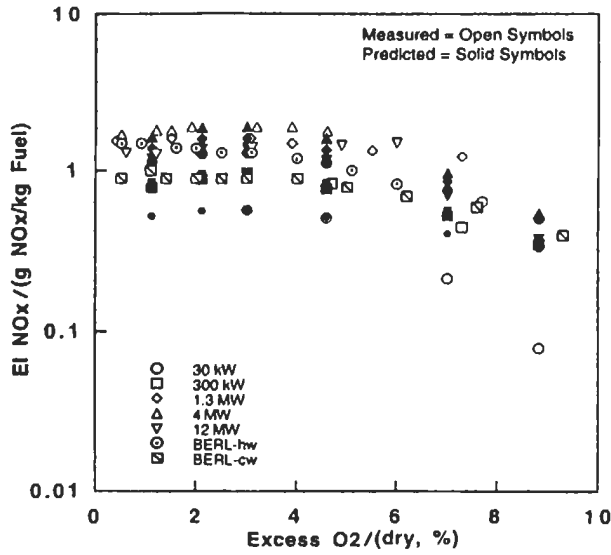


Fig. 5.85 (b): Excess air dilution scaling. Comparison between measured NO_x (open symbol) and predicted (solid symbol) variations in NO_x emissions with excess air dilution level and from the scaling model [902] assuming perfect aerodynamic and thermal similarity. Reproduced by permission of Elsevier Science.

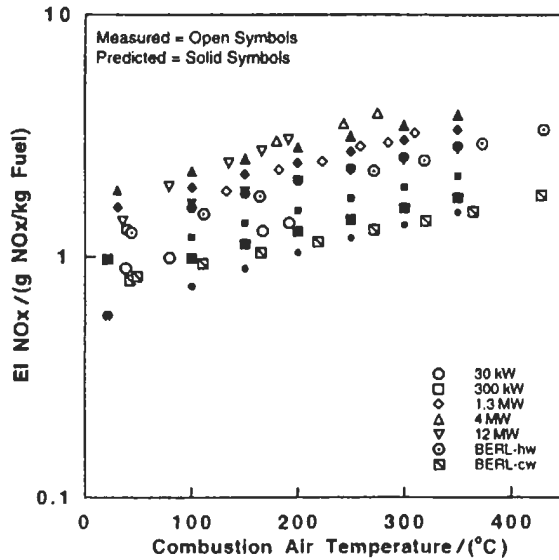


Fig. 5.85 (c): Combustion air preheat scaling. Comparison between measured NO_x emission levels versus combustion air temperature (open symbols) and predicted NO_x emission levels from the scaling model [902] assuming perfect aerodynamic and thermal similarity. Reproduced by permission of Elsevier Science.

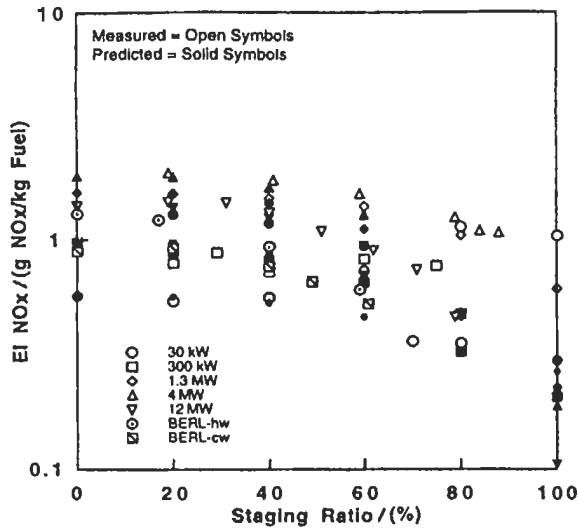


Fig. 5.85 (d): Fuel staging effects. Comparison between measured NO_x emission levels versus fuel staging ratio (open symbols) and predicted NO_x emission levels from the scaling model [902] assuming perfect aerodynamic and thermal similarity. Reproduced by permission of Elsevier Science.

model predictions and measurements for the dependence of NO_x emissions on fuel staging ratio. Finally, Fig. 5.85 indicate that the simple burner scaling model presented in “The SCALING 400 Model” appears to largely account for most major trends seen in the NO_x emissions performance of this class of burners and furnaces.

The reaction mechanism of NO_x is highly dependent on temperature and on duration of exposure to the necessary conditions (see Fig. 5.86) [903]. With high combustion

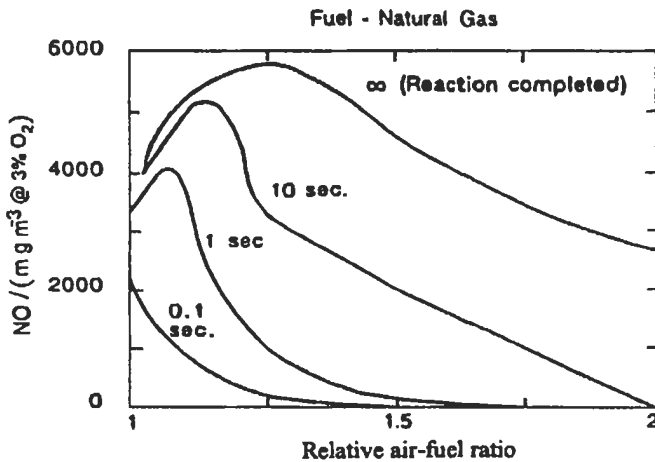


Fig. 5.86: Effect of relative air / fuel ratio and residence time on NO_x production [903]. Cited by Saacke Limited [903].

chamber temperatures, it is therefore important to keep the time spent in the high temperature zone as short as possible. These results can be achieved by constructing the burner appropriately, and by optimizing the shape of the combustion chamber.

Re-Burning

Natural gas reburning for NO_x control is currently a mature technology, which has been successfully demonstrated at full-scale boilers. In re-burning (NO recycling) approach (see chapter 1), a lean primary combustion stage is followed by a fuel-rich re-burning zone, where additional fuel is injected, with the remaining combustion air being introduced downstream of the re-burning zone. The chemical mechanism of re-burning involves the recycling of NO formed in the primary stage by reactions with hydrocarbon radical species (cyano compounds which mainly CN and HCN) in the fuel-rich re-burning stage. Under fuel-rich conditions, these cyano compounds may react preferentially to form N_2 and consequently reduce NO.

Natural gas re-burning is a practical technique for controlling emissions of nitrogen oxides (NO_x) from existing utility and large industrial boilers fired by any fossil fuel or waste material. In most boilers, this highly effective and flexible process can reduce NO_x emissions by 60-70 % using natural gas (total heat input).

The gas re-burning process reduces emissions without replacing or modifying existing burner equipment and required no chemical reagents or catalysts. In coal-fired boilers, SO_2 , particulate, and CO_2 are also reduced.

In gas re-burning, natural gas is injected into an upper region of the boiler to convert NO_x in combustion gases to N_2 . The overall process design and reactions involve three zones of the boiler as shown in Fig. 5.87:

- a. **Primary combustion zone.** In the primary combustion zone, existing burners fired by coal, oil, or gas are turned down by 10 to 20 %. The burners or cyclones may be operated at the lowest excess air consistent with normal commercial operation to minimize NO_x formation and to provide appropriate conditions for re-burning.
- b. **Gas re-burning zone.** Natural gas (between 10 to 20 % of boiler heat input) is injected above the primary combustion zone. This creates a fuel-rich region where hydrocarbon radicals react with NO_x to form N_2 . Gas re-burning injectors require new boiler-wall penetration on most boilers units.
- c. **Burnout zone.** A separate overfire air system redirects air from the primary combustion zone to a location downstream of the gas re-burning reaction zone to ensure complete combustion of unreacted fuel and combustible gases. This separate overfire air system requires boiler penetrations and ducting.

Full-scale field evaluations have amassed a growing body of performance data on gas re-burning in a variety of electric utility applications. The Gas Research Institute (GRI) has cosponsored these demonstrations with commercialization partners and research organizations that include the Electric Power Research Institute (EPRI), U.S. Department of Energy (DOE), U.S. Environmental Protection Agency (EPA), state agencies, gas companies, and electric utilities [904]. A summary of such full-scale field gas re-burning evaluations is given in Table 5.5.

Representative NO_x emissions reduction for a pilot-scale cyclone-fired pulverized coal combustor with reburning [905] are shown in Fig. 5.88. The effectiveness of re-burning in reducing NO_x emissions is dependent on the re-burning fuel. The largest reductions are achieved when the re-burning fuel is nitrogen free. In full-scale

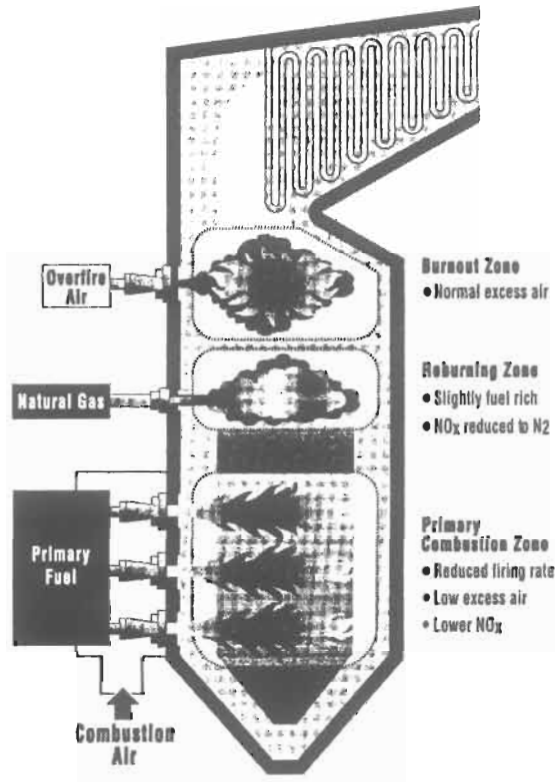


Fig. 5.87: Gas re-burning takes place in three boiler zones and converts NO_x to N₂ [904]. Reproduced by permission of Gas Research Institute.

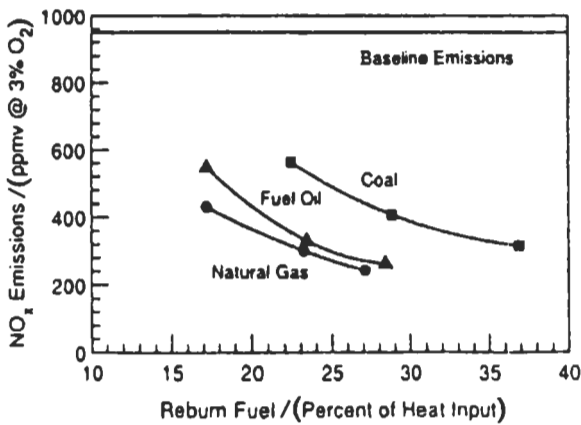


Fig. 5.88: The effect of re-burning on NO_x emissions from a pilot-scale cyclone boiler burning pulverized bituminous coal (1.4 wt % N daf) [905] re-burning fuel: ■ coal; ▲ fuel oil; ● natural gas. Fixed excess air = 15 %. Also shown are the base line NO_x emissions [118]. Reproduced by permission of The Combustion Institute.

Table 5.5: Full-scale gas re-burning field evaluation [904]. Reproduced by permission of Gas Research Institute.

Location	Size (MW)	Type	NO _x Control level
Ohio Edison – Niles	108	Cyclone	40-60 %
Illinois Power – Hennepin (with sorbent)	71	Tangential	60-70 %
Kansas P & L – Lawrence (close coupled)	300	Tangential	60 %
P.S. Colorado – Cherokee (with low burners)	158	Wall	75 %
CWLP-Lakeside (with sorbent)	33	Cyclone	60 %

natural gas fired furnaces, reductions of NO_x emissions of up to 50 %, corresponding to 40-50 ppmv at 3 % O₂, have been reported [906]. In coal fired furnaces, reduction in NO_x emissions of up to 70 % for cyclone-fired boilers, corresponding to approximately 200 ppmv [907-908], and reduction in the 40-50 % for tangentially-fired and wall-fired boilers, corresponding to 100-150 ppmv, have been reported using natural gas as the re-burning fuel [906]. Measurements in a pilot-scale furnace with re-burning have shown up to 60 % reduction in NO_x emissions and relatively small increase in N₂O emissions (< 10 ppmv) using pulverized coal as a re-burning fuel [909].

Eastman Kodak Company's cyclone boiler (Unit No. 43), located in Rochester, New York, has been retrofitted with the gas reburn technology developed by the Babcock and Wilcox (B & W) Company to reduce NO_x emissions in order to comply with the New York State regulations adopted in conformance with the Title 1 of the Clean Air Act Amendments (CAAA) of 1990 [883]. At the peak load, the ozone nonattainment required NO_x reduction from baseline levels necessary to meet the presumptive limit for cyclone boilers in this regulation is 56 %. Eastman Kodak Company and Gas Research Institute (GRI) are co-sponsoring this project. Equipment installation for the gas reburn system (using natural gas) was performed in September 1995. The maximum continuous rating (MCR) for boiler No. 43 is 220,000 kg per hour of steam flow (or approximately equivalent to 60 MWe) [883].

5.1.6.2 Post-Combustion Techniques

Nitrogen Oxides Techniques

While the combustion modifications discussed above are effective in reducing NO_x emissions, many of these techniques are approaching the limits of their capabilities for reducing NO_x emissions. Therefore, some form of post-combustion techniques for NO_x removal will be required.

Figure 5.89 shows a representative comparison of the NO-removal efficiencies of the three additives as a function of product gas temperature for SNCR in a laboratory-scale reactor [910]. It is seen that the maximum NO-removal efficiencies for all three additives are comparable and can exceed 90 %, but that the temperature window for NO-removal for cyanuric acid is shifted to somewhat higher temperatures. The NO-removal efficiency is dependent on the ratio of the NO concentration in the flue gas to the concentration of injected additive (NO/RN). In general NO-removal efficiency increases as the additive-to-NO ratio (RN/NO) increases. In practice, for RN/NO molar ratio of 0.8-1.5, the NO-removal efficiencies are found to be in excess of 50 % [911]. One possible by-product of the NO-removing reaction sequence is N₂O formed by the reaction of NO with NH or NCO.

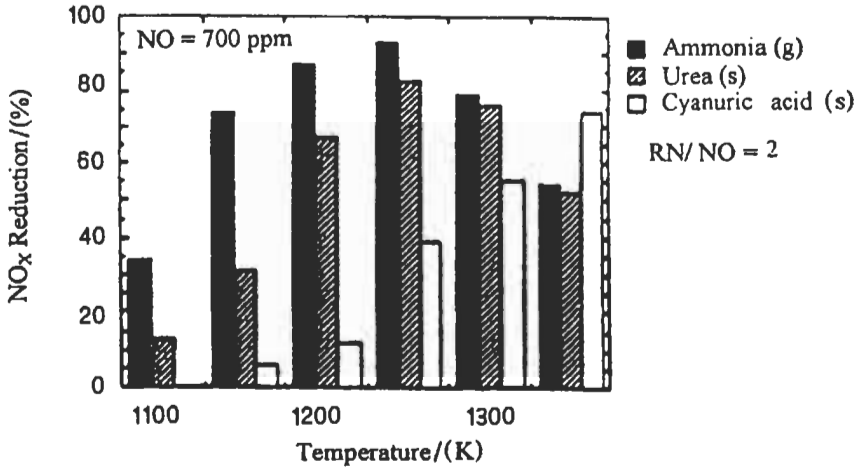


Fig. 5.89: The dependence of NO_x-removal efficiency on temperature for a pilot-scale selective non-catalytic reduction process for various nitrogen additives[118, 910]. Reproduced by permission of The Combustion Institute.

Catalysts to assist the NO-removal reaction (SCR) have found wide spread application in coal-fired boilers and also have applied in natural gas and oil-fired power stations, in stationary gas turbines [912]. The advantages of SCR over SNCR are somewhat higher NO-removal efficiencies and lower operating temperatures. Typical temperature ranges for SCR are between 500-700 K, while for SNCR are 1100-1400 K. The lower temperature limit for SCR is set by reaction rate and by formation and deposition of ammonia and sulfur salts. Typical NO-removal efficiencies and ammonia slips for SCR for a pulverized coal fired utility boiler are shown in Fig. 5.90. NO-removal

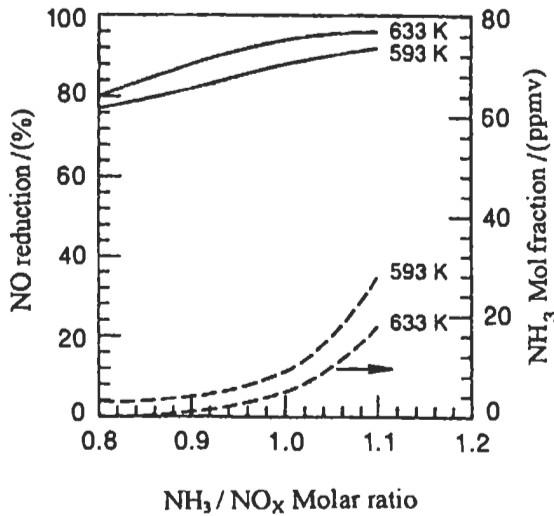


Fig. 5.90: Representative NO_x-removal efficiency and NH₃ slip for the selective catalytic reduction process [118, 913]. Reproduced by permission of The Combustion Institute.

efficiencies in the range of 80-90 %, with ammonia slips generally less than 5 ppmv, are achievable in practice [913].

Public Service Electric and Gas (PSE & G) [882] have evaluated the effectiveness of post-combustion NO_x control technologies on a wet-bottomed, coal-fired utility boiler. The technologies under study were conventional urea-based SNCR, horizontal in duct and air heater SCR and a combination of SNCR and SCR designated as SNCR/SCR Hybrid. In 1993 PSE & G, in partnership with EPRI, conducted a three month demonstration of urea based SNCR on one half of Mercer Unit 2. Building on these results, in 1994, PSE & G installed plate-type catalyst in the horizontal ductwork evaluation, on SNCR/SCR Hybrid demonstration was performed. Alexander et al [882] have discussed the success of commercial SNCR system in controlling NO_x emissions with respect to reliability and longer-term performance results.

Furthermore, the application of SNCR technology to a municipal solid waste boiler is shown in Fig. 5.91 (a). Multiple injection levels are used to maintain NO_x reduction efficiencies at acceptable levels as boiler load changes. Most of the current applications for these technologies have been on smaller municipal solid waste or biomass fueled boilers, where the appropriate temperature range is located in the upper furnace (Fig. 5.91 (a)). In large utility units, the proper temperature range occurs in the convection pass cavities, making application, especially on retrofits, more challenging. For these applications, overall control may be limited to the 20 to 40 % ranges. New boiler applications may require special design of the boiler convection pass with a dedicated open cavity in an optimal temperature window for the reaction to occur (Fig. 5.91 (b)). The application of selective catalytic reaction (SCR) is the most effective method

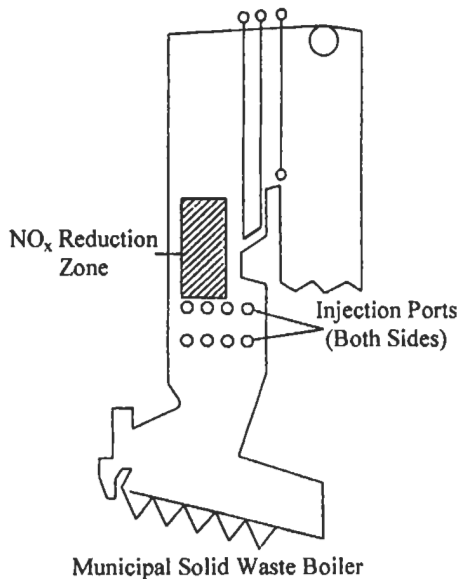


Fig. 5.91 (a): Typical SNCR application [126]. Reproduced by permission of the Babcock and Wilcox Company.

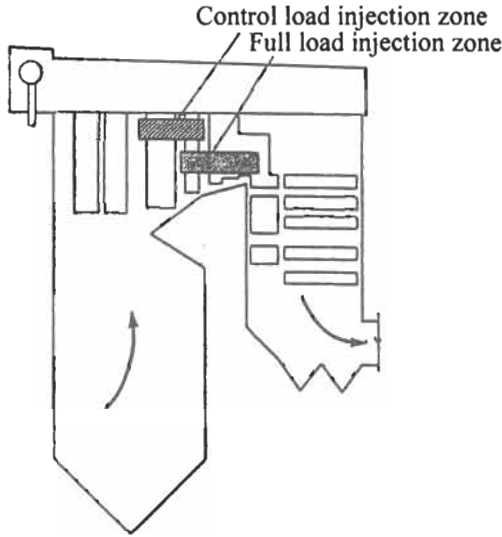


Fig. 5.91 (b): Coal-fired utility boiler with SNCR. Temperature window location at full and part load [126]. Reproduced by permission of the Babcock and Wilcox Company.

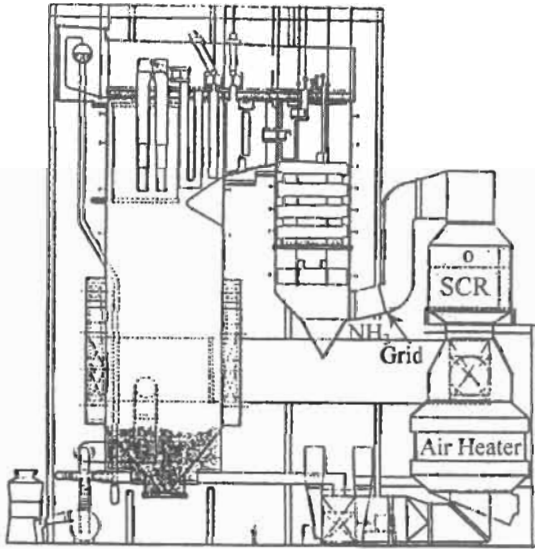


Fig. 5.91 (c): New utility boiler with SCR [126]. Reproduced by permission of the Babcock and Wilcox Company.

(in post-combustion) of reducing NO_x emissions especially where high removal efficiencies (70 to 90 %) are required. Typical example of new and retrofit application is shown in Fig. 5.91 (c). There are more than 400 SCR systems throughout the world.

Sulfur Dioxide Techniques

Man is responsible for the majority of the SO₂ emitted to the atmosphere. Annual worldwide emissions are estimated to be 180 to 200 million tons, nearly half of which are from industrial sources. The two principal industrial sources are fossil fuel combustion and metallurgical ore refining. The use of coal by the utilities has grown from 320 million tons in 1970 to 758 million tons in 1988. If no SO₂ emission controls had been implemented in 1970, it is estimated that SO₂ emissions from U.S. electric utilities would have grown to about 34.7 million tons per year by 1988.

In chapter 1 we have described the mechanism by which SO₂ is converted to sulfuric acid in acid rain. The pH scale is the method used to quantify the acidity of acid rain. The scale is defined by:

$$\text{pH} = \log_{10} [\text{H}^+] \quad (5.80)$$

where [H⁺] is the concentration of hydrogen ions in solution. A pH below 7 is considered acidic, while a value above 7 is alkaline. The pH of pure distilled water is 7. If rainwater contained no sulfuric or nitric acid, its pH would be approximately 5.7 due to absorption of carbon dioxide (CO₂) from the atmosphere. The contributions of man-made SO₂ and nitrogen oxides (NO_x) further reduce the pH of rainwater. No uniformly accepted definition exists as to what pH constitutes acid rain. Some authorities believe that a pH of about 4.6 is sufficient to cause sustained damage to lakes and forests [126].

Legislative action described in chapter 1 has been responsible for most industrial SO₂ controls. Therefore, a variety of SO₂ controls processes and technologies are in use and others are in various stages of development. This section presents the application of these technologies to reduce SO₂ in boilers. Commercialized processes include wet, semi-dry (slurry spray with drying) and completely dry processes. Of these, the wet SO₂ scrubber has been the dominant worldwide technology for the control of SO₂ from utility power plants. Wet flue gas desulfurization (FGD) systems will be described in this section with other systems, especially dry FGD systems. The utilities primarily used two strategies for control, switching to low sulfur coal and installing scrubbers. By 1988, the average sulfur content of fuels burned was 1.34 % for coal and 1.09 % for oil. With fuel switching alone, SO₂ emissions for electric utilities would have been 21.25 million tons in 1988; however, scrubbers, primarily wet, removed 7.65 million tons of SO₂ in 1988. In U.S., 68000 MW of FGD capacity were installed between 1970 and 1990. In Japan, 32000 MW of capacity were added during this period, while in Germany, 48000 MW of capacity were installed in this period, and the rest of the world accounts for approximately 40000 MW. Of the 180000 MW of worldwide FGD capacity, 85 % are wet scrubbers with the balance being predominantly dry scrubbers. Wet scrubbing processes are often categorized by reagent. Table 5.6 lists several scrubber processes and, of these, the limestone process has been the most widely applied.

Wet scrubbers offer the following advantages:

1. As an alternative to fuel switching, the utility can use its normal source of fuel supply.
2. As an alternative to and in contrast to other traditional and emerging flue gas desulfurization methods, wet scrubbers provide high SO₂ removal efficiency and high reagent utilization.

Table 5.6: Wet scrubber processes [126]. Reproduced by permission of Babcock and Wilcox Company.

Limestone ---
With no oxidation inhibition (natural oxidation)
With inhibited oxidation
With in situ forced oxidation
With ex situ forced oxidation
With soluble organic or inorganic buffers
Lime ---
With inorganic buffers (such as magnesium oxide)
With buffers
Dual alkali ---
Sodium carbonate/calcium hydroxide
Sodium carbonate/calcium carbonate
Soda ash ---
With regeneration by steam stripping
Without regeneration
Magnesium oxide with thermal regeneration

Wet scrubbers. The most popular wet scrubber design is the spray tower depicted in Fig 5.92 (a). The tower is designed so that, at maximum load, the average superficial gas velocity does not exceed the design gas velocity. For most spray towers, the average gas velocity varies from about 2.4 to 4 m s⁻¹ based upon scrubber outlet conditions. A typical design velocity for a limestone-wet scrubber is about 3.1 m s⁻¹ [126].

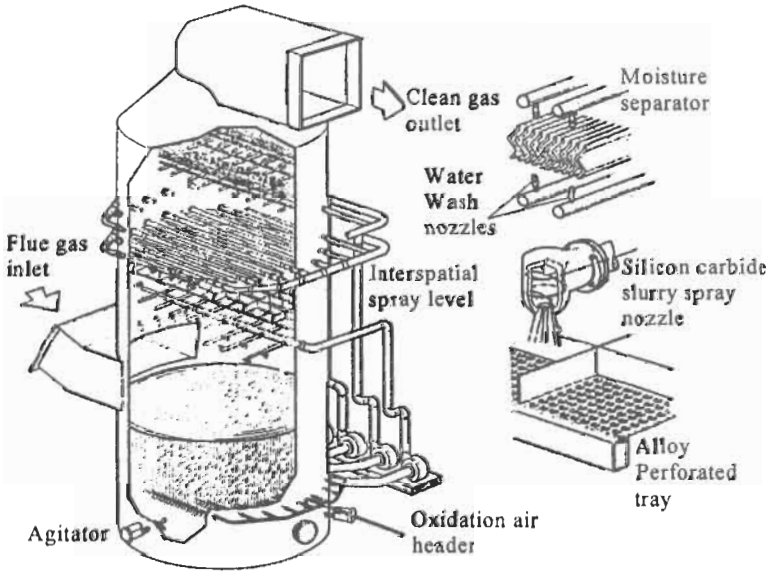


Fig. 5.92 (a): Wet flue gas desulfurization scrubber module [126]. Reproduced by permission of the Babcock and Wilcox Company.

Because the flue gas enters the absorber from the side, gas flow nonuniformity in the tower is a potential problem. This nonuniformity reduces overall SO_2 removal performance and aggravates mist eliminator carryover. The absorber design depicted in Fig. 5.92 (a) incorporates a sieve or perforated plate tray, which reduces flue gas flow maldistribution. The design of the tower is influenced by the reagent (lime or limestone), the desired SO_2 removal level, the tradeoff between fan power and recirculation slurry pump power, and several other factors. Spray nozzles are used in wet scrubbers to control the mixing of slurry with flue gas. The operating pressures typically vary between about 34 and 138 kPa. The large tank at the bottom of the tower is called the reaction tank or the recirculation tank. The volume of this tank permits several chemical and physical processes to approach completion. Flue gas enters the side of the scrubber module at a temperature of 121 to 177 °C and is evaporatively cooled to its adiabatic saturation temperature by a slurry spray. The scrubber inlet must be designed to prevent deposition of slurry solid at the wet-dry interface. Flue gas passes vertically upward through the scrubber. In the unit illustrated in Fig. 5.92 (a), the gas flow is distributed uniformly by a specially designed perforated plate or sieve tray. This tray serves as a gas-liquid contacting device. Above the tray, flue gases pass through several spray levels where additional gas-liquid contact is achieved. Each spray level consists of a set of headers and spray nozzles.

The design of the flue from the exit of the wet scrubber to the stack is an important facet of the system design. First, the flue gas leaves the mist eliminator saturated with water vapor. Second, some carryover of slurry droplets smaller than 20 microns is inevitable. These droplets will usually be slightly acidic and may contain high concentrations of dissolved chlorides. The flue gases will contain some residual SO_2 and ample oxygen to oxidize some of the SO_2 to SO_3 . Because the flue gas is saturated with water vapor, surface condensation is inevitable. This condensate can become severely acidic (pH less than 1), and calcium salts can deposit on the walls. Reheating the flue gas that is leaving the scrubber has been accomplished by various systems:

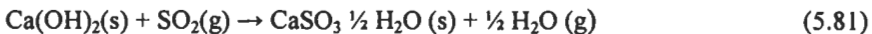
1. steam coil heaters,
2. mixing with some hot flue gas which is bypassed around the scrubber,
3. mixing with hot air,
4. mixing with hot gases generated by combustion of a clean fuel, and
5. regenerative heat exchangers, which transfer heat from the hot flue gas at inlet to the cooler flue gas at outlet.

Finally, the evaporation of droplets from the scrubber concentrates the corrosive constituents in the slurry. As a result, operation without flue gas reheat, i.e., with a wet stack, has become popular in the U.S. Under these conditions, the flues from the scrubber to the stack are lined with corrosion resistant materials, and the stack is lined with acid resistant brick or other suitable material. A drainage system is also included to accommodate condensation of water vapor.

Wet scrubber – limestone and lime FGD processes. All of the limestone and lime processes listed in Table 5.6 are classified as nonregenerable. This means that the reagent is consumed by the process and must therefore be continually replenished. In North America, most limestone wet FGD systems feature on-site wet grinding for slurry preparation. In most cases, the system of choice is a closed loop ball mill. The limestone grind is usually expressed as a percent passing a certain sieve size. The coarsest limestone grind used in wet FGD systems is one where about 70 % passes through a 200 mesh (75 micron) [126].

Lime based FGD systems are common in the U.S. Three types of slaking systems are used: the detention slaker, the paste slaker and the ball mill slaker. The detention slaker is the simplest but produces the poorest quality slaked lime. The paste slaker, while producing high quality lime, is the most complex system and grit separation can be troublesome. The ball mill slaker produces an intermediate slaked lime quality but requires no postslaking separation of the grit and slaked lime. All lime/limestone FGD wet scrubbers require fresh water for mist eliminator wash. This fresh water is usually combined with recycle water from the clarifier, thickener and/or vacuum filter to provide the total wash flow. A typical limestone based wet scrubbing process using in situ forced oxidation is depicted in Fig. 5.92 (b). In this example, the reagent preparation system includes a closed circuit ball mill system producing a slurry of ground limestone to a fineness of 95 % minus 325 mesh (44 microns). The water used in the milling system is recycled from the spent slurry dewatering system. The feed slurry is pumped to the absorber reaction tank at a controlled rate to maintain the pH of the slurry in this tank at a set point of 5.5. Air is also pumped to this reaction tank and distributed by spargers located near the bottom. The oxygen in the air reacts with any sulfite present in the slurry to produce gypsum (calcium sulfate dihydrate).

The slurry is pumped from the reaction tank to the spray headers shown in Fig. 5.92 (a). The slurry is sprayed counter currently into the flue gas where it absorbs the SO₂. The slurry falls to the perforated plate tray where additional SO₂ is absorbed into the froth created by the interaction of the flue gas and slurry on the tray. The slurry then drains back to the reaction tank. Figure 5.92 (c) illustrates a typical flow sheet for an FGD process using a lime produced from a dolomitic limestone. This lime contains about 5 % magnesium oxide (MgO), 90 % calcium oxide and 5 % inert. Within the process, the MgO is converted to MgSO₃, where, because of its relatively high solubility (approximately 10 g l⁻¹), the sulfite acts as a buffer to increase the SO₂ capacity of the slurry. The overall reaction is:



In this instance, a closed circuit ball mill system is used to produce a slaked lime:



The absorber towers used for this process are smaller than their limestone counterparts because the L/G required to achieve a comparable level of SO₂ absorption is typically only about 20 % of L/G for the limestone units. The dominant design variable for all FGD wet scrubbers is the ratio of slurry flow to gas flow in the tower (L/G). SO₂ absorption in a wet scrubber and its subsequent reaction with alkaline earth materials such as limestone is an elementary acid-base reaction. However, the chemical processes involved are complex. SO₂ is a relatively insoluble gas in water. Calcium carbonate (CaCO₃) has a low solubility in water. The principal reaction products are calcium sulfite hemihydrate (CaSO₃ · ½ H₂O) and calcium sulfate dihydrate (CaSO₄ · 2 H₂O), or gypsum. Both of these salts also have low solubilities. In wet FGD systems, magnesium oxide is used as an additive and it reacts with SO₂ to form magnesium sulfite. Because magnesium sulfite is highly soluble, the sulfite ion is the primary reactant in the gas-liquid interface as follows:

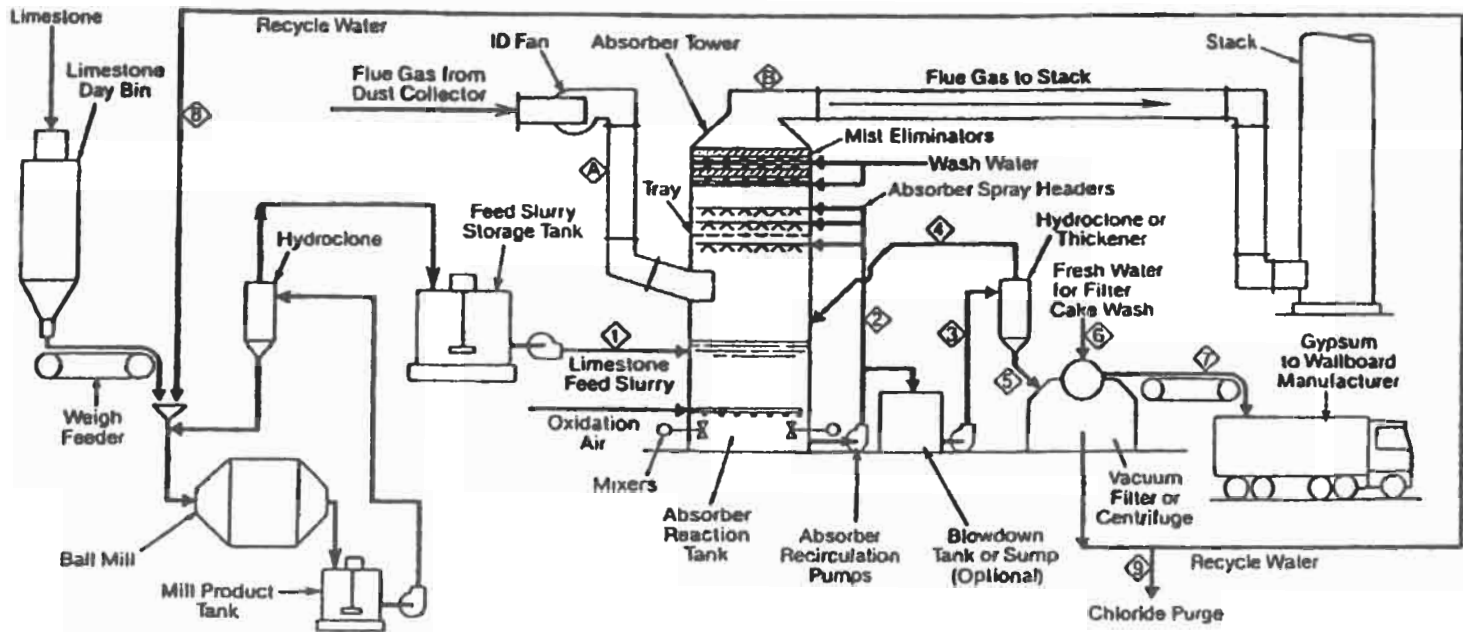


Fig. 5.92 (b): Wet scrubber FGD system flow diagram [126]. Reproduced by permission of the Babcock & Wilcox Company.

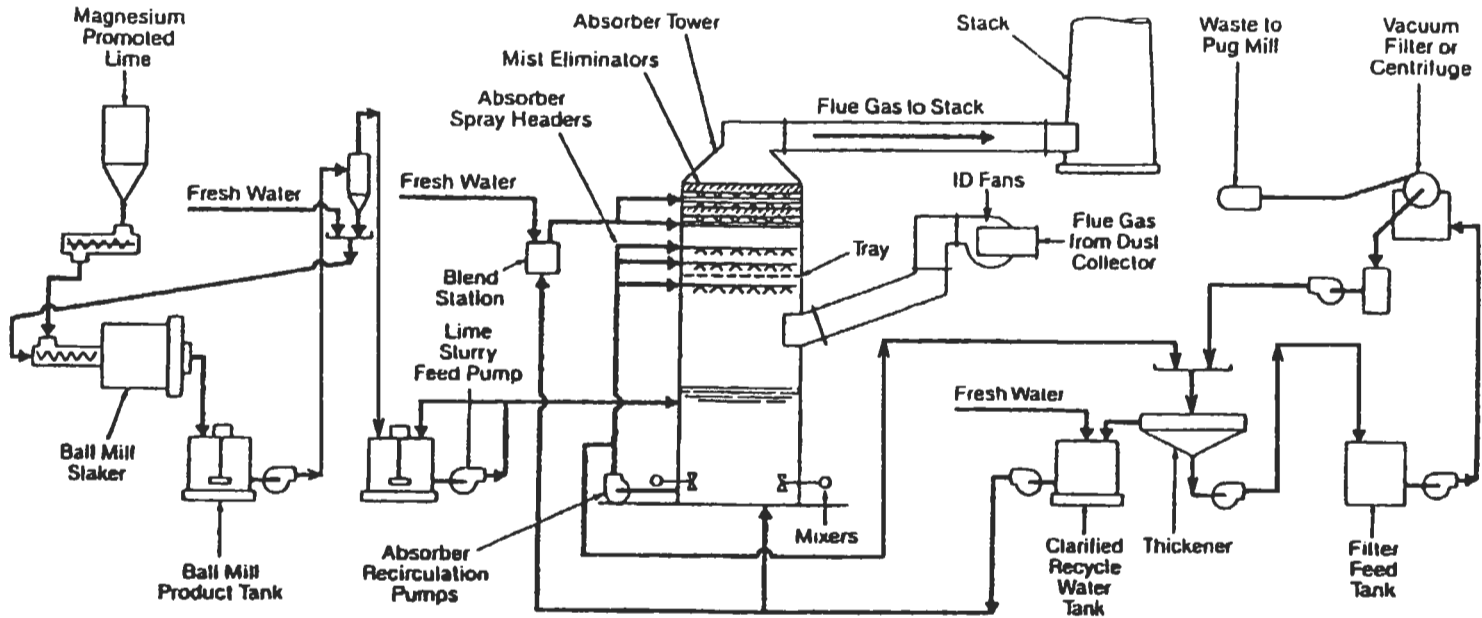


Fig. 5.92 (c): Wet lime FGD system flow schematic [126]. Reproduced by permission of Babcock & Wilcox Company.



Sodium carbonate can also be added to the lime/limestone system for a similar benefit. The total concentration of dissolved alkaline species such as CO_3^{2-} , HCO_3^- , SO_3^{2-} and OH^- in the slurry is referred to as dissolved alkalinity. If the dissolved alkalinity is sufficiently high, the scrubber may become gasphase diffusion controlled. This is illustrated in Fig. 5.93. Under these conditions the rate of SO_2 absorption is dependent only upon the amount of interfacial surface area.

Dry scrubbers. Dry scrubbing is the principal alternative to wet scrubbing for SO_2 control on utility boilers. Since 1980, 7200 MW of dry scrubbers have been installed at U.S. electric utilities. Dry scrubbing is also a popular choice for smaller industrial applications and for combined HCL and SO_2 control on waste-to-energy units. The advantages of dry scrubbing over wet scrubbing include [126]:

1. less costly construction materials,
2. dry waste products,
3. fewer unit operations, and
4. simplicity of operation.

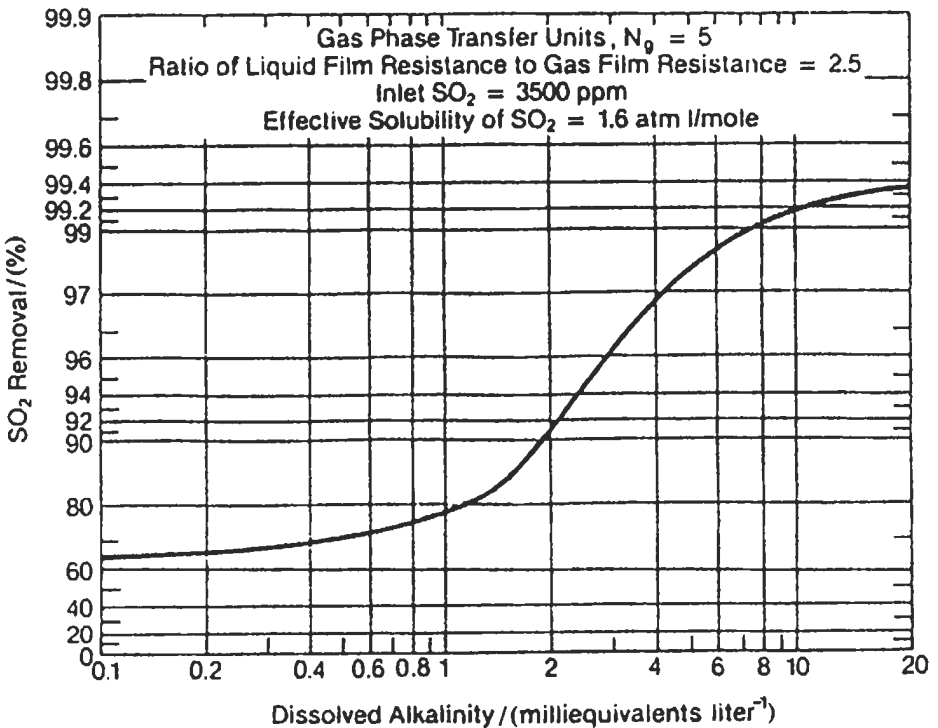
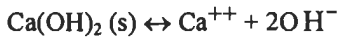


Fig. 5.93: Influence of dissolved alkalinity on SO_2 performance (1 milliequivalent = 50 ppm CaCO_3) [126]. Reproduced by permission of the Babcock & Wilcox Company.

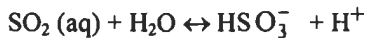
Dry scrubbing is sometimes referred to as spray absorption, spray drying or semi-wet scrubbing. It involves spraying a highly atomized slurry or aqueous solution of an alkaline reagent into the hot flue gas to absorb the SO_2 . Figure 5.94 (a) depicts a utility size dry scrubber installation coupled with a bag house. Unlike a wet scrubber installation, the dry scrubber is positioned before the dust collector. Flue gases leaving the air heater at a temperature of 121 to 177 °C enter the dry scrubber through an array of Turbo-Diffusers as shown in Fig. 5.94 (b) for a horizontal flow design. The quantity of water in the atomized spray is limited so that it completely evaporates in suspension. SO absorption takes place primarily while the spray is evaporating and the flue gas is adiabatically cooled by the spray. The difference between the temperature of flue gas leaving the dry scrubber and the adiabatic saturation temperature is known as the approach temperature. Reagent stoichiometry and approach temperature are the two primary variables, which dictate the scrubber's SO_2 removal efficiency. The predominant reagent used in dry scrubbers is slaked lime. The system shown in Fig. 5.94 (c) consists of storage facilities for pebble lime (CaO), a ball mill slaking system, a system for mixing slaked lime with recycled material from the dust collector, the dry scrubber and the dust collector. SO_2 absorption in a dry scrubber is similar to that attained by wet scrubbing. The majority of the reactions take place in the aqueous phase; the SO_2 and the alkaline constituents dissolve into the liquid phase where ionic reactions produce relatively insoluble products. The reaction path can be described as follows:



Absorption (5.85)



Dissolution (5.86)



Hydrolysis (5.87)

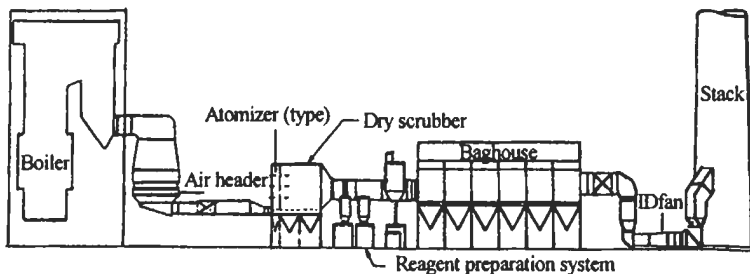


Fig. 5.94 (a): Dry scrubber emissions control system configuration [126]. Reproduced by permission of the Babcock & Wilcox Company.

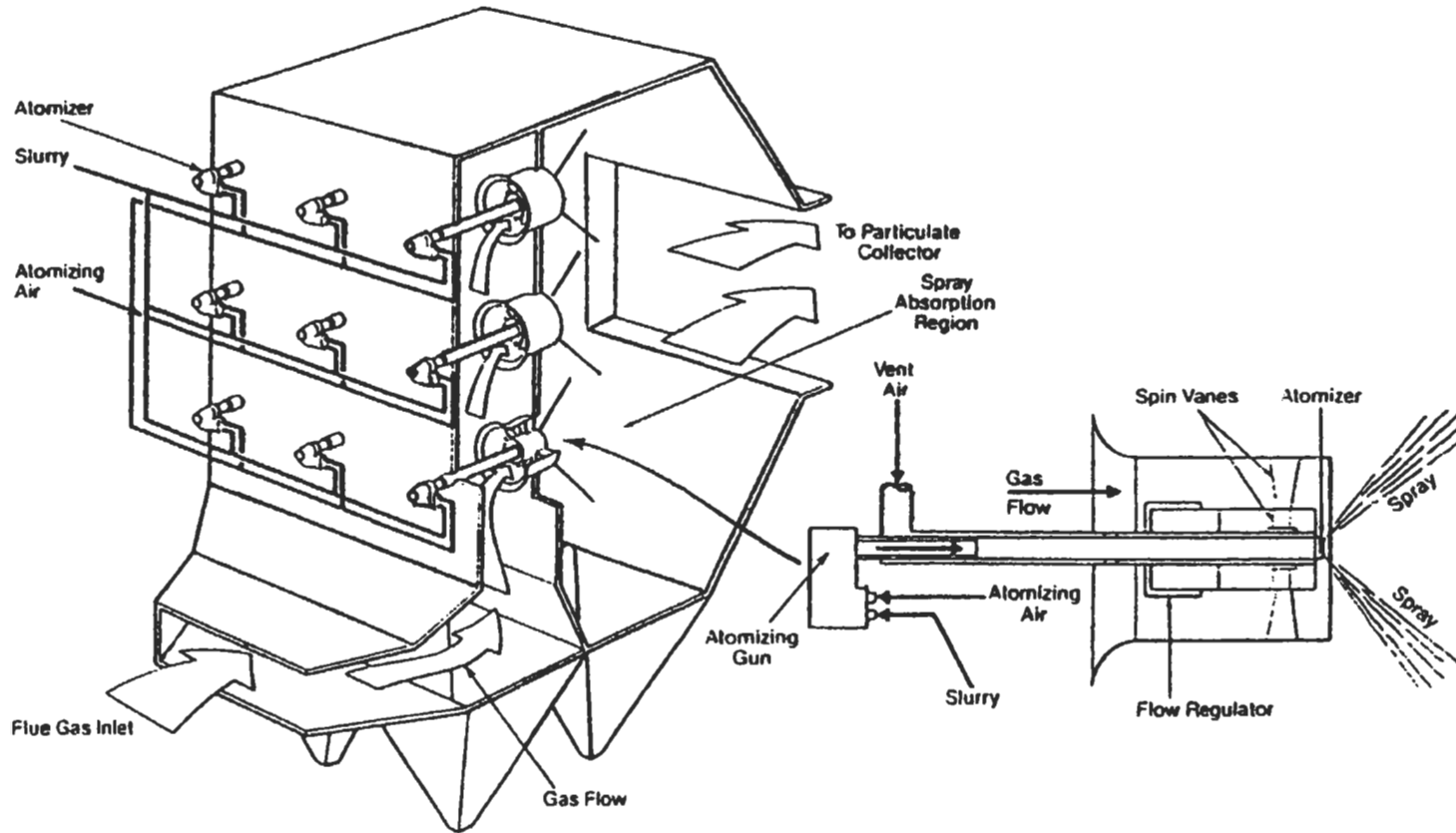


Fig. 5.94 (b): Dry scrubber reactor module, horizontal flow configuration showing Turbo-Diffuser insert [126].
 Reproduced by permission of the Babcock & Wilcox Company.

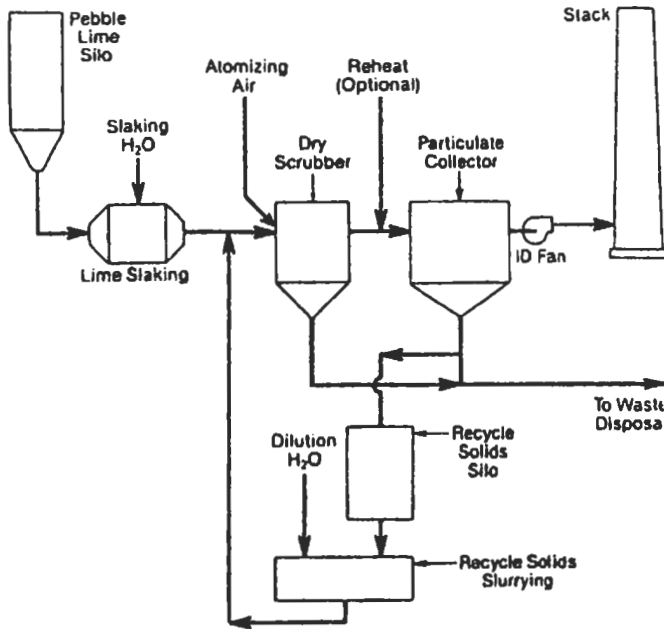
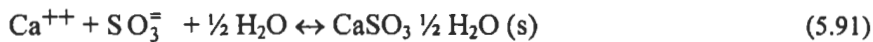


Fig. 5.94 (c): Dry FGD scrubber system schematic [126]. Reproduced by permission of the Babcock & Wilcox Company.



Neutralization



Precipitation

These dry scrubber reactions usually take place in the pH range of 10 to 12.5. In wet scrubbers, the reaction scheme occurs below a pH of 7. Dry scrubbers are normally sized for a certain gas phase residence time, which depends on the design approach temperature and the degree of atomization.

Other examples of commercialized FGD technology include:

1. furnace sorbent injection,
2. nacholite/trona injection, and
3. activated carbon

Furnace sorbent injection has developed during the past 20 years. The technology involves the pneumatic injection of limestone, dolomite or hydrated lime at a gas temperature of 1093 to 1260 °C. Normally; the injection point is near the nose of the boiler (see Fig. 5.94 (d)). Using hydrated lime, 50 to 60 % SO₂ capture is achievable with a calcium/sulfur ratio of 2.

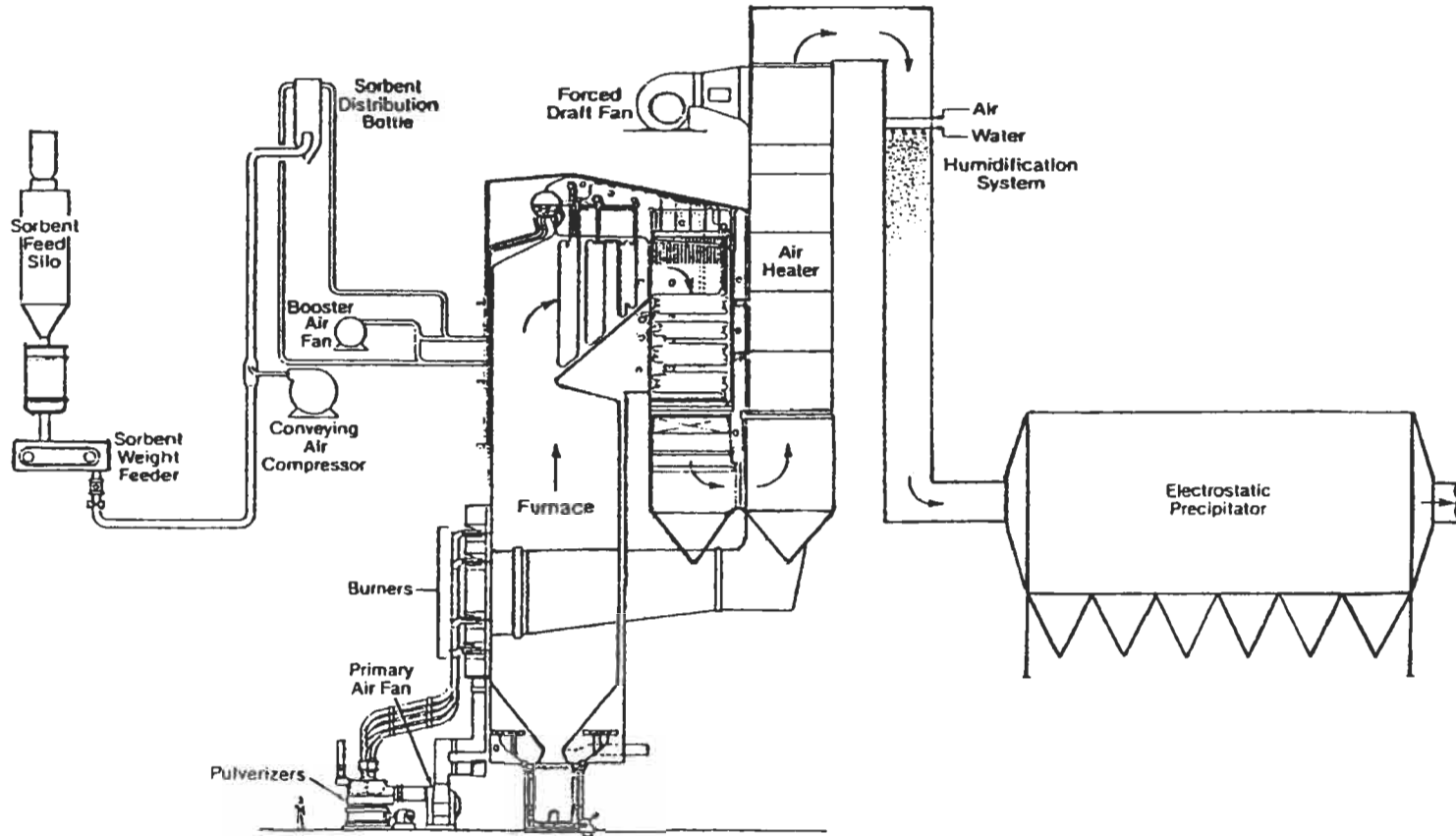


Fig. 5.94 (d): furnace sorbent injection system for SO₂ control – includes humidifier system to enhance particulate collection and SO₂ removal efficiency [126]. Reproduced by permission of the Babcock & Wilcox Company

5.1.6.3 Combination of NO_x and SO₂ Control Techniques

The field evaluations in Table 5.7 show that gas re-burning can provide NO_x reductions of 50 to 60 % during normal plant operation. However, the gas re-burning can be integrated with existing burner equipment or combined with other NO_x-control techniques, including low-NO_x burners, SCR, and SNCR to enhance overall NO_x reduction capability to meet emission regulations. Some of these variations are described further below:

(i) **Close-coupled gas re-burning.** This promising and cost-effective technique is applicable to tangentially and wall-fired boiler units (see section 5.2). Existing or modified burners are used to inject natural gas at the top of the primary combustion zone, thus eliminating the need for new boiler penetrations for gas injectors. Overfire air ensures burnout of the re-burning fuel. When applied to tangentially-fired boilers, close-coupled re-burning employs the existing windbox opening for gas re-burning injectors. NO_x reduction potential appears to be comparable to standard gas re-burning.

(ii) **Gas re-burning/low-NO_x burners.** Gas re-burning can be combined with low-NO_x burners to increase the overall NO_x reduction to 75 %. With this combination technique, the following NO_x emissions from large (> 200 MWe) boilers at full load have been achieved in practice [905], 40-50 ppmv (at 3 % O₂) for natural gas, 70-80 ppmv for light oils, 90-130 ppmv for heavy oils containing approximately 0.3 wt % N₂. Also, 10 ppmv NO_x (at 3 % O₂) was reported for a small (1.5 MWt) natural gas fire-tube boiler using a combination of a low-NO_x (staged) burner, flue gases re-circulation, and overfire air [896]. The NO_x emissions reductions achieved by combining low-NO_x burners with overfire air in pulverized coal boilers depend on the coal type and firing configuration. In tangentially-fired boilers, NO_x emissions as low as 220-370 ppmv (at 3 % O₂) have been reported, while in wall-fired boilers, NO_x levels as low as 250-440 ppmv have been achieved [914]. In all cases, reductions in NO_x emissions were accompanied by modest increases in CO emissions (typically less than 40 ppmv). Figure 5.95 shows NO_x re-burning technology combined with low-NO_x burners in

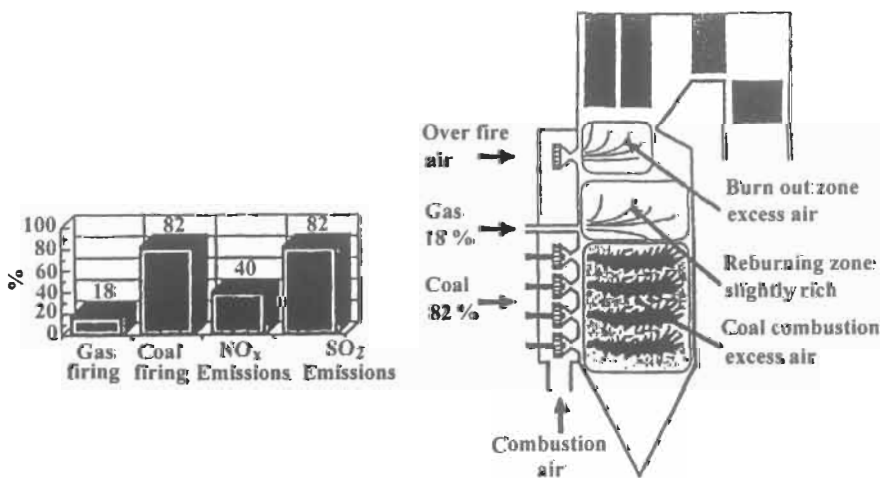


Fig. 5.95: NO_x re-burning [915]. Reproduced by permission of EPRI.

pulverized coal boiler, where 82 % coal is used in the primary zone and 18 % natural gas was injected into re-burning zone [916]. They found a reduction of NO_x (40 %) and SO_2 (83 %).

(iii) **Advanced gas re-burning.** These developmental technology combines gas re-burning with selective non-catalytic reduction (SNCR), in which urea or ammonia is injected to further reduce NO_x . Gas re-burning widens the temperature range in which injection of the reagent is most effective. Based on pilot-scale data, advanced gas re-burning should achieve an 80 % NO_x reduction level, while limiting natural gas use to about 10 % of the boiler full load. The NO_x emissions reductions achieved by combining low excess air, air staging, fuel staging and flue gas re-circulation in pulverized brown coal boilers (150 – 600 MWe) was 200 mg m^{-3} [917].

The effectiveness of the various control technologies individually or when combined, in achieving specific emissions levels are summarized in Table 5.7 [118]. Recently, Han et al [918] have presented results of the application of the Two-Stage Lagrangian (TSL) model of Broadwell and Lutz to the basic and advanced reburning processes in a 300 kW natural gas fired Boiler Simulator Facility (BSF). This TSL model allows continuous chemical reaction during the mixing while preserving some of the important characteristics of the jet. The model predicts 50 to 80 % NO_x removal depending on the thermal input of the reburning fuel, initial concentration of NO_x , and injection temperature of the overfire air and N-agent. Figure 5.96 shows the schematic of the facility with the modeling schemes used in each stage. Required inputs for each stage are also indicated. First, the main burner region is modeled as a plug flow reactor (PFR) and solved using CHEMKIN-II subroutines with the known temperature profile. Then, the injection of the reburning fuel is modeled with the TSL model assuming that the 8 separate jets do not interact with each other and the jet injection temperature is kept low (300 K) due to the water-cooling of the ejectors. The TSL model is used up to the point where the amount of entrainment equals the main flux and complete mixing is assumed from the point onward. The spraying of N-agent is assumed to lead to uniform mixing since the liquid droplets are probably well distributed and evaporated as they fill the duct. Chemically, urea is modeled as its two decomposition products NH_3 and HNCO . The overfire air injection is modeled similarly as the injection of the reburning fuel, but assuming normal injection. For comparison with TSL predictions, Fig. 5.97 shows the results obtained by Zamansky et al [919] using the time-distributed mixing model (ODF). The major difference between their model and the model of Han et al [918] is that the main flue gas is entrained into the jet in the current model, whereas the jet species are added to the main flue gas in their model. They [918] observed that quantitative prediction is not achieved with the ODF model due to the small change in stoichiometric ratio in the re-burning zone. Figure 5.97 shows the prediction of the NO remaining after the advanced re-burning processes with different N-agent injection temperatures using the TSL model, when the re-burning zone was kept just slightly rich. The results for the basic re-burning are also provided. For basic re-burning, i.e., re-burning without the addition of N-agent, the model [918] estimates 51 % remaining NO in terms of the ratio of the final to initial NO mole fraction. The experimental result, in which water was sprayed at various temperatures instead of N-agent, shows the remaining NO to be between 49 to 53 %. For the advanced reburning process which injects the N-agent at various positions, and thus at different temperatures (1380 K ~ 1650 K), the model predicts 30 to 40 % remaining NO depending upon the N-agent injection temperatures.

Table 5.7: NO_x emissions control technologies and potential emission reduction [118]. Reproduced by permission of The Combustion Institute.

Fuel	Combustion source	Control Technology*	Estimated NO _x emissions	
			% reduction	NO _x (ppmv @ 3% O ₂)
Natural gas	Boilers	LNB+OFA+FGR	70-80	20-50
		Re-burning	50-60	30-50
		SCR	80-90	20-30
Fuel oil	Boilers	LNB+OFA+FGR	70-80	70-100
		SCR**	80-90	30-50
Pulverized coal	Wall-fired/tangential-fired boilers	LNB+OFA	60-70	150-250
		Re-burning	50-60	100-150
		SNCR**	30-75	100-200
		SCR**	80-90	80-100
	Cyclone-fired boilers	Re-burning	50-60	150-200
		SNCR	30-75	200-350
		SCR	80-90	100-150

* LNB = Low-NO_x burner, OFA = Overfire air, FGR = Flue gas re-circulation, SCR = Selective catalytic reduction, SNCR = Selective non-catalytic reduction. ** In conjunction with LNB + OFA

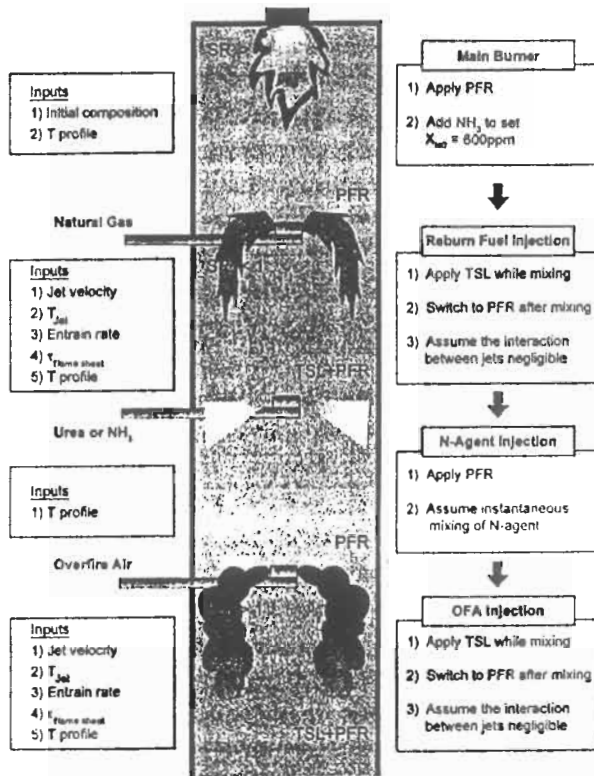


Fig. 5.96: The modeling scheme applied to each stage with the model input required [918]. Reproduced by permission of Elsevier Science.

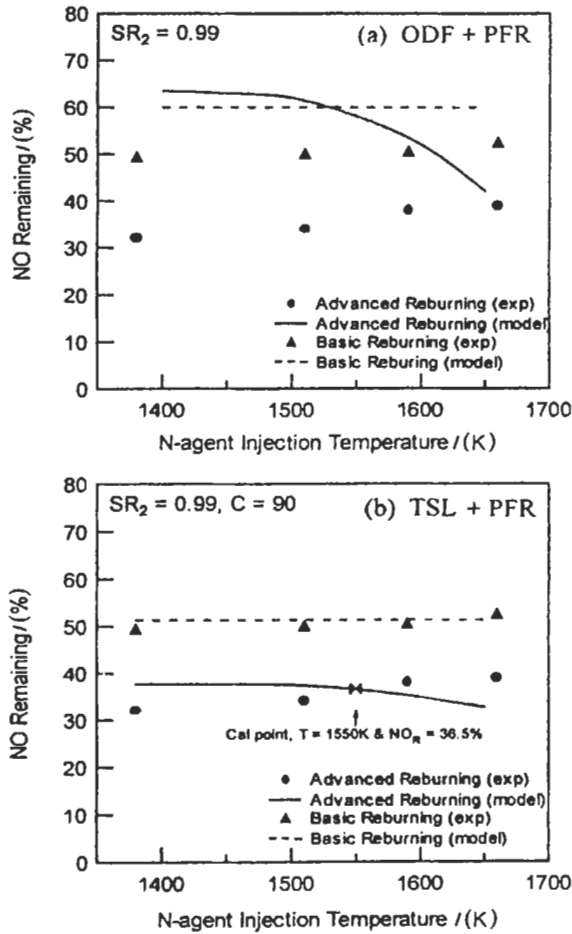


Fig. 5.97: The comparison between (a) time-distributed mixing model (ODF) and (b) TSL, model result, for advanced and basic re-burning prediction [918]. Reproduced by permission of Elsevier Science.

Terry et al [881] have investigated the integrated dry NO_x , SO_2 emissions control system which combines low- NO_x burners, overfire air, selective non-catalytic reduction (SNCR), and dry sorbent injection with humidification to reduce by up to 70 % both NO_x and SO_2 emissions from a 100 MW coal-fired utility boiler. The urea-based SNCR system was tested with the unmodified boiler in 1992. At full load, it reduced NO_x emissions by about 35 % with an associated ammonia slip limit of 10 ppm. Babcock and Wilcox XCL burners and a dual-zone overfire air system were retrofit to the top-fired boiler in mid-1992 and demonstrated a NO_x reduction of nearly 70 % across the load range. Integrated testing of the combustion modifications and the SNCR system were conducted in 1993 and showed that the SNCR system could reduce NO_x emission by an additional 45 % while maintaining 10 ppm of ammonia slip limit at full load.

Public Service Company of Colorado (PSCO) proposed the Integrated Dry NO_x/SO_2 Emissions Control System to the U.S. Department of Energy (DOE) as part of the third

round of the Clean Coal Technology Program (CCT-III) [881]. The proposed system was the first demonstration of low-NO_x burners, overfire air (OFA) ports, and urea-based selective non-catalytic reduction (SNCR) on a top-fired-utility-coal boiler. The integrated system also includes dry sorbent injection (DSI) using both sodium and calcium-based reagents and flue-gas humidification to control sulfur dioxide (SO₂) emissions. Figure 5.98 shows a simplified schematic of the Integrated Dry NO_x/SO₂ Emissions Control System at Arapahoe Unit 4. Installation of the integrated system to Arapahoe Unit 4 was completed in August 1992 and tested in mid 1995. About 70 % reduction in the emissions of NO_x and SO₂ through the integration of existing and emerging technologies was achieved, while minimizing capital expenditures and limiting waste production to dry solids that can be handled with conventional ash removal equipment. This innovative demonstration project is estimated to cost \$ 27411000 [881].

Table 5.8 summarizes the costs and reduction level of NO_x [904]. Compared with technologies that provide NO_x reductions greater than 50 %, gas re-burning is moderate in its capital cost-about \$ 30 to \$ 35 per kilowatt for a 500 MW plant. Operating costs consists primarily of the incremental cost of natural gas over the fuel it replaces.

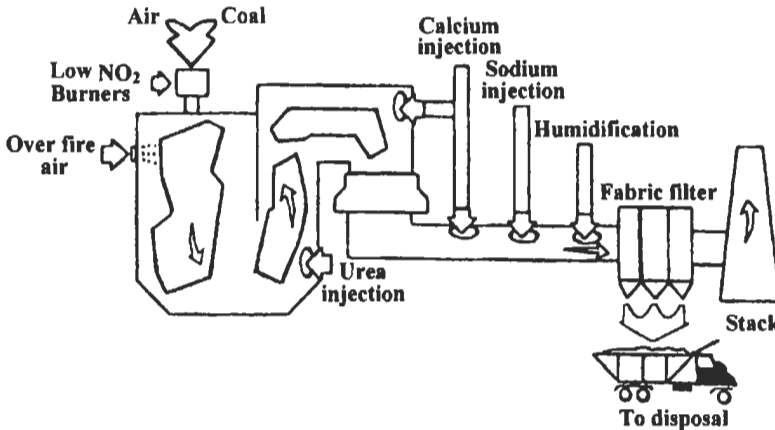


Fig. 5.98: Integrated dry NO_x/SO₂ emissions control system [881]. Reproduced by permission of the American Institute of Chemical Engineers.

Table 5.8: Approximate capital costs and reduction level of NO_x control technologies* [904]. Reproduced by permission of Gas Research Institute.

Technology	Capital cost (\$/kW)	NO _x Reduction % level
Low NO _x burner	10-20	30-50
Selective non-catalytic reduction (SNCR)	10-20	30-50
Close-coupled gas re-burning	20-25	50-60
Gas re-burning	30-35	50-70
Advanced gas re-burning**	40-45	70-90
Gas re-burning/low-NO _x burner	45-50	70-80
Selective catalytic reduction (SCR)	90-125	70-90

* Typical 500 MW coal-fired units, ** Based on pilot-scale data.

5.2 Tangentially-Fired Furnaces (TFFs)

5.2.1 Introduction

Tangentially-fired furnaces (TFFs) are units of polygon shape with four, six, eight or more sides; with fuel and air to be admitted in a tangential manner from the furnace corners or near them. The idea is to direct the flames at an imaginary circle in the middle of the furnace, in such a way, to bring about a vortex motion, which would be, by itself, moving upwards. Therefore, furnaces of such type are essentially vortex combustion units. In the last years, tangentially-fired furnaces have become more attractive in the field of power station firing systems. They have been used extensively throughout the world with wide applications in many types of steam boilers, including both small and high capacity units [582, 920-926]. These furnaces are quite suitable for many types of fuels including coal [920], oil [582, 921], and gas [921, 927].

The main advantages of TFF are:

1. The efficient mixing, due to vortex, rapid contact between fuel and air, and flames interaction, that would ensure a reliable combustion with uniform temperature distribution.
2. Uniform heat flux to the furnace walls; consequently failures due to high thermal stresses have been avoided.
3. The air and fuel streams can be admitted inclined either upward or downward from the horizontal, a feature that is used to vary the amount of heat absorbed by the furnace walls and to control the superheater temperature.
4. Vortex motion at the furnace center prevents or minimizes slugging of the furnace walls, erosion due to impingement and local over-heating.
5. NO_x in tangentially fired unit is lower than other firing types. NO_x emissions from TF boilers are about half the values from wall firing systems.
6. Tangential-firing technique is characterized by lower carbon losses (do not exceed 1%), and greater adaptability for the combustion of "difficult" fuels (e.g. fuels with low calorific value, high melting-point ash, or low volatile content).

One of the disadvantages of tangentially-fired systems is that any trouble occurring in any burner will affect badly the firing control and causes flames instability.

Tangentially-fired units are currently being designed with single or double chamber furnaces. The units can be characterized by squares, rectangles, or polygons of horizontal cross-sections in the corners of which the burners are positioned.

Two main types of burners are used in tangentially-fired furnaces having either vertical or horizontal slots. The advantage of horizontal burners is that a tier can be tilted to adjust temperature levels. In the USA, the practice is to use tiltable horizontal slot burners whereas in the USSR, vertical slots fixed-types are preferred. A schematic diagram of a tangentially-fired system is shown in Fig. 5.99 (a).

The prediction of operating characteristics, flow pattern, and the model of mixing in tangentially-fired furnaces has not yet been adequately investigated. Moreover, the matter regarding a safe stable ignition of the furnace, meaning the mutual interaction of flames and the effect of extinction of one burner or more on the overall stability, has been barely touched (El-Mahallawy et al [927]). Nevertheless in the last few years, this particular type of furnaces has become attractive not only because of its inherently low

NO_x emission [928] but also due to the existing uniformity of heat flux to the furnace walls without flame impingement or local overheating.

Romadin [929] collected some descriptive figures for TFF and advised with the square cross-sectional shape over others. Because of its peculiar aerodynamics, the flow inside the TFF as well as the combustion mode were found difficult and complicated to be numerically modeled or simulated. However, a number of trials has been made, based mostly on empirical assumptions, some of them were introduced by Lowe et al [920], Bueters et al [921], Benesch and Kremer [922] and Robinson [923]. The report submitted for the case of explosion of the tangentially-fired boiler No. 1 of Abu-Qir power station in Egypt, by El-Mahallawy et al [927], represents the only available reference that studied the effect of destabilization of a flame of one burner on the other flames in the furnace.

The objective of this section is to widen the knowledge about the tangentially fired furnaces under the integrated treatment of flow, combustion and heat transfer phenomena in addition to the effect of the burners deviation angle from the furnace diagonals on the furnace performance. It is also, to establish a database with enough details to assist the development and validation of mathematical models of tangentially-fired furnaces. All of these are discussed and reviewed in section 5.2.2. To fulfill all of these requirements, El-Mahallawy and his research group; Habib, Abdel Hafez, Kamel, Safar, Naseef, and Zakaria [926, 927, 930-932] have constructed and designed a square cross-section model furnace. The furnace corners were prepared for mounting one to three levels of burners on a provision to facilitate the burner movement.

5.2.2 General Background

Overview

Tangentially-fired furnaces (Fig 5.99 a and b) are evolved from problems met within producing large cyclone combustors (Fig. 5.99 c) and furnaces with up to 30 or more separate burners. Large cyclone combustors are expensive to be constructed because of their circular shape and due to the difficulty of keeping dynamic; kinematic, thermal and chemical similarities, and the wall temperature distribution the same between small and large size cyclones.

Many tangentially-fired units have been placed in operation all over the world since 1927. In tangential firing system, the fuel is admitted at the corners of the combustion chamber or near them through alternate compartments. Distribution dampers proportion the air to the individual fuel and air compartments. Thus, it is possible to vary the distribution of the air over the height of wind box, to vary the relative velocity of these air streams, and to change the rate of mixing of the fuel and air in the furnace. Fuel and air nozzles tilt in harmony to raise or lower the flame envelope in the furnace to control furnace heat absorption in the superheater, exit gas temperature and thus the heat absorption in the re-heater sections. The furnace wall heat absorption is controlled by deviation of nozzles from the furnace diagonal. The fuel and air streams from each corner of the furnace are directed tangentially to the circumference of a circular vortex in the center of the furnace as shown in Fig. 5.99 (b), so that it is called tangential-firing. The number of tiers of the burners can be one (Whaley and Rankin [933]), two (Martin et al [934]), three (Shagalova et al [935] and Blakeslee and Burbach [936]), four (Piper et al [937] and Boyd et al [938]), and

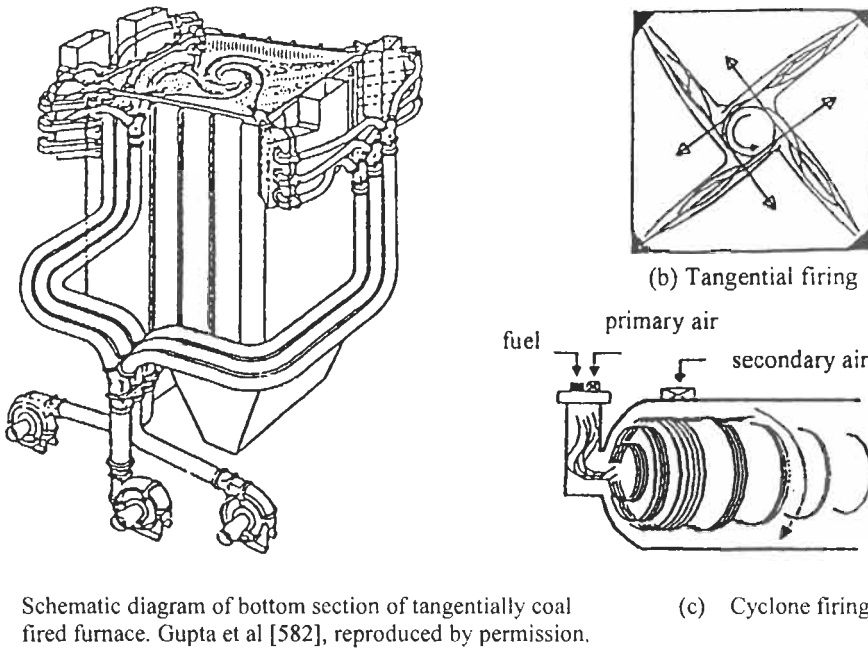


Fig. 5.99: Tangential and cyclone firing systems.

five (Bueters et al [921], Cetegen and Richter [924] and Burrington et al [939]). As market-driven philosophies for controlling NO_x become more prominent, the proper economic assessment of controlling NO_x techniques will be essential [940].

In operation of a TFF, a large vortex is created in the furnace as illustrated in Figs. 5.99 (b) and 5.100. The size of this vortex depends on the burner tilt angles and dimensions of the furnace. Stable burning in the TFF is achieved by the configuration of the boiler (and burner arrangement), rather than by the individual burners. When the boiler is fired in the tangential firing manner, each flame impinges upon the adjacent flame, creating a recirculating flow and stabilizing the latter flame. Therefore, precise control over local air/fuel ratios is not necessary, because lean or rich zones become entrained in the vortex and are blended for efficient combustion. Tangentially-fired systems are best suited for difficult fuels (coal, coal-water fuel, sludge oil, municipal refuse, and industrial waste fuel) because of the rapid contacting of the fuel and air, flame impingement, and the increased particulate residence time due to vortex motion (Whaley and Rankin [933], Hamilton [941] and Joseph [942]). The TF units have a good record in being able to meet emission regulations on NO_x as a result of their flexibility and the ability to control the heat release rate [943].

Burner outlet air velocities are of great importance for the operation of a furnace. Low velocities of primary and secondary air (16 to 20 m s^{-1}) are not suitable for coals having high volatile contents, as ignition can occur in or near the burner causing unavoidable slugging and distortion problems. Higher velocities (approximately 24 m s^{-1}) under the same conditions can correct such problems. Conversely, very high primary air velocities are undesirable as large coal particles can centrifuge out of the main combustion zone as unburnt carbon. For oil-fired combustion systems, air

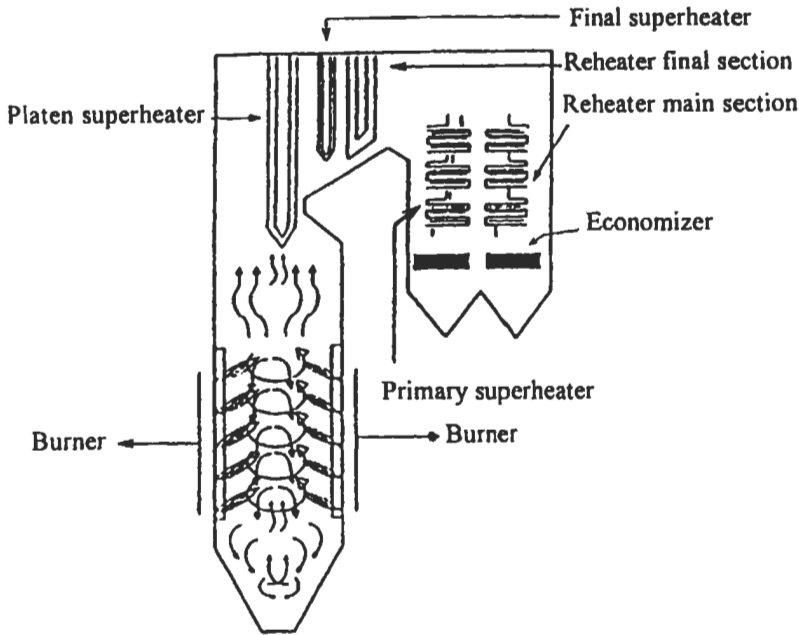


Fig. 5.100: Typical tangentially fired boiler.

velocity at the burner exit reaches 80 m s^{-1} . Due to the low levels of swirl, it is not expected that the processing vortex core will occur in tangentially-fired furnaces.

Configuration

The different arrangements of the single and multiple TF furnaces are shown in Figs 5.101 and 5.102 (Lawn [944]). The most advantageous shape of TF furnace is the square one; however, rectangles are frequently used. Single-chamber furnaces are usually rated up to 500 MW. Greater output is obtained by using two separate units per boiler, or double furnaces as shown in Fig. 5.102. A further alternative is two boilers with double furnaces. Octagonal furnaces are more complicated in design than the other arrangements; however, they can be doubled up to increase heat output, as shown in Fig. 5.102. The TF furnace is sized first to provide sufficient volume for complete combustion of the fuel, second to generate a specified amount of steam, and third to maintain furnace wall tube metal temperatures within allowable limits. Bueters et al [945] have stated that the relative typical furnace sizes for various fuels are as indicated in Fig. 5.103.

Romadin [929] collected some constructional and descriptonal considerations for tangentially-fired furnaces. Romadin indicated that the most advisable shape for tangentially-fired furnaces is the square one, and concluded that in case of utilizing rectangular shape TFF, the aerodynamics of the flow would be distorted if the ratio of the sides of the rectangle is greater than 1.25 to 1.35. He also recommended that the angle of inclination of burners axes from the diagonals of the furnace (θ) to be 4° - 6° for square furnaces and 6° - 8° for the rectangle ones. In general, to standardize the angle of inclination (θ), he suggested to confine it to the value of 5° .

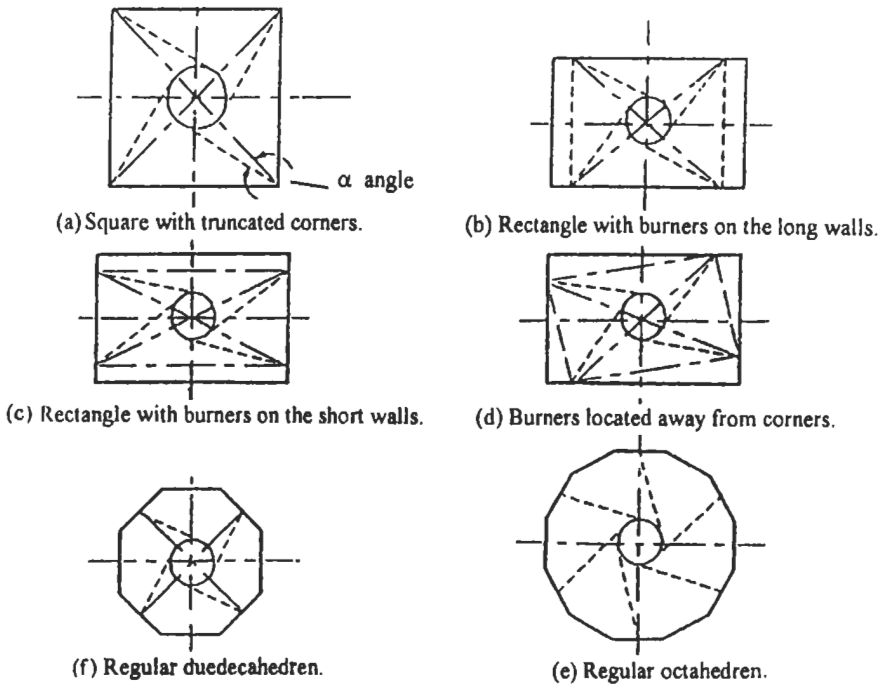


Fig. 5.101: Arrangements of single TF furnaces [944].

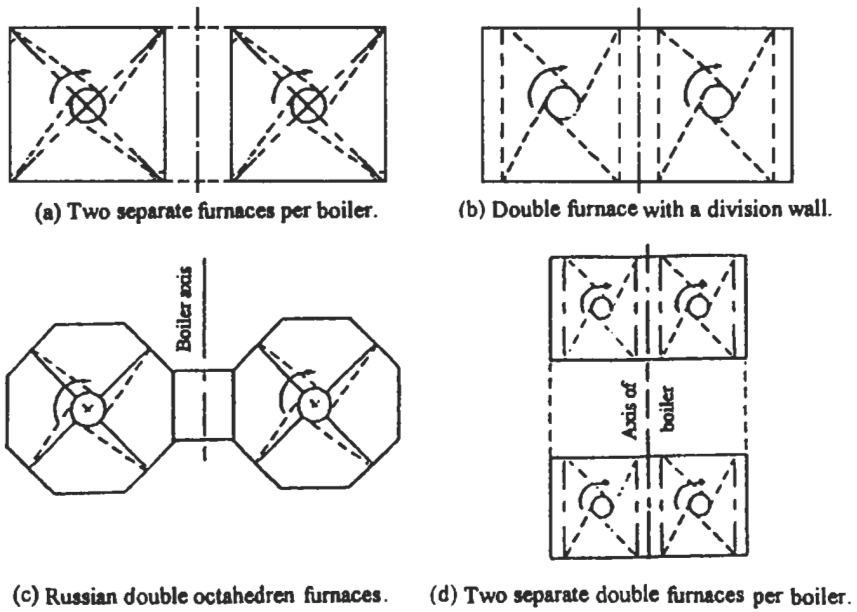


Fig. 5.102: Arrangements of multiple TF furnaces [944].

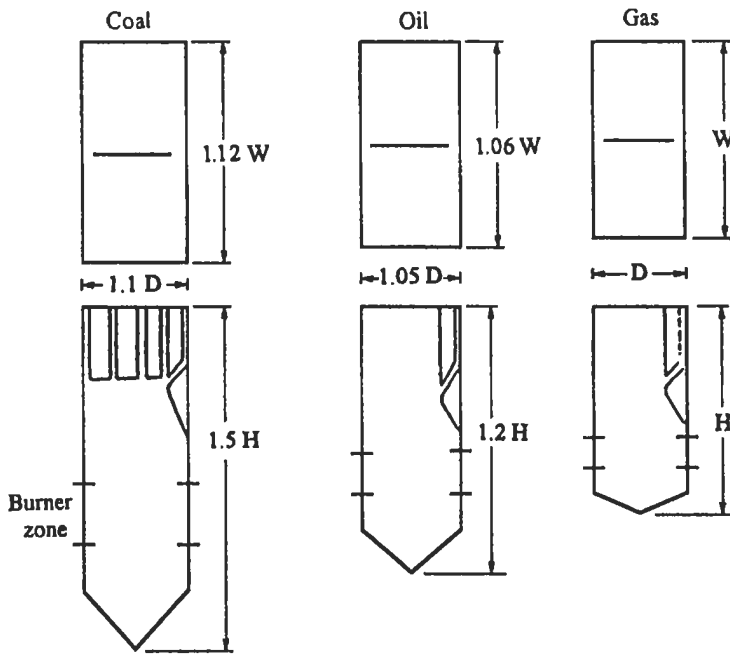


Fig. 5.103: Relative sizes of TF furnace wall for different fuels [945].

In this case, the diameter of the imaginary circle of flames tangency in the middle of the furnace (d_i) of a square-shape furnace can be calculated as:

$$d_i = 2a_f \sin(\theta) = 0.125a_f \quad (5.92)$$

where a_f is the length of the burners square's side, and θ is the angle between burners axes and the furnace's diagonal.

The length of the tangent (L_{\tan}) to the imaginary circle from the burner exit can also be calculated as:

$$L_{\tan} = 0.707 a_f \cos(\theta) \quad (5.93)$$

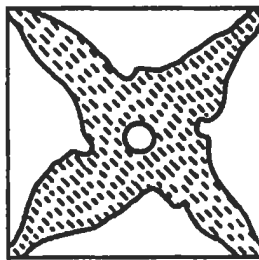
Romadin indicated that, the case of the furnaces with higher value of (θ) is not justified. He referred to the experience of operation of a furnace which was 7.168 x 6.656 m in cross section with a burners rectangle of 5.67 x 4.95 m. In this furnace, when θ was increased to 13.27° , the efficiency of the furnace was sharply decreased and the enthalpy of gases at the end of the furnace was increased by 7.6 %. Another case was confirmed by an experiment carried out in Germany; in which the furnace was equipped with three levels of burners, but the angle, θ was increased with transition from the bottom level to the upper one. It was unexpectedly found that, with this arrangement of burners, the loss due to unburnt carbon considerably increased, which made it necessary to return to the initial layout with constant angle. Also Romadin mentioned that, increasing the number of burners levels improves the occupation of the furnace by the

flames as shown in the plan view of Fig. 5.104. Compared with the conventional cyclone combustion, tangentially-fired furnaces operate at much lower swirl numbers, and therefore particulate separation is rather poor. The central vortex formed in a tangentially-fired furnace is much weaker and merely serves to stabilize the position of the flame in the furnace. He also concluded that the selection and design of tangentially-fired furnaces depend on a number of local features such as the fuel and burners.

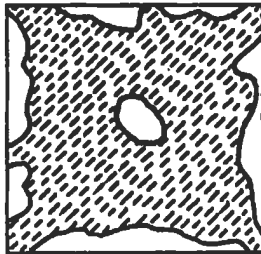
Lee and Lau [946] have mentioned that, tangential firing is favored on units rated at more than 400 t h^{-1} steam. But, units rated at less than 400 t h^{-1} steam utilize either wall or tangential firing. More utility boilers, particularly for low-volatile or low-grade coals, are equipped with TF systems.

5.2.3 Flame Stability

Flame stabilization is an interesting combustion problem and many studies have been carried out to determine the effect of different parameters on the stability of both laminar [947-949] and turbulent [950, 951] flames. Based on the theory of continuous wrinkled laminar flame, the effect of Reynolds number on the ratio of turbulent to laminar burning velocity was estimated [952]. Flammability limits, as defined by the leanest and the richest concentrations, which support a flame, have been determined by many investigators, including the works [953, 954] on the relations between temperature, pressure and these limits. It has been found that the flammability limits are broadened by increasing the temperature and pressure [24]. Correlations have been obtained for blow-off, blowout and flashback data for open burner flames in tubes of



(a) One tier of burners is in operation.



(b) Three tiers of burners are in operation.

Fig. 5.104: The dependence of the flame vortex size on the number of ignited tiers of burners [929].

different diameters at various fuel concentrations [561, 955]. Blow-off phenomenon has also been attributed [477, 956] to a reduction in the reaction rate caused by an enthalpy loss due to shear flow.

A better understanding of stable and safe ignition of the fuel-air mixture and the subsequent reliable operation are of important interest to engineers. Therefore, El-Mahallawy et al [930, 931] have measured the influence of fuel-flow rate and inclination angle θ on flame stability in a tangentially-fired furnace model. Also, they studied the effect of flame extinction of some burners on the other flames and on the vortex size. They have used a square cross-section model furnace, as shown in Fig. 5.105. The dimensions and shape were selected to simulate the tangentially-fired boilers of Abu-Qir thermal plant in Egypt. The model furnace cross-section is 0.6 x 0.6 m and the height is 1.0 m. The furnace was surrounded at the four sides by a water-cooling jacket. Each of the four corners of the furnace has been designed to accommodate a maximum of three LPG burners in three levels. A simple mechanism is designed for each burner to adjust the angle of inclination (θ) of the burner axis relative to the diagonal of the furnace in the horizontal plane. Plate 5.1 shows the produced flames in one level.

Ignition Limits

Seven different test runs were performed for each burner–inclination angle. Angles of inclination of 0° , 6° and 8° are used. One or more burners are ignited at a defined A/F ratio, while the others are shut off. By gradually opening the fuel valves for the shut off burners, the fuel-flow rates at which mixtures from these burners start to ignite can be determined. A complete set of the stability curves are obtained by changing the fuel-flow rate for the initially-ignited burners repeatedly.

The operating conditions for each run are given in Table 5.9. The dotted lines represent burners, which are initially shut off and then opened gradually; while the solid lines correspond to burners, which are kept ignited throughout the experiments. In the first four runs of Table 5.9, burners are either ignited or not lit while in the last three runs some of the burners were tripped. The following is a description for the experiments shown in Table 5.9. The results are presented in terms of plots of the equivalence ratios ϕ_e and ϕ_i for the extinguished and ignited burners, respectively, the average velocity of the initially-extinguished burners $U_{0,av}$, and the momentum flux of the initially-ignited burners.

Effect of Burner Tripping

Cases of non-tripped burners (test runs 1-4). In test run 1, two adjacent burners 1 and 2 are ignited at various A/F ratios; while burners 3 and 4 are not lit. The fuel is simultaneously and gradually introduced to burners 3 and 4 until ignition occurs. The burner- inclination angle θ was 6° or 8° . The fuel-flow rates at ignition of burners 3 and 4 were measured. The results are shown in Fig. 5.106. The resulting curves represent the ignition lines for burners 3 and 4.

The figure shows that three regions may be identified. Region I shows the non-ignitable zone and region II represents the ignitable zone for all burners, while region III represents an ignitable zone for burner 4 and a non-ignitable zone for burner 3. Burners 3 and 4 do not ignite at low values of momentum flux for burners 1 and 2 of less than 38 and 32 $\text{kg m}^{-1} \text{s}^{-2}$ for 6° and 8° , respectively, despite the increase in fuel-flow rates. In this

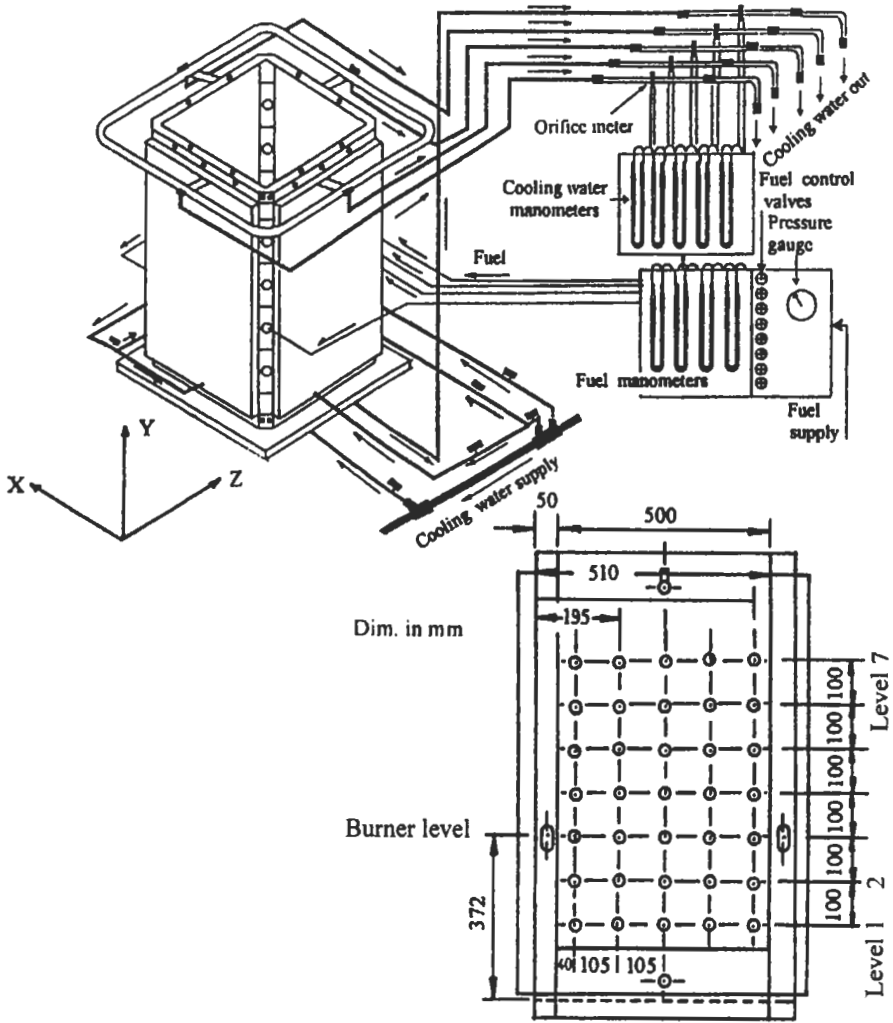









Fig. 5.105: General view and arrangement of measuring tappings of the tangentially fired model furnace [932].



Plate 5.1: Direct flame photograph ($A/F = 17$, $\theta = 6^\circ$) [932].

Table 5.9: Operating conditions of different runs [931]. Reproduced by permission of Elsevier Science.

Run No.	Diag. sketch of operating situation	Initially Ignited burners	Initially extinguished burners	Tripped burners
1		1, 2	3, 4	-
2		2, 4	1, 3	-
3		2, 3, 4	1	-
4		1	2, 3, 4	-
5		1	3, 4	2
6		1	2, 4	3
7		1	2, 3	4

- Refers to a tripped burner.
- Refers to an initially ignited burner.
- Refers to an initially extinguished burner.

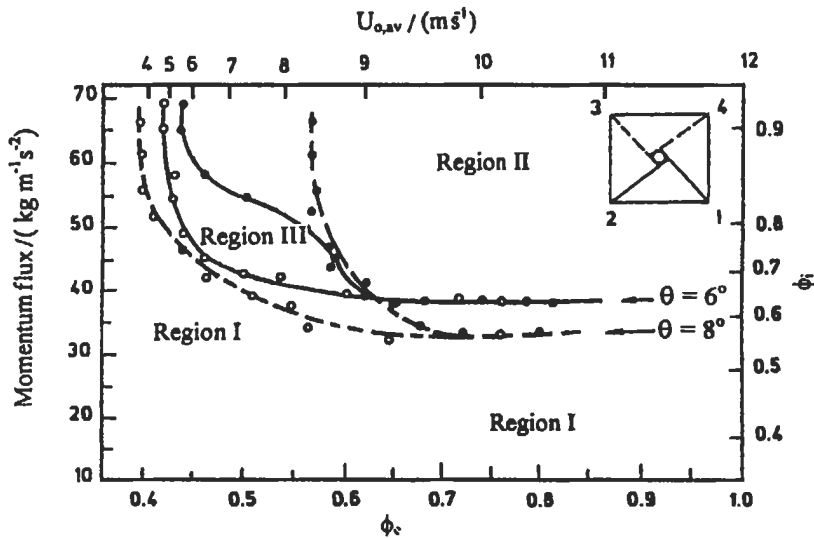


Fig. 5.106: Ignition curves of burners 3 (●) and 4 (○) [931]. Reproduced by permission of Elsevier Science.

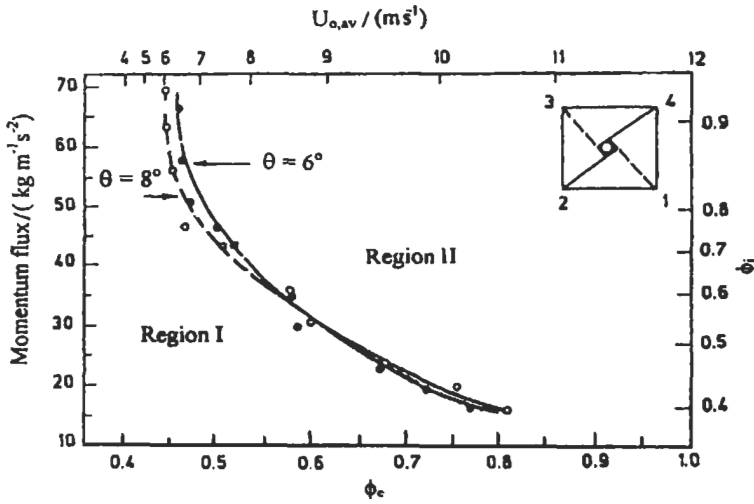


Fig. 5.107: Ignition curves of burners 1 (O) and 3 (●) [931]. Reproduced by permission of Elsevier Science.

part of region I, the momentum-fluxes of burners 1 and 2 are not enough for their flames to reach the mixtures of burners 3 and 4 and to initiate ignition. Above these limits of momentum-flux, ignition of burner 3 occurs at higher values of its equivalence ratio ϕ_e than for burner 4.

In test-run 2, two burners in opposite corners (burners 2 and 4) are ignited at various A/F ratios, while burners 1 and 3 are not lit. The fuel is introduced gradually to burners 1 and 3 until ignition occurs. The burner-inclination angle θ is 6° or 8° . The results are illustrated in Fig. 5.107, which indicates that ignition of the mixture of burners 1 and 3 started at the same time for each run. This is attributed to the symmetry of the flames in this case. It is also shown from the same figure that ignition occurs at high ϕ_e for low momentum fluxes of burners 2 and 4 and at low ϕ_e values for high momentum-fluxes.

In test run 3, burners 2, 3 and 4 were initially ignited at various fuel-flow rates, while burner 1 was not lit. Figure 5.108 illustrates the results and indicates that the flame stability is not significantly affected by the inclination angle, a result that could also be obtained for the above test case.

Figure 5.109 illustrates the results of test run 4 at $\theta = 6^\circ$. Burner 1 was ignited at various fuel-flow rates, while burners 2, 3 and 4 were not lit. The curves represent the ignition lines for these three burners. The results show that for momentum-fluxes of less than $15 \text{ kg m}^{-1} \text{ s}^{-2}$, burners 2, 3 and 4 do not ignite despite the increase in the fuel-flow rates. Regions I and II present extreme cases. Region III presents the conditions at which only burners 2 and 4 are ignited. In region IV, burner 4 is ignited while burner 3 is ignited in region VI.

Cases of Tripped-Burners (test-runs 5-7). In test run 5, burner 2 is tripped throughout the run, burner 1 is ignited at various fuel-flow rates, while burners 3 and 4 are not lit. The fuel is allowed to flow to burners 3 and 4 simultaneously and gradually until ignition occurs. The test-run is performed with burner-inclination angles of 6° or 8° . Figure 5.110 indicates that ignition of burners 3 and 4 occurs-simultaneously. The figure shows that relatively low values of the momentum flux of burner 1 are required for the ignition of the two burners for the case of inclination angle $\theta = 8^\circ$.

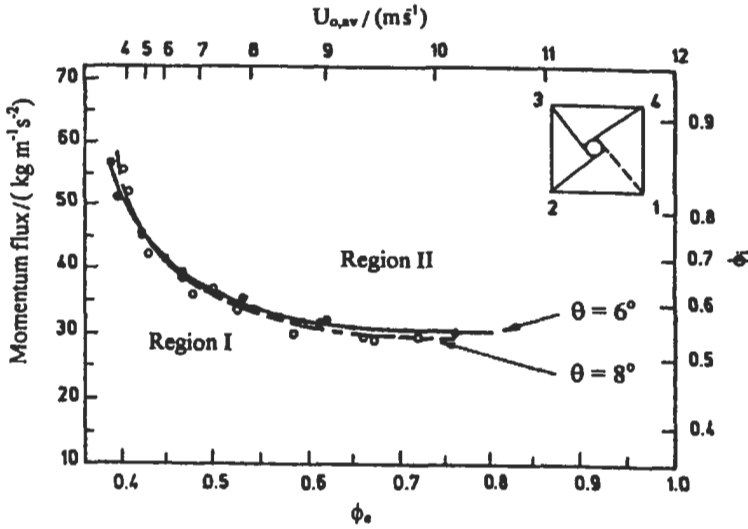


Fig. 5.108: Ignition curves of burner 1 [931]. Reproduced by permission of Elsevier Science.

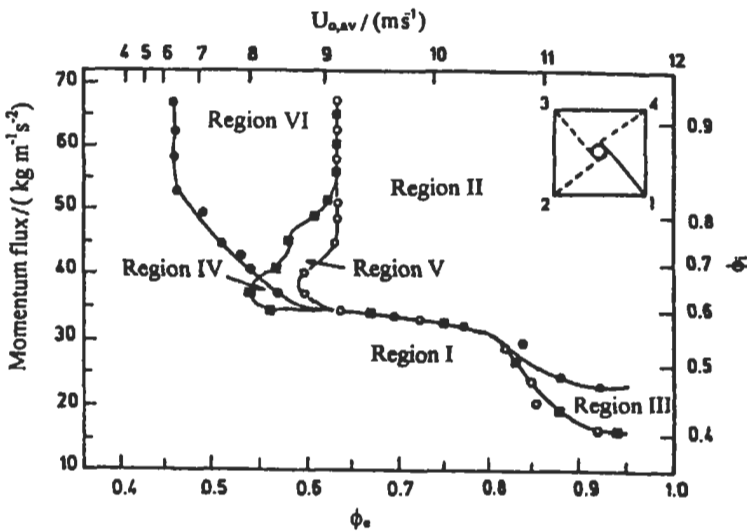


Fig. 5.109: Ignition curves of burners 2 (O), 3 (●) and 4 (■) at $\theta = 6^\circ$ [931]. Reproduced by permission of Elsevier Science.

Figure 5.111 shows the ignition curves for test-run 6. In this test-run, burner 3 is tripped throughout the run, burner 1 is ignited at various fuel-flow rates, while burners 2 and 4 are not lit. It is seen that for a momentum flux for burner 1 of less than $20 \text{ kg m}^{-1} \text{ s}^{-2}$, the influence of the vortex direction on burner ignition is insignificant and, therefore, the ignition curves of burners 2 and 4 coincide with each other at both angles of inclination. Above this value, the vortex direction becomes significant and ignition of burner 4 occurs at lower values of equivalence ratios as compared to burner 2.

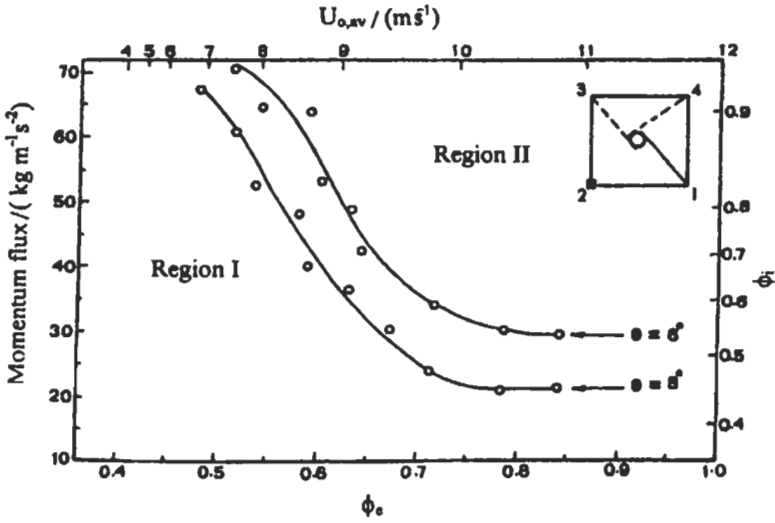


Fig. 5.110: Ignition curves of burners 3 and 4. Burner 2 is tripped [931]. Reproduced by permission of Elsevier Science.

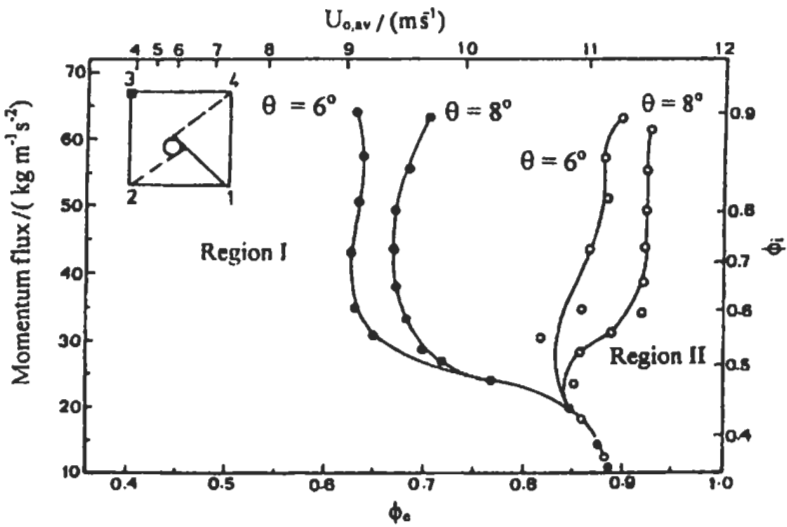


Fig. 5.111: Ignition curves of burners 2 (O) and 4 (●), burner 3 is tripped [931]. Reproduced by permission of Elsevier Science.

In test-run 7, burner 4 is tripped throughout the run, burner 1 is ignited at various fuel-flow rates, while burners 2 and 3 are not lit. The results show that burners 2 and 3 do not ignite at momentum-flux values for burner 1 of less than 52 and 45 $\text{kg m}^{-2} \text{s}^{-2}$ for 6° and 8° , respectively. Ignition of burners 2 and 3 is limited to the range of their equivalence ratios of 0.5-0.87.

Temperature-Contours Maps Just Before Ignition

Figure 5.112 exhibits temperature-contours maps in the furnace for test run 3 for $\theta = 6^\circ$ and 8° , respectively, just before ignition of burner 1. The contours maps for the two figures show that the temperature levels in the vicinity of burner 1 are greater for the case of $\theta = 8^\circ$ and ignition of this burner is, therefore, expected to occur at lower values of ϕ_e than for $\theta = 6^\circ$.

Figure 5.113 shows temperature-contours maps corresponding to test-run 4 for $\theta = 6^\circ$ and 8° , respectively, just before ignition of burner 4. The contours maps of Figs. 5.113 (a) and (b) show that the temperature around burner 4 is higher than for burner 2. It is, therefore, anticipated that burner 4 will ignite more readily at low values of ϕ_e than burner 2. This statement is confirmed by the stability limits of Fig. 5.109.

Inclination Angle and Core-Vortex Size

From the above discussions, it could be shown that the ignition curves for 6° and 8° inclination angles have similar trends. However, they have in some cases, different values of equivalence ratio at which ignition of distinguished burners occurs. It is also noted that, generally, ignition order of all burners in these test runs follows the vortex direction. In the case of $\theta = 8^\circ$, it is also shown that the vortex is larger in size and therefore its influence on the ignition of burners is significant.

The significance of the core size can be explained by examining the influence of the number of initially ignited burners of test-runs 1-4 on burners ignition and stability inside the furnace. Comparisons of Figs. 5.107, 5.108 and 5.109 indicate that burner ignition occurs faster (at lower ϕ_e) as the number of initially ignited burners increases.

Enough attention should be taken during the operation of such kind of furnaces to avoid flame failure of some burners. This will avoid any explosion, which may happen

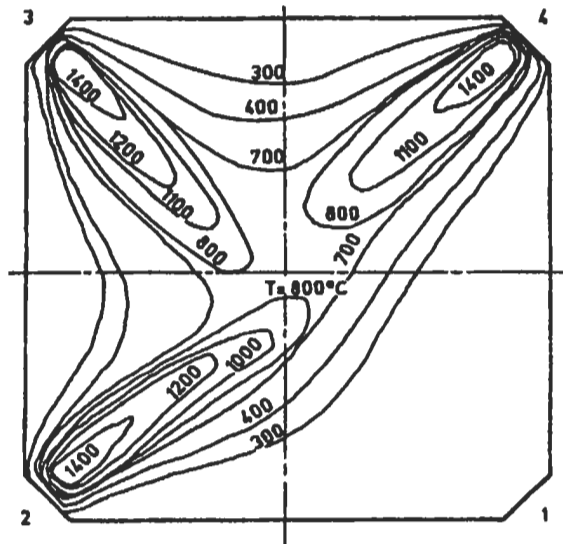


Fig. 5.112(a): Temperature - contours map for $\theta = 6^\circ$, $\phi_{2,3,4} = 0.6$ and $\phi_1 = 0.45$ [931]. Reproduced by permission of Elsevier Science.

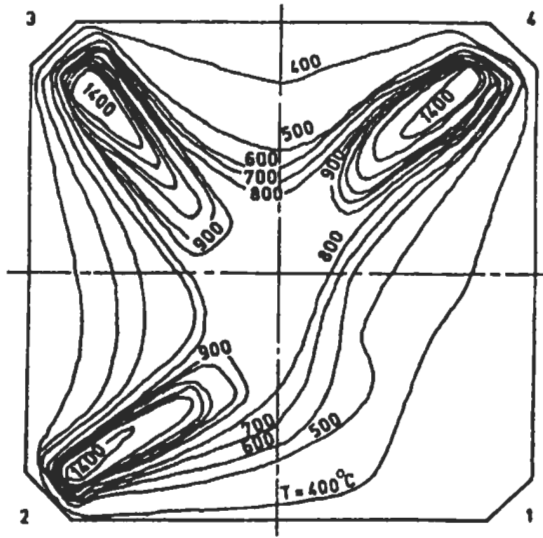


Fig. 5.112(b): Temperature- contours map for $\theta = 8^\circ$, $\phi_{2,3,4} = 0.6$ and $\phi_1 = 0.45$ [931].
 Reproduced by permission of Elsevier Science.

after forming an unburnt fuel cloud. This is similar to the case which took place in the tangentially natural gas-fired boilers of Abu-Qir power station, on 1984 in Egypt (boiler capacity is 450 ton stream h^{-1}).

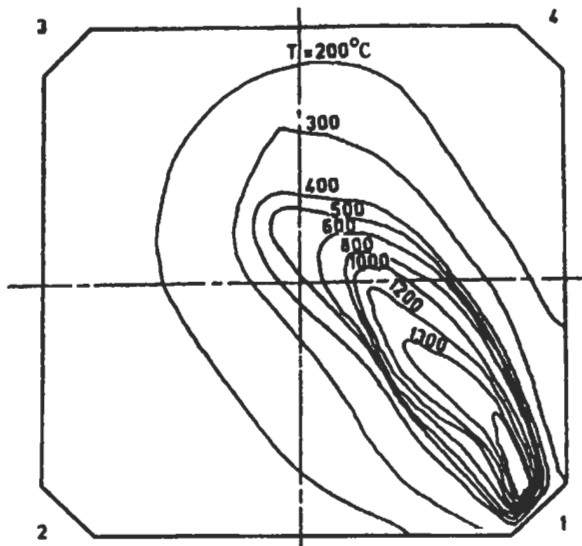


Fig. 5.113(a): Temperature- contours map for $\theta = 6^\circ$, $\phi_{2,3,4} = 0.45$ and $\phi_1 = 0.6$ [931].
 Reproduced by permission of Elsevier Science.

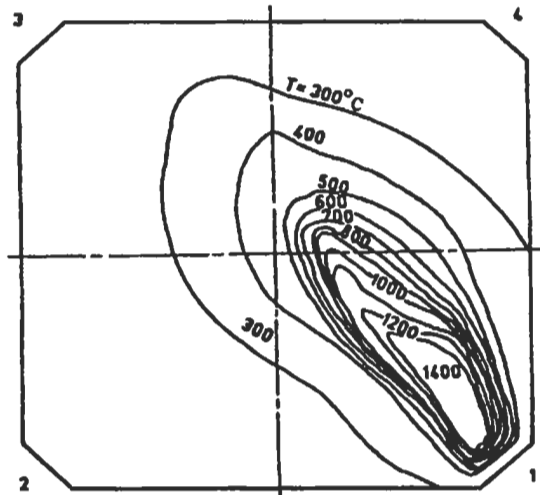


Fig. 5.113(b): Temperature- contours map for $\theta = 8^\circ$, $\phi_1 = 0.6$ and $\phi_{2,3,4} = 0.45$ [931]. Reproduced by permission of Elsevier Science.

5.2.4 Flow, Combustion, and Heat Transfer

The efficient burning of fuel in the combustion chamber as well as the transfer of heat to water and steam generated are essential for the economical working of power plants. Therefore, the above described tangentially-fired model furnace has been used by El-Mahallawy and Zakaria [932] to investigate the effect of the different parameters on the measured temperature distribution and its contours at the burners level, the concentration contours of combustion products, and the total heat transfer to the furnace walls. The analysis comprises the effect of the inclination angle on temperature and gas analysis distributions all over the furnace volume. These results are shown in Figs. 5.114 to 5.118.

Figure 5.114 shows the temperature contours maps at the third level, burners level, of the tested furnace at burners inclination angles 0, 6, and 8 degrees. Since the burners operate at the same conditions during the tests, the isothermal contours shape depend on the aerodynamics in the combustion space. The figure shows that at burner level the highest rate of temperature rise is found, for angle 8° , near to the walls which are exposed also to the highest gas temperature. Downstream of each burner a higher temperature region is characterized but for zero angle this region possesses relatively lower temperature. With respect to the central region of the furnace, it is characterized by high temperature but the temperature value decreases towards the furnace center in case of 8 and 6 degrees due to the anticipated recirculation of combustion products and entrained air. The temperature value in the center of the furnace, at that level, is lower in case of 8 degree, due to higher recirculation and enlargement of the circle of tangency than for 6 degree. The constant concentration contours of the combustion gases (CO_2 , O_2 and CO) were obtained at the burners level for the three inclination angles and the results for CO_2 are shown in Fig 5.115. The figure shows that, at the centerline of burner level there is a gradual increase of CO_2 concentration towards the furnace center with nearly constant concentration at the vortex region. The effect of recirculation of

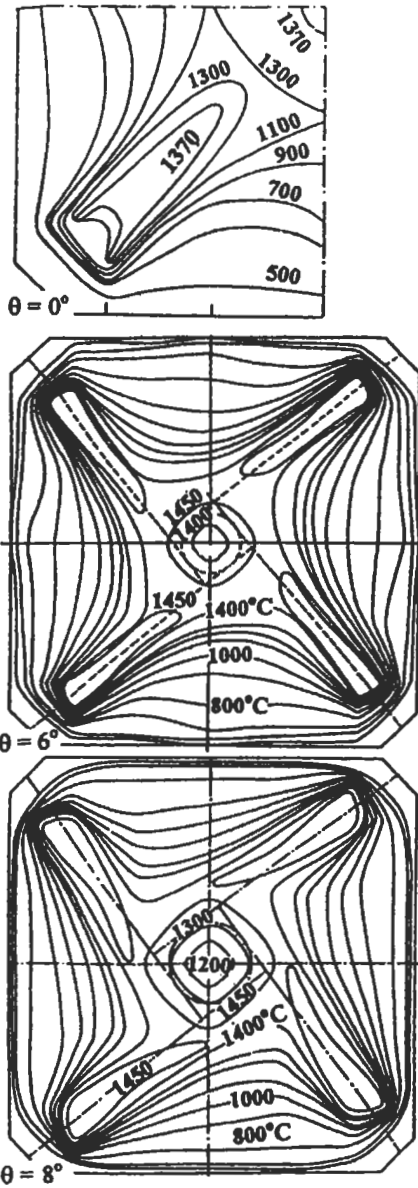


Fig. 5.114: Temperature contours map at the burners level, $A/F = 17$ [932].

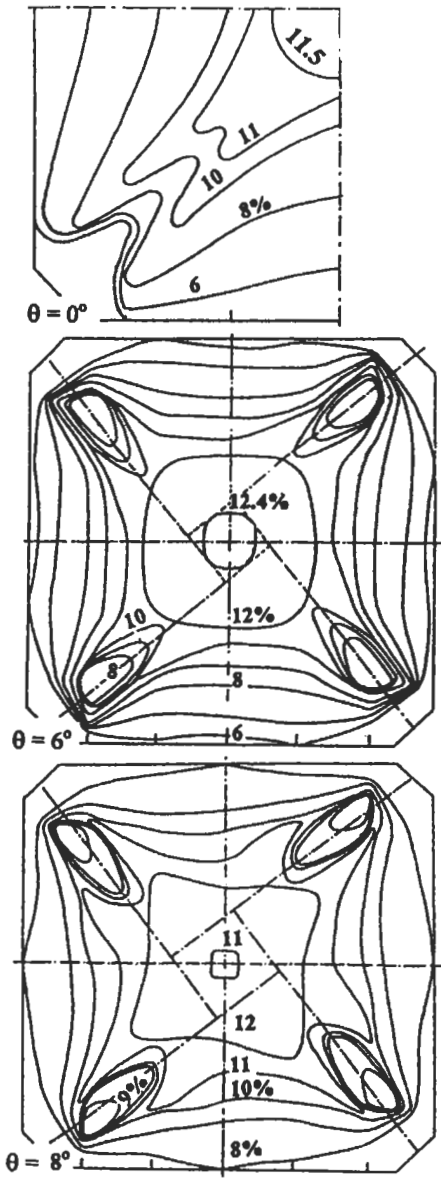


Fig. 5.115: Carbon dioxide contours map at the burners level, $A/F = 17$ [932].

entrained air with combustion products on gases concentrations can be characterized by a slightly higher percentage of CO_2 (8%) near to the furnace walls for 8 degrees, but with relatively lower values for 6 and zero degrees.

Maximum CO_2 occurs at the zone where fuel to air ratio is almost stoichiometric and well mixed. Since the input conditions are the same for the three test angles then the

vortex formation possesses the direct effect on the burning rate and oxidation of CO at the furnace center as the inclination angle increases. The vortex formation does not only improve the combustion process at the core zone but also has an effect on this process in the downstream region of each burner due to the recirculation of the hot gases to this region. The percentages of CO₂ are higher for angles 6° and 8° as compared with 0 degree, and take place in the outer boundary of the vortex due to higher reaction rates.

The inspection of oxygen and carbon monoxide concentrations zones indicated, as expected, that the zone of high values of CO₂ and CO correspond to low oxygen concentration. Moreover, the results show considerable quantities of free oxygen in the zones near the walls and virtually no CO concentration within these zones. Local regions of oxygen deficiency (0.5 %) in the flame core, on the jet axis, and in the vortex core with high CO concentration (1.2-1.5 %), reveal the weakness of mixing in spite of the excess air input to the burners.

The effect of the angle of inclination between the burners axis and the furnace diagonal on the distribution of the gas temperature and the concentration of CO₂ at different levels of the furnace, as well as, the effect of this angle on heat transfer to furnace walls will be given in the following parts (Fig. 5.116 – 5.118).

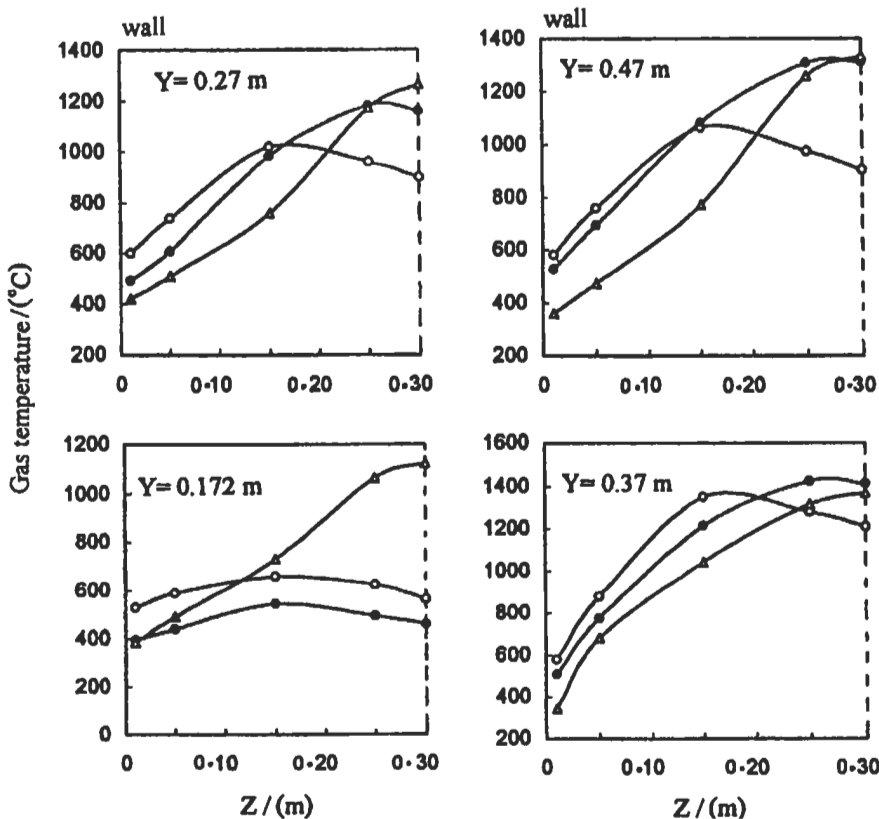


Fig. 5.116: Effect of inclination angle on the average temperature distribution at different levels of the model furnace O 8°, ● 6°, Δ 0° [932].

Effect of the inclination angle on the gas temperature. The cross section of the furnace is divided into five square rings and the average of the measured values is taken for each ring. The averages of the temperature measurements, for each angle are shown individually in Fig. 5.116. At the first level (the vertical height $Y = 0.172$ m), the averages of the temperatures are higher for angle 8° than for angle 6° with nearly uniform distribution as compared to the angle 0° .

The higher recirculation gases with entrained air at the furnace center, at all levels, arranged the temperature in a descending and ascending order at the furnace center and near the furnace walls especially for 8° inclination angle. Average gases concentration asserts this distribution.

Effect of the inclination angle on the gases concentration. Distribution of the average concentrations of CO_2 , CO and O_2 are obtained all over the furnace and the results for CO_2 are shown in Fig. 5.117. The results show lower values of CO_2 at the outer zones for 0° and 6° inclination angles as compared to angle 8° . Since for angle 0° the burners can be treated as opposed jets, a higher percentage of CO_2 is found at the furnace center. For the angles 6° and 8° , the recirculated gases with entrained air reach

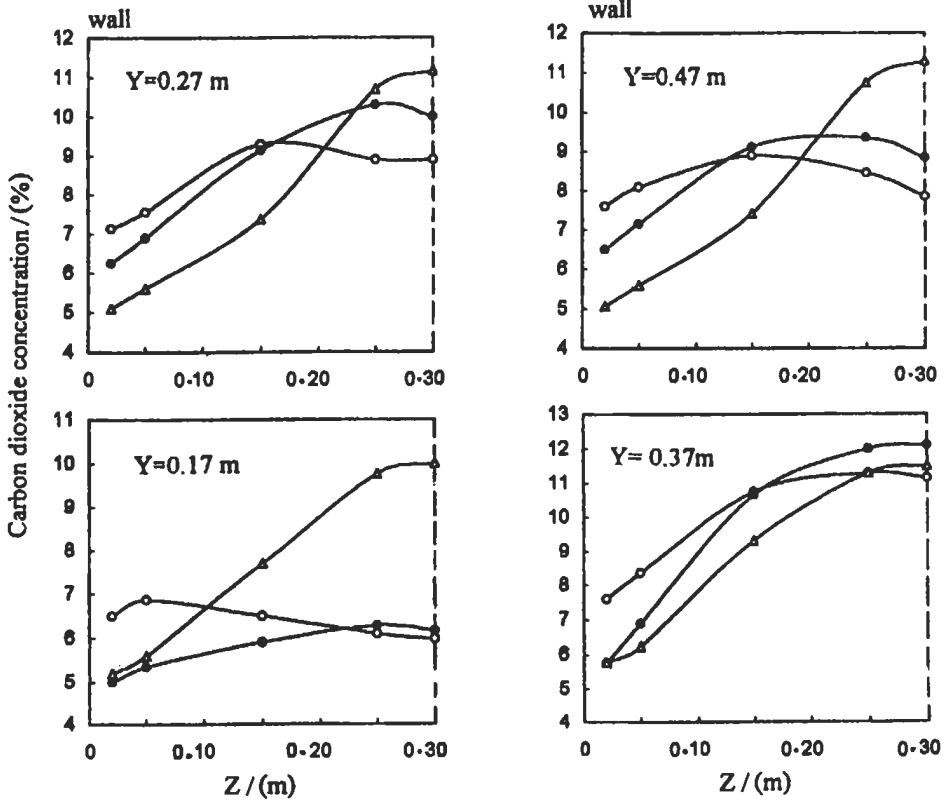


Fig. 5.117: Effect of inclination angle on the average carbon dioxide distribution at different levels of the model furnace O 8° , ● 6° , Δ 0° [932].

the furnace core causing a downward flow. As it descends, the downward flow widens which, together with its increasing volume due to heating, indicates gradual mixing with outer rotating flow of the primary flame.

Effect of inclination angle on the heat transfer. The total heat transfer to the furnace walls is calculated by measuring the cooling water mass flow rate and its temperature rise. The percentages of the total heat transfer as shown in Fig. 5.118 equal to 23.39%, 31.6% and 37% of the total heat input for the burners inclination angles of 0, 6 and 8 degrees respectively.

In order to model the above experimental results, El-Mahallawy et al [957] have developed a computer model to calculate the heat transfer to the furnace walls and they validate the model using the measured values of the different gas properties and the zoning method of analysis. The furnace volume, Fig. 5.119, has been divided in the three directions x , y , and z into 5, 7, and 15 divisions, respectively, to form rectangular parallelepiped gas elements with a total number of 525 gas elements. The walls of the furnace, Fig. 5.119, have been divided in x and y directions into 5 and 7 divisions, respectively to form rectangular surface elements with a total of 35 surface elements. The gas element is coordinated by (ig, jg, kg) and the surface element is coordinated by (is, js) . Each surface element receives radiation from all gas elements as shown in Fig. 5.120. The radiation from any gas element (ig, jg, kg) to surface element (is, js) is defined as $q_R(ig, jg, kg-is, js)$.

The input data of gas temperature and gases species concentrations of CO_2 , O_2 , and CO of each gas zone in the furnace volume had been fed to a computer program [957] for the three values of burners angles ($\theta = 0, 6$, and 8 degrees.). The fuel mass flow rate is 8 kg h^{-1} while the air / fuel ratio is 17. The surface emissivity (ϵ_s) of the furnace wall

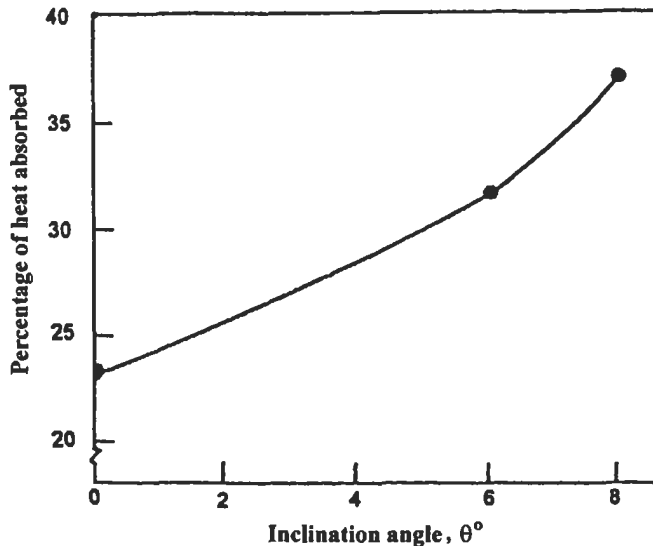


Fig. 5.118: Effect of inclination angle on the total heat absorbed by the furnace walls as a percentage of the total heat input [932].

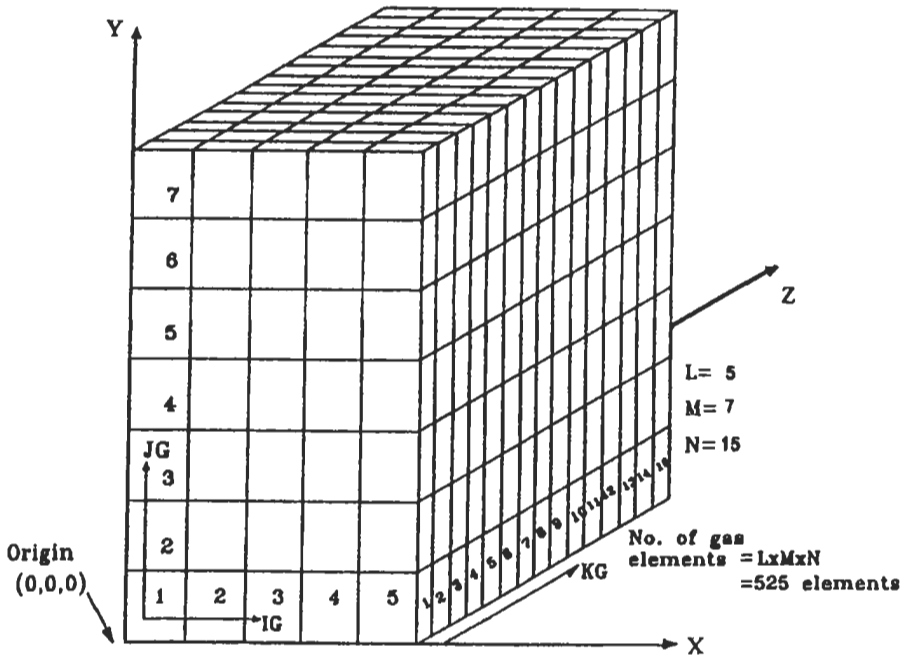


Fig. 5.119: Combustion gases division inside the furnace [957].

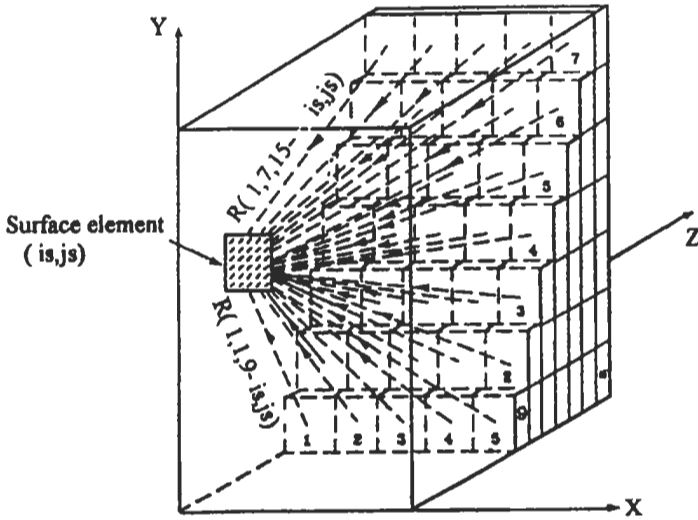


Fig. 5.120: Radiation transfer from gas elements to surface element (is, js) [957].

material and the average wall surface temperature are taken to be 0.9 and 400 K, respectively. The output of the program is the radiation properties of combustion gases and the radiative, convective, and total heat fluxes to the furnace walls.

The gas element emits radiation in all directions from its bounding surfaces, with an emissivity (ϵ_g) and gas temperature (T_g). The gas volume is considered as an absorbing-emitting medium with no scattering. The multi-reflection/scatter at surface wall elements is estimated to be as, $0.5 (1+\epsilon_g)$. Accordingly, the radiative heat q_R ($ig, jg, kg-is, js$), incident on any wall element (is, js) and coming from a gas volume element (ig, jg, kg), is expressed by Eq. 5.38. The view factor and transmissivity in the equation are described by arrays having five dimensions (ig, jg, kg, is, js). But each of T_g and ϵ_g is coordinated by an array having three dimensions (ig, jg, kg). The total radiative heat (kJ h^{-1}) received by surface element (is, js) is the summation of the radiative heat incident from all gas elements to this surface element as shown in Fig. 5.120 and this is given by:

$$q_{R, (is, js)} = \sum_{kg=1}^N \sum_{jg=1}^M \sum_{ig=1}^L q_{R} (ig, jg, kg - is, js) \quad (5.94)$$

where, N is the number of divisions in z direction, M is the number of divisions in y -direction, and L is the number of divisions in x -direction.

Radiative heat flux ($\text{kJ h}^{-1} \text{m}^{-2}$) at a surface element (is, js) is evaluated by dividing the total radiative heat reaching this element by surface element area. The total gas emissivity is divided into luminous emissivity and non-luminous emissivity. The source of luminous emissivity is the soot concentration, while the sources of non-luminous emissivity are carbon dioxide and water vapor, which are produced due to combustion. The luminous and non-luminous parts of the flame emissivity are calculated following the same procedures given in section 5.1.4.

The convective heat transferred from each gas element to its adjacent surface element is calculated by Eq. 5.40. The convective heat transfer coefficient, in case of forced convection, is a function of Nusselt number (Nu), Reynolds number (Re), and Prandtl number (Pr) (see section 5.1.3). The Nusselt number is a dimensionless group, and is a measure of the rate of heat transfer by convection. It can be expressed as a function of the Reynolds number which describes the flow, and the Prandtl number which is a property of the fluid, as follows [958];

$$Nu = 0.037 (Re)^{0.8} (Pr)^{0.333} \quad (5.95)$$

Computational results. The calculated radiative heat flux using the above procedure is given in Figs. 5.121 to 5.123 for values of θ equal 6, 8 and zero degrees, respectively. These figures show that the distributions of the heat flux on the furnace walls are almost identical with the maximum values existing at the burners level. The highest values are shown corresponding to the maximum value of θ , which is 8 degrees in this case.

The convective heat flux distributions on the furnace walls are shown in Figs. 5.124 and 5.125 for values of θ equal to 6 and 8 degrees, respectively. Again higher values of the heat flux correspond to the highest value of θ , the same trend as for the radiation flux. The high values of the convective heat flux occur at burners level.

Figure 5.126 shows the distribution of the total heat flux for the case of zero θ . The values of the total heat flux are lower than the values of the radiative heat flux for the cases of $\theta = 6$ and 8 degrees. The distribution of this total heat flux is shown

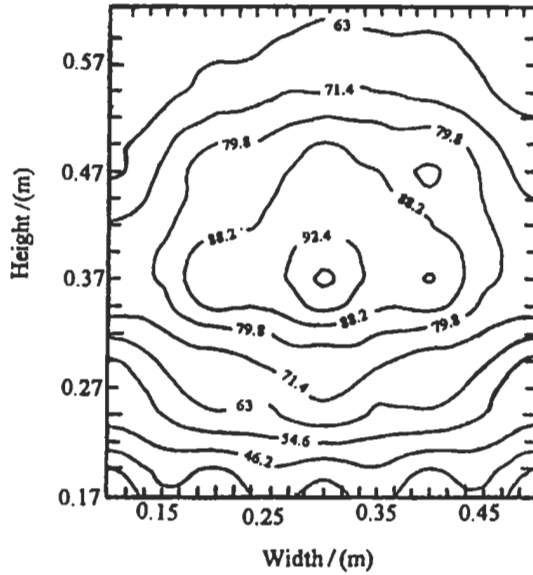


Fig. 5.121: Radiative heat flux ($10^3 \text{ kJ m}^{-2} \text{ h}^{-1}$) at $\theta = 6^\circ$ [957].

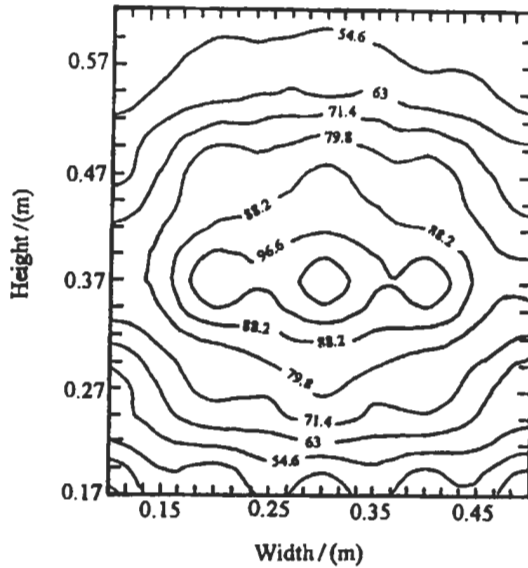


Fig. 5.122: Radiative heat flux ($10^3 \text{ kJ m}^{-2} \text{ h}^{-1}$) at $\theta = 8^\circ$ [957].

also to have the same trend as for the radiative and convective heat fluxes, with the maximum values occurring at the burners level. The high values of heat flux either total, radiative or convective which lay at burners level are expected due the high gas temperatures and velocities at this level.

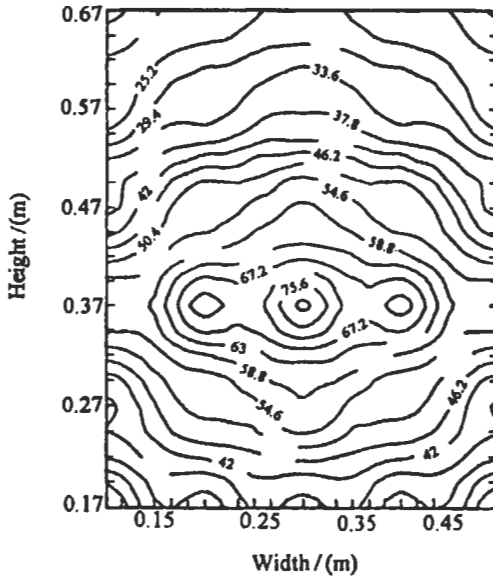


Fig. 5.123: Radiative heat flux ($10^3 \text{ kJ m}^{-2} \text{ h}^{-1}$) at $\theta = 0^\circ$ [957].

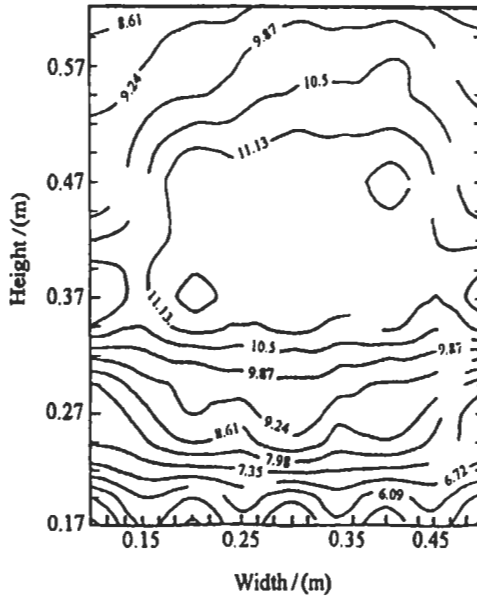


Fig. 5.124: Convective heat flux ($10^3 \text{ kJ m}^{-2} \text{ h}^{-1}$) at $\theta = 6^\circ$ [957].

Figures 5.127 and 5.128 show a fair agreement between the calculated and experimental heat flux, with a maximum difference of the order $\pm 11\%$. It is shown from the distributions of these heat fluxes that the difference between the maximum and minimum values is small as compared to those of the conventional furnaces. This is considered as one of the main advantages of the tangentially-fired furnaces.

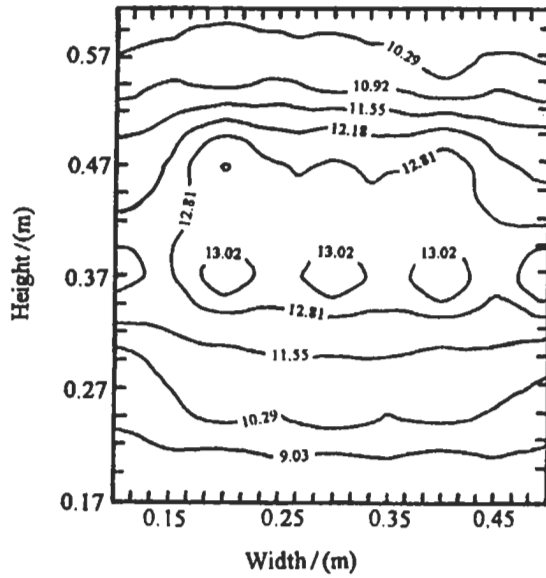


Fig. 5.125: Convective heat flux ($10^3 \text{ kJ m}^{-2} \text{ h}^{-1}$) at $\theta = 8^\circ$ [957].

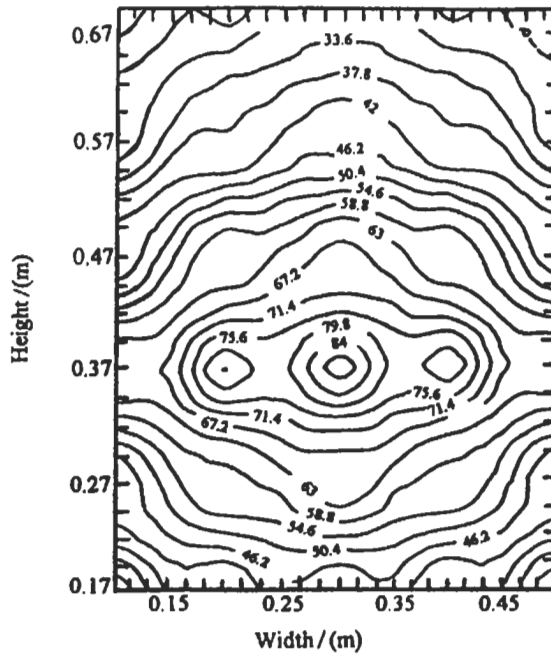


Fig. 5.126: Calculated total heat flux ($10^3 \text{ kJ m}^{-2} \text{ h}^{-1}$) at $\theta = 0^\circ$ [957].

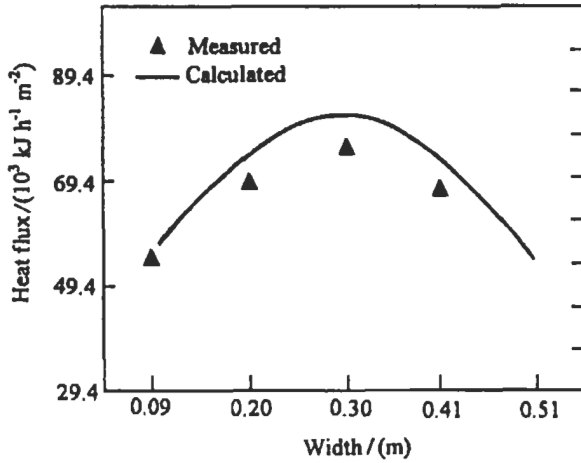


Fig. 5.127: Comparison between measured and calculated heat flux at $J_s = 2$ and $\theta = 6^\circ$ [957].

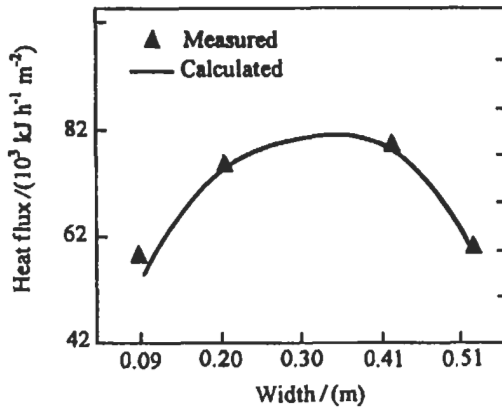


Fig. 5.128: Comparison between measured and calculated heat flux at $J_s = 5$ and $\theta = 6^\circ$ [957].

5.2.5 Modeling of Large Scale TFFs

Proper design of tangentially-fired furnaces requires a detailed description of the flow and thermal characteristics of the firebox. In large boiler models, several problems are encountered related to the increased grid sizes. Therefore, an advanced method has to be developed to overcome numerical problem associated with large grids. However, several numerical computations and field tests that applied to the tangentially-fired boiler have been investigated by many investigators [921-924, 935, 938, 959-979]. Flow, mixing, fuel burnout, and heat transfer were the main targets in their studies. The following presents the background to the TFF modeling with some results from these models.

Background to the Modeling of TFFs

The flow inside tangentially-fired furnaces is known to have its own peculiar aerodynamics, it is quite complicated in such a way that it is not easy to reach a satisfactory model to describe it. Previous trials to get a converged model have been based mostly on empirical assumptions, that is because the lack of data on multi-tier units. Robinson [923] has constructed a three dimensional model of a large tangentially fired furnace of the type used in power station boilers. This model is based on a set of differential equations governing the transport of mass, momentum, and energy, together with additional equations constituting subsidiary models of the turbulence, chemical reaction, and radiative heat transfer phenomena. The thirteen governing differential equations are converted to finite-difference form and solved by iteration procedure that utilizes the tridiagonal matrix algorithm. Nevertheless, the model is validated against experimental data acquired on two large furnaces. It is found that the model is successful in predicting several overall trends of the furnace behavior, but is inaccurate in predicting the details. The study is considered to be a successful demonstration of the potential help by such methods when applied to large tangentially-fired furnaces.

Categen and Richter [924] has discussed the results of the detailed temperature, heat flux and performance measurements conducted on a 420 MW tangentially coal-fired utility boiler (with 5 levels of burners) for several operating conditions (load, excess air, and coal flow at 6 degrees burner tilt-up) and compared them with predictions obtained from a three dimensional heat transfer model. The Monte-Carlo calculation technique for simulation of radiative heat transfer within the boiler furnace has been used. The gas temperatures are obtained from an iterative solution of the total energy balance. For simplification in heat transfer analysis, the total emissivity was assumed as a uniform value of 0.7.

Another study has been done by Platefoot [959] on the same boiler presented in Ref. 830. In this study, a numerical model has been developed which predicts heat fluxes to the selected points on the tube assemblies in the superheater pass of the boiler. The results of this model have been compared with heat fluxes calculated from measured steam tube wall temperatures as obtained from the boiler tests conducted at Liddell power station. The correlation between predicted and measured heat fluxes was poor at location near the furnace exit where the radiant heat transfer was dominant. The correlation was improved at locations further up the gas pass where convective heat transfer became increasingly more significant.

Boyd et al [938] described a computer code predicting fully three-dimensional turbulent gas and particle flow, combustion and heat transfer within a pulverized coal fired utility boiler. Input data for the model includes actual furnace operating conditions and coal properties. Radiative heat transfer is handled by the discrete transfer method. In this method, the furnace is divided into $6 \times 6 \times 17$ Cartesian cells, each having uniform temperature and absorption coefficient. A discrete number of the rays are tracked to the center of each wall cell from the surrounding walls. The incident heat flux at a point is obtained by integrating overall rays to that point. Bueters et al [921] used a computer model to predict the performance of tangentially-fired furnaces. This was achieved by a simple model, which viewed the furnace as an equivalent rectangular parallelepiped divided into 20 to 30 horizontal slices. Bianca et al [960] summarized the results of an experimental study designed to simulate and measure the effects of furnace aerodynamics (flow patterns, fuel-air mixing and ash particulate deposition) on the

corrosion problem in a utility coal fired steam generator. The units presented in the study are 156 MW, tangentially-fired pulverized coal utility boilers. They simulated the overall furnace flow patterns, burner-furnace mixing, and particle flow and deposition patterns. But, more work is required to develop experimental procedures that qualitatively correlate fuel/air mixing and ash/slag deposition patterns in laboratory models with actual field conditions.

Mironov et al [961] have studied the aerodynamics of the corner-fired furnace and their connection with the combustion of pulverized anthracite duff. An experimental study was made of the aerodynamics of a hot furnace with slot-type corner burners with two-stage air supply. Hot and cold tests were carried out on a boiler of 40.3 kg s^{-1} design steam capacity having a combustion chamber of square cross section, $7.7 \times 7.7 \text{ m}$ in plan, fitted with burners in a two-stage arrangement.

Lowe et al [962] adopted a model for a large tangentially-fired pulverized coal boiler with a furnace of thermal input of 900 MW. This furnace uses five levels; each having four burners with a firing circle, in the middle, of 2.5 m. Their predicted results were based on some empirical flow patterns and on dividing the furnace into 45 cylindrical zones. Using some numerical analysis techniques, they predicted the temperature distribution within the furnace. In their model they used a slicing technique in conjunction with:

1. Equation for the emissivity of CO_2 and water vapor.
2. A flow model for tangential firing.
3. Definition of the heat release (combustion zone).
4. A suitable radiation formulation.
5. Reasonably rapid computer solutions.

Benesch and Kremer [922] developed a mathematical model for fluid flow and mixing in tangentially-fired furnaces, which enabled the calculation of the transient behavior of flow and mixing in the furnace. Combustion has been considered as far as influencing the flow pattern, buoyancy forces caused by volume expansion during combustion, and the motion of coal particles in the combustion chamber. In their investigation, they had not coupled it with heat transfer calculation inside the furnace.

Shagalove et al [935] has studied the effect of the ratio of the burner height to width on the aerodynamics of TF furnace. The furnace considered in the study has three levels of burners fired with coal. When this ratio is greater than 4, the gas stream readily attaches to the wall, causing gas corrosion and slugging. Reducing this ratio increases the stability of the gas streams leaving the burners and of the central vortex flow. Radial different tangential velocity profiles can be obtained by varying burner tilt. The "disjointed" flow regime occurs when the upper burners are tilted upward by 20° , the lower burners are tilted downward by 20° , and the intermediate nozzles are left horizontal. Then, the diameter of the vortex core region can be reduced from $d_i/b = 0.85$ to 0.5, where b is the dimension of the longest side of the furnace. On the other side, the "jointed" flow regime occurs when the upper burners are tilted upward by 20° , the lower burners are tilted upward by 20° , and the intermediate nozzles are left horizontal.

Three-Dimensional Modeling for TFFs

Some of the boilers currently being operated in power stations are tangentially-fired with pulverized coal/oil or gas fuels. A fully three-dimensional numerical model is developed by Boyd et al [963] to predict the gas flow, particle trajectories, and

combustion and heat transfer in the furnace. This involves solving three-dimensional elliptic equations for gas flows, turbulence modeling, gas mixing, coal particle combustion modeling and a radiation transfer model. The complex task can be broken down into sub-models which can be to some extent, be experimentally verified. Their [963] numerical computations are based on the TEACH code developed at Imperial College [964]. The boiler modeling study by Boyd et al [963] is one of the four identical Liddell Power Station units. Each tower boiler comprises two rectangular furnaces sharing a central water wall (500 MWe). The furnaces are tangentially wall-fired from four groups of burners as shown in Fig. 5.129, and having dimensions of 10.69 x 8.86 x 31 m. Each vertical burner group consists of 8 pulverized-coal and primary air inlet ports with adjacent secondary airports above and below which supply approximately 80 % of the combustion air. The burner groups are directed at angles of 28° and 40° to the wall normal to achieve a central swirling fireball. One pulverized coal mill supplies each of the 8 levels of burners, but only 7 mills are required to maintain full load.

The predicted velocity vectors (from the above model [963]) in the plane of the heated jet are shown in Fig. 5.130 (a). The general clockwise swirling flow pattern set up by the tangential burners is apparent. However, the patterns in this rectangular cross-section furnace are not axisymmetric. Flow from the 40° burners is deflected hard against the north and south walls due to the interaction with the 28° jets. This behavior was confirmed by hot-wire anemometry in the Liddell boiler [965]. The vertical velocity profile at the furnace outlet plane just below the superheaters is shown in Fig. 5.130 (b). Vertical velocities are lowest in the center and highest at the 40° burner corners.

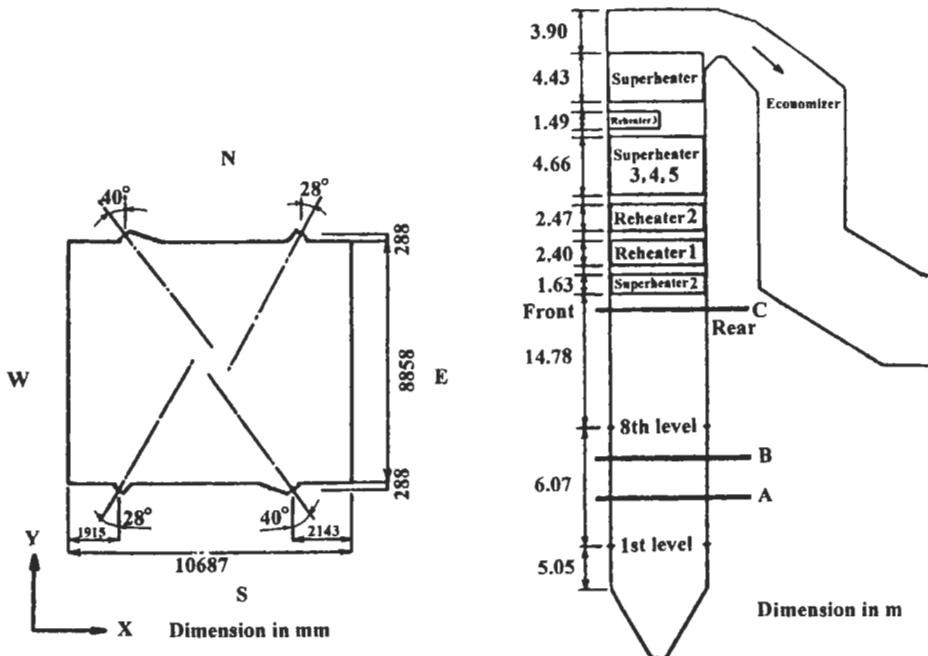


Fig. 5.129: Plan and elevation of Liddell 500 MWe boiler furnace. A, B and C are measurement plane locations in scale model [963]. Reproduced by permission of Department of Chemical Engineering, The University of Melbourne, Australia.

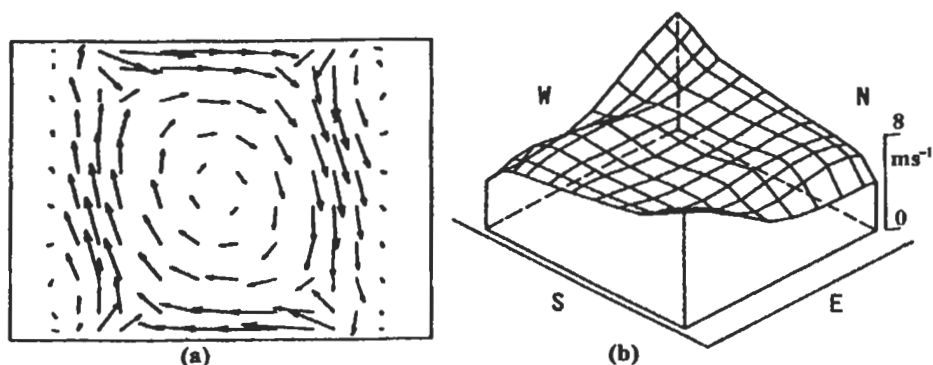


Fig. 5.130: Predicted velocities for cold flow Liddell boiler [963]. Reproduced by permission of Department of Chemical Engineering, The University of Melbourne, Australia.

- (a) Horizontal velocity vectors ($1\text{mm} = 1\text{ m/s}$) at plane A.
 (b) Vertical velocities at outlet (plane C).

The predicted and measured mixture fraction, f , distributions for the south wall with 28° burner are shown in Fig. 5.131. These are presented at three vertical heights indicated in the Fig. 5.129 elevation as A, B, and C. The lowest level is in the plane of the heated region of the jet which is the center one-third of the slit. Predictions and measurements are in good agreement. Plane A shows the penetration of the jet from the southern to the northern wall, along the western side. At plane B, mixing is well advanced and the jet has spread along the northern wall following the clockwise circulation. At plane C, mixing is fairly complete and there is no much variation in f across the profile. Overall, the measured profiles show a slightly higher mixing rate than the predictions as is evident in plane B. This implies that the turbulent exchange coefficients are higher than expected which in turn may be related to higher turbulence levels.

An integrated computational fluid model, including coal combustion and radiative heat transfer, is used by Knill et al [966] to model the flow in a 420 MWe tangentially-fired pulverized-coal boiler. Calculations are made with the boiler operated at 100 % and 45 % load, and compared with existing temperature and gas composition data above the burner belt. Local grid refinement is then applied around the corner windboxes. Local grid refinement allows accurate modeling of the flow gradients near the burner without substantially increasing the total computational requirements. With the finer grid, complex flow patterns of the multiple jets are better resolved. They [966] have used a commercial computational fluids package, TASCflow3D, to model the tangentially-fired coal boiler. TASCflow3D contains several novel methods to solve a variety of fluid flows in a robust, efficient and accurate manner.

The boiler used in the computation by Knill et al [966] is shown in Fig. 5.132, and details of the inlet conditions are summarized in Table 5.10. At full load, fuel was injected through 4 burner levels (B, C, D, and E) in each corner of the boiler. Secondary air was injected between the coal injectors to maintain a stoichiometry near 1.0. Overfire air (OFA) was injected above the burners to complete the combustion. At 45 % load, coal was only fired through the middle two burner-elevations (C, D). Sufficient secondary air was injected in the burner belt to maintain a stoichiometry of only 0.7.

Table 5.10: Inlet conditions [966]. Reproduced by permission of ASME.

Test condition	Full load	45 % load
Load (MWe)	405	182
Excess air (%)	21	47
Burner tilt (degrees up)	6	0
Coal flow (kg h ⁻¹)	1.48×10^5	6.83×10^4
Prim. Air flow (kg h ⁻¹)	2.81×10^5	1.30×10^5
Prim. Air temp. (K)	343	344
Sec. Air flow (kg h ⁻¹)	9.68×10^5	3.67×10^5
Overfire air (kg h ⁻¹)	2.32×10^5	3.36×10^5
Sec. OFA air temp. (K)	593	540

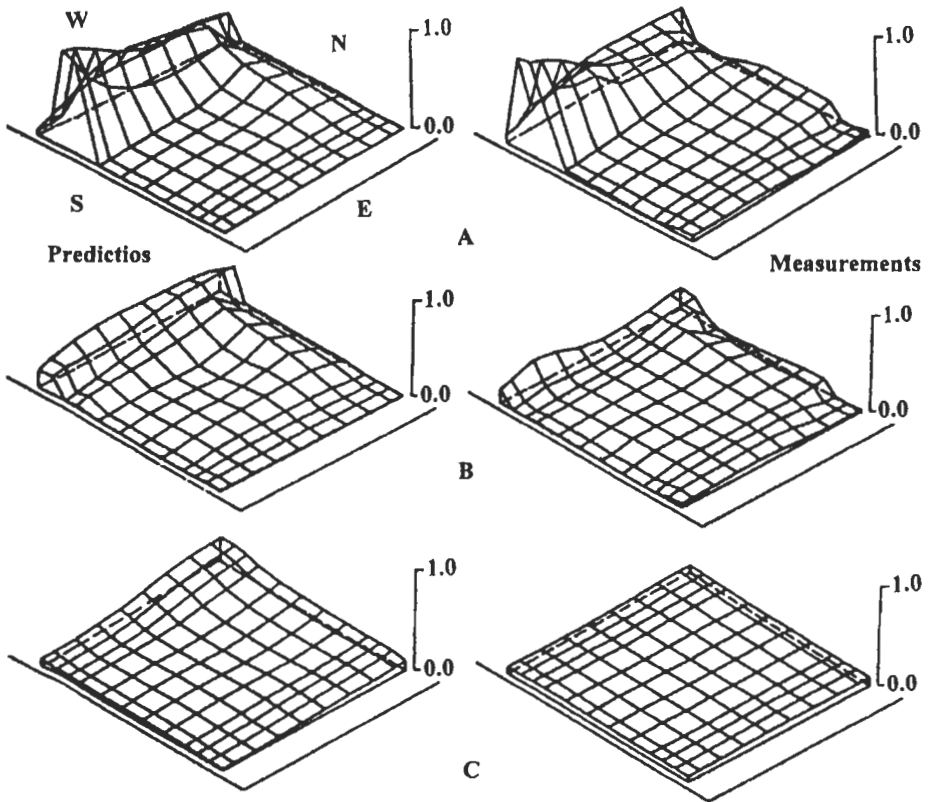


Fig. 5.131: Predicted and measured mixture fraction profiles for south wall 28° burner shown at planes A, B and C. Marked inlet stream is the centre one-third of 28° burner slit at the plane A level [963]. Reproduced by permission of Department of Chemical Engineering, The University of Melbourne, Australia.

Unlike the full load case, most of the air was fired through the overfire airports. A $19 \times 19 \times 50$ grid was constructed to represent the firebox section of the boiler. The convention adopted for the study was to associate the vertical direction as the Z coordinate and the K computational direction. The X and Y directions were associated with I and J computational directions, respectively, to maintain a right-handed grid.

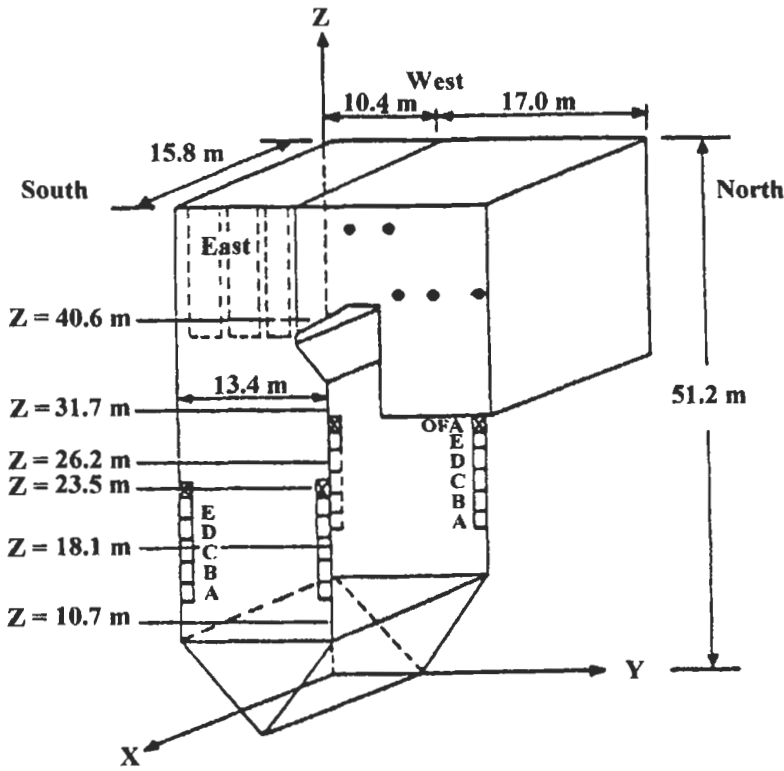


Fig. 5.132: Conesville tangentially fired boiler [966]. Reproduced by permission of ASME.

Calculations were first completed on this coarse regular grid to illustrate the influence of grid refinement on the calculation. The regular grid is considered as the coarsest grid to be suitable for tangentially-fired boiler simulation [967]. Separate calculations were performed using a grid, which was refined by a factor of three in the horizontal plane around each column burner. The refinement is extended 5 nodes in both the I and J directions to better resolve the jets as shown in Fig. 5.133. It was assumed that the flow enters perpendicular to each injection face and is balanced between all injectors. The flow was then seeded with a temperature of 1200 K around the burners to initiate devolatilization. Particles were injected each iteration and solved alternately with the hydrodynamic equations. This procedure was used for the first 100 iterations after which the particle injection frequency was reduced to once every 10 iterations.

Their results [966] show that the jet behavior influenced the circulation in the boiler. In the full load, improved prediction of the jet increased the tangential velocity near the walls. At $z = 27$ m, the swirl number was 0.4 for the regular grid compared to 0.8 for the embedded grid. The added swirl in the embedded grid influenced the general features of the flow. Particles tended to remain near the outside of the furnace in the embedded case. This, in turn, influenced the O_2 and temperature in and above the burner belt (see Figs. 5.134 and 5.135). A particle relaxation factor of 0.2 was applied to the particle sources of the hydrodynamic equations.

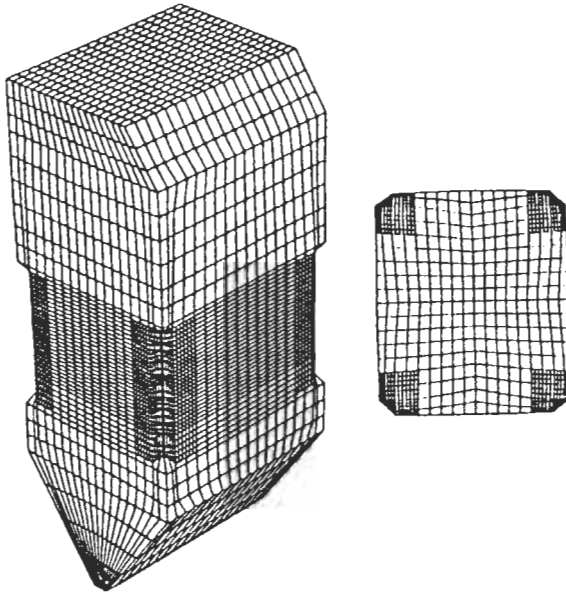


Fig. 5.133: Computational grid with grid embedding [966]. Reproduced by permission of ASME.

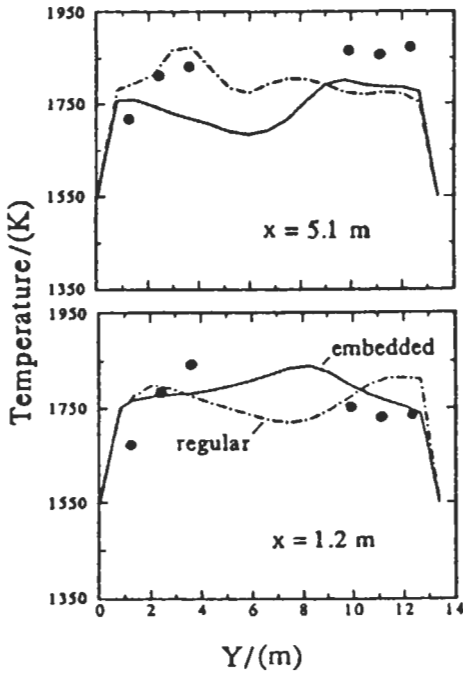


Fig. 5.134: Comparison of full load temperature distribution at 27 m elevation [966]. Reproduced by permission of ASME.

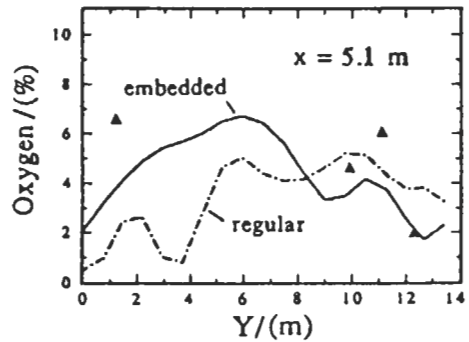


Fig. 5.135: Comparison of full load oxygen concentration at 27 m elevation [966]. Reproduced by permission of ASME.

The model [967] described in section 5.1.5.2 has been also validated using operational data from a tangentially coal fired 500-MWe boiler. The results demonstrate that the model has practical application for both the solution of operational problems and the optimization of the combustion performance of utility furnaces. A combustion optimization investigation on a tangentially-fired furnace indicates that potentially significant improvements are possible via modification of boiler operating parameters. The details of the model are also given elsewhere [968, 969]. The studies on the tangentially-fired furnaces involved the use of grids with around 20000 cells. For the swirl-burner wall-fired boiler (Bayswater, NSW), a finer grid was necessary to accurately model the burners. The nonuniform Cartesian grid used for the Bayswater furnace was 78 x 18 x 78 giving 109512 cells. A converged Bayswater solution [970] typically required 600 iterations and a CPU time of approximately 5 h on a Fujitsu VP2200 Supercomputer when commencing the solution process. Coal particles are tracked from each primary port cell. The particle size distribution is represented by a Rosin-Rammler function fitted to the measured distribution. Tracking is repeated to achieve adequate random particle dispersion. The model tracks around 10000 particle trajectories depending upon the burner geometry.

The Liddell boiler is simulated by Boyd and Kent [873] using the above model. This boiler is a 500-MWe unit with two tangentially-fired furnaces separated by a common central water wall (see more details in Figs. 5.129 and 5.136). The model predictions were compared with test data [971] which included burner and furnace exit plane gas

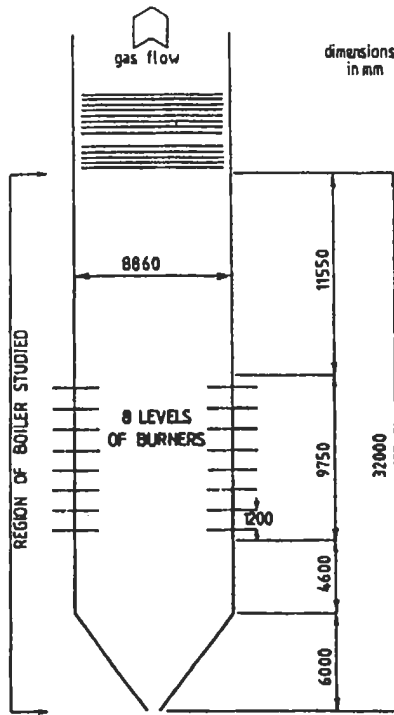


Fig. 5.136: Liddell boiler elevation [873]. Reproduced by permission of American Chemical Society (ACS).

temperatures and oxygen concentrations, wall incident radiative fluxes, and overall coal burnout. In general the wall heat fluxes were well predicted as were the temperature patterns in the burner zone; the peak temperature predicted in the furnace were however high by around 100°C .

Figure 5.137 shows the predicted (from the above model) and measured relationship between pulverized fuel fineness and the flue gas unburnt carbon loss. As expected the boiler test results showed a monotonic increase in percent unburnt carbon loss with increasing + 300 μm pulverized fuel size fraction. The model was able to reproduce this effect quite closely. The other parameter which in practice is found to have a major impact on unburnt carbon loss is the level of excess air in the flue gas. The predicted and measured relationships between excess air level and flue gas unburnt carbon loss are illustrated in Fig. 5.138. The slope of the predicted relationship is very close to that measured.

Experimental results obtained during trials of a flue gas online carbon in flyash analyzer revealed a correlation between burner tilt position and unburnt carbon loss. As illustrated in Fig. 5.139, the measured trend in flue gas unburnt carbon loss versus burner tilt is in good agreement with the predictions. A significant finding of the predictions was the considerable degree of unburnt carbon finding its way to the furnace ash hopper.

5.2.6 Emission and Emission Control

Emission

Regarding the emissions from TFF, Bueters [980] has presented a two-part paper for NO_x emissions from TF utility boilers. The first part was theoretical, and the second was practical. This study and Ref. 981 have approximately addressed the same topic.

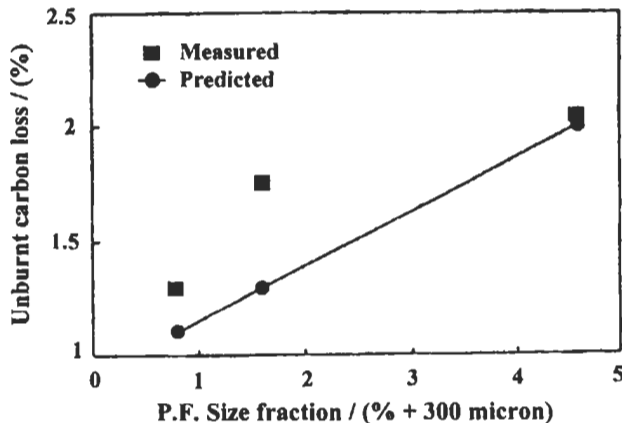


Fig. 5.137: Predicted and measured flue gas unburnt carbon losses plotted against pulverized fuel fineness [873]. Reproduced by permission of American Chemical Society (ACS).

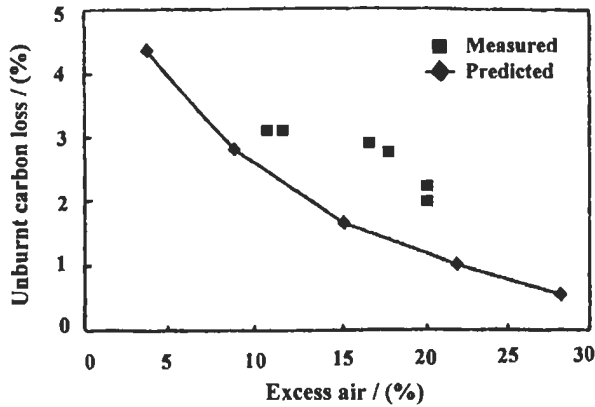


Fig. 5.138: Predicted and measured flue gas unburnt carbon losses plotted against furnace excess air level [873]. Reproduced by permission of American Chemical Society.

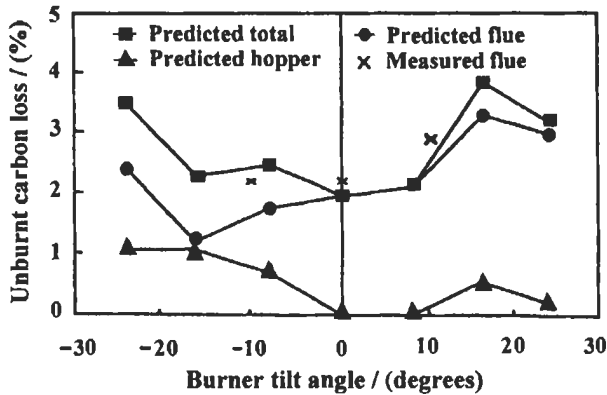


Fig. 5.139: Predicted flue, hopper, and total unburnt carbon and measured flue unburnt carbon loss plotted against burner tilt angle [873]. Reproduced by permission of American Chemical Society.

The main objective in their studies was the development of NO_x prediction capability and the factors influencing its formation. The factors involved in the design of large boiler furnaces and the current design practice in relation to NO_x emission control are considered.

Gregory et al [982] have conducted a field measurement program on utility boilers to determine the optimum location in the boiler ducting for extracting representative gas samples for continuous monitoring. The measurements are performed on seven fossil fuel-fired power boilers ranging in size from 125 to 800 MW, with the exception of one boiler was front wall-fired, all the other boilers were tangentially-fired. Concentration profiles for two pollutants, SO₂ and NO, and for two stable combustion products, CO₂ and O₂, as well as the velocity and temperature profiles were measured to establish the degree of point-to-point and duct-to-duct stratification of gaseous species.

Furthermore, the size distribution and composition of particulate emissions from two oil-fired utility boilers were determined under representative normal operating conditions by Piper et al [937]. In addition, the variability of particulate size and

compositional characteristics with changes in excess air level and fuel atomization quality was obtained from one boiler as an indication of the fluctuations in particulate emissions, which could be anticipated as a result of variable operating practices. The two test boilers included a 360 MW tangentially-fired boiler and a 345 MW face-fired boiler. The two boilers were burning a low sulfur (0.24 %) fuel oil. The tangentially-fired boiler is, a twin furnace steam generation unit with balanced draft. The unit is designed with the capability of firing coal, oil or natural gas fuels. Each furnace contains 16 steam-atomized burners. There are four elevations; each elevation containing four equally spaced burners. The burners can be tilted from a 30° downward to 30° upward position by superheat furnace and re-heat furnace tilt controls in the control room. The average values of NO_x for the TF unit and face-fired unit are 185 ppm and 261 ppm, respectively.

Habelt and Selker [981] have discussed the operating practices, that influence the formation of NO_x in utility steam power plants when fired with natural gas, oil or coal. NO_x emission data from a number of tangentially-fired utility boilers are presented to illustrate the NO_x emission level which can be expected from existing units, and the reductions which can be achieved through modifications of operating procedures. As a result of this study, the standard NO_x emissions for tested tangentially-fired units are given. These standard values are presented for gas, oil and coal firing at 3% excess oxygen as shown in Table 5.11. Based on the results of the study, the researchers have established a set of means to the operators of steam generating units for reducing NO_x emissions. These means are explained as follows:

Excess air. NO_x emissions increase as excess air is increased with all fuels. Operating at 10% higher excess air than the established minimum will normally increase NO_x emission by 20% for all fuels.

Nozzle tilt. The fuel and air nozzle tips can be tilted from the horizontal position by ± 30 degrees. Minimum NO_x emissions were generally at horizontal tilt position.

Air flow distribution. Increasing the percentage of air flow through the fuel compartments increases the rate of fuel-air mixing and increases NO_x formation by 20% on oil firing. The same change on coal firing results in only 10 % increase in NO_x emissions. A 20 % increase in NO_x emissions was observed with gas firing with a high percentage of air flow through either the fuel or air compartments.

Load reduction. A decrease in load reduces NO_x emissions with all fuels. The NO_x reduction for a 25 % reduction in load was 50 % on gas-fired units and 25 % on coal and oil-fired units.

Flue gas recirculation. Reductions in NO_x emissions of 35 % on oil and 60 % on gas firing were achieved with 30 % gas re-circulation.

Over-fire air operation. NO_x emissions decrease as over-fire air is increased. For coal and oil firing, the reduction in NO_x emissions averaged 38 %. For natural gas firing, the reduction in NO_x emissions averaged 50 %.

Table 5.11: Standard NO_x emissions for different fuel type.

Fuel type	kg /10 ⁶ kj fired	ppm
Gas	0.086	175
Oil	0.13	230
Coal	0.3	525

Fuel nitrogen. Fuel nitrogen is considered only with oil and coal firing. The indications were that NO_x emissions are influenced by fuel nitrogen with oil firing.

Water injection. Water injection has been demonstrated to be effective in reducing NO_x emissions on one gas-fired unit.

Emission Control

The NO_x reduction technologies available for both in-furnace and post combustion control processes are meeting the challenges posed by the regulatory environment (see chapters 1 and 2). The most cost effective solution for a desired NO_x emission level will require optimizing the total NO_x control system. Modern low NO_x tangentially firing systems have been investigated and summarized by several investigators [934, 936, 937, 980-995]. The following presents some applications of the low NO_x techniques in large scale TFF.

Application of combustion modification and post-combustion techniques. All the low NO_x techniques described in section 5.1.6 can be applied in tangentially-fired furnaces. Table 5.5 shows the application of re-burning techniques to full-scale tangentially-fired furnaces. Re-burning technique offers substantial NO_x reduction in tangentially-fired boilers [992] and a reduction of about 67 % in NO_x can be achieved by this technique [984, 991].

Burrington et al [939] studied the effect of the over-fire air (OFA) in TF boilers on NO_x formation. This study presented the findings of a program designed to investigate and evaluate the effectiveness of employing over-fire air as a method of reducing NO_x emission levels from tangentially fired boilers burning western U.S. coal types. The test programs investigated the effect of variations in excess air, unit slagging, load and over-fire air on unit performance and emission level. Additionally, the effect of biasing the combustion air through various out of-service fuel nozzle elevations was also investigated. The effect of over-fire air operation on water-walls corrosion potential was evaluated during thirty days baseline and over-fire air corrosion coupon test. The program was conducted on two tangentially-fired units designed with over-fire air registers (unit 1 has 6 levels of burners and unit 2 has 5 levels, both of them are fired with coal). In both boilers, re-heat outlet temperatures are controlled by fuel nozzle tilt and spray de-superheating. The following constituents were measured: NO_x , SO_x , CO, O_2 , and total hydrocarbon.

Blakeslee and Burbach [936] have studied various methods of reducing NO_x emissions on a gas-fired 250 MW TF boiler. These included the use of the water injection, operating without air pre-heat and staged combustion by the use of "over-fire" air, as well as the variation of operating conditions such as excess air, firing rate and fuel-air distribution. The use of "over-fire" air on the 250 MW unit reduced the NO_x emissions to less than 100 ppm. Water injection and elimination of the air pre-heat gave similar results.

Commercially-available, low-cost options for achieving NO_x compliance on pulverized coal-fired tangential boilers which require approximately 5 % to 50 % reductions has been presented by Mazzi and Haythornthwaite [985]. Often reduced NO_x and economic benefits (e.g. increased efficiency, reduced maintenance) can be achieved simultaneously. They presented in their work [986] the actual performance data based upon direct experience concerning the application of combustion tuning and fuel system modifications on eleven coal-fired, dry-bottom tangential boilers in the U.S.A. Frequently, combustion tuning efforts fall short of required NO_x reduction goal because

it is known how to inexpensively overcome common limiting factors (e.g. unburnt carbon, slugging).

In 1995, Morris and Sweeney [1987] have presented the results from both short term optimization testing and long term emission monitoring obtained during the first time of application of the controlled-flow, split-flame (CF/SF) low-NO_x burner design, used on wall-fired boilers, to a boiler having a tangential firing design. Installation of this burner system occurred without the modification of water-walls, or addition of separated over-fire air. During testing of the prototype tangential low-NO_x (TLN) burner system, it was found that a combination of optimized burners along with vertical secondary air staging provided the desired emission reduction over the entire boiler load range.

Two U.S.A. Department of Energy Innovative Clean Coal Technology Projects demonstrate advanced combustion techniques for the reduction of nitrogen oxides (NO_x) emission from coal-fired boilers [1990]. The primary objective of these demonstrations is to determine the performance of different low NO_x combustion technologies applied in a stepwise fashion to a 500 MW wall-fired boiler and a 180 MW tangentially-fired (T-fired) boiler. A target of achieving 50 % NO_x reduction has been established for each project. NO_x emissions results for those technologies that have been installed and tested to date are discussed and presented by Hardman and Sorge [1990].

In 1996, Thompson et al [1989] have summarized the post-retrofit operation and NO_x emissions experience for tangentially-fired units ranging in size from 135 to 250 MWe. The small units are older divided-furnace (8-corners) designs with only two burner elevations, whereas the larger units are twin-furnace (8-corners) superheat/reheat design (four burner elevations each) with a total of eight pulverizers. All units were retrofit with low-NO_x concentric firing systems (LNCFS) which included low-NO_x burners and over-fire air (OFA). One 250 MWe unit was recently retrofit with a state-of-the-art controls system under a jointly funded project with EPRI. In their work [1989] they address start-up and operational issues concerning the burner nozzle flame attachment and overheating, pulverizer high efficiency exhauster modifications and operation with a high sulfur slugging coal. NO_x emission guarantees were generally met without difficulty at full load, but trade-off between NO_x emissions and steam temperatures was necessary at reduced loads.

The applications of the post-combustion techniques in boilers are discussed in details in section 5.1.6. Michele et al [1995] have shown that SNCR technologies strongly depend on the thermal field downstream the lances as well as the spray characteristics, and the mixing between the atomized chemicals and the flue gases. In pulverized coal wall-fired and tangentially-fired boilers a reduction in NO_x of 30-75 % (100-200 ppm @ 3 % O₂) can be achieved using SNCR technique, while a reduction in NO_x of 80-90 % (80- 100 ppm @ 3 % O₂) can also be achieved using SCR technique. The application of SCR and SNCR techniques together with the combustion modification technique is called integrated technique, and this will be discussed in the following section.

Integrated NO_x control techniques. Martin et al [1934] have characterized a dry-calcium-based sorbent SO₂ capture technique combined with an offset auxiliary air low-NO_x burner. A 380 kW (1.37 million kJ h⁻¹) two-burner levels, tangentially-fired, pilot-scale facility has been used in this study. The experimental combustor used for this program is an approximate 1 to 14 geometric scaling of an existing modern design of a tangentially-fired boiler. Illinois number 6 bituminous coal was the fuel used during these experiments. Baseline tests showed that the facility property simulates full-scale

temperatures and emission levels. Dry sorbent SO₂ test results suggest that for enhanced sorbent SO₂ capture, injection should take place away from the burner zone where temperatures are low, and that the time the sorbent particles spend in the optimal temperature range should be extended as much as possible through sorbent injection methods and temperature profile modification.

Cohen et al [994] have investigated the cost impact of various NO_x control options for three cases of a coal-fired 400 MWe tangential unit designed to achieve 0.043 kg /10⁶ kj, NO_x (73 ppmvd @ 3 % O₂ dry volume). The steam generator operating parameters at top load are described in Table 5.12, with assumed typical Eastern Bituminous coal with fuel and ash properties. In each case they assumed different NO_x emission levels leaving the steam generator. In-furnace control via a tangential firing system will limit NO_x to levels of 0.173, 0.13, and 0.086 kg /10⁶ kj, for cases A, B, and C respectively (see Fig. 5.140) by using various degrees of air staging in the furnace. From these NO_x emission levels, a selective catalytic reduction system was integrated upstream of an air heater to achieve the final desired outlet NO_x emission level of 0.043 kg /10⁶ kj. A graphical description of the overall NO_x control design cases A, B, and C is shown in Figure 5.140.

The principal method of controlling NO_x formation in a tangentially-fired boiler is "air staging". Both local and global air staging are used to minimize O₂ availability during the critical early phases of combustion when the reactive volatile nitrogen species are released. Staging the combustion process creates fuel rich conditions in the firing zone, which promotes conversion of volatile nitrogen species to molecular nitrogen. The local air staging design features—flame attachment coal nozzles and offset secondary air nozzles—plus, a reduced firing zone heat release rate, will be the same for all three cases. Figure 5.141 shows a comparison of cases A, B and C firing system design arrangements. The principle difference among the three cases arrangements is the design of the global air staging, overfire-air (OFA) system. This approach is appropriate since the quantity and location of OFA injection significantly influence NO_x emissions.

Case studies A, B and C employ SCR as the basis for lowering the various NO_x emission levels leaving the steam generator to the required outlet NO_x level of 0.043 kg /10⁶ kj. A summary of the SCR design criteria is shown in Table 5.13. In terms of maintaining high NO_x reduction efficiency and low ammonia slip (unreacted ammonia), selective catalytic reduction is without equal. The SCR method was chosen over other possible post combustion techniques to achieve the desired outlet NO_x concentration, based upon demonstrated long-term performance and reliability.

Table 5.12: Summary of pulverized coal tangential steam generator parameters [994]. Reproduced by permission of ASME.

Maximum continuous rating	1335400 kg h ⁻¹
Superheater outlet temperature	452 °C
Superheater outlet pressure	180 bar
Reheater flow	1235606 kg h ⁻¹
Reheater outlet temperature	451 °C
Reheater inlet pressure	41 bar
Reheater inlet temperature	336 °C
Feedwater inlet temperature	252 °C

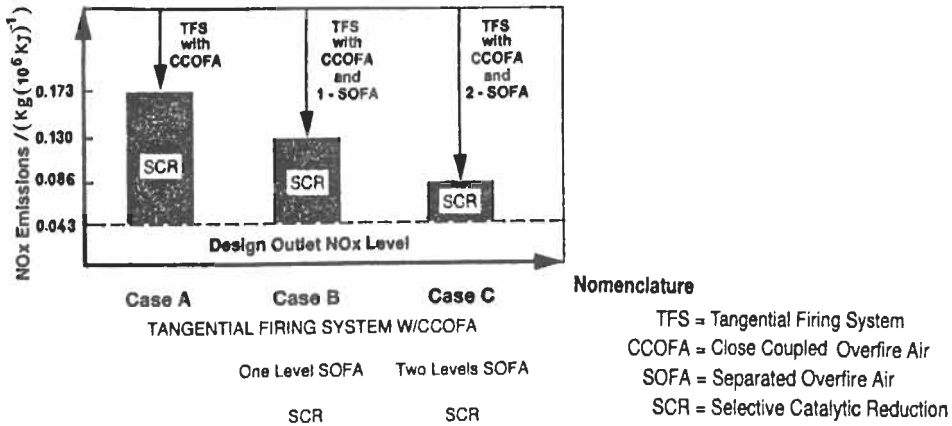


Fig. 5. 140: Total integrated NO_x control system [994]. Reproduced by permission of ASME.

SCR technology is a reduction process in which an ammonia vapor reacts over a catalyst, to reduce NO_x (95 % NO in the flue gases) to nitrogen and water vapor (see chapters 1, 4 and 5). For the proposed eastern bituminous coal (1.6 % sulphur by weight), the optimum operating temperature range is 338 °C to 400 °C. Based on this temperature window, the SCR reactor chamber is located between the economizer and air preheater. The physical dimensions of the SCR reactors for each case are shown in Fig. 5.142. An ammonia injection grid is installed upstream of the SCR reactor. At this location, a dilute mixture of ammonia and air is uniformly injected into the flue gases through a network of pipes and nozzles. This gridwork of pipes ensures a uniform distribution of ammonia before the flue gases pass through the active catalyst layers. Ammonia can be supplied in either aqueous (25 to 32 % by weight ammonia) or anhydrous form. Aqueous ammonia is more safe to store and handle. The case studied assumed equipment for an anhydrous system. A flow schematic for anhydrous ammonia system is shown in Fig. 5.143.

Table 5.13: Post-combustion control – selective catalytic reduction (SCR) [994]. Reproduced by permission of ASME.

	Case A	Case B	Case C
Inlet NO _x , kg / 10 ⁶ kg	0.173	0.13	0.086
Inlet NO _x , ppmvd at 3 % O ₂	293	219	146
Outlet NO _x , kg / 10 ⁶ kg	0.043	0.043	0.043
Outlet NO _x , ppmvd at 3 % O ₂	73	73	73
NO _x removal efficiency, %	75	66.67	50
Unreacted ammonia			
Exiting SCR, ppmvd at 3 % O ₂	5	5	5
Catalyst service life, years	2	2	2

Note: All cases are based on a new 400 MW steam generator firing an Eastern Bituminous coal.

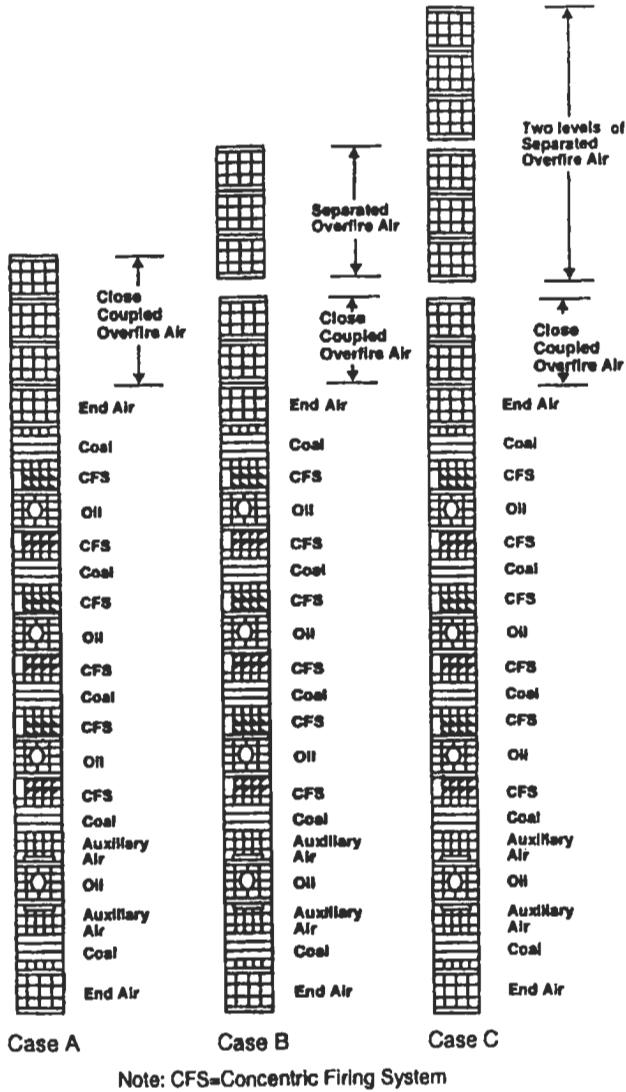


Fig. 5. 141: Tangential windbox design arrangements [994]. Reproduced by permission of ASME.

The total integrated system concepts consisting of both the firing and SCR system components were analyzed on a relative differential cost basis. The differential capital costs as well as the leveled capital and operating costs were compared for each of the cases studied (see Figs. 5.144 and 5.145). A summary of the assumed economic evaluation factors is presented in Table 5.14. When comparing the relative capital costs of the firing equipment versus the SCR for each case, it is apparent that maximizing in-furnace reduction is very effective in reducing overall system costs. From Fig. 5.144, the relative differential capital costs of case A (i.e., highest use of SCR, NO_x reduction = 75 %) versus case C (i.e., lowest use of SCR, NO_x reduction = 50 %), represented

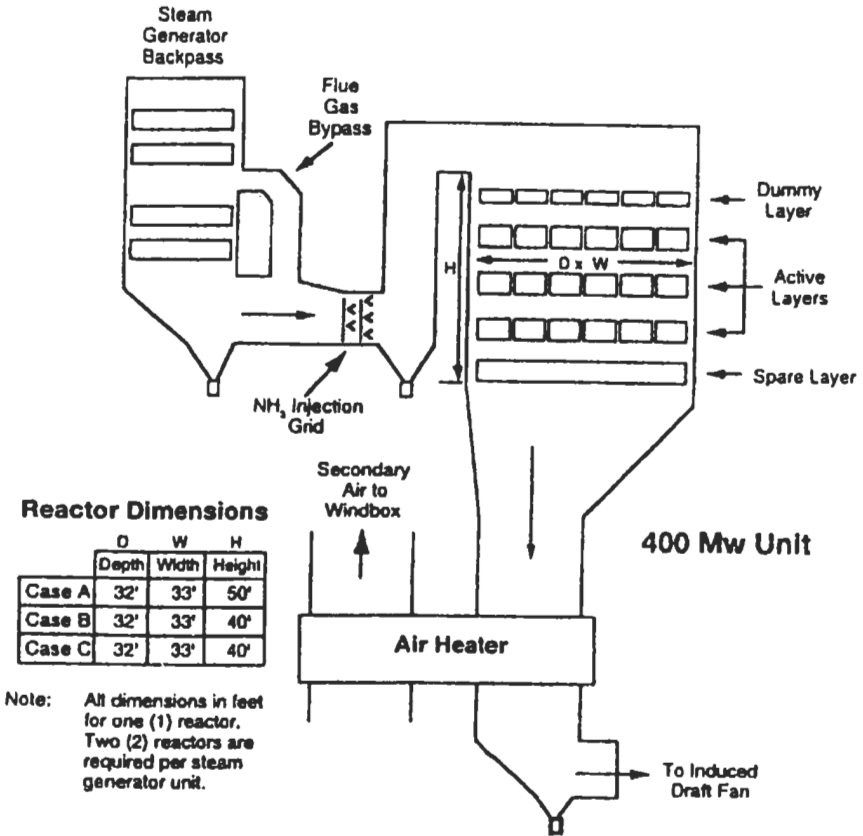


Fig. 5. 142: Arrangement of SCR system [994]. Reproduced by permission of ASME.

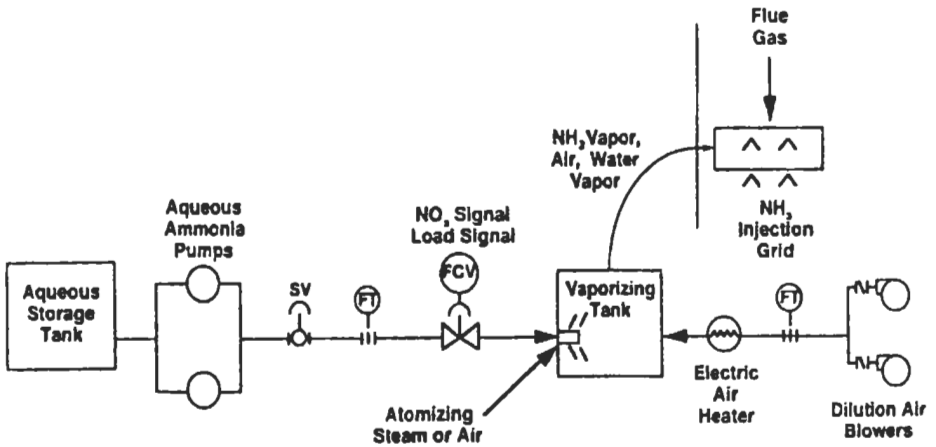


Fig. 5.143: Schematic of aqueous ammonia system Aqueous ammonia (25 – 32 % by weight NH₃) [994]. Reproduced by permission of ASME.

Table 5.14: Summary of economic evaluation parameters [994]. Reproduced by permission of ASME.

Discount rate	8 %
Escalation rate	4 %
Unit service life	30 year
Capacity factor	70 %
Auxiliary power (energy charge)	\$ 0.08 /kW h
Catalyst material cost	\$ 410 /ft ³
Anhydrous ammonia	\$ 200 /ton

All evaluated operating costs were determined on an annualized cost basis in 1992 dollars.

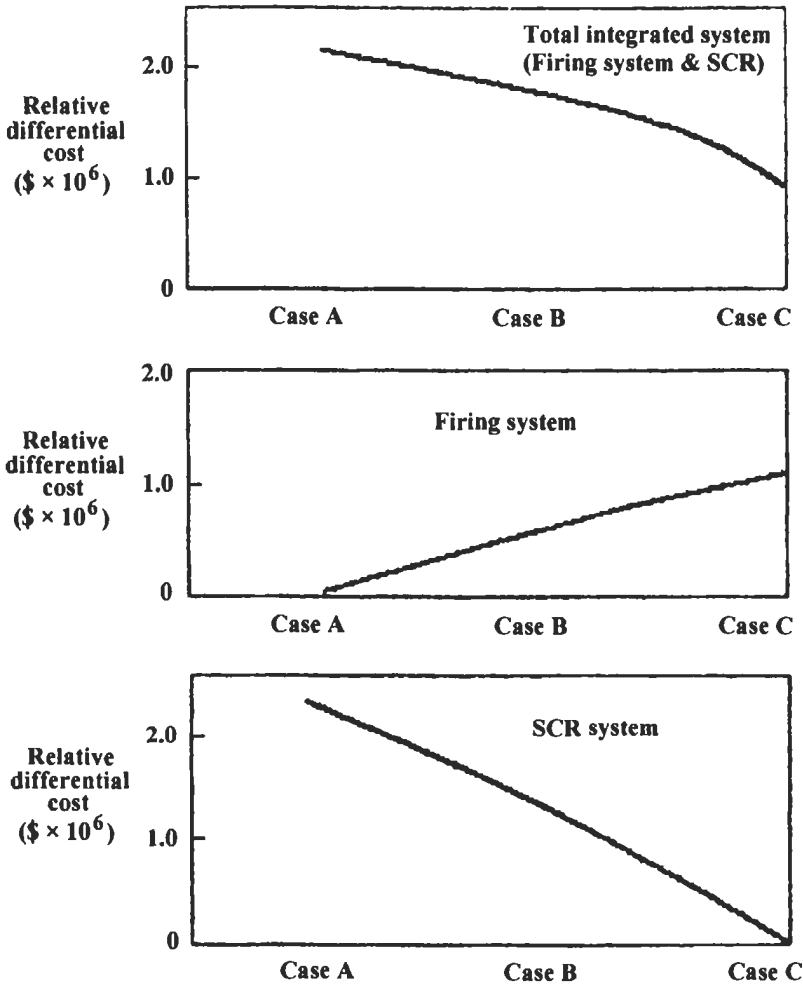


Fig. 5. 144: Differential capital costs [994]. Reproduced by permission of ASME.

more than a twofold increase in relative differential costs. When levelized capital and operating differential costs were compared, case A was more than four times the relative differential cost of case C. (see Fig. 5.145).

In order to obtain the most optimized design, a cost analysis was performed for three new units firing system/SCR combinations. As was shown in the evaluation, maximizing in-furnace techniques provided the most cost effective design approach. The higher NO_x reductions achieved in the furnace allowed for significant decreases in catalyst volume. This is translated to lower SCR operating costs through reduced catalyst replacement, lower power consumption and ammonia usage. Consequently, maximizing in-furnace NO_x reduction within an overall integrated system design proved to be an effective strategy for meeting the NO_x emission requirements of $0.038 \text{ kg } 10^{-6} \text{ kj}$ in a new 400 MWe coal-fired steam generator.

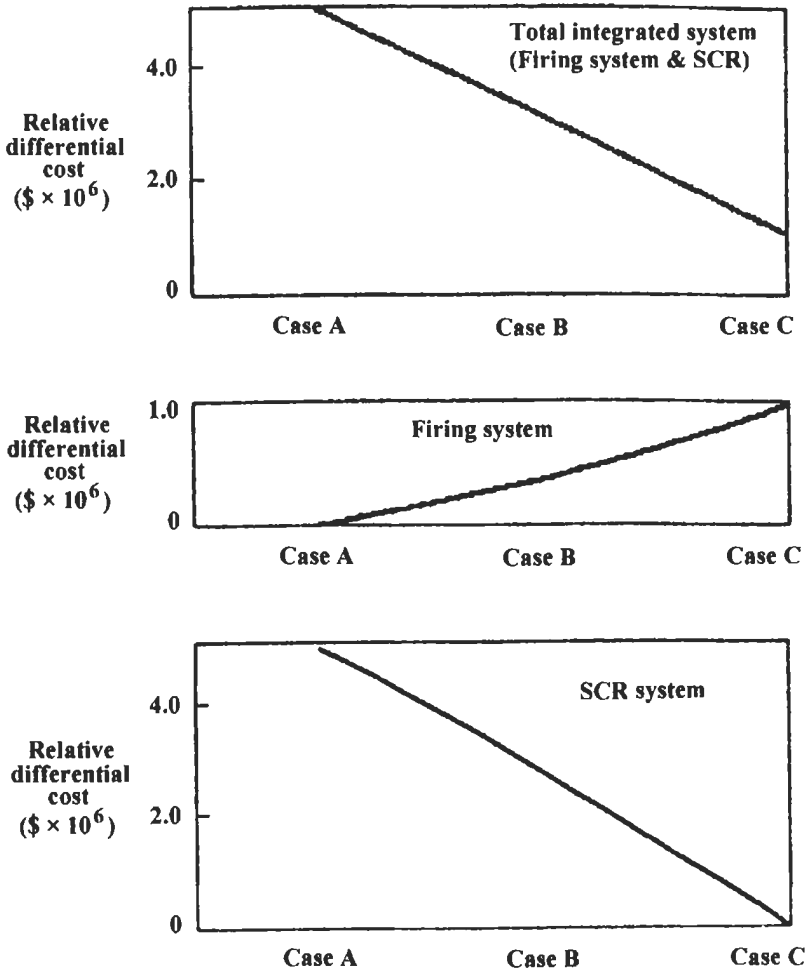


Fig. 5. 145: Levelized differential capital and operating costs [994]. Reproduced by permission of ASME.

5.3 Fluidized-Bed Furnaces (FBFs)

Fluidization is the technique by which beds of particulate solid materials come into contact with upward moving fluids. Under such conditions, the pressure drop through the bed remains substantially unchanged whatever the fluid flow rate. Fluidized-bed combustion is of the concurrent type. It differs from the cyclone furnace in that sulfur is removed during the combustion process. In addition, fluidized-bed combustion occurs at lower temperature, resulting in lower production of NO_x as well as the avoidance of slagging problems with some coals. The use of fluidized bed furnace, with the stages connected to it, has resulted in the development of new types of models. Pilot plants of this type have already been built and are used for scaling-up the studies of their performance.

The fluidized-bed combustor has been under development since the 1950s with the aim of perfecting the process and comparing its reliability and economy with SO_2 post combustion scrubbing. Fluidized beds have been in use for many decades in chemical-industry applications where intimate mixing and contact between reactants are desired. Such contact in fluidized turbulent state enhances heat and mass transfer and reduces time of reaction, plant size, and power requirement. Fluidized-beds have even been proposed for use in nuclear-power reactors. When used for coal, fluidized-bed combustion results in high combustion efficiency and low combustion temperature.

Some of the problems facing the development of fluidized-bed combustors include those that are associated with feeding the coal and limestone into the bed, the control of carbon carry-over with the flue gases, the regeneration or disposal of calcium sulfate, the quenching of combustion by the cooling water within the bed, and variable-load operation. Fluidized-bed combustors may be used with either a conventional steam power plant (Rankine cycle) or a combined gas-steam power plant (Brayton-Rankine) cycle. In the conventional power plant application, the bed can be of the atmospheric or pressurized type. Atmospheric-beds utilize both forced and induced-draft fans. Pressurized-beds use compressors to supply combustion air at pressures of up to 10 bar, which results in slightly higher heat-transfer rates.

A considerable amount of attention has been devoted to a wide range of research work on fluidization [996-1151]. However, coal gasification, in plants and underground gasification, is receiving more attention in some areas where coal is plenty. Moreover, investigations on burning low-grade fuels such as oil shales refused solids, and shredded tires have been carried out around the world, not only on pilot but also on large-scale plants. Burning of solid fuels, still being a complex process, passes through the stages of devolatilization and charring before the char combustion even takes place. The process of combustion itself is affected by number of factors such as particle size, porosity, composition, and, more important, the mechanism of combustion. While the shrinking particle mechanism prevails in case of a certain range of size and type, the shrinking core or the progressive combustion of particle occurs in some different sizes and types. The process of burning solid fuels is sometimes, and at relatively high temperature, suffers the cinder formation. The problem of unreacted particles sometimes occurs in cases of coal particles of large sizes (> 6 mm).

As an example of fluidized-bed combustors, crushed coal, between 6 to 20 mm in maximum, is injected into the bed just above an air-distribution grid in the bottom of the bed as shown in Fig. 5.146. The air flows upwards through the grid from the air plenum

into the bed, which now becomes the furnace where combustion of the mixture takes place. The products of combustion leaving the bed contain a large portion of unburned carbon particles are collected in a cyclone separator, which separates these particles from the gas by imparting a centrifugal acceleration to the mixture. They are then returned back to the fluidized bed to complete their combustion. In the considered example, the boiler water tubes are located in the furnace.

Combustion of liquid fuel involves the stages of heating, evaporation and combustion of a vapor-gas mixture. In this respect, the main reason for incomplete combustion is the degree of mixing of the fuel and the oxidant, which depends on the nature of fuel supply and the basic bed hydrodynamics. The use of gaseous fuel is to simplify the process at starting up and to reduce the quantity of harmful venting to the atmosphere.

Experimental work on fluidized-bed heat transfer has been highly concerned with attempts to develop empirical correlations for the prediction of bed to surface heat transfer coefficient to the surrounding enclosure. Although, the basic mechanisms have been recognized, no adequate fundamental models exist from which reliable bed-to-surface heat transfer coefficients can be predicted, so recourse has to be made to empirical correlations. These correlations disagree widely between themselves over a range of operating conditions and, at best, have only limited accuracy over restricted parts of those ranges. The reason for the deficiency of these correlations are that they have been principally developed from ambient temperature tests with relatively small bed to surface temperature difference so they do not include adequate allowance for the effect of temperature level on thermal properties. Moreover, tests were carried out in small-scale equipment, which had an excessive influence on the bed behavior.

In the following sections, the physical fundamental aspects of fluidized-beds are explained. Section 5.3.1 presents the application of FBF, while section 5.3.2 introduces some details about the phenomenon of fluidization. Section 5.3.3 deals with a background to combustion and emission, and section 5.3.4 presents a background to heat transfer in the fluidized-bed. Furthermore, section 5.3.5 describes some of the computational and experimental results of heat transfer in a rectangular cross-section fluidized-bed model, and section 5.3.6 presents the emission and emission control in FBF.

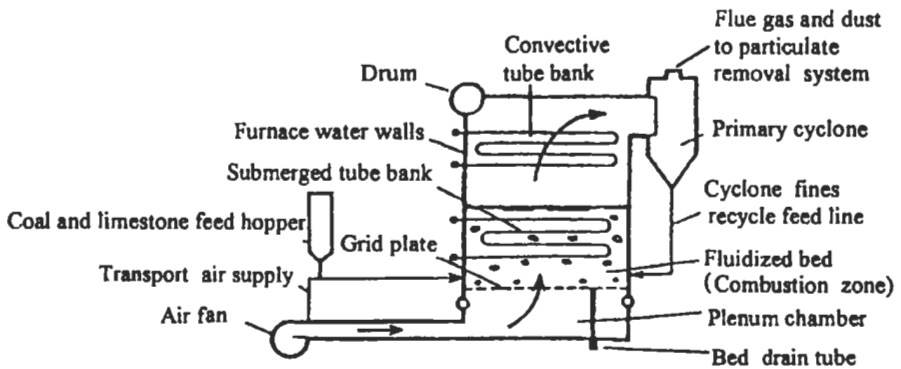


Fig. 5.146: Schematic of a fluidized bed combustion steam generator [6]. Reproduced by permission of Marcel Dekker Inc.

5.3.1 Application of FBC

The simplest use of FBC (fluidized bed combustor), from a thermal point of view, is destruction of low-calorific-value wastes; the combustor may be adiabatic without heat extraction, but the heat in the flue gases may be used for heating or drying. Second in complexity, are combustors with heat recovery, hot water boilers, for example for district heating. The third type of application in degree of complexity is in plants for electric power generation, with sizes ranging from small ($< 100 \text{ MW}_{\text{th}}$) combined heat and power generation plants for district heating systems or for industrial use, to electric-power utility applications with desired sizes of $1000 \text{ MW}_{\text{th}}$ and above ($300\text{-}600 \text{ MW}_e$) [1047].

The power producing FBC is usually an atmospheric pressure CFB (Circulating fluidized-bed) supplying steam to a Rankine cycle. A simplified scheme of such a process is shown in Fig. 5.147 (a). The efficiency of electric power production is further increased in a combined cycle with a pressurized FBC serving as the heat source for both the steam and the gas turbine cycle, Fig. 5.147 (b). The fluidized-bed is cooled by the evaporator and superheater of the steam cycle to the desired temperature of operation, $800\text{-}900 \text{ }^\circ\text{C}$. The bed temperature is limited by the release of alkali metals, which might cause corrosion to downstream turbine components. This problem can be solved; if a part of the fuel is devolatilized in a carbonizer, and the gas produced is burned in the flue gas from the PFBC to raise the temperature of the gas entering the turbine as shown in Fig. 5.147 (c) [1014, 1015]. The Topping cycle [1016] shown in Fig. 5.147 (d) is a proposed arrangement, which is similar to that of Fig. 5.147 (e), but simpler in the sense that an atmospheric pressure CFB burns the more or less devolatilized char. Figure 5.147 (e) shows the biomass fluidized-bed converter in combined cycle. The German High Temperature Winkler (HTW) gasifier operating at 25 bar pressure [1017, 1018], for gasification of brown coal, has some similarities with the biomass gasifier in Fig. 5.147 (e). At the present, most combustors are atmospheric CFBs, and only few commercial PFBCs (Fig. 5.147 (b)) are in operation.

The Stationary fluidized-bed (SFB), non-circulating combustor, Fig. 5.148 (a), (c), was the first method tried for combustion of solid fuels. Depending on the heating value of the fuel, the bed contains heat transfer surfaces to maintain the desired bed temperature around $850 \text{ }^\circ\text{C}$. The bed remains in the bubbling mode of fluidization, supported by the bottom of the combustion chamber through which air for combustion and fluidization is supplied. When more air is supplied per unit of cross-sectional area, the fluidization velocity becomes higher, and a considerable flow of bed material is carried away from the dense bottom bed. The particle suspension fills the entire combustion chamber with a density declining upwards; the bed is circulating, Fig. 5.148 (b), (d). A flow of particles, typically around $10 \text{ kg m}^{-2} \text{ s}^{-1}$, follows the gas out of the combustor and is separated from the gas by a particle separator, usually a cyclone. The SFB and CFB can be applied at atmospheric pressure, Fig. 5.148 (a), (b), as well as at higher pressures, 12-20 bar, Fig. 5.148 (c), and (d). One of the obvious differences between the atmospheric and pressurized combustors is the pressure vessel surrounding the pressurized designs. The walls of the combustion chambers often consist of conventional boiler heat transfer surfaces in the form of membrane-tube panels. Principal designs of FBC with characteristic fluidization velocities, mean particle sizes, and temperatures are shown in Fig. 5.148 (d). In the SFB, heat is not transferred all over the furnace by the bed material as in the CFB, but is only transferred to the walls surrounding the bed and to heat transfer surfaces in the bed itself.

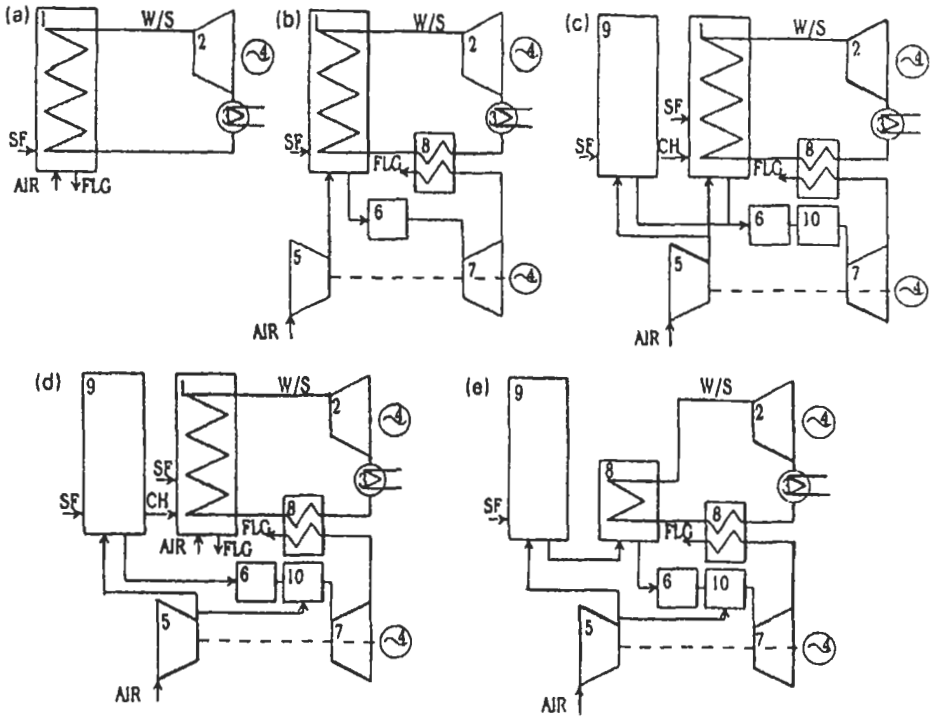


Fig. 5.147: Applications of fluidized-bed combustion. Simplified flow diagrams.

(a) Atmospheric FBC in Rankine cycle. (b) Pressurized FBC in combined cycle. (c) Same as (b) but with afterburning. (d) Topping cycle with atmospheric FBC. (e) Biomass fluidized bed converter in combined cycle. 1- Combustion chamber, 2- Steam turbine, 3- Condenser, 4- Generator, 5- Compressor, 6- Particle Filter, 7- Gas turbine, 8- Heat exchanger, 9- Carbonizer, devolatilizer, and 10- Gas turbine combustor. FLG-Flue gas. W/ S – Water or steam (steam upstream of the turbine and water downstream of the condenser). SF-Solid fuel. CH-Char [1047]. Reproduced by permission of Elsevier Science.

5.3.2 The Phenomenon of Fluidization

Fluidization is a phenomenon which occurs when a system (bed) starts to behave in many respects similar to a liquid due to a reduction of internal friction forces and cohesion. Beyond the point of incipient fluidization two different phenomena may occur. If at higher gas velocities the bed maintains the balance between the average drag forces on the particles by increasing their average interdistance; it is said to be **homogeneous fluidization**. On the other hand this balance may be maintained at increasing gas velocities by creating gas bubbles¹ while leaving the interparticle distance essentially unaffected; this is called **heterogeneous fluidization**.

¹ Gas bubbles are formed close to the gas distributor which grow due to coalescence while they move in upward direction. These gas bubbles look similar to those in a boiling liquid and provoke an intense mixing of the solid particles.

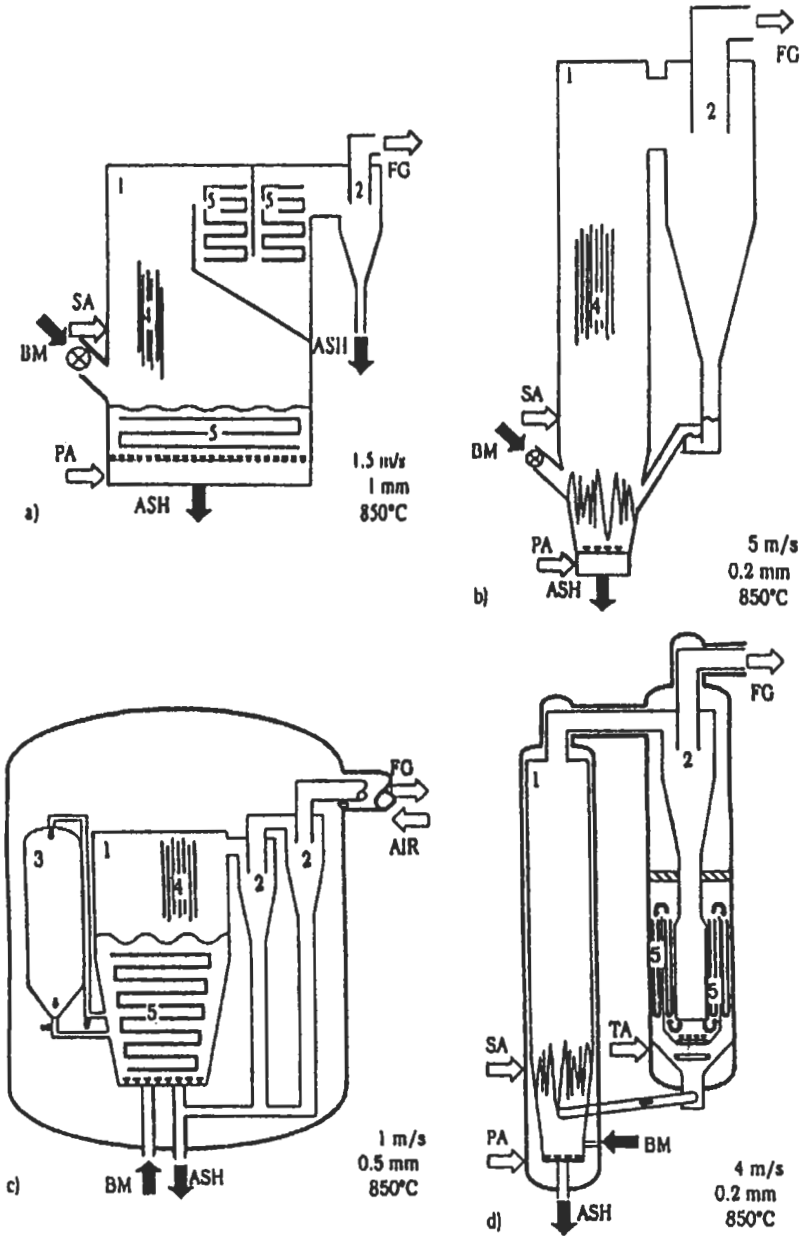


Fig. 5.148: Principal designs of FBC with characteristic fluidization velocities, mean particle sizes and temperature. Atmospheric (a) stationary, (b) circulating FBC. Pressurized (c) stationary and (d) circulating FBC. (The figures are not comparable in size). 1- Combustion chamber, 2- Cyclone, 3- Bed ash vessel, 4- Membrane-tube wall, 5- Heat exchanger tube bundle. BM- Bed material: fuel, sand and limestone. PA-Primary air. SA-Secondary air. TA-Tertiary air. FG-Flue gas. ⇒ Gas flow. → Particle flow. = Water/steam tube. — Wall of pressure vessel [1047]. Reproduced by permission of Elsevier Science.

A bed of particles offers resistance to fluid flow through it. As the velocity of flow increases, the drag force exerted on the particle increases. If the fluid is flowing downward through a bed of particles, it will tend to compact it. If the fluid flow is upwards through the bed, the drag force will tend to cause the particles to rearrange themselves within the bed to offer less resistance to the fluid flow. With further increase in the upward fluid velocity, the expansion continues and a stage will be reached where the drag forces exerted on the particles will be sufficient to support the weight of the particles. In this state, the fluid/particle system begins to behave like a fluid and it will flow under a hydrostatic head. This is the point of *incipient fluidization*.

At the *commencement of fluidization* the bed is more or less uniformly expanded and, up to this point, it makes little difference whether the fluid is a liquid or a gas. If the fluid is a liquid, the bed continues to expand uniformly with increase in the liquid velocity. If the fluid is a gas, the uniform expansion behavior is soon lost except with fine particles (< 0.01 mm), and the system becomes unstable with cavities containing few solids are formed. Over the flow range between incipient fluidization and the onset of bubbling, the bed is in a *quiescent state*. Figure 5.149 shows the behavior of the bed particles with the increase of the fluidizing fluid flow rate.

General Terminology

The terms *incipient fluidization* and *quiescent* are defined in the above section to distinguish between two conditions; first, the point when it begins to exhibit liquid-like properties and second, the point at which bubbles appear. The term *particulate² fluidization* refers to the condition in which the particles are uniformly dispersed within the fluid and the bed expands uniformly. Beyond the quiescent state, when bubbles appear within the bed, the condition is referred to as *aggregative fluidization*.

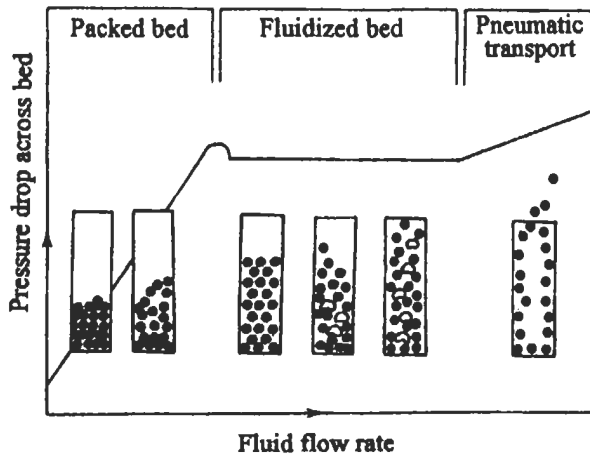


Fig. 5.149: Behavior of the bed particles with the increase of the fluidizing fluid flow rate [1043].

² particulate = Continuous = Dense.

At gas velocities highly exceeding those necessary to fluidize the bed, the bulk of the gas over and above that necessary to fluidize the bed flows as bubbles. Thus, the *bubble³ phase* contains very few particles. The boiling appearance exhibited by a bed in a highly agitated state under the action of a large number of bubbles rising through the bed, has led people to speak of "*turbulent*" fluidized beds.

Gas-fluidized beds of fine irregular particles are inclined to *channeling*. As the fluid flow rate through the bed is increased, instead of the bed expanding uniformly, the fluid opens up channels through the bed. Then, having created a path flow velocity. *Slugging* bed occurs in the case of deep and narrow gas-fluidized beds, where there is a tendency for bubbles to grow and coalesce as they rise through the bed until they occupy the whole cross-sectional area of the bed. The slug of gas rises through the tube carrying particles ahead of it until instability occurs and the solids collapse back to the bed. Bubbling, slugging and channeling may all result in reduced contacting efficiency. Certain crystalline materials with low sphericity will not be fluidized. Nevertheless, they can be handled by *spouted bed* techniques. In this technique the material is entrained in an air jet, which carries it up the center towards the top of the bed where it becomes de-entrained and flows back down the walls of the bed so that a vigorous circulation is maintained [1041]. Figure 5.150 shows the main visual features for each of the different regimes.

Minimum and Maximum Fluidization Velocity

One of the points of interest in the fluidized-bed operation is the possible range of fluidization velocities. For homogeneous fluidization, this range will be situated between the minimum fluidization velocity and the terminal velocity of the particles, because at the latter velocity all particles will be blown out of the vessel. In the intermediate range stable fluidization is possible as explained in the introduction. In heterogeneous fluidization it may be rather difficult to depict the upper velocity limit, especially if a range of particle sizes is presented in the bed. Moreover in some cases, particle entrainment is tolerated or even desired (circulating fluid beds).

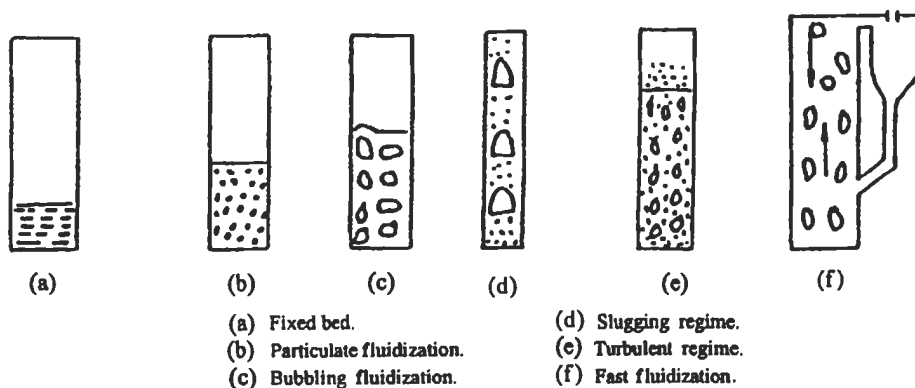


Fig. 5.150: Schematic diagram showing the main visual features for each of different regimes.

³ Bubble = Discontinuous = Lean

a) Minimum fluidization velocity. Figure 5.151 shows a fluidized bed with several pressure taps to illustrate the phenomena of incipient fluidization. The pressure drop across the bed is given in Fig. 5.152 as a function of the superficial velocity. As a pertinent point, the pressure drop across the gas distributor plate is important, as it must assure a regular distribution over the cross section. At incipient fluidization ($U = U_{mf}$), it should be a large fraction of, or be equal to, the pressure drop over the fluidized bed for accurate measurements of U_{mf} . Therefore, such measurements may not be possible in fluidized-beds that are especially designed for much higher velocities, since the pressure drop over the gas distributor plate at U_{mf} could be unacceptably low giving erroneous results.

Empirical expressions are available to give the value of U_{mf} for a particular powder in terms of the physical properties of the solid particles and of the fluidizing gas. They are mostly based on the principle of taking a gas velocity, pressure drop relationship for a packed bed of particles and extending it to the point where the particles become fluidized and the gas velocity through the bed is U_{mf} . Darcy's law gives the velocity of gas moving in laminar flow through a bed of porous material of depth H as:

$$U = C \frac{\Delta P}{H} \tag{5.96}$$

where ΔP is the pressure drop through the bed, and C is the permeability of the medium which are functions of both fluid viscosity and the fraction of voids in the bed. On the assumption that a bed of particles could be considered equivalent to an assembly of parallel cylindrical channels with internal surface and volume equal to the particle surface and pore volume respectively, and by combining Eq. 5.96 with the Hagen- Poiseuille equation

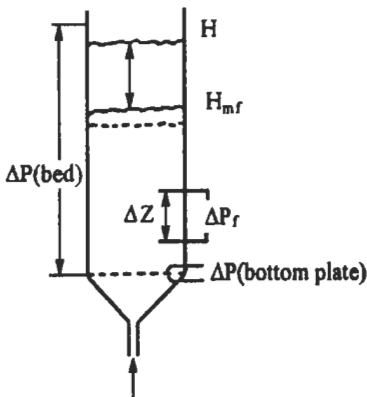


Fig. 5.151: Sketch of a homogeneous fluidized bed with pressure indications [997]. Reproduced by permission of Taylor & Francis Books, Inc.

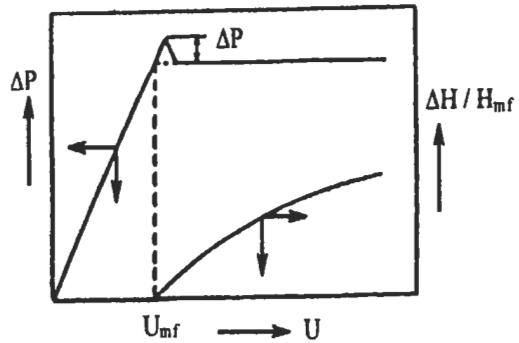


Fig. 5.152: Pressure drop over the homogeneous fluidized bed and relative expansion, both as a function of the superficial velocity [997]. Reproduced by permission of Taylor & Francis Books, Inc.

for laminar flow through cylindrical tubes of diameter, d [996], then the gas velocity is found to be:

$$U = \frac{d^2}{32\mu} \cdot \frac{\Delta P}{H} \quad (5.97)$$

and hence:

$$U = \frac{\gamma^3}{K\mu S^2} \frac{\Delta P}{H} \quad (5.98)$$

where γ is the bed void fraction, μ is the fluid viscosity, S is the particle surface area per unit volume of bed, and K is a constant. Now for spherical particles of diameter d_p :

$$S = \frac{6(1-\gamma)}{d_p} \quad (5.99)$$

and by substituting for S in Eq. 5.98:

$$U = \frac{\gamma^3 d_p^2}{(1-\gamma)^2 36K\mu} \frac{\Delta P}{H} \quad (5.100)$$

Since the pores in real materials are not straight, the actual paths taken by the fluid are sinuous and on the basis of experimental evidence, a proposed value for K of 5 that enables Eq. 5.100 to be written in the following form [996]:

$$U = \frac{\gamma^3}{180(1-\gamma)^2} \frac{d_p^2}{\mu} \frac{\Delta P}{H} \quad (5.101)$$

This equation is known as the Carman-Kozeny equation and it applies to a wide range of conditions in which the fluid flows through porous solids. For beds of non-spherical particles, it is necessary to introduce a sphericity factor Φ defined as:

$$\Phi = \frac{\text{surface area of sphere of volume equal to that of particle}}{\text{surface area of particle}}$$

For perfect spheres, $\Phi = 1$ and for other shapes, $0 < \Phi < 1$. The Carman-Kozeny equation may now be used to obtain an expression for the pressure drop through a vertical bed of particles of height H_{mf} :

$$\frac{\Delta P}{H_{mf}} = \frac{180(1-\gamma)^2 \mu U}{\gamma^3 (\Phi d_p)^2} \quad (5.102)$$

Now, at the point of minimum fluidization the force exerted by the upward flowing fluid is equal to the gravitational force acting on the particles:

$$\frac{\Delta P}{H_{mf}} = (1 - \gamma_{mf})(\rho_p - \rho_g)g \quad (5.103)$$

where γ_{mf} is the void fraction at minimum fluidization, and ρ_p and ρ_g are the densities of particles and gas, respectively. Substituting the appropriate values of voidage and gas velocity in Eq. 5.102 and combining it with Eq. 5.103 gives:

$$(1 - \gamma_{mf})(\rho_p - \rho_g)g = \frac{180(1 - \gamma_{mf})^2}{\gamma_{mf}^3} \frac{\mu U_{mf}}{(\Phi d_p)^2} \quad (5.104)$$

From which the minimum fluidization velocity is found to be;

$$U_{mf} = \frac{\gamma_{mf}^3}{180(1 - \gamma_{mf})} \frac{(\rho_p - \rho_g)(\Phi d_p)^2 g}{\mu} \quad (5.105)$$

The Carman-Kozeny equation is strictly applicable only to conditions of laminar flow, where the pressure drop is due solely to viscous energy losses. With beds of particles greater than about 150 μm in diameter, inertia forces become important and it is then necessary to use the Ergun equation [996] in the determination of U_{mf} :

$$\frac{\Delta P}{H} = \frac{150(1 - \gamma)^2}{\gamma^3} \frac{\mu U_{mf}}{(\Phi d_p)^2} + \frac{1.75(1 - \gamma)\rho_g U_{mf}^2}{\gamma^3 \Phi d_p} \quad (5.106)$$

The first (laminar) term is important for small particles; the second term becomes increasingly important for larger particles. Combining Eqs. 5.103 and 5.106 results in [997]:

$$Ar = \frac{150(1 - \gamma_{mf}) Re_{mf}}{\gamma_{mf}^3} + \frac{1.75}{\gamma_{mf}^3} Re_{mf}^2 \quad (5.107)$$

$$Ar = \frac{\rho_g d_p^3 (\rho_p - \rho_g) g}{\mu^2}, \text{ Archimedes number} \quad (5.108)$$

where $Re_{mf} = \frac{\rho_g U_{mf} d_p}{\mu}$, Reynolds number at incipient fluidization

Wen and Yu [998] found that for a range of particle types and sizes, the following two empirical relationships were valid:

$$\frac{1 - \gamma_{mf}}{\Phi^2 \gamma_{mf}^3} \cong 11 \quad ; \quad \frac{1}{\Phi \gamma_{mf}^3} \cong 14 \quad (5.109)$$

They combined these with the Ergun equation and obtained the generalized correlation:

$$\text{Re}_{mf} = [(33.7)^2 + 0.0408 \text{Ar}]^{1/2} - 33.7 \quad (5.110)$$

For fine particles (<100 μm), this can be further simplified to:

$$U_{mf} = \frac{g d_p^2 \rho_p}{1650 \mu} \quad (5.111)$$

The particle diameter can be approximated by:

$$d_p = 1 / \sum_i (X_i / d_{p,i}) \quad (5.112)$$

where X_i is the weight fraction of particles with diameter of approximately $d_{p,i}$, and

$$d_{p,i} = [d_{p,i}(\text{max}) + d_{p,i}(\text{min})] / 2 \quad (5.113)$$

or if particles are non spherical

$$d_p = 1 / \sum_i (X_i / \Phi_i d_{p,i}) \quad (5.114)$$

b) Maximum fluidization velocity. If the maximum fluidization velocity is limited by the terminal velocity of the particles, its value easily follows the drag force equation:

$$C_D (0.5 \rho_g U_{\text{max}}^2) (0.25 \pi d_p^2) = 0.1667 \pi d_p^3 g (\rho_p - \rho_g) \quad (5.115)$$

$$\text{and } U_{\text{max}} = \frac{8}{6} \left[\frac{d_p (\rho_p - \rho_g) g}{C_D \rho_g} \right]^{0.5} \quad (5.116)$$

where C_D is the drag coefficient for a sphere, which is a well-known function of the Reynolds number as shown in Fig. 5.153.

At very low Reynolds numbers, the Stokes law presents the theoretical solution for the drag force, F_d on a smooth rigid sphere; where:

$$F_d = 3 \pi \mu U d_p \quad (5.117)$$

and with the definition equation of the drag force on a sphere [997],

$$F_d = C_D (0.5 \rho_g U^2) (0.25 \pi d_p^2) \quad (5.118)$$

this results in: $C_D = 24/\text{Re}$

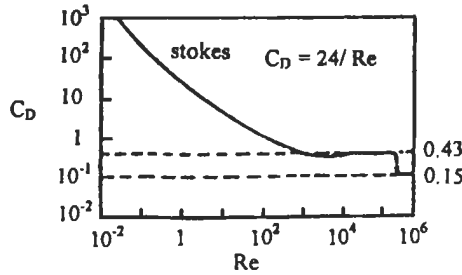


Fig. 5.153: Drag coefficient as a function of the Reynolds number [1997]. Reproduced by permission of Taylor & Francis Books, Inc.

At very high Reynolds numbers, the drag coefficient becomes constant:

$$C_D = 0.44 \quad \text{for } 10^4 < Re < 2 \times 10^5$$

Particle Characterization

Geldart [1054] has classified the behavior of solid particles fluidized by gases into four main groups: A, B, C, and D as shown in Fig. 5.154. The figure summarizes Geldart’s classification. Group A consists of materials having a small mean size and/or a low particle density. Beds of powders in this group expand considerably before bubbling commences and all bubbles rise faster than the interstitial gas. Cracking catalysts are typical examples of this group of solids. Group B contains materials in the mean size range of 40 to 500 μm and density, ρ_p, greater than 1400 kg m⁻³. There is no appreciable bed expansion before bubbling commences and most bubbles rise more quickly than the interstitial gas. Powders that are cohesive and consequently very difficult to fluidize belong to group C. Group D consists of large and dense particles. The largest bubbles rise more slowly than the interstitial gas, so that gas flows into the base of the bubble and out of the top. The gas velocity in the dense phase of the bed is high and the flow regime around the particles may be turbulent. Group D powders are also capable of forming a stable spout.

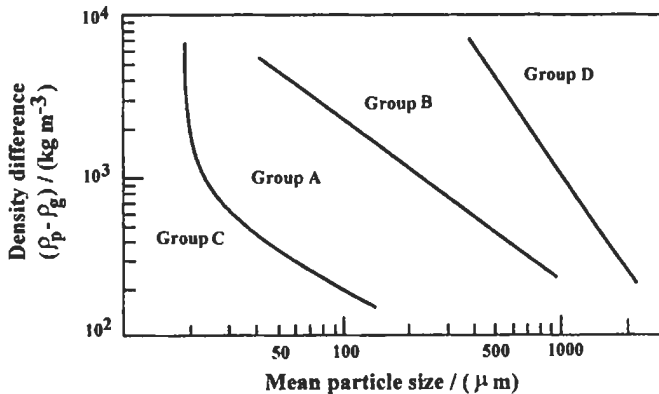


Fig. 5. 154: Powder classification diagram for fluidization by air at ambient conditions [1997]. Reproduced by permission of Taylor & Francis Books, Inc.

Packed Beds

A bed of particles sitting stationary on a perforated grid through which a gas is passing is generally referred to as a fixed or packed-bed. In moving packed beds, the solids move with respect to the walls of the column. In either case the particles do not move relative to each other. As the gas flows through the solids, it exerts a drag force on the particles, causing a pressure drop across the bed.

If the gas flow rate through the fixed bed is increased, the pressure drop continues to increase, until the superficial gas velocity reaches a critical value known as the minimum fluidization velocity, U_{mf} . This is defined as the velocity at which the fluid drag is equal to the weight of particles minus its buoyancy, and the fixed bed transforms into an incipient fluidized-bed. In this regime the body of solids behaves like a liquid, since the pressure drop across the bed equals to the weight of the bed.

Bubbling Bed

Bubbles in fluidized beds behave in many different ways. To examine the causes of fluidization nonuniformity, Trawinski [999] took into consideration the frictional forces between particles. Starting with the concept that bubbles appear in the bed as soon as the fluid velocity is high enough to cause the interparticle forces-the surface friction forces-to hinder the uniform expansion of the bed, and the required quantity of fluidizing medium can no longer pass through the interstices between the particles. In Trawinski's opinion, bubbles have a stable shell of particles and float in the fluidized bed flowing past this shell, just as in a viscous liquid; the bubbles move under the action of Archimedean forces and obey Stokes's law. According to Trawinski, the bubble dimensions are determined by the residence time at the point of formation (on the gas-distributing grid), which in turn depends on the friction forces that must be overcome when the bubble separates from the grid. The excess static pressure (according to Bernoulli's law) inside the bubble causes it to expand as long as it remains on the grid and is fed through the grid openings. The bubbles break away when they acquire sufficient buoyancy to overcome the friction between the particles.

Harrison and Leung [1000] suggested that bubbles above a certain size would be destroyed by the entrainment of solids from the wake under the action of internal gas circulation within the bubble. Rietema [1001] has reported that the average density of the dense phase will increase for beds of finer material as the superficial gas velocity is increased above the bubble point and that the density of the dense phase increases with height above the distributor. He suggested that this was because bubbles, when once formed, increase in size by draining gas from the expanded continuous phase as they rise through the bed. Since the rise velocity of bubbles is much greater than the superficial gas velocity, when working with beds of finer particles, the total gas hold up is decreased and the bed height therefore drops.

Grace and Venta [1002] found that there was a growth when two bubbles coalesced and then, after the resultant enlarged bubble had reached its final shape, it would tend to shrink by about 15% of its maximum size. When a bubble was observed to split, there was a decrease in the size of the two formed as compared with that of the original. The random initial particle distribution, the nonuniformity of the flow around the particles, and the growth and rise of bubbles cause a random and pulsating motion of the particles in a fluidized-bed and an intensive mixing of the particles. Rowe [1003] assumed that

the presence of bubbles in gas-fluidized bed imports a high degree of order to the motion of the gas and solids.

Recently, Campos et al [1072] have described the mass transfer between the bubble and dense phases in a fluidized-bed, used as a coke combustor. The experimental technique allowed quantification of the mass transfer rate during bubble formation and during a bubble's rise through the bed. The combustion experiments were performed at 1 atm and 1223 K, in a fluidized-bed (diameter of 120 mm) of sand (average diameter 325 μm) with static heights of 0.1-0.21 m. The bubbling flow rate ranged from 2.5 to 5 times that at incipient fluidization. The coke particles were 3 or 3.5 mm in diameter. Results indicate that the equivalent bed height, L_{eq} is independent of the bubbling air flow rate. The mean value $L_{eq} = 50$ mm suggests that for shallow beds the mass transferred during bubble formation is a significant part of the total mass transferred. The measured mass transfer factor between phases during a bubble's rise is independent of the bubbling air flow rate and substantially lower than the theoretical predictions of Kunii and Levenspiel [1073]. This disagreement is explained by the fact that the theoretical model is for an isolated bubble and does not account for the strong interaction between consecutive bubbles: this increases the bubble velocity and induces their coalescence, leading to a decrease in mass transferred between phases.

Bubble rise velocity. The rise velocity, U_B , of gas bubbles in fluid beds is an important parameter in the design of processes that depend on gas-solid contact. If U_B is much greater than the minimum fluidization velocity, gas bypassing can occur and be a serious problem; if on the other hand $U_B < U_{mf}$ gas-particle contact can be good. Calculation of U_B for a given type of bed material and gas flow rate is therefore essential. However, the problem is quite complicated particularly when freely bubbling beds are concerned, and it is doubtful whether there is any generally agreed procedure. For single bubbles of gas rising in beds of liquids of low viscosity, it was [996] shown experimentally that:

$$U_B = 0.711\sqrt{gd_B} \quad (5.119)$$

where d_B is the diameter of the sphere with the same volume as the bubble. It was first suggested by Davidson and Harrison [1004] that this equation may also be applied to single bubbles of gas rising in fluidized-beds, and the proposal has gained a wide measure of acceptance. In freely bubbling beds, however, bubbles undergo coalescence as they rise through the bed, a process which involves the acceleration of a trailing bubble velocity being higher than that given by Davies-Taylor equation. Davidson and Harrison [1004] also proposed on theoretical grounds that the average velocity of a bubble in a swarm should be given by the natural rising velocity of an isolated bubble plus the upward velocity of the particulate phase between the bubbles:

$$\bar{U}_B = (U - U_{mf}) + 0.711(gd_B)^{0.5} \quad (5.120)$$

Although the validity of this equation is doubtful [1005], it is widely used in reactor design calculation [1006].

A mechanistic model of bubble coalescence was proposed by Darton et al [1007], which leads to an equation predicting bubble diameter, closely similar to those resulting from empirical studies. The model is based on the assumption that bubbles tend to rise

in vertical streams from the distributor but the lateral movement occurs during coalescence between neighboring streams, the distance traveled by two bubbles before coalescence being proportional to their horizontal separation (Figure 5.155). From the work of Harrison and Leung [1008], the average separation between bubbles is taken to be twice the radius of the spherical region enclosing the bubble and its wake. Assuming the two-phase theory to apply, the variation of bubble diameter with height is then calculated to be:

$$d_B = \frac{0.54(U - U_{mf})^{0.4} (h + 4\sqrt{A_0})^{0.8}}{g^{0.2}} \quad (5.121)$$

where d_B is the diameter of the sphere with the same volume as that of the bubble, h is the height above the distributor, g is the acceleration due to gravity, and A_0 is the so-called "catchment area" which is taken to be the area of distributor per orifice; A_0 is considered to be zero for a porous plate distributor. The units in Eq. 5.121 are SI. Although this is a mechanistic model, the expression for d_B contains an empirical constant, 0.54, derived from the work of Werther [1009] and Rowe and Everett [1010] but the agreement that produces with a wide range of experimental observations is nevertheless quite good.

Concerning mass transfer from the bubble to dense phase, a great amount of theoretical and experimental work has been undertaken, the latter using either tracer techniques or promoting catalytic reactions. To overcome the complexity of mass transfer and experimentation, Sit and Grace [1011] have studied the interphase transfer rate from isolated bubbles rising in an incipiently fluidized bed.

Slugging

For a given bed, the size of the bubble increases, as the fluidizing velocity or the bed height is increased. If the bed is small in cross section and deep, the bubble may increase to a size comparable to the diameter or width of the bed. In this case the bubble passes through the bed, this phenomenon is known as slugging. A necessary condition for the formation of slugs is that the maximum stable bubble size must be greater than 0.6 times the diameter of the bed [1011]. Slugging does not occur in all beds. The pressure drop across the bed fluctuates rapidly. The transition from the bubbling to turbulent bed does not take place suddenly. The transition appears to start at the upper surface of the bed and then moves downwards. There is no general correlation for the calculation of the velocity of transition from the bubbling to the turbulent bed.

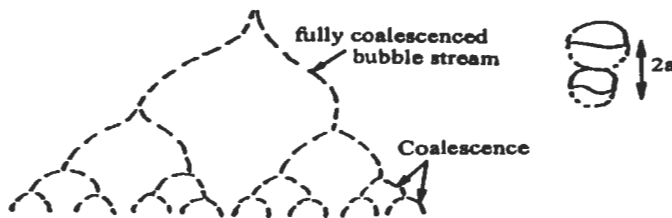


Fig. 5.155: Bubble paths during coalescence. The process should be visualized in three dimensions [996].

Bed Expansion

A packed bed expands as the upward fluid velocity through it is increased. Beyond the point of fluidization, further expansion is very dependent on particles size and particle size distribution, the design of the bed structures, and particularly on the design of the distributor.

Godard and Richardson [1012] have published results illustrating the expansion behavior of fine materials fluidized at pressures between 1 and 14 atmospheres where no bubbles tend to form. The behavior, in this case, is similar to that of liquid/solid systems where the voidage, γ , can be related to the superficial velocity, U_f and a coefficient U_i in the following form, Jottrand [1013].

$$\frac{U_f}{U_i} = \gamma^n \quad (5.122)$$

However, for the gas fluidized-system, U_i is generally in excess of the terminal falling velocity for the particle in the fluid and the index, n , is somewhat higher than that predicted for the fluidization of uniform spheres in a liquid.

For the bubble rise velocity given by the Davies Taylor relationship (Eq. 5.119) and for an isolated bubble, and with the assumption of that there will be no gas "short circuiting" through chains of bubbles nor interaction between bubbles in swarms, then the contribution of bubble flow to overall bed expansion may be allowed for, in terms of the bubble residence time within the bed, as:

$$\frac{H}{H - H_{mf}} = \frac{0.71}{U - U_{mf}} g^{0.5} V_B^{1/6} \quad (5.123)$$

where H is the height of the fluidized-bed at the superficial gas velocity U , H_{mf} is the bed height under minimum fluidizing conditions, V_B is the bubble volume, and U_{mf} is the gas velocity at minimum fluidization.

For a slugging bed, the bubble rise velocity will be less than that given by the Davies Taylor equation and bed expansion will be correspondingly increased. Matsen [1019] has shown that the maximum height of a slugging bed is given by:

$$\frac{H_{max}}{H_{mf}} = 1 + \frac{U - U_{mf}}{U_B} \quad (5.124)$$

where U_B is the modified rise velocity for the slugging conditions, which is given by:

$$U_B = 0.35 (g d_B)^{1/2} \quad (5.125)$$

The *two-phase theory* was proposed originally by Twoomy and Johnstone [1020], and it states that all gases in excess of that necessary to just fluidize the bed pass through in the form of bubbles. Thus, if Q_T is the total volumetric flow rate into the bed, Q_{mf} is the minimum fluidization flow rate and Q_B is the bubble flow rate, then:

$$Q_T = Q_B + Q_{mf} \quad (5.126)$$

In terms of the superficial velocities U and U_{mf} , and dividing through by the bed area, A , then:

$$\frac{Q_B}{A} = U - U_{mf} \quad (5.127)$$

In recent years, however, a large number of experimental studies have been reported in which the flow of bubble gas in freely bubbling beds has been measured, and the general conclusion drawn has been that; in the majority of systems, the two-phase theory overestimates the visible bubble flow, in some cases by a considerable amount; for a review see Twoomy and Johnstone [1021]. In other words, in these systems a large quantity of gas flows through the emulsion-phase than is predicted by the theory. It has been suggested, therefore, that Eq. 5.127 can be put in the following form:

$$\frac{Q_B}{A} = U - U_{mf}(1 - nf_0) \quad (5.128)$$

where n is a positive number and f_0 is the volume fraction of bed occupied by bubbles. In the "ideal" two-phase theory of course, $n = 0$, and the larger n becomes the larger is the emulsion-phase flow and the greater is the departure from ideality.

In order to obtain n , Lockett et al [1022] showed theoretically that for idealized circular (two-dimensional) and spherical (three-dimensional) bubbles, the values of n are 1 and 2, respectively. Their treatment was based on the concept of a bubble acting as a low-resistance short circuit for interstitial gas with the through-flow gas velocity being respectively $2 U_{mf}$ and $3 U_{mf}$ in the circular and spherical bubbles. The gas through-flow idea was also used by Grace and Harrison [1023] who found a value of $n = 4.3$ in an experimental study of 274 μm particles of magnesite in a two-dimensional bed. Grace and Cliff [1024] have shown that the measured deviations from the ideal two-phase theory vary over a wide range and that the value of n not only differs from one system to another but, that within a given system, it can also vary with bed height and gas velocity.

Distributor (or Grid) Design

Experience shows that the distributor must fulfill the following functions to achieve successful application of a required gas-fluidized bed process;

1. Distribute gas uniformly over the cross-sectional area of the bed.
2. Prevent or minimize backflow of solid particles through it into the wind box below.
3. Support the weight of the solids during periods when the bed is shut down.
4. Resist thermal stresses, corrosion, erosion, and blockage.
5. Give minimum pressure drop sufficient to achieve equal flow through the openings.

Figure 5.156 displays some common examples of grids and distributors. A flat perforated plate or wire mesh (type a), is commonly used for laboratory scale operations. A single dished perforated plate (type b) is used to withstand well heavy loads and thermal stresses in large-diameter beds. Two staggered perforated plates (type c) retain the advantages of single plate-ease of design and construction with good

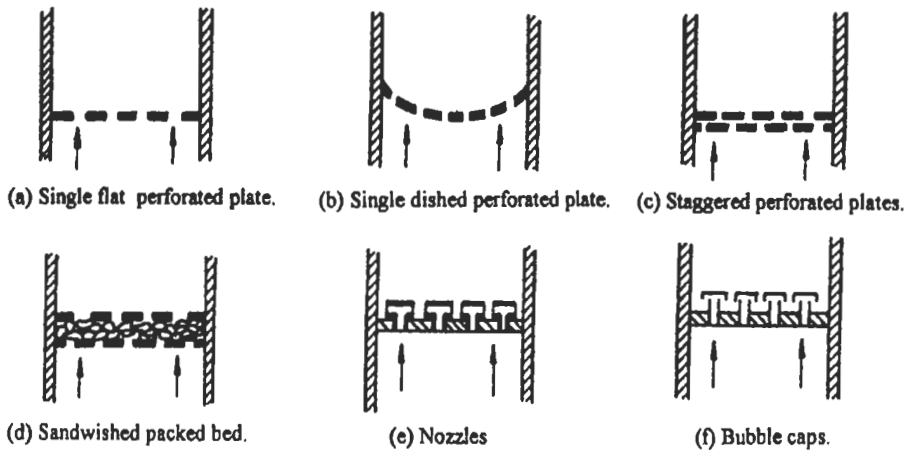


Fig. 5.156: Types of grids and distributors [1024].

gas distribution; while countering the fall of fine particles through the orifices when the bed is shut down. Type (d), a packed bed of granular material sandwiched by two perforated plates, is a good distributor. Nozzles (type e) and bubble caps (type f) have been used to prevent solids from falling through the distributor.

5.3.3 Combustion in FBF

The fluidized-bed combustion techniques have been refined and expanded through numerous scientific and engineering investigations, both experimental and theoretical. At present, a copious number of mathematical and experimental results is available. Because of the nature of fluidized-bed reactors, the combustion of gaseous and liquid fuels is not as popular as the combustion of solid fuels; coal for instance. Therefore, and to satisfy the interest of majority of researchers and designers, some light will be focused on the combustion of coal in fluidized-beds, before going deep inside the subject of heat transfer in fluidized-bed combustors. Table 5.15 shows the comparison of principal gas-solid contacting combustion processes [1055].

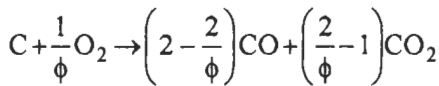
Dealing with coal, the combustion of carbon particle is the cornerstone of the whole subject. Several mathematical models and empirical formulae have been made available to date to express the rate of carbon combustion. Kool [1025] arrived at a simplified expression describing the overall rate of char combustion by adopting a shrinking particle model with constant particle density. For different types of coal combustion; progressive conversion model has been dealt with by many investigators, e.g., Prins and Van Swaaij [1026], and Levenspiel [1027]. However, and after being subjected to combustion in the bed for quite sometime, coal particles are found partly burned. This was interpreted by the fact that some types of coal, and for some larger particles, are burned according to the shrinking core mode of combustion. Wen and Ishida [1028] argued, after extensive studies of numerous systems, that the shrinking unreacted core model describes the combustion of coal particles with air more satisfactorily than any other model. Abdel-Hafez in his work [1029] reported that the experimental investigation has shown that, shrinking unreacted core of particle is applicable in

Table 5.15: Comparison of principal gas-solid contacting combustion process. Grase, J. R. (1986). Canadian J. Chem. Eng., 64, p. 353. Reproduced by permission of Canadian Journal of Chemical Engineering.

Property	Packed Bed	Fluidized Bed	Fast Bed	Pneumatic Transport
Application in boilers	Stoker fired	Bubbling fluidized	Circulating fluidized	Pulverized coal fired
Mean particle diameter (mm)	<300	0.03-3	0.05-0.5	0.02-0.08
Gas velocity through combustor zone (m/s)	1-3	0.5-3	3-12	15-30
Typical U/U_t	0.01	0.3	2	40
Gas motion	Up	Up	Up	Up
Gas mixing	Near plug flow	Complex two phases	Dispersed plug flow	Near plug flow
Solids motion	Static	Up & down	Mostly up, some down	Up
Solid-solids mixing	Negligible	Usually near perfect mixing	Near perfect mixing	Near plug flow
Overall voidage	0.4-0.5	0.5-0.85	0.85-0.99	0.98-0.998
Temperature gradient	Large	Very small	Small	May be significant
Typical bed-to-surface heat transfer coefficient, (W/m^2K)	50-150	200-550	100-250	50-100
Attrition	Little	Some	Some	Considerable
Agglomeration	Considerable	Some	No problem	No problem

case of burning bituminous coal of particle size $D > 3$ mm. He also reported that the well-known fragmentation of anthracite during burning makes the shrinking core model inapplicable to this type of coal.

For any of the investigators to derive an overall reaction rate for core combustion, every resistance regarding every reaction step must be taken into consideration. Moreover, the effective chemical reaction that takes place at the particle core surface is generally described by the reaction:



where the mechanism factor, ϕ , takes values between 1 and 2. The results of Ross and Davidson [1030] confirmed that ϕ takes the value 1 for large particles and approaches 2 for small particles ($D < 1$ mm). They also showed an agreement with the suggested expression of Wen and Dutta [1031] regarding ϕ for different particle size diameters.

The applicability of the shrinking core models is, in general, found to increase for larger diameters and higher bed temperatures. The latter may be attributed to the argument that the impurities in the ash such as calcium and potassium are molten at elevated temperatures, resulting in ash sintering and hence poor diffusion of oxygen into the core.

Prediction of carbon loss required special char combustion kinetics valid through the very high conversion targeted in industry (typically $> 99.5\%$), and valid for a wide range of particle temperature histories occurring in full-scale furnaces. Therefore, Hurt et al [1057] have presented high-temperature kinetics data for five coal chars in the form of time-resolved burning profiles that include the late stages of combustion. Their work [1057] describes the development and validation of the Carbon Burnout Kinetic Model (CBK), a coal-general kinetics package that is specifically designed to predict the total extent of carbon burnout and ultimate fly ash carbon content for prescribed temperature/oxygen histories typical of pulverized coal combustion systems. The model combined the single-film treatment of char oxidation with quantitative descriptions of thermal annealing, statistical kinetics, statistical densities, and ash inhibition in the late stages of combustion. In agreement with experimental observations, the CBK model predicts (1) low reactivities for unburned carbon residues extracted from commercial ash samples, (2) reactivity loss in the late stages of laboratory combustion, (3) the observed sensitivity of char reactivity to high-temperature heat treatment on seconds and subseconds time scales, and (4) the global reaction inhibition by mineral matter in the late stages of combustion observed in single-particle imaging studies. The model ascribes these various char deactivation phenomena to the combined effects of thermal annealing, ash inhibition, and the preferential consumption of more reactive particles, the relative contributions of which vary greatly with combustion conditions. The success of their approach [1057] (Fig. 5.157) suggests that annealing kinetics is similar for different types of chars. In addition, attempts to broaden the database in Fig. 5.157 to include other carbon types led to wide variability about the predictive curve. Much more work is needed to understand and accurately describe annealing kinetics under all conditions for a wide variety of parent materials.

Furthermore, Ilic et al [1062] have developed a mathematical model to describe the dynamic behavior of a porous char particle during combustion in a fluidized-bed. The model of the char particle involves two exothermic reactions: $C + O_2 = x CO + y CO_2$ -heterogeneous reaction on the internal and external char particle surfaces, and $CO + O = CO_2$ -heterogeneous reaction inside the char particle. The temperature and gas concentration fields inside the char particle are defined by partial differential equations of heat and mass balance. Changes of internal surface area and porosity during combustion are included in the mathematical model. The mathematical model results were compared with experiments done in a laboratory fluidized-bed reactor, with three

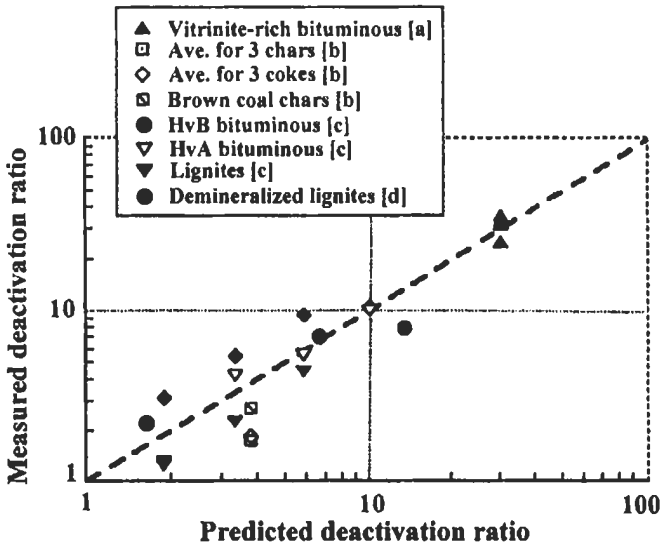


Fig. 5.157: Comparison of predicted deactivation factors with measured values from the literature for a variety of char types and heat treatment conditions [1057]. Data sources: (a) Beeley et al [1058]; (b) McCarthy [1059]; (c) Jenkins et al [1060]; (d) Radovic et al [1061]. Reproduced by permission of Elsevier Science.

types of coal chars of 5.1 and 15 mm. The bed temperature was in the range 500- 700 °C, as the oxidation of CO in the bed out of char particles could be ignored. Their results show the change of burning rates of the char particles depending on temperature and coal types. Over analysis of the burning rate profiles, the different combustion regimes were detected. Correspondence between the burning rate profiles, obtained by measurements of flue gas concentrations, and the calculated profiles of the unreacted carbon within the char particle showed that the model successively followed the burning rate and combustion regime changes with the bed temperature and coal type.

The experimental fluidized-bed reactor that has been used by Ilic et al [1062] is shown in Fig. 5.158. Three Serbian coals were chosen: anthracite Vrska Cuka, brown coal Aleksinac and lignite Kolubara. Prior to the experiments in the fluidized-bed, chars were prepared by heating up at 900 °C in a laboratory oven in inert atmosphere. Then the char particles were cooled and preserved from getting wet. Proximate and ultimate analysis, and some physical properties of the char particles are given in Table 5.16 (see also chapter 1). The dry and cold, having room temperature, char particles were introduced into the hot fluidized-bed reactor. With a thermocouple in the bed and a gas sample probe above the bed, the bed temperature and gas concentrations of O₂, CO and CO₂ were continuously measured during the experiments. Bed temperatures were chosen to avoid intensive oxidation of CO in the bed, that is; the bed temperature was in the range between 500 and 700 °C. Inert material of the fluidized-bed was silica sand with the mean particle diameter of 0.5 mm, while the bed height was 80 mm. Fluidizing velocity was in the range 0.46-0.53 m s⁻¹ for all of the experiments. Using burning rate profiles, one can detect the combustion regime of char particles. Figure 5.159 shows the changes of burning rate profiles with reaction temperature and burning particle size

Table 5.16: Proximate and ultimate analysis of the investigated chars. Malden et al [1062], reproduced by permission.

	Kolubara lignite	Aleksinac brown coal	Vrska Cuka anthracite
Proximate:			
Ash (%)	25.7	21.8	7.4
C _{fix} (%)	74.3	78.2	92.6
Volatile (%)	0	0	0
Heating value (Mj/kg)	23.7	24.3	30.5
Ultimate:			
C (%)	68.4	68.2	89.0
H (%)	1.0	1.2	1.4
N (%)	0.3	0.5	0.4
O (%)	4.6	8.3	1.8

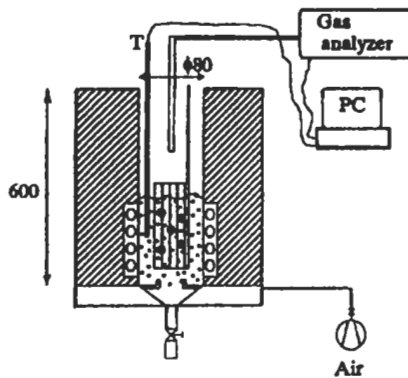


Fig. 5.158: Experimental setup for char combustion investigation in fluidized bed. (Dimensions in mm). Malden et al [1062], reproduced by permission..

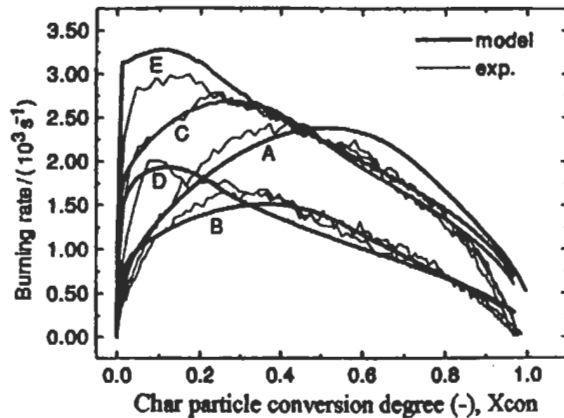


Fig. 5.159: Burning rate profiles for the Aleksinac brown coal char for different bed temperatures and char particle sizes, experimental and model results; T_b = 500 °C: A- d = 5mm , B- d = 10 mm; T_b = 600 °C: C- d = 5 mm, D- d = 10 mm; T_b = 700 °C : E- d = 5mm. Malden et al [1062], reproduced by permission.

of chars for the Aleksinac brown coal. As the reaction temperature increases, the moment of the maximum burning rate shifts toward the initial period of combustion, and the maximum burning rate increases. In addition, a similar shift of the moment of the maximum burning rate is for increasing particle diameter, but in that case the maximum burning rate decreases. These characteristics were detected by measurement during the experiments and predicted with the mathematical model also.

Currently, combustion of wastes was regarded in the first place as a means of destroying wastes, and only in the second place as an energy source. As a consequence to the oil crisis, thermal energy began to be produced (in paper and wood industries) on a large scale from wood wastes. In a first step, this was achieved by adapting existing industrial boilers such as Metalica, Manotehnica and CTFI to biomass combustion. Later, several new types of biomass-fired boilers appeared with better performance. These boilers, with capacities varying from 0.694 to 1.806 kg s⁻¹ steam, still had low efficiencies and high pollutant emissions [1063]. The next step was the design of a 2.778 kg s⁻¹ fluidized-bed steam boiler, burning sunflower shells. This type of boiler equipped most oil factories and was also used for burning lignite resulted from wood processing [1064]. Based on this potential and on the interest shown by industrial units, researches continued at ICPET Cercetare (in Romania) to develop a more efficient and environmental friendly technology. Experiments were made both on a laboratory scale facility and on a 1 MW_t circulating fluidized-bed combustion (CFBC) pilot plant [1065].

A 1 MW_t CFBC pilot plant is shown in Fig. 5.160 – the first CFBC plant built in Romania. It was originally designed for lignite with heating value higher than 5000 kJ kg⁻¹ and size range of 0 - 10 mm, or oil shales with 3800 kJ kg⁻¹ and 7 %

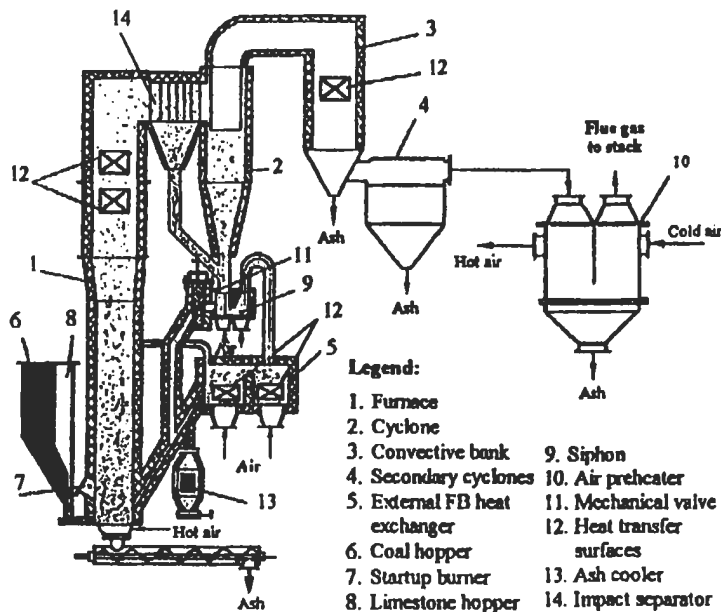


Fig. 5. 160: The 1 MW_t CFBC pilot plant. Reproduced by permission of Dragos Liviu [1065], ICPET CERCETARE ROMANIA.

fuel oil support [1066]. The main components for the 1 MW_t CFBC pilot plant are; Furnace, cyclone, loop seal, external fluidized bed heat exchanger (FBHE), convective pass, and air preheater. The combustion takes place in the furnace, both in the dense bed from the bottom and above it, where the particle density is lower. The start-up of the plant is achieved by means of a fuel oil burner that warms the fluidized-bed up to the solid fuel ignition temperature, when the combustion process is initiated. Two water circuits ensure the cooling of the plant. The main cooling circuit consists of heat transfer surfaces located in the fluidized-bed ash cooler, the furnace and the convective channel. The secondary circuit cools the ash screw conveyer and the fixed bed ash cooler. The solid fuel is introduced into the fluidized-bed by means of screw conveyers. During the fluidizing process, fuel particles are mixed with recirculated ash particles, and burnt as they are elutriated in the upper part of the furnace. The test rig is equipped with a tangentially entry single cell cyclone, where the coal and ash particles are centrifugally separated from the flue gas and fall through a dust into the siphon. The hot flue gases are evacuated at the upper part through a 90° turn and sent in the convective pass. Preparations have been made for biomass combustion on the 1 MW_t circulating fluidized-bed combustion (CFBC) pilot plant. Several feeding solutions have been tried, and for wood chips, sawdust and low bulk density materials, the most suitable proved to be a screw conveyer fitted with a system of fixed and rotating blades having the purpose of preventing fuel from arching. Bed material was consisted of ash from lignite combustion, with particle size under 2 mm. The packed ash bed had a height of 0.6 m. The feeding system worked much better with sawdust, and this allowed to achieve higher temperatures in the upper furnace and the recirculation loop. Oxygen content in flue gas was 4 %, but with very high carbon monoxide emissions. Other problems were encountered during the tests with sorghum waste, since its structure made it very difficult to mill and feed [1068]. Because of its very low density, it was immediately carried in the upper zone of the furnace, with no time to burn completely. In order to reduce the velocity in the lower part of the furnace, fluidizing airflow was reduced to a minimum, but this has led to the reduction of thermal load down to 40 %. As it can be seen in Fig. 5.161, temperatures were very low in the furnace, so the volatile matters practically stayed less than two seconds in the high temperature zone.

Furthermore, a fluidized-bed combustor pilot plant is designed and constructed by Shamsuddin and Sopian [1068] at the Combustion Research Laboratory, Universiti Kebangsaan Malaysia. The combustor is made up of 0.6 m x 0.9 m rectangular bed filled with sand up to 0.4 m height, static. A bank of heat transfer tubes is imbedded in the bed to absorb 50 % of heat released by the fuel. The remaining heat is transferred to tubes placed on the wall of the freeboard area. Experimental studies were carried out in the pilot plant using palm oil solid wastes. The combustion temperatures were maintained in the range 800-900 °C. The performance of the combustor was evaluated in terms of combustion and boiler efficiencies and flue gas emissions monitored. Figure 5.162 shows a typical temperature profile of combustion of palm solid wastes in the fluidized-bed boiler. During this experimental run, 540 kg palm shell and fiber mixture with a size range of 7-10 mm was consumed in 130 minutes. After an initial rise in temperature, the bed was maintained at a mean temperature of 780 °C within 60 minutes of feeding with palm shell and fiber waste. Steam rate of 600 kg h⁻¹ at atmospheric pressure is produced from the boiler. It was observed that upon introduction into the boiler through the feeding chute, all the heavier shells dropped onto the fluidizing bed. The residence time in the freeboard was approximately 2.5 seconds.

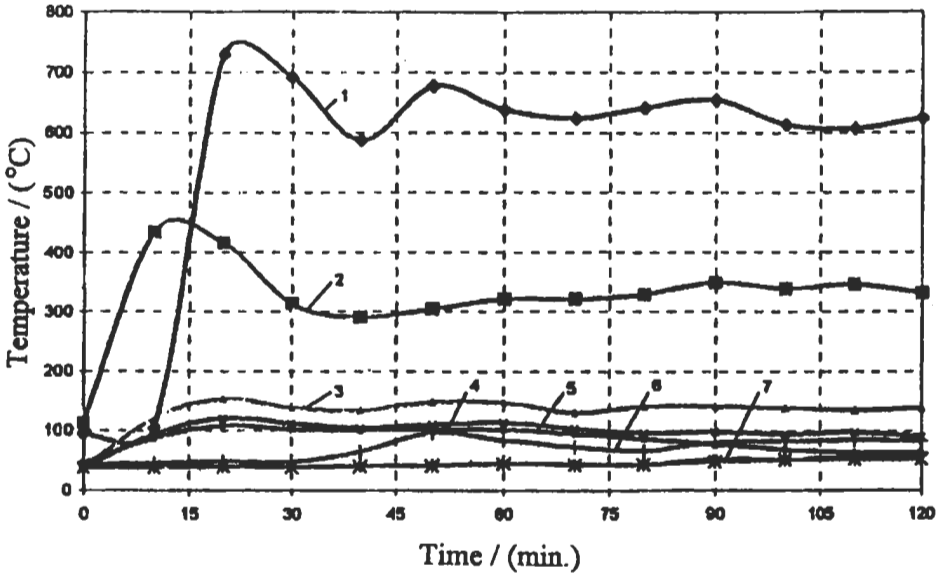


Fig. 5.161: Temperature variation at sorghum combustion on the 1 MW, CFBC pilot plant
 Legend: 1 - bed, 2 - furnace 1, 3 - furnace 2, 4 - furnace exit, 5 - stack, 6- FBHE exit, and 7- FBHE in [1065]. Reproduced by permission of Dragos Liviu [1065], ICPET CERCETARE ROMANIA.

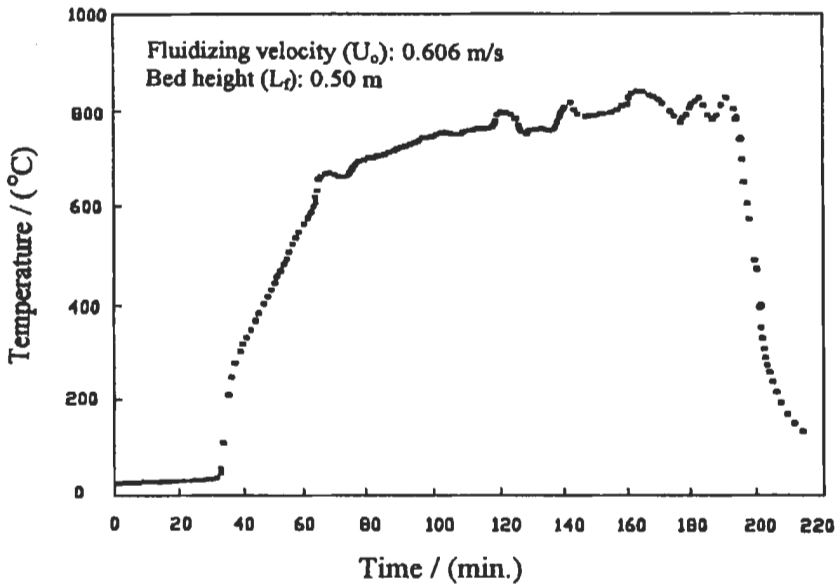


Fig. 5.162: Temperature profile of fluidizing bed fuelled by palm solid wastes [1068]. Reproduced by permission of ASME.

They estimated [1068] the boiler efficiency indirectly by energy losses from the boiler. Total energy losses is calculated from the following:

- i. Heat loss in the flue gas,
- ii. Heat loss through boiler walls,
- iii. Energy loss in unburnt fuel in ash,
- iv. Energy loss in flue due to CO, and
- v. Heat loss in water vapour in flue gas.

Figure 5.163 shows the effect of excess air on boiler efficiency. The results indicate that a boiler efficiency of 72 % is the maximum at excess air of 20-30 % when the boiler is fuelled with palm solid wastes. In comparison, boiler efficiencies of 80-82 % are achievable [1069], when the same boiler is fuelled with low quality coal from Sarawak. The reason for the lower efficiency could be due to the lower density of palm solid wastes as compared to coal.

5.3.4 Background to Heat Transfer

There is an enthusiastic and worldwide interest in the subject of heat transfer characteristics in fluidized-beds. The nature of combustion and the unique features of how energy is transferred from the combustion products to the surrounding enclosures distinguish the fluidized-bed heat transfer characteristics from those occurred in conventional heat vessels like boilers.

The direct contact between burning fuel and particles on one hand, and between hot particles and the components of the boiler on the other, would yield heat transfer coefficients three or more times higher than those of traditional boilers as indicated by Radovanovic [997], Shafey and Fan [1032], and Broughton [1033]. The combustion characteristics in the bed would also lead to moderate uniform temperatures within the fluidized part and therefore wear and tear on boiler parts due to hot spots are far more less. Few studies have been under-taken to investigate the simultaneous combustion and heat transfer in fluidized-bed using gaseous fuels (Bondarenko and Nekhlebayev [1034], Michaels and Beacham [1035], Jammaluddin, and Islam [1036]).

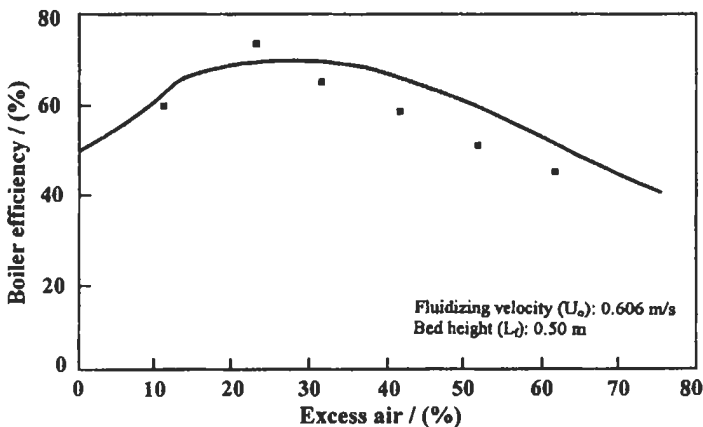


Fig. 5. 163: Effect of excess air on boiler efficiencies fuelled by palm solid wastes [1068]. Reproduced by permission of ASME.

The component of heat transfer by convection from the gases has been studied and is assumed to be of major importance in large particle fluidization. The second component is the unsteady conduction from the circulating particles contacting the heat transfer surface through a thin gas film for a certain residence time. While, radiation is significant from bed material to the freeboard walls and other objects for temperatures higher than 800 °C.

The total heat transfer coefficient is not simply the sum of the three components mentioned above. Although, this assumption can be considered for preliminary calculations of heat transfer. Each of these components increases on the expense of the other and these components of heat transfer are now reviewed.

Heat Transfer from Emulsion Phase

Staub [1037] presented a simplified model of the heat transfer to tube banks immersed in fluidized-beds. He assumed that the bed is divided into multiple particles upflow channels and particles downflow channels, and considered lateral particles exchange between flow channels. He neglected the inlet effects due to the distributor and the exit effects due to disengagement at the top of the dense bed region. The turbulent flow model given was supported by limited solids flow measurements. A mixing length concept is defined by the bed height needed to keep the mean lateral flow exchange of particles equals to their axial through flow rate. Wide range of gas pressures and temperatures, and particle sizes of 350 to 2600 μm were used in the model, and it offers an average value for Nusselt number as a function of Nusselt numbers of upflow and downflow regions, together with what so-called time and space average ratio. Adams [1038] concluded an approximate formula for gas convective Nusselt number in large-particle fluidized beds. The gas convective Nusselt number is obtained as a result of analysis of the three-dimensional viscous flow within interstitial channels adjacent to the heat transfer surface.

The fundamental element of the gas convective dominant heat transfer model of Adams [1039], was the analysis of flow within the interstitial channels adjacent to the heat transfer surface. The model was based upon a boundary layer analysis of flow within these channels with separate treatment of the two-dimensional flow near the channel center and three-dimensional, but Stoke's flow in the cusped corners is formed at particle contact points. For the fluidized-bed regime, the thermal state of the average particles is assumed to be such that the temperature distribution along the particle surface is linear.

The combined hydrodynamic and heat transfer model was described by Adams and Welty [1040]. They showed that emulsion phase and bubble phase contributions are due to gas convection and are considered separately. The emulsion phase contribution is determined from analysis of gas flow within interstitial channels bounded by particle surfaces and the tube wall. The geometry of this flow is simplified by using a boundary layer/inviscid core model with two-dimensional boundary layer flow near the channel center and three-dimensional, but Stoke's flow near particle contact points. The bubble phase heat transfer is determined by using conventional two dimensional boundary layer theories.

Adams [1041] reported an approximate model of bubble phase convective heat transfer to a horizontal tube immersed in a two-dimensional fluidized-bed. The model makes use of the exact solution for the inviscid flow field within a single two-

dimensional slow bubble. Bubble convective heat transfer accounts for about 30% or less of the total heat transfer for most cases of interest. As Adams [1042] continued his research [1039-1041], he studied the effect of contact time and particle thermal properties on the emulsion phase heat transfer by a coupled analysis of gas convection and transient conduction within spherical particles. The emulsion phase heat transfer to a surface immersed in large particle fluidized-bed depends upon the flow around and thermal response of individual particles. Heat transfer from the particles to the wall does not occur by direct conduction but involves the intervening gas. Thus, the rate of heat transfer to the wall depends upon the details of the interstitial gas flow as influenced by the mechanical and thermal presence of the solid particles. The accepted model of the time-averaged Nusselt number for a surface immersed in a bubbling gas fluidized-bed was expressed by Botterill [1043] (see Eq. 5.183):

The instantaneous emulsion phase heat transfer due to the combined effects of particle and gas convection is:

$$\text{Nu}_{em} = \frac{X_s}{S_p} \text{Nu}_s + \left(1 - \frac{X_s}{S_p}\right) \text{Nu}_{2D} \quad (5.129)$$

where X_s is Stoke's region edge location from particle contact point, S_p is half the distance between particle centers, and Nu_s and Nu_{2D} are the Nusselt numbers based upon the heat transfer rate of Stoke's region and the two-dimensional heat transfer rate, respectively.

In order to extrapolate Adams work [1042] to calculate the average heat transfer, complete information regarding the hydrodynamic characteristics of the bed is required. Among the parameters required are the emulsion phase voidage, the emulsion phase mean residence time (i.e. Fourier number), the bubble contact fraction, and the average interstitial gas velocity. Adams [1044] studied these parameters through an approximate analytical model of heat transfer to a horizontal tube immersed in a large particle bed with a single bubble contacting this tube. He concluded that the bubble phase heat transfer is highly dependent upon the hydrodynamic characteristics of the tube-bubble geometry. This model provided the instantaneous velocity distribution at the tube surface from which the instantaneous heat transfer rates could be determined. Heat transfer, bubble contact fraction, and emulsion phase residence times were determined locally for a horizontal tube of 50.8 mm diameter, and with sand particles of 1.3 mm mean diameter and dolomite particles with mean diameter of 2.0, 2.8, 4.0, and 6.6 mm.

Decker and Glicksman [1045] showed that the exact prediction of conduction requires detailed knowledge of particle, surface roughness geometry, and particle arrangement at the surface. They deduced the value of conduction heat transfer for particle roughness (γ/d_p) ranging from 10^{-2} to 10^{-4} mm to be averaged as:

$$h_d = 12 K_g/d_p \quad (5.130)$$

where K_g is the thermal conductivity of the gas and d_p is the particle diameter. In addition, they [1045] indicated that it is necessary for large particles to consider the thermal behavior of an individual particle adjacent to the heat transfer surface. They formulated the thermal time constant, τ_{CL} , for a temperature change of the particle adjacent to the wall as:

$$\tau_{CL} \sim \rho_p C_p d_p^2 / 36K_g \quad (5.131)$$

The particle thermal time constant was noted to be much larger than the particle residence time. They stated that the overall heat transfer rate between the emulsion and the wall for large particles is the sum of the conductive and convective components.

Model of Chen and Pei [1046] considered a spherical or cylindrical heating surface immersed in a fluidized-bed. A thermal boundary layer is, from time to time, renewed by the moving particles and fluidizing fluid. An average thickness of the boundary layer was assumed to deal with the total heat transfer coefficient. The maximum heat transfer coefficient could be obtained in the form of two semi-empirical formulae, for immersed flat plates:

$$Nu_0 = 0.074 Ar^{0.2} P_r^{1/3} (\rho_p C_p / \rho_{fd} C_{fd})^{1/3} \quad 20 < Ar < 2 \times 10^4 \quad (5.132)$$

and

$$Nu_0 = 0.013 Ar^{0.37} P_r^{1/3} (\rho_p C_p / \rho_{fd} C_{fd})^{1/3} \quad 2 \times 10^4 < Ar < 10^7 \quad (5.133)$$

Also, the maximum values of heat transfer coefficient have been the field of work of Botterill [1070]. He reported different correlations for the optimum condition of operation.

Kubie [1071] divided the models of heat transfer between the emulsion phase of gas-fluidized bed and immersed surface into two groups. The first group of models considers the bed microscopically, by evaluating heat transfer between the surface and the individual bed particles. The first disadvantage associated with those models is that the solution can only be obtained numerically. Secondly, the models shall only be accurate for short particle residence times, when the heat does not penetrate beyond the first layer of particles. Thirdly, in order to reconcile the theoretical results with the available experimental evidence, a gas film must be introduced between the surface and the first layer of particles.

Models of the second group consider the bed macroscopically by assuming that the bed consists of a continuous emulsion of particles and fluidizing gas, and gas bubbles, which constitute the discrete phase. The advantage of these models is its simplicity and the reasonable agreement with the experimental evidence for large packet residence times. Nevertheless, the models have a major disadvantage; that is the assumption of constant voidage emulsion which does not hold in the vicinity of the surface and, therefore results in unrealistic high heat transfer rates for short packet residence times. Kubie [1071] introduced a model assuming that the emulsion phase in the bulk of bed to be isothermal and of constant voidage. The heat transfer mechanism was assumed to have a transient conduction during the time of emulsion residence on surface. The variation of voidage was studied on the plane normal to the heat transfer surface. Accordingly, the time-mean heat transfer coefficient (\bar{h}_T) was approximated by:

$$\frac{\bar{h}_T d_p}{K_{em}} = \left[\frac{K_{em} R_c}{d_p} + \frac{\sqrt{\pi}}{2} \left(\frac{D_{v,em} \tau_{rs}}{d_p^2} \right)^{0.5} \right]^{-1} \quad (5.134)$$

where R_c is the contact resistance, K_{em} and $D_{v,em}$ are respectively thermal conductivity and diffusivity of the emulsion phase in the bulk of the bed, and τ_{rs} are the mean packet residence time.

Heat Transfer by Radiation

Sekely and Fisher [1074] reported experimental and analytical results for radiant heat transfer in fluidized-beds. The experiments were carried out by transmitting heat from a source through a transparent wall and by maintaining the wall at the bulk bed temperature. The radiative heat source was made of a graphite cylinder. Under conditions where the criteria are met, for both uniform particle temperature and constant flux, the expression for radiant heat transfer into the bed takes a particularly simple time-independent form:

$$q_p = \frac{dT}{dt} C_p \rho \frac{4\pi R_p^2}{3} = 4\pi\sigma R_p^2 F_p (T_s^4 - T_p^4) \quad (5.135)$$

where q_p is the heat transfer rate (energy/time) associated with a given particle wall contact area, F_p is the configuration factor, and T_s is the wall temperature.

Baskakov et al. [1075] used a technique to measure the radiative heat transfer coefficient by changing temperatures of two spheres of two Biot numbers immersed in the bed. One sphere had an oxidized surface (emissivity 0.8) and the other had a silver-plated surface (emissivity 0.1). They noted that the radiative coefficient increased by a factor of 7-8 as the surface temperature of the sphere was increased from 433 K up to 1003 K, whilst the bed was maintained at a temperature of 1123 K. The effective emissivity of the fluidized-bed in contact with the glass surface was found to be dependent on both the surface and bed temperatures. The Stefan-Boltzmann equation would only predict a four-fold increase in the transfer coefficient for a surface varying in temperature from 0.0 K to the bed temperature at constant bed and body emissivities:

$$\varepsilon_{eff} = q_{rad} / \sigma T_p^4 \quad (5.136)$$

The emissivity of a free surface of a fluidized-bed coincides with that for $T_s = T_b$ and decreases with the increase in bed temperature. The radiative component in the total heat transfer coefficient is independent of the particle diameter (within the tested range) and of the fluidizing velocity (during intensive fluidization).

Kolar et al. [1076] proposed the modified alternate slab model. The model assumes that the bed was made up of alternate slabs of gas and solid. The solid slabs are further subdivided into a convenient number of slices. The bed and heat transfer surfaces are considered gray while the gas is radiatively transparent. The model is examined for the prediction of radiative contribution in an air-sand system for various bed and operating parameters; particle size, bed and surface temperatures, and fluidizing velocity.

Typically, heat is transferred between the bed and the immersed surface by conduction and radiation through the emulsion phase, and by radiation through the bubble phase. The heat transfer coefficients for each of these processes were denoted by h_{dem} , $h_{r,em}$ and $h_{r,b}$, respectively. Assuming radiative and conductive components to be additive, the overall heat transfer coefficient, h_o , could be written as:

$$h_0 = (1 - \gamma_B)(h_{\text{dem}} + h_{r,\text{em}}) + \gamma_B h_{r,B} \quad (5.137)$$

where γ_B is the fractional heat transfer surface area, which is exposed to bubbles:

$$\gamma_B = 0.08553 \left[U_{\text{mf}}^2 \left[\left(\frac{U}{U_{\text{mf}}} \right) - 1 \right]^2 / g d_p \right]^{0.1948} \quad (5.138)$$

The bubble phase heat transfer coefficient was given by:

$$h_{r,B} = 2\sigma \left(\frac{1}{\epsilon_p} + \frac{2}{\epsilon_s} - 1 \right)^{-1} \frac{(T_b^4 - T_s^4)}{(T_b - T_s)} \quad (5.139)$$

The total radiative heat transfer coefficient h_r , was also given by:

$$h_r = h_{r,\text{em}} + h_{r,B} \quad (5.140)$$

Borodulya et al [1077] wrote different equations for the unsteady packet-to-surface heat transfer using a Pile model. The Pile model can be considered to consist of plane-parallel reflecting-absorbing and radiating plates. The plates (elementary layers) are characterized by their reflection and absorption coefficients and by their emissivities, which depend on the properties and concentration of particles forming the dispersed medium. A temperature gradient within the dispersed medium is absent. The fluidized-bed may be regarded as isothermal due to the agitation of particles. The radiative heat transfer in the system can be considered as occurring between two surfaces, each of which has its own emissivity and temperature.

Makhorin et al [1078] studied the effect of bed temperature and superficial gas velocity on the emissivity of the bed. They used photopyrometry to measure the particle temperature, and they measured the heat transferred by radiation only using a hot sight glass. They found that the bed temperature had a slight inverse effect on the bed's total emissivity. There are some other experimental techniques for the measurement of particle temperature which include the thermocouple [1079, 1080], photographic [1081], and fiber optic pyrometer [1082, 1083]. More detailed comparisons between the different methods have been given by LaNauze and Jung [1084].

Borodulya et al [1085] determined the degree of blackness of the surface of an isothermal inhomogeneous fluidized-bed as a whole, and of the emulsion phase and bubbles forming it. They used a window of the instrument for measuring the radiation flux (a radiometer) and a specified segment of the heat exchanger wall. The radiation flux received by the instrument varied periodically as the emulsion was replaced by the boiling bubble. In calculating the radiation flux, they considered each bubble in the bed independently. This is due to the high optical density of the emulsion separating the bubble. For $\epsilon_b \geq \epsilon_{\text{em}}$, the degree of blackness of the surface of an inhomogeneous fluidized-bed will be shown later in section 5.3.5:

According to the assumption of Decker and Glicksman [1045] for large-particle isothermal beds ($d_p > 1$ mm), the effective emissivity is only a function of particle emissivity and backscatter function [1086]. It does not depend on bed temperature,

particle diameter or particle volume fraction. Brewster [1087] made an analytical solution of the problem of emission into a black wall at zero degree assuming gray particles with constant properties. The effective emissivity is given by:

$$\epsilon_{\text{eff}} = \frac{\epsilon_p}{(1 - \epsilon_p)B} \left\{ \sum_{n=0}^4 \frac{4!}{n!(4-n)!} \frac{(\eta-1)^n}{(\zeta+n)} \left[\zeta \left(1 + \frac{2B(1-\epsilon_p)}{\epsilon_p} \right)^{0.5} + n \right] - \eta^4 \right\} \quad (5.141-a)$$

where $\eta = T_{\text{wa}} / T_b$ (5.141-b)

and $\zeta = \frac{3f_v \delta}{d_p} \left\{ \epsilon_p \left[2(1 - \epsilon_p)B + \epsilon_p \right] \right\}^{0.5}$ (5.141-c)

where B is the back-scatter fraction, (0.667), f_v is the particle volume fraction, (0.5), δ/d_p is the ratio of center-to-center particle spacing diameter, (0.5), n is the real part of refractive index [1086], and δ is the non-isothermal layer thickness which exists in the bed near the wall. In general the effective bed emissivity increases as T_{wa} increases for a given value of T_b . However for a given value of T_{wa} , the effective emissivity decreases with increasing T_b .

Total Heat Transfer

The knowledge of the total heat transfer between fluidized beds and immersed surface is of importance in the development of the fluidized bed boilers and various chemical processes. The total heat transfer coefficient, h_0 can be considered as the sum of the following five components [997, 1089];

- i. Conduction from the emulsion phase as a function of contact time (τ_{rs}), and the particle conductive component, h_d .
- ii. Gas convection transfer in the emulsion phase, $h_{c,em}$
- iii. Gas convection in passing bubbles, $h_{c,B}$
- iv. Radiation in the emulsion phase, $h_{r,em}$
- v. Radiation in the lean phase, when a bubble passes, $h_{r,B}$

Thus:

$$h_0 = (1 - \gamma_B)(h_d + h_{c,em} + h_{r,em}) + \gamma_B(h_{c,B} + h_{r,B}) \quad (5.142)$$

Jamalluddin and Islam [1036] studied the effects of size, configuration, and orientation of the immersed surface on the heat transfer coefficient in gaseous fuel fluidized-bed combustion system. Copper tube coils of two different diameters (0.098, 0.069 m) and number of turns (2, 4), respectively, were used as the immersed heat transfer surface, and also a copper cylinder of 0.05 m diameter, 0.05 m height in two different orientations (vertical and horizontal) was used. A mixture of gaseous fuel (methane of 96%) and air was introduced to the fluidized-bed tube of 0.15 m diameter, and chamotte particles of 1.55 mm average diameter were used as bed material with initial bed heights of 0.025 and 0.05 m. The overall heat transfer coefficient, h_0 , particle Nusselt, Nu_p and Reynolds, Re_p numbers were calculated as follows:

$$h_0 = \dot{m}_{wa} C_{wa} (T_{wa,o} - T_{wa,i}) / A_c \Delta T_m \quad (5.143)$$

where, \dot{m}_{wa} , C_{wa} , $T_{wa,o}$, and $T_{wa,i}$ are the mass flow rate, specific heat, outlet and inlet temperature of water, respectively. A_c is the total outside area of the heat transfer surface. ΔT_m is the mean temperature difference:

$$\Delta T_m = [\Delta T_1 - \Delta T_2] / 2.303 \log[\Delta T_1 / \Delta T_2],$$

where $\Delta T_1 = T_b - T_{wa,i}$, $\Delta T_2 = T_b - T_{wa,o}$ and T_b is the bed temperature.

Then:

$$Nu_p = h_0 d_p / K_g \text{ and } Re_p = d_p U_p \rho_g / \mu_g \quad (5.144)$$

where d_p , K_g , U_g , μ_g are the particle diameter, gas thermal conductivity, velocity, and viscosity, respectively.

In the 0.025 m bed [1036], the highest heat transfer coefficient was obtained from the coil of 0.098 m diameter because both the turns of the coil were immersed in the burning bed. The heat transfer coefficient in the cylinder (in horizontal position) was low because the cylinder covered a greater area of the distributor plate, therefore, it caused hindrance to the fluidization of the bed. In the 0.05 m bed, the highest heat transfer coefficient was obtained from coil of 0.069 m diameter because its four turns were completely immersed with a large exposed heat transfer area in the burning bed. The overall heat transfer coefficients for the immersed surface were found to vary from 487 to 907 $\text{kJ h}^{-1} \text{m}^{-2} \text{K}^{-1}$.

Recently, four different experimental methods for estimating heat transfer in a 12 MW_{th} circulating fluidized-bed boiler has been investigated by Andersson and Leckner [1088]. The methods are compared for a case of normal operating conditions, and the measured heat transfer coefficients are presented. In the central part of the combustion chamber, where most of the cooling surface is located, the cross-sectional average suspension density normally varies in the range of 10-20 kg m^{-3} , and the heat transfer coefficient is around 130 $\text{W m}^{-1} \text{K}^{-1}$ with a scatter of $\pm 15\%$ due to the different methods. The methods are critically analyzed and the heat transfer data are compared with relevant literature data [1088].

Heat Transfer to Horizontal and Vertical Tube Banks

In this section, the heat transfer to horizontal tube banks will be described first, then followed by the heat transfer to vertical tube bundles.

Horizontal tube banks. One of the most promising recent trends in improving boilers is the low-temperature combustion of solid fuels in a fluidized-bed by removing the heat from the combustion zone with the aid of a cooling surface made in the form of horizontal tube banks in staggered or in line arrangement. The results of investigations of the gasification and combustion of solid fuel in suspended state, indicate that the zone of active combustion in such systems does not exceed 200 mm from the level of the gas-distributing grid. Therefore, if heat-exchange surfaces are to be situated in such zone to ensure low-temperature combustion of the fuel, the surfaces have to be compact and optimally arranged.

Korolev and Syromyatnikov [1090] investigated the hydrodynamic and the structure of the fluidized-bed in the inter tube space to give the suitable arrangement of the tubes in the bundle. They reported that when the horizontal pitch increases, the flow pattern changes. At a speed close to the rate which coincides with the onset of fluidization, the gas cavity does not form under the tubes but between them. When fluidization number (the ratio of the superficial gas velocity to the linear velocity of gas at onset of fluidization) > 1 , the air flows from this cavity in the form of bubbles that are also the outer surfaces of the bundles; there the particles lie motionless. Korolev and Syromyatnikov [1090] also noted that in the staggered arrangement of the bundle, the flow around the tubes inside the bundle and on the outside is approximately equal, and the entire bed is more mobile than with the in-line through the inside of the bundle. The following expression for the mean porosity of a staggered bundle based on the experimental data is:

$$\frac{1 - \gamma_{\text{bun}}}{1 - \gamma_o} = 1.25\theta^{-0.4} Ar^{-0.03} \quad (5.145)$$

which is correct in the ranges $1.2 \leq \theta \leq 5$; $200 \leq Ar \leq 406000$

where γ_{bun} , γ_o are the porosity of the bed in the inter tube space of the bundle and the packed bed, respectively.

The local characteristics of heat transfer from horizontal staggered tube banks immersed in fluidized-beds were investigated experimentally by Chandran et al [1091]. The tube bundle experiments were carried out in a 0.305 m square, and open-loop fluidized-bed. While the single tube experiments consisted of two fluidized beds, one for operation at atmospheric pressure and the other for operation at pressures up to 50 kPa. Either for a ten-row tube bundle or a single tube, the steady-state heat transfer measurements were obtained in air fluidized-beds of glass beads.

The complex trend found for the variation of local heat transfer coefficients with variations in circumferential position, particle size, gas flow rate, and system pressure indicates a need for mechanistic modeling of the heat transfer process. Zabrodsky et al [1089] reported the experimental results for heat transfer coefficients between immersed-in-line and staggered-bundles of horizontal smooth tubes and air fluidized-beds of large particles. Their comparisons with existing correlations lead to the following conclusions;

- i. The horizontal pitch significantly affects the heat transfer from a tube bundle, while the influence of the vertical pitch is relatively insignificant.
- ii. The simplified theoretical equation for the conductive heat transfer is:

$$h_d = 7.2K_{fd}(1 - \gamma)^{2/3} / d_p \quad (5.146)$$

The gas convective component of heat transfer coefficient is determined as:

$$h_c = B^* U_s^{0.2} C_g \rho_g d_p \quad (5.147)$$

where, B^* is a constant equals 26.6. Thus, the semi-empirical equation for the overall

heat transfer coefficient leads to:

$$h_t = 7.2K_{fd}(1 - \gamma)^{2/3} / d_p + B^*U_s^{0.2}C_g\rho_g d_p \quad (5.148)$$

Goshayeshi et al [1092] studied the time-average local heat transfer coefficients for arrays of horizontal tubes immersed in a hot fluidized-bed. Propane was burned in a combustion chamber and the hot gases were directed into the 0.3 x 0.6 m test section through a distributor plate. Bed temperatures up to 1005 K were achieved. The effects of superficial gas velocity, particle size, and bed temperature on the heat transfer were studied. Heat transfer for the top, middle, and bottom tubes were also compared with those for a single tube.

Other investigators (e.g. Grewal and Saxena [1093], Krause and Peters [1094], and Goel, et al [1095]) studied the effect of surface roughness and finned tubes on heat transfer in a gas fluidized-bed. Grewal and Saxena [1093] reported that on smooth tubes, the mechanism of heat transfer between boiler tubes and the fluidized-bed is very complicated because of the involvement of many fluidized-bed variables such as particle size, size distribution, particle shape, particle density, particle and gas thermal properties, reactor geometry, and type of gas distributor; and the variations in heat transfer tube design such as size, shape, spacing (gap), pitch and material. For rough tubes, in addition to the above variables, one will have to include in the analysis of heat transfer process such variables as the type of surface roughness, size of surface roughness, and pitch to particle diameter ratio.

Vertical tube bundle in a fluidized-bed. Borodulya et al [1096] studied the overall heat transfer coefficient for the vertical tube bundles in the fluidized-beds of pressures of 1.1, 2.6, 4.1 and 8.1 MPa and at ambient temperature. Tube bundles of three different pitches were employed. The overall heat transfer coefficients were reported as a function of the fluidizing velocity. They concluded that the heat transfer coefficient from vertical tube bundle to bed increases with the rise of pressure and with the increase in particle diameter.

Morooka et al [1097] carried out their experiments on a bed made of a transparent acrylic plastic column. They concluded that the local weight-mean diameter of the solid particles in the dilute zone increases with decreasing height from the dense fluidized-surface and with increasing gas velocity. Also, the heat transfer coefficient is nearly independent of the heat transfer tube diameter and is only slightly affected by the lateral location of the tube.

Fundamental and engineering aspects of fluidized-combustion were reviewed by Beér [1098]. He discussed the relevance of available information on the kinetics of carbon-oxygen and carbon dioxide reaction to the combustion of coal in the fluidized-beds. Also, the rates of heat transfer to tubes immersed in the bed were studied. Little difference was found between heat transfer coefficient of vertically or horizontally arranged tubes. Beér has found that heat transfer coefficient in the bed was increased with increasing fluidizing velocity and bed temperature. He also explained that the increase of the heat transfer coefficient with the decrease of particle density is due to the transport of the oxidant penetrated with the fluidizing gas to the coal particle, the pyrolysis and combustion of the coal particle in the fluidized-bed, and also the attrition of coal particles in the bed. In addition to those, it is due to the reactions taking place in the free board above the fluidized-bed.

5.3.5 Experimental and Computational Study of Heat Transfer

In this section, the heat and mass transfer to the surrounding walls, distributor plate, immersed surfaces, and to a tube bank located in the free board will be considered.

Calculation of Different Modes of Heat Transfer

El-Mahallawy et al [1099] have studied the heat transfer to the surrounding walls for a gas-fired fluidized-bed. In the analysis of heat transfer to the bed wall, the distinction between the heat transfer in the fluidizing part and in the free-board of the bed is made. The contribution of the heat transfer by radiation either from the hot particles in the fluidizing part or from the hot combustion products and the horizontal luminous surface of the fluidizing sand to the free-board wall is considered. Both the wall heat transfer coefficient and the particle convective heat transfer coefficient are calculated. Figure 5.164 shows the fluidized-bed system used in this investigation, and it consists of the air and fuel supply as well as the cooling water with the necessary auxiliaries which facilitate its operation and control. The figure also shows the mixing pipe with mixing chamber, and sand collector. The furnace is a rectangular parallelepiped. Its inner cross-sectional area is 0.550×0.245 m and its height is 0.450 m. The furnace is surrounded by a cooling water jacket. It has a perforated copper plate with screwed plugs which ensures uniform distribution of the flowing mixture of fuel gas (LPG) and air, and permits the required pressure to convey sand particles. Several experimental runs have been performed [1099], and during these runs the air-fuel ratio is varied by varying the fuel mass flow rate while keeping the mass flow rate of air constant to maintain the total momentum nearly constant. The mass air-fuel ratio was varied between 18 to 22.

For the calculation of the heat transfer to the bed walls, the bed is considered to be divided into two main parts, a fluidizing part which is exposed to the combustion gases and sand particles, while the upper part, free-board, above the fluidizing part is exposed to exhaust gases only. The different modes of heat transfer are shown in Fig. 5.165.

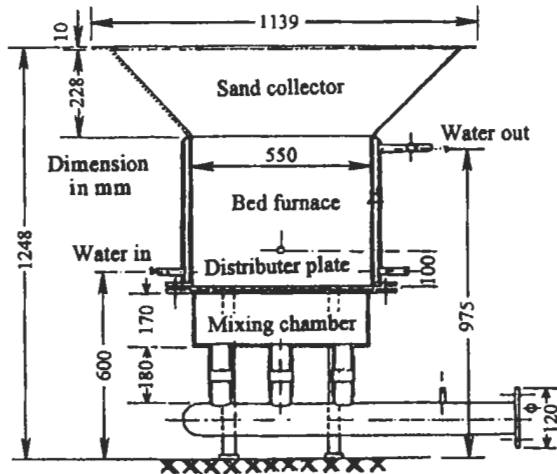


Fig. 5.164: Test rig layout [1099].

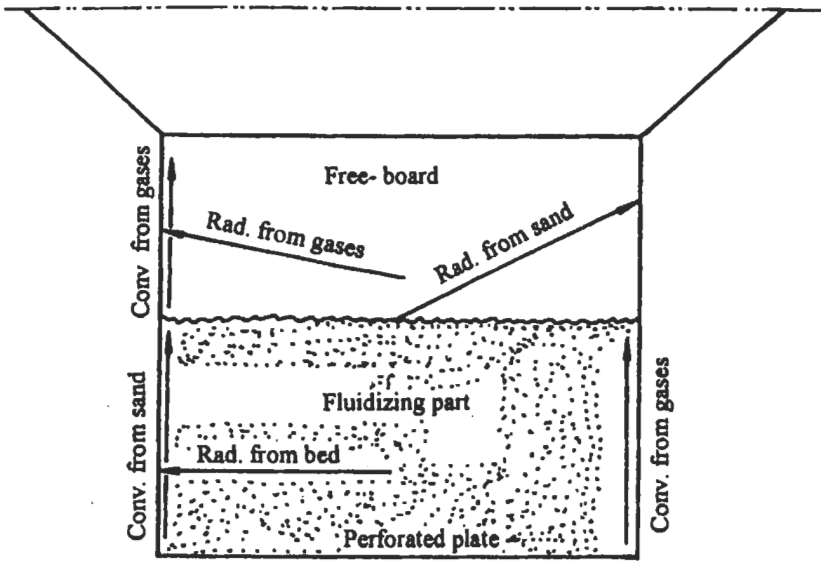


Fig. 5.165: The different heat transfer modes in the fluidized bed combustor [1099].

It is worth to notify the following legend for the next section to ease understanding the different equations; b, bed, c, convection, d, conduction, f, free-board, g, gases, p, particle, s, sand, r, radiation, w, wall or water, and t, total, contact.

Heat transfer to the free-board wall. The heat transfer to the free-board wall consists of heat transfer by convection from gases and heat transfer by radiation from the hot horizontal surface of the fluidizing sand and from combustion products.

The convective heat transfer, q_{cf} to the free board wall is calculated by [1100]:

$$q_{cf} = h_{cf} A_f (T_g - T_w) \tag{5.149}$$

where A_f is the inner surface area, T_w is the temperature of the inner wall surface, and T_g is the average temperature of the gases ($0.5 (T_b + T_{ex})$), where T_b and T_{ex} are the temperature of the bed and exhaust, respectively.

The coefficient of the heat transfer by convection (h_{gf}) for parallel flow is calculated using the following equation [1100]:

$$Nu_{gf} = h_{gf} D_b / K_{gf} = 0.022 Re_{gf}^{0.8} Pr_{gf}^{0.43} \beta \tag{5.150}$$

where K_{gf} , Pr_{gf} , ν_{gf} , are the thermal conductivity, Prandtl number, and the kinematic viscosity of gases, and they are taken at the average temperature of gases. D_b is the equivalent diameter of the bed. In the above equation, Reynolds number is defined as:

$$Re_{gf} = U_g D_b / \nu_{gf} \tag{5.151}$$

$$= [(A/F + 1) \dot{m}_f / \rho_{gf} A_c] [4A_c / P_b] / \nu_{gf}$$

where A_c and P_b are the cross-sectional area and the wetted perimeter of bed, respectively, and the correction factor (β) can be estimated from the relation [1100];

$$\beta = 1.38 (X_b/D_b)^{-0.12} \quad (5.152)$$

where X_b is half the height of the bed.

The radiative heat transfer, q_{rf} to the free board wall is given by:

$$q_{rf} = q_{rs} + q_{rg} \quad (5.153)$$

The radiative heat transfer from gases in the bed to the free-board wall, q_{rg} is calculated by Eq. 5.38 and Ref. 1100. Also, the radiative heat transfer from sand to the free-board wall, q_{rs} is calculated by Eq. 5.38 with replacing $((\epsilon_s + 1)/2)$ by ϵ_s and ϵ_g by ϵ_b (emissivity of the bed), while the configuration factor, VF, in this equation is taken from Refs. 1100, 1101..

The distribution of the dimensionless radiative and convective heat transfer to the free-board wall is shown in Fig. 5.166 (a). The luminous radiation from the hot sand represents about 70 % from the total to this part, and the convective heat from gases represents about 14 % and the rest is the heat transfer by radiation from combustion gases.

The radiative heat transfer coefficient from bed to the free-board wall is determined as:

$$h_{rf} = h_{rs} + h_{rg} \quad (5.154)$$

The coefficients of heat transfer by radiation from sand and gases are obtained by:

$$h_{r,s} = q_{rs} / A_f (T_b - T_w), \quad \text{and} \quad h_{rg} = q_{rg} / A_f (T_g - T_w) \quad (5.155)$$

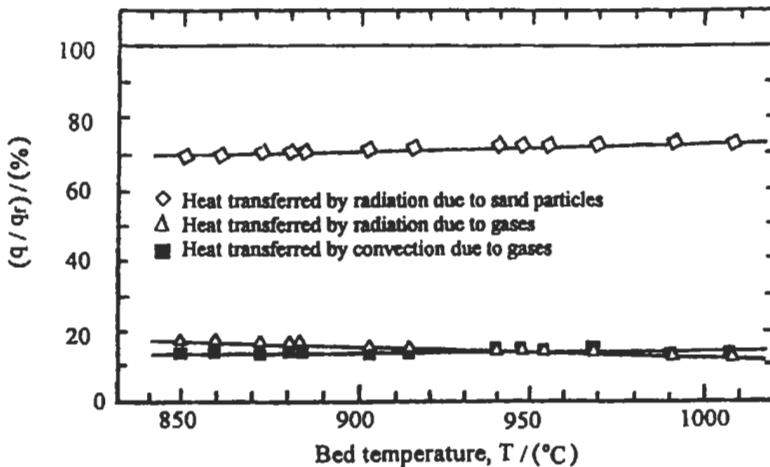


Fig. 5.166 (a): Distribution of the different modes of heat transfer in the free board [1099].

Heat transfer to the fluidizing part wall. The overall heat transfer coefficient in the fluidizing part is determined from the relation:

$$h_b = q_b / A_b (T_b - T_w) \quad (5.156)$$

where A_b is the wall surface area, and q_b is the heat transferred to the fluidizing part wall, and it is estimated by subtracting the heat transferred to the upper wall from the heat absorbed by the cooling water (q_w).

$$q_b = q_w - q_f \quad (5.157)$$

The heat transferred to the free-board wall (q_f) is equal to the summation of the convective and the radiative heat transfer.

$$q_f = q_{cf} + q_{rf} \quad (5.158)$$

The radiative heat transfer to the fluidizing part wall is calculated by:

$$q_{rb} = h_{rb} A_b (T_b - T_w) \quad (5.159)$$

The radiative coefficient of heat transfer, h_{rb} is calculated by [1102]:

$$h_{rb} = 20.5 \epsilon_b [(T_b/100)^4 - (T_w/100)^4] / (T_b - T_w) \quad (5.160)$$

The effective emissivity of the bed, ϵ_b is given by Ref. 1103.

The convective heat transfer to the fluidizing part wall is estimated by subtracting the summation of the convective and radiative heat transfer to the free-board and the radiative heat transfer to the fluidizing part wall from the heat absorbed by the cooling water jacket.

$$q_{cb} = q_w - (q_{cf} + q_{rf} + q_{rb}) \quad (5.161)$$

The convective heat transfer coefficient (h_{cb}) is calculated by;

$$h_{cb} = \frac{q_{cb}}{A_b (T_b - T_w)} \quad (5.162)$$

The convective heat transfer coefficient to the fluidizing part wall is equal to the sum of both the convective heat transfer coefficient of particles and gases, therefore:

$$h_{cp} = h_{cb} - h_{cg} \quad (5.163)$$

where h_{cg} is the convective heat transfer coefficient of gases and is calculated by [1104]:

$$Nu_{gb} = h_{cg} d_p / k_{gb} = 0.0175 Ar^{0.46} Pr^{0.33} (U_{m,f}/U_{max})^{0.3} \quad (5.164)$$

The minimum fluidizing velocity is given by [443]:

$$U_{m.f} = d_p^2 (\rho_p - \rho_{gb}) g / 1650 \mu_{gb} \tag{5.165}$$

The distribution of the dimensionless radiative and convective heat is shown in Fig. 5.166 (b). For the fluidizing part, the radiative heat is 24 % and the convective heat is 76 %. As shown in Fig. 5.166 (c), about 10 % of the total heat (to the fluidizing part and free-board) is transferred to the free-board, and 90 % to the fluidizing part wall. For the free-board, the calculations showed that of this 10 %, 8.6 % is by radiation and 1.4 % is by convection, and for the radiative heat 7 % is luminous and 1.6 % is nonluminous.

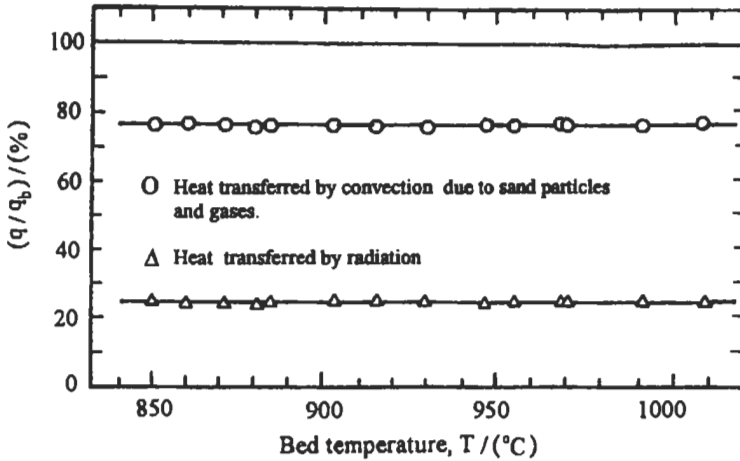


Fig. 5.166 (b): Distribution of the different modes of heat transfer in the fluidizing part [1099].

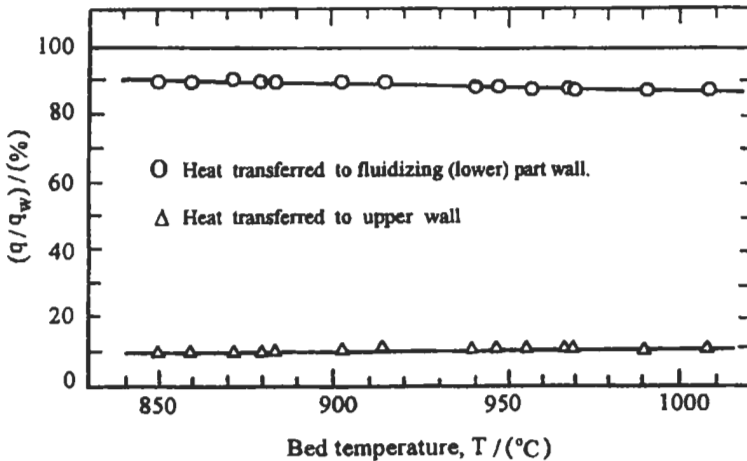


Fig. 5.166 (c): Distribution of heat transfer to the fluidizing part and free-board [1099].

Also, the calculations showed that for the fluidizing part 68 % of the total heat transferred (to the bed and the free-board) is by convection, from which 51 % from sand and 17 % from the gases. The radiation represents 22 % of this total heat.

Empirical formulae, based on the experimental results (Figs. 5.167 and 5.168), for the total heat transfer coefficient in the fluidizing part and the particle heat transfer coefficient are obtained as follows:

$$Nu_b = h_b d_p / K_{gb} = 0.56 Ar^{0.2} \tag{5.166}$$

where $Ar = d_p^3 \rho_p \rho_{gb} / \mu_{gb}^2 g$.

$$\text{and } Nu_p = h_p d_p / K_{gb} = 1.3 + 0.145 Re_p^{0.6} Pr_{gb}^{0.33} \tag{5.167}$$

where $Re_p = U_p d_p / \nu_{gb}$

The constants of the above equations are determined by fitting the values of the experimental curves, and the results are shown to be in reasonable agreement with Refs. 1106 and 1107.

Heat Transfer to the Distributor Plate

The study of heat transfer to the gas distributor of fluidized bed furnaces is of significant importance to the design engineer. A wealth of papers and books has been published studying the heat transfer in fluidized beds as described in section 5.3.4, but few authors were concerned with the problem of heat transfer to the gas distributor. Therefore, in this section the effect of the bed temperature on the heat transfer to the distributor will be discussed. The bed temperature was varied from 650 °C to 1100 °C (by changing the air to fuel (LPG) ratio). The effect of three average particle diameters (1200, 1500 and 1800 μm) on the heat transfer to the distributor plate was also demonstrated.

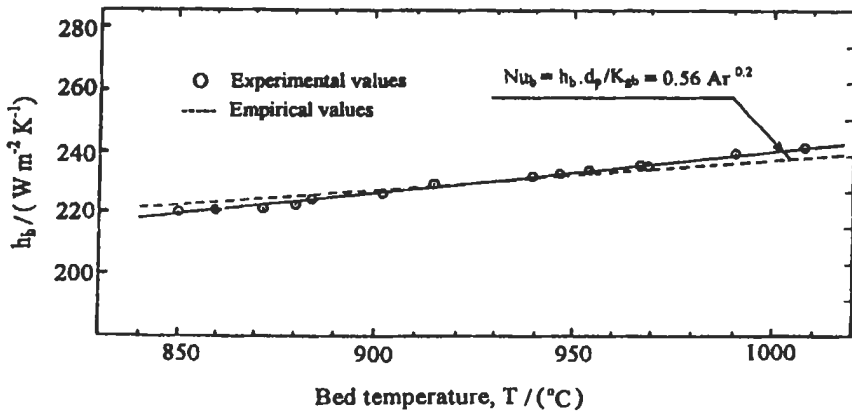


Fig. 5.167: The variation of the wall heat transfer coefficient in the fluidizing part with the bed temperature [1099].

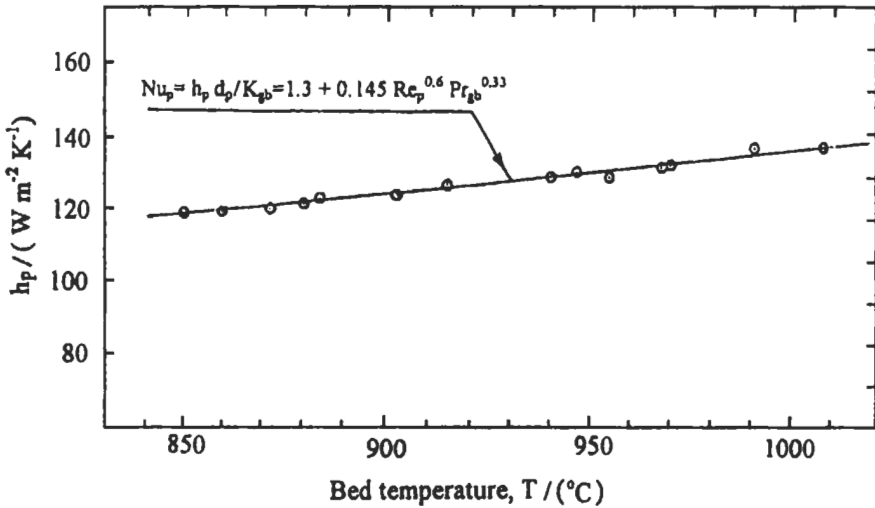


Fig. 5.168: Variation of the particle heat transfer coefficient with bed temperature [1099].

The general layout of the fluidized-bed is given in Fig. 5.164, while the description of the distributor plate was given by El-Mahallawy and Mahmoud [1108]. The distributor was made of a copper plate 0.6 x 0.3 m, and 0.013 m thickness. One hundred and sixty two nozzles were screwed into the plate and each nozzle had an exit hole of 2.5 mm diameter. The plate was water-cooled using 17 coil-tubes embedded into the plate, and the plate had nine thermocouples fixed on its surface to measure its temperature.

For the calculation of heat transfer by radiation to the plate, Eq. 5.38 is used with total emissivity calculated from Ref. 416. The heat transfer coefficient by convection from hot gases to the relatively cold plate is obtained using a procedure described by Xavier and Davidson [1109], and its variation with particle diameter is shown in Fig. 5.169. The total heat transfer coefficient, h_t , is calculated from the heat absorbed by the cooling water, q_t , the average surface temperature of the plate, and the temperature of the bed materials adjacent to the plate. The conductive heat transfer coefficient is calculated from:

$$h_d = h_t - (h_r + h_c) \tag{5.168}$$

Figure 5.169 reveals that the overall heat transfer coefficient h_t decreases as the particle diameter increases. This could be attributed to the increase of the total surface area in the case of small particles. The radiation heat transfer coefficient, h_r has no significant change with particle diameter as shown in the figure. It was proved experimentally by Pikashov et al [1110] that the particle diameter had only a slight effect on the emmissivity of the bed. He also proved that the shape of the particles can have a dominant effect on the emmissivity of the bed. Also, Fig. 5.169 shows that the increase in particle diameter results in a reduction of the conductive heat transfer coefficient, h_d . This depends on the contact area between the particles and the plate. This is quite understood, since for large particles the contact area between the particles

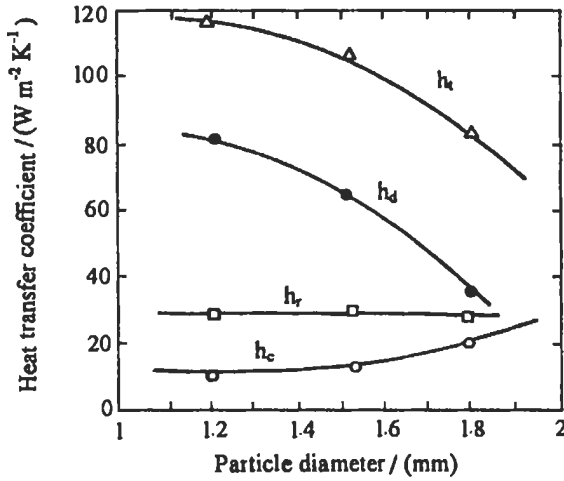


Fig. 5.169: Variation of overall, h_t , conduction, h_d , radiation, h_r and convection, h_c , heat transfer coefficients to the distributor plate with particle diameter [1108].

and the plate is lower than that for smaller particles.

The variation of the total heat transfer to the distributor plate with bed temperature is shown in Fig. 5.170 for different particle diameters. The figure shows that this heat increases with the increase of the bed temperature and the decrease of particle diameter. For a particle diameter of 1200 μm , the total heat was found to represent a percentage of 6 and 8% from the total chemical energy of the fuel input for bed temperatures of 650 and 1250 $^\circ\text{C}$, respectively.

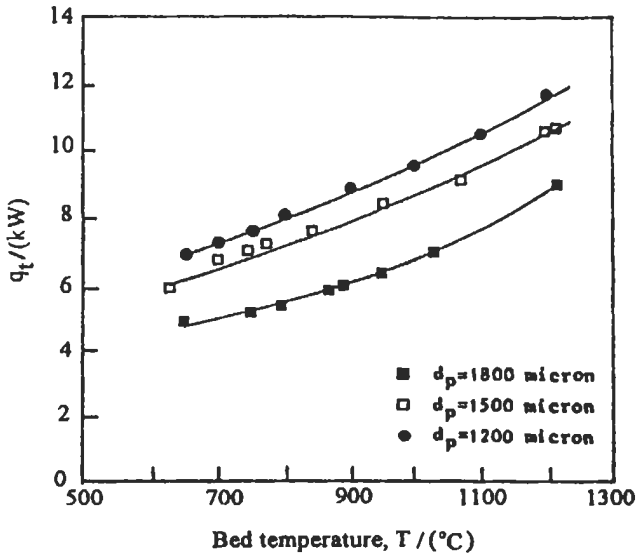


Fig. 5.170: Variation of total heat transfer to the distributor plate with bed temperature for different particle diameters [1108].

From the above described experimental results, two empirical formulae for the total and conductive heat transfer coefficients are obtained as:

$$\text{Nu}_t = 4.1 \times 10^{-5} A_r^{0.5} (d_p/D)^{-1.1} \quad (5.169)$$

$$\text{Nu}_d = 3.7 \times 10^{-10} A_r^{0.9} (d_p/D)^{-2.45} \quad (5.170)$$

where A_r is the Archimedes No., D is the hydraulic diameter of the bed and d_p is the particle diameter.

Heat Transfer to Immersed Bodies

Although there is a vast literature in the subject of heat transfer in fluidized-beds, there is a great need to verify the data accumulated by experimental work under conditions that assemble the practice, i.e. firing conditions. The influence of various factors on heat transfer between the fluidized-bed and the immersed body needs to be clarified. Also, a governing correlation for the estimation of total heat transfer coefficient to immersed body needs to be formulated directly from the experimental results. Therefore, El-Mahallawy et al [1111] have studied the effect of bed temperature, particle diameter, tube diameter, and orientation on the heat transfer coefficient between the bed and an immersed body under firing conditions. They have used the same fluidized-bed described above. The heat transfer mechanism between the fluidized material and the immersed body is multi disciplinary including: (i) the inter phase gas convective component; which would be of influential weight for flows of high Reynolds number, (ii) the unsteady conduction component between the solid particles and the immersed body and (iii) the radiative component.

The immersed bodies used in the fluidized-bed described above are copper coils of different tube diameters. They are positioned inside the furnace horizontally and vertically to study the effect of orientation method. Three coil-tube diameters are used. These are 4, 6, and 8 mm outer diameter, and 2.5, 4, and 6 mm inner diameter, respectively. A series of experiments was performed in order to study the effect of different parameters on the heat transfer coefficient between fluidized-bed material and the immersed copper coils.

The heat transfer to the coil is obtained from the enthalpy rise of the circulating water flowing through the coil. The temperature of the inner surface of the coil is obtained from the empirical relation governing the heat transfer for fully developed turbulent flow in smooth tubes as given by Mikheyev [529];

$$\text{Nu} = 0.023 \text{Re}^{0.8} \text{Pr}^{0.3} \quad (5.171)$$

where Nu , Re and Pr are Nusselt number, Reynolds number and Prandtl number respectively. The outer temperature is obtained from the conduction equation in cylindrical wall as given by Holman [1112]. The total heat transfer coefficient h_t is thus obtained using Newton's equation of convection;

$$q_{\text{coil}} = h_t S_o (t_b - t_{\text{coil}}) \quad (5.172)$$

where q_{coil} is the total heat transferred to the coil, S_o is the outer surface area of the coil,

t_b is the bed temperature, and t_{coil} is the outer surface temperature of the coil. The calculated total heat transfer coefficient under different parameters are shown in Figs. 5.171 to 5.173.

Influence of bed temperature. Figure 5.171 shows the variation of total heat transfer coefficient with bed temperature. The fluidized particles are of the same average diameter, 1500 microns, while the immersed coils are made of a 6 mm outer diameter tube, and have a 70 mm coil diameter. The figure shows that for both coils, horizontal or vertical, the heat transfer coefficient initially increases with the increase in bed temperature till it attains a maximum at about 1173 K and then followed by a steady decline. It is evident that the heat transfer coefficient exhibits comparatively higher values for the horizontal coils.

The process of changing bed temperature leads to changing many influential parameters that affect the heat transfer mechanism in fluidized-beds; including: (I) fluid superficial gas velocity, (ii) the volumetric specific heat of gases, (iii) the thermal conductivity and (iv) the residence time.

In contrast to the expectation that the heat transfer coefficient would steadily increase with the increase of the superficial stream velocity, the results show clearly that the initial increase of the heat transfer coefficient is followed by a steady decline. This conclusion could certainly be anticipated and explained. It is also being confirmed by previous investigators [1043, 1113] who have investigated a wide range of superficial velocities. Increasing the superficial fluid velocity would result in increasing both the fluid velocity and bed voidage. The former causes an increase in the heat transfer coefficient but the latter would have the opposite effect.

The volumetric specific heat of gases C_p is three orders of magnitude smaller than that of solid particles. It may be thought that there is no power dependence of h_t on C_p . On the other hand, some authors [1043] predicted that h_t increases with an increase in C_p at high pressures and gas velocities.

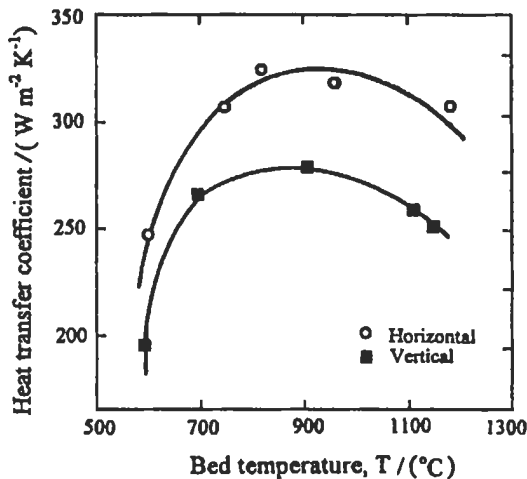


Fig. 5. 171: Total heat transfer coefficient versus bed temperature for particle diameter 1500 microns using coil of 6 mm outer tube diameter [1111].

The gas thermal conductivity is the physical property that has the greatest influence on heat transfer. It was reported that the initial increase in h_t with temperature t_b of the fluidized-bed results from the increase in k_{gb} with t_b . As the temperature increases, the residence time decreases at the heat transfer surface as the intense bubbly flow creates more intense particle circulation.

Influence of particle diameter. The experimental observations for the range of particle diameter (1200-1800 micron) showed that the total heat transfer coefficient decreases with the increase of particle diameter (Fig. 5.172).

To analyze this observation, it is required to show the effect of particle diameter on the three components of heat transfer coefficient. For the conductive component of heat transfer coefficient, there is a strong inverse dependence with the particle diameter. This is due to two reasons. The first is that the decrease in particle diameter means larger surface area of the particles for the same bed height. The second reason is that the decrease in particle diameter means a decrease in the path of conductive transfer between particles and surface.

On the other hand, the convective component of heat transfer coefficient which results from the convection from interstitial gases to immersed heat transfer surface increases with the increase in particle diameter. This is due to the fact of dependence of convective heat transfer on Reynolds number, which is increased by increasing particle diameter. The radiative component is not affected by particle diameter.

For the above range of particle sizes, the effect of inverse dependence of the conductive component is stronger than that of the direct dependence of the convective component which is more sound in coarser particles.

Influence of tube diameter. Increasing the tube diameter (4 mm, 6 mm, 8 mm) resulted in a decrease of the heat transfer coefficient. This dependence is related to the appreciable decrease in the temperature of the solid particles as they flowed around the

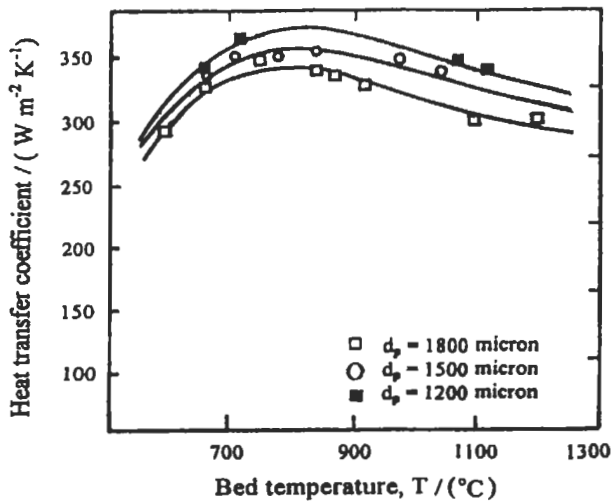


Fig. 5.172: The effect of particle diameter on the total heat transfer coefficient [1111].

coil. Under otherwise equal conditions, the cooling of the particles will be greater i.e., h_t will be smaller. The second reason is that packets of solid particles are thrown aside from the heat transfer surface of small dimensions by the action of gas bubbles, and the total replacement of the packets causes increase in h_t , while in larger dimensions, the gas bubbles will only move the packet along the surface so that h_t will be less.

Influence of coil diameter. Increasing the coil diameter resulted in a decrease of heat transfer coefficient. This is due to the increase of surface area, which results in more disturbances to the flow that affects bubbles behavior and growth. It is also due to the increase of the cooling effect of the surrounding particles associated with the presence of the coils body at higher cooling potential (Fig. 5.173).

Influence of method of orientation. It was observed that horizontal coils have higher values of heat transfer coefficients than vertical coils, Fig. 4.171. Besides that the horizontal coil covers a greater area of the distributor plate, the disturbance of the flow and the bubble growth are more compared to the case of vertical coil. This increases the collisions of moving particles to the coil, thus increasing the heat transfer by conduction.

Correlation for the total heat transfer coefficient. The experimental results are used to calculate Archimedes and Nusselt numbers. The following correlation, based on experimental results, is obtained:

$$Nu = 0.0035 Ar^{0.4673} (D/d_p)^{0.516} \quad (5.173)$$

where D is the hydraulic diameter. A comparison between this correlation and the experimental data is shown in Fig. 5.174.

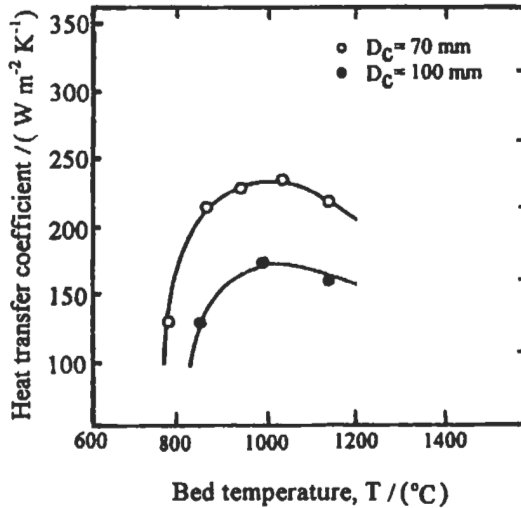


Fig. 5.173: Effect of coil diameter on the total heat transfer coefficient [1111].

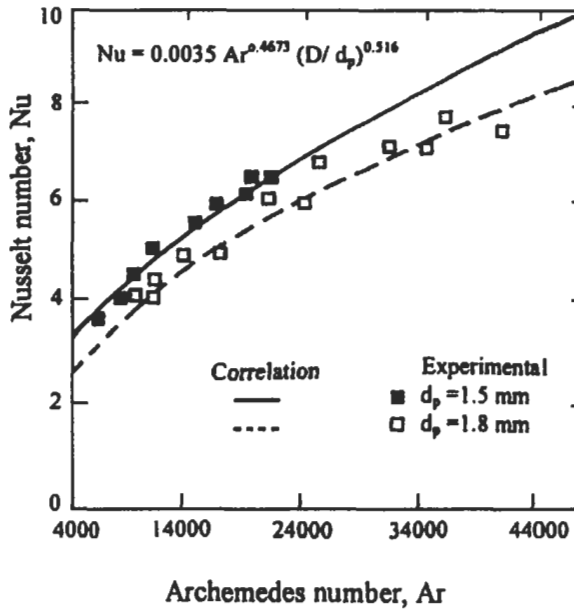


Fig. 5.174: Comparison between correlation and experimental results [1111].

Heat Transfer in a Bubbling Fluidized-Bed Combustor

The interrelationships between heat and mass transfer in large particles ($d_p > 1$ mm) fluidized-bed model are considered experimentally and theoretically in this section. Abdel-Hafez et al [1114, 1115] have investigated the effect of bed temperature on the different modes of heat and mass transfer coefficients. In their analysis of heat transfer to the bed wall, a distinction between the heat transfer in the fluidizing medium part and in the free-board part is made.

The layout of their fluidized-bed test rig [1114, 1115] with its attached necessary systems is shown in Fig. 5.175 (a). The rig is equipped with the necessary controlling and measuring devices. The furnace itself consists of three sequential vertical stages (the bed and two free-board parts), mixing pipe with mixing box, exhaust collector and chimney, Fig. 5.175 (a). The first stage, which is the furnace, is a rectangular cuboid with an inner cross-sectional area of 0.550×0.245 m, an outer cross-sectional area of 0.570×0.265 m and a height of 0.370 m surrounded by a cooling jacket of 0.570×0.265 m inner cross-section, 0.590×0.285 m outer cross-section and 0.350 m height. The second part is a four-row horizontal staggered tube bank (inside and outside tube diameters of 0.022 and 0.028 m, respectively), through which water is passed, and is located in the lower part of the free-board whereas the flue gases flowing in cross flow over the tubes. The staggered arrangement has a 0.068 m horizontal tube-to-tube spacing, and a 0.075 m vertical row-to-row spacing. The total number of tubes is 26 and the exposed length of the bundle to the flowing gases is 0.245 m. The lower first row of the tube bank is 0.395 m above the surface of the fixed bed and 0.445 m above the distributor plate. The water flow rate through each row is accurately controlled and monitored, whereas the inlet and exit temperatures are recorded.

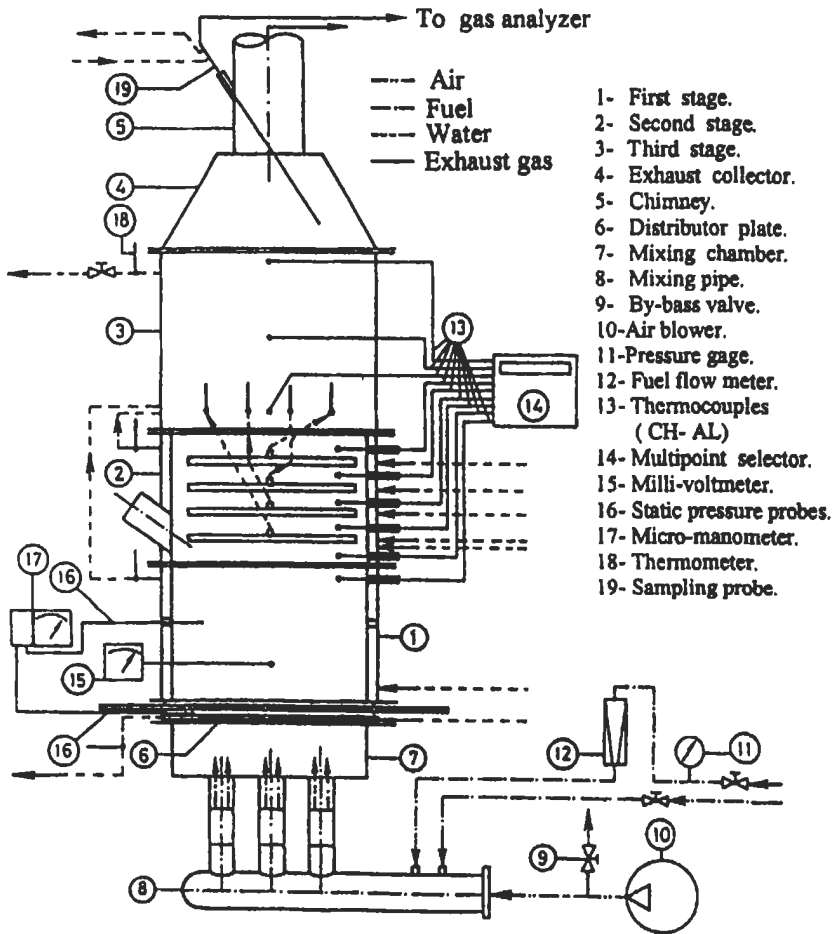


Fig. 5.175 (a): The fluidized bed test rig layout [1115]. Reproduced by permission of John Wiley and Sons Limited.

The experiments were conducted with constant rate of cooling water and air mass-flow rate. The experimental results were recorded under different bed temperatures, which were adjusted through the fuel-air mass ratio, while the height of the static bed is 0.05 m, and the minimum fluidization velocity is from 0.43 m s^{-1} to 0.5 m s^{-1} corresponding to bed temperature from 1114 K to 1429 K, respectively.

The experimental technique is based on measuring the different local average quantities, which are required to calculate the different modes of heat transfer from the bed to the three stages of the fluidized-bed combustor. The heat balance technique is applied to guarantee the reliability of the measured quantities. Bed temperature is measured by fine wire thermocouple, which is immersed in the bed at 0.16 m above the distributor plate.

Nine identical thermocouples are located in such arrangement that one of them is used for measuring the temperature of the free-board right above the fluidization zone and a group of five for measuring the temperatures in between the rows of the staggered

tube bank. The last three thermocouples are anchored at three different points in one of the fire tubes. All thermocouples are connected to multi-point selector. Temperatures reading from nine thermocouples are corrected for radiation. Fuel mass flow rate (LPG) and air mass flow rate were measured as well as the species concentration (O_2 , CO and CO_2) of the exit exhaust gases. The range of fuel flow rate was 16 to 25 $kg\ h^{-1}$, while the range of mass air to fuel ratio was 24 to 38. Measurements of species concentration at the chimney showed a complete combustion. Therefore, by knowing the chemical composition of the fuel and volumetric analysis of the combustion products, the overall air fuel ratio could be obtained. Mass flow rate of cooling water through each of different cooling stages, together with the temperature rise across, are recorded for the purpose of heat balance. Also, the pressure drop across the bed is measured, by means of micromanometer, to estimate the Archimedes number, which in turn is used to investigate the bed characteristics.

Computational method. Figure 4.175 (b) shows the different modes of heat transfer. To estimate the heat transfer coefficients of the different modes, in the fluidized-bed, the first stage is divided into two parts: a fluidizing medium part and a free-board part. The fluidizing part is exposed to the sand particles and combustion gases, while the free-board part is exposed to the exhaust gases only. The heat transfer to the surface of the free-board, q_f is by convection and radiation due to both gases and sand particles, and these are calculated by the same way described before in this section.

The radiative heat transfer to the fluidizing part wall. The radiative heat transfer to the wall in contact with the fluidizing part is calculated from the following equation [1077]:

$$q_{rb} = \sigma \epsilon_{net} A_b \left[\left(\epsilon_{eff} / \epsilon_b \right) (T_b^4 - T_w^4) \right] \quad (5.174)$$

where

$$\epsilon_{net} = \left(\frac{1}{\epsilon_b} + \frac{1}{\epsilon_w} - 1 \right)^{-1}$$

where, ϵ_w is the emissivity of the wall of the bed. The degree of blackness of the surface of an inhomogenous fluidized-bed is determined from the following equation [1085]:

$$\epsilon_b = \frac{\Omega}{\Omega^*} \epsilon_p^{0.31} + \left(1 - \frac{\Omega}{\Omega^*} \right) \epsilon_p^{0.485} \quad (5.175)$$

where ϵ_p is the particle emissivity, and Ω^* is the fraction of the heat exchange surface in contact with the bubbles in the maximum inhomogeneity bed, ($\Omega^* = 0.614$). The value of Ω can be calculated from the following formula [1085]:

$$\Omega = 1.56 \frac{Re_b - Re_{m,f}}{Ar^{0.5}} = 1.56 \frac{d_p (U_{g,b} - U_{m,f})}{v_{g,b} Ar^{0.5}} \quad (5.176)$$

$$\text{where } Re_b = \frac{U_{g,b} d_p}{v_{g,b}}, \quad Re_{m,f} = \frac{U_{m,f} d_p}{v_{g,b}}, \quad Ar = \frac{\rho_{g,b} d_p^2 \rho_{bk} g}{\mu_{g,b}^2}$$

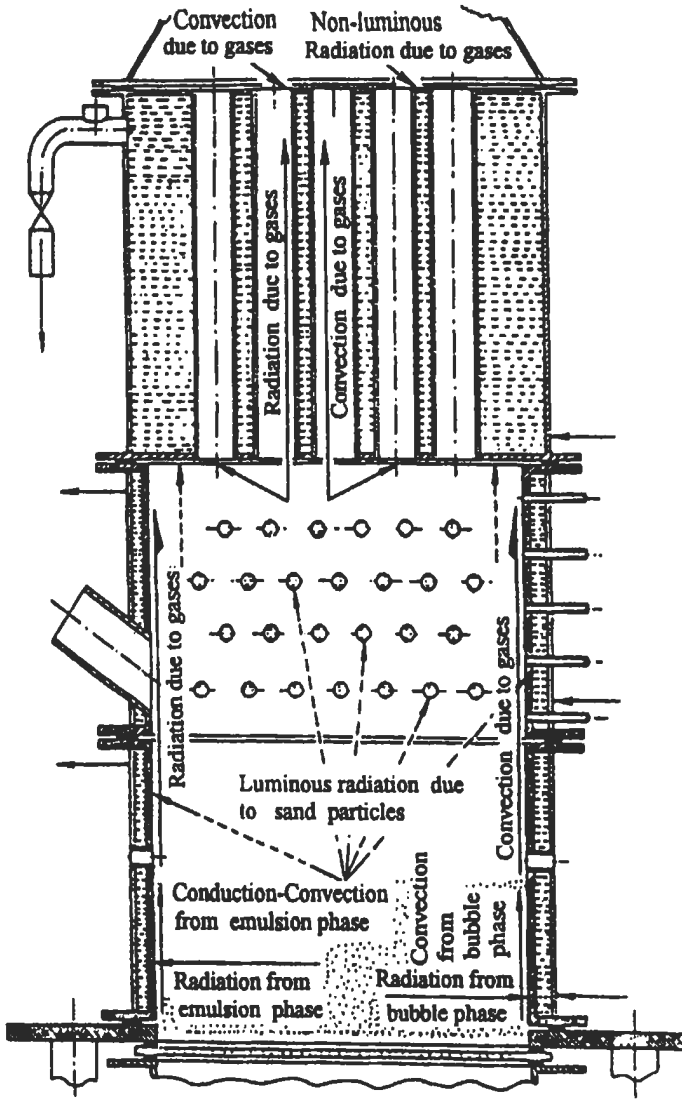


Fig. 5.175 (b): Heat transfer modes to the different stages of the fluidized bed [1115]. Reproduced by permission of John Wiley and Sons Limited.

The bulk density (ρ_{bk}) during the fluidization is calculated from the following equation [1043, 1116]:

$$\Delta P = H_{m,f} (\rho_{bk}) (1 - \gamma_{m,f}) g \tag{5.177}$$

where ΔP is the pressure drop across bed height (hydraulic resistance of the fluidized-bed), and $H_{m,f}$ and $\gamma_{m,f}$ are the bed height and the voidage of minimum fluidization, respectively.

The Reynolds number and Archimeds number are related to each other through the relation [998, 1116] which is used to determine Reynolds number at minimum fluidization.

$$Ar = \frac{150 (1 - \gamma_{m.f})}{\gamma_{m.f}^3} Re_{m.f} + \frac{1.75}{\gamma_{m.f}^3} Re_{m.f}^2 \quad (5.178)$$

The radiative heat transfer, in turn, is divided into radiation in the lean phase where bubbles pass (q_{rl}) and radiation in the dense phase; q_{rd} :

$$q_{rl} = \gamma_B q_{rb} \quad (5.179)$$

$$q_{rd} = (1 - \gamma_B) q_{rb} \quad (5.180)$$

The bubble fraction, or bubble voidage (γ_B), has been dealt with in Ref. 1117. The bubble fraction increases with the bed temperature due to the increase in superficial velocity. The superficial velocity increases with the bed temperature as a result of the decrease in density of gases while the minimum fluidization velocity decreases slightly with increasing operating temperature. This is because the increasing viscosity of the gas is the controlling factor.

The conduction constant in the emulsion phase. The total heat transfer to the fluidizing part wall by combined convective from bubble phase and conduction-convection from emulsion phase, q_{comb} is estimated by subtracting the summation of the convective and radiative heat transfer to the free-board wall, q_f , and the radiative heat transfer to the fluidizing part wall, q_{rb} , from the heat absorbed by the cooling water jacket of the bed and free board, q_{bf} , that is:

$$q_{comb} = q_{bf} - (q_f + q_{rb}) \quad (5.181)$$

The overall heat transfer coefficient (h_{comb}) is calculated by;

$$h_{comb} = \frac{q_{comb}}{A_b (t_b - t_w)} \quad (5.182)$$

For the combined conductive-convective heat transfer due to both emulsion and voidage phases for a large particle in fluidized-beds ($d_p > 1$ mm), the expression proposed by Refs. 1043 and 1042 is considered:

$$Nu_{comb} = \gamma_B [Nu]_B + (1 - \gamma_B) [Nu]_{em} \quad (5.183)$$

where Nu_B is the Nusselt number describing the gas phase convection associated with the bubble, and Nu_{em} is the Nusselt number describing the heat transfer between the emulsion and the wall. Also:

$$Nu_{\text{comb}} = \frac{h_{\text{comb}} d_p}{K_{\text{gb}}} \quad (5.184)$$

The Nusselt number, Nu_B , due to bubble voidage may be estimated using this correlation [1045];

$$Nu_B = 0.664 \left[\frac{(U_B + 3U_{m.f}) d_p}{v_{g,b}} \right]^{0.5} Pr_{g,b}^{0.33} \left(\frac{d_p}{L} \right)^{0.5} \quad (5.185)$$

where U_B is the bubble rise velocity, $U_{m.f}$ is the minimum fluidization velocity, and L is the average bubble length, ($L = H_b$).

Decker and Glicksman [1045] found that for large particles the emulsion phase heat transfer is correlated by:

$$Nu_{\text{em}} = C^* + 0.05 (1 + 2\gamma_B) \frac{U_{m.f}}{v_{gb}} d_p Pr \quad (5.186)$$

where C^* is the conduction constant, and $C^* = Nu_d$ which will be described next.

Mass transfer coefficient of moving particles. As it was previously mentioned about the importance of the interrelationships between heat and mass transfer in fluidized-bed and the effect of each on the other, the coefficient of mass transfer of moving particles in the bed to the enclosing wall is calculated. The average contact time, τ_t in a fluidized-bed is necessarily, first, estimated in the following manner [1118]:

$$\tau_t = \left[\frac{\pi}{6(1 - \gamma_b)} \right]^{1/3} \frac{d_p}{U_p} \quad (5.187)$$

When $(H_b/H_{mf}) > 3$, the prevailing case in this work, the bed voidage (γ_b) is estimated as [1119]:

$$\frac{1 - \gamma_b}{1 - \gamma_{m.f}} = e^{-\left(3gH_b/U_p^2\right)} \quad (5.188)$$

where H_b is the height of the bed and U_p is the mean-particle velocity; estimated as [1105];

$$U_p = U_{m.f} / \gamma_{m.f} \quad (5.189)$$

Secondly, the average film thickness (δ) for turbulent flow regime in the bed is found to be [1118]:

$$\delta = 0.0597 d_p \frac{M^*}{N^*} \quad (5.190)$$

where, $N^* = 0.2902 (d_p/U_p \tau_t)^{0.8} (d_p U_g / \nu)^{0.2}$

and $M^* = [1 + (N^*)^{1.2}]^{1.8} - (N^*)^{1.8}$

Finally, the average mass transfer coefficient of a moving particle from the bed to the wall is given by [1118]:

$$h_D = \frac{2D_v}{\sqrt{\pi D_v \tau_t}} + \frac{\delta}{\tau_t} \left\{ e^{D_v \tau_t / \delta^2} \left[1 - \operatorname{erf} \sqrt{\frac{D_v \tau_t}{\delta^2}} \right] - 1 \right\} \quad (5.191)$$

where D_v is the thermal diffusivity. The particle cooling time τ_c is considered as one of the parameters interrelating the heat and mass transfer in the bed. It is estimated from Fourier number, F_o , as [1120]:

$$F_o = \left(\frac{D_v \tau_c}{d_p^2} \right) = 4.8 \times 10^{-3} (T_w / T_b)^{3.25} (H_b / d_p)^{2.27} \quad (5.192)$$

Experimental and computational results. In this section, the effect of the bed temperature on the characteristics of heat transfer to different parts of the fluidized-bed is discussed and this includes: i) The characteristics of the heat transfer to the bed walls by conduction, convection and radiation, ii) The contact time of a circulating particle between the bed and the walls, iii) The cooling time of a moving particle, and finally an empirical formula describing the total heat transfer coefficient from the bed to the walls is suggested.

Heat transfer to the fluidizing medium and free-board walls. The quantities of the heat transfer to the fluidizing medium and the free-board walls are displayed in Fig. 5.176. The figure shows that the heat transfer to the fluidizing medium wall increases with the bed temperature up to a certain limit, then it decreases with further increase in bed temperature.

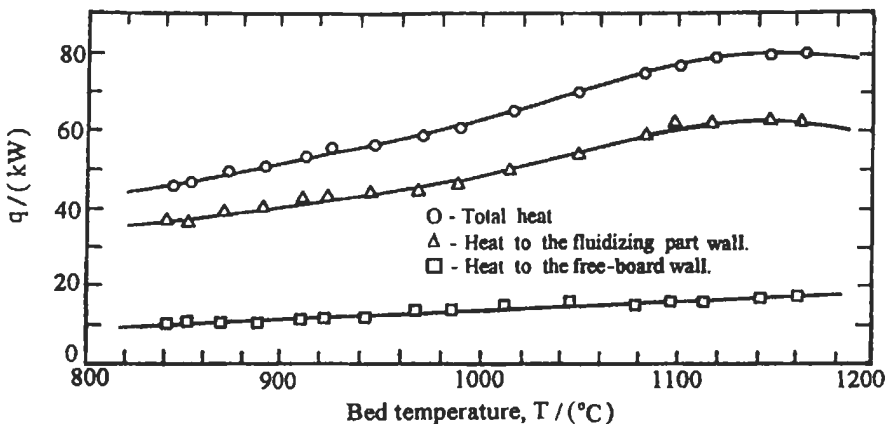


Fig. 5.176: Heat transfer to the fluidizing part and free-board [1114].

The plot of heat transfer coefficient against bed temperature, Fig. 5.177, proved that the coefficient undergoes a maximum value at a bed temperature above which the convection heat transfer coefficient due to emulsion phase decreases again. The increase in heat transfer coefficient is due to the fact that near the walls, the particles motion acts as promoter to erode away any gas film, thus, it reduces its resistance effect. The convective heat transfer coefficient due to bubble phase increases with the increase in the bed temperature.

For the heat transfer to the free-board, the effect of bed temperature on the total heat transfer, the radiative heat transfer due to both sand particles and gases; and the gases convective heat transfer can be studied with the aid of Fig. 5.178. The total radiative heat

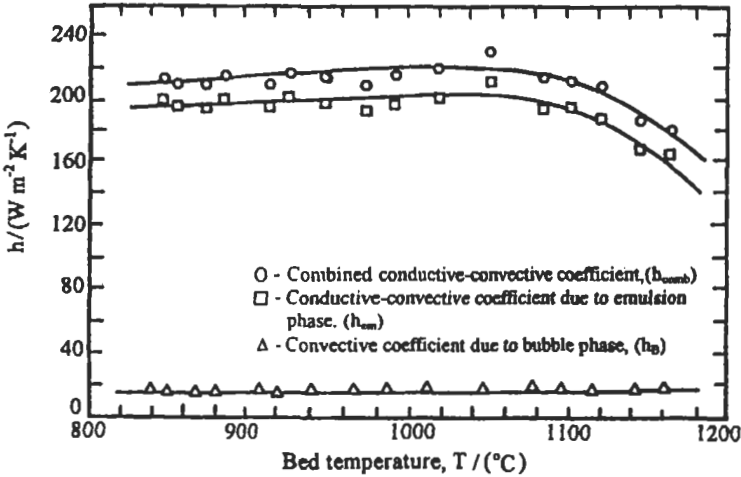


Fig. 5.177: Combined conductive-convective heat transfer coefficients of fluidizing medium walls as a function of bed temperature [1114].

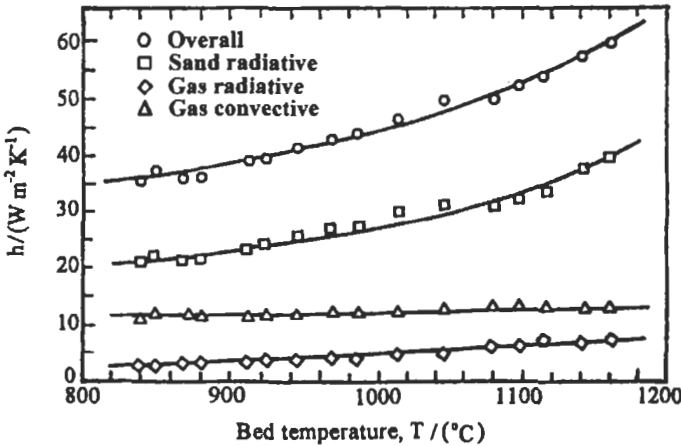


Fig. 5.178: Heat transfer coefficients of free-board walls as a function of bed temperature [1114].

transfer is equal to the sum of the luminous and the nonluminous components. The heat transfer of the luminous radiation depends on the bed temperature and degree of blackness of the surface of an inhomogeneous fluidized-bed, while the heat transfer of the nonluminous radiation depends on the gases emissivity and temperature. Most of these quantities increase by increasing the bed temperature, and consequently, the radiative heat transfer will increase.

Contact and cooling times. The calculations of residence (contact) time and thermal (cooling) time help to interpret the decrease in heat transfer coefficient at bed temperature higher than 1060 °C, (Fig. 5.177). The same phenomenon occurred previously when El-Mahallawy et al [1111] studied, under the same conditions, the heat transfer coefficient between the bed and the immersed coils. It is clear that the contact time increases with the increase of bed temperature (Fig. 5.179). It is, also noted that the cooling time of a particle decreases with the increase of bed temperature up to 1060 °C above which it increases. The initial decrease in cooling time is due to the increase of the bed temperature and the thermal diffusivity at a constant bed height, while the subsequent increase in cooling time is due to the increase in bed height as a consequence of bed temperature.

As for the effect of bed temperature on the convective heat transfer due to emulsion phase, the cooling time and the contact time can be viewed with regards to Figs. 5.177 and 5.178. With the increase of bed temperature, the contact and cooling times of particle converge, while the heat transfer coefficient due to emulsion phase increases. With bed temperature higher than 1060 °C, the reverse takes place. This explains why the heat transfer coefficient decreases when $t_b > 1060$ °C.

The mass transfer coefficient. The mass transfer coefficient of a moving particle increases with the increase of bed temperature, Fig. 5.180. The increase in the mass transfer coefficient is related to the additional relative velocity arising from the terminal velocity of the particle and failure of the particle to respond completely to the oscillations of the fluid. Consequently, the particles act with the fluid to improve the heat transfer between them.

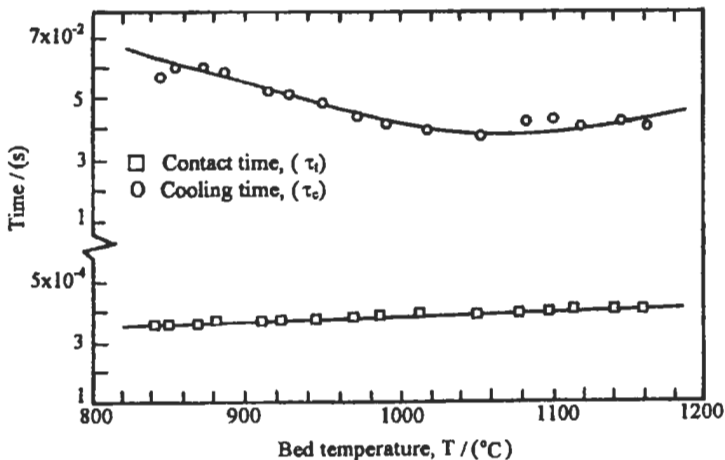


Fig. 5.179: Variation of the average contact time of the fluid masses and the cooling time of the particle with the bed temperature [1114].

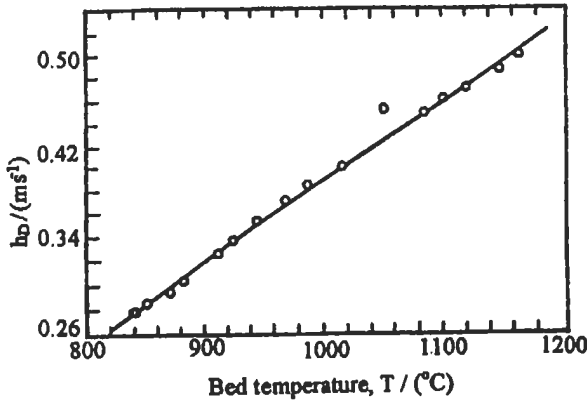


Fig. 5.180: The mass transfer coefficient of a moving particle in the fluidizing medium part as a function of bed temperature [1114].

Empirical formula for the heat transfer coefficients. The Nusselt number describing the heat transfer between the emulsion and the wall consists of two components, the conduction and the convection terms. The conduction term, C^* , is plotted against Archimedes number, Fig. 5.181. It is evident that the conduction term is not constant as it was claimed in the literatures. Decker and Glicksman [1045], proposed that the conduction term is equal to 6 for irregular shaped particles with sphericity much less than unity.

The following correlation is based on the experimental results and is describing the conduction term of the fluidizing part in the bed:

$$Nu_d = C^* = -41.5315 + 0.008 Ar - 4.617 \times 10^{-7} Ar^2 + 8.755 \times 10^{-12} Ar^3 \quad (5.193)$$

The experimental values are found to lie along the calculated values from Eq. 5.193 with a scatter not exceeding $\pm 3.3\%$ (see Fig. 5.181). It is clear that the conduction Nusselt number is not constant in the range of operating bed temperatures. Decker and Glicksman [1045] pronounced that “the conduction constant equals 12, which is halved to approximately 6 for irregular particles with sphericity much less than unity for a range of bed temperatures below 800 °C.

The total heat transfer coefficient could also be correlated by:

$$Nu_t = -15.2567 + 0.0031 Ar - 1.779 \times 10^{-7} Ar^2 + 3.415 \times 10^{-12} Ar^3 \quad (5.194)$$

Figure 5.182 shows the experimental values of the total heat transfer coefficient and those calculated by the above equation with a scatter not exceeding $\pm 3.8\%$.

Heat Transfer to a Horizontal Tube Bundle

The effect of the variation of bed temperature on the characteristics of heat transfer to any array of a horizontal staggered water tube bundle located in the free-board region of a bubbling gas-fired fluidized-bed combustor is shown in Figs. 5.183 and 5.184 with

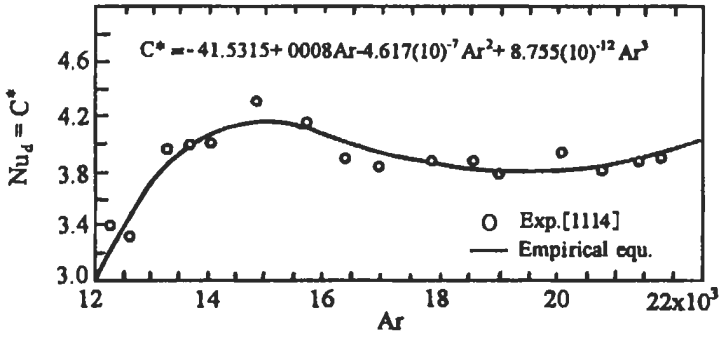


Fig. 5.181: Plot of $Nu_d = f(Ar)$ [1114].

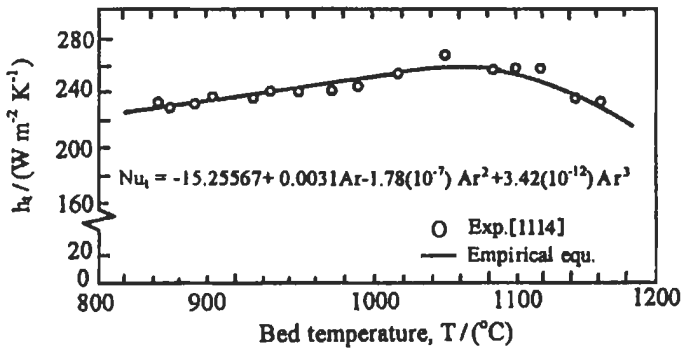


Fig. 5.182: Plot of total wall heat transfer coefficient against bed temperature [1114].

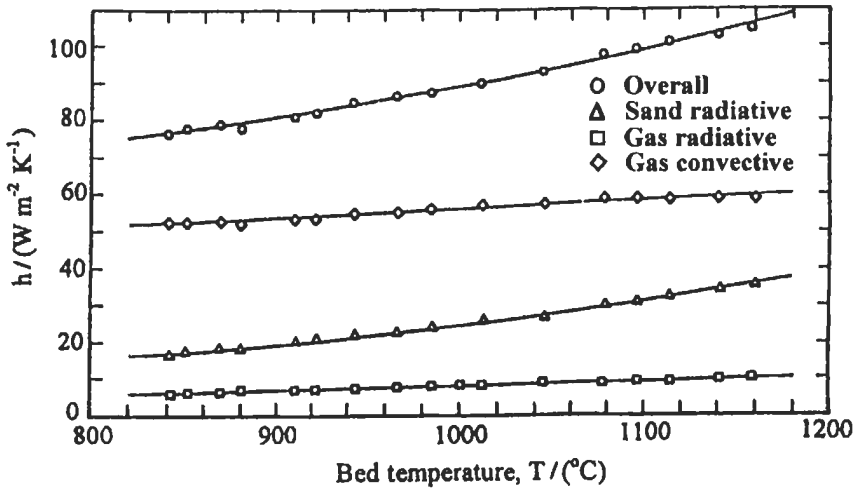


Fig. 5.183: Heat transfer coefficients vs. bed temperature for the first row [1115]. Reproduced by permission of John Wiley and Sons Limited.

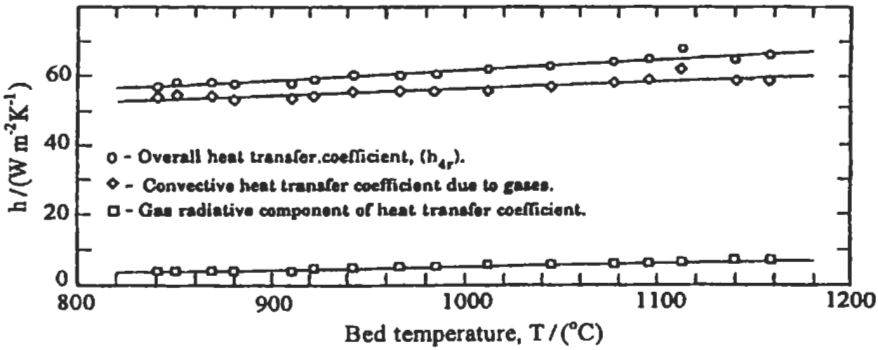


Fig. 5.184: Heat transfer coefficients vs. bed temperature for the fourth row [1115]. Reproduced by permission of John Wiley and Sons Limited.

the contribution of each component of heat transfer to first and fourth rows of the bundle. The heat transfer by gas convection to all rows shows, generally, higher values than those of other radiative components. This means that the superficial gas velocity has more impact on the heat transfer to the bundle. However, the variation of radiative heat transfer from the bed material is more affected by the variation in bed temperature. According to the assumption of Decker and Glicksman [1045] for large particle isothermal beds ($d > 1$ mm as in the above case), the effective emissivity of the bed is a function of particle emissivity, and does not depend on the bed temperature, particle diameter or particle volume fraction. Therefore, the increase in heat transfer by radiation from the bed material to the considered bundle is due to the increase in bed temperature in the first place, and secondly owing to the increase in the view factor between the bed surface and the rows of the bundle. The bed height increases with the increase in bed temperature, so that bed surface is becoming closer to the bundle as the bed temperature increases. The increase in the gas component of radiative heat transfer is mainly due to the increase in gas temperature in the fee-board with the increase of bed temperature.

By accumulating the convective heat transfer to each row, summing up the areas of rows, and calculating the logarithmic mean temperature, the average convective heat transfer coefficient could be obtained. Consequently, the Nusselt number is determined at the average gas temperature. The Reynolds number of gases for each row indicates laminar flow; thus the average magnitude of Reynolds number is estimated and so is the Prandtl number. Owing to the flow pattern of gases over the tubes, the Prandtl number is associated with the exponent $1/3$ [1121]. The resultant formula for the average convective heat transfer coefficient from the bed to the horizontal staggered tube bundle can be correlated by [1115]:

$$Nu = 0.025 Re^{0.92} Pr^{1/3} \quad (5.195)$$

where, $Re = \frac{S_T}{S_T - d_o} U_g d_b / \nu_{g,av.}$, and S_T is the transversal spacing between the tubes, while d_o is the outer diameter of the tube.

Figure 5.185 shows the relation between $Nu/Pr^{1/3}$ and Re with a maximum scatter of $\pm 2.6\%$.

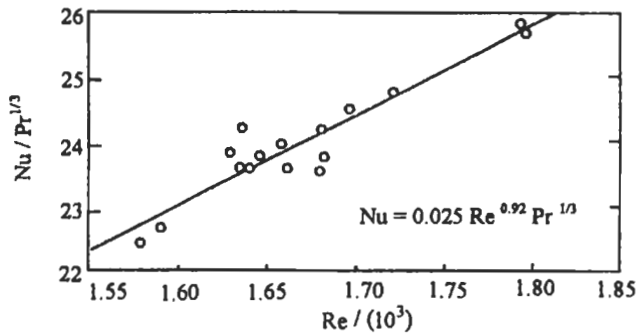


Fig. 5.185: Plot of $Nu / Pr^{1/3}$ vs. Re for the bundle [1115]. Reproduced by permission of John Wiley and Sons Limited.

5.3.6 Emission and Emission Control

This section describes the emission and emission control in FBF, where several investigators have concentrated their work in this field [1122-1151].

Emission

The overall gaseous emission characteristics are now fairly well known from tests in commercial-scale FBC boilers [1122, 1123], but nevertheless, differences between observations in different plants are not readily explained. Table 5.17 shows some representative examples from careful measurements of emissions. Some trends are seen in Table 5.17 with respect to type of combustor: the NO emission is low for CFB in relation to SFB, and also in comparison to pressurized SFB, whereas the relationship is reversed for N_2O . Performance data, such as presented in Table 5.17, can be influenced by changes in a great number of parameters, some of them are illustrated in Fig. 5.186. This figure can be explained as follows [1047]:

Table 5.17: Emission from commercial size FBC boilers burning bituminous coals. Bed temperature around 850 °C, excess air around 25 % average values [1047]. Reproduced by permission of Elsevier Science.

Plant	Nucla [1124]	Örebro [1125]	TVA [1126, 1127]	Värtan [1128]
Type	CFB	CFB	SFB	PFBC
Size, MW _{th}	350	165	500	2 x 200
Fuel, bituminous coal	Salt Creek and local	Polish and English	High sulphur bituminous	Polish
Combustion efficiency, %	98-99	Not given	97*	(> 99) [1129]
Limestone addition @ 90 %	3.0	2.2	2.3*	about 2
Sulphur capture: Ca/S molar ratio				
NO ppm @ 6 % O ₂	70	50	165-180	175
N ₂ O ppm @ 6 % O ₂	100	120	35	12-36
CO ppm @ 6 % O ₂	90	70	150	..**

* For optimum conditions with maximum fly ash recirculation.

** Very low at full load

Parameter (horizontal axis)	Effluent (vertical axis)			
	$1-\eta_o$	SO ₂	N ₂ O	NO
Solids residence time (recirculation)	↘	↘	→	→
Calcium addition, Ca/S molar ratio	→	↘	→	↗
Bed temperature	↘	↘	↘	↗
Excess air	→	→	→	→
Air staging	→	→	→	→
Pressure	→	→	→	→

Fig. 5. 186: Effect of an increase in principal influencing parameters on combustion efficiency and emissions of SO₂, N₂O and NO [1047]. Reproduced by permission of Elsevier Science.

Residence time. Recirculation (CFB) and bed height (PFBC) increase residence time and improve combustion efficiency as well as sulphur capture efficiency, whereas the effect on NO and N₂O is not clear.

Calcium addition. Calcium addition obviously leads to sulphur capture, but it also may somewhat reduce the N₂O emission and raise the NO emission.

Bed temperature. A rise in bed temperature improves burn-up, reduces the N₂O emission, but increases the NO emission, and if the temperature rises substantially above 850 °C, the sulphur capture in an atmospheric combustor will deteriorate.

Excess air. An abundant supply of oxygen is beneficial for combustion and for sulphur capture. Unfortunately, formation of NO and N₂O is enhanced.

Air staging. Air staging may reduce the oxygen supply to zones in the combustor which are important for combustion and sulphur capture and may thus reduce the efficiencies of these processes, whereas it probably leads to some NO reduction. In an SFB combustor, on the other hand, air staging comprises the entire bed; secondary air supplied sufficiently far above the bed is beneficial for NO reduction, but it also increases the probability of reducing condition in the bed, which negatively affects sulphur capture and may lead to corrosion of heat transfer surfaces. In an SFB fired with biofuels, air (or flue gas) supply to the free-board is necessary to provide mixing for burn-up of volatiles [1047].

The use of low calorific value or high sulphur content coal mixed with biomass is interesting due the complementary properties of the two fuels, since, as opposed to the typical characteristics of low quality coals, biomass has low ash and sulphur contents, and a high volatile concentration that is favorable to a clean combustion of the coals under consideration. With the scope of this concept, Kakaras et al [1148] have performed a series of experiments in a lab-scale Atmospheric Bubbling Fluidized-Bed Combustor (ABFBC), using the fossil fuels of Megalopolis pre-dried lignite and

Götteborn hard coal with biomass material, i.e. wood matter from pressed oil-stone (WPOS) and straw. During the trials, the applicability limits of the coal partial substitution by biomass as a function of the excess air ratio were determined, taking also into account the special features of the combustion technology used. In this way, the effects on combustion behavior, flue gas emissions, volatiles release, residual matter and the ash tendency for agglomerates and deposits formation were thoroughly examined. The obtained results showed that co-combustion is technically feasible and could be extended in large-scale firing installations, provided that difficulties arising mainly from the ash melting in high temperatures can be industrially confronted.

The emissions of CO, SO₂, NO_x and N₂O in relation to the biomass percentage in the fuel blend with parameters; the excess air ratio, and the Ca/S ratio are illustrated in Fig. 5.187, in order to evaluate the combustion behavior of the two biomass fuels, when these are burned in combination with pre-dried lignite. Combustion efficiency can be well characterized by the emissions and mostly by the unburnt fuel content of the ash and the CO emission. Specifically, when the biomass percentage in the fuel blend is increased [1148]:

- CO emission is decreased until the WPOS presence in the blend reaches up to 20 % and it can be controlled when the excess air ratio ranges from 1.58 (7.7 % O₂) to 1.69 (8.5 % O₂). The relevant range for the case of straw is 1.7 (8.6 % O₂) / 1.8 (9.3 % O₂). Generally, the CO emission control is directly dependent on the combustion conditions (fluidizing velocity, mixing, temperature, particle size) and the appropriate excess air ratio for each fuel blend.
- SO₂ emission is reduced due to the low S-content of the biomass materials and the greater sulphur retention, arising from the enhanced CaO & MgO percentages in the ash composition. The only exception was the blend of 80 % lignite-20 % WPOS, where the SO₂ values were higher than the reference case and this could be connected to the lower Ca/S ratio and consequently the decrease of the natural desulphurisation rate.
- NO_x emissions are increased when WPOS is burned with pre-dried lignite and the opposite will happen when straw is used. This is mainly caused by the different percentages of nitrogen in the biomass fuels, which is the major source for NO_x formation in fluidized-bed combustion, where the temperature is low.
- N₂O emission is reduced or remains at the same level for all the test cases despite the different biomass nitrogen contents. The determinant factor for this reduction is the improved ignition and the subsequent improvement of the combustion efficiency, as the temperature increases in much higher rate [1151].

The effect of combustion of coal blends on the emissions in fluidized-bed reactor has been investigated by Boavida et al [1149]. Five blends prepared by mixing two coals based on their petrological characterization, in varying amounts, were selected to study the possibility of reducing NO_x, N₂O, and SO₂ emissions. The results showed that some blends have the opposite behavior concerning the release of NO_x and SO₂ in relation to parent coals, and the emissions were higher than expected. The N₂O amounts observed in almost all blends tested, were found to be lower than the predicted values [1149]. With some blends, the mixing levels intended to reduce SO₂ were not always found to correspond to those for simultaneous decrease of NO_x (see Figs. 5.188 to 5.191. Figures 5.188 and 5.189 show the dependence of the release of NO_x and N₂O with fuel ratio, that is Fixed Carbon / Volatile Matter, and fuel N / C ratio, at T = 780 °C.

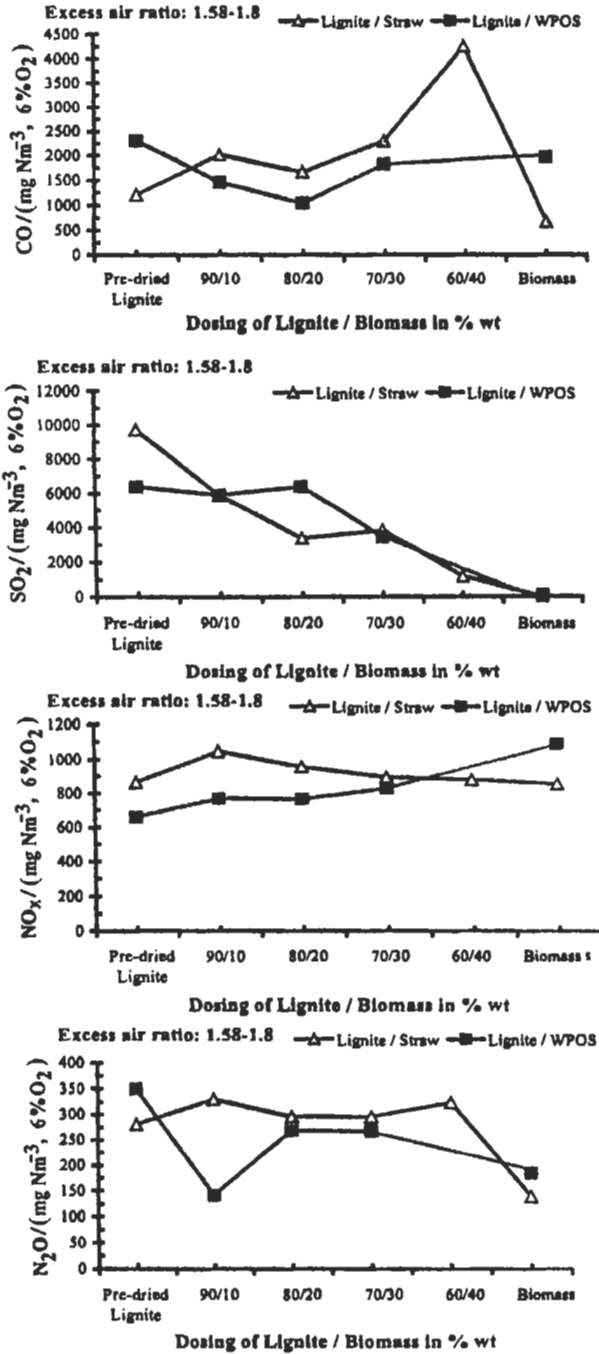


Fig. 5. 187: CO, SO₂, NO_x, N₂O emissions in relation to the pre-dried Lignite/biomass (WPOS & Straw) percentages in the fuel blend with parameters, the excess air ratio, and the Ca/S ratio. Emmanuel Kakaras, NTUA [1148], reproduced by permission.

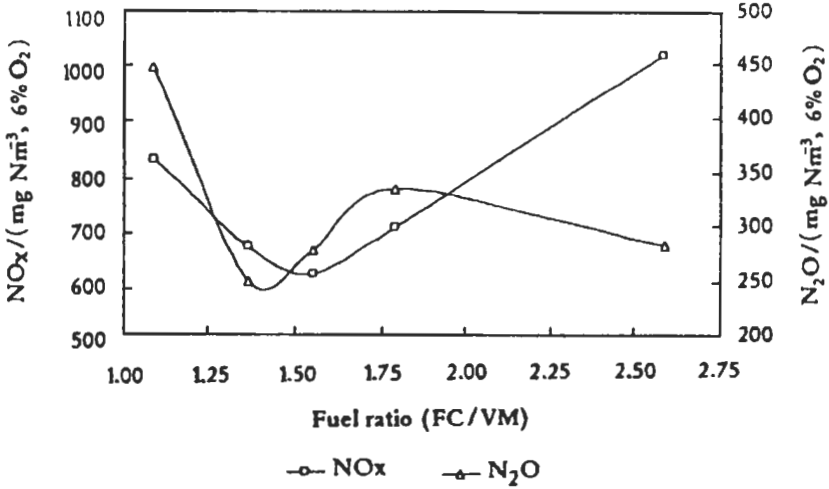


Fig. 5. 188: NO_x and N₂O emissions of the five single coals versus fuel ratio (Fixed carbon/Volatiles) for T = 780 °C. Ibrahim Gulyurtlu et al [1149], reproduced by permission.

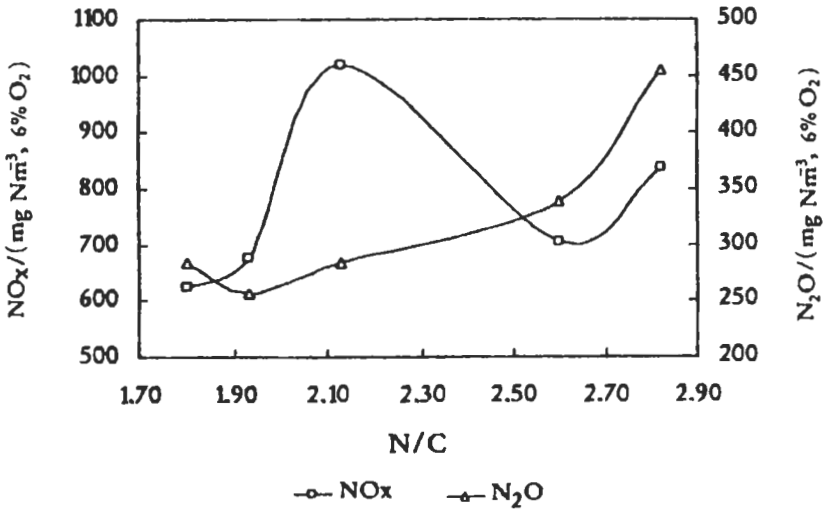


Fig. 5. 189: NO_x and N₂O emissions of the five single coals versus Nitrogen / Carbon ratio (N/C) for T = 780 °C. Ibrahim Gulyurtlu et al [1149], reproduced by permission.

It can be seen that fuel ratio is a very important factor in NO_x emissions and values between 1.25 and 2.0 appear to minimize the amounts of NO_x released. Furthermore, there is an optimum value, around 1.6, that could be taken as a reference. For N₂O, it is the N/C ratio that appears to be more influential and gives a better correlation with levels formed. At 780 °C, when N₂O emission was found to be higher, increasing values were recorded with a rise in N/C ratio. In Figs. 5.190 and 5.191, it can be seen that N₂O emissions increases with the increment of coal C5 in the mixture which is the coal with higher nitrogen content and higher N/C ratio as in the blend B2. Also, SO₂ emissions

increase with the increment of the coal with higher sulphur content (C1) in the blend, as can be seen in Table 5.18. This suggests that an opposite tendency exists concerning the released amounts of SO₂ and NO_x, thus turning impossible any attempt to reduce both emissions at the same time by varying the composition of the blends prepared as based on their petrological nature. They [1149] indicated that the petrological characterization to optimize the blend mixture was done to increase the reactivity which could fail in satisfying simultaneous removal of both SO₂ and NO_x with equal efficiency.

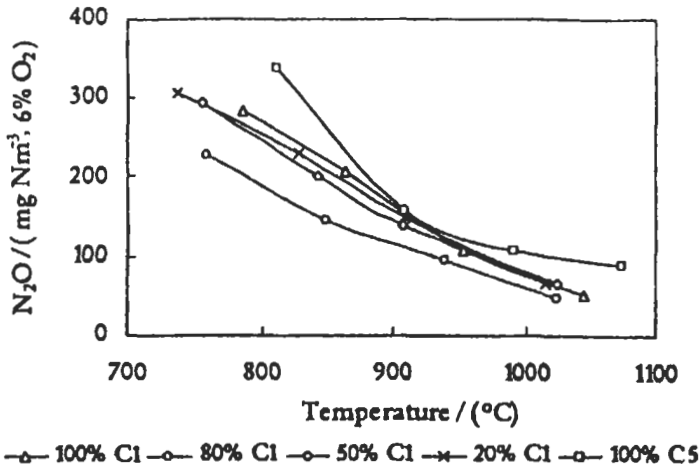


Fig. 5. 190: N₂O emissions of the different composition mixtures tested for blend B₂ versus temperature. Ibrahim Gulyurtlu et al [1149], reproduced by permission.

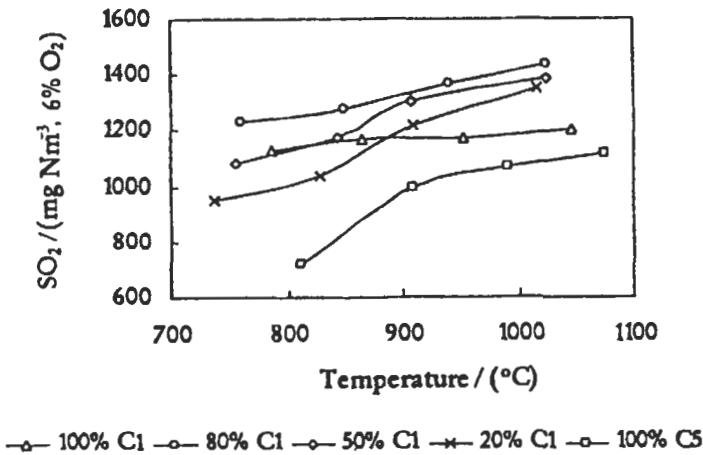


Fig. 5. 191: SO₂ emission of the different composition mixtures tested for blend B₂ versus temperature. Ibrahim Gulyurtlu et al [1149], reproduced by permission.

Table 5.18: Ultimate (daf, % wt) and proximate (db, % wt) analyses of individual coals. Ibrahim Gulyurtlu et al [1149], reproduced by permission.

Samples	C1	C2	C3	C4	C5
C	84.87	82.01	79.03	76.29	80.45
H	5.09	5.83	4.43	5.04	4.96
N	1.53	1.58	1.68	2.15	2.09
S	1.08	0.86	0.62	1.74	0.77
O	7.43	9.72	14.24	14.78	11.73
Volatiles	33.78	38.61	23.24	25.76	32.21
Fixed Carbon	52.26	52.51	60.27	28.20	57.59
Ash	13.96	8.88	16.49	46.04	10.23

The behavior of multicomponent briquettes, prepared by mixing two different particle sizes of coal and two different types of binder species has been investigated by Boavida et al [1150]. They burn single briquettes over a wide range of temperatures in a laboratory scale fluidized-bed combustor facility. Nitrogen (NO_x and N_2O) and sulphur (SO_2) oxides emissions resulting from the combustion of these briquettes were constantly monitored during the time of burning. The levels of O_2 , CO_2 and CO were also recorded during the same period. Their [1150] experimental results showed that coal particle size influenced burnout times and emission levels of some gaseous species.

Combustion tests [1150], with briquettes prepared using cement binder, showed a breakage tendency with an increase in temperature. Below 800°C , the breakdown of briquettes was not found to occur, however, at higher temperatures, it was observed a faster disintegration process that was enhanced as the temperature increased. This phenomenon appeared to take place with both fine cement briquettes (BCf) and coarse cement briquettes (BCc), and influenced the gaseous emission pattern. At relatively higher temperatures (880 and 950°C), two peaks were observed in the NO_x , N_2O and SO_2 emission profiles (as given in Figs. 5.192, 5.193, and 5.194) as functions of reaction time. This may be explained by the physical mechanical behavior of these briquettes, during the combustion process. When the briquette starts to burn, there is an increase of amounts of gaseous pollutants resulting from the rise of temperature due to the burning of the surface of the briquettes. It appears that there was a quick release of gaseous volatiles, which were rapidly oxidized. Then, at higher temperatures, with the surface burned away and due to internal stresses resulting from the temperature evolution inside briquette, it appears that the structure collapses resulting in formation of fine particles which increase the superficial area available for oxidation reaction.

Under reducing atmospheres near the fine particles, which resulted from the collapse of the briquette, with oxygen no longer available to react with fuel-N and fuel-S, it is possible that reactions leading to reduction of NO_x , N_2O , and SO_2 , start to take place; thus forming the first peak observed for these pollutant gases. During this period the fuel-N and fuel-S are probably converted mainly to HCN , NH_3 , N_2 , and H_2S ; their reduced species. With the gradual decrease in the carbon content as a result of the combustion of fine particles, once again, the level of oxygen begins to increase which could then give rise to mostly gas phase oxidation of the nitrogenous and sulphur species, which could result in further formation of gaseous pollutants, thus the second

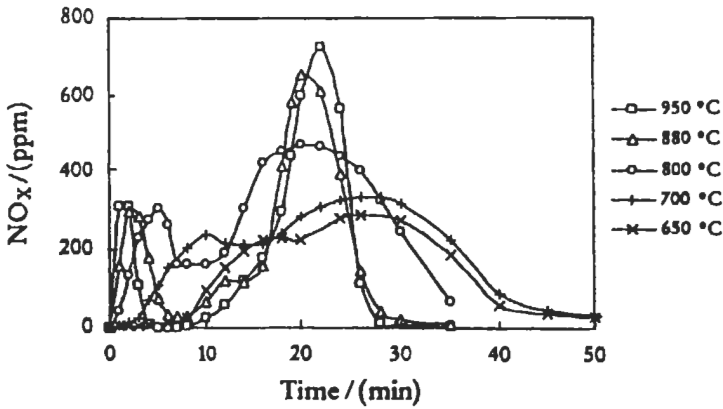


Fig. 5. 192: NO_x emission for the five initial set furnace temperatures tested for BCf briquettes, in ppm units. Ibrahim Gulyurtlu et al [1150], reproduced by permission.

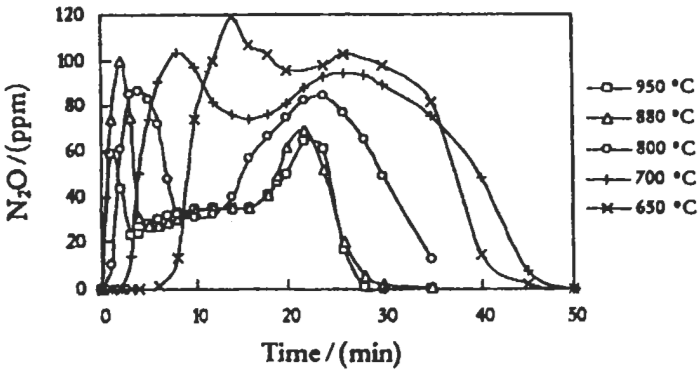


Fig. 5. 193: N₂O emissions for the five initial set furnace temperatures tested for BCf briquettes, in ppm units. Ibrahim Gulyurtlu et al [1150], reproduced by permission.

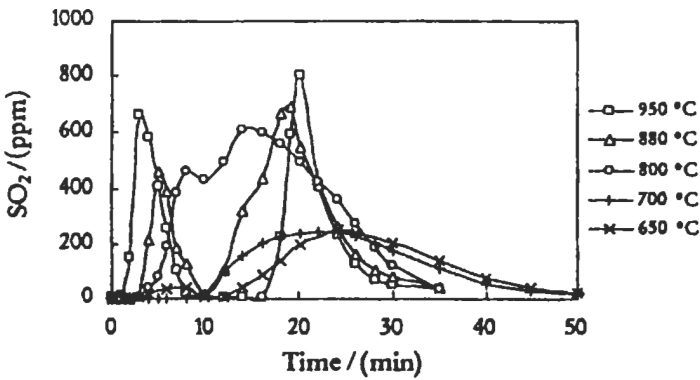


Fig. 5. 194: SO₂ emissions for the five initial set furnace temperatures tested for BCf briquettes, in ppm units. Ibrahim Gulyurtlu et al [1150], reproduced by permission.

peak appears. This second peak is normally higher, because it represents a longer combustion period. It can also be seen, in NO_x and SO_2 emission profiles, that peak values increase with temperature. At pre-set temperatures equal or above 800°C , the CO emissions consist in a single peak, which increases with a rise in temperature, along the period during which the oxygen is deficient combustion period. However, at temperatures below 800°C , CO emissions form two peaks. One at the initial period and the other at the final end period of combustion as shown in Fig. 5.195.

Emissions Control

Reduction of emissions by measures taken in the combustion chamber is one of the principal reasons for employing the fluidized-bed concept for combustion. Considering combustion efficiency, sulphur capture by limestone, and nitric oxide emissions, the optimum condition for an atmospheric pressure combustor at full load operation is characterized by a bed temperature of about 850°C and an excess-air ratio at, or slightly above 1.2 as described above. Pressurized combustors have basically the same conditions, but the optimization also concerns gas turbine requirements. When the emission of N_2O from coal combustion was discovered, the conditions for optimization changed, since the N_2O emission is high at 850°C and becomes lower at higher temperatures, opposite to NO and sulphur capture (Fig. 5.196). Therefore, it is important to reduce the N_2O emission without negatively affecting the emissions of NO and SO_2 . The following presents the application of the emission control method (described in chapter 1) in the CFB and PFB.

NO_x , N_2O , and CO emissions control. The NO_x emission from coal firing in FBF is generally lower than the emission from powder-coal-firing combustors. NO_x emissions between 200 ppm and 500 ppm are found in literature, and these values are decreasing with increasing installation size. The relatively low NO_x emission is partly due to the low combustion temperature. In the U.S.A, the standard for new coal-burning power plants is 360 ppm of NO_x for bituminous coal, and 300 ppm of NO_x for sub-bituminous coal. The NO_x emissions from industrial FBF meet these standards.

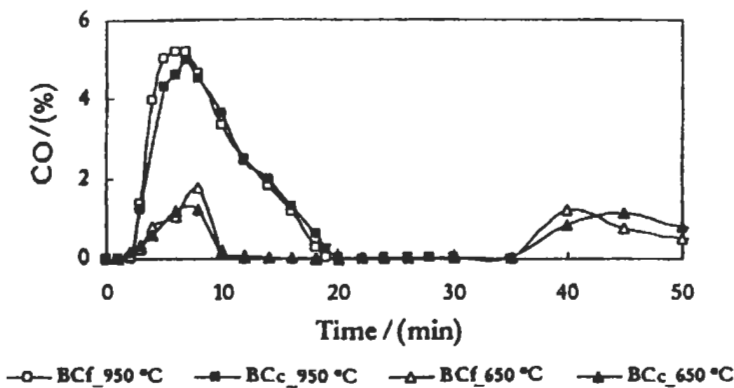


Fig. 5.195: CO profile emissions at initial set furnace temperature of 950 and 650°C for BCf and BCc briquettes, in % (v/v) units. Ibrahim Gulyurtlu et al [1150], reproduced by permission.

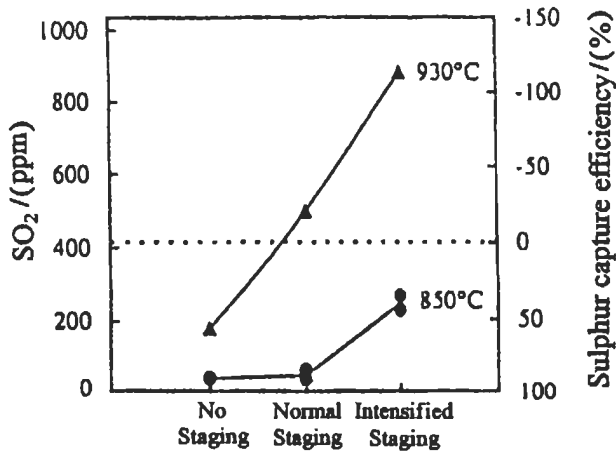


Fig. 5.196: SO₂ emission (or desulphurization efficiency η_s) for three cases of air supply at 850 °C and 930 °C at a constant total excess-air ratio of 1.2 and Ca/S = 3. Negative desulphurization efficiency means excess sulphur emission [1130]. Cited by Leckner [1047].

There are different common techniques which can be applied to reduce N₂O in CFB and PFB, and these techniques are as follows [1047]:

1. High bed temperature and/or low excess-air ratio in the combustion chamber. This technique affects both formation and destruction of N₂O and leads to a reduction of the N₂O emission. It normally increases the NO emission, which has to be handled by ammonia injection in the flue gases or by some other flue-gas treatment. Also, the SO₂ emission will be higher for a given limestone addition. Figure 5.196 shows that at a bed temperature of 930 °C and a normal air staging, there was no sulphur capture at all, despite limestone addition. This is due to a greater impact of reducing conditions in the bed at high temperature [1047]. However, from a thermodynamic point of view there is no limitation for sulphur capture at this temperature level as long as there is an excess air, as shown in Fig. 5.197, so a sufficiently good sulphur retention could have been achieved if the oxygen distribution in the bed had been even and reducing regions had been absent.
2. Change of air supply to the combustion chamber under otherwise normal conditions. This technique affects the combustion chamber processes directly by the arrangement of the air supply. Part of the total air is normally added to the combustion chamber as secondary air, few meters from the bottom. The bottom part of the combustor is then nominally substoichiometric. A case where all air is supplied from the bottom differs from a normal staging case by an improved capture of SO₂ and an enhanced emission of NO, where the effect on N₂O is small [1131]. Moreover, the N₂O formed there is mostly reduced on its way through the combustion chamber [1132], which is, as shown in Fig. 5.198, to some extent the case also for NO. However, reversed air staging has been proposed by Refs. 1134 and 1135. According to this strategy, stoichiometric air is supplied to the bottom of the combustion chamber, and the excess air is added in connection to the cyclone. This enhances sulphur capture

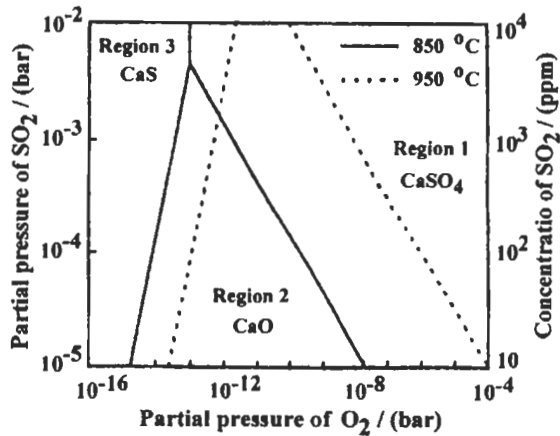


Fig. 5.197: Phase diagram for the system: CaO, CaS, CaSO₄, SO₂, and O₂ [1146]. Reproduced by permission of Elsevier Science.

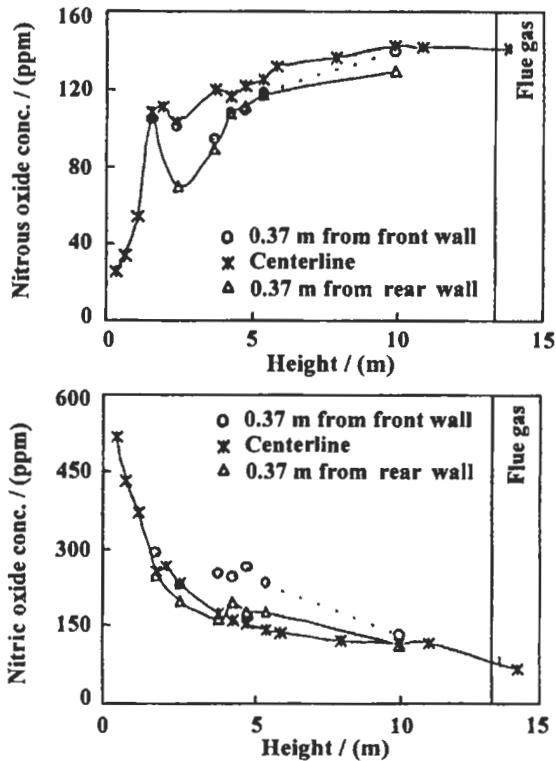


Fig. 5.198: Concentration of gases in a CFB combustion chamber on the centerline, 0.87 m from the wall, 0.87 m from the walls during combustion of bituminous coal [1133]. Data: bed temperature 850 °C, excess air 20 %, air fractions of primary and secondary air 0.65/0.35, fuel mass mean size 6mm, volatile content (dry and ash-free) 40 %. Gas concentrations are given in ppm as measured. No limestone was added [1132]. Reproduced by permission of Elsevier Science.

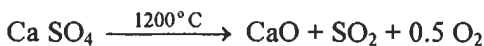
and yields a slightly higher NO concentration in the bottom zone. In the upper zone, after the main combustion activity, oxygen concentration has become low and so is the formation of N₂O, whereas NO and SO₂ finally reach about the same levels as during normal staging. In this case the N₂O concentration could be reduced to one-fourth (25 ppm) in a test case, without significantly changing the other emissions.

3. Normal operation conditions in the bed, but high temperature and/or low excess air in a special combustion space in a particle-free zone of the flue gas dust. In order to investigate this method, additional fuel (gas, oil, wood or coal) was burned in the cyclone of a CFB boiler [1136, 1137], where the particles are mostly found at the walls. An acceptable level of N₂O (less than 30 ppm) could be reached by a fuel addition corresponding to 8 % of the total fuel supplied to the boiler. Fuel injection into the free-board of a stationary FBC [1138] achieves a high N₂O reduction and some NO reduction by operating the bed sub-stoichiometrically in an air-staging procedure.
4. Addition of bed material that could work as a catalyst to influence formation and destruction of N₂O in the combustion chamber. MgO has been proposed as a catalyst [1139]. The activity of MgO is lower than that of CaO, but the material is not influenced by SO₂. Another catalyst that was investigated by Shimizu et al [1140] is Fe₂O₄, and this catalyst not only enhances the formation of NO, as do CaO and MgO, but in contrast to the other materials it hardly affects the formation of N₂O.
5. Two-stage combustion. The concept of two-stage FBC [1141] has been suggested [1142] for N₂O reduction in connection with stationary FBC. Coal is burned in the lower bed without limestone. Sulphur capture takes place in the upper bed consisting of lime. This lime also serves for reduction of N₂O, similarly to the above proposal. With total air supply to the bottom bed almost 50 % reduction of N₂O was attained in the upper bed, but with air staging the reduction increased to 80 % for unchanged 90 % sulphur capture [1142], and NO was greatly reduced.
6. The emission of carbon monoxide from CFB plants is not generally perceived to be a major problem. It is normally below the statutory limit. The emission depends on the fuel composition and the combustion temperature, particularly below 800 °C. Typical levels of emission are in the range of 15-200 ppm, as compared to 200-400 ppm in stoker-fired boilers.

Sulphur capture. The most important advantage of fluidized-bed combustion is the concurrent removal of the sulfur dioxide, SO₂, that results normally from the combustion of the sulfur content in the coal. Desulfurization is accomplished by the addition of limestone directly to the bed together with the crushed coal. Limestone is a sedimentary rock composed mostly of calcium carbonate (Ca CO₃) and sometimes some magnesium carbonate (Mg CO₃).

A high temperature must be avoided for two reasons;

1. Calcium sulphate begins to decompose and release SO₂ by:



2. In the region of 1400 °C thermal fixation of nitrogen occurs to produce NO_x; this may be 40 % of the total emission.

Table 5.17 shows that 90 % sulphur capture can be achieved by addition of a little more than twice the stoichiometric amount of calcium. For high sulphur coals, higher sulphur capture efficiencies may be desired, and higher limestone feed rates than a molar ratio of two are necessary. In atmospheric pressure combustors, the partial pressure of CO_2 is low enough for the limestone to calcine ($\text{CaCO}_3 \rightarrow \text{CaO} + \text{CO}_2$), but at high pressure applications, as seen from Fig. 5.199, the material does not calcine at a normal combustor temperatures, except in zones where combustion has not yet produced a sufficient CO_2 concentration [1143, 1144]. In the presence of oxygen, sulphation binds the SO_2 released by combustion ($\text{CaO} + \text{SO}_2 + \frac{1}{2} \text{O}_2 \rightarrow \text{CaSO}_4$). Under pressurized conditions, the limestone has normally not calcined and direct sulphation occurs ($\text{CaCO}_3 + \text{SO}_2 + \frac{1}{2} \text{O}_2 \rightarrow \text{CaSO}_4 + \text{CO}_2$). The rate of this reaction is maximum at a bed temperature between 815 and 870 °C, though a practical range of operation of fluidized-beds of 750 to 950 °C is common.

The initial porosity, as well as the presence of pores developed by calcination, has a decisive effect on the rate and capacity of SO_2 capture. However, the pores formed by calcination will be closed by the resulting CaSO_4 , since it has a larger molar volume ($46 \text{ cm}^3 \text{ mole}^{-1}$) than calcium carbonate ($36.9 \text{ cm}^3 \text{ mole}^{-1}$), and diffusion through a more or less dense product layer is a characteristic feature of sulphation under both atmospheric and pressurized conditions, as shown in Fig. 5.200 [1147]. The porous structure formed by calcination gives an initial advantage for the calcined stone compared to the directly sulphated one, as shown in Fig. 5.201, where sulphation of different types of limestone is compared in a thermobalance at 1 bar and 15 bar, exposed to combustion gases [1145]. The figure shows that for particle size range (200 - 400 μm), the directly sulphated limestone becomes more converted than the calcined one at longer exposure time.

Mjörnell et al [1147] have tested two limestones, 0.7 mm in size in a laboratory reactor, one size is a porous reactive, and another is a crystalline, and low-reactive, and both yielding conversions of 0.37 and 0.09 respectively as shown in Fig. 5.202. The limestones were used with the same coal in two atmospheric CFB boilers (40 and 165 MW) [1147].

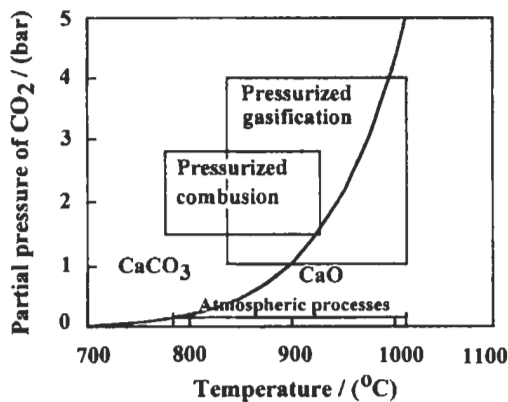


Fig. 5.199: Phase diagram. Equilibrium CO_2 partial pressure as a function of temperature [1143]. Regions of operation for various fluidized bed conversion processes are indicated. Cited by Leckner [1047].

The conversions obtained in the boiler were 0.4-0.45 for the reactive limestone, and slightly less for the unreactive one; considerably higher than in the laboratory. This is due to that the particles, originally having a mean size of 0.7 mm, breakdown into smaller pieces, but nevertheless remain for a sufficiently long time in the bed [1147].

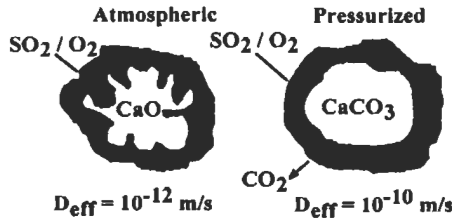


Fig. 5.200: Comparison of sulphation under atmospheric and pressurized conditions [1144, 1146]. Reproduced by permission of ASME.

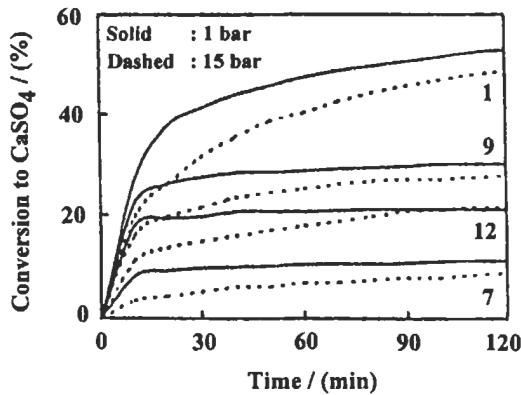


Fig. 5.201: Comparison of conversion to CaSO₄ for various limestones (numbered 1, 7, 9 and 12) measured in a thermobalance at 850 °C. Gas composition 0.3 % SO₂, 4 % O₂, 10 % CO₂ (1 bar) or 20 % CO₂ (15 bar), remainder N₂. Particle sizes 200-400 μm [1145]. Reproduced by permission of Elsevier Science.

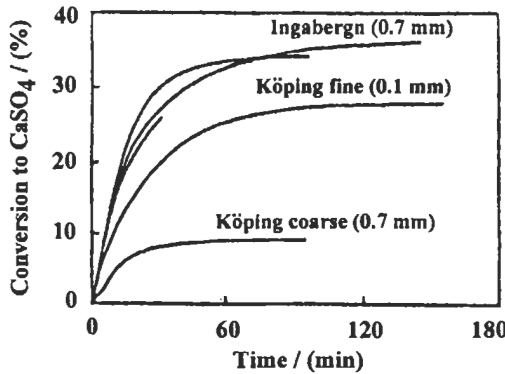


Fig. 5.202: Limestone conversion measured in a differential reactor. 10 % CO₂, 4 % O₂, 1500 ppm SO₂, temperature 850 °C, pressure 1 bar [1147]. Reproduced by permission of ASME.

Appendix A
Conversion Factors and Constants
(Tables A1 and A2)

Table A1: Conversion factors and constants

Quantity (length, area, volume...etc.)	Conversion	
	Symbol	Equivalence
Length	1 in	0.254×10^{-2} m
	1 ft	0.3048 m
Area	1 in ²	6.45×10^{-4} m ²
	1 ft ²	9.29×10^{-2} m ²
Volume	1 in ³	16.39×10^{-6} m ³
	1 ft ³	0.02832 m ³
	1 gal	$0.1605 \text{ ft}^3 = 4.546 \times 10^{-3} \text{ m}^3 = 4.546$ litre
	1 USgal	$0.1337 \text{ ft}^3 = 3.785 \times 10^{-3} \text{ m}^3$
Acceleration	Standard gravity	9.807 m s^{-2}
	ft s ⁻²	3.048 m s^{-2}
Density	1 b ft ⁻³	16.02 kg m^{-3}
	1 Slug ft ⁻³	515.4 kg m^{-3}
	1 lb in ⁻³	$27.68 \times 10^3 \text{ kg m}^{-3}$
Thermal conductivity	1 Btu ft ⁻¹ h ⁻¹ R ⁻¹	$1.731 \text{ J m}^{-1}\text{s}^{-1}\text{°C} = 1.731 \text{ W m}^{-1}\text{K}^{-1}$
	1 Cal cm ⁻¹ s ⁻¹ K ⁻¹	$418.7 \text{ J m}^{-1}\text{s}^{-1}\text{°C} = 418.7 \text{ W m}^{-1}\text{K}^{-1}$
Mass	1 lb	0.4536 kg
	1 slug	$32.17 \text{ lb} = 14.59 \text{ kg}$
	1 ton	$2240 \text{ lb} = 1016 \text{ kg}$
Force	1 lbf	9964 N
	1 kgf	$2.205 \text{ lbf} = 9.807 \text{ N}$
	1 dyne	10^{-5} N
Velocity	1 mile h ⁻¹	$1.467 \text{ ft s}^{-1} = 1.609 \text{ km h}^{-1}$
	1 knot	$1.689 \text{ ft s}^{-1} = 1.853 \text{ km h}^{-1}$
Pressure	1 bar	$10^5 \text{ Pa} = 14.5 \text{ lbf in}^{-2}$
	1 lbf in ⁻²	$0.07031 \times 10^{-1} \text{ kgf m}^{-2}$
	1 kgf cm ⁻²	0.9807 bar
	1 lbf ft ⁻²	47.88 N m^{-2}
	1 ft H ₂ O	$62.43 \text{ lbf ft}^{-2} = 2989 \text{ N m}^{-2}$
	1 mmHg	$1 \text{ torr} = 133.3 \text{ N m}^{-2}$
	inHg	$3.386 \times 10^3 \text{ Pa}$
Energy, work, heat	Btu	$1.055 \times 10^3 \text{ J} = 525$ calorie
	ft-lbf	1.356 J
	erg	$1 \times 10^{-7} \text{ J}$
	calorie	4.182 J
	1 kWh	3.6 MJ
	1 hph	2.685 MJ
	1 lbf ft	1.356 N m
Torque	1 tonf ft	3037 N m
	1 ft ³ min ⁻¹	$4.719 \times 10^{-4} \text{ m}^3 \text{ s}^{-1}$
Flow rate	1 gal min ⁻¹	$7.577 \times 10^{-5} \text{ m}^3 \text{ s}^{-1}$
Temperature	1 F (T _F)	$T_C = (T_F - 32)/1.8$ (°C)
	1°C (T _C)	$T_K = T_C + 273$ (°K)
	1 F (T _F)	$T_K = (T_F + 460)/1.8$ (°K)
	1 R (T _R)	$T_K = T_R/1.8$ (°R)
Viscosity, kinematic	centistoke	$10^{-6} \text{ m}^2 \text{ s}^{-1}$
	stock	$10^{-4} \text{ m}^2 \text{ s}^{-1}$
Viscosity, dynamic	ft ² s ⁻¹	$0.0929 \text{ m}^2 \text{ s}^{-1}$
	centi-poise	10^{-3} Pa
	(1 poise = 1 g cm ⁻¹ s ⁻¹)	
	1 lb ft ⁻¹ s ⁻¹	1.488 Pa s
1 slug ft ⁻¹ s ⁻¹	47.88 N s m^{-2}	

Table A2 (a): Physical constants.

Quantity	Conversion value
Universal gas constant	8.314 kJ kgmole ⁻¹ K ⁻¹
Standard acceleration of gravity	9.8066 m s ⁻²
Joule's constant	4.184 x 10 ⁷ erg cal ⁻¹
Avogadro's number	6.02 x 10 ²³ molecules g-mole ⁻¹
Boltzmann's constant (Universal gas constant / Avogadro's number)	1.38 x 10 ⁻¹⁶ erg molecule ⁻¹ K ⁻¹
Faraday's constant	9.625 x 10 ⁴ abs-coulombs g-equivalent ⁻¹
Planck's constant	6.62 x 10 ⁻²⁷ erg s
Stefan-Boltzmann constant	1.355 x 10 ⁻⁸ cal s ⁻¹ m ⁻² K ⁻⁴
Electronic charge	1.602 x 10 ⁻¹⁹ abs-coulomb
Speed of light	2.9979 x 10 ⁸ m s ⁻¹

Table A2 (b): Energy units and energy content of fuels.

1 Ton crude oil (1 Ton crude oil=7.3 barrel oil)	42 GJ (Giga Joule)
1 Ton LNG (Liquefied Natural Gas)	46 GJ
1 Ton LPG	47.1 GJ
1 Ton fuel oil	40.7 GJ
1 Ton kerosene	45.5 GJ
1 Ton gasoline	46.2 GJ
1 Ton coal	28.0 GJ
1 Ton wood	16 GJ
10 ³ kWh	3.6 GJ or 9.36 GJ (based on conversion efficiency of 0.385)
1000 m ³ NG (at standard condition and low calorithic value)	36 GJ
1 Thermal natural gas	0.1055 GJ (10 ⁵ Btu)
1 Ton Uranium	10 ⁴ Ton crude oil (based on normal reactor), 5x10 ⁵ Ton crude oil (based on fast reactor)
Quad	1.055x10 ¹⁸ J (10 ¹⁵ Btu)

Table A2 (c): Terms which are frequently used in reports employing the metric system of units.

1 billion	1000 million = 10 ⁹
1 trillion	1000 billion = 10 ¹²
1 kcal	1 kilocalorie = 3.968 Btu (British thermal units)
1 therm	10 ⁵ Btu = 25,200 kcal
1 thermie	1000 kcal
1 joule	10 ⁷ erg
1 metric ton	1000 kilograms = 0.985 ton = 1.1023 short ton
1 toe	1 ton of oil equivalent = 10 ⁷ kcal
1 Mtoe	1 million metric tons of oil equivalent = 10 ¹³ kcal
1 tce	1 ton of coal equivalent = 0.7 toe
1 Mtce	1 million tons of coal equivalent = 0.7 Mtoe
1 Mcf	1 thousand cubic feet = 28.3 cubic meters
1 TCF	1 trillion cubic feet = 28.3x10 ⁹ cubic meters
\$1 per Mcf	is approximately equivalent to \$40 per toe
f.o.b.	free on board
c.i.f.	cost including insurance and freight
GNP	Gross Nation Product
GDP	Gross Domestic Product

Appendix B
Thermal and Physical Parameters,
Properties, and Flammability Limits
of Gases and Vapors
(Tables B1 to B4)

Table B1: Main physical parameters of gases [8]

Name of substance and its chemical formula	Molecular mass, M	Density under standard conditions ρ , kg m ⁻³	Relative density with respect to air, ρ	volume of one kmole v , m ³ /kmole	Melting point, t_m , °C	Boiling point, t_b , °C	Critical point, t_c , °C	Critical pressure, P_c , MN m ⁻²	Critical density, ρ_c , kg m ⁻³
Nitrogen (N ₂)	28.016	1.2505	0.9673	22.4	-210.02	-195.81	-147.0	3.391	311
Ammonia (NH ₃)	17.031	0.7714	0.6967	22.08	-77.7	-33.4	132.3	11.27	235
Argon (Ar)	39.944	1.7839	1.3799	22.39	-189.3	-185.9	-122	4.861	531
Acetylene (C ₂ H ₂)	26.04	1.1709	0.9057	22.22	-81 ^{*1}	-83.6 ^{*2}	35.7	6.243	231
Acetone (C ₃ H ₆ O)	58.08	(2.595)	2.005	(22.41)	-94.3	56.1	235.5	4.714	273
Normal butane (C ₄ H ₁₀)	58.12	2.703	2.091	21.50	-135	0.5	152.0	3.793	228
Isobutane (C ₄ H ₁₀)	58.12	2.668	2.064	21.78	-145	-10.2	134.9	3.646	221
Normal butyl alcohol (C ₄ H ₁₀ O)	74.12	3.244	2.610	22.84	-89.8	117.7	288	4.959	-
Water (H ₂ O)	18.016	0.768	0.5941	23.45	0.0	100.0	374.15	22.114	307
Hydrogen (H ₂)	2.0156	0.08987	0.06952	22.43	-259.2	-252.78	-239	1.294	31
Air (dry)	28.96	1.2928	1.000	22.4	-213	-193	-140.7	3.763	310
Normal hexane (C ₆ H ₁₄)	86.17	(3.845)	2.970	(22.41)	-95.3	68.73	234.7	3.028	234
Helium (He)	4.003	0.1785	0.1381	22.42	-	-268.93	-267.9	0.228	69.3
Normal heptane (C ₇ H ₁₆)	100.19	4.459	3.450	22.47	-90.6	98.4	267.0	2.734	235
Carbon dioxide (CO ₂)	44.01	1.9768	1.5291	22.26	-56	-78.48	31.04	7.777	468
Normal decane (C ₁₀ H ₂₂)	142.3	(6.35)	4.91	(22.41)	-31	173	346	2.078	230
Diphenyl (C ₁₂ H ₁₀)	154.08	(6.89)	5.33	(22.41)	-70.5	255.3	496	3.116	-
Diphenyl ether (C ₁₂ H ₁₀ O)	168.8	(7.54)	5.83	(22.41)	80	287	-	-	-
Dichloromethane (CH ₂ Cl ₂)	84.94	(3.79)	2.93	(22.41)	-96.5	-40	245	4.449	-
Diethyl ether (C ₄ H ₁₀ O)	74.12	(3.30)	2.55	(22.41)	-129	34.6	194	3.606	264
Nitrogen oxide (N ₂ O)	44.016	1.9780	1.53	22.05	-90.8	-88.7	36.5	7.262	457
Hydrogen iodide (HI)	127.93	5.789	4.478	22.1	-51	-36	150	8.203	-
Oxygen (O ₂)	32.000	1.42895	1.1033	22.39	-218.83	-182.97	-118.4	5.067	410
Krypton (Kr)	83.7	3.74	2.89	22.38	-157.2	-153.2	-63.8	5.498	908
Xenon (Xe)	131.3	5.89	4.51	22.29	-111.9	-108.8	16.6	5.870	1110
Methane (CH ₄)	16.04	0.7168	0.5545	22.36	-182.5	-161.5	-82.1	4.635	162
Methylamine (CH ₃ N)	31.06	1.388	1.0737	22.37	-92.5	-6.5	156.9	7.448	-
Methyl alcohol (CH ₃ O)	32.04	1.426	1.103	22.47	-98	64.51	240	7.948	272
Neon (Ne)	20.183	0.8999	0.6961	22.43	-248.6	-246.1	-228.7	2.724	484
Nitrosyl chloride (NOCl)	65.465	2.9919	2.314	21.88	-61.5	-5.5	165	9.369	-
Ozone (O ₃)	48.000	2.22	1.71	21.6	-252	-112	-5	6.782	537
Nitrogen oxide (NO)	30.008	1.3402	1.0367	22.39	-163.5	-152	-93	6.778	52

*1 Triple point;

*2 Sublimation point

Table B1: (continued)

Name of substance and its chemical formula	Molecular mass, M	Density under standard conditions ρ , kg m ⁻³	Relative density with respect to air, ρ	volume of one kmole v, m ³ kmole ⁻¹	Melting point, t_m , °C	Boiling point, t_b , °C	Critical point, t_c , °C	Critical pressure, P_c , MN m ⁻²	Critical density, ρ_c , kg m ⁻³
Carbon monoxide (CO)	28.01	1.2500	0.9669	22.40	-205	-191.5	-140	3.489	301
Normal octane (C ₈ H ₁₈)	114.22	5.030	3.890	22.71	-57	-125.7	296.7	2.489	233
Normal pentane (C ₅ H ₁₂)	72.14	3.457	2.674	20.87	-135.5	36.1	196.6	3.371	232
Isopentane (C ₅ H ₁₂)	72.14	(3.22)	2.49	(22.41)	-160.0	28.0	187.8	3.332	234
Propane (C ₃ H ₈)	44.09	2.0037	1.550	22.00	-189.9	-42.6	96.8	4.253	220
Propylene (C ₃ H ₆)	42.08	1.915	1.481	21.96	-185.2	-47	92.0	4.616	233
Selenic acid (H ₂ SeO ₄)	80.968	3.6643	2.9002	21.82	-	-	-	-	-
Sulfur dioxide (SO ₂)	64.06	2.9263	2.2635	21.89	-75.3	-10.0	157.5	7.879	524
Sulfur trioxide (SO ₃)	80.06	(3.575)	2.765	(22.41)	-16.8	46	218.2	8.487	633
Hydrogen sulfide (H ₂ S)	34.08	1.5392	1.1906	22.14	-85.6	-60.4	100.4	8.996	349
Hydrogen phosphide (PH ₃)	34.04	1.530	1.183	22.25	-133.5	-87.5	51.3	6.527	-
Freon-11 (CF ₃ Cl)	137.4	(6.13)	4.74	(22.41)	-111	23.65	198.0	4.371	554
Freon-12 (CF ₂ Cl ₂)	120.92	5.510	4.262	21.95	-155	-29.8	111.5	3.920	555
Freon-13 (CFCl ₃)	114.47	(5.11)	3.95	(22.41)	-181	-81.50	28.75	3.861	581
Fluor (F ₂)	38.000	1.695	1.31	22.42	-120	-188	-101	5.566	-
Silicon fluoride (SiF ₄)	104.06	4.6905	3.7133	22.18	-90	-75	-14.1	3.714	-
Methyl fluoride (CH ₃ F)	34.03	1.545	1.195	22.03	-	-78	44.6	5.870	300
Chlorine (Cl ₂)	70.914	3.22	2.49	22.02	-100.5	-33.95	144	7.703	573
Hydrogen chloride (HCl)	36.465	1.6391	1.2679	22.25	-11.2	-85	51.4	8.252	420
Methyl chloride (CH ₃ Cl)	50.49	2.307	1.784	21.88	-91.5	-24.0	143.1	6.674	353
Chloroform (CHCl ₃)	119.39	5.283	4.087	22.60	-68.5	61.30	263.4	5.468	500
Cyan (C ₂ N ₂)	52.04	(2.765)	2.14	(22.41)	-34.4	-21	128.3	6.076	-
Hydrogen cyanide (HCN)	27.026	(1.205)	0.933	(22.41)	-14.2	-20.8	183.5	5.370	195
Ethane (C ₂ H ₆)	30.07	1.356	1.049	22.16	-183.6	-88.6	32.3	4.880	203
Ethylamine (C ₂ H ₇ N)	45.08	2.0141	0.706	22.37	-81	16.5	183	5.615	248
Ethylene (C ₂ H ₄)	28.05	1.2605	0.9750	22.24	-169.4	-103.5	9.2	5.057	227
Ethyl alcohol (C ₂ H ₆ O)	46.07	2.043	1.580	22.55	-114.5	78.3	243.1	6.380	276
Ethyl chloride (C ₂ H ₅ Cl)	64.52	(2.88)	2.225	(22.41)	-138.7	12.2	187.2	5.263	330

Note 1. Boiling point of some substances is above 0°C. Values of ρ for vapors of these substances under standard conditions are conventional, but they are used to calculate ρ at various temperatures and pressures.

2. Bracketed density values have been calculated with the aid of the formula for ideal gases, $\rho = M/22.41$.

Table B2 (a): Thermal and physical properties of monoatomic gases as a function of temperature [8].

$t, ^\circ\text{C}$	$\lambda \times 10^3$ $\text{W (m}^\circ\text{C)}^{-1}$	$\eta \times 10^6$ N s m^{-2}	Pr	$\nu \times 10^6$ $\text{m}^2 \text{s}^{-1}$	C_p $\text{kJ (kg}^\circ\text{C)}^{-1}$	$C_p/C_v=k$	$\alpha \times 10^2$ $\text{m}^2 \text{h}^{-1}$	$\rho,$ kg m^{-3}
Argon (Ar)								
0	16.5	21.1	0.663	11.8	0.519	1.67	6.41	1.784
100	21.2	26.9	0.661	20.6	0.519	1.67	11.2	1.305
200	25.6	32.2	0.653	31.2	0.519	1.67	17.2	1.030
300	29.9	36.9	0.640	43.4	0.519	1.67	24.4	0.850
400	33.9	41.1	0.628	56.7	0.519	1.67	32.6	0.724
500	37.9	45.2	0.619	72.0	0.519	1.67	42.0	0.627
600	39.4	48.5	0.604	87.0	0.519	1.67	51.9	0.558
Helium (He)								
0	143	18.7	0.684	105	5.204	1.67	55.2	0.1785
100	179	22.9	0.667	176	5.204	1.67	94.8	0.1305
200	213	27.0	0.660	270	5.204	1.67	143	0.1030
300	244	30.8	0.656	362	5.204	1.67	199	0.0850
400	276	34.3	0.648	474	5.204	1.67	263	0.0724
500	305	37.6	0.642	611	5.204	1.67	336	0.0627
600	333	40.3	0.631	723	5.204	1.67	-	0.0558
Krypton (Kr)								
0	8.88	23.4	0.656	6.28	0.249	1.67	3.44	3.74
100	11.6	30.6	0.656	11.2	0.249	1.67	6.13	7.74
200	14.3	37.3	0.648	17.2	0.249	1.67	9.59	2.16
300	16.7	43.2	0.637	24.3	0.249	1.67	13.7	1.73
400	19.3	48.5	0.625	32.0	0.249	1.67	18.4	1.516
500	21.7	53.4	0.611	40.5	0.249	1.67	23.7	1.32
600	24.1	59.2	0.612	50.6	0.249	1.67	29.8	1.17
Mercury Vapor								
200	7.68	45.1	0.620	-	-	-	-	-
300	9.36	55.3	0.618	-	-	-	-	-
400	11.0	65.8	0.616	18.1	0.104	1.67	10.4	3.64
500	12.7	74.5	0.613	24.1	0.104	1.67	13.8	3.16
600	14.4	85.0	0.612	31.1	0.104	1.67	17.5	2.80

Table B2 (b): Thermal and physical properties of diatomic gases as a function of temperature [8].

Air								
0	24.4	17.2	0.707	13.3	1.004	1.400	6.76	1.293
100	32.1	21.9	0.688	23.0	1.009	1.397	12.1	0.946
200	39.3	26.0	0.680	34.8	1.026	1.390	18.4	0.747
300	46.1	29.7	0.674	48.2	1.047	1.378	25.7	0.616
400	52.1	33.0	0.678	63.0	1.068	1.366	33.5	0.524
Carbon Monoxide (CO)								
0	23.3	16.6	0.740	13.3	1.0396	1.400	6.46	1.250
100	30.1	20.7	0.718	22.6	1.0446	1.397	11.3	0.916
200	36.5	24.4	0.708	33.8	1.0584	1.389	17.9	0.723
300	42.6	27.9	0.709	47.0	1.0802	1.379	23.8	0.596
400	48.5	31.2	0.711	61.8	1.1057	1.367	31.1	0.508
Hydrogen (H ₂)								
0	172	8.36	0.688	93.0	14.19	1.410	48.6	0.0899
100	220	10.3	0.677	157	14.45	1.398	83.4	0.0657
200	264	12.1	0.666	233	14.50	1.396	126	0.0519
300	307	13.8	0.655	323	14.53	1.395	178	0.0428
400	348	15.4	0.644	423	14.58	1.394	236	0.0364

Table B2 (b): continued.

$t, ^\circ\text{C}$	$\lambda \times 10^3$ $\text{W (m}^\circ\text{C}^{-1})$	$\eta \times 10^6$ N s m^{-2}	Pr	$\nu \times 10^6$ $\text{m}^2 \text{s}^{-1}$	$C_p (\text{kJ } ^\circ\text{C}^{-1})$	$C_p/C_v = k$	$\alpha \times 10^7$ $\text{m}^2 \text{h}^{-1}$	ρ kg m^{-3}
0	24.3	16.7	0.705	13.3	1.030	1.402	6.89	1.250
100	31.5	20.7	0.678	22.5	1.034	1.400	11.6	0.916
200	38.5	24.2	0.656	33.6	1.043	1.394	18.3	0.723
300	44.9	27.7	0.652	46.4	1.060	1.385	25.5	0.597
400	50.7	30.9	0.659	60.9	1.082	1.375	33.3	0.508
0	24.7	19.4	0.720	13.6	0.9148	1.397	6.80	1.429
100	32.9	24.1	0.686	23.1	0.9336	1.385	12.1	1.05
200	40.7	28.5	0.674	34.6	0.9630	1.370	15.6	0.826
300	48.0	32.5	0.673	47.8	0.9948	1.353	25.4	0.682
400	55.0	36.3	0.675	62.8	1.0236	1.340	33.3	0.580
0	14.7	14.0	0.780	7.09	0.8148	1.301	3.28	1.9767
100	22.8	18.2	0.733	12.6	0.9136	1.260	6.21	1.447
200	30.9	22.4	0.715	19.2	0.9927	1.235	9.83	1.143
300	39.1	26.4	0.712	27.3	1.0567	1.217	14.1	0.944
400	47.2	30.2	0.709	36.7	1.1103	1.205	19.1	0.802
0	8.4	12.1	0.874	4.14	0.607	1.272	1.70	2.926
100	12.3	16.1	0.863	7.51	0.662	1.243	3.14	2.140
200	16.6	20.0	0.856	11.8	0.712	1.223	4.48	1.690
300	21.2	23.8	0.848	17.1	0.754	1.207	7.25	1.395
400	25.8	27.6	0.834	23.3	0.783	1.198	10.0	1.187
0	23.7	12.0	1.06	19.4	2.102	1.28	6.92	0.588
100	33.5	15.9	0.94	30.6	1.976	1.30	13.2	0.464
200	44.2	20.0	0.91	44.3	2.014	1.29	20.6	0.384
300	55.9	24.3	0.90	60.5	2.073	1.28	29.8	0.326
400	69.8	28.3	0.90	80.5	2.138	1.28	39.8	0.286

Table B2 (d): Thermal and physical properties of Hydrocarbons of the methane series $\text{C}_n\text{H}_{2n+2}$ [8].

Butane (C_4H_{10})								
0	13.3	6.84	0.821	2.63	1.5918	1.097	1.16	2.593
100	23.5	9.26	0.798	4.87	2.0273	1.075	2.20	1.90
200	36.5	11.67	0.784	7.78	2.4556	1.061	3.57	1.50
300	51.9	14.02	0.761	11.3	2.8149	1.052	5.37	1.24
400	69.8	16.38	0.734	15.6	3.1292	1.046	7.64	1.05
Ethane (C_2H_6)								
0	19	8.60	0.746	6.41	1.6471	1.202	3.09	1.342
100	31.9	11.38	0.738	11.6	2.0674	1.154	5.64	0.983
200	47.5	14.12	0.741	18.2	2.4899	1.124	8.85	0.776
300	65.4	16.79	0.736	26.2	2.8696	1.105	12.8	0.640
400	85.5	19.32	0.726	35.6	3.2138	1.095	17.5	0.545

Table B2 (d): (Continued).

$t, ^\circ\text{C}$	$\lambda \times 10^3$ $\text{W (m}^\circ\text{C)}^{-1}$	$\eta \times 10^6$ N s m^{-2}	Pr	$\nu \times 10^6$ $\text{m}^2 \text{s}^{-1}$	C_p $\text{kJ (kg}^\circ\text{C)}^{-1}$	$C_p/C_v=k$	$\alpha \times 10^2$ $\text{m}^2 \text{h}^{-1}$	$\rho,$ kg m^{-3}
Heptane (C ₇ H ₁₆)								
0	10.7	5.39	0.812	-	1.6102	1.053	-	-
100	19.3	17.29	0.784	2.28	2.0197	1.042	10.5	3.27
200	30.5	9.62	0.771	3.72	2.4406	1.035	17.4	2.58
300	43.7	11.77	0.749	5.51	2.7849	1.030	26.6	2.13
400	59.4	13.93	0.722	7.68	3.0832	1.027	38.4	1.81
Hexane (C ₆ H ₁₄)								
0	11.2	5.90	0.841	-	1.6023	1.063	-	-
100	20.2	8.15	0.814	2.89	2.0231	1.050	12.8	2.813
200	32.0	10.39	0.796	4.68	2.4438	1.040	21.2	2.220
300	45.9	12.65	0.769	6.92	2.7909	1.035	32.4	1.833
400	62.5	14.91	0.738	9.60	3.0936	1.031	46.6	1.560
Methane (CH ₄)								
0	30.7	10.39	0.734	14.5	2.1654	1.314	7.13	0.7168
100	46.5	13.24	0.698	25.1	2.4484	1.268	13.0	0.525
200	63.7	15.89	0.703	38.2	2.8068	1.225	19.8	0.141
300	82.3	18.34	0.707	53.5	3.1753	1.193	27.3	0.342
400	102	20.69	0.717	71.9	3.5295	1.171	35.8	0.291
Octane (C ₈ H ₁₈)								
0	9.8	4.93	0.816	-	1.6144	1.046	-	-
100	17.7	6.79	0.776	1.82	2.0209	1.037	8.46	3.73
200	27.8	8.65	0.759	2.94	2.4488	1.030	13.9	2.945
300	40	40.49	0.729	4.32	2.7800	1.026	21.3	2.43
400	54.3	12.36	0.700	4.96	3.0756	1.023	30.7	2.07
Pentane (C ₅ H ₁₂)								
0	12.3	6.35	0.821	-	1.5931	1.077	-	-
100	22.0	8.65	0.796	3.67	2.0247	1.060	1.66	2.355
200	34.1	10.88	0.781	5.90	2.4476	1.049	2.69	1.86
300	48.6	13.24	0.763	8.62	2.7993	1.042	4.08	1.54
400	65.5	15.49	0.735	11.8	3.1075	1.037	5.81	1.31
Propane (C ₃ H ₈)								
0	15.2	7.50	0.762	3.81	1.5495	1.138	1.80	1.967
100	26.3	10.00	0.768	6.94	2.0168	1.102	3.26	1.44
200	40.1	12.45	0.763	10.9	2.4581	1.083	5.17	1.14
300	56.2	14.81	0.748	15.8	2.8345	1.070	7.61	0.939
400	74.8	17.16	0.727	21.6	3.1610	0.062	10.7	0.799

Table B2 (e): Thermal and physical properties of polyatomic gases [8].

$t, ^\circ\text{C}$	$\lambda \times 10^3$ $\text{W (m}^\circ\text{C)}^{-1}$	$\eta \times 10^6$ N s m^{-2}	Pr	$\nu \times 10^6$ $\text{m}^2 \text{s}^{-1}$	C_p $\text{kJ (kg}^\circ\text{C)}^{-1}$	$C_p/C_v=k$	$\alpha \times 10^2$ $\text{m}^2 \text{h}^{-1}$	$\rho,$ kg m^{-3}
Acetone (C ₃ H ₆ O)								
0	9.7	6.86	0.386	-	1.256	1.130	-	-
100	17.3	9.41	0.840	5.07	1.537	1.103	2.18	1.87
200	26.9	12.06	0.806	8.22	1.788	1.086	3.68	1.47
300	38.6	14.71	0.774	12.1	2.022	1.076	5.64	1.22
400	52.1	17.36	0.743	16.9	2.236	1.067	8.15	1.03
500	67.5	20.00	0.720	22.3	2.428	1.062	11.1	0.901
600	84.7	22.75	0.695	28.3	2.587	1.059	14.7	0.799
Ammonia (NH ₃)								
0	21.1	9.36	0.908	12.2	2.043	0.31	4.81	0.7714
100	34.0	13.04	0.852	23.2	2.219	1.28	9.78	0.564

Table B2 (e): (Continued).

200	48.8	16.67	0.818	38.0	2.399	1.26	16.5	0.445
300	65.5	20.59	0.812	56.4	2.583	1.24	24.8	0.368
400	84.0	24.32	0.796	78.7	2.747	1.22	35.1	0.313
500	103.6	28.15	0.793	105	2.918	1.20	47.0	0.272
600	124.4	31.97	0.792	134	3.082	1.19	60.6	0.241
Benzol (C ₆ H ₆)								
0	9.2	6.98	0.716	-	0.943	1.127	-	-
100	17.3	7.21	0.554	3.74	1.325	1.086	1.84	2.55
200	28.1	12.28	0.719	5.99	1.676	1.067	3.01	2.01
300	41.6	14.64	0.688	8.80	1.956	1.057	4.62	1.66
400	57.6	17.20	0.652	12.1	2.183	1.050	6.74	1.41
500	76.4	19.76	0.614	15.9	2.369	1.047	9.44	1.23
600	96.3	22.31	0.585	20.4	2.524	1.044	12.6	1.09
Chloromethyl (CH ₂ Cl)								
0	9.2	9.807	0.818	4.25	0.770	1.27	1.86	2.31
100	15.4	13.435	0.805	7.96	0.921	1.22	3.55	1.69
200	24.2	17.162	0.750	12.8	1.059	1.18	6.17	1.33
300	33.8	20.790	0.727	18.9	1.185	1.16	9.39	1.10
400	45	24.517	0.706	26.2	1.296	1.15	13.3	0.938
500	57.5	28.243	0.685	34.6	1.394	1.13	18.2	0.815
Cyclohexane (C ₆ H ₁₂)								
0	9.7	6.384	0.718	-	1.094	1.100	-	-
100	18.1	8.296	0.768	3.075	1.647	1.064	1.44	2.75
200	29.2	10.503	0.769	4.84	2.139	1.049	2.26	2.17
300	42.8	12.504	0.749	7.00	2.566	1.040	3.35	1.79
400	58.8	14.475	0.723	9.50	2.938	1.033	4.74	1.52
500	79.3	16.034	0.656	12.4	3.246	1.030	6.67	1.32
Ethyl Acetate (C ₄ H ₈ O ₂)								
0	9.1	6.91	0.892	-	1.168	1.088	-	-
100	16.6	9.47	0.832	5.16	1.465	1.069	1.42	2.88
200	26.3	12.06	0.798	8.32	1.742	1.056	2.39	2.27
300	38.3	14.61	0.765	12.2	2.005	1.049	3.67	1.87
400	52.2	17.06	0.733	16.9	2.257	1.043	5.21	1.60
500	68.2	19.71	0.723	22.4	2.499	1.038	7.06	1.39
Ethyl Ether (C ₄ H ₁₀ O)								
0	13	6.16	0.766	-	1.440	1.084	-	-
100	22.8	9.28	0.748	3.83	1.842	1.065	1.84	2.42
200	35.2	11.67	0.736	6.12	2.223	1.053	2.99	1.91
300	50	14.02	0.727	8.92	2.587	1.045	4.42	1.57
400	67.3	16.48	0.720	12.2	2.943	1.039	6.14	1.34
500	86.4	18.83	0.714	16.1	3.274	1.036	8.14	1.17
Toluene (C ₇ H ₈)								
0	13	6.609	0.748	-	1.023	1.097	-	-
100	-	8.855	-	-	1.411	1.068	-	-
200	-	11.013	-	4.65	1.750	1.054	-	2.38
300	-	13.239	-	6.75	2.047	1.045	-	1.96
400	-	15.396	-	9.23	2.294	1.040	-	1.667
500	-	17.456	-	12.0	2.504	1.036	-	1.45

Table B3: Enthalpy of combustion or heating values of some hydrocarbons at 25 °C [31].

Hydrocarbon	Formula	Liquid H ₂ O in products (negative of higher heating value)		Vapor H ₂ O in products (negative of lower heating value)	
		Liquid hydrocarbon, kJ kg ⁻¹ fuel	Gaseous hydrocarbon, kJ kg ⁻¹ fuel	Liquid hydrocarbon, kJ kg ⁻¹ fuel	Gaseous hydrocarbon, kJ kg ⁻¹ fuel
<i>Paraffin family</i>					
Methane	CH ₄	-	-55,496	-	-50,010
Ethane	C ₂ H ₆	-	-51,875	-	-47,484
Propane	C ₃ H ₈	-49,975	-50,345	-45,983	-46,353
Butane	C ₄ H ₁₀	-49,130	-49,500	-45,344	-45,714
Pentane	C ₅ H ₁₂	-48,643	-49,011	-44,983	-45,351
Hexane	C ₆ H ₁₄	-48,308	-48,676	-44,733	-45,101
Heptane	C ₇ H ₁₆	-48,071	-48,436	-44,557	-44,922
Octane	C ₈ H ₁₈	-47,893	-48,256	-44,425	-44,788
Decane	C ₁₀ H ₂₂	-47,641	-48,000	-44,239	-44,598
Dodecane	C ₁₂ H ₂₆	-47,470	-47,828	-44,109	-44,467
<i>Olefin family</i>					
Ethene	C ₂ H ₄	-	-50,296	-	-47,158
Propene	C ₃ H ₆	-	-48,917	-	-45,780
Butene	C ₄ H ₈	-	-48,453	-	-45,316
Pentene	C ₅ H ₁₀	-	-48,134	-	-44,996
Hexene	C ₆ H ₁₂	-	-47,937	-	-44,800
Heptene	C ₇ H ₁₄	-	-47,800	-	-44,662
Octene	C ₈ H ₁₆	-	-47,693	-	-44,556
Nonene	C ₉ H ₁₈	-	-47,612	-	-44,475
Decene	C ₁₀ H ₂₀	-	-47,547	-	-44,410
<i>Alkylbenzene family</i>					
Benzene	C ₆ H ₆	-41,831	-42,266	-40,141	-40,576
Methylbenzene	C ₇ H ₈	-42,437	-42,847	-40,527	-40,937
Ethylbenzene	C ₈ H ₁₀	-42,997	-43,395	-40,924	-41,322
Propylbenzene	C ₉ H ₁₂	-43,416	-43,800	-41,219	-41,603
Butylbenzene	C ₁₀ H ₁₄	-43,748	-44,123	-41,453	-41,828

Table B4 (a): Gaseous fuel characteristics.

Type	CO ₂	O ₂	N ₂	CO	H ₂	CH ₄	C ₂ H ₆	C ₃ H ₈	C ₄ H ₁₀	Illuminants and Others	SG	Heating Value kJ m ⁻³	
												Gross	Net
Natural	5.0	90.0	5.0	0.60	37,300	33,680
Natural	0.8	83.4	15.8	0.61	42,060	38,030
Natural	6.5	77.5	16.0	0.70	39,970	36,170
Natural	0.8	8.4	84.1	6.7	0.63	36,280	32,740
Natural	36.7	14.5	23.5	14.9	10.4*	1.29	79,460	72,980
Propane	2.2	97.3	0.5	1.55	95,290	87,840
Propane	2.0	72.9	0.8	24.3 #	1.77	93,280	86,280
Butane	6.0	94.0	2.04	119,580	110,300
Butane	5.0	66.7	28.3 \$	2.00	118,610	109,300
Refinery oil	0.2	0.6	1.2	6.1	4.4	72.5	1.00	61,470	56,770
Refinery oil	0.2	0.2	0.5	1.2	13.1	23.3	21.9	39.6	0.89	54,950	50,330
Oil gas	1.2	0.5	2.4	7.7	54.2	30.1	3.9	0.37	21,230	19,000
Coal gas	2.4	0.8	11.3	7.4	48.0	27.1	3.0	0.47	20,190	18,100
Coal gas	1.7	0.8	8.1	7.3	49.5	29.2	3.4	0.47	22,310	20,120
Coal gas	2.1	0.4	4.4	13.5	51.9	24.3	3.4	0.42	19,370	17,360
Coke oven	2.2	0.8	8.1	6.3	46.5	32.1	4.0	0.44	21,200	18,960
Producer	8.0	0.1	50.0	23.2	17.7	1.0	0.86	5,330	4,950
Producer	4.5	0.6	50.9	27.0	14.0	3.0	0.86	6,070	5,700
Blast furnace	11.5	60.0	27.5	1.0	1.02	3,430	3,430
Blue gas (water gas)	5.4	0.7	8.3	37.0	47.3	1.3	0.57	10,690	9,760
Blue gas (water gas)	5.5	0.9	27.6	28.2	32.5	4.6	0.7	0.70	9,690	8,900
Carburated water	3.6	0.4	5.0	21.9	49.6	10.6	2.5	6.1	0.54	19,970	17,170
Carburated water	6.0	0.9	12.4	26.8	32.2	13.5	8.2	0.66	19,740	16,800
Carburated water	0.7	0.3	5.8	11.7	28.0	36.1	17.4	0.63	31,290	28,680
Sewage	22.0	6.0	2.0	68.0	0.79	25,700	23,130

source: American Gas Association (1948)

*C₅H₁₂ #C₃H₆ \$C₄H₈

||At 60 and 30 in.Hg

Table B4 (b): Flammability limits (in terms of ϕ) of gases and vapors with air.

Compound	Formula	Flammability limits	
		Lean (ϕ) _L	Rich (ϕ) _R
<i>Paraffin hydrocarbons</i>			
Methane	CH ₄	0.464	1.64
Ethane	C ₂ H ₆	0.500	2.72
Propane	C ₃ H ₈	0.510	2.83
n-Butane	C ₄ H ₁₀	0.540	3.30
n-Pentane	C ₅ H ₁₂	0.540	3.59
n-Hexane	C ₆ H ₁₄	0.510	4.00
n-Heptane	C ₇ H ₁₆	0.530	4.50
n-Octane	C ₈ H ₁₈	0.500	4.25
n-Nonane	C ₉ H ₂₀	0.470	4.34
Decane	C ₁₀ H ₂₂	0.450	3.56
<i>Olefins</i>			
Ethene	C ₂ H ₄	0.41	> 6.10
Propene	C ₃ H ₆	0.48	2.72
Butene-1	C ₄ H ₈	0.53	3.53
<i>Acetylenes</i>			
Acetylene	C ₂ H ₂	0.390	-
<i>Aromatics</i>			
Benzene	C ₆ H ₆	0.430	3.36
Toluene	C ₇ H ₈	0.430	3.22
<i>Cyclic hydrocarbons</i>			
Cyclopropane	C ₃ H ₆	0.580	2.76
Cyclohexane	C ₆ H ₁₂	0.480	4.01
<i>Alcohols</i>			
Methyl alcohol	CH ₄ O	0.480	4.08
Propylene oxide	C ₃ H ₆ O	0.470	-
<i>Ketones</i>			
Methylethyl ketone	C ₄ H ₈ O	0.59	2.33
<i>Inorganic</i>			
Carbon monoxide + water vapor at 18 °C	CO	0.34	6.76
<i>Sulfides</i>			
Carbon disulfide	CS ₂	0.18	1.12

ϕ is the equivalence ratio

Data from Hibbard, R. and Barnett, C. M., "Basic Considerations in the Combustion of Hydrocarbon Fuels with Air", NACA Report 1300, Supt. Documents, U.S. Govt. Printing Office, Washington, D. C. (1959).

Appendix C
Thermochemical Data for Calculating
Enthalpy, Entropy and Equilibrium
Constants
(Tables C1 to C2)

Table C1: Value of constants $a_{i,0}$, $a_{i,1}$, and $a_{i,2}$ used to calculate the specific enthalpy for different components, $H_{p,T} = a_{i,0} + a_{i,1}T + a_{i,2}T^2$ J kmol.

Species	Coeff.	300-600 K	600-900	900-1200	1200-1500	1500-1800	1800-2100	2100-2400	2400-2700
H	a_0	2.11933873E+08	2.11933873E+08	2.11933873E+08	2.11933873E+08	2.11933873E+08	2.11933873E+08	2.11933871E+08	2.11933872E+08
	a_1	2.08000224E+04	2.08000224E+04	2.08000225E+04	2.08000224E+04	2.08000226E+04	2.08000227E+04	2.08000244E+04	2.08000232E+04
	a_2	-1.07043074E-08	-4.98788916E-09	-5.72290161E-08	-1.72964546E-08	-6.11339370E-08	-8.13525529E-08	-4.52247051E-07	-1.67942431E-07
O	a_0	2.42638975E+08	2.43042532E+08	2.43241578E+08	2.43227682E+08	2.43213925E+08	2.43348149E+08	2.43601094E+08	2.43846189E+08
	a_1	2.31310159E+04	2.15508268E+04	2.10477105E+04	2.10681323E+04	2.10897414E+04	2.09369786E+04	2.06884077E+04	2.04775093E+04
	a_2	-1.93684289E+00	-3.75253889E-01	-5.66083371E-02	-6.37997525E-02	-7.21882151E-02	-2.86869838E-02	3.24258031E-02	7.78187142E-02
CO	a_0	-1.19074843E+08	-1.18784517E+08	-1.19138797E+08	-1.20255497E+08	-1.21746805E+08	-1.23125148E+08	-1.24118150E+08	-1.24751652E+08
	a_1	2.77530876E+04	2.65619161E+04	2.73678854E+04	2.93294241E+04	3.14161320E+04	3.30152737E+04	3.39983842E+04	3.45443364E+04
	a_2	2.11143296E+00	3.33810419E+00	2.87920477E+00	2.01580193E+00	1.28476416E+00	8.20473767E-01	5.76971344E-01	4.59281270E-01
O ₂	a_0	-8.41215785E+06	-8.45191397E+06	-9.63044323E+06	-1.09722721E+07	-1.15398444E+07	-1.14482726E+07	-1.14681833E+07	-1.20684285E+07
	a_1	2.70290625E+04	2.69771916E+04	2.97883655E+04	3.21891516E+04	3.30048877E+04	3.29036661E+04	3.29180044E+04	3.34283795E+04
	a_2	4.00216465E+00	4.24434114E+00	2.56092717E+00	1.48471317E+00	1.19140109E+00	1.21933357E+00	1.21709190E+00	1.10854860E+00
H ₂	a_0	-8.29812911E+06	-8.68524335E+06	-7.94540381E+06	-7.05749859E+06	-7.12951482E+06	-8.19971133E+06	-9.52860058E+06	-1.05588885E+07
	a_1	2.71593329E+04	2.88539296E+04	2.71123210E+04	2.55149733E+04	2.55890349E+04	2.68165432E+04	2.81274067E+04	2.90145623E+04
	a_2	2.34388734E+00	5.04608356E-01	1.53326050E+00	2.25307859E+00	2.23644865E+00	1.88412604E+00	1.56062042E+00	1.36953764E+00
OH	a_0	3.03517944E+07	3.11850844E+07	3.18048979E+07	3.18406947E+07	3.12927076E+07	3.03158361E+07	2.90596928E+07	2.76408912E+07
	a_1	3.12403759E+04	2.80205033E+04	2.64802483E+04	2.63937908E+04	2.71499551E+04	2.82747281E+04	2.95100187E+04	3.07267458E+04
	a_2	-1.96353115E+00	1.17885458E+00	2.13902202E+00	2.18758760E+00	1.92637871E+00	1.60228142E+00	1.29835829E+00	1.03735187E+00
CO ₂	a_0	-4.03230243E+08	-4.05503928E+08	-4.08483718E+08	-4.11512707E+08	-4.14259995E+08	-4.16581324E+08	-4.18433637E+08	-4.19875521E+08
	a_1	2.60922057E+04	3.47353524E+04	4.19632451E+04	4.73511746E+04	5.12084346E+04	5.39008809E+04	5.57311040E+04	5.69714547E+04
	a_2	1.88716353E+01	1.05681278E+01	6.16578109E+00	3.76410765E+00	2.40818341E+00	1.62667211E+00	1.17424187E+00	9.07346009E-01
N ₂	a_0	-8.48870665E+06	-8.15039752E+06	-8.30119827E+06	-9.20740461E+06	-1.06561537E+07	-1.21905497E+07	-1.34149000E+07	-1.41919358E+07
	a_1	2.79875657E+04	2.66386780E+04	2.69570647E+04	2.85411443E+04	3.05633675E+04	3.23406182E+04	3.35518151E+04	3.42222002E+04
	a_2	1.65394210E+00	3.00876631E+00	2.84321096E+00	2.14938166E+00	1.44265519E+00	9.27500442E-01	6.27739960E-01	4.83069796E-01
H ₂ O	a_0	-2.51670196E+08	-2.51073876E+08	-2.50905014E+08	-2.51786159E+08	-2.53868761E+08	-2.56869912E+08	-2.60294536E+08	-2.63681212E+08
	a_1	3.13663182E+04	2.90462528E+04	2.85809153E+04	3.01026482E+04	3.29951226E+04	3.64564086E+04	3.98289095E+04	4.27371502E+04
	a_2	3.74585290E+00	6.02445106E+00	6.34115735E+00	5.68290412E+00	4.67710215E+00	3.67808667E+00	2.84717548E+00	2.22247437E+00
HO ₂	a_0	1.12693261E+07	1.06339344E+07	8.99965379E+06	6.49250293E+06	3.67631905E+06	1.17217261E+06	-6.99570234E+05	-2.07767848E+06
	a_1	2.93162152E+04	3.16375730E+04	3.55427676E+04	3.99743820E+04	4.39203425E+04	4.68255942E+04	4.86770492E+04	4.98621896E+04
	a_2	1.04649014E+01	8.32313467E+00	5.97991214E+00	4.01690032E+00	2.63260532E+00	1.78911102E+00	1.33093322E+00	1.07599099E+00
HCO	a_0	-2.16828479E+07	-2.17668051E+07	-2.35607937E+07	-2.64637350E+07	-2.94186195E+07	-3.20038732E+07	-3.44016103E+07	-3.67743036E+07
	a_1	2.93231500E+04	2.93939824E+04	3.36464775E+04	3.87855362E+04	4.29321831E+04	4.59280302E+04	4.82910807E+04	5.03279170E+04
	a_2	9.01416145E+00	9.18065505E+00	6.65015451E+00	4.37034172E+00	2.91342403E+00	2.04462380E+00	1.46197040E+00	1.02459349E+00

Table C1: (continued).

Species	Coeff.	300-600 K	600-900	900-1200	1200-1500	1500-1800	1800-2100	2100-2400	2400-2700
CH ₂ O	a ₀	-1.24898978E+08	-1.25060916E+08	-1.29573300E+08	-1.36254087E+08	-1.42196257E+08	-1.46823372E+08	-1.51280427E+08	-1.56193074E+08
	a ₁	2.41764875E+04	2.41138024E+04	3.48283320E+04	4.66833149E+04	5.50421026E+04	6.04080126E+04	6.47949598E+04	6.90090701E+04
	a ₂	1.92934297E+01	1.99950387E+01	1.36082123E+01	8.33670535E+00	5.39288193E+00	3.83561956E+00	2.75531734E+00	1.85108337E+00
CH ₃	a ₀	1.35608947E+08	1.35228966E+08	1.33206257E+08	1.29376074E+08	1.24353532E+08	1.18957692E+08	1.13791058E+08	1.09122277E+08
	a ₁	2.94845375E+04	3.07534777E+04	3.55448267E+04	4.22929825E+04	4.93120598E+04	5.55538783E+04	6.06493445E+04	6.46606558E+04
	a ₂	1.56346271E+01	1.45805220E+01	1.17310971E+01	8.75169455E+00	6.29569964E+00	4.48874414E+00	3.23149165E+00	2.36939828E+00
CH ₄	a ₀	-8.34851175E+07	-8.30734671E+07	-8.81345945E+07	-9.67536133E+07	-1.05577650E+08	-1.13464787E+08	-1.21167906E+08	-1.29085110E+08
	a ₁	2.14177977E+04	1.90162267E+04	3.09681012E+04	4.62223373E+04	5.86041078E+04	6.77390632E+04	7.53260754E+04	8.2121428E+04
	a ₂	2.44354806E+01	2.75331914E+01	2.04488870E+01	1.36835058E+01	9.33359331E+00	6.68582711E+00	4.81625862E+00	3.35731985E+00
H ₂ O ₂	a ₀	-1.45756190E+08	-1.46391590E+08	-1.48025870E+08	-1.50533020E+08	-1.53349200E+08	-1.55853350E+08	-1.57095480E+08	-1.57233200E+08
	a ₁	2.93162152E+04	3.16375730E+04	3.55427676E+04	3.99743820E+04	4.39203425E+04	4.68255942E+04	4.86770492E+04	4.98621896E+04
	a ₂	1.04649014E+01	8.32313467E+00	5.97991214E+00	4.01690032E+00	2.63260532E+00	1.78911102E+00	1.33093322E+00	1.07599009E+00
C ₂ H ₄	a ₀	4.37016000E+07	3.94582860E+07	3.23238000E+07	2.20911430E+07	1.13062860E+07	6.63657140E+06	-6.20085710E+06	-1.24880000E+07
	a ₁	1.54488570E+04	3.07260000E+04	4.80078570E+04	6.61271430E+04	8.09342860E+04	8.67414290E+04	9.94528570E+04	1.04815710E+05
	a ₂	4.67714290E+01	3.38157140E+01	2.27785710E+01	1.47857140E+01	9.71428570E+00	7.92857140E+00	4.78571430E+00	3.64285710E+00
C ₂ H ₅	a ₀	9.89740000E+07	9.59411430E+07	8.72300000E+07	7.77014290E+07	6.67354290E+07	5.40985710E+07	4.19860000E+07	2.92180000E+07
	a ₁	2.38457140E+04	3.40900000E+04	5.49614290E+04	7.17314290E+04	8.69714290E+04	1.01451430E+05	1.13370000E+05	1.24345710E+05
	a ₂	4.71428570E+01	3.86428570E+01	2.62142860E+01	1.88571430E+01	1.35714290E+01	9.42857140E+00	6.50000000E+00	4.14285710E+00
C ₂ H ₆	a ₀	-9.60484000E+07	-9.95071430E+07	-1.08725860E+08	-1.18998220E+08	-1.33986740E+08	-1.50643400E+08	-1.68548570E+08	-1.85072000E+08
	a ₁	2.13365710E+04	3.35870000E+04	5.57274430E+04	7.35932000E+04	9.43848570E+04	1.13527000E+05	1.31068570E+05	1.45154290E+05
	a ₂	5.65142860E+01	4.58071430E+01	3.25864290E+01	2.48400800E+01	1.76428570E+01	1.21500000E+01	7.85714290E+00	4.85714290E+00
CH ₂	a ₀	3.84896421E+08	3.83036791E+08	3.81129439E+08	3.79950662E+08	3.79263321E+08	3.78896830E+08	3.78515911E+08	3.78058590E+08
	a ₁	3.01201000E+04	2.95639000E+04	3.09097500E+04	3.54633000E+04	3.90823000E+04	4.26014000E+04	4.58851000E+04	4.87320000E+04
	a ₂	7.51000000E+00	8.05000000E+00	7.26500000E+00	5.26500000E+00	4.01500000E+00	3.00800000E+00	2.20500000E+00	1.59900000E+00
C ₂ H ₃	a ₀	2.84345000E+08	2.80870000E+08	2.80834500E+08	2.73723500E+08	2.72253000E+08	2.72100000E+08	2.72100000E+08	2.72100000E+08
	a ₁	3.66243000E+04	4.17522000E+04	4.63257000E+04	3.66567000E+04	-2.86170000E+04	-2.07394000E+05	-5.70102000E+05	-1.20334400E+06
	a ₂	2.32900000E+01	1.86100000E+01	1.58285000E+01	1.98930000E+01	4.21400000E+01	9.29300000E+01	1.81080000E+02	3.15475000E+02
C ₂ H ₂	a ₀	2.26724643E+08	2.25595052E+08	2.24016929E+08	2.22436505E+08	2.20978940E+08	2.20179414E+08	2.19628536E+08	2.19528536E+08
	a ₁	1.40515000E+04	2.11246000E+04	2.31062000E+04	2.80460000E+04	2.94349000E+04	3.19462000E+04	3.41880000E+04	3.60815000E+04
	a ₂	1.35500000E+01	6.85000000E+00	5.66600000E+00	3.50000000E+00	3.03600000E+00	2.31700000E+00	1.76950000E+00	1.36600000E+00

Table C2: Absolute ideal gas entropies at standard state pressure, S° (kJ kmol⁻¹ K⁻¹ at 1 bar).

T(K)	CO	CO ₂	H ₂	O ₂	H ₂ O	OH	O	H	NO	N ₂	NO ₂
298	197.653	213.795	130.684	205.142	188.833	183.703	161.060	114.718	210.761	191.611	239.953
0	-	-	-	-	-	-	-	-	-	-	-
100	165.850	179.105	102.145	173.306	152.390	149.587	135.947	92.011	177.034	159.813	202.431
200	186.025	199.975	119.437	193.486	175.486	171.591	152.156	106.417	198.753	179.988	225.732
300	197.833	214.025	130.864	205.322	189.038	183.892	161.198	114.847	210.950	191.791	240.183
400	206.234	225.334	139.215	213.874	198.783	192.465	167.432	120.826	219.535	200.180	251.321
500	212.828	234.924	145.738	220.698	206.523	199.063	172.202	125.466	226.267	206.740	260.685
600	218.313	243.305	151.077	226.455	213.037	204.443	176.063	129.257	231.890	212.175	268.865
700	223.062	250.773	155.608	231.272	218.719	209.004	179.314	132.458	236.765	216.866	276.149
800	227.271	257.517	159.549	235.924	223.803	212.979	182.118	135.236	241.091	221.016	282.714
900	231.066	263.668	163.060	239.936	228.430	216.523	184.590	137.684	244.991	224.757	288.684
1000	234.531	269.325	166.223	243.585	232.706	219.732	186.795	139.872	248.543	228.167	294.153
1100	237.719	274.555	169.118	246.928	236.694	222.677	188.787	141.855	251.806	231.309	299.190
1200	240.673	279.417	171.792	250.016	240.443	225.405	190.603	143.662	254.823	234.225	303.855
1300	243.426	283.956	174.281	252.886	243.986	227.949	192.272	145.328	257.626	236.941	308.194
1400	245.999	288.216	176.620	255.564	247.350	230.342	193.820	146.867	260.250	239.484	312.253
1500	248.421	292.224	178.833	258.078	250.560	232.598	195.260	148.303	262.710	241.878	316.056
1600	250.702	296.016	180.929	260.446	253.622	234.736	196.603	149.641	265.028	244.137	319.637
1700	252.861	299.592	182.929	262.685	256.559	236.769	197.866	150.905	267.216	246.275	323.022
1800	254.907	302.993	184.833	264.810	259.371	238.702	199.059	152.093	269.287	248.304	326.223
1900	256.852	306.232	186.657	266.835	262.078	240.551	200.184	153.215	271.258	250.237	329.265
2000	258.710	309.326	188.406	268.764	264.681	242.325	201.251	154.281	273.136	252.078	332.160
2100	260.480	312.265	190.088	270.613	266.191	244.020	202.268	155.294	274.927	253.836	334.921
2200	262.174	315.098	191.707	272.387	269.609	245.652	203.233	156.265	276.638	255.522	337.562
2300	263.802	317.805	193.268	274.090	271.948	247.225	204.163	157.185	278.279	257.137	340.089
2400	265.362	320.411	194.778	275.735	274.207	248.739	205.050	158.072	279.856	258.689	342.515
2500	266.865	322.918	196.234	277.316	276.396	250.200	205.899	158.922	281.370	260.183	344.846
2600	268.312	325.332	197.649	278.848	278.517	251.610	206.720	159.737	282.827	261.622	347.089
2700	269.705	327.658	199.017	280.329	280.571	252.974	207.506	160.520	284.232	263.011	349.248
2800	271.053	329.905	200.343	291.764	282.563	254.296	208.269	161.277	285.592	264.350	351.331
2900	272.358	332.085	201.636	283.157	284.500	255.576	209.000	162.005	286.902	265.647	353.344
3000	273.618	334.193	202.887	284.508	286.383	256.819	209.711	162.708	288.174	266.902	355.289
3200	276.023	338.218	205.293	287.098	289.994	259.199	211.063	164.051	290.592	269.295	359.000
3400	278.291	342.013	207.577	289.554	293.416	261.450	212.339	165.311	292.876	271.555	362.490
3600	280.433	345.595	209.757	291.889	296.676	263.588	213.544	166.499	295.031	273.689	365.783
3800	282.467	349.005	211.841	294.115	299.776	265.618	214.686	167.624	297.073	275.714	368.904
4000	284.396	352.243	213.837	296.236	302.742	267.559	215.778	168.691	299.014	277.638	371.866

Table C3: Value of constants $a_{i,0}$ and $a_{i,1}$ used to calculate the specific heat at constant pressure for different components, $C_{p,i}(T) = a_{i,0} + a_{i,1}T$ J kmole⁻¹K⁻¹(Eq. 1.39).

Species	Coeff.	300-600 K	600-900	900-1200	1200-1500	1500-1800	1800-2100	2100-2400	2400-2700
H	a_0	2.08000224E+04	2.08000224E+04	2.08000224E+04	2.08000224E+04	2.08000224E+04	2.08000224E+04	2.08000224E+04	2.08000224E+04
	a_1	-1.37250709E-25	-1.22099657E-25	-3.51147918E-25	-1.14524131E-25	-2.82522563E-25	-1.67998433E-25	-1.94735584E-25	-2.21472735E-25
O	a_0	2.31761125E+04	2.15696208E+04	2.10523687E+04	2.10674254E+04	2.10885880E+04	2.09371160E+04	2.06895727E+04	2.04786950E+04
	a_1	-3.91916348E+00	-7.67377397E-01	-1.17270750E-01	-1.27293911E-01	-1.43519722E-01	-5.71273915E-02	6.45802760E-02	1.55295924E-01
OH	a_0	3.13150943E+04	2.80592627E+04	2.64962557E+04	2.63973691E+04	2.71479236E+04	2.82708066E+04	2.95057435E+04	3.07224972E+04
	a_1	-3.99221644E+00	2.32713033E+00	4.26549969E+00	4.37106394E+00	3.85202919E+00	3.20492584E+00	2.59735941E+00	2.07545176E+00
N ₂	a_0	2.80314477E+04	2.66572063E+04	2.69585590E+04	2.85332574E+04	3.05522335E+04	3.23304131E+04	3.35446935E+04	3.42185448E+04
	a_1	3.26224050E+00	5.99609433E+00	5.67927621E+00	4.29896496E+00	2.88834490E+00	1.85826209E+00	1.25777341E+00	9.67227581E-01
O ₂	a_0	2.71128148E+04	2.69771272E+04	2.97614449E+04	3.21672704E+04	3.29972694E+04	3.29057273E+04	3.29212528E+04	3.34276542E+04
	a_1	7.87113027E+00	8.46714839E+00	5.13352215E+00	2.98155742E+00	2.38727494E+00	2.43782766E+00	2.43240952E+00	2.21683133E+00
H ₂	a_0	2.70385408E+04	2.88353045E+04	2.71309664E+04	2.55331203E+04	2.55939323E+04	2.68112127E+04	2.81200880E+04	2.90108099E+04
	a_1	4.85316457E+00	1.04369284E+00	3.05874846E+00	4.49447796E+00	4.46812790E+00	3.76905947E+00	3.12341336E+00	2.74000774E+00
CO	a_0	2.78039433E+04	2.65786704E+04	2.73647523E+04	2.93177722E+04	3.14035376E+04	3.30056482E+04	3.39927501E+04	3.45418899E+04
	a_1	4.16361160E+00	6.65303470E+00	5.75340080E+00	4.03403862E+00	2.57365520E+00	1.64423712E+00	1.15575908E+00	9.19205918E-01
CO ₂	a_0	2.59374573E+04	3.46377405E+04	4.19033232E+04	4.73143210E+04	5.11852520E+04	5.38860740E+04	5.57218528E+04	5.69659795E+04
	a_1	3.78497169E+01	2.11913725E+01	1.23597477E+01	7.54297052E+00	4.82452519E+00	3.25805342E+00	2.35114119E+00	1.81605183E+00
CH ₄	a_0	2.17798645E+04	1.90541557E+04	3.08756532E+04	4.61168476E+04	5.85311294E+04	6.76974915E+04	7.52974634E+04	8.20923356E+04
	a_1	4.83403019E+01	5.49395059E+01	4.09124283E+01	2.74055164E+01	1.86921113E+01	1.33822062E+01	9.63798542E+00	6.72125061E+00
H ₂ O	a_0	3.14225699E+04	2.90766735E+04	2.85914975E+04	3.00995521E+04	3.29840455E+04	3.64420810E+04	3.98147790E+04	4.27252616E+04
	a_1	7.44257456E+00	1.20206995E+01	1.26684739E+01	1.13610583E+01	9.35454816E+00	7.35879426E+00	5.69745764E+00	4.44758747E+00
CH ₂ O	a_0	2.44418562E+04	2.41198920E+04	3.47394882E+04	4.65958730E+04	5.49895836E+04	6.03842429E+04	6.47804979E+04	6.89909737E+04
	a_1	3.81685249E+01	3.99052966E+01	2.72410383E+01	1.67098483E+01	1.08057888E+01	7.67732785E+00	5.51268196E+00	3.70621511E+00
HCO	a_0	2.94159369E+04	2.93967213E+04	3.36135247E+04	3.87500931E+04	4.29073603E+04	4.59136475E+04	4.82817513E+04	5.03193404E+04
	a_1	1.78817858E+01	1.83280527E+01	1.33068112E+01	8.75364182E+00	5.83547316E+00	4.09319559E+00	2.92589610E+00	2.05111806E+00
HO ₂	a_0	2.93060749E+04	3.16150810E+04	3.55144500E+04	3.99460993E+04	4.38964877E+04	4.68086223E+04	4.86673384E+04	4.98582356E+04
	a_1	2.09111020E+01	1.66440219E+01	1.19658851E+01	8.04258549E+00	5.27328770E+00	3.58390262E+00	2.66479606E+00	2.15272933E+00

Table C3: (continued).

Species	Coeff.	300-600 K	600-900	900-1200	1200-1500	1500-1800	1800-2100	2100-2400	2400-2700
CH ₃	a ₀	2.95204952E+04	3.07463563E+04	3.55142869E+04	4.22543176E+04	4.92750788E+04	5.55233540E+04	6.06263189E+04	6.46440124E+04
	a ₁	3.11965327E+01	2.91368736E+01	2.34615393E+01	1.75117084E+01	1.26011829E+01	8.98560610E+00	6.46873961E+00	4.74260007E+00
H ₂ O ₂	a ₀	2.93060749E+04	3.16150810E+04	3.55144500E+04	3.99460993E+04	4.38964877E+04	4.68086223E+04	4.86673384E+04	4.98582356E+04
	a ₁	2.09111020E+01	1.66440219E+01	1.19658851E+01	8.04258549E+00	5.27328770E+00	3.58390262E+00	2.66479606E+00	2.15272933E+00
C ₂ H ₄	a ₀	1.40276670E+04	3.12805000E+04	4.96280000E+04	6.61733330E+04	8.00233330E+04	9.08166670E+04	9.90833330E+04	1.05293330E+05
	a ₁	9.70900000E+01	6.58950000E+01	4.40800000E+01	2.96000000E+01	2.00000000E+01	1.38000000E+01	9.75000000E+00	7.10000000E+00
C ₂ H ₅	a ₀	2.28956670E+04	3.42115000E+04	5.50533330E+04	7.20250000E+04	8.72000000E+04	1.01508330E+05	1.14290000E+05	1.24840000E+05
	a ₁	9.64000000E+01	7.74650000E+01	5.25000000E+01	3.75500000E+01	2.70500000E+01	1.88500000E+01	1.26000000E+01	8.10000000E+00
C ₂ H ₆	a ₀	2.10286670E+04	3.36680000E+04	5.62100000E+04	7.39500000E+04	9.46200000E+04	1.14163330E+05	1.31033330E+05	1.44746670E+05
	a ₁	1.13900000E+02	9.18400000E+01	6.48000000E+01	4.95000000E+01	3.52000000E+01	2.40000000E+01	1.57500000E+01	9.90000000E+00
C ₂ H ₂	a ₀	1.40515000E+04	2.11246000E+04	2.31062000E+04	2.80460000E+04	2.94349000E+04	3.19462000E+04	3.41880000E+04	3.60815000E+04
	a ₁	2.71000000E+01	1.37600000E+01	1.13330000E+01	7.00000000E+00	6.07300000E+00	4.63500000E+00	3.53900000E+00	2.73200000E+00
CH ₂	a ₀	3.01201000E+04	2.95639000E+04	3.09097500E+04	3.54633000E+04	3.90823000E+04	4.26014000E+04	4.58851000E+04	4.87320000E+04
	a ₁	1.50000000E+01	1.61000000E+01	1.45300000E+01	1.05300000E+01	8.03000000E+00	6.01700000E+00	4.41000000E+00	3.19900000E+00
C ₂ H ₃	a ₀	3.66243000E+04	4.17522000E+04	4.63257000E+04	3.66567000E+04	-2.86170000E+04	-2.07394000E+05	-5.70102000E+05	-1.20334400E+06
	a ₁	4.65800000E+01	3.72200000E+01	3.16570000E+01	3.97860000E+01	8.42800000E+01	1.85860000E+02	3.62160000E+02	6.30950000E+02
n-C ₃ H ₇	a ₀	2.37140000E+04	5.61430000E+04	9.34290000E+04	1.11357000E+05	1.35500000E+05	1.48290000E+05	1.67000000E+05	1.83900000E+05
	a ₁	1.68100000E+02	1.09050000E+02	6.57140000E+01	4.95240000E+01	3.28570000E+01	2.57140000E+01	1.66670000E+01	9.52380000E+00
C ₃ H ₆	a ₀	1.93500000E+04	4.60000000E+04	7.49500000E+04	1.01507000E+05	1.17400000E+05	1.33730000E+05	1.61193000E+05	1.61193000E+05
	a ₁	1.56330000E+02	1.08330000E+02	7.40000000E+01	5.08570000E+01	3.99040000E+01	3.05714000E+01	1.79520000E+01	1.79520000E+01
C ₃ H ₈	a ₀	1.65140000E+04	4.99140000E+04	9.05500000E+04	1.19710000E+05	1.40700000E+05	1.61230000E+05	1.79114000E+05	1.95990000E+05
	a ₁	1.93760000E+02	1.33570000E+02	8.56670000E+01	6.00470000E+01	4.55710000E+01	3.39050000E+01	2.51430000E+01	1.79520000E+01
C ₈ H ₁₈	a ₀	2.77000000E+04	1.18300000E+05	1.71200000E+05	3.13400000E+05	3.53500000E+05	4.07400000E+05	4.48200000E+05	4.91000000E+05
	a ₁	4.74800000E+02	3.11400000E+02	2.49500000E+02	1.22860000E+02	9.47600000E+01	6.38100000E+01	4.38100000E+01	2.57000000E+01

Table C4: Coefficients of equilibrium constant for Eq. 1.81 to be used in calculating K_1 to K_{14} for 14 chemical equilibrium reactions.

Equilibrium Constant	Chemical reaction equations	A_1	A_2	A_3	A_4	A_5	A_6	A_7	A_8	A_9	A_{10}	A_{11}	A_{12}
K_1	$\text{CO}_2 \leftrightarrow \text{CO} + 0.5 \text{O}_2$	-4.7060	4.5548	-1.9275	0.6914	-0.2143	0.0568	-0.0118	0.6918	0.7740	-0.1600	0.0297	-0.0053
K_2	$\text{CO} \leftrightarrow \text{C} + 0.5 \text{O}_2$	-23.3871	13.5989	-5.6463	2.0147	-0.6290	0.1745	-0.0436	-7.0178	2.4494	-0.4831	0.0876	-0.0146
K_3	$\text{CH}_4 \leftrightarrow \text{C} + 2 \text{H}_2$	-12.3506	13.1975	-5.5245	1.9729	-0.6151	0.1704	-0.0425	3.4195	2.3113	-0.4651	0.0856	-0.0144
K_4	$\text{HCN} \leftrightarrow \text{C} + 0.5 \text{H}_2 + 0.5 \text{N}_2$	-12.6282	9.5942	-4.0164	1.4348	-0.4479	0.1243	-0.0310	-1.1652	1.6762	-0.3401	0.0622	-0.0104
K_5	$\text{H}_2\text{O} \leftrightarrow \text{H}_2 + 0.5 \text{O}_2$	-5.1798	4.0998	-1.6966	0.6008	-0.1828	0.0461	-0.0081	-0.2380	0.7418	-0.1478	0.0290	-0.0066
K_6	$\text{H}_2\text{O} \leftrightarrow \text{OH} + 0.5 \text{H}_2$	-5.6771	4.7100	-1.9572	0.6958	-0.2168	0.0510	-0.0143	-0.0217	0.8372	-0.1692	0.0317	-0.0055
K_7	$0.5 \text{H}_2 \leftrightarrow \text{H}$	-4.2669	3.6898	-1.5150	0.5328	-0.1618	0.0418	-0.0086	0.2000	0.6740	-0.1360	0.0268	-0.0063
K_8	$0.5 \text{O}_2 \leftrightarrow \text{O}$	-4.8419	4.1600	-1.7225	0.6135	-0.1940	0.0570	-0.0163	0.1700	0.7458	-0.1456	0.0235	-0.0021
K_9	$1.5 \text{O}_2 \leftrightarrow \text{O}_3$	-8.23556	2.3730	-0.9800	0.3462	-0.1077	0.0299	-0.0075	-5.3797	0.4183	-0.0869	0.0158	-0.0026
K_{10}	$0.5 \text{N}_2 \leftrightarrow \text{N}$	-12.1749	7.8225	-3.2406	1.1510	-0.3568	0.0984	-0.0249	-2.7519	1.4098	-0.2776	0.0501	-0.0068
K_{11}	$0.5 \text{N}_2 + 0.5 \text{O}_2 \leftrightarrow \text{NO}$	-2.2991	1.4798	-0.6119	0.2102	-0.0593	0.0126	-0.0015	-0.5281	0.2562	-0.0520	0.0080	-0.0003
K_{12}	$\text{NO}_2 \leftrightarrow \text{NO} + 0.5 \text{O}_2$	2.0772	0.9404	-0.3968	0.1434	-0.0450	0.0125	-0.0031	3.1992	0.1675	-0.0320	0.0059	-0.0010
K_{13}	$\text{NH}_3 \leftrightarrow 0.5 \text{N}_2 + 1.5 \text{H}_2$	4.3247	0.9087	-0.3926	0.1381	-0.0427	0.0119	-0.0030	5.3672	0.1264	-0.0338	0.0062	-0.0010
K_{14}	$2\text{HNO}_3 + \text{NO} \leftrightarrow 3 \text{NO}_2 + \text{H}_2\text{O}$	7.6818	0.5958	-0.2475	0.1101	-0.0781	0.0699	-0.0526	8.4100	0.1200	-0.0600	0.0533	-0.0400

Appendix D
Equilibrium Composition and
Adiabatic Temperatures for Some
Gaseous and Liquid Fuels
(Tables D1 to D4)

Solution Method for the Equilibrium Program Described in Section 1.5.4

The method of solving the equations described in section 1.5.4 is similar to that given by Kopa et al. [46] and Agrawal and Gupta [39] with minor modifications. The method of solving Eqs. 1.34(a) and 1.82 to 1.95 together with these given in Table C4 (Appendix C) is as follows:

1. A trial value of equilibrium temperature T_{ad} is assumed and the equilibrium constants K_1 - K_{14} are computed at this temperature.
2. It is easy to assume the number of moles of the compounds $A(H_2)$, $B(H_2O)$, $C(CO_2)$ and $D_1^{0.5}(N_2)$, therefore the mole fractions of all other species are expressed in terms of $A(H_2)$, $B(H_2O)$, $C(CO_2)$, $D(\sqrt{N_2})$ by using the equations given in Table C4 (Appendix C), with the known values of K_1 - K_{14} and having $P_e = P_i$.
3. Eqs. 1.87 to 1.89 and 1.91 are rewritten in the forms:

$$F(A, B, C, D) = 0 \quad (1.D1)$$

$$G(A, B, C, D) = 0 \quad (1.D2)$$

$$H(A, B, C, D) = 0 \quad (1.D3)$$

$$J(A, B, C, D) = 0 \quad (1.D4)$$

4. The four Eqs. 1.D1 to 1.D4 with the four unknowns (A , B , C and D) are linearized by using Taylor series expansion and neglecting higher-order small terms.

$$F = F_o + F_A \delta A + F_B \delta B + F_C \delta C + F_D \delta D \quad (1.D5)$$

$$G = G_o + G_A \delta A + G_B \delta B + G_C \delta C + G_D \delta D \quad (1.D6)$$

$$H = H_o + H_A \delta A + H_B \delta B + H_C \delta C + H_D \delta D \quad (1.D7)$$

$$J = J_o + J_A \delta A + J_B \delta B + J_C \delta C + J_D \delta D \quad (1.D8)$$

where,

$F_A = \partial F / \partial A$, etc. and $F_o = F(A_o, B_o, C_o, D_o)$, etc.

The maximum number of iterations required to achieve a convergence of (10^{-7}) is between 4 and 7. Once A , B , C and D are computed, the composition of the equilibrium products is readily obtained.

5. Once the equilibrium composition of the products is known, the total number of moles of the products, N_p , is computed from Eq. 1.90 and the enthalpy of the products is calculated and compared with that of reactants.

If they do not tally, the assumed value of T_{ad} is either increased (if $H_r < H_p$) and the steps outlined are obtained by interpolation. As the temperature and the energy have no linear relation, exact equivalence $H_p = H_r$ is difficult to achieve.

In order to save computer time, a maximum difference of 20 J mole^{-1} fuel between H_r and H_p is to be considered acceptable. This difference has negligible effect on T_{ad} .

The method of solution for the constant-volume cases is entirely analogous to the foregoing.

For four-mixture fuels it is important to keep the number of moles of the four fuels equals unity (i.e. $a_1 + a_2 + a_3 + a_4 = 1$).

Figure D1 shows the flow chart for a computer program to solve the above equations and compute the equilibrium composition and final state of the products at constant volume or pressure.

Source of thermochemical data:

Specific heats are taken from the work of Prothero [47] and Eq. 1.18, while equilibrium constant values are those given in JANAF Tables [13] and fitted by Agrawal and Gupta [39] with Eq. 1.81 Both are used as thermochemical data in the above described program.

Equilibrium composition and adiabatic temperature calculations

A comparison of the results obtained by the above described program with those of Agrawal and Gupta [39] and Steffensen et al [48] shows a good agreement within ± 4 °C. Table D1 (Appendix D) shows the output results from the program for methane-air flame at atmospheric pressure and initial temperature of 298K. The computed results for adiabatic flame temperature at constant-pressure and constant-volume combustion for CH₄, C₃H₈, C₈H₁₈ and natural gas are shown in Table D2 (Appendix D), while Tables D3 (a), (b) in the same appendix show some of the output results for natural gas-air mixtures (see the composition for Egyptian natural gas in chapter 2) at different pressures (Table D3 (a)), initial temperatures (Table D3 (b)). Also some results for propane-air mixture are given in Table D4 at different pressures.

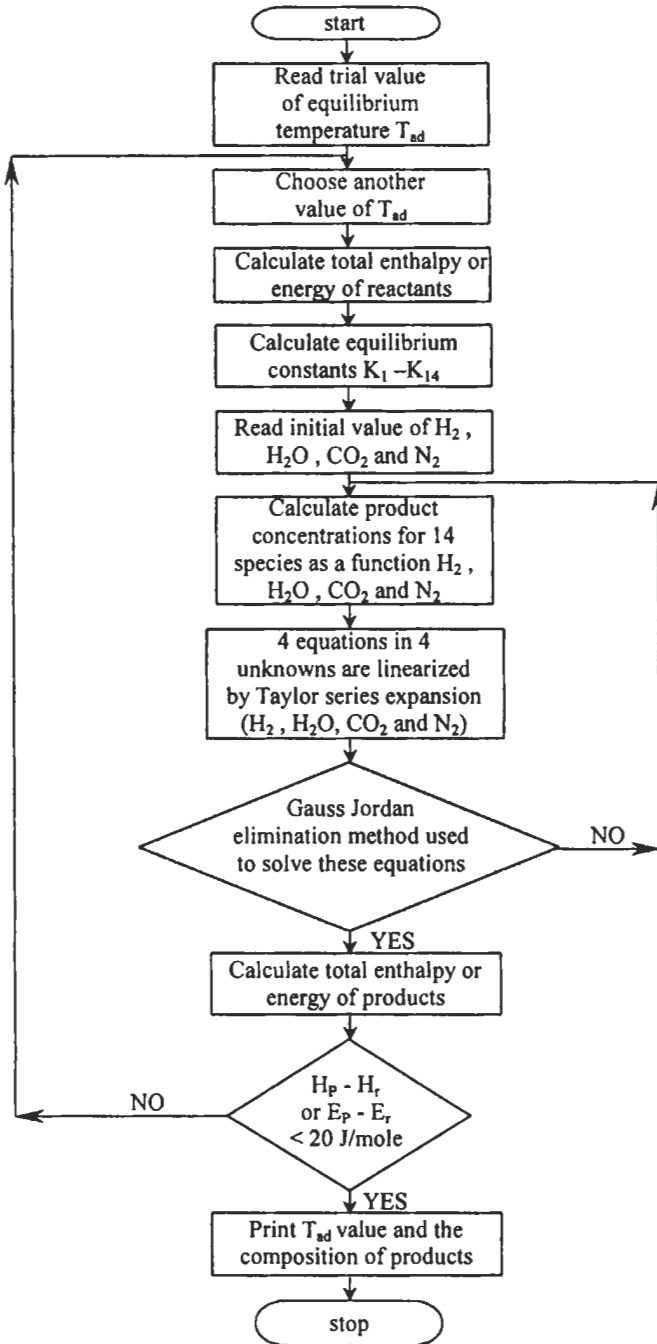


Fig. D1: Computer program flow chart to compute the equilibrium composition and final products.

Table D1: Output of the adiabatic program for equilibrium composition and adiabatic temperature at constant pressure combustion.

No. of carbon for fuel1 is	C1 = 1	No. of carbon for fuel2 is	C2 = 0
No. of hydrogen for fuel1 is	H1 = 4	No. of hydrogen for fuel2 is	H2 = 0
No. of moles for fuel1 is	Z1 = 0.243	No. of moles for fuel2 is	Z2 = 0.000
Equivalence ratio is	PHI = 1.00	Equivalence ratio is	PHI = 1.00
No. of carbon for fuel3 is	C3 = 0	No. of carbon for fuel4 is	C4 = 1
No. of hydrogen for fuel3 is	H3 = 0	No. of hydrogen for fuel4 is	H4 = 0
No. of moles for fuel3 is	Z3 = 0.000	No. of moles for fuel4 is	Z4 = 0.083
Equivalence ratio is	PHI = 1.00	Equivalence ratio is	PHI = 1.00
Atomic ratio of carbon to oxygen is	RCO = 0.3340	Mole fraction of fuel is	XFUEL = 0.3009
Atomic ratio of hydrogen to oxygen is	RHO = 0.9959	Mole fraction of air is	XAIR = 0.69907
Atomic ratio of nitrogen to oxygen is	RNO = 3.7602	Molecular weight of reactants is	WMU = 21.643
Total number of moles reactants is	SUMI = 3.323	Total no. of atoms is	ATS = 5.94
Stoichiometric air fuel ratio	SAFR = 13.692	No. of calculations	NC = 24
Actual air fuel ratio	AAFR = 13.692	No. of change in temperature	NT = 15
Enthalpy of products	HPRO = -4350.6 cal	Equilibrium pressure	PE = 1.02 atm
Enthalpy of reactants	HREA = -4348.5 cal	Total mole fractions	XSUM = 0.99945
The difference in enthalpy	XDX = -2.137	Total no. of product moles	SUME = 2.65
Initial temperature	TI = 298.00 K	Expansion ratio	ER = 5.826
Initial pressure	PI = 1.02 atm	Ratio of mole reactants to mole products	RS = 1.2535
Adiabatic temperature	T _{ad} = 2176.213 K	Weight of the products	WME = 27.13
H ₂ = 0.1774E-01	H ₂ O = 0.1648E+00	CO ₂ = 0.7905E-01	N ₂ = 0.6923E+00
O = 0.2067E-04	O ₂ = 0.8210E-04	O ₃ = 0.7905E-13	H = 0.6462E-03
OH = 0.8064E-03	CO = 0.4360E-01	C = 0.3128E-15	CH ₄ = 0.2366E-13
N = 0.0000E+00	NO = 0.2306E-03	NO ₂ = 0.5619E-08	NH ₃ = 0.3144E-07
HNO ₃ = 0.1144E-14	HCN = 0000E+00		

Table D2: Comparison between adiabatic flame temperature T_{ad} for CH_4 , C_3H_8 and LNG at different initial pressures, P_i , and equivalence ratios, ϕ . The initial temperature is, $T_i = 298$ K.

Fuel	Initial conditions			Constant pressure	Constant volume combustion	
	ϕ	P_i (atm)	T_i (K)	T_{ad} (K)	P_c (atm) (equil. pres.)	T_{ad} (K)
CH_4	0.8	1	298	1994	8.1	2379
	0.8	10	298	2002	81	2407
	1	1	298	2225	8.9	2588
	1	10	298	2268	90.6	2673
	1.25	1	298	2096	9	2525
	1.25	10	298	2099	89.7	2550
C_3H_8	0.8	1	298	2041	8.5	2428
	0.8	10	298	2050	85.6	2464
	1	1	298	2267	9.4	2631
	1	10	298	2317	96.3	2727
	1.25	1	298	2162	9.7	2599
	1.25	10	298	2169	97.5	2635
C_8H_{18}	0.8	1	298	2051	8	2436
	0.8	10	298	2061	86.1	2476
	1	1	298	2275	9.5	2641
	1	10	298	2328	97.2	2739
	1.25	1	298	2176	9.8	2615
	1.25	10	298	2184	99	2654
LNG (0.9 CH_4 + 0.1 C_2H_6)	1	1	298	2277	-	-
C_2H_6	1	1	298	2269	-	-

Table D3 (a): Equilibrium temperatures and concentrations for natural gas-air combustion at 300 K, and different initial pressures and equivalence ratios.

ϕ	P_i , atm	0.1	1	10	100
0.5	T_{ad} , K	1481.9	1482.7	1482.8	1482
0.5	H ₂	1.48E-06	4.75E-07	1.50E-07	4.75E-08
0.5	H ₂ O	9.78E-02	9.78E-02	9.78E-02	9.78E-02
0.5	CO ₂	5.12E-02	5.12E-02	5.12E-02	5.12E-02
0.5	N ₂	7.51E-01	7.51E-01	7.51E-01	7.51E-01
0.5	O	3.19E-06	1.02E-06	3.22E-07	1.02E-06
0.5	O ₂	9.98E-02	9.74E-02	9.94E-02	9.94E-02
0.5	H	5.54E-08	1.00E-08	1.78E-09	3.17E-10
0.5	OH	9.74E-05	5.51E-05	3.10E-05	1.74E-05
0.5	CO	1.93E-06	6.20E-07	1.96E-07	6.20E-08
0.7	T_{ad} , K	1837.3	1842.5	1844.8	1845.4
0.7	H ₂	1.33E-04	4.44E-05	1.44E-05	4.57E-06
0.7	H ₂ O	1.34E-01	1.34E-01	1.34E-01	1.34E-01
0.7	CO ₂	7.00E-02	7.02E-02	7.03E-02	7.03E-02
0.7	N ₂	7.35E-01	7.35E-01	7.35E-01	7.35E-01
0.7	O	1.30E-04	4.31E-05	1.39E-05	4.42E-06
0.7	O ₂	5.76E-02	5.73E-02	5.73E-02	5.74E-02
0.7	H	1.77E-05	3.38E-06	6.19E-07	1.11E-07
0.7	OH	1.27E-03	7.36E-04	4.20E-04	2.37E-04
0.7	CO	2.74E-04	9.19E-05	2.98E-05	9.47E-06
0.7	NO	2.48E-03	2.52E-03	2.54E-03	2.55E-03
1	T_{ad} , K	2169.2	2232.9	2277.3	2305.3
1	H ₂	6.07E-03	3.69E-03	2.10E-03	1.12E-03
1	H ₂ O	1.75E-01	1.80E-01	1.83E-01	1.85E-01
1	CO ₂	8.18E-02	8.73E-02	9.15E-02	9.42E-02
1	N ₂	7.06E-01	7.09E-01	7.12E-01	7.14E-01
1	O	6.06E-04	2.28E-04	6.95E-05	1.82E-05
1	O ₂	7.47E-03	4.73E-03	2.60E-03	1.26E-03
1	H	1.17E-03	4.12E-04	1.25E-04	3.34E-05
1	OH	4.47E-03	2.94E-03	1.70E-03	8.92E-04
1	CO	1.45E-02	9.51E-03	5.72E-03	3.16E-03
1	NO	2.19E-03	2.01E-03	1.63E-03	1.22E-03
1.3	T_{ad} , K	2058.1	2063.2	2072.4	2074.5
1.3	H ₂	4.27E-02	4.36E-02	4.27E-02	4.29E-02
1.3	H ₂ O	1.79E-01	1.79E-01	1.81E-01	1.81E-01
1.3	CO ₂	5.47E-02	5.43E-02	5.46E-02	5.48E-02
1.3	N ₂	6.59E-01	6.59E-01	6.59E-01	6.60E-01
1.3	O	1.93E-05	2.03E-06	2.38E-07	2.44E-08
1.3	O ₂	3.51E-05	3.60E-06	4.30E-07	4.43E-08
1.3	H	1.57E-03	1.50E-04	1.72E-04	5.52E-05
1.3	OH	7.27E-04	2.37E-04	8.22E-05	2.64E-05
1.3	CO	6.16E-02	6.28E-02	6.18E-02	6.24E-02
1.3	NO	1.10E-04	1.27E-05	1.27E-05	4.09E-06
1.6	T_{ad} , K	1835.8	1838.2	1839.1	1839.5
1.6	H ₂	9.92E-02	9.93E-02	9.94E-02	9.93E-02
1.6	H ₂ O	1.55E-01	1.56E-01	1.56E-01	1.56E-01
1.6	CO ₂	3.79E-02	3.79E-02	3.78E-02	3.79E-02
1.6	N ₂	6.11E-01	6.12E-01	6.12E-01	6.12E-01
1.6	O	1.99E-07	2.07E-08	2.11E-09	2.12E-10
1.6	O ₂	1.38E-07	1.44E-08	1.46E-09	1.47E-10
1.6	H	4.78E-04	1.54E-04	4.92E-05	1.56E-05
1.6	OH	5.34E-05	1.73E-05	5.53E-06	1.75E-06
1.6	CO	9.47E-02	9.50E-02	9.50E-02	9.51E-02
1.6	NO	3.49E-06	1.10E-06	3.63E-07	1.15E-07

Table D3 (b): Equilibrium temperatures and concentrations for propane-air combustion at atmospheric pressure, and different initial temperatures and equivalence ratios.

ϕ	T_i , K	300	400	600	900
0.5	T_{ad} , K	1509.1	1746.4	1991.2	2232
0.5	H ₂	5.52E-07	8.20E-06	6.92E-05	3.55E-04
0.5	H ₂ O	8.06E-02	8.04E-02	7.90E-02	7.80E-02
0.5	CO ₂	6.05E-02	6.04E-02	6.02E-02	5.80E-02
0.5	N ₂	7.57E-01	7.56E-01	7.55E-01	7.51E-01
0.5	O	1.46E-06	2.27E-05	1.96E-04	1.02E-03
0.5	O ₂	1.00E-01	9.90E-02	9.79E-02	9.50E-02
0.5	CO	1.08E-06	2.20E-05	2.30E-04	1.43E-03
0.5	OH	6.30E-05	3.65E-04	1.43E-03	4.09E-03
0.5	H	1.48E-08	6.43E-07	1.27E-05	1.27E-04
0.5	NO	9.27E-04			
0.7	T_{ad} , K	1880.2	2097.6	2299.7	2475.5
0.7	H ₂	5.00E-05	2.70E-04	9.40E-04	2.29E-03
0.7	H ₂ O	1.11E-01	1.09E-01	1.07E-01	1.02E-01
0.7	CO ₂	8.31E-02	8.22E-02	7.90E-02	7.26E-02
0.7	N ₂	7.44E-01	7.42E-01	7.39E-01	7.32E-01
0.7	O	6.04E-05	3.25E-04	1.17E-03	3.04E-03
0.7	O ₂	5.80E-02	5.67E-02	5.61E-02	5.64E-02
0.7	CO	1.56E-04	9.80E-04	3.85E-03	9.81E-03
0.7	OH	8.30E-04	2.42E-03	5.42E-03	9.73E-03
0.7	H	4.85E-06	5.06E-05	2.98E-04	1.08E-03
0.7	NO	2.87E-03		8.15E-03	
1	T_{ad} , K	2270.7	2405	2404	2649.8
1	H ₂	3.39E-03	5.48E-03	8.27E-03	1.15E-02
1	H ₂ O	1.48E-01	1.46E-01	1.37E-01	1.29E-01
1	CO ₂	1.02E-01	9.40E-02	8.26E-02	7.10E-02
1	N ₂	7.21E-01	7.15E-01	7.07E-01	6.98E-01
1	O	3.32E-04	8.67E-04	1.94E-03	3.89E-03
1	O ₂	5.97E-03	9.53E-03	1.33E-02	1.79E-02
1	CO	1.27E-02	2.08E-02	3.08E-02	4.10E-02
1	OH	3.27E-03	5.86E-03	9.33E-03	1.40E-02
1	H	4.85E-04	1.21E-03	2.62E-03	5.03E-03
1	NO	2.47E-03	4.07E-03	6.00E-03	
1.3	T_{ad} , K	2130.2	2330.2	2515	2665.1
1.3	H ₂	3.39E-02	3.20E-02	3.18E-02	3.35E-02
1.3	H ₂ O	1.52E-01	1.52E-01	1.48E-01	1.40E-01
1.3	CO ₂	6.61E-02	6.37E-02	5.99E-02	5.38E-02
1.3	N ₂	6.73E-01	6.72E-01	6.68E-01	6.61E-01
1.3	O	5.62E-06	6.94E-05	4.71E-04	1.66E-03
1.3	O ₂	1.07E-05	1.38E-04	9.12E-04	2.86E-03
1.3	CO	7.35E-02	7.54E-02	7.87E-02	8.35E-02
1.3	OH	3.90E-04	1.61E-03	4.74E-03	9.50E-03
1.3	H	1.69E-03	2.03E-03	4.70E-03	9.11E-03
1.3	NO	7.39E-05		1.48E-03	
1.6	T_{ad} , K	1901.4	2122.3	2349.8	2559.9
1.6	H ₂	8.33E-02	7.97E-02	7.65E-02	7.37E-02
1.6	H ₂ O	1.30E-01	1.32E-01	1.33E-01	1.31E-01
1.6	CO ₂	4.34E-02	4.01E-02	3.76E-02	3.52E-02
1.6	N ₂	6.27E-01	6.26E-01	6.25E-01	6.21E-01
1.6	O	6.21E-08	1.87E-06	3.19E-05	2.75E-04
1.6	O ₂	4.25E-08	1.34E-06	2.35E-05	2.04E-04
1.6	CO	1.16E-01	1.19E-01	1.22E-01	1.23E-01
1.6	OH	2.96E-05	2.07E-04	1.04E-03	3.50E-03
1.6	H	2.31E-04	1.01E-03	3.46E-03	8.85E-03
1.6	NO	2.21E-06	2.47E-05	1.70E-04	

Table D4: Equilibrium temperatures and concentrations for propane-air combustion at 300 K, and different initial pressures and equivalence ratios.

ϕ	P_i , atm	0.1	1	10	100
0.5	T_{ad} , K	1508.9	1509.1	1509.3	1509.3
0.5	H ₂	1.74E-06	5.52E-07	1.75E-07	5.53E-08
0.5	H ₂ O	8.05E-02	8.06E-02	8.06E-02	8.03E-02
0.5	CO ₂	6.05E-02	6.05E-02	6.05E-02	6.05E-02
0.5	N ₂	7.57E-01	7.57E-01	7.57E-01	7.57E-01
0.5	O	4.61E-06	1.46E-06	4.60E-07	1.47E-07
0.5	O ₂	1.00E-01	1.00E-01	1.00E-01	1.00E-01
0.5	CO	3.39E-06	1.08E-06	3.41E-07	1.08E-07
0.5	OH	1.10E-04	6.30E-05	3.55E-05	2.00E-05
0.5	H	8.27E-08	1.48E-08	2.63E-09	4.68E-10
0.5	NO	9.25E-04	9.27E-04	9.27E-04	9.27E-04
0.7	T_{ad} , K	1874.6	1880.2	1882.5	1883.8
0.7	H ₂	1.52E-04	5.00E-05	1.64E-05	5.20E-06
0.7	H ₂ O	1.10E-01	1.11E-01	1.11E-01	1.11E-01
0.7	CO ₂	8.30E-02	8.31E-02	8.32E-02	8.33E-02
0.7	N ₂	7.44E-01	7.44E-01	7.44E-01	7.44E-01
0.7	O	1.80E-04	6.04E-05	1.96E-05	6.25E-06
0.7	O ₂	5.76E-02	5.80E-02	5.83E-02	5.82E-02
0.7	CO	4.67E-04	1.56E-04	5.03E-05	1.64E-05
0.7	OH	1.43E-03	8.30E-04	4.74E-04	2.68E-04
0.7	H	2.55E-05	4.85E-06	8.86E-07	1.60E-07
0.7	NO	2.80E-03	2.87E-03	2.90E-03	2.91E-03
1	T_{ad} , K	2200.4	2270.7	2322.4	2355.9
1	H ₂	5.38E-03	3.39E-03	1.97E-03	1.10E-03
1	H ₂ O	1.44E-01	1.48E-01	1.51E-01	1.52E-01
1	CO ₂	9.59E-02	1.02E-01	1.07E-01	1.11E-01
1	N ₂	7.16E-01	7.21E-01	7.23E-01	7.25E-01
1	O	8.38E-04	3.32E-04	1.02E-04	2.70E-05
1	O ₂	9.58E-03	5.97E-03	3.31E-03	1.56E-03
1	CO	1.86E-02	1.27E-02	7.86E-03	4.57E-03
1	OH	4.90E-03	3.27E-03	1.94E-03	1.02E-03
1	H	1.30E-03	4.85E-04	1.53E-04	4.29E-05
1	NO	2.68E-03	2.47E-03	2.73E-03	5.03E-03
1.3	T_{ad} , K	2115.2	2130.2	2134.6	2137.4
1.3	H ₂	3.39E-02	3.39E-02	3.38E-02	3.39E-02
1.3	H ₂ O	1.50E-01	1.52E-01	1.52E-01	1.52E-01
1.3	CO ₂	6.61E-02	6.61E-02	6.60E-02	6.63E-02
1.3	N ₂	6.73E-01	6.73E-01	6.74E-01	6.74E-01
1.3	O	4.54E-05	5.62E-06	5.99E-07	6.18E-08
1.3	O ₂	8.67E-05	1.07E-05	1.16E-06	1.19E-07
1.3	CO	7.34E-02	7.35E-02	7.31E-02	7.39E-02
1.3	OH	1.08E-03	3.90E-04	1.27E-04	4.09E-05
1.3	H	1.99E-03	6.90E-04	2.24E-04	7.23E-05
1.3	NO	2.02E-04	7.39E-05	2.44E-05	7.90E-06
1.6	T_{ad} , K	1897.6	1901.4	1902.7	1903.1
1.6	H ₂	8.31E-02	8.33E-02	8.33E-02	8.34E-02
1.6	H ₂ O	1.30E-01	1.30E-01	1.30E-01	1.30E-01
1.6	CO ₂	4.34E-02	4.34E-02	4.34E-02	4.34E-02
1.6	N ₂	6.26E-01	6.27E-01	6.27E-01	6.27E-01
1.6	O	5.83E-07	6.21E-08	6.34E-09	6.40E-10
1.6	O ₂	3.99E-07	4.25E-08	4.34E-09	4.37E-10
1.6	CO	1.16E-01	1.16E-01	1.16E-01	1.16E-01
1.6	OH	9.02E-05	2.96E-05	9.47E-06	3.01E-06
1.6	H	7.10E-04	2.31E-04	7.39E-05	2.34E-05
1.6	NO	6.60E-06	2.21E-06	7.73E-07	2.45E-07

Appendix E
Transport Properties
(Tables E1 and E2)

Table E1: Intermolecular force parameters.

Substance	Molecular weight M	Lennard-Jones parameters [54]		Substance	Molecular weight M	Lennard-Jones parameters [54]	
		Si (Å)*	ε / κ (K)			Si (Å)	ε / κ (K)
<i>Light elements</i>				C ₂ H ₄	28.05	4.232	205
H ₂	2.016	2.915	38.0	C ₂ H ₆	30.07	4.418	230
He	4.003	2.576	10.2	C ₃ H ₆	42.08	-	-
<i>Noble gases</i>				C ₃ H ₈	44.09	5.061	254
Ne	20.183	2.789	35.7	n-C ₄ H ₁₀	58.12	-	-
Ar	39.944	3.418	124	i-C ₄ H ₁₀	58.12	5.341	313
Kr	83.80	3.498	225	n-C ₅ H ₁₂	72.15	5.769	345
<i>Simple polyatomic substances</i>				n-C ₆ H ₁₄	86.17	5.909	413
Air	28.97	3.617	97.0	n-C ₇ H ₁₆	100.20	-	-
N ₂	28.02	3.681	91.5	n-C ₈ H ₁₈	114.22	7.451	320
O ₂	32.00	3.433	113	n-C ₉ H ₂₀	128.25	-	-
O ₃	48.00	-	-	Cyclohexane	84.16	6.093	324
CO	28.01	3.590	110	C ₆ H ₆	78.11	5.270	440
CO ₂	44.01	3.996	190	<i>Other organic compounds</i>			
NO	30.01	3.470	119	CH ₄	16.04	3.822	137
N ₂ O	44.02	3.879	220	CH ₃ Cl	50.49	3.375	855
SO ₂	64.07	4.290	252	CH ₂ Cl ₂	84.94	4.759	406
Cl ₂	70.91	4.115	357	CHCl ₃	119.39	5.430	327
Br ₂	159.83	4.268	520	CCl ₄	153.84	5.881	327
<i>Hydrocarbons</i>				C ₂ N ₂	52.04	4.38	339
CH ₄	16.04	3.822	137	COS	60.08	4.13	335
C ₂ H ₂	26.04	4.221	185	CS ₂	76.14	4.438	488

* 1 Å = Angstrom unit = 10⁻¹⁰m = 0.1 nm (nano meter)

Table E2: Functions for the prediction of transport properties of gases at low densities [55].

$(\kappa T / \varepsilon)$ or $(\kappa T / \varepsilon_{AB})$	$\Omega_\eta = \Omega_\lambda$ (for viscosity and thermal conductivity)	$\Omega_{D_{AB}}$ (for mass diffusivity)	$(\kappa T / \varepsilon)$ or $(\kappa T / \varepsilon_{AB})$	$\Omega_\eta = \Omega_\lambda$ (for viscosity and thermal conductivity)	$\Omega_{D_{AB}}$ (for mass diffusivity)
0.30	2.785	2.662	2.60	1.081	0.9878
0.35	2.628	2.476	2.70	1.069	0.9770
0.40	2.492	2.318	2.80	1.058	0.9672
0.45	2.368	2.184	2.90	1.048	0.9576
0.50	2.257	2.066	3.00	1.039	0.9490
0.55	2.156	1.966	3.10	1.030	0.9406
0.60	2.065	1.877	3.20	1.022	0.9328
0.65	1.982	1.798	3.30	1.014	0.9256
0.70	1.908	1.729	3.40	1.007	0.9186
0.75	1.841	1.667	3.50	0.9999	0.9120
0.80	1.780	1.612	3.60	0.9932	0.9058
0.85	1.725	1.562	3.70	0.9870	0.8998
0.90	1.675	1.517	3.80	0.9811	0.8942
0.95	1.629	1.476	3.90	0.9755	0.8888
1.00	1.587	1.439	4.00	0.9700	0.8836
1.05	1.549	1.406	4.10	0.9649	0.8788
1.10	1.514	1.375	4.20	0.9600	0.8740
1.15	1.482	1.346	4.30	0.9553	0.8694
1.20	1.452	1.320	4.40	0.9507	0.8652
1.25	1.424	1.296	4.50	0.9464	0.8610
1.30	1.399	1.273	4.60	0.9422	0.8568
1.35	1.375	1.253	4.70	0.9382	0.8530
1.40	1.353	1.233	4.80	0.9343	0.8492
1.45	1.333	1.215	4.90	0.9305	0.8456
1.50	1.314	1.198	5.00	0.9269	0.8422
1.55	1.296	1.182	6.00	0.8963	0.8124
1.60	1.279	1.167	7.00	0.8727	0.7896
1.65	1.264	1.153	8.00	0.8538	0.7712
1.70	1.248	1.140	9.00	0.8379	0.7556
1.75	1.234	1.128	10.0	0.8242	0.7424
1.80	1.221	1.116	20.0	0.7432	0.6640
1.85	1.209	1.105	30.0	0.7005	0.6232
1.90	1.197	1.094	40.0	0.6718	0.5960
1.95	1.186	1.084	50.0	0.6504	0.5756
2.00	1.175	1.075	60.0	0.6335	0.5596
2.10	1.156	1.057	70.0	0.6194	0.5464
2.20	1.138	1.041	80.0	0.6076	0.5352
2.30	1.122	1.026	90.0	0.5973	0.5256
2.40	1.107	1.012	100.0	0.5882	0.5170
2.50	1.093	0.9996			

REFERENCES

1. World Energy Outlook, WEO, Ch. 3, International Energy Agency, 1998 37.
2. World Energy Council, WEC, Ch. 2, Edition of Survey of Energy Resources (SER), Crude Oil and Natural Gas Liquids, 1998 38.
3. B. L. Capehart, W. C. Turner, and W. J. Kennedy, "Guide to Energy Management", Second Ed. The Fairmont Press, Inc., Lilburn, GA30247, USA, 1997.
4. The Energy Dimension of Climate Change and Energy and Climate Change, part IV, IEA/OECD Paris, 1997.
5. Energy in Europe, 1999 Annual Energy Review, January 2000.
6. E. L. Keating, "Applied Combustion", Marcel Dekker, Inc., New York, 1993.
7. R. O. C. Norman, and D. J. Waddington, "Modern Organic Chemistry", Mills and Soon Limited, Second Ed., London, 1975.
8. E. I. Kazantsev, "Industrial Furnaces", Translated from the Russian by I. V., Savin, Mir Publishers, Moscow, 1977.
9. R. A. Strehlow, "Fundamentals of Combustion", International Textbook Company, Scranton, Pennsylvania, 1968.
10. Djong-Gie, Oei, Automotive Engineering, SAE, The Engineering Society for Advancing Mobility Land Sea Air and Space, Int., Feb. 1997 115.
11. V. A. Kirillin, V. V. Sychev and A. E. Sheindlin, "Engineering Thermodynamics", Mir Publishers, Moscow, 1976.
12. W. C. Gardiner, Jr. (Ed.), "Combustion Chemistry", Springer-Verlag, New York, 1984 481.
13. JANAF Thermochemical Tables, Stull, D. R., et al. Dow Chemical, Midland, Michigan, 1971.
14. C. K. Westbrook, and L. L. Chase, "Chemical Kinetics and Thermochemical Data for Combustion Applications", Lawrence Livermore Laboratory, UCID-17833, Rev.3, Feb. 19 1983.
15. G. Dixon-Lewis, "Computer modeling of combustion reaction in flowing system with transport", Ch. 2 of "Combustion Chemistry", (W. C. Gardiner, Jr. Ed.), Springer Verlag, New York, 1984.
16. S. El-Din Habik, and S. A. El-Sherif, Port-Said Engineering Research Journal,

- Faculty of Engineering of Port-Said, Suez Canal University, 1997 1 (1).
17. S. El-Din Habik, S. A. El-Sherif, Pech Cho and Duane L. Abata, *Combust. Sci. and Technol.* 1999 148 93.
 18. S. A. El-Sherif, *Fuel*, 1998 77 (14) 1539.
 19. S. El-Din Habik, *Journal of Engineering and Applied Science*, Faculty of Engineering, Cairo University, June 1998 45 (3) 375.
 20. S. El-Din Habik, *Journal of Engineering and Applied Science*, Faculty of Engineering, Cairo University, 1996 43 (5) 1217.
 21. G. Dixon-Lewis, D. Bradley, and S. El-Din Habik, *Combust. Flame*, 1991 86 12.
 22. R. A. Strehlow, "Combustion Fundamentals", N. Chigier Consulting Ed., McGraw-Hill Book Company, New York, London, 1984.
 23. W. C. Reynolds, "The Element Potential Method for Chemical Equilibrium Analysis; Implementation of the Interactive Program STANJAN", Mechanical Engineering Dept. Stanford University, 1986. Instructors may contact Prof. Reynolds (wcr@thermo.stanford.edu) for a copy of the program.
 24. I. Glassman, "Combustion", Academic Press, New York, San Francisco, London, 1977.
 25. J. M. Smith, "Chemical Engineering Kinetics", McGraw-Hill, Chemical Engineering Series, Third Edition, 1981.
 26. D. L. Baulch, C. J. Cobos, R. A. Cox, P. Frank, G. Hayman, Th. Just, J. A. Kerr, T. Murrells, M. J. Pilling, J. Troe, R. W. Walker, and J. Warnatz, *Combust. Flame*, 1994 98 59.
 27. J. Vandooren, Oldenhove de L. Guertechin, and P. J. Van Tiggelen, *Combust. Flame*, 1986 64 127.
 28. J. Warnatz, "Rate coefficients in the C/H/O System", "In Combustion Chemistry" (W. C. Gardiner Jr. Ed.), Ch.5, Springer-Verlag, New York, 1984.
 29. European Committee, CEC Kinetic Data Evaluation Group, Summary (Provisional) of preferred rate data for combustion modeling, 1989.
 30. W. J. Tsang, *Phys. Chem. Ref. Data*, 1987 16 3.
 31. G. J. VanWynen, and R. E. Sonntag, "Fundamentals of Classical Thermodynamics, S.I. Version", 2nd Ed. John Wiley, 1976.
 32. D. D. Agrawal, and C. P. Gupta, *Trans. ASME, J. Eng. Power*, 1977 99 246.
 33. S. Gordon, and B. J. McBride, "Computer Program for Calculation of Complex Chemical Equilibrium Compositions, Rocket Performance, Incident and Reflected Shocks and Chapman Jouguet Denotations", NASA, SP-273, 1971.
 34. C. Olikara, and G. L. Borman, *SAE*, 1975 750468.
 35. J. H. Harker, and D. A. Allen, *J. Inst. Fuel*, 1969 42 183.
 36. D. A. Miller, and S. G. McConnel, *J. Inst. Fuel*, 1972 45 43.
 37. J. H. Harker, *J. Inst. Fuel*, 1967 40 206.

38. D. D. Agrawal, S. P. Sharma, and C. P. Gupta, *J. Inst. Fuel*, 1975 48 104.
39. D. D. Agrawal, and C. P. Gupta, *Trans. ASME, J. Eng. Power*, 1977 99 246.
40. C. G. W. Sheppard, "Electrical Phenomena in Flame", Ph.D. Thesis, Dept. of Mech. Engineering, University of Leeds, U.K., 1971.
41. G. Dixon-Lewis, and J. B. Greenberg, *J. Inst. Fuel*, 1975 48 132.
42. K. T. Rhee, and S. I. Chang, *Combust. Sci. and Technol.*, 1985 44 75.
43. S. El-Din Habik, "Burning Properties of Solid Fuels", Ph.D. Thesis, Department of Mechanical Engineering, Leeds University, U.K., 1986.
44. D. Bradley, G. Dixon-Lewis, S. El-Din Habik, L.K. Kwa, and S. El-Sherif, *Combust. Flame*, 1991 85 105.
45. D. Bradley, S. El-Din Habik, and S. El-Sherif, *Combust. Flame*, 1991 87 336.
46. R. D. Kopa, B. R. Hollander, F. H. Hollander, and Kimura, *H.S.AE. Prog. in Tech.*, 1964 7 10.
47. A. Prothero, *Combust. Flame*, 1969 13 399.
48. R. J. Steffensen, J. T. Agnew, and R. A. Olsen, "Combustion of hydrocarbons property tables", Purdue University, Lafayette, Ind., *Bulletin*, 1966 122.
49. G. J. Van Wylen and R. E. Sonntag "Fundamentals of Classical Thermodynamics", SI Version 3rd Ed., John Wiley and Sons, Inc., New York, London, Sydney, Toronto, 1985.
50. D. C. Look, and H. J. Sauer, "Engineering Thermodynamics", PWS Publishers, Boston, 1986.
51. E. H. Kennard, "Kinetic Theory of Gases", McGraw-Hill, New York, 1938.
52. R. B. Bird, W. E. Stewart, and E. N. Lightfoot, "Transport Phenomena", Wiley International Edition, Toppan Company, Ltd., Tokyo, Japan 1960.
53. S. Chapman, and T. G. Cowling, "Mathematical Theory of Non-Uniform Gases", Cambridge University Press, Second Edition, 1951.
54. J. O. Hirschfelder, C. F. Curtiss, and R. B. Bird, "Molecular Theory of Gases and Liquids", Wiley, New York, 1954.
55. J. O. Hirschfelder, R. B. Bird, and E. L. Spotz, *Chem. Revs.*, 1949 44 205.
56. R. C. Reid, J. M. Prausnitz, and B. E. Poling, "The Properties of Gases and Liquids", McGraw-Hill, 3rd Ed. (1977), 4th Ed., 1987.
57. C. F. Curtiss, and J. O. Hirschfelder, *J. Chem. Phys.*, 1949 17 550.
58. C. R. Wilke, *J. Chem. Phys.*, 1950 18 517.
59. E. A. Mason, and C. S. Saxena, *Phys. Fluids*, 1958 1 361.
60. G. Dixon-Lewis, Sorgotto, I. (Ed.), *Ubstutyti du Unouabtu/Chemicci dell "Universita Padova"*, Italy, 1974 113.
61. G. Dixon-Lewis, *Coll. Int. Berthelot-Vieille Mallard Le Chatelier (Actes)*, 1st, 1981 1 284.
62. R. J. Kee, G. Dixon-Lewis, J. Warnatz, M. Coltrin, and J. Miller, "A FORTRAN

- Computer Code, Package for the Evaluation of Gas Phase Multi-Component Transport Properties”, SAND RR-8246, Sandia National Laboratories, Livermore, CA, 1980.
63. R. Svehla, and B. McBride, “Fortran IV Program Package for Thermodynamic and Transport Calculations in Complex Chemical Systems”, NASA Tech. Note TN S7185, NASA Washington D.C., Jan. 1973.
 64. D. Stull, and A. Prophet (Eds.), Joint Army/Navy/Air Force Thermochemical Tables, NSRDS NBS No.37, National Standard Reference Data System, National Bureau of Standards, U.S. Government Printing Office (1969), 2nd Ed., 1986.
 65. G. Dixon-Lewis, Twenty-Third Symposium on Combustion (International), The Combustion Institute, Pittsburgh, 1991 305.
 66. R. J. Kee, J. A. Miller, G. H. Evans, and G. Dixon-Lewis. Twenty-Second Symposium (International) on Combustion, The Combustion Institute, Pittsburgh, 1989 1479.
 67. N. Peters, and B. Rogg, (Eds) “Reduced Kinetic Mechanisms for Applications in Combustion Systems”, Springer-Verlag, Berlin Heidelberg New York, 1993.
 68. K. Seshadri, Twenty-Sixth Symposium (International) on Combustion, The Combustion Institute, Pittsburgh, 1996.
 69. J. A. Miller, Twenty-Sixth Symposium (International) on Combustion, The Combustion Institute, Pittsburgh, 1996 461.
 70. G. Patnaik, K. Kailasanath, and R. S. Sinkovits, Twenty-Sixth Symposium (International) on Combustion, The Combustion Institute, Pittsburgh, 1996 899.
 71. R. M. Fristrom, “Flame Structure and Processes”, Oxford University Press, Inc., Oxford, New York, Toronto, 1995.
 72. K. M. Leung, and R. P. Lindstedt, *Combust. Flame*, 1995 102 129.
 73. B. Zuo, and V. D. Bulck, *Combust. Flame*, 1998 113 615.
 74. B. Yang, and S. B. Pope, *Combust. Flame*, 1998 112 85.
 75. J. W. Bozzelli, and A. M. Dean, *Int. J. Chem. Kinet.*, 1995 27 1097.
 76. V. Dupont, and A. Williams, *Combust. Flame*, 1998 114 103.
 77. GRI Mech. Version 2.11 9/6/95, www address, <http://www.gri.org>, 1995.
 78. C. K. Westbrook, and F. L. Dryer, Eighteenth Symposium (International) on Combustion, The Combustion Institute, Pittsburgh, 1981 749.
 79. E. Oran, and J. Boris, *Progress in Energy and Combustion Science*, 1981 7 1.
 80. J. Warnatz, Eighteenth Symposium (International) on Combustion, The Combustion Institute, Pittsburgh, 1981 369.
 81. M. Evans, “Current theoretical concepts of steady state flame propagation”, *Chem. Rev.*, 1952 51 363.
 82. D. A. Frank-Kamenetzki, “Diffusion and Heat Exchange in Chemical Kinetics”, Princeton University Press, Princeton, 1955.

83. N. Semenov, *Chemical Kinetics and Chain Reactions*, Oxford, UK, 1935.
84. Ya. B. Zeldovich, "Combustion Theory", National Advisory Committee for 76 Aeronautics, Technical Report F.TS-1226-LA, Air Material Command, Washington D.C. (Trans. From Russian), 1949.
85. J. O. Hirschfelder, C. F. Curtiss, and R. B. Bird, "Molecular Theory of Gases and Liquids", Wiley, New York, 1954.
86. D. B. Spalding, *Phil. Trans. Roy. Soc. London*, 1956 249.
87. D. B. Spalding, and P. L. Stephenson, *Proc. Roy. Soc. London*, 1971, A324.
88. L. D. Smoot, W. Hecker, and G. Williams, *Combust. Flame*, 1976 26 323.
89. G. Dixon-Lewis, *Fourth Symposium (International) on Combustion*, The Combustion Institute, 1954 263.
90. G. Dixon-Lewis, *Proc. Roy. Soc.*, 1976 A298.
91. G. Dixon-Lewis, *Proc. Roy. Soc. London*, 1968 A307.
92. G. Dixon-Lewis, *Combust. Flame*, 1970 15 197.
93. G. Dixon-Lewis, *Proc. Roy. Soc. London*, 1972 A330.
94. G. Dixon-Lewis, *Phil. Trans. Roy. Soc. London*, 1979 A292.
95. G. Dixon-Lewis, *Combust. Flame*, 1979 36 1.
96. G. Dixon-Lewis, *Phil. Trans. Roy. Soc. Lond.*, 1981 A 303.
97. G. Dixon-Lewis, *Combust. Sci. and Technol*, 1983 34 1.
98. G. Dixon-Lewis, *J. Archivum Combust.*, 1984 4 279.
99. G. Dixon-Lewis, T. David, P. H. Gaskell, S. Fukutani, H. Jinno, J. Miller, R. J. Kee, D. Smooke, N. Petter, E. Effelsberg, J. Warnatz, and F. Behrendt, *Twentieth Symposium (International) on Combustion*, The Combustion Institute, Pittsburgh, 1985 1893.
100. G. Dixon-Lewis, and M. Missaghi, *Twenty-Second Symposium (International) on Combustion*, The Combustion Institute, Pittsburgh 1989 1461.
101. M. J. Prather, and J. A. Logan, *Twenty-Fifth Symposium (International) on Combustion*, The Combustion Institute, Pittsburgh, 1994 1513.
102. M. W. Holdgate, "A Perspective of Environmental Pollution", Cambridge University Press, Cambridge, 1979.
103. B. J. Alloway, and D. C. Ayres, "Chemical Principles of Environmental Pollution", Blackie Academic Professional, 1st Ed., 1993.
104. N. de Nevers, "Air Pollution Control Engineering", McGraw-Hill, Inc., New York, International Edition, 1995.
105. D. H. Meadows, D. L. Meadows, and J. Randers, "Beyond the limits", Earthscan publications, London, 1992.
106. K. Speakman, *Emission Control – Statutory Requirements*, in Dunderdale, J. (Ed.) *Energy and the Environment*, Roy. Soc. of Chem., Cambridge, 1990.
107. B. Moldan, and J. L. Schnoor, *Environmental Science Technology*, 1992 26 14.

108. S. A. El-Sherif, *Engineering Research Journal*, Helwan University, Faculty of Engineering, Mataria, Cairo, June, 1999 63.
109. S. M. Correa, and M. D. Smooke, *Twenty-Third Symposium (International) on Combustion*, The Combustion Institute, Pittsburgh, 1990 289.
110. P. C. Malte, and D. T. Pratt, *Combust. Sci. Technol.*, 1974 8 25.
111. C. P. Fenimore, *Thirteenth Symposium (International) on Combustion*, The Combustion Institute, Pittsburgh, 1971 373.
112. C. T. Bowman, *Prog. Energy Combust. Sci.*, 1975 1 33.
113. G. A. Lavoie, J. B. Heywood, and J. C. Keck, *Combust. Sci. Technol.*, 1970 1 313.
114. J. O. L. Wendt, and J. M. Ekmann, *Combust. Flame*, 1975 25 355.
115. R. C. Flagan, and J. H. Seinfeld, "Fundamentals of Air Pollution Engineering", Prentice Hall Inc., New Jersey, 1988.
116. C. Poppe, S. Sivasegaram, and J. H. Whitelaw, *Combust. Flame*, 1998 113 13.
117. O. Q. Zhou, L. G. Neal, R. Rolli, J. Haslbeck and A. Chang, *Twenty-Sixth Symposium (International) on Combustion*, The Combustion Institute, Pittsburgh, 1996 2091.
118. C. T. Bowman, *Twenty-Fourth Symposium (International) on Combustion*, The combustion Institute, Pittsburgh, 1992 859.
119. V. Dupont, and A. Williams, *Combust. Flame*, 1998 114 103.
120. M. C. Drake, and R. J. Blint, *Combust. Sci. Technol.*, 1991 75 261.
121. J. A. Miller, and C. T. Bowman, *Pro. Energy Combust. Sci.*, 1989 15 287.
122. M. C. Drake, and R. J. Blint, *Combust. Flame*, 1991 83 185.
123. P. Glarborg, J. A. Miller, and R. J. Kee, *Combust. Flame*, 1986 65 177.
124. P. C. Malte, and D. T. Pratt, *Combust. Sci. Technol.*, 1974 9 221.
125. P. Dagaut, F. Lecomte, S. Chevailier, and M. Cathonnet, *Combust. Flame*, 1999 119 494.
126. Babcock and Wilcox a McDermott Company, "Steam, its Generation and Use", ch. 34, 40th Edition, Ed. S.C. Stultz and J. B. Kitto, Barberton, USA, 1992.
127. R. E. Dickinson, and R. J. Cicerone, *Nature*, 1986 319 109.
128. R. Wayne, "Chemistry of Atmospheres", Oxford Univer. Press, Oxford, 1991.
129. S. Arrhenius, "On the Influence of Carbonic Acid in the Air upon the Temp. of the ground", London, Edinburgh, Dublin Philos. Mag. J. Sci., 1896 41 237.
130. Intergovernmental Panel on Climate Change, *Climate change 1992*, J. T. Houghton, B. A. Callander and S. K. Varney (Eds.), Cambridge University Press, 1994 1-200.
131. J. T. Houghton, G. J. Jenkins, and J. J. Ephraims, "Climate Change: the IPCC Assessment", Cambridge University Press, Cambridge, 1990.
132. Intergovernmental Panel on Climate Change (IPCC), 1996.

133. H. Alnakeeb, M. A. Ibrahim, S. Ragab, The Fourteenth Petroleum Conference, Organized by Ministry of Petroleum in Egypt, October 1998 12.
134. P. N. Cheremisinoff, "Air Pollution Control and Design for Industry", Marcel Dekker, Inc., New York, Basel and Hong Kong, 1993.
135. I. Ionel, Proc. of the Mediterranean Combustion Symposium, Antalya – Turkey, June 20-25, 1999 399.
136. G. Dixon-Lewis, Proc. Roy. Soc. Lond. A, 1970 317 235.
137. G. Dixon-Lewis, "Complex Chemical Reaction Systems (J. Warnatz and W. Jager, Eds".) Springer Series in Chemical Physics, Springer-Verlag, Heidelberg, 1987 47 265.
138. G. Dixon-Lewis, "Dynamic of Reactive Systems, part I (A. L. Kuhl, J. R. Bowen, J. C. Leyer and A. Borisov, Eds.) Progr. in Astronaut. and Aeronaut., 1988 113.
139. G. Dixon-Lewis, and G. L. Isles, Trans. Faraday Soc., 1957 53 193.
140. G. Dixon-Lewis, and G. L. Isles, Seventh Symposium (International) on Combustion, Butterworths, London, 1959 475.
141. G. Dixon-Lewis, and I. G. Shepherd, Fifteenth Symposium (International) on Combustion, The Combustion Institute Pittsburgh 1975 1483.
142. G. Dixon-Lewis, and D. J. Williams, "Comprehensive Chemical Kinetics (C. H. Bamford and C. F. H. Tipper, Eds.), Amsterdam, Elsevier, Ch. 1, 1977 17.
143. G. Dixon-Lewis, and S. M. Islam, Nineteenth Symposium (International) on Combustion, The Combustion Institute, Pittsburgh 1983 283.
144. M. A. Cherian, P. Rhodes, R. J. Simpson, and G. Dixon-Lewis, Eighteenth Symposium (International) on Combustion, The Combustion Institute, Pittsburgh, 1981 385.
145. G. Dixon-Lewis, V. Giovangigli, R. J. Kee, J. A. Miller, B. Rogg, M. D. Smook, G. Stahl, and J. Warnatz, paper presented at 12 th ICDERS, Univ., Michigan, Ann Arbor, 1989.
146. G. Dixon-Lewis, D. Bradley, and S. El-Din Habik, J. Archivum Combust., 1987, 7 85.
147. D. Bradley, G. Dixon-Lewis, and S. El-Din Habik, Combust. Flame, 1989 77 41.
148. G. Dixon-Lewis, D. Bradley. and S. El-Din Habik, Joint Meeting of the British and French Section of the Combustion Institute, Rouen, France, 17-21 April, 1989 309.
149. D. Bradley, G. Dixon-Lewis, S. El-Din Habik, and S. A. El-Sherif, Engineering research Bulletin, University of Helwan, Faculty of Eng. and Tech. Mataria, Cairo. , 1991 7.
150. D. Bradley, G. Dixon-Lewis, S. El-Din Habik, and E. M. J. Mushi, Twentieth Symposium (International) in Combustion, The Combustion Institute, Pittsburgh, 1985 931.

151. D. Bradley, G. Dixon-Lewis, and S. El-Din Habik, International Specialists Meeting on Coal Dust, Lisbon, Portugal, 1987.
152. S. El-Sherif, "The Role of Gas Phase Chemical Kinetics in the Combustion of Liquid and Solids," Ph.D. Thesis, Department of Mechanical Engineering, University of Leeds, 1990.
153. S. El-Sherif, Engineering Research Bulletin, University of Helwan, Faculty of Eng. and Tech., Mataria, Cairo, Egypt, 1993 1 (1).
154. M. A. Abu-Elenin, A. Y. Abdalla, S. El-Din Habik, S. A. El-Sherif, and M. A. Shahien, First International Conference on Engineering Research, Development and Application at Faculty of Engineering and Technology, Port-Said, Egypt. 26-28 November, 1991.
155. S. El-Din Habik, Scientific Engineering Bulletin, Port-Said, Egypt, 1993 5 (2) 57.
156. S. El-Din Habik, Scientific Engineering Bulletin, Port-Said, Egypt, 1993 5 (2) 131.
157. P. L. Stephenson, and R. G. Taylor, Combust. Flame, 1973 20 231.
158. J. Warnatz, Ber Bunsengas., Phys. Chem., 1978 82 834.
159. J. Warnatz, Ber Bunsengas., Phys. Chem., 1979 83 950.
160. D. Bradley, Z. Chen, S. A. El-Sherif, S. El-Din Habik, G. John, and G. Dixon-Lewis, Combust. Flame, 1994 96 80.
161. C. K. Westbrook, and F. L. Dryer, Combust. Flame, 1980 37 171.
162. J. E. Dove, and J. Warnatz, Ber, Bunsengas, Phys. Chem., 1983 87 1040.
163. L. Monchick, and E. A. Mason, J. Chem. Phys., 1961 35 1676.
164. L. Monchick, Munn, R., J., and Mason, E. A., J. Chem. Phys., 1966 45 3051.
165. R. A. Svehla, Technical Report R-132, NASA, Washington, D. C. 1962.
166. J. Warnatz, Combust. Sci. and Tech., 1983 34 177.
167. G. Dixon-Lewis, M. M. Sutton, and A. Williams, Proc. Roy. Soc. Lond., 1970 A317 227.
168. M. J. Day, G. Dixon-Lewis, and Thompson, K. Proc. Roy. Soc. Lond., 1972 A330 199.
169. A. D. Snyder, and G. B. Skinner, Combust. Flame, 1964 8 164.
170. G. Dixon-Lewis, J. B. Greenberg, and F. A. Goldsworthy, Fifteenth Symposium ((International) on Combustion, The Combustion Institute, Pittsburgh, 1975 717.
171. D. L. Baulch, and D. D. Drysdale, Combust. Flame, 1974 23 215.
172. Oldenhove de L. Guertechin, J. Vandooren, and P. J. J. Van Tiggelen, Chim. Physique, 1983 80 583.
173. G. Dixon-Lewis, and A. Williams, Eleventh Symposium (International) on Combustion, The Combustion Institute, Pittsburgh, 1967 951.

174. G. Tsatsaronis, *Combust. Flame*, 1978 33 217.
175. C. K. Westbrook, Nineteenth Symposium (International) on Combustion, The Combustion Institute, Pittsburgh, 1982 153.
176. F. N. Egolfopoulos, P. Cho, and C. K. Law, *Combust. Flame*, 1989 76 375.
177. G. J. Langley, and Burgess, A. R. *Proc. Roy. Soc. Lond.*, 1989 A421 259.
178. J. A. Miller, R. E. Mitchell, M. D. Smooke, and R. J. Kee, Nineteenth Symposium (International) on Combustion, The Combustion Institute, Pittsburgh, 1982 181.
179. G. John, Ph.D. Thesis, Department of Mechanical Engineering, University of Leeds, U.K., 1992.
180. N. H. Heniker, Methanol as an Alternate Fuel, Conference Report, Engineering Foundation Conference, 1974 1.
181. E. L. Clark, in *Future Automotive Fuels* (J. M. Colucci and N. E. Gallopoulos, Eds.), Plenum, New York, 1977.
182. J. A. Bolt, SP-254, SAE, 1964.
183. J. C. Ingamells, and R. H. Lindquist, SAE paper no. 750121, 1975.
184. W. J. Most, and J. P. Longwell, SAE paper no. 750119, 1975.
185. J. A. Harrington, and R. M. Pilot, *Trans. SAE*, paper no. 750420, 1975 395.
186. O.L. Gülder, *Proceedings of the Sixteenth IECEC*, ASME, 1981 2 1160.
187. O.L. Gülder, *Proceedings of the Alcohol Fuel Technology, Fourth International Symposium*, 1982 1 347.
188. O. L. Gülder, Nineteenth Symposium (International) on Combustion, The Combustion Institute, Pittsburgh, 1982 275.
189. A. Koenig, W. Lee, and W. Beruhardt, SAE paper no. 760545, 1976.
190. Yu. A. Borisov, Yu. V. Klopov, and V. N. Prostov, *Combustion, Explosion and Shock Waves* (Translated from Russian), 1986 22 2.
191. J. O. Olsson, I. B. M. Olsson, and L. L. Andersson, *J. Phys. Chem.*, 1986 91 4160.
192. L. L. Andersson, B. Christenson, A. Høglund, J. O. Olsson, and L. G. Rosengren *Prog. Astronautics Aeronautics*, 1985 95 164.
193. G. Paczko, P. M. Lefdal, and N. Peters, Twenty first Symposium (International) on Combustion, The Combustion Institute, Pittsburgh, 1986 735.
194. D. F. Cooke, M. G. Dodson, and A. Williams, *Combust. Flame*, 1971 16 233.
195. J. Vandooren, and P. J. Van Tiggelen, Eighteenth Symposium (International) on Combustion, The Combustion Institute. Pittsburgh, 1981 473.
196. D. Aronowitz, R. J. Santoro, F. L. Dryer, and I. Glassman, Seventeenth Symposium (International) on Combustion, The Combustion Institute, Pittsburgh, 1979 633.
197. H. H. Grotheer, and S. Kelm, Third International Seminar on Flame Structure,

- Alma-Ata, USSR Academy of science, Novosibirsk, 1989.
198. W. P. Hess, and F. P. Tully, *Phys. Chem.*, 1989 93 1944.
 199. E. A. Lissi, G. Massiff, and A. E. Villa, *J. Chem. Soc. Farad. Trans.*, 1 1973 69 346.
 200. J. Vandooren, Oldenhove, L. de Guertechin, and P. J. Van Tiggelen, *Combust. Flame*, 1986 64 127.
 201. W. J. Tsang, *J. Phys. Chem. Ref. Data*, 1987 16 (3) 471.
 202. M. Cathonnet, *Combust. Sci. Technol.*, 1994 98 265.
 203. C. K. Westbrook, and W. I. Pitz, *Combust. Sci. Technol.*, 1984 37 117.
 204. C. J. Jachimowski, *Combust. Flame*, 1984 55 213.
 205. P. Dagaut, M. Cathonnet, J.C. Boetiner, and F. Gaillard, *Combust. Sci. Technol.*, 1987 56 23.
 206. T. M. Sloane, *Combust. Sci. Technol.*, 1992 83 77.
 207. S. El-Din Habik, F. M. El-Mahallawy, and A. M. Barakat, *J. of Engineering and Applied Science, Faculty of Engineering, Cairo University*, No. 6 Dec. 1997 1155.
 208. A. T. Droege, and F. D. Tully, *J. Phys. Chem.*, 1986 90 1949.
 209. R. W. Walker, "Rate Constants for Reactions in Gas Phase Hydrocarbon Oxidation Reaction Kinetics and Energy Transfer". Specialist periodical report. The Chemical Society (Ed.). London, 1977 2 296.
 210. J. A. Kerr, and A. Trotman-Dickenson, *Translation Faraday Society*, 1959 55 921.
 211. D.J. Hautman, R. J. Santoro, F. L. Dryer, and I. Glassman, *J. Chem. Kinetics*, 1981 13 149.
 212. A. F. Trotman-Dickenson, *Advances in Free Radical Chemistry*, 1965 1.
 213. G. Dixon-Lewis, M. M. Sutton, and A. Williams, *Disc. Faraday Soc.*, 1962 33 205.
 214. G. Jahn, *Der Zundvorgang in Gasmischen*, Berlin, Oldenbourg, Berlin 1934.
 215. D. A. Senior, *Combust. Flame*, 1961 5 7.
 216. R. Edse, and L. R. Jr. Lawrence, *Combust. Flame*, 1969 13 479.
 217. T. G. Scholte, and P. B. Vaags, *Combust. Flame*, 1959 3 495.
 218. H. Edmondson, and M. P. Heap, *Combust. Flame*, 1971 16 161.
 219. R. Günther, and G. Janisch *Chem-Ing. Techn.*, 1971 43 975.
 220. R. Günther, and G. Janisch *Combust. Flame*, 1972 19 49
 221. W. A. Strauss, and R. Edse, *Seventh Symposium (International) on Combustion*, Butterworths, London, 1959 377.
 222. J. T. Agnew, and L. B. Graiff, *Combust. Flame*, 1961 5 209.
 223. G. E. Andrews, and D. Bradley, *Combust. Flame*, 1973 20 77.

224. T. Iijima, and T. Takeno, *Combust. Flame*, 1986 65 35.
225. G. E. Andrews, and D. Bradley, *Combust. Flame*, 1972 18 133.
226. C. K. Wu, and C. K. Law, Twentieth Symposium (International) on Combustion, The Combustion Institute, 1984 1941.
227. G. Yu, C. K. Law, and C. K. Wu, *Combust. Flame*, 1986 63 339.
228. C. K. Law, D. L. Zhu, and G. Yu, Twenty-First Symposium (International) on Combustion, The Combustion Institute, 1986 1419.
229. G. E. Andrews, and D. Bradley, *Combust. Flame*, 1972 19 275.
230. J. Vandooren, J. Peeters, and P. J. Van Tiggelen, Fifteenth Symposium (International) on Combustion, The Combustion Institute, Pittsburgh, 1975 745.
231. G. Dixon-Lewis, and G. L. Isles, *Proc. Roy. Soc. Lond.*, 1969 A308 517.
232. T. G. Scholte, and P. B. Vaags, *Combust. Flame*, 1959 3 511.
233. K. T. Aung, M. I. Hassan, and G. M. Faeth, *Combust. Flame*, 1998 112 1.
234. T. G. Scholte, and P. B. Vaags, *Combust. Flame*, 1959 3 503.
235. G. P. R. Mack, and B. A. Thrush, *J Chem. Soc. Faraday Trans.*, 1973 I 69 208.
236. N. Washida, R. J. Martinez, and K. D. Z. Bayes, *Naturf. A*, 1974 29 251.
237. R. M. Fristrom, and A. A. Westenberg, *Flame Structure*, McGraw-Hill, New York, 1965.
238. T. P. Coffee, *Combust. Flame*, 1984 55 161.
239. J. Warnatz, J. Bockham, A. Moser, and H. W. Wenz, Nineteenth Symposium (International) on Combustion, The Combustion Institute, Pittsburgh, 1983 197.
240. C. K. Westbrook, and F. L. Dryer, *Prog. Energy Combust. Sci.*, 1984 10 1-57.
241. J. Vandooren, and P. J. Van Tiggelen, Sixteenth Symposium (International) on Combustion, The Combustion Institute, Pittsburgh, 1977 1133.
242. J. Peeters, and G. Mahnen, In *Combustion Institute European Symposium* (F. Weinberg, Ed.), New York, Academic press, 1973 53.
243. J. H. Bechtel, R. J. Blint, C. J. Dasch, and D. R. Weinberger. *Combust. Flame*, 1981 42 197.
244. C. K. Law, Twenty Second Symposium (International) on Combustion, The Combustion Institute, Pittsburgh, 1989 1381.
245. L. Yamaoka, and H. Tsuji, Twentieth Symposium (International) on Combustion, The Combustion Institute, Pittsburgh, 1984 1883.
246. S.A. El-Sherif, *Engineering Research Journal*, Helwan University, Faculty of Engineering, Mataria, Cairo, Egypt, April 1999 62 161.
247. V. S. Babkin, and L. S. Kozachenko, *Combustion, Explosions and Shock Waves*, 1966 2 46.
248. D. Bradley, A. K. Kwa, A. K. C. Lau, M. Missaghi, and S. B. Chin, *Combust. Flame*, 1988 71 109.

249. R. S. Cant, and K. N. C. Bray, Twenty Second Symposium (International) on Combustion, The Combustion Institute, Pittsburgh, 1989 791.
250. F. A. Williams, Combustion Theory. Addison Wesley Pub. Co. Reading, Mass, 1965.
251. D. D. Agrawal, Combust. Flame, 1981 42 243.
252. D. Smith, and J. T. Agnew, Sixth Symposium (International) on Combustion. The Combustion Institute, New York, Academic Press, 1957 83.
253. A. C. Egerton, and A. H. Lefebvre, Proc. Roy. Soc., 1954, 222A, 206.
254. J. Diederichsen, and H. G. Wolfhand, Trans. Farad., Soc., 1954 52 (403) 1103.
255. S. P. Sharma., D. D. Agrawl, and C. P. Gupta, Eighteenth Symposium (International) on Combustion, The Combustion Institute, Pittsburgh, 1981 493.
256. A. M. Garforth, and C. S. Rallis, Combust. Flame, 1978 31 53.
257. S. El-Din Habik, "Liquid Fuel System in Low Pressure," Internal Report, Ref. No. T55, April 1989, University of Leeds, England.
258. S. J. Cook, and R. F. Simmons, Combust. Flame, 1982 46 177.
259. J. O. Hirschfelder, C. F. Curtiss, and R. B. Bell, "Molecular Theory of Gases and Liquids," John Wiley and Sons, New York, 1960.
260. G. S. Bahn, "Approximate Thermochemical Tables for Some C-H-O Species," NASA report, NASA-CR-2178, 1973.
261. T. Tsuboi, and K. Hashimoto, Combust. Flame, 1981 42 61.
262. T. S. Norton, and F. L. Dryer, Combust. Sci. Technol., 1989 63 107.
263. J. O. Olsson, L. S. Karlsson, and L. L. Andersson, J. Phys. Chem., 1986 90 (9) 1458.
264. R. Akrich, C. Vovelle, and R. Delbourgo, Combust. Flame, 1978 32 171.
265. R. R. Baldwin, M. E. Fuller, J. S. Hillman, D. Jackson, and R. W. Walker, J. Chem. Soc. Farad. Trans. I, 1974 70 635.
266. J. F. Pauwels, M. Carlier, P. Dovelde, and L. R. Sochet, Combust. Sci. Technol., 1989 64 97.
267. J. B. Vandooren, V. P. Balakhin, and P. J. Van Tiggelen, J. Archivum combust., 1981 1 229.
268. H. K. Kwa, "Heat Release Rates in Gaseous Flames", Ph.D. Thesis, Department of Mechanical Engineering, University of Leeds, 1987.
269. T. P. Coffee, Combust. Sci. Tech., 1985 43 333.
270. G. J. Gibbs, and H. F. Calcote, J. Chem. Eng., 1959 4 (3) 226.
271. M. Metghalchi, and J. C. Keck, Combust. Flame, 1982 48 191.
272. K. Seshodri, Twenty-Sixth Symposium (International) on Combustion, The Combustion Institute, Pittsburgh, 1996 831.
273. W. H. Wiser, and G. R. Hill, Fifth Symposium (International) on Combustion, Reinhold, New York, 1954 553.

274. S. El-din Habik, *Scientific Engineering Bulletin, Faculty of Engineering, Port-Said, Egypt*, 1993, 5 (1) 83.
275. M. Hirano, K. Oda, T. Hirano, and K. Akita, *Combust. Flame*, 1981 40 341.
276. S. Koda, K. Oda, M. Hirano, T. Hirano, and K. Akita, *Combust. Flame*, 1982 46 17.
277. Zeldovich, a, B., *Acta Physicochim URSS*, 1946 21 577.
278. D. L. Baulch, D. D. Drysdale, D. G. Horne, and A. C. Lloyd, *Evaluated Kinetics Data for High Temperature Reactions" vol. I, Butterworths, London*, 1973.
279. R.M. Fristrom, R. Prescott, and C. Grunfelder, *Combust. Flame*, 1957 1 100.
280. J. H. Bechtel, R. J. Blint, C. J. Dasch, and D. R. Weinburgur, *Combust. Flame*, 1981 42 197.
281. D. A. Stephenson, *Seventeenth Symposium (International) on Combustion, The Combustion Institute, Pittsburgh*, 1978 993.
282. J. M. Singer, *Fourth Symposium (International) on Combustion, Williams & Wilkins, Baltimore*, 1953 352.
283. F. A. Smith, *Chem. Rev.*, 1937 21 389.
284. E. Z. Bartholome, *Electrochem*, 1949 53 191.
285. M. Metghalchi, and J. C. Keck, *Combust. Flame*, 1980 38 143.
286. M. N. Hamid, Ph.D. Thesis, Department of Mechanical Engineering, Leeds University, 1986.
287. O. M. F. Elbahar, *The Eight International Conference for Mechanical Power Engineering, Alexandria, Egypt*, 1993 12.
288. C. M. Vagelopoulos, F. M. Egolfopoulos, and C. K. law, *Twenty-Fifth Symposium (International) on Combustion, The Combustion Institute, Pittsburgh*, 1994 341.
289. J. D. Naber, D. L. Siebers, S. S. Di Julio, , and C. K. Westbrook, *Combust. Flame*, 1994 99 192.
290. C. P.Fenimore, and G. W. Jones, *Ninth Symposium (International) on Combustion, The Combustion Institute, Pittsburgh*, 1963 597.
291. T. Singh, and R. F. Sawyer, *Thirteen Symposium (International) on Combustion, The combustion institute, Pittsburgh*, 1971 103.
292. R. Hennessy, C. Robinson, and D. B. Smith, *Twenty-First Symposium (International) on Combustion, The Combustion Institute, Pittsburgh*, 1988 761.
293. R. Günther, and G. Janisch "Messwerte de Flammgeschwindigkeit von Gasen", *Cheni-Ing-Technik*, 1959 43 975.
294. W. C. Johnston, *Soc. Auto. Eng. J.*, 1947 55-62.
295. M. S. Haniff, A. Melvin, D. B. Smith, and A. Williams, *J. of Inst. of Energy, Dec.*, 1989 229.
296. D. Burgess, and M. Hertzberg, *I. S. N A. Translation*, 1975 14 129.
297. L. Ubbelohde, and E. Koelliker, *J. Gasbeleucht*, 1916 59 49.

298. H. Passauer, *Gas and Wasserfach*, 1930 73 313.
299. K. Bunte, and A. Steding, *Gas and Wasserfach*, 1928 71 673 701- 731.
300. E. Hartmann, "Der Verbrennungs mehanismus des Kohlenoxyds und seiner Gemische mit Gasen und Dampfen," Dissert., University of Karlsruhe, 1931.
301. V. S. Babkin, and Yu. G. Kononenko, *Fiz. Goren. Vzryva* 1967 3 268. [English translation: *Combustion, Explosion and Shock Waves*, 1970 3 168].
302. A. R. T. Denues, and W. J. Heff, *J. Am. Chem. Soc.*, 1940 62 3045.
303. R. E. Bloz, and H. Burlage, *Jet Propulsion*, 1955 25 265.
304. M. Gilbert, *Sixth Symposium (International) on Combustion*, Reinhold, New York, 1957 74.
305. M. Gerstein, O. Levine, and E. L. Wong, *J. Am. Chem. Soc.*, 1951 73 418.
306. G. L. Dugger, "Effect of Initial Temperature on Flame Speed of Methane-Air, Propane-Air, and Ethylene-Air Mixtures," *NACA Rept.* 1952 1061.
307. K. Wohl, and N. B. Kapp, "Flame Stability at Variable Pressures," *Meteor Rept. UAC-42, Res. Dept., United Aircraft Corp.* (Oct. 1949).
308. L. Sieg, *Angew. Chem.*, 1951 63 143.
309. F. R. Caldwell, H. P. Broida, and J. J. Dover, *Ind. Eng. Chem.*, 1951 43 2731.
310. W. H. Clingman, R. S. Brokaw, and R. N. Pease, *Fourth Symposium (International) on Combustion*, Williams & Wilkins, Baltimore, 1953 310.
311. M. Gerstein, O. Levine, and E. L. Wong, "Fundamental Flame Velocities of Pure Hydrocarbons, I: Alkanes, Alkenes, Alkynes, Benzen and Cyclohexane," *NACA RM E 50 G 24*, 1950.
312. G. H. Morgan, and W. R. Kane, *Fourth Symposium (International) on Combustion*, Williams & Wilkins, Baltimore, 1953 313.
313. J. Diederichsen, and H. G. Wolfhard, *Trans. Farad. Soc.*, 1956 52 1102.
314. W. A. Rosser, H. Wise, and J. Miller, *Seventh Symposium (International) on Combustion*, Butterworth, London, 1959 175.
315. Unpublished Natl. Bur. Stds. Results, 1955 2.
316. H. T. Henderson, and G. R. Hill, *J. Phys. Chem.*, 1956 60 874.
317. W. H. Wiser, and G. R. Hill, "The Kinetics of Combustion of Methyl Alcohol," *Tech. Rept. No. 4, Air Force Combustion Contract No. AF 33 (038) (20839)*, University of Utah, 1952.
318. J. M. Singer, J. Grumer, and E. B. Cook, *Proc. Gas Dynamics Symposium on Aerothermochemistry*, Northwestern University, Evanston, Illinois, 1956 139.
319. G. Dixon-Lewis, and M. J. G. Wilson, *Trans. Faraday Soc.*, 1951 46 1106.
320. J. Manton, G. Von Elbe, and B. Lewis, *Fourth Symposium (International) on Combustion*, Williams & Wilkins, Baltimore, 1953 358.
321. D. Bradley, and G. Hundy, *Thirteenth Symposium (International) on Combustion*, The Combustion Institute, Pittsburgh, 1971 575.

322. H. F. Coward, and F. J. Hartwell, *J. Chem. Soc.*, 1932 2676.
323. J. Corsiglia, *Am. Gas Assoc. Monthly*, 1931 13 437.
324. V. S. Babkin, L. S. Kozachenko, and I. L. Kuznetsov, *Zh. Prikl. Mekhan. Tekhn. Fiz.* 3, 145 (1964). (English Translation): TT66-61882 1966.
325. J. H. Grover, E. N. Fales, and A. G. Scurlock, *Ninth Symposium (International) on Combustion*, Academic Press, New York, 1963 21.
326. E. B. Cook, and T. A. Kubala, *Eighth Symposium (International) on Combustion*, Williams & Wilkins, Baltimore, 1962 537.
327. J. Combourieu, Thesis, Paris, 1960.
328. V. P. Karpov, and A. S. Sokolik, *Dokl. Akad. Nauk SSSR* 1961 138, 874. [English translation: *Proc. Acad. Sci. USSR, Phys. Chem. Sec.*, 1961 138 (457)].
329. R. E. Bolz, and H. Burlage, "Propagation of Free Flame in Laminar and Turbulent Flow Fields," NASA Tech. Note D-551, 1960.
330. A. Barrassin, R. Lisbet, J. Combourieu, and P. Laffitte, *Bull. Soc. Chim. France*, 1967 7 2521.
331. K. Wohl, and L. Shore, *Ind. Eng. Chem.*, 1955 47 828.
332. J. Manton, and B. B. Milliken, *Proceedings of the Gas Dynamics Symposium on Aerothermochemistry*, Northwestern University, Evanston, Illinois, 1956 151.
333. H. Edmondson, and M. P. Heap, *Combust. Flame*, 1970 14 195.
334. V. G. Piskunov, B. I. Shraer, and M. A. Glikin, *Gazovaya Promyshlennost*, 1969 14 36.
335. C. Halpern, *J. Res. Natl. Bur. Std.*, 1963 67A 71.
336. H. Edmondson, and M. P. Heap, *Combust. Flame*, 1969 13 472.
337. I. Fells, and H. G. Rutherford, *Combust. Flame*, 1969 13 130.
338. U. Bonne, W. Jost, and H. G. Wagner, *Fire Res. Abstr. Rev.*, 1962 4.
339. T. G. Scholte, and P. B. Vaags, *Combust. Flame*, 1959 3 495.
340. W. H. Clingman, and R. N. Pease, *J. Am. Chem. Soc.*, 1956 78 1775.
341. G. I. Kozlov, *Seventh Symposium (International) on Combustion*, Butterworths, London, 1959 142.
342. S. A. Weil, "Burning Velocities of Hydrocarbon Flames," *Inst. Gas Tech., Chicago, Res. Bull.*, 1961 (30).
343. R. Lindow, *Brennstoff Wärme Kraft*, 1968 20 8.
344. S. B. Reed, J. Mineur, and J. P. McNaughton, *J. Inst. Fuel*, 1971 44 149.
345. N. V. Lavrov, and S. F. Evlanov, *Gazovaya Promyshlennost* 13 42 1968 [English translation: NLL, Boston Spa, England, M 9215 1989].
346. L. Khitrin, *Technical Physics of the USSR*, 1936 39 (3) 926.
347. F. H. Garner, R. Long, and G. R. Ashforth, *Fuel Lond.*, 1949 49 272.
348. Von. H. Sachsse, and E. Bartholome, *Elektrochem.*, 1949 53 183.

349. H. F. Calcote, C. M. Barnett, and M. R. Irby, paper presented at meeting of the American Chemical Society, Atlantic City, NJ, 1949.
350. M. Gerstein, O. Levine, and E. Wong, *Ind. Eng. Chem.*, 1951 43 2770.
351. R. E. Albright, D. P. Heath, and R. H. Thena, *Ind. Eng. Chem.*, 1951 44 2490.
352. D. M. Simon, and E. L. Wong. NACA, RME, 5-1, Hog, 1951.
353. G. L. Dugger, and D. D. Graab, NACA, T. N. 2680, 1952.
354. F. H. Garner, R. Long, and B. Thorley, *Fuel Lond.*, 1954 29 394.
355. P. Wagner, and G. L. Dugger, *J. Am. Chem. Soc.*, 1955 74 227.
356. S. Heimel, and R. C. Weast, Sixth Symposium (International) on Combustion, Reinhold, New York, 1957 296.
357. J. Warnatz, Twentieth Symposium (International) on Combustion. The Combustion Institute, Pittsburgh, 1984 845.
358. J. W. Linnett, H. S. Pickering, and P. Wheatley, *J. Trans. Farad. Soc.*, 1951 47 974.
359. R. Friedman, and E. Burke, *Ind. Eng. Chem.*, 1951 43 2772.
360. C. K. Westbrook, *Combust. Sci. Technol.*, 1980 23 191.
361. J. Warnatz, *Combust. Sci. Technol.*, 1981 26 203.
362. V. S. Babkin, A. V. Vyon, and L. S. Kozachenko, *Combust. Explos. Shock Waves*, 1967 3 221.
363. J. Rappeneau, *Combustion Researches and Reviews* 40, Butterworths, London, 1957.
364. V. K. Zotin, and A. V. Talantov, N-1, 115 [English translation: *Sov. Aeronaut.*, 1968 9 60].
365. D. M. Simon, *J. Am. Chem. Soc.*, 1951 73 422.
366. P. L. Walker, and C. C. Wright, *J. Am. Chem. Soc.*, 1952 74 3769.
367. C. K. Westbrook, J. Warnatz, and W. J. Pitz, Twenty-Second Symposium (Int.) on Combustion, The Combustion Institute, Pittsburgh, 1989 893.
368. D. Bradley, A. K. C. Lau, and M. Lawes, *Phil. Trans. R. Soc. Lond.*, 1992 A338 359.
369. R. G. Abdel-Gayed, D. Bradley, and M. Lawes, *Proc. Roy. Soc. Lond.*, 1987 A414 389.
370. W. A. Al-Masseeh, D. Bradley, P. H. Gaskell, and A. K. C. Lau, Twenty-Third Symposium (International) on Combustion. The Combustion Institute, Pittsburgh, 1991 825.
371. Y. B. Zeldovich, and D. A. Frank-Kamenetski, *Zh. Fiz. Khim*, Mosk 1938 12 100.
372. F. A. Williams, "Combustion Theory", 2nd Ed., Benjamin/Cummings, Menlo Park, CA, 1985.
373. Y. B. Zeldovich, G. I. Barenblatt, V. B. Librovich, and G. M. Makhviladze, *The*

- Mathematical Theory of Combustion and Explosions, Consultants Bureau, New York, 1985.
374. D. B. Spalding, *Combust. Flame*, 1957 1 287.
375. D. Bradley, P. H. Gaskell, and A. K. C. Lau, Twenty-third Symposium (International) on Combustion, The Combustion Institute, Pittsburgh, 1991 685.
376. F. A. Williams, Twenty-Fourth (International) Symposium on Combustion, The Combustion Institute, Pittsburgh, 1992 1.
377. F. L. Dryer, "The Phenomenology of Modeling Combustion Chemistry," Bartok, W. and Sarofim A. F. (Eds.), *Fossil Fuel Combustion*, John Wiley and Sons, New York, 1989 121.
378. N. Peters, and B. Rogg, *Lecture Notes in Physics*, MIS, Springer-Verlag 1994.
379. S. H. Lam, and D. A. Goussis, Twenty-Second (International) Symposium on Combustion, The Combustion Institute, Pittsburgh, 1988 931.
380. U. Mass, and S. B. Pope, *Combust. Flame*, 1992 88 239.
381. C. Kennel, J. Gottgens, and N. Peters, Twenty-Third (International) Symposium on Combustion, The Combustion Institute, Pittsburgh, 1990 479.
382. C. K. Westbrook, and F. L. Dryer, *Combust. Sci. Technol.*, 1981 27 31.
383. J. Warnatz, Twenty-Fourth Symposium (International) on Combustion, The Combustion Institute, Pittsburgh, 1992 553.
384. R. B. Edelman, and O. F. Fortune, *AIAA paper*, 1969 69.
385. E. Ranzi, A. Sogaro, P. Gaffuri, G. Pennati, C. K. Westbrook, and W. J. Pitz, *Combust. Flame*, 1994 99 201.
386. H. Pitsch, N. Peters, and K. Seshadri, Twenty-Sixth Symposium (International) on Combustion, The Combustion Institute, Pittsburgh, 1996 763.
387. A. A. Amsden, P. J. O'Rourke, and T. D. Butler, "KIVA-II: A Computer Program for Chemically Reactive Flows with Sprays," Los Alamos National Laboratory Report, LA-11560-MS, 1989 .
388. Y. Hardalupas, C. H. Liu, and J. H. Whitelaw, *Combust. Sci. Technol.*, 1994 97 157.
389. G. L. Dugger, D. M. Simon, and M. Gerstein, "Laminar Flame Propagation," Ch. IV in *NACA Report*, 1959 1300.
390. O. L. Gülder, *Combust. Sci. and Technol.*, 1986 33 179.
391. M. Metghalchi, and J. C. Keck, "Laminar Burning Velocity of Iso-Octane-Air-Methane and Methanol-Air Mixtures at High Temperature and Pressure," fall meeting of Combustion Institute (Eastern Section) 1977.
392. E. H. James, *SAE Paper No.* 870170.
393. B. Benkoussan, M.Phil, Thesis, Department of Mechanical Engineering, University of Leeds, U. K, 1988.
394. C. B. Henery, and R. H. Robert, "Properties of Aircraft Fuels," *NACA Tech. Not.*, 1956 3266-3280.

395. V. S. Babikin, A. V. V'Yun, and L. S. Kozachenko, *Fizika Goreniyai Vzryva*, 1967 3 3.
396. D. Bradley, R. A. Hicks, M. Lawes, C. G. W. Sheppard, and R. Woolley, *Combust. Flame*, 1998 115 126.
397. S. G. Davis, H. Wang, K. Brezinsky, and C. K. Law, *Twenty-Sixth Symposium (International) on Combustion*, The Combustion Institute, Pittsburgh, 1996 1025.
398. M. Hori, N. Matsunaga, P. Malte, and N. M. Marinov, *Twenty Fourth Symposium (International) on Combustion*, The Combustion Institute, Pittsburgh, 1992 909.
399. D. X. Du, R. L. Axelbaum, and C. K. Law, *Combust. Flame*, 1995 102 11.
400. S. A. El-Sherif, *Fuel*, 2000 79 567.
401. R. Viskanta, *International Symposium on Transport Phenomena in Combustion*, ISTP-8, 1995.
402. J. R. Howell, M. J. Hall, J. L. Ellzey, "Heat Transfer in Porous Media and Two-Phase Flow", (Bayazitonglu, Y., and Sathuvalli, U. B. Eds.), ASME HTD-302, New York, 1995 1.
403. R. Mital, J. P. Gore, R. Viskanta, and S. Singh, in *Proceeding of 1995 Joint Thermal Meeting on Combustion Fundamentals and Applications*, Central and Western States and Mexican National Sections of the Combustion Institute, Pittsburgh, 1995 32.
404. P. F. Hsu, J. R. Howell, and R. D. Matthews, *ASME J. Heat Transfer*, 1993 115 744.
405. P. F. Hsu, W. D. Evans, and J. R. Howell, *Combust. Sci. Technol*, 1993 90 149.
406. A. Williams, R. Wooley, and M. Lawes, *Combust. Flame*, 1992 89 157.
407. R. Ruiz, and S. N. Singh, *Proceedings of International Gas Research Conference*, Orlando, FL, 1992 2410.
408. V. Khanna, L. Goel, and J. L. Ellzey, *Combust. Sci., Technol*, 1994 99 133.
409. M. R. Kulkarni, K. P. Chavali, and R. E. Peck, *Proceedings of the Western States Section of the Combustion Institute*, Berkeley, CA, 1992.
410. P. H. Bouma, R. L. G. M. Eggels, and L. P. H. de Goey, *Proceedings of the Third International Conference on Combustion Technologies for a Clean Environment*, Lisbon, Portugal, 1995.
411. D. K. Min, and H. D. Shin, *Int. J. Heat and Mass Transfer*, 1991 34 (2) 341.
412. R. Mital, J. P. Gore, and R. Viskanta, *Combust. Flame*, 1997 111 175.
413. M. D. Rumminger, R. W. Dibble, N. H. Heberle, and D. R. Crosley, *Twenty-Sixth Symposium (International) on Combustion*, The Combustion Institute, 1996 1795.
414. L. B. Younis, and R. Viskanta, *Int. J. Heat Mass Transfer*, 1993 36 1425.
415. B. Karlovitz, D. W. Denniston, D. H. Knapschaefer, and F. E. Wells, *Fourth Symposium (International) on Combustion*, The Combustion Institute,

- 1953 613.
416. H. Tsuji, *Prog. in Energy and Combust. Sci.*, 8, 93 (1982).
 417. H. Tsuji, ASME-JSME Thermal Engineering Conference, Honolulu, Hawaii, 1983 4 11.
 418. H. B. Keller, *Applications of Bifurcation Theory* (P. Rabonowitz, Ed.), Academic press, New York, 1977.
 419. V. Giovangigli, and M. D. Smooke, *Combust. Sci. Technol.*, 1987 53 23.
 420. P. A. Libby, and F. A. Williams, *Combust. Flame*, 1982 44 287.
 421. P. A. Libby, and F. A. Williams, *Combust. Sci. Technol.*, 1983 31 1.
 422. P. A. Libby, and F. A. Williams, *Combust. Sci. Technol.*, 1984 37 221.
 423. P. A. Libby, A. Linan, and F. A. Williams, *Combust. Sci. Technol.*, 1983 34 257.
 424. N. Darabiha, S. M. Candel, V. Giovangigli, and M. D. Smooke, *Combust. Sci. Technol.*, 1988 60 267.
 425. G. Dixon-Lewis, and I. G. Shepherd, Fifteenth Symposium (International) on Combustion, The Combustion Institute, Pittsburgh, 1975 1483.
 426. S. Kalamatianos, Y. K. Park, and D. G. Vlachos, *Combust. Flame*, 1998 112 45.
 427. W. A. Abd Al-Masseeh, D. Bradley, P. H. Gaskell, and A. K. C. Lau, Twenty-Third Symposium (International) on Combustion, The Combustion Institute, Pittsburgh, 1991 825.
 428. J. M. Rhine, and R. J. Tucker, "Modeling of Gas-Fired Furnaces and Boiler, and other Industrial Heating Processes", British Gas plc in association with McGraw-Hill Book Company, London and New York, 1991.
 429. A. D. Gosman, and K. Y. M. Lai, International Symposium on Refined Modeling of Flows, IAHR, Paris, 1982.
 430. D. Bradley, S. B. Chain, P. H. Gaskell, A. K. C. Lau, and M. Missaghi, International Conference on Computers in Engine Technology, Institution of Mechanical Engineering, London, 1987 315.
 431. A. Y. Abdalla, D. Bradley, S. B. Chain, and C. Lam., *Prog Astro. Aero.* 1984 95 356.
 432. D. Bradley, Twenty-Fourth Symposium (International) on Combustion, The Combustion Institute, Pittsburgh, 1992 247.
 433. K. N. C. Bray, Twenty-Sixth Symposium (International) on Combustion, The Combustion Institute, Pittsburgh, 1996 1.
 434. WM. T. Ashurst, Twenty-Fifth Symposium (International) on Combustion, The Combustion Institute, Pittsburgh, 1992 1075.
 435. S. P. Burke, and T. E. W. Schumann, *Ind. Eng. Chem.*, 1928 20 (10).
 436. H. C. Hottel, and W. R. Hawthorne, Third Symposium (International) on Combustion, Baltimore, 1949 254.
 437. K. Wohl, C. Gazly, and N. Kapp, Third Symposium (International) on

- Combustion, Baltimore, 1949 288.
438. W. R. Hawthorne, D. S. Weddel, and H. C. Hottel, Third Symposium (International) on Combustion, Baltimore, 1949 266.
439. J. Du, and R. L. Axelbaum, Twenty-Sixth Symposium (International) on Combustion, The Combustion Institute, Pittsburgh, 1996 1137.
440. R. G. Abdel-Gayed, D. Bradley, and A. K. C. Lau, Twenty-Second Symposium (International) on Combustion, The Combustion Institute, Pittsburgh., 1989 731.
441. G. K. Batchelor, Proc. Roy. Soc. (London), 1952 A213 349.
442. G. I. Taylor, Proc. Roy. Soc. (London), 1935 A151 421.
443. R. Borghi, In Recent Advances in Aerospace Sciences, Plenum Press, New York, 1985.
444. J. Abraham, F. A. Williams, and F. V. Bracco, SAE paper 850345, 1985.
445. R. G. Abdel-Gayed, D. Bradley, and F. K. Lung, Combust. Flame, 1989 76 213.
446. R. G. Abdel-Gayed, and D. Bradley, Combust. Flame, 1985 62 61.
447. B. E. Launder, and D. B. Spalding, Comp. Meth. Appl. Engng., 1974 3 269 289.
448. R. W. Bilger, Combust. Sci. Tech., 1975 11 215.
449. W. P. Jones, In Prediction Methods for Turbulent Flows (Kollmann, W Ed.), Hemisphere, 1980 380.
450. W. P. Jones, and J. H. Whitelaw, Combust. Flame 1982 48 1.
451. B. E. Launder, G. J. Reece, and W. Rodi, J. Fluid Mech., 1975 68 537.
452. F. A. Williams "Structure of flamelets in turbulent reacting flow and influence of combustion on turbulence fields", Lecture Notes in Engineering, Springer , 1989 40 195.
453. J. C. Hermanson, M. G. Mungal, and P. E. Dimotakis, AIAA-85-0142.
454. P. E. Dimotakis, AIAA-89-0262.
455. A. M. Masri, R. W. Bilger, and R. W. Dibble, Combust. Flame, 1988 712 245.
456. W. Kollmann, and J. Y. Chen, "The interaction of turbulence and chemical kinetics", In Major Research Topics in Combustion, (M. Y. Hussaini, , A. Kumar, and R. G. Voigt, Eds.), Springer-Verlag, New York, Inc. 1992.
457. J. Swithenbank, B. C. R. Ewan, S. B. Chin, L. Shao, and Wu, Y., "Mixing power concept in scramjet combustor design", In Major Research Topics in Combustion, (M. Y. Hussaini, A. Kumar, and R. G. Voigt, Eds.), Springer-Verlag, New York, Inc. 1992.
458. P. A. Libby, "Comments on the interaction of turbulence and chemical kinetics", In Major Research Topics in Combustion, (M. Y. Hussaini, A. Kumar, and R. G. Voigt, Eds.), Springer-Verlag, New York, Inc. 1992.
459. R. W. Bilger, Prog. in Energy and Combustion Sciences", 1976 1 87.
460. P. A. Libby, and F. A. Williams, AIAA J., 1981 19 261.

461. Y. C. Chen, W. Kollmann, and R. W. Dibble, *Combust. Sci. Technol*, 1989 64 315.
462. S. K. Liew, K. N. C. Bray, and J. B. Moss, *Combust. Sci. Technol.*, 1981 27 69.
463. S. K. Liew, and K. N. C. Bray, *Combust. Flame*, 1984 56 199.
464. N. Peters, *Twenty-First Symposium (International) on Combustion*, The Combustion Institute, 1986 1231.
465. S. M. Correa, "Relevance of nonpremixed laminar flames to turbulent combustion", In *Major Research Topics in Combustion*, (M. Y. Hussaini, A. Kumar, and R. G. Voigt, Eds.), Springer-Verlag, New York, Inc. 1992.
466. P. Nilsson, and X. S. Bai, *Experimental Thermal and Fluid Science*, 2000 21.
467. R. Borghi, *Prog. Energy Combust. Sci.*, 1988 14 245.
468. A. C. Benim, and K. J. Syed, *Proc. of the Mediterranean Combustion Symposium*, Antalya – Turkey, June 20-25 1999 1050.
469. P. Moreau, *Turbulent flame development in a high velocity premixed flow*, ONERA T. P., 1977 5.
470. P. Moreau, and R. Borghi, *Experimental and theoretical studies of nitrogen oxides production in a turbulent premixed flow*, ONERA T. P., 1980 1.
471. F. M. El-Mahallawy, S. A. Farag, and M. A. Abdel Rahman, *The Fourth International Conference for Mechanical Power Engineering*, Faculty of Engineering, Cairo University, Oct. 1982.
472. B. Lewis, and G. Von Elbe, *The Journal of Chemical Physics*, 1943 11 75.
473. B. Lewis, and G. Von Elbe, "Combustion, Flame and Explosions of Gases", Academic press, New York, 1951.
474. G. Von Elbe, and M. Mentser, *The Journal of Chemical Physics*, 1945 13 89.
475. K. Wohl, N. M. Kapp, and C. Gazley, *Third Symposium on Combust., Flame and Explosion Phenomena*, Williams and Wilkins Co., Baltimore, 1949 3.
476. D. W. Van Krevelen, and H. A. G. Chermin, *Seventh Symposium (International) on Combustion*, Butter-Worths Scientific Publications, London, 1959.
477. S. B. Reed, *Combustion and Flame*, 1967 11 177.
478. W. P. Jensen, and C. W. Shipman, *Seventh Symposium on Combustion*, Butter-Worth Scientific Publications London, 1959.
479. I. V. Bepalov, *Physical Principles of the Working Process in Combustion Chambers of Jet Engines* by Raushenbakh et al., Translated from Russian, Clearinghouse for Federal Scientific and Technical Information, U.S.A., AD 658 372 May, 1967 366.
480. S. A. Beltagui, and N. R. L. Maccallum, *European Combustion Symposium*, Academic Press, London and New York, 1973 559.
481. G. G. Bafuwa, and N. R. L. Maccallum, *European Combustion Symposium*, Academic Press, London and New York , 1973 565.

482. G. V. S. N. Rao, and V. Sriramulu, *Combust. Flame*, 1979 34 (2) 203.
483. H. P. Schmid, P. Habisreuther, and W. Leuckel, *Combust. Flame*, 1998 113 79.
484. M. Philipp, S. Hoffmann, P. Habisreuther, B. Lenze, and H. Eickhoff, *Twenty-Fourth Symposium (International) on Combustion*, The Combustion Institute, Pittsburgh, 1992 361.
485. T. M. Farag, M. Arai, M. Shimizu, and H. Hiroyasu, *Bulletin of the JSME*, October, 1983 26 220.
486. S. Yuasa, *Combust. Flame*, 1986 66 181.
487. R. W. Schefer, M. Namazian, and J. J. Kelly, *AIAA*, 1994 32 1844.
488. F. M. El-Mahallawy, E. S. Mahdi Ali, and M. Rashad, *Heat and Fluid Flow in Power System Components*, (Rezk, A. M., Ed.), Pergaman Press, Oxford, 1979 283-292.
489. F. M. El-Mahallawy, E. S. Mahdi Ali, H. A. Kamhawy, and M. R. Taha, *Third International Conference for Mechanical Power Engineering*, Monofia University, Egypt. 1980.
490. F. M. El-Mahallawy, E. S. Mahdi Ali, and A. S. El-Ghoroury, *AMSE Proceeding International Conference*, Athens, France, June, 1984 27-29.
491. J. M. Beér, and N. A. Chigier, *Combustion Aerodynamics*, Applied Science Publisher Ltd, London, 1972.
492. A. E. Smart, B. Jones, and N. T. Jewell, *AIAA*, 1976 76 141.
493. B. Prade, and B. Lenze, *Twenty-Fourth Symposium (International) on Combustion*, The Combustion Institute, Pittsburgh, 1992 369.
494. A. J. Lightman, R. D. Richmond, and L. Krishnamurthy, paper No. AIAA-80-1544, *AIAA 15th. Thermophysics Conference*, Snowmass, Co., 1980.
495. A. R. Masri, B. B. Dally, R. S. Barlow, and C. D. Carter, *Twenty-Fifth Symposium (International) on Combustion*, The Combustion Institute, Pittsburgh, 1994 1301.
496. Y-C Cheng, C-C Chang, K-L Pan, and J. T. Yang, *Combust. Flame*, 1998 115 51.
497. D. Bradley, P. H. Gaskell, X. J. Gu, M. Lawes, and M. J. Scoott, *Combust. Flame*, 1998 115 515.
498. Y. S. Gil, H. S. Jung, and S. H. Chung, *Combust. Flame*, 1998 113 348.
499. P. Bailly, D. Garre`ton, O. Simonin, P. Bruel, M. Champion, B. Deshaies, S. Duplantier, and S. Sanquer, *Twenty-Sixth Symposium (International) on Combustion*, The Combustion Institute, Pittsburgh, 1996 923.
500. A. G. Bakroziis, D. D. Papailiou, and P. Koutmos, *Combust. Flame*, 1999 119 291.
501. I. D. Kalogirou, and D. D. Papailion, *AIAA*, 1994 162 237.
502. D. Trimis, *Verbrennungsvorgänge in porösen inerten Medien*, BEV 95, 5, ESYTEC, Erlangen, 1996.

503. P. A. Libby, and F. A. Williams, *Turbulent Reacting Flows*, ABACUS Press, Tunbridge Wells, UK, 1993.
504. D. Feikema, R. H. Chen, and J. F. J. Driscoll, *Combust. Flame*, 1991 86 347.
505. F. Takahashi, and W. J. Schmoll, *Twenty-Third Symposium (International) on Combustion*. The Combustion Institute, Pittsburgh, 1990 677.
506. J. T. Yang, C. C. Chang, and M. T. Lin, *Ninth Congress on Cogeneration and Utility, Industrial and Independent Power Generation*, Vienna, Austria, ASME paper 95-CTP-44, 1995.
507. C. M. Müller, H. Breitbach, and N. Peters, *Twenty-Fifth Symposium (International) on Combustion*, The Combustion Institute, Pittsburgh, 1994 1099.
508. F. M. El-Mahallawy, M. M. Hassan, and I. A. El-Desokey, *4th International Conference of Fluid Mechanics (ICFM4)*, Alexandria, 1992 1.
509. W. Leuckel, and N. Fricker, *Journal of Institute of Fuel*, 1976 103.
510. C. S. Schmid, R. Weber, and P. A. Roberts, IFRF Doc. No. K70/a/2.
511. D. Bradley, and A. K. C. Lau, *Pure and Applied Chemistry*, 1990 62 803.
512. D. Bradley, *Fundamental Aspects of Gaseous Combustion*, "Combustion Flow Diagnostics" (D. F. G. Durao, M. V. Heitor, J. H. Whitelaw and P. O. Witze Eds), Kluwer Academic Publishers, Series E, Applied Sciences, Dordrecht, Boston, London, 1992, 207, 47.
513. K. N. C. Bray, P. A. Libby, and J. B. Moss, *Combust. Flame*. 1985 61 87.
514. K. N. C. Bray, M. Champion, and P. A. Libby, *Combust. Sci. Technol.*, 1988 59 463.
515. K. N. C. Bray, M. champion, and P. A. Libby, *Twenty-Second Symposium (International) on Combustion*, The Combustion Institute, Pittsburgh, 1989 763.
516. M. V. Heitor, A. M. K. P. Taylor, and J. H. Whitelaw, *Exp. Fluids*, 1985 3 323.
517. D. Bradley, A. K. C. Lau, and M. Missaghi, *Combust. Sci. Technol.*, 1989 64 119.
518. D. B. Spalding, *Chem. Engng. Sci.*, 1971 26 95.
519. S. S. Girimaji, and S. B. Pope, *Material Element Deformation in Isotropic Turbulence*, FDA-89-14, Cornell University, 1989.
520. S. M. Correa, and W. Shyy, *Prog. Energy Combust. Sci.*, 1987 13 249.
521. P. H. Gaskell, and A. K. C. Lau, *Int. J. Num. Meth. Fluids*, 1988 8 617.
522. W. A. Abd El-Masseeh, D. Bradley, P. H. Gaskell, and A. K. C. Lau, *Seventh Symposium on Turbulent Shear Flows*, 1989 21.
523. C. k. Westbrook, and W. J. Pitz, *Prog. Astro. Aero.*, 1984 95 211.
524. W. A. Abd El-Masseeh, D. Bradley, P. H. Gaskell, A. Ishikawa, and A. K. C. Lau, *Twenty-Third Symposium (International) on Combustion*, The Combustion Institute, Pittsburgh, 1991 825.
525. I. E. Megahed, F. M. El-Mahallawy, and, K. H. Khalil, "Flow, Mixing and

- Heat Transfer in Furnaces", (D.B. Spalding, K. H. Khalil, F. M. El-Mahallawy, and E. E. Khalil. Eds.), HMT Pergamon Press, 1978 2 93.
526. F. M. El-Mahallawy, S. A. Farag, M. M. Hassan, and S. M. Khalifa, The Third International Conference for Mechanical Power Engineering, Faculty of Engineering, El-Monofia University, Egypt, 1980.
527. A. D. Gosman, "Heat and Mass Transfer in Recirculating Flows", Academic Press, London, 1969.
528. H. Schlichting, "Boundary Layer Theory Trans.", Sixth Edition, McGraw -Hill Book Co., New York, 1968.
529. M. Mikheyev, "Fundamental of Heat Transfer", Mir Publishers, Mosco, 1968.
530. I. E. Megahed, F. M. El-Mahallawy, and, K. H. Khalil, "Flow, Mixing and Heat Transfer in Furnaces", (D. B. Spalding, K. H. Khalil, F. M. El-Mahallawy, and E. E. Khalil. Eds.), HMT Pergamon Press, 1978 2 131.
531. F. M. El-Mahallawy, S. Farag, and Khalifa, Engineering Research Journal, Faculty of Engineering, Helwan University, Mataria, 2001.
532. E. Mallard, and H. L. Le Chatelier, Annales des Mines, 1883 4 343.
533. G. Damköhler, Elektrochem. Angew. Phys. Chem., 1940 46 601.
534. K. I. Shchelkin, Zh. Eksp. i Teoret. Fiz., 1943 13 520.
535. B. Karlovitz, Fourth Symposium (International) on Combustion, Williams and Wilkins Co, 1953 60.
536. L. M. Bollinger, and D. T. Williams, Third Symposium (International) on Combustion, Williams and Wilkins Co., 1949 176.
537. H. Hottel, G. Williams, A. Scurlock, Third Symposium (International) on Combustion, Williams and Wilkins Co, 1949 21.
538. B. Karlovitz, Dennistone and Wells, Third Symposium (International) on Combustion, Williams and Wilkins Co., 1949 613.
539. D. Bradley, and R. Abdel Gayed, Sixteen Symposium (International) on Combustion, The Combustion Institute, Pittsburgh, 1976 1725.
540. G. Andrews, D. Bradley, and S. Lwakabamba, Combust. Flame, 1975 24 285.
541. P. A. Libby, and F. A. Williams. Ann. Rev. Fluid Mech., 1976 8 351.
542. K. N. C. Bray, Topics in Applied Physics vol. 44, Turbulent Reacting Flows, (P. A. Libby, and F. A. Williams, Eds, Springier-Verag, 1980 115.
543. D. Bradley, In Internal Combustion Engineering. Science and Technology (J. Wearing Ed), Elsevier, 1990.
544. H. Kobayashi, T. Tamura, K. Maruta, T. Niioka, and F. A. Williams, Twenty-Sixth Symposium (International) on Combustion, The Combustion Institute, Pittsburgh, 1996 389.
545. J. Furukawa, T. Hirano, and F. A. Williams, Combust. Flame, 1998 113 487.
546. B. F. Magnussen, and B. H. Hjertager, Sixteenth Symposium (International) on Combustion, The Combustion Institute, 1977 719.

547. D. B. Spalding, Thirteenth Symposium (International) on Combustion, The Combustion Institute, 1971 649.
548. D. R. Ballal, and A. H. Lefebvre, Proc. Roy. Soc., 1975 A344 217.
549. R. G. Abdel-Gayed, and D. Bradley, Phil. Trans. Roy. Soc., 1981 301 1.
550. R. G. Abdel-Gayed, D. Bradley, and M. Lawes, Proc. Roy. Soc., London, 1987 A414 389.
551. D. Bradley, J. Hynes, M. Lawes, and C. G. W. Sheppard, International Conference on Combustion in Engines, Institution of Mechanical Engineers, London, 1988 17.
552. G. P. Beretta, M. Rashidi, and J. C. Keck, Combust. Flame, 1983 52 217.
553. R. G. Abdel-Gayed, D. Bradley, M. Lawes, and F. K. K. Lung, Twenty-First-Symposium (International) on Combustion, The Combustion Institute, Pittsburgh, 1986 49.
554. A. Lipatnikov, and J. Chomiak, Proc. of the Mediterranean Combustion Symposium, Antalya-Turkey, June 20-25, 1999 1038.
555. K. N. C. Bray, in Turbulent Reacting Flows (P. A. Libby and F. A. Williams, Eds.), Springer-Verlag, Berlin, 1980 115.
556. J. O. Hinze, "Turbulence", 2nd Edition, McGraw Hill, New York, 1975.
557. Wm. T. Ashurst, Combust. Sci. Technol., 1995 104 19.
558. S. S. Ibrahim, R. S. Cant, and K. N. C. Bray, in Dynamics of Deflagrations and Reactive Systems: Flames (A. L. Kuhl, J. C. Leyer, A. A. Borisov, and W. A. Sirignano, Eds.) Progress in Asronautics and Aeronautics, 1991 141 177.
559. A. N. Lipatnikov, and J. Chomiak, Fourth International Symposium on Engineering Turbulence Modeling and Measurements, 1998.
560. I. Sawai, M. Kunugi, and H. Jinno, Fourth Symposium (International) on Combustion, Baltimore, 1953 805.
561. S. P. Sharma, and C. Mohan, "Fuels and Combustion", Tata McGraw-Hill Publishing Company Limited, New Delhi, 1984.
562. R. Gunther, Gaswarne, 1966 15 376.
563. H. A. Becker, Fifteenth Symposium (International) on Combustion, The Combustion Institute, Pittsburgh, 1975 601.
564. S. J. Yagi, Soc. Chem. Ind. (Japan), 1943 46 (608) 821.
565. H. A. Becker, and D. Liang, Combust. Flame, 1978 32 115 .
566. F. M. El-Mahallawy, S. A. Farag, and N. I. Beshara, First Specialists Meeting (International) of the Combustion Institute, Universite' de Bordeaux I-France, 20-24 Juillet, 1981 123.
567. H. A. Becker, and S. Yamazaki, Combust. Flame, 1978 33 123.
568. H. A. Becker, and S. Yamazaki, Sixteenth Symposium (International) on Combustion, The Combustion Institute, Pittsburgh, 1977 681.
569. F. C. Lockwood, F. M. El-Mahallawy, and D. B. Splading, Combust. Flame,

- 1974 23 283.
570. Ibrahim, M. A. Said and F. M. El-Mahallawy, *Combust. Flame*, 1985 60 141.
571. F. M. El-Mahallawy, H. Heikel, and M. A. Ismail, *The Fourth International Conference for Mechanical Power Engineering*, Faculty of Engineering, Cairo University, Egypt, 1982.
572. H. N. Powell, and W. G. Browne, *Six Symposium on Combustion (International)*, Reinhold Publishing Corporation, 1957.
573. I. Saural, M. Kunugi, and H. Jinno, *Fourth Symposium on Combustion (International)*, Reinhold Publishing Corporation, 1953.
574. F. G. Roper, C. Smith, and Cunningham, *Combust. Flame*, 1977 29 115.
575. A. K. Shaha, *Combustion and Fuel Technology*, Oxford, IBH Publishing Co., 1974.
576. E.S. Mahdi Ali, F. M. El-Mahallawy, and M. Zakeria, *The Fourth International Conference for Mechanical Power Engineering*, Faculty of Engineering, Cairo University, Egypt, 1982 33.
577. N. A. Chigier, and J. M. Beèr, *Trans. ASME*, 86, J. Basic Eng. 1964.
578. F. M. El-Mahallawy, A. S. Elasfour, N. M. Rafat, and M. M. Youssef, *Scientific Engineering Bulletin*, Faculty of Engineering, Cairo University, 1983 163.
579. L. Boguslawski, and Cz. O. Popiel, *J. Fluid Mech.*, 1979 90 (3) 531.
580. M. Barchilon, R. Curtet, *J. Basic Eng. (Trans. ASME)*, 1964 777.
581. M. W. Thring, and M. P. Newby, *Fourth Symposium (International) on Combustion*, The Combustion Institute, Baltimore, 1953 789.
582. A. K. Gupta, D. G. Lilley, and N. Syred, "Swirl Flows" ABACUS Press. N. Y., USA, 1984.
583. F. M. El-Mahallawy, Z. S. Safar, A. Rezk, and A. S. Elghoroury, *Engineering Research Journal*, Faculty of Engineering, Helwan University, Matria, 2001.
584. N. M. Kerr, and D. Fraser, "Effect of Swirl on Axisymmetrical Turbulent Jets" Part I, Kerr and Fraser Paper, May, 1965.
585. N. M. Kerr, *J. of the Institute of Fuel*, Dec., 1965 577.
586. Leuckel, W., "Swirl Intensities, Swirl Types and Energy Losses of Different Swirl Generating Devices", Doc. No. GO2/a/16, International Flame Foundation, Ijmuiden, Holland, 1968.
587. O. M. Knio, A. S. Worlikar, and H. N. Najm, *Twenty-Sixth Symposium (International) on Combustion*, The Combustion Institute, Pittsburgh, 1996 203.
588. A. Mestre, "Efficiency and Pollutant Formation Studies in a Swirling Flow Combustor" *Aerospatial Research Center*, Chatillon, France, 1974.
589. S. A. Beltagui, and N.R.L. Maccallum, *J. of the Institute of Fuel*, Dec., 1976 183.
590. Y. H. El-Banhawy, "Open and Confined Spray Flames" Ph.D. Thesis, Univ. of London, England, 1980.

591. G. E. Ahmad, M. K. Andrews, and S. F. Sharif, Twentieth Symposium (International), The Combustion Institute, Pittsburgh, 1984 259.
592. T. Toshimi, H. D. Shin, and A. Ishio, *Combust. Flame*, 1981 41 261.
593. F. C. Gouldin, J. S. Depsky, and S. I. Lee, *AIAA*, 1985 23 95.
594. J. J. Keller, and M. P. Escudier, *AIAA J.* 23rd Aerospace Sciences Meeting Jan. 1985.
595. Sturgess, G. J. and Sayed, A. "Calculation of Confined Swirling Flows" *AIAA J. Aerospace Science Meeting*, Jan. 1985.
596. U. S. Choi, and R. W. Lyvzkowski, "The Effect of Swirl on the Development of Recirculation Flow Patterns in a Swirl Combustor", *ASME*, N. Y., USA Feb., 1986.
597. O. Kawaguchi, and H. Akiyama, International Gas Research Conference, 547, Toronto, Canada, Sept., 1987.
598. M. S. Ramavajjala, and A. K. Gupta, 7th International Conference of Mech. Power Eng., Cairo Univ., vol. II, Dec., 1990.
599. M. Arai, T. M. Farag. and H. Hiroyasu, International Gas Turbine Congress, Tokyo, October, 1983 221.
600. F. M. El-Mahallawy, K. H. Khalil, and Y. H. El-Banhawy, "Heat and Mass Transfer" Series, (B. Spalding, K. H. Khalil, F. M. El-Mahallawy, and E. E. Khalil. Eds.), Pergamon Press, 1978 49.
601. K. H. Khalil, F. M. El-Mahallawy, and Y. H. El-Banhawy, *The Bulletin of the Faculty of Engineering, Cairo University*, 1975.
602. E. E. Khalil, F. M. El-Mahallawy, and N. M. Rafat, *The First Conference of Mechanical Power Engineering, Faculty of Eng., Cairo University*, Feb., 1977.
603. F. M. El-Mahallawy, M. A. Hassan, M. A. Ismail, and H. Zafan, *ASME*, 94-GT-441.
604. F. M. El-Mahallawy, M. A. Hassan, M. A. Ismail, and H. Zafan, *Engineering Research Journal, Faculty of Engineering of El-Mataria, University of Helwan, Egypt*, 1994 5.
605. F. M. El-Mahallawy, and M. A. Habib, *The First Conference of Mechanical Power Eng., Faculty of Eng. Cairo University*, Feb. 1977.
606. F. M. El-Mahallawy, E.S. Mahdi Ali, and M. Khalifa, *The First Mechanical Power Engineering Conference, Cairo University*, Feb., 1977.
607. F. M. El-Mahallawy, and F. Y. Ghali, *The Second Mechanical Power Engineering Conference, Ain Shams University*, Sept. 1978.
608. F. M. El-Mahallawy, and A. A. Hassan,; *The First Conference of the Mechanical Power Engineering, Faculty of Engineering, Cairo University*, Feb., 1977.
609. F. M. El-Mahallawy, B. A. Khalifa, and M. A. Shahin, *The Fourth International Conference for Mechanical Power Engineering, Faculty of Engineering, Cairo University*, Oct. 1982.

610. A. D. Gosman, W. M. Pun, A. K. Runchal, D. B. Spalding, and M. Wolfshtein, "Heat and Mass Transfer in Recirculating Flows", Academic, Press, London, 1969.
611. J. G. Cogoli, D. Gray, and R. H. Essenhigh, *Combust. Sci. Technol.*, 1977 16 165.
612. T. Abbas, P. Costen, and F. C. Lockwood, *Combust. Flame*, 1992 91 346
613. P. A. Gillis, and P. J. Smith, nineteenth., ACS National Meeting, Toronto, Canada, 1990 33 (2) 215.
614. A. D. Gosman, "Lecture 7, The computer program, prediction of the performance of combustion chambers and furnaces", A short Course presented at Pennsylvania State University, Pennsylvania, April 19-21, 1978.
615. S. V. Patanker, "Numerical Heat Transfer and Fluid Flow, Computational Methods in Mechanics and Thermal Sciences", Hemisphere Publishing Corp., Washington DC, 1980.
616. A. D. Gosman, L. S. Caretto, S. V. Patankar, and D. B. Spalding, *Proceeding of the Third International Conference on Numerical Methods in Fluid Dynamics*, 1973 2.
617. C. K. Wu, L. E. Chen, J. Li, H. Y. Wang, J. B. Wei, H. Q. Zhan, and F. Y. Zhu, *Twenty-Second Symposium (International) on Combustion*, The Combustion Institute, 1988 193.
618. F. C. Lockwood, S. M. A. Rizvi, G. K. Lee, and H. Whaley, *Twentieth Symposium (International) on Combustion*, The Combustion Institute, 1984 513.
619. P. J. Strkowaski, A. Krothapalli, and D. Wishart, *AIAA Journal*, 1993 31 (11) 2033.
620. G. Monnot, "Principles of Turbulent Fired Heat", Gulf Publishing Company, 1985.
621. S. W. Kim, and J. J. Bemson, *AIAA Journal*, 1993 31 (5) 806.
622. W. B. Fu, J. B. Wei, H. Q. Zhan, W. C. Sun, L. Zhao, Y. L. Chen, H. Q. Han, W. S. Huang, and C. K. Wu, *Twenty-First Symposium (International) on Combustion*, The Combustion Institute, Pittsburgh, 1986 567.
623. R. Weber, *Twenty-Sixth Symposium (International) on Combustion*, The Combustion Institute, Pittsburgh, 1996 3343.
624. K. H. Khalil, F. M. El-Mahallawy, and H. A. Moneib, *Sixteenth Symposium (International) on Combustion*, The Combustion Institute, Pittsburgh, 1976 135.
625. F. M. El-Mahallawy, F. C. Lockwood, and D. B. Spalding,; *Combustion Institute European Symposium*, 1973.
626. F. M. El-Mahallawy, M. A. Hassan, and M. H. Eid, *International Journal of Energy and Research*, John Wiley and Sons Publisher 1995 24 (5) 373.
627. N. Fricker, and W. Leuckel, *International Flame Research Foundation, Doc. No. GO2/9/18, Final Report*, 1969.

628. M. L. Mather and N. R. Maccalum, *J. Inst. Fuel*, 1967 238.
629. J. Chedaille, W. Leuckel, and A. K. Chesters, *J. Inst. Fuel*, 506, Dec., 1966.
630. A. Y. Kuo, "Combustion", McGraw-Hill, New York, 1987.
631. A. H. Lefbver, "Gas Turbine Combustion", Mc Graw-Hill, New York, 1983.
632. A. K. Jasuja, "Atomization of crude oil and residual fuel oils", ASME paper 78/GT/83.
633. G. M. Faeth, *Prog. Energy Combust. Sci.*, 1983 9 1.
634. F. M. El-Mahallawy, A. S. Elasfour, and E. Mahdi Ali, *Scientific Engineering Bulletin, Faculty of Engineering, Cairo University*, 1979 10.
635. A. Chernov, and N. Bessrebrennikov, "Fundamentals of Heat Engineering and Hydraulic", Mir publishers, Moscow, 1969.
636. F. M. El-Mahallawy, *Scientific Engineering Bulletin, Faculty of Engineering, Cairo University*, 1978 8.
637. F. M. El-Mahallawy, A. S. Elasfour, and E. Mahdi Ali, *Proceeding of the Seventh International Heat Transfer Conference, IHTC, Munchen*, 1982 529.
638. M. H. Eid, "Heat transfer by radiation in a cylindrical oil-fired flame tube", Ph. D. Thesis, Cairo University, Egypt, 1982.
639. J. M. Beér, "Methods for Calculation Radiation Heat Transfer From Flames in Combustors and Furnaces", in *Heat Transfer in Flame*, John Wiley and Sons, New York, 1974 29.
640. V. Isachenko, V. Osipova, and A. Sukomel, "Heat transfer", Mir Publishers, Moscow, 1969 263.
641. K. C. Schadow, E. Gutmark, K. J. Wilson, and R. A. Smith, *AIAA J.*, 1990 6 407.
642. M. B. Gibbs, and A. Williams, *J. Institute Energy*, 1983 74.
643. R. H. Chen, J. F. Driscoll, J. Kelly, M. Namaziam, and R. W. Schefer *Combust. Sci. Technol.*, 1990, 71 197.
644. A. A. Desoky, A. S. K. Halaf, and F. M. El-Mahallawy, *Int. J. Hydrogen Energy*, 1990 15 (3) 203.
645. F. M. El-Mahallawy, and A. S. Abbas, *The Second Mechanical Power Engineering Conference, Ain Shams University*, Sept. 1978.
646. F. M. El-Mahallawy, E. E. Khalil, and O. Abdel Aal, *The Fourth International Conference for Mechanical Power Engineering, Cairo University*, Oct. 1982.
647. F. M. El-Mahallawy, M. A. Abu El-Enin, and A. A. El-Atroush, *The Bulletin of the Faculty of Engineering, Alexandria University, Faculty of Engineering Press*, 1987.
648. E.S. Mahdi Ali F. M. El-Mahallawy, and M. Khalifa, *Scientific Engineering Bulletin, Faculty of Engineering, Cairo University*, 1979 10.
649. F. M. El-Mahallawy, K. H. Khalil, and A. H. Abdel Hafiz, "Flow, Mixing and Heat Transfer in Furnaces, (B. Spalding, K. H. Khalil, F. M. El-Mahallawy, and

- E. E. Khalil. Eds.), HMT Pergamon Press, 1978 2 224.
650. K. H. Khalil, F. M. El-Mahallawy, E. E. Khalil, and A. H. Abdel-Hafiz, Proceeding of Second Conference of Mechanical Power Engineering, Faculty of Engineering, Ain Shams University, 23-28 Sept., 1978.
651. F. M. El-Mahallawy, E.S. Mahdi Ali, S. M. Negm, and N. M. Rafat, Proceedings of Second Conference of Mechanical Power Engineering, Faculty of Engineering, Ain Shams University, 23-28 Sept. 1978.
652. F. M. El-Mahallawy, M. A. Hassan, and M. M. Abdou, Engineering Bulletin, Helwan University, Mataria, 1990 1 100.
653. A. H. Abdel Hafez, and M. R. Taha, Engineering Research Journal, Faculty of Engineering, Helwan University, March 1995 3.
654. A. H. Abdel Hafez, F. M. El-Mahallawy, and A. M. Shehata, ASME COGEN-Turbo, 1994 513.
655. Y. Kamotani, and I. Gerber, AIAA J., 1972 10 1425.
656. A. H. Abdel Hafez, Engineering Research Journal, Faculty of Engineering, Helwan University, Mataria, 1999.
657. F. M. El-Mahallawy, E. S. Mahdi Ali, H. A. Kamhawy, and M. R. Taha, Third International Conference for Mechanical Power Engineering, Monofia University, Egypt, 1980.
658. F. M. El-Mahallawy, E. Mahdi Ali, and M. Rashad, The Second Mechanical Power Engineering Conference, Ain Shams University, Sept., 1978.
659. R. F. Huang, and C. T. Lin, Combust. Sci. Technol., 1994 100 139 .
660. Y-C Chen, C-C Chang, K-L Pan, and J-T Yang, Combust. Flame, 1998 115 51.
661. F. M. El-Mahallawy, E. S. Mahdi Ali, and A. S. El-Ghoroury, AMSE Proceeding International Conference, Athen, France, 1984.
662. P. A. Libby, and F. A. Williams, Turbulent reacting flows, "Topics in Applied Physics" Springer Verlag, New York, 1981.
663. F. E. Marble, and J. E. Broadwell, The coherent flame model of non premixed combustion, Project Squid Report, TRW-9-PU, 1977.
664. S. M. Cannon, B. S. Brewster, and L. D. Smoot, Combust. Flame, 1999 119 233
665. A. Bentebiche, D. Veynante, and E. Esposito, Mediterranean Combustion Symposium, Antalya – Turkey, June 20-25, 1999 527.
666. W. Vicente, N. Fueyo, and C. Dopazo, Combust. Sci. Technol., 2000 153 468.
667. D. Benedetto, S. Pasini, M. Falcitelli, C. La Marca, and L. Tognotti, Combust. Sci. Technol., 2000 153.
668. S. P. Nandula, R. W. Pitz, R. S. Barlow, and G. J. Fiechtner, AIAA, 96-0937 1996.
669. S. B. Pope, Combustion Theory Modelling, 1997 1 41.
670. H. P. Mallampalli, T. H. Fletcher, and J. Y. Chen, J. Eng. Gas Turbines Power, 1998 120 703.

671. A. C. Benim, *Int. J. Num. Methods Fluids*, 1990 11 697.
672. I. Z. Hu, and S. M. Correa, *Twenty-Sixth Symposium (International) on Combustion*, The Combustion Institute, Pittsburgh, 1996 307.
673. S. Candel, and Al, *Combust. Sci. and Technol.*, 1994 98 245.
674. A. J. H. Teekaram, *3rd European Conference on Industrial Furnaces and Boilers*, Portugal, 1995.
675. E. Djavdan, N. Darabiha, V. Giovangeli, and S. J. Candel, *Physics*, 1991 III 1 651.
676. A. Oksanen, and E. Maki Mantila, *3rd European Conference*, Portugal, 1995.
677. G. Brown, and A. Roshko, *J. Fluid Mech.*, 1974 64 775.
678. S. V. Patanker, and D. B. Spalding, *Int. J. Heat Mass Transfer*, 1972 15 (1787) 307.
679. H. P. Mallampalli, T. H. Fletcher, and J. Y. Chen, "Updated CH₄/NO_x global mechanism used for modeling lean premixed turbulent combustion of natural gas", <http://www2.et.byu.edu/~tom/gas-turbines/updated-5step.html>, 1998.
680. C. T. Bowman, R. K. Hanson. D. F. Davidson, J. W. C. Gardiner, V. Lissianski, G. P. Smith, D. M. Golden, M. Frenklach, H. Wang. and, M.V. Lissianski, *GRI-Mech 2.11*. <http://www.gri.org>, 1995.
681. J. Y. Chen, *Combust. Sci. and Technol.*, 1988 57 89.
682. H. P. Mallampalli, T. H. Fletcher, and J. Y. Chen, "Evaluation of CH₄/NO_x global mechanism used for modeling lean premixed turbulent combustion of natural gas", In *Fall Meeting of the Western States Section of the Combustion Institute*, University of Southern California Los Angeles, CA., Oct. 28-29, 1996.
683. B. E. Launder, *J. Fluid Mech.*, 1975 67 569.
684. M. M. Gibson, and B. E. Launder, *J. Fluid Mech.*, 1978 86 491.
685. B. A. Younis, "On modeling the effects of streamline curvature on turbulent shear flows", PhD Thesis, University of London, 1984.
686. S. B. Pope, *Combust. Sci. Technol.*, 1981 25 159.
687. K. R. Ehrhardt, "Development of a hybrid model for the prediction of nitric oxides emission of furnace" *Energy Lab. Report*, Massachusetts Inst. of Technology, 1993.
688. G. De Michele, S. Ligasacchi, S. Pasini, and L. Tognotti, *Int. Symp. Of AFRC*, Baltimore, Oct. 1996.
689. D. Benedetto, S. Pasini, T. Ranzi, C. Faravelli, L. La Marca, and Tognotti, *The Fourth International Conference on Technologies and Combustion for a Clean Environment*, Lisbona, 7-10 Luglio, 1997.
690. C. La Marca, "NO_x Formation and Emissions Control in Oil-Fired Boiler", Thesis in Chemical Engineering, University of Pisa, 1996.
691. B. P. Breen, and H.S. Hura, *The 1993 International Joint Power Generation Conference*, Kansas City, Missouri, Oct. 17-22, 1993.

692. P. Kilpinen, M. Hupa, P. Glarborg, and S. Hadvig, "Reburning": Parametric study of natural gas reburn chemistry using kinetic modeling", Report 87-89309-25-1 Nordisk Gsteknisk Center, Maggio, 1990.
693. G. De Michele, S. Pasini, A. Tozzi, "Simulation of heat transfer and combustion in gas and oil-fired furnaces", The Combustion Institute, Sezione Italiana e Sovietica, Pisa, Italia, Nov. 5-7, 1990.
694. E. Ranzi, T. Faravelli, P. Gaffuri, A. Sogaro, A. D'Anna, and A. Ciajolo, *Combust. Flame*, 1997 108 24.
695. S.G. Dukelow, "The Control of Boilers", 2nd Edition, Instrument Society of America, 1991.
696. A.L. Kohan, and H.M. Spring, "Boiler Operator's Guide", 3rd Ed., McGraw-Hill, Inc., New York, 1991.
697. S.P. Langley, *Mem Natl. Acad. Sci.*, 1883 2 147.
698. R. M. Goody, "Atmospheric Radiation, Theoretical Basis", Clarendon Press, Oxford, 1964 I .
699. C. Christiansen, *Ann. Phys., Wied.*, 1883 19 267.
700. W.E. Sumpner, *Proc. Phys. Soc. London*, 1894 94 10.
701. Edward P. Hyde, *Nat. Bur. Stand. U.S. Bull.*, 1907 3 81.
702. O. A. Saunders, *Proc. Phys. Soc. London*, 1928 41 569.
703. B. Gebhart, "Heat Transfer", 2nd Edition. McGraw-Hill Book Company, New York, 1971 150-163.
704. Nusselt, Wilhelm, "Graphische Bestimmung des Winkelverhältnisses beider Wärmestrahlung", *V.D.I.Z.*, 1928 72 673.
705. J. M. Hammersley, and D. C. Handscomb, "Monte Carlo Methods", John Wiley and Sons, Inc., New York, 1964.
706. Metropolis, Nicholas, and S. Ulam, "The Monte Carlo Method", *J. Am. Stat. Assoc.*, 1949 44 (247) 335.
707. Khan, Herman, "Application of Monte Carlo", Rept. No. RM-1237-AEC, (AEC, No. AECU-3259), Rand Corp., April 27, 1956.
708. J. R. Howell, "Monte Carlo Treatment of Data Uncertainties in Thermal Analysis", *J. Spacecr Rockets*, 1973 10 (6) 411 .
709. Denis J. Zigrang, *AIAA paper 75-710*, May, 1975.
710. N. J. McCormick, and I. Kuscer, "Singular eigen-function expansion in neutron transfer theory", in "Advances in Nuclear Science and Technology", (E. J. Henley and j. Lewins, Eds.), Academic Press, New York, 1973 7 181.
711. E. C. Gritton, and A. Leonard, *J. Quant. Spectrosc. Radiat. Transfer* 1970 10 1095.
712. Y. Yener, M. N. Ozisik, and C. E. Siewert, *J. Quant. Spectrosc., Radiat. Transfer*, 1976 16 165.
713. M. M. R. Williams, " The wiener-hopf technique. An alternative to the singular

- eigen-function method", in "Advances in Nuclear Science and Technology", (E. J. Henley and J. Lewins, Eds.), Academic Press, New York, 1973 7 283.
714. R. G. Deissler, *J. Heat Transfer*, 1964 86 (2) 240.
715. R. John Howell, and Perlmutter, Morris, *AIChE. J.*, 1964 10 (4) 562.
716. R. P. Bobco, *J. Heat Transfer*, 1967 89 (4) 313.
717. S. Rosseland, "Theoretical Astrophysics, Atomic Theory and the Analysis of Stellar Atmospheres and Envelopes", Clarendon Press, Oxford, 1936.
718. H. Douglas Sampson, *J. Quat. Spectrosc. Radiat. Transfer*, 1965 5 (1) 211.
719. M. M. Abu-Romia, and C. L. Tien, *J. Heat Transfer*, 1967 89 (4) 321.
720. R. W. Patch, *J. Quant. Spectrosc. Radiat. Transfer*, 1967 7 (4) 611.
721. S. Chandrasekhar, "Radiative Transfer", Dover Publications, Inc., New York, 1960.
722. A. Schuster, *Astrophys. J.*, 1905 21 (1).
723. B. G. Carlson, and K. D. Lathrop, "Transport Theory-the Method of Discrete Ordinates", in *Computing Methods in Reactor Physics*, Gordon and Breach, New York, 1968.
724. K. J. Daniel, N. M. Laurendeau, and F.P. Incropera, "Predictions of radiation absorption and scattering in turbid water bodies", *ASME J. Heat Transfer*, 1979 101 (1) 63.
725. A. S. Eddington, "The Internal Constitution of the Stars", Dover Publications, Inc., New York, 1959.
726. F. A. Milne, "Thermodynamics of the Stars", "Handbuch der Astrophysite", vol. 3 Springer-Verlag., OHG, Berlin, 1930 65.
727. Cheng, Ping, *AIAA J.*, 1966 4 (2) 238.
728. Krook, Max, *Astrophys.J.*, 1955 122 (3) 488.
729. Y. Bayazitoglu, and J. Higeyni, *AIAA J.*, 1979 17 (4) 424.
730. Karkow, Burton, H. J. Babrov, G.J. Maclay, and A.L. Shabott, *Appl. Opt.*, 1966 5 (11) 1791.
731. D. K. Edwards, and M. M. Weiner, *Combust. Flame*, 1966 10 (2) 202.
732. H.C. Hottel, "Radiant Heat Transmission", in Williams H. McAdams (Ed) "Heat Transmission", 3rd Ed., Chapter 4, McGraw-Hill Book Company, New York, 1954.
733. H. C. Hottel, and E. S. Cohen, *AIChE. J.*, 1958 4 (1) 3.
734. Thomas H. Einstein, "Radiant Heat Transfer to Absorbing Gases Enclosed Bbetween Parallel Flat Plates with Flow and Conduction", NASA TRR-154, 1963.
735. F. M. El-Mahallawy, "Effect of Scale and Shape of the Combustion Zone in Gas Turbine Combustion Chambers", Ph.D. Thesis, Cairo University, 1967.
736. H. C. Hottel, and A.F. Sarofim, "Radiative Transfer", McGraw Hill Book Company, New-York, 1967.

737. Siegel, Robert, and John R. Howell, "Thermal Radiation Heat Transfer", 2nd Ed., Hemisphere Publishing Corporation, Mc Graw-Hill Book Company, New York, 1981.
738. A. A. Rezk El-Monem, "Experimental and Analytical Investigation of Wall Heat Flux in Boiler Furnaces", Ph.D. Thesis, Department of Mechanical Engineering, Cairo University, Egypt, 1986.
739. Schwarzschild, K. *Gas. Wiss. Gottingen, Nachr. Math-Phys. Klasse 1*, 41 1906.
740. D. K. Edwards, and A. Balakrishnan, *Int. J. Heat Mass Transfer*, 1973 16 25.
741. R. D. Skocypec, D. V. Walters, and R. O. Buckius, *J. Quant. Spectrosc. Radiat. Transfer*, 1986 28 425.
742. H. C. Van de Hulst, *Light Scattering by Small Particles*, Chapman and Hall Ltd., New York, 1957.
743. S. C. Lee, and C. L. Tien, Eighteenth Symposium (International) on Combustion. The Combustion Institute, Pittsburgh, 1981 1159.
744. S. Chippet, and W.A. Gray, *Combust. Flame*, 1978 31 149.
745. D. G. Goodwin, and M. Mitchner, ASME paper 84-HT-41, 1984.
746. J. T. Twitty, and J. A. Weinman, *J. Appl. Meteorology*, 1971 10 725.
747. J. M. Beér, and J. Clause, *J. Inst. Fuel*, 1962 44 437.
748. A. R. Jones, *Prog. Energy Combust. Sci.*, 1979 5 73.
749. F. C. Lockwood, and N. G. Shah, "An improved flux model for the calculation of radiation heat transfer in combustion chamber", ASME, 76-HT-55, 1977.
750. P. Docherty, and M. Fairweather, *Combust. Flame*, 1988 71 79.
751. A. D. Gosman, and F. C. Lockwood, Fourteenth Symposium (International) on Combustion, The Combustion Institute, Pittsburgh, 1973.
752. D. B. Spalding, "Heat and Mass Transfer in Recirculating Flows", Academic Press, 1969.
753. N. Selcuk, and R. G. Siddall, *Int. J. Heat Mass Transfer*, 1976 19 313.
754. J. S. Truelove, "One-Dimensional Radiative Transfer in Plane Cylindrical and Spherical Geometries Using the Discrete Ordinates Approximations", UKAER Report, AERE-R8479, 1976.
755. G. Cox, *Combust. Sci. Technol.*, 1977 17 75.
756. Y. R. Sivathanu, and J. P. Gore, *JSRT*, 1993 49 269.
757. J. W. Hartick, M. Tacke, G. Frughtel, E. P. Hassel, and Janicka, J., Twenty-Sixth Symposium (International) on Combustion, The Combustion Institute, Pittsburgh, 1996 75.
758. A. S. Abbas, and F. C. Lockwood, Twenty First Symposium (International) on Combustion, The Combustion Institute, Pittsburgh, 1986.
759. F. M. El-Mahallawy, and A. A. Rezk El-Monem, *Journal of Engineering and Applied Science*, Faculty of Engineering, Cairo University, Egypt, April, 1999 46 (2) 257.

760. F. M. El-Mahallawy, Bulletin of the Faculty of Engineering, Cairo University, Egypt, 1973-1974 16.
761. F. M. El-Mahallawy, "Theoretical Analysis of Radiant, Convective and Total Heat Transfer in Different Shape Combustion Zones", "Flow, Mixing and Heat Transfer in Furnaces", HMT Series, (B. Spalding, K. H. Khalil, F. M. El-Mahallawy, and E. E. Khalil. Eds.), Pergamon Press, 1978 2.
762. F. M. Yowakim, F. M. El-Mahallawy, and S. A. Farag, Mech, Eng. Bulletin, Cairo University, Egypt, 1974-1975 7.
763. N. M. Rafat, and F. M. El-Mahallawy, The Bulletin of the Faculty of Engineering, Cairo University, Egypt, 1968 177.
764. N. M. Rafat, F. M. El-Mahallawy, and E. Mahdi Ali, Bulletin of the Faculty of Engineering, Cairo University, Egypt, 1973-1974 17.
765. F. M. El-Mahallawy, and N. M. Rafat, "Effect of Scale and Shape of Combustion Zones on Heat Transfer in Furnaces", "Flow, Mixing and Heat Transfer in Furnaces", HMT Series, (B. Spalding, K. H. Khalil, F. M. El-Mahallawy, and E. E. Khalil. Eds.), Pergamon Press, 1978 2.
766. F. M. El-Mahallawy, S. A. Farag, and F. M. Yowakim, Proceeding of First Conference of Mechanical Power Engineering, Cairo University, Feb., 1977 2.
767. N. M. Rafat, and F. M. El-Mahallawy, The Bulletin of Faculty of Engineering, Cairo University, Egypt, 1965.
768. F. M. El-Mahallawy, M. B. Khalil, and S. A. Farag, J. Heat and Mass Transfer, 1976 3 (5) 421.
769. F. M. El-Mahallawy, E. E. Khalil, and O. Abdel Aal, ASME, 184-GT-1983.
770. F. M. El-Mahallawy, E. S. Mahdi Ali, and M. H. Eid, The Fourth International Conference for Mechanical Power Engineering, Cairo University, 15-18 October, 1982.
771. F. M. El-Mahallawy, E. Mahdi, Ali, H. Salem, Y. El-Banhawy, and H. Moneib, Proceeding Eighth IASTED International Symposium, "Flame properties and heat transfer characteristics in a model of water tube boiler furnace" ACTA Press, Zurich, 1983.
772. F. M. El-Mahallawy, E.S. Mahdi Ali, H. Salem, Y. El-Banhawy, and H. Moneib,; Proceedings Eighth IASTED International Symposium, "Experimental study of confined spray flame in a model flame tube of fire tube boiler", ACTA Press, Zurich, 1983.
773. F. M. El-Mahallawy, E.S. Mahdi Ali, E. E. Khalil, H. Salem, Y. H. El-Banhawy, and H. Moneib, "Effect of burner loading on flame structure and heat transfer characteristics of a large cylindrical oil fired flame tube", 20th, Joint Propulsion Conference, ATAA, Cincinnati, Ohio, 1984.
774. F. M. El-Mahallawy, E.S. Mahdi Ali, H. Salem, H. El-Banhawy, and H. A. Moneib, "Modeling of heat transfer from flame in utility steam generator", AMSE: International Conference held in Athens From 27-29 June, 1984.
775. F. M. El-Mahallawy, T. I. Sabry, F. A. Ramadan, and H. R. El-Shoubashy, The

- Eighth International Conference for Mechanical Power Engineering, Alexandria University, Egypt, April, 27-29, 1993.
- 776 M. Beér, János "Methods of Calculating Radiative Heat Transfer from Flames in Combustors and Furnaces", in N. H. Afgan and J. M. Beér, Eds., "Heat Transfer in Flames", Scripta Book Co., Washington, D. C., 1974 29.
- 777 W. Richer, and G. Bauersfeld, "Radiation Models for use in Complete Mathematical Furnace Models", I.V.D., University of Stuttgart, Chapter (II), 1973.
- 778 F. R. Steward, and H. K. Gürtüz, "Mathematical Simulation of an Industrial Boiler by the zone Method of Analysis", in N. H. Afgan and J. M. Beér, Eds., "Heat Transfer in Flame", Scrieta Book Co., Washington, D. C., 1974 47.
- 779 J. M. Beér, N. A. Chigier, and K. B. Lee, Ninth Symposium (International) on Combustion, The Combustion Institute, Pittsburgh, 1963.
- 780 W. H. McAdams, "Heat transmission", McGraw-Hill, New York, 1954.
- 781 F. M. El-Mahallawy, Z. S. Safar, H. Selim, E. E. Khalil, H. Salem, Y. H. El-Banhawy, H. A. Moneib, A. A. M. Rezk, M. H. Eid, M. Shaaban, and M. Shahein, "Rationalization of Fuel Combustion in Boilers and Industrial Furnaces in Egypt", University Linkage Project No. 81008, Supreme Council of Universities, F. R. C. U., Cairo, Egypt, Mid-Year Report, 1984.
- 782 S. I. Evans, and R. J. Sarjant, *J Inst. Fuel*, 1931.
- 783 K. McNaughton, and C. Sinclair, *J. Fluid Mech.*, June, 1966 25 (2) 367.
- 784 K. P. Perry, *Proc. Inst. Mech. Engrs.*, London, 1954 168 (30) 775.
- 785 G. G. Thurlow, *Proc. Inst. Mech. Engrs.*, London, 1954 168 (30) 797.
- 786 V. A. Smirnov, G. E. Verevochkin, and P. M. Brdlick, *International Journal of Heat and Mass Transfer*, London, 1961 2 1-7.
- 787 R. Gardon, and J. C. Akfirat, "Heat transfer characteristics of impinging two-dimensional air jets", *ASME, Journal of Heat Transfer*, vol. 88, Series C, 1966 (3) 101.
- 788 K. Kataoka, and T. Mizushina, *Proc. of the 5th IHTC*, Tokyo, 1974 II 305.
- 789 F. M. El-Mahallawy, A. S. Elasfour, and M. M. Shabaan, *The Fourth International Conference for Mechanical Power Engineering Faculty of Engineering, Cairo University, Egypt, 1982.*
- 790 H. A. Becker, H. C. Hottel, and G. C. Williams, *Eleventh Symposium (International) on Combustion, The Combustion Institute, Pittsburgh, 1967.*
- 791 R. J. Baker, P. Hutchinson, E. E. Khalil, and J. H. Whitelaw, *Fifteenth Symposium (International) on Combustion, The Combustion Institute, Pittsburgh, 1975 553.*
- 792 L. Wu, *Inst. Fuel J.*, 1969 42 316.
- 793 C. J. Hoogendoorn, C. M. Ballintijn, and W. R. Dorresteyn, *Inst. Fuel, J.* 1970 43 511.
- 794 S. E. Elgobashi, and W. M. Pun, *Fifteenth Symposium (International) on*

- Combustion, The Combustion Institute, Pittsburgh, 1975 .
- 795 L. Wu, and N. Fricker, *Inst. Fuel J.*, 1976 49 144.
- 796 M. H. Lewis, and L. D. Smoot, *Combust. Flame*, 1981 42 183.
- 797 B. Lenze, Nineteenth Symposium (International) on Combustion, The Combustion Institute, Pittsburgh, 1982 565.
- 798 M. M. Hassan, F. C. Lockwood, and H. A. Moneib, *Combust. Flame*, 1982 51 249.
- 799 F. M. El-Mahallawy, Rationalization of Fuel Combustion in Boilers and Industrial Furnaces in Egypt, First Annual Report, University Linkage Project no. 81008, Cairo University, Egypt, 1982.
- 800 F. M. El-Mahallawy, Rationalization of Fuel Combustion in Boilers Industrial Furnaces in Egypt, Second Annual Report, University Linkage Project no. 81008, Cairo University, Egypt, 1983.
- 801 F. M. El-Mahallawy, M. A. Abu-El-Enin, and A. K. Abd El-Samed *Scientific Bulletin of the Faculty of Engineering, Ain Shams University, Egypt* 1986 19 (2) 194.
- 802 F. M. El-Mahallawy, M. A. Abu El-Enin, and M. M. Bakry, *The Bulletin of the Faculty of Engineering, Alexandria University, Egypt*, 1986 25.
- 803 F. M. El-Mahallawy, M. A. Abu El-Enin, and A. A. El-Atroush, *The Bulletin of the Faculty of Engineering, Alexandria University, Egypt*, 1986-1987 25-26 539.
- 804 S. S. Wahid, A. M. El-Kersh, F. M. El-Mahallawy, and M. A. Wahhab, 2nd Minia Conference on Energy and its Applications, Egypt, 12-14 Jan, 1988 9.
- 805 F. M. El-Mahallawy, E. Mahdi Ali, E. E. Khalil, H. Salem, Y. H. El-Banhawy, and H. A. Moneib, "Multi flame characteristics in a model water tube boiler furnaces", *AMSE Proceedings International Conference, Athens, France, Jan 27-29, 1984* 32 359.
- 806 S. S. Wahid, A. M. El-Kersh, F. M. El-Mahallawy, and M. A. Wahhab, 2nd Minia Conference of Energy and its Applications, 12-14 Jan, 1988 64.
- 807 S. A. El-Sherif, *Engineering Research Journal, Faculty of Engineering of El-Mataria, University of Helwan, Cairo, Egypt*, April 1999, 62 161.
- 808 D. Bradley, S. El-Din Habik, and J. R. Swithenbank, Twenty-First Symposium (International) on Combustion, The Combustion Institute, Pittsburgh, 1988 249.
- 809 D. Bradley, S. El-Din Habik, and M. A. M. Jamel, First International Colloquium Explosibility of Industrial Dusts, Baranow, Polish Academy of Sciences, Part I, 1984 4.
- 810 D. Bradley, S. A. El-Sherif, and S. El-Din. Habik, Eighth International Conference for Mechanical Power Engineering, Alexandria University, April 27-29, 1993.
- 811 S. El-Din. Habik, and El-Sherif, Port-Said, Egypt, *Eng. Res. J.*, 3, 1998.
- 812 S. A. El-Sherif, *Engineering Research Bulletin, University of Helwan, Faculty*

- of Engineering,, Mataria, Cairo, Egypt, Oct., 1994 5.
- 813 S. El-Din Habik, Engineering Research Bulletin, University of Helwan, Faculty of Engineering, Mataria, Cairo, Egypt , 1998 58.
- 814 N. Kayakol, Ph. D. thesis, Middle East Technical University, Türkiye, 1998.
- 815 N. Selcuk, and N. Kayakol, Int. J. Heat Mass Transfer, 1997 40 213.
- 816 N. Selcuk, and N. Kayakol, ASME HDT- 1996 325 (3) 151.
- 817 N. Kayakol, N. Selcuk, Campell I, and Gülder ,Ö L., Experimental Thermal and Fluid Science, 2000 21 134.
- 818 A. H. Lefebvre, and M. V. Herbert, Inst. of Mechanical Engineers 1960.
- 819 N. Fricker, L. Van Hyden, and S. Michelfelder, IFRF Doc. No. F 35/2/5, 1971.
- 820 S. Michelfelder, and T. M. Lowes, Report on the M^2 trails, IFRF Doc. no. F 36/2/4, 1974.
- 821 D. R. Shoffstall, Burner Design Criteria for the Control of NO_x in N.C. Combustion. EPA-60012-76-098 a, 1976.
- 822 A. M. Godridge, and A. W. Read, Prg. Energy Combust. Sci., 1976 2 83.
- 823 L. Lamb, J. Inst. Fuel, 1972 43 443.
- 824 J. A. Arcsott, J. Gibb, and R. Jenner, The Application on N. E. diffusion theory on Monte-Carlo methods to predict the heat transfer performance of a 500 MW power station boiler from isothermal thermal flow data, Heat Transfer in Furnaces, 1978 674.
- 825 D. Anson, A. M. Godridge, and E. Hammond, Fourth Symposium on Flames and Industry. Predictive Methods for Industrial Flames, Imperial College, London, 19-20 Sept., 1972.
- 826 B. R. Adams, and P. J. Smith, Combust. Sci. and Technol., 1993 88 293.
- 827 M. D. G. Carvalho, and F. C. Lockwood, "Mathematical Simulation of an End-Port Regenerative Glass Furnace", Proc. Institution of Mechanical Engineers, No. C2, 1985 199.
- 828 B. E. Launder, and D. B. Spalding, "Mathematical Models of Turbulence", Academic Press, 1972.
- 829 F. C. Lockwood, and A. S. Naguib, Combust. Flame, 1975 24 109.
- 830 J. N. Richardson, Jr. H. C. Howard, and Jr. R. W. Smith, Proc. Fourth Symposium (International) on Combustion, The Combustion Institute, 1953.
- 831 F. C. Lockwood, and N. G. Shah, Eighteenth Symposium (International) on Combustion, The Combustion Institute, 1981.
- 832 L. S. Caretto, A. D. Gosman, S. V. Patanker, and, D. B. Spalding Proc. 3rd International Conf. on Numerical Methods in Fluid Mechanics, Springer Verlag, 1972.
- 833 M. A. Abdel-Rahman, F. M. El-Mahallawy, and F. C. Lockwood, First European Conference on Industrial Furnaces and Boilers, Luchpon, Portugal, 21-24 March, 1988.

- 834 L. N. Patel, IFAC Symposium on Automation and Instrumentation for Power Plants, Ramamoorthy, M. (Ed.), 1989 201.
- 835 L. N. Patel, Conference on Thermal System, 22-23 Feb. B. H. U., Varanasi, 1986.
- 836 D. Anson, A. M. Godridge, and E. Hammond, Fourth Symposium on Flame and Industry, 19-20 Sept. Institute of Fuel, London, 1972 150.
- 837 S. J. Zibas, and S. A. Idem, "Boiler heat transfer modeling using CEMS data with application to fouling analysis", PWR-Vol. 30, Joint Power Generation Conference, ASME 1996 2.
- 838 H. N. Sharan, Journal of the Institute of Fuel, 1963 36 268.
- 839 G. H. Babcock, and S. Wilcox, Steam, Its Generation and Use, The Babcock and Wilcox Co., New York, 1955.
- 840 A. Bloch, E. Karasin, B. Chudnovsky, A. Talanker, B. Milshtein, and S. Pesler, "Expert diagnostic system for combustion and heat transfer processes in steam boiler furnaces", ASME Power Div. Publ. PWR (Fairfield, Nj, (USA)) ASME, 1997 32 619.
- 841 A. G. Blokh, "Heat Transfer in Steam Boiler Furnaces", (79 Madison Avenue, New York, NY 10016 (USA)) Hemisphere Publ. Corporation, 1987 283.
- 842 A. Sanyal, and R. Chandan, A role model for IPPs, Proc. AM. Power Conf. (Chicago, IL, (USA)) Illinois Inst of Technology, 1998 1 352.
- 843 C. Delle-Site, E. Sciubba, and M. Trissati, "Influence of fouling on the heat transfer characteristics of boiler tubes", ASME Adv. Energy Syst. Div. Publ. Aes. (Fairfield, NJ, (USA)) ASME, 1997 37 271.
- 844 G. Bergeles, D. Bouris, M. Yianneskis, S. Balabani, A. Kravaritis, and S. Itskos, "Effects of fouling on the efficiency of heat exchangers in lignits utility boilers", App. Therm. Eng., No. S-10, 1997 17 739.
- 845 S. Esaki, M. Kawaji, X. Shen, H. Tran, and C. Dees, Nippon-Kikai-Gakkai-Ronbunshu, B., 1997 63 (607) 993.
- 846 H. Hayasaka, N. Matsumura, and K. Kudo, Nippon-Kikai-Gakkai-Ronbunshu, B., 1996 62 (599) 2806.
- 847 P. Coelho, P. Meunier, and M. Carvalho, "Diagnosis of combustion and heat transfer phenomena in a utility boiler", ASME Heat Transfer Div. Publ. HTD, (New York, NY, (USA)) ASME, 1994 296 119.
- 848 R. K. Boyd, and J. H. Kent, Energy Fuels, 1994 8 (1) 124.
- 849 J. Ströhle, H. Knaus, U. Schnell, and K. R. G. Hein, Combust. Sci. Technol., 2000 153.
- 850 P. J. Coelho, J. M. Goncalves, M. G. Carvalho, and D. N. Trivic, Int. J. Heat Transfer, 1998 41 (4-5) 745.
- 851 Z. Guo, and S. Maruyama, "Three-dimensional radiative transfer in anisotropic, and nongray media", ASME Pressure Vessels Piping Div. Publ. PVP. (Fairfield, NJ, (USA)) ASME, 1998 377 (2) 101.

- 852 R. Schneider, Beitrag Zur Numerischen Berechnung Dreidimensionaler Reagierender Strömungen in Industriellen Brennkammern, VDI Verlag, Düsseldorf, 1998.
- 853 H. Knaus, R. Schneider, X. Han, J. Ströhle, U. Schnell, and K. R. G. Hein, Fourth International Conference on Combustion Technology for a Clean Environment, Libson, 1997.
- 854 M. N. Özisik, Radiative Transfer and Interaction with Conduction and Convection, Wiley, New York, 1973.
- 855 A. G. De Marco, F. C. Lockwood, La rivista dei combustibili, 1975 29 (5-6) 184.
- 856 W. A. Fiveland, J. Heat Transfer, 1984 106 699.
- 857 E. H. Chui, G. D. Raithby, Numerical Heat Transfer, Part B, 1993 23 269.
- 858 M. F. Modest, Radiative Heat Transfer, McGraw Hill, Singapore, 1993.
- 859 J. Liu, H. M. Shang, and Y. S. Chen, Numerical Heat Transfer, Part B, 1997 31 423.
- 860 W. A. Fiveland, AIAA J. Thermophysics, 1988 2 (4) 309.
- 861 J. P. Dormall, and G. D. Raithby, Numerical Heat Transfer, 1984 7 147.
- 862 C. M. Rhie, and W. L. Chow, AIAA Journal, 1983 21 (11) 1525.
- 863 H. Knaus, J. Maier, U. Schnell, and K. R. G. Hein, 4th Europe. Conf. on Industrial Furnaces and Boilers, Proto., 1997.
- 864 B. Risio, R. Schneider, U. Schnell, K. R. G. Hein, Proc., ECCOMAS 96, Paris, 1996 374.
- 865 U. Schnell, R. Schneider, H. C. Magel, B. Risio, J. Lepper, and K. R. G. Hein, 3rd Int. Conf. on Combust. Technol. for a Clean Environment, Lisbon, 1995.
- 866 N. J. Selcuk, Heat Transfer, 1985 107 648.
- 867 P. J. Coelho, J. M. Goncalves, and M. G. Carvalho, A flow/heat transfer problems, In Numerical Method in Thermal Problems, Ed. R. Lewis and P. Durbetaki, 1995 9 Part 1 378.
- 868 W. W. Yuen, A. K. Ma, and E. E. Takara, "Evaluation of radiative heat transfer using the generalized zonal method and absorption mean beam length concept", Developments in Radiative Heat Transfer, ASME HTD, 1992 203 269.
- 869 P. F. Hsu, Z. Tan, and J. R. Howell, "Application of the YIX method to radiative heat transfer within a mixture of highly anisotropic scattering particles and non-gray gas", Developments in Radiative Heat Transfer, ASME HTD, 1992 203 285.
- 870 W. A. Fiveland, and R. A. Wessel, "Numerical model for predicting performance of three-dimensional pulverized fuel fired furnaces", ASME J. Eng. Gas Turbines Power, 1988 110 117.
- 871 H. Aoki, S. Tanno, T. Miura, and S. Ohnishi, JSME Int. Journal, Sep. II, 1992 35 428.
- 872 K. C. Smyth, J. H. Miller, R. C. Dorfman, W. G. Mallard, and A. R. Santoro,

- Combust. Flame, 1985 62 157.
- 873 R. K. Boyd, and J. H. Kent, Energy and Fuels, 1994 8 124.
- 874 A. Milson, and N. Chigier, Combust. Flame, 1966 12 675.
- 875 A. El-Askary, "Theoretical and experimental investigation heat transfer by oblique impinging jet flames of industrial size", Ph. D. Thesis, Prach University, 1982.
- 876 G. Anderson, and E. Streisno, "Heat transfer from flame impinging on flat and cylindrical surface", J. Heat Transfer, Trans. of ASME, Feb., 1963 49.
- 877 E. Schulte, "Impingement heat transfer rates from torch flames", J. Heat Transfer, Trans. of ASME, May, 1972 231.
- 878 F. M. El-Mahallawy, F. C. Lockwood, and M. M. Shabaan, Port-Said Eng. Res. J., Faculty of Eng. of Port-Said, Egypt, 1999 5 (1).
- 879 E. P. Keramida, H. H. Liakos, M. A. Founti, and N. C. Markatos, Proc. of the Mediterranean Combustion Symposium, Antalya – Turkey, June 20-25, 1999 629.
- 880 H. H. Liakos, M. K. Koukou, M. A. Founti, and N. C. Markatos, Fourth Computational Fluid Dynamics' 98 Conference Athens, Greece, 1998 984.
- 881 H. Terry, M. Larry, S. Randy, and H. Thurston-J, , Environmental-Progress May, 1995 14 (2) 115.
- 882 H. Alexander, W. Albert, R. Rpland, and L. John-H, Proceeding of the Air and Waste Management Association's, Annual Meeting and Exhibition, 1996, Air and Waste Management Assoc., Pittsburgh, PA, USA, 16 P. 6-RP 139.07.
- 883 H. Farzan, GJ Maringo, CT. Beard, GE. Weed, and J. Pratapas, "NO_x on control using natural gas reburn on an industrial cyclone boiler", Power American Society of Mechanical Engineers, Power Division (Publication), PWR, ASME, New York, NY, USA, 1996 30 835.]
- 884 L. G. Frank, G. V. James, L. D. Steven, and S. S. Jonathan, International Exhibition and Conference for the Power Generation Industries Power Generation, PennWell Pub and Exhib, Houston, TX, USA, 1998 201.
- 885 M. Reinhard, and S. E. Todd, Proceedings of the American Power Conference, Iiinois Inst. of Technology, Chicago, IL, USA, 1995 57 (2) 1204.
- 886 D. J. Philip, T. J. Robert, and B. E Jr. George, "Masland industries boiler plant emissions study RACT proposal and system retrofit", ASME, Power Division (Publication), PWR, ASME, New York, NY, USA, 1995 27 133.
- 887 L. F. Anthony, B. W. Ronald, Andrew, W. McClaine, and H. Matthew, Proceedings of the International Technical Conference on Coal Utilization and Fuel Systems, Coal and Slurry Technology Assoc., Washington, DC, USA, 1997 759.
- 888 K. S. Michael, and D. P. Peter, "Illinois power's on line operator advisory system to control NO_x and improve boiler efficiency: An Update", Proceedings of the American Power Conference, Illinois Inst. of Technology, Chicago, IL, USA, 1997 59-1 331.

- 889 C. Joseph, "NO of the American Power Conference, Vol. 57-2, 1995, Illinois Inst. of Technology, Chicago, IL, USA, p. 1204. and CO: Semi Empirical Model for Boilers" Proceedings of the American Power Conference, Illinois Inst. of Technology, Chicago, IL, USA, 1997 59-2 785.
- 890 J. K. Joe, A. W. Jeffery, and R. B. Peter, "Low NO_x burner retrofits and enhancements for a 518 MW oil and gas fired boiler", Environmental control fuels and combustion technologies, ASME, Environmental Control Division Publication, EC, Vol. 1, ASME, New York, NY, USA, 1995 325.
- 891 K. C. Hopkins, D. O. Czerniak, C. Youssef, L. Radak, and J. Nylander, ASME paper 91-JPGC-EC-3, presented at the International Power Generation Conference, San Diego, CA, October 6-10, 1991.
- 892 J. Feese, and S. Turns, *Combust. Flame*, 1998 113 66.
- 893 C. Wiles, and B. Gerhold, "NO_x reduction from a gas turbine using exhaust gas re-circulation", ASME paper NO. 80-JPGC/GT-5, 1980.
- 894 B. P. Breen, "Emissions from continuous combustion systems", (W. Cornelius and W. G. Agnew, Eds.), Plenum Press, 1972 325.
- 895 Q. Wang, M. A. D'wLuchi, and D. J. Sperling, *Air Waste Manage Assoc.*, 1990 40 1275.
- 896 S. C. Yang, J. H. Pohl, S. J. Bortz, and R. J. Yang, Paper 92-42, Spring Meeting of the Western States Section of The Combustion Institute, March, 1992.
- 897 S. A. El-Sherif, and M. A. Ismail, *Engineering Research Journal*, Helwan University, Faculty of Engineering, Mataria, Cairo, Egypt, 1999 65.
- 898 F. M. El-Mahallawy, S. El-Din Habik, and E.S. El-Shabrawy, *Engineering Research Journal*, Helwan University, Faculty of Engineering, Mataria, Cairo, Egypt, August, 1999 64.
- 899 S. C. Li, F. A. Williams, *Combust. Flame*, 1999 118 399.
- 900 J. Grusha, and M. S. McCartney, Development and evaluation of the ABB combustion engineering low NO_x concentric firing systems, Proc., Joint Symposium on Stationary Combustion NO_x Control, 1991.
- 901 R. A. Lisauskas, R. J. Snodgrass, S. A. Johnson, and D. Eskinazi, Experimental investigation of retrofit low NO_x combustion systems, Proc., Joint Symposium on Stationary Combustion NO_x Control, 1985.
- 902 T. C. A. Hsieh, W. J. A. Dahm, and J. F. Driscoll, *Combust. Flame*, 1998 114 54.
- 903 Saacke, Low NO_x technology, Combustion and Energy Systems, Data Sheet TV46 issues 45/CO/12/95.
- 904 Natural Gas Re-Burning, Cost-Effective NO_x Reduction for Utility Boilers, Gas Research Institute, 8600 West Bryn Mawr Avenue, Chicago, Illinois 60631 GRI-93/0059, 1993 (brochure).
- 905 R. A. Lisauaskas, and C. A. Penterson, An advanced low-NO_x combustion system for gas and oil firing, Proc., Joint Symposium on Stationary Combustion NO_x Control, 1991.

- 906 Proceedings of the Re-burning Workshop, Nordic Gas Technology Center Report, ISBN 87-89309-33-2, January, 1991.
- 907 R. W. Borio, R. D. Lewis, M. B. Keogh, R. C. Booth, R. E. Hall, R. A. Lott, A. Kokkino, D. F. Gyorke, S. Durrani, H. J. Johnson, and J. J. Kienle, Reburn technology for NO_x control on a cyclone-fired boiler, Proc. 1991, Joint Symposium on Stationary Combustion NO_x control.
- 908 A. S. Yagiela, G. J. Maringo, R. J. Newell, and H. Farzan, Update on coal re-burning for reduction NO_x in cyclone boilers, Proc. Joint Symposium on Stationary Combustion NO_x Control, 1991.
- 909 V. Reddy, L. J. Muzio, and G. S. Samuelsen, Pilot scale evaluation of nitrous oxide production from coal re-burning, Paper 91-74, Western States Section Combustion Institute Meeting, October, 1991.
- 910 L. J. Muzio, T. A. Montgomery, G. C. Quartucy, J. A. Cole, and J. C. Kramlich, N_2O formation in selective non-catalytic reduction processes, Proc. Joint Symposium on Stationary NO_x Control, 1991.
- 911 R. M. A. Irons, H. J. Price, and R. T. Squires, Tailoring ammonia-based SNCR for installation in power station boilers, Proc. Joint Symposium on Stationary NO_x Control, 1991.
- 912 P. A. May, L. M. Campbell, and K. L. Johnson, Environmental and economic evaluation of gas turbine NO_x control, Proc. Joint Symposium on Stationary NO_x Control, 1991.
- 913 B. K. Speronello, J. M. Chen, M. Durilla, and R. M. Heck, Application of composite NO_x SCR catalysts in commercial systems, Proc. Joint Symposium on Stationary NO_x Control, 1991.
- 914 A. Kokkinos, J. E. Cichanowicz, R. E. Hall, and C. B. J. Sedman, Air Waste Manage. Assoc., 1991 41 1251.
- 915 B. Folsom, C. Hong, T. Sommer, and J. M. Pratapas, in the Proceeding of the 1993 Joint Symposium on Stationary Combustion NO_x Control, Maimi Beach Fl., EPRI Report TR 103265-V2, Palo Alo, Ca, 1993 7A 15-34.
- 916 L. K. Chan, A. F. Sarofim, and J. M. Beér, Combust. Flame, 1983 52 37.
- 917 K. R. G. Hein, The Combustion Institute, Section Francaise – British section, Rounne – France 18/21 Avril, 1989.
- 918 D. Han, M. G. Mungal, V. M. Zamansky and T. J. Tyson, Combust. Flame, 1999 119 483.
- 919 V. M. Zamansky, M. S. Sheldon, and P. M. Maly, Western States Section, The Combustion Institute 1998 Spring Meeting, Berkeley, CA, Paper No. 98S-30, 1998.
- 920 A. Lowe, T. F. Wall, and I. McStewart, Fifteenth Symposium (International) on Combustion, The Combustion Institute, Pittsburgh, 1975 261.
- 921 K. Bueters, J. Cogoli, and W. Hobelt, Fifteenth Symposium (International) on Combustion, The Combustion Institute, Pittsburgh, 1975.
- 922 W. Benesch, and H. Kremer, Twentieth Symposium (International) on

- Combustion, The Combustion Institute, Pittsburgh, 1984.
- 923 G. F. Robinson, *J. Inst. of Energy*, 1985 58 (436) 116.
- 924 B. M. Cetegen, and W. Richter, "Heat transfer modelling of a large coal fired utility boiler and comparisons with field data, vol. 1, publ. By ASME, New York, NY, USA, 1987 225.
- 925 M. T. Raz mikov, and Yu. M. Lipov, "Steam Boilers of Thermal Power Stations", Mir publishers, Moscow, 1985.
- 926 M. W. Thing, and M. P. Newby, Fourth Symposium (International) on Combustion, The Combustion Institute, Williams and Wikins Co., 1953 789.
- 927 F. M. El-Mahallawy, M. M. Kamel, Z. S. Safer, and M. A. A. Habib, "Report on the Explosion of Boiler No. 1 of Abu-Qir power plant", FRCU of The Supreme Council of Universities, April 7, 1986.
- 928 S. M. McCartney, and R. J. Colette, Proceedings of the 1982 Joint Symposium on Stationary Combustion NO_x control, EPRT CS-3182, 1983.
- 929 V. P. Romadin, "Furnaces with corner firing tangential burners". *Thermal Eng.*, 1973 20 (7) 79.
- 930 A. H. Abdel-Hafez, F. M. El-Mahallawy, M. A. Habib, and N. Naseef, *Engineering Research Bulletin*, Faculty of Eng. and Tech., Helwan University, Cairo, 1989 11.
- 931 M. A. Habib, F. M. El-Mahallawy, A. H. Abdel-Hafez, and N. Naseef, *Energy*, 1992 17 (3) 283.
- 932 F. M. El-Mahallawy, and M. Zakaria, *Engineering Research Journal*, Faculty of Engineering of El-Mataria, University of Helwan, Cairo, Egypt, 1999.
- 933 H. Whaley, and D. M. Rankin, "Coal-Water Fuel Combustion in Boiler" *Canada Energy Mines and Resources*, Canada, 1987 88 (9) 75.
- 934 R. J. Martin, J. T. Killy, S. Ohimine, and E. K. Chu, "Pilot-scale characterization of dry sorbet injection for SO₂ control in a low NO_x tangential system", *Engineering for Gas Turbines and Power*, ASME Trans, 1988 110 (1) 111.
- 935 S. L. Shagalove, L. V. Yur'ev, D. I. Parparov, and I. N. Shnitser, *Thermal Engineering*, 1979 2 78-81.
- 936 C. E. Blakeslee, and H. E. Burbach, *J. Air Pollution Control Assoc.*, 1973 23 (1) 37-42.
- 937 B. F. Piper, S. Hersh, and D. J. Mormile, "Particulate Emission Characteristics of Oil-fired Utility Boilers", Consolidated Edison Co. of New York, Report No.: RPRI-CS-1995, New York, Aug., 1981 95.
- 938 R. K. Boyd, A. Lowe, and J. Feg, "Three-dimensional modelling of a pulverized-coal fired utility furnace" *International Symposium on Coal Combustion*, Beijing (People of Reb. China), Sep. 1987.
- 939 R. L. Burrington, D. John Cavers, and Selker Ambrose, "Overfire Air Technology for Tangentially Fired Utility Boilers Burning Western U.S. Coal" *Industrial Environmental Research Triangle Park, N.C. 27711*. Report No. EPA/600/7-77/117, USA, Oct., 1977 332.

- 940 J. L. Marion, D. P. Towle, R. C. L. Kunkel, and R. C. Flesh, "Development of ABB-CE's tangential firing system 2000 (TFS 2000th System)", EPRI/EPA 1993 Joint Symposium on Stationary Combustion NO_x Control.
- 941 T. J. Hamilton, "Computer Control System for Multifuel Industrial Boilers", Power Engineering, Haneywell, Dec. , 1979 79 (12) 56.
- 942 Singer G. Joseph, "Combustion in Fossil Power System", Combustion Engineering Inc. 1000 Prospect Hill Rd., Windsor, CT. 06095, USA, 1981.
- 943 E. Munde-Lcanada, and M. Rossano-Roman, Proc. of the 5th Power Plant Dynamics, Control and Testing Symposium, Knoxville, TN, USA, May 21-23, 1983 1 901.
- 944 C. J. Lawn, "Principles of Combustion Engineering for Boilers", Mir Publishers Academic press Limited 24/28 Road London, 1987 498.
- 945 K. A. Bueters, "NO_x emissions from tangentially-fired utility boilers" AIChE Symposium Series, V71 N148, Combustion Eng. Inc., Windsor, Conn USA, 1973 85.
- 946 G. K. Lee, and I. L. Lau, J. of the Institute of Energy, 1985 III (437) 197.
- 947 E. Mallard, and H. Le Chatelier, Ann. Mines, 1883 4, 379.
- 948 N. N. Semenov, NACA Tech Memo., 1951 1282, WA.
- 949 C. Tanford, and R. N. Pease, J. Chem. Phys., 1947 15, 861.
- 950 G. Damkohler, NACA Tech. Memo. , 1947 1112, WA.
- 951 K. I. Schelkin, NACA Tech. Memo. , 1947 1110, WA.
- 952 D. T. Williams, and L. M. Bollinger, Third Symposium (International) on Combustion, 1949 176.
- 953 H. F. Coward, and G. W. Jones, U.S. Bur. Mines B 503, Washington, DC, 1952.
- 954 G. W. Jones, and R. E. Kennedy, U.S. Bur. Mines Rep. Invest. 3826, Washington, DC, 1949.
- 955 B. Lewis, and G. Von Elbe, Combustion, Flame and Explosion of Gases, Academic Press, New York, NY, 1952.
- 956 B. Karlovitz, D. W. Denniston, D. H. Knapschaefer, and F. E. Wells, Fourth Symposium (International) on Combustion, 1953 613.
- 957 F. M. El-Mahallawy, Z. Safer, A. Rezk, and S. Abd El-Raouf Kandil , Second International Conference on Engineering Research, ICER'95, Faculty of Engineering of Port-Said, Suez Canal University, Egypt, 19-21 Dec., 1995.
- 958 H. Schlichting, "Boundary-Layer Theory", Seventh Edition, McGraw-Hill Book Company, New York, U.S.A., 1979 212 292.
- 959 Platefoot, "Measurement and prediction of the tube metal temperature and heat flux in a large boiler", Third Australasian Conference on Heat and Mass Transfer, Melbourne, Aust., May 13-15, 1985 283.
- 960 J. D. Bianca, W. P. Bauer, and J. G. McGowan, Combustion Engineering Inc. Pennsylvania, USA, 1981.

- 961 S. N. Mironov, V. G. Yudaev, and A. G. Ivanov, *Them. Eng.*, 1964 11 (4) 17.
- 962 A. Lowe, T. F. Wall, and I. McStewart, *Fifteenth Symposium (International) on Combustion*, The Combustion Institute, Pittsburgh, 1975 1245.
- 963 R. K. Boyd, K. J. Roscarel, and J. H. Kent, *Third Australian Conference on Heat and Mass Transfer*, Melbourne Conference May, 1985 10125 51.
- 964 A. D. Gosman, and F. J. K. Iderian, *TEACH-T: A General Computer Program for Two-Dimensional, Turbulent Recirculating Flows*, Fluids Section Report, Mech. Eng. Dept., Imperial College, 1976.
- 965 R. K. Boyd, and J. H. Kent, *Eighth Australian Fluid Mechanics Conference*, 1B14-17, 1983.
- 966 K. J. Knill, E. Chui, and P. M. Hughes, "Application of grid refinement in modeling a tangentially fired coal boiler", *FACT, Combustion Modeling, Cofiring and NO_x Control*, ASME, 1993 17 115.
- 967 P. A. Gillis, and P. J. Smith, *Twenty-Third Symposium (International) on Combustion*, The Combustion Institute, Pittsburgh, 1990 981.
- 968 L. Y. Chen, P. P. Mann, and J. H. Kent, *Twenty Fourth Symposium (International) on Combustion*, The Combustion Institute, Pittsburgh, 1992 1381.
- 969 X. L. Luo, R. K. Boyd, and J. K. Kent, *J Inst. Energy*, 1991 64 230.
- 970 P. Benyon, A. Mann, R. Boyd, J. Kent, T. Langrish, A. Lowe, J. Crawford, A. Stuart, and A. Miller, *5th Australian Supercomputing Conference*, Melbourne, 1992.
- 971 A. Lowe, "The instrumentation of a large utility boiler for the determination of the effects of mineral matter on heat transfer", *Slugging and Fouling Due to Impurities in Combustion Gases*, The Engineering Foundation, Copper Mountain, Co., 1984.
- 972 M. Xu, J. Yuan, S. Ding, H. Cao, *Applied Mechanics and Engineering*, Mar. 30, 1998 155 369.
- 973 X. Liu, and X. Xu, "Numerical simulation of the two-phase flow and combustion in the tangential-firing boiler furnace by using the ALE algorithm and trajectory model", *Proceedings of the 1997, International Symposium on Multiphase Fluid, Non-Newtonian Fluid and Physico-Chemical, Fluid Flows, ISMNP'97, Int. Acad Publ.*, 1997 46.
- 974 X. Han, Z. Zhao, and M. Zhang, "Mathematical modeling for heat transfer process in tangential-fired boiler furnace", *Combust. Sci. Technol.*, Aug. 35, 1996 2 (3) 292.
- 975 Z. Zhao, and M. Zhang, *Proceeding of the Chinese Society of Electrical Engineering*, Jan., 1997 17 (1) 54.
- 976 R. C. Kunkel, M. Palkes, *International Power Generation Conference*, San Diego, CA, 1991.
- 977 K. F. Cen, and J. R. Fan, *International Power Generation Conference*, San Diego, CA, USA, p. 1, 1991.

- 978 J. N. Cannon, B. W. Webb, and M. Queiroz, "Testing of a tangential coal-fired power plant with water cooled probes", ASME, Petroleum Division (Publ.), 1991 33 49.
- 979 X. Y. Zhou, C. G. Zheng, and Y. Y. Ma, "Comparison of several discrete arithmetic schemes for simulating a constrained jet and a lab-scale tangential fired furnace", *Computer Methods in Applied Mechanics and Engineering*, 1996 130 (3-4) 279.
- 980 K. A. Bueters, AICHE Symposium Series, Combustion Eng. Inc., Windsor, Conn., USA, 1973 71 (148) 85-102.
- 981 W. W. Habelt, and A. P. Selker, "Operating procedures and prediction for NO_x control in steam power plants", Central States Section of the Combustion Institute Spring Technical Meeting, Madison, Wisconsin, USA, Mar. 26-27, (1974) 18.
- 982 M. W. Gregory, A. R. Crawford, E. H. Manny, and W. Bartok, "Determination of the magnitude of SO₂, CO₂ and O₂ stratification in the ducting of fossil fuel fired power plant.", Exxon Research and Engineering Company Linden, New Jersey, Presented at the 69th Annual Meeting of the Air Pollution Control Association Portland, Oregon, 27-July, 1976 76-356.
- 983 E. L. Jr Morris, and T. W. Sweeney, "Application of controlled flow/split flame low NO_x burners on a tangentially fired boiler", ASME, New York, USA, 4-JPGC-EC-6, 1994 1.
- 984 T. J. May, E. G. Rindahl, T. Booker, J. C. Opatrny, Keen, T. Robert, M. E. Light, A. Sanyal, T. M. Sommer, B. A. Folsom, and J. M. Pratapas, "Gas reburning in tangentially-fired, wall-fired and cyclone-fired boilers, ASME, Fuel and Combustion Technologies Division (Pub.) FACT-18, 1994 221.
- 985 E. A. Mazzi, and M. Haythornthwaite Sheila, "Experience with combustion tuning and fuel system modifications to inexpensively reduce NO_x emissions from eleven coal-fired tangential boilers", ASME, Environmental Control Division (Pub.) EC., 1997 5 219.
- 986 J. C. Hower, F. Rathbone, Robl, T. L., G. A. Thomas, B. O. Haeberlin, and A. S. Trimble, "Case study of the conversion of tangential and wall-fired units to low-NO_x combustion: Impact on fly ash quality", *Waste-Management*, 1998 17 (4) 219.
- 987 E. L. Jr Morris, and T. W. Sweeney, "Controlled flow, split flame low NO_x burners system performance on a tangentially fired boiler", ASME, Environmental Control Division (Pub.) EC., 1995 1 69.
- 988 J. E. Gabrielson, A. A. Lookman, J. P. Bionda, and S. J. Nix, "Results of NO_x retrofit of Kentucky utilities Ghent 1 tangentially fired unit", ASME, Environmental Control Division (Pub.) EC., 1995 1 61.
- 989 R. E. Thompson, G. H. Shiomoto, and F. P. Haumesser, "Post-retrofit operating and NO_x emissions experience on five tangential-fired units", ASME, Environmental Control Division (Pub.) EC., 1996 1 77.
- 990 R. R. Hardman, and J. N. Sorge, Proceeding of the American Power Conference,

- Vol. 54, pt. 1, Publ. By Illinois Inst of Technology, Chicago, IL, USA, 1992 745.
- 991 M. B. Cohen, J. Klingspor, and G. E. Bresowar, "State of the art emissions control technology for new tangentially fired pulverized coal utility steam generators", ASME, New York, NY, USA, 1991 1.
- 992 R. C. LaFlesh, J. L. Marion, D. P. Towle, C. Q. Maney, G. DeMichele, S. Pasini, S. Betacchi, A. Piantanida, G. Gall, and G. Mainini, "Application of reburning technologies for NO_x emissions control on oil and pulverized coal tangentially fired boilers", ASME, New York, NY, USA, 1991 1.
- 993 J. P. Bionda, J. E. Gabrielson, and K. I. Andrews, "Nitric oxide emission reductions on a 520 MW tangentially fired pulverized coal unit", ASME, New York, NY, USA, 1993 1.
- 994 M. B. Cohen, T. D. Hellewell, R. C. Kunkel, and K. A. Nowak, "Integrating NO_x control technologies for new tangential coal fired steam generators", ASME, Fuel and Combustion Technologies Division (Pub.) FACT-, 1993 17 251.
- 995 G. De Michele, M. Graziadio, P. Mazzel, and M. Cioni, "SNCR application on a tangentially oil-fired boiler", ASME, Fuel and Combustion Technologies Division (Pub.) FACT-, 1993 17 229.
- 996 J. G. Yates. "Fundamentals of Fluidized Bed Chemical Processes", The Butterworths, London, 1983 6.
- 997 M. Radovanovic, "Fluidized Bed Combustion" Hemisphere Publishing Corporation Washington, USA, 1986 95.
- 998 C. Y. Wen, and Y. H. Yu, *AIChE, J.*, 1966 12 610.
- 999 H. Trawinski, "Effektive Zöhigkeit und Inhomogenität von Wirbelschichten", *Chem Ing. Techn.*, 1953 25 (5) 229.
- 1000 D. Harrison, and L. S. Leung, *Trans. Inst. Chem. Eng.*, 1961 39 409.
1001. K. Rietema, "International Symposium on Fluidization", Netherlands University Press, Amsterdam, 1967 154.
1002. J. R. Grace, J. Venta, and J. Canda, *Chem. Eng.*, 1973 15 110.
1003. P. N. Rowe, "The Delayed Bubbling of Fluidized Beds of Fine Particles", *Chem. Engng. Sci.*, Pergamon Press, 1969 24 (2) 415.
1004. J. F. Davidson, and D. Harrison, "Fluidized Particles", Cambridge University Press, 1963.
1005. R. M. Davidson, D. Harrison, R. C. Darton, and R. D. La Nauze, "In Chemical Reactor Theory", Ed. Lapidus, I, and Amundson, N. R., Chapter 10, Prentice, Hall, New York, 1977.
1006. D. Kunü, and O. Levenspiel, "Fluidization Engineering", Wiley, New York, 1969.
1007. R. C. Darton, R. D. Lanauze, J. E. Davidson, and D. Harrison, *I. Trans. Chem. Engrs.*, 1977 55 274.

1008. D. Harrison, and L. S. Leung, "Symposium on the Interaction Between Fluid and Solids", Ed. Rottenburg, P. A., (127), Institution of Chemical Engineers, 1962.
1009. J. Werther, I. Trans. Chem. Engrs., 1974 52 149.
1010. P. N. Rowe, and D. J. Everett, I. Trans. Chem. Engrs., 1972 50 42.
1011. S. P. Sit, and J. R. Grace, Chem., Engng. Sci., 1978 33 1115.
1012. K. Godard, and J. F. Richardson, "Fluidization Tripartite Chemical Engineering Conf., Montreal, 126. Institution of Chemical Engineers, London, 1968.
1013. R. J. Jottrand, Appl. Chem. London, Suppl. Issue, 2, S17, 1952.
1014. J. D. McClung, C. Kastner, R. Dellefield, and S. Sears, in Proceedings of the Twelfth International Conference on Fluidized Bed Combustion, Ed. Rubow, I. N., and Commonwealth, G., ASME, New York, 1993 1047.
1015. W. Schemenau, and C. van den Berg, in VDI Conference "Wirbelschichtfeuerungen", VDI-Berichte 1081, VDI-Verlag, Düsseldorf, 1993 19.
1016. S. G. Daves, M. Mordecai, D. Brown, and G. K. Burnard, in Proceedings of the Thirteenth International Conference on Fluidized Bed Combustion, Ed. Heinschel, K. J., ASME, New York, 1995 1275.
1017. K. Stahl, and M. Neergaard, VGB Kraftwerkstechnik, 1996 76 306.
1018. W. Adlhoeh, J. Keller, and P. K. Herbert, VGB Kraftwerkstechnik, 1992 72 345.
1019. J. M. Matsen, Chem. Eng. Prog. Symp. Series, 1970 66 (101) 47.
1020. R. D. Twoomy, and H. F. Johnstone, Chem. Engng. Prog., 1952 48 220.
1021. R. D. Twoomy, and H. F. Johnstone, Chem Engng. Sci., 1974 29 327.
1022. M. J. Lockett, J. F. Davidson, and D. Harrison, Chem. Engng. Sci., 1967 22 1059.
1023. J. R. Grace, and D. Harrison, Chem. Engng. Sci., 1969 24 497.
1024. J. R. Grace, and R. Clift, Chem. Engng. Sci., 1974 29 327.
1025. R. J. M. Kool, "Dynamic Modeling and Identification of a Coal-Fired Pressurized Fluidized Bed Combustor", Ph.D. Thesis, Delft University, The Netherlands WTHD, 1985 175.
1026. W. Prins, and W. P. N. Van Swaaij, "Fluidized Bed Combustion of a Single Carbon Particle", Twente University of Technology, Department of Chemical Engineering, The Netherlands, 1986.
1027. O. Levenspiel, "Chemical Reaction Engineering", J. Wiley, New York, 1972 360.
1028. C. Y. Wen, and M. Ishida, "Chemical Engineering Science" 1971 26 1031.
1029. A. H. Abdel Hafez, J. of Chemical Engineering Science, 1988 43 (4) 839.
1030. I. B. Ross, and J. S. Davidson, Trans. Inst. Chem. Eng., 1981 59 108.
1031. C. Y. Wen, and S. Dutta, Addison Wesley Publishing Corporation, 1978.

1032. H. M. Shafey, and L. T. Fan, , The Bulletin of Faculty of Engineering, Assiut University, Egypt, 1984 109.
1033. J. Broughton, "Fluidized Beds Combustion and Application", Applied Science Publishers, ch. 9, 1983 305.
1034. D. T. Bondarenko, and Yu. P. Nekhlebayev, "Investigation of natural-gas combustion in a fluidized-bed limestone calciner", Soviet Research, Heat Transfer, 1984 16 (2) 133.
1035. H. J. Michaels, and B. Beacham, 4th Symposium on Fluidized Combustion: Systems and Application, London, IA-4, 1980.
1036. A. S. Jammaluddin, and M. N. Islam, "Study of heat transfer in a natural gas fuel fluidized bed combustion system". Discussion on paper of Ref. 46, IV, 8, 1980.
1037. F. W. Staub, "Solids circulation in turbulent fluidized beds and heat transfer to immersed tube banks", ASME, J. of Heat Transfer, 1979 101 391.
1038. R. L. Adams, "An approximate formula for gas convection dominant heat transfer in large-particle fluidized beds", ASME, J. of Heat Transfer, 1981 103 395.
1039. R. L. Adams, "Extension of the Adams-Welty fluid bed heat transfer model to the packed bed case", ASME, J. of Heat Transfer, 1981 103 602.
1040. R. L. Adames, and J. R. Welty, "An analytical study of bubble and adjacent tube influence on heat transfer to horizontal tube in a gas fluidized bed", ASME, J. of Heat Transfer, 1982 104 206.
1041. R. L. Adams, "An approximate model of bubble phase convective heat transfer to a horizontal tube in a large particle fluid bed", ASME, J. of Heat Ttransfer, 1982 104 565.
1042. R. L. Adams, "Coupled gas convection and unsteady conduction effects in fluid bed heat transfer based on a single particle model", Int. J. Heat Mass Transfer, Pergamon Press, 1982 25 (12) 1819.
1043. J. S. M. Botterill, "Fluid Bed Heat Transfer". Academic Press. Inc., Ltd., London, 1975.
1044. R. L. Adams, "Heat transfer in large particle bubbling fluidized beds", ASME, J. of Heat Transfer, 1984 106 85.
1045. N. Decker, and L. R. Glicksman, "Heat transfer in large particle fluidized beds". Int. J. Heat transfer, Pergamon Press, 1983 26 (9) 1307.
1046. P. Chen, and D. C. T. Pei, Int. J. Heat Mass Transfer, 1985 28 (3) 375.
1047. Bo. Leckner, Prog. Energy Combust. Sci., 1998 24 31.
1048. H. M. Shafey, A. M. Abd El-Ghany, and A. M. Nassib, J. Heat Mass Transfer, 1993 36 (9) 2281.
1049. R. Donald, van der Vaart, Ind. Eng. Chem. Res., 1992 31 999.
1050. J. A. M. Kulpers, W. Prins, and W. P. M. van Swaaij, AIChE Journal, July, 1992 38 7.

1051. A. A. Fatani, and I. E. Megahd, *Energy*, 1993 18 (7) 727.
1052. Y. Flitris, and P. Hatzikonstantinou, *Computers Chem. Engng.*, 1993 17 (9) 885.
1053. A. W. Siebert, D. Highgate, and M. Newborough, *Applied Thermal Engineering*, 1999 19 37.
1054. D. Geldart, *Powder Technology*, 1972 6 201.
1055. J. R. Grace, *Canadian J. Chem. Eng.*, 1986 64 353.
1056. D. Geldart, *Gas Fluidization Technology*, John Wiley and Sons, Chichester, 1986 88.
1057. R. Hurt, J-K Sun, and M. Lunden, *Combust. Flame*, 1998 113 181.
1058. T. Beeley, J. Crelling, J. Gibbins, R. Hurt, M. Lunden, C. Man, J. Williamson, and N. Yang, *Twenty-sixth Symposium (International) on Combustion*, The Combustion Institute, Pittsburgh, 1996.
1059. D. J. McCarthy, *Fuel*, 1982 61 298.
1060. R. G. Jenkins, B. N. Nandi, and P. L. Jr Walker, *Fuel*, 1973 52 288.
1061. L. R. Radovic, P. L. Jr Walker, and R. G. Jenkins, *Fuel*, 1983 62 849.
1062. M. S. Ilic, S. N. Oka, and B. B. Vesna, *Proc. of the Mediterranean Combustion Symposium*, Antalya – Turkey, June 20-25, 1999 866.
1063. M. Dumitru, N. Scarlat, and co., *Research and experiments for the efficient utilization of wood wastes and biomass for clean energy production: Creating a database regarding the nature and volume of industrial wood wastes and biomass*, ICPET Cercetare work S4-12-97 (in Romanian).
1064. N. Rănoiu, C. Cazacu, and co, *Solid Fuel Combustion Equipment*, Ed. Tehnică, 1995 (in Romanian).
1065. L. Dragos, M. Macavescu, A. Savu, M. Gîrjoabă, *Proc. of the Mediterranean Combustion Symposium*, Antalya – Turkey, June 20-25, 1999 832.
1066. L. Dragos, M. Gîrjoabă, and C. Fluerau, *Researches for the utilization of solid wastes in CFBC boilers*, 1st South-East Symposium, *Fluidized Beds in Energy Production*, Chemical and Process Engineering and Ecology, Ohrid, 1997.
1067. A.I. Savu, L. Dragos, and co., *Experiments regarding biomass combustion on the 1 MWt pilot plant with circulating fluidized bed combustion*, ICPET Cercetare work S4-9-96 (in Romanian).
1068. A. H. Shamsuddin, and K. Sopian, "Combustion of oil palm solid wastes in fluidised bed combustor" IECEC paper, ASME, 1995 2 (160) 565.
1069. A. M. Kamsani, "Combustion of Sarawak low-quality coal in a fluidized bed boiler", Msc Thesis, Universiti Kebangsaan Malaysia, Bangi, 1995.
1070. J. S. M. Botterill, ; "Fluid Bed Heat Transfer", Academic Press, 1975.
1071. J. Kubie, *Int. J. Heat Mass Transfer*, 1985 28 (7) 1345.
1072. J. B. L. M. Campos, O. D. S. Mota, and A. M. F. R. Pinto, *Combust. Flame*, 1999 116 (105).

1073. D. Kunii, and O. Levenspiel, *Ind. Eng. Chem. Fundam.*, 1968 7 446.
1074. J. Sekely, and R. J. Fisher, "Bed to Wall Radiation Heat Transfer in a Gas-Solid Fluidized Bed", *Chem. Engng. Sci.*, Pergamon Press., 1969 24 833.
1075. A. P. Baskakov, B. V. Berg, O. K. Vitt, N. F. Filippovsky, V. A. Kirakosyan, J. M. Goldobin, and V. K. Maskaev, "Heat Transfer to Objects Immersed in Fluidized Beds", *Powder Technology*, El Sevier Sequoia S.A., Lausanne-Netherland, 1973 24 273.
1076. A. K. Kolar, N. S. Grewal, and S. C. Saxena, "Investigation of Radiative Contribution in a High Temperature Fluidized-Bed using the Alternate-Slab Model", *Int. J. Heat Mass Transfer*, 1979 22 (12) 1695.
1077. V. A. Borodulya, and V. I. Kovensky, *Int. J. Heat Mass Transfer*, 1984 26 (2) 287.
1078. K. E. Makhorin, V. S. Pikashov, and G. P. Kuchin, "Measuring Particle Temperature and Emissivity in a High Temperature Fluidized Bed, Fluidization, Cambridge University Press, 1978.
1079. T. M. Linjewile, V. S. Gururajan, and P. K. Agarwal, *Fuel*, 1993 72 813.
1080. F. Winter, M. E. Prah, and H. Hofbauer, *Combust. Flame*, 1997 108 302.
1081. J. F. Stubington, *Chem. Eng. Res. Des.*, 1985 63 241.
1082. T. Joutsenoja, J. Stenberg, and R. Hernberg, *Combust. Sci. Technol.*, 1996 121 123.
1083. T. M. Linjewile, A.S. Hull, and P. K. Agarwal, *Fuel*, 1994 73 1880.
1084. R. D. La Nauze, and R. D., and K. Jung, *Australian Coal Science Conference, Australian Institute of Energy, Adelaide*, 1988 31.
1085. V. A. Borodulya, and V. I. Kovenskü, *J. of Engng. Phys. (Inzh-Fiz. Zhu.)*, 1984 46 (2) 205.
1086. M. Q. Brewster, and C. L. Tien, "Radiative transfer in packed fluidized beds; dependent versus independent scattering", *ASME, J. of Heat Transfer*, 1982 104 573.
1087. M. Q. Brewster, "Effective absorptivity and emissivity of particulate media with application to a fluidized bed", *ASME, J. of Heat Transfer*, 1986 108 710.
1088. B. A. Andersson, and Bo. Leckner, *J. Heat and Mass Transfer*, 1992 45 (12) 3353.
1089. S. S. Zabrodsky, Yu. G. Epanov, D. M. Galershtein, S. C. Saxena, and A. K. Kolar, *Int. J. Heat Mass Transfer*, 1981 24 (4) 571.
1090. V. N. Korolev, and N. I. Syromyatnikov, "Hydrodynamics of a bed in the inter tube space of staggered and in-line tube bundles", *J. of Engng. Phys. (Inzh.-Fiz. Zhu)*, 1980 38 (5) 514.
1091. R. Chandran, J. C. Chen, and F. W. Staub, "Local heat transfer coefficients around horizontal tubes in fluidized beds", *ASME, J. of Heat Transfer*, 1980 102 152.
1092. A. Goshayeshi, J. R. Welty, R. L. Adams, and N. Alavizadeh, "Local heat

- transfer coefficients for horizontal tube arrays in high temperature large-particle fluidized beds; an experimental study", ASME, J. of Heat Transfer, 1986 108 108.
1093. N. S. Grewal, and S. G. Saxena, "Effects of surface roughness on heat transfer from horizontal immersed tubes", ASME, J. of Heat Transfer, 1979 101 397.
 1094. W. B. Krause, and A. R. Peters, "Heat transfer from horizontal serrated finned tube in a air-fluidized bed of uniformly sized particles" ASME, J. of Heat Transfer, 1983 105 (2) 319.
 1095. I. Goel, S. C. Saxena, and A. F. Dolidovich, "Heat transfer from rough and finned horizontal tubes in a gas fluidized bed", ASME, J. of Heat Transfer, 1984 106 (1) 91.
 1096. V. A. Borodulya, V. L. Ganzha, A. I. Prodberezsky, S. N. Upadhyay, and S. C. Saxena, Int. J. Heat Mass Transfer, Pergamon Press., 1983 26 (11) 1577.
 1097. S. Morooka, Y. Maruyama, K. I. Kawazulshi, S. I. Higashi, and Y. Kato, Japaneas Society Chem. Engrs., Heat Transfer, 1979 8 1.
 1098. J. M. Beér, Sixteenth Symposium on Combustion, Cambridge, Massachusetts, August, 1976.
 1099. F. M. El-Mahallawy, Z. S. Safar, and S. G. Sharobeem, Fifth International Conference of Mechanical Power Engineering, Faculty of Engineering, Ain Shams University, Cairo, 13-15 Oct. 1984.
 1100. V. P. Isachenko, V. A. Osipova, and A. S. Sukomel, "Heat Transfer" English Ed. Mir Publisher, Moscow, 1977.
 1101. W. H. Giedt, "Principles of Engineering Heat Transfer", 2nd. Ed., East-West Press. Privated Ltd. Bombay, 1967.
 1102. S. S. Zabrodsky, Int. J. Heat and Mass Transfer, 1973 16 241.
 1103. J. S. M. Botterill, "Fluidized Bed Behaviour, Fluidized Beds: Combustion and Application, Applied Science Publishers, 1983.
 1104. A. P. Baskakov, and U. M. Surpun, I.C.E., April, 1972.
 1105. J. M. Beér, B. M. Gibbs, and F. J. Periera, Fourth Symposium on Fluidized Combustion, London, 1980.
 1106. N. N. Varygin, and I. G. Mortynshin, Khim Mashinostroenie, Russian, 1959 5 6.
 1107. E. R. G. Eckert, and R. M. Drake, "Heat and Mass Transfer", 2nd Ed. McGraw-Hill, New York, 1959.
 1108. F. M. El-Mahallawy, and H. M. Mahmoud, Engineering Research Journal, Faculty of Engineering of Mataria, University of Helwan, Cairo, Egypt, 1999.
 1109. A. M. Xavier, and Davidson, "Heat Transfer to Surface Immersed in Fluidized Beds", Fluidization, Cambridge University Press, 1978.
 1110. V. S. Pikashov, S. S. Zabrodsky, K. E. Makhorin, and A. I. Ilchenko, Proceedings of the Academy of Sciences of B.S.S.R., Physical and Energetics Series, 1969 2 100.

1111. F. M. El-Mahallawy, Z. S. Safar, and M. A. Yehia, *Engng. Res. Journal, Faculty of Engineering of Mataria, Helwan University*, June, 1998 57 53.
1112. J. P. Holman, "Heat Transfer", International student edition, Mc-Graw-Hill International book company, 1981.
1113. H. M. Shafey, "Clean heat & power generation & energy saving using fluidized bed technology", F.R.C.U., 830216.
1114. A. H. Abdel-Hafez, F. M. El-Mahallawy, Z. S. Safar, and S. G. Sharobeem, *The Eighth International Conference for Mechanical Power Engineering, Alexandria University, Alexandria, Egypt, April 27-29, 1993* 3.
1115. A. H. Abdel-Hafez, F. M. El-Mahallawy, Z. S. Safar, and S. G. Sharobeem, *International Journal of Energy Research*, 1997 21.
1116. R. Clift, J. P. K. Seville, S. C. Moore, and C. Chavarie, "Comments on Buoyancy in Fluidized Bed", *Chem. Engng. Sci.*, Pergamon Press., 1987 42 (1) 191.
1117. S. G. Sharobeem, "Heat Transfer in a Gas-Fired Fluidized Bed Heat Generator", Ph. D. Thesis, Cairo University, Egypt, 1991.
1118. D. T. Wasan, and M. S. Ahluwalia, "Consecutive Film and Surface Renewal Mechanism for Heat or Mass Transfer from a Wall", *Chem. Engng. Sci.*, Pergamon Press, 1969 24 1535.
1119. S. S. Zabrodsky, *Hydrodynamics and Heat Transfer in Fluidized Beds*, the M.I.T. Press, 1966.
1120. A. A. Akhundov, "Heat and mass transfer in fluidized-bed heat treatment of granular silicate particles", *Soviet Research, Heat Transfer*, 1982 14 (3) 77.
1121. F. P. Incropera, and D. P. Dewitt, "Introduction to Heat Transfer", John Wiley and Sons, Inc. USA, 1985.
1122. M. Takeshita, *Environmental Performance of Coal Fired FBC, IEACR/75, IEA Coal Research, Londone*, 1994.
1123. B. Leekner, *International Journal of Energy Research*, 1992 16 351.
1124. M. A. Freidman, T. J. Heller, and T. J. Boyd, in *Proceeding of the Eleventh International Conference on Fluidized Bed Combustion*, Ed. Anthony, E. J., ASME New York, 1991 381.
1125. B. Leckner, M. Karlsson, M. Mjörnell, and U. J. Hagman, *Inst. Energy*, 1992 65 122.
1126. W. R. Carson, E. A. Stephens, J. M. Castleman, and J. M. Wheddon, in *Proceeding of the Twelfth International Conference on Fluidized Bed Combustion*, Ed. Rubow, I. N. and Commonwealth, G., ASME, New York, 1993 1021.
1127. R. A. Brown, and L. Muzio, in *Proceedings of the Eleventh International Conference on Fluidized Bed Combustion*, Ed. Anthony, E. J., ASME, New York, 1991 719.
1128. A. Dahl, in *Proceedings of the Twelfth International Conference on Fluidized Bed Combustion*, Ed. Rubow, I. N. and Commonwealth, G., ASME, New

- York, 1993 931.
1129. M. J. Mudd, and W. P. Reinhart, in Proceedings of the Thirteenth International Conference on Fluidized Bed Combustion, Ed. Heinschel, K. J., ASME, New York, 1995 925.
 1130. A. Lyngfelt, K. Bergqvist, F. Johnsson, I. E. Åmand, and B. Leckner, in Gas Cleaning at High Temperatures, Ed., Clift, R., and Seville, J. P. K. Blackie Academic & Professional, Glasgow, 1993 470.
 1131. A. Lyngfelt, and B. Leckner, Fuel, 1993 72 1553.
 1132. L. E. Åmand,, and B. Leckner, Fuel, 1994 73 1389.
 1133. J. P. Hämäläinen, and M. J. Aho, in Proceeding of the Sixth International Workshop on Nitrous Oxide Emissions, Ed. Hupa, M., and Matinlinna, J., ÅAU/HUT/VTT/NIRE/IFP/USEPA, Turku, 1994 601.
 1134. A. Lyngfelt, L. E. Åmand, and B. Leekner, in Proceedings of the Thirteenth International Conference on Fluidized Bed Combustion, Ed. Heinschel, K. J., ASME, New York, 1995 1049.
 1135. A. Lyngfelt, L. E. Åmand, and B. Leckner, Energy Fuels, 1995 9 386.
 1136. B. Leckner, and L. Gustavsson, J. Inst. Energy, 1991 64 176.
 1137. L. Gustavsson, and B. Leckner, Ind. Eng. Chem. Res., 1996 34 1419.
 1138. H. Hoseda, M. Harada, and T. Hiram, in Proceeding pf the Sixth International Workshop on Nitrous Oxide Emissions, Ed. Hupa, M., and Matinlinna, J., ÅAU/HUT/VTT/NIRE/IFP/USEPA, Turku, 1994 179.
 1139. M. Klein, H. Köser, and J. rosenthal, VGB-Konferenz: Chemie im Kraftwerk 1991. Vereinigung der Grosskraft-werkbetreiber Essen, also presented as abstract in Fifth International Workshop on N2O Emissions, NIRE/IFP/EPA/SCEJ, Tsukuba, 1992 223.
 1140. T. Shimizu, T. Togashi, M. Miura, E. Karahashi, T. Yamaguchi, M. Tonsyo, and M. Inagaki, in Proceeding of the Sizxth International Workshop on Nitrous Oxide Emissions, Ed. Hupa, M., and Matinlinna, J., ÅAU / HUT / VTT / NIRE / IFP / USEPA, Turku, 1994 155.
 1141. L. O. Ingesson, Fourth European Coal Utilization Conference. Industrial Presentation Group, Essen, September, 1984 1 127.
 1142. T. Shimizu, M. Miura, T. Togashi, M. Tonsho, M. Inagaki, and M. Matsukata, in Proceeding of the Thirteenth International Conference on Fluidized Bed Combustion, Ed. Heinschel, K. J., ASME, New York 1995 1083.
 1143. K. Iisa, and M. Hupa, J Inst. Energy, 1992 65 201.
 1144. K. Iisa, C. Tullin, and M. Hupa, in Proceedings of the Thirteenth International Conference on Fluidized Bed Combustion, Ed. Anthony, E. J., ASME, New York, 1995 83.
 1145. P. Yrjas, K. Iisa, and M. Hupa, Fuel, 1995 74 395.
 1146. A. Lyngfelt, and B. Leckner, Chem. Eng. Sci., 1993 48 1131.
 1147. M. Mjörnell, B. Leckner, M. Karlsson, and A. Lyngfelt, in Proceedings of the

- Eleventh International Conference on Fluidized Bed Combustion, Ed. Anthony, E. J., ASME, New York, 1991 655.
1148. E. Kakaras P. Vourliotis, P. Grammelis, and D. Vamvuka, Proc. of the Mediterranean Combustion Symposium, Antalya – Turkey, June 20-25, 1999 941.
1149. D. Boavida, P. Abelha, I. Gulyurtlu, and I. Cabrita, Proc. of the Mediterranean Combustion Symposium, Antalya – Turkey, June 20-25, 1999 928.
1150. D. Boavida, P. Abelha, I. Gulyurtlu, and I. Cabrita, Proc. of the Mediterranean Combustion Symposium, Antalya – Turkey, June 20-25, 1999 854.
1151. E. Kakaras, and P. Vourliotis, J. Inst. Energy, March, 1995 68 22.

Index

- Absorption coefficient 540
- Activation energy 32
- Adiabatic flame temperature 26
- Advanced gas re-burning 625
- Aerodynamics 424
- Aggregative fluidization 679
- Air and fuel staging 602
- Air pollutant 57
- Air pollution 55
 - air pollution standards 59
- Air quality 55
- Air staging 602
- Alcohols and phenols 11
- Aldehydes 11
- Alkanes 9
- Alkenes 10
- Alkynes 10
- Annular jet 380
- Aromatic compounds 10
- Arrhenius constant 31
- Asymmetric confined jets 402
- Auto-ignition 85
- Automobile air pollutants 62
- Avogadro's constant 28
- Bacharach soot number 534, 536
- Beam length 540
- Bed expansion 689
- Blockage ratio 294, 305-309
- Blow-off velocity 280
- Blow out 81, 283-293
- Bluff bodies 478
- Boltzmann constant 28
- Boundary velocity gradient 281
- Boilers
 - fire-tube 500, 501
 - high pressure 501
 - industrial 503
 - low pressure 501
 - water-tube 500, 502
- Bubble phase 703
- Bubble rise velocity 687
- Bubbling bed 686
- Bunsen flame 280, 334
- Burners
 - arrangement 558
 - configuration 603
 - geometry 325, 415
 - tripping 636-642
- Burning velocity correlation 199-207, 222
 - closed system 338
 - eigen value 209
 - horizontal flat flames 342
 - premixed flames 82
- Burning velocity measurements 82
 - propagation methods
 - constant explosion 84
 - double kernel 84
 - tube 84
 - stationary methods
 - cone angle 83
 - flat flame burner 83
 - opposed flame 84
 - pressure drop 84
 - total area 83
- Burnout zone 607
- Carbon burnout kinetic model 691, 693
- Central recirculation zone 286, 390
- Chain branching 30
- Chain termination 30
- Chemical equilibrium 34
- Char particles 135
- Chemical kinetics 27, 29
- Circulating fluidized-bed 138
- Clean air act 59
- Coaxial confined jets 398
- Coaxial jets 380
- Coefficient of convective heat transfer 529
- Coefficient of thermal conductivity 44
- Co-flowing jets 406
- Coherent flame model 487
- Cold models 397

- Combustion
 - aerodynamics 424
 - air swirling 380, 411, 454
 - efficiency 462
 - modeling 483
 - modification techniques 20, 88, 73, 366
 - stoichiometry 20
- Conduction constant 725
- Cone swirler 538
- Confined flames 423
- Contact time 729
- Convective heat transfer 528
- Cooling time 729
- Core-vortex 642
- Critical boundary velocity 281
- Cyclone firing 631
- Deactivation 693, 694
- Diffusion
 - forced 47
 - ordinary 47
 - thermal 47
- Diffusion coefficient 44
- Diffusion flame
 - diffusion flame length 263
 - opposed diffusion flames 268
- Diffusion method 510
- Dilution zone 451
- Disc stabilizer 293
- Discrete-ordinates method 569
- Distributor 690
- Distributor plate 714, 715
- Dry scrubbers 613
- Eddy break up model 490
- Eddy diffusivity 264, 349
- Eddy dissipation concept 276
- Effective origin 379
- Elementary reactions 29
- Elementary steps 29
- Emissions 67, 483, 597, 663, 733
 - emission control 624, 666
 - emission reduction 74, 734
 - NO_x emission
 - nitric oxide 64, 65
 - nitrogen dioxide 66
 - nitrogen oxide 609, 666, 735
 - So_x emission 66, 625
 - sulfur dioxide formation 66, 613, 667
 - sulfur trioxide formation 66, 741
- Emissive power, 552
- Emissivity 527, 551
 - gas 443
 - luminous 551
 - non-luminous 552
- Emitting medium 509
- Emulsion phase 700
- Energy sources 2
- Enthalpy 18
- Enthalpy of formation 22
- Entrainment 380, 385, 388
- Entropy 17, 19, 26
- Equilibrium 27
 - composition 38
 - constant 31, 37
 - modeling 37
 - temperature 38
- Equivalence ratio 21
- Ethane flames 108, 182
- Ethers 11
- Exchange coefficient 404
- Exothermic reaction 23
- External flue gas recirculation 598
- Extinction 269
- Fire-tube boiler 500, 501
- Flame
 - curvature 346
 - envelope 357
 - extinction pattern 252
 - height 347, 352
 - impingement 588
 - length 263
 - modeling
 - laminar flame model 86
 - turbulent flame model 272, 311, 487 - 489, 490, 490 - 497
 - stability limits 283, 287
 - stabilization
 - laminar flame 80
 - turbulent flame 283, 290, 365, 478
 - strain 253
 - stretch 253
 - structure 110, 123, 129, 145, 160, 168, 220, 250, 170
 - temperature 82
 - thickness 137
- Flame tubes
 - circular cross section
 - horizontal 531
 - vertical 545
 - elbow flame tubes 464
 - square cross section
 - horizontal 552
- Flash back 81, 283
- Flat flames 342
- Flow pattern 424
- Flue gas recirculation 68, 598, 665
- Fluidization

- aggregative 679
- heterogeneous 677
- homogeneous 677
- incipient 679
- particulate 679
- Fluidized-bed
 - packed bed 686
 - slugging bed 688
 - spouted bed 680
- Fluidized-bed combustor 676 -678
 - atmospheric 676, 709
 - bubbling bed 686, 721
 - circulating bed 676
 - deep bed 135
 - pressurized 676
 - stationary 676
- Flux and discrete ordinates method 515
- Forced diffusion 47
- Forced flow reversal 412, 460
- Forward rate coefficient 97, 99
- Forward reaction 30
- Free board 710, 711
- Free jets 378
- Fuel 7
 - additives 226
 - cell principles 14
 - cells 14
 - fuel to air velocity ratio (FAVR) 295
300
 - nitrogen 666
 - nitrogen oxide 70
 - staging 69, 602
- Furnace geometry 415
- Gas
 - constant 16
 - emissivity 543
 - radiation 514
 - reburning 69, 602
 - reburning zone 607
- Geometrical view factor 528
- Gibbs function 35
- Greenhouse warming 74
- Heat
 - flux 535, 549, 564, 566
 - flux meter 593
 - liberation 438, 440
 - liberation in flame tubes 440
 - release 473
- Heat transfer in fluidized-bed
 - distributor plate 714
 - fluidizing part 712, 725
 - free board 710, 727
 - immersed bodies 717
- Heterogeneous Fluidization 677
- High hydrocarbon fuels 212
- Hollow cone stabilizer 293
- Horizontal flame tube 531
- Horizontal flat flame 326
- Horizontal tube bundle 730
- Hydrogen flames 93
- Ideal gas 15, 16
- Ignition limits 636
- Impinging jet 590
- Incipient fluidization 679
- Inclination angle of air and fuel streams
646-648
- Integrating factor 510
- Internal convection 331
- Internal energy 26
- Internal flue gas recirculation 69, 665
- Internal recirculation 382
- Jet- like flames 301
- Jets
 - annular 380
 - coflowing 406
 - confined 387
 - asymmetric 402
 - coaxial 398
 - swirling 411
 - free 378
 - swirling 386
 - wall 381
- Jet stirred reactor 316
- Karlovitz stretch factor 336, 270
- Kinetic theory of gases 27
- Kinetics
 - of carbon monoxide 67
 - of nitrogen compounds 63
 - of sulfur dioxide 66
 - of sulfur trioxide 66
- Laminar burning velocity 114, 124, 130,
151, 157, 186, 191
- Laminar flame propagation 86
- Laminar flame stabilization 80
- Laminar flamelet model 311
- Laminar premixed flames modeling 86
 - computational method 87
 - conservation of energy 91, 92
 - conservation of total mass 88
- Laminar premixed flame kinetic
mechanisms 93
 - ethane-air 108
 - formaldehyde-oxygen- nitrogen 96
 - hydrogen-air 93
 - hydrogen-carbon monoxide 96
 - methane-air 98

- methanol-air 100
- methanol-air-water
- natural gas-air 105
- propane-air 106
- Large industrial boilers 503
- Laser Doppler Velocimetry 300
- Lean extinction limit 283-290
- Legislation of air pollution 59
- Lewis number 49, 271
- Lifted turbulent jet flames 301-302, 374
- Lift-off heights 301, 302
- Limits of flammability 22
- Liquified petroleum gas 12
- Local energy flux 510
- Low NO_x burners 69, 602
- Mass ratio 399, 400
- Mass transfer coefficient 727
- Mean beam length 514
- Methane flames 98
- Methanol flames 100
- Milne- Eddington approximation 512
- Mixing 378, 397
- Mixing in cold models 397
- Mixture fraction 399, 400, 401, 412, 431, 432, 434, 436
- Mixture strength 21
- Modeling of tangentially-fired furnaces
 - large TFF 654
 - TFF 656-663
- Molecularity of reaction 31
- Moment method 507
- Monte Carlo method 513
- Multi-jet burners 407
- Natural gas flames 12, 105, 184
- Nitrogen compounds 65, 226
- Nitric oxide (NO) 64, 65
 - fuel 70
 - prompt 69
 - thermal 68
- Nitric oxide reduction technologies
 - air-staging 602
 - flue gas recirculation 598-600
 - fuel staging 602
 - reburning 607-609
 - steam injection 601
 - water injection 601
- Nitrogen dioxide 66
- Non-stoichiometric mixtures 21
- Non-streamlined bodies 290
- Nusselt number 529, 591-593
- Oil reserves 2
- Optical thickness 509
- Over-ventilated flame 261
- Packed beds 686
- Particle characterization 685
- Particulate fluidization 679
- Percent theoretical air 22
- Pollutant 57
 - emissions reduction techniques 67
 - formation 63
 - oxidation kinetics 63
 - reduction techniques in vehicles 74
- Porous burner 241
- Post-combustion technique 71, 609, 666
- Potential parameters 94
- Power plant 504
- Prandtl number 48
- Pre-combustion 73
- Pre-exponential factor 214
- Pressure drop method 84
- Primary zone 451
- Probability density function 274
- Prompt NO 65, 69
- Propane flames 106
- Proved oil reserves 3
- Proximate analysis 695
- Radiation
 - calculations 524
 - flux and discrete ordinates method 515
 - radiation flux density 446
 - radiation intensity 508
 - radiation models 509-524
 - radiative energy 505
 - radiative flux 520
 - radiative physical constants 519
 - zonal method of analysis 522
 - annular division algorithm 539
 - Monte carlo method 513
 - spherical division algorithm 540
- Rate coefficient 31
- Rate constants 30
- Reaction kinetics 30
- Reaction mechanisms 93-108
- Reaction rate 149
- Real gas 41
- Reburning 607-609
- Recirculation zone 409, 410
 - central 452, 476, 480
 - size 409, 418
 - strength 409, 410, 450, 458
 - wall 388
- Reduced chemical kinetic models 213
- Reduced reaction mechanism 213
- Relative air- fuel ratio 22
- Residence time 734
- Reversed flow 412, 414

- Reversed flow furnace 413, 460
- Reversed mass flow rate 426, 477, 478
- Reversed reaction 30
- Rich extinction limit 283 - 290
- Richardson ratio 352
- Rotational parameters 94
- Sampling system 431, 434
- Scattering
 - anisotropic 585-587
 - isotropic 585-587
 - medium 509
- Schmidt number 48
- Scrubber
 - dry 619-622
 - wet 614-619
- Second law of thermodynamics 17
- Selective catalytic reduction 609-612, 669
- Selective non-catalytic reduction 609-611
- Similarity 77, 605
- Single and multiple tangentially- fired furnaces 632
- Slugging 688
- Solid cone stabilizer 293
- Solid fuels 13
- Soot concentration 444
- Sorbent injection technologies 73
- Source function 508
- Source term 404
- Spherical division algorithm 540
- Spherical harmonics method 513
- Square cross-section flame tube 552
- Stability
 - diffusion flames 287-290
 - premixed flames 283-287
- Stabilizer shape 291-294
- Staged combustion 69
 - air staging 602
 - fuel staging (reburning) 69
- Stationary fluidized-bed 676
- Steam boilers 500
- Steam injection 601
- Stochastic model 489
- Strain rate 314
- Stretched flame 269, 270
- Sulfur capture 744
- Sulfur reduction techniques 73
 - ordinary diffusion 47
 - theory of viscosity 44
 - thermal conductivity 46
- Sulfur dioxide techniques 66, 613
- Sulfur trioxide 66
- Swirl number 386, 387, 393
- Swirling jet 386
- Tangential-firing 629-635
- Thermal flame height 355
- Thermal NO 68
- Thermochemical calculations 22
- Three-dimensional CRFD model 490-497
- Three-dimensional division algorithm 527
- Three-dimensional modeling of TFF 656 - 663
- Tracer techniques 397
- Transport
 - parameters 92
 - phenomena 41, 44
 - properties 49
- Tube banks 700
- Tunnel burner 318
- Turbulence scales 271
- Turbulent
 - burning 270
 - burning velocity 332
 - diffusion flame
 - confined 423
 - horizontal flat 326
 - vertical free 319
 - flame models 315, 517
 - coherent flame model 487-489
 - CRFD model 490-497
 - $k-\epsilon$ model 272
 - laminar flamelet 311
 - stochastic model 489-490
 - kinetic energy 404
 - mixing 424, 430
 - vertical free flames 320
 - viscosity 272, 404
- Turbulent flame regimes 271
- Two-dimensional division algorithm 526
- Two-flux method 511, 515
- Two-phase theory 689
- Two swirling confined jets 411
- Ultimate analysis 138, 695
- Under-ventilated flame 261, 262
- Universal gas constant 28
- View factor 472, 528
- Viscosity 44
- Viscous dissipation 323, 331
- Visible flame height 360
- Wall jet 381
- Water-in-oil emulsion 536
- Water injection 601
- Wet and dry scrubbing 73, 613
- Zonal method 515, 522, 566-569

FUNDAMENTALS AND TECHNOLOGY OF COMBUSTION

F. El-Mahallawy and S. El-Din Habik

Fundamentals and Technology of Combustion is a valuable scientific and technical reference for engineers and scientists, as well as for postgraduate students in the academic community, establishing a link between principles and practical applications in the field of combustion. Containing descriptions of fundamental and combustion processes, along with an extensive survey of combustion research technology, this book takes account of mathematical combustion modelling of the processes covering premixed and diffusion flames, where many chemical and physical processes compete in complex ways for both laminar and turbulent flows.

Chapters include:

Combustion Fundamentals

Laminar Premixed Flames

Turbulent Premixed and Diffusion Flames

Characteristics of Turbulent Confined Diffusion Flames

Combustion, Heat Transfer and Emission in Boilers and Furnaces

This book is brought to you by Elsevier Energy, publisher of the world's leading collection of primary research journals and a range of complementary magazines, newsletters and books. This highly respected programme encompasses: fossil fuels, renewable energy, nuclear power, policy & economics, and electric power.

Visit the Elsevier Energy Programme online at www.energyinfo.net



elsevier energy

Cover image reproduced from *Stochworkbook*
1999, Scott and Daughters Publishing, Inc.

